Final Technical Report for ONR Award under Grant N00014-07-1-0395 MARSnet: Mission-aware Autonomous Radar Sensor Network for Future Combat Systems 12/8/06 to 12/31/09.

Qilian Liang
Department of Electrical Engineering
416 Yates Street, Room 518
University of Texas at Arlington
Arlington, TX 76019-0016
Phone: 817-272-1339; Fax: 817-272-2253
E-mail: liang@uta.edu

Abstract

This ONR award has significantly helped the PI and his research group to survive and develop. Major achievements include students training, technology transfer to DoD product, and research accomplishments. Eight Ph.D students and eight M.S. students have been supported by this ONR project. Of these 16 Ph.D/M.S. students, 4 Ph.D students and 4 M.S. students are women. In this ONR project, we have systematically studied radar sensor networks, which include sense-through-foliage target detection using FOPEN radar and radar sensor network, UWB radar for Sense-through-foliage channel modeling and foliage clutter modeling, waveform design and diversity in radar sensor networks, multi-target detection in radar sensor networks, UWB noise radar for sense-through-wall channel modeling, and compressive sensing for radar and radar sensor networks, etc. Sixty-five papers have been produced during this project and are attached to this final technical report.

Our research results on Foliage Penetration (FOPEN) radar and radar sensor networks have been transferred to US Air Force for their laser imaging through clouds product. The algorithms from this ONR project could be integrated into existing Navy and Marine Corps' radar sensor systems such as Tactical Remote Sensor System (TRSS), Joint Surveillance Target Attack Radar System (JSTARS), Tier II Pioneer Unmanned Aerial System (UAS), Expeditionary Tactical Area Surveillance Sysem (ETASS), Critical Area Protection System (CAPS), etc. The research will directly benefit DoD netcentricity based programs and concepts including Navy FORCEnet, Distributed Common Ground System (DCGS), Transparent Urban Structures (TUS) program, etc.

1 Students Training

The PI strives to create a research-intensive educational environment and establish and maintain a strong network sensing group at UT-Arlington to develop the next generation of educators, researchers, and entrepreneurs who will drive future innovation in radars, communications, and networks.

Report Documentation Page

Form Approved
OMB No. 0704-0188

Public reporting burden for the collection of information is estimated to average 1 hour per response, including the time for reviewing instructions, searching existing data sources, gathering and maintaining the data needed, and completing and reviewing the collection of information. Send comments regarding this burden estimate or any other aspect of this collection of information, including suggestions for reducing this burden, to Washington Headquarters Services, Directorate for Information Operations and Reports, 1215 Jefferson Davis Highway, Suite 1204, Arlington VA 22202-4302. Respondents should be aware that notwithstanding any other provision of law, no person shall be subject to a penalty for failing to comply with a collection of information if it does not display a currently valid OMB control number.

1. REPORT DATE	2. REPORT TYPE	3. DATES COVERED
JAN 2010	**N/A**	**-**

4. TITLE AND SUBTITLE	5a. CONTRACT NUMBER
MARSnet: Mission-aware Autonomous Radar Sensor Network for Future Combat Systems 12/8/06 to 12/31/09.	5b. GRANT NUMBER
	5c. PROGRAM ELEMENT NUMBER
6. AUTHOR(S)	5d. PROJECT NUMBER
	5e. TASK NUMBER
	5f. WORK UNIT NUMBER
7. PERFORMING ORGANIZATION NAME(S) AND ADDRESS(ES) **University of Texas at Arlington Office of Sponsored Pojects P.O. Box 19145 Arlington, TX 76019-0016**	8. PERFORMING ORGANIZATION REPORT NUMBER
9. SPONSORING/MONITORING AGENCY NAME(S) AND ADDRESS(ES) **Office of Naval Research Arlington, VA 22203-1995**	10. SPONSOR/MONITOR'S ACRONYM(S)
	11. SPONSOR/MONITOR'S REPORT NUMBER(S)

12. DISTRIBUTION/AVAILABILITY STATEMENT
Approved for public release, distribution unlimited

13. SUPPLEMENTARY NOTES
The original document contains color images.

14. ABSTRACT

15. SUBJECT TERMS

16. SECURITY CLASSIFICATION OF:			17. LIMITATION OF ABSTRACT	18. NUMBER OF PAGES	19a. NAME OF RESPONSIBLE PERSON
a. REPORT	b. ABSTRACT	c. THIS PAGE			
unclassified	**unclassified**	**unclassified**	**UU**	**816**	

Eight Ph.D students (Qingchun Ren, Haining Shu, Xinsheng Xia, Jing Liang, Emily Lei Xu, Ji Wu, Steve Iverson, and Davis Kirachaiwanich) and eight M.S. students (Rahul Sawant, Hung Ly, Hong-Sam Le, Mukta Athavale, Varsha Bolar, Siddhartha Mukkamala, Mamta Desai, Ashith Kumar) have been supported by this ONR project. Of these 16 graduate students, 4 Ph.D students and 4 M.S. students are women. Four PhD students have graduated during this project:

1. Haining Shu, PhD Dissertation: Wireless Sensor Network Lifetime Analysis and Energy Efficient Techniques, August 2007.

2. Qingchun Ren, PhD Dissertation: Medium Access Control (MAC) Layer Design and Data Query Processing for Wireless Sensor Networks, December 2007.

3. Xinsheng Xia, PhD Dissertation: Cross-Layer Design for Wireless Ad Hoc Sensor Networks, December 2007.

4. Jing Liang, Ph.D Dissertation: Radar and Non-Radar Sensor Networks, August 2009.

Besides, five M.S. students (Rahul Sawant, Hung Ly, Hong-Sam Le, Mukta Athavale, Varsha Bolar) have completed their degrees during this project. With two new PhD students (Ishrat Maherin and Julie Chen) and two new MS students (Urmi Desai and Sanil Fulani) joining us in January 2010, we have six PhD students and five M.S. students in this group.

2 Recognitions and Honors Associated with this ONR Award

During this project, the PI has received the following recognitions and honors associated with this award.

- Promoted to Associate Professor with tenure in early 2008 (Promotion and Tenure dossier submitted in Fall 2007).
- 2007 U.S. Air Force Summer Faculty Fellowship Program Award.
- 2009 U.S. Air Force Summer Faculty Fellowship Program Award.
- Lead Guest Editor, Special Issue on *Radar and Sonar Sensor Networks*, *EURASIP Journal on Wireless Communications and Networking*, 2009.

3 Technology Transition to DoD Product

A technology outcome from this ONR project, sense-through-foliage target detection using UWB radar and UWB radar sensor networks, has been transferred to AFRL/RHX for the application of wideband concepts to laser cloud penetration for the purpose of airborne imaging for Air Force. This product is being implemented in Brooks City AFB in San Antonio, TX, and will be deployed in 2011-2013 for Air Force.

Forests and buildings favor asymmetric threats because the warfighter has a limited sensing capability. Forest and buildings provide excellent concealment from observation, ambush, and escape, as well as provide secure bases for enemy Command & Control (C2), weapons caches, and Improvised Explosive Device (IED)/ Weapon of Mass Destruction (WMD) assembly. These have become "the high ground" in fourth-generation warfare, providing a significant strategic advantage.

We believe that solving the sense-through-foliage target detection will significantly benefit sense-through-wall and other subsurface sensing problems. In [42][31], we studied sense-through-foliage target detection using ultra-wideband (UWB) radars. We proposed a Discrete-Cosine-Transform (DCT)-based approach for sense-through-foliage target detection when the echo signal quality is good, and a Radar Sensor Network (RSN) and DCT-based approach when the echo signal quality is poor. A RAKE structure which can combine the echos from different cluster-members was proposed for clusterhead in the RSN. We compared our approach with the ideal case when both echos are available, i.e., echos with target and without target. We also compared our approach against the scheme in which 2-D image was created via adding voltages with the appropriate time offset as well as the matched filter-based approach. We observed that the matched filter-based couldn't work well because the UWB channel has memory. Simulation results show that our DCT-based scheme works much better than the existing approaches, and our RSN and DCT-based approach can be used for target detection successfully while even the ideal case fails to do it. Based on this study, AFRL/RHX has applied it to the application of wideband concepts to laser cloud penetration for the purpose of airborne imaging. According to the AFRL/RHX officer, Dr. Richard A. Albanese in USAF AFMC 711 HPW, the laser imaging through clouds will come to operational fruition in the coming three-five years.

This technology also has its Naval relevance. It will help Marine Corps and expeditionary war-fighters to make the forest and wall transparent. It will directly benefit Navy's Transparent Urban Structures (TUS) program. Sense-through-foliage algorithms resulting from this research could be integrated into emerging net-centric Navy and Marine Corps Command & Control and Intelligence, Surveillance, and Reconnaissance (C2 and ISR) acquisition programs through a Service Oriented Architecture (SOA).

4 Research Accomplishments

4.1 An Overview

Perhaps this is the first research project in this world that is fully dedicated to radar sensor networks. In this ONR project, we have extensively studied radar sensor networks, and have produced 65 papers, of which 20 journal papers and 25 conference papers have been published or accepted, and the other 20 papers are still in the review process. In summary, we have made significant contributions in the following aspects of radar sensor networks:

- sense-through-foliage target detection using FOPEN radar and radar sensor network [3][29][31] [36][39][42][43],
- UWB radar for Sense-through-foliage channel modeling and foliage clutter modeling [1][19][23] [40][44][62],
- waveform design and diversity in radar sensor networks [2][8][9][13][21][22][32][38][47][61][65],
- radar sensor network optimization [25][46],
- MIMO radar [22][65],
- multi-target detection in radar sensor networks [7][24][28][35][48][55],
- sensor network for threat assessment [5][11][27][35][37],

- virtual MIMO sensor networks [4][41][45][51],
- UWB sensor network optimization [6][54][57],
- energy efficiency in wireless sensor networks [12][14][16][20][52],
- resource allocation in wireless sensor networks [15][18][49][50][53],
- cross layer design for sensor networks [10][14],
- passive geolocation in electronic warfare [26][30][56][63],
- UWB noise radar for sense-through-wall channel modeling [33],
- compressive sensing for radar and radar sensor networks [58][59][60][64].

The most significant research results in each category are described in the following section. All publications are included in the Appendix.

4.2 Most Significant Research Results

4.2.1 UWB Radar Sensor Networks for Sense-through-Foliage Target Detection

In [31][42], we studied sense-through-foliage target detection using FOPEN UWB radar sensor network. We proposed a Discrete-Cosine-Transform (DCT)-based approach for sense-through-foliage target detection using a single UWB radar when the echo signal quality is good, and a Radar Sensor Network (RSN) and DCT-based approach when the echo signal quality is poor. A RAKE structure which can combine the echos from different cluster-members was proposed for clusterhead in the RSN. We compared our approach with the ideal case when both echos are available, i.e., echos with target and without target. We also compared our approach against the scheme in which 2-D image was created via adding voltages with the appropriate time offset as well as the matched filter-based approach. We observed that the matched filter-based couldnt work well because the UWB channel has memory. Simulation results show that our DCT-based scheme works much better than the existing approaches, and our RSN and DCT-based approach can be used for target detection successfully while even the ideal case fails to do it.

4.2.2 UWB Radar for Outdoor Propagation Channel Modeling in Foliage Environment

In [1], we studied the statistical modeling for outdoor non-line-of-sight (NLOS) channel in rich scattering and slowly time-varying foliage environment based on extensive data collected using both narrowband and ultra-wideband (UWB) radars. The multi-path contributions arrive at the receiver are grouped into clusters. The time of arrival of clusters can be modeled as a Poisson arrival process, while within each cluster, subsequent multipath contributions or rays also arrive according to a Poisson process. However, the parameters are quite different along with the frequency. We also observed that the amplitude of multipath channel at each path can be more accurately characterized by log-logistic distribution (LLD) other than log-normal, Weibull or Rayleigh due to the best goodness-of-fit and smallest root mean square error (RMSE).

4.2.3 Network-enabled Electronic Warfare for Target Recognition Based on Radar Sensor Networks

Network-enabled Electronic Warfare (NEW) is to develop modeling and simulation effort to explore the advantages and limitations of network-enabled electronic warfare concepts. The advantages of linking multiple electronic support measures (ESM) and electronic attack (EA) assets to achieve improved capabilities across a networked battle force have yet to be quantified. In [2], we utilized radar sensors as ESM and EA assets to demonstrate the advantages of NEW in Collaborative Automatic Target Recognition (CATR). Signal (waveform) design for Radar Sensor Networks (RSN) in NEW was studied theoretically. The conditions for waveform coexistence and the interferences among waveforms in RSN were analyzed. We applied the NEW to CATR via waveform diversity combining and proposed maximum-likelihood (ML)-ATR algorithms for non-fluctuating targets as well as fluctuating targets. Simulation results indicated that our NEW-CATR performs much better than the single sensor-based ATR algorithm for non-fluctuating targets and fluctuating targets.

4.2.4 Biologically-Inspired Target Recognition in Radar Sensor Networks

One of the great mysteries of the brain is cognitive control. How can the interactions between millions of neurons result in behavior that is coordinated and appears willful and voluntary? There is consensus that it depends on the prefrontal cortex (PFC). Many PFC areas receive converging inputs from at least two sensory modalities. Inspired by human's innate ability to process and integrate information from disparate, network-based sources, we applied human-inspired information integration mechanisms to target detection in cognitive radar sensor network [3]. Humans' information integration mechanisms have been modelled using maximum-likelihood estimation (MLE) or soft-max approaches. We applied these two algorithms to cognitive radar sensor networks target detection. Discrete-cosine-transform (DCT) was used to process the integrated data from MLE or soft-max. We applied fuzzy logic system (FLS) to automatic target detection based on the AC power values from DCT. Simulation results showed that our MLE-DCT-FLS and soft-max-DCT-FLS approaches perform very well in the radar sensor network target detection, whereas the existing 2-D construction algorithm doesn't work in this study.

4.2.5 Channel Selection in Virtual MIMO Sensor Networks

In [4], we presented two practical algorithms for selecting a subset of channels in virtual multiple-input multiple-output (MIMO) wireless sensor networks (WSNs) to balance the MIMO advantage consumption of sensor cooperation. If intracluster node-to-node multihop needs be taken into account, the maximum spanning tree searching (MASTS) algorithm, with respect to the cross-layer design, always provides a path connecting all sensors. When the WSN is organized in a manner of cluster-to-cluster multihop, the singular-value decomposition-QR with threshold (SVD-QR-T) approach selects the best subset of transmitters while keeping all receivers active. The threshold is adaptive by means of fuzzy c-means (FCM). These two approaches are compared by simulation against the case without channel selection in terms of capacity, bit error rate (BER), and multiplexing gain with water filling or equal transmission power allocation. Despite less multiplexing gain, when water filling is applied, MASTS achieves higher capacity and lower BER than virtual MIMO without channel selection at moderate-to-high signal-to-noise ratio (SNR), whereas SVD-QR-T by FCM provides the lowest BER at high SNR; in the case of no water filling and equal transmission power allocation, MASTS still offers the highest capacity at moderateto- high SNR, but SVD-QR-T

by FCM achieves the lowest BER. Both algorithms provide satisfying performances with reduced resource consumption.

4.2.6 A New Ternary Code Design for Radar Sensor Networks

Based on the zero correlation zone (ZCZ) concept, we [21] presented the definition and properties of a set of new ternary codes - ZCZ sequence-pair set (ZCZPS) and proposed a method to use the optimized punctured sequence-pair along with Hadamard matrix in the zero correlation zone in order to construct the optimized punctured ZCZ sequence-pair set (optimized punctured ZCZPS). According to property analysis, the optimized punctured ZCZPS has good autocorrelation and cross correlation properties when Doppler shift is not large. We applied it to radar target detection. The simulation results showed that the optimized punctured ZCZ sequence-pairs (optimized punctured ZCZPS) outperform other conventional pulse compression codes, such as the well known polyphase codeP4 code. We have applied our triphase coded waveform to radar sensor network. In [21], we performed some theoretical studies on coexistence and interferences of phase coded waveforms in RSN. We analyzed our ternary codes properties, especially their optimized cross correlation property of any two sequence pairs in the set. We applied our ternary codes and equal gain combination technique to target recognition and evaluated the performances versus different number of radars in RSN with Doppler shift or time delay. Simulation results showed that detection performances of RSN with our optimized punctured ZCZPS (with or without Doppler shift) are much better than those of single radar.

4.2.7 Orthogonal Pulse Compression Codes for MIMO Radar System

Inspired by recent advances in MIMO radar, in [22], we introduced orthogonal pulse compression codes to MIMO radar system in order to gain better target direction finding performance. We proposed the concept and the design methodology for the optimized triphase phase coded waveforms that is the optimized punctured Zero correlation Zone (ZCZ) sequence-Pair Set (ZCZPS). The method is to use the optimized punctured sequence-pair along with Hadamard matrix in the ZCZ. According to codes property analysis, our proposed phase coded waveforms could provide optimized autocorrelation and cross correlation properties in ZCZ. Then we presented a generalized MIMO radar system model using our proposed codes and simulate the target direction finding performance in the system. The simulation results showed that diversity gain could be obtained using our orthogonal pulse compression codes for MIMO radar system. The more antennas used, the better target direction finding performance provided.

4.2.8 Compressive Sensing in Radar Sensor Networks

Motivated by recent advances on Compressive Sensing (CS) and high data redundancy among radars in radar sensor networks, we studied CS for radar sensor networks [58]. We demonstrated that the sense-through-foliage UWB radar signals are very sparse, which means CS could be applied to radar sensor networks to tremendously reduce the sampling rate. We applied SVD-QR and maximum likelihood algorithms to CS for radar sensor networks. SVD-QR could vastly reduce the number of radar sensors, and CS is applied to the selected radar sensors for data compression. Simulations are performed and our compression ratio could be 192:1 overall.

References

[1] Jing Liang, Qilian Liang, "Outdoor Propagation Channel Modeling in Foliage Environment," accepted by *IEEE Trans on Vehicular Technology*. [Pages 12-46 in this Report]

[2] Qilian Liang, Xiuzhen Cheng, Sherwood Samn, "NEW: Network-enabled Electronic Warfare for Target Recognition," *IEEE Trans on Aerospace and Electronic Systems*, vol. 46, no. 1, Jan 2010. [Pages 47-76 in this Report]

[3] Qilian Liang, "Biologically-Inspired Target Recognition in Radar Sensor Networks," *EURASIP Journal on Wireless Communications and Networking*, Paper ID: 523435, vol. 2010. [Pages 77-102 in this Report]

[4] Jing Liang, Qilian Liang, "Channel Selection Algorithms in Virtual MIMO Wireless Sensor Networks," *IEEE Trans on Vehicular Technology.*, vol. 58, no. 3, pp. 2249-2257, June 2009. [Pages 103-111 in this Report]

[5] Qilian Liang, Xiuzhen Cheng, "KUPS: Knowledge-based Ubiquitous and Persistent Sensor networks for Threat Assessment," *IEEE Transactions on Aerospace and Electronic Systems*, vol. 44, no. 3, pp. 1060-1069, July 2008. [Pages 112-121 in this Report]

[6] Qingchun Ren, Qilian Liang, " Throughput and energy-efficiency Aware Ultra Wideband Communication in Wireless Sensor Networks: A Cross-Layer Approach," *IEEE Transactions on Mobile Computing*, vol. 7, no. 7, pp. 805-816, July 2008. [Pages 122-133 in this Report]

[7] Hung Ly, Qilian Liang, "Diversity in Radar Sensor Networks: Theoretical Analysis and Application to Target Detection," *International Journal of Wireless Information Networks*, vol. 16, no. 4, 2009. [Pages 134-141 in this Report]

[8] Lei Xu, Qilian Liang, "Optimized Punctured ZCZ Sequence-pair Set: Design, Analysis and Application to Radar System", accepted by *EURASIP Journal on Wireless Communications and Networking,* Paper ID: 254837, vol. 2010. [Pages 142-164 in this Report]

[9] Qilian Liang, "Automatic Target Recognition Using Waveform Diversity in Radar Sensor Networks", *Pattern Recognition Letters (Elsevier),* vol. 29, no. 2, pp. 377-381, 2008. [Pages 165-169 in this Report]

[10] Xinsheng Xia, Qilian Liang, "Cross-Layer Design for Mobile Ad Hoc Networks Using Interval Type-2 Fuzzy Logic Systems", *International Journal of Uncertainty, Fuzziness and Knowledge-Based Systems*, Vol. 16, no. 3, pp. 391-407, June 2008. [Pages 170-185 in this Report]

[11] Qingchun Ren, Qilian Liang, Dechang Chen, "A Fuzzy Logic-Based Secure MAC Protocol Aiming at Denial of Service (DoS) Attacks in Wireless Sensor Networks", accepted by *Information Sciences (Elsevier).* [Pages 186-205 in this Report]

[12] Haining Shu, Qilian Liang, Jean Gao, "Wireless Sensor Network Lifetime Analysis Using Interval Type-2 Fuzzy Logic Systems", *IEEE Transactions on Fuzzy Systems*, vol. 16, no. 2, pp. 416-427, April 2008. [Pages 206-217 in this Report]

[13] Qilian Liang, "Radar Sensor Networks: Algorithms for Waveform Design and Diversity with Application to ATR with Delay-Doppler Uncertainty", *EURASIP Journal on Wireless Communications and Networking*, Article ID: 89103, pp. 1-9, vol. 2007. [Pages 218-226 in this Report]

[14] Qilian Liang, Lingming Wang, Qingchun Ren, " Fault tolerant and energy efficient cross-layer design in wireless sensor networks", *International Journal on Sensor Networks*, vol. 2, no. 3/4, pp. 248-257, 2007. [Pages 227-236 in this Report]

[15] Liang Zhao, Qilian Liang, "Hop-Distance Estimation in Wireless Sensor Networks with Applications to Resources Allocation," *EURASIP Journal on Wireless Communications and Networking*, Paper ID: 84256, pp. 1-8, vol. 2007. [Pages 237-244 in this Report]

[16] Haining Shu, Qilian Liang, Jean Gao, "Distributed sensor deployment using fuzzy logic systems," *International Journal on Wireless Information Networks*, vol. 14, no. 3, pp. 163-173, 2007. [Pages 245-255 in this Report]

[17] Liang Zhao, Qilian Liang, "Energy-Efficient Self-Organization for Wireless Sensor Networks: A Fully Distributed Approach", *International Journal of Distributed Sensor Networks*, vol. 3, no. 4, pp. 347-369, 2007. [Pages 256-285 in this Report]

[18] Qingchun Ren, Qilian Liang, "Energy and quality aware query processing in wireless sensor database systems", *Information Sciences (Elsevier)*, vol. 177, no. 10, pp. 2188-2205, May 2007. [Pages 286-303 in this Report]

[19] Jing Liang, Qilian Liang, Sherwood Samn, "A Propagation Environment Modeling in Foliage," accepted by *EURASIP Journal on Wireless Communications and Networking*, Paper ID: 873070, vol. 2010. [Pages 304-334 in this Report]

[20] Xinsheng Xia, Qilian Liang, "Latency-aware and Energy Efficiency Tradeoffs for Wireless Sensor Networks," *International Journal on Sensor Networks*, vol. 5, no. 1, 2010. [Pages 335-342 in this Report]

[21] Lei Xu, Qilian Liang, "Radar Sensor Network Using A New Ternary Codes: Theory and Application," submitted to *IEEE Trans on Aerospace and Electronic Systems*. [Pages 343-374 in this Report]

[22] Lei Xu, Qilian Liang, "Orthogonal Pulse Compression Codes for MIMO Radar System", submitted to *IEEE Trans on Aerospace and Electronic Systems*. [Pages 375-402 in this Report]

[23] Qilian Liang, "Wireless Channel Modeling in Foliage Environment: UWB versus Narrowband", submitted to *IEEE Trans on Vehicular Technology*. [Pages 403-433 in this Report]

[24] Hung Ly, Qilian Liang, "Collaborative Multi-Target Detection in Radar Sensor Networks", submitted to *International Journal of Wireless Information Networks.* [Pages 434-453 in this Report]

[25] Jing Liang, Qilian Liang, "Design and Analysis of Distributed Radar Sensor Networks," submitted to *IEEE Transactions on Parallel and Distributed Systems*. [Pages 454-463 in this Report]

[26] Jing Liang, Qilian Liang, "Passive Geolocation of RF Emitters by A Netcentric Small Unmanned Aerial System," submitted to *(Wiley) Wireless Communications and Mobile Computing*. [Pages 464-485 in this Report]

[27] Qilian Liang, "Human-inspired favor weak fuzzy logic systems: theory and applications," submitted to *IEEE Trans on Systems, Man, and Cybernetics, Part b: Cybernetics*. [Pages 496-524 in this Report]

[28] Hong Sam Le, Qilian Liang, "Multi-target Identification and Classification in Cognitive Radar Sensor Networks," submitted to *International Journal of Wireless Information Networks*. [Pages 515-527 in this Report]

[29] Jing Liang, Qilian Liang, "Sense-Through-Foliage Target Detection Using UWB Radar Sensor Networks," submitted to *Pattern Recognition Letter (Elsevier)*. [Pages 528-562 in this Report]

[30] Qilian Liang, Sherwood Samn, "Passive Geolocation Based on Wireless Channel Estimation," submitted to *IEEE Trans on Aerospace and Electronic Systems*. [Pages 563-582 in this Report]

[31] Qilian Liang, "UWB Radars for Sense-through-Foliage Target Detection," submitted to *IEEE Trans on Geoscience and Remote Sensing*. [Pages 583-610 in this Report]

[32] Lei Xu, Qilian Liang, Ting Jiang, "A ternary pulse compression code: design and application to radar system," accepted by *IEEE International Conference on Acoustic, Speech, and Signal Processing (ICASSP)*, March 2010, Dallas, TX. [Pages 611-614 in this Report]

[33] Jing Liang, Qilian Liang, Sherwood Samn, Ram Narayanan, "Sense-Through-Wall Channel Modeling Using UWB Noise Radar," *IEEE Globecom, International Workshop on Multi-Gigabit MM-Wave and Tera-Hz Wireless Systems*, Nov 2009, Honolulu, Hawaii. [Pages 615-619 in this Report]

[34] Lei Xu, Qilian Liang, "A Set of Triphase Coded Waveforms: Design and Application to Radar System," *IEEE Military Communication Conference*, Oct 2009, Boston, MA. [Pages 620-626 in this Report]

[35] Hong-Sam Le, Qilian Liang, "Situation Assessment via Multi-Target Identification and Classification in Radar Sensor Networks," *IEEE Military Communication Conference*, Oct 2009, Boston, MA. [Pages 627-632 in this Report]

[36] Qilian Liang, "Biologically-Inspired Target Recognition in Radar Sensor Networks," *IEEE International Conference on Wireless Algorithms, Systems, and Applications*, August 2009, Boston, MA. [Pages 633-642 in this Report]

[37] Qilian Liang, "Situation Understanding Based on Heterogeneous Sensor Networks and Human-Inspired Favor Weak Fuzzy Logic System," *IEEE International Conference on Communications*, June 2009, Dresden, Germany. [Pages 643-647 in this Report]

[38] Lei Xu, Qilian Liang, "Radar Sensor Network Using a New Triphase Coded Waveform: Theory and Application," *IEEE International Conference on Communications*, June 2009, Dresden, Germany. [Pages 648-652 in this Report]

[39] Jing Liang, Qilian Liang, "UWB Radar Sensor Networks Detection of Targets in Foliage Using Short-Time Fourier Transform," *IEEE International Conference on Communications*, June 2009, Dresden, Germany. [Pages 653-657 in this Report]

[40] Qilian Liang, Xiuzhen Cheng, "Wireless Channel Modeling in Foliage Environment: UWB versus Narrowband," *IEEE Military Communication Conference*, November 2008, San Diego, CA. [Pages 658-663 in this Report]

[41] Jing Liang, Qilian Liang, "A Graph Theoretical Algorithm for Virtual MIMO Channel Selection in Wireless Sensor Networks," *IEEE Military Communication Conference*, November 2008, San Diego, CA. [Pages 664-669 in this Report]

[42] Qilian Liang, Sherwood Samn, Xiuzhen Cheng, "UWB Radar Sensor Networks for Sense-through-Foliage Target Detection," *IEEE International Conference on Communications*, May 2008, Beijing, China. [Pages 670-674 in this Report]

[43] Jing Liang, Qilian Liang, Sherwood Samn, "A Differential Based Approach for Sense-Through-Foliage Target Detection using UWB Radar Sensor Networks," *IEEE International Conference on Communications*, May 2008, Beijing, China. [Pages 675-679 in this Report]

[44] Jing Liang, Qilian Liang, Sherwood Samn, "Foliage Clutter Modeling Using the UWB Radar," *IEEE International Conference on Communications*, May 2008, Beijing, China. [Pages 680-684 in this Report]

[45] Jing Liang, Qilian Liang, "Channel Selection Algorithms in Virtual MIMO Sensor Networks," *ACM MobiHoc 2008, First ACM Workshop on Heterogeneous Sensor and Actor Networks*, May 2008, Hong Kong. [Pages 685-692 in this Report]

[46] Jing Liang, Qilian Liang, "Image Fusion on Radar Sensor Networks," *International Conference on Heterogeneous Networking for Quality, Reliability, Security and Robustness (Qshine)*, Workshop on Mobile Content Quality of Experience, Vancouver, Canada, August 2007. [Pages 693-696 in this Report]

[47] Qilian Liang, Sherwood Samn, "NEW-CATR: Network-enabled Electronic Warfare for Collaborative Automatic Target Recognition," *IEEE Military Communication Conference*, Oct 2007, Orlando, FL. [Pages 697-703 in this Report]

[48] Hung Ly, Qilian Liang, "Collaborative Multi-Target Detection in Radar Sensor Networks," *IEEE Military Communication Conference*, Oct 2007, Orlando, FL. [Pages 704-710 in this Report]

[49] Rahul Sawant, Qilian Liang, Dan Popa, Frank Lewis, "Experimental Path Loss Models for Wireless Sensor Networks," *IEEE Military Communication Conference*, Oct 2007, Orlando, FL. [Pages 711-717 in this Report]

[50] K. Xing, X. Cheng, L. Ma, and Q. Liang, "Superimposed Code Based Channel Assignment in Multi-Radio Multi-Channel Wireless Mesh Networkss," *ACM MobiCom 2007*, pp. 15-26, Montreal, QC, Canada, Sept 2007. [Pages 718-729 in this Report]

[51] Jing Liang, Qilian Liang, "SVD-QR-T Approach for Virtual MIMO Channel Selection in Wireless Sensor Networks," *IEEE International Conference on Wireless Algorithms, Systems, and Applications*, Chicago, IL, August 2007. [Pages 730-737 in this Report]

[52] Qingchun Ren, Qilian Liang, "Performance Analysis of Energy Detection for Cognitive Radio Wireless Networks," *IEEE International Conference on Wireless Algorithms, Systems, and Applications*, Chicago, IL, August 2007. [Pages 738-745 in this Report]

[53] Sejal Raje, Qilian Liang, "Time synchronization in network-centric sensor networks," *IEEE Radio and Wireless Symposium*, Jan 2007, Long Beach, CA. [Pages 746-749 in this Report]

[54] Lingming Wang, Qilian Liang, "UWB Sensor Networks in Hostile Environment: Interference Analysis and Performance Study," *IEEE Radio and Wireless Symposium*, Jan 2007, Long Beach, CA. [Pages 750-753 in this Report]

[55] Haining Shu, Qilian Liang, "Data Fusion in Multi-Target Radar Sensor Network," *IEEE Radio and Wireless Symposium*, Jan 2007, Long Beach, CA. [Pages 754-757 in this Report]

[56] Jing Liang, Qilian Liang, "RF Emitter Location Using A Network of Unmanned Aerial Vehicles," submitted to *IEEE 2010 International Conference on Wireless Communications, Networking and Information Security (WCNIS2010)*. [Pages 758-763 in this Report]

[57] Lingming Wang, Qilian Liang, "UWB Sensor Networks in Hostile Environment: Interference Analysis and Performance Study," *Handbook of Wireless Mesh & Sensor Networking*, McGraw-Hill International, NY, 2007. [Pages 764-782 in this Report]

[58] Qilian Liang, "Compressive Sensing in Radar Sensor Networks," submitted to *IEEE International Radar Conference*, Washington DC, May 2010. [Pages 783-786 in this Report]

[59] Ji Wu, Qilian Liang, Sherwood Samn, "Compressive sensing of sense-through-wall UWB noise radar signals," to be submitted to *IEEE Military Communications*, Washington DC, May 2010. [Pages 787-790 in this Report]

[60] Ji Wu, Qilian Liang, "An Amplitude Based Approach for Adaptive Compressive Sampling of UWB Noise Radar Signal," submitted to *IEEE International Radar Conference*, Washington DC, May 2010. [Pages 791-794 in this Report]

[61] Lei Xu, Qilian Liang, "Waveform design and optimization for radar sensor networks," to be submitted to *IEEE Globecom*, Miami, FL, Nov 2010. [Pages 795-798 in this Report]

[62] Jing Liang, Qilian Liang, "Outdoor Propagation Channel Modeling in Foliage Environment," to be submitted to *IEEE Globecom*, Miami, FL, Nov 2010. [Pages 799-804 in this Report]

[63] Qilian Liang, "TDoA Algorithm for Passive Geolocation Based on Channel Estimation," to be submitted to *IEEE Military Communications*, San Jose, CA, Oct 2010. [Pages 805-808 in this Report]

[64] Qilian Liang, Ji Wu "Sparsity and Compressive Sensing of Sense-through-Foliage Radar Signals," to be submitted to *IEEE Military Communications*, San Jose, CA, Oct 2010. [Pages 809-812 in this Report]

[65] Lei Xu, Qilian Liang, "Orthogonal Pulse Compression Codes for MIMO Radar System," submitted to *IEEE International Radar Conference*, Washington DC, May 2010. [Pages 813-816 in this Report]

Outdoor Propagation Channel Modeling in Foliage Environment

Jing Liang and Qilian Liang, *Senior Member, IEEE*

Department of Electrical Engineering

University of Texas at Arlington

E-mail: jliang@wcn.uta.edu, liang@uta.edu

Abstract

In this paper, we study the statistical modeling for outdoor non line-of-sight (NLOS) channel in rich scattering and slowly time-varying foliage environment based on extensive data collected using both narrowband and ultra-wideband (UWB) radars. The multi-path contributions arrive at the receiver are grouped into clusters. The time of arrival of clusters can be modeled as a Poisson arrival process, while within each cluster, subsequent multipath contributions or rays also arrive according to a Poisson process. However, the parameters are quite different along with the frequency. We also observe that the amplitude of multipath channel at each path can be more accurately characterized by log-logistic distribution (LLD) other than log-normal, Weibull or Rayleigh due to the best goodness-of-fit and smallest root mean square error (RMSE).

Index Terms : Channel modeling, foliage, outdoor, log-logistic, goodness-of-fit, narrowband, UWB

1 Introduction and Motivation

The performance of communications systems in foliage is confined to propagation channels. An accurate characterization model is crucial in degradation improvement for sensing-through-foliage detection, tracking and classification. The radio channels can be categorized in a number of different ways, such as narrowband versus wideband, indoor versus outdoor, etc. In the narrowband situation, the bandwidth of signals are much smaller than both the carrier frequency and the coherence bandwidth of the channel [1], therefore the multipath reflections are not easy to resolve in

the receiving signals. On the contrary, the signal bandwidth of wideband is on the order of or lager than the coherent bandwidth of the channel, and thus the multipath components in the received are resolvable. As for indoor or outdoor environment, in general, the former tends to induce higher multiple scattering and diffraction due to obstacles inside while the latter is more likely to bring on large-scale fading.

There have been many efforts undertaken to investigate propagation channels. In narrowband mobile radio channels, Rayleigh, Rician and Nakagami distributions have been commonly used for the flat fading modeling, and a narrowband model close to additive white Gaussian noise (AWGN) with strong specular interference for aeronautical telemetry [2]. [3]-[5] studied radiowave propagation in foliage using narrowband signals. For wideband channels, the Ultra-Wideband (UWB) pulse is one of the most interesting signal due to the exceptional range resolution, strong penetrating capability and low power. IEEE has standardized UWB indoor multipath channel [6] on a basis of Saleh and Valenzuela (S-V) channel model [7]. Compared to indoor situation, measurements and models are inadequate for UWB outdoor propagations. [8] has applied UWB radar-like test apparatus to obtain propagation delays, which serves as a preliminary investigation into UWB channel for rural terrain, but more extensive measurements and further analysis are absent for statistical characterization. [9] has characterized UWB channels for outdoor office environment by S-V model with modifications on the ray arrival times and amplitude statistics to fit the empirical data. However, these parameters may not fit foliage environment as trees and branches provide different scattering from that of indoor. Some experimental outdoor studies other than UWB are presented in [10]-[12]. [10] proposes that instead of Rayleigh, Weibull provides better fit to spatially and temporally extended spiking data. [11] shows that the foliage is impulsively corrupted with multipath fading, which leads to inaccuracy of the K-distribution model. [12] models the aeronautical telemetry channel gain using a complex gaussian random variable.

Foliage is a special environment goes somewhere in between indoor and outdoor cases. Like indoor environment, the foliage contains a wealth of multiple scattering owning to rough surfaces of branches and leaves, thus a dominant line-of-sight (LOS) is less likely to present. Moreover, due to the wind the movement of leaves, branches and even the tree trunks contribute to the time-varing

fading phenomenon and therefore the channel can not be as stationary as the one indoor. In such a situation, it's more accurate to apply both narrowband and ultra-wide band (UWB) radar to model the propagation channel, as we believe that foliage is composed of intervening materials that are electromagnetically dispersive, which contributes to the strong frequency dependence of propagation, and thus a narrowband-wideband study would assist with the better understanding of channel characterization. In our investigation, narrowband signals have been tried at 200 and 400 MHz respectively, while UWB radar emissions are at a relatively low frequency-typically between 100 MHz and 3 GHz. Each frequency component in a radar signal will sense the foliage in a slightly different manner, therefore provides differences in multipath pulses.

The rest of this paper is organized as follows. In Section 2, we summarize the measurement and collection of the data. In Section 3, we apply CLEAN algorithm to extract channel impulse response (CIR) for 200MHz, 400MHZ, and UWB signals. Section 4 presents the channel model in view of temporal characterization as well as statistic model comparison. We conclude our work in Section 5.

2 Measurement Setup

The foliage penetration measurement effort began in August 2005 and continued through December 2005. The measurements were taken in Holliston, Massachusetts. The data used in this paper were measured in November. The foliage is made up of both deciduous and conifer trees with higher percentage of deciduous. Generally the hight of trees are above 25 meters. Fig. 1 illustrated the largely defoliated but dense forest at this time.

The foliage experiment was constructed on a seven-ton man lift, which had a total lifting capacity of 450 kg. The limit of the lifting capacity was reached during the experiment as essentially the entire measuring apparatus was placed on the lift. Fig. 2 shows the lift. This picture was taken in September with the foliage largely still present. The lift was a 4-wheel drive diesel platform that was driven up and down a graded track 25 meters long with an experimental length of 20 meters. This track served as a strip map synthetic aperture radar track and the extra 5 meters accommodated the length of the lift. The measurement system was moved to twelve equally parted

locations named '0','2','4','5','6','8','10','12','14','16','18' and '20' on the track. At each location along the track, 35 pulses taken 3 seconds apart have been obtained for the transmitted and received signal respectively. Each sample in the pulse is spaced at 50 picoseconds interval, and 16,000 samples were collected for each pulse for a total time duration of 0.8 microseconds. The accomplished data structure is shown in Fig. 3.

The principle pieces of equipment secured on the lift under a weather shield are listed below:

- dual antenna mounting stand
- two antennas
- 200MHz, 1KW Amplifier, power supply, pre-amp
- 400MHz, 1KW Amplifier, power supply, pre-amp
- Barth pulse source (Barth Electronics, Inc. model 732 GL) for UWB
- Tektronix model 7704 B oscilloscope
- rack system
- HP signal Generator
- IBM laptop
- custom RF switch and power supply
- weather shield (small hut)

The general equipment layout is shown as a schematic in Fig. 4. A photographic side view of the equipment platform on the lift is illustrated in Fig. 5. Individual transmit and receive antennas have been used as it was believed that circulators did not exist for wideband signals in 2005. Antennas are EMCO ridged waveguide horns (Microwave Horn, EMCO 3106) over a frequency range of 200MHz to 2 GHz. An 5.486-meter (18-foot) distance between antennas was chosen to reduce the signal coupling between the transmitter and the receiver [13]. The system was pointing at the specified 91.44 meters (300 feet) one way distance. Beyond 91.44 meters (300

feet) the received signal disappeared into the noise. The transmit and receive antenna required two degrees of rotational freedom (azimuth and elevation). The antennas could be adjusted during the course of the experiment while having sufficient stability not to become misaligned during wind gusts in excess of 40 mph. The position along the track was changed and the rotation angle down range adjusted at each measurement location such that it the centerline of the RF beam made a series of parallel measurements along the track.

The preamplifiers were Henry Radio model 50B-200 and 50B-400 for 200 and 400 MHz respectively. The Henry Radio power amplifiers were TEMPO-2002A and TEMPO-2400A for 1 KW pulsed at 200 and 400MHz respectively. Each amplifier was specified at a minimum bandwidth of 2 MHz around it center frequency. The source for all of the narrow band or continuous wave signals was an Agilent 8648A signal generator. The UWB pulse generator uses a coaxial reed switch to discharge a charge line for a very fast rise time pulse outputs. The model 732 pulse generator provides pulses of less than 50 picoseconds (ps) rise time, with amplitude from 150 V to greater than 2 KV into any load impedance through a 50 ohm coaxial line. The generator is capable of producing pulses with a minimum width of 750 ps and a maximum of 1 microsecond. This output pulse width is determined by charge line length for rectangular pulses, or by capacitors for 1/e decay pulses. A Yagi antenna (Antenna Research Associates LPC-2010-C) which contained the Barth pulse was applied in transmit primarily to spread the beam of the wideband pulse. The signal output was displayed on a computer-controlled digital storage oscilloscope (Tektronix model 7704 B). Please see Fig. 6 for system schematic diagram and Fig. 7 for EMCO 3106 gain and beamwidth.

3 Channel Impulse Response Based on the Measured Data and CLEAN Algorithm

We calculated the averaged transmitted and received signals of 35 measured pulses at each location (12 locations) for 200MHz, 400MHz and UWB respectively. The transmitted and averaged received signals at location '4' for different frequencies are shown from Fig. 8 to 10. According to [14] a minimum of 9 samples are necessary to average out small-scale fading to permit the true shape

of the power decay profile (PDP) to be recovered. We believe the average of 35 samples offers satisfactory removal of both small-scale fading and noise. Note that at a different location (e.g. '0"2"6'...) the result will be slightly different. However, for simplicity and conciseness, illustration at one location is sufficient to show the essential properties.

As in foliage, the received signal is made up of distorted and time shifted pulses, the complicated multipath channel impulse response (CIR) can be modeled as follows [15]

$$r(t) \approx \sum_{n} a_n p_n(t - \tau_n) e^{j\phi_n} \tag{1}$$

where a_n, p_n and τ_n are referred to as the amplitude, unit pulse, time delay, and phase angle of the n^{th} propagation path respectively.

Generally speaking, time domain, frequency-domain and with sliding correlator are three basic techniques to characterize the channel [16]. If high-resolution channel modeling is required, a deconvolution algorithm, such as the CLEAN [17] can be used to extract the CIR. It was initially introduced in [18] to enhance radio astronomical maps of the sky, and has also been employed in both narrowband [17] and UWB [19]-[21].

The CLEAN algorithm is an iterative, high-resolution, subtractive deconvolution procedure that is capable resolving dense multipath components which are usually irresolvable by conventional inverse filtering [22]. It generates multiple taps by "cleaning" the similarities between the measurement and the template, and thus constructs a discrete CIR in time. There have been some enhanced versions of CLEAN proposed recently [15][17][23]-[25].

Our steps involved [25] are:

1. Calculate the autocorrelation of the transmitted signal $R_{ss}(t)$ and the cross-correlation of the transmitted with the received waveform $R_{sy}(t)$.

2. Find the largest correlation peak in $R_{sy}(t)$, record the normalized amplitudes α_k and the relative time delay τ_k of the correlation peak.

3. Subtract $R_{ss}(t)$ scaled by α_k from $R_{sy}(t)$ at the time delay τ_k.

4. If a stopping criterion (a minimum threshold on the peak correlation) is not met, go step 2. otherwise stop.)

The stopping criterion should be decided on a basis of noise level. Choosing the good stopping criterion is important because the deconvolution must go deep enough to be correct but CLEAN algorithms start to diverge when the noise is cleaned too deep. A good compromise is slightly below the noise level, typically 0.5σ, where σ is the standard deviation of noise. Since each CIR (12 CIR for 12 locations) we obtained is based on the 35 averaged pulses (noise has been averaged out), we searched the total number of clean components.

Given the transmission, reception and the CLEAN processing described above, the obtained CIR of location '4' are illustrated from Fig. 11 to 13. Note that we plot the absolute value of the UWB channel for the comparison between the outdoor UWB channel (Fig. 13) with the indoor S-V model [7] (Fig. 14). Generally, these figures show that

1. Compare Fig. 13 with Fig. 14, similar to the discrete channel impulse in S-V model, impulse responses in foliage arrive in clusters. There are subsequent rays within each cluster. This is also a typical phenomenon for Fig. 11 and 12. Due to the complex layout of trees, foliage is a rich scattering environment, which leads to multipath components in propagtion channels.

2. Channels are frequency dependent. It has been observed that the intervening materials, such as foliage and soil, have dielectric properties that are strongly frequency dependent. This in part explains the differences of 200MHz, 400MHz and UWB CIR .

The phase angles ϕ_n will be assumed a *priori* to be statistically independent random variables with a uniform distribution over $[0, \pi)$. We believe that this is self-evident and needs no experimental justification.

We have experimentally derived multipath propagation channels for foliage environment using 200MHz, 400MHz and UWB signals. Based on the large ensemble of CIR, a statistical model will be proposed in the next Section.

4 Outdoor Channel Modeling

4.1 Temporal Characterization

We start with the physical realization that rays obtained through CLEAN arrive in clusters, which is not consistent with a simple Poisson arrival-time model. Similar observations were found in modeling urban mobile radio channels [26]. Observe CIR at 200MHz, 400MHz and UWB for 12 locations, such as some of those given in Fig. 11 to 13, like in S-V model, the time axis of multipath contributions are divided into "bins", with the probability of a ray arriving within a given "bin". In the S-V model, the arrival of clusters is modeled as a Poisson arrival process with a rate Λ, while within each cluster, subsequent multipath contributions or rays also arrive according to a Poisson process with a rate λ (see Fig. 15). Given that 1) S-V model retains the basic features of a constant-rate Poisson arrival-time process and mutually independent path gain, 2) it appears to be extendable by adjusting its parameters to present different measured channel responses, 3) the parameter analysis is relatively simple, we model the foliage temporal properties on a basis of S-V, and therefore link up the outdoor and indoor multipath environment. Moreover, this model can be explained from a physical viewpoint, therefore making it more readily extendable to other foliage environment.

The time arrival of clusters in foliage can be modeled as a Poisson arrival process with a rate Λ. The first arriving ray of a cluster is formed by the transmitted signal following a more-or-less "direct" path to the receiver. Such a path, comprises mostly open spaces, goes through a few, but not too many, tree trunks and branches. Subsequent clusters result from reflections from farther trunks, branches and leaves. Within each cluster, subsequent multipath contributions or rays also arrive according to a Poisson process with a rate λ. These rays within a cluster are formed by multiple "weaker" reflections from tree trunks, branches, leaves and other potential animals (e.g., birds and squirrels).

We define:

- T_l = the arrival time of the first path of the l-th cluster;
- $\tau_{k,l}$ = the delay of the k-th path within the l-th cluster relative to the first path arrival time

T_l;

- Λ = the cluster arrival rate;
- λ = the ray arrival rate, i.e., the arrival rate of the paths within each cluster.

By definition, we have $\tau_{0l} = T_l$. The distributions of the cluster arrival time and the ray arrival time are given by

$$p(T_l|T_{l-1}) = \Lambda \exp\left(-\Lambda(T_l - T_{l-1}), l > 0\right)$$
$$p(\tau_{k,l}|\tau_{(k-1),l}) = \lambda \exp\left(-\lambda(\tau_{k,l} - \tau_{(k-1),l})\right), k > 0 \quad (2)$$

It is worth mentioning that clusters generally overlap. Deciding which ray belongs to a particular cluster can be difficult from time to time. Let Γ and γ denote power-delay time constants for the clusters and the rays respectively (see Fig.15). Typically, $\Gamma > \gamma$, and the expected power of the rays in a cluster decay faster than the expected power of the first ray of the next cluster. Note that if $T_l - T_{l-1}$ is large enough such that $e^{-\frac{T_l - T_{l-1}}{\gamma}} \ll e^{-\frac{T_l - T_{l-1}}{\Gamma}}$, then the lth and $(l-1)th$ cluster will appear separate. In our analysis, the cluster is determined in such a way that within each cluster, the gain of rays decay. Then we observe $\bar{T}_l$, i.e., the averaged arrival time of the first path within clusters, and $\bar{\tau}_{k,l}$, i.e., the averaged arrival rate of the paths within each cluster.

Table 1 listed the parameters of Λ and λ, which are averaged values of 12 locations for 200MHz, 400MHz and UWB impulse responses respectively. As for indoor UWB data, we refer [27]. The higher Λ and λ of UWB implies its exceptional range resolution compared to narrowband signals. Lower Λ and λ of outdoor UWB than those of indoor means indoor environment typically have a richer multiple scattering due to the effect of superstructure (such as walls, furniture, doors for indoor environment), that provides stronger reflections other than trunks, branches and leaves. Higher value of Λ and λ for clusters and rays would be expected if denser trees are present. At the same time, we believe some weak rays may appear to be miss detected due to our measurement sensitivity.

4.2 Statistical Distribution of Channel Amplitude

In the IEEE UWB indoor channel model [6], the clutter approach was adopted (same as S-V model), but a lognormal distribution was suggested for characterizing the multipath gain amplitude, and an additional log-normal variable was introduced for representing the fluctuations of the total multipath gain. In this Section we propose that log-logistic model would better characterize the multipath gain for both outdoor narrowband and UWB channels.

4.2.1 Statistic Models

Log-logistic distribution (LLD) [28] is a special case of Burr's type-XII distribution [29] as well as a special case of the kappa distribution proposed by Mielke and Jonson [30]. Lee *et al.* employed the LLD for frequency analysis of multiyear drought durations [31], whereas Shoukri *et al.* employed LLD to analyse extensive Canadian precipitation data [32], and Narda & Malik used LLD to develop a model of root growth and water uptake in wheat [33]. In spite of intensive application in precipitation and stream-flow data, so far the log-logistic distribution (LLD) statistical model has never been applied to foliage channel modeling to the best our knowledge.

This model is intended to be employed on a basis of higher kurtosis and longer tails, as well as its statistical similarity to log-normal and Weibull distributions. PDF for LLD on a basis of different of μ and σ are illustrated in Fig. 16. As we shall see that this model provides the best curve fit compared to lognormal, Weibull and Rayleigh.

Here we use the two-parameter distribution with parameters μ and σ. The PDF for this distribution is given by

$$f(x) = \frac{e^{\frac{lnx-\mu}{\sigma}}}{\sigma x(1+e^{\frac{lnx-\mu}{\sigma}})^2}, \quad x > 0,\ \sigma > 0 \tag{3}$$

where μ is scale parameter and σ is shape parameter. The mean of the the LLD is

$$E\{x\} = e^{\mu}\Gamma(1+\sigma)\Gamma(1-\sigma) \tag{4}$$

The variance is given by

$$Var\{x\} = e^{2\mu}\{\Gamma(1+2\sigma)\Gamma(1-2\sigma) - [\Gamma(1+\sigma)\Gamma(1-\sigma)]^2\} \tag{5}$$

while the moment of order k is

$$E\{x^k\} = \sigma e^{\mu} B(k\sigma, 1 - k\sigma),\ k < \frac{1}{\sigma} \tag{6}$$

where

$$B(m, n) = \int_0^1 x^{m-1}(1-x)^{n-1} dx \tag{7}$$

Similarly, the log-normal distribution [34] is a two-parameter distribution with parameters μ and σ. The PDF for this distribution is given by

$$f(x) = \frac{1}{x\sigma\sqrt{2\pi}} e^{-\frac{(lnx-\mu)^2}{2\sigma^2}},\quad x > 0, \sigma > 0 \tag{8}$$

where μ is the scale parameter and σ is the shape parameter.

The Weibull distribution, which is named after Waloddi Weibull, can be made to fit measurements that lie between the Rayleigh and log-normal distribution [35].

The Weibull distribution is also a two-parameter distribution with parameters a and b. The PDF for this distribution is given by

$$f(x) = ba^{-b}x^{b-1}e^{-(x/a)^b},\quad x > 0, a > 0,\ b > 0 \tag{9}$$

where b is the shape parameter and a is the scale parameter.

The Rayleigh distribution, whose real and imaginary components are Gaussian, has the PDF as follows:

$$f(x) = \frac{x}{b^2} e^{-\frac{x^2}{2b^2}},\quad b > 0 \tag{10}$$

If a and b are the parameters of the Weibull distribution, then the Rayleigh distribution with parameter b is equivalent to the Weibull distribution with parameters $a = \sqrt{2}b$ and $b = 2$.

4.2.2 Maximum Likelihood Estimation

On a basis of CIR amplitude from 12 different locations, we apply Maximum Likelihood Estimation (MLE) approach to estimate the parameters for log-logistic, log-normal, Weibull and Rayleigh models respectively. MLE is often used when the sample data are known and parameters of the underlying probability distribution are to be estimated [36] [37]. It is generalized as follows:

Let y_1, y_2, $\cdots$, y_N be N independent samples drawn from a random variable $\mathbf{Y}$ with m parameters θ_1, θ_2, $\cdots$, θ_m, where $\theta_i \in \theta$, then the joint PDF of y_1, y_2, $\cdots$, y_N is

$$L_N(\mathbf{Y}|\theta) = f_{Y|\theta}(y_1|\theta_1, \theta_2, \cdots, \theta_m) f_{Y|\theta}(y_2|\theta_1, \theta_2, \cdots, \theta_m) \cdots f_{Y|\theta}(y_n|\theta_1, \theta_2, \cdots, \theta_m) \tag{11}$$

When expressed as the conditional function of $\mathbf{Y}$ depends on the parameter θ, the likelihood function is

$$L_N(\mathbf{Y}|\theta) = \prod_{k=1}^{N} f_{Y|\theta}(y_k|\theta_1, \theta_2, \cdots, \theta_m) \tag{12}$$

The maximum likelihood estimate of θ_1, θ_2, $\cdots$, θ_m is the set of values $\hat{\theta}_1$, $\hat{\theta}_2$, $\cdots$, $\hat{\theta}_m$ that maximize the likelihood function $L_N(\mathbf{Y}|\theta)$.

As the logarithmic function is monotonically increasing, maximizing $L_N(\mathbf{Y}|\theta)$ is equivalent to maximizing $\ln(L_N(\mathbf{Y}|\theta))$. Hence, it can be shown that a necessary but not sufficient condition to obtain the ML estimate $\hat{\theta}$ is to solve the likelihood equation

$$\frac{\partial}{\partial \theta} \ln(L_N(\mathbf{Y}|\theta)) = 0 \tag{13}$$

We obtain $\hat{\mu}$ and $\hat{\sigma}$ for log-logistic, $\hat{\mu}$ and $\hat{\sigma}$ for log-normal, $\hat{a}$ and $\hat{b}$ for weibull and $\hat{b}$ for Rayleigh respectively, which are shown in Table 2. We also explore the standard deviation (STD) error of each parameter. These descriptions are also shown in Table 2 in the form of ε_x, where x denotes different parameter for each model. It is obvious that log-logistic model provides smaller STD errors than those of log-normal.

4.2.3 Goodness-of-fit in curve and RMSE

We may also observe that to what extend does the PDF curve of the statistic model match that of CIR amplitude by root mean square error (RMSE). Let i (i=$1, 2, \cdots, n$) be the sample index of CIR amplitude, c_i is the corresponding PDF value whereas $\hat{c}_i$ is the PDF value of the statistical model with estimated parameters by means of MSE. RMSE is obtained through

$$\texttt{RMSE} = \sqrt{\frac{1}{n}\sum_{i=1}^{n}(c_i - \hat{c}_i)^2} \tag{14}$$

where n is the sample index. The RMSE for 200MHz, 400Hz and UWB have been listed in Table 3. It demonstrates that LLD turns out to be the model that fits the channel data best.

One may also draw the above conclusion from the Fig. 17 and 18, which describe the the goodness-of-fit by curves. In Fig. 17, the absolute gains of all our resolved paths have been plotted in terms of histogram. It can be easily seen that Rayleigh model provides the worst goodness-of-fit compared to LLD, log-normal and Weibull. Also, Weibull is not a good choice due to the inaccurate kurtosis and high tails. Compare LLD with log-normal, it is obvious that LLD is able to provide higher kurtosis, sharper slope, and lower tail. In other word, LLD provides generally better goodness-of-fit than that of log-normal. Fig. 18 uses cumulated statistical methodology to show the general better goodness-of-fit provided by LLD model.

The above investigations show that LLD can better characterize the amplitude of outdoor multipath impulse responses other than log-normal, Weibull and Rayleigh models for both narrowband and UWB cases.

5 Conclusions and Future Work

This paper presented propagation measurement results of 200MHz, 400MHz and UWB signals in Holliston foliage in November with largely defoliated but dense forest. Like indoor environment, foliage contains a wealth of multiple scattering owning to rough surfaces of trunks, branches and leaves. CLEAN algorithm was used to resolve dense multipath components which were usually irresolvable by conventional inverse filtering.

We came to following conclusions: 1) foliage non line-of-sight (NLOS) channels are generally frequent dependent, which is illustrated by different temporal and amplitude properties of channel impulse response (CIR) based on three measurement frequencies. This is due to the fact that foliage is made up of intervening materials that have dielectric properties associated with frequencies. 2) The temporal characterizations of CIR for both narrowband and UWB are similar to those of S-V model for indoor environment. Therefore we model the time arrival of clusters as a Poisson process with a rate Λ and subsequent multipath contributions using another Poisson process with a rate λ. The analysis result of Λ and λ are shown in Table 1. The capability of multipath resolution

(from high to low) is that $UWB > 200MHz > 400MHz$, and indoor environment typically has a richer multiple scattering than that of outdoor. 3) The amplitude of multipath channels can be more accurately characterized by log-logistic distribution (LLD) other than log-normal, Weibull or Rayleigh. We apply maximum likelihood estimation (MLE) approach to estimate the parameters for those models based on CIR amplitude. Table 2 and 3 show that LLD provides smaller STD errors and root-mean-square-error (RMSE). Additionally, the better fit provided by LLD is visually shown in Fig. 17 and 18. Our model is extendable by adjusting temporal and LLD parameters to represent the channels within the same foliage at different season or other foliage environment. This model can be easily used in simulation and analysis for planning wireless networks, designing fixed terrestrial and satellite communication services.

The channels discussed in this paper are very slowly time varying. At each location, 35 pulses were taken 3 seconds apart, having roughly 0.9 correlation coefficient at each location. Generally, foliage are time varying from time to time because of changes with the seasons or due to movement on windy days. For future work, we may collect extensive data to explore the time varying nature of foliage propagation channels.

Acknowledgement

This work was supported in part by the Office of Naval Research (ONR) Grant N00014-07-1-0395, N00014-07-1-1024, N00014-03-1-0466, and National Science Foundation (NSF) under Grant CNS-0721515.

References

[1] J. G . Proakis, *Digital Communications*, 4th ed., New York: McGraw-Hill, 2001.

[2] M. Rice, R. Dye and K. Welling, "Narrowband Channel Model for Aeronautical Telemetry", *IEEE Transactions on Aerospaace and Electronic Systems*, vol. 36, pp. 1371-1377, Otc. 2000.

[3] T. Fernandes, R. Caldeirinha et. al., "A Discrete RET model for Millimeter-Wave Propagation in Isolated Tree Formations", *IEICE Transactions on Communications*, vol. E88-B, pp. 2411 - 2418, June, 2005.

[4] R. F. S. Caldeirinha, "Radio Charaterisation of Single Trees at micro- and millimetre wave frequencies", Phd Thesis, University of Glamorgan, United Kingdom, April 2001.

[5] Neil C. Rogers, A. Seville, J. Richter, D. Ndzi, R. Caldeirinha, A. Shukla, M. Al-Nuaimi, K. Craig, and J. Austin, "A generic model of 1-60GHz radio propagation trough vegetation - Final report", *Tech. Rep., Radiocommunications Agency*, May 2002.

[6] IEEE 802.15.SG3a, "Channel modeling sub-committee report final", *IEEE P802.15-02/490r1-SG3a*, Feb. 2003.

[7] A. A. Saleh and R. A. Valenzuela, "A statistical model for indoor multipath propagation", *IEEE Journal on Selected Areas in Communications*, vol. 5, no.2, pp. 128-137, Feb. 1987.

[8] M. Z. Win, F. Ramírez-Mireles, R. A. Scholtz and M. A. Barnes, "Ultra-Wide Bandwidth (UWB) signal propagation for outdoor wireless communications", *Proc. of VTC 1997*, vol. 1, pp. 251-255, May 1997.

[9] C. W. Kim, X. Sun, L. C. Chiam, B. Kannan, F. P. S. Chin and H. K. Garg, "Characterization of ultra-wideband channels for outdoor office environment", *IEEE Wireless Communications and Networking Conference*, vol. 2, pp. 950-955, Mar. 2005.

[10] F. L. Posner , "Spiky sea clutter at high range resolutions and very low grazing angles", *IEEE Transactions on Aerospace and Electronic Systems*, vol. 38, pp. 58-73, Jan. 2002.

[11] Watts, S., "Radar detection prediction in K-distribution sea clutter and thermal noise", *IEEE Transactions on Aerospace and Electronic Systems*, AES-23, pp. 40-45, Jan 1987.

[12] M. Rice, A. Davis and C. Bettweiser, "Wideband Channel Model for Aeronautical Telemetry", *IEEE Transactions on Aerospace and Electronic Systems*, vol. 40, pp. 57-69, Jan. 2004.

[13] J. A. Henning, "Design and Performance of An Ultra-Wideband Foliage Penetrating Noise Radar", Masters Thesis, University of Nebraska, May 2001.

[14] C. W. Kim, X. Sun, L. C. Chiam, B. Kannan, F. P. S. Chin and H. K. Garg, "Characterization of ultra-wideband channels for outdoor office environment"in *Proc. IEEE WCNC, 13-17*, March 2005, pp. 950-955.

[15] R. J. -M. Cramer, R. A. Scholtz and M. Z. Win, "Evaluation of an ultra-wide-band propagation channel", *IEEE Transactions on Antennas and Propagation*, vol. 50, pp. 561 - 570, May 2002.

[16] T. S. Rappaport, *Wireless Communications: Principles and Practice*, 2nd ed., Upper Saddle River, NJ: Prentice-Hall, 2002.

[17] R. G. Vaughan and N. L. Scott, "Super-resolution of pulsed multipath channels for deplay spread characterization", *IEEE Transactions on Wireless Communications*, vol. 47, pp. 343-347, Mar. 1999.

[18] J. A. Högbom, "Aperture Synthesis with a non-regular distribution of interferometer baselines", *Astronomy and Astrophysics Supplement Ser.*, vol. 15, pp. 417-426, 1974.

[19] P. C. Richardson, W. Xiang and W. Stark, "Modeling of ultra-wideband channels within vehicles", *IEEE Journal on selected areas in communications*, vol. 24, pp. 906-912, Apr. 2006.

[20] B. M. Donlan, D. R. McKinstry, R. M. Buehre, "The UWB indoor channel: large and small scale modeling", *IEEE Transactions on Wireless Communications*, vol. 5, pp. 2863-2873, Oct. 2006.

[21] W. Yang and Z. Naitong, "A new multi-template CLEAN algorithm for UWB channel impulse response characterization", in *Proc. Int. Conf. Coommun. Technol.*, Nov. 2006, pp. 1-4.

[22] A. F. Molisch, "Ultrawideband propagtion channels: Theory, measurement and modeling", *IEEE Transactions on Vehicular Technology*, vol. 54, Sept. 2005, pp. 1528-1545.

[23] S. M. Yano, "Investigating the ultra-wideband indoor wireless channel", in *Proc. 55th IEEE Veh, Technol. Spring Conf.*, vol. 3, pp. 1200-1204, May 2002.

[24] Z. Irahhauten, G. J. M. Janssen, H. Nikookar, A. Yarovoy, and L. P. Ligthart, "UWB Channel Measurements and Results for Office and Industrial Environments", in *Proc. IEEE 2006 International Conference on Ultra-Wideband*, pp. 225-230, Sept, 2006.

[25] J. H. Reed, *An introduction to Ultra Wideband Communication Systems*, Prentice Hall, 2005.

[26] G. L. Turin, F. D. Clapp, T. L. Johnston, S. B. Fine, and D. Lavry, "A statistical model of urban multipath propagation", *IEEE Transactions on Vehicular Technology*, vol. VT-21, pp. 1-9, Feb. 1972.

[27] M. -G. Di Benedetto and G. Giancola, *Understanding ultra wideband Radio Fundamentals*, Prentice Hall, 2004.

[28] R. C. Gupta, O. Akman and S. Lvin, "A Study of Log-Logistic Model in Survival Analysis", *Biometrical Journal*, 41, pp. 431-443, 1999.

[29] I. W. Burr, "Cumulative frequency functions", *Ann. Math. Statist.*, 13, 215-232, 1942.

[30] P. W. Mielke, and E. S. Johnson, "Three-parameter kappa distribution maximum likelihood estimates and likelihood ratio tests", *Monthly Weather Rev.*, 101, 701-709, 1973.

[31] K. S. Lee, J. Sadeghipour and J. A. Dracup, "An approach for frequency analysis of multiyear dought duration", *Wat. Resour. Res.* 22(5), 655-662, 1986.

[32] M. M. Shoukri, I. U. H. Mian, and D. S. Tracy, " Sampling properties of estimators of the log-logistic distribution with application to Canadian precipitation data", *Can. J. Statist.* 16(3), 223-236, 1988.

[33] N. K. Narda and R. K. Malik, "Dynamic model of root growth and water uptake in wheat", *Indian J. Agric. Engng* 3(3&4), 147-155, 1993.

[34] E. Limpert, W. Stahel and M. Abbt, "Log-normal Distributions across the Sciences: Keys and Clues", *BioScience*, 51 (5), pp. 341C352, 2001.

[35] W. Weibull, "A statistical distribution function of wide applicability", J. Appl. Mech.-Trans. ASME 18(3), 293-297, 1951.

[36] Devore, *Probability and Statistics for Engineering and the Sciences*, Monterey, CA: Brooksi-Cole, 1982.

[37] M. Barkat, *Signal deteciton and estimation*, 2nd, London: Artech house, 2005.

List of Tables

1 Temporal Parameters for Channel Models 19

2 Estimated Parameters for Statistic Model 19

3 Root Mean Square Error (RMSE) Comparison between Statistic Models 19

Table 1: Temporal Parameters for Channel Models

Scenario	$\Lambda(1/ns)$	$\lambda(1/ns)$
200MHz	0.012	0.4
400MHz	0.004	0.128
Outdoor UWB	0.04	0.8
Indoor UWB Extreme NLOS	0.0667	2.1

Table 2: Estimated Parameters for Statistic Model

PDF	Log-Logistic	Log-normal	Weibull	Rayleigh
200MHz	$\hat{\mu} = -3.79907$ $\hat{\sigma} = 0.43948$ $\varepsilon_\mu = 0.0517626$ $\varepsilon_\sigma = 0.0250518$	$\hat{\mu} = -3.69473$ $\hat{\sigma} = 0.811659$ $\varepsilon_\mu = 0.0550099$ $\varepsilon_\sigma = 0.0390963$	$\hat{a} = 0.0388139$ $\hat{b} = 1.00543$ $\varepsilon_a = 0.0027934$ $\varepsilon_b = 0.00456447$	$\hat{b}$=0.0474046
400MHz	$\hat{\mu} = -3.75666$ $\hat{\sigma} = 0.482505$ $\varepsilon_\mu = 0.071783$ $\varepsilon_\sigma = 0.035901$	$\hat{\mu} = -3.61265$ $\hat{\sigma} = 0.917049$ $\varepsilon_\mu = 0.0795182$ $\varepsilon_\sigma = 0.0565477$	$\hat{a} = 0.0447926$ $\hat{b} = 0.903163$ $\varepsilon_a = 0.00458706$ $\varepsilon_b = 0.0536079$	$\hat{b}$=0.0609159
Outdoor UWB	$\hat{\mu} = -3.30616$ $\hat{\sigma} = 0.590192$ $\varepsilon_\mu = 0.202988$ $\varepsilon_\sigma = 0.101636$	$\hat{\mu} = -3.13344$ $\hat{\sigma} = 1.12623$ $\varepsilon_\mu = 0.225245$ $\varepsilon_\sigma = 0.164277$	$\hat{a} = 0.080002$ $\hat{b} = 0.765597$ $\varepsilon_a = 0.0222858$ $\varepsilon_b = 0.106023$	$\hat{b}$=0.141188

Table 3: Root Mean Square Error (RMSE) Comparison between Statistic Models

PDF	Log-Logistic	Log-normal	Weibull	Rayleigh
200MHz	5.7016	6.2850	8.8810	9.7562
400MHz	5.9023	6.5635	9.7056	10.3359
UWB	2.1867	2.4756	3.0136	4.8975

List of Figures

1 Foliage environment in November 20

2 This figure shows the lift with the experiment. The antennas are at the far end of the lift from the viewer under the roof that was built to shield the equipment from the elements. This picture was taken in September with the foliage largely still present. The cables coming from the lift are a ground cable to an earth ground and one of 4 tethers used in windy conditions. 21

3 Measured data file structure. '0' - '20' are 12 equally parted locations with an experimental length of 20 meters. At each location, 35 pulses of 200MHz, 400MHz and UWB signals are measured respectively. 21

4 Antenna layout 22

5 The experiment on top of the lift under the hut built for weather protection. The black box in the foreground is a weather resistant box that held the oscilloscope and Barth pulser during the testing. 22

6 System schematic diagram 23

7 EMCO 3106 technical data (a) gain (b) half power beamwidth 24

8 Measurement of 200MHz and 35 pulses average : (a) transmitted pulse (b) received echoes 25

9 Measurement of 400MHz and 35 pulses average: (a) transmitted pulse (b) received echoes 26

10 Measurement of UWB and 35 pulses average: (a)transmitted pulse (b) received echoes 27

11 200MHz channel impulse response by CLEAN from 35-pulse averaged transmitting and receiving signals 28

12 400MHz channel impulse response by CLEAN from 35-pulse averaged transmitting and receiving signals 28

13 UWB channel impulse response by CLEAN from 35-pulse averaged transmitting and receiving signals 29

14 An illustration of the channel impulse in S-V model. 29

15 An illustration of the double exponential decay of the cluster power profile and the ray power profile within clusters in S-V model. 30
16 An illustration of log-logistic probability density function. 30
17 Goodness-of-fit illustration by density (a)CIR for 200MHz (b)CIR for 400MHz (c)CIR for UWB 31
18 Goodness-of-fit illustration by cumulated probability (a)CIR for 200MHz (b)CIR for 400MHz (c)CIR for UWB 32



Figure 1: Foliage environment in November



Figure 2: This figure shows the lift with the experiment. The antennas are at the far end of the lift from the viewer under the roof that was built to shield the equipment from the elements. This picture was taken in September with the foliage largely still present. The cables coming from the lift are a ground cable to an earth ground and one of 4 tethers used in windy conditions.

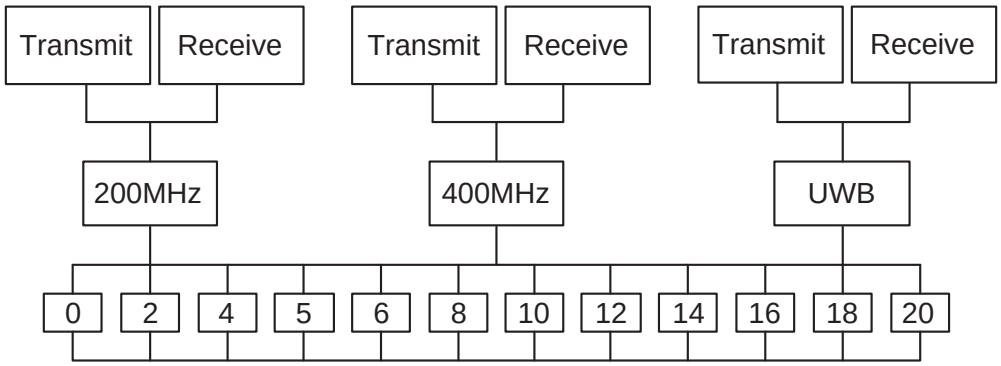


Figure 3: Measured data file structure. '0' - '20' are 12 equally parted locations with an experimental length of 20 meters. At each location, 35 pulses of 200MHz, 400MHz and UWB signals are measured respectively.

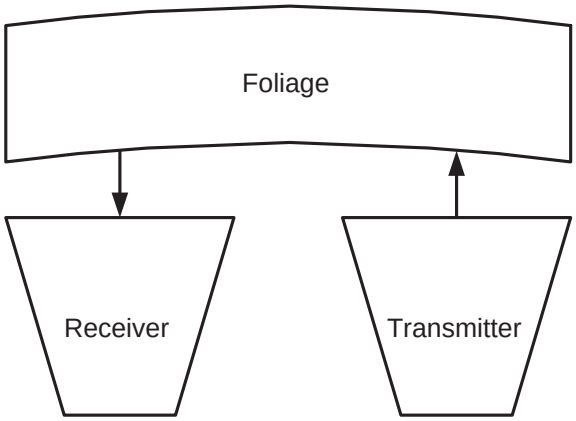


Figure 4: Antenna layout



Figure 5: The experiment on top of the lift under the hut built for weather protection. The black box in the foreground is a weather resistant box that held the oscilloscope and Barth pulser during the testing.

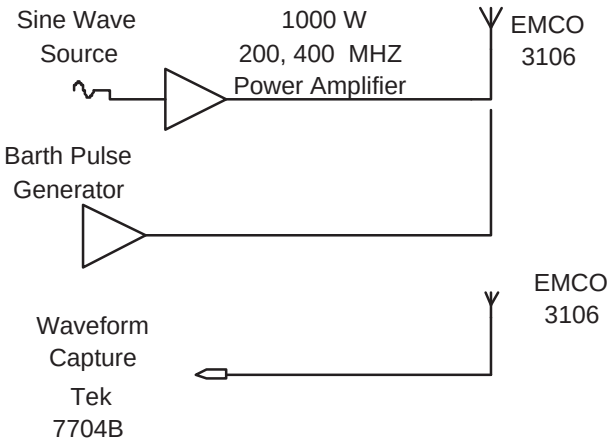
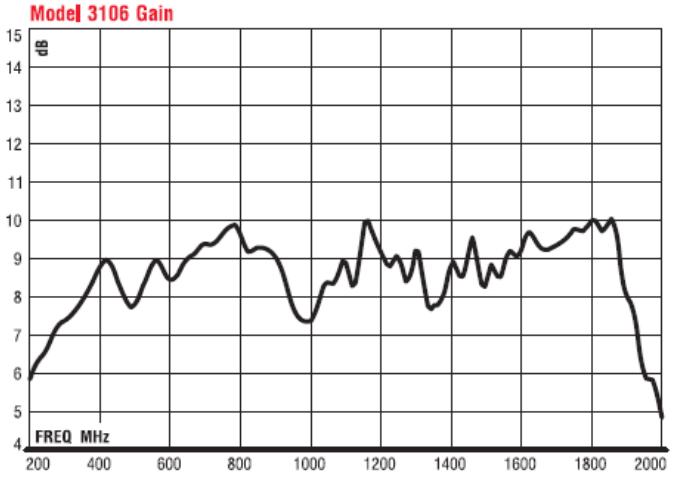
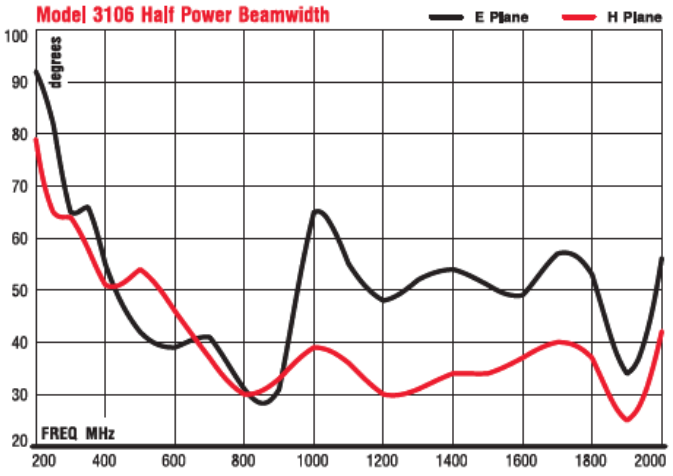


Figure 6: System schematic diagram

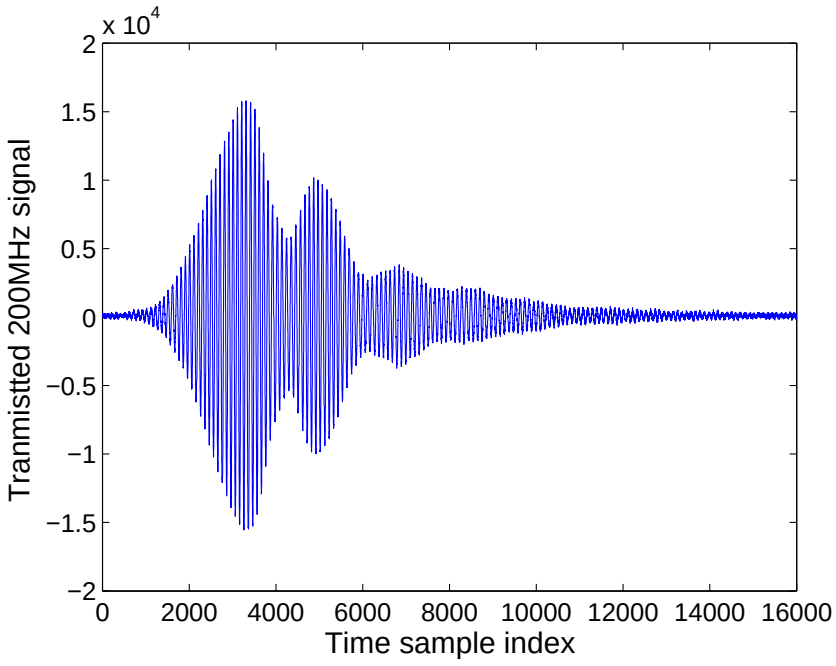


(a)

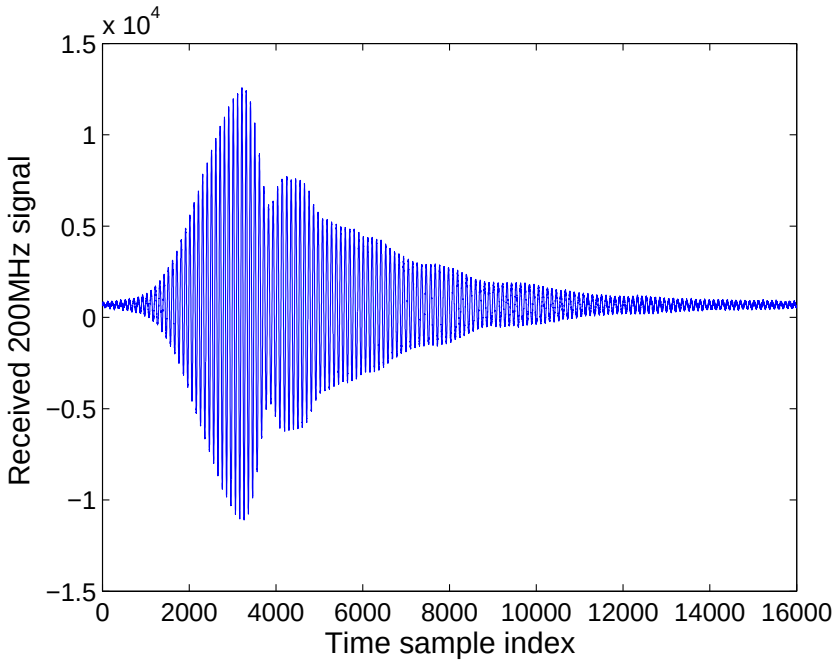


(b)

Figure 7: EMCO 3106 technical data (a) gain (b) half power beamwidth

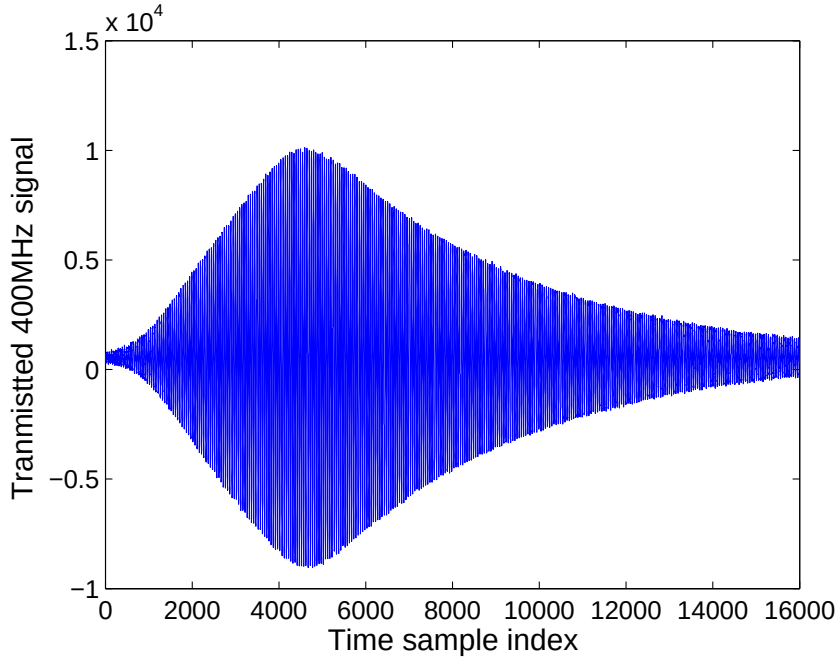


(a)

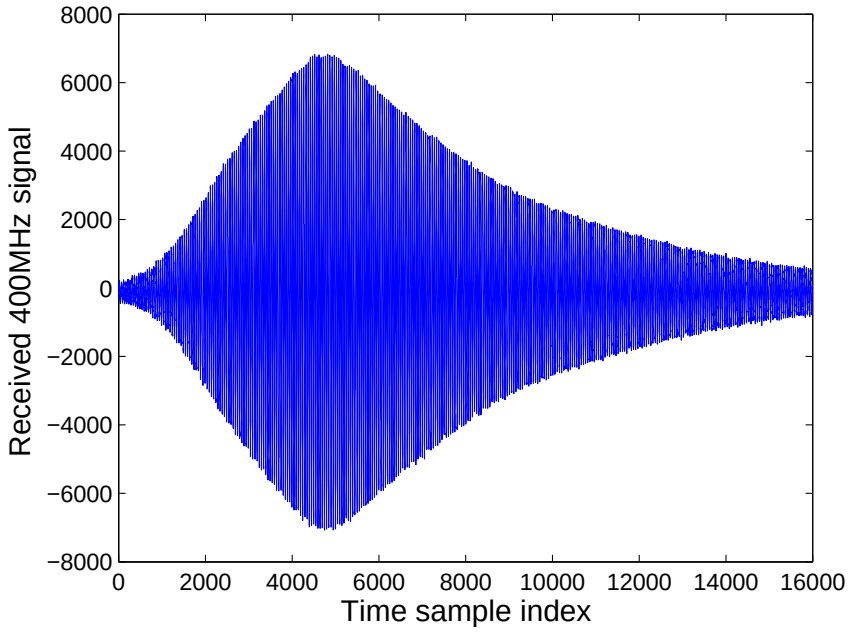


(b)

Figure 8: Measurement of 200MHz and 35 pulses average : (a) transmitted pulse (b) received echoes

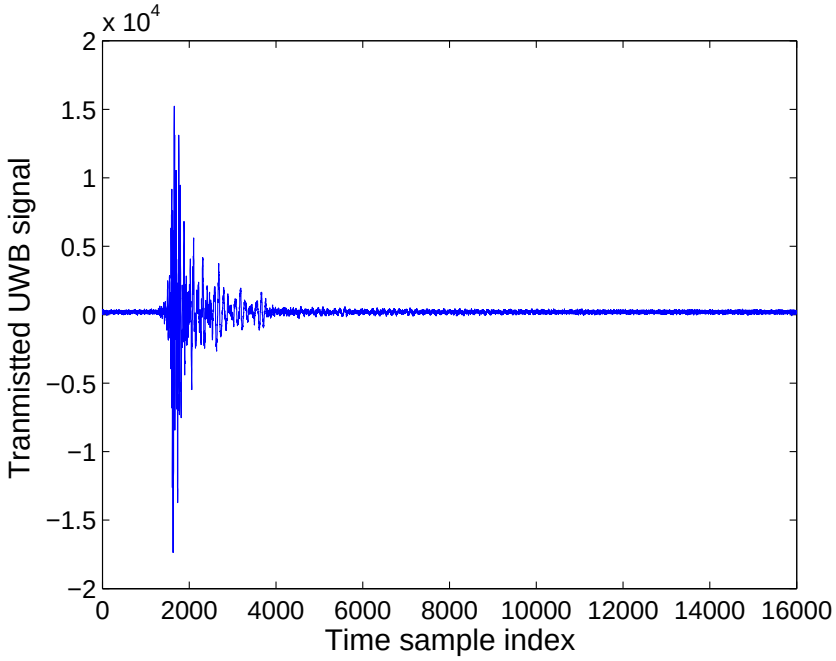


(a)

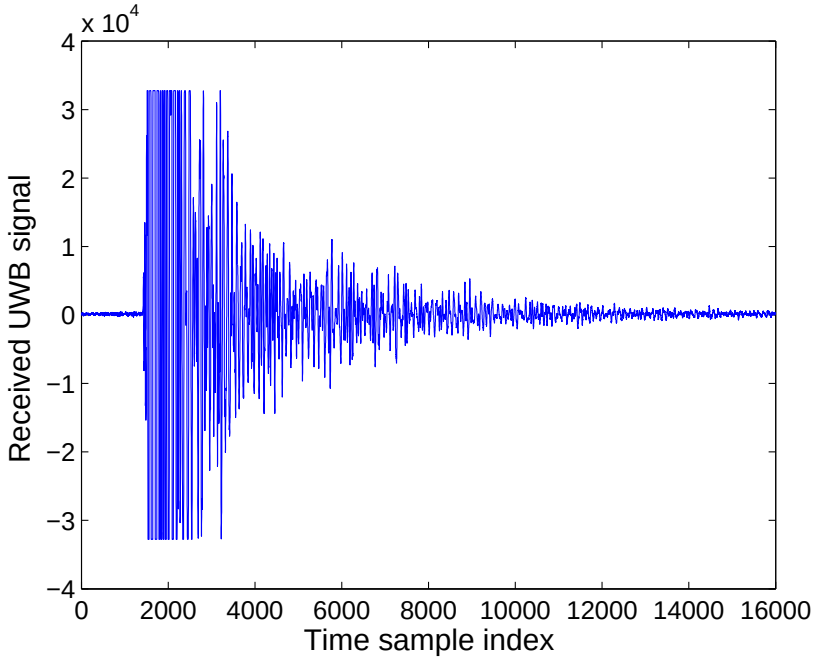


(b)

Figure 9: Measurement of 400MHz and 35 pulses average: (a) transmitted pulse (b) received echoes



(a)



(b)

Figure 10: Measurement of UWB and 35 pulses average: (a)transmitted pulse (b) received echoes

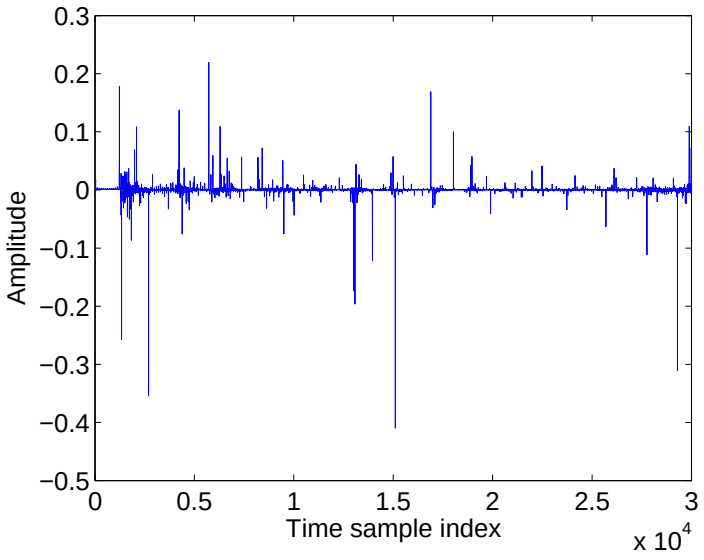


Figure 11: 200MHz channel impulse response by CLEAN from 35-pulse averaged transmitting and receiving signals

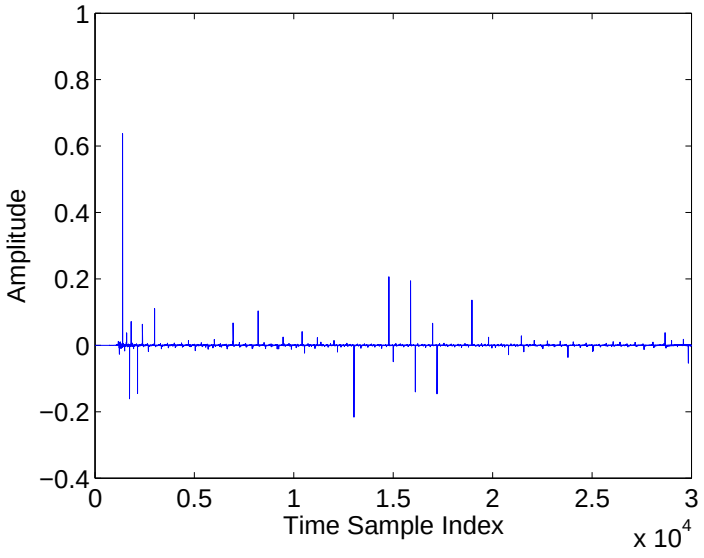


Figure 12: 400MHz channel impulse response by CLEAN from 35-pulse averaged transmitting and receiving signals

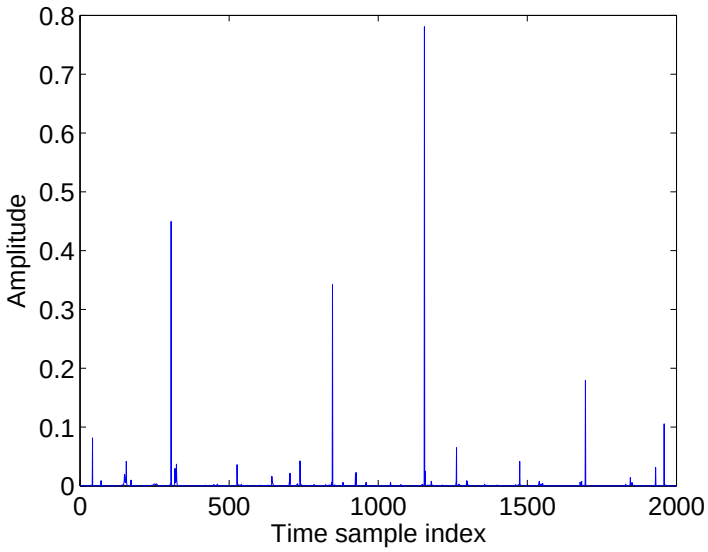


Figure 13: UWB channel impulse response by CLEAN from 35-pulse averaged transmitting and receiving signals

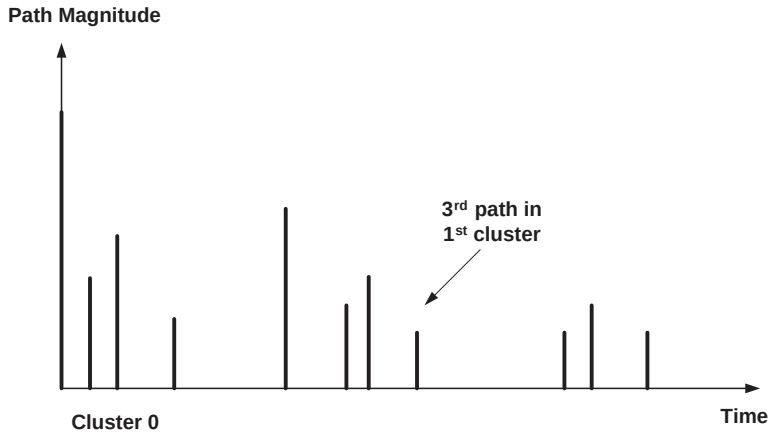


Figure 14: An illustration of the channel impulse in S-V model.

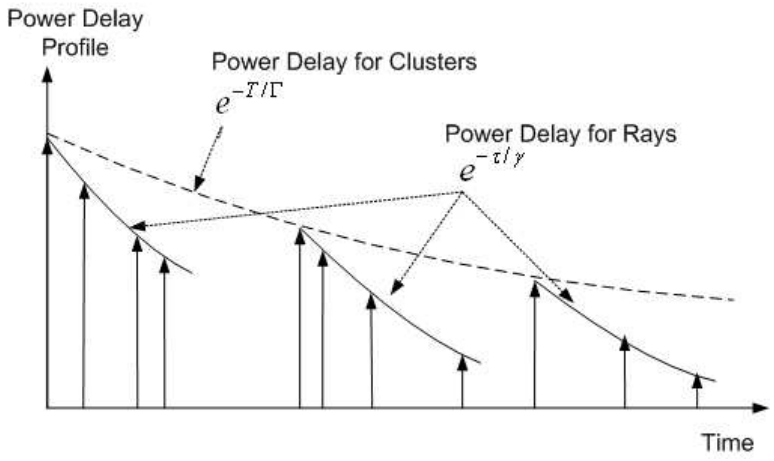


Figure 15: An illustration of the double exponential decay of the cluster power profile and the ray power profile within clusters in S-V model.

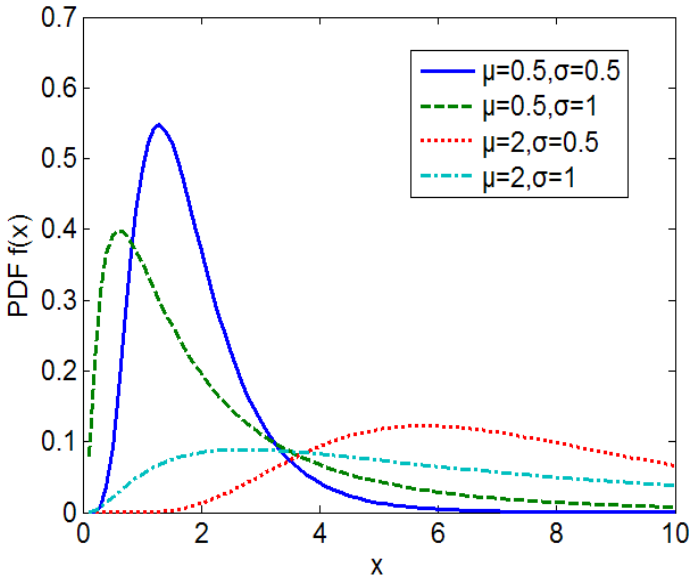
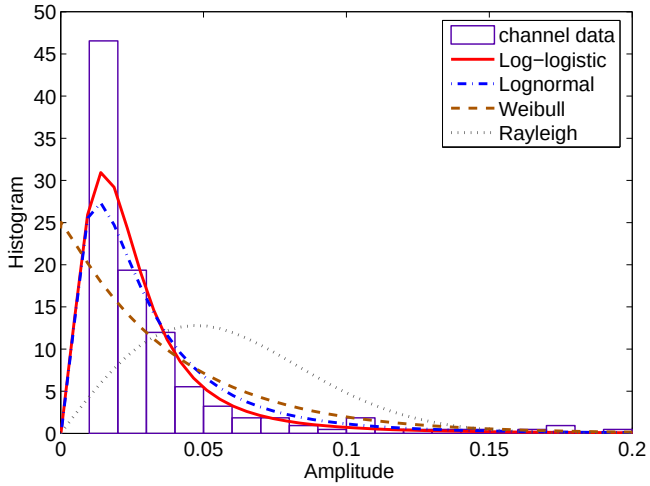
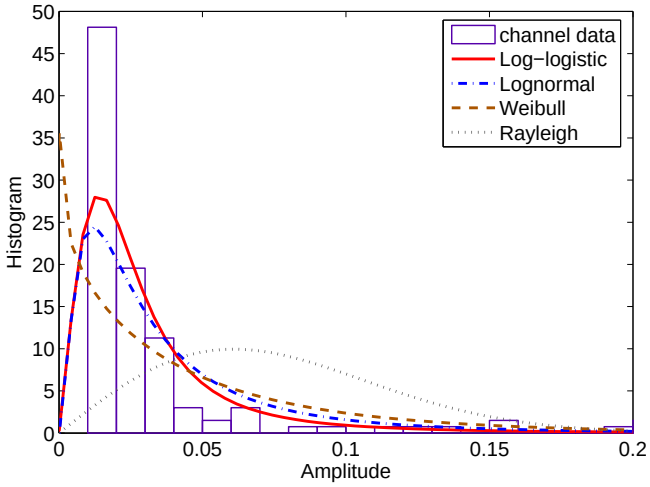


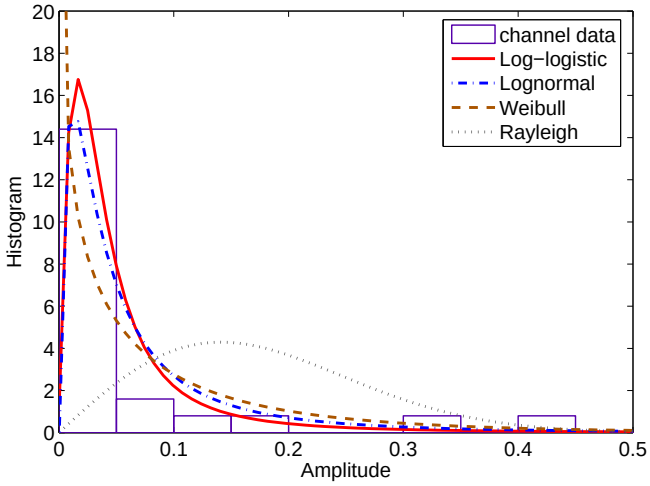
Figure 16: An illustration of log-logistic probability density function.



(a)

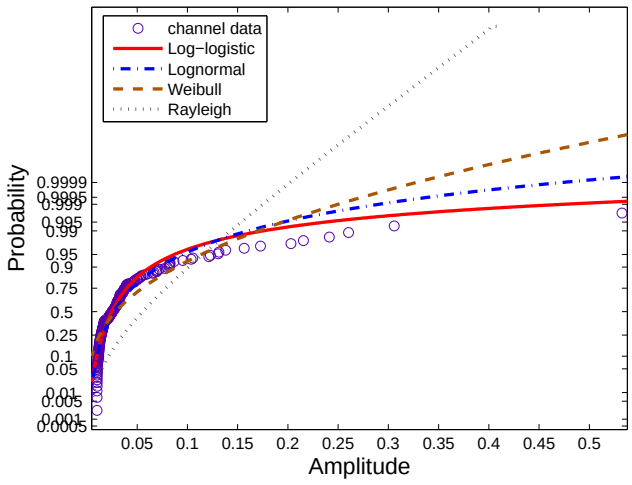


(b)

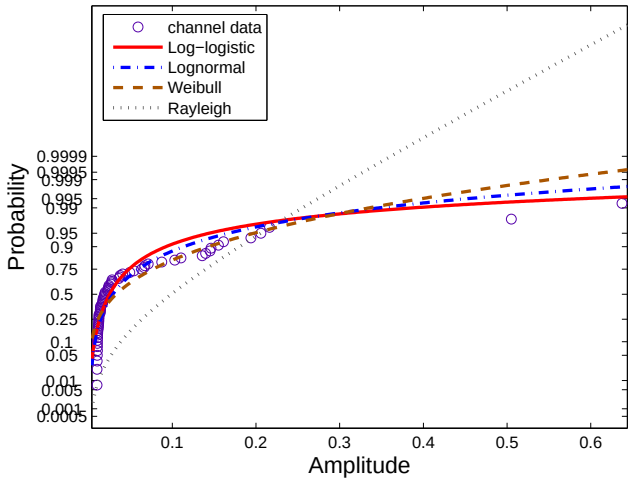


(c)

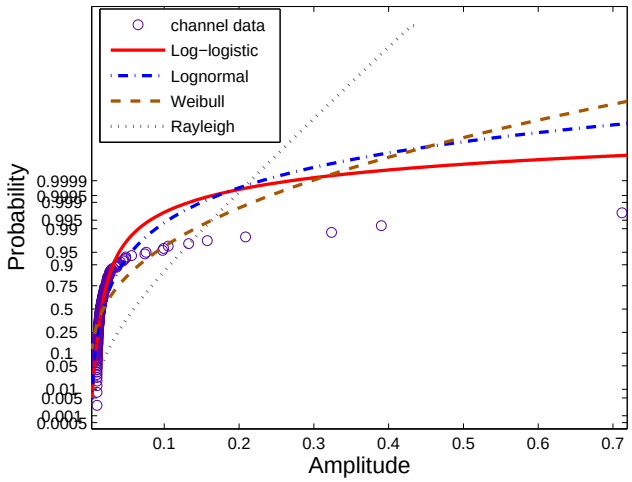
Figure 17: Goodness-of-fit illustration by density (a)CIR for 200MHz (b)CIR for 400MHz (c)CIR for UWB



(a)



(b)



(c)

Figure 18: Goodness-of-fit illustration by cumulated probability (a)CIR for 200MHz (b)CIR for 400MHz (c)CIR for UWB

NEW: Network-enabled Electronic Warfare for Target Recognition

Qilian Liang	Xiuzhen Cheng	Sherwood W. Samn
Dept of Electrical Engineering	Dept of Computer Science	Air Force Research Laboratory/RHX
University of Texas at Arlington	George Washington University	Brooks City Base
Arlington, TX 76019-0016, USA	Washington, DC 20052, USA	San Antonio, TX 78235, USA
E-mail: liang@uta.edu	E-mail: cheng@gwu.edu	E-mail: Sherwood.samn@brooks.af.mil

Abstract

Network-enabled Electronic Warfare (NEW) is to develop modeling and simulation effort to explore the advantages and limitations of network-enabled electronic warfare concepts. The advantages of linking multiple electronic support measures (ESM) and electronic attack (EA) assets to achieve improved capabilities across a networked battle force have yet to be quantified. In this paper, we utilize radar sensors as ESM and EA assets to demonstrate the advantages of NEW in Collaborative Automatic Target Recognition (CATR). Signal (waveform) design for Radar Sensor Networks (RSN) in NEW is studied theoretically. The conditions for waveform coexistence and the interferences among waveforms in RSN are analyzed. We apply the NEW to CATR via waveform diversity combining and propose maximum-likelihood (ML)-ATR algorithms for non-fluctuating targets as well as fluctuating targets. Simulation results indicate that our NEW-CATR performs much better than the single sensor-based ATR algorithm for non-fluctuating targets and fluctuating targets.

Index Terms : Network-enabled electronic warfare, radar sensor networks, waveform diversity, collaborative automatic target recognition, maximum-likelihood, interferences.

1 Introduction and Motivation

In current and future military operational environments such as Global War on Terrorism (GWOT) and Maritime Domain Awareness (MDA), war fighters require technology that can support their information needs in manner that is independent of their location and consistent with their level of command or responsibility and operational situation. To support this need, the U.S. Department of Defense (DoD) has developed the concept of Network Centric Warfare (NCW), defined as "*military operations that exploit state-of-the-art information and networking technology to integrate widely dispersed human decision makers, situational and targeting sensors, and forces and weapons into a highly adaptive, comprehensive system to achieve unprecedented mission effectiveness*" [1]. Network-enabled Electronic Warfare (NEW) is the form of electronic combat used in NCW. Focus is placed on a network of interconnected, adapting systems that are capable of making choices about how to survive and achieve their design goals in a dynamic environment. The goal of NEW is to develop modeling and simulation effort to explore the advantages and limitations of network-enabled electronic warfare concepts. The advantages of linking multiple electronic support measures (ESM) and electronic attack (EA) assets to achieve improved capabilities across a networked battle force have yet to be quantified [2]. In this paper, we utilize radar sensors as ESM and EA assets to demonstrate the advantages of NEW in Collaborative Automatic Target Recognition (CATR). The network of radar sensors should operate with multiple goals managed by an intelligent platform network that can manage the dynamics of each radar to meet the common goals of the platform, rather than each radar operates as an independent system. Therefore, it is significant to perform signal design and processing and networking cooperatively within and between platforms of radar sensors and their communication modules. This need is also testified by the recent solicitations from the U.S. Office of Naval Research [2][3]. For example, in [3], it is stated that "Algorithms are sought for fused, and/or, coherent cross-platform Radio Frequency (RF) sensing. The focus of this

effort is to improve surveillance utilizing a network, not fusion of disparate sensor products. The algorithms should be capable of utilizing RF returns from multiple aspects in a time-coordinated sensor network."

In this paper, we study waveform design and diversity algorithms for radar sensor networks. Waveform diversity is the technology that allows one or more sensors on board a platform to automatically change operating parameters, e.g., frequency, gain pattern, and pulse repetition frequency (PRF), to meet the varying environments. It has long been recognized that judicious use of properly designed waveforms, coupled with advanced receiver strategies, is fundamental to fully utilize the capacity of the electromagnetic spectrum. However, it is the relatively recent advances in hardware technology that are enabling a much wider range of design freedoms to be explored. As a result, there are emerging and compelling changes in system requirements such as more efficient spectrum usage, higher sensitivities, greater information content, improved robustness to errors, reduced interference emissions, etc. The combination of these changes is fueling a worldwide interest in the subject of waveform design and the use of waveform diversity techniques.

Most existing works on waveform design and selection are focused on single radar or sonar system. In 1974, Fitzgerald [8] demonstrated the inappropriateness of selection of waveforms based on measurement quality alone: the interaction between the measurement and the track can be indirect, but must be accounted for. Since then, extensive works on waveform design have been reported. Bell [6] used information theory to design radar waveforms for the measurement of extended radar targets exhibiting resonance phenomena. In [5], the singularity expansion method was used to design discriminant waveforms such as K-pulse, E-pulse, and S-pulse. Sowelam and Tewfik [23] developed a signal selection strategy for radar target classification, and a sequential classification procedure was proposed to minimize the average number of necessary signal transmissions. Intelligent waveform selection was studied in [4][12], but the effect of Doppler shift was not con-

sidered. In [16], time-frequency-based generalized chirps were used as waveform for detection and estimation. In [15], the performance of constant frequency (CF) and linear frequency modulated (LFM) waveform fusion from the standpoint of the whole system was studied, but the effect of clutter was not considered. In [24], a new time-frequency signal decomposition algorithm based on the S-method was proposed and evaluated on the high-frequency surface-wave radar (HFSWR) data, and demonstrated that it provided an effective way for analyzing and detecting maneuvering air targets with significant velocity changes, including target signal separation from the heavy clutter. In [25], CF and LFM waveforms were studied for a sonar system, but it was assumed that the sensor is non-intelligent (i.e., waveform can't be selected adaptively). All the above studies and design methods focused on the waveform design or selection for a single active radar or sonar system. In [21], cross-correlation properties of two radars were briefly mentioned and the binary coded pulses using simulated annealing [7] are highlighted. However, the cross-correlation of two binary sequences such as binary coded pulses (e.g. Barker sequence) is much easier to study than that of two analog radar waveforms.

In this paper, we focus on the waveform diversity and design for radar sensor networks using the constant frequency (CF) pulse waveform. Comparing to previous works, this paper has the following novelties:

1. Our focus is placed on a network of interconnected, adapting radar systems that are capable of making choices about how to survive and achieve their design goals in a dynamic environment.

2. We study waveform design and diversity for radar sensors networks. In Space-Time Adaptive Processing (STAP) [18], the waveform (pulse) design is essentially for a single radar system. The pulse is sent repeatedly at different time and echo is received and processed by an antenna array, and no interference exists among pulses if the pulse repetition interval is large enough.

3. We investigate collaborative automatic target recognition using radar sensor networks and compare it against single radar system in CATR.

4. Simulations are performed for nonfluctuating targets as well as fluctuating targets, and a real world application example, sense-through-foliage target detection, is presented.

The rest of this paper is organized as follows. In Section 2, we study the coexistence of radar waveforms. In Section 3, we analyze the interferences among radar waveforms. In Section 4, we propose a RAKE structure for waveform diversity combining and present a maximum-likelihood (ML) algorithm for CATR. In Section 5, we provide simulation results on ML-CATR. In Section 6, we conclude this paper and discuss future research.

2 Co-existence of Radar Waveforms

In radar sensor networks (RSN), radar sensors interfere with each other and the signal-to-interference-ratio may be very low if the waveforms are not properly designed. In this paper, we introduce orthogonality as one criterion for waveform design in RSN to make radars coexistence. In addition, since the radar channel is narrow-band, we will also consider the bandwidth constraint.

In our radar sensor networks, we choose the CF pulse waveform, which can be defined as

$$x(t) = \sqrt{\frac{E}{T}} \exp(j2\pi\beta t) \quad -T/2 \leq t \leq T/2 \tag{1}$$

where β is the RF carrier frequency in radians per second. In radar, ambiguity function (AF) is an analytical tool for waveform design and analysis, which succinctly characterizes the behavior of a waveform paired with its matched filter. The ambiguity function is useful for examining resolution, side lobe behavior, and ambiguities in both range and Doppler for a given waveform [18]. For a single radar, the matched filter for waveform $x(t)$ is $x^*(-t)$, and the ambiguity function of CF pulse

waveform is

$$\begin{aligned} A(\tau, F_D) &= \left| \int_{-T/2+\tau}^{T/2} x(t) \exp(j2\pi F_D s) x^*(t-\tau) dt \right| \\ &= \left| \frac{E \sin[\pi F_D (T - |\tau|)]}{T \pi F_D} \right| \quad -T \leq \tau \leq T \end{aligned} \tag{2}$$

We can simplify this AF in the following three special cases:

1. When $\tau = 0$,

$$A(0, F_D) = \left| \frac{E \sin(\pi F_D T)}{T \pi (F_D)} \right|; \tag{3}$$

2. when $F_D = 0$,

$$A(\tau, 0) = \left| \frac{E(T - |\tau|)}{T} \right|; \tag{4}$$

3. and when $\tau = F_D = 0$,

$$A(0, 0) = E \tag{5}$$

Note that the above ambiguity is for one radar only (no coexisting radar).

For radar sensor networks, the waveforms from different radars interfere with each other. We choose the waveform for radar i as

$$x_i(t) = \sqrt{\frac{E}{T}} \exp[j2\pi(\beta + \delta_i)t] \quad -T/2 \leq t \leq T/2 \tag{6}$$

which means that there is a frequency shift δ_i for radar i. To minimize the interference from one waveform to another, optimal values for δ_i should be determined to make the waveforms orthogonal to each other, i.e., let the cross-correlation between $x_i(t)$ and $x_n(t)$ be 0,

$$\int_{-T/2}^{T/2} x_i(t) x_n^*(t) dt = \frac{E}{T} \int_{-T/2}^{T/2} \exp[j2\pi(\beta + \delta_i)t] \exp[-j2\pi(\beta + \delta_n)t] dt \tag{7}$$

$$= E \text{sinc}[\pi(\delta_i - \delta_n)T] \tag{8}$$

If we choose

$$\delta_i = \frac{i}{T} \tag{9}$$

where i is a dummy index, (8) can be written as

$$\int_{-T/2}^{T/2} x_i(t)x_n^*(t)dt = \begin{cases} E & i = n \\ 0 & i \neq n \end{cases} \tag{10}$$

Therefore choosing $\delta_i = \frac{i}{T}$ in (6) yields orthogonal waveforms, i.e., the waveforms can coexist if the carrier spacing is a multiple of $1/T$ between two radar waveforms. In other words, orthogonality amongst carriers can be achieved by separating the carriers by a multiple of the inverse of waveform pulse duration. With this design, all the orthogonal waveforms can work simultaneously. However, there may exist time delay and Doppler shift ambiguity which may interfere with other waveforms in RSN.

3 Interferences of Waveforms In Radar Sensor Networks

3.1 RSN with Two Radar Sensors

We are interested in analyzing the interference from one radar to another if there exist time delay and Doppler shift. For a simple case where there are two radar sensors (i and n), the ambiguity function of radar i (considering the interference from radar n) is

$$\begin{aligned} A_i(t_i, t_n, F_{D_i}, F_{D_n}) &= \left| \int_{-\infty}^{\infty} [x_i(t)\exp(j2\pi F_{D_i}t) + x_n(t-t_n)\exp(j2\pi F_{D_n}t)]x_i^*(t-t_i)dt \right| && (11) \\ &\leq \left| \int_{-T/2+\max(t_i,t_n)}^{T/2+\min(t_i,t_n)} x_n(t-t_n)\exp(j2\pi F_{D_n}t)x_i^*(t-t_i)dt \right| \\ &\quad + \left| \int_{-T/2+t_i}^{T/2} x_i(t)\exp\left(j2\pi F_{D_i}t\right)x_i^*(t-t_i)dt \right| && (12) \\ &= \left| \int_{-T/2+\max(t_i,t_n)}^{T/2+\min(t_i,t_n)} x_n(t-t_n)\exp(j2\pi F_{D_n}t)x_i^*(t-t_i)dt \right| \\ &\quad + \left| \frac{E\sin[\pi F_{D_i}(T-|t_i|)]}{T\pi F_{D_i}} \right| && (13) \end{aligned}$$

To make the analysis easier, it is generally assumed that the radar sensor platform has access to the Global Positioning Service (GPS) and the Inertial Navigation Unit (INU) timing and navigation

data [3]. In this paper, we assume that the radar sensors are synchronized and that $t_i = t_n = \tau$. Then (13) can be simplified as

$$A_i(\tau, F_{D_i}, F_{D_n}) \approx |E\text{sinc}[\pi(n - i + F_{D_n}T)]| + \left|\frac{E\sin[\pi F_{D_i}(T - |\tau|)]}{T\pi F_{D_i}}\right| \tag{14}$$

We have the following three special cases:

1. If $F_{D_i} = F_{D_n} = 0$, and δ_i and δ_n follow (9), (14) becomes

$$A_i(\tau, 0, 0) \approx \left|\frac{E(T - |\tau|)]}{T}\right| \tag{15}$$

2. If $\tau = 0$, (14) becomes

$$A_i(0, F_{D_i}, F_{D_n}) \approx |E\text{sinc}[\pi(n - i + F_{D_n}T)]| + \left|\frac{E\sin(\pi F_{D_i}T)}{T\pi F_{D_i}}\right| \tag{16}$$

3. If $F_{D_i} = F_{D_n} = 0$, $\tau = 0$, and δ_i and δ_n follow (9), (14) becomes

$$A_i(0, 0, 0) \approx E \tag{17}$$

3.2 RSN with M Radar Sensors

Our analysis on an RSN with two radar sensors can be extended to the case of M radars. Assuming that the time delay τ for each radar is the same, then the ambiguity function of radar 1 (considering interferences from all the other $M - 1$ radars with CF pulse waveforms) can be expressed as

$$A_1(\tau, F_{D_1}, \cdots, F_{D_M}) \approx \sum_{i=2}^{M} |E\text{sinc}[\pi(i - 1 + F_{D_i}T)]| + \left|\frac{E\sin[\pi F_{D_1}(T - |\tau|)]}{T\pi F_{D_1}}\right| \tag{18}$$

Similarly, we have the following three special cases:

1. $F_{D_1} = F_{D_2} = \cdots = F_{D_M} = 0$, and the frequency shift δ_i in (6) for each radar follows (9), then (18) becomes

$$A_1(\tau, 0, 0, \cdots, 0) \approx \left|\frac{E(T - |\tau|)]}{T}\right| \tag{19}$$

Comparing it against (4), we notice that a radar may exist that can get the same signal strength as that of the single radar in a single radar system (no coexisting radar) when the Doppler shift is 0.

2. If $\tau = 0$, then (18) becomes

$$A_1(0, F_{D_1}, F_{D_2}, \cdots, F_{D_M}) \approx \sum_{i=2}^{M} |E\text{sinc}[\pi(i - 1 + F_{D_i}T)]| + \left| \frac{E \sin(\pi F_{D_1} T)}{T\pi F_{D_1}} \right| \quad (20)$$

Comparing to (3), a radar in RSN has higher interferences when unknown Doppler shifts exist.

3. $F_{D_1} = F_{D_2} = \cdots = F_{D_M} = 0$, $\tau = 0$, and δ_i in (6) follows (9), then (18) becomes

$$A_1(0, 0, 0, \cdots, 0) \approx E \quad (21)$$

4 NEW for Collaborative Automatic Target Recognition

In NEW, the radar sensors are networked together in an ad hoc fashion. They do not rely on a preexisting fixed infrastructure, such as a wireless backbone network or a base station. They are self-organizing entities that are deployed on demand in support of various events surveillance, battlefield, disaster relief, search and rescue, etc. Scalability concern suggests a hierarchical organization of radar sensor networks with the lowest level in the hierarchy being a cluster. As argued in [9] [10] [13] [17], in addition to helping with scalability and robustness, aggregating sensor nodes into clusters has additional benefits:

1. conserving radio resources such as bandwidth;

2. promoting spatial code reuse and frequency reuse;

3. simplifying the topology, e.g., when a mobile radar changes its location, it is sufficient for the nodes in the attended clusters to update their topology information;

4. reducing the generation and propagation of routing information; and,

5. concealing the details of global network topology from individual nodes.

In RSN, each radar can provide its waveform parameters such as δ_i to its clusterhead radar, and the clusterhead radar can combine the waveforms from its cluster members.

In RSN with M radars, the received signal for clusterhead (assume it's radar 1) is

$$r_1(u,t) = \sum_{i=1}^{M} \alpha(u) x_i(t - t_i) \exp(j2\pi F_{D_i} t) + n(u,t) \tag{22}$$

where $\alpha(u)$ stands for radar cross section (RCS), which can be modeled using non-zero constants for non-fluctuating targets and four Swerling target models for fluctuating targets [18]; F_{D_i} is the Doppler shift of the target relative to waveform i; t_i is the delay of waveform i, and $n(u,t)$ is the additive white Gaussian noise (AWGN). In this paper, we propose a RAKE structure for waveform diversity combining, as illustrated by Fig. 1. The RAKE structure is so named because it reminds the function of a garden rake, each branch collecting echo energy similarly to how tines on a rake collect leaves. This figure summarizes how the clusterhead works. The received signal $r_1(u,t)$ consists of echoes triggered by the waveforms from each radar sensor, and $x_i^*(t - t_i)$ is used to retrieve the amplified waveform from radar i (amplified by the target RCS) based on the orthogonal property presented in Sections 2 and 3, and then this information is time-averaged for diversity combining.

%%%%% **Insert Figure 1 here** %%%%%

According to this structure, the received $r_1(u,t)$ is processed by a bank of matched filters, then the output of branch 1 (after integration) is

$$\begin{aligned} & Z_1(u;t_1,\cdots,t_M,F_{D_1},\cdots,F_{D_M}) \\ = & \int_{-T/2}^{T/2} r_1(u,t)x_1^*(t-t_1)ds \qquad (23) \\ = & \int_{-T/2}^{T/2}[\sum_{i=1}^{M}\alpha_i(u)x_i(t-t_i)\exp(j2\pi F_{D_i}t)+n(u,t)]x_1^*(t-t_1)dt \qquad (24) \end{aligned}$$

Assuming $t_1 = t_2 = \cdots = t_M = \tau$, then based on (18),

$$\begin{aligned} Z_1(u;\tau,F_{D_1},\cdots,F_{D_M}) \approx & \sum_{i=2}^{M}\alpha(u)E\text{sinc}[\pi(i-1+F_{D_i}T)] \\ + & \frac{\alpha(u)E\sin[\pi F_{D_1}(T-|\tau|)]}{T\pi F_{D_1}}+n(u,\tau) \qquad (25) \end{aligned}$$

Similarly, we can get the output for any branch m ($m = 1,2,\cdots,M$),

$$\begin{aligned} Z_m(u;\tau,F_{D_1},\cdots,F_{D_M}) \approx & \sum_{i=1,i\neq m}^{M}\alpha(u)E\text{sinc}[\pi(i-m+F_{D_i}T)] \\ + & \frac{\alpha(u)E\sin[\pi F_{D_m}(T-|\tau|)]}{T\pi F_{D_m}}+n(u,\tau) \qquad (26) \end{aligned}$$

Therefore $Z_m(u;\tau,F_{D_1},\cdots,F_{D_M})$ consists of three parts, namely signal (reflected signal from radar m waveform): $\frac{\alpha(u)E\sin[\pi F_{D_m}(T-|\tau|)]}{T\pi F_{D_m}}$, interferences from other waveforms: $\sum_{i=1,i\neq m}^{M}\alpha(u)E\text{sinc}[\pi(i-m+F_{D_i}T)]$, and noise: $n(u,\tau)$.

We can also have the following three special cases for $|Z_m(u;\tau,F_{D_1},\cdots,F_{D_M})|$:

1. When $F_{D_1} = \cdots = F_{D_M} = 0$,

$$Z_m(u;\tau,0,0,\cdots,0) \approx \frac{E\alpha(u)(T-|\tau|)]}{T}+n(u,\tau) \qquad (27)$$

which means that if there is no Doppler mismatch, there is no interference from other waveforms.

2. If $\tau = 0$, (26) becomes

$$\begin{aligned} & Z_m(u; 0, F_{D_1}, \cdots, F_{D_M}) \\ \approx & \sum_{i=1, i\neq m}^{M} \alpha(u) E \text{sinc}[\pi(i - m + F_{D_i} T)] + \frac{\alpha(u) E \sin[\pi F_{D_m} T]}{T \pi F_{D_m}} + n(u) \end{aligned} \tag{28}$$

3. If $\tau = 0$, and $F_{D_1} = \cdots = F_{D_M} = 0$, (26) becomes

$$Z_m(u; 0, 0, 0, \cdots, 0) \approx E\alpha(u) + n(u) \tag{29}$$

Doppler mismatch happens quite often in target search where target velocity is not yet known. However, in target recognition, generally high-resolution measurements of targets in range ($\tau = 0$) and Doppler are available, therefore (29) will be used for CATR.

How to combine all the Z_m's ($m = 1, 2, \cdots, M$) is very similar to the diversity combining in wireless communications to combat channel fading, and the combination schemes may be different for different applications. In this paper, we are interested in applying the RSN waveform diversity to CATR, e.g., recognition that the echo on a radar display is that of an aircraft, ship, motor vehicle, bird, person, rain, chaff, clear-air turbulence, land clutter, sea clutter, bare mountains, forested areas, meteors, aurora, ionized media, or other natural phenomena via collaborations among different radars. Early radars were "blob" detectors in that they detected the presence of a target and gave its location in range and angle, and radar began to be more than a blob detector and could provide recognition of one type of target from another [21]. It is known that small changes in the aspect angle of complex (multiple scatter) targets can cause major changes in the radar cross section (RCS). This has been considered in the past as a means of target recognition, and is called *fluctuation of radar cross section with aspect angle*, but it has not had much success [21]. In [19], a parametric filtering approach was proposed for target detection using airborne radar. In [14], knowledge-based sensor networks were applied to threat assessment. In this paper,

we propose maximum likelihood collaborative automatic target recognition (ML-CATR) algorithms for non-fluctuating targets as well as fluctuating targets.

4.1 ML-CATR for Non-fluctuating Targets

In some sources, the non-fluctuating target is identified as a "Swerling 0" or "Swerling 5" model [22]. For non-fluctuating targets, the RCS $\alpha_m(u)$ is just a constant α for a given target. In (29), $n(u,\tau)$ is a zero-mean Gaussian random variable for a given τ, so $|Z_m(u;0,0,\cdots,0)|$ follows a Rician distribution because signal $E\alpha(u)$ is a positive constant, $E\alpha$, for a non-fluctuating target. Let $y_m \stackrel{\triangle}{=} |Z_m(u;0,0,\cdots,0)|$, then the probability density function (pdf) of y_m is

$$f(y_m) = \frac{2y_m}{\sigma^2}\exp[-\frac{(y_m^2+\lambda^2)}{\sigma^2}]I_0(\frac{2\lambda y_m}{\sigma^2}) \tag{30}$$

where

$$\lambda = E\alpha, \tag{31}$$

σ^2 is the noise power (with I and Q sub-channel power $\sigma^2/2$), and $I_0(\cdot)$ is the zero-order modified Bessel function of the first kind. Let $\mathbf{y} \stackrel{\triangle}{=} [y_1, y_2, \cdots, y_M]$, then the pdf of $\mathbf{y}$ is

$$f(\mathbf{y}) = \prod_{m=1}^{M} f(y_m) \tag{32}$$

Our CATR is a multiple-category hypothesis testing problem, i.e., to decide a target category (e.g. aircraft, ship, motor vehicle, bird, etc) based on $r_1(u,t)$. Assume there are totally N categories and a category n target has RCS α_n, therefore the ML-CATR algorithm to decide a target category C can be expressed as,

$$C = \arg\max_{n=1}^{N} f(\mathbf{y}|\lambda = E\alpha_n) \tag{33}$$

$$= \arg\max_{n=1}^{N} \prod_{m=1}^{M} \frac{2y_m}{\sigma^2}\exp[-\frac{(y_m^2+E^2\alpha_n^2)}{\sigma^2}]I_0(\frac{2E\alpha_n y_m}{\sigma^2}) \tag{34}$$

4.2 ML-CATR for Fluctuating Targets

Fluctuating target modeling is more realistic in which the target RCS is drawn from either the Rayleigh or chi-square of degree four pdf. The Rayleigh model describes the behavior of a complex target consisting of many scatters, none of which is dominant. The fourth-degree chi-square models targets having many scatters of similar strength with one dominant scatter. Based on different combinations of pdf and decorrelation characteristics (scan-to-scan or pulse-to-pulse decorrelation), four Swerling models are used [18]. In this paper, we focus on the "Swerling 2" model which is a Rayleigh distribution with pulse-to-pulse decorrelation. The pulse-to-pulse decorrelation implies that each individual pulse results in an independent value for RCS α.

For the Swerling 2 model, the RCS $|\alpha(u)|$ follows a Rayleigh distribution and its I and Q subchannels follow zero-mean Gaussian distributions with a variance γ^2. Assume

$$\alpha(u) = \alpha_I(u) + j\alpha_Q(u) \tag{35}$$

and $n(u) = n_I(u) + jn_Q(u)$ follows a zero-mean complex Gaussian distribution with a variance σ^2 for the I and Q subchannels. Therefore according to (29), $Z_m(u; 0, 0, 0, \cdots, 0)$ is a zero-mean Gaussian random variable with a variance $E^2\gamma^2 + \sigma^2$ for the I and Q subchannels, which means $y_m \stackrel{\triangle}{=} |Z_m(u; 0, 0, \cdots, 0)|$ follows a Rayleigh distribution with a parameter $\sqrt{E^2\gamma^2 + \sigma^2}$,

$$f(y_m) = \frac{y_m}{E^2\gamma^2 + \sigma^2} \exp(-\frac{y_m^2}{E^2\gamma^2 + \sigma^2}) \tag{36}$$

The mean value of y_m is $\sqrt{\frac{\pi(E^2\gamma^2+\sigma^2)}{2}}$, and the variance is $\frac{(4-\pi)(E^2\gamma^2+\sigma^2)}{2}$. The variance of signal is $\frac{(4-\pi)E^2\gamma^2}{2}$ and the variance of noise is $\frac{(4-\pi)\sigma^2}{2}$.

Let $\mathbf{y} \stackrel{\triangle}{=} [y_1, y_2, \cdots, y_M]$, then the pdf of $\mathbf{y}$ is

$$f(\mathbf{y}) = \prod_{m=1}^{M} f(y_m) \tag{37}$$

Assume there are totally N categories and a category n target has a RCS $\alpha_n(u)$ (with a variance

γ_n^2), so the ML-ATR algorithm to decide a target category C can be expressed as,

$$C = \arg\max_{n=1}^{N} f(\mathbf{y}|\gamma = \gamma_n) \quad (38)$$

$$= \arg\max_{n=1}^{N} \prod_{m=1}^{M} \frac{y_m}{E^2\gamma_n^2 + \sigma^2} \exp(-\frac{y_m^2}{E^2\gamma_n^2 + \sigma^2}) \quad (39)$$

5 Simulations and Real World Application Example

5.1 Computer Simulations

Radar sensor networks will be required to detect a broad range of target classes. Too often, the characteristics of objects that are not of interest (e.g., bird) are similar to those of threat objects (e.g., missile). Therefore, new techniques to discriminate threat against undesired detections (e.g. birds, etc.) are needed. We applied our ML-CATR to this important application, to recognize a target from many target classes. We assume that the domain of target classes is known a priori (N in Sections 4.1 and 4.2), and that the RSN is confined to work only on the known domain.

For non-fluctuating target recognition, our targets have 5 classes with different RCS values, which are summarized in Table 1 [21]. We applied the ML-CATR algorithms in Section 4.1 (for the non-fluctuating target case) to classify an unknown target as one of these 5 target classes. At each average SNR value, we ran Monte-Carlo simulations for 10^5 times for each target. The average SNR value is based on the average power from all targets (signal variance), so the actual SNRs for bird and missile are much lower than the average SNR value. For example, at the average SNR=16dB, the bird target SNR=-33.1646dB, and the missile target SNR=0.8149dB; and at average SNR=20dB, the bird target SNR=-29.1646dB, and the missile target SNR=4.8149dB. In Fig. 2(a)(b), we plotted the probability of the ATR error in bird and missile recognition when they are assumed as non-fluctuating targets. These figures indicate that a single radar system can't perform well in both recognitions, whose probability of the ATR error is above 10%, which can't

be used for real-world ATR. However, the 5-radar RSN and 10-radar RSN can maintain very low ATR errors. In Fig. 2(c), we plotted the average probability of the ATR error for all 5 targets recognition. Since the other 3 targets (different aircrafts) have much higher SNRs, their ATR error is lower, which makes the average probability of ATR error lower.

%%%%% **Insert Table 1 here** %%%%%

%%%%% **Insert Figure 2 here** %%%%%

For fluctuating target recognition, we assume the fluctuating targets follow the "Swerling 2" model (Rayleigh distribution with pulse-to-pulse decorrelation), and assume the RCS value listed in Table 1 to be the standard deviation (std) γ_n of RCS $\alpha_n(u)$ for target n. We applied the ML-CATR algorithm in Section 4.2 (for the fluctuating target case) for target recognition within the 5 targets domain. Similarly we ran Monte-Carlo simulations at each SNR value. In Fig. 3(a)(b)(c), we plotted the ATR performance for fluctuating targets and compared the performances of a single-radar system, a 5-radar RSN, and a 10-radar RSN. Observe that the two RSNs perform much better than the single radar system. The ATR error for the missile is higher than that of bird because the Rayleigh distribution of the missile has a lot of overlap with its neighbor targets (aircrafts). Comparing Fig. 2(a)(b)(c) to Fig. 3(a)(b)(c), it is clear that higher SNRs are needed for the fluctuating target recognition comparing to the non-fluctuating target recognition. According to Skolnik [21], the radar performance with a probability of recognition error (p_e) less than 10% is good enough. Our RSN with waveform-diversity can achieve a probability of ATR error much less than 10% for each target ATR as well as the average ATR for all targets. However, the single radar system has a probability of ATR error much higher than 10%. Fig. 3(c) also tells us that the

average probability of ATR error of a single-radar system is impossible to be less than 10% even at an extremely high SNR. Our RSN with waveform diversity is very promising for real-world ATR.

%%%%% **Insert Figure 3 here** %%%%%

5.2 Real World Application Example

We verified our approach based on a real world application example, sense-through-foliage target detection from U.S. Air Force Research Laboratory. The target is a trihedral reflector (as shown in Fig. 4) in a forest. We plot two collections using UWB radars in Figs. 5a and 5b. Fig. 5a has no target on range, and Fig. 5b has target at samples around 13,900. We plot the echo differences between Figs. 5a and 5b in Fig. 5c. However, it is impossible to identify whether there is any target and where there is target based on Fig. 5c, which means *single radar doesn't work even in ideal case*. Since significant pulse-to-pulse variability exists in the echoes, this motivates us to explore the spatial and time diversity using radar sensor networks approach. The echoes, i.e., RF responses by the pulse of each cluster-member radar, are combined by the clusterhead using the RAKE structure in Fig. 1.

%%%%% **Insert Figure 4 here** %%%%%

%%%%% **Insert Figure 5 here** %%%%%

We ran simulations for an RSN with 30 radar sensors, and plot the power of AC values in Figs. 6a and 6b for the two cases (with target and without target) respectively. Observe that in Fig. 6b, the power of AC values (around sample 13,900) where the target is located is non-fluctuating

(monotonically increase then decrease). Although some other samples also have very high AC power values, it is very clear that they are quite fluctuating and the power of AC values behaves like random noise because generally the clutter has Gaussian distribution in the frequency domain.

%%%%% **Insert Figure 6 here** %%%%%

6 Conclusions and Future Works

We have studied the constant frequency pulse waveform design and diversity in radar sensor networks. We showed that the waveforms can coexist if the carrier frequency spacing is a multiple of $1/T$ between two radar waveforms. We made analysis on interferences among waveforms in RSN and proposed a RAKE structure for waveform diversity combining in RSN. As an application example, we applied the waveform design and diversity to CATR in RSN and proposed ML-CATR algorithms for non-fluctuating targets as well as fluctuating targets. Simulation results show that an RSN using our waveform diversity-based ML-ATR algorithms performs much better than a single radar system for non-fluctuating targets and fluctuating targets recognition. We also validated our RSN approach via a real-world sense-through-foliage target detection example.

In our future research, we will investigate the CATR when multiple targets coexist in RSN, and the number of targets are time-varying. In this paper, we used spatial diversity combining. For multi-target ATR, we will further investigate spatial-temporal-frequency combining for waveform diversity in RSN.

Acknowledgment

The research of Liang was supported in part by the U.S. Office of Naval Research (ONR) under Grant N00014-07-1-0395, N00014-07-1-1024, N00014-03-1-0466, and National Science Foundation (NSF) under Grant CNS-0721515 and CNS-0831902. The research of Cheng was supported in part by the NSF CAREER award CNS-0347674 and NSF under Grant CNS-0721699 and CNS-0831852.

References

[1] ONR BAA 06-016, "Command and Control and Combat Systems (C2 and CS)", http://www.onr.navy.mil/02/baa/expired.asp.

[2] ONR BAA 07-009, "Electronic Warfare Discovery and Invention (D&I)," http://www.onr.navy.mil/02/baa/.

[3] ONR BAA 07-017, "NET-SENTRIC Surveillance," http://www.onr.navy.mil/02/baa/.

[4] P. Baggenstoss, "Adaptive pulse length correction (APLECORR): a strategy for waveform optimization in ultrawideband active sonar," *IEEE Trans on Oceanic Engineering*, vol. 23, no. 1, pp. 1-11, 1998.

[5] C. E. Baum, et al, "The singularity expansion method and its application to target identification", *Proc. of the IEEE*, vol 79, no. 10, Oct 1991.

[6] M. R. Bell, "Information theory and radar waveform design", *IEEE Trans on Information Theory*, vol. 39, no. 5, pp. 1578-1597, Sept 1993.

[7] H. Deng, "Synthesis of binary sequences with good correlation and cross-correlation properties by simulated annealing," *IEEE Trans on Aerospace and Electronic Systems*, vol. 32, no. 1, Jan 1996.

[8] R. Fitzgerald, "Effects of range-Doppler coupling on chirp radar tracking accuracy," *IEEE Trans on Aerospace and Electronic Systems*, vol. 10, pp. 528-532, July 1974.

[9] T.-C. Hou and T-J. Tsai, " An access-based clustering protocol for multihop wireless ad hoc networks," *IEEE J. Selected Areas in Communications*, vol. 19, no. 7, pp. 1201-1210, July 2001.

[10] A. Iwata, C. C. Chiang, G. Pei, M. Gerla, and T. W. Chen, " Scalable routing strategies for ad hoc networks," *IEEE J. Selected Areas in Communications*, vol. 17, pp. 1369-1379, 1999.

[11] R. A. Johnson and E. L. Titlebaum, "Range Doppler Uncoupling in the Doppler Tolerant Bat Signal", *Proc. of IEEE Ultrasonics Symposium*, New York, pp. 64-67, 1972.

[12] D. Kershaw and R. Evans, "Optimal waveform selection for tracking system", *IEEE Trans on Information Theory*, vol. 40, no. 5, pp. 1536-1550, 1994.

[13] C. R. Lin and M. Gerla, "Adaptive clustering in mobile wireless networks," *IEEE J. Selected Areas in Communications*, vol. 16, pp. 1265-1275, 1997.

[14] Q. Liang, X. Cheng, "KUPS: Knowledge-based Ubiquitous and Persistent Sensor Networks for Threat Assessment", *IEEE Trans on Aerospace and Electronic Systems*, vol. 44, no. 3, July 2008.

[15] R. Niu, P. Willett, and Y. Bar-Shalom, "Tracking consideration in selection of radar waveform for range and range-rate measurements", *IEEE Transactions on Aerospace and Electronic Systems*, Vol. 38, No. 2, 2002.

[16] A. Papandreou, G. F. Boudreaux-Bartels, and S. M. Kay, "Detection and estimation of generalized chirps using time-frequency representation", *Twenty-Eighth Asilomar Conference on Signals, Systems and Computers*, vol. 1, pp. 50-54, Oct. 1994.

[17] C. E. Perkins, "Chapter 4, Cluster-Based Networks," *Ad Hoc Networking*, Edited by C. E. Perkins, pp. 75-138, Addison-Wesley, 2001.

[18] M. A. Richards, *Fundamentals of Radar Signal Processing*, McGraw-Hill Companies, New York, 2005.

[19] J. Roman, M. Rangaswamy, D. Davis, Q. Zhang, B. Himed, and J. Michels, "Parametric adaptive matched filter for airborne radar applications," *IEEE Trans. Aerosp. Electron. Syst.*, vol. 36, no. 2, pp. 677-692, 2000.

[20] T. K. Sarkar and N. Sangruji, "An adaptive nulling system for a narrow-band signal with a look-direction constraint utilizing the conjugate gradient method," *IEEE Trans. Antennas Propagat.*, vol. 37, no. 7, pp. 940-944, July 1989.

[21] M. I. Skolnik, *Introduction to Radar Systems*, 3rd ed, New York, McGraw Hill, 2001.

[22] P. Swerling, "Probability of detection for fluctuating targets", *IRE Trans on Information Theory*, vol. 6, pp. 269-308, April 1960.

[23] S. Sowelam and A. Tewfik, "Waveform selection in radar target classification," *IEEE Trans on Information Theory*, vol. 46, no. 3, pp. 1014-1029, 2000.

[24] L. Stankovic, T. Thayaparan, M. Dakovic, "Signal Decomposition by Using the S-Method with Application to the Analysis of HF Radar Signals in Sea-Clutter," *IEEE Trans. on Signal Processing*, vol. 54, no. 11, pp.4332-4342, Nov. 2006.

[25] Y. Sun, P. Willett, and R. Lynch, "Waveform fusion in sonar signal processing", *IEEE Transactions on Aerospace and Electronic Systems*, Vol. 40, No. 2, 2004

List of Tables

1 RCS values at microwave frequency for 5 targets. 22

Table 1: RCS values at microwave frequency for 5 targets.

Index n	Target	RCS
1	Bird	0.01
2	Conventional unmanned winged missile	0.5
3	Small single-engine aircraft	1
4	Small fighter aircraft or 4 passenger jet	2
5	Large fighter aircraft	6

List of Figures

1 Waveform diversity combining by clusterhead in RSN. 23

2 Probability of ATR error for *non-fluctuating* targets at different average SNR (dB) values. (a) bird, (b) missile, (c) the average probability of ATR error for 5 targets. . 24

3 Probability of ATR error for *fluctuating* targets at different average SNR (dB) values. (a) bird, (b) missile, (c) the average probability of ATR error for 5 targets. 25

4 The target (a trihedral reflector) is shown on the stand at 300 feet from the measurement lift. 26

5 Measurement of UWB radar. (a) Expanded view of traces (no target) from sample 13,001 to 15,000. (b) Expanded view of traces (with target) from sample 13,001 to 15,000. (c) The differences between (a) and (b). 27

6 Power of AC values based on radar sensor networks approach. (a) No target (b) With target in the field (in samples around 13,900). 28

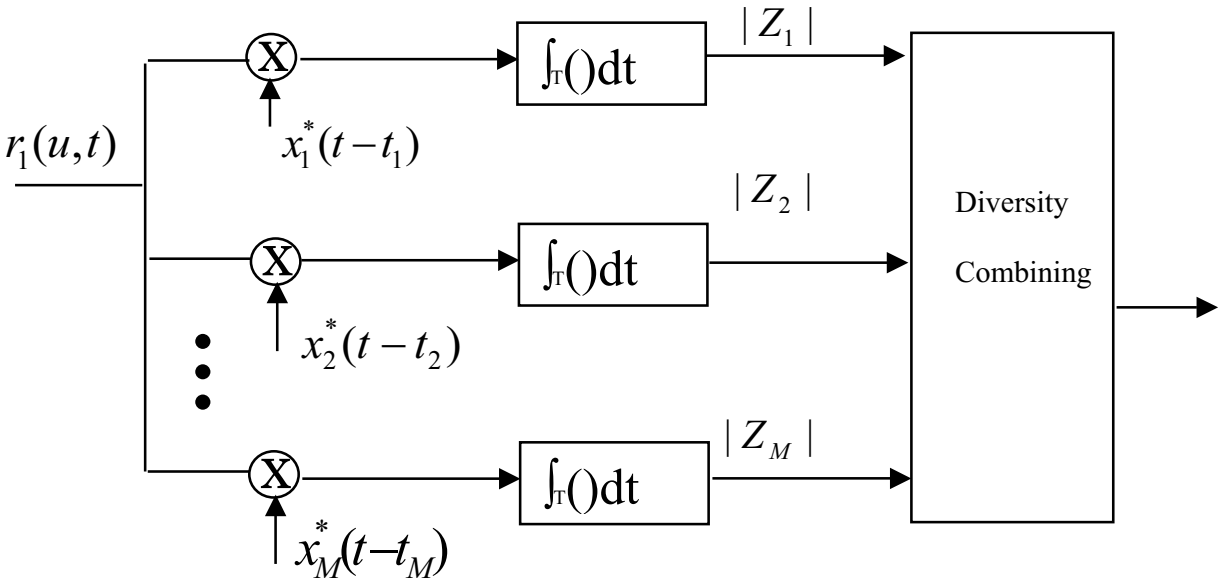
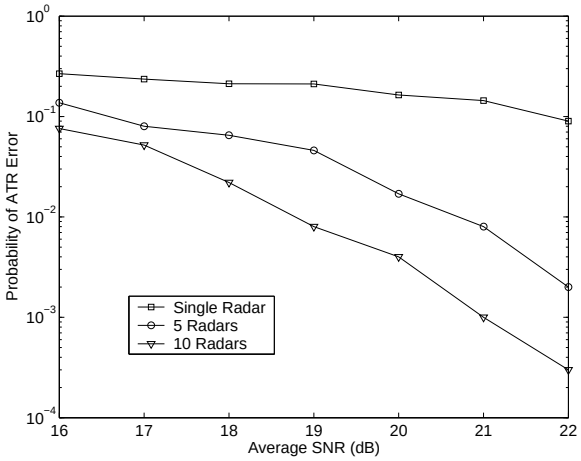
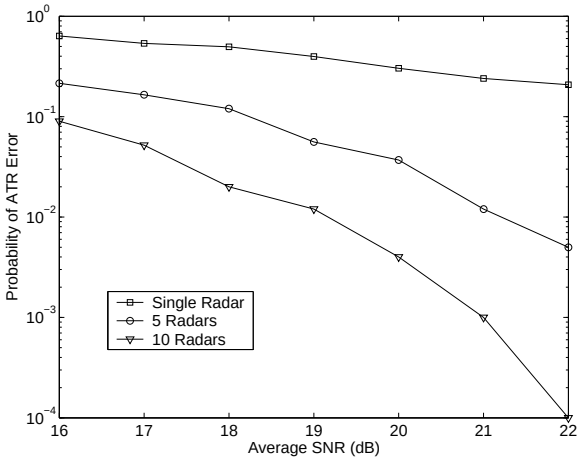


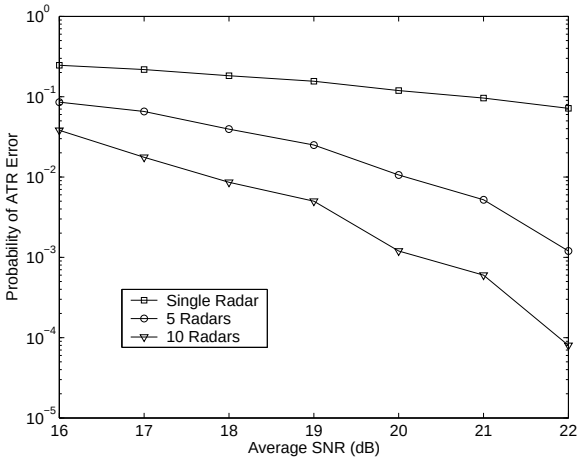
Figure 1: Waveform diversity combining by clusterhead in RSN.



(a)

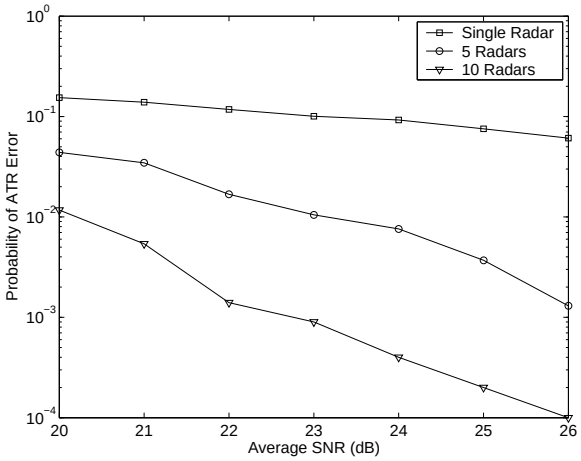


(b)

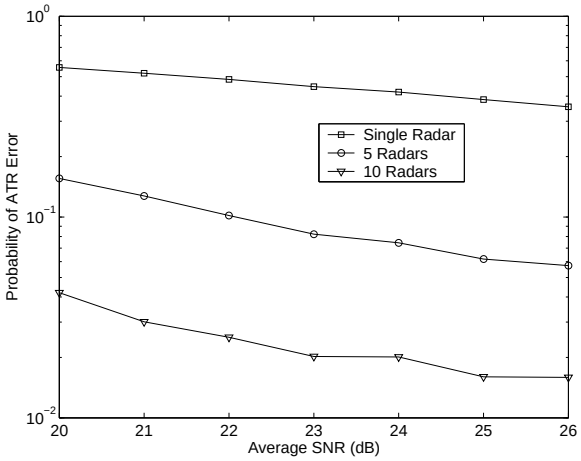


(c)

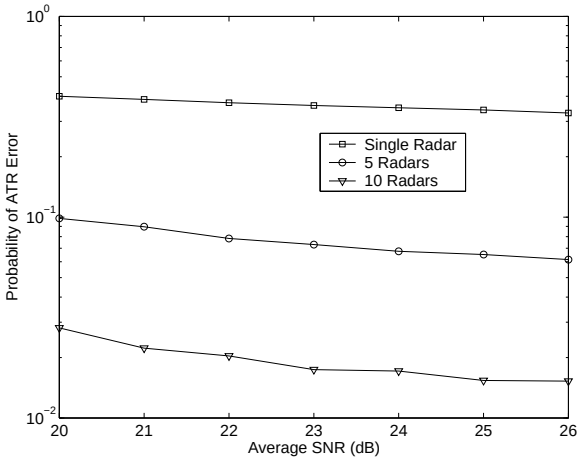
Figure 2: Probability of ATR error for *non-fluctuating* targets at different average SNR (dB) values. (a) bird, (b) missile, (c) the average probability of ATR error for 5 targets.



(a)



(b)

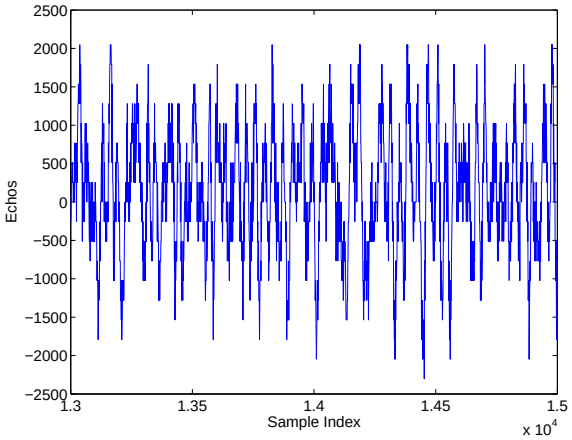


(c)

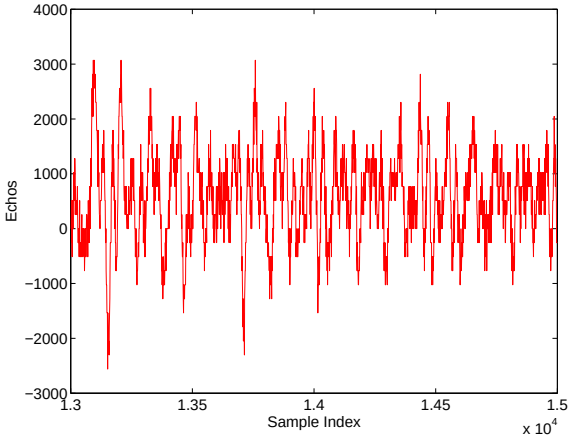
Figure 3: Probability of ATR error for *fluctuating* targets at different average SNR (dB) values. (a) bird, (b) missile, (c) the average probability of ATR error for 5 targets.



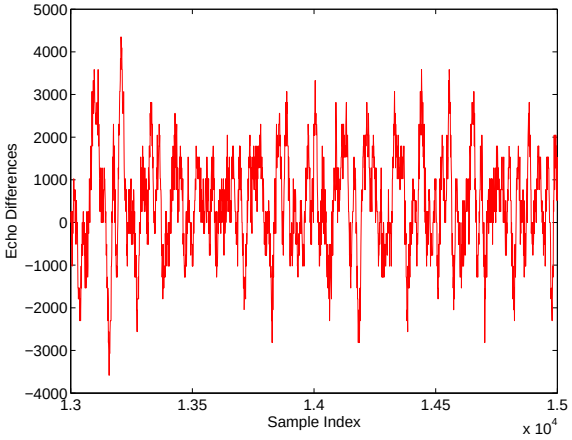
Figure 4: The target (a trihedral reflector) is shown on the stand at 300 feet from the measurement lift.



(a)

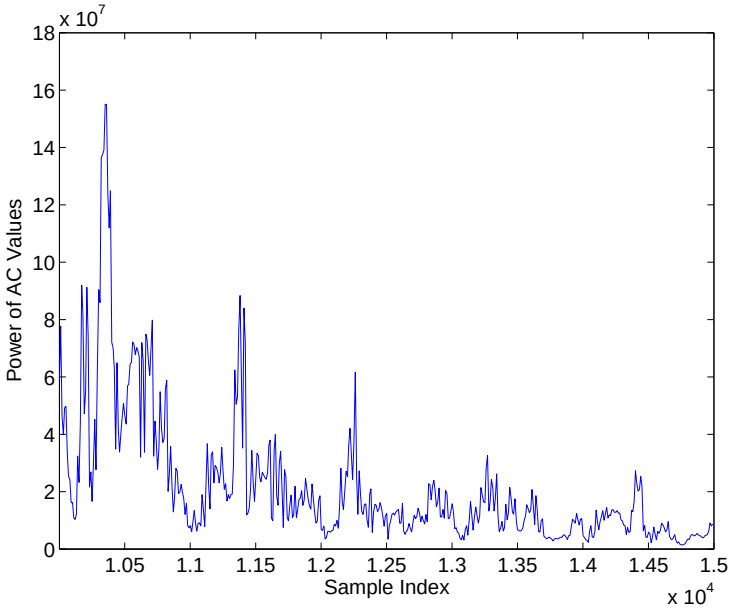


(b)

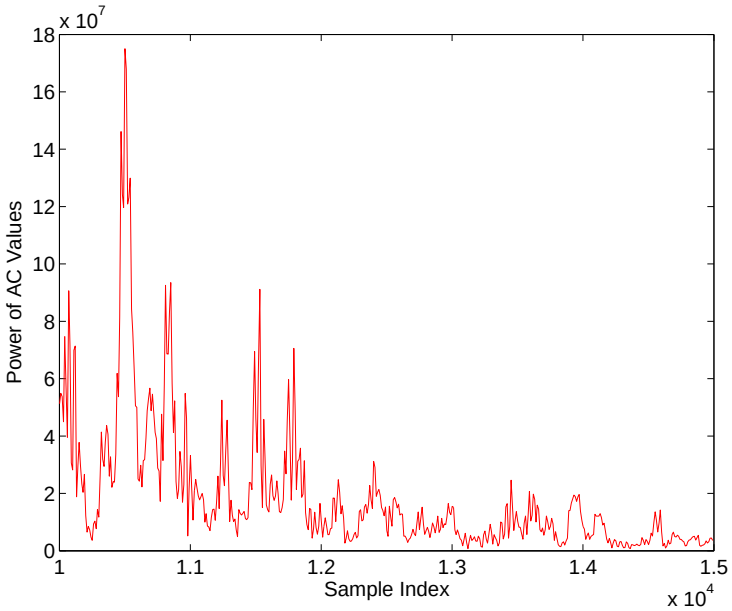


(c)

Figure 5: Measurement of UWB radar. (a) Expanded view of traces (no target) from sample 13,001 to 15,000. (b) Expanded view of traces (with target) from sample 13,001 to 15,000. (c) The differences between (a) and (b).



(a)



(b)

Figure 6: Power of AC values based on radar sensor networks approach. (a) No target (b) With target in the field (in samples around 13,900).

Biologically-Inspired Target Recognition in Radar Sensor Networks*

Qilian Liang

Department of Electrical Engineering

University of Texas at Arlington

Arlington, TX 76019-0016, USA

E-mail: liang@uta.edu

Abstract

One of the great mysteries of the brain is cognitive control. How can the interactions between millions of neurons result in behavior that is coordinated and appears willful and voluntary? There is consensus that it depends on the prefrontal cortex (PFC). Many PFC areas receive converging inputs from at least two sensory modalities. Inspired by human's innate ability to process and integrate information from disparate, network-based sources, we apply human-inspired information integration mechanisms to target detection in cognitive radar sensor network. Humans' information integration mechanisms have been modelled using maximum-likelihood estimation (MLE) or soft-max approaches. In this paper, we apply these two algorithms to cognitive radar sensor networks target detection. Discrete-cosine-transform (DCT) is used to process the integrated data from MLE or soft-max. We apply fuzzy logic system (FLS) to automatic target detection based on the AC power values from DCT. Simulation results show that our MLE-DCT-FLS and soft-max-DCT-FLS approaches perform very well in the radar sensor network target detection, whereas the existing 2-D construction algorithm doesn't work in this study.

*Some material in this paper has been presented at International Conference on Wireless Algorithms, Systems, and Applications, August 2009, Boston, MA.

Index Terms : Biologically-inspired, information integration, prefrontal cortex (PFC), cognitive radar sensor networks, fuzzy logic systems, automatic target recognition, maximum-likelihood estimation.

1 Introduction and Motivation

Humans display a remarkable capability to perform visual and auditory information integration despite noisy sensory signals and conflicting inputs. Humans are adept at network visualization, and at understanding subtle implications among the network connections. To date, however, human's innate ability to process and integrate information from disparate, network-based sources has not translated well to automated systems. Motivated by the above challenges, we apply human information integration mechnisms to cognitive radar sensor networks. A cognitive network is one that is aware of changes in user needs and its environment, adapts its behavior to those changes, learns from its adaptations, and exploits knowledge to improve its future behavior. A cognitive radar sensor network consists of multiple networked radar sensors and radar sensors sense and communicate with each other collaboratively to complete a mission. In real world, cognitive radar sensor network information integration is necessary in different applications. For example, in an emergency natural disaster scenario, such as China Wenchuan earthquake in May 2008, Utah Mine Collapse in August 2007, or West Virginia Sago mine disaster in January 2006, cognitive radar sensor network-based information integration for first responders is critical for search and rescue. Danger may appear anywhere at any time, therefore, first responders must monitor a large area continuously in order to identify potential danger and take actions. Due to the dynamic and complex nature of natural disaster, some buried/foleage victims may not be found with image/video sensors, and UWB radar sensors are needed for penetrating the ground or sense-through-wall. Unfortunately, the radar data acquired are often limited and noisy. Unlike medical imaging or synthetic aperture radar imaging

where abundance of data is generally available through multiple looks and where processing time may not be crucial, practical cognitive radar sensor networks are typically the opposite: availability of data is limited and required processing time is short. This need is also motivated by the fact that humans display a remarkable capability to quickly perform target recognition despite noisy sensory signals and conflicting inputs. Humans are adept at network visualization, and at understanding subtle implications among the network connections. To date, however, human's innate ability to process and integrate information from disparate, network-based sources for situational understanding has not translated well to automated systems. In this paper, we apply human information integration mechanisms to information fusion in cognitive radar sensor network.

The rest of this paper is organized as follows. In Section 2, we introduce the human information integration mechanisms and their mathematical modeling. In Section 3, we introduce the radar sensor network data collection. In Section 4, we apply the human information integration mechanisms to cognitive radar sensor network. In Section 5, we apply fuzzy logic system for target detection as a post-processing for Section 4. In Section 6, we conclude this paper.

2 Human Information Integration Mechanisms

One of the great mysteries of the brain is cognitive control. How can the interactions between millions of neurons result in behavior that is coordinated and appears willful and voluntary? There is consensus that it depends on the prefrontal cortex (PFC) [14][16]. A schematic diagram of some of the extrinsic and intrinsic connections of the PFC is depicted in Fig. 1 [14]. Many PFC areas receive converging inputs from at least two sensory modalities [3][9]. For example, the dorsolateral (DL) (areas 8, 9, and 46) and ventrolateral (12 and 45) PFC both receive projections from visual, auditory, and somatosensory cortex. Furthermore, the PFC is connected with other cortical regions that are themselves sites of multimodal convergence. Many PFC areas (9, 12, 46, and 45) receive

inputs from the rostral superior temporal sulcus, which has neurons with bimodal or trimodal (visual, auditory, and somatosensory) responses [2][17]. The arcuate sulcus region (areas 8 and 45) and area 12 seem to be particularly multimodal. They contain zones that receive overlapping inputs from three sensory modalities [17]. Observe, for example, that mid-dorsal area 9 directly processes and integrates visual, auditory, and multimodal information. Regarding the functional model/mechanisms of different PFC areas (in Fig. 1): mid-dorsal area 9, dorsolateral area 46, and ventrolateral areas 12, 45, and orbital and medial areas 10, 11, 13, 14, different models and rules have been reported in the literature [6][18][4][5].

Recently, a maximum-likelihood estimation (MLE) approach was proposed for multi-sensory data fusion in human [6]. In the MLE approach [6], sensory estimates of an environmental property can be represented by $\hat{S}_j = f_i(S)$ where S is the physical property being estimated, f is the operation the nervous system performs to derive the estimate, and $\hat{S}$ is the perceptual estimate. Sensory estimates are subject to two types of error: random measurement error and bias. Thus, estimates of the same object property from different cues usually differ. To reconcile the discrepancy, the nervous system must either combine estimates or choose one, thereby ignoring the other cues. Assuming that each single-cue estimate is unbiased but corrupted by independent Gaussian noise, the statistically optimal strategy for cue combination is a weighted average [6]

$$\hat{S}_c = \sum_{i=1}^{M} w_i \hat{S}_i \tag{1}$$

where $w_i = \frac{1/\sigma_i^2}{\sum_j 1/\sigma_j^2}$ and is the weight given to the ith single-cue estimate, σ_i^2 is that estimates variance, and M is the total number of cues. Combining estimates by this MLE rule yields the least variable estimate of S and thus more precise estimates of object properties.

Besides, some other summation rules have been proposed in perception and cognition such as soft-max rule: $y = (\sum_{i=1}^{M} x_i^n)^{\frac{1}{n}}$ [5] where x_i denotes the input from an input source i, and M is the total number of sources. In this paper, we will apply MLE and soft-max human brain information

integration mechanisms to cognitive radar sensor network information integration.

3 Radar Sensor Networks Data Measurement and Collection

Our work is based on the sense-through-foliage UWB radar sensor networks. The foliage experiment was constructed on a seven-ton man lift, which had a total lifting capacity of 450 kg. The limit of the lifting capacity was reached during the experiment as essentially the entire measuring apparatus was placed on the lift. (as shown in Fig. 2). The principle pieces of equipment secured on the lift are: Barth pulser, Tektronix model 7704 B oscilloscope, dual antenna mounting stand, two antennas, rack system, IBM laptop, HP signal Generator, Custom RF switch and power supply and Weather shield (small hut). The target is a trihedral reflector (as shown in Fig. 3). Throughout this work, a Barth pulse source (Barth Electronics, Inc. model 732 GL) was used. The pulse generator uses a coaxial reed switch to discharge a charge line for a very fast rise time pulse outputs. The model 732 pulse generator provides pulses of less than 50 picoseconds (ps) rise time, with amplitude from 150 V to greater than 2 KV into any load impedance through a 50 ohm coaxial line. The generator is capable of producing pulses with a minimum width of 750 ps and a maximum of 1 microsecond. This output pulse width is determined by charge line length for rectangular pulses, or by capacitors for 1/e decay pulses.

For the data we used in this paper, each sample is spaced at 50 picosecond interval, and 16,000 samples were collected for each collection for a total time duration of 0.8 microseconds at a rate of approximately 20 Hz. We plot the transmitted pulse (one realization) in Fig. 4a) and the received echos in one collection in Fig. 4b (averaged over 35 pulses). The data collections were extensive. 20 different positions were used, and 35 collections were performed at each position using UWB radar sensor networks.

4 Human-Inspired Sense-through-Foliage Target Detection

In Figs. 5a and 5b, we plot two collections of UWB radars. Fig. 5a has no target on range, and Fig. 5b has target at samples around 13,900. We plot the echo differences between Figs. 5a and 5b in Fig. 5c. However, it is impossible to identify whether there is any target and where there is target based on Fig. 5c. Since significant pulse-to-pulse variability exists in the echos, this motivate us to explore the spatial and time diversity using Radar Sensor Networks (RSN).

In RSN, the radar sensors are networked together in an ad hoc fashion. They do not rely on a preexisting fixed infrastructure, such as a wireline backbone network or a base station. They are self-organizing entities that are deployed on demand in support of various events surveillance, battlefield, disaster relief, search and rescue, etc. Scalability concern suggests a hierarchical organization of radar sensor networks with the lowest level in the hierarchy being a cluster. As argued in [11] [8] [7] [19], in addition to helping with scalability and robustness, aggregating sensor nodes into clusters has additional benefits:

1. conserving radio resources such as bandwidth;
2. promoting spatial code reuse and frequency reuse;
3. simplifying the topology, e.g., when a mobile radar changes its location, it is sufficient for only the nodes in attended clusters to update their topology information;
4. reducing the generation and propagation of routing information; and,
5. concealing the details of global network topology from individual nodes.

In RSN, each radar can provide their pulse parameters such as timing to their clusterhead radar, and the clusterhead radar can combine the echos (RF returns) from the target and clutter. In this paper, we propose a RAKE structure for combining echos, as illustrated by Fig. 6. The integration

means time-average for a sample duration T and it's for general case when the echos are not in discrete values. It is quite often assumed that the radar sensor platform will have access to Global Positioning Service (GPS) and Inertial Navigation Unit (INU) timing and navigation data [15]. In this paper, we assume the radar sensors are synchronized in RSN. In Fig. 6, the echo, i.e., RF response by the pulse of each cluster-member sensor, will be combined by the clusterhead using a weighted average, and the weight w_i is determined by the two human-inspired mechanisms.

We applied the human-inspired MLE algorithm to combine the sensed echo collection from $M = 30$ UWB radars, and then the combined data are processed using discrete-cosine transform (DCT) to obtain the AC values. Based on our experiences, echo with a target generally has high and nonfluctuating AC values and the AC values can be obtained using DCT. We plot the power of AC values in Figs. 7a and 7b using MLE and DCT algorithms for the two cases (with target and without target) respectively. Observe that in Fig. 7b, the power of AC values (around sample 13,900) where the target is located is non-fluctuating (somehow monotonically increase then decrease). Although some other samples also have very high AC power values, it is very clear that they are quite fluctuating and the power of AC values behaves like random noise because generally the clutter has Gaussian distribution in the frequency domain.

Similarly, we applied the soft-max algorithm ($n = 2$) to combine the sensed echo collection from $M = 30$ UWB radars, and then used DCT to obtain the AC values. We plot the power of AC values in Figs. 7a and 7b using soft-max and DCT algorithms for the two cases (with target and without target) respectively. Observe that in Fig. 8b, the power of AC values (around sample 13,900) where the target is located is non-fluctuating (somehow monotonically increase then decrease).

We made the above observations. However, in real world application, automatic target detection is necessary to ensure that our algorithms could be performed in real time. In Section 5, we apply fuzzy logic systems to automatic target detection based on the power of AC values (obtained via

MLE-DCT or soft-max-DCT).

We compared our approaches to the scheme proposed in [20]. In [20], 2-D image was created via adding voltages with the appropriate time offset. In Figs. 9a and 9b, we plot the 2-D image created based on the above two data sets (from samples 13,800 to 14,200). The sensed data from 30 radars are averaged first, then plotted in 2-D [20]. However, it's not clear which image shows there is target on range.

5 Fuzzy Logic System for Automatic Target Detection

5.1 Overview of Fuzzy Logic Systems

Figure 10 shows the structure of a fuzzy logic system (FLS) [12]. When an input is applied to a FLS, the inference engine computes the output set corresponding to each rule. The defuzzifer then computes a crisp output from these rule output sets. Consider a p-input 1-output FLS, using singleton fuzzification, *center-of-sets* defuzzification [12] and "IF-THEN" rules of the form

$$R^l : \text{IF } x_1 \text{ is } \mathrm{F}_1^l \text{ and } x_2 \text{ is } \mathrm{F}_2^l \text{ and } \cdots \text{ and } x_p \text{ is } \mathrm{F}_p^l, \text{ THEN } y \text{ is } \mathrm{G}^l.$$

Assuming singleton fuzzification, when an input $\mathbf{x}' = \{x_1', \ldots, x_p'\}$ is applied, the degree of firing corresponding to the lth rule is computed as

$$\mu_{\mathrm{F}_1^l}(x_1') \star \mu_{\mathrm{F}_2^l}(x_2') \star \cdots \star \mu_{\mathrm{F}_p^l}(x_p') = \mathcal{T}_{i=1}^{p} \mu_{\mathrm{F}_i^l}(x_i') \tag{2}$$

where $\star$ and $\mathcal{T}$ both indicate the chosen t-norm. There are many kinds of defuzzifiers. In this paper, we focus, for illustrative purposes, on the center-of-sets defuzzifier [12]. It computes a crisp output for the FLS by first computing the centroid, c_{G^l}, of every consequent set G^l, and, then computing a weighted average of these centroids. The weight corresponding to the lth rule consequent centroid

is the degree of firing associated with the lth rule, $\mathcal{T}_{i=1}^{p}\mu_{\mathrm{F}_i^l}(x_i')$, so that

$$y_{cos}(\mathbf{x}') = \frac{\sum_{l=1}^{M} c_{\mathrm{G}^l}\mathcal{T}_{i=1}^{p}\mu_{\mathrm{F}_i^l}(x_i')}{\sum_{l=1}^{M}\mathcal{T}_{i=1}^{p}\mu_{\mathrm{F}_i^l}(x_i')} \tag{3}$$

where M is the number of rules in the FLS. In this paper, we design a FLS for automatic target recognition based on the AC values obtained using MLE-DCT or soft-max-DCT.

5.2 FLS for Automatic Target Detection

Observe that in Figs. 7 and 8, the power of AC values are quite fluctuating and have lots of uncertainties. FLS is well known to handle the uncertainties. For convenience in describing the FLS design for Automatic Target Detection (ATD), we first give the definition of *footprint of uncertainty* of AC power values and *region of interest* in the footprint of uncertainty.

Definition 1 (Footprint of Uncertainty) *Uncertainty in the AC power values and time index consists of a bounded region, that we call the* footprint of uncertainty *of AC power values. It is the union of all AC power values.*

Definition 2 (Region of Interest (RoI)) *An RoI in the footprint of uncertainty is a contour consisting of a large number (greater than 50) of AC power values where AC power values increase then decrease.*

Definition 3 (Fluctuating Point in RoI) $P(i)$ *is called a* fluctuating point *in the RoI if* $P(i-1), P(i), P(i+1)$ *are non-monotonically increasing or decreasing.*

Our FLS for automatic target detection will classify each ROI (with target or no target) based on two antecedents: *the centroid of the ROI* and *the number of fluctuating points in the ROI*. The linguistic variables used to represent these two antecedents were divided into three levels: *low*, *moderate*, and *high*. The consequent – the possibility that there is a target at this RoI – was divided

into 5 levels, *Very Strong, Strong, Medium, Weak, Very Weak*. We used trapezoidal membership functions (MFs) to represent *low*, *high*, *very strong*, and *very weak*; and triangle MFs to represent *moderate*, *strong*, *medium*, and *weak*. All inputs to the antecedents are normalized to 0–10.

Based on the fact the AC power value of target is non-fluctuating (somehow monotonically increase then decrease), and the AC power value of clutter behaves like random noise because generally the clutter has Gaussian distribution in the frequency domain, we design a fuzzy logic system using rules such as:

R^l : IF *centroid of a RoI* (x_1) is F_l^1, and *the number of fluctuating points in the ROI* (x_2) is F_l^2,

THEN the possibility that there is a target at this RoI (y) is G^l.

where $l = 1, \ldots, 9$. We summarize all the rules in Table 1. For every input (x_1, x_2), the output is computed using

$$y(x_1, x_2) = \frac{\sum_{l=1}^{9} \mu_{\mathrm{F}_l^1}(x_1)\mu_{\mathrm{F}_l^2}(x_2)c_{avg}^l}{\sum_{l=1}^{9} \mu_{\mathrm{F}_l^1}(x_1)\mu_{\mathrm{F}_l^2}(x_2)} \tag{4}$$

We ran simulations to 1000 collections in the real world sense-through-foliage experiment, and found that our FLS performs very well in the automatic target detection based on the AC power values obtained from MLE-DCT or soft-max-DCT, and achieve probability of detection $p_d = 100\%$ and false alarm rate $p_{fa} = 0$.

6 Conclusions

Inspired by human's innate ability to process and integrate information from disparate, network-based sources, we applied human-inspired information integration mechanisms to target detection in cognitive radar sensor network. Humans' information integration mechanisms have been modelled using maximum-likelihood estimation (MLE) or soft-max approaches. In this paper, we applied these two algorithms to cognitive radar sensor networks target detection. Discrete-cosine-transform

(DCT) was used to process the integrated data from MLE or soft-max. We applied fuzzy logic system (FLS) to automatic target detection based on the AC power values from DCT. Simulation results showed that our MLE-DCT-FLS and soft-max-DCT-FLS approaches performed very well in the radar sensor network target detection, whereas the existing 2-D construction algorithm couldn't work in this study.

Acknowledgement

This work was supported in part by U.S. Office of Naval Research (ONR) under Grant N00014-07-1-0395, N00014-07-1-1024, N00014-03-1-0466, and National Science Foundation (NSF) under Grant CNS-0721515.

References

[1] D. K. Barton, *Radar System Analysis and Modeling*, Artech House, Boston, MA, 2006.

[2] C. Bruce C, R. Desimone, C. G. Gross, "Visual properties of neurons in a polysensory area in superior temporal sulcus of the macaque," *J. Neurophysiol.*, vol. 46 369 84, 1981.

[3] D. A. Chavis, D. N. Pandya, "Further observations on cortico-frontal connections in the rhesus monkey," *Brain Res.*, vol. 117, pp. 369386, 1976.

[4] B. A. Dosher, G. Sperling, and S. A. Wurst, "Tradeoffs between stereopsis and proximity luminance covariance as determinants of perceived 3D structure," *Vision Research*, vol. 26, No. 6, pp. 973-990, 1986.

[5] N. V. S. Graham, "Visual pattern analyzers," pp. xvi, 646, New York, NY, US: Oxford University Press, 1989.

[6] J. M. Hillis, M. O. Ernst, M. S. Banks, and M. S. Landy, "Combining sensory information: Mandatory fusion within, but not between, senses," *Science*, vol. 298, No. 5598, pp. 1627-1630, 2002.

[7] T.-C. Hou and T-J. Tsai, " An access-based clustering protocol for multihop wireless ad hoc networks," *IEEE J. Selected Areas in Communications*, vol. 19, no. 7, pp. 1201-1210, July 2001.

[8] A. Iwata, C. C. Chiang, G. Pei, M. Gerla, and T. W. Chen, " Scalable routing strategies for ad hoc networks," *IEEE J. Selected Areas in Communications*, vol. 17, pp. 1369-1379, 1999.

[9] E. G. Jones, T. P. S. Powell, An anatomical study of converging sensory pathways within the cerebral cortex of the monkey," *Brain*, vol. 93, pp. 793-820, 1970.

[10] Q. Liang, "Biologically-Inspired Target Recognition in Radar Sensor Networks," *International Conference on Wireless Algorithms, Systems, and Applications*, August 2009, Boston, MA.

[11] C. R. Lin and M. Gerla, "Adaptive clustering in mobile wireless networks," *IEEE J. Selected Areas in Communications*, vol. 16, pp. 1265-1275, 1997.

[12] J. M. Mendel, *Uncertain Rule-Based Fuzzy Logic Systems*, Prentice-Hall, Upper Saddle River, NJ, 2001.

[13] E. K. Miller, "The prefrontal cortex: complex neural properties for complex behavior," *Neuron*, vol. 22, pp. 1517, 1999.

[14] E. K. Miller, J. D. Cohen, "An Integrative Theory of Prefrontal cortex function," *Annu. Rev. Neurosci.*, vol. 24, pp. 167, 2001.

[15] ONR BAA 07-017, "NET-SENTRIC Surveillance," http://www.onr.navy.mil/02/baa/.

[16] R. C. OReilly, "Biologically Based Computational Models of High-Level Cognition," *Science*, Oct 2006.

[17] D. N. Pandya, C. Barnes, "Architecture and connections of the frontal lobe," *The Frontal Lobes Revisited*, ed. E Perecman, pp. 41 72. New York: IRBN, 1987.

[18] D. G. Pelli, "Uncertainty explains many aspects of visual contrast detection and discrimination," *Journal of the Optical Society of America*, vol. A, No. 2, pp. 1508-1532, 1985.

[19] C. E. Perkins, "Chapter 4, Cluster-Based Networks," *Ad Hoc Networking*, Edited by C. E. Perkins, pp. 75-138, Addison-Wesley, 2001.

[20] P. Withington , H. Fluhler, and S. Nag , "Enhancing homeland security with advanced UWB sensors," *IEEE Microwave Magazine*, Sept 2003.

List of Tables

1 The rules for target detection. Antecedent 1 is *centroid of a RoI*, Antecedent 2 is *the number of fluctuating points in the ROI*, and Consequent is *the possibility that there is a target at this RoI*. 14

Table 1: The rules for target detection. Antecedent 1 is *centroid of a RoI*, Antecedent 2 is *the number of fluctuating points in the ROI*, and Consequent is *the possibility that there is a target at this RoI*.

Rule #	Antecedent 1	Antecedent 2	Consequent
1	low	low	medium
2	low	moderate	weak
3	low	high	very weak
4	moderate	low	strong
5	moderate	moderate	medium
6	moderate	high	weak
7	high	low	very strong
8	high	moderate	strong
9	high	high	medium

List of Figures

1 Schematic diagram of some of the extrinsic and intrinsic connections of the PFC. Most connections are reciprocal; the exceptions are indicated by arrows. The frontal eye field (FEF) has variously been considered either adjacent to, or part of, the PFC. 15

2 This figure shows the lift with the experiment. The antennas are at the far end of the lift from the viewer under the roof that was built to shield the equipment from the elements. This picture was taken in September with the foliage largely still present. The cables coming from the lift are a ground cable to an earth ground and one of 4 tethers used in windy conditions. 16

3 The target (a trihedral reflector) is shown on the stand at 300 feet from the lift. . . 17

4 Transmitted pulse and received echos in one experiment. (a) Transmitted pulse. (b) Received echos. 18

5 Measurement with 35 pulses average. (a) Expanded view of traces (no target) from sample 13,001 to 15,000. (b) Expanded view of traces (with target) from samples 13,001 to 15,000. (c) The differences between (a) and (b). 19

6 Echo combining by clusterhead in RSN. 20

7 Power of AC values using MLE-based information integration and DCT. (a) No target (b) With target in the field. 21

8 Power of AC values using soft-max based information integration and DCT. (a) No target (b) With target in the field. 22

9 2-D image created via adding voltages with the appropriate time offset. (a) No target (b) With target in the field. 23

10 The structure of a fuzzy logic system. 24

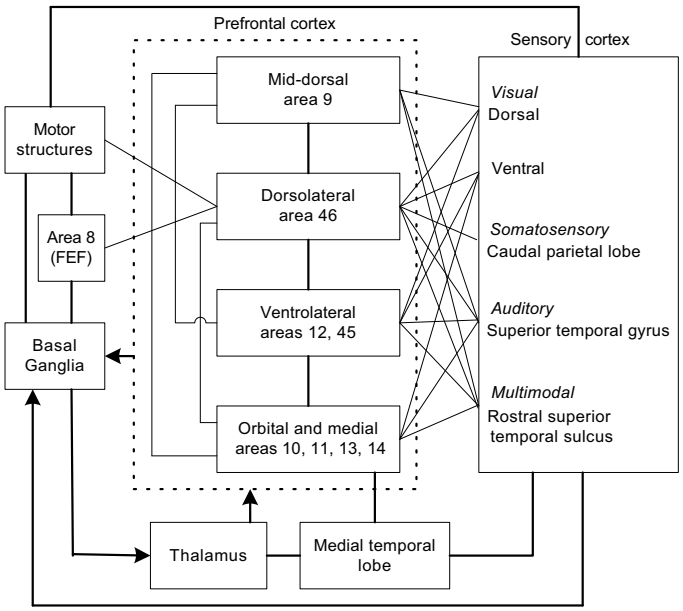


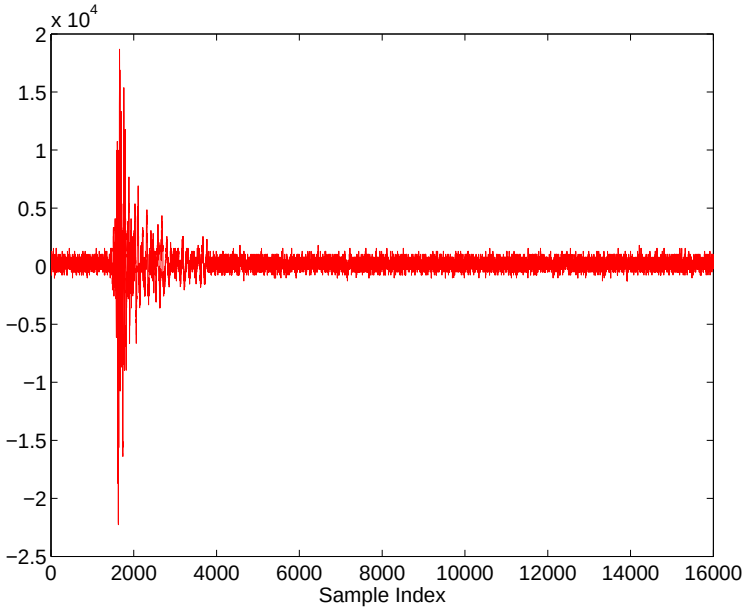
Figure 1: Schematic diagram of some of the extrinsic and intrinsic connections of the PFC. Most connections are reciprocal; the exceptions are indicated by arrows. The frontal eye field (FEF) has variously been considered either adjacent to, or part of, the PFC.



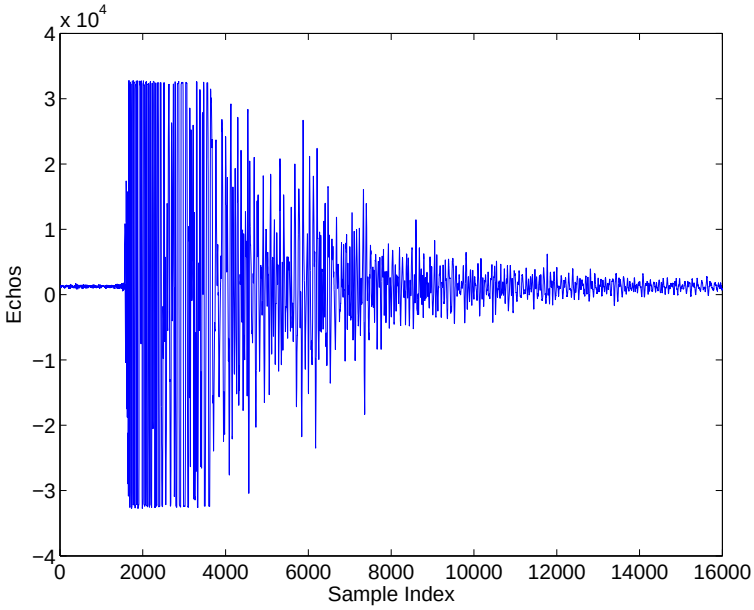
Figure 2: This figure shows the lift with the experiment. The antennas are at the far end of the lift from the viewer under the roof that was built to shield the equipment from the elements. This picture was taken in September with the foliage largely still present. The cables coming from the lift are a ground cable to an earth ground and one of 4 tethers used in windy conditions.



Figure 3: The target (a trihedral reflector) is shown on the stand at 300 feet from the lift.



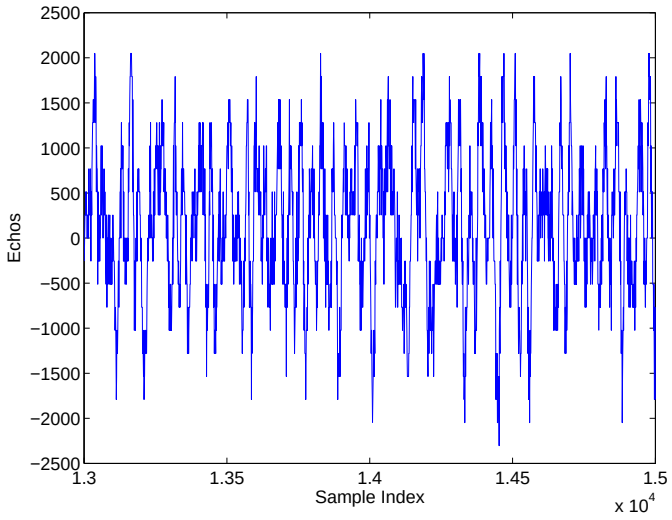
(a)



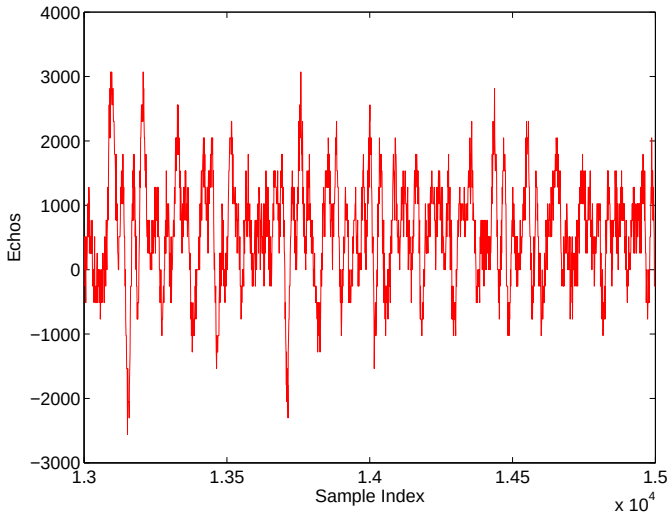
(b)

Figure 4: Transmitted pulse and received echos in one experiment. (a) Transmitted pulse. (b) Received echos.

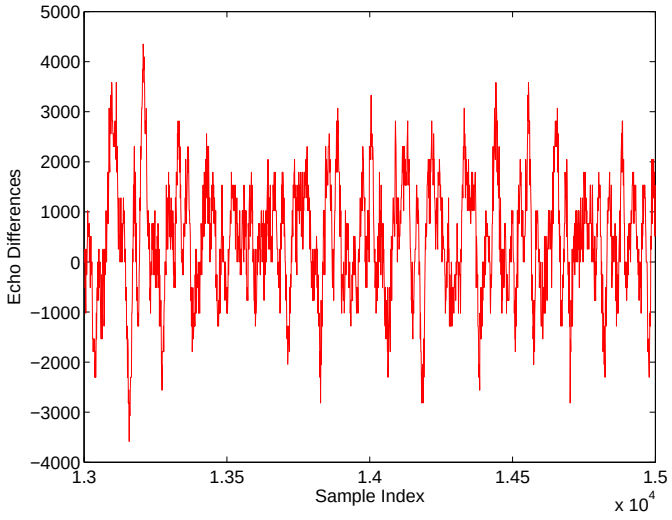
.



(a)



(b)



(c)

Figure 5: Measurement with 35 pulses average. (a) Expanded view of traces (no target) from sample 13,001 to 15,000. (b) Expanded view of traces (with target) from samples 13,001 to 15,000. (c) The differences between (a) and (b).

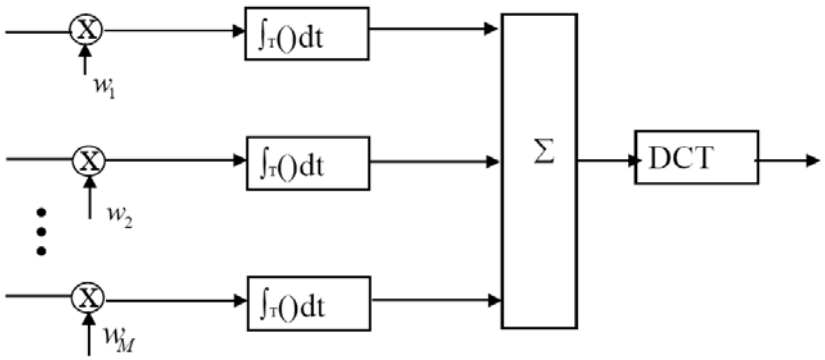
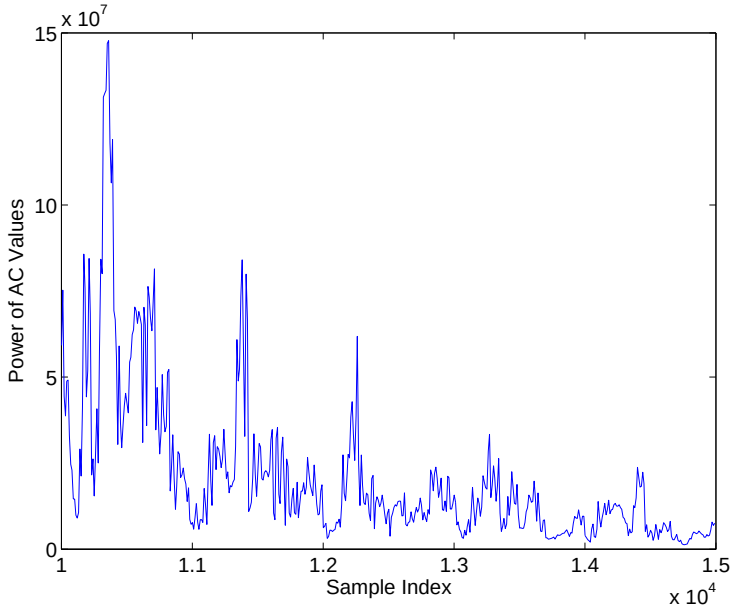
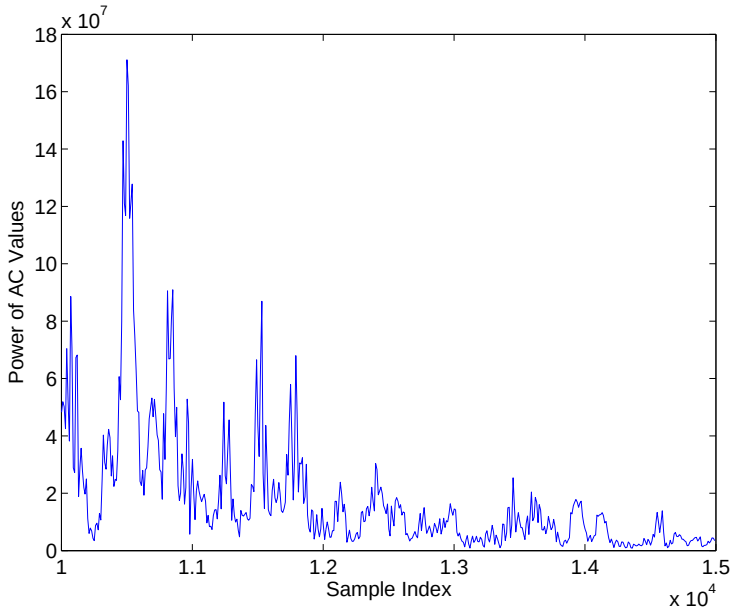


Figure 6: Echo combining by clusterhead in RSN.

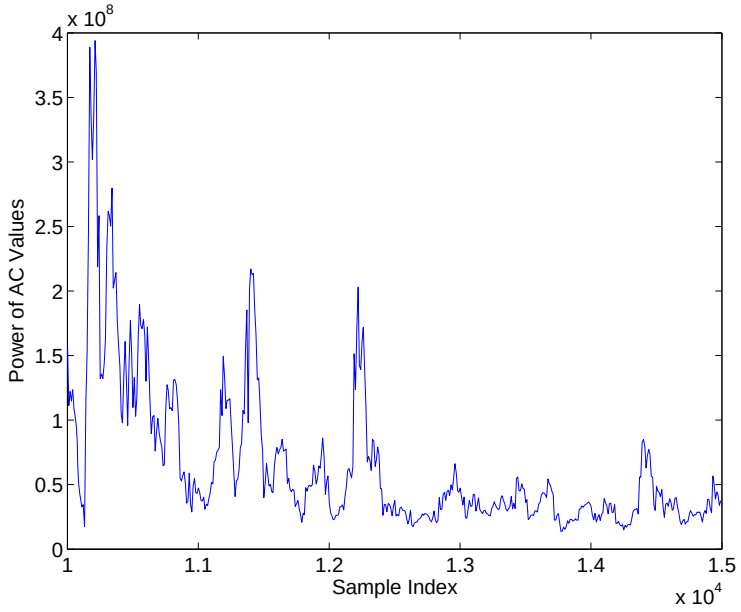


(a)

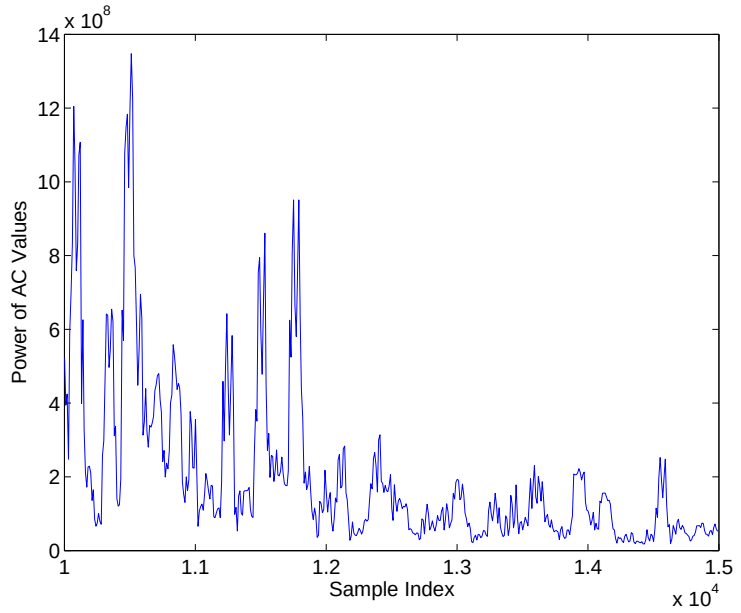


(b)

Figure 7: Power of AC values using MLE-based information integration and DCT. (a) No target (b) With target in the field.

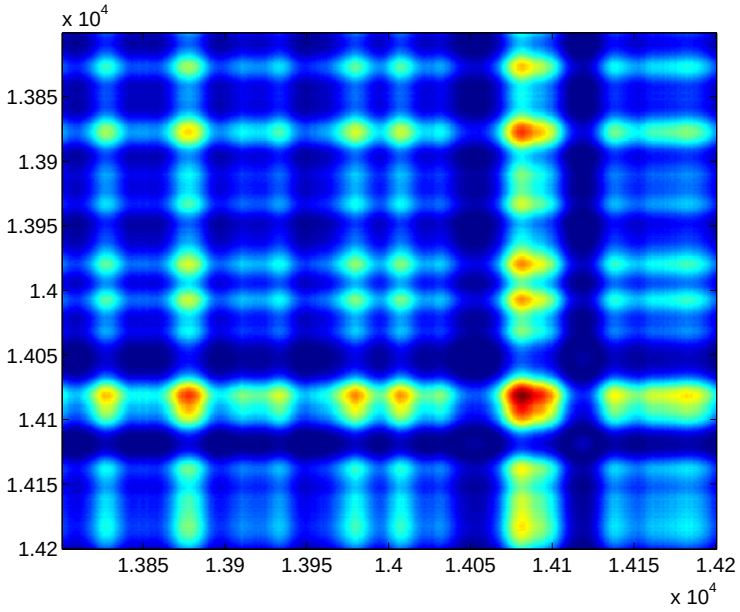


(a)

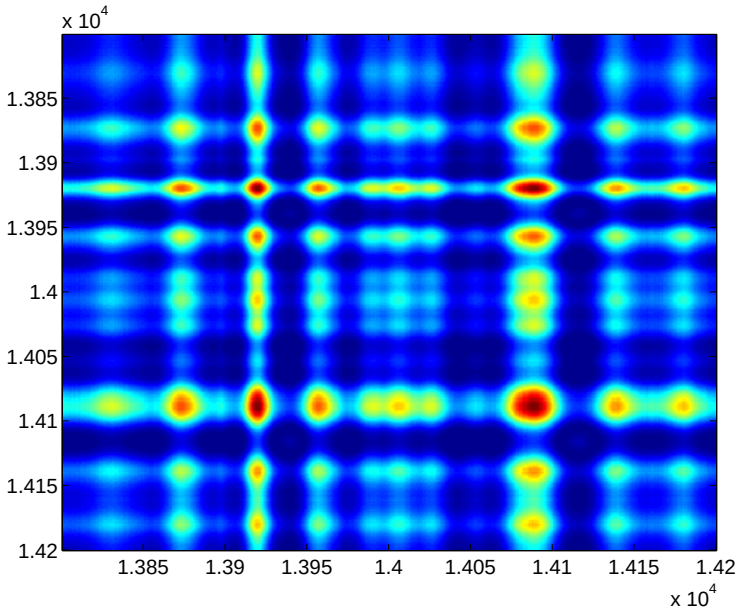


(b)

Figure 8: Power of AC values using soft-max based information integration and DCT. (a) No target (b) With target in the field.



(a)



(b)

Figure 9: 2-D image created via adding voltages with the appropriate time offset. (a) No target (b) With target in the field.

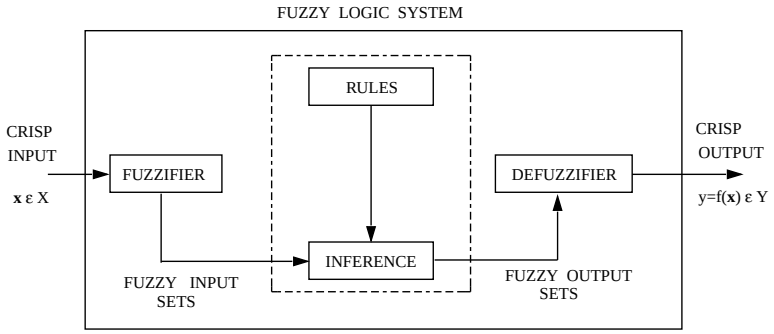


Figure 10: The structure of a fuzzy logic system.

Channel Selection in Virtual MIMO Wireless Sensor Networks

Jing Liang, *Student Member, IEEE*, and Qilian Liang, *Senior Member, IEEE*

***Abstract*—In this paper, we present two practical algorithms for selecting a subset of channels in virtual multiple-input–multiple-output (MIMO) wireless sensor networks (WSNs) to balance the MIMO advantage consumption of sensor cooperation. If intracluster node-to-node multihop needs be taken into account, the maximum spanning tree searching (MASTS) algorithm, with respect to the cross-layer design, always provides a path connecting all sensors. When the WSN is organized in a manner of cluster-to-cluster multihop, the singular-value decomposition-QR with threshold (SVD-QR-T) approach selects the best subset of transmitters while keeping all receivers active. The threshold is adaptive by means of fuzzy c-means (FCM). These two approaches are compared by simulation against the case without channel selection in terms of capacity, bit error rate (BER), and multiplexing gain with water filling or equal transmission power allocation. Despite less multiplexing gain, when water filling is applied, MASTS achieves higher capacity and lower BER than virtual MIMO without channel selection at moderate-to-high signal-to-noise ratio (SNR), whereas SVD-QR-T by FCM provides the lowest BER at high SNR; in the case of no water filling and equal transmission power allocation, MASTS still offers the highest capacity at moderate-to-high SNR, but SVD-QR-T by FCM achieves the lowest BER. Both algorithms provide satisfying performances with reduced resource consumption.**

***Index Terms*—Channel selection, fuzzy c-means (FCM), maximal spanning tree, singular-value decomposition-QR (SVD-QR), virtual multiple-input–multiple-output (MIMO), wireless sensor networks (WSNs).**

I. Introduction

VIRTUAL multiple-input–multiple-output (MIMO) communication-based wireless sensor networks (WSNs) have intensively been studied in recent years. Constrained by its physical size and limited battery, an individual sensor node is allowed to accommodate only one antenna. Numerical results show that if these sensors can be constructed into cooperative MIMO systems, over certain distance ranges, they may outperform single-input–single-output systems in energy consumption [1], [2].

Manuscript received October 24, 2007; revised March 28, 2008 and June 3, 2008. First published August 26, 2008; current version published May 11, 2009. This work was supported in part by the Office of Naval Research under Grant N00014-07-1-0395 and Grant N00014-07-1-1024 and in part by the National Science Foundation under Grant CNS-0721515 and Grant CNS-0831902. The review of this paper was coordinated by Prof. H. H. Nguyen.

The authors are with the Department of Electrical Engineering, University of Texas, Arlington, TX 76019 USA (e-mail: jliang@wcn.uta.edu; liang@uta.edu).

Color versions of one or more of the figures in this paper are available online at http://ieeexplore.ieee.org.

Digital Object Identifier 10.1109/TVT.2008.2004705

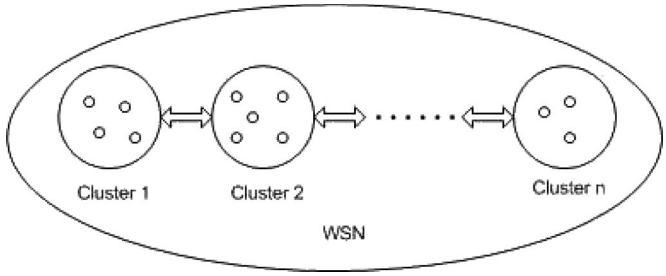


Fig. 1. Cooperative clusters in multihop WSNs.

To encompass both wireless and networking communications, virtual-MIMO-based WSNs have so far been extended by incorporating the multihop routings and hop-by-hop recovery schemes [3], [4]. This model is shown in Fig. 1. Assume that the multihop WSNs consist of n clusters. Here, the cluster refers to a group of closely gathered wireless sensors that have been cooperated as multiple transmitters or receivers. If each cluster consists of $c_i, i = 1, 2, \ldots, n$ sensor nodes, respectively, then the radio-frequency (RF) chains for this virtual MIMO WSN system will turn out to be $\prod_{i=1}^{n} c_i$, which implies tremendous circuit energy consumption, along with the increase in n. Provided that the energy and delay cost associated with the local information exchange have to be taken into account, cooperative virtual MIMO WSN may not always guarantee to be effective.

In this paper, we investigate a methodology called *channel selection*, with the aim of balancing the MIMO advantage and the complexity of sensor cooperation. This channel-selection-based virtual MIMO WSN model is shown in Fig. 2. It is a common scenario that sensor nodes (denoted by circles) are efficiently grouped into clusters by means of [5]–[8] while cluster heads (denoted by triangles) [9] offer centralized control over cooperative virtual MIMO channels. These cluster heads are not subject to strict energy constrains, but others are [2]. At first, channel side information (CSI) may be obtained by various channel estimation techniques, such as the reciprocity principle and a feedback channel [10]. Then, channel selection may be applied through subset selection algorithms using switches placed at either the transmitting or the receiving cluster head, or jointly working at both ends. Therefore, the best set of channels is selected to be active, whereas the remaining channels are not employed. Since, at some hops, transmissions are turned off, energy will be saved during the virtual MIMO communications [13], [14]. If the same total transmitting power is allocated to the best subset of channels, the performances after channel selection such as capacity and BER may even be better, compared to those before channel selection.

0018-9545/$25.00 © 2009 IEEE

Authorized licensed use limited to: University of Texas at Arlington. Downloaded on December 18, 2009 at 13:47 from IEEE Xplore. Restrictions apply.

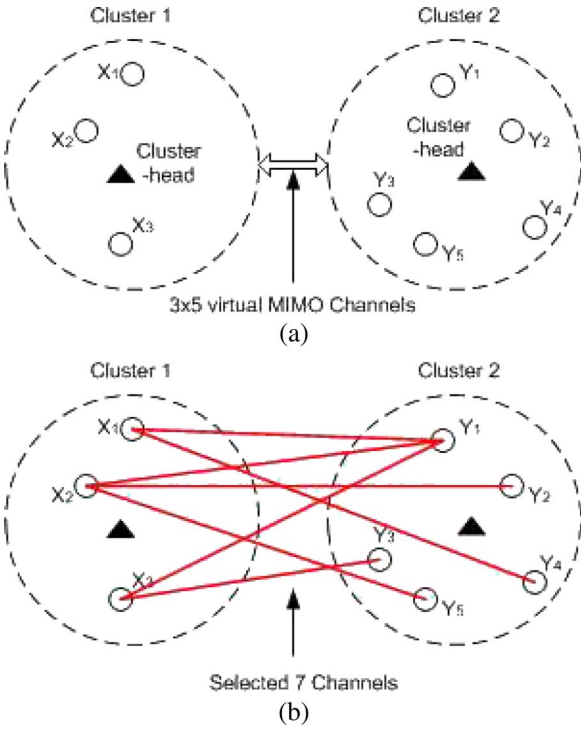


Fig. 2. System illustration for virtual MIMO channel selection. (a) Before channel selection. (b) After channel selection.

It is worth mentioning that the energy consumption introduced by collecting CSI is indispensable for the proper operation of virtual MIMO. In [1], MIMO fading channels are presented as a scalar matrix, which implies that CSI is assumed to be known; however, the overhead computation for CSI is ignored. Jayaweera [2] takes into account this extra training energy to provide a fair comparison and demonstrates that, if the system is designed with judicious parameters, significant energy efficiency can be achieved after all.

This paper proposes two channel-selection algorithms for different situations. One is the maximum spanning tree searching (MASTS) approach; the other is singular-value decomposition-QR with threshold (SVD-QR-T) by fuzzy c-means (FCM). In general, Monte Carlo simulation results show that, in spite of less multiplexing gain, when water filling is applied, MASTS achieves higher capacity and lower BER than virtual MIMO without channel selection at moderate-to-high signal-to-noise ratio (SNR), whereas SVD-QR-T by FCM provides the lowest BER at high SNR; in the case of no water filling and equal transmission power allocation, MASTS still offers the highest capacity at moderate-to-high SNR, but SVD-QR-T by FCM achieves the lowest BER. Both approaches provide satisfying performances with reduced RF resource compared with the case without channel selection.

The remainder of this paper is organized as follows: Section II proposes the MASTS and SVD-QR-T by FCM algorithms with concrete examples for virtual MIMO channel selection. Section III estimates their performances in terms of capacity, BER, and multiplexing gain. Section IV draws the conclusion.

II. Channel-Selection Algorithm

A. Problem Formulation

Among the existing research on conventional MIMO channel selection, four criteria have been used.

1) Capacity maximization: In previous works [15]–[17], channel capacity is used as the optimality criterion, i.e., antennas that achieve the largest capacity are active.
2) Minimum error rate: Apart from maximization of capacity based on the Shannon theory, Heath and Paulraj [18] derived another criteria from the aspect of minimum error rate when coherent receivers, either maximum likelihood, zero forcing, or a minimum mean-square error linear receiver is employed.
3) SNR maximization: In [19], antenna selection is performed only at the receiver based on the largest instantaneous SNR using space-time coding (STC). It is analytically shown that the full diversity advantage promised by MIMO can fully be exploited using this criterion as long as the space-time code employed has full spatial diversity.
4) Cross-layer optimal scheduling: In addition to the physical layer, some related works have adopted the graph theory approach to consider the cross-layer design. Choi *et al.* performed the optimal antenna assignment for spatial multiplexing by Hungarian algorithm using a weighted bipartite matching graph [20] and took into account users' quality-of-service (QoS) requirement with a clique-searching algorithm for antenna selection [21].

Although the aforementioned criteria have provided dazzling mathematical standards, one problem is how to accommodate them in the WSN rather than traditional communications; the other problem is how to encompass intracluster or intercluster multihop connectivity to better support the networking capability and QoS requirement.

We shall answer these questions in two steps.

1) If intracluster sensor-to-sensor multihop must be taken into account, we suggest the MASTS algorithm based on Kruskal's theory [22] from the aspect of graph theory. The idea behind the scheme is that selected channels not only provide better channel gain but also act as a connected path between two arbitrary sensor nodes to perfectly serve the upper layer routing and networking. Take Fig. 2(b) as an example; these channels denoted by red lines have been selected based on MASTS. It is obvious that, between any two nodes $X_iY_j, i = 1, 2, 3, j = 1, \ldots, 5$; $X_iX_j, i = 1, 2, 3, j = 1, 2, 3, i \neq j$; or $Y_iY_j, i = 1, \ldots, 5, y = 1, \ldots, 5, i \neq j$, there is a path connecting them through single hop or multihop. Due to the inherent link layer connectivity, MASTS can be referred to as a cross-layer design.
2) If the WSN is organized in a manner of cluster-to-cluster multihop (as shown in Fig. 1), we propose an SVD-QR-T virtual MIMO channel-selection approach employing FCM to virtually provide an adaptive threshold. Since current multihop theory and routing algorithms can be applied by the upper layers, we only focus on the physical

Authorized licensed use limited to: University of Texas at Arlington. Downloaded on December 18, 2009 at 13:47 from IEEE Xplore. Restrictions apply.

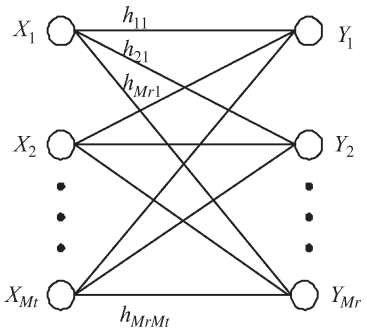


Fig. 3. Graphic channel model for virtual MIMO.

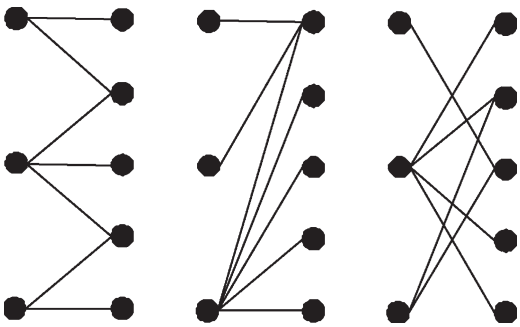


Fig. 4. Examples of spanning trees for a 3×5 virtual MIMO.

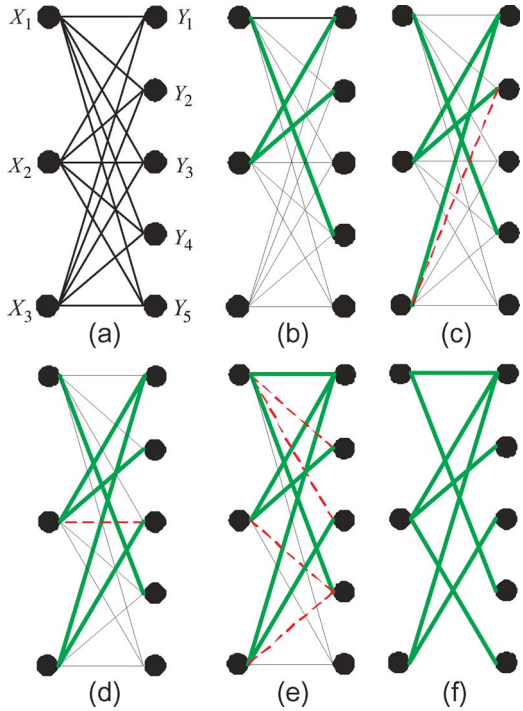


Fig. 5. MASTS algorithm.

layer design. This approach selects the $rt \times M_r$ best subsets of channels (see Section II-C1 for rt; M_r is the number of receivers) while keeping rt transmitting sensors and all of the receiving sensors active.

B. MASTS

1) MASTS Design: A virtual MIMO communication scenario can simply be presented by equation $\mathbf{Y} = \mathbf{HX} + \mathbf{n}$, where $\mathbf{H}$ is an $Mr \times Mt$ channel matrix and $\mathbf{n}$ denotes the random Gaussian noise. The MIMO channel model with M_t transmitting sensors and M_r receiving nodes is shown in Fig. 3, where each receiver observes a superposition of the M_t transmitted signals corrupted by the flat fading and additive white Gaussian noise. Each h_{ij}, where $i = 1, 2, \ldots, M_r$ and $j = 1, 2, \ldots, M_t$, represents the channel gain from transmitter j to receiver i [23], which is assumed to be Rayleigh independent identically distributed (i.i.d.). The additive noise also has i.i.d. entries $n_j \sim \mathcal{CN}(0, \sigma^2)$. From the aspect of graph theory, the vertex set and edge set consist of sensors and channels, respectively, and Fig. 3 shows a connected graph [24], i.e., there is a path connecting two arbitrary nodes, with h_{ij} denoting its edge weight.

Global connectivity is usually required for WSNs [25], [26]. When node-to-node multihop needs to be considered, the channel selection scheme has to incorporate routing connectivity inside a cluster, aside from pure physical communications. A spanning tree [24] suggests an algorithm in which, in an arbitrary graph, all the vertices are connected with the minimum necessary edges, i.e., there is no isolated vertices under the condition of the least possible edge number. For example, when $Mt = 3$ and $Mr = 5$, some of the possible spanning trees are shown in Fig. 4.

The MASTS approach is to compute a spanning tree with the maximum sum of edge weight, i.e., to select the maximum sum of channel gain while realizing the connectivity of all the sensors. Note that, for an arbitrary graph of n vertices, its spanning tree consists of n vertices and $n - 1$ edges [24]. Since there are $Mt + Mr$ vertices, the number of edges to be selected by the MASTS algorithm is a fixed $Mt + Mr - 1$, which means that MASTS always chooses $Mt + Mr - 1$ channels. The MASTS algorithm can be presented in three steps.

Step 1: Select the three edges with the highest weight and their vertices.

Step 2: Enlarge the subgraph by edges with decreasing weight, and make sure that no cycles are formed.

Step 3: Continue Step 2 until the number of edges in the enlarged subgraph is equal to $Mt + Mr - 1$. This final subgraph is the spanning tree with the maximum sum of weight.

2) Example of MASTS: As a virtual MIMO graph contains the same information as that of channel gain matrix $\mathbf{H}$, we illustrate the MASTS algorithm in Fig. 5 and though matrices $\mathbf{H}_b\mathbf{H}_c\mathbf{H}_d\mathbf{H}_e\mathbf{H}_g$.

Fig. 5(a) shows the original virtual MIMO graph. Fig. 5(b) shows the subgraph with the three highest edge weights. These edges are denoted by $\langle\rangle$ in matrix $\mathbf{H}_b$, i.e.,

$$\mathbf{H}_b = \begin{bmatrix} 0.6211 & \langle 0.7536 \rangle & 0.6595 \\ 0.5602 & \langle 0.6596 \rangle & 0.1834 \\ 0.2440 & 0.2141 & 0.6365 \\ \langle 0.8220 \rangle & 0.6021 & 0.1703 \\ 0.2632 & 0.6049 & 0.5396 \end{bmatrix}.$$

This is Step 1.

Authorized licensed use limited to: University of Texas at Arlington. Downloaded on December 18, 2009 at 13:47 from IEEE Xplore. Restrictions apply.

Note that, among the three selected entries, 0.8220 has a different row index from that of 0.7536 or 0.6595, so enlarging this subgraph with any of the remaining edges will absolutely not form a cycle.

Thus, the second step starts with selecting the edge with the fourth highest weight, which is shown in Fig. 5(c) and by matrix $\mathbf{H}_c$, i.e.,

$$\mathbf{H}_c = \begin{bmatrix} 0.6211 & \langle 0.7536\rangle & \langle 0.6595\rangle \\ 0.5602 & \langle 0.6596\rangle & 0.1834\times \\ 0.2440 & 0.2141 & 0.6365 \\ \langle 0.8220\rangle & 0.6021 & 0.1703 \\ 0.2632 & 0.6049 & 0.5396 \end{bmatrix}.$$

Note that, after the selection of entry 0.6595, entry 0.1834 will no longer be selected; else, a cycle $X_2Y_1X_3Y_2$ will form. Thus, we note entry 0.1834 with "$\times$" and use a dashed line to represent the unavailability of the corresponding edge in Fig. 5(c). This implies the following criteria:

Criteria: Any four entries with index $(i,j)(i,q)(p,j)(p,q)$, where $i,\ p \le Mr,\ i \ne p;\ j,\ q \le Mt,\ j \ne q$, form a cycle. If any three have been selected, the remaining one should be eliminated.

Based on this condition, we continually select entries as shown in Fig. 5(d)–(f) and matrices $\mathbf{H}_d\mathbf{H}_e\mathbf{H}_f$, i.e.,

$$\mathbf{H}_d = \begin{bmatrix} 0.6211 & \langle 0.7536\rangle & \langle 0.6595\rangle \\ 0.5602 & \langle 0.6596\rangle & 0 \\ 0.2440 & 0.2141\times & \langle 0.6365\rangle \\ \langle 0.8220\rangle & 0.6021 & 0.1703 \\ 0.2632 & 0.6049 & 0.5396 \end{bmatrix}$$

$$\mathbf{H}_e = \begin{bmatrix} \langle 0.6211\rangle & \langle 0.7536\rangle & \langle 0.6595\rangle \\ 0.5602\times & \langle 0.6596\rangle & 0 \\ 0.2440\times & 0 & \langle 0.6365\rangle \\ \langle 0.8220\rangle & 0.6021\times & 0.1703\times \\ 0.2632 & 0.6049 & 0.5396 \end{bmatrix}$$

$$\mathbf{H}_g = \begin{bmatrix} 0.6211 & 0.7536 & 0.6595 \\ 0 & 0.6596 & 0 \\ 0 & 0 & 0.6365 \\ 0.8220 & 0 & 0 \\ 0 & 0.6049 & 0 \end{bmatrix}.$$

As we only have to select $3+5-1=7$ edges, the edges shown in Fig. 5(f) represented by nonzero entries in matrix $\mathbf{H}_g$ are the channels finally selected.

C. SVD-QR-T by FCM

1) SVD-QR-T Design: When cluster-to-cluster multihop turns out to be a major concern and intracluster node-to-node multihop can be ignored, the SVD-QR-T by FCM may work as a practical virtual MIMO channel-selection approach for the physical layer, and multihop theory and routing algorithms can be applied by the upper layers. Singular value decomposition (SVD) has been applied to MIMO channel decomposition in [23] and [27], and sensor node selection in [28]. However, these studies are theoretical analysis only, and no algorithm about which channels will physically be selected in practice has been proposed.

We propose SVD-QR-T in three steps.

1) Given the channel gain matrices $\mathbf{H} \in R^{Mr\times Mt}$ and $r = rank(\mathbf{H}) \le \min(Mt, Mr)$, determine a numerical estimate rt of the rank r by calculating the SVD, i.e.,

$$\mathbf{H} = \mathbf{U}\Sigma\mathbf{V}^T \tag{1}$$

where $\mathbf{U}$ is an $Mr \times Mr$ matrix of orthonormalized eigenvectors of $\mathbf{H}\mathbf{H}^T$, $\mathbf{V}$ is an $Mt \times Mt$ matrix of orthonormalized eigenvectors of $\mathbf{H}^T\mathbf{H}$, and Σ is the diagonal matrix $\Sigma = \mathrm{diag}(\sigma_1, \sigma_2, \ldots, \sigma_i, \ldots, \sigma_r)$, where $\sigma_i = \sqrt{\lambda_i}$. λ_i is the ith eigenvalue of $\mathbf{H}\mathbf{H}^T$, and σ_i is the singular value of $\mathbf{H}$ and $\sigma_1 \ge \sigma_2 \ge \cdots \ge \sigma_r > 0$. In many practical cases, $\sigma_1, \sigma_2, \ldots, \sigma_{rt}$ are much larger than $\sigma_{rt+1}, \ldots, \sigma_r$; thus, we may set a threshold to pick up valuable $\sigma_i, i = 1, 2, \ldots, rt$, and discard those trivial singular values to save resource but maintain a satisfying performance. Sometimes, rt can be much smaller than rank r, e.g., even 1. In this paper, we use FCM to determine rt.

2) Partition

$$\mathbf{V} = \begin{bmatrix} \mathbf{V}_{11} & \mathbf{V}_{12} \\ \mathbf{V}_{21} & \mathbf{V}_{22} \end{bmatrix} \tag{2}$$

where $\mathbf{V}_{11} \in R^{rt\times rt}$, $\mathbf{V}_{12} \in R^{rt\times(Mt-rt)}$, $\mathbf{V}_{21} \in R^{(Mt-rt)\times rt}$, and $\mathbf{V}_{22} \in R^{(Mt-rt)\times(Mt-rt)}$.

3) Using QR decomposition with column pivoting, determine $\mathbf{E}$ such that

$$\left[\mathbf{V}_{11}^T, \mathbf{V}_{21}^T\right]\mathbf{E} = \mathbf{Q}\mathbf{R} \tag{3}$$

where $\mathbf{Q}$ is a unitary matrix, $\mathbf{R} \in R^{rt\times Mt}$ forms an upper triangular matrix with decreasing diagonal elements, and $\mathbf{E}$ is the permutation matrix. The positions of 1 in the first rt columns of $\mathbf{E}$ correspond to the rt ordered *most significant* transmitters.

2) FCM—Unsupervised Clustering for Adaptive Threshold: In this section, we propose the FCM clustering approach to divide singular values $\sigma_1, \sigma_2, \ldots, \sigma_r$ into two clusters that provide a virtual adaptive threshold so the cluster with higher center would remain for active channels.

FCM clustering is a data clustering technique where each data point belongs to a cluster to a certain degree specified by a membership grade. This technique was originally introduced by Bezdek [29] as an improvement on earlier clustering methods. Here, we briefly summarize it.

Definition 1 (Fuzzy C-Partition): Let $\mathbf{X} = x_1, x_2, \ldots, x_n$ be any finite set, $\mathbf{V}_{cn}$ be the set of real $c \times n$ matrices, and c be an integer, where $2 \le c < n$. The *fuzzy c-partition space* for $\mathbf{X}$ is the set

$$M_{fc} = U \in V_{cn} | u_{ik} \in [0,1] \qquad \forall i,k \tag{4}$$

where $\sum_{i=1}^{c} u_{ik} = 1 \forall k$, and $0 < \sum_{k=1}^{n} u_{ik} < n \forall i$. Row i of matrix $U \in M_{fc}$ contains values of the ith membership function u_i in the fuzzy c-partition U of $\mathbf{X}$.

Authorized licensed use limited to: University of Texas at Arlington. Downloaded on December 18, 2009 at 13:47 from IEEE Xplore. Restrictions apply.

Definition 2 (FCM Functionals) [29]: Let J_m: $M_{fc} \times \mathcal{R}^{cp} \rightarrow \mathcal{R}^{+}$ be

$$J_m(\mathbf{U}, \mathbf{v}) = \sum_{k=1}^{n} \sum_{i=1}^{c} (u_{ik})^m (d_{ik})^2 \tag{5}$$

where $\mathbf{U} \in M_{fc}$ is a fuzzy c-partition of X; $\mathbf{v} = (\mathbf{v}_1, \mathbf{v}_2, \ldots, \mathbf{v}_c) \in \mathcal{R}^{cp}$, where $\mathbf{v}_i \in \mathcal{R}^p$, is the cluster center of prototype u_i, $1 \leq i \leq c$; and

$$(d_{ik})^2 = \|\mathbf{x}_k - \mathbf{v}_i\|^2 \tag{6}$$

where, in turn, $\| \cdot \|$ is any inner product induced norm on $\mathcal{R}^p$, weighting exponential $m \in [1, \infty)$, and u_{ik} is the membership of $\mathbf{x}_k$ in fuzzy cluster u_i. $J_m(\mathbf{U}, \mathbf{v})$ represents the distance from any given data point to a cluster weighted by that point's membership grade.

The solutions of

$$\min_{\mathbf{U} \in M_{fc}, \mathbf{v} \in \mathcal{R}^{cp}} J_m(\mathbf{U}, \mathbf{v}) \tag{7}$$

are the least squared error stationary points of J_m. An infinite family of fuzzy clustering algorithms—one for each $m \in (1, \infty)$—is obtained using the necessary conditions for solutions of (7), as summarized in the following:

Theorem 1 [29]: Assuming $\| \cdot \|$ to be an inner product induced norm, fix $m \in (1, \infty)$, let $\mathbf{X}$ have at least $c < n$ distinct points, and define the sets $(\forall k)$

$$I_k = \{i | 1 \leq i \leq c; d_{ik} = \|\mathbf{x}_k - \mathbf{v}_i\| = 0\} \tag{8}$$

$$\tilde{I}_k = \{1, 2, \cdots, c\} - I_k. \tag{9}$$

Then, $(\mathbf{U}, \mathbf{v}) \in M_{fc} \times \mathcal{R}^{cp}$ is globally minimal for J_m only if (ϕ denotes an empty set)

$$I_k = \phi \Rightarrow u_{ik} = 1 \Big/ \left[\sum_{j=1}^{c} \left(\frac{d_{ik}}{d_{jk}} \right)^{2/(m-1)} \right] \tag{10}$$

or

$$I_k \neq \phi \Rightarrow u_{ik} = 0 \qquad \forall i \in \tilde{I}_k \text{ and } \sum_{i \in I_k} u_{ik} = 1 \tag{11}$$

$$\mathbf{v}_i = \sum_{k=1}^{n} (u_{ik})^m \mathbf{x}_k \Big/ \sum_{k=1}^{n} (u_{ik})^m \qquad \forall i. \tag{12}$$

Bezdek proposed the iterative method presented here [29] to minimize $J_m(\mathbf{U}, \mathbf{v})$.

1) Fix c, $2 \leq c < n$; choose any inner product norm metric for $\mathcal{R}^p$; and fix m, $1 \leq m < \infty$. Initialize $\mathbf{U}^{(0)} \in M_{fc}$ (e.g., randomly choose its elements from the values between 0 and 1).
2) Then, at step $l (l = 1, 2, \ldots)$, calculate the c fuzzy cluster centers $\mathbf{v}_i^{(l)}$ using (12) and $\mathbf{U}^{(l)}$.
3) Update $\mathbf{U}^{(l)}$ using (10) or (11).
4) Compare $\mathbf{U}^{(l)}$ and $\mathbf{U}^{(l-1)}$ using a convenient matrix norm: If $\|\mathbf{U}^{(l)} - \mathbf{U}^{(l-1)}\| \leq \varepsilon_L$, stop; otherwise, return to Step 2.

3) Example of SVD-QR-T by FCM: We use the example given here to illustrate the application of SVD-QR-T by FCM to MIMO-WSN channel selection.

Step 1: Assume that the estimated channel gain is

$$\mathbf{H} = \begin{bmatrix} 0.6211 & 0.7536 & 0.6595 \\ 0.5602 & 0.6596 & 0.1834 \\ 0.2440 & 0.2141 & 0.6365 \\ 0.8220 & 0.6021 & 0.1703 \\ 0.2632 & 0.6049 & 0.5396 \end{bmatrix}$$

which is the same as that in MASTS. By matrix computation, we get

$$\mathbf{V} = \begin{bmatrix} -0.5856 & -0.5075 & -0.6321 \\ -0.6574 & -0.1589 & 0.7366 \\ -0.4743 & 0.8469 & -0.2406 \end{bmatrix}$$

$$\mathrm{diag} = (\Sigma) = (2.0017, 0.6347, 0.2572).$$

Use FCM to divide $\mathrm{diag}(\Sigma)$ into two clusters, we get

$$\mathbf{v} = \begin{bmatrix} 2.0010 \\ 0.4445 \end{bmatrix}$$

$$\mathbf{U} = \begin{bmatrix} 1.0000 & 0.0190 & 0.0114 \\ 0.0000 & 0.9810 & 0.9886 \end{bmatrix}.$$

Entry 1.0000 at $\mathbf{U}$ means that the membership degree of 2.0017 belonging to the cluster with center 2.0010 is 1.0000. Therefore, the cluster with higher center is composed of only 2.0017; then, 2.0017 is chosen, and $rt = 1$.

Step 2: Obtain $\mathbf{V}_{11}$ and $\mathbf{V}_{21}$ from $\mathbf{V}$, i.e.,

$$\mathbf{V}_{11} = -0.5856$$

$$\mathbf{V}_{21} = \begin{bmatrix} -0.6574 \\ -0.4743 \end{bmatrix}.$$

Based on $[\mathbf{V}_{11}^T \mathbf{V}_{21}^T]$, get $\mathbf{E}$ by QR as

$$\mathbf{E} = \begin{bmatrix} 0 & 1 & 0 \\ 1 & 0 & 0 \\ 0 & 0 & 1 \end{bmatrix}.$$

As $rt = 1$, choose the first column of $\mathbf{E}$ as

$$\mathbf{E}(:, rt) = \begin{bmatrix} 0 \\ 1 \\ 0 \end{bmatrix}$$

Step 3: Analyzing $\mathbf{E}(:, rt)$, 1 appears on the second row; thus, the second column of $\mathbf{H}$ is selected to construct $\mathbf{H}_s$, which is

$$\mathbf{H}_s = \begin{bmatrix} 0 & 0.7536 & 0 \\ 0 & 0.6596 & 0 \\ 0 & 0.2141 & 0 \\ 0 & 0.6021 & 0 \\ 0 & 0.6049 & 0 \end{bmatrix}.$$

Authorized licensed use limited to: University of Texas at Arlington. Downloaded on December 18, 2009 at 13:47 from IEEE Xplore. Restrictions apply.

This implies that the channels to be selected are those that connect the second transmitting sensor and all the receiving sensors, i.e., the cluster head would select transmitter 2 and all the receivers to be active while not employing other transmitting sensors.

As we may see, the row index in which 1 appears in $\mathbf{E}(:, rt)$ particularly determines which transmitters to be selected, so, with regard to SVD-QR-T by FCM, $rt \times M_r$ channels are selected to be active.

Note that the transmitting nodes are reduced due to the typically doubled power consumption in transmit mode [30], [31]. In any case that the receiving sensors spend more energy than the transmitters, we may simply apply the preceding approach into a transposed channel gain matrix $\mathbf{H}^T$, and some receivers will be turned off.

III. Performance Analysis

In the previous section, we have illustrated our proposed channel-selection approaches step by step. In this section, we would like to discuss the capacity, bit error rate (BER), and multiplexing gain of virtual MIMO after applying the MASTS and SVD-QR-T by FCM approaches with and without water filling.

A. Capacity

When both channel state information at the transmitter (CSIT) and channel state information at the receiver (CSIR) are known, the water-filling technique can be utilized to optimally allocate power P_i at the independent parallel channel i [23]. The sum of capacities on each of these independent parallel channels is the maximal capacity of the virtual MIMO. This capacity can be expressed as

$$C = \max_{\sum P_i \le P} \sum_{i=1}^{r} B \log_2 \left(1 + \frac{P_i}{\sigma^2}\lambda_i\right) \tag{13}$$

where P is the total power constraint for transmitting sensors, r is the rank of $\mathbf{H}$, and λ_i is the eigenvalue of $\mathbf{H}\mathbf{H}^T$. Since the SNR at the ith channel at full power is $\text{SNR}_i = \lambda_i P/\sigma^2$, the capacity (13) can also be given in terms of the power allocation P_i as

$$C = \max_{\sum P_i \le P} \sum_{i=1}^{r} B \log_2 \left(1 + \frac{P_i}{P}\text{SNR}_i\right) \tag{14}$$

where

$$\frac{P_i}{P} = \begin{cases} 1/\text{SNR}_0 - 1/\text{SNR}_i, & \text{SNR}_i \ge \text{SNR}_0 \\ 0, & \text{SNR}_i < \text{SNR}_0 \end{cases} \tag{15}$$

for some cutoff value SNR_0. The final capacity is given as

$$C = \sum_{\text{SNR}_i \ge \text{SNR}_0} B \log_2 \left(\frac{\text{SNR}_i}{\text{SNR}_0}\right). \tag{16}$$

The value of SNR_0 must numerically be found, owing to the nonexistence of a closed-form solution for continuous distributions of SNR [32]. Due to the randomness of the channel gain matrix, we employ Monte Carlo simulations to analyze the capacity performances on MASTS and SVD-QR-T by FCM with five steps.

1) Use Jake's model [33] to randomly generate an independent $M_t \times M_r$ Rayleigh channel model.
2) Follow the MASTS and SVD-QR-T by FCM channel selection algorithms, respectively, to select the channels.
3) Obtain eigenvalue λ_{ig} and its rank r_g for $\mathbf{H}_g$. Note that λ_{ig} is totally different from the λ_i of $\mathbf{H}$. Similarly, we can obtain λ_{is} and r_s for $\mathbf{H}_s$.
4) Assuming $B = 1$ Hz, calculate the capacity for the three virtual MIMO systems based on (13)–(16).
5) Apply Monte Carlo simulations 10 000 times, and obtain the average value for different values of the SNR.

The simulation result is shown in Fig. 6(a). It shows that, when the SNR is lower than 5 dB, SVD-QR-T by FCM provides a larger capacity than MASTS, but both of them are smaller than virtual MIMO without channel selection. Nevertheless, MASTS grows larger than a full virtual MIMO when the SNR reaches around 8.5 dB. It clearly shows that MASTS can offer the largest capacity at high SNR.

It is not always the case that both CSIT and CSIR are known. If only CSIR is obtained, water-filling power optimization cannot be applied, and we may simply allocate equal power to each transmitter; therefore, the capacity becomes

$$C = \sum_{i=1}^{r} B \log_2 \left(1 + \frac{\text{SNR}_i}{M_t}\right). \tag{17}$$

Here, we also apply Monte Carlo simulations 10 000 times to obtain the average capacity for these three systems, respectively, which is shown in Fig. 6(b).

It shows that SVD-QR-T by FCM provides a higher capacity than a virtual MIMO without channel selection if the SNR is less than 10 dB and a higher capacity than that of MASTS if the SNR is less than 2.5 dB. MASTS outweighs virtual MIMO without channel selection in capacity from 0 dB, and this advantage is more obvious, along with the increase in SNR. The advantage of MASTS in capacity at high SNR lies in the fact that the maximum channel gain is one of the selection goals. The advantage of SVD-QR-T by FCM over virtual MIMO without channel selection at low SNR is due to the optimized power allocation.

B. BER

Assuming binary phase-shift keying (BPSK) is used for modulation and maximal ratio combining is employed for diversity combination, then the BER is [34]

$$P_b = \left(\frac{1-\mu}{2}\right)^L \sum_{k=0}^{L-1} \binom{L-1+k}{k} \binom{1+\mu}{2}^k \tag{18}$$

Authorized licensed use limited to: University of Texas at Arlington. Downloaded on December 18, 2009 at 13:47 from IEEE Xplore. Restrictions apply.

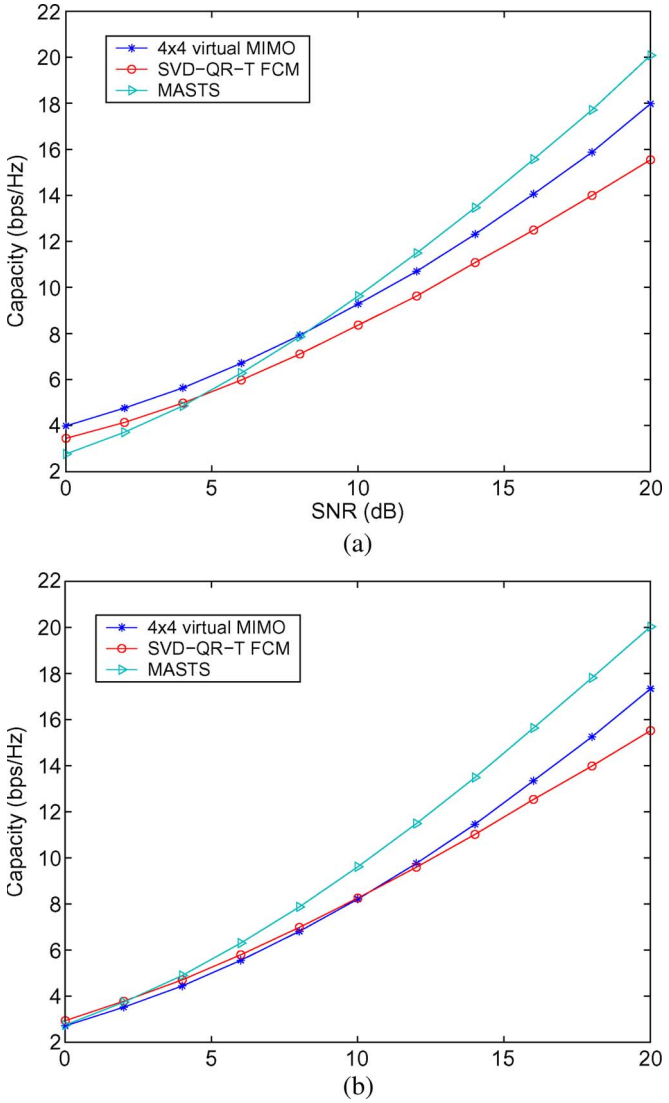


Fig. 6. Capacity for a 4 × 4 virtual MIMO (a) with and (b) without water filling.

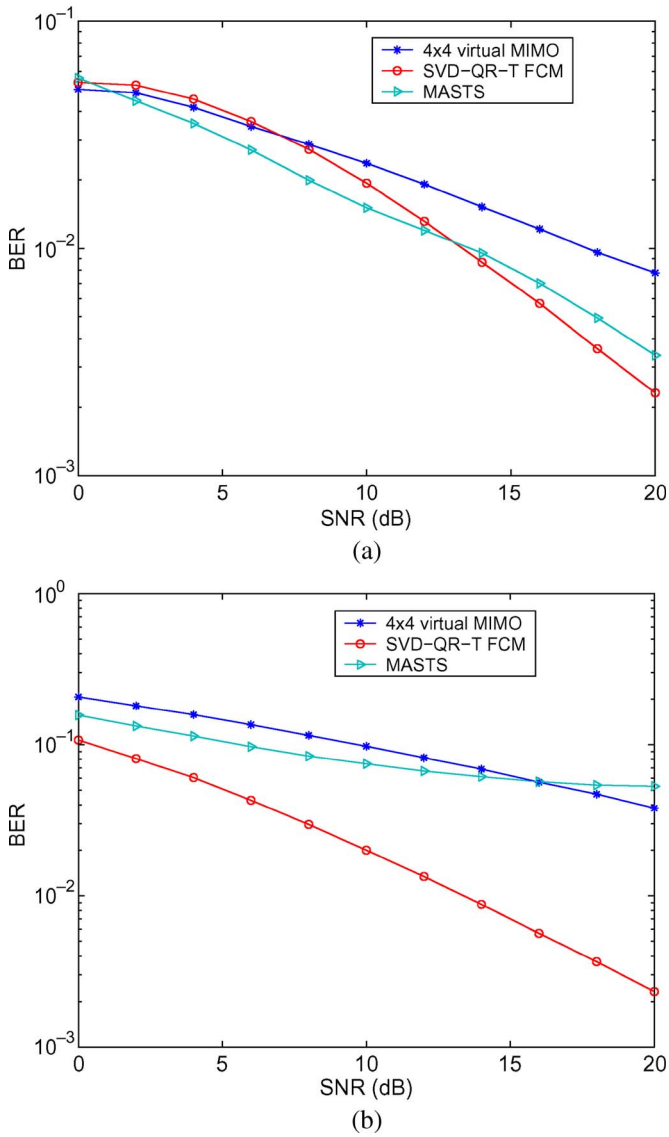


Fig. 7. BER for a 4 × 4 virtual MIMO employing BPSK (a) with and (b) without water filling.

where

$$\mu = \sqrt{\frac{\frac{P}{\sigma^2}}{1+\frac{P}{\sigma^2}}}. \tag{19}$$

However, for clarity and mathematical simplicity, in our study, we do not apply any STC. Since no diversity gain is adopted, BER can be denoted as

$$P_b = \frac{1}{r}\sum_{i=1}^{r}\left(\frac{1-\sqrt{\frac{\mathrm{SNR}_i}{1+\mathrm{SNR}_i}}}{2}\right). \tag{20}$$

The Monte Carlo simulation results for BER are shown in Fig. 7. In Fig. 7(a), water filling is adopted. SVD-QR-T by FCM offers lower BER than virtual MIMO without channel selection when the SNR is higher than about 7 dB. It also provides the lowest BER after the SNR grows to 13 dB. MASTS achieves the lowest BER when the SNR is in the range of 1.3–13.3 dB. Fig. 7(b) shows the situation without water filling. The advantage of SVD-QR-T by FCM is better demonstrated in this situation, whereas MASTS outperforms virtual MIMO without channel selection when the SNR is lower than around 16 dB. This is because SVD-QR-T by FCM chooses the best subset of equivalent parallel channels, so that the SNR_i allocated at each parallel is larger than that of MASTS and full virtual MIMO, as P/σ^2 grows larger.

C. Multiplexing Gain

The maximal multiplexing gain is the number of equivalent multiple parallel spatial channels [35]. It is also referred to as the degrees of freedom to communicate [36], which is related to the row and column numbers of $\mathbf{H}$, $\mathbf{H}_g$, and $\mathbf{H}_s$. It has been derived in [36] that the maximal multiplexing gain provided by $M_r \times M_t$ MIMO is

$$MG = \min(M_t, M_r). \tag{21}$$

Authorized licensed use limited to: University of Texas at Arlington. Downloaded on December 18, 2009 at 13:47 from IEEE Xplore. Restrictions apply.

However, the accurate multiplexing gain is

$$MG = rank(\mathbf{H}) \tag{22}$$

since it is possible that $\mathbf{H}$ is not of full rank. As SVD-QR-T by FCM selects rt transmitters and all receivers, the maximal multiplexing gain offered by SVD-QR-T by FCM is

$$MG_s = \min(rt, M_r). \tag{23}$$

Note that $rt \leq r \leq M_r$; therefore, the accurate multiplexing gain for SVD-QR-T by FCM is

$$MG_s = rt. \tag{24}$$

Concerning MASTS, all transmitting and receiving sensors are active, and the maximal multiplexing gain is

$$MG_g = rank(\mathbf{H}_g). \tag{25}$$

If water filling is applied, less multiplexing gain will be offered, as some singular values with SNR lower than SNR_0 will be cut off.

Under the premise that $\mathbf{H}$ is of full rank, we obtain the multiplexing gain simulation result in Fig. 8. In case of water filling, Fig. 8(a) shows that, when $M_t = M_r = 10$, the multiplexing gains for MASTS and SVD-QR-T by FCM are 4 and 3.5, respectively, if the SNR is 0 dB. They increase to 8.2 and 5, respectively, if the SNR becomes 20 dB in Fig. 8(b). Note that, although, along the increase in SNR, the multiplexing gain of both algorithms increases, this characteristic is more obvious for MASTS. In case of no water filling, the SNR does not have an impact on the multiplexing gain. The simulation result is shown in Fig. 8(c).

IV. Conclusion

This paper is a preliminary work on the virtual MIMO channel-selection problem in practice. Two approaches with concrete examples are proposed from the aspect of pure physical design and cross-layer consideration, respectively. We have not only presented the channel-selection algorithms but have also provided a detailed performance analysis with Monte Carlo simulations. We demonstrate that, under the same total transmission power constraint, either with or without water filling, the virtual MIMO after MASTS channel selection can offer higher capacity than full virtual MIMO at moderate-to-high SNR, whereas SVD-QR-T by FCM can provide the lowest BER performance at moderate-to-high SNR. The major limitation of this work is that the proposed two approaches are based on a quasi-static channel environment and feasible CSI.

Future research tracks might concern the following: 1) the extension of the proposed algorithm to integrate with STC to exploit spatial diversity to further optimize system performances and 2) application of channel-selection approaches to radar sensor networks [37].

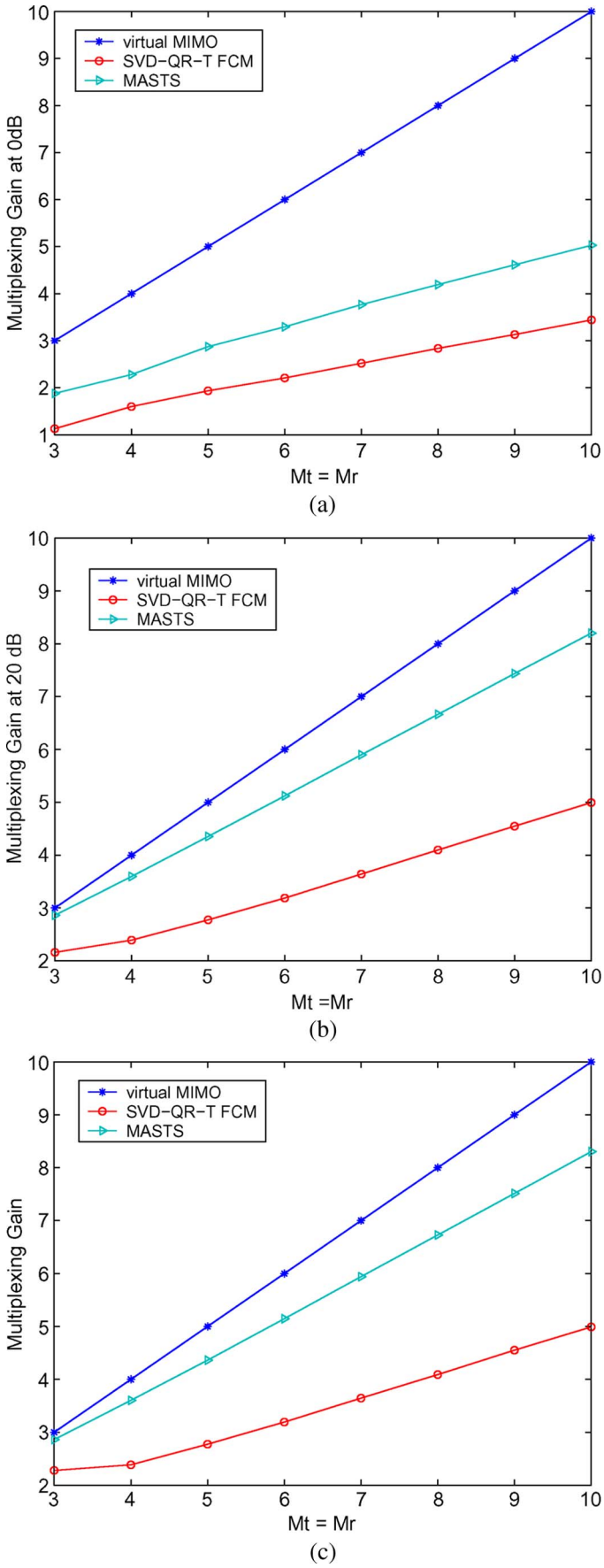


Fig. 8. Multiplexing gain with water filling at (a) SNR = 0 dB and (b) SNR = 20 dB, and (c) without water filling.

Authorized licensed use limited to: University of Texas at Arlington. Downloaded on December 18, 2009 at 13:47 from IEEE Xplore. Restrictions apply.

REFERENCES

[1] S. Cui and A. Goldsmith, "Energy-efficiency of MIMO and cooperative MIMO techniques in sensor networks," *IEEE J. Sel. Areas Commun.*, vol. 22, no. 6, pp. 1089–1098, Aug. 2004.

[2] S. K. Jayaweera, "Virtual MIMO-based cooperative communication for energy-constrained wireless sensor networks," *IEEE Trans. Wireless Commun.*, vol. 5, no. 5, pp. 984–989, May 2006.

[3] A. del Coso, U. Spagnolini, and C. Ibars, "Cooperative distributed MIMO channels in wireless sensor networks," *IEEE J. Sel. Areas Commun.*, vol. 25, no. 2, pp. 402–414, Feb. 2007.

[4] Y. Yuan, Z. He, and M. Chen, "Virtual MIMO-based cross-layer design for wireless sensor networks," *IEEE Trans. Veh. Technol.*, vol. 55, no. 3, pp. 856–864, May 2006.

[5] O. Younis and S. Fahmy, "Distributed clustering in ad-hoc sensor networks: A hybrid, energy-efficient approach," in *Proc. IEEE Conf. Comput. Commun. (INFOCOM)*, Hong Kong, Mar. 2004, pp. 629–640.

[6] T. J. Kwon and M. Gerla, "Clustering with power control," in *Proc. Mil. Commun. Conf.*, Atlantic City, NJ, Nov. 1999, pp. 1424–1428.

[7] S. Bandyopadhyay and E. Coyle, "An energy-efficient hierarchical clustering algorithm for wireless sensor networks," in *Proc. IEEE Conf. Comput. Commun. (INFOCOM)*, San Francisco, CA, Apr. 2003, pp. 1713–1723.

[8] A. D. Amis, R. Prakash, T. H. P. Voung, and D. T. Huynh, "Max-min d-cluster formation in wireless ad hoc networks," in *Proc. IEEE Conf. Comput. Commun. (INFOCOM)*, Tel-Aviv, Israel, Mar. 2000, pp. 32–41.

[9] Q. Liang, "Clusterhead election for mobile ad hoc wireless network," in *Proc. IEEE Int. Symp. PIMRC*, Beijing, China, Sep. 2003, pp. 1623–1628.

[10] M. Bengtsson and B. Ottersten, "Optimal and suboptimal transmit beamforming," in *Handbook of Antennas in Wireless Communications*, L. C. Godara, Ed. Boca Raton, FL: CRC, 2001.

[11] Q. Ling and T. Li, "Blind MIMO channel estimation based on structured transmit delay," in *Proc. IEEE ICASSP*, Toulouse, France, May 2006, pp. 761–764.

[12] T. Li, Q. Ling, and Z. Ding, "Space-time diversity design for blind estimation and equalization over frequency selective channels," in *Proc. IEEE ICASSP*, Philadelphia, PA, Mar. 2005, pp. iii/441–iii/444.

[13] D. A. Gore and A. J. Paulraj, "MIMO antenna subset selection with space-time coding," *IEEE Trans. Signal Process.*, vol. 50, no. 10, pp. 2580–2588, Oct. 2002.

[14] A. Gorokhov, D. A. Gore, and A. J. Paulraj, "Receive antenna selection for MIMO flat-fading channels: Theory and algorithms," *IEEE Trans. Inf. Theory*, vol. 49, no. 10, pp. 2687–2696, Oct. 2003.

[15] A. F. Molisch, M. Z. Win, and J. H. Winters, "Capacity of MIMO systems with antenna selection," in *Proc. Int. Conf. Commun.*, 2001, pp. 570–574.

[16] D. A. Gore, R. U. Nabar, and A. Paulraj, "Selecting an optimal set of transmit antennas for a low rank matrix channel," in *Proc. Int. Conf. Acoust., Speech, Signal Process.*, 2000, pp. 2785–2788.

[17] S. Sandhu, R. U. Nabar, D. A. Gore, and A. Paulraj, "Near optimal antenna selection of transmit antennas for a MIMO channel based on Shannon capacity," in *Proc. 34th Asilomar Conf.*, Nov. 1999, pp. 567–571.

[18] R. W. Heath, Jr. and A. Paulraj, "Antenna selection for spatial multiplexing systems based on minimum error rate," in *Proc. IEEE Int. Control Conf.*, 2001, pp. 2276–2280.

[19] I. Bahceci, T. M. Duman, and Y. Altunbasak, "Antenna selection for multiple-antenna transmission systems: Performance analysis and code construction," *IEEE Trans. Inf. Theory*, vol. 49, no. 10, pp. 2669–2681, Oct. 2003.

[20] Y. J. Choi, J. Kim, and S. Bahk, "Downlink scheduling with fairness and optimal antenna assignment for MIMO cellular systems," in *Proc. Global Telecommun. Conf.*, 2004, vol. 5, pp. 3165–3169.

[21] Y. J. Choi, J. Kim, and S. Bahk, "Optimal antenna assignment considering QoS under MIMO environments," in *Proc. IEEE Int. Conf. Commun.*, Jun. 2004, vol. 7, pp. 4216–4221.

[22] J. B. Kruskal, "On the shortest spanning subtree and the traveling salesman problem," in *Proc. Amer. Math. Soc.*, 1956, vol. 7, pp. 48–50.

[23] A. Goldsmith, *Wireless Communications*. Cambridge, U.K.: Cambridge Univ. Press, 2001.

[24] D. B. West, *Introduction to Graph Theory*, 2nd ed. New Delhi, India: Prentice–Hall, 2005.

[25] X. Cheng *et al.*, "Strong minimum energy topology in wireless sensor networks: NP-completeness and heuristics," *IEEE Trans. Mobile Comput.*, vol. 2, no. 3, pp. 248–256, Jul.–Sep. 2003.

[26] X. Cheng *et al.*, "Polynomial-time approximation scheme for minimum connected dominating set in ad hoc wireless networks," *Networks*, vol. 42, no. 4, pp. 202–208, 2003.

[27] S. Chen, S. A. Billings, and W. Luo, "Orthogonal least squares methods and their application to nonlinear system identification," *Int. J. Control*, vol. 50, no. 5, pp. 1873–1896, 1989.

[28] Q. Liang and L. Wang, "Redundancy reduction in wireless sensor networks using SVD-QR," in *Proc. IEEE Mil. Commun. Conf.*, Atlantic City, NJ, Oct. 2005, pp. 1857–1861.

[29] J. C. Bezdek, *Pattern Recognition With Fuzzy Objective Function Algorithms*. New York: Plenum, 1981.

[30] S. Singh, M. Woo, and C. S. Raghavendra, "Power-aware routing in mobile ad hoc networks," in *Proc. ACM/IEEE MOBICOM*, 1998, pp. 181–190.

[31] M. Stemm and R. Katz, "Measuring and reducing energy consumption of network interfaces in hand-held devices," in *Proc. 3rd Int. Workshop Mobile Multimedia Commun.*, Sep. 1996, pp. 1–7.

[32] M.-S. Alouini and A. J. Goldsmith, "Capacity of Rayleigh fading channels under different adaptive transmission and diversity-combining techniques," *IEEE Trans. Veh. Technol.*, vol. 48, no. 4, pp. 1165–1181, Jul. 1999.

[33] J. G. Proakis, *Digital Communications*, 4th ed. New York: McGraw-Hill, 2001.

[34] G. L. Stüber, *Principles of Mobile Communication*, 2nd ed. Norwell, MA: Kluwer, 2001.

[35] R. Heath, Jr. and A. Paulraj, "Switching between multiplexing and diversity based on constellation distance," in *Proc. Allerton Conf. Commun., Control Comput.*, Oct. 2000, pp. 212–221.

[36] L. Zheng and D. N. C. Tse, "Diversity and multiplexing: A fundamental tradeoff in multiple-antenna channels," *IEEE Trans. Inf. Theory*, vol. 49, no. 5, pp. 1073–1096, May 2003.

[37] J. Li and P. Stoica, "MIMO radar-diversity means superiority," in *Proc. 14th Ann. Workshop Adaptive Sensor Array Process.*, Lexington, MA, Jun. 2006.



Jing Liang (S'06) received the B.S. and M.S. degrees from Beijing University of Posts and Telecommunications, Beijing, China, in 2003 and 2006, respectively, both in electrical engineering. She is currently working toward the Ph.D. degree in electrical engineering with the Department of Electrical Engineering, University of Texas, Arlington.

Her current research interests include radar sensor networks, collaborative and distributed signal processing, wireless communications, wireless networks, and fuzzy logic systems.



Qilian Liang (M'01–SM'05) received the B.S. degree from Wuhan University, Wuhan, China, in 1993, the M.S. degree from Beijing University of Posts and Telecommunications, Beijing, China, in 1996, and the Ph.D. degree from the University of Southern California, Los Angeles, in May 2000, all in electrical engineering.

Since August 2002, he has been with the Department of Electrical Engineering, University of Texas, Arlington (UTA), where he is currently an Associate Professor. Prior to that, he was a Member of Technical Staff with Hughes Network Systems Inc., San Diego, CA. He is the author of more than 130 journal and conference proceeding papers and six book chapters. He is also the holder of six pending U.S. patents. His research interests include sensor networks, wireless communications, wireless networks, communication systems and communication theory, signal processing for communications, fuzzy logic systems and applications, and collaborative and distributed signal processing.

Dr. Liang was the recipient of the 2002 IEEE TRANSACTIONS ON FUZZY SYSTEMS Outstanding Paper Award, the 2003 U.S. Office of Naval Research Young Investigator Award, the 2005 UTA College of Engineering Outstanding Young Faculty Award, and the 2007 U.S. Air Force Summer Faculty Fellowship Program Award.

Authorized licensed use limited to: University of Texas at Arlington. Downloaded on December 18, 2009 at 13:47 from IEEE Xplore. Restrictions apply.

KUPS: Knowledge-Based Ubiquitous and Persistent Sensor Networks for Threat Assessment

QILIAN LIANG, Senior Member, IEEE
University of Texas at Arlington

XIUZHEN CHENG, Member, IEEE
The George Washington University

We propose a knowledge-based ubiquitous and persistent sensor network (KUPS) for threat assessment, in which "sensor" is a broad characterization. It refers to diverse data or information from ubiquitous and persistent sensor sources such as organic sensors and human intelligence sensors. Our KUPS for threat assessment consists of two major steps: situation awareness using fuzzy logic systems (FLSs) and threat parameter estimation using radar sensor networks (RSNs). Our FLSs combine the linguistic knowledge from different intelligent sensors, and our proposed maximum-likelihood (ML) estimation algorithm performs target radar cross section (RCS) parameter estimation. We also show that our ML estimator is unbiased and the variance of parameter estimation matches the Cramer-Rao lower bound (CRLB) if the radar pulses follow the Swerling II model. Simulations further validate our theoretical results.

Manuscript received August 10, 2006; revised February 28, 2007; released for publication August 20, 2007.

IEEE Log No. T-AES/44/3/929753.

Refereeing of this contribution was handled by J. P. Y. Lee.

The work of Liang was supported by the U.S. Office of Naval Research (ONR) under Grant N00014-07-1-0395 and ONR Young Investigator Program Award under Grant N00014-03-1-0466.

The work of Cheng was supported by the National Science Foundation (NSF) CAREER award under Grant CNS-0347674.

Authors' addresses: Q. Liang, Dept. of Electrical Engineering, University of Texas at Arlington, Arlington, TX 76019-0016, E-mail: (liang@uta.edu); X. Cheng, Dept. of Computer Science, The George Washington University, Washington, D.C. 20052.

0018-9251/08/$25.00 © 2008 IEEE

I. INTRODUCTION AND MOTIVATION

In current and future military operational environments, such as global war on terrorism (GWOT) and maritime domain awareness (MDA), warfighters require technologies evolved to support information needs regardless of location and consistent with the user's level of command or responsibility and operational situation. To support this need, the U.S. Department of Defense (DoD) has developed the concept of network centric warfare (NCW), defined as "*military operations that exploit state-of-the-art information and networking technology to integrate widely dispersed human decision makers, situational and targeting sensors, and forces and weapons into a highly adaptive, comprehensive system to achieve unprecedented mission effectiveness*" [1].

The DoD has defined three levels of data fusion for NCW. the level 1 data fusion combines data from single or multiple sensors and sources to provide the best estimate of objects and events in the battlespace in terms of their position, kinematics (e.g. tracks), identity, or identification features. In [14], decision fusion rules were studied in multi-hop wireless sensor networks. In [10], a fuzzy logic approach for postdetection signal integration and detection was proposed, and a functional paradigm for fuzzy data fusion was presented in [25]. However, too often in level 1 data fusion, the characteristics of objects that are not of interest will be similar to those of threat objects. The conventional approach to false alarm control is to reduce sensitivity of the radar in areas of clutter, using sensitivity time control (STC) [26]. In [11], we proposed a maximum-likelihood (ML) automatic target recognition (ATR) algorithm using constant frequency (CF) waveform design and diversity, assuming perfect delay and Doppler. In [12], we applied linear frequency modulation (LFM) waveform design and diversity to ATR with delay-Doppler uncertainty. Level 2 data fusion focuses on situation assessment. This requires recognition of objects/entities in the regions of interest, as well as recognizing activities of these objects, and inferring their relationships. Level 3 data fusion is threat assessment, which requires inferring the intent of objects/entities, or groups of objects, in the regions of interest. Higher level data fusion also needs lower level data fusion results. In level 2/3 data fusion, some works have been reported. A situation/threat assessment fusion system was proposed in [3]. Other approaches include multiple attribute decision making [4], Bayesian networks [21], etc. In [6], an intelligent threat assessment processor using genetic algorithms and fuzzy logic was proposed. In [20], threat assessment was studied in tactical airborne environments. In [9], neural network was applied to threat assessment for automated visual surveillance.

Authorized licensed use limited to: University of Texas at Arlington. Downloaded on December 18, 2009 at 13:49 from IEEE Xplore. Restrictions apply.

In [5], an intelligent assistant to provide automatic situation and threat advice in the Air Defence Ground Environment was proposed. In [2], a situation and threat assessment model based on group analysis was studied.

Despite these above advances, current shortfalls in warfighting functionality result from limitations in technology. For example, accurate and timely information about battlespace objects and events is not available to support warfighter decision making (including reliable location, tracking, combat identification, and targeting information). While massive amounts of data will be generated by penetrating persistent sensors, warfighters require technologies that not only integrate information from diverse sources but also provide indications of information significance in ways that support the user's tactical decision needs regardless of location and are consistent with the user's level of command or responsibility and operational situation. Assuming the availability of object track and identity information, automated decision tools that transform this information into actionable knowledge for the decision maker are required. The tools and technologies to resolve these shortfalls must address data fusion, particularly at levels 2/3 [1]. In this paper, we propose a knowledge-based ubiquitous and persistent sensor network (KUPS) for threat assessment.

The rest of this paper is organized as follows. In Section II, we introduce the new concept of KUPS, and in Section III, we propose knowledge-based situation awareness using intelligence (INT) sensors. In Section IV, we propose a fine target recognition and threat assessment scheme that employs an ML estimation algorithm for threat target radar cross section (RCS) parameter estimation using radar sensor networks (RSNs). Finally, we conclude this paper and discuss future research directions in Section V.

II. INTRODUCTION TO KNOWLEDGE-BASED UBIQUITOUS AND PERSISTENT SENSOR NETWORKS: A NEW CONCEPT

In this paper, we propose an NCW model entitled knowledge-based ubiquitous and persistent sensor network (KUPS), in which "sensor" is a broad characterization concept. It means ubiquitous and persistent sensors sources such as the following.

1) Organic sensors (e.g., radar, electro-optic and infrared, acoustic, and nonacoustic) deployed on air, ground, surface, or unattended platforms.

2) Signal intelligence (SIGINT) including electronic intelligence (ELINT) and communication intelligence (COMINT). For example, it can assign meaningful metadata to each collection, and the metadata is the standardized characterization of data providing descriptors (such as stability, activity, membership, or structure).

3) Human intelligence (HUMINT), e.g., to identify specific people/cells/groups and relationships.

4) Measurement and signatures intelligence (MASINT), e.g., to provide specific weapon system identifications, chemical compositions and material content.

5) Imagery intelligence (IMINT), e.g., to track vehicles through urban area.

6) Open source intelligence (OSINT), e.g., to provide text data collection.

All these sources of information need to be integrated via "sensor networking" to accomplish a mission. In this paper, we apply KUPS to threat assessment, and the organic sensors we use are pulse Doppler radars.

Our KUPS for threat assessment is a hierarchical and recursive architecture which consists of two major steps.

Step 1, Situation Awareness: Performing knowledge-based situation awareness using INT sensors (e.g. SIGINT, HUMINT sensors). Fuzzy rules are used to represent the linguistic knowledge uncertainties from HUMINT sensors, and fuzzy logic systems (FLSs) are used to perform knowledge-based decision making on situation awareness (e.g., threat or nonthreat). If it is assessed as a nonthreat, stops; if it is assessed as a potential threat to issue an indication & warning (I&W), then go to Step 2 for further target recognition and threat assessment.

Step 2, Fine Target Recognition and Threat Assessment: Performing target RCS value estimation using RSNs. We propose an ML estimation algorithm to estimate target RCS parameter value using RSNs. Based on the estimated RCS parameter, the KUPS will advise what kind of target this threat is. The ML estimation algorithm can help to estimate the RCS parameter θ (parameter in a Rayleigh distribution for fluctuating target). However, the same RCS parameters may mean different targets, threats or nonthreats. For example, for $\theta = 2$, the target can be a small flighter aircraft, a small pleasure boat, a bicycle [26], or any other similar size target. This example illustrates that RCS-based level 1 data fusion (e.g., [11, 12]) without considering other context such as geographical information (from OSINT) has very clear disadvantages. So we have to use Step 1 to make the decision first, and only an I&W requires further classification for further action. Sometimes it may be a false alarm based on fine target recongition, therefore Step 2 will make final threat assessment.

Step 2 results can be feedback to Step 1 recursively to further tune the parameters in FLS design. Fig. 1 depicts the relationship between Steps 1 and 2. We discuss these two steps in the following sections.

Authorized licensed use limited to: University of Texas at Arlington. Downloaded on December 18, 2009 at 13:49 from IEEE Xplore. Restrictions apply.

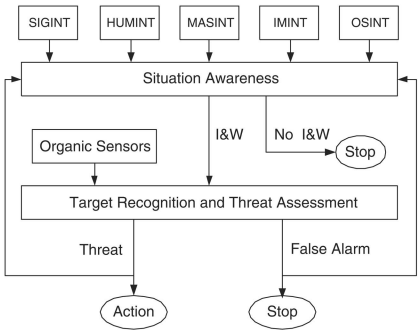


Fig. 1. Relations of Steps 1 and 2.

III. KNOWLEDGE-BASED SITUATION AWARENESS USING INT SENSORS

In knowledge-based situation assessment using INT sensors, fuzzy rules are used to represent the linguistic and numerical knowledge uncertainties from INT sensors, and FLSs are used to perform knowledge-based decision making on threat assessment. We give a brief introduction on FLSs first.

A. Overview of Fuzzy Logic Systems

In general, an FLS is a nonlinear mapping of an input data (feature) vector to a scalar output [16]. Fig. 2 shows the structure of an FLS [16]. When an input is provided to an FLS, the inference engine computes the output set corresponding to each rule. The defuzzifier then computes a crisp output from these rule output sets. Consider a p-input 1-output FLS, using singleton fuzzification, center-of-sets defuzzification [18, 16], and "IF-THEN" rules of the form

$$R^l:\ \text{IF } x_1 \text{ is } \mathrm{F}_1^l \text{ and } x_2 \text{ is } \mathrm{F}_2^l \text{ and } \cdots$$
$$\text{and } x_p \text{ is } \mathrm{F}_p^l, \text{ THEN } y \text{ is } \mathrm{G}^l.$$

Assuming singleton fuzzification, when an input $\mathbf{x}' = \{x_1', \ldots, x_p'\}$ is applied, the degree of firing corresponding to the lth rule is computed as

$$\mu_{\mathrm{F}_1^l}(x_1') \star \mu_{\mathrm{F}_2^l}(x_2') \star \cdots \star \mu_{\mathrm{F}_p^l}(x_p') = \mathcal{T}_{i=1}^{p} \mu_{\mathrm{F}_i^l}(x_i') \qquad (1)$$

where $\star$ and $\mathcal{T}$ both indicate the chosen t-norm (minimum or product operation) [16], and $\mu_{\mathrm{F}_i^l}(x_i')$ is the membership grade of fuzzy set F_i^l for input x_i'. There are many kinds of defuzzifiers [16, 18]. In this paper, we focus, for illustrative purpose, on the center-of-sets defuzzifier [18]. It computes a crisp output for the FLS by first computing the centroid c_{G^l} of every consequent set G^l, and then computing a weighted average of these centroids. The weight corresponding to the lth rule consequent centroid is the degree of firing (firing strength) associated with the lth rule, $\mathcal{T}_{i=1}^{p} \mu_{\mathrm{F}_i^l}(x_i')$, so that

$$y_{\cos}(\mathbf{x}') = \frac{\sum_{l=1}^{M} c_{\mathrm{G}^l} \mathcal{T}_{i=1}^{p} \mu_{\mathrm{F}_i^l}(x_i')}{\sum_{l=1}^{M} \mathcal{T}_{i=1}^{p} \mu_{\mathrm{F}_i^l}(x_i')} \qquad (2)$$

where M is the number of rules in the FLS. Readers can refer to [16, 18] for details on FLS. Reference [16] provides a very good tutorial on FLS, and [18] gives an introduction to and directions on FLS development [18].

B. Knowledge-Based Situation Awareness using FLSs

In our FLS design for situation awareness, we consider the following knowledge-based antecedents.

1) The first antecedent is the number of switches from the nonmaneuvering set (constant behavior in speed, acceleration, and direction, etc.) to the maneuvering set (varying behavior in speed, acceleration, and direction, etc). When a target is beginning a maneuver from a nonmaneuvering class, the tracking system can switch the algorithms applied to the problem from a nonmaneuvering set to the maneuvering set. The errors in distance from where the tracker estimates the position of a target between the actual position can be very large when the incorrect motion models are applied to the problem. Additionally, when the tracker does finally catch up to the target after the maneuver, the track will "jump" across the operator's scope giving a very unrealistic and unreliable picture of what that target is actually doing. So a threat target will quite often switch from a nonmaneuvering set to the maneuvering set, and vice versa, to avoid being tracked all the time. This knowledge can be used as an antecedent for situation awareness.

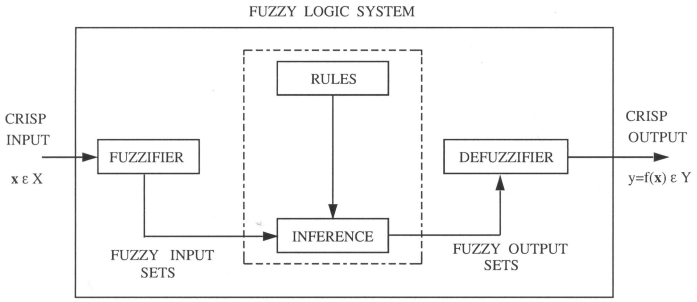


Fig. 2. Structure of FLS.

Authorized licensed use limited to: University of Texas at Arlington. Downloaded on December 18, 2009 at 13:49 from IEEE Xplore. Restrictions apply.

TABLE I
Fuzzy Rules used in KUPS

Rule #	Ante 1	Ante 2	Ante 3	Consequent
1	low	low	low	weak
2	low	low	moderate	medium
3	low	low	high	strong
4	low	moderate	low	very weak
5	low	moderate	moderate	weak
6	low	moderate	high	medium
7	low	high	low	very weak
8	low	high	moderate	weak
9	low	high	high	medium
10	moderate	low	low	medium
11	moderate	low	moderate	strong
12	moderate	low	high	very strong
13	moderate	moderate	low	weak
14	moderate	moderate	moderate	medium
15	moderate	moderate	high	strong
16	moderate	high	low	very weak
17	moderate	high	moderate	weak
18	moderate	high	high	medium
19	high	low	low	medium
20	high	low	moderate	strong
21	high	low	high	very strong
22	high	moderate	low	weak
23	high	moderate	moderate	medium
24	high	moderate	high	strong
25	high	high	low	very weak
26	high	high	moderate	weak
27	high	high	high	Moderate

Note: Ante 1 is number of switches from nonmaneuvering set to maneuvering set or vice versa. Ante 2 is frequency of appearance of such type of target. Ante 3 is importance of geolocation of target. Consequent is the possibility that target is a threat.

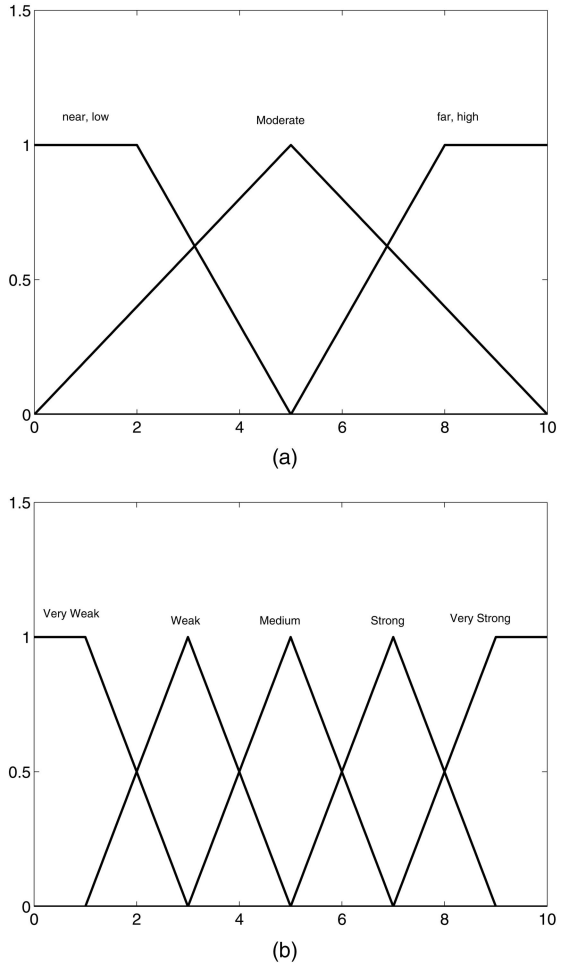


Fig. 3. MFs used to represent linguistic labels. (a) MFs for antecedents. (b) MFs for consequent.

2) The second antecedent is the frequency of appearance of such type of target based on some a priori knowledge such as archival radar data. Generally threat targets are new compared to archival radar data.

3) The third antecedent is the importance of geolocation of this target based on the geographical information systems (GISs). Examples of important geolocations include large metroplexes, landmarks, military bases, airports, etc. Threats happen quite often in such areas.

The above three antecedents are all knowledge based and it can be collected from the INT sensors. A typical rule using the above three antecedents can be:

> IF the number of switches from nonmaneuvering set to the maneuvering set is high, and the frequency of appearance of such target is low, and the importance of geolocation of such type of target is high, THEN the possibility that an I&W needs to be issued is very strong.

The linguistic variables used to represent each antecedent are divided into three levels: low, moderate, and high. The consequent—the possibility that an I&W needs to be issued—is divided into 5 levels, very strong, strong, medium, weak, very weak. So we need to set up $3^3 = 27$ (because every antecedent has 3 fuzzy subsets, and there are 3 antecedents) rules for this FLS. Table I summarizes the fuzzy rules we use in this paper. We use trapezoidal membership functions (MFs) to represent low, and high, and triangle MFs to represent moderate. We show these MFs in Fig. 3.

For input (x_1, x_2, x_3), the output is computed using

$$y(x_1, x_2, x_3) = \frac{\sum_{l=1}^{27} \mu_{\mathrm{F}_l^1}(x_1)\mu_{\mathrm{F}_l^2}(x_2)\mu_{\mathrm{F}_l^3}(x_3)c_{\mathrm{avg}}^l}{\sum_{l=1}^{27} \mu_{\mathrm{F}_l^1}(x_1)\mu_{\mathrm{F}_l^2}(x_2)\mu_{\mathrm{F}_l^3}(x_3)} \quad (3)$$

where $\mu_{\mathrm{F}_l^i}(x_i)$ $(i = 1,2,3)$ represents the antecedent i membership degree (in the lth rule) when the input is x_i and the membership functions are plotted in Fig. 3. By repeating these calculations for $\forall x_i \in [0,10]$, we obtain a hypersurface $y(x_1, x_2, x_3)$. This equation represents the nonlinear mapping between three inputs and one output of the FLS. Since it's a 4-D surface (x_1, x_2, x_3, y), it's impossible to be plotted visually.

Authorized licensed use limited to: University of Texas at Arlington. Downloaded on December 18, 2009 at 13:49 from IEEE Xplore. Restrictions apply.

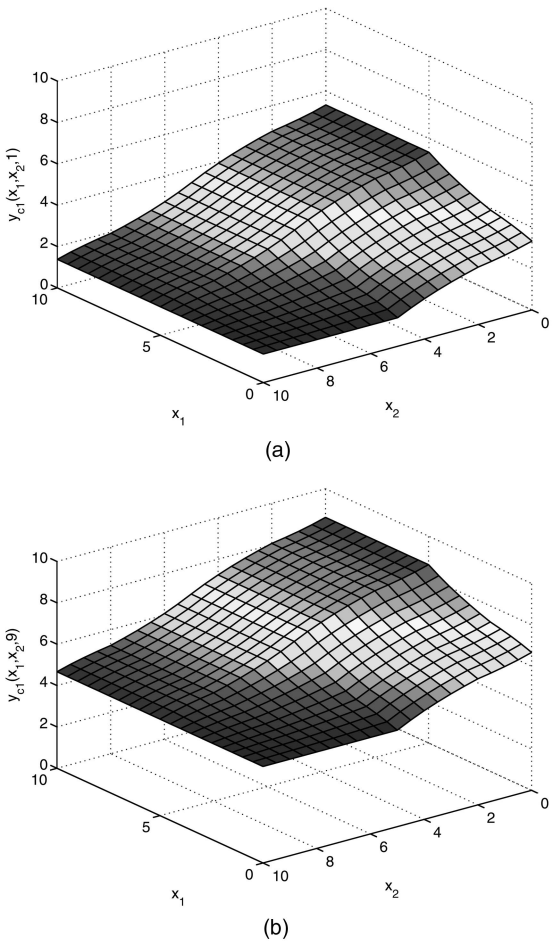


Fig. 4. Threat assessment surface for fixed importance of geolocation of this target (x_3). (a) When $x_3 = 1$. (b) When $x_3 = 9$.

If we have $x_3 = 1$, and two other antecedents x_1 and x_2 are variables, the output is computed using

$$y(x_1,x_2,1) = \frac{\sum_{l=1}^{27} \mu_{\mathrm{F}_l^1}(x_1)\mu_{\mathrm{F}_l^2}(x_2)\mu_{\mathrm{F}_l^3}(1)c_{\cos}^l}{\sum_{l=1}^{27} \mu_{\mathrm{F}_l^1}(x_1)\mu_{\mathrm{F}_l^2}(x_2)\mu_{\mathrm{F}_l^3}(1)}. \quad (4)$$

This equation represents the nonlinear mapping between three inputs (one of which is fixed) and one output of the FLS. By repeating these calculations for $\forall x_1 \in [0,10]$ and $\forall x_2 \in [0,10]$, we obtain a hypersurface $y(x_1,x_2,1)$, as plotted in Fig. 4(a). In contrast, if we have $x_3 = 9$, and two other antecedents x_1 and x_2 are variables, we obtain another surface $y(x_1,x_2,9)$, as plotted in Fig. 4(b). Observe that from Fig. 4, the importance of geolocation of a target (x_3) makes a big difference in situation awareness, and the number of switches from nonmaneuvering set to the maneuvering set or vice versa (x_1) and the frequency of appearance of such target (x_2) also play a very important role even when the importance of geolocation (x_3) is the same.

IV. FINE TARGET RECOGNITION AND THREAT ASSESSMENT

A. Target RCS Value Estimation using RSNs

1) *RCS and RCS Voltage for Fluctuating Target*: Most radar analysis and measurement programs emphasize RCS measurements, which are proportional to received power. RCS is the fictional area over which the transmitter power density must be intercepted to collect a total power that would account for the received power density. Typical values of RCS for targets of interest range from 0.01 m^2 to hundreds of square meters [26]. Fluctuating target modeling is more realistic in which the target RCS is drawn from either the Rayleigh/exponential or chi-square of degree four probability density function (pdf). The Rayleigh/exponential model describes the behavior of a complex target consisting of many scatters, none of which is dominant. The fourth-degree chi-square model targets have many scatters of similar strength with one dominant scatter. Based on different combinations of pdf and decorrelation characteristics (scan-to-scan or pulse-to-pulse decorrelation), four Swerling models are used [24]. In this paper, we focus on "Swerling II" model which is an exponential distribution with pulse-to-pulse decorrelation. The pulse-to-pulse decorrelation implies that each individual pulse results in an independent value for RCS. Sometimes the RCS voltage value (square root of RCS) is of interest, particularly for use in simulations to model the composite echo from a multiple-scatter target. The RCS voltage value is the square root of RCS, so the pdf of RCS voltage follows a Rayleigh distribution [24]. In this paper, we apply radar sensor networks to estimate the RCS value.

2) *Introduction to Radar Sensor Networks*: In [11], we performed the following theoretical studies on CF pulse waveform design and diversity in RSNs: 1) the conditions for waveform coexistence, 2) interferences among waveforms in RSN, and 3) waveform diversity combining in RSN.

For RSNs, the waveforms from different radars interfere with each other. We choose the waveform for radar i as

$$x_i(t) = \sqrt{\frac{1}{T}}\exp[j2\pi(\beta + \delta_i)t], \qquad -T/2 \le t \le T/2 \quad (5)$$

where β is the RF carrier frequency in radians per second, and δ_i is a frequency shift for radar i. To minimize the interference from one waveform to the other, optimal values for δ_i should be determined to have the waveforms orthogonal to each other, i.e., let the cross-correlation between $x_i(t)$ and $x_n(t)$ be 0. We showed that choosing $\delta_i = i/T$ in (5) can have orthogonal waveforms, i.e., the waveforms can

Authorized licensed use limited to: University of Texas at Arlington. Downloaded on December 18, 2009 at 13:49 from IEEE Xplore. Restrictions apply.

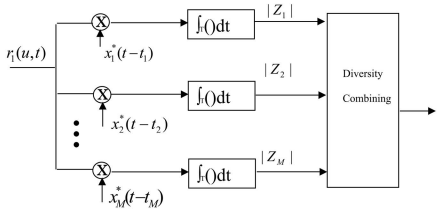


Fig. 5. Waveform diversity combining by clusterhead in RSN.

coexist if the carrier spacing is $1/T$ between two radar waveforms.

In RSN, the radar sensors are networked together in an ad hoc fashion. They do not rely on a preexisting fixed infrastructure, such as a wireline backbone network or a base station. They are self-organizing entities that are deployed on demand in support of various event surveillance, battlefield, disaster relief, search and rescue, etc. Scalability concern suggests a hierarchical organization of RSNs with the lowest level in the hierarchy being a cluster. As argued in [15], [8], [7], [22], in addition to helping with scalability and robustness, aggregating sensor nodes into clusters has additional benefits:

1) conserving radio resources such as bandwidth,
2) promoting spatial code reuse and frequency reuse,
3) simplifying the topology, e.g., when a mobile radar changes its location, it is sufficient for the nodes in attended clusters to update their topology information,
4) reducing the generation and propagation of routing information,
5) concealing the details of global network topology from individual nodes.

In RSN, each radar can provide its waveform parameters such as δ_i to its clusterhead radar, and the clusterhead radar can combine the waveforms from its cluster members.

In RSN with M radars, the received signal for clusterhead (assume it's radar 1) is

$$r_1(u,t) = \sum_{i=1}^{M} \alpha(u) x_i(t-t_i)\exp(j2\pi F_{D_i} t) + n(u,t) \tag{6}$$

where $x_i(t)$ is the transmitted CF waveform, $\alpha(u)$ stands for voltage of RCS, F_{D_i} is the Doppler shift of target relative to waveform i, t_i is the delay of waveform i, and $n(u,t)$ is the additive white Gaussian noise (AWGN). In [11], we proposed a RAKE structure for waveform diversity combining, as illustrated by Fig. 5.

According to this structure, the received $r_1(u,t)$ is processed by a bank of matched filters, then the output of branch 1 (after integration and before taking the envelope) is [11]

$$\begin{aligned} Z_1(u;t_1,\ldots,t_M,F_{D_1},\ldots,F_{D_M}) &= \int_{-T/2}^{T/2} r_1(u,t)x_1^*(t-t_1)dt \qquad (7)\\ &= \int_{-T/2}^{T/2}\left[\sum_{i=1}^{M}\alpha(u)x_i(t-t_i)\exp(j2\pi F_{D_i}t)+n(u,t)\right]x_1^*(t-t_1)dt \qquad (8)\end{aligned}$$

where $\int_{-T/2}^{T/2} n(u,t)x_1^*(t-t_1)dt$ can easily be proved to be AWGN. Let

$$n(u,t_1) \triangleq \int_{-T/2}^{T/2} n(u,t)x_1^*(t-t_1)dt. \tag{9}$$

Assuming $t_1 = t_2 = \cdots = t_M = \tau$, then according to interference analysis in [11],

$$Z_1(u;\tau,F_{D_1},\ldots,F_{D_M}) \approx \sum_{i=2}^{M}\alpha(u)\mathrm{sinc}[\pi(i-1+F_{D_i}T)] + \frac{\alpha(u)\sin[\pi F_{D_1}(T-|\tau|)]}{T\pi F_{D_1}} + n(u,\tau). \tag{10}$$

Similarly, we can get the output for any branch m $(m = 1,2,\ldots,M)$,

$$Z_m(u;\tau,F_{D_1},\ldots,F_{D_M}) \approx \sum_{i=1,i\neq m}^{M}\alpha(u)\mathrm{sinc}[\pi(i-m+F_{D_i}T)] + \frac{\alpha(u)\sin[\pi F_{D_m}(T-|\tau|)]}{T\pi F_{D_m}} + n(u,\tau). \tag{11}$$

Therefore $Z_m(u;\tau,F_{D_1},\ldots,F_{D_M})$ consists of three parts, signal (reflected signal from radar m waveform): $\alpha(u)E\sin[\pi F_{D_m}(T-|\tau|)]/T\pi F_{D_m}$, interferences from other waveforms: $\sum_{i=1,i\neq m}^{M}\alpha(u)E\mathrm{sinc}[\pi(i-m+F_{D_i}T)]$, and noise: $n(u,\tau)$.

We can have three special cases for $Z_m(u;\tau,F_{D_1},\ldots,F_{D_M})$.

1) When $F_{D_1} = \cdots = F_{D_M} = 0$,

$$Z_m(u;\tau,0,0,\ldots,0) \approx \frac{\alpha(u)(T-|\tau|)}{T} + n(u,\tau) \tag{12}$$

which means if there is no Doppler mismatch, there will be no interference from other waveforms.

2) If $\tau = 0$, then (11) becomes

$$Z_m(u;0,F_{D_1},\ldots,F_{D_M}) \approx \sum_{i=1,i\neq m}^{M}\alpha(u)\mathrm{sinc}[\pi(i-m+F_{D_i}T)] + \alpha(u)\mathrm{sinc}[\pi F_{D_m}T] + n(u). \tag{13}$$

3) If $\tau = 0$, and $F_{D_1} = \cdots = F_{D_M} = 0$, then (11) becomes

$$Z_m(u;0,0,0,\ldots,0) \approx \alpha(u) + n(u). \tag{14}$$

Authorized licensed use limited to: University of Texas at Arlington. Downloaded on December 18, 2009 at 13:49 from IEEE Xplore. Restrictions apply.

Doppler mismatch happens quite often in target search where target velocity is not known yet. However, in target recognition, generally high-resolution measurements of targets in range ($\tau = 0$) and Doppler are available, so (14) will be used for RCS value estimation.

How to combine all the Z_ms ($m = 1,2,\ldots,M$) is very similar to the diversity combining in communations to combat channel fading, and the combination schemes may be different for different applications. In this paper, we are interested in applying RSN waveform diversity to estimate the RCS parameter γ^2, and we propose an ML algorithm for RCS parameter estimation.

3) *Maximum Likelihood Algorithm for RCS Parameter Estimation*: For the Swerling II model, the RCS voltage $|\alpha(u)|$ follows a Rayleigh distribution and the I and Q subchannels of $\alpha(u)$ follow zero-mean Gaussian distributions with a variance γ^2 (the RCS average power value). Assume

$$\alpha(u) = \alpha_I(u) + j\alpha_Q(u) \tag{15}$$

and $n(u) = n_I(u) + jn_Q(u)$ follows a zero-mean complex Gaussian distribution with a variance σ^2 for the I and Q subchannels.

According to (14),

$$|Z_m(u;0,0,0,\ldots,0)| \approx |\alpha(u) + n(u)|. \tag{16}$$

Since $\alpha(u)$ and $n(u)$ are zero-mean complex Gaussian random variables, $\alpha(u) + n(u)$ is a zero-mean Gaussian random variable with a variance $\gamma^2 + \sigma^2$ for the I and Q subchannels, which means $y_m \triangleq |Z_m(u;0,0,\ldots,0)|$ follows a Rayleigh distribution with parameter $\sqrt{\gamma^2 + \sigma^2}$,

$$f(y_m) = \frac{y_m}{\gamma^2 + \sigma^2} \exp\left[-\frac{y_m^2}{2(\gamma^2 + \sigma^2)}\right]. \tag{17}$$

The mean value of y_m is $\sqrt{\pi(\gamma^2 + \sigma^2)/2}$, and its variance is $(4-\pi)(\gamma^2 + \sigma^2)/2$. The variance of signal is $(4-\pi)\gamma^2/2$ and the variance of noise is $(4-\pi)\sigma^2/2$.

Let $\mathbf{y} \triangleq [y_1, y_2, \ldots, y_M]$, then the pdf of $\mathbf{y}$ is

$$f(\mathbf{y}) = \prod_{m=1}^{M} f(y_m) \tag{18}$$

$$= \prod_{m=1}^{M} \frac{y_m}{\gamma^2 + \sigma^2} \exp\left[-\frac{y_m^2}{2(\gamma^2 + \sigma^2)}\right] \tag{19}$$

let

$$\theta \triangleq \gamma^2 \tag{20}$$

then (19) can be expressed as

$$f(\mathbf{y}) = \prod_{m=1}^{M} \frac{y_m}{\theta + \sigma^2} \exp\left[-\frac{y_m^2}{2(\theta + \sigma^2)}\right]. \tag{21}$$

Therefore the ML algorithm to estimate the RCS average value (θ) can be represented as

$$\hat{\theta}_{\mathrm{ML}}(\mathbf{y}) = \arg\sup_{\theta \in R^+} f(\mathbf{y})$$

$$= \arg\sup_{\theta \in R^+} \prod_{m=1}^{M} \frac{y_m}{\theta + \sigma^2} \exp\left[-\frac{y_m^2}{2(\theta + \sigma^2)}\right]. \tag{22}$$

Maximizing $f(\mathbf{y})$ is equivalent to maximizing $\log f(\mathbf{y})$ (natural logarithm),

$$\log f(\mathbf{y}) = \sum_{m=1}^{M} \left[\log\left(\frac{y_m}{\theta + \sigma^2}\right) - \frac{y_m^2}{2(\theta + \sigma^2)}\right]. \tag{23}$$

Since it is a continuous function for $y_m > 0$ and $\theta > 0$, a necessary condition for the ML estimation is

$$\frac{\partial}{\partial\theta} \log f(\mathbf{y})|_{\theta = \hat{\theta}_{\mathrm{ML}}(\mathbf{y})} = \frac{\sum_{m=1}^{M} y_m^2 - 2M(\theta + \sigma^2)}{2(\theta + \sigma^2)^2} = 0 \tag{24}$$

which has the unique solution

$$\hat{\theta}_{\mathrm{ML}}(\mathbf{y}) = \frac{\sum_{m=1}^{M} y_m^2}{2M} - \sigma^2. \tag{25}$$

Considering $\theta \geq 0$,

$$\hat{\theta}_{\mathrm{ML}}(\mathbf{y}) = \max\left[\frac{\sum_{m=1}^{M} y_m^2}{2M} - \sigma^2, 0\right]. \tag{26}$$

Since

$$\frac{\partial^2}{\partial\theta^2} \log f(\mathbf{y})|_{\theta = \hat{\theta}_{\mathrm{ML}}(\mathbf{y})} = -\frac{4M^3}{(\sum_{m=1}^{M} y_m^2)^2} < 0 \tag{27}$$

this solution gives the unique maximum of $\log f(\mathbf{y})$. The expectation of $\hat{\theta}_{\mathrm{ML}}(\mathbf{y})$ is

$$E_\theta[\hat{\theta}_{\mathrm{ML}}(\mathbf{y})] = \int_0^\infty \frac{\sum_{m=1}^{M} y_m^2}{2M} f(y_m) dy_m - \sigma^2 \tag{28}$$

$$= \int_0^\infty \frac{\sum_{m=1}^{M} y_m^2}{2M} \frac{y_m}{\theta + \sigma^2} \exp\left[-\frac{y_m^2}{2(\theta + \sigma^2)}\right] dy_m - \sigma^2$$

$$= \theta. \tag{29}$$

Therefore it's an unbiased estimator.

Fisher's information for this case can be computed via

$$I_\theta = -E_\theta\left[\frac{\partial^2}{\partial\theta^2} \log f(\mathbf{y})\right]$$

$$= -E_\theta\left[\frac{M(\theta + \sigma^2) - \sum_{m=1}^{M} y_m^2}{(\theta + \sigma^2)^3}\right]. \tag{30}$$

The mean value of y_m is $\sqrt{\pi(\theta + \sigma^2)/2}$, and its variance is $(4-\pi)(\theta + \sigma^2)/2$. So the Cramer-Rao lower bound (CRLB) is

$$\mathrm{Var}_\theta[\hat{\theta}(\mathbf{y})] \geq \frac{1}{I_\theta} = \frac{(\theta + \sigma^2)^2}{M}. \tag{31}$$

Authorized licensed use limited to: University of Texas at Arlington. Downloaded on December 18, 2009 at 13:49 from IEEE Xplore. Restrictions apply.

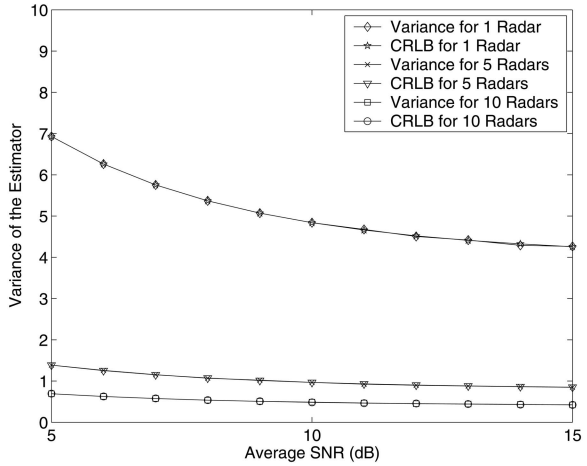


Fig. 6. Variance of RCS ML estimator with different number of radars in RSN.

Since $(\partial/\partial\theta)\log f(\mathbf{y})$ in (24) is of the form $k(\theta)[\hat{\theta}_{\mathrm{ML}}(y) - E_\theta[\hat{\theta}(\mathbf{y})]$ for

$$k(\theta) = \frac{M}{(\theta + \sigma^2)^2} \tag{32}$$

we conclude that $\hat{\theta}_{\mathrm{ML}}(\mathbf{y})$ can achieve the CRLB theoretically [17]. From (31), it's clear that CRLB is inversely proportional to the number of radars M in RSN, which means RSN with larger M will have much lower CRLB. This conclusion is drawn based on the assumption that the radar pulses are independent (in time and space) and follow a Rayleigh distribution, which is the Swerling II model [24].

4) *Simulations*: For fluctuating target with an RCS parameter $\theta = 2$ (Rayleigh distribution), we ran Monte Carlo simulations for 10^6 realizations at each SNR value, and we applied the ML estimation algorithm to estimate the parameter $\hat{\theta}$ for each realization. In Fig. 6, we plotted the variance of the RCS ML estimator with different number of radars in RSN. Observe the following.

1) The actual variance of $\hat{\theta}$ matches exactly with the CRLB for different numbers of radars in RSN, which validates our theoretical results: our ML estimator on the RCS parameter is an unbiased estimator and the variance of the parameter estimation matches CRLB.

2) The actual variance of $\hat{\theta}$ reduces as M increases, and numerically it is reversely proportional to M as we have shown in Section IVA.

B. Threat Assessment

Based on the estimated RCS value (for fine target recognition) and situation awareness-related I&W, threat can be assessed. For example, if an I&W was issued in Step 1 (situation awareness) on an unidentified flying object, we proceed with Step 2. In Step 2, based on Step 2 RCS value estimation, the target, for example, could be recognized as a bird, a missile, or other because a bird has an average RCS value of 0.01 m^2 and a conventional unmanned winged missle has an average RCS value of 0.5 m^2 [24]. A bird means the I&W is a false alarm, and a missile means the I&W is a threat and immediate actions need to be taken. The threat assessment results can be feedback to Step 1 to tune the design parameters of the FLS using training methods (for example, the steepest descent algorithm [13]).

V. CONCLUSIONS AND FUTURE WORKS

We have proposed a KUPS for threat assessment, of which "sensor" is a broad characterization concept, and it can be organic sensors, HUMINT sensors, SIGINT sensors, etc. Our KUPS for threat assessment consists of two major steps: situation awareness based on FLSs, fine target recognition (using RSNs), and threat assessment. Our FLSs can combine the linguistic knowledge from different intelligent sensors which contains lots of uncertainties. We propose an ML estimation algorithm for target RCS parameter estimation. Theoretically we show that our ML estimator is unbiased and the variance of parameter estimation matches the CRLB. Simulations further validate these theoretical results.

The proposed techniques will increase the sensitivity and performance of existing and future NCW, enhancing ship self-defense modes against stealthy, sea skimming, and antiship cruise missiles. In future works, we will also infer intent of objects/entities, or groups of objects, in the regions of interest. We will also study methods for constructing and learning a wide variety of models of threat behavior and methods for reasoning with uncertain and incomplete information for assessing threats from object activities.

ACKNOWLEDGMENT

Dr. Liang would like to thank ONR Program Officer Dr. Rabinder N. Madan for his direction and insightful discussion on RSNs.

REFERENCES

[1] Command and Control and Combat Systems (C2 and CS). ONR BAA 06-016.

[2] Cai, Y. et al.
A situation and threat assessment model based on group analysis.
In *Proceedings of the 2005 International Conference on Machine Learning and Cybernetics*, Aug. 2005, 356–361.

[3] Choi, J. W., Joo, J. W. and Cho, D. L.
Situation/threat assessment fusion system (STAFS).
In *Proceedings of the Fifth International Conference on Information Fusion*, July 2002, 1374–1380.

Authorized licensed use limited to: University of Texas at Arlington. Downloaded on December 18, 2009 at 13:49 from IEEE Xplore. Restrictions apply.

[4] Changwen, Q., and You, H.
A method of threat assessment using multiple attribute decision making.
In *6th International Conference on Signal Processing*, Aug. 2002, 1091–1095.

[5] Dall, I. W.
Threat assessment without situation assessment.
In *Proceedings of Information, Decision and Control*, Feb. 1999, 365–370.

[6] Gonsalves, P. et al.
Intelligent threat assessment processor (ITAP) using genetic algorithms and fuzzy logic.
In *Proceedings of the Third International Conference on Information Fusion*, 2000.

[7] Hou, T.-C., and Tsai, T-J.
An access-based clustering protocol for multihop wireless ad hoc networks.
IEEE Journal of Selected Areas in Communications, **19**, 7 (July 2001), 1201–1210.

[8] Iwata, A., Chiang, C. C., Pei, G., Gerla, M., and Chen, T. W.
Scalable routing strategies for ad hoc networks.
IEEE Journal of Selected Areas in Communications, **17** (1999), 1369–1379.

[9] Jan, T.
Neural network based threat assessment for automated visual surveillance.
In *IEEE International Joint Conference on Neural Networks*, vol. 2, July 2004, 1309–1312.

[10] Leung, S. W., Minett, J. W., Siu, Y. M., and Lee, M. K.
A fuzzy approach to signal integration.
IEEE Transactions on Aerospace and Electronic Systems, **38**, 1 (Jan. 2002), 346–351.

[11] Liang, Q.
Waveform design and diversity in radar sensor networks: Theoretical analysis and application to automatic target recognition.
In *IEEE International Workshop on Wireless Ad Hoc and Sensor Networks*, June 2006, New York.

[12] Liang, Q.
Radar sensor networks: Algorithms for waveform design and diversity with application to atr with delay-Doppler uncertainty.
EURASIP Journal on Wireless Communications and Networking, (2007), 1–9.

[13] Liang, Q., and Mendel, J. M.
Interval type-2 fuzzy logic systems: Theory and design.
IEEE Transactions on Fuzzy Systems, **8**, 5 (Oct. 2000), 535–550.

[14] Lin, Y., Chen, B., and Varshney, P. K.
Decision fusion rules in multi-hop wireless sensor networks.
IEEE Transactions on Aerospace and Electronic Systems, **41**, 2 (2005), 476–489.

[15] Lin, C. R., and Gerla, M.
Adaptive clustering in mobile wireless networks.
IEEE Journal of Selected Areas in Communications, **16** (1997), 1265–1275.

[16] Mendel, J. M.
Fuzzy logic systems for engineering : A tutorial.
Proceedings of the IEEE, **83**, 3 (Mar. 1995), 345–377.

[17] Mendel, J. M.
Lessons in Estimation Theory for Signal Processing, Communications, and Control.
Upper Saddle River, NJ: Prentice-Hall, 1995.

[18] Mendel, J. M.
Uncertain Rule-Based Fuzzy Logic Systems.
Upper Saddle River, NJ: Prentice-Hall, 2001.

[19] Manley, J. E., Mineart, G. M., and Sheridan, A. E.
Underwater marine domain awareness for first responders: A low cost approach.
MTS/IEEE TECHNO-OCEAN '04 vol. 3, 2004, 1695–1700.

[20] Nguyen, X. T.
Threat assessment in tactical airborne environments.
In *Proceedings of the Fifth International Conference on Information Fusion*, July 2002.

[21] Okello, N., and Thorns, G.
Threat assessment using Bayesian networks.
In *Proceedings of the Sixth International Conference of Information Fusion*, vol. 2, 2003, 1102–1109.

[22] Perkins, C. E.
Cluster-based networks.
In C. E. Perkins (Ed.), *Ad Hoc Networking*, Reading, MA: Addison-Wesley, 2001, 75–138.

[23] Roman, J., Rangaswamy, M., Davis, D., Zhang, Q., Himed, B., and Michels, J.
Parametric adaptive matched filter for airborne radar applications.
IEEE Transactions on Aerospace and Electronic Systems, **36**, 2 (2000), 677–692.

[24] Richards, M. A.
Fundamentals of Radar Signal Processing.
New York: McGraw-Hill, 2005.

[25] Singh, R. P., Bailey, W. H.
Fuzzy logic applications to multisensor-multitarget correlation.
IEEE Transactions on Aerospace and Electronic Systems, **33**, 3 (July 1997), 752–769.

[26] Skolnik, M. I.
Introduction to Radar Systems (3rd ed.).
New York, McGraw-Hill, 2001.

[27] Swerling, P.
Probability of detection for fluctuating targets.
IRE Transactions on Information Theory, **6** (Apr. 1960), 269–308.

[28] Petterson, G. et al.
Multi-source integration and temporal situation assessment in air combat.
1999 Information, Decision and Control, (Feb. 1999), 371–375.

[29] Steinberg, A. N.
An approach to threat assessment.
In *2005 8th International Conference on Information Fusion*, vol. 2, July 2005.

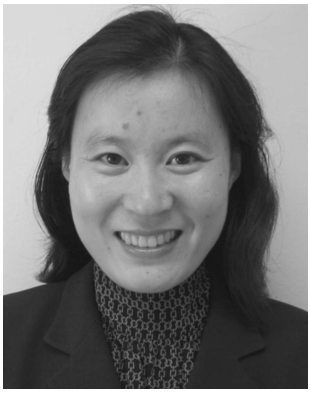
Authorized licensed use limited to: University of Texas at Arlington. Downloaded on December 18, 2009 at 13:49 from IEEE Xplore. Restrictions apply.



Qilian Liang (M'01—SM'05) received the B.S. degree from Wuhan University in 1993, M.S. degree from Beijing University of Posts and Telecommunications in 1996, and Ph.D. degree from University of Southern California (USC), Los Angeles, in May 2000, all in electrical engineering.

He joined the faculty of the University of Texas at Arlington in August 2002 and is currently an associate professor. Prior to that he was a member of the technical staff in Hughes Network Systems Inc. at San Diego, CA. His research interests include sensor networks, wireless communications, wireless networks, communication system and communication theory, signal processing for communications, fuzzy logic systems and applications, collaborative and distributed signal processing.

Dr. Liang has published more than 120 journal and conference papers, 6 book chapters, and has 6 U.S. patents pending. He received the 2002 IEEE Transactions on Fuzzy Systems Outstanding Paper Award, the 2003 U.S. Office of Naval Research (ONR) Young Investigator Award, and the 2005 UTA College of Engineering Outstanding Young Faculty Award.



Xiuzhen (Susan) Cheng (M'02) received her M.S. and Ph.D. degrees in computer science from the University of Minnesota–Twin Cities, in 2000 and 2002, respectively.

She is an associate professor in the Department of Computer Science at the George Washington University. Her current research interests include wireless and mobile computing, sensor networking, wireless and mobile security, and approximation algorithm design and analysis.

Dr. Cheng has served on the editorial boards of several technical journals and in the technical program committees of various professional conferences/workshops. She was the program cochair of the first International Conference on Wireless Algorithms, Systems, and Applications (WASA06). She worked as a program director in the National Science Foundation for six months in 2006. She received the NSF CAREER Award in 2004.

Authorized licensed use limited to: University of Texas at Arlington. Downloaded on December 18, 2009 at 13:49 from IEEE Xplore. Restrictions apply.

Throughput and Energy-Efficiency-Aware Protocol for Ultrawideband Communication in Wireless Sensor Networks: A Cross-Layer Approach

Qingchun Ren, *Student Member*, *IEEE*, and Qilian Liang, *Senior Member*, *IEEE*

Abstract—In this paper, we propose an efficient MAC protocol: the throughput maximized MAC protocol (TM-MAC), inspired by the availability that a number of ultrawideband (UWB) transmission parameters can be tuned to better match the requirements of data flow. In TM-MAC, we implement a concurrent multiuser access scheme instead of a mutual exclusion method such as TDMA and random access. For multiuser interference, we establish a model to adaptively adjust the data transmission rate to generate the expected signal to interference noise ratio (SINR) at the receiver side for reliable communications. We also analyze the relationship among the theoretical maximum channel capacity, achievable maximum channel capacity, and data transmission rate. According to network topology, TM-MAC redivides each piconet into several subsets in which communication pairs can make communication simultaneously and achieve the maximum throughput using the highest data rate. In subset formation, we propose a general analytical framework that captures the unique characteristics of shared wireless channel and throughput variance, as well as allows the modeling of a large class of systemwide throughput maximization via the specification of the per-link utilization function. For algorithm essential parameters design, we consider the influence of traffic type on the system performance. Heavy tailed distribution, compared to Poisson distribution for most existing work, is exploited to accurately model the real traffic to achieve the adaptation of our algorithm. Simulation results show that our algorithm can maximize throughput to achieve short latency.

Index Terms—Wireless sensor networks, ultrawideband communication, MAC protocl, network throughput, energy efficiency, multiuser access control, multiuser interference, mutual exclusion.

1 Introduction

Recent developments in integrated circuit technology have brought about the construction of a small and low-cost sensor node with signal processing and wireless communication capabilities. A wireless sensor network (WSN) can be thought of as an ad hoc network consisting of sensor nodes that are linked by a wireless medium to perform distributed sensing tasks. Distributed WSNs have increasing applications as they hold the potential to renovate many segments of our economies and lives from environment monitoring to manufacture and business asset management [1].

Within the past 40 years, advances in analog, digital electronics, and ultrawideband (UWB) signal theory have enabled system designers to propose some practical UWB communication systems such as in [2]. Currently, numerous companies and government agencies are investigating the potential of UWB to deliver on its promises. A wide range of UWB applications have been demonstrated [3], [4]. According to the Federal Communications Commission (FCC), a UWB system is defined as any radio system that has a 10-dB bandwidth larger than 20 percent of its center frequency or has a 10-dB bandwidth equal to or larger than 500 MHz [5]. Two different UWB communications systems —impulse-based systems (I-UWB) and multicarrier systems (MC-UWB))—have been pursued recently. UWB has several features that differentiate it from conventional narrowband systems [6]:

- Large instantaneous bandwidth enables fine time resolution for network time distribution, precision location capability, or use as a radar.
- Short duration pulses are able to provide robust performance in dense multipath environments by exploiting more resolvable paths.
- Low-power spectral density allows coexistence with existing users and has a Low Probability of Intercept (LPI).
- Data rate may be traded for power spectral density and multipath performance.

However, no existing wireless network successfully takes those above advantages because of the lack of an efficient medium access control technology. As a general principle, the role of the MAC module is to allow multiple users to share a common resource. Chandra et al. [7] defined a set of parameters that characterize a MAC independently of the underlying transmission technique and multiple access method. They are

• *The authors are with the Department of Electrical Engineering, University of Texas at Arlington, Arlington, TX 76019-0016. E-mail: ren@wcn.uta.edu, liang@uta.edu.*

Manuscript received 12 Jan. 2007; revised 27 June 2007; accepted 17 Sept. 2007; published online 24 Sept. 2007.
For information on obtaining reprints of this article, please send e-mail to: tmc@computer.org, and reference IEEECS Log Number TMC-0016-0107.
Digital Object Identifier no. 10.1109/TMC.2007.70765.

1536-1233/08/$25.00 © 2008 IEEE Published by the IEEE CS, CASS, ComSoc, IES, & SPS

Authorized licensed use limited to: University of Texas at Arlington. Downloaded on December 18, 2009 at 13:51 from IEEE Xplore. Restrictions apply.

- throughput, defined as the percentage of channel capacity used during data transmission,
- delay, that is, the average time spent by a packet in a MAC queue, and
- degree of fairness that states that access to the medium is fair if all nodes have a similar chance of obtaining medium access.

Conventional wireless MAC protocols assume that simultaneous transmissions result in transmission errors and thus employ mutual exclusion mechanisms to avoid them. Moreover, from a layered architecture aspect, the functions executed by MAC should be defined without taking into account the underlying physical layer, which is seen by MAC as a black box offering the service of transferring bits in the form of signals appropriately for the channel. Following this approach, there are some MAC protocols that appeared for UWB communication systems. In the European funded project Ultra-wideband Concepts for Ad-hoc Networks (U.C.A.N.) [8], a TDMA-based MAC protocol is proposed. This MAC protocol is an adaptation for UWB from the IEEE 802.15.3 [9] draft standard for the narrow-band wireless personal area network (WPAN). Ding et al. [10] studied the impact of channel acquisition time with different MAC protocols including centralized TDMA and distributed CSMA/CA methods. In [11], a single transceiver approach for UWB and a companion MAC layer based on busy tone multiple access (BTMA) was proposed. BTMA reduces the time and energy spent on collision as compared to handshaking protocols.

However, the design of an efficient MAC protocol for UWB systems should investigate some possible MAC enhancements that will take into account the inherent advantages of UWB technology. In [12], a scheme providing distributed medium access through pulse sense was proposed, which is similar to carrier sense in the narrow-band system. Moreover, UWB is flexible in the reconfiguration process of transmission data rate and power. Thus, another approach for MAC protocol design is proposed. Opposite to mutual exclusion MAC protocols, this kind of MAC protocol for UWB systems tries to allow simultaneous transmission and to adapt to multiuser interference. Cuomo et al. [13] outlined key issues to design a multiaccess scheme based on UWB. They selected a distributed mechanism to handle radio resource sharing and presented a general framework of radio resource sharing to UWB wireless ad hoc networks. A UWB-tailored MAC algorithm —the uncoordinated, wireless, baseborn medium access for UWB communication networks ($(UWB)^2$) is proposed in [14]. $(UWB)^2$ takes advantage of the multiple access capabilities offered by time hopping (TH) codes and relies for the access to a common channel on the high multiple user interference (MUI) robustness provided by the processing gain of impulse radio (IR).

In this paper, inspired by the availability that a number of transmission parameters can be tuned to better match the requirements of data flow for UWB communication, we propose a MAC protocol: throughput maximized MAC protocol (TM-MAC). In TM-MAC, we implement concurrent multiuser access instead of mutual exclusion methods such as TDMA and random access. Cross-layer design techniques are exploited by combining the MAC layer and physical layer together for the optimization tasks on network throughput and energy efficiency. On a MAC layer, according to the network topology, TM-MAC redivides each piconet into several throughput-maximized subsets, in which communication pairs can make communication simultaneously and achieve the maximum throughput using the highest data rate. For subset formation, we propose a general analytical framework that captures the unique characteristics of shared wireless channel and throughput variance, as well as allows the modeling of a large class of systemwide throughput maximization via the specification of per-link utilization function. On a physical layer, we analyze the relationship among the theoretical maximum channel capacity, the achievable maximum channel capacity, and the data transmission rate. For multiuser interference, we establish a model to adaptively adjust the data rate to generate the expected signal to interference noise ratio (SINR) at the receiver side.

The remainder of this paper is organized as follows: In Section 2, we summarize our motivations for our work. Then, we analyze the impact of simultaneous transmissions on throughput in Section 3. Section 4 describes the details of our TM-MAC algorithm. Simulation results are given in Section 5. Section 6 concludes the paper.

2 Our Motivations

2.1 Energy Constraint

The biggest challenge for the designers of WSNs is to develop systems that will run unattended for years. This calls for not only robust hardware and software but also lasting energy resources. However, the current generation of sensor nodes is battery powered, where available energy is limited, and replacing or recharging batteries may be impractical or uneconomical in many cases. Battery lifetime is a major constraint. Even though future generations can be powered by ambient energy sources (sunlight, vibrations, etc.) [15], the current provided is very low. Thus, energy consumption is still heavily constrained. From both perspectives, protocols and applications designed for WSNs should be highly efficient and optimized in terms of energy.

Generally, a sensor node consists of a microprocessor, data storage, sensors, analog-to-digital converters (ADCs), a data transceiver, an energy source, and controllers that tie those pieces together [1]. Moreover, using multiple access instead of mutual exclusion access methods, one of the main energy wasting sources is the idle waiting for next arrival data packets, which is caused by burst traffic. Consequently, communications, not only transmitting but also receiving or merely scanning channel for communication, can use up to half of the energy [16].

One approach implements energy reservation through reducing the amount of information exchanged over the network and considers the problem of reducing power consumption on wireless interfaces. The research in [17] points out a bit rate of 100 kilobits per second ($Kbps$) over 5 meters with no more than 1 mW power consumption. Hence, UWB is the best choice in terms of energy efficiency for energy-constrained WSNs. For the energy consumption

Authorized licensed use limited to: University of Texas at Arlington. Downloaded on December 18, 2009 at 13:51 from IEEE Xplore. Restrictions apply.

problem for generic WSNs, we have done some work in [18] and [19]. Our proposed energy-efficient MAC protocols not only reserve energy to extend network lifetime but also own the capability to solve the accumulative clock drift problem without network synchronization. In this paper, we extend our previous work to UWB communication systems.

2.2 Physical Layer Properties

The Shannon channel capacity theory defines the theoretical maximum data transmission rate, at which error-free digits can be transmitted over a bandwidth-limited channel in the presence of noise, usually expressed in the form as the following:

$$C = Wlog_2\left(1 + \frac{S}{N}\right), \quad (1)$$

where C is the channel capacity in bits per second, W is the bandwidth in hertz, and $\frac{S}{N}$ is the signal-to-noise ratio (SNR).

In UWB communication systems, even though bandwidth is finite, the bandwidth is at least 500 MHz or the transmitted signal has a 10 dB bandwidth larger than 20 percent of its center frequency based on the FCC standard. Compared with the narrowband system, information-theoretic results in [20] and [21] show that the Shannon-capacity of a multipath fading with an Additive White Gaussian Noise (AWGN) wideband channel is a linear function of SNR, as shown in (2):

$$C = \xi \times SNR. \quad (2)$$

Moreover, for the I-UWB system, the data transmission rate R can be formulated as follows:

$$R = \frac{1}{N_s N_h T_c}, \quad (3)$$

where N_s is the number of pulses transmitted at the pulse repetition time, N_h is the number of frames (pulses) per information bit, and T_c is the bin duration.

Note that UWB is flexible in the reconfiguration process of transmission data rate and power due to the availability of a number of transmission parameters such as N_s, N_h, and T_c, which can be tuned to better match the requirements of data flow. Therefore, for a given level of interference at a receiver, a sender can tune its rate by adjusting the code in order to achieve the desired bit error rate (BER) in UWB systems.

2.3 Systemwide Optimization through the Cross-Layer Approach

Lessons learned from developing network protocols for WSNs in the last couple of years show that using the traditional layered networking approach has several drawbacks in the resulting performance and efficiency of systems. Quite often, significant improvements are possible for network protocols, but they require a significant amount of information to be passed along the layers of the system. Although in principle this approach allows independence among various protocols, it incurs significant overhead in parameter transfer. Moreover, improvements performed on a specific layer can cause impairments and even be counterproductive for other layers. Therefore, optimization can be more effective when taking into account the overall system and using all available knowledge. In other words, the cross-layer design approach is a viable approach for resource-constrained WSNs.

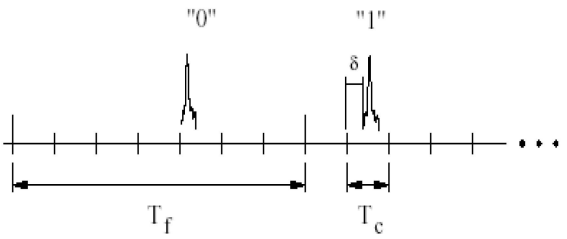


Fig. 1. UWB signal waveform with PPM, the model of Win-Scholtz [25].

3 Theoretic Analysis on the Variance of Network Throughput

3.1 Network Model

Due to the limited transmission range of current UWB signals, UWB technology is considered for short-range communications. The network model assumed in this paper is that of "piconet" or clustered architecture. A piconet is a collection of devices consisting of one master or piconet controller (PNC) device and the remaining slave devices. The PNC is responsible for scheduling the communication between slaves. Each piconet can have only one PNC and up to 255 slaves. A device can be a PNC in only one piconet, but it can be a slave in multiple piconets simultaneously. In this network, we assume that all nodes have the same communication and computing capabilities. Since clustering method design is not the target of this paper, we assume that we can set up this hierarchical clustering topology for a randomly deployed network through certain existing methods such as the energy-efficient self-organization (ESO) [22] algorithm.

3.2 Physical Layer Model

The UWB physical model, on which the design of our protocol is based, is described in this section. The most common and traditional way of emitting a UWB signal is by radiating pulses that are very short in time. IR transmits extremely short pulses, giving rise to wide spectral occupation in the frequency domain (bandwidth from near DC to a few gigahertz). The way by which the information data symbols modulate the pulses may vary. Pulse Position Modulation (PPM) and Pulse Amplitude Modulation (PAM) are commonly adopted modulation schemes [23], [24]. In addition to modulation, in order to shape the spectrum of the generated signal, data symbols are encoded using pseudo-random or pseudonoise (PN) codes. Fig. 1 reports an example of signal waveform, each characterized by a TH code word. Here, T_f is the frame duration and $T_f = N_h T_c$.

During information propagation, we consider the multi-path-affected UWB radio channel. The presence of multiple paths between the transmitter and the receiver makes the channel exhibit time-variant properties. Due to the distortion, the received signal often has little resemblance with the transmitted waveform. Two popular UWB channel models are used in most research. They are the S-V model

Authorized licensed use limited to: University of Texas at Arlington. Downloaded on December 18, 2009 at 13:51 from IEEE Xplore. Restrictions apply.

[26] and the IEEE 802.15.3a [27] model. We use the IEEE 802.15.3a model in this paper. The impulse response of a channel is described as

$$h(t) = \sum_{j=1}^{L(t)} \alpha_j(t)\delta(t - \tau_j(t)), \tag{4}$$

where $\delta(t)$ is the Dirac function. $\alpha_j(t)$ and $\tau_j(t)$ are the channel gain and the delay measured at time t for the jth path. $L(t)$ is the number of paths observed at time t.

Then, the signal $r(t)$ at the receiver side can be expressed as follows:

$$\begin{aligned} r(t) &= x(t) * h(t) + \omega(t) + n(t) \\ &= \sum_{j=1}^{L(t)} \alpha_j(t)x(t - \tau_j(t)) + \omega(t) + n(t), \end{aligned} \tag{5}$$

where $x(t)$ is the transmitted signal, $\omega(t)$ is the multiuser interference, and $n(t)$ is AWGN noise.

Supposing there are N pairs of communicating UWB terminals, with each pair consisting of one transmitter and one receiver, and using one pseudorandom code, N links are active and the $SINR$ at the ith link's receiver is formed as follows [13]:

$$SINR_i = \frac{P_i g_{ii}}{R_i(\eta_i + T_f\sigma^2 \sum_{k=1,k\neq i}^{N} P_k g_{ki})} \quad (i = 1, 2, \cdots, N), \tag{6}$$

where R_i is the binary bit rate of the ith link, P_i is the average power emitted by the ith link's transmitter, g_{ij} is the path gain from the ith link's transmitter to the jth link's receiver, η_i is the background noise energy plus interference from other non-UWB systems, and σ^2 is a dimensional parameter depending on the shape of monocycle.

Even though the parameters characterizing the channel impulse response in (5) are time varying, we can generally assume, however, that this rate of variation is slow compared to the pulse rate. In other words, we can assume the channel to be stationary within an observation time T, which is larger than the average pulse repetition period. Under this assumption, (5) can be rewritten as follows:

$$r(t) = \sum_{j=1}^{L(t)} \alpha_j x(t - \tau_j(t)) + \omega(t) + n(t). \tag{7}$$

In this case, the total multipath gain g, which measures the total amount of energy collected over $L(t)$ pulses, is determined as follows:

$$g = \sum_{j=1}^{L(t)} |\alpha_j|^2. \tag{8}$$

Note that $g \leq 1$ and is related with the attenuation suffered by the transmitted pulses during propagation. In multipath environments, g decreases with distance according to the path-loss model [28] as follows:

$$g = \frac{g_0}{d^\beta}, \tag{9}$$

where g_0 is the reference value for power gain evaluated at $d_0 = 1m$ and β is the exponent of power or energy attenuation law.

3.3 The Impact of Simultaneous Transmissions on Network Throughput

Within a network, piconets can be treated as independent of each other since the distance among piconets is long enough to permit us to ignore the interference among them (the piconet formation scheme can ensure that this assumption is held). Thus, the analysis on the change of network throughput can be simplified into a set of independent analysis on the change of throughput for individual piconets. Then, combining all results together linearly, we can obtain the impact of simultaneous transmission on the aggregate throughput. In the following parts, the discussions focus on the impact of simultaneous transmissions on the throughput within a piconet.

According to the noisy channel coding theorem: If the data transmission rate is less than the channel capacity, there exist channel codes (and decoders) that make it possible to achieve reliable communication. Otherwise, it is not possible to make the probability of error tend toward zero with any code. In this paper, the theoretic maximum channel capacity (C_{t-max}) is defined as the largest channel capacity implied by the channel state, and the achievable maximum channel capacity (C_{a-max}) is defined as the largest channel capacity that is acquired using the highest data rate to make reliable communication. From (2) and (6), it is noted that C is in inverse proportion to R, that is, $C \propto \frac{1}{R}$. We derive the data rate referring to C_{a-max}, noted as R_{a-max}, to achieve our goal—trying to not only enhance the data rate to shorten the transmission latency but also ensure reliable communication. The value of R_{a-max} is calculated as follows:

$$R_{a-max,i} = \sqrt{\frac{\xi P_i g_{ii}}{\eta_i + T_f\sigma^2 \sum_{k=1,k\neq i}^{N} P_k g_{ki}}}. \tag{10}$$

For estimating the throughput of a piconet in which there are N pairs of communication terminals making communication simultaneously with data packets R_{a-max}, the throughput (TH_{put}) of this piconet is calculated as follows:

$$TH_{put} = \sum_{i=1}^{N} \sqrt{\frac{\xi P_i g_{ii}}{\eta_i + T_f\sigma^2 \sum_{k=1,k\neq i}^{N-1} P_k g_{ki}}}. \tag{11}$$

For an existing piconet, if we add m more pairs of communication terminals, what is the influence on the throughput of this piconet? Through analyzing the change of throughput when adding a different number of communication pairs or picking up the same number of communication pairs but located at different positions, we try to obtain the criterion for the formation of a simultaneous transmission subset.

In order to simplify the description, we let $U_i \triangleq T_f\sigma^2 \sum_{k=1,k\neq i}^{N} P_k g_{ki}$. Without losing generality, we let the newly added communication pairs be pair $N+1$ to pair $N+m$. For existing communication pairs (that is, pair 1 to pair N), the new achieved channel capacity $C'_{a-max,i}$ is

$$C'_{a-max,i} = \sqrt{\frac{\xi P_i g_{ii}}{\eta_i + U_i + T_f\sigma^2 \sum_{k=N+1}^{N+m} P_k g_{ki}}} \quad (i = 1, \cdots, N). \tag{12}$$

Moreover, the achieved channel capacity for new communication pairs $C_{a-max,i}$ is

Authorized licensed use limited to: University of Texas at Arlington. Downloaded on December 18, 2009 at 13:51 from IEEE Xplore. Restrictions apply.

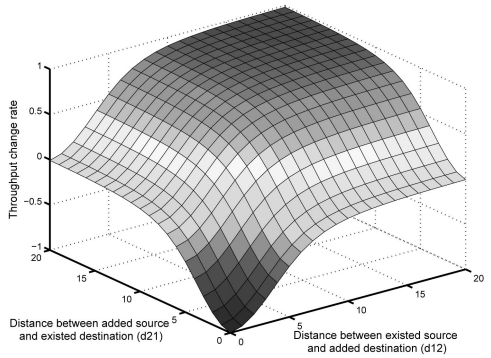


Fig. 2. Relationship between the throughput change rate and the strength of multiuser interference.

$$C_{a-max,i} = \sqrt{\frac{\xi P_i g_{ii}}{\eta_i + T_f \sigma^2 \sum_{k=1,k\neq i}^{N+m} P_k g_{ki}}} \quad (i = N+1, \cdots, N+m). \tag{13}$$

Based on the results in (12), (13), and (11), the influence of adding more simultaneous transmissions on the throughput of a piconet is expressed as the change of piconet throughput, denoted as $\triangle TH_{put}$ and calculated using (14):

$$\begin{aligned} \triangle TH_{put} &= TH'_{put} - TH_{put} \\ &= \sum_{i=1}^{N} \sqrt{\frac{\xi P_i g_{ii}}{\eta_i + U_i + T_f \sigma^2 \sum_{k=N+1}^{N+m} P_k g_{ki}}} \\ &\quad + \sum_{i=N+1}^{N+m} \sqrt{\frac{\xi P_i g_{ii}}{\eta_i + T_f \sigma^2 \sum_{k=1,k\neq i}^{N+m} P_k g_{ki}}} \\ &\quad - \sum_{i=1}^{N} \sqrt{\frac{\xi P_i g_{ii}}{\eta_i + U_i}}. \end{aligned} \tag{14}$$

We also obtain the relationship between the new data rate $R'_{max,i}$ and the original data rate $R_{max,i}$ for node i $(i = 1, \cdots, N)$, as shown in (15). Note that adding some communication pairs into an existing network will decrease the highest data rate, which ensures reliable communication since $\frac{T_f \sigma^2 \sum_{k=N+1}^{N+m} P_k g_{ki}}{\xi P_i g_{ii}}$ is always positive:

$$\frac{1}{R'^2_{a-max,i}} = \frac{1}{R^2_{a-max,i}} + \frac{T_f \sigma^2 \sum_{k=N+1}^{N+m} P_k g_{ki}}{\xi P_i g_{ii}}. \tag{15}$$

From (14) and (15), we observe that, when adding more communication pairs, the change of piconet throughput is related to the negative influence caused by degrading the highest data rate for existing communication pairs and the positive influence due to permitting more communication pairs to work concurrently. Thus, from a networkwide perspective, letting more nodes work concurrently does not definitely mean to upgrade or degrade the throughput of a piconet. There is a watershed for it. That is, when the negative influence is equal to or smaller than the positive influence of adding some communication pairs into a net that existed, the network performance in terms of throughput will be improved or at least will not be degraded. Consequently, we can formulate the criterion that guarantees the network throughput to be improved when allowing more simultaneous communication pairs as follows:

TABLE 1
Typical Values for Parameters in (17)

Parameter	Typical Value	Parameter	Typical Value
T_f	100 ns	σ^2	1.9966×10^{-3}
η	$2.568 \times 10^{-21}\ V^2 s$	P	$1\ \mu W$
d	1 m	ξ	$\log_2^e$
g_0	7.9433×10^{-6}		

$$\begin{aligned} &\sum_{i=1}^{N} \sqrt{\frac{\xi P_i g_{ii}}{\eta_i + U_i}} - \sum_{i=1}^{N} \sqrt{\frac{\xi P_i g_{ii}}{\eta_i + U_i + T_f \sigma^2 \sum_{k=N+1}^{N+m} P_k g_{ki}}} \\ &\leq \sum_{i=N+1}^{N+m} \sqrt{\frac{\xi P_i g_{ii}}{\eta_i + T_f \sigma^2 \sum_{k=1,k\neq i}^{N+m} P_k g_{ki}}}. \end{aligned} \tag{16}$$

First, we consider the $N = 1$ and $m = 1$ scenario as our analysis basis. We assume that the distance between transmitters and receivers is the same for each communication pair (that is, $d_{ii} = d$), thus each communication pair can use the same power to transmit. Moreover, the noise floor for communication is fixed. Thus, (14) is changed to

$$\begin{aligned} \triangle TH_{put} = &\sqrt{\frac{\xi P g_0}{\eta d_{22}^{\beta} + T_f \sigma^2 P g_0 (\frac{d_{22}}{d_{12}})^{\beta}}} + \sqrt{\frac{\xi P g_0}{\eta d_{11}^{\beta} + T_f \sigma^2 P g_0 (\frac{d_{11}}{d_{21}})^{\beta}}} \\ &- \sqrt{\frac{\xi P g_0}{\eta d_{11}^{\beta}}}. \end{aligned} \tag{17}$$

In this case, $\triangle TH_{put}$ is a function of the distance between the original existing communication pair's transmitter and the added communication pair's receiver (d_{12}), the distance between the added communication pair's transmitter and the original existed communication pair's receiver (d_{21}), that is, $\triangle TH_{put} = f(d_{12}, d_{21})$. We define the throughput change rate of a piconet as $\frac{\triangle TH_{put}}{TH_{put}}$. Based on (17), we plot the piconet throughput change rate versus the strength of multiuser interference. Fig. 2 shows the hypersurface for $\forall d_{12}, d_{21} \in [0, 20]$. Table 1 shows the parameters we use.

Note that, to ensure the throughput to be enhanced when adding one or more communication pairs, the shortest distance for d_{12} and d_{21} should be at least equal to a threshold d_{min}, which is related with the choice of transmission power (P), environment noise strength (η), environment exponential (β), symbol time (T_f), monocycle shape (σ^2), and power gain (g_0) evaluated at $d_0 = 1m$, except the distance between the transmitter and the receiver of the originally existing communication pair. That is,

$$d_{min} = \left\{ \left(\frac{1}{(\sqrt{\frac{1}{\eta}} - \sqrt{\frac{1}{\eta + T_f \sigma^2 P \frac{g_0}{d_{max}^{\beta}}}})^2} - \eta \right) (g_0 T_f \sigma^2 P)^{-1} \right\}^{\frac{1}{\beta}}. \tag{18}$$

Authorized licensed use limited to: University of Texas at Arlington. Downloaded on December 18, 2009 at 13:51 from IEEE Xplore. Restrictions apply.

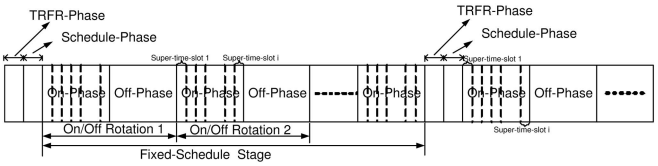


Fig. 3. System time scheme structure.

4 Throughput-Maximized MAC Protocol (TM-MAC) Design

We have proposed an energy-efficient MAC protocol, ASCEMAC, in [18] for WSNs. ASCEMAC intelligently forces nodes to power on and off their batteries alternately to implement communication, as well as to reduce energy consumption on collision and idle listening to extend network lifetime. However, for UWB communication systems, TDMA-based and contention-based mutual exclude media access control schemes are not the best choice anymore in terms of spectrum efficiency. Motivated by this challenge, we propose our algorithm: throughput-maximized MAC protocol especially for UWB communication systems.

TM-MAC divides the system time into four phases: *Traffic-Rate and Failure-Rate (TRFR) Phase*, *Schedule-Broadcast Phase*, *On-Phase*, and *Off-Phase*. TRFR message, TRFR-Phase duration design, matching schedule establishment and maintenance, schedule interval design, and time-slot allocation mechanisms for TM-MAC are the same as in ASCEMAC. Although, in TM-MAC, during the On-Phase, the further divided supertime slots are occupied by subsets individually. TM-MAC, based on the network topology, is responsible for further dividing a network into a set of subsets in which communication pairs can make communication simultaneously. Consequently, TM-MAC cannot only inherit the advantages of ASCEMAC but also maximizes network throughput.

4.1 Introduction to ASCEMAC

ASCEMAC leverages the characteristics of the free-running timing method and the advantages of the fuzzy logic system on uncertain problems. In ASCEMAC, the timing-rescheduling scheme and time-slot allocation algorithm provide an approach to remove the tight dependency on network synchronization for energy-efficient MAC protocols, which is a critical constraint for network upgrading and expanding. Furthermore, considering the heterogeneous nature of WSN, a traffic-strength-based and network-density-based designing model is built. This model equips the system with the capability to determine essential algorithm parameters adaptively, which greatly influences system performance in terms of energy reservation and communication capability. In addition, adaptive methods for parameter adjustment are utilized. In opposition to existing network synchronization schemes, ASCEMAC is a control-center-exhaustion scheme. It is data-gathering nodes whose energy is more abundant and easier to recharge than data-collection nodes that are in charge of most working loads to form a matching operation among nodes.

T (2 bits)	SRC (8 bits)	AR_d (8 bits)	SR_d (8 bits)	FR (8 bits)	OR (8 bits)

T packet type
SRC source address
AR_d data arrival rate
SR_d data service rate
FR transmission failure rate
OR buffer overflowing rate

Fig. 4. TRFR message format.

ASCEMAC protocol divides system time into four phases: *TRFR-Phase*, *Schedule-Phase*, *On-Phase*, and *Off-Phase* (Fig. 3).

- *TRFR-Phase*. It is preserved for data-collection nodes to send TRFR messages (Fig. 4) to data-gathering nodes.
- *Schedule-Phase*. It is preserved for data-gathering nodes to locally broadcast phase-switching schedules.
- *Off-Phase*. It is preserved for data-collection nodes to power off their radios. In this phase, there is no communication, but data storing and sensing may happen.
- *On-Phase*. It is preserved for data-collection nodes to power on their radios to carry on communication.

At the end of each *On-Phase*, nodes go on "vacation"—*Off-Phase*—for a period of time. Thus, new arrivals during an *On-Phase* can be served in first-in, first-out (FIFO) order. Although new arrivals occurring during an *Off-Phase*, rather than going into service immediately, wait until the end of this *Off-Phase*, they are then served in the *On-Phase* and in FIFO order. Interarrival time and service time for data packets are independent and follow general distribution $F(t)$ and $G(s)$ individually. For the average interarrival time $\frac{1}{\lambda}$, we have $0 < \frac{1}{\lambda} = \int_0^\infty tdF(t)$. Similarly, for the average service time μ, we have $0 < \mu = \int_0^\infty sdG(s)$.

According to the received schedule messages (Fig. 5), nodes set up their own phase-switching schedules, which ensure them to switch to the same phase simultaneously.

ASCEMAC utilizes two techniques to make its scheme robust and feasible to use the free-running timing method [29], which allows nodes to run on their own clocks and makes a contribution to save the energy used by setting up and maintaining the global or common timescale. First, schedule messages are broadcasted. Leveraging the property of broadcast, schedule messages can reach all data-collection nodes at the same time once ignoring the difference of propagation time of them (it is reasonable since the propagation time within a cluster is between 0.1 and 1 microseconds). Moreover, nodes go to the *On-Phase* immediately after receiving schedule messages. Second, in a schedule message, all time references, such as On-Duration

T (2 bits)	SRC (8 bits)	D_{off} (8 bits)	D_{on} (8 bits)
SRC_1 (8 bits)	$DEST_1$ (8 bits)	D_{df1} (8 bits)	D_{s1} (8 bits)
SRC_2 (8 bits)	$DEST_2$ (8 bits)	D_{df2} (8 bits)	D_{s2} (8 bits)

SRC_i (8 bits)	$DEST_i$ (8 bits)	D_{dfi} (8 bits)	D_{si} (8 bits)

T packet type
SRC source address
D_{off} off phase duration
D_{on} on phase duration
D_{si} supper time slot duration for node i
D_{dfi} supper time slot starts defer time
SRC_i source address for ith supper time slot
$DEST_i$ destination address for ith supper time slot

Fig. 5. Schedule message packet format for ASCEMAC.

Authorized licensed use limited to: University of Texas at Arlington. Downloaded on December 18, 2009 at 13:51 from IEEE Xplore. Restrictions apply.

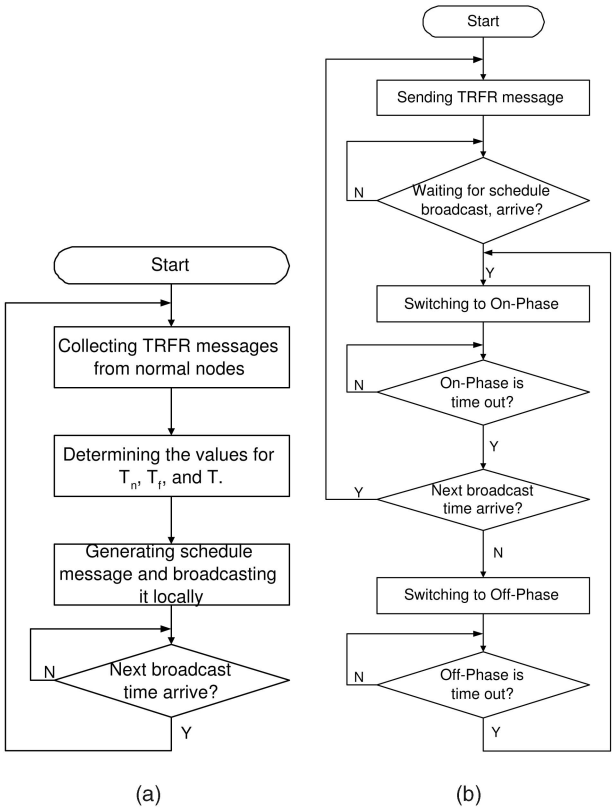


Fig. 6. Flow chart for (a) data-gathering nodes and (b) data-collection nodes to establish and maintain matching schedules in ASCEMAC.

and Off-Duration, are relative values rather than absolute values. This property can eliminate errors introduced by sending time and access time.

Note that, based on schedule messages and nodes' local clocks, phase-switching schedules are supposed to be established at each node to ensure matching operations if there is no clock drift. However, mismatching operations among nodes are unavoidable since there are always clock-drifts caused by unstable and inaccurate frequency standards. Therefore, it is possible that transmitters have powered on their radios to send messages, but the receivers' radios are still powered off. Those mismatching operations cause communication to fail. Moreover, with the accumulative clock drift becoming bigger and bigger, the impact on communications turns more and more serious. The solution in ASCEMAC is to rebroadcast the schedule message, which forces data-collection nodes to remove accumulative clock drifts and to reestablish matching schedules.

Although, how can data-collection nodes know the time of next schedule broadcast so as to power on their radios? The solution is that ASCEMAC includes reschedule interval information in the schedule messages. To preestimate the value of the schedule interval, a rescheduling-FLS is designed to monitor the influence of accumulative clock drifts, the variance of traffic strength, and the service capability on communications. Then, ASCEMAC can adjust the schedule interval and power-on/off duration adaptively. ASCEMAC uses

$$T_i = \xi_i \times T_{i-1} \tag{19}$$

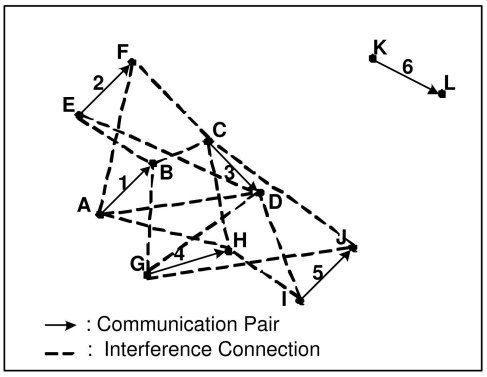


Fig. 7. Network graph G.

as the interval adjustment function, where T_i is the interval for the ith schedule broadcast and ξ_i is the ith adjustment factor determined by our rescheduling-FLS.

Hence, each node within a cluster is synchronized to a reference packet (schedule message) that is injected into the physical channel at the same instant. Furthermore, after the same period of time specified by T_n, all nodes switch to the *Off-Phase* and stay there for a T_f period. Finally, all nodes switch back to the *On-Phase*. Phase is circulatedly switched in this way (see Fig. 6).

4.2 Optimizing Piconet Throughput

The network is represented as a directed graph $G = (V, E)$. V is the set of nodes in a piconet. $e = (u, v)$ is an edge in E if and only if nodes u and v are the transmitter and receiver of a communication pair. Fig. 7 shows an example, in which nodes A, C, E, G, I, and K are transmitters, whereas B, D, F, H, J, and L are receivers. If a receiver is located within another transmitter's communication range or interference untolerable range formulate by (18), throughput degradation will not be avoided when they communicate simultaneously. This interference is denoted by dotted lines.

In our algorithm, the interference caused by the newly added communication pairs is intolerable when the created throughput is smaller than the original one. Otherwise, it is tolerable. We consider all communication pairs in a piconet to generate the interference tolerable graph $G' = (V', E')$ according to (18). $V' \subset E$, that is, each point in G' is a communication pair in G. $e' = (u', v')$ is an edge in E' if and only if the achieved throughput is bigger than the throughput generated by those two terminals separately. According to the network topology, we utilize the conclusion acquired in (18) to detect the intolerable interference from other communication pairs. Fig. 8a presents the inference tolerable graph for the graph in Fig. 7.

We generate the potential subset to form graph G''. $G'' = (V_1, V_2, E'')$ is a bit-partite graph such that $V_1 = V'$ and each point in V_2 presents all cliques and subcliques in G'. $e'' = (u'', v'')$ is an edge in E'' if and only if $u'' \in V_1$, $v'' \in V_2$, and u'' belongs to one of the cliques in G' represented by v''. Fig. 8b represents the potential group formation graph for the inference tolerable graph shown in Fig. 8a.

Each clique in G' represents a potential subset of communication pairs making simultaneous communication to enhance throughput. We represent each point in V_1 as an one-off source that is granted and must to be used once in

Authorized licensed use limited to: University of Texas at Arlington. Downloaded on December 18, 2009 at 13:51 from IEEE Xplore. Restrictions apply.

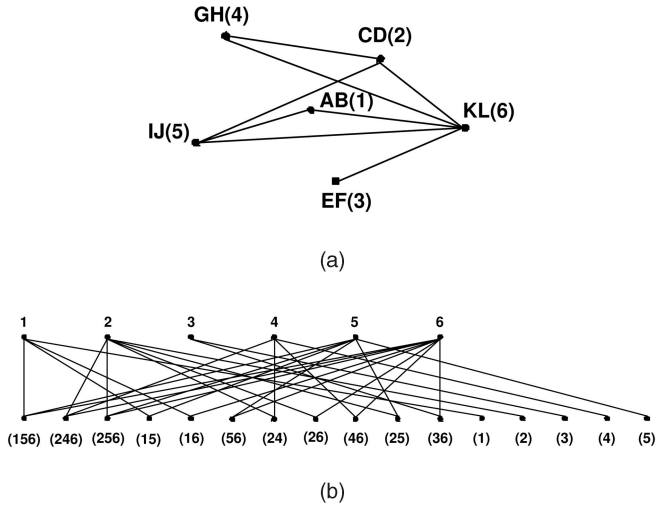


Fig. 8. (a) Interference tolerable graph G' and (b) Potential Group formation graph G''.

supertimeslot. Then, the subset formation in a piconet represents the optimal classification for all nodes within a piconet, and a point in V_2 is permitted to occupy the channel mutually excluded if and only if it can contribute to achieve higher throughput and one-off source is still available.

Let I_{ij} be an indicator function such that $I_{ij} = 1$ if the point $j \in V_2$ is allocated with channel by point $i \in V_1$ and $I_{ij} = 0$ otherwise. Let $TH'_{put,j}$ be the subthroughput generated by point j. Then, the channel allocation problem can be represented as a set of the following linear constraints:

$$\begin{aligned} &\forall i, \quad \sum_j I_{ij} = 1, \\ &\forall j, \forall i, \quad r_j = TH'_{put,j} \times \sum_i I_{ij}, \end{aligned} \tag{20}$$

where r_j is the subthroughput generated by point j in V_2 and the unit for it is pks/sec. Note that this set of constraints captures the location-dependent interference on piconet throughput characteristics of UWB communication systems.

The utility function $U(r)$ for a throughput r is defined as

$$U(r) = r. \tag{21}$$

Since our goal for subset optimization is to improve piconet throughput as much as possible, maximizing the piconet throughput problem can be modeled by the following equations:

$$Maximize \quad \sum_j U(r_j).$$

Subject to

$$\begin{aligned} &\forall i, \quad \sum_j I_{ij} = 1, \\ &\forall j, \forall i, \quad r_j = TH'_{put,j} \times \sum_i I_{ij}. \end{aligned} \tag{22}$$

4.3 Essential Parameters Design

The studies in [18] and [19] have shown that essential algorithm parameters such as power-on/off duration and schedule-broadcast interval, which greatly influence system performance in terms of energy reservation and communication capability. How to adaptively determine the value for those essential parameters of TM-MAC is the main task in this section.

4.3.1 Off-Phase Duration (T_f)

It is now recognized [30], [31] that traffic in wired and wireless communication networks is better described by heavy-tailed distributions rather than by Poisson, Gaussian, or other classical distributions with exponentially decreasing tails. In this paper, we model network arrivals as a Pareto distribution, a heavy-tailed distribution. The probability mass function is given in (23):

$$f(x) = \alpha k^{\alpha} x^{-\alpha-1}, \quad 1 < \alpha < 2, \quad k > 0, \quad x \geq k, \tag{23}$$

and its cumulative distribution function is given by

$$F(x) = 1 - \left(\frac{k}{x}\right)^{\alpha}, \tag{24}$$

where k represents the smallest value the random variable can take.

In this case, we establish an embedded-Markov chain to express the packet arrive process for each user. $N(t)$ is the number of data packets in buffer at time t. N_n^- stands for the queue length when the nth data packet arrives (the current arrival data packet not included). Even though the queue length of each user does not own a Markov property anymore, N_n^-, $n \geq 0$ forms a Markov chain, an embedded-Markov chain. The average arrival interval ($\frac{1}{\lambda}$) is given as

$$\frac{1}{\lambda} = \int_k^{\infty} x dF(x) = \frac{\alpha k}{\alpha - 1}. \tag{25}$$

During *Off-Phase*, there are about $T_{f,i} \times \lambda_i$ data packets that arrived at node i. We assume that the buffer size for node i is B_s. Then, the duration, denoted by t_i, within which node i's buffer can be fully filled with arrived data packets, is given by $t_i = \frac{B_s}{\lambda_i}$. Considering the first criteria, $T_{f,i}$ for node i should be no longer than t_i. In this algorithm, we let

$$T_{f,i} = t_i = \frac{B_s}{\lambda_i} = B_s\left(\frac{\alpha_i k_i}{\alpha_i - 1}\right). \tag{26}$$

We assume that B_s is a constant, $\alpha_i = \alpha$ for all users, while k_i follows a uniform distribution at range $[0, k^*]$. Note that the cumulative density function for $T_{f,i}$ is given as

$$F_{T_{f,i}}(t_{f,i}) = P\{T_{f,i} \leq t_{f,i}\} = F_K\left(\frac{t_{f,i}(\alpha - 1)}{\alpha B_s}\right). \tag{27}$$

Since

$$F_K(k) = \frac{k}{k^*}, \tag{28}$$

then

$$F_{T_{f,i}}(t_{f,i}) = \frac{t_{f,i}(\alpha - 1)}{\alpha k^* B_s}. \tag{29}$$

Since, within a cluster, there are multiple nodes that have various traffic arrival rates, the duration for all nodes will

Authorized licensed use limited to: University of Texas at Arlington. Downloaded on December 18, 2009 at 13:51 from IEEE Xplore. Restrictions apply.

not be the same. If we let the *Off-Phase* duration for an entire cluster $T_{f,tot}$ be equal to the ith user, $T_{f,tot} = T_{f,i}$. Moreover, for a new arrival to an idle system, rather than going into service immediately, it waits for the end of the vacation period and arrivals are served following a first-come-first-in order. Therefore, the longer $T_{f,tot}$ is, the longer the data packets waiting in the buffer for transmission are. We leverage the $GI^*/G/1$ with the vacation model to model our system. Through analysis, we try to get the relationship between the average waiting time ($\bar{W}_j$) for the jth user and $T_{f,tot}$, that is, $\bar{W}_j = f_j(T_{f,tot})$.

Based on this conclusion, we try to get the probability (p_j) for data packets out of date for jth when the *Off-Phase* duration is equal to $T_{f,tot}$, given in (31):

$$p_j = P\{\bar{W}_j \geq W_{max}\} = 1 - F_{T_{f,tot}}(f_j^{-1}(W_{max})). \quad (30)$$

Since $T_{f,tot} = T_{f,i}$, (31) is rewritten as follows:

$$p_{ij} = P\{\bar{W}_{ij} \geq W_{max}\} = 1 - F_{T_{f,i}}(f_j^{-1}(W_{max})), \quad (31)$$

where p_{ij} is the probability of data packets out of date for a jth user when letting an ith user's *Off-Phase* duration for the entire cluster.

For a system with an *Off-Phase* duration $T_{f,i}$ and total data packets out of date probability $\Sigma_j p_j$, we represent our objective function as

$$arg\max_i \quad J(T_{f,i}) = arg\max_i \{\beta T_{f,i} - \gamma \sum_j p_{ij}\}, \quad (32)$$

where β and γ are systems parameters that respectively represent the "latency constant" and the "penalty constant," which are tuned to achieve the desired trade-off between maximizing the energy reservation period and minimizing the buffer overflowing rate.

4.3.2 On-Phase Duration (T_n)

During *On-Phase*, normal nodes start to send data packets through competition. Users, who have data packets to send, access the channel to make communication. If we let the duration for the *On-Phase* of nodes be $T_{n,tot}$, the total number of data packets (N_i) arrived is given in (33) since the traffic arrival process is independent of the data transmission process. Generally, there are two parts for N_i: one is the data packets arrived during the *Off-Phase*, denoted by $N_{f,i}$, and the other is the data packets arrived during the *On-Phase*, denoted by $N_{n,i}$:

$$N_i = N_{f,i} + N_{n,i} = \lambda_i(T_{f,tot} + T_{n,tot}). \quad (33)$$

In our *On-Phase* duration and *Off-Phase* duration design, we not only try to extend the power-off time to reserve energy (through avoiding more idle listening), but also need to ensure that the data packets are up to date. Considering that the active duration ($T_{n,i}$) should be long enough for all received data packets to be sent out, then we have

$$R_{b,i}T_{n,i} = \lambda_i(T_{n,i} + T_{f,tot}). \quad (34)$$

Solving (34) for $R_{b,i}$, we get

$$R_{b,i} = \frac{\lambda_i(T_{n,i} + T_{f,tot})}{T_{n,i}}. \quad (35)$$

TABLE 2
Number of Different Kinds of Subsets Generated with Various Node Density

	5 pairs	10 pairs	15 pairs	20 pairs	30 pairs	40 pairs
1-pair subset	1.648	2.964	4.198	5.782	8.398	10.635
2-pairs subset	0.824	1.368	2.175	3.058	5.081	7.293
3-pairs subset	0.464	0.62	0.856	1.134	1.908	2.677
4-pairs subset	0.078	0.61	0.771	1.105	1.429	1.687

From another aspect of obtaining a satisfied data successful transmission rate to acquiring data rate, that is, $\hat{R}_{b,i}$ for node i acquired in (10), we define the objective function for T_f as

$$U(T_{n,i}) = \sum_j |R_{b,j} - \hat{R}_{b,j}|. \quad (36)$$

Then, the optimum task is shown as follows:

$$T_{n,tot} = arg\min_i U(T_{n,i}). \quad (37)$$

5 Performance Evaluation

We performed extreme simulations to evaluate the performance of our algorithm, TM-MAC. A network with an number of communication pairs, which is composed of a transmitter and a receiver, is set up, and the radio range (radius) of nodes is 20 m. For each communication pair, the distance between the transmitter and the receiver is fixed at 1 m. Those communication pairs are deployed randomly in an area of $50 \times 50\ \mathrm{m}^2$ and have no mobility. This network can be treated as one piconet in a large-scale system. Other parameters for a physical layer are the same, as in Table 1.

We deploy five to 40 communication pairs separately in the same region. Then, we form simultaneous transmission subsets using our TM-MAC. We observe that the number of various subsets generated is 1-pair subset, 2-pair subset, 3-pair subset, and 4-pair subset, which means that, in a subset, there is one communication pair, two communication pairs, three communication pairs, and four communication pairs. We run Monte Carlo simulations and make an average operation on those results to remove the randomness of simulation results. The results are shown in Table 2. We also observed the chance for each communication pair to be classified into different subsets (see Table 3).

Note that in Tables 2 and 3, three to four percent of communication pairs are being classified into 1-pair, 2-pair, or 3-pair subset. With increasing node density, there is a greater chance to form a 4-pair subset, that is, there is a 10 percent higher probability for a 40-communication-pairs scenario than for a five-communication-pairs scenario.

Within a piconet, we made simulations to check the actual throughput achieved by a different subset. Under various node densities from five to 40 communication pairs, we plot throughput versus total communication pairs within the same piconet we set up (See Fig. 9a). Note that a subset, within which there are more communication pairs making communication simultaneously, acquires higher throughput. In a 40-communication-pairs scenario, the

Authorized licensed use limited to: University of Texas at Arlington. Downloaded on December 18, 2009 at 13:51 from IEEE Xplore. Restrictions apply.

TABLE 3
Percentage of Communication Pairs Being Classified into within Different Kinds of Subsets for Various Node Density

%	5 pairs	10 pairs	15 pairs	20 pairs	30 pairs	40 pairs
1-pair subset	32.96	29.64	27.987	28.91	27.993	26.587
2-pair subset	32.96	27.36	29	30.58	33.873	36.465
3-pair subset	27.84	18.6	17.12	17.01	19.08	20.078
4-pair subset	6.24	24.4	25.893	23.5	19.053	16.87

throughput achieved by a four-pair subset is 119.309 Kbps, which is around two times the throughput achieved by a 1-pair subset. Moreover, with the node density increase, the largest throughput that can be achieved is decreased since the interference coming from other users is increased.

We compared our TM-MAC against IEEE 802.15.3a, which uses a mutually excluded scheme to implement media access control—the TDMA scheme. We check the achieved throughput, the transmission time needed for a certain traffic load, and the longest latency for data packets for our TM-MAC and IEEE 802.15.3a (See Figs. 9b, 10a, and 10b). Note that our TM-MAC can achieve higher throughput than IEEE 802.15.3a at around 5.97 percent to 25.358 percent. Given same amount of traffic to networks, which run TM-MAC and IEEE 802.15.3a separately, the transmission time needed for TM-MAC is shorter than the one for 80.215.3a. The reduced ratio for various node densities from 40 communication pairs to five communication pairs is located within the range from 10.358 percent to 32.18 percent. Since IEEE 802.15.3a uses the mutually excluded scheme for media access control, the communication for various communication pairs is carried out serially, while, for TM-MAC, some communication pairs can make communication simultaneously. The longest latency for TM-MAC is shorter than IEEE 802.15.3a. The decreased ratio is from 18.554 percent to 65.869 percent.

6 Conclusions

In this paper, we proposed a MAC protocol: the throughput maximized MAC protocol (TM-MAC). In TM-MAC, we implemented a multiuser access way instead of a mutual

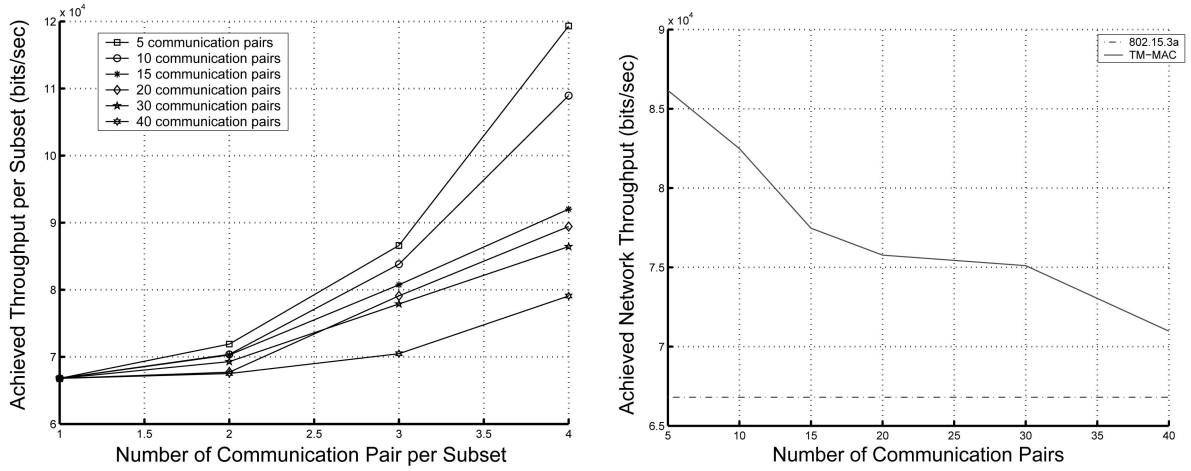


Fig. 9. (a) Throughput achieved per subset and (b) average throughput achieved.

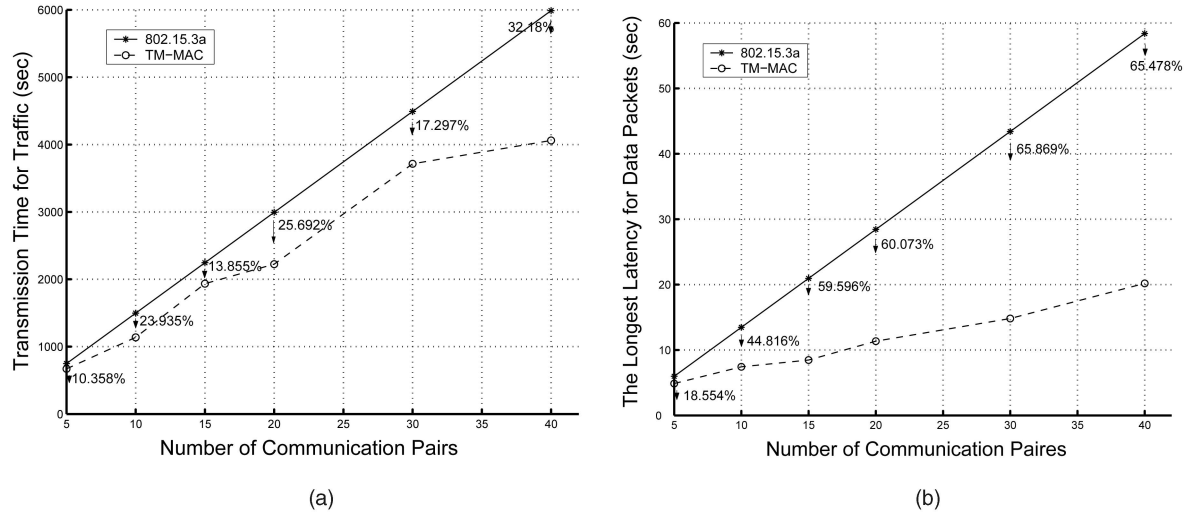


Fig. 10. (a) Transmission duration needed and (b) longest latency for data packet.

Authorized licensed use limited to: University of Texas at Arlington. Downloaded on December 18, 2009 at 13:51 from IEEE Xplore. Restrictions apply.

exclusion method such as TDMA and random access. Since the cross-layer design approach is a good solution to reach the target of highly energy-efficient WSNs, we combined a MAC layer and a physical layer together to optimize the throughput of a network. On a MAC layer, according to the network topology, TM-MAC redivides each piconet into several subsets in which communication pairs can make communication simultaneously and achieve the maximum throughput using the highest data rate. For subset formation, we proposed a general analytical framework that captures the unique characteristics of a shared wireless channel and a throughput variance and allows the modeling of a large class of systemwide throughput maximizing models via the specification of per-link utilization functions. On a physical layer, we analyzed the relationship among the theoretical maximum channel capacity, the achievable maximum channel capacity, and the data rate. For a multiuser interference, we established a model to adaptively adjust the data rate to ensure certain SNR at the receiver side.

Simulation results demonstrate that TM-MAC can implement throughput maximization to achieve short latency and transmit the same number of data packets over a network during a shorter period.

ACKNOWLEDGMENTS

This work was supported by the US Office of Naval Research (ONR) under Grants N00014-07-1-0395, N00014-03-1-0466, and N00014-07-1-1024 and by the US National Science Foundation (NSF) under Grant CNS-0721515.

REFERENCES

[1] D. Culler, D. Estin, and M. Srivastava, "Guest Editors' Introduction: Overview of Sensor Networks," *Computer*, vol. 37, no. 8, pp. 41-49, 2004.

[2] P.K. Dutta, A.K. Arora, and S.B. Bibyk, "Towards Radar-Enabled Sensor Networks," *Proc. Fifth Int'l Conf. Information Processing in Sensor Networks (IPSN '06)*, pp. 467-474, Apr. 2006.

[3] R.J. Fontana, E.R.A. Ameti, L. Beard, and D. Guy, "Recent Advances in Ultra Wideband Communications Systems," *Proc. 2002 IEEE Conf. Ultra Wideband Systems and Technologies*, pp. 129-133, May 2002.

[4] R.J. Fontana, "Recent System Applications of Short-Pulse Ultra-Wideband (UWB) Technology," *IEEE Trans. Microwave Theory Techniques*, vol. 52, no. 9, pp. 2087-2104, 2004.

[5] *Standard, ET Docket 98-153, First Report and Order in the Matter of Revision of Part 15 of the Commissions Rules Regarding Ultra-Wideband Transmission Systems*, Federal Communication Commission (FCC 02-48), Apr. 2002.

[6] J.H. Reed, *An Introduction to Ultra Wideband Communication Systems.* Prentice Hall, 2005.

[7] A. Chandra, V. Gummallla, and J.O. Limb, "Wireless Medium Access Control Protocols," *IEEE Comm. Survey and Tutorials*, vol. 3, no. 2, 2000.

[8] *Ultra Wideband Concepts for Ad-Hoc Networks (UCAN)*, http://www.prorec-projekte.de/ucan/, 2008.

[9] *I. 802.15.3-2003, IEEE Standard for Information Technology—Telecommunications and Information Exchange between Systems—Local and Metropolitan Area Networks Specific Requirements Part 15.3: Wireless Medium Access Control (MAC) and Physical Layer (PHY) Specifications for High Rate Wireless Personal Area Networks (WPANS)*, IEEE, Sept. 2003.

[10] J. Ding, L. Zhao, S.R. Medidi, and K.M. Sivalingam, "MAC Protocols for Ultra-Wide-Band (UWB) Wireless Networks: Impact of Channel Acquisition Time," *Proc. Int'l Conf. Internet, Performance, and Control of Networks (ITCOM '02)*, pp. 97-106, July 2002.

[11] N.J. August and D.S. Ha, "An Efficient UWB Radio Architecture for Busy Signal MAC Protocols," *Proc. IEEE Conf. Ultra Wideband Systems and Technologies*, pp. 325-334, May 2004.

[12] N.J. August, H. Lee, and D.S. Ha, "Pulse Sense: A Method to Detect a Busy Medium in Pulse-Based Ultra Wideband (UWB) Networks," *Proc. IEEE Conf. Ultra Wideband Systems and Technologies*, pp. 366-370, May 2004.

[13] F. Cuomo, C. Martello, A. Baiocchi, and F. Capriotti, "Radio Resource Sharing for Ad Hoc Networking with UWB," *IEEE J. Selected Areas in Comm.*, vol. 20, no. 9, pp. 1722-1732, Dec. 2002.

[14] M.-G.D. Benedetto, L.D. Nardis, M. Junk, and G. Giancola, "$(uwb)^2$: Uncoordinated, Wireless, Baseborn, Medium Access Control for UWB Communication Networks," *J. Mobile Networks and Applications*, special issue on WLAN Optimization at the MAC and Network Levels, vol. 10, no. 5, pp. 663-674, 2005.

[15] F. Zhao and L. Guibas, *Wireless Sensor Networks: An Information Processing Approach.* Morgan Kaufmann, 2004.

[16] M. Stemm and R.H. Katz, "Measuring and Reducing Energy Consumption of Network Modules in Hand-Held Devices," *IEICE Trans. Comm.*, vol. 8, no. E80-B, pp. 1125-1131, Aug. 1997.

[17] S. Biaz and Y.D. Barowski, "Gangs: An Energy Efficient MAC Protocol for Sensor Networks," *Proc. 42nd Ann. Southeast Regional Conf. (ACMSE '04)*, pp. 82-87, Apr. 2004.

[18] Q. Ren and Q. Liang, "An Energy-Efficient Mac Protocol for Wireless Sensor Networks," *Proc. IEEE Global Telecomm. Conf. (GLOBECOM '05)*, pp. 157-161, Dec. 2005.

[19] Q. Ren and Q. Liang, "A Contention-Based Energy-Efficient MAC Protocol for Wireless Sensor Networks," *Proc. IEEE Wireless Comm. and Networking Conf. (WCNC '06)*, Apr. 2006.

[20] I.E. Teletar and D.N.C. Tse, "Capacity and Mutual Information of Wideband Multipath Fading Channels," *IEEE Trans. Information Theory*, vol. 46, no. 4, pp. 1384-1400, July 2000.

[21] S. Verdu, "Spectral Efficiency in the Wideband Regime," *IEEE Trans. Comm.*, vol. 48, no. 6, pp. 1319-1343, June 2002.

[22] L. Zhao, X. Hong, and Q. Liang, "Energy-Efficient Self-Organization for Wireless Sensor Networks: A Fully Distributed Approach," *Proc. IEEE Global Telecomm. Conf. (Globecom '04)*, pp. 2726-2732, Nov. 2004.

[23] M.L. Welborn, "System Considerations for Ultra Wideband Wireless Networks," *Proc. IEEE Radio and Wireless Conf.*, pp. 628-634, Aug. 2001.

[24] I. Guvenc and H. Arslan, "On the Modulation Options for UWB Systems," *Proc. IEEE Military Comm. Conf. (MILCOM '03)*, pp. 892-897, Oct. 2003.

[25] M. Win and R. Scholtz, "Ultra-Wide Bandwidth Time-Hopping Spread-Spectrum Impulse Radio for Wireless Multiple-Access Communication," *IEEE Trans. Comm.*, vol. 48, no. 4, pp. 679-691, Dec. 2000.

[26] A.A.M. Saleh and R.A. Valenzuela, "A Statistical Model for Indoor Multipath Propagation," *IEEE J. Selected Areas in Comm.*, vol. 5, no. 2, pp. 128-137, Feb. 1987.

[27] *IEEE Document I. 802.15.SG3a, Channel Modeling Sub-Committee Report Final*, IEEE, 2003.

[28] M.D. Benedetto and G. Giancola, *Understanding Ultra Wide Band Radio Fundamentals.* Prentice Hall, 2004.

[29] J.E. Elson, "Time Synchronization in Wireless Sensor Networks," PhD dissertation, Computer Science Dept., Univ. of California, Los Angeles, 2003.

[30] K. Park and W. Willinger, *Self-Similar Network Traffic and Performance Evaluation.* John Wiley & Sons, 2000.

[31] G. Anandalingam and S. Raghavan, *Telecommunications Network Design and Management.* Springer, 2002.

Authorized licensed use limited to: University of Texas at Arlington. Downloaded on December 18, 2009 at 13:51 from IEEE Xplore. Restrictions apply.



Qingchun Ren received the BS and MS degrees from the University of Electrical Science and Technology of China in 1997 and 2003, respectively, both in electrical engineering. She is currently working toward the PhD degree in electrical engineering at the University of Texas, Arlington. Since August 2003, she has been a research assistant in the Wireless Communication Network Group, University of Texas, Arlington. Her research interests include sensor networks (energy efficiency, cross layer design, optimal sensor deployment, etc.), fuzzy logic systems, query processing for sensor database systems, cognitive radio systems, and underwater acoustic sensor networks. She is a student member of the IEEE.



Qilian Liang received the BS degree from Wuhan University in 1993, the MS degree from the Beijing University of Posts and Telecommunications in 1996, and the PhD degree from the University of Southern California (USC) in May 2000, all in electrical engineering. He joined the faculty of the University of Texas, Arlington, in August 2002. Prior to that, he was a member of the technical staff at Hughes Network Systems, Inc., San Diego. His research interests include sensor networks, wireless communications, wireless networks, communication system and communication theory, signal processing for communications, fuzzy logic systems and applications, and collaborative and distributed signal processing. He has published more than 120 journal and conference proceedings, six book chapters, and has six US patents pending. He received the 2002 *IEEE Transactions on Fuzzy Systems* Outstanding Paper Award, the 2003 US Office of Naval Research (ONR) Young Investigator Award, the 2005 UTA College of Engineering Outstanding Young Faculty Award, and the 2007 AFOSR Summer Faculty Fellowship Program Award. He is a senior member of the IEEE.

▷ **For more information on this or any other computing topic, please visit our Digital Library at** www.computer.org/publications/dlib.

Authorized licensed use limited to: University of Texas at Arlington. Downloaded on December 18, 2009 at 13:51 from IEEE Xplore. Restrictions apply.

Int J Wireless Inf Networks (2009) 16:209–216
DOI 10.1007/s10776-009-0097-x

Diversity in Radar Sensor Networks: Theoretical Analysis and Application to Target Detection

Hung D. Ly · Qilian Liang

Published online: 27 June 2009
© Springer Science+Business Media, LLC 2009

Abstract We study a diversity scheme based on waveform design and space-time adaptive processing to improve the detection performance of radar sensor networks in the presence of certain types of interference. To reduce the interference between radar sensors and maximize the signal-to-interference-plus-noise ratio, we use an orthogonality criterion to design waveforms for radar sensors. Besides, performance of radar sensor networks depends largely on clutter which is extended in both angle and range and is spread in Doppler frequency. By using the space-time adaptive processing, effects of clutter can be suppressed. We also propose a receiver for diversity combining and, as an application example, we investigate the detection performance of radar sensor networks using the proposed diversity scheme. Simulation results for both non-fluctuating targets and fluctuating targets show that the performance of the proposed scheme is superior to that of the single radar with the spatial-temporal diversity only.

Keywords Waveform design · Space-time adaptive processing · Diversity · Target detection · Radar sensor networks

H. D. Ly (✉)
Department of Electrical and Computer Engineering, Texas A&M University, College Station, TX 77843, USA
e-mail: hungly@tamu.edu

Q. Liang
Department of Electrical Engineering, University of Texas at Arlington, Arlington, TX 76013, USA
e-mail: liang@uta.edu

1 Introduction

Radar sensor network (RSN) consists of collaboratively operating radar sensors which have capabilities of sensing, signal processing and wireless communication. Sensors are deployed ubiquitously on airborne unmanned vehicles and networked together in an ad-hoc fashion to perform various tasks such as surveillance, battlefield, disaster relief, search and rescue, etc. RSN has advantages compared to a single radar in improving the system sensitivity, reducing obscuration effects and vulnerability, and increasing the detection performance. However, some challenging problems such as networking between sensors, canceling effects of interference, power efficient communication, and reducing complexity of signal processing schemes need to be considered. Only few work on these aspects has been done. Kadambe [1] recently proposed a minimax entropy-based technique to reduce the processing complexity in the RSN. In [2], relative merits of the RSN and the balance between increased performance, complexity and cost were discussed. In this paper, we propose a method to design the waveform to cancel the interference between sensors and maximize the signal-to-interference-plus-noise ratio (SINR). In literature on the waveform design, Fitzgerald [3] demonstrated the inappropriateness of waveform selection based on measurement quality alone: the interaction between the measurement and the track can be indirect, but must be taken into account. Bell [4] used the information theory to design waveform for the measurement of extended radar targets exhibiting resonance phenomena. Baum [5] used the singularity expansion method to design some discriminant waveforms. However, these design methods were used for the single radar only. In [6], the RSN for automatic target recognition was studied, but clutter and jammer were not considered.

Performance of the RSN depends largely on clutter which is extended in both angle and range and is spread in Doppler frequency because of motion of the platform and target. Space-Time Adaptive Processing (STAP) or spatial-temporal diversity has become an excellent technique to suppress effects of clutter. STAP refers to the simultaneous processing of the spatial samples from an array antenna and the temporal samples provided by the echoes from multiple pulses of a coherent processing interval. A considerable amount of work has been done to develop STAP for processing data from airborne or space-borne radars to reliably detect moving targets of interest in the presence of strong clutter returns and jamming [7–9]. By combining waveform design and spatial-temporal diversity, we can perform spatial-temporal-frequency diversity in RSN. Our studies show that the proposed diversity scheme can improve the detection performance with a low false alarm probability.

The rest of this paper is organized as follows. In Sect. 2, we propose a method to design waveforms. Spatial-temporal diversity and interference analysis are discussed in Sect. 3. In Sect. 4, we propose a diversity combining scheme and analyze detection performance for non-fluctuating targets as well as fluctuating targets. Simulation results and performance analysis are discussed in Sect. 5, and in Sect. 6, we conclude the paper.

2 Waveform Design

Sensors in the RSN may interfere with one another and SINR may be very low if waveforms are not properly chosen. Consider the constant frequency pulse waveform for radar i:

$$x_i(t) = \sqrt{\frac{E}{T}}\exp(j2\pi(f+\Delta_i)t), 0 \le t \le T. \tag{1}$$

where E is the waveform energy, T is the waveform pulse duration and Δ_i is a frequency shift for radar sensor i. To minimize the interference between radar sensors, we need to find a set of frequency shifts $\{\Delta_i\}_{i=0}^{M-1}$ (M is the number of radar sensors) for which the waveforms are orthogonal. Let $\mathrm{cov}(k,l)$ denote the cross-correlation between the waveforms $x_k(t)$ and $x_l(t)$.

$$\begin{aligned}\mathrm{cov}(k,l) &= \int_0^T x_k(t)x_l^*(t)dt, \\ &= E\mathrm{sinc}((\Delta_k-\Delta_l)T)\exp(j\pi(\Delta_k-\Delta_l)T).\end{aligned} \tag{2}$$

If $\pi(\Delta_k-\Delta_l)T = i\pi$, the waveforms $x_k(t)$ and $x_l(t)$ are orthogonal. A set of frequency shifts $\{\Delta_i\}_{i=0}^{M-1}$ therefore can be chosen such that:

$$\Delta_i = \Delta_k - \Delta_l = \frac{i}{T}, i = 0,1,\ldots,M-1. \tag{3}$$

Based on (3), we are sure that the waveforms can co-exist if the frequency shift is i/T between two waveforms, i.e., orthogonality among waveforms can be achieved by separating frequencies of waveforms by multiplying an integer with the inverse of the waveform pulse duration.

3 Spatial-Temporal Diversity and Interference Analysis

3.1 Spatial-Temporal Diversity

At each sensor, we use a receiver with an array antenna, depicted in Fig. 1, which consists of an N-element uniform linear array with inter-element spacing h_i and K pulse repetition interval (PRI) time taps. Consider a signal $s_i(t) = A\exp(j\Omega_i t)$ impinging on the array. If the angle of arrival wave relative to the array is θ, the signal observed at the nth array element is

$$\begin{aligned}g_n(t) &= A\exp\left\{j(\Omega_i(t-\frac{nh_i}{c}\sin\theta)+\phi_0)\right\}, \\ & n = 0,1,\ldots,N-1\end{aligned} \tag{4}$$

where the phase offset ϕ_0 accounts for the absolute phase at the first element. We consider N samples formed from N array elements at time t_0 and map these N element samples into a vector form to have a snapshot of the array at a fixed time.

$$\begin{aligned}\mathbf{g} &= A_1\left[1 \;\; \exp(-\frac{j2\pi h_i}{\lambda_i}\sin\theta) \;\; \ldots \;\; \exp(-\frac{j2\pi(N-1)h_i}{\lambda_i}\sin\theta)\right]' \\ &= A_1\mathbf{a}_s(\overline{\theta}_i)\end{aligned} \tag{5}$$

Here, $A_1 = A\exp(j(\Omega_i t+\phi_0)), \overline{\theta}_i = \frac{h_i}{\lambda_i}\sin\theta$ is the normalized angle, $(.)'$ denotes the transpose operation, and $\mathbf{a}_s(\overline{\theta}_i)$ is the spatial steering vector.

$$\mathbf{a}_s(\overline{\theta}_i) = \left[1 \quad \exp(-j2\pi\overline{\theta}_i) \quad \ldots \quad \exp(-j2\pi(N-1)\overline{\theta}_i)\right]'. \tag{6}$$

Since the target is in motion, the normalized Doppler shift at the target induced on sensor i at angle θ is

$$\begin{aligned}\overline{f}_{di} &= \frac{2v_iT}{\lambda_i}\sin\theta \\ &= \beta\overline{\theta}_i\end{aligned} \tag{7}$$

where v_i is the velocity of sensor i and $\beta = \frac{2v_iT}{h_i} = \frac{4v_iT}{\lambda_i}|_{h_i=\frac{\lambda_i}{2}}$. Each vector of array outputs from successive pulses due to the target will have a temporal linear phase progression, i.e., at the kth PRI, snapshot of the target takes the form [9, 10]

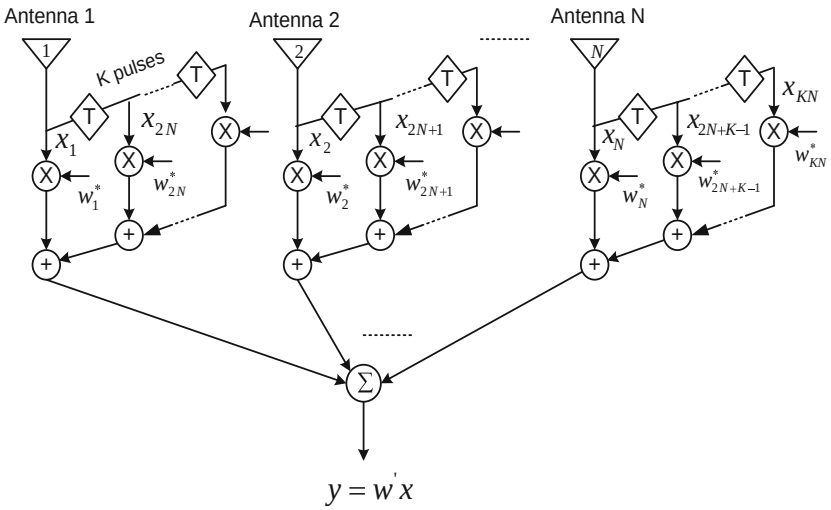


Fig. 1 Receiver configuration

$$\mathbf{e}(\overline{\theta}_i,\overline{f}_{di}) = \exp(j2\pi(k-1)\overline{f}_{di})\mathbf{a}_s(\overline{\theta}_i), \quad k = 1,2,\ldots,K. \tag{8}$$

If K pulses are to be processed in a coherent pulse interval, the KN dimensional space-time steering vector corresponding to a possible target at look angle θ and Doppler frequency $\overline{f}_{di}$ is given by

$$\mathbf{e}(\overline{\theta}_i,\overline{f}_{di}) = \mathbf{b}_t(\overline{f}_{di}) \otimes \mathbf{a}_s(\overline{\theta}_i), \tag{9}$$

where $\otimes$ denotes the Kronecker product and $\mathbf{b}_t(\overline{f}_{di})$ is the K-dimensional Doppler steering vector

$$\mathbf{b}_t(\overline{f}_{di}) = \begin{bmatrix} 1 & \exp(j2\pi\overline{f}_{di}) & \ldots & \exp(j2\pi(K-1)\overline{f}_{di}) \end{bmatrix}'. \tag{10}$$

By introducing the complex weighting vector $\mathbf{w}_i$, the output response of the space-time beamformer can be maximized for any desired angle of arrival. More specifically, let $\mathbf{x}_i$ and y_i denote the received data and beamformer output at sensor i, respectively.

$$y_i = \mathbf{w}_i'\mathbf{x}_i. \tag{11}$$

In any case, the optimum weight vector, $\mathbf{w}_i \in \mathcal{C}^{NK}$, that maximizes SINR, satisfies

$$\mathbf{w}_i = \mathbf{R}_i^{-1}\mathbf{e}(\overline{\theta}_i,\overline{f}_{di}), \tag{12}$$

where $\mathbf{R}_i \in \mathcal{C}^{NK\times NK}$ is the interference-plus-noise covariance matrix.

3.2 Interference Analysis

In this section, we focus on clutter and jamming. Note that the interference between sensors can be canceled by the orthogonality of waveforms and noise can be modeled by the normal process.

(1) *Clutter*: Clutters generate unwanted radar returns that may interfere with the desired signal. In many scenarios, the dominant interference is not noise, but clutter. Consequently, the signal-to-clutter ratio (SCR) is often of more important than the signal-to-noise ratio (SNR). The integrated clutter can be generally approximated as the sum of N_c elemental clutter patches. For clutter patch i, the space-time data vector [9] is

$$\begin{aligned} \mathbf{p}_i &= \gamma_i \mathbf{b}_t(\overline{f}_{d_{ci}}) \otimes \mathbf{a}_s(\overline{\theta}_{ci}) \\ &= \gamma_i \mathbf{u}_i \end{aligned} \tag{13}$$

where γ_i is a complex scalar random variable that accounts for the amplitude and phase of the ith clutter patch, $\mathbf{u}_i = \mathbf{b}_t(\overline{f}_{d_{ci}}) \otimes \mathbf{a}_s(\overline{\theta}_{ci})$, and $\mathbf{b}_t(\overline{f}_{d_{ci}})$ and $\mathbf{a}_s(\overline{\theta}_{ci})$ are the temporal vector and spatial vector of clutter signal from clutter patch i, respectively. $\overline{f}_{d_{ci}}$ and $\overline{\theta}_{ci}$ are the normalized Doppler shift and angle of arrival of clutter patch i, respectively. The total clutter vector equals to

$$\begin{aligned} \mathbf{x}_c &= \sum_{i=1}^{N_c} \mathbf{p}_i \\ &= \sum_{i=1}^{N_c} \gamma_i \mathbf{b}_t(\overline{f}_{d_{ci}}) \otimes \mathbf{a}_s(\overline{\theta}_{ci}) \\ &= \sum_{i=1}^{N_c} \gamma_i \mathbf{u}_i. \end{aligned} \tag{14}$$

The covariance matrix of the clutter is given by

$$\begin{aligned} \mathbf{R}_c &= \mathbb{E}\{\mathbf{x}_c\mathbf{x}_c'\} \\ &= \sum_{i=1}^{N_c}\sum_{j=1}^{N_c} \mathbb{E}\{\gamma_i\gamma_j'\}\mathbf{u}_i\mathbf{u}_j' \end{aligned} \tag{15}$$

where $\mathbb{E}\{x\}$ denotes the expectation of the random variable x.

(2) *Jamming*: Jamming signals are generated by hostile interfering signal sources that seek to degrade the performance of radar sensors by mechanisms such as degrading SINR by increasing the noise level or generating false detection to overwhelm the radar with false targets. One of the most common forms of jamming is a simple noise jammer that radiates a relatively high-power waveform at the victim sensor from a specific platform. A commonly employed model for N_j jamming signals [7]

$$\mathbf{x}_{ja} = \sum_{m=1}^{N_j} z_m \otimes \mathbf{a}_j(\overline{\theta}_m) \tag{16}$$

where z_m contains voltage samples of the mth jammer waveform taken at PRI. The different jammer waveforms are uncorrelated with each other.

4 Diversity Combining and Target Detection

Sensors in the network are assigned waveforms with specific parameters and they can provide their parameters about waveforms to the cluster-head which collects and combines waveforms from cluster members. The received signal at sensor i consists of the desired signal and interference

$$\mathbf{x}_i(u,t) = \alpha_i(u)\mathbf{e}(\overline{\theta}_i, \overline{f}_{di})s_i(t-\tau_i) + \mathbf{d}_i(u,t) \tag{17}$$

where the pair of variables (u,t) is for a random process, e.g., $x(u,t)$ is a random process and only variable u is for the random variable, e.g., $\alpha_i(u)$ is a random variable. $\mathbf{d}_i(u,t) = \mathbf{x}_{ci}(u,t) + \mathbf{x}_{jai}(u,t) + \mathbf{x}_{ini}(u,t) + \mathbf{n}_i(\mathrm{u,t})$ presents the overall interference, i.e., the sum of the clutter vector $\mathbf{x}_{ci}(u,t)$, the jammer vector $\mathbf{x}_{jai}(u,t)$, the interference between sensors $\mathbf{x}_{ini}(u,t)$, and the background white noise $\mathbf{n}_i(u,t)$. $\alpha_i(u)$ is a random variable that models the radar cross section (RCS), $\mathbf{e}(\overline{\theta}_i,\overline{f}_{di})$ is a spatial-temporal steering vector that models the target return for a specific angle-Doppler, and $s_i(t-\tau_i)$ is the return of waveform with delay τ_i. The data at the output of the ith sensor is the multiplication of the received data $\mathbf{x}_i(u,t)$ and the spatial-temporal weight vector $\mathbf{w}_i$:

$$\begin{aligned} y_i(u,t) &= \mathbf{w}_i^{'}\mathbf{x}_i(u,t), \\ &= \mathbf{w}_i^{'}\big(\alpha_i(u)\mathbf{e}(\overline{\theta}_i,\overline{f}_{di})s_i(t-\tau_i) + \mathbf{d}_i\big), \\ &= \alpha_i(u)s_i(t-\tau_i)L_i(\overline{\theta}_i,\overline{f}_{di}) + D_i, \end{aligned} \tag{18}$$

where $D_i \triangleq \mathbf{w}_i^{'}\mathbf{d}_i$ and $L_i(\overline{\theta}_i,\overline{f}_{di}) \triangleq \mathbf{w}_i^{'}\mathbf{e}(\overline{\theta}_i,\overline{f}_{di})$. Assuming the RSN with M sensors, the received signal $r(u,t)$ at the cluster-head is

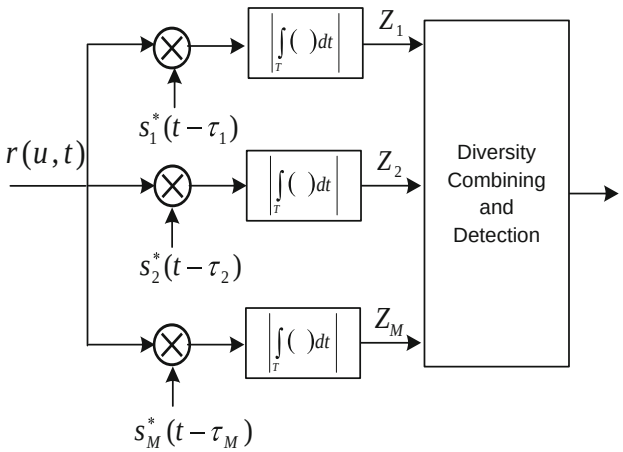


Fig. 2 Receiver at the clusterhead for diversity combining

$$\begin{aligned} r(u,t) &= \sum_{i=1}^{M} y_i(u,t), \\ &= \sum_{i=1}^{M}\big\{\alpha_i(u)s_i(t-\tau_i)L_i(\overline{\theta}_i,\overline{f}_{di}) + D_i\big\}. \end{aligned} \tag{19}$$

Note that $\alpha_i(u)$ can be modeled using non-zero constants for non-fluctuating targets and four Swerling target models for fluctuating targets [11]. At the cluster-head, we propose a receiver as shown in the Fig. 2 to combine waveforms. According to this receiver, the received signal $r(u,t)$ is processed by a bank of matched filters. After integration, the output of the branch 1 is given by

$$\begin{aligned} Z_1(u) &= \left|\int_0^T r(u,t)s_1^*(t-\tau_1)dt\right|, \\ &= \left|\sum_{i=1}^{M}\alpha_i(u)L_i(\overline{\theta}_i,\overline{f}_{di})\int_0^T s_i(t-\tau_i)s_1^*(t-\tau_1)dt\right. \\ &\quad \left. + \sum_{i=1}^{M}\int_0^T s_1^*(t-\tau_1)D_i dt\right|, \end{aligned} \tag{20}$$

$$= |Z_{11}(u) + Z_{12}(u)|, \tag{21}$$

where $()^*$ denotes the conjugate operation. $Z_{11}(u)$ and $Z_{12}(u)$ are defined as below

$$\begin{aligned} Z_{11}(u) &\triangleq \sum_{i=1}^{M}\alpha_i(u)L_i(\overline{\theta}_i,\overline{f}_{di})\int_0^T s_i(t-\tau_i)s_1^*(t-\tau_1)dt \\ &= \sum_{i=2}^{M}\alpha_i(u)L_i(\overline{\theta}_i,\overline{f}_{di})\int_0^T s_i(t-\tau_i)s_1^*(t-\tau_1)dt \\ &\quad + E\alpha_1(u)L_1(\overline{\theta}_1,\overline{f}_{d1}). \end{aligned} \tag{22}$$

$$Z_{12}(u) \triangleq \sum_{i=1}^{M} \int_{0}^{T} s_1^*(t-\tau_1) D_i dt. \tag{23}$$

Based on (3), $Z_{11}(u)$ can be rewritten as

$$Z_{11}(u) = E\alpha_1(u) L_1(\overline{\theta}_1, \overline{f}_{d1}). \tag{24}$$

Assuming that waveforms are designed properly. Hence, the interference between sensors is negligible. Since the detection performance of RSN is greatly affected by the clutter, we consider the clutter the primary interference source. The overall interference can be given by

$$\begin{aligned} \mathbf{d}_i &= \mathbf{c}_i(\overline{f}_{d_{ci}}, \overline{\theta}_{ci}) + \mathbf{n}_i, \\ &= \sum_{j=1}^{N_c} \gamma_{ij} \mathbf{u}_{ij} + \mathbf{n}_i, \end{aligned} \tag{25}$$

where $\mathbf{u}_{ij} = \mathbf{b}_t(\overline{f}_{d_{cij}}) \otimes \mathbf{a}_s(\overline{\theta}_{cij})$. Thus, $Z_{12}(u)$ becomes

$$Z_{12}(u) = \sum_{i=1}^{M} \int_{0}^{T} \mathbf{w}_i' \mathbf{d}_i s_1^*(t-\tau_1) dt. \tag{26}$$

Since γ_{ij} is a complex random variable, we assume γ_{ij} is a complex Gaussian random variable. Hence, it is not difficult to prove that Z_{12} is a complex Gaussian noise $n(u)$. The output of the branch 1 becomes

$$Z_1(u) \approx |E\alpha_1(u) L_1(\overline{\theta}_1, \overline{f}_{d1}) + n(u)|. \tag{27}$$

Similarly, the output of the ith branch ($i = 1, 2, \ldots, M$) is

$$Z_i(u) \approx |E\alpha_i(u) L_i(\overline{\theta}_i, \overline{f}_{di}) + n(u)|. \tag{28}$$

Based on (28), we can recognize that the output of the ith branch is composed of the signal from sensor i and noise. Note that when computing $Z_i(u)$, we still have to estimate the interference-plus-noise covariance matrix.

The purpose of detection problem is to figure out the presence and motion of the desired targets such as missiles, tanks, fighter aircrafts, other tactical weapons from the enemy, illegal intruders at the border of the country, over-speeded vehicles or strange ships at sea, etc. Here, we apply the spatial-temporal-frequency diversity to improve the detection performance and use a maximum likelihood criterion to analyze the detection performance of RSN for both non-fluctuating targets and fluctuating targets. The detection problem in RSN can be formulated as follows:

$$\begin{aligned} &H_0 : \textit{Target is not present} \\ &H_1 : \textit{Target is present} \end{aligned} \tag{29}$$

4.1 Non-fluctuating Targets

Non-fluctuating targets can be modeled as the Swerling 0 or equivalently Swerling V [11, 12]. The radar cross section (RCS) $\alpha_i(u)$ of non-fluctuating targets is constant and unknown. We assume that $\alpha_i(u) = \alpha(u), i = 1, 2, .., M$. Under hypothesis $H_0, Z_i(u)$ follows the Rayleigh distribution whose probability density function (pdf) is

$$f(z_i|H_0) = \frac{2z_i}{\sigma^2} \exp\left(-\frac{z_i^2}{\sigma^2}\right). \tag{30}$$

Under hypothesis $H_1, Z_i(u)$ follows the Rician distribution whose pdf with the parameter m_i is

$$f(z_i|H_1) = \frac{2z_i}{\sigma^2} \exp\left(-\frac{z_i^2 + m_i^2}{\sigma^2}\right) I_0\left(\frac{2m_i z_i}{\sigma^2}\right), \tag{31}$$

where $m_i = E\alpha(u) L_i(\overline{\theta}_i, \overline{f}_{di}), \sigma^2/2$ is the noise power for each branch I, Q, and $I_0(.)$ is the zero-order modified Bessel function of the first kind. We assume that $Z_1, Z_2, \ldots, Z_m$ are independent random variables. Let $\mathbf{z} \triangleq [Z_1, Z_2, \ldots, Z_M]$, the joint pdf of the random vector $\mathbf{z}$ for each hypothesis:

$$f(z|H_0) = \prod_{i=1}^{M} \frac{2z_i}{\sigma^2} \exp\left(-\frac{z_i^2}{\sigma^2}\right), \tag{32}$$

$$f(z|H_1) = \prod_{i=1}^{M} \frac{2z_i}{\sigma^2} \exp\left(-\frac{z_i^2 + m_i^2}{\sigma^2}\right) I_0\left(\frac{2m_i z_i}{\sigma^2}\right). \tag{33}$$

4.2 Fluctuating Targets

In practice, RCS is normally fluctuating. Based on different combinations of pdf and decorrelation (pulse to pulse or scan to scan), Swerling [11] proposed four Swerling models. He also showed that the statistics associated with Swerling I and II models are applied to targets consisting of many small RCS scatters of comparable RCS values, while the statistics associated with Swerling III and IV models are applied to targets consisting of one large scatter and many small equal RCS scatters [12]. In this paper, we focus on the Swerling II model. The magnitude $|\alpha(u)|$ of Swerling II targets fluctuates independently from pulse to pulse according to a chi-square probability density function with two degree of freedom.

$$\alpha(u) = \alpha_I(u) + j\alpha_Q(u), \tag{34}$$

where $\alpha_i(u)$ and $\alpha_Q(u)$ follow Gaussian distribution with the variance $\rho^2/2$ for each branch I, Q. Under hypothesis $H_0, Z_i(u)$ follows the Rayleigh distribution whose pdf is

$$f(z_i|H_0) = \frac{2z_i}{\sigma^2} \exp\left(-\frac{z_i^2}{\sigma^2}\right). \tag{35}$$

Under hypothesis $H_1, Z_i(u)$ follows the Rayleigh distribution whose pdf is given by

$$f(z_i|H_1) = \frac{2z_i}{\sigma_i^2}\exp\left(-\frac{z_i^2}{\sigma_i^2}\right), \tag{36}$$

where $\sigma_i = \sqrt{(EL_i(\overline{\theta}_i,\overline{f}_{di}))^2\rho^2 + \sigma^2}$. We assume that $Z_1, Z_2, \ldots, Z_m$ are independent random variables. Let $\mathbf{z} \triangleq = [Z_1, Z_2, \ldots, Z_M]$, the joint pdf of the random vector $\mathbf{z}$ for each hypothesis:

$$f(z|H_0) = \prod_{i=1}^{M}\frac{2z_i}{\sigma^2}\exp\left(-\frac{z_i^2}{\sigma^2}\right), \tag{37}$$

$$f(z|H_1) = \prod_{i=1}^{M}\frac{2z_i}{\sigma_i^2}\exp\left(-\frac{z_i^2}{\sigma_i^2}\right). \tag{38}$$

5 Simulation Results and Discussion

5.1 Data Model

We use the modified Joint Domain Localized algorithm proposed by Adve et al. [13] to determine the space-time weights at sensors. The data generation scheme uses the physical model presented by Ward [8]. As mentioned in the section III, the clutter is modeled as a sum of the contributions of many discrete far field sources. Here, amplitude of each discrete source is a complex Gaussian random variable whose average power is set by a chosen clutter-to-noise ratio (CNR). The normalized Doppler shift associated with each clutter source depends on the velocity of the platform. Thermal noise is modeled as a Gaussian white noise process. The average power is set to unity allowing the clutter and target powers to be referenced to the white noise power. Simulations do not consider the effects of jammers. Parameters used in simulations are listed in the Table 1 [13]. The interference-plus-noise covariance matrix $\mathbf{R}_d$ is given

$$\mathbf{R}_d = \mathbf{R}_n + p_c(k)\mathbf{R}_c \tag{39}$$

Table 1 Parameters used in simulations

Parameters	Values
Array elements	8
Pulses	8
Element spacing	$\lambda_i/2$
Pulse Repetition Frequency (PRF)	1024 Hz
The number of clutter sources	181
Target normalized Doppler shift	1/3
Thermal noise power	Unity
Clutter to noise ratio (CNR)	50 dB
The number of Doppler bins in LPR	3
The number of Angle bins in LPR	3
(LPR: Local Processing Region)	

where $\mathbf{R}_n$ is the covariance of noise, $\mathbf{R}_c$ is the clutter covariance computed in (15), and $p_c(k)$ is a random variable used to model the clutter power of the kth range cell. $p_c(k)$ often follows *Weibull* or gamma distribution. Since, in homogeneous environments, the average clutter power does not depend on k, we assume the average CNR equals 50 dB.

5.2 Detection Performance Analysis

In RSN, each sensor transmits a known waveform. This waveform is reflected back from the target toward the receiving sensor. RSN's tasks are to detect the existence of the target and to estimate its unknown parameters, e.g., range, speed and direction. Figure 3a presents the probability of miss-detection P_{MD} as a function of SCNR and $P_{FA} = 10^{-6}$ while Fig. 3b presents the miss-detection probability P_{MD} as the function of false alarm probability

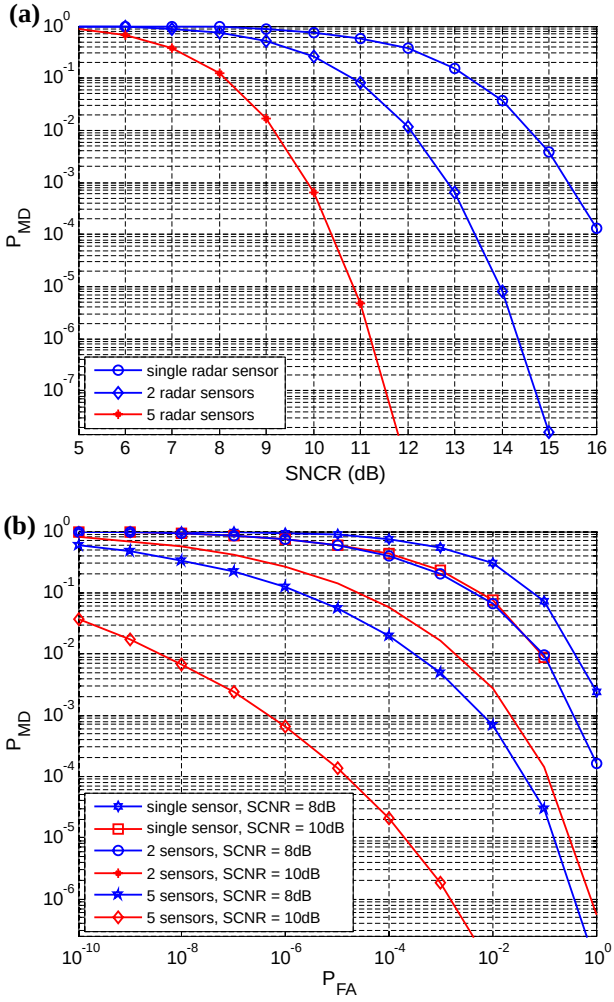


Fig. 3 Non-fluctuating target models

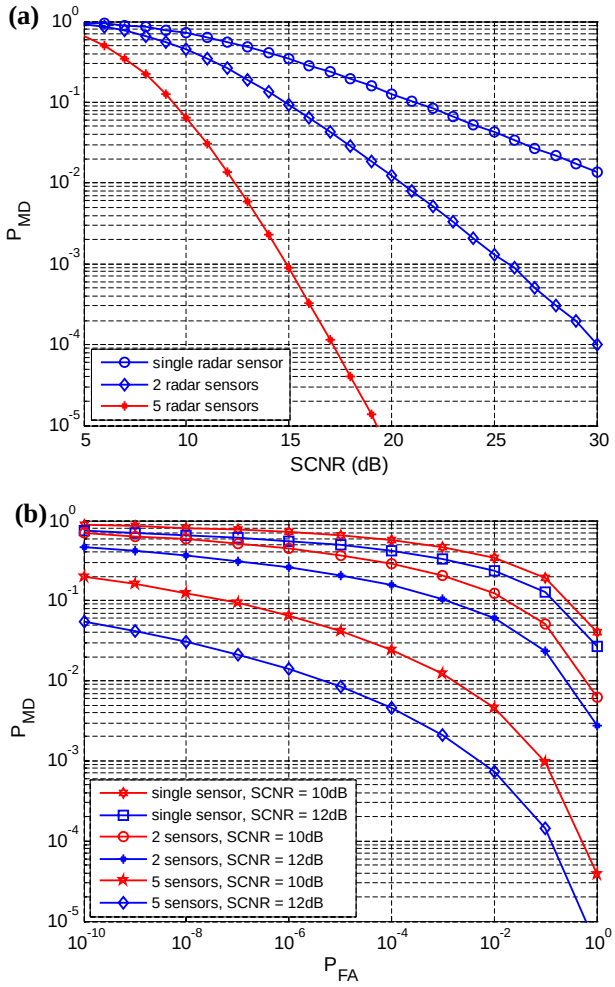


Fig. 4 Fluctuating target models

P_{FA}, SCNR = 8 dB and SCNR = 10 dB for non-fluctuating targets. Similarly, Fig. 4a presents the probability of miss-detection P_{MD} as a function of SCNR and $P_{FA} = 10^{-6}$ while Fig. 4b presents the miss-detection probability P_{MD} as the function of false alarm probability P_{FA}, SCNR = 10 dB and SCNR = 12 dB for fluctuating targets.

Based on these results, we recognize that the probability of miss-detection P_{MD} at the same SCNR decreases when the number of radar sensors in the network increases, e.g., at SCNR = 10 dB, P_{MD} of the 5-radar RSN is much lower than that of the 2-radar RSN. It is desirable for P_{MD} to be as low as possible. In the real world, P_{MD} less than 10% is reasonable. We can observe that it is very difficult to achieve this P_{MD} with a single radar at low P_{FA} and if possible, the SCNR must be very high. However, the 5-radar RSN can maintain very low P_{MD} at a low P_{FA}.

We also notice that it requires more SCNR with fluctuating targets than with non-fluctuating targets to achieve the same P_{MD}. For example, when we use 5 radar sensors and P_{MD} is about 10%, SCNR is 9.3 dB for fluctuating targets but less than 9 dB for non-fluctuating targets. At the same values of P_{MD} and SCNR, P_{FA} for non-fluctuating targets is lower than for fluctuating targets. Therefore, depending on specific scenarios, we can choose P_{FA} and SCNR logically in order to get the desired detection performance.

6 Conclusions

We investigated and applied the spatial-temporal-frequency diversity to improve the detection performance of RSN. We also proposed a receiver for diversity combining in RSN. The probability of miss-detection as a function of the false alarm probability and the signal-to-clutter-plus-noise is analyzed for both non-fluctuating targets and fluctuating targets. Simulation results showed that the detection performance of the proposed diversity scheme-based radar sensor network is much better than that of single radar system using the spatial-temporal diversity only.

Acknowledgements This work was supported by the Office of Naval Research (ONR) Young Investigator Award under Grant N00014-03-1-0466

References

1. S. Kadambe, *Feature Discovery and Sensor Discrimination in a Network of Distributed Radar Sensors for Target Tracking*, HRL Laboratories, LLC, 2001.
2. C. J. Baker and A. L. Hume, Netted radar sensing, *IEEE A&E Systems Magazine*, February 2002.
3. R. Fitzgerald, Effects of range-doppler coupling on chirp radar tracking acuracy, *IEEE Transaction on Aerospace and Electronic Systems*, Vol. 10, pp. 528–532, 1974.
4. M. R. Bell, Information theory and radar waveform design, *IEEE Transaction on Information Theory*, Vol. 39, No. 5, pp. 1578–1597, 1993.
5. C. E. Baum, et al, The singularity expansion method and its application to target identification, *Proceedings of the IEEE*, Vol. 79, No. 10, 1991.
6. Q. Liang, Waveform design and diversity in radar sensor networks: theoretical analysis and application to automatic target recognition, *Int. Workshop on Wireless Ad Hoc and Sensor Networks*, June 2006, New York.
7. W. L. Melvin, A STAP overview, *IEEE A&E Systems Magazine*, Vol 19, No. 1, pp. 19–35, 2004
8. J. Ward, *Space-time Adaptive Processing for Airborne Radar*, Lincoln Lab Technical Report 1015, December 1994.
9. J. R. Guerci, *Space-time Adaptive Processing for Radar*, Artech House, 2003.
10. M. A. Richards, *Fundamentals of Radar Signal Processing*, McGraw-Hill, New York, 2005.
11. P. Swerling, Probability of detection for fluctuating targets, *IRE Transaction on Information Theory*, Vol IT-6, pp. 269–308, 1960.
12. B. R. Mahafza, *Radar Systems Analysis and Design*, Chapman & Hall, 2005.

13. R. S. Adve et al., Practical joint domain localized adaptive processing in homogeneous and non-homogeneous environments: part I—homogeneous environments, *IEE Part F: Proceedings on Radar, Sonar and Navigation*, October 1999.
14. H. D. Ly and Q. Liang, Spatial-temporal-frequency diversity in radar sensor networks, *IEEE Military Communications Conference*, October 2006, Washington DC.

Author Biographies



Hung D. Ly received his BS degree from Posts and Telecommunications Institute of Technology (PTIT), Vietnam in May 2002 and his MS degree from the University of Texas at Arlington in August 2007, both in Electrical Engineering. From June 2002 to July 2005, he was a lecturer at the Faculty of Telecommunication Engineering 1, PTIT. Since August 2007, he has been pursuing his PhD degree in Electrical and Computer Engineering at Texas A&M University. His general research interests are in the areas of network information theory, wireless communications and wireless network security.



Dr. Qilian Liang is an Associate Professor in the Department of Electrical Engineering of University of Texas at Arlington, where he has been since August 2002. Prior to this he was a Member of Technical Staff in Hughes Network Systems Inc at San Diego, California. He received the Electrical Engineering BS degree from Wuhan University, China, in 1993. From the Beijing University of Posts and Telecommunications in 1996 he received MS degree in Electrical Engineering. He received PhD degree in Electrical Engineering from University of Southern California (USC) in May 2000. His research interests include Sensor networks (energy efficiency, cross layer design, information integration, etc), wireless communications, wireless networks, communication theory, fuzzy logic systems and applications, signal processing for communications, collaborative and distributed signal processing. He has published more than 120 journal and conference papers, 6 book chapters, and has 6 U.S. patents pending. He received 2002 IEEE Transactions on Fuzzy Systems Outstanding Paper Award, 2003 U.S. Office of Naval Research (ONR) Young Investigator Award, 2005 UTA College of Engineering Outstanding Young Faculty Award, and 2007 AFOSR Summer Faculty Fellowship Program Award.

Optimized Punctured ZCZ Sequence-pair Set: Design, Analysis and Application to Radar System

Lei Xu and Qilian Liang

Department of Electrical Engineering

University of Texas at Arlington

Arlington, TX 76010-0016 USA

Email: xu@wcn.uta.edu, liang@uta.edu

Abstract

Based on the zero correlation zone (ZCZ) concept, we present the definitions and properties of a set of new ternary codes –ZCZ sequence-Pair Set (ZCZPS), and propose a method to use the optimized punctured sequence-pair along with Hadamard matrix to construct an optimized punctured ZCZ sequence-pair set (OPZCZPS) which has ideal autocorrelation and cross correlation properties in the zero correlation zone. Considering the moving target radar system, the correlation properties of the codes will not be severely affected when Doppler shift is not large. We apply the proposed codes as pulse compression codes to radar system and the simulation results show that optimized punctured ZCZ sequence-pairs outperform other conventional pulse compression codes, such as the well known polyphase code–P4 code.

Index Terms : ternary, zero correlation zone, optimized punctured ZCZ sequence-pair, phase coded waveform

1 Introduction

Pulse compression is known as a technique to raise the signal to maximum sidelobe (signal-to-sidelobe) ratio to improve the target detection and range resolution abilities of the radar system. This technique allows a radar to simultaneously achieve the energy of a long pulse and the resolution of a short pulse without the high peak power which is required by a high energy short duration pulse [1]. One of the waveform designs suitable for pulse compression is phase-coded waveform design. The phase-coded waveform design is that a long pulse of duration T is divided into N subpulses each of width T_s. Each subpulse has a particular phase, which is selected in accordance with a given code sequence. The pulse compression ratio equals the number of subpulses $N = T/T_s \approx BT$, where the bandwidth is $B \approx 1/T_s$. In general, a phase-coded waveform with longer code word, in other words, higher pulse compression ratio, can have lower sidelobe of autocorrelation, relative to the mainlobe peak, so its main peak can be better distinguished. The relative lower sidelobe of autocorrelation is very important since range sidelobes are so harmful that they can mask main peaks caused by small targets situated near large targets. In addition, the cross-correlation property of the pulse compression codes should be considered in order to reduce the interference among radars when we choose a set of pulse compression codes to work in a Radar Sensor Network (RSN).

Much time and effort was put for designing sequences with impulsive autocorrelation functions (ACFs) and cross correlation functions (CCFs) for radar target ranging and target detection. On one hand, for aperiodic sequences, it is known that for most binary sequences of length $N(N > 13)$ the attainable sidelobe levels are approximately $\sqrt{N}$ [2] [3] and the mutual peak cross correlations of the same-length sequences are much larger and are usually in the order of $2\sqrt{N}$ to $3\sqrt{N}$. Later, set of binary sequences of length N with autocorrelation sidelobes and cross-correlation peak values of approximately $\sqrt{N}$ are studied in paper [4]. Besides, the small set of Kasami sequences and the Bent sequences could achieve maximum correlation values of approximately $\sqrt{N}$. In addition to binary sequences, polyphase codes, with better Doppler tolerance and lower range sidelobes such as the Frank and P1 codes, the Butler-matrix derived P2 code, the linear-frequency derived P3 and P4 codes were provided and intensively analyzed in [5] [6] [7]. Quadiphase [8] code could also reduce poor fall-off of the radiated spectrum and mismatch loss in the receiver pulse compression filter of biphase codes. Nevertheless, the range sidelobe of the polyphase codes can not be low enough to avoid

masking returns from targets. Hence, considerable work has been done to reduce range sidelobes for the radar system. By suffering a small S/N loss, the authors in [11] present several binary pulse compression codes to greatly reduce sidelobes. In the previous paper [12], pulse compression using a digital-analog hybrid technique is studied to achieve very low range sidelobes for potential application to spaceborne rain radar. In the paper[13], time-domain weighting of the transmitted pulse is used and is able to achieve a range sidelobe level of -55 dB or better in flight tests. These sidelobe suppression methods, however, degrade the receiving resolution because of wider mainlobe.

On the other hand, for periodic sequences, the lowest periodic ACF that could be achieved for binary sequences, as in the case of m-sequences [9] or Legendre sequences, is $|R_i(\tau \neq 0) = 1|$. GMW [10] has the same periodic ACF properties, but posses larger linear complexity. Considering the non-binary case, it is possible to find perfect sequences, such as two valued Golomb sequences, Ipatov ternary sequences, Frank sequences, Chu sequences, and modulatable sequences. However, it should be noted that for both binary and non-binary cases, it is impossible for the sequences to have perfect ACF and CCF simultaneously although ideal CCFs could be achieved alone. One can synthesize a set of non-binary sequences with impulsive ACF and the lower bound of CCF: $R_{ij} = \sqrt{N}, \forall \tau, i \neq j$ [14][15], which is governed by Welch bound and Sidelnikov bound.

So far in the previous work, range sidelobes could hardly reach as low as zero. In addition, it has also been well proven that it is impossible to design a set of codes with ideal impulsive autocorrelation function and ideal zero cross-correlation functions, since the corresponding parameters have to be limited by certain bounds, such as Welch bound [14], Sidelnikov bound [15], Sarwate bound [16], Levenshtein bound [17], etc. To overcome these difficulties, the new concepts, generalized orthogonality (GO), also called Zero Correlation Zone (ZCZ) is introduced. Based on ZCZ [18][19][20] concept, we propose a set of ternary codes– ZCZ sequence-pair set, which can reach zero autocorrelation sidelobe during Zero Correlation Zone and zero mutual cross correlation peaks during the whole period. We also present and analyze a method to construct such ternary codes and subsequently apply them to a radar detection system. The method is that optimized punctured sequence-pair joins together with Hadamard matrix to construct optimized punctured ZCZ sequence-pairs set. An example is presented, investigated and studied in the radar targets detection

simulation system for the performance evaluation of the proposed ternary codes. Because of the outstanding property performance and well target detection performance in simulation system, the newly proposed codes can be useful candidates for pulse compression application in radar system.

The rest of the paper is organized as follows. Section 2 introduces the definitions and properties of ZCZPS. In Section 3, the optimized punctured ZCZPS is introduced, and a method using optimized punctured sequence-pair and Hadamard matrix to construct such codes is given and proved. In Section 4, the properties and ambiguity function of optimized punctured ZCZPS are simulated and analyzed. The performance of optimized punctured ZCZPS is investigated in radar targets detection system by comparing with P4 code in section 5. In Section 6, conclusions are drawn on optimized punctured ZCZPS.

2 The Definitions and Properties of ZCZ Sequence-pair Set

Zero Correlation Zone (ZCZ)is a new concept provided by Fan et.al [20] [21] in which the autocorrelation and cross correlation sidelobes are zero while the time delay is kept within ZCZ instead of the whole period of time domain. There has been considerable interest in constructing [22][23][24][25][26] new classes of ZCZ sequences in ZCZ and studying their properties [27].

Here, we introduce sequence-pair into the ZCZ concept to construct ZCZ sequence-pair set. We consider ZCZPS $(\mathbf{X}, \mathbf{Y})$, $\mathbf{X}$ is a set of K sequences of length N and $\mathbf{Y}$ is a set of K sequences of the same length N:

$$\mathbf{x}^{(p)} \in \mathbf{X} \quad p = 0, 1, 2, ..., K-1 \tag{1}$$

$$\mathbf{y}^{(q)} \in \mathbf{Y} \quad q = 0, 1, 2, ..., K-1 \tag{2}$$

The autocorrelation function (ACF) (here we use autocorrelation to stand for the cross correlation between two different sequences of a sequence-pair to distinguish the cross correlation between two different sequence-pairs) of sequence-pair $(\mathbf{x}^{(p)}, \mathbf{y}^{(p)})$ is defined by:

$$R_{\mathbf{x}^{(p)}\mathbf{y}^{(p)}}(\tau) = \sum_{i=0}^{N-1} x_i^{(p)} y_{(i+m) \mod N}^{(p)*}, 0 \le m \le N-1 \tag{3}$$

The cross correlation function of two sequence-pairs $(\mathbf{x}^{(p)}, \mathbf{y}^{(p)})$ and $(\mathbf{x}^{(q)}, \mathbf{y}^{(q)}), p \neq q$ is defined by:

$$C_{\mathbf{x}^{(p)}\mathbf{y}^{(q)}}(\tau) = \sum_{i=0}^{N-1} x_i^{(p)} y_{(i+m) \mod N}^{(q)*}, 0 \le m \le N-1 \tag{4}$$

Where $\tau = mT_s$ is the time delay and T_s is the bit duration.

For pulse compression sequences, some properties are of particular concern in the optimization for any design in engineering field. They are the peak sidelobe level, the energy of autocorrelation sidelobes and the energy of their mutual cross correlation [4]. Therefore, the peak sidelobe level which represents a source of mutual interference and obscures weaker targets can be presented as $\max_K |R_{x^{(p)}y^{(p)}}(\tau)| = 0, \tau$ is among the zero correlation zone for ZCZPS. Another optimization criterion for the set of sequence-pairs is the energy of autocorrelation sidelobes joined together with the energy of cross correlation. By minimizing the energy, it can be distributed evenly, and the peak autocorrelation sidelobe and the cross correlation level can be minimized as well [4]. Here, the energy of ZCZPS can be employed as:

$$E = \sum_{p=0}^{K-1} \sum_{\tau=1}^{Z_0} R^2_{\mathbf{x}^{(p)}\mathbf{y}^{(p)}}(\tau) + \sum_{p=0}^{K-1} \sum_{q=0, q\neq p}^{K-1} \sum_{\tau=0}^{Z_0} C_{\mathbf{x}^{(p)}\mathbf{y}^{(q)}}(\tau) \tag{5}$$

According to (5), it is obvious to see that the energy can be kept low while minimizing the autocorrelation sidelobes and cross correlation values of any two sequence-pairs within Zero Correlation Zone.

Hence, the ZCZPS can be constructed by minimizing the autocorrelation sidelobe of a sequence-pair and cross correlation value of any two sequence-pairs in ZCZPS.

Definition 2-1 Assume $(\mathbf{X}, \mathbf{Y})$ to be a sequence-pair set of K sequence-pairs and each sequence-pair is of N bit length. If all the sequence-pairs in the set satisfy the following equation:

$$\begin{aligned} R_{\mathbf{x}^{(p)}\mathbf{y}^{(q)}}(\tau) &= \sum_{i=0}^{N-1} x_i^{(p)} y_{(i+m) \mod (N)}^{(q)*} = \sum_{i=0}^{N-1} y_i^{(p)} x_{(i+m) \mod (N)}^{(q)*} \\ &= \begin{cases} \lambda N, & \text{for } m = 0, p = q \\ 0, & \text{for } m = 0, p \neq q \\ 0, & \text{for } 0 < |m| \leq Z_0 \end{cases} \end{aligned} \tag{6}$$

where $p, q = 1, 2, 3, ..., K-1, i = 0, 1, 2, ..., N-1$, $0 < \lambda \leq 1$ and $\tau = mT_s$. Then $(\mathbf{x}^{(p)}, \mathbf{y}^{(p)})$ is called a ZCZ sequence-pair, $ZCZP$ is an abbreviation, and $(\mathbf{X}, \mathbf{Y})$ is called a ZCZ sequence-pair set, $ZCZPS(N, K, Z_0)$ is an abbreviation.

3 Optimized Punctured ZCZ Sequence-pair Set

3.1 Definition of Optimized Punctured ZCZ Sequence-pair Set

Matsufuji and Torii have provided some methods of constructing ZCZ sequences in [28] [31]. In this section, a set of novel ternary codes, namely the optimized punctured ZCZ sequence-pair set, is constructed by applying the optimized punctured sequence-pair [32] to the Zero Correlation Zone. Here, optimized punctured ZCZPS is a specific kind of ZCZPS.

Definition 3-1 [32] Sequence $\mathbf{u} = (u_0, u_1, ..., u_{N-1})$ is the punctured sequence for $\mathbf{v} = (v_0, v_1, ..., v_{N-1})$,

$$u_j = \begin{cases} 0, & \text{if } u_j \text{ is punctured} \\ v_j, & \text{if } u_j \text{ is Non-punctured} \end{cases} \tag{7}$$

Where P is the number of punctured bits in sequence $\mathbf{u}$. Suppose $v_j \in (-1, 1)$ and $u_j \in (-1, 0, 1)$, $\mathbf{u}$ is P-punctured binary sequence, $(\mathbf{u}, \mathbf{v})$ is called a punctured binary sequence-pair.

Definition 3-2 [32] The autocorrelation of punctured sequence-pair $(\mathbf{u}, \mathbf{v})$ is defined as

$$R_{\mathbf{uv}}(\tau) = R_{\mathbf{uv}}(mT_s) = \sum_{i=0}^{N-1} u_i v_{(i+m) \mod N}, 0 \le m \le N-1 \tag{8}$$

If the punctured sequence-pair has the following autocorrelation property:

$$R_{\mathbf{uv}}(mT_s) = \begin{cases} E, & \text{if } m \equiv 0 \text{mod} N \\ 0, & \text{otherwise} \end{cases} \tag{9}$$

the punctured sequence-pair is called an optimized punctured sequence-pair [32]. Where, $E = \sum_{i=0}^{N-1} u_i v_i = N - P$, is the energy of punctured sequence-pair.

Definition 3-3 If $(\mathbf{X}, \mathbf{Y})$ in Definition 2-1 is constructed by optimized punctured sequence-pair and a certain matrix, such as Hadamard matrix or an orthogonal matrix, where

$$x_i^{(p)} \in (-1, 1), \quad i = 0, 1, 2, ..., N-1$$

$$y_i^{(q)} \in (-1, 0, 1), \quad i = 0, 1, 2, ..., N-1$$

Then

$$R_{\mathbf{x}^{(p)}\mathbf{y}^{(q)}}(\tau)=\sum_{i=0}^{N-1}x_i^{(p)}y_{(i+m)\ \bmod N}^{(q)*}=\begin{cases}\lambda N, & \text{for } m=0, p=q\\ 0, & \text{for } m=0, p\neq q\\ 0, & \text{for } 0<|m|\leq Z_0\end{cases} \tag{10}$$

where $0<\lambda\leq 1$ and $\tau=mT_s$, then $(\mathbf{X},\mathbf{Y})$ can be called an optimized punctured ZCZ sequence-pair set. $OPZCZPS(N,K,Z_0)$ is an abbreviation.

3.2 Design of Optimized Punctured ZCZ Sequence-pair Set

Based on an optimized punctured binary sequence-pair of odd length and a Hadamard matrix, an optimized punctured ZCZPS can be constructed on following steps:

Step 1: Considering an optimized punctured binary sequence-pair $(\mathbf{u},\mathbf{v})$ of odd length, the length of each sequence is N_1

$$\mathbf{u}=u_0,u_1,...,u_{N_1-1},u_i\in(-1,1),$$

$$\mathbf{v}=v_0,v_1,...,v_{N_1-1},v_i\in(-1,0,1),$$

$$i=0,1,2,...,N_1-1,N_1\ is\ odd$$

Step 2: A Hadamard matrix $\mathbf{B}$ (the Hadamard matrix is made up of a set of Walsh sequences) of order N_2 is used here. N_2, the length of each sequence, is equal to the number of the sequences in the matrix. Here, any Hadamard matrix order is possible and $\mathbf{b}^{(p)}$ is the row vector of the matrix.

$$\mathbf{B}=[\mathbf{b}^{(0)};\mathbf{b}^{(1)};...;\mathbf{b}^{(N_2-1)}],$$

$$\mathbf{b}^{(p)}=(b_0^{(p)},b_1^{(p)},...,b_{N_2-1}^{(p)}),$$

$$R_{\mathbf{b}^{(p)}\mathbf{b}^{(q)}}=\begin{cases}N_2, & \text{if } p=q\\ 0, & \text{if } p\neq q\end{cases}$$

Step 3: Doing bit-multiplication on the optimized punctured binary sequence-pair and each row of the

Hadamard matrix $\mathbf{B}$, then sequence-pair set $(\mathbf{X}, \mathbf{Y})$ is obtained,

$$\mathbf{b}^{(p)} = (b_0^{(p)}, b_1^{(p)}, ..., b_{N_2-1}^{(p)}), p = 0, 1, ..., N_2 - 1,$$

$$x_j^{(p)} = u_{j \mod N_1} b_{j \mod N_2}^{(p)}, 0 \le p \le N_2 - 1, 0 \le j \le N - 1,$$

$$\mathbf{X} = (\mathbf{x}^{(0)}; \mathbf{x}^{(1)}; ...; \mathbf{x}^{(N_2-1)}),$$

$$y_j^{(p)} = v_{j \mod N_1} b_{j \mod N_2}^{(p)}, 0 \le p \le N_2 - 1, 0 \le j \le N - 1,$$

$$\mathbf{Y} = (\mathbf{y}^{(0)}; \mathbf{y}^{(1)}; ...; \mathbf{y}^{(N_2-1)})$$

Here, the optimized punctured binary sequence-pairs are of odd lengths and the lengths of Walsh sequence are $2^n, n = 1, 2, ...$ It is easy to see that $gcd(N_1, N_2) = 1$, common divisor of N_1 and N_2 is 1, then $N = N_1 * N_2$. The sequence-pair set $(\mathbf{X}, \mathbf{Y})$ is the optimized punctured ZCZPS and $N_1 - 1$ is the Zero Correlation Zone Z_0. The length of each sequence in optimized punctured ZCZPS is $N = N_1 * N_2$ that depends on the product of length of optimized punctured sequence-pair and the length of Walsh sequence in Hadamard matrix. The number of sequence-pairs in optimized punctured ZCZPS rests on the order of the Hadamard matrix. The sequence $\mathbf{x}^{(p)}$ in sequence set $\mathbf{X}$ and the corresponding sequence $\mathbf{y}^{(p)}$ in sequence set $\mathbf{Y}$ construct a sequence-pair $(\mathbf{x}^{(p)}, \mathbf{y}^{(p)})$ that can be used as a pulse compression code.

The correlation property of the sequence-pairs in optimized punctured ZCZPS is:

$$\begin{aligned} R_{\mathbf{x}^{(p)}\mathbf{y}^{(q)}}(\tau) &= R_{\mathbf{uv}}(m \mod N_1) R_{\mathbf{b}^{(p)}\mathbf{b}^{(q)}}(m \mod N_2) \\ &= \begin{cases} EN_2, & \text{if } m = 0 \text{ and } p = q \\ 0, & \text{if } 0 < |m| \le N_1 - 1 \text{ and } p = q \\ 0, & \text{if } 0 \le |m| \le N_1 - 1 \text{ and } p \ne q \end{cases} \end{aligned} \tag{11}$$

where $N_1 - 1$ is the Zero Correlation Zone Z_0 and $\tau = mT_s$.

Proof:

1) When $p = q$,

$$\tau = 0, R_{\mathbf{uv}}(0) = E, R_{\mathbf{b}^{(p)}\mathbf{b}^{(q)}}(0) = N_2, R_{\mathbf{x}^{(p)}\mathbf{y}^{(q)}}(0) = R_{uv}(0) R_{b^{(p)}b^{(q)}}(0) = EN_2;$$

$$0 < |\tau| \le (N_1 - 1)T_s, R_{\mathbf{uv}}(\tau) = 0, R_{\mathbf{x}^{(p)}\mathbf{y}^{(q)}}(\tau) = R_{\mathbf{uv}}(m \mod N_1) R_{\mathbf{b}^{(p)}\mathbf{b}^{(q)}}(m \mod N_2) = 0;$$

2) When $p \neq q$,

$$\tau = 0, R_{\mathbf{b}^{(p)}\mathbf{b}^{(q)}}(0) = 0, R_{\mathbf{x}^{(p)}\mathbf{y}^{(q)}}(0) = R_{\mathbf{uv}}(0)R_{b^{(p)}b^{(q)}}(0) = 0;$$

$$0 < |\tau| \leq (N_1 - 1)T_s,$$

$$R_{\mathbf{uv}}(\tau) = 0, R_{\mathbf{x}^{(p)}\mathbf{y}^{(q)}}(\tau) = R_{\mathbf{uv}}(m \mod N_1)R_{b^{(p)}b^{(q)}}(m \mod N_2) = 0.$$

According to Definition **2-1**, the OPZCZPS constructed by the above method is a ZCZPS.

4 Properties of Optimized Punctured ZCZ Sequence-pair Set

Considering the optimized punctured ZCZPS constructed by the method mentioned in the last section, the autocorrelation and cross correlation properties can be simulated and analyzed. For example, the optimized punctured ZCZPS $(\mathbf{X}, \mathbf{Y})$ is constructed by 31-length optimized punctured binary sequence-pair $(\mathbf{u}, \mathbf{v}), \mathbf{u} = [+++-----+-+-+++-----+--+--+++-++-], \mathbf{v} = [++++000+0+0+++0000+00+00+++0++0]$ (using $'+'$ and $'-'$ symbols for $'1'$ and $'-1'$) and Hadamard matrix $\mathbf{H}$ of order 4. We follow the three steps presented in Section **3.2** to construct the optimized punctured ZCZPS. The number of sequence-pairs here is 4, and the length of each sequence is $31 * 4 = 124$. The first row of each matrix $\mathbf{X} = [\mathbf{x}^{(1)}; \mathbf{x}^{(2)}; \mathbf{x}^{(3)}; \mathbf{x}^{(4)}]$ and $\mathbf{Y} = [\mathbf{y}^{(1)}; \mathbf{y}^{(2)}; \mathbf{y}^{(3)}; \mathbf{y}^{(4)}]$ constitute a certain optimized punctured ZCZP $(\mathbf{x}^{(1)}, \mathbf{y}^{(1)})$. Similarly, the second row of each matrix $\mathbf{X}$ and $\mathbf{Y}$ constitute another optimized punctured

ZCZ sequence-pair $(\mathbf{x}^{(2)}, \mathbf{y}^{(2)})$ and so on.

$$
\begin{aligned}
\mathbf{x}^{(1)} &= [+++\,+---+-+-+++----+--+--++++-+++-+++++---+\\
&\quad +-+-+++----+--+--+++-++-+++++---+-+-+++\\
&\quad ----+--+--+++-+++-+++++---+-+-++++-----+--\\
&\quad +--+++-++-],\\
\mathbf{y}^{(1)} &= [+++\,+000+0+0+++0000+00+00+++0++0+++\,+000\\
&\quad +0+0+++0000+00+00+++0++0+++\,+000+0+0+++\\
&\quad 0000+00+00+++0++0+++\,+000+0+0+++0000+00\\
&\quad +00+++0++0];\\
\mathbf{x}^{(2)} &= [+-+--+----------+--+-++++---++-++++---+-++--+\\
&\quad +++++-++-+-+--++--+-+---++-+--+-------+-\\
&\quad -+-++--+-++-+++----+-++-++++++++-++-+-+--+\\
&\quad ++--+---++],\\
\mathbf{y}^{(2)} &= [+-+-000-0-0-+-0000+00-00+-+0+-0-++-+000\\
&\quad +0+0+-+0000-00+00-+-0-+0+-+-000-0-0-+-\\
&\quad 0000+00-00+-+0+-0-++-+000+0+0+-+0000-00\\
&\quad +00-+-0-+0].
\end{aligned}
$$

Here, optimized punctured ZCZ sequence-pairs $(\mathbf{x}^{(1)}, \mathbf{y}^{(1)})$ and $(\mathbf{x}^{(2)}, \mathbf{y}^{(2)})$ are studied as two examples in the following parts.

4.1 Autocorrelation and Cross Correlation Properties

The autocorrelation property and cross correlation property of 124-length sequence-pairs in the optimized punctured ZCZ sequence-pair set $(\mathbf{X}, \mathbf{Y})$ are shown in Figs. 1 and 2.

From the Figs. 1 and 2, the peak autocorrelation sidelobe of ZCZPS can be as low as 0 while the time delay is kept within $Z_0 = N_1 - 1 = 30$ (Zero Correlation Zone) and the cross correlation value is kept as

low as 0 during the whole time domain. And it is always true that the cross correlation values of optimized punctured ZCZPS are zero over the whole period and the sidelobe of autocorrelation of ZCZPS could be kept as low as 0 among ZCZ.

We still have to confess that the energy loss of the proposed codes is no less than 1.7 db due to reference mismatch. However, the perfect periodic ACF and CCF achieved simultaneously during the ZCZ zone and the codes' structure could make up for it. It is known that a suitable criterion for evaluating code of length N is the ratio of the peak signal mainlobe divided by the peak signal sidelobe (PSR) of their autocorrelation function, which can be bounded by [33]

$$[PSR]_{dB} \leq 20log_2 N = [PSR_{max}]_{dB} \tag{12}$$

The only aperiodic uniform phase codes that can reach the PSR_{max} are the Barker codes whose length is equal or less than 13. Considering the periodic sequences, the m-sequences or Legendre sequences could achieve the lowest periodic ACF of $|R_i(\tau \neq 0) = 1|$. For non-binary sequences, it is possible to find perfect sequences of ideal ACF. Golomb codes are a kind of two-valued (biphase) perfect codes which obtain zero periodic ACF but result in large mismatch power loss. The Ipatov code shows a way of designing code pairs with perfect periodic autocorrelation (the cross correlation of the code pair) and minimal mismatch loss. In addition, zero periodic autocorrelation function for all nonzero shifts could be obtained by polyphase codes, such as Frank and Zadoff codes. However, for both binary and non-binary periodic sequences, it is not possible for the sequences to have perfect ACF and CCF simultaneously although ideal CCFs could be achieved alone. Comparing with the above codes, the proposed ternary codes could obtain perfect periodic ACF during the ZCZ and the reference sequence is made of (-1,0,1) which is much less complicated than other perfect ternary codes such as Ipatvo code. The reference code for Ipatov code is of a three-element alphabet which might not always be integer.

Nevertheless, considering multi targets in the system, multiple peaks of the autocorrelation function of the proposed codes might affect on the range resolution. The range resolution could be limited as $T_s < \tau < N_1 T_s$ or $\tau > NT_s$. Here, T_s is one bit duration, N_1 is the length of an optimized punctured sequence-pair and N is the length of an optimized punctured ZCZ sequence-pair. In the Fig. 1, $N_1 = 31$. Otherwise, some digital signal processing methods could also be introduced to distinguish the peaks. On the another hand,

there may also be the concern that multiple peaks of single transmitting signal reflected from one target may affect determining the main peak of ACF. As a matter of fact, the matched filter here could shift at the period of ZCZ length to track each peak instead of shifting bit by bit after the first peak is acquired. Hence, in this way could it be working more efficiently. Alike the tracking technology in synchronization of CDMA system, checking several peaks instead of only one peak guarantee the precision of P_D and avoidance of P_{FA}. In addition, those obtained peaks could be averaged before the detection in order to reduce the effect of random noise in the channel so that the detection performance could be improved.

To sum up, the new code could achieve perfect ACF and CCF in the ZCZ simultaneously according to Fig. 1 and 2, and its PSR can be as large as infinite.

4.2 Ambiguity Function

When the transmitted impulse is reflected by a moving target, the reflected echo signal includes a linear phase shift which corresponds to a Doppler shift F_d [33]. As a result of the Doppler shift F_d, the main peak of the autocorrelation function is reduced. The SNR is degraded and the sidelobe structure is also changed because of the Doppler shift.

The ambiguity function which is usually used to analyze the radar performance within Doppler shift and time delay is defined in [33]:

$$A(\tau, F_D) \equiv |\int_{-\infty}^{\infty} x(s) e^{j2\pi F_D s} x^*(s-\tau) ds| \equiv |\hat{A}(\tau, F_D)| \tag{13}$$

where τ is the time delay between transmitting signal and matched filter, and F_D is the Doppler shift.

In [29], PAF (Periodic Ambiguity Function) is introduced by Levanon as an extension of the periodic autocorrelation for Doppler shift. And the single-periodic complex envelope is [30]:

$$A_{periodic}(\tau, F_D) \equiv |\frac{1}{T}\int_0^T x(s+\frac{\tau}{2}) e^{j2\pi F_D s} x^*(s-\frac{\tau}{2}) ds| \equiv |\hat{A}_{periodic}(\tau, F_D)| \tag{14}$$

Where T is one period of the signal.

We are studying sequence-pairs in this research, so we use different codes for transmitting part and receiving part. The single-period ambiguity function for ZCZPS can be rewritten as

$$A_{pair}(\tau, F_D) \equiv |\hat{A}_{pair}(\tau, F_D)| = |\frac{1}{T}\int_0^T x^{(p)}(s+\frac{\tau}{2}) e^{j2\pi F_D s} y^{(q)*}(s-\frac{\tau}{2}) ds| \tag{15}$$

Where $p, q = 0, 1, 2..., K-1$, $T = NT_s$ is one period of the signal and T_s is one bit duration. At the same time, when $p = q$, equation (15) can be used to analyze the autocorrelation property within Doppler shift; and when $q \neq p$, equation (15) can be used to analyze the cross correlation performance within Doppler shift. Equation (15) is plotted in Fig. 3 in a three-dimensional surface plot to analyze the radar performance of optimized punctured ZCZPS within Doppler shift. Here, maximal time delay is 1 unit (normalized to length of the code, in units of NT_s) and maximal Doppler shift is 5 units for cross correlation and 3 units for autocorrelation (normalized to the inverse of the length of the code, in units of $1/NT_s$).

In Fig.3(a), there is relative uniform plateau suggesting low and uniform sidelobes. This low and uniform sidelobes minimize target masking effect in Zero Correlation Zone of time domain, where $Z_0 = 30$, $-30\tau_c \leq \tau \leq 30\tau_c$. From Fig. 3(b), considering cross correlation property between any two optimized punctured ZCZ sequence-pairs of the ZCZPS, we can see that the optimized punctured ZCZPS is tolerant of Doppler shift when Doppler shift is not large. When the Doppler shift is zero, or the target is not moving, cross correlation sidelobe of our proposed code is zero in the whole time domain.

Since synchronizing techniques develop exponentially in the industrial world, time delay between transmitting signal and matched filter can, to some extent, be precisely estimated. Therefore, it is necessary to investigate the property of our proposed code when we have the output of the matched filter at the expected time $\tau = 0$. When $\tau = 0$, the ambiguity function can be expressed as:

$$|\hat{A}_{pair}(0, F_D)| = |\frac{1}{T}\int_0^T x^{(p)}(s) y^{(q)*}(s) e^{(j2\pi F_D s)} ds| \tag{16}$$

And the Doppler shift performance without time delay is presented in the Fig. 4.

Fig. 4(a) illustrates that without time delay of matched filter but having the Doppler shift less than 1 unit, the autocorrelation value of optimized punctured ZCZPS falls sharply during one unit, and the trend of the amplitude over the whole frequency domain decreases as well. Fig. 4(b) shows that there are some convex surfaces in the cross correlation performance. From Figs.4(a) and 4(b), when Doppler frequencies equal to multiples of the pulse repetition frequency ($PRF = 1/PRI = 1/Ts$), all the ambiguity values turn to zero except when Doppler frequency is equal to 2 PRF for cross correlation. That is the same as many widely used pulse compression binary code such as the Barker code. Overall, the ambiguity function performances of optimized punctured ZCZP can be as efficient as conventional pulse compression binary

code.

5 Application to Radar System

According to [33], P_D (Probability of Detection), P_{FA} (Probability of False Alarm) and P_M (Probability of Miss) are three probabilities of most interest in the radar system. Note that $P_M = 1 - P_D$. Therefore, we simulated the above three probabilities of using 124-length optimized punctured ZCZ sequence-pair in radar system in this section. The performance of radar system using 124-length P4 code is also studied in order to compare with the performance of optimized punctured ZCZ sequence-pairs of corresponding length. In the simulation model, 10^5 times of Monte-Carlo simulation has been run for each SNR value. The Doppler shift frequency is a random variable that is kept less than 1 unit (normalized to the inverse of the length of the code, in units of $1/NT_s$), and the expected peak time of the output of the matched filter is at $\tau = 0$.

From Fig. 5, the probabilities of miss target detection P_M of the system using 124-length optimized punctured ZCZP are lower than 124-length P4 code especially when the SNR is not high. When SNR is higher than 18 dB, both probabilities of miss targets of the system approach zero. However, the probabilities of miss targets of P4 code fall more quickly than optimized punctured ZCZP.

We plotted the detection probability P_D versus false alarm probability P_{FA} of the coherent receiver. We have simulated the performance at different SNR values. Because of the limited space, we only chose SNR at 12 db and 14 dB. Fig. 6 shows performance of 124-length optimized punctured ZCZP and performance of the same length P4 code when the SNR is 12dB and 14dB. Within the same SNR value either 12dB or 14dB, the detection probabilities of optimized punctured ZCZ sequence-pair are much larger than detection probabilities of P4 code, and meanwhile P_{FA} of the first code are also smaller than P_{FA} of the latter code. Stating differently, optimized punctured ZCZ sequence-pair has higher target detection probability while keeping a lower false alarm probability. Furthermore, observing Fig. 6, 124-length optimized punctured ZCZ sequence-pair even has much better performance at 12dB SNR than P4 code of corresponding length at 14dB SNR.

6 Conclusions

The definition and properties of a set of newly provided ternary codes–ZCZ sequence-pair set were discussed in this paper. Based on optimized punctured sequence-pair and Hadamard matrix, we have investigated a constructing method for a specific ZCZPS–optimized punctured ZCZPS made up of a set of optimized punctured ZCZPs along with studying its properties. The significant advantage of the optimized punctured ZCZPS is a considerably reduced sidelobe as low as zero in the zero correlation zone and zero mutual cross correlation value in the whole time domain. According to the radar system simulation results shown in Figs. 5 and 6, it is easy to observe that 124-length optimized punctured ZCZPS has better performance than P4 code of the same length when the target is not moving very fast in the system. A general conclusion can be drawn that the optimized punctured ZCZPS consisting of optimized punctured ZCZ sequence-pairs can effectively increase the variety of candidates for pulse compression codes. Because of the ideal cross correlation properties of optimized punctured ZCZPS, our future work would focus on the application of the optimized punctured ZCZPS in multiple radar systems.

References

[1] S. Ariyavisitakul, N. Sollenberger, and L. Greenstein, *Introduction to Radar System*, Tata McGraw-Hill, 2001.

[2] A. M. Boehmer, "Binary pulse compression codes," *IEEE Trans. Informaion Theory*, vol.IT-13, pp.156-167, Apr. 1967.

[3] R. Turyn, "On Barker codes of even length," *Proc. IEEE*, vol.51,9.1256, Sep. 1963.

[4] U. Somaini, "Bianry sequences with good autocorrelation and cross correlation properties," *IEEE Transactions on Aerospace and Electronic Systems*, AES-11, 6, 1226-1231, Nov. 1975.

[5] R. L. Frank, "Polyphase codes with good nonperiodic correlation properties", *IEEE Transactions on Information Theory,* IT. -9, pp. 43-45, Jan. 1963.

[6] B. L. Lewis and F. F. Kretschuner, "A new class of polyphase pulse compression codes and techniques", *IEEE Transactions on Aerospace and Electronic Systems,* AES-17, pp. 364-372, May. 1981.

[7] B. L. Lewis and F. F. Kretschuner, "Linear frequency modulation derived polyphase pulse compression codes", *IEEE Transactions on Aerospace and Electronic Systems,* AES-18, pp. 637-641, Sep. 1982.

[8] J. W. Taylor, Jr. and H. J. Bilinchikoff, "Quadriphase code–a radar pulse compression signal with unique characteristics", *IEEE Transactions on Aerospace and Electronic Systems,* AES-24, pp. 156-170, Mar. 1988.

[9] S. W. Golomb, *Shift register sequences*, Holden-Day, 1967, Revised edn: Aegean Park Press, Laguna Hills, CA, 1982.

[10] R. A. Scholtz and L. R. Welch, "GMW sequences", *IEEE Transactions on Information Theory,* IT. -30, pp. 548-553, Jan. 1984.

[11] R. Sato and M. Shinrhu, "Simple mismatched filter for binary pulse compression code with small PSL and small S/N loss [radar]", *IEEE Transactions on Aerospace and Electronic Systems,* AES-39(2), pp. 711-718, Apr. 2003.

[12] K. Sato, H. Horie, H. Hanado and H. Kumagai, "A digital-analog hybrid technique for low range sidelobe pulse compression", *IEEE Transactions on Aerospace and Electronic Systems,* AES-39(7), pp. 1612-1615, Jul. 2001.

[13] A. Tanner, S. L. Durden, R. Denning, E. Im, F. K. Li, W. Ricketts and W. Wilson, "Pulse compression with very low sidelobes in an airborne rain mapping radar", *IEEE Transactions on Aerospace and Electronic Systems,* AES-32(1), pp. 211-213, Jan. 2004.

[14] L. R. Welch, "Lower bounds on the maximum cross correlation of signals," *IEEE Trans. Inform. Theory*, IT-20, (3), pp. 397-399, 1974.

[15] V. M. Sidelnikov, "On mutual correlation of sequences," *Soviet Math doklady*, 12,pp. 197-201, 1971.

[16] D. V. Sarwate and M .B. Pursley, "Crosscorrelation properties of pseudorandom and related sequences," *Proc. IEEE*, 68, (3), pp. 593-620, 1980.

[17] P. G. Boyvalenkov, D. P. Danev and S.P. Bumova, "Upper bounds on the minimum distance of spherical codes," *IEEE Trans. Inform. Theory*, 42, (5), pp. 1576-1581, 2002.

[18] P. Z. Fan and M. Darnell, *Sequence design for communications applications,* Research Studies Press, John Wiley & Sons Ltd, London, 1996.

[19] P. Z. Fan and M. Darnell, "On the construction and comparison of period digital sequences sets," *IEE Proc. Commun.*, 144, (6), pp. 111-117, 1997.

[20] P. Z. Fan, N. Suehiro, N. Kuroyanagi and X. M. Deng, "A class of binary sequences with zero correlation zone," *IEE Electron.Letter*, 35 (10): 777-779, 1999.

[21] P. Z. Fan and L. Hao, "Generalized Orthogonal Sequences and Their Applications in Synchronous CDMA Systems," *IEICE Trans.Fundamentals*, E832A(11): 1 16, 2000.

[22] X. Tang and W. H. Mow, "A new systematic construction of zero correlation zone sequences based on interleaved perfect sequences," *IEEE Trans. Inform. Theory*, 54, (12), pp :5729 - 5734, Dec. 2008.

[23] Z. C. Zhou, X. H. Tang; G. Gong;, "A new class of sequences with zero or low correlation zone based on interleaving technique," *IEEE Trans. Inform. Theory*, 54, (9), pp: 4267-4273, Sep.2008.

[24] Z. C. Zhou; X. H. Tang;, "A new class of sequences with zero correlation zone based on interleaved perfect sequences," *Information Theory Workshop, 2006. ITW '06 Chengdu. IEEE*, 22-26, pp: 548 - 551, Oct. 2006.

[25] S. Matsufuji, "Two families of sequence pairs with zero correlation zone," *Parallel and Distributed Computing, Applications and Technologies, 2003. PDCAT'2003. Proceedings of the Fourth International Conference on*, 27-29, pp:899 - 903, Aug. 2003 .

[26] S. Matsufuji, K. Takatsukasa, Y. Watanabe, N. Kuroyanagi, N. Suehiro, "Quasi-orthogonal sequences," *Wireless Communications, 2001. (SPAWC '01). 2001 IEEE Third Workshop on Signal Processing Advances in*, 20-23, pp:255 - 258, Mar. 2001.

[27] X. H. Tang, P. Z. Fan, S. Matsufuji, "Lower bounds on correlation of spreading sequence set with low or zero correlation zone," *Electronics Letters*, 36, (6), pp:551 - 552, 16 Mar. 2000.

[28] S. Matsufuji, N Suehiro , N Kuroyanagi and P Z Fan, "Two types of polyphase sequence set for approximately synchronized CDMA systems," *IEICE Trans. Fundamentals*, E862A(1): 229-234, Jan. 2003.

[29] N. Levanon and A. Freedman, "Periodic ambiguity function of CW signals with perfect periodic autocorrelation", *IEEE Transactions on Aerospace and Electronic Systems,* AES-28(2), pp. 387-395, Apr. 1992.

[30] L. W. Couch, "Effects of modulation nonlinearity on the range response of FM radars", *IEEE Transactions on Aerospace and Electronic Systems,* AES-9(4), pp. 598-606, Jul. 1973.

[31] H. Torii, M. Nakamura and N. Suehiro, "A new class of zero correlation zone sequences," *IEEE Trans. Inform. Theory*, 50: 559-565, Mar. 2004.

[32] T. Jiang, *Research on Quasi-Optimized Binary Signal Pair and Perfect Punctured Binary Signal Pair Theory,* Ph.D Dissertation: Yanshan University, 2003.

[33] M. A. Richards, *Fundamentals of Radar Signal Processing,* McGraw-Hill, 2005.

List of Figures

1 Periodic autocorrelation property of optimized punctured ZCZPS 19

2 Periodic cross correlation property of optimized punctured ZCZPS 19

3 Ambiguity function of 124-length ZCZPS: (a) autocorrelation (b) cross correlation 20

4 Doppler shift of 124-length ZCZPS (τ=0): (a) autocorrelation (b) cross correlation 21

5 Probability of miss targets detection : 124-length optimized punctured ZCZ sequence-pair VS. 124-length P4 code 22

6 Probability of detection versus probability of false alarm of the coherent receiver : 124-length optimized punctured ZCZ sequence-pair VS. 124-length P4 code 22

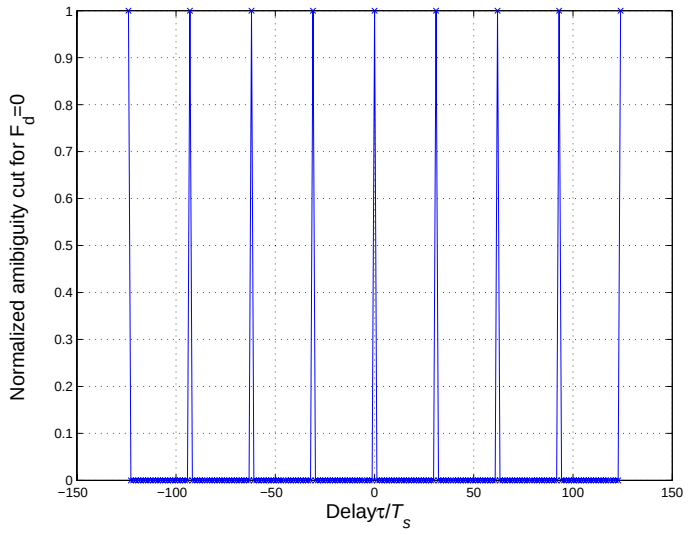


Figure 1: Periodic autocorrelation property of optimized punctured ZCZPS

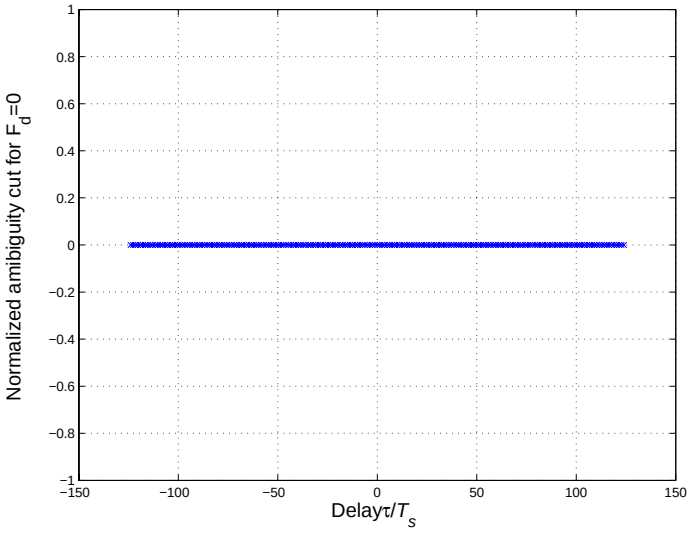
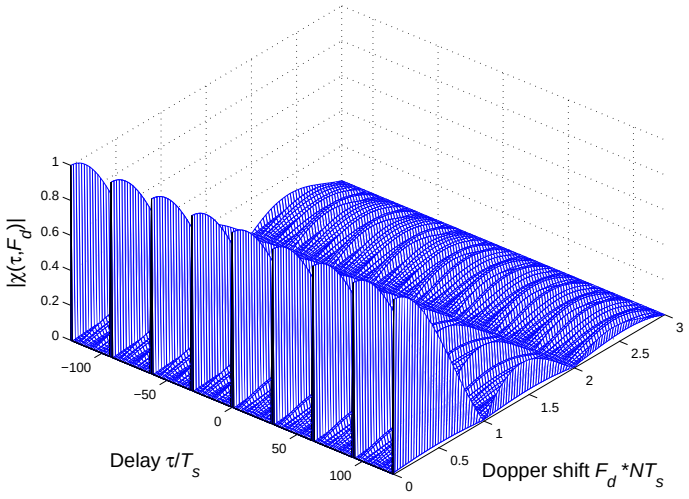
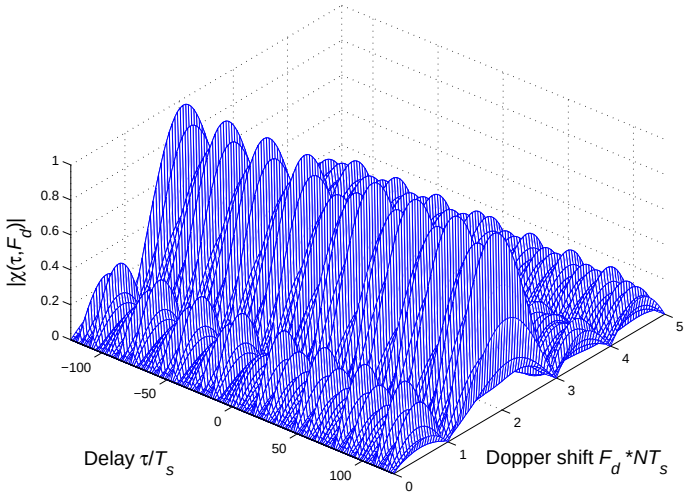


Figure 2: Periodic cross correlation property of optimized punctured ZCZPS

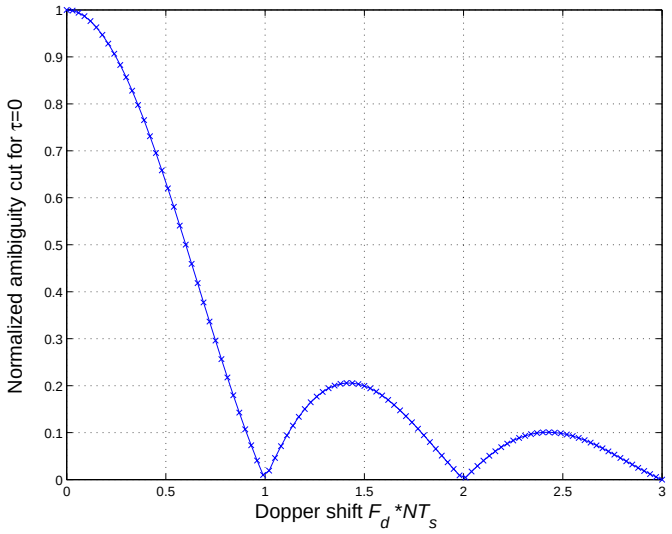


(a)

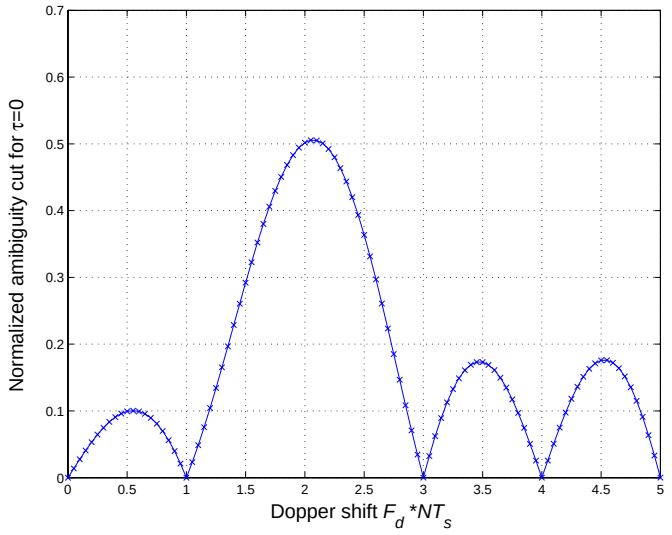


(b)

Figure 3: Ambiguity function of 124-length ZCZPS: (a) autocorrelation (b) cross correlation



(a)



(b)

Figure 4: Doppler shift of 124-length ZCZPS (τ=0): (a) autocorrelation (b) cross correlation

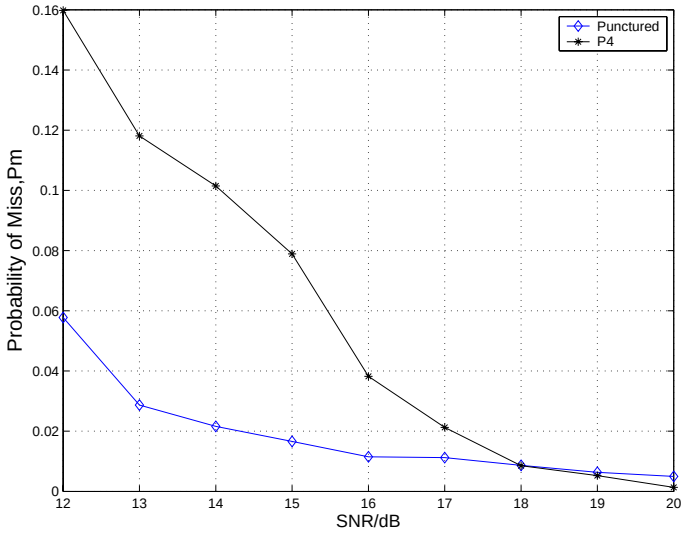


Figure 5: Probability of miss targets detection : 124-length optimized punctured ZCZ sequence-pair VS. 124-length P4 code

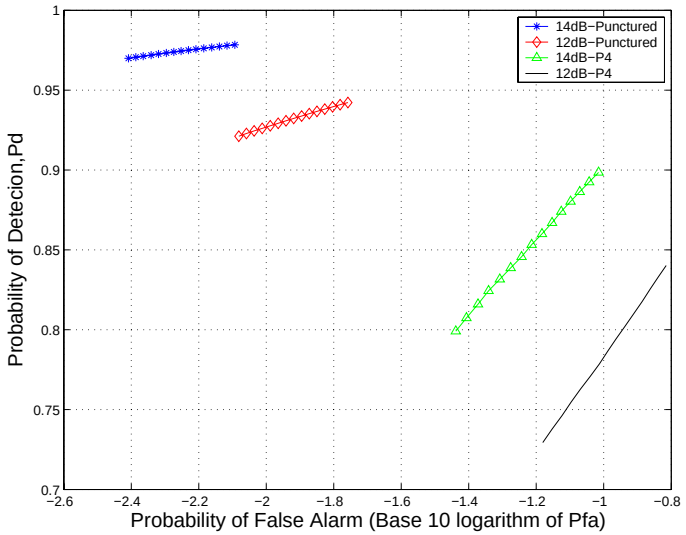


Figure 6: Probability of detection versus probability of false alarm of the coherent receiver : 124-length optimized punctured ZCZ sequence-pair VS. 124-length P4 code

Available online at www.sciencedirect.com
ScienceDirect
Pattern Recognition Letters 29 (2008) 377–381
Pattern Recognition Letters
www.elsevier.com/locate/patrec

Automatic target recognition using waveform diversity in radar sensor networks

Qilian Liang *

Department of Electrical Engineering, University of Texas at Arlington, 416 Yates Street, Rm 518, Arlington, TX 76019-0016, USA

Received 12 June 2006; received in revised form 4 October 2007
Available online 1 November 2007

Communicated by B. Kamgar-Parsi

Abstract

In this paper, we perform a number of theoretical studies on constant frequency (CF) pulse waveform design and diversity in radar sensor networks (RSN): (1) the conditions for waveform co-existence, (2) interferences among waveforms in RSN, (3) waveform diversity combining in RSN. As an application example, we apply the waveform design and diversity to automatic target recognition (ATR) in RSN and propose maximum-likehood (ML)-ATR algorithms for non-fluctuating target as well as fluctuating target. Simulation results show that our waveform diversity-based ML-ATR algorithm performs much better than single-waveform ML-ATR algorithm for non-fluctuating targets or fluctuating targets. Conclusions are drawn based on our analysis and simulations.
© 2007 Elsevier B.V. All rights reserved.

Keywords: Radar sensor networks; Waveform diversity; Automatic target recognition; Maximum-likelihood; Interferences; Ambiguity function

1. Introduction

The network of radar sensors should operate with multiple goals managed by an intelligent platform network that can manage the dynamics of each radar to meet the common goals of the platform, rather than each radar to operate as an independent system. Therefore, it is significant to perform signal design and processing and networking cooperatively within and between radar sensors. In this letter, we will study waveform design and diversity for radar sensor networks.

In the existing works on waveform design and selection, Bell (1993) used information theory to design radar waveform for the measurement of extended radar targets exhibiting resonance phenomena. In (Baum, 1991) singularity expansion method was used to design some discriminant waveforms such as K-pulse, E-pulse, and S-pulse. Sowelam and Tewfik (2000) developed a signal selection strategy for radar target classification, and a sequential classification procedure was proposed to minimize the average number of necessary signal transmissions. All the above studies and design methods were focused on the waveform design or selection for a single active radar or sensor. In (Skolnik, 2001) cross-correlation properties of two radars are briefly mentioned and the binary coded pulses using simulated annealing (Deng, 1996) are highlighted. However, the cross-correlation of two binary sequences such as binary coded pulses (e.g. Barker sequence) are much easier to study than that of two analog radar waveforms. In this paper, we will focus on the waveform diversity and design for radar sensor networks using constant frequency (CF) pulse waveform.

The rest of this paper is organized as follows. In Section 2, we study the co-existence of radar waveforms. In Section 3, we analyze the interferences among radar waveforms. In Section 4 we propose a RAKE structure for waveform

* Tel.: +1 817 272 1339; fax: +1 817 272 2253.
E-mail address: liang@uta.edu

0167-8655/$ - see front matter © 2007 Elsevier B.V. All rights reserved.
doi:10.1016/j.patrec.2007.10.016

diversity combining and propose maximum-likelihood (ML) algorithms for automatic target recognition (ATR). In Section 5, we provide simulation results on ML-ATR. In Section 6, we conclude this paper and provide some future works.

2. Co-existence of radar waveforms

For radar sensor networks, the waveforms from different radars will interfere with each other. We choose constant frequency (CF) pulse waveform for radar i as

$$x_i(t) = \sqrt{\frac{E}{T}}\exp[\mathrm{j}2\pi(\beta+\delta_i)t], \quad -T/2 \leqslant t \leqslant T/2 \tag{1}$$

which means there is a frequency shift δ_i for radar i. To minimize the interference from one waveform to the other, optimal values for δ_i should be determined to have the waveforms orthogonal to each other, i.e., let the cross-correlation between $x_i(t)$ and $x_n(t)$ be 0

$$\begin{aligned}\int_{-T/2}^{T/2} x_i(t)x_n^*(t)\mathrm{d}t &= \frac{E}{T}\int_{-T/2}^{T/2}\exp[\mathrm{j}2\pi(\beta+\delta_i)t] \\ &\quad\times\exp[-\mathrm{j}2\pi(\beta+\delta_n)t]\mathrm{d}t \\ &= E\mathrm{sinc}[\pi(\delta_i-\delta_n)T]\end{aligned} \tag{2}$$

If we choose

$$\delta_i = \frac{i}{T} \tag{3}$$

where i is a dummy index, then (2) can have two cases

$$\int_{-T/2}^{T/2} x_i(t)x_n^*(t)\mathrm{d}t = \begin{cases} E & i=n \\ 0 & i\neq n \end{cases} \tag{4}$$

So choosing $\delta_i = \frac{i}{T}$ in (1) can have orthogonal waveforms, i.e., the waveforms can co-exist if the carrier spacing is $1/T$ between two radar waveforms. However, orthogonality among the reflected waveforms (echoes) may not hold because of time delay and doppler shift ambiguity during transmission and reflection, so we need to study the interferences of waveforms in RSN.

3. Interferences of waveforms in radar sensor networks

3.1. RSN with two radar sensors

We are interested in analyzing the interference from one radar to another if there exist time delay and doppler shift. For a simple case where there are two radar sensors (i and n), the ambiguity function of radar i (considering interference from radar n) is

$$\begin{aligned}A_i(t_i,t_n,F_{D_i},F_{D_n}) = \Big|\int_{-\infty}^{\infty}[x_i(t)\exp(\mathrm{j}2\pi F_{D_i}t). \\ +x_n(t-t_n)\exp(\mathrm{j}2\pi F_{D_n}t)]x_i^*(t-t_i)\mathrm{d}t\Big|\end{aligned} \tag{5}$$

$$\begin{aligned}&\leqslant \Big|\int_{-T/2+\max(t_i,t_n)}^{T/2+\min(t_i,t_n)} x_n(t-t_n) \\ &\quad\exp(\mathrm{j}2\pi F_{D_n}t)x_i^*(t-t_i)\mathrm{d}t\Big| \\ &\quad+\Big|\int_{-T/2+t_i}^{T/2} x_i(t) \\ &\quad\exp(\mathrm{j}2\pi F_{D_i}t)x_i^*(t-t_i)\mathrm{d}t\Big| \\ &= \Big|\int_{-T/2+\max(t_i,t_n)}^{T/2+\min(t_i,t_n)} x_n(t-t_n) \\ &\quad\exp(\mathrm{j}2\pi F_{D_n}t)x_i^*(t-t_i)\mathrm{d}t\Big| \\ &\quad+\left|\frac{E\sin[\pi F_{D_i}(T-|t_i|)]}{T\pi F_{D_i}}\right|\end{aligned} \tag{6}$$

To make analysis easier, we assume $t_i = t_n = \tau$, then (6) can be simplified as

$$\begin{aligned}A_i(\tau,F_{D_i},F_{D_n}) &\approx |E\mathrm{sinc}[\pi(n-i+F_{D_n}T)]| \\ &\quad+\left|\frac{E\sin[\pi F_{D_i}(T-|\tau|)]}{T\pi F_{D_i}}\right|\end{aligned} \tag{7}$$

3.2. RSN with M radar sensors

It can be extended to an RSN with M radars. Assuming time delay τ for each radar is the same, then the ambiguity function of radar 1 (considering interferences from all the other $M-1$ radars with CF pulse waveforms) can be expressed as

$$\begin{aligned}A_1(\tau,F_{D_1},\ldots,F_{D_M}) &\approx \sum_{i=2}^{M}|E\mathrm{sinc}[\pi(i-1+F_{D_i}T)]| \\ &\quad+\left|\frac{E\sin[\pi F_{D_1}(T-|\tau|)]}{T\pi F_{D_1}}\right|\end{aligned} \tag{8}$$

4. Waveform diversity and combining with application to ATR

In RSN, The radar sensors are networked together in an ad hoc fashion. Scalability concern suggest a hierarchical organization of radar sensor networks with the lowest level in the hierarchy being a cluster. In RSN, each radar can provide their waveform parameters such as δ_i to their clusterhead radar, and the clusterhead radar can combine the waveforms from its cluster members. In RSN with M radars, the received signal for clusterhead (assume it is radar 1) is

$$r_1(u,t) = \sum_{i=1}^{M}\alpha(u)x_i(t-t_i)\exp(\mathrm{j}2\pi F_{D_i}t) + n(u,t) \tag{9}$$

where $\alpha(u)$ stands for complex radar cross section (RCS) and its magnitude can be modeled using non-zero con-

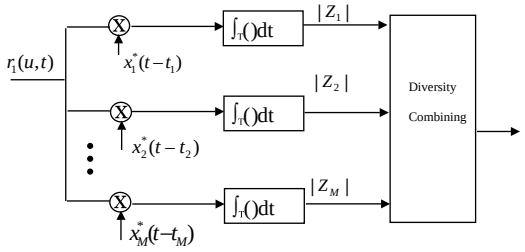


Fig. 1. Waveform diversity combining by clusterhead in RSN.

stants for non-fluctuating target and four Swerling target models for fluctuating target (Richards, 2005); F_{D_i} is the doppler shift of target relative to waveform i; t_i is delay of waveform i, and $n(u,t)$ is additive white Gaussian noise (AWGN). RCS may vary with aspect angle, and the radars have been assumed to be calibrated in such that RCS can be extracted in terms of meaningful units. In this paper, we propose a RAKE structure for waveform diversity combining, as illustrated by Fig. 1.

According to this structure, the received $r_1(u,t)$ is processed by a bank of matched filters, then the output of branch 1 (after integration) is

$$|Z_1(u;t_1,\ldots,t_M,F_{D_1},\ldots,F_{D_M})| = \left|\int_{-T/2}^{T/2} r_1(u,t)x_1^*(t-t_1)\mathrm{d}s\right| \tag{10}$$

$$= \left|\int_{-T/2}^{T/2}\left[\sum_{i=1}^{M}\alpha_i(u)x_i(t-t_i)\exp(\mathrm{j}2\pi F_{D_i}t)+n(u,t)\right]x_1^*(t-t_1)\mathrm{d}t\right| \tag{11}$$

where $\int_{-T/2}^{T/2} n(u,t)x_1^*(t-t_1)\mathrm{d}t$ can easily be proved to be AWGN, so

$$|n(u,t_1)| \triangleq \left|\int_{-T/2}^{T/2} n(u,t)x_1^*(t-t_1)\mathrm{d}t\right| \tag{12}$$

follows Rayleigh distribution. Assuming $t_1=t_2=\cdots=t_M=\tau$, then based on (8),

$$|Z_1(u;\tau,F_{D_1},\ldots,F_{D_M})| \approx \sum_{i=2}^{M}|\alpha(u)E\mathrm{sinc}[\pi(i-1+F_{D_i}T)]| + \left|\frac{\alpha(u)E\sin[\pi F_{D_1}(T-|\tau|)]}{T\pi F_{D_1}}\right| + |n(u,\tau)| \tag{13}$$

Similarly, we can get the output for any branch m $(m=1,2,\ldots,M)$,

$$|Z_m(u;\tau,F_{D_1},\ldots,F_{D_M})| \approx \sum_{i=1,i\neq m}^{M}|\alpha(u)E\mathrm{sinc}[\pi(i-m+F_{D_i}T)]| + \left|\frac{\alpha(u)E\sin[\pi F_{D_m}(T-|\tau|)]}{T\pi F_{D_m}}\right| + |n(u,\tau)| \tag{14}$$

If $\tau=0$, and $F_{D_1}=\cdots=F_{D_M}=0$, then (14) becomes

$$|Z_m(u;0,0,0,\cdots,0)| \approx |E\alpha(u)| + |n(u)| \tag{15}$$

Doppler mismatch happens quite often in target search where target velocity is not yet known. In the study of ATR in this paper, we assume that there is no delay and doppler uncertainty, so (15) will be used.

ATR has been extensively studied. In statitical approaches, conditional Gaussian (with Rayleigh in magnitude) models have been used for ATR with SAR data by O'Sullivan et al. (2001), DeVore and O'Sullivan (2002, 2003, 2004). Their models are Gaussian when one conditions on parameters such as aspect angle. Conditional Gaussian was also used for ATR with range profile data by Jacobs and O'Sullivan (2000). DeVore and O'Sullivan also tried out a Rician model (Devore et al., 2000) although it didn't perform well in their particular SAR application. Besides, Rician model was also used by Ehrman and Lanterman (2004a,b, 2003a,b) on ATR via comparing the RCS of targets detected by passive radar system to the simulated RCS of known targets. All these studies are for single radar system. We are interested in studying ATR using RSN and comparing it against the signle radar system.

4.1. ML-ATR for non-fluctuating targets

For non-fluctuating target, the magnitude of RCS $\alpha_m(u)$ is just a constant α for a given target. In (15), $|n(u,\tau)|$ follows Rayleigh distribution since $n(u,\tau)$ is a Gaussian random variable for given τ, so $|Z_m(u;0,0,\ldots,0)|$ follows Rician distribution because signal $E|\alpha|$ is a constant. Let $y_m \triangleq |Z_m(u;0,0,\ldots,0)|$, then the probability density function (pdf) of y_m is

$$f(y_m)=\frac{2y_m}{\sigma^2}\exp\left[-\frac{(y_m^2+\lambda^2)}{\sigma^2}\right]I_0\left(\frac{2\lambda y_m}{\sigma^2}\right) \tag{16}$$

where

$$\lambda = E|\alpha|, \tag{17}$$

σ^2 is the noise power (with I and Q sub-channel power $\sigma^2/2$), and $I_0(\cdot)$ is the zero-order modified Bessel function of the first kind. Let $\boldsymbol{y} \triangleq [y_1,y_2,\ldots,y_M]$, then the pdf of $\boldsymbol{y}$ is

$$f(\boldsymbol{y})=\prod_{m=1}^{M}f(y_m) \tag{18}$$

Our ATR is a multiple-category hypothesis testing problem, i.e., to decide a target category (e.g. aircraft, ship, motor vehicle, bird, etc.) based on $r_1(u,t)$. Assume there are totally N categories and category n target has RCS α_n, so the ML-ATR algorithm to decide a target category C can be expressed as

$$C = \arg\max_{n=1}^{N} f(\boldsymbol{y}|\lambda=E|\alpha_n|) \tag{19}$$

$$= \arg\max_{n=1}^{N}\prod_{m=1}^{M}\frac{2y_m}{\sigma^2}\exp\left[-\frac{(y_m^2+E^2|\alpha_n|^2)}{\sigma^2}\right]\times I_0\left(\frac{2E|\alpha_n|y_m}{\sigma^2}\right) \tag{20}$$

4.2. ML-ATR for fluctuating targets

Fluctuating target modeling is more realistic in which the target complex RCS (magnitude) is drawn from either the Rayleigh or chi-square of degree four pdf (Richards, 2005). In this paper, we will focus on "Swerling 2" model (Swerling, 1960) which is Rayleigh distribution with pulse-to-pulse decorrelation. For Swerling 2 model, the magnitude of complex RCS $|\alpha(u)|$ follows Rayleigh distribution and its I and Q sub-channels follow zero-mean Gaussian distributions with variance γ^2. Assume

$$\alpha(u) = \alpha_I(u) + j\alpha_Q(u) \tag{21}$$

and $n(u) = n_I(u) + jn_Q(u)$ follows zero-mean complex Gaussian distribution with variance σ^2 for the I and Q sub-channels. According to (11), (14), and (15),

$$|Z_m(u;0,0,0,\ldots,0)| \approx |E\alpha(u) + n(u)| \tag{22}$$

is a more accurate approximation. Since $\alpha(u)$ and $n(u)$ are zero-mean complex Gaussian random variables, so $E\alpha(u) + n(u)$ is a zero-mean Gaussian random variable with variance $E^2\gamma^2 + \sigma^2$ for the I and Q sub-channels, which means $y_m \triangleq |Z_m(u;0,0,\ldots,0)|$ follows Rayleigh distribution with parameter $\sqrt{E^2\gamma^2 + \sigma^2}$:

$$f(y_m) = \frac{y_m}{E^2\gamma^2 + \sigma^2} \exp\left(-\frac{y_m^2}{E^2\gamma^2 + \sigma^2}\right) \tag{23}$$

Table 1
RCS values at microwave frequency for 5 targets

Index n	Target	RCS (m^2)
1	Bird	0.01
2	Conventional unmanned winged missile	0.5
3	Small single-engine aircraft	1
4	Small flighter aircraft or 4 passenger jet	2
5	Large flighter aircraft	6

Let $\boldsymbol{y} \triangleq [y_1, y_2, \cdots, y_M]$, then the pdf of $\boldsymbol{y}$ is

$$f(\boldsymbol{y}) = \prod_{m=1}^{M} f(y_m) \tag{24}$$

Assume there are totally N categories and category n target has complex RCS $\alpha_n(u)$ (with variance γ_n^2), so the ML-ATR algorithm to decide a target category C can be expressed as

$$C = \arg\max_{n=1}^{N} f(\boldsymbol{y}|\gamma = \gamma_n) \tag{25}$$

$$= \arg\max_{n=1}^{N} \prod_{m=1}^{M} \frac{y_m}{E^2\gamma_n^2 + \sigma^2} \exp\left(-\frac{y_m^2}{E^2\gamma_n^2 + \sigma^2}\right) \tag{26}$$

5. Simulations

Radar sensor networks will be required to detect a broad range of target classes. Too often, the characteristics of objects that are not of interest (e.g., bird) will be similar to those of threat objects (e.g., missile). Therefore, new techniques to discriminate threat against undesired detections (e.g. birds, etc.) are needed. We applied our ML-ATR to this important application, to recognize a target from many target classes. We assume that the domain of target classes is known a priori (N in Sections 4.1 and 4.2), and that the RSN is confined to work only on the known domain.

For non-fluctuating target recognition, our targets have 5 classes with different RCS values, which are summarized in Table 1 Skolnik, 2001. For fluctuating target recognition, we assume the fluctuating targets follow "Swerling 2" model (Rayleigh with pulse-to-pulse decorrelation), and assume the RCS value listed in Table 1 to be the standard deviation (std) γ_n of RCS $\alpha_n(u)$ for target n. We applied the ML-ATR algorithms in Section 4.1 (for non-fluctuating target case) and Section 4.2 (for fluctuating target case) to classify an unknown target as one of these 5 target classes. At each average SNR value, we ran Monte-Carlo simulations for 10^5 times for each target. In Fig. 2a and b, we plot the average probability of ATR error for all 5 targets recognition (non-

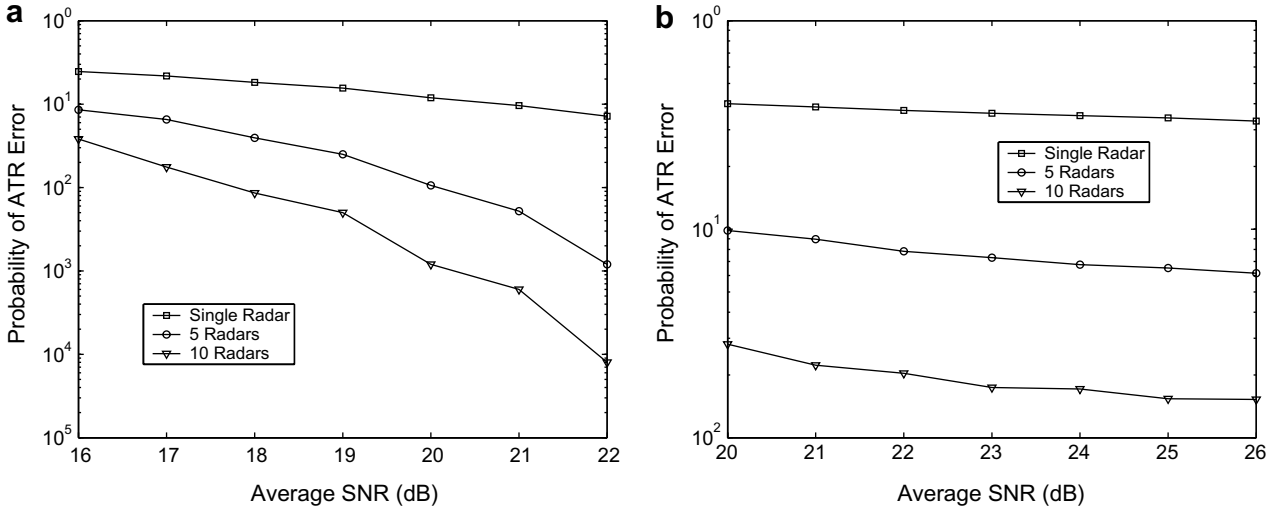


Fig. 2. Probability of ATR error for 5 targets. (a) *non-fluctuating* targets, (b) *fluctuating* targets.

fluctuating and fluctuating targets). Our RSN with waveform diversity can have average probability of ATR error much less than 10%. However, the single radar system has probability of ATR error much higher than 10%. Observe that even if the single radar works at much higher SNR, it still could not achieve low probability of ATR error because the single radar system is not very sensitive to the SNR. This clearly demonstrates that waveform diversity in RSN can tremendously improve the ATR performance, and break the performance floor of single radar system.

6. Conclusions

We have studied constant frequency pulse waveform design and diversity in radar sensor networks. We showed that the waveforms can co-exist if the carrier frequency spacing is $1/T$ between two radar waveforms. We made analysis on interferences among waveforms in RSN and proposed a RAKE structure for waveform diversity combining in RSN. As an application example, we applied the waveform design and diversity to automatic target recognition (ATR) in RSN and proposed maximum-likehood (ML)-ATR algorithms for non-fluctuating target as well as fluctuating target. Simulation results show that RSN using our waveform diversity-based ML-ATR algorithm performs much better than single radar system for non-fluctuating targets and fluctuating targets recognition.

Acknowledgements

This work was supported by the U.S. Office of Naval Research (ONR) under Grant N00014-03-1-0466, N00014-07-1-0395, and N00014-07-1-1024.

The author would like to thank ONR Program Officer Dr. Rabinder N. Madan for his direction and insightful discussion on radar sensor networks, and an anonymous reviewer for his/her constructive review comments, all of which we have incoporated into the new version.

References

Baum, C.E. et al., 1991. The singularity expansion method and its application to target identification. Proc. IEEE 79 (10).

Bell, M.R., 1993. Information theory and radar waveform design. IEEE Trans. Informat. Theory 39 (5), 1578–1597.

Deng, H., 1996. Synthesis of binary sequences with good correlation and cross-correlation properties by simulated annealing. IEEE Trans. Aerosp. Electron. Systems 32 (1).

DeVore, M.D., O'Sullivan, J.A., 2002. Performance complexity study of several approaches to automatic target recognition from SAR images. IEEE Trans. AES 38 (2), 632–648.

DeVore, M.D., O'Sullivan, J.A., 2003. Target-centered models and information-theoretic segmentation for automatic target recognition. Multidim. Systems Signal Process. 14, 139–159.

DeVore, M.D., O'Sullivan, J.A., 2004. Quantitative statistical assessment of conditional models for synthetic aperture radar. IEEE Trans. Image Process. 13 (2), 113–125.

Devore, M.D., Lanterman, A.D., O'Sullivan, J.A., 2000. ATR performance of a Rician model for SAR images. In: Sadjadi, F.A. (Ed.), Proc. SPIE Automatic Target Recognition X, vol. 4050, Orlando, FL, April, pp. 34–45.

Ehrman, L.M., Lanterman, A.D., 2003. Target identification using precomputed radar cross sections and a coordinated flight model. In: Kurzenhauser, P., Spickler, B. (Eds.), Third Multinational Conference on Passive and Covert Radar, Univ. of Washington Applied Physics Laboratory, October 21–23, 2003.

Ehrman, L.M., Lanterman, A.D., 2003. Automated target recognition using passive radar and coordinated flight models. In: Sadjadi, F.A. (Ed.). Proc. SPIE Automatic Target Recognition XIII, vol. 5094, April 2003.

Ehrman, L.M., Lanterman, A.D., 2004a. Robust algorithm for automated target recognition using precomputed radar cross sections. In: Sadjadi, F.A. (Ed.), Proc. SPIE Automatic Target Recognition XIV, vol. 5426, April 12–16.

Ehrman, L.M., Lanterman, A.D., 2004b. A Robust algorithm for automatic target recognition using passive radar. In: 36th IEEE Southeastern Symposium on System Theory, Atlanta, GA, March 14–16.

Jacobs, S.P., O'Sullivan, J.A., 2000. Automatic target recognition using sequences of high resolution radar range-profiles. IEEE Trans. Aerosp. Electron. Systems 36 (2), 364–382.

O'Sullivan, J.A., DeVore, M.D., Kedia, V., Miller, M.I., 2001. SAR ATR performance using a conditionally gaussian model. IEEE Trans. AES 37 (1), 91–108.

Richards, M.A., 2005. Fundamentals of Radar Signal Processing. McGraw-Hill Companies, New York.

Skolnik, M.I., 2001. Introduction to Radar Systems, third ed. McGraw Hill, New York.

Sowelam, S., Tewfik, A., 2000. Waveform selection in radar target classification. IEEE Trans. Informat. Theory 46 (3), 1014–1029.

Swerling, P., 1960. Probability of detection for fluctuating targets. IRE Trans. Informat. Theory 6, 269–308.

International Journal of Uncertainty, Fuzziness and Knowledge-Based Systems
© World Scientific Publishing Company

CROSS-LAYER DESIGN FOR MOBILE AD HOCNETWROKS USING INTERVAL TYPE-2 FUZZY LOGIC SYSTEMS

XINSHENG XIA and QILIAN LIANG

Department of Electrical Engineering, University of Texas at Arlington
416 Yates Street, Nedderman Hall, Rm 518
Arlington, Texas 76019-0016 USA
xia@wcn.uta.edu, liang@uta.edu

Received (10-02-2006)
Revised (11-02-2007)
Accepted (25-05-2007)

In this paper, we introduce a new method for packet transmission delay analysis and prediction in mobile ad hoc networks. We apply a fuzzy logic system (FLS) to coordinate physical layer and data link layer. We demonstrate that type-2 fuzzy membership function (MF), i.e., the Gaussian MFs with uncertain variance is most appropriate to model BER and MAC layer service time. Two FLSs and one neural network: a singleton type-1 FLS, an interval type-2 FLS and back-prop neural network (NN) are designed to predict the packet transmission delay based on the BER and MAC layer service time. Simulation results show that the interval type-2 FLS performs much better than the type-1 FLS in transmission delay prediction. And FLSs performs better than back-prop NN. We use the forecasted transmission delay to adjust the transmission power, and it shows that the interval type-2 FLS performs much better than a type-1 FLS, and FLSs are performs better than back-prop NN in terms of energy consumption, average delay and throughput. Besides, we obtain the performance bound based on the actual transmission delay.

Keywords: wireless Ad Hoc networks, cross-layer design, fuzzy logic system, interval type-2 fuzzy sets, packet transmission delay analysis and prediction

1. Introduction

The demand for Quality of Service (QoS) in mobile ad hoc networks is growing in a rapid speed. To enhance the QoS, we consider the combination of physical layer and data-link layer together, a cross-layer approach. A strict layered design is not flexible enough to cope with the dynamics of the mobile ad hoc networks [1]. Cross-layer design could introduce the layer interdependencies to optimized overall network performance. The general methodology of cross-layer design is to maintain the layered architecture, capture the important information that influence other layers, exchange the information between layers and implement adaptive protocols and algorithms at each layer to optimize the performance.

Lots of previous works have focused on cross-layer design for QoS provision. Liu

et al [2] combine the AMC at physical layer and ARQ at the data link layer. Ahn et al [3] use the info from MAC layer to do rate control at network layer for supporting real-time and best effort traffic. Akan et al [4] propose a new adaptive transport layer suite including adaptive transport protocol and adaptive rate control protocol based on the lower layer information.

Some works related to energy efficiency have been reported. Banbos proposes a power-controlled multiple access schemes in [5]. This protocol reveals the trade-off of the transmitter power cost and backlog/delay cost in power control schemes. Zhu [6] proposes a minimum energy routing scheme, which consider the energy consumption for data packets as well as control packets of routing and multiple access. In [7], Sichitiu proposes a cross-layer scheduling method. Through combining network layer and MAC layer, a deterministic, schedule-based energy conservation scheme is proposed. This scheme drives its power efficiency from eliminating idle listening and collisions.

However, cross-layer design can produce unintended interactions among protocols, such as an adaptation loops. It is hard to characterize the interaction at different layers and joint optimization across layers may lead to complex algorithm.

In this paper, we discuss one of the parameters for QoS: packet transmission delay. And our algorithm is quite different from all the previous works. We propose to use interval type-2 Fuzzy Logic System (FLS) for packet transmission delay analysis and prediction, and we compare it against a singleton type-1 FLS. After applying FLSs, better performances could be achieved. Also, the fuzzy method could be flexible and simpler to implement.

We apply the transmission delay predictors to control the transmission power. The simulation achieves performance parameters of average delay, energy consumption and throughput. Assume we know the actual transmission delay, we also get these parameters as the performance bounds. Table 1 is the acronyms used in the paper.

The remainder of this paper is structured as following. In section 2, we introduce the preliminaries. In section 3, we make an overview of fuzzy logic systems. In section 4, we apply the FLS to the cross-layer design. Simulation results and discussions are presented in section 5. In section 6, we conclude this paper.

2. Preliminaries

2.1. *Pysical layer design*

The physical layer is the interface between the wireless medium and the MAC [8]. The principle of OFDM is to divide a high-speed binary signal to be transmitted over a number of low data-rate subcarriers. A key feature of the IEEE 802.11a PHY is to provide 8 PHY modes with different modulation schemes and coding rates, making the idea of link adaptation feasible and important, as listed in Table 2. BPSK, QPSK, 16-QAM and 64-QAM are the supported modulation schemes. The OFDM provides a data transmission rates from 6 to 54MBPS. The higher code rate

Table 1. Acronyms

AMC	*Adaptive Modulation and Coding*
BER	*Bit Error Rate*
BPSK	*Binary Phase Shift Keying*
CSMA/CA	*Carrier − Sense Multiple Access with Collision Avoidance*
FLS	*Fuzzy Logic System*
MAC	*Medium Access Control*
MF	*Membership Function*
NN	*Neural Network*
OFDM	*Orthogonal Frequency Division Multiplexing*
QAM	*Quadrature Amplitude Modulation*
QPSK	*Quality of Service*
QoS	*Quadrature Phase Shift Keying*
RMSE	*Root Mean Square Errors*

of 2/3 and 3/4 are obtained by puncturing the original rate 1/2 code.

Table 2. Eight PHY Modes of the IEEE802.11A PHY

Mode	*Modulation*	*CodeRate*	*DataRate*	*BpS∗*
1	*BPSK*	1/2	6*Mbps*	3
2	*BPSK*	3/4	9*Mbps*	4.5
3	*QPSK*	1/2	12*Mbps*	6
4	*QPSK*	3/4	18*Mbps*	9
5	$16-QAM$	1/2	24*Mbps*	12
6	$16-QAM$	3/4	36*Mbps*	18
7	$64-QAM$	2/3	48*Mbps*	24
8	$64-QAM$	3/4	54*Mbps*	27

*Bytes per OFDM Symbol

2.2. *MAC layer design*

The 802.11 MAC uses Carrier-Sense Multiple Access with Collision Avoidance (CSMA/CA) to achieve automatic medium sharing between compatible stations. In CSMA/CA, a station senses the wireless medium to determine if it is idle before it starts transmission. If the medium appears to be idle, the transmission may proceed, else the station will wait until the end of the in-progress transmission. A station will ensure that the medium has been idle for the specified inter-frame

interval before attempting to transmit.

Besides carrier sense and RTS/CTS mechanism, an acknowledgment (ACK) frame will be sent by the receiver upon successful reception of a data frame. Only after receiving an ACK frame correctly, the transmitter assumes successful delivery of the corresponding data frame. The sequence for a data transmission is: RTS-CTS-DATA-ACK.

A mobile node will retransmit the data packet when finding failing transmission. Retransmission of a signal packet can achieve a certain probability of delivery. There is a relationship between the probability of delivery p and retransmission times n [9]:

$$n = 1.451n\frac{1}{1-p} \tag{1}$$

The IEEE 802.11 standard requires that a data frame is discarded by the transmitter's MAC after certain number of unsuccessful transmission attempts. According to the requirement of probability of delivery, we choose the minimum number of retransmission.

When MAC layer acquires access to the channel, the nodes will exchange the RTS-CTS-DATA-ACK packets. After the transmitters receive an ACK packet, a packet is transmitted successfully. In this paper, we assume that there will be always best-effort traffic present that can be locally and rapidly rate controlled in an independent manner at each node to yield necessary low delays and stable throughputs.

2.3. *Bit error rate*

BER is the percentage of bits with errors divided by the total number of bits that have been transmitted, received or processed over a given time period. It is a measure of transmission quality. The high BER means high packets loss rate. Requests for resends will increase delay. For delay sensitive traffic requires a very low BER.

2.4. *MAC layer service time*

There are three basic processes when the MAC layer transmits a packet [10]: the decrement process of the backoff timer, the successful packet transmission process that takes a time period of T_{suc} and the packet collision process that takes a time period of T_{col}. Here, T_{suc} is the random variable representing the period that the medium is sensed busy because of a successful transmission, and T_{col} is the random variable representing the period that the medium is sensed busy by each station due to collisions. The MAC layer service time is the time interval from the time instant that a packet becomes the head of the queue and starts to contend for transmission, to the time instant that either the packet is acknowledged for a successful transmission or the packet is dropped. This time is important when we examine the performance of higher protocol layers.

2.5. *Packet transmission delay*

The packet delay represents the time it took to send the packet between the transmitter and the next-hop receiver, including the deferred time and the time to fully acknowledge the packet. The packet transmission delay between the mobile nodes includes three parts: the wireless channel transmission delay, the Physical/MAC layer transmission delay, and the queuing delay [11].

Defining D as the distance between two nodes and C as the light speed, the wireless channel transmission delay as:

$$Delay_{ch} = \frac{D}{C} \tag{2}$$

The Physical/MAC layer transmission delay will be decided by interaction of the transmitter and the receive channel, the node density and the node traffic intensity etc. The queuing delay is decided by the mobile node I/O system-processing rate, the subqueue length in the node. In order to make the system "stable", the rate at which node transfers packets intended for its destination must satisfy all nodes that the queuing lengths will not be infinite and the average delays will be bounded.

2.6. *Energy*

A mobile node consumes significant energy when it transmits or receives a packet. But we will not consider the energy consumed when the mobile node is idle.

The distance between two nodes are variable in the mobile ad hoc networks and the power loss model is used. To send the packet, the sender consumes [12],

$$P_{tx} = P_{elec} + \epsilon_{fs} \cdot d^2 \tag{3}$$

and to receive the packet, the receiver consumes,

$$P_{rx} = P_{elec} \tag{4}$$

Where P_{elec} represents the power that is necessary for digital processing, modulation, and ϵ_{fs} represents the power dissipated in the amplifier for the free space distance d transmission.

2.7. *One-step markov path model*

The mobile nodes are roaming independently with variable ground speed. The mobility model is called one-step Markov path model [13]. The probability of moving in the same direction as the previous move is higher than other directions in this model, which means this model has memory. Fig.1. shows the probability of the six directions.

3. Overview of Interval Type-2 Fuzzy Logic Systems

Fig. 2. shows the structure of a type-2 FLS [14]. It is very similar to the structure of a type-1 FLS [15]. For a type-1 FLS, the *output processing* block only contains the

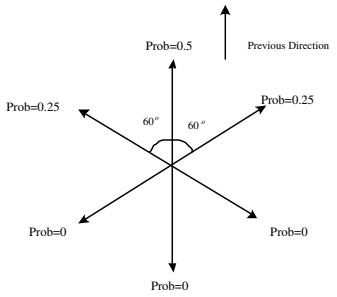


Fig. 1. One-step Markov Path Model

defuzzifier. We assume that the reader is familiar with type-1 FLSs, so that here we focus only on the similarities and differences between the two FLSs.

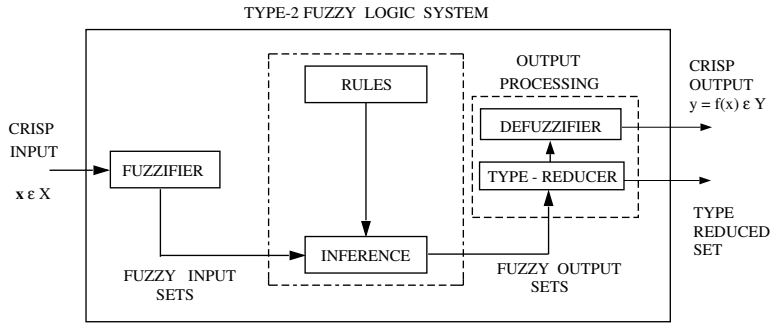


Fig. 2. The structure of a type-2 FLS

In order to emphasize the importance of the type-reduced set, we have shown two outputs for the type-2 FLS, the type-reduced set and the crisp defuzzified value.

The fuzzifier maps the crisp input into a fuzzy set. This fuzzy set can, in general, be a type-2 set.

In the type-1 case, we generally have "IF-THEN" rules, where the lth rule has the form "R^l : IF x_1 is F_1^l and x_2 is F_2^l and $\cdots$ and x_p is F_p^l, THEN y is G^l", where: x_is are inputs; F_i^ls are antecedent sets ($i = 1, \ldots, p$); y is the output; and G^ls are consequent sets. The distinction between type-1 and type-2 is associated with the nature of the membership functions, which is not important while forming rules; hence, the structure of the rules remains exactly the same in the type-2 case, the only difference being that now some or all of the sets involved are of type-2; so, the lth rule in a type-2 FLS has the form "R^l : IF x_1 is $\tilde{\mathrm{F}}_1^l$ and x_2 is $\tilde{\mathrm{F}}_2^l$ and $\cdots$ and x_p is $\tilde{\mathrm{F}}_p^l$, THEN y is $\tilde{\mathrm{G}}^l$".

In the type-2 case, the inference process is very similar to that in type-1. The

inference engine combines rules and gives a mapping from input type-2 fuzzy sets to output type-2 fuzzy sets. To do this, one needs to find unions and intersections of type-2 sets, as well as compositions of type-2 relations.

In a type-1 FLS, the defuzzifier produces a crisp output from the fuzzy set that is the output of the inference engine, i.e., a type-0 (crisp) output is obtained from a type-1 set. In the type-2 case, the output of the inference engine is a type-2 set; so, "extended versions" (using Zadeh's Extension Principle [16]) of type-1 defuzzification methods was developed in [14]. This extended defuzzification gives a type-1 fuzzy set. Since this operation takes us from the type-2 output sets of the FLS to a type-1 set, this operation was called "type-reduction" and the type-reduced set so obtained was called a "type-reduced set" [14]. To obtain a crisp output from a type-2 FLS, we can defuzzify the type-reduced set.

General type-2 FLSs are computationally intensive, because type-reduction is very intensive. Things simplify a lot when secondary membership functions (MFs) are interval sets (in this case, the secondary memberships are either 0 or 1). When the secondary MFs are interval sets, the type-2 FLSs were called "interval type-2 FLSs". In [17], Liang and Mendel proposed the theory and design of interval type-2 fuzzy logic systems (FLSs). They proposed an efficient and simplified method to compute the input and antecedent operations for interval type-2 FLSs, one that is based on a general inference formula for them. They introduced the concept of upper and lower membership functions (MFs) and illustrate their efficient inference method for the case of Gaussian primary MFs. They also proposed a method for designing an interval type-2 FLS in which they tuned its parameters.

In an interval type-2 FLS with *singleton fuzzification* and meet under minimum or product t-norm, the result of the input and antecedent operations, F^l, is an interval type-1 set, i.e., $F^l = [\underline{f}^l, \overline{f}^l]$, where $\underline{f}^l$ and $\overline{f}^l$ simplify to

$$\underline{f}^l = \underline{\mu}_{\tilde{\mathrm{F}}_1^l}(x_1) \star \ldots \star \underline{\mu}_{\tilde{\mathrm{F}}_p^l}(x_p) \tag{5}$$

and

$$\overline{f}^l = \overline{\mu}_{\tilde{\mathrm{F}}_1^l}(x_1) \star \ldots \star \overline{\mu}_{\tilde{\mathrm{F}}_p^l}(x_p) \tag{6}$$

where x_i $(i = 1, \ldots, p)$ denotes the location of the singleton.

In this paper, we use center-of-sets type-reduction, which can be expressed as:

$$Y_{\cos}(Y^1, \cdots, Y^M, F^1, \cdots, F^M) = [y_l, y_r] = \int_{y^1} \cdots \int_{y^M} \int_{f^1} \cdots \int_{f^M} 1 \Big/ \frac{\sum_{i=1}^{M} f^i y^i}{\sum_{i=1}^{M} f^i} \tag{7}$$

where $Y_{\cos}$ is an interval set determined by two end points, y_l and y_r [17]; $f^i \in F^i = [\underline{f}^i, \overline{f}^i]$; $y^i \in Y^i = [y_l^i, y_r^i]$, and Y^i is the centroid of the type-2 interval consequent set $\tilde{\mathrm{G}}^i$; and, $i = 1, \ldots, M$. Because $Y_{\cos}$ is an interval set, we defuzzify it using the average of y_l and y_r; hence, the defuzzified output of an interval type-2 FLS is

$$f(\mathbf{x}) = \frac{y_l + y_r}{2} \tag{8}$$

4. Modeling BER and MAC Layer Service Time Using Interval Type-2 Membership Function

4.1. *BER analysis and modeling ber*

Let p be the probability that bit is error in any given time. So p can be described as a random variable with a known mean value E_a.

Now, at any given time the bit is error with probability p and the bit is correct with probability 1-p. Since the bit is either error or correct, the number of the bits it is error(E_b) for a fixed length transmission bits is binomial random variable. The length of the transmission bits is N_t, The probability that E_b takes any value x is :

$$P\{E_b = x\} = \mathrm{C}_x^{N_t}\mathrm{p}^x(\text{1-p})^{N_t-x} \tag{9}$$

As the number of the length of the transmission bits increase, the binomial distribution is approximated to a Gaussian distribution, with mean $\mu = pN_t$ and variance $\sigma^2 = p(1\text{-}p)N_t$.

In this paper, we set up membership functions (MFs) for BER. We get the original data from 10000 Monte-Carlo simulations. From the original data of BER shown in Table 2, we randomly decomposed the whole data sets into ten segments and computed the mean m_i and std σ_i of the BER of the ith segment, $i = 1, 2, \cdots, 10$. We also computed the mean m and std σ of the entire BER. To see which value –m_i or σ_i– varies more, we normalized the mean and std of each segment using m_i/m, and σ_i/σ, and we then computed the std of their normalized values, σ_m and σ_{std}.

Table 3. Mean and std values for ten segments and the entire BER, and their normalized std.

BER	mean	std
Segment 1	0.016613	0.033315
Segment 2	0.015618	0.027857
Segment 3	0.015528	0.017401
Segment 4	0.016206	0.02107
Segment 5	0.015721	0.017148
Segment 6	0.016298	0.029309
Segment 7	0.017062	0.037428
Segment 8	0.016253	0.022871
Segment 9	0.016448	0.023194
Segment 10	0.016237	0.020675
Entire Traffic	0.016198	0.025829
Normalized std	0.029161	0.26184

As we see from the last row of Table 3, $\sigma_m \ll \sigma_{std}$. We conclude, therefore, that if the BER of each segment (small number of simulations)are Gaussian, then the membership function for BER (in large number of simulations) is more appropriate

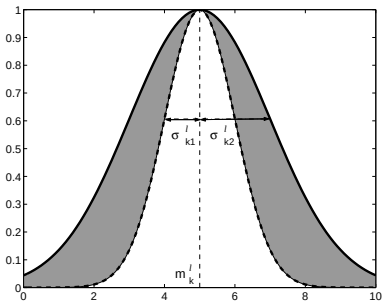


Fig. 3. Type-2 Gaussian MF with uncertain standard deviation

to be modeled as Gaussian with uncertain standard deviation. One example of type-2 Gaussian MF with uncertain standard deviation is shown in Fig.3.

4.2. *MAC layer service time analysis and modeling*

Recent research by Zhai, kwon and Fang [10] discovered that the lognormal distribution could match for the MAC layer service time. i.e., if the MAC layer service time for the packet i is s_i, then

$$\log_{10} s_i \sim \mathcal{N}(\cdot; m, \sigma^2) \tag{10}$$

We, therefore, tried to model the logarithm of the MAC layer service time, to see if a Gaussian MF can match its nature. We got the original data from simulation. We decomposed the whole data sets into ten segments and computed the mean m_i and std σ_i of the logarithm of the MAC layer service time of the ith segment, $i = 1, 2, \cdots, 10$. We also computed the mean m and std σ of the entire logarithm of the MAC layer service time. To see which value –m_i or σ_i– varies more, we normalized the mean and std of each segment using m_i/m, and σ_i/σ, and we then computed the std of their normalized values, σ_m and σ_{std}.

As we see from the last row of Table 4, $\sigma_m \ll \sigma_{std}$. We conclude, therefore, that if the logarithm of the MAC layer service time of each segment (small number of simulations)are Gaussian, then the membership function for the logarithm of the MAC layer service time(in large number of simulations) is more appropriate to be modeled as Gaussian with uncertain standard deviation. One example of type-2 Gaussian MF with uncertain standard deviation is shown in Fig.3.

5. Cross-layer Design Using Interval Type-2 Fuzzy Logic System

As we introduce in the section 2, the high BER means high packets loss rate. Requests for resends will increase latency. For delay sensitive traffic requires a very low BER. And the MAC layer service time is important when we examine the performance of higher protocol layers. So we could know BER and MAC layer service

Table 4. Mean and std values for ten segments and the entire logarithm of MAC layer service time, and their normalized std.

MAC layer service time	mean	std
Segment 1	-1.1902	0.44295
Segment 2	-1.1929	0.44698
Segment 3	-1.1967	0.45237
Segment 4	-1.1959	0.44835
Segment 5	-1.1917	0.43598
Segment 6	-1.1924	0.44779
Segment 7	-1.1976	0.45687
Segment 8	-1.1996	0.45554
Segment 9	-1.1923	0.45068
Segment 10	-1.1997	0.462
Entire Traffic	-1.1949	0.44981
Normalized std	0.0028746	0.016421

time will manage the packet transmission delay between the mobile nodes. We are now ready to evaluate the packet transmission delay using fuzzy logic systems.

We predict packet transmission delay based on the following two antecedents:

- Antecedent 1. BER.
- Antecedent 2. MAC layer service time.

The consequent is depicted as the packet transmission delay. The linguistic variables used to represent the BER and MAC layer service time were divided into three levels: *low*, *moderate*, and *high*. The consequent – the packet transmission delay was divided into 5 levels, *vert low, low, moderate, high and very high*.

We designed questions such as:

IF *BER* is *low* and *MAC layer service time* is *high*, THEN the packet transmission delay is _____.

So we need to set up $3^2 = 9$ (because every antecedent has 3 fuzzy sub-sets, and there are 2 antecedents) rules for this FLS. We summarized these rules in Table 5.

We used Guassian membership functions (MFs) to represent the antecedents and the consequent.

Fig.4. show the FLS application for the cross-layer design.

When a mobile node sends out a packet, it will first predict the packet transmission delay using the FLS algorithm. After that, the node could adjust the transmission power according to the predicted packet transmission delay. That means if the predicted packet transmission delay is larger, we will increase the transimission power. Similar rules can be obtained for other cases. Therefore average delay, energy consumption and throughput performances will change.

Table 5. Fuzzy Rules and Consequent

$Antecedent1$	$Antecedent2$	$Consequent$
Low	Low	$VeryLow$
Low	$Moderate$	Low
Low	$High$	$Moderate$
$Moderate$	Low	Low
$Moderate$	$Moderate$	$Moderate$
$Moderate$	$High$	$High$
$High$	Low	$Moderate$
$High$	$Moderate$	$High$
$High$	$High$	$VeryHigh$

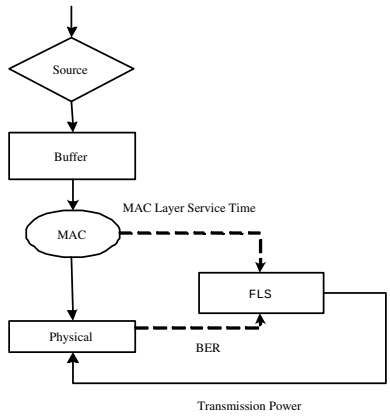


Fig. 4. FLS application for cross-layer design

6. Simulations

We implemented the simulation model using the OPNET modeler. The simulation region is 300×300 meters. There were 12 mobile nodes in the simulation model, and the nodes were roaming independently with variable ground speed between 0 to 10 meters per second. The mobility model was called one-step Markov path model. The movement would change the distance between mobile nodes. We assumed the collecting data distribution of the mobile node was exponential distribution and the arriving interval was 0.2 second and the length of the packet is 512 bits.

For type-1 FLS, We chose Gaussian membership function as antecedents; for interval type-2 FLS, we used Gaussian primary MF's with fixed mean and uncertain std for the antecedents. The initial 9 rules were designed according to Table 5. We followed the training algorithm proposed in [17]. In [19], the Back-prop NN is the

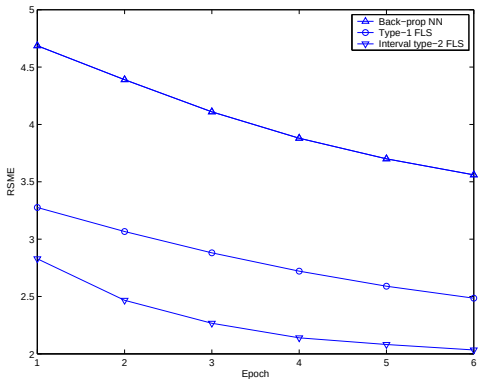


Fig. 5. The RMSE of packet transmission delay prediction for two FLS approaches

best non-fuzzy design. We chose Back-prop NN as a comparision. We set the Back-prop as two input, one output, 4 layers and 540 connectivity. The steepest decent algorithm was used to train all the parameters based on the 300 data sets. After training, the rules were fixed, and we tested the FLS based on the remaining 300 data sets.

In Fig.5., we summarized the root-mean-square-errors (RMSE) between the estimated packet transmission delay and the actual delay.

$$RMSE = \sqrt{\frac{1}{300}\sum_{i=301}^{600}[d(i) - f(i)]^2} \tag{11}$$

where d(i) was the actual packet transmission delay and f(i) was the estimated delay.

The simulation result shows that the interval type-2 FLS for packet transmission delay analysis and prediction outperforms the type-1 FLS, and two FLSs outperform Back-prop NN.

In the following performance simulation, we assume we could know the actual transmission delay. We just use it as a ideal case to get the performance parameters as the bounds.

6.1. *Average delay*

We used the average delay parameter to evaluate the network performance. Each packet was labeled a timestamp when it was generated by the source sensor node. When its destination sensor node received it, the time interval was the transmission delay.

$$Average\,Delay = \frac{\sum_{i=1}^{K} D_i}{K} \tag{12}$$

Fig.6. summaried the delay performance of the four algorithms. The type-2 FLS algorithm was better than the type-1 FLS algorithm. The type-2 FLS predictor could reduce the average delay by up to 20% than type-1 FLS predictor. Two FLS were better than Back-prop NN algorithm. And the ideal case was get by using actual transmission delay as the predictor outcome, and it was the best performance among the three.

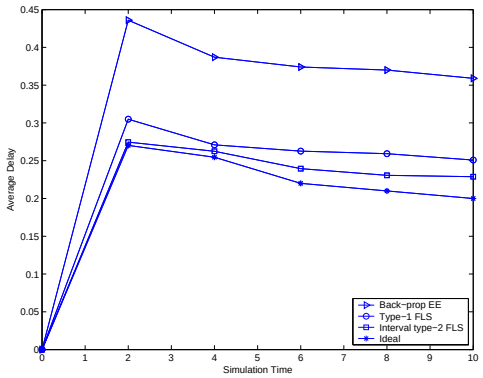


Fig. 6. Average Delay for Three Algorithms

6.2. *Energy efficiency*

It was not convenient to recharge the battery, so the energy efficiency was extremely important for mobile ad hoc networks. In the wireless mobile ad hoc networks, we used the parameter: the remaining energy to describe the energy efficiency.

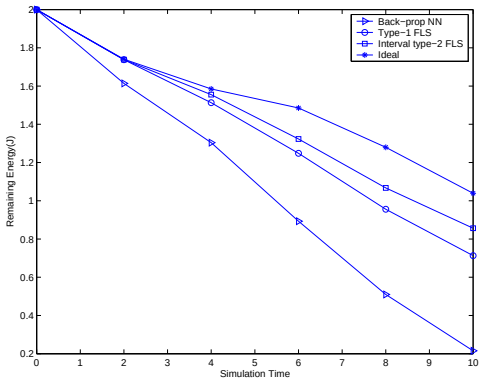


Fig. 7. Remaining Energy for Three Algorithms

The fuzzy computing consumed energy. In [20], we knew the energy comsumed by computing was far less than that comsumed by communication. We could only consider the commmunication energy comsuption for energy efficiency.

Fig.7. showed the remaining energy of the four algorithms. We assumed that the energy of each sensor is 2.0J and we adopted CSMA/CA protocol to solve the packets collision problem. If a sensor node transmitted Num_s packets (each packet cost 1 second) and receives Num_r packets (each packets also cost 1 second) and it was roaming in the network for T_m, we could get the remaining energy E_i of this sensor node [11]:

$$E_i = 2.0 - (3 \times 10^{-5} \times T_m + 1.2 \times 10^{-3} \times 1 + 6 \times 10^{-4} \times 1) \tag{13}$$

Same as the average delay, for the performance of the energy consumption, the type-2 FLS algorithm was better than the type-1 FLS algorithm. The type-2 FLS predictor could reduce the energy consumption by up to 21% than the type-1 FLS predictor. Two FLSs were better than Back-prop NN algorithm. The ideal case was set as the low bound.

6.3. *Networks efficiency*

The mobile ad hoc networks were used to collect data and transfer packets. The throughput of packets transmitted was one of the parameters to evaluate the networks efficiency. In our simulation, we assumed the collecting data distribution of the mobile node was Poisson distribution and the arriving interval was 0.2 second.

Observing from Fig.8., the type-2 FLS algorithm was better than the type-1 FLS algorithm. The type-2 FLS predictor could increase the throughput by up to 45% than the typ-1 FLS predictor. Two FLSs were better than Back-prop NN algorithm. And the ideal case was set as the high bound.

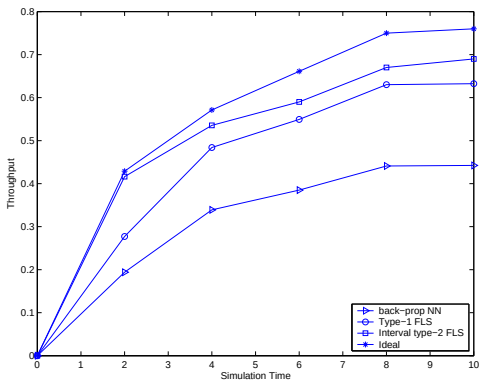


Fig. 8. Throughput for Three Algorithms

We introduce the fuzzy logic system in the cross-layer design. Compared with other algorithms for cross-layer design, the fuzzy method could be flexible and simpler to implement. We could predict the packet transmission delay according to the information just from physical layer and MAC layer. So we have potential application advantage. We use the FLSs as the predictors and we could control the transmission power according the outcomes of the predictors. Simulation results show that the type-2 FLS algorithm is better than the type-1 FLS algorithm. Two FLSs were better than Back-prop NN algorithm. And we could set the ideal case as the performance bounds.

7. Conclusion

Cross-layer design is a effective method to improve the performance of the mobile ad hoc network. We applied the fuzzy logic system to coordinate physical layer and data-link layer. We select BER and MAC layer service time as antecedents to analyze and predict the packet transmission delay. And we apply a type-1 FLS and an interval type-2 FLS for the packet transmission delay analysis and prediction. Simulation results show that the interval type-2 FLS for packet transmission delay analysis and prediction outperforms the type-1 FLS. Two FLSs are better than Back-prop NN algorithm. We use the FLSs as the predictors and we could control the transmission power according the outcomes of the predictors. Simulation results show that the type2 algorithm is better than the type1 algorithm. Two FLSs are better than Back-prop NN algorithm. And we could set the ideal case as the performance bounds.

Acknowledgment

This work was supported by the U.S. Office of Naval Research (ONR) Young Investigator Award under Grant N00014-03-1-0466.

1. A. J. Goldsmith and S. B. Wicker, " Design Challenges for Energy-Constrained Ad Hoc Wireless Networks", *IEEE Wireless Comm.,* vol. 9, no. 4 , pp. 8-27, 2002.
2. Q. Liu, S. Zhou and G. Giannakis, " Cross-Layer Combining of Adaptive Modulation and Coding with Truncated ARQ over Wireless Links", *IEEE Transactions on Wireless Communications*, vol. 3 , no.5 , pp. 1746 - 1755, Sept. 2004.
3. G. Ahn, A. Campbell, A. Veres and L. Sun, " Support Service Differentiation for Real-Time and Best-Effort Traffic in Stateless Wireless Ad Hoc Networks (SWAN)", *IEEE Transactions on Mobile Computing*, vol. 1, no. 3, pp. 192 - 207, July-Sept. 2002.
4. O. B. Akan and I. F. Akyildiz, " ATL, An Adaptive Transport Layer Suite for Next Generation on Wireless Internet", *IEEE Journal on Selected Areas in Communcations*, June 2004.
5. N. Bambos and S. Kandukuri, " Power-Controlled Multiple Access Schemes for Next-Generation Wireless Packet Networks ," *IEEE Wireless Communications*, June 2002.
6. J. Zhu, C. Qiao and X. Wang, " A Comprehensive Minimum Energy Routing Scheme for Wireless Ad Hoc Networks ," *IEEE INFOCOM2004.*
7. M. L. Sichitiu, " Cross-Layer Scheduling for Power Efficiency in Wireless Sensor Networks ," *IEEE INFOCOM2004.*

8. D. Qiao, S. Choi and K. G. Shin, " Goodput Analysis and Link Adaption for IEEE 802.11a Wireless LANs", *IEEE Transactions On Mobile Computing*, Oct. 2002.
9. L. H. Bao and J. J. Garcia-Luna-Aceves, " Hybrid Channel Access Scheduling in Ad Hoc Networks", *IEEE Computer Society,* Washington, DC, USA.
10. H. Zhai, Y. Kwon and Y. Fang, "Peformance analysis of IEEE 802.11 MAC protocols in wireless LANs", *Wireless Communication and Mobile Computing*, pp. 917-931, 2004.
11. X. Xia and Q. Liang, "Latency-aware and energy efficiency tradeoffs for sensor networks", *15th IEEE PIMRC(Personal, Indoor and Mobile Radio Communications), 2004.*
12. W. B. Heinzelman, A. P. Chandrakasan and H. Balakrishnan, " An application-specific protocol architecture for wireless microsensor networks ," *IEEE Transactions on Wireless Communications*, vol. 1 no. 4, Oct 2002.
13. T. C. Hou and T. J. Tsai, "Adaptive clustering in a hierarchical ad hoc network", *Proc. Int. Computer Symp.,Tainan, Taiwan,R.O.C.*, Dec. 1998, pp. 171-176.
14. N. N. Karnik, J. M. Mendel and Q. Liang, "Type-2 fuzzy logic systems", *IEEE Transactions On Fuzzy Systems*, vol. 7, no. 6, pp. 643-658, Dec. 1999.
15. J. M. Mendel, "Fuzzy logic systems for engineering: a tutorial", *Proc. of the IEEE*, vol. 83, no. 3, pp. 345-377, March 1995.
16. L. A. Zadeh, " The concept of a linguistic variable and its application to approximate reasoning - I", *Information Sciences*, vol. 8, pp. 199-249, 1975.
17. Q. Liang and J. M. Mendel, "Interval type-2 fuzzy logic systems: theory and design", *IEEE Transactions on Fuzzy Systems*, vol. 8, no. 5, pp. 535-550, Oct 2000.
18. C. Lu et al, " RAP: a real-time communication architecture for large-scale wireless sensor networks", *Proceeding of the eighth IEEE real-time and embedded technology and applications Symposium*, San Jose, California, pp. 55 - 66, Sept. 25 - 27, 2002.
19. J. Jang, " ANFIS: Adaptive-Network-Based Fuzzy Inference System", *IEEE Transactions on Systems, MAN and Cybernetics*, vol. 23, no. 3 May/Jun 1993.
20. A. Y. Wang and C. G. Sodini, " A simple energy model for wireless microsensor transceivers", *IEEEE Global Telecommunications Conference, 2004. GLOBECOM '04*, Nov. 29 - Dec. 3, 2004, Dallas, Texas, vol 5, pp:3205 - 3209.

A Fuzzy Logic Based Secure MAC Protocol Aiming at Denial of Service (DoS) Attacks in Wireless Sensor Networks

Qingchun Ren, Qilian Liang
Department of Electrical Engineering
University of Texas at Arlington
Arlington, TX 76019-0016 USA
E-mail: ren@wcn.uta.edu; liang@uta.edu

Dechang Chen
Department of Preventive Medicine and Biometrics
Uniformed Services University of the Health Sciences
Bethesda, MD 20814-4799 USA
dchen@usuhs.mil

Abstract

Security problems caused by Denial of Service(DoS) attacks for wireless sensor networks (WSNs) are important and hot research issues. Without proper security mechanisms, WSNs will be confined to limited and controlled environments. This negates numerous promises WSNs hold. However, current works on Media Access Control (MAC) for WSNs mainly concentrate on balancing the efficiency and fairness of common channel access. In this paper, we propose a secure MAC protocol for WSNs: fuzzy logic based secure media access control (FSMAC) protocol. In FSMAC, a security system is embedded into the existing MAC sub-layer. Therefore, the operation mechanism of the original MAC protocol, i.e., CSMA/CA, and its interfaces with the network layer and the physical layer remain unchanged. This breaks through the concept that unless the developers of WSNs take security into account at design time, the protocols they depend on will remain vulnerable to DoS attacks. Moreover, fuzzy logic system is applied for intrusion detection and defense. FSMAC is a fully distributed and non-agent-based method. Appropriate countermeasures are also adopted to reduce the destruction of attacks. Simulations were performed to demonstrate the effectiveness of our approach in terms of detection probability, false alarm rate, data packet successful transmission rate, energy consumption and network lifetime.

Keywords: DoS Attack; Fuzzy Logic Systems; Secure MAC protocol; Distributed WSN; Attack Monitoring; Defense, Collision Attack; Exhaustion Attack; Unfairness Attack.

1. Introduction

A wireless sensor network (WSN) can be thought as an ad hoc network, which consists of sensor nodes linked by wireless medium to perform distributed sensing tasks. Recent developments in integrated circuit technology have

allowed the construction of small and low-cost sensor nodes with signal processing and wireless communication capabilities. Distributed WSNs have increasing applications. They hold the potential to revolutionize many segments of our economy and lives from environmental monitoring, to manufacturing and business asset management[5]. However, individual sensor nodes are resource - energy, bandwidth, computation, and memory - constrained devices.

Most of WSNs actively monitor their surroundings, therefore it is easy to deduce information other than the data monitored[30]. Such unwanted information leakage often results in privacy breaches. Moreover, the wireless communication schemes employed by sensor networks facilitate eavesdropping and packet injection by adversaries. To ensure operation safety, secrecy of sensitive data and privacy for people in sensor environments, security algorithms are eagerly needed for WSNs.

Generally, denial of service (DoS) attacks[37] aim at disabling normal functions via wasting network resources, which could have been utilized by systems to provide useful services to legitimate clients. They can be carried out either by flooding victim nodes with network traffic or sending requests that cause victim nodes to behave unpredictably. DoS attacks on WSNs can be carried not only by attackers within an organization for having the authority to access the network, but also by attackers outside the organization. For DoS attacks, the target resources may be file system space, process space, network bandwidth and network connections. There are two main kinds of DoS attacks: system-oriented DoS attacks and congestion-based DoS attacks. System-oriented DoS attacks exploit vulnerabilities in operating systems and the implementations of protocol stack. Congestion-based DoS attacks take advantage of the weakness inside the network design. On the other hand, according to the number of attack sources, there are single-source DoS attacks and multi-source DoS attacks. A single-source DoS attack is originated only at one host, and a multi-source DoS attack floods the victim with a barrage of attack packets coming from multiple hosts. DoS attacks on WSNs may be carried at network layer and MAC layer. On network layer, DoS attacks will result in a disruption of routing functionalities. While on MAC layer, DoS attacks can potentially disrupt channel access and cause the resource wastage in terms of bandwidth and energy.

Currently, agent-based intrusion detection[38][1], signature-based intrusion detection [32] [12] [31], anomaly detection [27], encryption[40][7][39] and authentication schemes[8][33] are popular and effective security methods for networks. They can cooperate together, or work individually to improve system security. However, these secure methods are disabled or degraded when they are applied to WSNs to defend DoS attacks. The reasons are: (a) Complex cryptography is too onerous to be completed by capacity-limited sensor nodes; (b) The cooperation among sensor nodes within a distributed WSN consume extra resource; (c) It is impractical to employ particular sensor nodes to conduct intrusion detection in WSNs; (d) It is very easy for enemies to compromise some sensor nodes to get the access authority.

DoS attacks are increasingly common and critical in computer networks in recent years. Without proper security mechanisms, computer networks will be

confined to limited and controlled environments, and negate many of promises they hold. DoS attacks have been studied extensively for wired networks, e.g., Internet, however there is a lack of equivalent researches for WSNs. Moreover, security in WSNs is complicated by the constrained capabilities of sensor nodes and the properties of their deployment:

- Wireless links make WSNs more susceptible to link attacks ranging from passive eavesdropping, active impersonating, message replaying to message distorting;
- Sensor nodes, roaming in a hostile environment with relatively poor physical protection, have the non-negligible possibility of being compromised;
- WSNs, unlike fixed networks, have dynamic topology and group membership, which can dramatically increase the complexity to administrate authorization.

Wireless media are shared by all nodes in a network. This means all nodes can transmit at any point, which may cause contention over the common channel. It is necessary to provide a fair and efficient method to share the media among all nodes. The media access control (MAC) protocol is responsible for deciding when competing nodes can access the share media.

Numerous MAC protocols have been proposed for wireless communications networks. They can be divided into two broad categories according to whether contention exists or not:

- Schedule-based MAC protocols: For this kind of MAC protocol, a central authority specifies when and for how long each controlled node may transmit over the shared medium. Hence, there is no collision during transmission process, such as FDMA, TDMA, CDMA, FCDMA and SDMA[10];
- Contention-based MAC protocols: As its name implies, all nodes access the common channel through competition, such as CSMA, CSMA/CA, IEEE802.11, WMACA[34].

In CSMA/CA, before transmitting a packet, a node first listens to the channel for a short period of time. If it does not sense any traffic, it assumes that the channel is idle and starts data transmission. Moreover, CSMA/CA introduces a three-way handshake to make hidden nodes aware of upcoming transmissions, so collisions at common neighbors can be avoided. The working process is described below, where the timing of successful data packet transmissions is shown in Fig. 1.

1. The sender initiates the handshake by transmitting a Request-To-Send (RTS) control packet announcing its intended data transmission;
2. The receiver responds with a Clear-To-Send (CTS) packet, which informs all neighbors of the receiver of the upcoming transmission;
3. Data packets are finally guaranteed to be collision-freely transmitted.

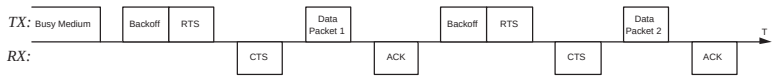


Figure 1: The timing of successful data packet transmissions in CSMA/CA protocol.

In literature, some secure protocols have been proposed for wireless network. In [35], wired equivalent privacy (WEP) is added to IEEE 802.11[25] standard to bring security into wireless networks. It employs the well-known and believed-secure RC4[29] cipher to bring the security level of wireless systems close to that of wired ones. Perrig proposed a security protocol for WSNs: SPINS[26]. It has two secure building blocks - SNEP and TESLA. SNEP includes data confidentiality, two-party data authentication, and evidence of data freshness. TESLA provides authenticated broadcast for severely resource-constrained environments. But, WEP and SPINS cannot effectively deal with the security problems in WSNs caused by DoS attacks. Even though some intrusion detection algorithms for wireless networks are proposed in [3][4][6][10], they are all agent-based. Therefore, additional nodes are needed to execute intrusion detection.

Security problems of WSNs are attracting more and more researchers attention. Our research in this paper focuses on the internal DoS attacks on MAC layer. We propose a fuzzy logic based secure MAC protocol - FSMAC to improve system immunity on DoS attacks. Compared to existing secure protocols, FSMAC has advantages as following.

- Security system is embedded into the existing MAC sub-layer. The operation mechanism of original MAC protocol - CSMA/CA, and the interfaces with the network layer and the physical layer remain unchanged. This breaks through the concept that unless the developers of WSNs take security into account at design time, the protocols they depend on will remain vulnerable to DoS attacks.
- Fuzzy logic theory is innovatively utilized to design a security system for intrusion detection and defense.
- FSMAC is a fully distributed and non-agent-based method.

The rest of this paper is organized as follows: In Section 2, we provide some preliminaries on fuzzy logic systems. The classification on potential DoS attacks and the selection on intrusion indicators are discussed in Section 3. Our algorithm design is described in Section 4, including the intrusion detection method and appropriate countermeasures. Simulation results are provided in Section 5. Then, Section 6 concludes this paper.

2. Preliminaries: Fuzzy Logic Systems

Fig.2 shows the structure of a fuzzy logic system (FLS) [23]. When an input is applied to a FLS, the inference engine computes the output set corresponding

to each rule. The defuzzifier then computes a crisp output from these rule output sets. Consider a p-input 1-output FLS, using singleton fuzzification, *center-of-sets* defuzzification [21] and "IF-THEN" rules of the form [22]

$$R^l : \text{IF } x_1 \text{ is } \mathrm{F}_1^l \text{ and } x_2 \text{ is } \mathrm{F}_2^l \text{ and } \cdots \text{ and } x_p \text{ is } \mathrm{F}_p^l, \text{ THEN } y \text{ is } \mathrm{G}^l.$$

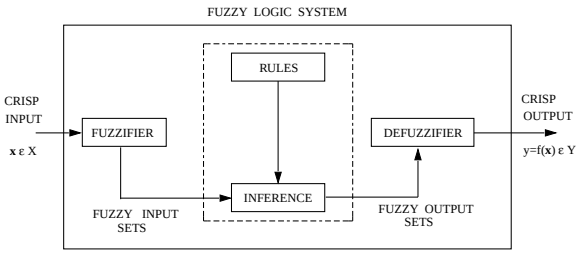


Figure 2: Structure of a fuzzy logic system.

Assuming singleton fuzzification, when an input $\mathbf{x}' = \{x_1', \ldots, x_p'\}$ is applied, the degree of firing corresponding to the l-th rule is computed as

$$\mu_{\mathrm{F}_1^l}(x_1') \star \mu_{\mathrm{F}_2^l}(x_2') \star \cdots \star \mu_{\mathrm{F}_p^l}(x_p') = \mathcal{T}_{i=1}^{p} \mu_{\mathrm{F}_i^l}(x_i') \tag{1}$$

where $\star$ and $\mathcal{T}$ both indicate the chosen t-norm. There are many kinds of defuzzifiers. In this paper, we focus, for illustrative purposes, on the height defuzzifier [22]. It computes a crisp output for the FLS by first computing the height, $\bar{y}^l$, of every consequent set G^l, and, then computing a weighted average of these heights. The weight corresponding to the l-th rule consequent height is the degree of firing associated with the l-th rule, $\mathcal{T}_{i=1}^{p} \mu_{\mathrm{F}_i^l}(x_i')$, so that

$$y_h(\mathbf{x}') = \frac{\sum_{l=1}^{M} \bar{y}^l \mathcal{T}_{i=1}^{p} \mu_{\mathrm{F}_i^l}(x_i')}{\sum_{l=1}^{M} \mathcal{T}_{i=1}^{p} \mu_{\mathrm{F}_i^l}(x_i')} \tag{2}$$

where M is the number of rules in the FLS.

3. Denial of Service Attacks on MAC Layer of Wireless Sensor Networks

CSMA/CA protocol mainly concentrates on how to utilize common channel efficiently and fairly when it is designed. It also assumes that each node accesses the common channel following the same multiple access scheme strictly. This assumption is the premise to guarantee the common channel be shared successfully and efficiently among nodes. However, it leaves chances for DoS attacks on MAC layer through violating this rule on purpose.

By analyzing the working mechanism of CSMA/CA protocol, the characteristics of DoS attacks and the limited capabilities of WSNs, potential DoS attacks on MAC layer of WSNs can be classified into three categories: collision attack, unfairness attack and exhaustion attack. Based on the classification of DoS attacks, we correspondingly choose our indicators for intrusion detection.

3.1. DoS Attack Classification

1. Collision Attack
   In collision attacks, adversaries conduct attacks through sending attack packets onto the busy channel. Those attack packets will collide with control packets (RTS, CTS and ACK) and data packets from normal sensor nodes. In Fig.3, grey rectangles stand for packets sent by collision attackers. Collision is supposed to happen when there is an overlap between a normal sensor node's transmission and a collision attacker's transmission. In this case, data transmissions of normal sensor nodes will fail due to collision.

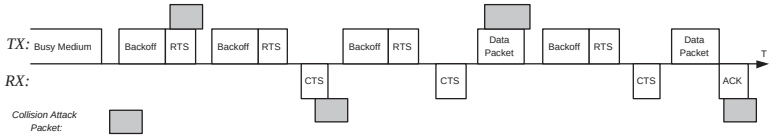


Figure 3: Failure transmissions due to collision attacks

2. Unfairness Attack
   In the unfairness attack case, attackers have higher chance to access common channel than other normal sensor nodes. Unfairness attackers send attack packets to the common channel immediately once sensing channel is idle. In that sense, unfairness attackers prevent other normal sensor nodes from transmitting. In Fig. 4, grey rectangles stand for packets coming from unfairness attackers.

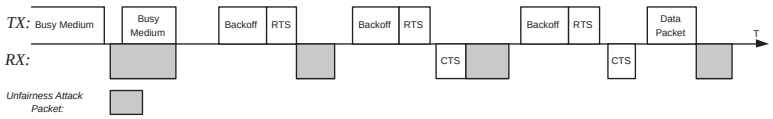


Figure 4: Failure transmissions due to unfairness attacks

3. Exhaustion Attack
   Exhaustion attacks are supposed to happen when adversaries abnormally send a great amount of RTS to normal sensor nodes. RTS/CTS-based MAC protocols are transmitter invitation MAC protocols. That means, when a receiver receives a RTS successfully, it must respond to that invitation with a CTS. Moreover, adversaries are compromised from normal sensor nodes, which makes the receiver unable to tell whether RTS is sent by normal sensor nodes or by adversaries. Under this condition, if adversaries send RTS to normal sensor nodes repeatedly, normal sensor nodes have to respond to those RTS incessantly with CTS, which will lead to the exhaustion of battery resources of those normal sensor nodes.

3.2. Intrusion Indicator Design

When collision attacks intrude the network, attackers send massive packets into the common channel when the detecting channel is busy. As a result, more RTS, CTS, ACK and even data packets may be destroyed due to collisions caused by attackers (See Fig.3). Moreover, the average latency of data packet is prolonged because of more retransmitting RTS packets and data packets.

Under normal condition, without any attacks, it is fair for each node to transmit data over the common channel from a long-term statistical view, since nodes have to wait for a random time before sending RTS to try to hold the common channel (see Fig.1), and only the first successful one can be allowed to transmit data over the common channel. Data packets of normal sensor nodes have to wait for longer time at MAC layer, when unfairness attackers prevent other normal sensor nodes from transmitting by holding the channel ahead of time.

Differing from collision attacks and unfairness attacks, exhaustion attackers work almost in the same way as other normal sensor nodes, except for sending RTS repeatedly to some normal sensor nodes. As a result, the arrival rate of RTS at victim nodes will increase dramatically. Besides this, data packets should wait for longer time, since the common channel is more utilized for transmitting RTS by attackers.

From above analysis, we can see that intrusions may be detected by monitoring abnormal alterations of some sensitive network parameters, which include the following.

- A great number of RTS packets are received by victim nodes for exhaustion attacks;
- Average waiting time becomes very long for both unfairness attacks and collision attacks;
- Collision takes place considerably often during collision attacks.

In our algorithm, we choose the arrival rate (R_{RTS}), average waiting time (T_w) and collision rate (R_c) as our intrusion indicators.

- Collision Rate (R_c): R_c is the collision number detected by a node per second.
- Average Waiting-Time (T_w): T_w is the waiting time of a data packet at MAC layer.
- RTS Arrival Rate (R_{RTS}): R_{RTS} is the number of RTS received successfully by a node per second.

Fixing a network's traffic strength, node density, node capacity, etc., we add collision attacks, unfairness attacks and exhaustion attacks respectively into this network, which runs on CSMA/CA protocol. Table 1 displays a set of mean and variance values for R_{RTS}, T_w and R_c. There is no DoS attacks for

normal scenarioes. Collision attacks, unfairness attacks and exhaustion attacks are introduced into collision attack scenarioes, unfairness attack scenarioes and exhaustion attack scenarioes separately.

Table 1: Mean and variance values for R_{RTS}, T_w and R_c

$Mean/Variance$	R_{RTS}	$T_w(ms)$	R_c
$Normal\ Scenario$	9.9/2.14	4/0.0	0.07/0.19
$Collision\ Attack\ Scenario$	6.0/4.78	290/370	146/157.19
$Unfairness\ Attack\ Scenario$	5.9/4.72	180/370	0.15/0.35
$Exhaustion\ Attack\ Scenario$	22.1/14.3	270/410	1.8/2.16

Note that different attacks result in different abnormal changes on R_{RTS}, T_w, R_c:

- When a collision attacker intrudes a network, the mean values of R_c is about 2084 times bigger and T_w is about 71 times longer than the normal value;
- For unfairness attack, the mean value of T_w is about 44 times longer than the normal value;
- For exhaustion attacks, the mean values of R_{RTS} is about doubled and T_w is about 66 times longer than the normal value.

Those sharp changes in Table 1 verify the feasibility of our intrusion detection algorithm. Thus, once we detect some unusual changes on R_{RTS}, T_w or R_c, we can infer, with certain reliability, that there are DoS attacks intruding the network. Based on this analysis, we design our FLS to implement intrusion detection.

4. Fuzzy Logic Based Secure MAC (FSMAC) Algorithm Description

The structure of our proposed secure MAC algorithm is shown in Fig.5. We improve the security of MAC layer through adding two special modules - intrusion detection module and intrusion defense module - into the original MAC layer. Each sensor node has its own security system.

In FSMAC, the intrusion module of each sensor node monitors R_{RTS}, T_w and R_c, and periodically judges whether intrusion exists or not. If intrusion is found, the defense module of this sensor node will be trigged by FLS intrusion detection module. Defense module will inform physical layer and MAC layer to switch to different RF band to make transmission, or pause for a while. Then, after a period of time, sensor node will switch back to the original RF band, or restart information exchanging over the network. Intrusion detection will be resumed also.

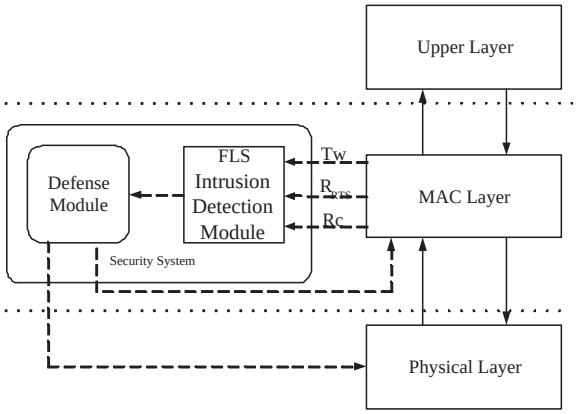


Figure 5: Secure MAC algorithm model

4.1. Intrusion Detection Strategy

From Table 1, we notice that various intrusion indicators are not identically sensitive to different DoS attacks. Collision attacks significantly increase data average waiting time and data packet collision rate, unfairness attacks significantly increase the data average waiting time only and exhaustion attacks increase RTS arrival rate and data average waiting time so much. It looks like the abnormal change on the data average waiting time T_w can indicate these three kinds of DoS attacks. However, measurements are usually corrupted by noise; hence, they are uncertain. To increase the accuracy of our intrusion detection, we choose all three intrusion indicators, i.e., R_{RTS}, T_w and R_c, to make the decision.

Moreover, since the distributed DoS attacks (DDoS)[36] can use many computers to launch a coordinated DoS attack against one or more targets, it is possible for more than one type of DoS attacks to appear within a system. Through monitoring R_{RTS}, T_w and R_c simultaneously, we can make intrusion decision without classifying the attack type.

Based on above considerations, it is an essential part that how to combining those three intrusion indicators together. There are two main approaches: linear combination methods and nonlinear combination schemes. For linear combination, the probability of intrusion found P_{if} can be expressed as $P_{if} = \alpha \times R_{RST} + \beta \times T_w + \gamma \times R_c$. The key task is to determine the values for combination factors α, β and γ for optimizing the performance in terms of higher detection probability and lower false alarm rate. There are maximum likelihood (ML)[11], equal gain (EG) and maximal-ratio combining (MRC) methods[2].

In [25], we proposed a soft decision scheme for parameter combination. The advantage of using soft decision is that a very small fluctuation of any indicators value can be effectively reduced. The decision function is as following:

$$y(x) = \frac{1}{1 + exp[-A(x - C)]} \tag{3}$$

Notes:

- Parameter A determines the slope of the curve.
- Parameter C determines the center of the curve.

The shape of curve is adaptively adjusted through adjusting parameters A and C. The intrusion probabilities obtained are:

- Probability of collision attack (P_c): P_c is the probability of collision attack found. It directly relates to R_c;
- Probability of exhaustion attack (P_e): Pe is the probability of exhaustion attack found. It directly relates to RRTS;
- Probability of unfairness attack (Pu): Pu is the probability of unfairness attack found. It directly relates to T_w;
- Probability of total (Pt): Pt directly relates to probability of successful data packet transmission (P_{st}).

The working process is depicted in Fig. 6.

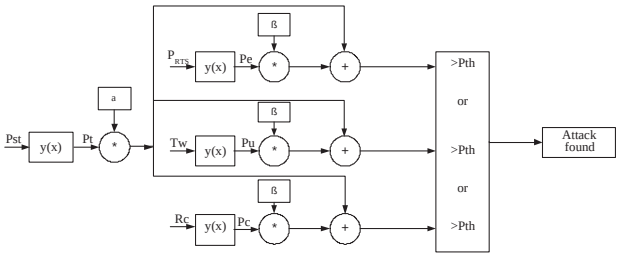


Figure 6: Intrusion probability process flow.

For the nonlinear combination approach, the FLS optimizes combination through rules and fuzzy logic. FLS nonlinearly maps a set of input data into an output; the output case decomposes into a collection of independent multi-input/sign-output systems. The richness of fuzzy logic is that there are an enormous number of possibilities that lead to lots of different mappings. Moreover, a FLS is well-known for being able to handle linguistic characterizations and uncertainty of data. As an extension of our previous work, we design a fuzzy logic model for intrusion detection in this paper.

4.2. Fuzzy Logic Intrusion Detection Module Design

Designing a FLS can be viewed as given a set of input-out pairs, tuning is essentially equivalent to determining a system that provides an optimal fit to the input-output pairs, with respect to a cost function. There exists a multitude of design methods that can be used to construct FLSs that have different

properties and characteristics. There are data-intensive ways, computational simplicity approaches, recursive methods, offline ways and application specific approaches[19].

Each sensor node monitors R_{RTS}, T_w and R_c, which are the inputs (or antecedents) of FLS intrusion detection module (See Fig.5). Then according to the output (or consequent) - possibility of intrusion found by FLS intrusion detection module, the security system makes a decision whether intrusion exists or not.

There are three main steps for our FLS design:

- Fix the shapes and parameters of all the antecedent and consequent membership functions ahead of time. The data establish the rules and no tuning is used.
- Fix the shapes and parameters of the antecedent membership functions ahead of time. Use the training data to tune the consequent parameters.
- Fix the shapes of all the antecedent and consequent membership functions ahead of time. Use the training data to tune the antecedent and consequent parameters.

Based on the preceding steps, for our FLS, the linguistic variables used to represent R_{RTS} and R_c are divided into two levels: Low and $High$; and those that are used to represent T_w are divided into two levels: $Short$ and $Long$. The result - the possibility that a sensor node finds intrusion - is divided into 5 levels, $Very\ Low$, Low, $Moderate$, $High$ and $Very\ High$. We show the membership functions in Fig.7(a) and Fig.7(b). From these two figures we can see that every antecedent has 2 fuzzy subsets, so we need to set up $2^3 = 8$ (because every antecedent has 2 fuzzy subsets, and there are 3 antecedents) rules for this FLS.

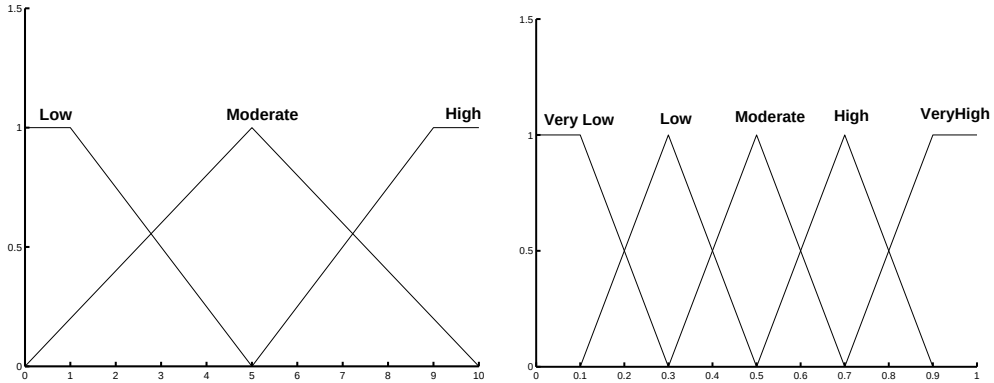


Figure 7: (a) Antecedent, and (b) consequent membership functions.

Based on the fact that when any type of DoS attacks (i.e., collision attacks, unfairness attacks or exhaustion attacks) intrudes a network, R_{RTS}, T_w or R_c becomes sharply high/long. The sharper the change is, the more the possibility of detecting intrusion is. We design a fuzzy logic system using rules such as:

R^l: IF *collision rate* (x_1) *of a node detected* is *High*, *average waiting time* (x_2) *of a node collected* is *Long*, and *RTS arrival rate* (x_3) *of a node received* is *Low*, THEN *the possibility* (y) *that a intrusion found by this node* is *High*.

Where $l = 1,2,\ldots,8$. We summarize all the rules in Table 2. Ante1 is collision rate, Ante2 is average waiting time, Ante3 is RTS arrival rate. Consequent is the possibility that intrusion is found.

Table 2: Rules for intrusion detection.

Rule	*Ante*1	*Ante*2	*Ante*3	*Consequent*
1	*Low*	*Short*	*Low*	*VeryLow*
2	*Low*	*Short*	*High*	*Moderate*
3	*Low*	*Long*	*Low*	*Moderate*
4	*Low*	*Long*	*High*	*High*
5	*High*	*Short*	*Low*	*Moderate*
6	*High*	*Short*	*High*	*Low*
7	*High*	*Long*	*Low*	*High*
8	*High*	*Long*	*High*	*VeryHigh*

Defuzzification produces a crisp output for the FLS from the fuzzy sets that appear at the output of the inference block. Many defuzzifiers have been proposed in the literature, such as centroid defuzzifier, center-of-sums defuzzifier, height defuzzifier and center-of-sets defuzzifier[23]. One criterion for the choice of a defuzzifier is computational simplicity. Based on this criterion, in our design, for every input(x_1,x_2,x_3), the output is computed using

$$y(x_1, x_2, x_3) = \frac{\sum_{l=1}^{8} \bar{y}^l \mu_{\mathrm{F}_1^l}(x_1)\mu_{\mathrm{F}_2^l}(x_2)\mu_{\mathrm{F}_1^3}(x_3)}{\sum_{l=1}^{8} \mu_{\mathrm{F}_1^l}(x_1)\mu_{\mathrm{F}_2^l}(x_2)\mu_{\mathrm{F}_3^l}(x_3)} \tag{4}$$

The height of the five fuzzy sets depicted in Fig.7(b) are $\bar{y}_1$=0.1, $\bar{y}_2$=0.3, $\bar{y}_3$=0.5, $\bar{y}_4$=0.7, $\bar{y}_5$=0.9.

4.3. Design and Optimization of FLS

FLS can incorporate numerical and linguistic knowledge into a unified framework, just like what we have done in this paper. The FLS design is very flexible based on different choices of antecedent and consequent membership functions such as triangular, trapzoidal, Gaussian, or sigmoid functions. Generally piecewise linear membership functions (such as triangular or trapzoidal)

are preferred, because of their simplicity and efficiency with respect to computability. In this paper, we use triangular and trapzoidal membership functions to illustrate our design of FLS. The rules are coming from experts' (i.e., the authors') linguistic knowledge, and then the antecedents and consequent are represented using membership functions. Such methodology has been popularly used, such as the FLS designs in topology design for wireless personal area networks [13], connection admission control in ATM networks[14]. Nonlinear membership functions such as Gaussian and Sigmoid membership functions could be used in this application as well with higher computational complexity. To optimize our design in real world, some membership tuning and optimization methods such as least mean square (LMS), SVD-QR, etc could be used, for example, LMS was used in [15][16][17], and SVD-QR was used in [18].

4.4. Defense Module Design

When intrusions are found, the defense module is triggered, taking some countermeasures to reduce the effects of attackers on the network. In fact, it is an energy waste or unsafe action for normal sensor nodes to transmit or receive information during the intrusion period. That is, transmission or reception is almost unsuccessful or spied by attackers when enemies attack a network. Thus it is an appropriate and effective choice for normal nodes to switch to different RF bands to make transmission or to pause for a while.

In this paper, we focus on intrusion detection. So just as an example, we choose pausing for a while to implement defense. There is no information on attacks, thus we can't know the duration of attacks. Therefore, after a period of sleep, nodes should wake up to resume data communication and intrusion detection. Nodes will stay at this state until intrusion is found again. At the sleep mode, there is no transmitting or receiving, but sensing (such as collecting data of temperature, humidity, or degree of air pollution) still continues.

In order to make our secure algorithm available for general WSNs, in which there is no center control, our defense scheme, such as the intrusion detection scheme, is also distributed.

5. Simulation and Performance Analysis

We used the simulator OPNET to run simulations. A network with 30 nodes is set up and the radio range (radius) of each node is 50m. Those nodes are randomly deployed in an area of $100 \times 100m^2$ and have no mobility. In order to simplify the analysis about the performance of our security MAC algorithm, we exclude the factors coming from physical layer and network layer in our experiments. Table 3 summarizes the parameters used by our simulations. Packet size is 1000 bytes. The destination for each node's traffic is randomly chosen from its neighbors. As in [20][24], data packets arrive according to a Poisson process with certain rate in our simulations.

All sensor nodes are set initially with energy of 2J. We use the same energy consumption model as in [9] for the radio hardware. To transmit an l-symbol

Table 3: Physical layer parameters.

W_{wmin}	32	W_{wmax}	1024
MAC Header	34 bytes	ACK	38 bytes
CTS	38 bytes	RTS	44 bytes
SIFS	10 μsec	DIFS	50 μsec
ACK-Timeout	212 μsec	CTS-Timeout	348 μsec

message a distance d, the radio expends:

$$E_{Tx}(l,d) = E_{Tx-elec(l)} + T_{Tx-amp(l,d)} = l \times E_{elec} + l \times e_{fs} \times d^2 \quad (5)$$

and to receive this message, the radio expends:

$$E_{Rx} = l \times E_{elec} \quad (6)$$

The electronics energy, E_{elec}, as described in [9], depends on factors such as coding, modulation, pulse-shaping and matched filtering. The amplifier energy, $e_{fs} \times d^2$ depends on the distance to the receiver and the acceptable bit error rate. In this paper, we choose: $E_{elec} = 50nJ/sym$, $e_{fs} = 10pJ/sym/m^2$.

The attacker is an abnormal sensor node, which has been captured and reprogrammed by enemies successfully before the system starts to work. In our simulations, attackers start the intrusion randomly, and each attack lasts for a random length of period.

We define a parameter metrics to testify the performance of our algorithm.

- Possibility of detection (P_d): the possibility of nodes making correct detection when there is an attack;
- False alarm rate (P_{fd}): the possibility of nodes making false detection when there is no attack;
- Data packet successful transmission rate (R_{st}): the rate of successful transmit data packets to all data packets transmitted;
- Average energy consumption (E_{av})(J/Pk): the energy consumed per successful transmission data packet;
- Time of first node dead (T_s)(Second): the time that the first node, in the network, runs out of power. When the energy of a node is used up, we assume this node is dead.

We separately test the influences of each DoS attack - collision attack, unfairness attack and exhaustion attack. In each experiment, there is only one type of attack introduced. We compared our FSMAC against original CSMA/CA protocol. In Fig.8, we plot the simulation time versus the successful transmission rate. Observe that the data packet successful transmission rate for FSMAC has

been increased about 25% for each DoS attack. In Fig.9, we compared the average energy consumption for successful data transmission of these two schemes. Observed that, our FSMAC outperforms the original CSMA/CA for about 5% less energy consumption per data packet. In Table 4, FSMAC extends the time of first node dead about two times, compared to the original CSMA/CA scheme.

For CSMA/CA without any attacks, the time of first node dead is about 200s. But Table 4 even shows FSMAC has longer lifetime than CSMA/CA without any attack. The reason is that some sensor nodes switch to the sleep state when intrusion found. At sleep state, some energy is reserved for no transmitting and receiving. For three different types of attacks, the false alarm rate of our algorithm is 0, and the probability of detection is 100%.

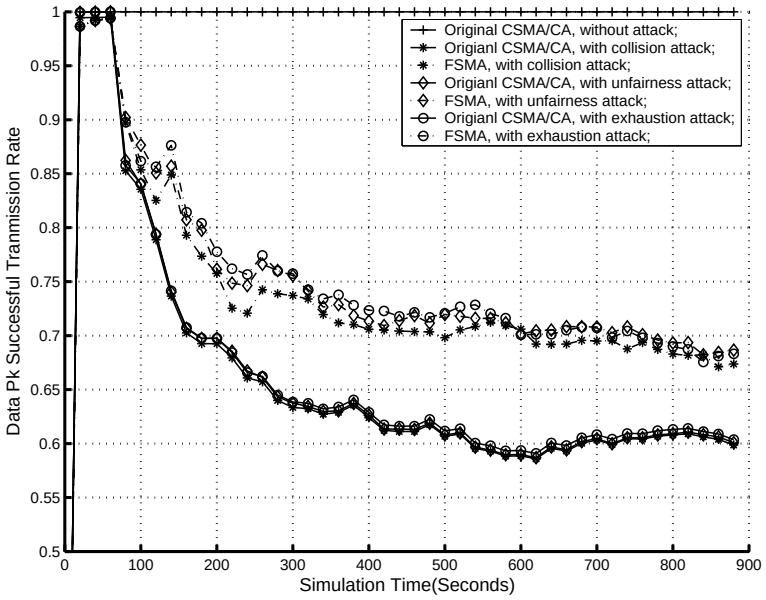


Figure 8: Rate of data packet successful transmission.

Table 4: Time that the first node dies.

	Collision Attack		Unfairness Attack		Exhaustion Attack	
	CSMA/CA	FSMAC	CSMA/CA	FSMAC	CSMA/CA	FSMAC
Ts	126s	271s	107s	229s	126	275s

We also test the impact of combining DoS attack. That is, three types of DoS attacks intrude the network together(See Fig. 10 and 11).

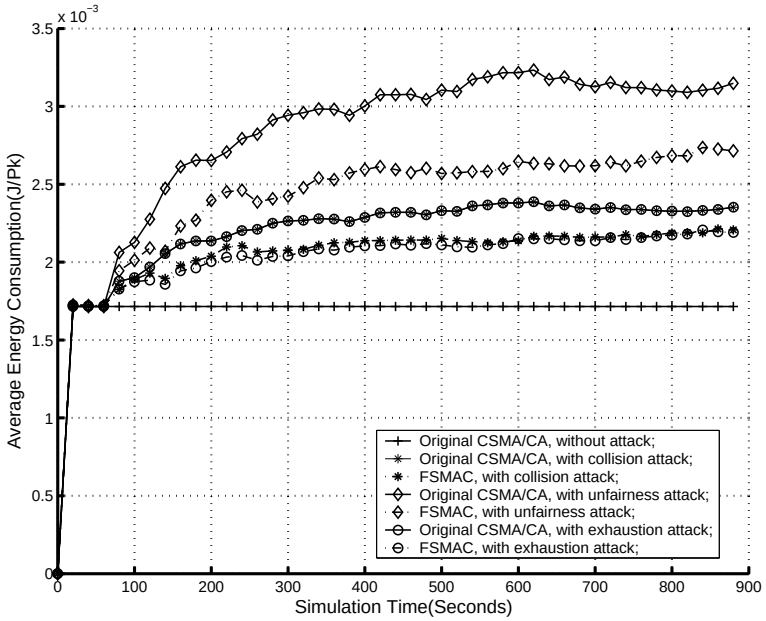


Figure 9: Average energy consumption.

6. Conclusion

In this paper, we classify popular DoS attacks on MAC layer of WSNs into three categories: collision attack, unfairness attack and exhaustion attack. We firstly choose RTS arrival rate, average waiting-time and collision rate as our indicators for intrusion detection. Based on the classification of DoS attacks and selection of intrusion indictors, we propose a secure MAC protocol for WSNs - FSMAC, a fully distributed method. In our algorithm, a fuzzy logic system is designed for decision making on intrusion detection. The simulation results have demonstrated that:

- Our algorithm can detect all intrusions without any false alarm;
- Failure data transmission, caused by DoS attacks, could be alleviated 25% by our secure method;
- Half energy is reserved through reducing the energy waste for failure transmission caused by DoS attacks.

Acknowledgement

This work was supported in part by the U.S. Office of Naval Research (ONR) under Grant N00014-07-1-0395, N00014-07-1-1024, and National Science Foun-

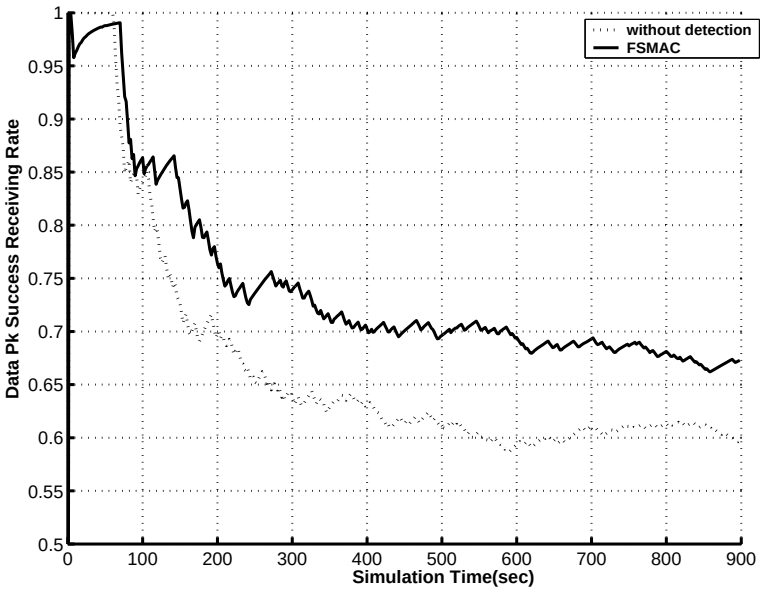


Figure 10: Rate of successful data packet transmission.

dation (NSF) under Grant CCF-0956438, CCF-0627322, CNS-0831902, and CNS-0721515.

[1] S. Banerjee, C. Grosan, and A. Abraham, Ideas: intrusion detection based on emotional ants for sensors, in Proc. 5th International Conference on Intelligent Systems Design and Applications 2005 (ISDA 05), Sept. 2005, pp. 344–349.

[2] D. Brennan, Linear diversity combining techniques, in Proc. the Institute of Radio Engineers (IRE), June 1959, pp. 1075-1102.

[3] H. Chan and A. Perrig, Security and privacy in sensor networks, Computer, vol. 36, no. 10, pp. 103-105, 2003.

[4] M. K. Chirumanilla and B. Ramamurthy, Agent based intrusion detection and response system for wireless lans, in Proc. IEEE International Conference on Communications 2003 (ICC 03), May 2003, pp. 492-496.

[5] D. Culler, D. Estin, and M. Srivastava, Guest editors introduction: overview of sensor networks, vol. 37, no. 8, pp. 41-49, 2004.

[6] J. E. Dickerson, J. Juslin, O. Koukousoula, and J. A. Dickers, Fuzzy intrusion detection, in Proc. Joint 9th IFSA World Congress and 20th NAFIPS International Conference, July 2001, pp. 2165-2170. 24.

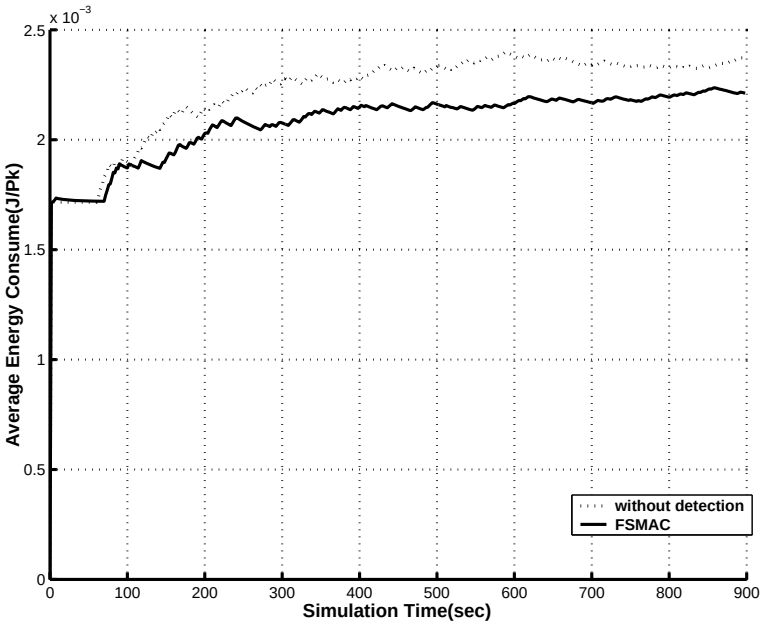


Figure 11: Average energy consumption.

[7] R. Du, H. Tu, and W. Song, An efficient key management scheme for secure sensor networks, in Proc. 6th International Conference on Parallel and Distributed Computing, Applications and Technologies 2005 (PDCAT2005), Dec. 2005, pp. 279-283. 23.

[8] N. Engelbrecht and W. T. Penzhorn, Secure authentication protocols used for low power wireless sensor networks, in Proc. IEEE International Symposium on Industrial Electronics 2005 (ISIE 2005), June 2005, pp. 1777-1782.

[9] W. B. Heinzelman, A. P. Chandrakasan, and H. Balakrishnan, An application-specific protocol architecture for wireless microsensor networks, IEEE Trans. Wireless Commun., vol. 1, no. 4, pp. 660-670, Oct. 2002.

[10] O. Kachirski and R. Guha, Effective intrusion detection using multiple sensors in wireless ad hoc networks, in Proc. 36th Hawaii International Conference on System Sciences (HICSS03), Jan. 2003.

[11] S. M. Kay, Fundamentals of Statistical Signal Processing: Estimation Theory. NJ: Prentice- Hall, 1993.

[12] A. Konar, U. K. Chakraborty and P. P. Wang, Supervised learning on a fuzzy Petri net, Information SciencesInformatics and Computer Science: An International Journal, Vol.172 no.3–4, Jun. 2005 pp.397–416.

[13] Q. Liang, Designing power aware self-reconfiguring topology for mobile wireless personal area networks using fuzzy logic, IEEE Transactions on Systems, Man, and Cybernetics, Part C, vol. 33, no. 3, August 2003.

[14] Q. Liang, N. N. Karnik, and J. M. Mendel, Connection admission control in ATM network using survey-based type-2 fuzzy logic systems, IEEE Transactions on Systems, Man, and Cybernetics, Part C, vol. 30, no. 3, pp. 529–539, August 2000.

[15] Q. Liang, J. M. Mendel, Interval type-2 fuzzy logic systems: theory and design", IEEE Transactions on Fuzzy Systems, vol. 8, no. 5, pp. 535–550, Oct 2000.

[16] Q. Liang, J. M. Mendel, Equalization of time-varying nonlinear channels using type-2 fuzzy adaptive filters, IEEE Transactions on Fuzzy Systems, vol. 8, no. 5, pp. 551–563, Oct 2000.

[17] Q. Liang, J. M. Mendel, Overcoming time-varying co-channel interference using type-2 fuzzy adaptive filters, IEEE Transactions on Circuits and Systems, II, vol. 47, no. 12, pp. 1419–1428, Dec 2000.

[18] Q. Liang, J. M. Mendel, Design interval type-2 fuzzy logic systems using SVD-QR method: rule reduction, International Journal of Intelligent Systems, vol. 15, no. 10, pp. 939–957, Oct 2000.

[19] C. T. Lin and C. S. G. Lee, Neural Fuzzy Systems. NJ: Prentice-Hall, 1996.

[20] A. Manjeshwar, Q. Zeng, and D. P. Agrawal, An analytical model for information retrieval in wireless sensor networks using enhanced apteen protocol, IEEE Trans. Parallel Distrib. Syst., vol. 13, no. 12, pp. 1290-1302, Dec. 2002.

[21] E. H. Mamdani, Applications of fuzzy logic to approximate reasoning using linguistic synthesis, vol. 26, no. 12, pp. 1182-1191, 1977.

[22] J. M. Mendel, Uncertain Rule-Based Fuzzy Logic Systems: Introduction and New Directions. Prentice-Hall, 2001.

[23] J. M. Mendel, Fuzzy logic systems for engineering: a tutorial, Proceedings of the IEEE, vol. 83, no. 3, pp. 345-377, Mar. 1995.

[24] V. P. Mhatre, C. Rosenberg, D. Kofman, R. Mazumdar, and N. Shroff, A minimum cost heterogeneous sensor network with a lifetime constraint, vol. 4, no. 1, pp. 4-15, Jan. 2005.

[25] P802.11, Ieee standard for wireless lan medium access control (mac) and physical layer (phy) specifications, Nov. 1997.

[26] A. Perrig, R. Szewczyk, V. Wen, D. Culler, and J. D. Tygar, Spins: security protocols for sensor networks, Wireless Networks, vol. 8, no. 5, pp. 521-534, 2002.

[27] S. T. Powers and J. He, A hybrid artificial immune system and Self Organising Map for network intrusion detection, Information Sciences, Vol. 178, no.15, pp. 3024–3042, Aug. 2008.

[28] Q. Ren and Q. Liang, Secure media access control (mac) in wireless sensor networks: intrusion detections and countermeasures, in Proc. 15th IEEE International Symposium on Personal, Indoor and Mobile Radio Communications, 2004 (PIMRC2004), Sept. 2004, pp. 3025-3029.

[29] R. L. Rivest, The rc4 encryption algorithm, in Technical Report of RSA Data Security, Inc., Mar. 1992.

[30] E. Shi and A. Perrig, Designing secure sensor networks, IEEE Wireless Commun. Mag., vol. 11, no. 6, pp. 38-43, 2004.

[31] D. Shih , H. Chiang and C. D. Yen, Classification methods in the detection of new malicious emails, Information SciencesInformatics and Computer Science: An International Journal, June 2005 Vol.172 no.1-2, pp.241–261,

[32] T. Shon and J. Moon, A hybrid machine learning approach to network anomaly detection, Information Sciences Vol. 177 no. 18, pp. 3799–3821, 2007.

[33] P. Taejoon and K. G. Shin, Soft tamper-proofing via program integrity verification in wireless sensor networks, vol. 4, no. 3, pp. 297-309, 2005.

[34] C. K. Toh, Ad Hoc Mobile Wireless Networks: Protocols and Systems, Prentice-Hall, 2002.

[35] J. Walker, Unsafe at any key size: an analysis of the wep encapsulation, in IEEE 802.11 doc 00-362, Oct. 2000.

[36] A. D. Wood and J. A. Stankovic, Defeating distributed denial of service attacks, IT Professional, vol. 2, no. 4, pp. 36-42, 2000.

[37] A. D. Wood and J. A. Stankovic, Denial of service in sensor networks, IEEE Trans. Comput., vol. 35, no. 10, pp. 54-62, 2002.

[38] D. Xiao, C. Chen and G. Chen, Intrusion detection based security architecture for wireless sensor networks, in Proc. IEEE International Symposium on Communications and Information Technology 2005 (ISCIT2005), Oct. 2005, pp. 1412-1415.

[39] A. Yasinsac and J. Childs, Formal analysis of modern security protocols, Information Sciences, Vol. 171, no. 1–3, pp. 189-211, Mar. 2005.

[40] Y. Zhen and G. Yong, A robust group-based key management scheme for wireless sensor networks, in Proc. IEEE Wireless Communications and Networking Conference, 2005 (WCNC2005), Mar. 2005, pp. 1915-1920.

Wireless Sensor Network Lifetime Analysis Using Interval Type-2 Fuzzy Logic Systems

Haining Shu, *Student Member, IEEE,* Qilian Liang, *Senior Member, IEEE,* and Jean Gao, *Member, IEEE*

***Abstract*—Extending the lifetime of the energy constrained wireless sensor networks is a crucial challenge in sensor network research. In this paper, we present a novel approach based on fuzzy logic systems to analyze the lifetime of a wireless sensor network. We demonstrate that a type-2 fuzzy membership function (MF), i.e., a Gaussian MF with uncertain standard deviation (std) is most appropriate to model a single node lifetime in wireless sensor networks. In our research, we study two basic sensor placement schemes: square-grid and hex-grid. Two fuzzy logic systems (FLSs): a singleton type-1 FLS and an interval type-2 FLS are designed to perform lifetime estimation of the sensor network. We compare our fuzzy approach with other nonfuzzy schemes in previous papers. Simulation results show that FLS offers a feasible method to analyze and estimate the sensor network lifetime and the interval type-2 FLS in which the antecedent and the consequent membership functions are modeled as Gaussian with uncertain std outperforms the singleton type-1 FLS and the nonfuzzy schemes.**

***Index Terms*—Fuzzy logic system, interval type-2 fuzzy sets, lifetime distribution, network lifetime analysis, wireless sensor networks.**

I. Introduction

RESEARCH on sensor networks was originally motivated by military applications. Starting around 1980, networked microsensors technology has been widely used in military applications. One example of such applications is the cooperative engagement capability developed by the U.S. Navy. This network-centric warfare system consists of multiple radars collecting data on air targets [1]. Other military sensor networks include acoustic sensor arrays for antisubmarine warfare such as the fixed distributed system and the advanced deployable system, and unattended ground sensors such as the remote battlefield sensor system and the tactical remote sensor system.

Nowadays, although the majority of sensors are still wired, wireless sensors provide significant advantages over wired sensors. Two main problems within wired sensor networks—cost and delays in deployment—are tackled when low-cost sensors and communication networks become available.

Manuscript received January 12, 2006; revised June 29, 2006, September 7, 2006, and November 22, 2006. This work was supported by the U.S. Office of Naval Research Young Investigator Award under Grant N00014-03-1-0466.

H. Shu and Q. Liang are with the Department of Electrical Engineering, University of Texas at Arlington, Arlington, TX 76019 USA (e-mail: shu@wcn.uta.edu; liang@uta.edu).

J. Gao is with the Department of Computer Science and Engineering, the University of Texas at Arlington, Arlington, TX 76019 USA (e-mail: gao@cse.uta.edu).

Color versions of one or more of the figures in this paper are available online at http://ieeexplore.ieee.org.

Digital Object Identifier 10.1109/TFUZZ.2006.890668

Wireless sensor networks have recently come into research notability because they developed many other nonmilitary applications, from environment and habitat monitoring to industrial process control to infrastructure security [3] and transportation automation. One networked sensing experiment on Great Duck Island [2] provides a small lens into an expansive future of such applications. The experiment was conducted by a team of computer engineers from the University of California, Berkeley. To date, 190 wireless sensors have been deployed on a small island ten miles off the coast of Maine to study the nesting behaviors of petrels. Biologists are now monitoring the petrels on the island from their offices, browsing data from sensors linked by satellite.

A wireless sensor network consists of certain amount of small and energy-constrained nodes. Basic components of a sensor node include a single or multiple sensor modules, a wireless transmitter–receiver module, a computational module, and a power supply module. Such networks are normally deployed for data collection where human intervention after deployment, to recharge or replace node batteries, may not be feasible, resulting in limited network lifetime. Most applications have prespecified lifetime requirements, for instance, the petrels monitoring application in [2] has a lifetime requirement of at least nine months. Thus estimation of lifetime of such networks prior to deployment becomes a necessity. Prior works on evaluating lifetime have considered networks where sensor nodes are randomly deployed. Reference [4] gives the upper bound on lifetime that any network with the specified number of randomly deployed nodes, source behavior, and energy can reach while [6] discusses the upper bounds on lifetime of networks with cooperative cell based strategies. Network lifetime of fixed deployment schemes were recently studied in [7]. Jain and Liang observed that in wireless sensor networks, the behavior of a single node lifetime demonstrates the nature of normal Gaussian distribution, which brings the first light of exploring the network lifetime behavior given the knowledge of nodes' lifetimes [7].

In this paper, we address the issue of lifetime analysis and estimation for wireless sensor networks in which the sensor nodes are deployed at desired locations. Our approach is entirely different from all prior research. Instead of trying out various probability basis, we propose to apply an interval type-2 fuzzy logic system (FLS) for lifetime analysis and estimation in a wireless sensor network. We demonstrate that a type-2 fuzzy membership function (MF), i.e., a Gaussian MF with uncertain variance, is most appropriate to model a single node lifetime in wireless sensor networks. Two FLSs—a singleton type-1 FLS and an interval type-2 FLS—are constructed for lifetime analysis and

1063-6706/$25.00 © 2008 IEEE

Authorized licensed use limited to: University of Texas at Arlington. Downloaded on December 18, 2009 at 14:08 from IEEE Xplore. Restrictions apply.

estimation. Simulations are implemented on two basic placement schemes: square-grid and hex-grid. We believe that these two schemes can serve as basis for evaluating more complex schemes for their lifetime performance prior to deployment and help justify the deployment costs. We set up our *fuzzy logic lifetime evaluator* and compare it against the first-node-die methods in [26] and [27] and the upper bounds in [4].

The rest of this paper is organized as follows. In Section II, we detail two sensor deployment schemes used for this paper and the basic concepts on network coverage, connectivity, and lifetime. Section III gives an overview of interval type-2 fuzzy logic systems. In Section IV, we demonstrate that a single node lifetime can be modeled with Gaussian MFs. We observe that a type-2 Gaussian MF with uncertain variance is most appropriate to model a single node lifetime in wireless sensor networks. We apply this knowledge and design an interval type-2 FLS in Section V to estimate network lifetime. A singleton type-1 FLS is constructed as well for performance comparison. Simulation results and discussions are presented in Section VI. Section VII concludes this paper.

II. Preliminaries

A sensor network is designed to perform high-level information processing tasks such as target detection and tracking. Applications of sensor networks are widely ranging and can vary significantly in modes of deployment, application requirements, sensing models, and quality of service. In this section, we discuss the key assumptions related to our approach, then formally characterize the basic modes of sensor placement in this paper, followed by the concept of coverage, connectivity, and network lifetime.

A. Assumptions and Notations

The approach of network lifetime analysis developed in this paper is based on the following assumptions about the wireless sensor networks.

- Sensor nodes are placed in a two-dimensional field. Nodes operate with very limited energy resources, which shape the aspects of the node performance, for instance, the node's processing ability, sensing, and communication range. We assume all sensor nodes originally deployed are identical in power configuration and functionality.
- Sensing and communications between sensor nodes are through radio links. We make the assumption that the radio range for a node is a disk of radius r around the node where r is taken as the same for all nodes. A sensor node can detect or sense any target or event within its *sensing range*, denoted by R_s. We also define a *communication range* R_c, which is the distance beyond which the transmitted signal is received with signal-to-noise ratio below the acceptable threshold level. In this paper, we assume the communication range R_c to be equal to the sensing range R_s.
- To be more energy efficient, direct communication between any pair of sensor nodes is allowed only if the Euclidean distance r between them satisfies $r \leq R_c$. Such a pair of nodes is called neighboring nodes. Since communication within communication range R_c is by broadcast, all immediate neighbors hear what a node transmits. Communication between nonneighboring nodes is achieved via peer-to-peer communication and may consists several short hops to relay the transmitted message.
- Since the communication range R_c denotes the maximum distance of direct communication between two sensor, a sensor network is said to be deployed with *minimum density* when the Euclidean distance between all neighboring nodes is $r = R_c$.

B. Basic Modes of Sensor Placement

Sensor placement directly affects power resource management and background data processing, which is carried out with various sensed data in distributed sensor networks. An intelligent sensor placement enlarges the field coverage, facilitates the operation of sensors (detecting, communication, data aggregation, etc.), and minimizes the excessive communications in fulfilling a task.

The simplest placement modes involve uniform or regular placement of sensor nodes such that each sensor node in the network has the same number of neighbors. A sensor placement mode that regulates two neighbors per sensor node has been described in [10]. According to [7], we use the *square-grid* and *hex-grid* placement modes illustrated in Fig. 1(a) and (b), respectively. Square-grid mode in Fig. 1(a) shows that each sensor node in the network has four neighbors, and in the Hex-grid mode in Fig. 1(b), the number of neighbors for every sensor node is three. We believe that these three elementary placement modes [10], [7] can serve as basis for other placement schemes, because a placement scheme of any complexity can be decomposed into two-neighbor, three-neighbor, and four-neighbor groups.

r in Fig. 1(a) and (b) denotes communication range. Sensor nodes in both square-grid and hex-grid are equidistant from their respective neighbors. According to our assumption, both grids are deployed with minimum density.[1]

C. Coverage and Connectivity

Coverage and connectivity are two important performance metrics of networks, and hence a discussion on them becomes imperative before the lifetime of the network can be defined.

Coverage scales the adequacy with which the network covers the sensor field. A sensor with sensing range R_s is said to cover or sense a circular region of radius R_s around it. If every point in the sensor field is within distance R_s from at least one sensor node, then the network is said to provide complete or 100% coverage.

Various levels of coverage are acceptable depending on the applications. In critical applications, complete coverage is required at all times. Any loss of coverage leads to a sensing gap in the field. Such gaps cause breach of security in case of surveillance applications. Also, in applications that require data with high precision, a sensing gap leads to inaccuracies. For such networks, any loss of coverage renders the network nonfunctional,

[1]The *hex-grid* is observed to have lower density than the *square-grid*. Rough calculation shows that with 36 nodes deployed, the network with *square-grid* covers an area of approximate $25r^2$, and the *hex-grid* covers an area of approximate $48r^2$, almost double that of the *square grid*.

Authorized licensed use limited to: University of Texas at Arlington. Downloaded on December 18, 2009 at 14:08 from IEEE Xplore. Restrictions apply.

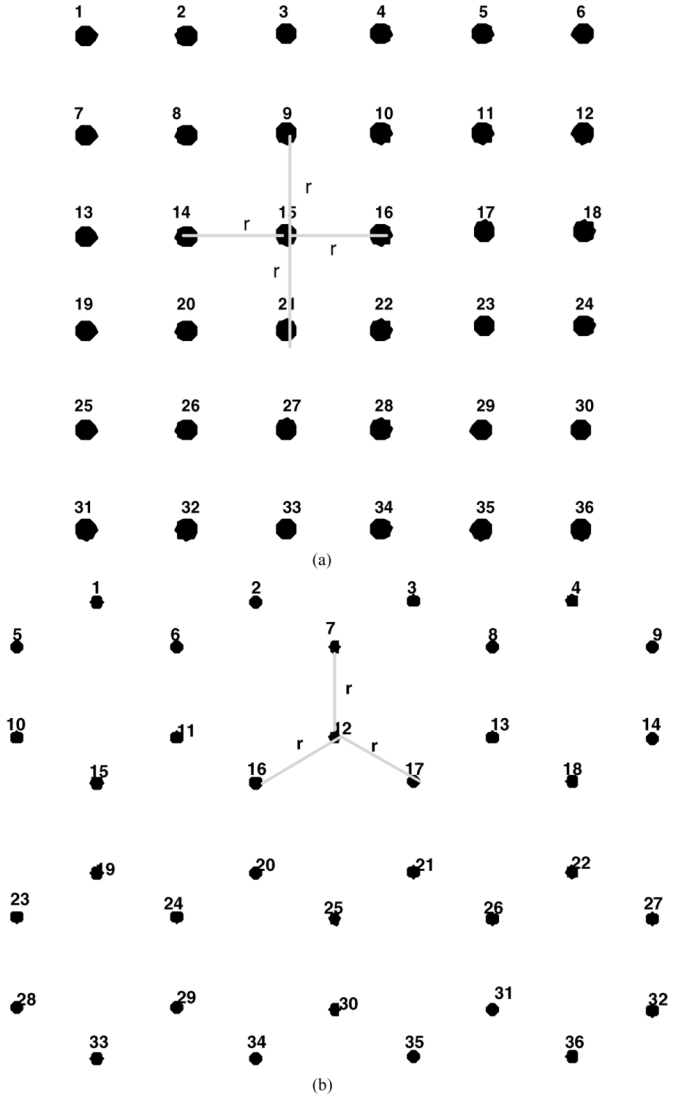


Fig. 1. Two placement modes for a 36-node sensor network. r in both grids denotes the communication range: (a) square-grid and (b) hex-grid.

while in some other applications a small loss of coverage may be acceptable.

Connectivity scales the adequacy with which nodes are able to communicate with their peers. One of the strengths of sensor networks arises from their ability to aggregate data collected from different sensor nodes. This requires adequate communication between sensor nodes. Any node should be able to communicate with any other node for proper functioning of the network. If a large number of nodes fail due to lack of energy, a part of the network may get completely disconnected from the rest. In this paper, we assume that only 100% connectivity is acceptable and the network fails with any loss of connectivity. An example of a sensor placement scheme that concentrates mainly on coverage as its parameter of interest can be found in [11], where a sensor placement algorithm for grid coverage has been proposed.

In our analysis, we require the network to provide complete coverage and connectivity. We give equal importance to both parameters and declare the network nonfunctional if either of them falls below their desired levels.

D. Network Lifetime

The basic definition of lifetime or, more precisely, the post-deployment active lifetime of a network is the cumulative active time measured from deployment until network failure. Based on the levels of coverage and connectivity required to deem a network functional, network failure can be interpreted in different ways. Since we assume that a wireless sensor network is fully functioning with complete coverage and connectivity, network failure corresponds to the first loss of coverage or connectivity.

In this paper, we concentrate on finding the minimum lifetime of a network, the worst case scenario. To be able to evaluate this minimum lifetime, we need to know the lifetime of a single sensor node, the minimum number of node failures that cause network failure, and the positional relationship[2] between the failed nodes.

Consider the square-grid and hex-grid networks deployed with minimum density. Both networks survive the failure of a single node without loss of either connectivity or coverage implying that the minimum number of node failures that can lead to network failure is greater than one. Now looking into the square-grid network in Fig. 2(a), apparently failure of nodes 20 and 21 causes loss of coverage. Similarly, failure of nodes 20 and 25 in the hex-grid network brings the coverage down to less than 100%. It comes to a conclusion that the failure of any two neighboring nodes causes loss of coverage and hence network failure.

Thus the minimum number of node failures that cause network failure is two, and these two nodes must be adjacent to each other (neighbors). A network may undergo multiple node failures and still be connected and covered if any of the failed nodes are not neighbors. But the absolute minimum number of node failures that can cause network failure is two.

III. Introduction to Type-2 Fuzzy Sets and Interval Type-2 Fuzzy Logic Systems: An Overview

A. Introduction to Type-2 Fuzzy Sets

The concept of type-2 fuzzy sets was introduced by Zadeh [12] as an extension of the concept of an ordinary fuzzy set, i.e., a type-1 fuzzy set. Type-2 fuzzy sets have grades of membership that are themselves fuzzy [14]. A type-2 membership grade can be any subset in [0,1]—the *primary membership;* and, corresponding to each primary membership, there is a *secondary membership* (which can also be in [0,1]) that defines the possibilities for the primary membership. A type-1 fuzzy set is a special case of a type-2 fuzzy set; its secondary membership function is a subset with only one element, crisp grades of membership. Type-2 fuzzy sets allow us to handle linguistic uncertainties, as typified by the adage "words can mean different things to different people." A fuzzy relation of higher type (e.g., type-2) has been regarded as one way to increase the fuzziness of a relation, and, according to Hisdal, "increased fuzziness in a description means increased ability to handle inexact information in a logically correct manner [15]."

Fig. 3 shows an example of a type-2 set. The domain of the membership grade corresponding to $x = 4$ is also shown. The

[2]Positional relationship between two nodes can be that the two nodes are diagonal, adjacent, or completely unrelated.

Authorized licensed use limited to: University of Texas at Arlington. Downloaded on December 18, 2009 at 14:08 from IEEE Xplore. Restrictions apply.

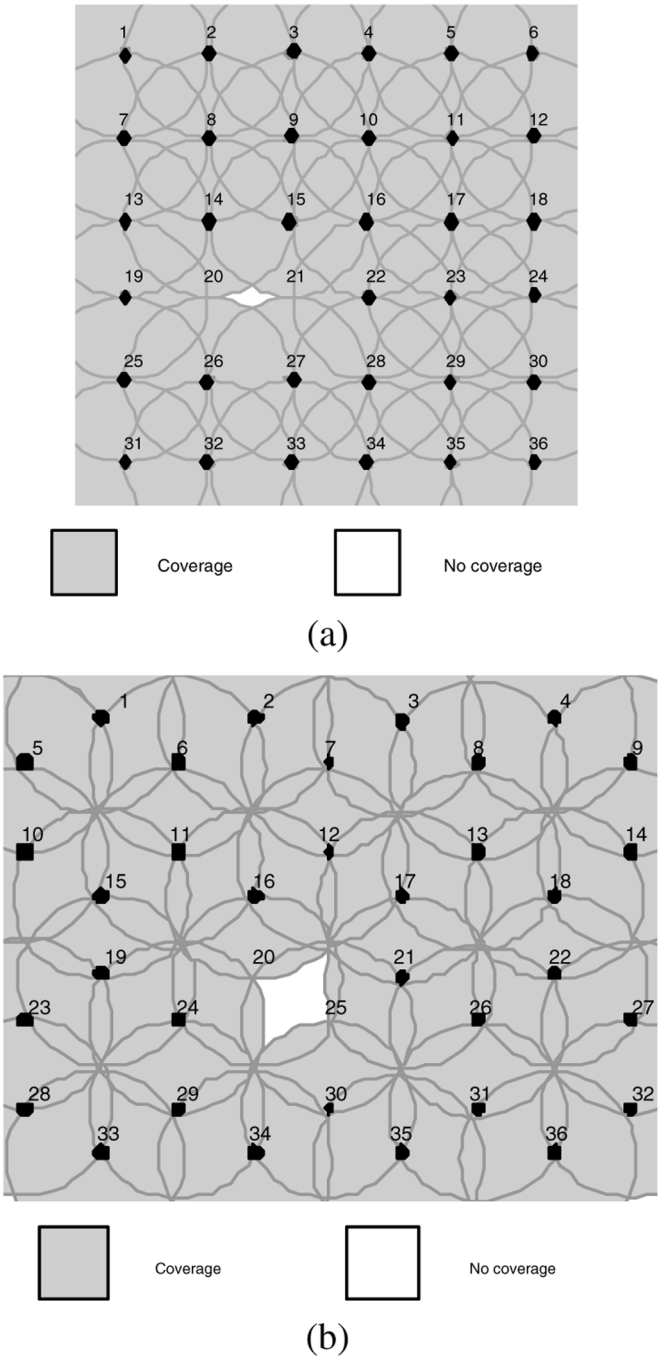


Fig. 2. Loss of coverage due to failure of two neighboring nodes: (a) Square-grid: failure of nodes 20 and 21 causes loss of coverage. (b)Hex-grid: failure of nodes 20 and 25 causes loss of coverage.

membership grade for every point is a Gaussian type-1 set contained in [0,1]; we call such a set a "Gaussian type-2 set". When the membership grade for every point is a crisp set, the domain of which is an interval contained in [0,1], such type-2 sets are called "interval type-2 sets" and their membership grades "interval type-1 sets" [8]. Interval type-2 sets are very useful when we have no other knowledge about secondary memberships.

An interval type-2 fuzzy set can be represented by its *upper* and *lower* MFs [18]. An upper MF and a lower MF are two type-1 MFs that are bounds for the footprint of uncertainty (the

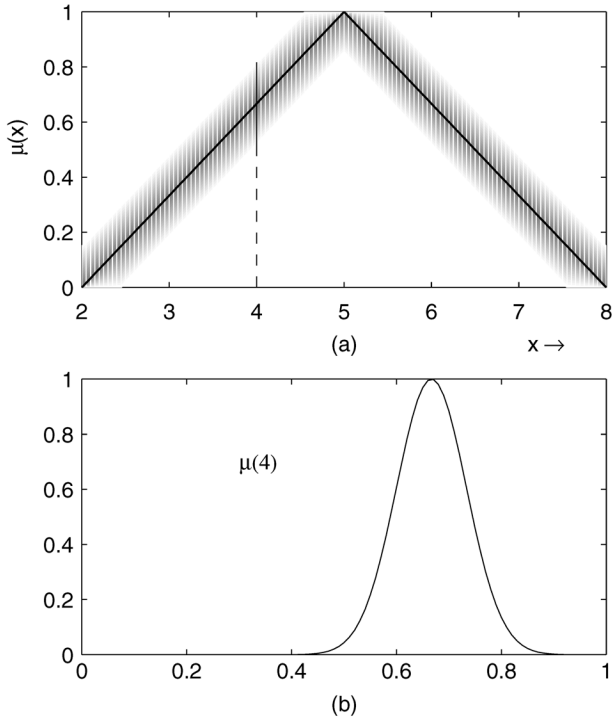


Fig. 3. (a) Pictorial representation of a Gaussian type-2 set. The secondary memberships in this type-1 fuzzy set are shown in (b) and are Gaussian. Note that this set is called a Gaussian type-2 set because all its secondary membership functions are Gaussian. The "principal" membership function (the bold line), which is triangular in this case, can be of any shape.

union of all primary membership grades) of an interval type-2 MF. The upper MF is a subset that has the maximum membership grade of the footprint of uncertainty; and, the lower MF is a subset that has the minimum membership grade of the footprint of uncertainty.

We use an overbar (underbar) to denote the upper (lower) MF. For example, let $\tilde{F}_k^l(x_k)$ denote the type-2 MF for the kth antecedent of the lth rule; then the upper and lower MFs of $\mu_{\tilde{F}_k^l}(x_k)$ are $\bar{\mu}_{\tilde{F}_k^l}(x_k)$ and $\underline{\mu}_{\tilde{F}_k^l}(x_k)$, respectively, so that

$$\mu_{\tilde{F}_k^l}(x_k) = \int_{q^l \in [\underline{\mu}_{\tilde{F}_k^l}(x_k), \bar{\mu}_{\tilde{F}_k^l}(x_k)]} 1/q^l \qquad (1)$$

where $\int$ denotes the union of individual points of each set in the continuum.

Example 1: Gaussian Primary MF With Uncertain Standard Deviation: Consider the case of a Gaussian primary MF having a fixed mean m_k^l and an uncertain standard deviation that takes on values in $[\sigma_{k1}^l, \sigma_{k2}^l]$, i.e.,

$$\mu_k^l(x_k) = \exp\left[-\frac{1}{2}\left(\frac{x_k - m_k^l}{\sigma_k^l}\right)^2\right], \quad \sigma_k^l \in \left[\sigma_{k1}^l, \sigma_{k2}^l\right] \quad (2)$$

where $k = 1, \ldots, p$; p is the number of antecedents; $l = 1, \ldots, M$; and M is the number of rules. The upper MF $\bar{\mu}_k^l(x_k)$ is (see Fig. 4)

$$\bar{\mu}_k^l(x_k) = \mathcal{N}\left(m_k^l, \sigma_{k2}^l; x_k\right) \qquad (3)$$

Authorized licensed use limited to: University of Texas at Arlington. Downloaded on December 18, 2009 at 14:08 from IEEE Xplore. Restrictions apply.

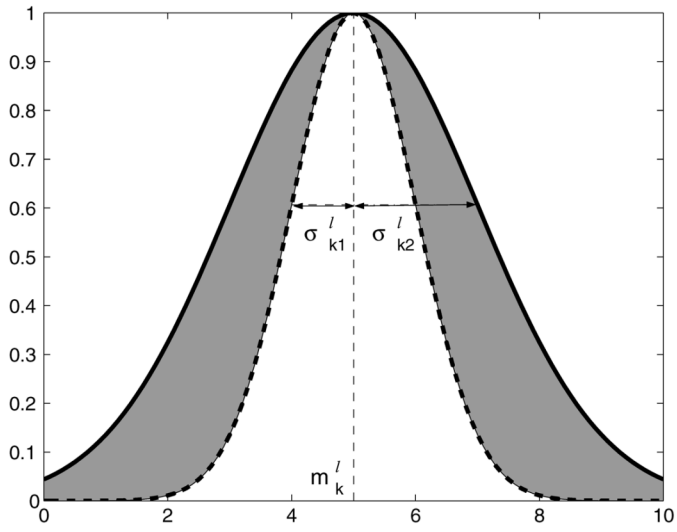


Fig. 4. Type-2 Gaussian MF with uncertain standard deviation. The thick solid lines denote upper MFs, and the thick dashed lines denote lower MFs. The shaded regions are the footprints of uncertainty for interval secondaries. The center of the Gaussian MFs is five, and the variance varies from 1.0 to 2.0.

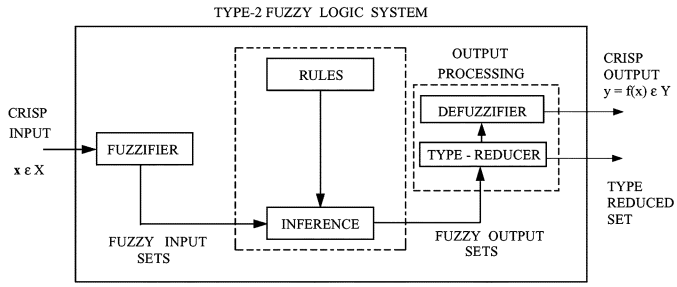


Fig. 5. The structure of a type-2 FLS. In order to emphasize the importance of the type-reduced set, we have shown two outputs for the type-2 FLS, the type-reduced set, and the crisp defuzzified value.

and the lower MF $\underline{\mu}_k^l(x_k)$ is (see Fig. 4)

$$\underline{\mu}_k^l(x_k) = \mathcal{N}(m_k^l, \sigma_{k1}^l; x_k) \tag{4}$$

□

This example illustrates how to define $\bar{\mu}$ and $\underline{\mu}$, so that it is clear how to define these membership functions for other situations (e.g., triangular, trapezoidal, bell MFs).

B. Introduction To Type-2 Fuzzy Logic Systems: An Overview

Fig. 5 shows the structure of a type-2 FLS [8]. It is very similar to the structure of a type-1 FLS [13]. For a type-1 FLS, the *output processing* block only contains the defuzzifier. We assume that the reader is familiar with type-1 FLSs, so that here we focus only on the similarities and differences between the two FLSs. The fuzzifier maps the crisp input into a fuzzy set. This fuzzy set can, in general, be a type-2 set.

In the type-1 case, we generally have "IF-THEN" rules, where the lth rule has the form "R^l: IF x_1 is F_1^l and x_2 is F_2^l and $\cdots$ and x_p is F_p^l, THEN y is G^l," where x_is are inputs; F_i^ls are antecedent sets $(i = 1, \ldots, p)$; y is the output; and G^ls are consequent sets. The distinction between type-1 and type-2 is associated with the nature of the membership functions, which is not important while forming rules; hence, the structure of the rules remains exactly the same in the type-2 case, the only difference being that now some or all of the sets involved are of type-2; so, the lth rule in a type-2 FLS has the form "R^l: IF x_1 is $\tilde{F}_1^l$ and x_2 is $\tilde{F}_2^l$ and $\cdots$ and x_p is $\tilde{F}_p^l$, THEN y is $\tilde{G}^l$."

In the type-2 case, the inference process is very similar to that in type-1. The inference engine combines rules and gives a mapping from input type-2 fuzzy sets to output type-2 fuzzy sets. To do this, one needs to find unions and intersections of type-2 sets as well as compositions of type-2 relations.

In a type-1 FLS, the defuzzifier produces a crisp output from the fuzzy set that is the output of the inference engine, i.e., a type-0 (crisp) output is obtained from a type-1 set. In the type-2 case, the output of the inference engine is a type-2 set; so, "extended versions" (using Zadeh's extension principle [12]) of type-1 defuzzification methods was developed in [8]. This extended defuzzification gives a type-1 fuzzy set. Since this operation takes us from the type-2 output sets of the FLS to a type-1 set, this operation was called "type-reduction" and the type-reduced set so obtained was called a "type-reduced set" [8]. To obtain a crisp output from a type-2 FLS, we can defuzzify the type-reduced set.

General type-2 FLSs are computationally intensive, because type-reduction is very intensive. Things simplify a lot when secondary MFs are interval sets (in this case, the secondary memberships are either zero or one). When the secondary MFs are interval sets, the type-2 FLSs were called "interval type-2 FLSs." In [18], Liang and Mendel proposed the theory and design of interval type-2 FLSs. They proposed an efficient and simplified method to compute the input and antecedent operations for interval type-2 FLSs, one that is based on a general inference formula for them. For interval type-2 FLSs, Liang and Mendel defined the concept of upper and lower MFs and illustrate their efficient inference method for the case of Gaussian primary MFs. They also proposed a method for designing an interval type-2 FLS in which they tuned its parameters.

In an interval type-2 FLS with *singleton fuzzification* and meet under minimum or product t-norm, the result of the input and antecedent operations F^l is an interval type-1 set, i.e., $F^l = [\underline{f}^l, \bar{f}^l]$, where $\underline{f}^l$ and $\bar{f}^l$ simplify to

$$\underline{f}^l = \underline{\mu}_{\tilde{\mathrm{F}}_1^l}(x_1) \star \ldots \star \underline{\mu}_{\tilde{\mathrm{F}}_p^l}(x_p) \tag{5}$$

$$\bar{f}^l = \bar{\mu}_{\tilde{\mathrm{F}}_1^l}(x_1) \star \ldots \star \bar{\mu}_{\tilde{\mathrm{F}}_p^l}(x_p) \tag{6}$$

where $x_i (i = 1, \ldots, p)$ denotes the location of the singleton.

In this paper, we use center-of-sets type reduction, which can be expressed as

$$\begin{aligned} Y_{\cos}(Y^1, \ldots, Y^M, F^1, \ldots, F^M) &= [y_l, y_r] \\ &= \int_{y^1} \cdots \int_{y^M} \int_{f^1} \cdots \int_{f^M} 1 \Big/ \frac{\sum_{i=1}^M f^i y^i}{\sum_{i=1}^M f^i} \end{aligned} \tag{7}$$

where $Y_{\cos}$ is an interval set determined by two end points y_l and y_r; $f^i \in F^i = [\underline{f}^i, \bar{f}^i]$; $y^i \in Y^i = [y_l^i, y_r^i]$ and Y^i is the centroid of the type-2 interval consequent set $\tilde{G}^i$; and $i =$

Authorized licensed use limited to: University of Texas at Arlington. Downloaded on December 18, 2009 at 14:08 from IEEE Xplore. Restrictions apply.

$1, \ldots, M$. Because $Y_{\cos}$ is an interval set, we defuzzify it using the average of y_l and y_r; hence, the defuzzified output of an interval type-2 FLS is

$$f(\mathbf{x}) = \frac{y_l + y_r}{2}. \tag{8}$$

C. Applications of Interval Type-2 Fuzzy Logic Systems

Liang and Mendel have developed theory and design methods for the most useful kind of type-2 FLSs, interval type-2 FLSs [18], and have applied them to a number of very important applications, such as the following.

1) Fading channel equalization [19] and cochannel interference elimination [20]. The channel states in a fading channel or channel with cochannel interferences are uncertain, and they validated that an interval type-2 fuzzy set, Gaussian primary membership function with uncertain mean, can be used to represent such uncertainties.
2) Network video traffic modeling and classification [16]. MPEG variable bit rate traffic are very bursty. They validated that the I, P, and B frame sizes are log-normal with fixed mean and uncertain variance, so an interval type-2 fuzzy sets can be used to model the bursty video traffic and an interval type-2 fuzzy logic system with such type-2 fuzzy set are demonstrated performing much better than a Bayesian classifier.
3) Connection admission control for ATM network [17]. Connection admission control is actually a decision making problem. Different factors such as incoming real-time video/audio packet sizes, non–real time packet sizes, and buffer sizes are uncertain. They applied an interval type-2 fuzzy logic to handle these uncertainties.

IV. Modeling Node Lifetime With Gaussian Membership Functions

Though applications of sensor networks vary with task requirements, sensor nodes retain the basic elements within any sensor network. Behavior of individual sensor in a manner determines the network performance. As we have discussed in Section II-C, failure of sensor nodes due to lack of energy may cause the network to function improperly or completely break down. Thus it becomes significantly important to characterize a single node behavior before going into the network layer. A distinct identity of sensor nodes and wireless sensor network is its constrained energy resources, which is widely measured by the node and network lifetime. In this section, we study the lifetime behavior for single sensor node and try to find its probability characters from real network data.

Since wireless sensor nodes are severely energy constrained due to their compact form, hardware design and protocol approaches for different layers must take energy efficiency into account to increase the lifetime of sensor networks. However, a fundamental question—"what is the nature of sensor network lifetime?" has not been answered yet. Because the lifetime of each individual node is not a constant but a random variable, it follows that the network lifetime is also a random variable. Recently, Jain and Liang [7] showed that in a wireless sensor network where the workloads are very well balanced, the behavior of a single node lifetime demonstrates the nature of normal Gaussian distribution. Their observation was also justified by the knowledge of probability and random process in [7]. Fig. 6 illustrates the real node lifetime distribution in a hex-grid sensor network.

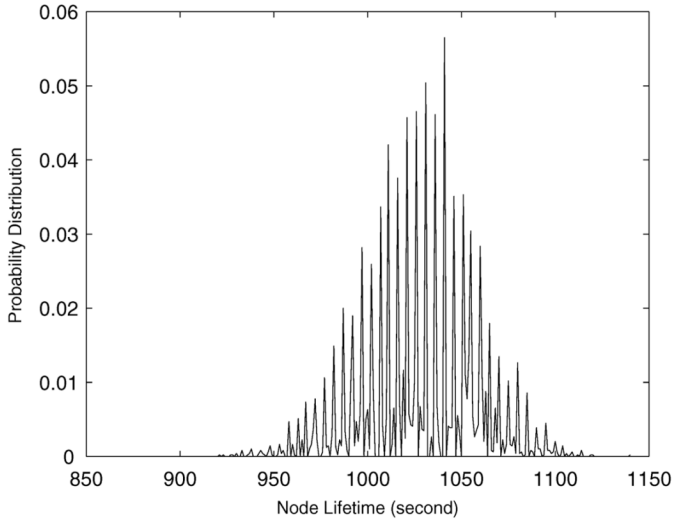


Fig. 6. A single node lifetime distribution in a hex-grid sensor network.

TABLE I
Mean and STD Values for Seven Segments and the Entire Node Lifetime, and Their Normalized STD

Node Lifetime Data	Mean	Std
Segment 1	1027.4	30.182
Segment 2	1028.9	29.819
Segment 3	1026.3	30.798
Segment 4	1028.7	30.917
Segment 5	1028	29.944
Segment 6	1027	29.975
Segment 7	1027.9	30.306
Entire Data Set	1027.7	30.292
Normalized STD	0.00082783	0.013105

In the paper, we are first interested in setting up a precise MF for the single node lifetime. From the original data of single node lifetime shown in Table I, we decomposed the whole data sets into seven segments and computed the mean μ_i and standard deviation σ_i of node lifetime for each segment, $i = 1, 2, \ldots 7$. The mean μ and standard deviation σ for the entire data set were also computed. We are also interested to know which value—mean μ_i or standard deviation σ_i—varies more. We first normalized the mean μ_i and standard deviation σ_i of each segment using μ_i/μ and σ_i/σ. Then we computed the standard deviation of their normalized values σ_m and σ_{std}. Results are presented in the end of Table I.

From the last row of Table I, we see that $\sigma_m \ll \sigma_{\text{std}}$, which means standard deviation σ_i varies much more than the mean value μ_i. Therefore we conclude that if the single node lifetime follows normal Gaussian distribution, it is most appropriate to be modeled as a Gaussian MF with uncertain standard deviation. This result justifies the use of the Gaussian MFs to model single node lifetime in Section V.

Authorized licensed use limited to: University of Texas at Arlington. Downloaded on December 18, 2009 at 14:08 from IEEE Xplore. Restrictions apply.

V. Sensor Network Lifetime Analysis Using Interval Type-2 Fuzzy Logic Systems

In Section IV, we came to a conclusion that in wireless sensor networks, the single node lifetime can be well modeled by a type-2 Gaussian MF with uncertain variance. This result offers a truly original approach to probe into the trait of network lifetime. Referring to [4], [6], and [7], prior research on sensor network lifetime are mostly heuristic or application and protocol driven. In this paper, we propose to apply fuzzy logic systems to sensor network lifetime analysis, more specifically to evaluate or estimate network lifetime using interval type-2 FLSs. We name our network lifetime evaluation system *type-2 fuzzy logic lifetime evaluator (FLLE2).*

From the overview of type-2 FLSs in Section III-B, we know that in a type-2 FLS, when p inputs are applied to the system, the inference engine computes the output set corresponding to each rule. After the unique type-reduction operation, the defuzzifier computes a crisp output from these rule output sets. We next expatiate the input–output parameters, type-2 antecedent and consequent MFs and fuzzy rules precisely designed for evaluating sensor network lifetime.

A. Antecedent and Consequent Membership Functions

Let N be the number of sensor nodes deployed in a sensor network. All sensor nodes are initially configured with the same battery level. After a period of time during which several tasks (detecting, target tracking and communication, etc.) were carried out by different sensors, the network is left with sensor nodes at various battery levels. We assume the sensor network of interest at this point retains complete coverage and connectivity and all sensor nodes are still alive. The problem of evaluating network lifetime is formulated like this:

> Given a set of data representing the various battery levels of all N alive sensor nodes, denoted by $p(1), \ldots, p(N)$, estimate the cumulative alive time T of the network measured from the point of interest until network failure, where $p(i)$ is the current battery level of sensor node i.

The $N \times 1$ values of battery levels, $p(1), \ldots, p(N)$, are taken as input to the FLLE2 and the alive time T of the network measured from the point of interest until network failure is taken as the output of FLLE2.

We depict one antecedent as "the remaining battery level of sensor node i" and the consequent as "the cumulative network alive time from the point of interest until network failure" The linguistic variables to represent the antecedent are divided into three levels—*high, moderate,* and *low*—and the consequent is divided into five levels—*very high, high, moderate, low,* and *very low*.

Antecedent and consequent membership functions are chosen based on the result in Section IV. An interval type-2 Gaussian MF with uncertain standard deviation is illustrated in Fig. 4. In this paper, all antecedents and consequents use the same type of MFs and the MF parameters are initialized consistently.

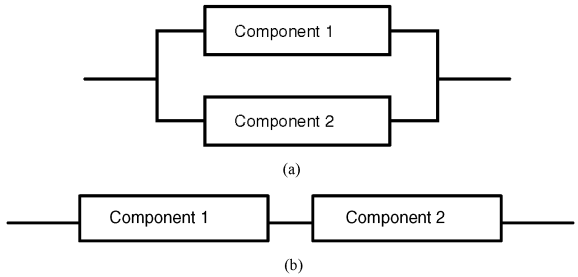


Fig. 7. RBDs for a system of two components. (a) RBD with parallel connected components and (b) RBD with series connected components.

B. Rules Design

We apply *reliability theory* from control system to design the fuzzy rules. In this section, we first treat the basics of reliability theory and then demonstrate how this knowledge is extracted for rules design with two simple examples.

1) Basics of Reliability Theory: For the sensor network lifetime issue studied in this paper, reliability theory provides a feasible method to design fuzzy rules. To understand this, we introduce the reliability block diagram (RBD). RBD is a graphical representation of the components of the system and provides a visual representation of the way components are reliability-wise connected. Thus the effect of the success or failure of a component on the system performance can be evaluated.

Consider a system with two components. If this system is such that a single component failure can render the system nonfunctional, then we say that the components are reliability-wise connected in series. If the system fails only when both its components fail, then we say that the components are reliability-wise connected in parallel. Note that the physical connection between the component may or may not be different from their reliability-wise connection. The RBDs for both cases are given in Fig. 7. Any complex system can be realized in the form of a combination of blocks connected in series and parallel.

2) Rules Design Using Reliability Theory: In our analysis, the wireless sensor network is the system under consideration, and the sensor nodes are the components of the system. We detail below how to design rules with the knowledge of reliability theory referring to the two basic RBDs in Fig. 7. We make the assumption that the workload among all components (sensor nodes) is very well balanced.

Example 1: Setup Fuzzy Rules for Parallel System in Fig. 7(a): In the parallel system, crisp logic claims that the system (network) fails only when both components (sensor nodes) fail. In fuzzy logic systems, the rules can be set up as one example shown below:

> IF the remaining battery level of component 1 (sensor node 1) is *high* and the remaining battery level of component 2 (sensor node 2) is *moderate*, THEN the lifetime of the system (network) is *very high*.

Example 1: Setup Fuzzy Rules for Series system in Fig. 7(b): In the series system, crisp logic claims that the system (network) fails when either component fails. In fuzzy logic systems, the rules can be set up as one example shown below:

Authorized licensed use limited to: University of Texas at Arlington. Downloaded on December 18, 2009 at 14:08 from IEEE Xplore. Restrictions apply.

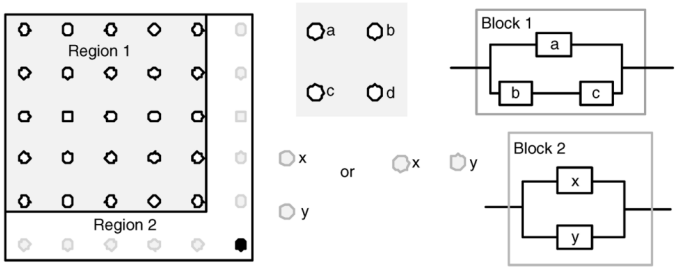


Fig. 8. RBD of a single node in a square grid. Nodes belonging to region-1 are modeled as block-1, and nodes belonging to region-2 are modeled as block-2.

IF the remaining battery level of component 1 (sensor node 1) is *low* and the remaining battery level of component 2 (sensor node 2) is *moderate*, THEN the lifetime of the system (network) is *low*.

Note that the parallel and series systems are the essential ways to model two sensor nodes. A wireless sensor network consisting of multiple sensor nodes can be hierarchically represented in the reliability block diagram.

C. Case Studies: Rules Design

1) Square-Grid Sensor Network: As defined in Section II-D, the minimum network lifetime is the time to failure of any two neighboring nodes. We know that the failure of any single node does not cause network failure. The failure of any node coupled with the failure of any of its neighbors causes network failure. Using this definition, we build the RBD for the square-grid as shown in Fig. 8.

Fig. 8 shows the RBD block for a single node in the network. A node can be modeled in two ways depending on its position in the sensor field. This distinction based on its position is made due to a simple observation that nodes at the right edge of the sensor field (region-2) do not have any right neighbor (node b), as opposed to nodes in region-1. Also, nodes at the bottom edge of the sensor field (region-2) do not have a bottom neighbor (node c), as opposed to the nodes in region-1. Note that as every node in a square-grid, node a has four neighbors, but its relationship with only two neighbors is modeled in its RBD block. This is because the relationship with the other two neighbors will be modeled when their RBD blocks are constructed. If this is not followed, then the relationship between every node–neighbor pair will be modeled twice.

We abstract three antecedents from the RBD of block-1 in Fig. 8.

- Antecedent 1—The remaining battery level of node a.
- Antecedent 2—The minimum remaining battery level of node b and c.
- Antecedent 3—The remaining battery level of node d.

The consequent is depicted as "minimum network lifetime." The linguistic variables to represent the antecedent are divided into three levels, and the consequent is divided into five levels as detailed in Section V-A. A total of $27 = 3^3$ rules (three antecedents and each has three fuzzy subsets) are set up for square-grid block-1. Table II gives the complete 27 designed rules.

TABLE II
COMPLETE 27 RULES FOR SQUARE-GRID BLOCK-1

Rule Number	Antecedent 1	Antecedent 2	Antecedent 3	Consequent
1	Low	Low	Low	Very Low
2	Moderate	Low	Low	Very Low
3	High	Low	Low	Low
4	Low	Moderate	Low	Low
5	Moderate	Moderate	Low	Moderate
6	High	Moderate	Low	High
7	Low	High	Low	Moderate
8	Moderate	High	Low	High
9	High	High	Low	Very High
10	Low	Low	Moderate	Very Low
11	Moderate	Low	Moderate	Low
12	High	Low	Moderate	Moderate
13	Low	Moderate	Moderate	Moderate
14	Moderate	Moderate	Moderate	High
15	High	Moderate	Moderate	Very High
16	Low	High	Moderate	Moderate
17	Moderate	High	Moderate	High
18	High	High	Moderate	Very High
19	Low	Low	High	Low
20	Moderate	Low	High	Moderate
21	High	Low	High	Moderate
22	Low	Moderate	High	High
23	Moderate	Moderate	High	Very High
24	High	Moderate	High	Very High
25	Low	High	High	High
26	Moderate	High	High	Very High
27	High	High	High	Very High

TABLE III
COMPLETE NINE RULES FOR SQUARE-GRID BLOCK-2

Rule Number	Antecedent 1	Antecedent 2	Consequent
1	Low	Low	Very Low
2	Moderate	Low	Low
3	High	Low	Moderate
4	Low	Moderate	Low
5	Moderate	Moderate	High
6	High	Moderate	Very High
7	Low	High	Moderate
8	Moderate	High	Very High
9	High	High	Very High

Two antecedents are chosen based on the RBD of block-2 in Fig. 8, and consequent is defined the same as in block-1. A total of $9 = 3^2$ rules shown in Table III are constructed in this scheme.

- Antecedent 1—The remaining battery level of node x.
- Antecedent 2—The remaining battery level of node y.

2) Hex-Grid Sensor Network: The analysis for the hex-grid is carried out on the same lines as that of the square-grid. Fig. 2(b)

Authorized licensed use limited to: University of Texas at Arlington. Downloaded on December 18, 2009 at 14:08 from IEEE Xplore. Restrictions apply.

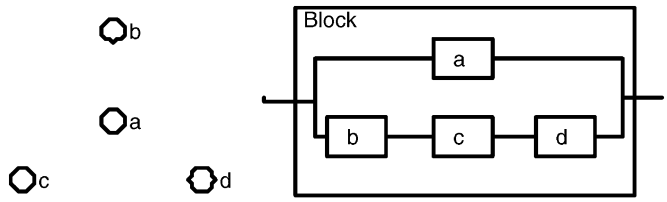


Fig. 9. RBD block for a single node in the hex-grid.

shows that as in the case of a square grid, two neighboring node failures cause network failure. The RBD block of a single node is shown in Fig. 9.

Since the relation between a node and all of its neighbors is modeled by its corresponding RBD block, the RBD blocks for the neighbors are not constructed, as this causes the relationship between the nodes to be considered twice. In the hex-grid network, things simplify a lot when we abstract two antecedents from its hexagonal structure. The two antecedents are listed below.

- Antecedent 1—The remaining battery level of node a.
- Antecedent 2—The minimum remaining battery level of node b, c, and d.

Consequent definition, levels to represent antecedent and consequent are consistent with Section V.A. A total of $9 = 3^2$ rules for hex-grid network are constructed consistently with square-grid network block-2 as listed in Table III.

VI. Simulation and Discussion

In the previous sections, we have theoretically addressed the approach to analyze wireless sensor network lifetime using interval type-2 fuzzy logic systems. Research on the single node lifetime justified the use of Gaussian MFs with uncertain standard deviation (std) to model node lifetime and type-2 fuzzy logic systems for the network lifetime likewise. We are now ready to validate the feasibility of our approach. In this section, we will train the design parameters of FLLE2 with collected data and test our new FLLE2. We devised a *Type-1 fuzzy logic lifetime evaluator* (FLLE1) using singleton type-1 fuzzy logic system to compare the performance with FLLE2. FLLE1 is trained using the same algorithm as FLLE2.

A. Energy Consumption Model and Test Data Generation

Simulation is implemented on two deployment modes: square-grid and hex-grid. For both modes, we consider the basic units in Fig. 8 block-1 and Fig. 9 and deploy the network with minimum density (referring to Section II-A). Our explicit goal is to evaluate the remnant active time of a network when some sensor nodes have consumed certain amount of energy in task performing. Thus we initialize the remaining power level of all sensor nodes by random variables within [0,10] J.

A radio energy consumption model has been well studied in LEACH (Energy-Efficient Communication Protocols for Wireless Microsensor Networks) [26] and ESO (Energy-Efficient Self-Organization for Wireless Sensor Networks) [27]. Different applications consume energy resources in different manners. According to the path-loss model in wireless communication, the energy E needed to transmit over distance d is proportionate to d^β, where β is the path-loss exponent depending on the specific propagation environment. For example, β will have a larger value for long-distance transmission than for short-distance transmission. In order to save energy resources and decrease interference, power control is widely used in wireless communications such that the radio could be adjusted for a certain range of output power level. The following model is adopted from [26], where perfect power control is assumed.

To transmit l bits over distance d, the sender's radio spends

$$E_{TX}(l,d) = E_{TX-elec}(l) + E_{TX-\mathrm{amp}}(l,d) = \begin{cases} lE_{\mathrm{elec}} + l\epsilon_{\mathrm{fs}}d^2 & d < d_0 \\ lE_{\mathrm{elec}} + l\epsilon_{\mathrm{mp}}d^4 & d \geq d_0 \end{cases} \quad (9)$$

and to receive this message, the receiver's radio spends

$$E_{RX}(l,d) = E_{RX-\mathrm{elec}} = lE_{\mathrm{elec}}. \quad (10)$$

The electronics energy E_{elec} depends on factors such as digital coding, modulation, filtering, and spreading of the signal, whereas the amplifier energy $\epsilon_{\mathrm{fs}}d^2$ in free space or $\epsilon_{\mathrm{mp}}d^4$ in multipath environment depends on the distance to the receiver and the acceptable bit-error rate. For the simulations described in later sections, the communication energy parameters are set as $d_0 = 86.2$ m, the radio dissipates $E_{\mathrm{elec}} = 50$ nJ per bit to run the transmitter or receiver circuitry, $\epsilon_{\mathrm{fs}} = 10$ pJ/bit/m^2, and $\epsilon_{\mathrm{mp}} = 0.0013$ pJ/bit/m^4.

In our simulation, we use the formula in (9) under the circumstances $d < d_0$. Sensor nodes take turn to transmit data to their immediate neighbors by broadcast until network failure. We assume the transmission alternation is determined by the remaining power level of individual sensor nodes at the beginning of each epoch. The sensor node with the lowest power level gets to transmit with the least probability. We also make the assumption that the transmitted data bits per turn is a constant such that the energy dissipation varies only with the transmitting distance. We ran simulations for square-grid and hex-grid wireless sensor networks using the OPNET platform set up in [27]. The actual sensor network lifetime can be obtained for different sensor battery level [0,10] J settings.

We run 50 Monte-Carlo simulations to collect data sets, each of which contains $N = 600$ lifetime data for square-grid and hex-grid networks, respectively. Each data set consists of battery levels of four nodes and actual network lifetime. In our FLS network lifetime analysis, we used 300 data sets for training, and the remaining 300 data sets were used for testing.

B. Simulation Results and Discussion

We designed the FLLE2 and FLLE1 for a square-grid wireless sensor network. The initial 27 rules were designed according to Table II. The antecedent and consequent MFs for FLLE1 and FLLE2 are plotted in Fig. 10. Then we tuned the parameters of FLLE1 and FLLE2 using steepest descent algorithm. We followed the training algorithm proposed in [18] for FLLE2. Three hundred data sets were used for training. Both FLLE1 and FLLE2 were trained for six epochs. After training, the parameters of FLLE1 and FLLE2 were fixed and the remaining 300 data sets were used for testing.

Authorized licensed use limited to: University of Texas at Arlington. Downloaded on December 18, 2009 at 14:08 from IEEE Xplore. Restrictions apply.

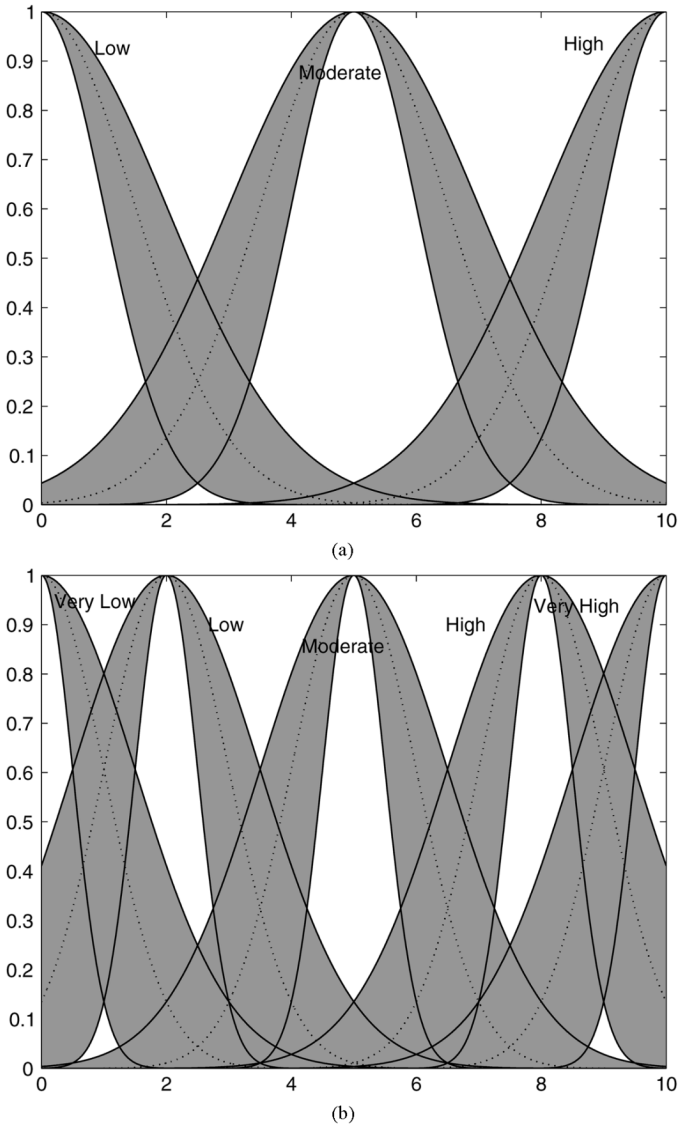


Fig. 10. Membership functions. (a) Antecedent MFs: MFs with shaded regions are for FLLE2 and MFs with dashed lines are for FLLE1. (b) Consequent MFs: MFs with shaded regions are for FLLE2 and MFs with dashed lines are for FLLE1.

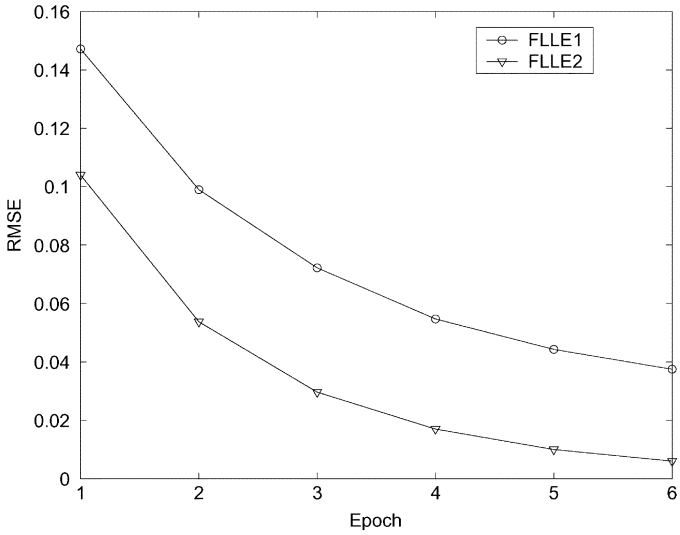


Fig. 11. Square-grid: RMSE of FLLE1 and FLLE2.

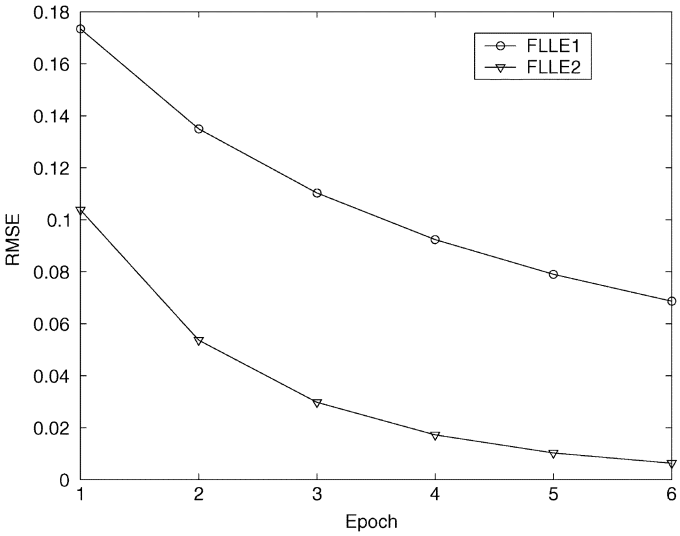


Fig. 12. Hex-grid: RMSE of FLLE1 and FLLE2.

In Fig. 11, we summarized the root mean square errors (RMSEs) between the estimated lifetime and the actual lifetime. Observe that the RMSEs of both FLLE1 and FLLE2 for square-grid wireless sensor network decrease along with the tuning epoch and the FLLE2 performs much better than the FLLE1. For example, FLLE1 takes down RMSE from initial 0.1472 to around 0.037 at the sixth epoch while FLLE2 reduces RMSE from 0.104 to 0.006. FLLE2 achieves nearly 83.8% reduction in RMSE compared to FLLE1 at the sixth epoch.

Similarly, we designed a FLLE1 and a FLLE2 for hex-grid wireless sensor network. The initial nine rules were set according to Table III. The same antecedent and consequent MFs as in square-grid network were used. We then trained and tested the FLLE1 and FLLE2. In Fig. 12, we plotted the RMSE between the estimated lifetime and the actual lifetime. Results show that the FLLE1 and the FLLE2 for hex-grid sensor network decrease the RMSE along with the tuning epoch and FLLE2 outperforms FLLE1 likewise. For example, FLLE1 takes down RMSE from initial 0.1734 to around 0.069 at the sixth epoch while FLLE2 reduces RMSE from 0.1038 to 0.006. FLLE2 achieves nearly 91.3% reduction in RMSE comparing to FLLE1 at the sixth epoch.

Next, we implement the basic units of square-grid and hex-grid into a wireless sensor network and compare the performance of FLLE1 and FLLE2 with the general nonfuzzy approach. We estimate the network lifetime in five consecutive windows. In each observing window, we run Monte Carlo simulation 100 times. We compare our fuzzy logic based evaluators with the first node die methods used in [26] and [27] and normalized the network lifetime to the upper bound of data gathering sensor activities proposed in [4]. Simulation results are presented in Figs. 13 and 14.

In both figures, we observe that the estimated lifetimes from FLLE2 and the first node die method are tight to the upper bound, and our fuzzy approach FLLE2 outperforms the nonfuzzy first node die method. Comparing the performance of FLLE1 and FLLE2, the results again validate the feasibility of modeling the sensor node lifetime with the type-2 interval fuzzy logic system.

Authorized licensed use limited to: University of Texas at Arlington. Downloaded on December 18, 2009 at 14:08 from IEEE Xplore. Restrictions apply.

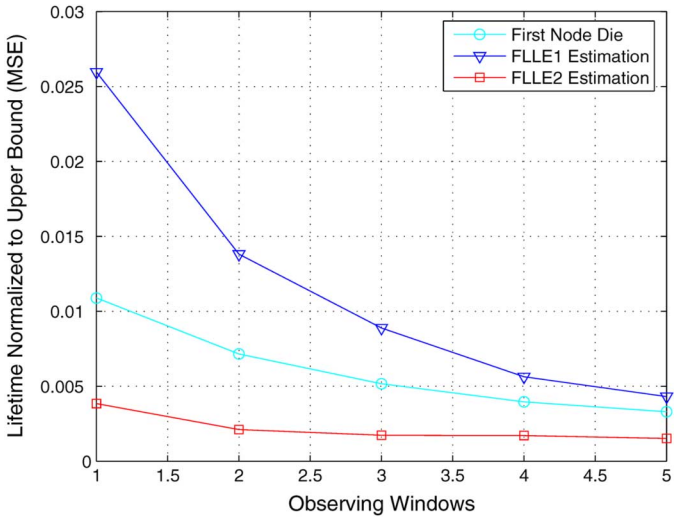


Fig. 13. Square-grid: fuzzy estimation and nonfuzzy approach.

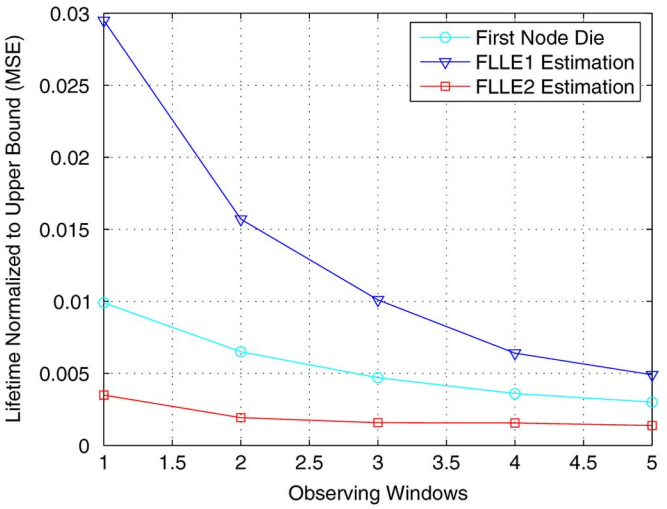


Fig. 14. Hex-grid: fuzzy estimation and nonfuzzy Approach.

Up to the present, we have discussed the basic units of square-grid and hex-grid wireless sensor networks. Now, let $N_{\min}$ be the number of sensor nodes required to be deployed with minimum density (referring to Section II-A). For square-grid sensor network, the network RBD in Fig. 8 consists of $(\sqrt{N_{\min}}-1)^2$ block-1s and $2(\sqrt{N_{\min}}-1)$ block-2s in series, the whole square grid network can actually be decomposed into multiple blocks serial connected together and the method of setting up rules can be applied likewise. Similarly, in hex-grid sensor network, $N_{\min}/2$ RBD blocks in Fig. 9 connected in series represent the network, which can be decomposed the same way as in the square-grid sensor network. While designing the FLSs, if the number of antecedents is more than three, we can union-rule configuration [28] to eliminate the rule explosion.

VII. Conclusions and Future Works

In this paper, we described a new method based on fuzzy logic systems to analyze and estimate the network lifetime for wireless sensor networks. Our approach is illuminated by the research that a single node lifetime behaves the nature of normal Gaussian distribution. However, we showed that if the single node lifetime follows normal Gaussian distribution, it is most appropriate to be modeled as a Gaussian MF with uncertain standard deviation. We then set up the fuzzy logic lifetime evaluator based on interval type-2 FLSs for lifetime estimation and test its performance using real lifetime data. Simulation results convincingly justified the feasibility of applying type-2 FLSs into wireless sensor network lifetime analysis. We believe that our approaches opens up a new vision for research on wireless sensor network lifetime analysis.

Our future work will focus on lifetime evaluation under the circumstances that the task scheduling is variable and how the estimated network lifetime could be used to accommodate the scheduling change.

Acknowledgment

The authors would like to thank L. Zhao for providing help on network lifetime simulations.

References

[1] C. Y. Chong and S. P. Kumar, "Sensor networks: Evolution, opportunities, and challenges," *Proc. IEEE*, vol. 91, pp. 1247–1256, Aug. 2003.
[2] A. Mainwaring, J. Polastre, R. Szewczyk, D. Culler, and J. Anderson, "Wireless sensor networks for habitat monitoring," in *Proc. WSNA'02*, Atlanta, GA, Sep. 28, 2002, pp. 88–97.
[3] V. A. Kottapalli, A. S. Kiremidjian, J. P. Lynch, E. Carryer, and T. W. Kenny, "Two-tired wireless sensor network architecture for structural health monitoring," in *Proc. SPIE*, San Diego, CA, Mar. 2003.
[4] M. Bhardwaj, T. Garnett, and A. Chandrakasan, "Upper bounds on the lifetime of sensor networks," in *Proc. IEEE Int. Conf. Commun.*, 2001, pp. 785–790.
[5] M. Bhardwaj and A. P. Chandrakasan, "Bounding the lifetime of sensor networks via optimal role assignments," in *Proc. INFOCOM*, 2002, pp. 1587–1596.
[6] D. M. Blough and P. Santi, "Investigating upper bounds on network lifetime extension for cell-based energy conservation techniques in stationary ad hod networks," in *Proc. MOBICOM'2002*, Atlanta, GA, Sep. 2002, pp. 183–192.
[7] E. Jain and Q. Liang, "Sensor placement and lifetime of wireless sensor networks: Theory and performance analysis," in *Sensor Network Operations*, S. Phoha, T. F. LaPorta, and C. Griffin, Eds. New York: Wiley, 2005.
[8] N. N. Karnik, J. M. Mendel, and Q. Liang, "Type-2 fuzzy logic systems," *IEEE Trans. Fuzzy Syst.*, vol. 7, no. 6, pp. 643–658, Dec. 1999.
[9] J.-S. R. Jang, "ANFIS: Adaptive-network-based fuzzy inference system," *IEEE Trans. Syst., Man, Cybern.*, vol. 23, pp. 665–685, May/Jun. 1993.
[10] K. Kar and S. Banerjee, "Node placement for connected coverage in sensor networks," in *Extended Abstract Proc. WiOpt 2003*, Sophia-Antipolis, France, Mar. 2003.
[11] S. S. Dhillon, K. Chakrabarty, and S. S. Iyengar, "Sensor placement for grid coverage under imprecise detections," *FUSION*, 2002.
[12] L. A. Zadeh, "The concept of a linguistic variable and its application to approximate reasoning—I," *Inform. Sci.*, vol. 8, pp. 199–249, 1975.
[13] J. M. Mendel, "Fuzzy logic systems for engineering: A tutorial," *Proc. IEEE*, vol. 83, pp. 345–377, Mar. 1995.
[14] D. Dubois and H. Prade, *Fuzzy Sets and Systems: Theory and Applications*. New York: Academic, 1980.
[15] E. Hisdal, "The IF THEN ELSE statement and interval-valued fuzzy sets of higher type," *Int. J. Man-Machine Studies*, vol. 15, pp. 385–455, 1981.
[16] Q. Liang and J. M. Mendel, "MPEG VBR video traffic modeling and classification using fuzzy techniques," *IEEE Trans. Fuzzy Syst.*, vol. 9, no. 1, pp. 183–193, Feb. 2001.
[17] Q. Liang, N. Karnik, and J. M. Mendel, "Connection admission control in ATM network using survey-based type-2 fuzzy logic systems," *IEEE Trans. Syst., Man, Cybern., C*, vol. 30, no. 3, pp. 529–539, Aug. 2000.
[18] Q. Liang and J. M. Mendel, "Interval type-2 fuzzy logic systems: Theory and design," *IEEE Trans. Fuzzy Syst.*, vol. 8, no. 5, pp. 535–550, Oct. 2000.
[19] Q. Liang and J. M. Mendel, "Equalization of time-varying nonlinear channels using type-2 fuzzy adaptive filters," *IEEE Trans. Fuzzy Syst.*, vol. 8, no. 5, pp. 551–563, Oct. 2000.
[20] Q. Liang and J. M. Mendel, "Overcoming time-varying co-channel interference using type-2 fuzzy adaptive filters," *IEEE Trans. Circuits Syst. II*, vol. 47, no. 12, pp. 1419–1428, Dec. 2000.

Authorized licensed use limited to: University of Texas at Arlington. Downloaded on December 18, 2009 at 14:08 from IEEE Xplore. Restrictions apply.

[21] L.-X. Wang and J. M. Mendel, "Fuzzy basis functions, universal approximation, and orthogonal least squares learning," *IEEE Trans. Neural Netw.*, vol. 3, no. 5, pp. 807–814, Sep. 1992.
[22] D. Kececioglu, *Reliability Engineering Handbook*. Englewood Cliffs, NJ: Prentice-Hall, 1991, vol. 1, 2.
[23] L. M. Leemis, *Reliability: Probabilistic Models and Statistical Methods*. Englewood Cliffs, NJ: Prentice-Hall, 1995.
[24] A. Papoulis and S. U. Pillai, *Probability, Random Varibales and Stochastic Processes*, 4th ed. New York: McGraw-Hill, 2002.
[25] B. Healy, "The use of wireless sensor networks for mapping environmental conditions in buildings," ASHRAE Seminar, Jul. 2003 [Online]. Available: http://www.nist.gov/tc75/ASHRAESummer2003SeminarHealy.pdf
[26] W. R. Heinzelman, A. Chandrakasan, and H. Balakrishnan, "An application-specific protocol architecture for wireless microsensor networks," *IEEE Trans. Wireless Commun.*, vol. 1, no. 4, pp. 660–670, Oct. 2002.
[27] L. Zhao and Q. Liang, "Energy-efficient self-organization for wireless sensor networks: A fully distributed approach," in *Proc. IEEE GLOBECOM*, Dallas, TX, Nov. 2004, pp. 2728–2732.
[28] W. E. Combs and J. E. Andrews, "Combinatorial rule explosion eliminated by a fuzzy rule configuration," *IEEE Trans Fuzzy Syst.*, vol. 6, no. 1, pp. 1–11, Feb. 1998.



Haining Shu (S'04) received the B.S. degree in electronics and information systems from Peking University, China, in 1996 and the M.S. degree in electrical engineering from the University of Texas at Dallas in 2002. She is currently pursuing the Ph.D. degree in electrical engineering at the University of Texas at Arlington.

Prior to the master's program, she was a Systems Engineer with Telecom Planning and Research Institute, Beijing. Her research interests include fuzzy logic systems and applications, distributed source coding, sensor networks, and collaborative radar system.



Qilian Liang (SM'05) received the B.S. degree from Wuhan University, China, in 1993, the M.S. degree from Beijing University of Posts and Telecommunications, Beijing, China, in 1996, and the Ph.D. degree from the University of Southern California, Los Angeles, in 2000, all in electrical engineering.

He joined the Faculty of the University of Texas at Arlington in 2002. Prior to that he was a Member of Technical Staff with Hughes Network Systems Inc., San Diego, CA. His research interests include sensor networks (energy efficiency, cross-layer design, optimal sensor deployment, etc.), wireless communications, wireless networks, communication system and communication theory, signal processing for communications, fuzzy logic systems and applications, multimedia network traffic modeling and classification, and collaborative and distributed signal processing. He has published more than 100 journal and conference papers and five book chapters, and has six U.S. patents pending.

Dr. Liang received the 2002 IEEE Transactions on Fuzzy Systems Outstanding Paper Award, the 2003 Office of Naval Research Young Investigator Award, and the 2005 UTA College of Engineering Outstanding Young Faculty Award.



Jean Gao (M'96) received the B.S. and M.S. degrees in biomedical engineering from Shanghai Medical University, Shangai, China, and Rose-Hulman Institute of Technology, respectively. She received the Ph.D. degree in electrical engineering from Purdue University, West Lafayette, IN.

She is an Assitant Professor in the Computer Science and Engineering Department at the University of Texas at Arlington. Her research interests in computer vision and pattern recognition are object motion estimation, shape classification, multidimensional multiobject tracking, and reconstruction.

Dr. Gao was the recipient of the prestigious CAREER Award from the National Science Foundation.

Authorized licensed use limited to: University of Texas at Arlington. Downloaded on December 18, 2009 at 14:08 from IEEE Xplore. Restrictions apply.

Hindawi Publishing Corporation
EURASIP Journal on Wireless Communications and Networking
Volume 2007, Article ID 89103, 9 pages
doi:10.1155/2007/89103

Research Article

Radar Sensor Networks: Algorithms for Waveform Design and Diversity with Application to ATR with Delay-Doppler Uncertainty

Qilian Liang

Department of Electrical Engineering, University of Texas at Arlington, Room 518, 416 Yates Street, Arlington, TX 76019-0016, USA

Received 30 May 2006; Revised 28 November 2006; Accepted 29 November 2006

Recommended by Xiuzhen Cheng

Automatic target recognition (ATR) in target search phase is very challenging because the target range and mobility are not yet perfectly known, which results in delay-Doppler uncertainty. In this paper, we firstly perform some theoretical studies on radar sensor network (RSN) design based on linear frequency modulation (LFM) waveform: (1) the conditions for waveform coexistence, (2) interferences among waveforms in RSN, (3) waveform diversity in RSN. Then we apply RSN to ATR with delay-Doppler uncertainty and propose maximum-likeihood (ML) ATR algorithms for fluctuating targets and nonfluctuating targets. Simulation results show that our RSN vastly reduces the ATR error compared to a single radar system in ATR with delay-Doppler uncertainty. The proposed waveform design and diversity algorithms can also be applied to active RFID sensor networks and underwater acoustic sensor networks.

Copyright © 2007 Qilian Liang. This is an open access article distributed under the Creative Commons Attribution License, which permits unrestricted use, distribution, and reproduction in any medium, provided the original work is properly cited.

1. INTRODUCTION AND MOTIVATION

The goal for any target recognition system is to give the most accurate interpretation of what a target is at any given point in time. There are two classes of motion models of targets, one for maneuvering targets and one for nonmaneuvering (constant velocity and acceleration) targets. The area that is still lacking in target recognition is the ability to detect reliably when a target is beginning a maneuver where its speed and range are uncertain. The tracking system can switch the algorithms applied to the problem from a nonmaneuvering set to the maneuvering set when a target is beginning a maneuver. But when the tracker does finally catch up to the target after the maneuver and then perform ATR, the latency is too high. In time-critical mission situation, such latency in ATR is not tolerable. In this paper, we are interested in studying automatic target recognition with range and speed uncertainty, that is, delay-Doppler uncertainty, using radar sensor networks (RSN). The network of radar sensors should operate with multiple goals managed by an intelligent platform network that can manage the dynamics of each radar to meet the common goals of the platform rather than each radar to operate as an independent system. Therefore, it is significant to perform signal design and processing and networking cooperatively within and between platforms of radar sensors and their communication modules. In this paper, we are interested in studying algorithms on radar sensor network (RSN) design based on linear frequency modulation (LFM) waveform: (1) the conditions for waveform coexistence, (2) interferences among waveforms in RSN, (3) waveform diversity in RSN. Then we apply RSN to automatic target recognition (ATR) with delay-Doppler uncertainty.

In nature, diverse waveforms are transmitted by animals for specific applications. For example, when a bat and a whale are in the search mode for food, they emit a different type of waveform than when they are trying to locate their prey. The Doppler-invariant waveforms that they transmit are environment dependent [1]. Hence, in RSN, it may be useful to transmit different waveforms from different neighbor radars and they can collaboratively perform waveforms diversity for ATR. Sowelam and Tewfik [2] developed a signal selection strategy for radar target classification, and a sequential classification procedure was proposed to minimize the average number of necessary signal transmissions. Intelligent waveform selection was studied in [3, 4], but the effect of Doppler shift was not considered. In [5], the performance of constant

frequency (CF) and LFM waveform fusion from the standpoint of the whole system was studied, but the effects of clutter were not considered. In [6], CF and LFM waveforms were studied for sonar system, but it was assumed that the sensor is nonintelligent (i.e., waveform cannot be selected adaptively). All the above studies and design methods were focused on the waveform design or selection for a single active radar or sensor. In [7], cross-correlation properties of two radars are briefly mentioned and the binary coded pulses using simulated annealing [8] are highlighted. However, the cross-correlation of two binary sequences such as binary coded pulses (e.g., Barker sequence) are much easier to study than that of two analog radar waveforms. In [9], CF waveform design was applied to RSN with application to ATR without any delay-Doppler uncertainty. In this paper, we will focus on the waveform design fusion for radar sensor networks using LFM waveform.

The rest of this paper is organized as follows. In Section 2, we study the coexistence of LFM radar waveforms. In Section 3, we analyze the interferences among LFM radar waveforms. In Section 4, we propose a RAKE structure for waveform diversity combining and propose maximum-likelihood (ML) algorithms for ATR with delay-Doppler uncertainty. In Section 5, we provide simulation results on ML-ATR with delay-Doppler uncertainty. In Section 6, we conclude this paper and provide some future works.

2. COEXISTENCE OF LFM RADAR WAVEFORMS

In RSN, radar sensors will interfere with each other and the signal-to-interference-ratio may be very low if the waveforms are not properly designed. We will introduce orthogonality as one criterion for waveforms design in RSN to make them coexistence. Besides, the radar channel is narrowband, so we will also consider the bandwidth constraint.

In our radar sensor networks, we choose LFM waveform. The LFM waveform can be defined as

$$x(t) = \sqrt{\frac{E}{T}} \exp\left(j2\pi\beta t^2\right), \quad -\frac{T}{2} \le t \le \frac{T}{2}. \tag{1}$$

In radar, ambiguity function (AF) is an analytical tool for waveform design and analysis that succinctly characterizes the behavior of a waveform paired with its matched filter. The ambiguity function is useful for examining resolution, side lobe behavior, and ambiguities in both range and Doppler for a given waveform [10]. For a single radar, the matched filter for waveform $x(t)$ is $x^*(-t)$, and the ambiguity function of LFM waveform is [10]

$$\begin{aligned} A(\tau, F_D) &= \left| \int_{-T/2+\tau}^{T/2} x(t) \exp\left(j2\pi F_D t\right) x^*(t-\tau) dt \right| \\ &= \left| \frac{E \sin\left[\pi(F_D + \beta\tau)(T - |\tau|)\right]}{T\pi(F_D + \beta\tau)} \right|, \quad -T \le \tau \le T. \end{aligned} \tag{2}$$

Three special cases can simplify this AF:

(1) when $\tau = 0$,

$$A(0, F_D) = \left| \frac{E \sin\left(\pi F_D T\right)}{T\pi(F_D)} \right|; \tag{3}$$

(2) when $F_D = 0$,

$$A(\tau, 0) = \left| \frac{E \sin\left[\pi\beta\tau(T - |\tau|)\right]}{T\pi\beta\tau} \right|, \quad -T \le \tau \le T; \tag{4}$$

(3) and

$$A(0, 0) = E. \tag{5}$$

However, the above ambiguity is for one radar only (no coexisting radar).

For radar sensor networks, the waveforms from different radars will interfere with each other. We choose the waveform for radar i as

$$x_i(t) = \sqrt{\frac{E}{T}} \exp\left[j2\pi\left(\beta t^2 + \delta_i t\right)\right], \quad -\frac{T}{2} \le t \le \frac{T}{2} \tag{6}$$

which means there is a frequency shift δ_i for radar i. To minimize the interference from one waveform to the other, optimal values for δ_i should be determined to have the waveforms orthogonal to each other, that is, let the cross-correlation between $x_i(t)$ and $x_n(t)$ be 0,

$$\begin{aligned} &\int_{-T/2}^{T/2} x_i(t) x_n^*(t) dt \\ &= \frac{E}{T} \int_{-T/2}^{T/2} \exp\left[j2\pi\left(\beta t^2 + \delta_i t\right)\right] \exp\left[-j2\pi\left(\beta t^2 + \delta_n t\right)\right] dt \\ &= E \operatorname{sinc}\left[\pi(\delta_i - \delta_n) T\right]. \end{aligned} \tag{7}$$

If we choose

$$\delta_i = \frac{i}{T}, \tag{8}$$

where i is a dummy index, then (7) can have two cases:

$$\int_{-T/2}^{T/2} x_i(t) x_n^*(t) dt = \begin{cases} E, & i = n, \\ 0, & i \ne n. \end{cases} \tag{9}$$

So, choosing $\delta_i = i/T$ in (6) can have orthogonal waveforms, that is, the waveforms can coexist if the carrier spacing is $1/T$ between two radar waveforms. That is, orthogonality amongst carriers can be achieved by separating the carriers by an integer multiple of the inverse of waveform pulse duration. With this design, all the orthogonal waveforms can work simultaneously. However, there may exist time delay and Doppler shift ambiguity which will have interferences to other waveforms in RSN.

3. INTERFERENCES OF LFM WAVEFORMS IN RADAR SENSOR NETWORKS

3.1. RSN with two radar sensors

We are interested in analyzing the interference from one radar to another if there exist time delay and Doppler shift. For a simple case where there are two radar sensors (i and n), the ambiguity function of radar i (considering interference from radar n) is

$$A_i(t_i, t_n, F_{D_i}, F_{D_n}) \tag{10}$$

$$= \left| \int_{-\infty}^{\infty} [x_i(t) \exp(j2\pi F_{D_i} t) + x_n(t-t_n) \exp(j2\pi F_{D_n} t)] x_i^*(t-t_i)\, dt \right| \tag{11}$$

$$\leq \left| \int_{-T/2+\max(t_i,t_n)}^{T/2+\min(t_i,t_n)} x_n(t-t_n) \exp(j2\pi F_{D_n} t) x_i^*(t-t_i)\, dt \right| + \left| \int_{-T/2+t_i}^{T/2} x_i(t) \exp(j2\pi F_{D_i} t) x_i^*(t-t_i)\, dt \right| \tag{12}$$

$$= \left| \int_{-T/2+\max(t_i,t_n)}^{T/2+\min(t_i,t_n)} x_n(t-t_n) \exp(j2\pi F_{D_n} t) x_i^*(t-t_i)\, dt \right| + \left| \frac{E \sin[\pi(F_{D_i} + \beta t_i)(T - |t_i|)]}{T\pi(F_{D_i} + \beta t_i)} \right|. \tag{13}$$

To make analysis easier, we assume $t_i = t_n = \tau$ which is a reasonable assumption because radar sensors can be coordinated by the clusterhead to send out LFM waveforms. Then (13) can be simplified as

$$A_i(\tau, F_{D_i}, F_{D_n}) \approx |E \operatorname{sinc}[\pi(n-i+F_{D_n}T)]| + \left| \frac{E \sin[\pi(F_{D_i} + \beta\tau)(T - |\tau|)]}{T\pi(F_{D_i} + \beta\tau)} \right|. \tag{14}$$

Some special cases of (14) are listed as follows.

(1) If $F_{D_i} = F_{D_n} = 0$, then (14) becomes

$$A_i(\tau, 0, 0) \approx \left| \frac{E \sin[\pi\beta\tau(T - |\tau|)]}{\pi\beta T\tau} \right|. \tag{15}$$

(2) If $\tau = 0$, then (14) becomes

$$A_i(0, F_{D_i}, F_{D_n}) \approx |E \operatorname{sinc}[\pi(n-i+F_{D_n}T)]| + |E \operatorname{sinc}(\pi F_{D_i} T)|. \tag{16}$$

(3) If $F_{D_i} = F_{D_n} = 0$, $\tau = 0$, and δ_i and δ_n follow (8), then (14) becomes

$$A_i(0, 0, 0) \approx E. \tag{17}$$

3.2. RSN with M radar sensors

It can be extended to an RSN with M radars. Assuming time delay τ for each radar is the same, then the ambiguity function of radar 1 (considering interferences from all the other $M-1$ radars with CF pulse waveforms) can be expressed as

$$A_1(\tau, F_{D_1}, \ldots, F_{D_M}) \approx \left| \sum_{i=2}^{M} E \operatorname{sinc}[\pi(i-1+F_{D_i}T)] \right| + \left| \frac{E \sin[\pi(F_{D_1} + \beta\tau)(T - |\tau|)]}{T\pi(F_{D_1} + \beta\tau)} \right|. \tag{18}$$

Similarly, we can have three special cases.

(1) If $F_{D_1} = F_{D_2} = \cdots = F_{D_M} = 0$, then (18) becomes

$$A_1(\tau, 0, 0, \ldots, 0) \approx \left| \frac{E \sin[\pi\beta\tau(T - |\tau|)]}{\pi\beta T\tau} \right|. \tag{19}$$

Comparing it against (4), it shows that our derived condition in (6) can have a radar in RSN and it gets the same signal strength as that of a single radar (no coexisting radar) when the Doppler shift is 0.

(2) If $\tau = 0$, then (18) becomes

$$A_1(0, F_{D_1}, F_{D_2}, \ldots, F_{D_M}) \approx \left| \sum_{i=1}^{M} E \operatorname{sinc}[\pi(i-1+F_{D_i}T + \beta\tau T)] \right|. \tag{20}$$

Comparing to (3), a radar in RSN has more interferences when unknown Doppler shifts exist.

(3) If $F_{D_1} = F_{D_2} = \cdots = F_{D_M} = 0$, $\tau = 0$, and δ_i in (6) follows (8), then (18) becomes

$$A_1(0, 0, 0, \ldots, 0) \approx E. \tag{21}$$

4. APPLICATION TO ATR WITH DELAY-DOPPLER UNCERTAINTY

In RSN, the radar sensors are networked together in an ad hoc fashion. They do not rely on a pre-existing fixed infrastructure, such as a wireline backbone network or a base station. They are self-organizing entities that are deployed on demand in support of various events surveillance, battlefield, disaster relief, search and rescue, and so forth. Scalability concern suggests a hierarchical organization of radar sensor networks with the lowest level in the hierarchy being a cluster. As argued in [11–14], in addition to helping with scalability and robustness, aggregating sensor nodes into clusters has additional benefits:

(1) conserving radio resources such as bandwidth;
(2) promoting spatial code reuse and frequency reuse;
(3) simplifying the topology, for example, when a mobile radar changes its location, it is sufficient for only the nodes in attended clusters to update their topology information;

(4) reducing the generation and propagation of routing information; and,
(5) concealing the details of global network topology from individual nodes.

In RSN, each radar can provide their waveform parameters such as δ_i to their clusterhead radar, and the clusterhead radar can combine the waveforms from its cluster members.

In RSN with M radars, the received signal for clusterhead (assume it is radar 1) is

$$r_1(u,t) = \sum_{i=1}^{M} \alpha(u) x_i(t-t_i) \exp\left(j2\pi F_{D_i} t\right) + n(u,t), \quad (22)$$

where $\alpha(u)$ stands for radar cross section (RCS) and can be modeled using nonzero constants for nonfluctuating target and four Swerling target models for fluctuating target [10]; F_{D_i} is the Doppler shift of target relative to waveform i; t_i is delay of waveform i, and $n(u,t)$ is additive white Gaussian noise (AWGN). In this paper, we propose a RAKE structure for waveform diversity combining, as illustrated by Figure 1.

According to this structure, the received $r_1(u,t)$ is processed by a bank of matched filters, then the output of branch 1 (after integration) is

$$\begin{aligned} &\left| Z_1(u;t_1,\ldots,t_M,F_{D_1},\ldots,F_{D_M}) \right| \\ &\quad = \left| \int_{-T/2}^{T/2} r_1(u,t) x_1^*(t-t_1)\,ds \right| \\ &\quad = \left| \int_{-T/2}^{T/2} \left[\sum_{i=1}^{M} \alpha(u) x_i(t-t_i) \exp\left(j2\pi F_{D_i} t\right) + n(u,t) \right] \right. \\ &\qquad \left. \times x_1^*(t-t_1)\,dt \right|, \end{aligned} \quad (23)$$

where $\int_{-T/2}^{T/2} n(u,t) x_1^*(t-t_1)\,dt$ can easily be proved to be AWGN, let

$$n(u,t_1) \triangleq \int_{-T/2}^{T/2} n(u,t) x_1^*(t-t_1)\,dt \quad (24)$$

follow a white Gaussian distribution. Assuming $t_1 = t_2 = \cdots = t_M = \tau$, then based on (18),

$$\begin{aligned} &\left| Z_1(u;\tau,F_{D_1},\ldots,F_{D_M}) \right| \\ &\quad \approx \left| \sum_{i=2}^{M} \alpha(u) E \operatorname{sinc}\left[\pi(i-1+F_{D_i}T)\right] \right. \\ &\qquad \left. + \frac{\alpha(u) E \sin\left[\pi(F_{D_1}+\beta\tau)(T-|\tau|)\right]}{T\pi(F_{D_1}+\beta\tau)} + n(u,\tau) \right|. \end{aligned} \quad (25)$$

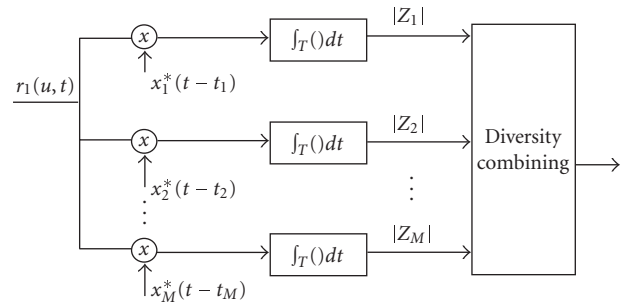


Figure 1: Waveform diversity combining by clusterhead in RSN.

Similarly, we can get the output for any branch m ($m = 1,2,\ldots,M$),

$$\begin{aligned} &\left| Z_m(u;\tau,F_{D_1},\ldots,F_{D_M}) \right| \\ &\quad \approx \left| \sum_{i=1,i\neq m}^{M} \alpha(u) E \operatorname{sinc}\left[\pi(i-m+F_{D_i}T)\right] \right. \\ &\qquad \left. + \frac{\alpha(u) E \sin\left[\pi(F_{D_m}+\beta\tau)(T-|\tau|)\right]}{T\pi(F_{D_m}+\beta\tau)} + n(u,\tau) \right|. \end{aligned} \quad (26)$$

So, $|Z_m(u;\tau,F_{D_1},\ldots,F_{D_M})|$ consists of three parts, signal (reflected signal from radar m waveform):

$$\left| \frac{\alpha(u) E \sin\left[\pi(F_{D_m}+\beta\tau)(T-|\tau|)\right]}{T\pi(F_{D_m}+\beta\tau)} \right|, \quad (27)$$

interferences from other waveforms:

$$\sum_{i=1,i\neq m}^{M} \left| \alpha(u) E \operatorname{sinc}\left[\pi(i-m+F_{D_i}T)\right] \right|, \quad (28)$$

and noise: $|n(u,\tau)|$. Delay-Doppler uncertainty happens quite often in target search and recognition where target range and velocity are not yet perfectly known.

We can also have three special cases for

$$\left| Z_m(u;\tau,F_{D_1},\ldots,F_{D_M}) \right|. \quad (29)$$

(1) When $F_{D_1} = \cdots = F_{D_M} = 0$,

$$\begin{aligned} &\left| Z_m(u;\tau,0,0,\ldots,0) \right| \\ &\quad \approx \left| \frac{\alpha(u) E \sin\left[\pi\beta\tau(T-|\tau|)\right]}{T\pi\beta\tau} + n(u,\tau) \right|. \end{aligned} \quad (30)$$

(2) If $\tau = 0$, then (26) becomes

$$\begin{aligned} &\left| Z_m(u;0,F_{D_1},\ldots,F_{D_M}) \right| \\ &\quad \approx \left| \sum_{i=1}^{M} \alpha(u) E \operatorname{sinc}\left[\pi(i-m+F_{D_i}T)\right] + n(u) \right|. \end{aligned} \quad (31)$$

(3) If $\tau = 0$ and $F_{D_1} = \cdots = F_{D_M} = 0$, then (26) becomes

$$\left| Z_m(u;0,0,0,\ldots,0) \right| \approx \left| E\alpha(u) + n(u) \right|. \quad (32)$$

How to combine all the Z_m's ($m = 1, 2, \ldots, M$) is very similar to the diversity combining in communications to combat channel fading, and the combination schemes may be different for different applications. In this paper, we are interested in applying RSN waveform diversity to ATR, for example, recognition that the echo on a radar display is that of an aircraft, ship, motor vehicle, bird, person, rain, chaff, clear-air turbulence, land clutter, sea clutter, bare mountains, forested areas, meteors, aurora, ionized media, or other natural phenomena. Early radars were "blob" detectors in that they detected the presence of a target and gave its location in range and angle, and radar began to be more than a blob detector and could provide recognition of one type of target from another [7]. It is known that small changes in the aspect angle of complex (multiple scatter) targets can cause major changes in the radar cross section (RCS). This has been considered in the past as a means of target recognition, and is called *fluctuation of radar cross section with aspect angle*, but it has not had much success [7]. In this paper, we propose a maximum-likelihood automatic target recognition (ML-ATR) algorithm for RSN. We will study both fluctuating targets and nonfluctuating targets.

4.1. ML-ATR for fluctuating targets with delay-Doppler uncertainty

Fluctuating target modeling is more realistic in which the target RCS is drawn from either the Rayleigh or chi-square of degree four pdf. The Rayleigh model describes the behavior of a complex target consisting of many scatters, none of which is dominant. The fourth-degree chi-square models targets having many scatters of similar strength with one dominant scatter. Based on different combinations of pdf and decorrelation characteristics (scan-to-scan or pulse-to-pulse decorrelation), four Swerling models are used [10]. In this paper, we will focus on "Swerling 2" model which is Rayleigh distribution with pulse-to-pulse decorrelation. The pulse-to-pulse decorrelation implies that each individual pulse results in an independent value for RCS α.

For Swerling 2 model, the RCS $|\alpha(u)|$ follows Rayleigh distribution and its I and Q subchannels follow zero-mean Gaussian distributions with variance γ^2. Assume

$$\alpha(u) = \alpha_I(u) + j\alpha_Q(u) \tag{33}$$

and $n(u) = n_I(u) + jn_Q(u)$ follows zero-mean complex Gaussian distribution with variance σ^2 for the I and Q subchannels. Observe (26), for given τ, F_{D_i} ($i = 1, \ldots, M$),

$$\begin{aligned}
&\sum_{i=1,\, i\neq m}^{M} \alpha(u) E \operatorname{sinc}\left[\pi\left(i - m + F_{D_i} T\right)\right] \\
&\qquad + \frac{\alpha(u) E \sin\left[\pi\left(F_{D_m} + \beta\tau\right)\left(T - |\tau|\right)\right]}{T\pi\left(F_{D_m} + \beta\tau\right)} \\
&= \alpha(u) E\Bigg[\sum_{i=1,\, i\neq m}^{M} \operatorname{sinc}\left[\pi\left(i - m + F_{D_i} T\right)\right] \\
&\qquad + \frac{\sin\left[\pi\left(F_{D_m} + \beta\tau\right)\left(T - |\tau|\right)\right]}{T\pi\left(F_{D_m} + \beta\tau\right)}\Bigg]
\end{aligned} \tag{34}$$

follows zero-mean complex Gaussian distributions with variance $E^2\gamma^2[\sum_{i=1,\, i\neq m}^{M} \operatorname{sinc}[\pi(i - m + F_{D_i}T)] + \sin[\pi(F_{D_m} + \beta\tau)(T - |\tau|)]/T\pi(F_{D_m} + \beta\tau)]^2$ for the I and Q subchannels. Since $n(u, \tau)$ also follows zero-mean Gaussian distribution, so $|Z_m(u; \tau, F_{D_1}, \ldots, F_{D_M})|$ of (26) follows Rayleigh distribution. In real world, the perfect values of τ and F_{D_i} are not known in the target search phase and the mean values of τ and F_{D_i} are 0, so we just assume the parameter of this Rayleigh distribution $b = \sqrt{E^2\gamma^2 + \sigma^2}$ (when τ and F_{D_i} equal to 0).

Let $y_m \triangleq |Z_m(u; \tau, F_{D_1}, \ldots, F_{D_M})|$, then

$$f(y_m) = \frac{y_m}{E^2\gamma^2 + \sigma^2} \exp\left(-\frac{y_m^2}{2\left(E^2\gamma^2 + \sigma^2\right)}\right). \tag{35}$$

The mean value of y_m is $\sqrt{\pi(E^2\gamma^2 + \sigma^2)/2}$ and the variance is $(4 - \pi)(E^2\gamma^2 + \sigma^2)/2$. The variance of signal is $(4 - \pi)E^2\gamma^2/2$ and the variance of noise is $(4 - \pi)\sigma^2/2$.

Let $\mathbf{y} \triangleq [y_1, y_2, \ldots, y_M]$, then the pdf of $\mathbf{y}$ is

$$f(\mathbf{y}) = \prod_{m=1}^{M} f(y_m). \tag{36}$$

Our ATR is a multiple-category hypothesis testing problem, that is, to decide a target category (e.g., different aircraft, motor vehicle, etc.) based on $r_1(u, t)$. Assume there are totally N categories and category n target has RCS $\alpha_n(u)$ (with variance γ_n^2), so the ML-ATR algorithm to decide a target category C can be expressed as

$$\begin{aligned}
C &= \arg \max_{n=1,\ldots,N} f(\mathbf{y} \mid \gamma = \gamma_n) \\
&= \arg \max_{n=1,\ldots,N} \prod_{m=1}^{M} \frac{y_m}{E^2\gamma_n^2 + \sigma^2} \exp\left(-\frac{y_m^2}{2\left(E^2\gamma_n^2 + \sigma^2\right)}\right).
\end{aligned} \tag{37}$$

4.2. ML-ATR for nonfluctuating targets with delay-Doppler uncertainty

In some sources, the nonfluctuating target is identified as "Swerling 0" or "Swerling 5" model [15]. For nonfluctuating target, the RCS $\alpha(u)$ is just a constant α for a given target. Observe (26), for given τ, F_{D_i} ($i = 1, \ldots, M$),

$$\begin{aligned}
&\sum_{i=1,\, i\neq m}^{M} \alpha(u) E \operatorname{sinc}\left[\pi\left(i - m + F_{D_i} T\right)\right] \\
&\qquad + \frac{\alpha(u) E \sin\left[\pi\left(F_{D_m} + \beta\tau\right)\left(T - |\tau|\right)\right]}{T\pi\left(F_{D_m} + \beta\tau\right)} \\
&= \alpha E\Bigg[\sum_{i=1,\, i\neq m}^{M} \operatorname{sinc}\left[\pi\left(i - m + F_{D_i} T\right)\right] \\
&\qquad + \frac{\sin\left[\pi\left(F_{D_m} + \beta\tau\right)\left(T - |\tau|\right)\right]}{T\pi\left(F_{D_m} + \beta\tau\right)}\Bigg]
\end{aligned} \tag{38}$$

is just a constant. Since $n(u, \tau)$ follows zero-mean Gaussian distribution, so $|Z_m(u; \tau, F_{D_1}, \ldots, F_{D_M})|$ of (26) follows

Table 1: RCS values at microwave frequency for 6 targets.

Index n	Target	RCS
1	Small single-engine aircraft	1
2	Large flighter aircraft	6
3	Medium bomber or jet airliner	20
4	Large bomber or jet airliner	40
5	Jumbo jet	100
6	Pickup truck	200

Rician distribution with direct path value

$$\lambda = \alpha E\Bigg[\sum_{i=1,\, i\neq m}^{M} \operatorname{sinc}\left[\pi(i-m+F_{D_i}T)\right] + \frac{\sin\left[\pi(F_{D_m}+\beta\tau)(T-|\tau|)\right]}{T\pi(F_{D_m}+\beta\tau)}\Bigg]. \tag{39}$$

Since τ and F_{D_i} are uncertain and zero-mean, so we just use the approximation

$$\lambda = \alpha E \tag{40}$$

which is obtained when τ and F_{D_i} equal to 0.

Let $y_m \triangleq |Z_m(u;\tau,F_{D_1},\ldots,F_{D_M})|$, then the probability density function (pdf) of y_m is

$$f(y_m) = \frac{2y_m}{\sigma^2}\exp\left[-\frac{(y_m^2+\lambda^2)}{\sigma^2}\right]I_0\left(\frac{2\lambda y_m}{\sigma^2}\right), \tag{41}$$

where σ^2 is the noise power (with I and Q subchannel power $\sigma^2/2$), and $I_0(\cdot)$ is the zero-order modified Bessel function of the first kind. Let $\mathbf{y} \triangleq [y_1, y_2, \ldots, y_M]$, then the pdf of $\mathbf{y}$ is

$$f(\mathbf{y}) = \prod_{m=1}^{M} f(y_m). \tag{42}$$

The ML-ATR algorithm to decide a target category C based on $\mathbf{y}$ can be expressed as,

$$\begin{aligned} C &= \arg\max_{n=1,\ldots,N} f(\mathbf{y} \mid \lambda = E|\alpha_n|) \\ &= \arg\max_{n=1,\ldots,N} \prod_{m=1}^{M} \frac{2y_m}{\sigma^2} \\ &\quad\times \exp\left[-\frac{(y_m^2+E^2\alpha_n^2)}{\sigma^2}\right]I_0\left(\frac{2E|\alpha_n|y_m}{\sigma^2}\right). \end{aligned} \tag{43}$$

5. SIMULATIONS

Radar sensor networks will be required to detect a broad range of target classes. In this paper, we applied our ML-ATR to automatic target recognition with delay-Doppler uncertainty. We assume that the domain of target classes is known a priori (N in Sections 4.1 and 4.2), and that the RSN is confined to work only on the known domain.

For fluctuating target recognition, our targets have 6 classes with different RCS values, which are summarized in Table 1 [7]. We assume the fluctuating targets follow "Swerling 2" model (Rayleigh with pulse-to-pulse decorrelation), and assume the RCS value listed in Table 1 to be the standard deviation (std) γ_n of RCS $\alpha_n(u)$ for target n. We applied the ML-ATR algorithm in Section 4.1 (for fluctuating target case) for target recognition within the six targets domain. We chose $T = 0.1$ ms and $\beta = 10^6$. At each average SNR value, we ran Monte-Carlo simulations for 10^5 times for each target. In Figures 2(a), 2(b), 2(c), we plot the average ATR error for fluctuating targets with different delay-Doppler uncertainty and compared the performances of single-radar system, 5-radar RSN, and 10-radar RSN. Observe these three figures.

(1) The two RSNs vastly reduce the ATR error comparing to a single-radar system in ATR with delay-Doppler uncertainty, for example, the 10-radar RSN can achieve ATR error 2% comparing against the single-radar system with ATR error 37% at SNR = 32 dB with delay-Doppler uncertainty $\tau \in [-0.1\,\mathrm{T}, 0.1\,\mathrm{T}]$ and $F_{D_i} \in [-200\,\mathrm{Hz}, 200\,\mathrm{Hz}]$.

(2) Our LFM waveform design can tolerate reasonable delay-Doppler uncertainty which are testified by Figures 2(b), 2(c).

(3) According to Skolnik [7], radar performance with probability of recognition error (p_e) less than 10% is good enough. Our 10-radar RSN with waveform diversity can have probability of ATR error much less than 10% for the average ATR for all targets. However, the single-radar system has probability of ATR error much higher than 10%. Our RSN with waveform diversity is very promising to be used for real-world ATR.

(4) Observe Figures 2(a), 2(c), the average probability of ATR error in Figure 2(c) is not as sensitive to the SNR as that in Figure 2(a), that is, ATR error curve slope becomes flat with higher delay-Doppler uncertainty, which means that the delay-Doppler uncertainty can dominate the ATR performance when it is too high.

For nonfluctuating target recognition, our targets have 6 classes with different RCS values, which are summarized in Table 1 [7]. We applied the ML-ATR algorithms in Section 4.2 (for nonfluctuating target case) to classify an unknown target as one of these 6 target classes. We chose $T = 0.1$ ms and $\beta = 10^6$. At each average SNR value, we ran Monte-Carlo simulations for 10^5 times for each target. In Figures 3(a), 3(b), 3(c), we plotted the probability of ATR error with different delay-Doppler uncertainty. Observe these figures.

(1) The two RSNs tremendously reduce the ATR error comparing to a single-radar system in ATR with delay-Doppler uncertainty, for example, the 10-radar RSN can achieve ATR error 9% comparing against the single-radar system with ATR error 22% at SNR = 22 dB with delay-Doppler uncertainty $\tau \in [-0.2T, 0.2T]$ and $F_{D_i} \in [-500\,\mathrm{Hz}, 500\,\mathrm{Hz}]$.

(2) Comparing Figures 2(a), 2(b), 2(c) against Figures 3(a), 3(b), 3(c), the gain of 10-radar RSN for fluctuating target recognition is much larger than that for nonfluctuating

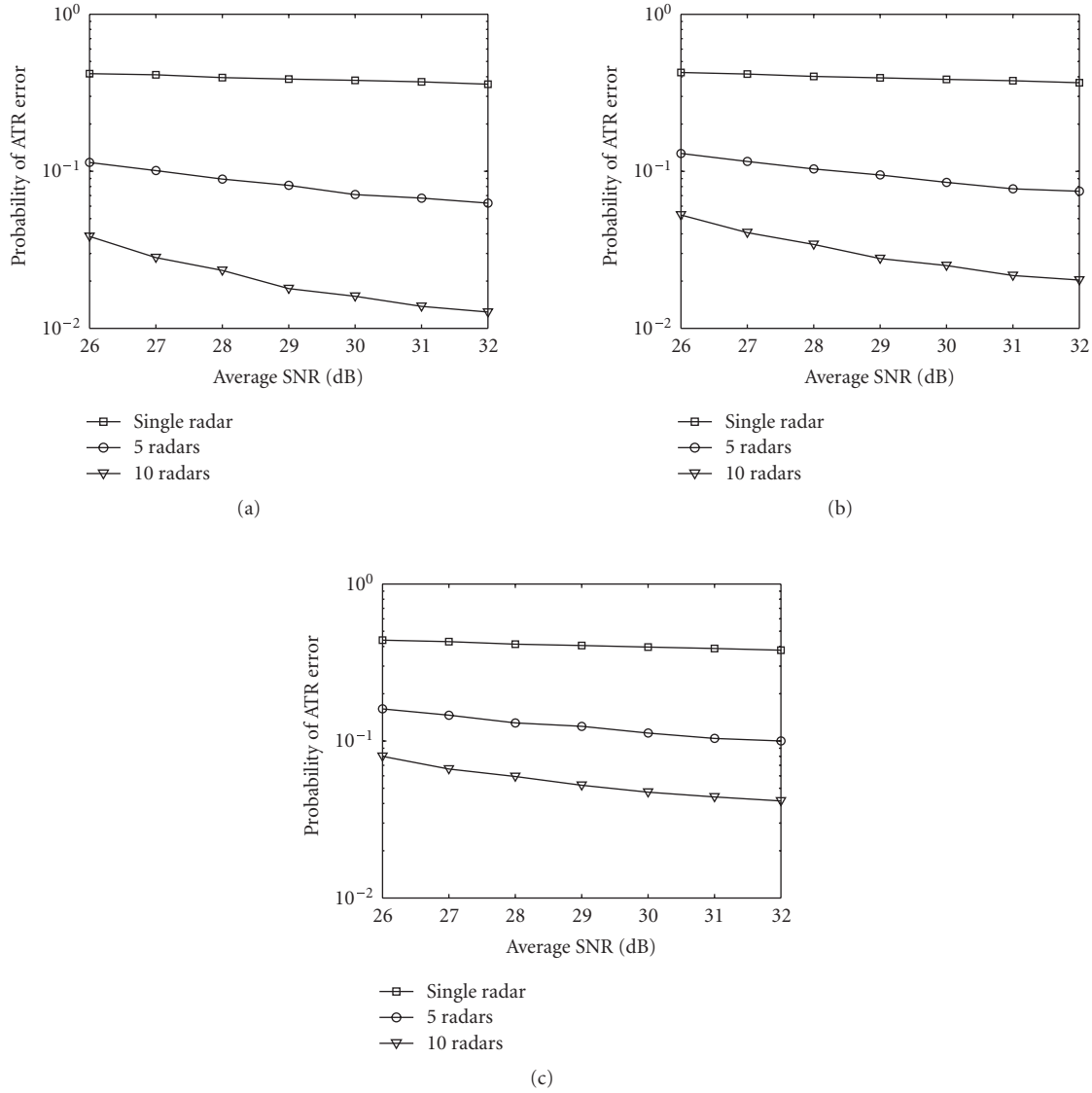


Figure 2: The average probability of ATR error for 6 *fluctuating* targets with different delay-Doppler uncertainty: (a) no delay-Doppler uncertainty, (b) with delay-Doppler uncertainty, $\tau \in [-0.1T, 0.1T]$ and $F_{D_i} \in [-200\,\text{Hz}, 200\,\text{Hz}]$, and (c) with delay-Doppler uncertainty, $\tau \in [-0.2T, 0.2T]$ and $F_{D_i} \in [-500\,\text{Hz}, 500\,\text{Hz}]$.

target recognition, which means our RSN has better capacity to handle the fluctuating targets. In real world, fluctuating targets are more meaningful and realistic.

(3) Comparing Figures 3(a), 3(b), 3(c) against Figures 2(a), 2(b), 2(c), the ATR needs much lower SNR for nonfluctuating target recognition because Rician distribution has direct path component.

6. CONCLUSIONS AND FUTURE WORKS

We have studied LFM waveform design and diversity in radar sensor networks (RSN). We showed that the LFM waveforms can coexist if the carrier frequency spacing is $1/T$ between two radar waveforms. We made analysis on interferences among waveforms in RSN and proposed a RAKE structure for waveform diversity combining in RSN. We applied the RSN to automatic target recognition (ATR) with delay-Doppler uncertainty and proposed maximum-likehood (ML)-ATR algorithms for fluctuating targets and nonfluctuating targets. Simulation results show that RSN using our waveform diversity-based ML-ATR algorithm performs much better than single-radar system for fluctuating targets and nonfluctuating targets recognition. It is also demonstrated that our LFM waveform-based RSN can handle the delay-Doppler uncertainty which quite often happens for ATR in target search phase.

The waveform design and diversity algorithms proposed in this paper can also be applied to active RFID sensor networks and underwater acoustic sensor networks because LFM waveforms can also be used by these active sensor

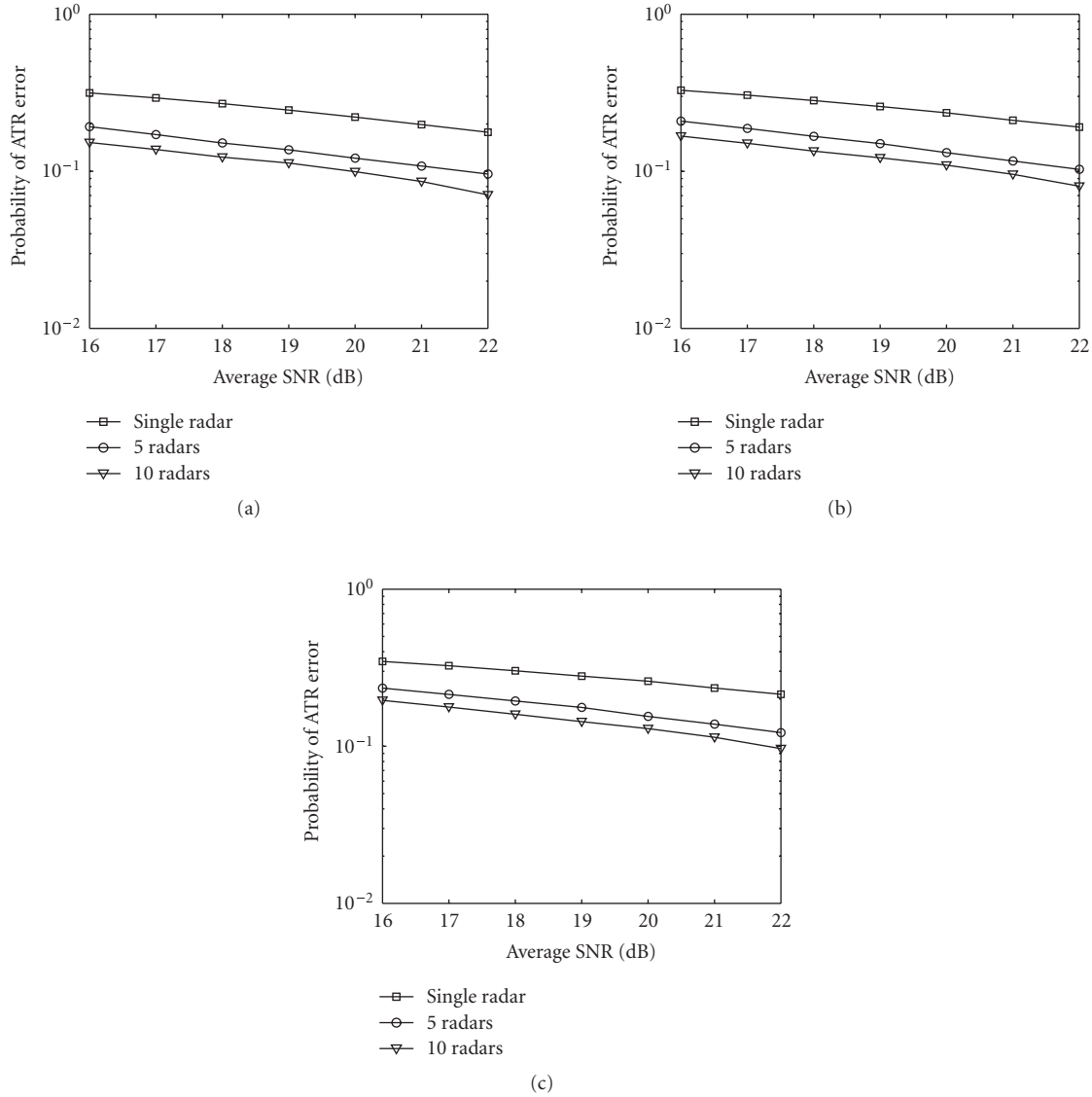


FIGURE 3: The average probability of ATR error for 6 *nonfluctuating* targets with different delay-Doppler uncertainty: (a) no delay-Doppler uncertainty, (b) with delay-Doppler uncertainty, $\tau \in [-0.1\,\mathrm{T}, 0.1\,\mathrm{T}]$ and $F_{D_i} \in [-200\,\mathrm{Hz}, 200\,\mathrm{Hz}]$, and (c) with delay-Doppler uncertainty, $\tau \in [-0.2\,\mathrm{T}, 0.2\,\mathrm{T}]$ and $F_{D_i} \in [-500\,\mathrm{Hz}, 500\,\mathrm{Hz}]$.

networks to perform collaborative monitoring tasks. In this paper, the ATR is for single-target recognition. We will continuously investigate the ATR when multiple targets coexist in RSN and each target has delay-Doppler uncertainty. In our waveform diversity combining, we have used spatial diversity combining in this paper. We will further investigate spatial-temporal-frequency combining for RSN waveform diversity.

ACKNOWLEDGMENTS

This work was supported by the US Office of Naval Research (ONR) Young Investigator Program Award under Grant no. N00014-03-1-0466. The author would like to thank ONR Program Officer Dr. Rabinder N. Madan for his direction and insightful discussion on radar sensor networks.

REFERENCES

[1] R. A. Johnson and E. L. Titlebaum, "Range-doppler uncoupling in the doppler tolerant bat signal," in *Proceedings of IEEE Ultrasonics Symposium*, pp. 64–67, Boston, Mass, USA, October 1972.

[2] S. M. Sowelam and A. H. Tewfik, "Waveform selection in radar target classification," *IEEE Transactions on Information Theory*, vol. 46, no. 3, pp. 1014–1029, 2000.

[3] P. M. Baggenstoss, "Adaptive pulselength correction (APLECORR): a strategy for waveform optimization in ultrawideband active sonar," *IEEE Journal of Oceanic Engineering*, vol. 23, no. 1, pp. 1–11, 1998.

[4] D. J. Kershaw and R. J. Evans, "Optimal waveform selection for tracking systems," *IEEE Transactions on Information Theory*, vol. 40, no. 5, pp. 1536–1550, 1994.

[5] R. Niu, P. Willett, and Y. Bar-Shalom, "Tracking considerations in selection of radar waveform for range and range-rate measurements," *IEEE Transactions on Aerospace and Electronic Systems*, vol. 38, no. 2, pp. 467–487, 2002.

[6] Y. Sun, P. Willett, and R. Lynch, "Waveform fusion in sonar signal processing," *IEEE Transactions on Aerospace and Electronic Systems*, vol. 40, no. 2, pp. 462–477, 2004.

[7] M. I. Skolnik, *Introduction to Radar Systems*, McGraw Hill, New York, NY, USA, 3rd edition, 2001.

[8] H. Deng, "Synthesis of binary sequences with good autocorrelation and cross-correlation properties by simulated annealing," *IEEE Transactions on Aerospace and Electronic Systems*, vol. 32, no. 1, pp. 98–107, 1996.

[9] Q. Liang, "Waveform design and diversity in radar sensor networks: theoretical analysis and application to automatic target recognition," in *Proceedings of International Workshop on Wireless Ad Hoc and Sensor Networks (IWWAN '06)*, New York, NY, USA, June 2006.

[10] M. A. Richards, *Fundamentals of Radar Signal Processing*, McGraw-Hill, New York, NY, USA, 2005.

[11] C. R. Lin and M. Gerla, "Adaptive clustering for mobile wireless networks," *IEEE Journal on Selected Areas in Communications*, vol. 15, no. 7, pp. 1265–1275, 1997.

[12] A. Iwata, C.-C. Chiang, G. Pei, M. Gerla, and T.-W. Chen, "Scalable routing strategies for ad hoc wireless networks," *IEEE Journal on Selected Areas in Communications*, vol. 17, no. 8, pp. 1369–1379, 1999.

[13] T.-C. Hou and T.-J. Tsai, "An access-based clustering protocol for multihop wireless ad hoc networks," *IEEE Journal on Selected Areas in Communications*, vol. 19, no. 7, pp. 1201–1210, 2001.

[14] M. Steenstrup, "Cluster-based networks," in *Ad Hoc Networking*, C. Perkins, Ed., chapter 4, pp. 75–138, Addison-Wesley, Reading, Mass, USA, 2001.

[15] P. Swerling, "Probability of detection for fluctuating targets," *IEEE Transactions on Information Theory*, vol. 6, no. 2, pp. 269–308, 1960.

Fault-tolerant and energy efficient cross-layer design for wireless sensor networks

Qilian Liang,* Lingming Wang and Qingchun Ren

Department of Electrical Engineering,
University of Texas at Arlington,
Arlington, TX 76019-0016, USA
E-mail: liang@uta.edu
E-mail: wang@wcn.uta.edu
E-mail: ren@wcn.uta.edu
*Corresponding author

Abstract: In wireless sensor networks, fault-tolerant and energy efficiency are two important topics. Some link failure may happen during data transmission and some threat can come from compromised nodes, which might relay incorrect information (packet) to the next node during routing. In this paper, we propose a Fault-tolerant and Energy Efficient Multipath-routing (FEEM) scheme aided with channel coding and interleaver, which is a cross-layer design approach. For multipath selection, we propose an Energy and Mobility-aware Geographical Multipath Routing (EM-GMR) scheme, which is based on Fuzzy Logic System (FLS) considering the remaining battery capacity, mobility and distance to the destination node. Simulation results show that our EM-GMR scheme can extend the network lifetime longer than the original geographical routing scheme which only considers distance to the destination location and this scheme can reduce the frame loss rate and link failure rate since mobility is considered. We demonstrate that even if certain paths have failure or are compromised, our FEEM scheme is still able to recover the transmitted message from failure with very low Bit Error Rate (BER) and Frame Error Rate (FER).

Keywords: wireless sensor networks; multipath routing; energy efficiency; fault-tolerant; channel coding.

Reference to this paper should be made as follows: Liang, Q., Wang, L. and Ren, Q. (2007) 'Fault-tolerant and energy efficient cross-layer design for wireless sensor networks', *Int. J. Sensor Networks*, Vol. 2, Nos. 3/4, pp.248–257.

Biographical notes: Qilian Liang received a PhD in Electrical Engineering from the University of Southern California (USC) in May 2000. He joined in the Faculty of the University of Texas at Arlington in August 2002. Prior to that he was a Member of Technical Staff in Hughes Networks Systems. His research Interests include sensor networks, wireless communications, signal processing for communications, etc. He has published more than 100 journals and conference papers. He received 2002 IEEE Transactions on Fuzzy Systems Outstanding Paper Award, 2003 US Office of Naval Research (ONR) Young Investigator Award and 2005 UTA College of Engineering Outstanding Young Faculty Award.

Lingming Wang is a PhD candidate in the Department of Electrical Engineering at the University of Texas at Arlington. Her research interests include sensor networks and physical layer communications.

Qingchun Ren is a PhD candidate in the Department of Electrical Engineering at the University of Texas at Arlington. Her research interests include sensor networks and MAC layer protocol design.

1 Introduction

Wireless sensor networking is an emerging technology that promises unprecedented ability to monitor and manipulate the physical world via a network of densely distributed wireless sensor nodes. The nodes can sense the physical environment in a variety of modalities, including acoustic, video, seismic, thermal, infrared, etc. In wireless sensor networks, there exists some challenges:

- The routing path (link) failure may happen during data transmission because of collision, node dying out (no battery), node busy or other accidents. Some applications require real-time information and data, which means retransmission is not possible.
- Security is an important topic for sensor networks, especially for the security-sensitive applications such as battlefield monitoring and homeland security. Traditional security mechanisms, such as authentication protocols, digital signature and encryption, can play important roles in achieving confidentiality, integrity, authentication and non-repudiation of communication in ad hoc networks, but these mechanisms are not sufficient by themselves for mobile sensor networks.

Copyright © 2007 Inderscience Enterprises Ltd.

- There exists energy constraint in wireless sensor networks because most sensors are battery operated, which means the operating Signal-to-Noise-Ratio (SNR) is very low and some energy efficiency schemes have to be developed.
- Sensor mobility may cause the existing point-to-point route invalid before another route must be chosen. In physical layer, sensor mobility generates channel fading during data transmission, which degrades the performance in terms of Bit Error Rate (BER) and Frame Error Rate (FER).

These challenges motivate us to design a fault-tolerant (tolerate link failure and compromised nodes) and energy efficient schemes for information and data transmission in wireless sensor networks. In this paper, we propose a Fault-tolerant and Energy Efficient Multipath-routing (FEEM) scheme aided with channel coding and interleaver in wireless sensor networks, which is a cross-layer approach.

Many routing protocols have been developed for ad hoc networks, which can be summarised as two categories: table-driven (e.g. destination sequenced distance vector (Bhagwat, 1994), cluster switch gateway routing (Chiang et al., 1997)) and source-initiated on-demand-driven (e.g. ad hoc on-demand distance vector routing (Perkins and Royer, 1999), dynamic source routing (Johnson and Maltz, 1996)). Lee and Gerla (2001) proposed a Split Multipath Routing protocol that builds maximal disjoint paths, where data traffic is distributed in two roots per session to avoid congestion and to use network resources efficiently. A Multipath Source Routing (MSR) scheme was proposed by Wang et al. (2001), which is an extension of Dynamic Source Routing (DSR). Their work focuses on distributing load adaptively among several paths. Nasipuri and Das (1999) presented the On-Demand Multipath Routing scheme, which is also an extension of DSR. In their scheme, alternative routes are maintained, which can be utilised when the primary one fails. Tsirigos et al. (2001) proposed a multipath routing scheme based on diversity coding. Three different paths are utilised to distribute the data and x-for-y diversity coding is used to offer protection against at most x lost blocks out of the total $x + y$ blocks. Security in ad hoc networks and sensor networks have been studied by some researchers. Zhou and Haas (1999) took advantage of inherent redundancy in ad hoc networks – multiple routes between nodes – to defend routing against denial of service attacks. Law et al. (2002) benchmarked some well-known cryptographic algorithms in search for the best compromise in security and energy efficiency on a typical sensor node. Deng et al. (2003) evaluated the performance of INSENS, an INtrusion-tolerant routing protocol for wireless sensor networks. Karlof and Wagner (2003) considered routing security in wireless sensor networks. However, none of these security-related approaches considered to solve this problem from physical layer design. In additions, energy efficient routing has been extensively studied by this community. In Xue and Li (2001), a location-aided power aware routing protocol was proposed. Singh et al. (1998) proposed power-aware routing and discussed different metrics in power-aware routing; Li et al. (2001) extended their work and proposed an online power aware routing in wireless ad hoc networks. A greedy distance routing (Bose and Morin, 1999) was proposed for unicast geographic routing. Greedy Perimeter Stateless Routing (GPSR) (Karp and Kung, 2000) was proposed as a mixture of greedy distance routing and perimeter protocol. A protocol named GEAR which stands for *Geographical and Energy-Aware Routing* was proposed by Yu et al. (2001), whose goal is to efficiently route a message to a geographic region while at the same time performing some load-balancing on the nodes used and thus avoiding energy depletion. But node mobility was not considered in this protocol. In this paper, we propose an Energy and Mobility-aware Geographical Multipath Routing (EM-GMR) scheme for wireless sensor networks and compare with Geographical Multipath Routing (GMR) scheme.

The rest of this paper is organised as follows. In Section 2, we present an EM-GMR in a wireless sensor network. In Section 3, we present our FEEM scheme Aided with Channel Coding and Interleaver. The simulation results and performance analysis are presented in Section 4 and in Section 5, we conclude this paper.

2 EM-GMR

In this paper, we propose an EM-GMR scheme. In the existing geographical routing approach (e.g. Jain et al., 2001), the path selection does not consider the remaining battery capacity of each node and its mobility, which are two very important factors for energy efficiency and network lifetime. Sensor mobility means the degree of channel fading and high mobility requires higher SNR for operating if the BER or FER requirements are given. In our EM-GMR, we consider *distance to the sensor node*, *remaining battery capacity* and *mobility* of each sensor node. The geographical location of destination is known to the source node (as in Jain et al., 2001) and the physical location of each sensor node can be estimated easily if the locations of three sensor nodes (within a communication range) are known in wireless sensor network. Our scheme is a fully distributed approach where each sensor only needs the above three parameters and we use Fuzzy Logic Systems (FLS) to handle these three parameters in the EM-GMR.

2.1 Preliminaries: overview of FLSs

A FLS includes fuzzifier, inference engine, rules and defuzzifier (Mendel, 1995). When an input is applied to a FLS, the inference engine computes the output set corresponding to each rule. The defuzzifer then computes a crisp output from these rule output sets. Consider a p-input 1-output FLS, using singleton fuzzification, *centre-of-sets* defuzzification (Mendel, 2001) and 'IF-THEN' rules of the form

$$R^l: \text{IF} x_1 \text{ is } \text{F}_1^l \text{and} x_2 \text{ is } \text{F}_2^l \text{ and } \cdots \text{and} x_p \text{ is } \text{F}_p^l,$$
$$\text{THEN} y \text{ is } \text{G}^l$$

Assuming singleton fuzzification, when an input $\mathbf{x}' = \{x_1', \ldots, x_p'\}$ is applied, the degree of firing corresponding to the lth rule is computed as

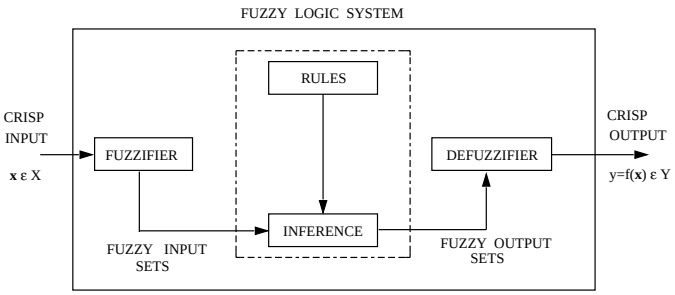
$$\mu_{\mathrm{F}_1^l}(x_1') \star \mu_{\mathrm{F}_2^l}(x_2') \star \cdots \star \mu_{\mathrm{F}_p^l}(x_p') = \mathcal{T}_{i=1}^{p} \mu_{\mathrm{F}_i^l}(x_i') \quad (1)$$

where $\star$ and $\mathcal{T}$ both indicate the chosen t-norm. There are many kinds of defuzzifiers. In this paper, we focus, for illustrative purposes, on the centre-of-sets defuzzifier (Figure 1) (Mendel, 2001). It computes a crisp output for the FLS by first computing the centroid, c_{G^l}, of every consequent set G^l, and then computing a weighted average of these centroids. The weight corresponding to the lth rule consequent centroid is the degree of firing associated with the lth rule, $\mathcal{T}_{i=1}^{p} \mu_{\mathrm{F}_i^l}(x_i')$, so that

$$y_{\cos}(\mathbf{x}') = \frac{\sum_{l=1}^{M} c_{\mathrm{G}^l} \mathcal{T}_{i=1}^{p} \mu_{\mathrm{F}_i^l}(x_i')}{\sum_{l=1}^{M} \mathcal{T}_{i=1}^{p} \mu_{\mathrm{F}_i^l}(x_i')} \quad (2)$$

where M is the number of rules in the FLS (Figure 1).

Figure 1 The structure of a FLS



2.2 FLS for node selection in multipath routing

In this paper, we assume that each sensor node keeps a table which has some information about its neighbour nodes: locations, battery level and mobility. The table is updated periodically by the locally broadcasted information (beacon) from each neighbour node. The structure of a beacon includes node ID, its position, battery level and mobility. We define a new term, *coherence time*, during which the three parameters (locations, battery level and mobility) do not change very much. Coherence time is the shortest time duration that a sensor node will send another beacon. Each sensor examines itself the status of the three parameters in every coherence time period and if a certain parameter has changed above a threshold, it will locally broadcast a beacon (Figure 2).

Figure 2 Structure of a beacon

Type	Self Node ID	Position_X	Position_Y	Energy	Mobility

There are one control channel and one data traffic channel in the sensor network. Direct Sequence Code-Division Multiple Access (DS-CDMA) is used and 64-bit Walsh sequence are used as spreading sequence. The control channel is a common channel which means every node in its local communication range is able to obtain the message and all 0's Walsh sequence is reserved for control channel. Each source node randomly generates M 64-bit Walsh sequences and a spreading sequence is used for each path. The spreading sequence is relayed to the next hop node via common control channel.

In our EM-GMR for M-path routing, the source node select M nodes in its communication range for the first hop relay. Assume there are N ($N > M$) nodes in its communication range, nodes who are further to the destination node than the source node are not considered. Choosing M nodes from remaining eligible nodes is based on a FLS (as will be described in detail). Starting the second hop, each node in the M-path selects its next hop node also using a FLS.

In our FLS design, we set up fuzzy rules for node selection based on the following three descriptors:

1 distance of a node to the destination

2 its remaining battery capacity and

3 its degree of mobility.

The linguistic variables used to represent the distance of a node to the destination were divided into three levels: *near*, *moderate* and *far* and those to represent its remaining battery capacity and degree of mobility were divided into three levels: *low*, *moderate* and *high*. The consequent – the possibility that this node will be selected – was divided into five levels, *Very Strong, Strong, Medium, Weak* and *Very Weak*. So we need to set up $3^3 = 27$ (because every antecedent has 3 fuzzy subsets and there are 3 antecedents) rules for this FLS.

A desired node to be included into the path should have near distance to the destination, high remaining battery capacity (so that the network life can last longer) and low mobility (so that channel fading will not be severe). Based on this fact, we design a FLS using rules summarised in Table 1. We used trapezoidal Membership Functions (MFs) to represent *near*, *low*, *far* and *high* and triangle MFs to represent *moderate* (Figure 3).

For every input (x_1, x_2, x_3), the output is computed using

$$y(x_1, x_2, x_3) = \frac{\sum_{l=1}^{27} \mu_{\mathrm{F}_l^1}(x_1) \mu_{\mathrm{F}_l^2}(x_2) \mu_{\mathrm{F}_l^3}(x_3) c^l}{\sum_{l=1}^{27} \mu_{\mathrm{F}_l^1}(x_1) \mu_{\mathrm{F}_l^2}(x_2) \mu_{\mathrm{F}_l^3}(x_3)} \quad (3)$$

where c^l is the centroid of consequent set. The output from FLS is degree of the possibility that this node will be selected into the path.

Our EM-GMR scheme consists of route discovery phase, route reconstruction phase and route deletion phase. In the route discovery phase, the source node uses a FLS to evaluate all eligible nodes (closer to the destination location) in its communication range based on the parameters of each node: distance to the destination, remaining battery capacity and degree of mobility. The source node chooses the top M nodes based on the degree of the possibility (output of FLS) that this node will be selected. The source node sends a Route Notification (RN) packet to each desired node and each desired node will reply using a REPLY packet if it is available. The structure of RN and REPLY is summarised in Figure 4. If after a certain period of time, the source node did not receive

REPLY from some desired node, it will pick the node with the $M + 1$st degree of selection possibility. In the second hop, the selected node in each path will choose its next hop node uses a FLS. As illustrated in Figure 5, node B needs to choose one node from eligible nodes C, D, E, F, H based on their three parameters and sends RN packet to the selected node and waits for REPLY. If the top one node is unavailable (selected by another path or busy), then the top second node will be selected. By this means, M paths can be set up.

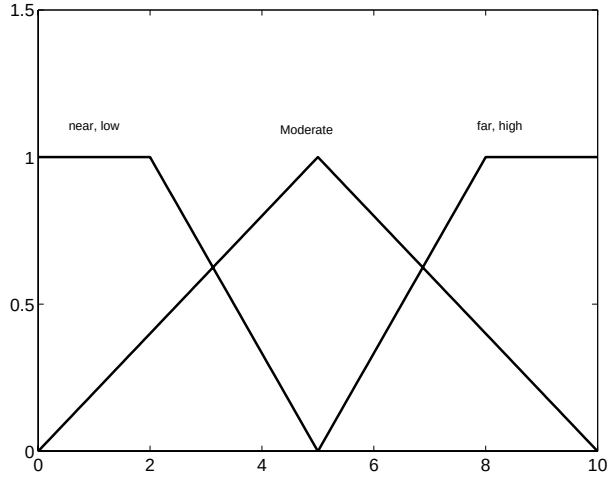
Table 1 The rules for node selection in multipath routing. Antecedent 1 (Ante 1) is distance of a node to the destination, Antecedent 2 (Ante 2) is its remaining battery capacity, Antecedent 3 (Ante 3) is its degree of mobility and Consequent is the possibility that this node will be included into the path

Rule #	*Ante 1*	*Ante 2*	*Ante 3*	Consequent
1	Near	Low	Low	Medium
2	Near	Low	Moderate	Weak
3	Near	Low	High	Very weak
4	Near	Moderate	Low	Medium
5	Near	Moderate	Moderate	Strong
6	Near	Moderate	High	Weak
7	Near	High	Low	Very strong
8	Near	High	Moderate	Strong
9	Near	High	High	Medium
10	Moderate	Low	Low	Weak
11	Moderate	Low	Moderate	Very weak
12	Moderate	Low	High	Very weak
13	Moderate	Moderate	Low	Medium
14	Moderate	Moderate	Moderate	Medium
15	Moderate	Moderate	High	Weak
16	Moderate	High	Low	Strong
17	Moderate	High	Moderate	Strong
18	Moderate	High	High	Weak
19	Far	Low	Low	Weak
20	Far	Low	Moderate	Very weak
21	Far	Low	High	Very weak
22	Far	Moderate	Low	Weak
23	Far	Moderate	Moderate	Weak
24	Far	Moderate	High	Very weak
25	Far	High	Low	Medium
26	Far	High	Moderate	Strong
27	Far	High	High	Medium

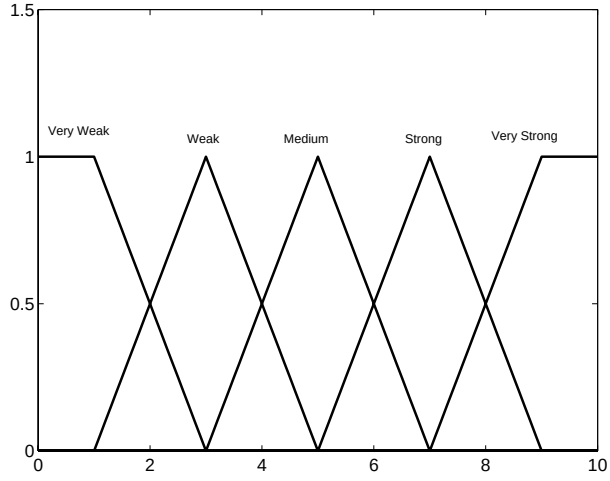
Each node is mobile, it may be possible that some node moves out of the communication range or some node dies out, which will lead to link failure, then a route reconstruction phase is started. The node immediately before the failure node in the routing path will apply FLS to determine the selection possibility for all its eligible neighbour nodes and choose the top one degree node (via RN-REPLAY procedure). The new node will determine its next node accordingly. Based on the source ID and destination location information in RN, it is easy to reconstruct the partial path failure.

The energy, mobility and physical location of each node are changing. It may be possible that a node (in path) observes that its next node is not the optimal after a while, then this node will initiate a route deletion phase. This node will send an RN packet to the optimal node via common control channel and this RN packet will also be received by the original relay node who will notice that the original path is deleted.

Figure 3 The MFs used to represent the linguistic labels (a) MFs for antecedents and (b) MFs for consequent



(a)



(b)

Figure 4 RN and REPLY packet structure

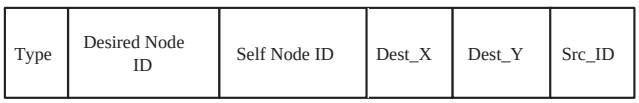
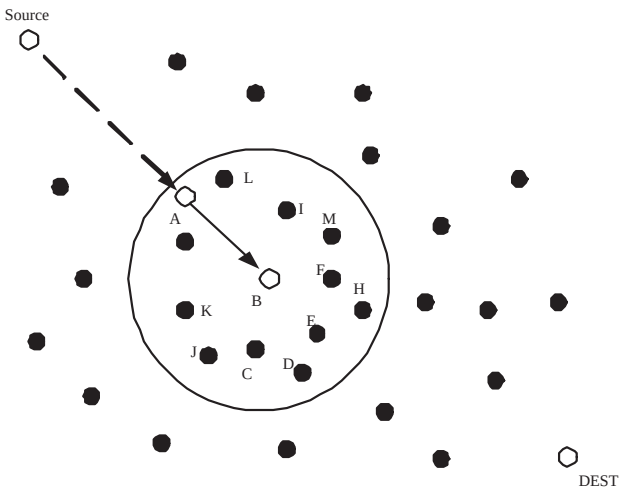


Figure 5 Illustration of node selection



3 FEEM Aided with channel coding

In our fault-tolerance, we will tolerate link failure and security-related problems. In the security part, there are two sources of threats to routing protocols. The first comes from external attacks. By injecting erroneous routing information, replaying old routing information or distorting routing information, an attacker could successfully partition a network or introduce excess traffic load into the network by causing retransmission and inefficient routing. This kind of attack can be overcome using cryptographic schemes such as digital signature to protect the routing information (Zhou and Haas, 1999). The second and also the more severe kind of threats comes from compromised nodes, which might relay incorrect information (packet) to the next node during routing. Detection of such incorrect information is difficult: merely requiring relayed information to be signed by each node would not work because compromised nodes are able to generate valid signatures using their private keys. In this paper, we focus on the second threat and our goal is: even if certain paths are compromised, the receiver node may still be able to recover message from errors. In this paper, we propose a FEEM scheme aided with channel coding and interleaver.

In our FEEM with channel coding and interleaver scheme. We apply convolutional coding to encode the information bits, then the code words are interleaved. Interleaver (Wicker, 1995) was used to eliminate the correlation of the noise/fading process affecting adjacent symbols in a received code word, but here we use interleaver to make sure that the incorrect symbols in one compromised path will be spread after de-interleaver so that the Viterbi decoder will perform well. The interleaved bits are inserted with some unique words (for demodulation purpose) and then these bits are modulated to symbols. By this means, a frame has been built. For M-path routing, we split the symbols in one frame to M equal-length bursts and each path transmits one burst in parallel. The receiver node demodulates each received burst from different path and provide soft-decision output. The receiver node combines all the soft-decision output from each burst according to the order when they are transmitted. In this paper, we use the demodulation algorithm we proposed in Liang (2003) for soft decision output. In case one or more bursts are lost due to link failure during transmission, the receiver node will provide 0's as the soft decision output. Then de-interleaving is performed to the soft-decision output and the de-interleaved data are used as the input to Viterbi decoder. The decoded output from Viterbi decoder are the information bits with possible errors due to compromised nodes (providing random data relay) and Additive White Gaussian Noise (AWGN). We summarise this scheme using a diagram in Figure 6.

4 Simulations

4.1 Sensor mobility and channel fading

Mobility of a sensor generates a doppler shift, which is a key parameter of fading channel. The doppler shift is

$$f_{\mathrm{d}} = \frac{v}{c} f_{\mathrm{c}} \tag{4}$$

where v is the speed of a sensor, c is the speed of light (3×10^8 m/s) and f_{c} is the carrier. In our simulation, we used the carrier is 5 GHz. For reference, if a sensor moves with speed 12 m/s, the doppler shift is 200 Hz.

We model channel fading in sensor networks as Rician fading. Rician fading occurs when there is a strong specular (direct path or line of sight component) signal in addition to the scatter (multipath) components. For example, in communication between two infraed sensors, there exist a direct path. The channel gain,

$$g(t) = g_I(t) + jg_Q(t) \tag{5}$$

can be treated as a wide-sense stationary complex Gaussian random process and $g_I(t)$ and $g_Q(t)$ are Gaussian random processes with non-zero means $m_I(t)$ and $m_Q(t)$, respectively and they have same variance σ_g^2, then the magnitude of the received complex envelop has a Rician distribution,

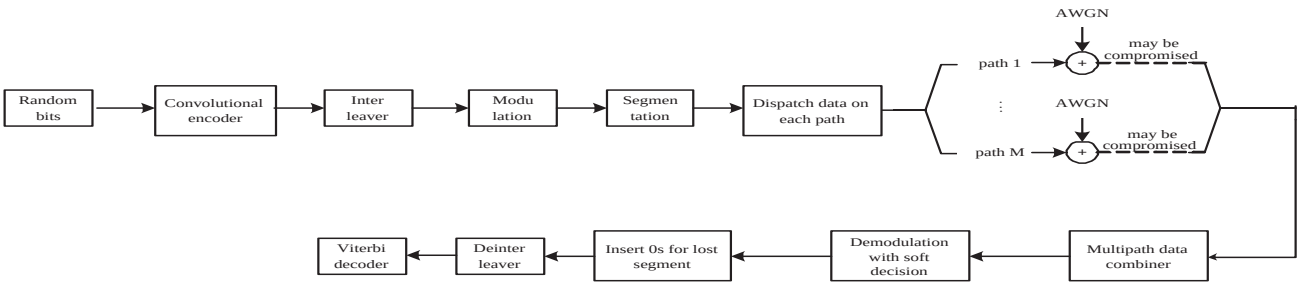
$$p_\alpha(x) = \frac{x}{\sigma^2} \exp\left\{-\frac{x^2+s^2}{2\sigma^2}\right\} I_0\left(\frac{xs}{\sigma^2}\right) \quad x \geq 0 \tag{6}$$

where

$$s^2 = m_I^2(t) + m_Q^2(t) \tag{7}$$

and $I_0(\cdot)$ is the zero order modified Bessel function. This kind of channel is known as Rician fading channel. A Rician channel is characterised by two parameters, Rician factor K which is the ratio of the direct path power to that of the multipath, that is, $K = s^2/2\sigma^2$, and the Doppler spread (or single-sided fading bandwidth) f_{d}. We simulate the Rician fading using a direct path added by a Rayleigh fading generator. The Rayleigh fade generator is based on Jakes (1993) model in which an ensemble of sinusoidal waveforms are added together to simulate the coherent sum of scattered rays with Doppler spread f_{d} arriving from different directions to the receiver. The amplitude of the Rayleigh fade generator is controlled by the Rician factor K. The number of oscillators to simulate the Rayleigh fading is 60.

Figure 6 The diagram of FEEM aided with channel coding and interleaver



4.2 Simulations of EM-GMR

We ran our simulations using OPNET. It was found that 59 sensors were deployed randomly in an area with size 10 km × 10 km and communication range (radius) was 1 k. Totally 59 sensors were deployed initially. The source and destination sensors were set with 2 J initially and 5 couples of source and destination nodes were communicating at the same time in this network. All the other sensors had initial energy from 0 to 2 J. Each node (including source and destination nodes) had moving speed ranging from 0 to 10 m/s and its moving speed changed in every 10 sec. The frame length was 512 symbol and symbol rate was 9.6 ksym/s in our simulation.

Each sensor locally broadcasted a beacon message in every 2 sec to keep link, so that neighbour table could be updated (including new neighbour joins in and old neighbours expire). These information are used for route discovery, reconstruction and deletion. The coherence time were set as 10 sec in our simulation.

We used the same energy consumption model as in Heinzelman (2002) for the radio hardware energy dissipation where the transmitter dissipates energy to run the radio electronics and the power amplifier and the receiver dissipates energy to run the radio electronics. We chose the path-loss exponent $p = 2$. To transmit an l-symbol message a distance d, the radio expends:

$$E_{\mathrm{T}x}(l,d) = E_{\mathrm{T}x-\mathrm{elec}}(l) + E_{\mathrm{T}x-\mathrm{amp}}(l,d)$$
$$= lE_{\mathrm{elec}} + l\epsilon d^2 \tag{8}$$

and to receive this message, the radio expends

$$E_{\mathrm{R}x}(l) = E_{\mathrm{R}x-\mathrm{elec}}(l) = lE_{\mathrm{elec}} \tag{9}$$

The electronics energy, E_{elec}, as described in Heinzelman (2002), depends on factors such as coding, modulation, pulse-shaping and matched filtering and the amplifier energy, ϵd^2 depends on the distance to the receiver and the acceptable bit error rate. In this paper, we chose: $E_{\mathrm{elec}} = 50$ nJ/sym, $\epsilon = 10$ pJ/sym/m^2. Same as Heinzelman (2002) and Wang et al. (1999), the energy for data aggregation is set as $E_{\mathrm{DA}} = 5$ nJ/sym/signal.

We compared our EM-GMR against the Geographical Multipath Routing (GMR) scheme where only distance to the destination is considered. In Figure 7, we plotted the simulation time versus the number of nodes dead. Observe that when 50% nodes (30 nodes) die out, the network lifetime for EM-GMR has been extended about $(175-125)/125 = 40\%$. In Figure 8, we compared the frame loss rate of these two scheme. Observe that our EM-GMR outperforms the GMR for about 20% less frame loss. The average latency during transmission (end-to-end) is 419.68 ms for our EM-GMR and 407.5 ms for GMR, and link failure rate for EM-GMR is 5.68% but for GMR is 10.42%.

4.3 Performance of FEEM for link failure

We evaluated our FEEM scheme using computer simulations. We ran our simulations for four-path FEEM and six-path transportation FEEM and assumed each path has 2% failure rate. QPSK modulation and convolutional codes with rate 1/2 and connections 101 and 111 (in binary) were used in the transmitting sensor (encoder) and receiver node (Viterbi decoder).

Figure 7 Simulation time versus number of nodes dead

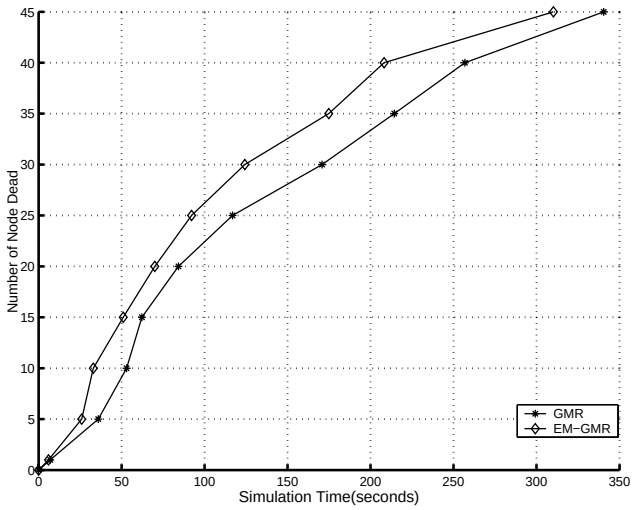
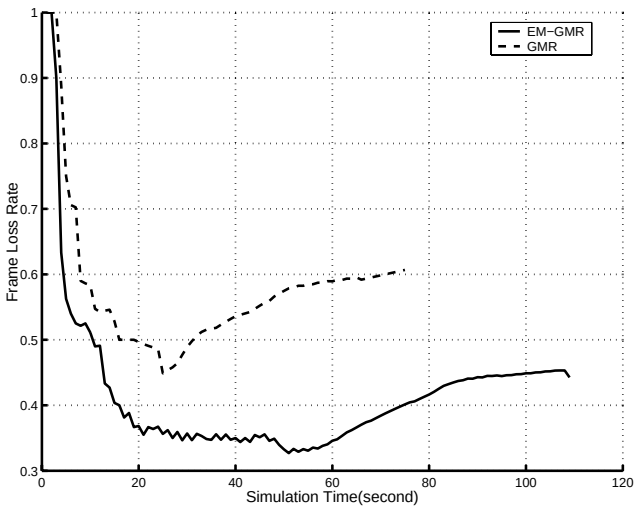


Figure 8 Simulation time versus frame loss rate

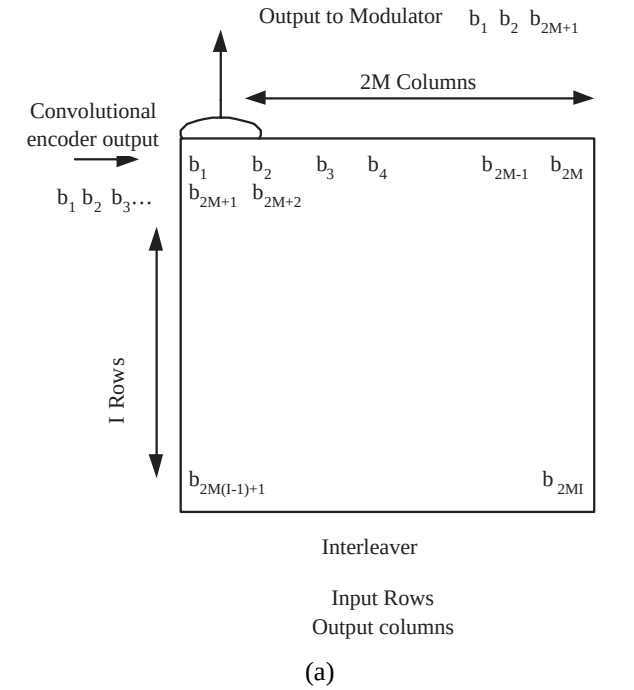


For four-path FEEM, a frame structure with 820 QPSK symbols (800 symbols payload and 20 symbols UW) were used. We used block interleaver with size 8×200 to interleave the payload bits (after channel coding). The interleaver and de-interleaver is shown in Figure 9(a) and (b) where $M = 4$ in this paper. Then we construct a frame by inserting UW and modulation. One frame is split to four equal-length bursts (205 sym/burst) for transmission. We ran Monte-Carlo Simulations for 10^5 frames at each E_b/N_0 value and compared its performance against 2-path diversity. In 2-path diversity, the transmitted symbols in each path are identical, but it will have big advantage if one path has failure during transportation. In the simulation, the frame in each path has 400 payload symbols and 10 UW symbol per burst without coding. Considering two paths, the total number of symbols (820 symbols) is the same as the FEEM per transportation.

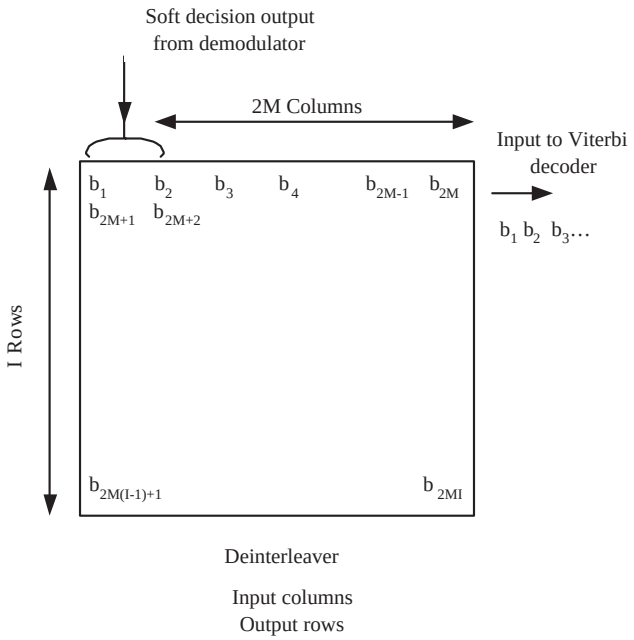
In Figure 10, we summarised the average BER versus E_b/N_0. Observe that the FEEM scheme has more than 3 dB

gain comparing to the 2-path diversity scheme. It clearly shows a BER floor for the FEEM scheme at high E_b/N_0 because there exists 2% failure rate for each path. But the performance of our FEEM is very good (e.g. BER $= 3\times10^{-4}$ at $E_b/N_0 = 5$ dB).

Figure 9 The interleaver and de-interleaver structures: (a) interleaver and (b) de-interleaver



(a)



(b)

In mobile wireless sensor networks, there exists channel fading during data transportation. In the simulation, we used Rician fading $K = 9$ dB and $f_d = 20$ Hz. We compared our FEEM scheme against the two-path diversity with Maximal Ratio Combination (MRC) scheme. Diversity is very powerful in combatting channel fading Stuber (2001) and MRC is the optimal combination scheme for diversity. We used the same frame structure as that in dual transportation scheme (Figure 11(b)). We ran Monte-Carlo Simulations for 2×10^5 frames at each E_b/N_0 value for four-path FEEM and diversity with MRC and summarised the results in Figure 12. Observe that four-path FEEM can achieve more than 1 dB gain at BER $= 10^{-3}$.

Figure 10 Average BER versus E_b/N_0 for four-path and six-path FEEM and 2-path diversity in static AWGN channel

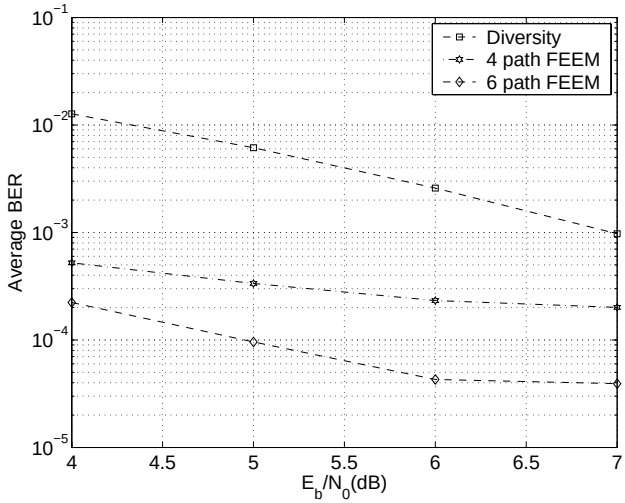
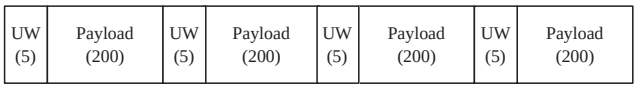
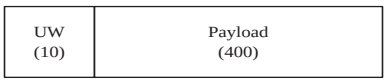


Figure 11 Frame structure (in symbols) we used in our simulations: (a) four-path FEEM and (b) 2-path diversity



(a)



(b)

In six-path FEEM, a frame structure with 930 QPSK symbols (900 symbols payload and 30 symbols UW) were used. We used block interleaver with size 12×150 to interleave the payload bits (after channel coding) and then then construct a frame by inserting UW and modulation. One frame is split to six equal-length bursts (155 sym/burst) for transmission.

We ran Monte-Carlo Simulations for 10^5 frames at each E_b/N_0 value and compared its performance against the 2-path diversity. The frame structure is provided in Figure 13(b). In Figure 10, we plotted the average BER versus E_b/N_0. Observe that more than 4 dB gain can be achieved using FEEM.

Similarly, we performed simulations for Rician fading channel $K = 9$ dB and $f_d = 20$ Hz, and compared our six-path FEEM against the two-path diversity with MRC. The simulation results are summarised in Figure 12, which demonstrates that more than 2 dB gain can be achieved using six-path FEEM. Observe Figures 10 and 12, for larger number of paths in FEEM, the performance is better, which means the fault is more tolerable.

Figure 12 Average BER versus E_b/N_0 for FEEM and diversity with MRC in Rician fading channel ($K = 9$ dB, $f_d = 20$ Hz)

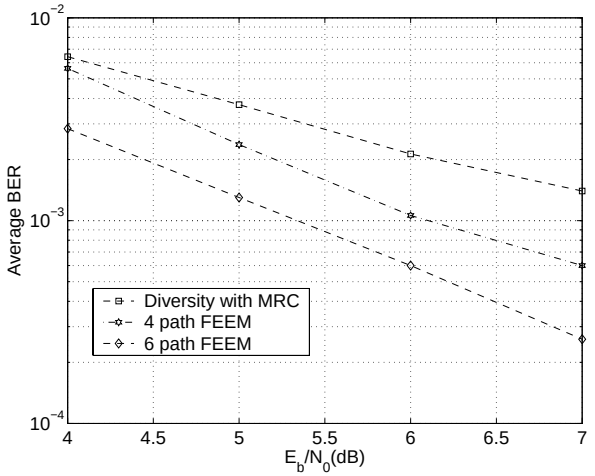
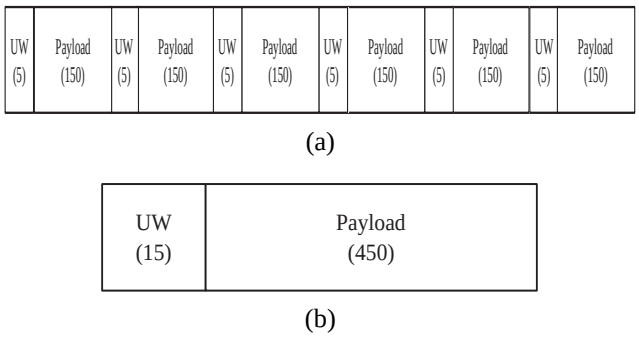


Figure 13 Frame structure (in symbols) we used in our simulations: (a) six-path FEEM and (b) 2-path diversity



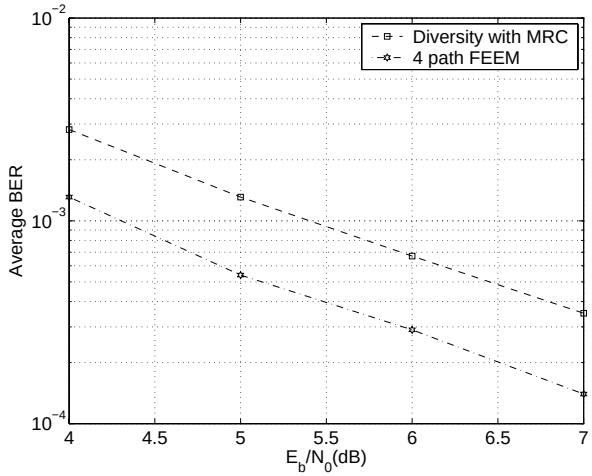
We also simulated the FER versus SNR. In Figure 14(a) and (b), we plotted the BER and FER versus SNR for Rician fading channel $K = 15$ dB, $f_d = 10$ Hz, respectively. Observe Figure 14(b), 1.5 dB gain can be achieved at FER = 2%.

4.4 Performance of FEEM for compromised nodes

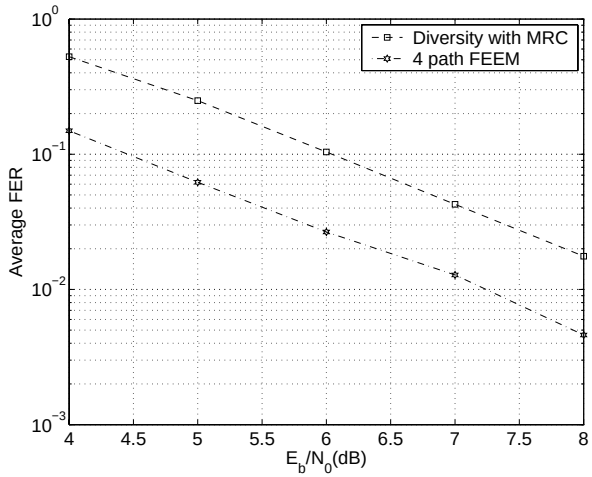
Due to space limitation, we only include the performance for secure multipath routing where each path has 1% probability to be compromised. When a path is compromised, the received burst from this path is some data with random value. We evaluated our FEEM scheme using computer simulations. We ran our simulations for six-path SEEM aided with channel coding and interleaver. We assumed that each path has probability 1% to be compromised. QPSK modulation and convolutional codes with rate 1/2 and connections 101 and 111 (in binary) were used in the transmitting sensor (encoder) and receiver node (Viterbi decoder). We used the frame structure plotted in Figure 13(a) for six-path FEEM. Block interleaver 12 × 300 (in bits) is used before modulation and de-interleaver 300 × 12 (in soft-decision symbol with resolution 3 bits per symbol) is used after demodulation.

In our channel coding, we introduced some redundancy (coding rate 1/2), so we compared our FEEM scheme against 2-path diversity, which means both schemes introduced the same amount of redundancy. The frame structure of each path in the 2-path diversity is plotted in Figure 13(b).

Figure 14 Average BER and FER versus E_b/N_0 for FEEM and diversity with MRC in Rician fading channel ($K = 15$ dB, $f_d = 10$ Hz): (a) BER and (b) FER



(a)



(b)

We ran Monte-Carlo simulations for 10^5 frames at each E_b/N_0 value for our FEEM scheme and diversity with MRC. We evaluated a four-path FEEM for Rician fading channel with random K from 9 to 12 dB and random f_d from 10 to 200 Hz and each path has 1% probability to be compromised. We ran Monte-Carlo Simulations for 10^5 frames at each E_b/N_0 value for our SEEM scheme and diversity with MRC, and the channel fading is different from frame to frame. In Figure 15, we summarised the average BER versus E_b/N_0. Observe that about 1.4 dB gain can be achieved at BER = 0.5%. We also evaluated a six-path FEEM for Rician fading channel with random K from 9 to 12 dB and random f_d from 10 to 200 Hz, and the BER is plotted in Figure 16. Observe that about 3 dB gain can be achieved at BER = 0.5%.

4.5 Performance analysis

Why our FEEM scheme can perform very well even with 2% link failure or 1% to be compromised in each path? This can be explained based on the successful example of

puncturing. Puncturing is often used to generate additional rates from a single convolutional code (Cain et al., 1979; Hagenauer, 1988). The basic idea behind puncturing is not to transmit some of the bits output by the convolutional encoder, thus increase the rate of the code. This increase in rate decrease the free distance of the code, but usually the resulting free distance is very close to the optimum one. The receiver inserts dummy bits to replace the punctured bits in the receiver, hence only one encoder/decoder pair is needed to generate several different code rates. In our M-path routing, the receiver node inserts 0's if one burst is lost during transmission or a compromised path provides random values to the receiver node. Then the receiver node de-interleaves the soft-decision output from demodulator (random value), which is very similar that some dummy bits are used to replace the bits from compromised path. But in our scheme, the effective puncturing pattern in terms of the number of bits and puncture location is time-varying from frame to frame.

Figure 15 Average BER versus E_b/N_0 for four-path FEEM and diversity with MRC in Rician fading channel with random K from 9 to 12 dB and random f_d from 10 to 200 Hz

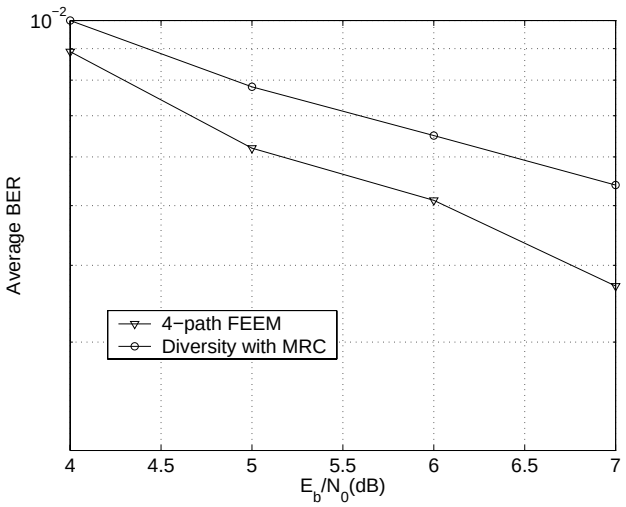
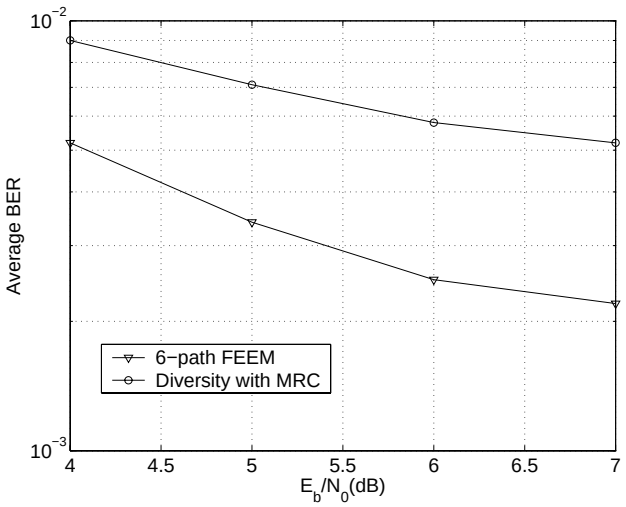


Figure 16 Average BER versus E_b/N_0 for six-path FEEM and diversity with MRC in Rician fading channel with random K from 9 to 12 dB and random f_d from 10 to 200 Hz



5 Conclusion

We have proposed an EM-GMR for wireless sensor networks. The remaining battery capacity, mobility and distance to the destination node of candidate sensors in the local communication range were taken into consideration for next hop relay node selection and a FLS was applied to the decision making. Simulation results showed that this scheme could extend the network lifetime about 40% comparing to the GMR scheme where only distance to the destination was considered. Besides, this scheme could tremendously reduce the frame loss rate and link failure rate since mobility was considered.

In wireless sensor networks, the energy is limited and some link failure may happen during data transmission. In additions, threat can come from compromised nodes, which might relay incorrect information (packet) to the next node during routing. Detection of such incorrect information is very difficult. In this paper, we proposed a FEEM aided with channel coding and interleaver scheme for wireless sensor networks to tolerate this. The M-path in multipath routing are selected using EM-GMR. Based on the simulation results, we draw the following conclusions:

1 our scheme performs much better than the diversity with MRC scheme in terms of BER

2 our FEEM can tolerate some link failures and compromised, which makes wireless sensor networks survivable and resilient

3 our FEEM scheme can work at low SNR (e.g. $E_b/N_0 = 5$ dB), which can save lots of energy because energy constraint is one of the most important topics in wireless sensor networks and existing studies show that most energy is consumed in communication-related activities in wireless sensor networks

4 the larger the number of paths in FEEM, the better the performance, which means the fault is more tolerable

5 the network lifetime can be extended using our FEEM scheme.

Acknowledgement

This work was supported by the US Office of Naval Research (ONR) Young Investigator Program Award under Grant N00014-03-1-0466.

References

Bhagwat, C.P. (1994) 'Highly dynamic destination-sequenced distance vector routing', *Proceedings. of ACM SIGCOMM'94*, pp.234–244.

Bose, P. and Morin, P. (1999) 'Online routing in triangulations', *Proceedings of Tenth International Symposium on Algorithm and Computation*, Springer-Verlag, pp.113–122.

Cain, J.B. Clark Jr., G.C. and Geist, J.M. (1979) 'Punctured convolutional codes of rate (n-1)/n and simplified maximum likelihood decoding', *IEEE Transactions on Information Theory*, Vol. 25, pp.97–100.

Chiang, C-C., et al. (1997) 'Routing in clustered multihop mobile wireless networks with fading channel', *Proceedings of IEEE Singapore International Conference on Networks*.

Deng, J., Han, R. and Mishra, S. (2003) 'A performance evaluation of intrusion-tolerant routing in wireless sensor networks', *IPSN 2003*.

Hagenauer, J. (1988) 'Rate compatible punctured convolutional codes and their applications', *IEEE Transactions on Communications*, Vol. 36, pp.389–400.

Heinzelman, W.B. (2002) 'An application-specific protocol architecture for wireless microsensor networks', *IEEE Transactions on Wireless Communications*, Vol. 1, No. 4, pp.660–670.

Jain, R., Puri, A. and Sengupta, R. (2001) 'Geographical routing using partial information for wireless sensor networks', *IEEE Personal Communications*, pp.48–57.

Jakes, W.C. (1993) *Microwave Mobile Communication*, New York, NY: IEEE Press.

Johnson, D. and Maltz, D. (1996) *Mobile Computing*, Kluwer Academic Publishers.

Karlof, C. and Wagner, D. (2003) 'Secure routing in sensor networks: attacks and countermeasures', *SNPA 2003*.

Karp, B. and Kung, H.T. (2000) 'GPSR: greedy perimeter stateless routing for wireless networks', *ACM MobiCom*, pp.243–254.

Law, Y.W., Dulman, S., Etalle, S. and Havinga, P. (2002) 'Assessing security-critical energy-efficient sensor networks', Department of Computer Science, University of Twente, *Technical Report TR-CTIT-02-18*, July 2002.

Lee, S.J. and Gerla, M. (2001) 'Split multipath routing with maximally disjoint paths in ad hoc networks', *ICC 2001*.

Li, Q., Aslam, J. and Rus, D. (2001) 'Online power-aware routing in wireless ad-hoc networks', *Proceedings of Annual ACM/IEEE International Conference on Mobile Computing and Networking (MobiCom)*, Rome, Italy, pp.97–107.

Liang, Q. (2003) 'Optimal demodulator for satellite-based wireless ATM networks', *IEEE International Conference on Communications (ICC)*, Alaska.

Mendel, J.M. (1995) 'Fuzzy logic systems for engineering: a tutorial', *Proceedings of the IEEE*, Vol. 83, No. 3, pp.345–377.

Mendel, J.M. (2001) *Uncertain Rule-Based Fuzzy Logic Systems*, Upper Saddle River, NJ: Prentice-Hall.

Nasipuri, A. and Das, S.R. (1999) 'An on-demand multipath routing for mobile ad hoc networks', *IEEE ICCCN 1999*, pp.64–70.

Perkins, C.E. and Royer, E. (1999) 'Ad hoc on demand distance vector routing', *Proceedings of Second IEEE Workshop on Mobile Computing Systems and Applications*.

Singh, S., Woo, M. and Raghavendra, C.S. (1998) 'Power-aware routing in mobile ad hoc networks', *Proceedings of Annual ACM/IEEE International Conference on Mobile Computing and Networking (MobiCom)*, Dallas, TX, pp.181–190.

Stuber, G.L. (2001) *Principles of Mobile Communication*, 2nd edition, Kluwer Academic Press.

Tsirigos, A., et al. (2001) 'Multipath routing in mobile ad hoc networks or how to route in the presence of frequent topology changes', *IEEE MILCOM 2001*, pp.878–883.

Wang, A. et al. (1999) 'Energy-scalable protocols for battery-operated microsensor networks', *Proceedings of IEEE Workshop on Signal Processing Systems (SiPS'99)*, Taipei, Taiwan, pp.483–492.

Wang, L., Shu, Y.T., Dong, M., Zhang, L.F. and Yang, W.W. (2000) 'Multipath source routing in wireless ad hoc networks', *Canadian Conference on Electrical and Computer Engineering*, Vol. 1, pp.479–483.

Wicker, S.B. (1995) *Error Control Systems for Digital Communication and Storage*, Upper Saddle River, NJ: Prentice Hall.

Xue, Y. and Li, B. (2001) 'A location-aided power-aware routing protocol in mobile ad hoc networks', *Proceedings of Globecom'2001*, San Antonio, TX, pp.2837–2841.

Yu, Y., Govindan, R. and Estrin, D. (2001) 'Geographical and energy aware routing: a recursive data dissemination protocol for wireless sensor networks', *Technical Report UCLA/CSD-TR-01-0023*, UCLA Computer Science Department.

Zhou, L. and Haas, Z.J. (1999) 'Securing ad hoc networks', *IEEE Networks, Special Issue on Network Security*.

Hindawi Publishing Corporation
EURASIP Journal on Wireless Communications and Networking
Volume 2007, Article ID 84256, 8 pages
doi:10.1155/2007/84256

Research Article

Hop-Distance Estimation in Wireless Sensor Networks with Applications to Resources Allocation

Liang Zhao and Qilian Liang

Department of Electrical Engineering, University of Texas at Arlington, Arlington, TX 76010, USA

Received 22 May 2006; Revised 7 December 2006; Accepted 26 April 2007

Recommended by Huaiyu Dai

We address a fundamental problem in wireless sensor networks, how many hops does it take a packet to be relayed for a given distance? For a deterministic topology, this hop-distance estimation reduces to a simple geometry problem. However, a statistical study is needed for randomly deployed WSNs. We propose a maximum-likelihood decision based on the conditional pdf of $f(r \mid H_i)$. Due to the computational complexity of $f(r \mid H_i)$, we also propose an attenuated Gaussian approximation for the conditional pdf. We show that the approximation visibly simplifies the decision process and the error analysis. The latency and energy consumption estimation are also included as application examples. Simulations show that our approximation model can predict the latency and energy consumption with less than half RMSE, compared to the linear models.

Copyright © 2007 L. Zhao and Q. Liang. This is an open access article distributed under the Creative Commons Attribution License, which permits unrestricted use, distribution, and reproduction in any medium, provided the original work is properly cited.

1. INTRODUCTION

The recent advances in MEMS, embedded systems, and wireless communications enable the realization and deployment of wireless sensor networks (WSN), which consist of a large number of densely deployed and self-organized sensor nodes [1]. The potential applications of WSN, such as environment monitor, often emphasize the importance of location information. Fortunately, with the advance of localization technologies, such location information can be accurately estimated [2–5]. Accordingly, geographic routing [6–8] was proposed to route packets not to a specific node, but to a given location. An interesting question arises as "how many hops does it take to reach a given location?" The prediction of the number of hops, that is, hop-distance estimation, is important not only in itself, but also in helping, estimate the latency and energy consumption, which are both important to the viability of WSN.

The question could become very simple if the sensor nodes are manually placed. However, if sensor nodes are deployed in a random fashion, the answer is beyond the reach of simple geometry. The stochastic nature of the random deployment calls for a statistical study.

The relation between the Euclidean distance and network distance (in terms of the number of hops), also referred to as hop-distance relation, catches a lot of research interest recently. In [9], Huang et al. defined the Γ-compactness of a geometric graph $G(V, E)$ to be the minimum ratio of the Euclidean distance to the network distance,

$$\gamma = \min_{i,j \in V} \frac{d(i,j)}{h(i,j)}, \tag{1}$$

where $d(i, j)$ and $h(i, j)$ are the Euclidean distance and network distance between nodes i and j, respectively. The constant value γ is a good lower bound, but might not be enough to describe the nonlinear relation between Euclidean distance and network distance. In fact, their relation is often treated as linear for convenience, for example, $[r/R] + 1$ is widely used to estimate the needed number of hops to reach distance r given transmission range R. Against this simple intuition, the relation between Euclidean distance and network distance is far more complex. Fortunately, a lot of probabilistic studies have been applied to this question. In [10], Hou and Li studied the 2D Poisson distribution to find an optimal transmission range. They found that the hop-distance distribution is determined not only by node density and transmission range, but also by the routing strategy. They showed results for three routing strategies, most forward with fixed radius, nearest with forward progress, and most forward with variable radius. Cheng and Robertazzi in [11] studied the one-dimensional Poisson point and found the pdf of r given the number of hops. They also pointed out that the 2D Poisson

point distribution is analogous to the 1D case, replacing the length of the segment by the area of the range. Vural and Ekici reexamined the study under the sensor networks circumstances in [12], and gave the mean and variance of multihop distance for 1D Poisson point distribution. They also proposed to approximate the multihop distance using Gaussian distribution. Zorzi and Rao derive the mean number of hops of the minimal hop-count route through simulations and analytic bounds in [8]. Chandler [13] derives an expression for t-hop outage probability for 2D Poisson node distribution. However, Mukherjee and Avidor [14] argue that one of Chandler's assumptions is relaxed, and thus his expression is in fact a lower bound on the desired probability. Using the same assumption, they also derive the pdf of the minimal number of hops for a given distance in a fading environment. Although these analytic results are available in the literature, their monstrous computational complexity limits their applications. Therefore, we try to approximate the hop-distance relation and simplify the decision process and error analysis in this paper. Considering the application of resource allocation, only large-scale path loss is considered, and thus the fading is ignored.

The rest of this paper is organized as follows. The number of hops prediction problem is addressed and solved in Section 2. Since this problem has no closed-form solution, we propose an attenuated Gaussian approximation and show how to simplify the error analysis in Section 2.1. Application examples are shown in Section 3. Section 4 concludes this paper.

2. ESTIMATION OF NETWORK DISTANCE BASED ON EUCLIDEAN DISTANCE

Suppose the sensor nodes are placed on a plane at random, and $N(A)$, the number of nodes in a given area A, follows two-dimensional Poisson distribution with average density λ. The problem of interest is to find the number of hops needed to reach a distance r away. We can make a maximum-likelihood (ML) decision,

$$\hat{H} = \arg\max f(r \mid H_n), \quad n = 1, 2, 3, \ldots, \tag{2}$$

where the event H_n can be described as "the minimum number of hops is n from the source to the specific node at Euclidean distance r." In the following discussion, we are trying to approximate $f(r \mid H_n)$ for 2D Poisson distribution. Note that $r < R$ implies H_1, that is, the specific node is within one hop from the source. We are more interested in multiple-hop distance relation, especially when n is moderately large.

2.1. Attenuated Gaussian approximation

Since $f(r \mid H_i)$ is awkward to evaluate even using numerical methods, we use histograms collected from Monte Carlo simulations as substitute to the joint pdf. All the simulation data are collected from a scenario where N sensor nodes were uniformly distributed in a circular region of radius of R_{Bound} meters. For convenience, polar coordinates were used. The source node was placed at $(0, 0)$. The transmission range was set as R meters. For each setting of (N, R_{Bound}, R), we ran 300 simulations, in each of which all nodes are redeployed at random. We ran simulations for extensive settings of node density λ and transmission range R. Due to space constraints, only the histograms for $(N = 1000, R_{\text{Bound}} = 200, R = 30)$ are plotted in Figure 1, which approximately shows that $f(r \mid H_i)$ approaches the normal when H_i increases. Table 1 lists the first-, second-, third-, and fourth-order statistics of $f(H, r)$.

Table 1: Statistics of $f(r \mid H_i)$.

Number of hops	Mean	STD	Skewness	Kurtosis
1	19.991	7.0651	−0.57471	−0.58389
2	45.132	7.8365	−0.16958	−1.0763
3	72.01	8.2129	−0.10761	−1.0332
4	99.45	8.391	−0.07938	−0.97857
5	127.14	8.5323	−0.06445	−0.93104
6	154.96	8.6147	−0.05341	−0.9004
7	182.68	8.573	−0.07738	−0.91687

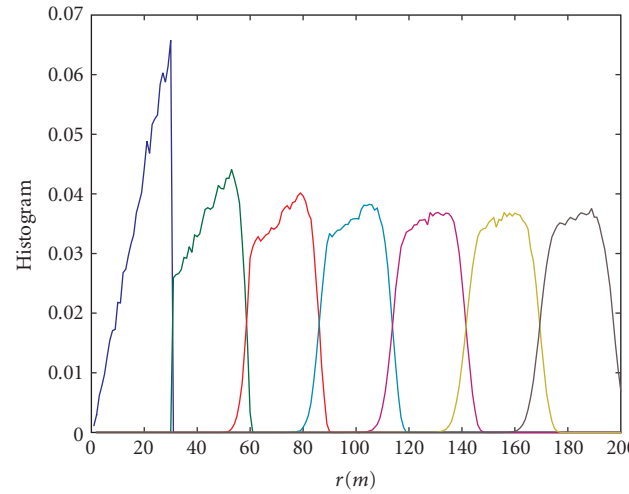


Figure 1: Histograms of hop-distance joint distribution ($N = 1000$, $R_{\text{Bound}} = 200$, $R = 30$).

Skewness is a third-order statistic used to measure of symmetry, or more precisely, the lack of symmetry. Skewness is zero for a symmetric distribution and positive skewness indicates right skewness while negatives indicates left skewness.

Definition 1 (see [15]). For a given sample set X,

$$m_3 = \frac{\Sigma(X - \overline{X})^3}{n}, \qquad m_2 = \frac{\Sigma(X - \overline{X})^2}{n}, \tag{3}$$

where $\overline{X}$ is the sample mean of X, and n is the size of X. Then a *sample estimate of skewness coefficient* is given by

$$g_1 = \frac{m_3}{m_2^{3/2}}. \tag{4}$$

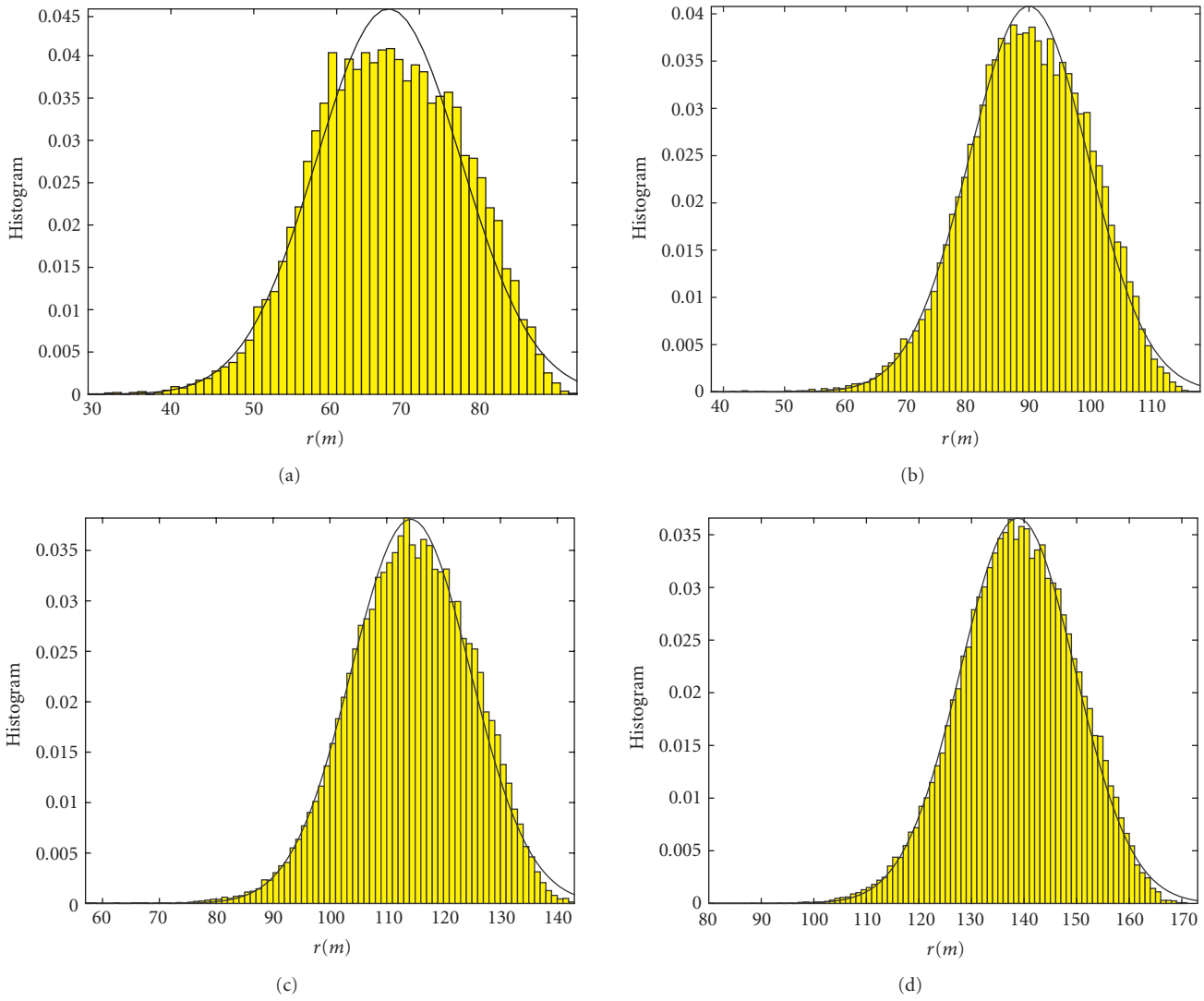


FIGURE 2: The histogram versus postulated distribution for end-to-end distances for given number of hops: (a) three hop; (b) four hop; (c) five hop; (d) six hop.

Kurtosis is a fourth-order statistic indicating whether the data are peaked or flat relative to a normal distribution.

Definition 2 (see [15]). A sample estimate of kurtosis for a sample set X is given by

$$g_2 = \frac{m_4}{m_2^2} - 3, \tag{5}$$

where $m_4 = \Sigma(X - \overline{X})^4/n$ is the fourth-order moment of $\overline{X}$ about its mean.

Skewness and kurtosis are useful in determining whether a sample set is normal. Note that the skewness and kurtosis of a normal distribution are both zero; significant skewness and kurtosis clearly indicate that data are not normal. Table 1 clearly shows that the skewness and kurtosis satisfy the Gaussianity condition within tolerance of error. Furthermore, The postulated distribution and histogram are drawn together in Figures 2(a), 2(b), 2(c), and 2(d), which clearly shows a close match for each case. Also, note that $f(r \mid H_n)$ attenuates exponentially with n increase, we need to introduce an attenuation factor to model this behavior.

Thus, the objective function can be approximated by

$$f(r \mid H_n) = \alpha^n \mathcal{N}(m_n, \sigma_n) = \frac{\alpha^n}{2\pi\sigma} e^{-(r-m_n)^2/2\sigma_n^2}, \tag{6}$$

where α is the equivalent attenuation base, m_n and σ_n are the mean and standard deviation (STD), respectively. Since $f(r \mid H_n)$ attenuates with n increasing, α must be less than 1. The specific values of these parameters can be estimated from simulations or computed numerically from the exact pdfs. Our extensive simulations show that even for only moderately large H_i, $f(r \mid H_i)$ has the following properties.

(1) $\sigma_n \approx \sigma_{n-1}$, which means that the neighboring joint pdfs have similar spread.

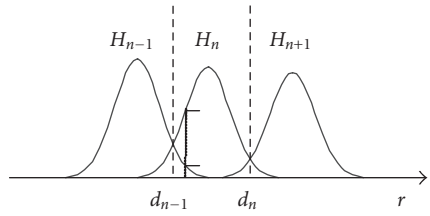


Figure 3: Gaussian approximation.

(2) $m_n - m_{n-1} \approx m_{n+1} - m_n$, which means that the joint pdfs are evenly spaced.
(3) $3 < (m_n - m_{n-1})/\sigma_n < 5$, which means the overlap between the neighboring joint pdfs is small but not negligible. (As a rule of thumbs, $Q(3)$ is considered relatively small and $Q(5)$ is regarded negligible.)
(4) $(m_n - m_{n-2})/\sigma_n \gg 5$, which means the overlap between the nonneighboring joint pdfs is negligible.
(5) $\alpha < 1$. For large density λ, $\alpha \to 1$. Along with property (1), this tell us that the neighboring joint pdfs have nearly identical shape.

As shown in the following discussion, these properties largely simplify the decision rule and the error analysis. Another interesting observation, besides these properties, is that the following equations do not stand true,

$$\begin{aligned} m_n &= nm_1, \\ m_n &= nR, \\ m_n &= (n-1)R + R/2. \end{aligned} \tag{7}$$

Although these equations sound plausible, they all give visible errors. The aforementioned estimator $[r/R] + 1$ for H_i, though widely used, is not good in the new light shed by this study.

2.2. Decision boundaries

Following (2), and observing the $f(r \mid H_i)$ in Figure 3, the decision is needed only between neighboring H_i, that is,

$$f(r \mid H_n) \underset{n+1}{\overset{n}{\gtrless}} f(r \mid H_{n+1}). \tag{8}$$

This is because, for a specific value of r, there are only two values of H_i with dominating $f(r \mid H_i)$, compared to which $f(r \mid H_i)$ for other values of H_i is negligible. Substituting (6) into (8), we obtain the decision boundary d_n between the regions H_n and H_{n+1},

$$\begin{aligned} d_n &= \frac{B + \sqrt{B^2 + AC}}{A}, \\ A &= \sigma_{n+1}^2 - \sigma_n^2, \\ B &= m_n\sigma_{n+1}^2 - m_{n+1}\sigma_n^2, \\ C &= m_n^2\sigma_{n+1}^2 - m_{n+1}^2\sigma_n^2 + 2\sigma_n^2\sigma_{n+1}^2 \ln\alpha. \end{aligned} \tag{9}$$

Using property (1),

$$d_n = \frac{m_{n+1}^2 - m_n^2 - 2\sigma_n^2 \ln\alpha}{2(m_{n+1} - m_n)}. \tag{10}$$

For large density λ, property (5) is applicable, (9) simplifies to

$$d_n = \frac{\sigma_n^2 m_{n+1} + \sigma_{n+1}^2 m_n}{\sigma_n^2 + \sigma_{n+1}^2}. \tag{11}$$

Applying property (1) to (11),

$$d_n = \frac{m_n + m_{n+1}}{2}. \tag{12}$$

No matter which approximate solution we choose for d_n, the decision rule is given by

$$r \underset{n}{\overset{n+1}{\gtrless}} d_n. \tag{13}$$

In other words,

$$\text{we decide } \hat{n} \quad \text{if } d_{\hat{n}-1} < r \le d_{\hat{n}}. \tag{14}$$

2.3. Error performance analysis

For our decision rule, a decision error occurs only when the required number of hops is n, but our decision $\hat{n} \neq n$. Thus, the probability of error for a specific r is

$$p(\epsilon \mid r) = \sum_{n \neq \hat{n}} f(H_n \mid r), \tag{15}$$

where $f(H \mid r)$ is related to $f(r \mid H_i)$ by the Bayesian rule. The total probability of error is obtained by integrating (15) over all possible r,

$$p(\epsilon) = \int p(\epsilon \mid r) f_r(r) dr. \tag{16}$$

According to property (4), only $f(r \mid H = n-1)$ and $f(r \mid H = n+1)$ could have outstanding value over the decision region $[d_{n-1}, d_n]$,

$$\begin{aligned} p(\epsilon) &\approx \sum_{n=2}^{\infty} \int_{d_{n-1}}^{d_n} f(r \mid H_{n-1}) p(H_{n-1}) + f(r \mid H_{n+1}) p(H_{n+1}) dr \\ &= \sum_{n=2}^{\infty} \alpha^{n-1} p(H_{n-1}) \left[Q\left(\frac{d_{n-1} - m_{n-1}}{\sigma_{n-1}} \right) - Q\left(\frac{d_n - m_{n-1}}{\sigma_{n-1}} \right) \right] \\ &\quad + \alpha^{n+1} p(H_{n+1}) \left[Q\left(\frac{m_{n+1} - d_n}{\sigma_{n+1}} \right) - Q\left(\frac{m_{n+1} - d_{n-1}}{\sigma_{n+1}} \right) \right]. \end{aligned} \tag{17}$$

Note that

$$\frac{d_n - m_{n-1}}{\sigma_{n-1}} - \frac{d_{n-1} - m_{n-1}}{\sigma_{n-1}} = \frac{d_n - d_{n-1}}{\sigma_{n-1}} \gg 1, \tag{18}$$

therefore, $Q((d_n - m_{n-1})/\sigma_{n-1})$ is negligible compared to $Q((d_{n-1} - m_{n-1})/\sigma_{n-1})$. Similarly, $Q((m_{n+1} - d_n)/\sigma_{n+1})$ is negligible. Equation (17) is approximated by

$$\begin{aligned} p(\epsilon) &\approx \alpha^3 p(H_3) Q\left(\frac{m_3 - d_2}{\sigma_3}\right) \\ &\quad + \sum_{n=3}^{\infty} \left[\alpha^{n-1} p(H_{n-1}) Q\left(\frac{d_{n-1} - m_{n-1}}{\sigma_{n-1}}\right) \right. \\ &\qquad \left. + \alpha^{n+1} p(H_{n+1}) Q\left(\frac{m_{n+1} - d_n}{\sigma_{n+1}}\right)\right] \\ &= \alpha^2 p(H_2) Q\left(\frac{d_2 - m_2}{\sigma_2}\right) \\ &\quad + \sum_{n=3}^{\infty} \alpha^n p(H_n) \left[Q\left(\frac{m_n - d_{n-1}}{\sigma_n}\right) + Q\left(\frac{d_n - m_n}{\sigma_n}\right)\right]. \end{aligned} \tag{19}$$

Substituting an appropriate solution of d_n into (19) would give us the probability of error within required accuracy. For example, if we choose (12),

$$\begin{aligned} p(\epsilon) &\approx \alpha^2 p(H_2) Q\left(\frac{m_3 - m_2}{2\sigma_2}\right) \\ &\quad + \sum_{n=3}^{\infty} \alpha^n p(H_n) \left[Q\left(\frac{m_n - m_{n-1}}{2\sigma_n}\right) + Q\left(\frac{m_{n+1} - m_n}{2\sigma_n}\right)\right]. \end{aligned} \tag{20}$$

Thanks to the Gaussian approximation, the error probability is given in forms of Q functions, which is tremendously simpler than the derivation from the original pdfs. This error process is general and applicable to other estimators. For example, even when we have to use a linear estimator due to limit of computation capacity, we can still use the above process to obtain the corresponding error probability.

3. APPLICATION EXAMPLES

We provide two application examples, latency and energy estimation, in this section. To emphasize the role of the number of hops in the estimation, we use general time and energy models. On how to derive the parameters such as T_{rx}, T_{tx} for a specific routing scheme, readers are referred to [16, 17].

3.1. Latency estimation

We use a simple time model, in which the latency increases linearly with the number of hops [18]. Suppose it takes T_{rx}, T_{tx} for a sensor node to process 1 bit of incoming and outgoing messages, respectively, and T_{pr} is the required time to transmit 1 bit of message through a band-limited channel. Therefore, the latency introduced for each hop is

$$T_{\text{hop}} = T_{tx} + T_{pr} + T_{rx}. \tag{21}$$

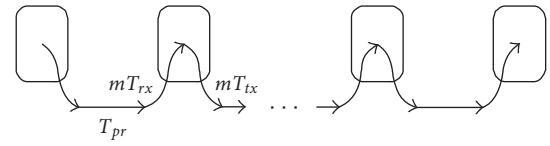


Figure 4: Time model.

Table 2: Energy consumption parameters

Name	Value
r_0	86.2 m
E_{elec}	50 nJ/bit
E_{DA}	5 nJ/bit
ϵ_{fs}	10 pJ/bit/m^2
ϵ_{mp}	0.0013 pJ/bit/m^4

As shown in Figure 4, given the end-to-end distance r, we can find the required number of hops $\hat{n}$ according to (13), thus, a good estimator of the total latency of an l-bit message is

$$l\hat{n}T_{\text{hop}}. \tag{22}$$

3.2. Energy consumption estimation

The following model is adopted from [19] where perfect power control is assumed. To transmit l bits over distance r, the sender's radio expends

$$E_{tx}(l, r) = \begin{cases} lE_{\text{elec}} + l\epsilon_{fs} r^2, & r < d_0, \\ lE_{\text{elec}} + l\epsilon_{mp} r^4, & r \geq d_0, \end{cases} \tag{23}$$

and the receiver's radio expends

$$E_{rx}(l, r) = lE_{\text{elec}}. \tag{24}$$

E_{elec} is the unit energy consumed by the electronics to process one bit of message, ϵ_{fs} and ϵ_{mp} are the amplifier factor for free-space and multipath models, respectively, and d_0 is the reference distance to determine which model to use. In fact, the first branch of (23) assumes a free-space propagation and the second branch uses a path-loss exponent of 4. The values of these communication energy parameters are set as in Table 2.

Let s_n denote the single-hop distance from the $(n-1)$th-hop to the nth-hop. Obviously, $s_n \leq R$. In our experimental setting, $R = 30m < d_0$ so that the free-space model is always used. This agrees well with most applications, in which multihop short-range transmission is preferred to avoid the exponential increase in energy consumption for long-range transmission. Naturally, the end-to-end energy consumption for sending l bit over distance r is given by

$$E_{\text{total}}(l, r) = \sum_{1}^{\hat{n}} \{E_{tx}(l, r_1) + E_{rx}(l)\}, \tag{25}$$

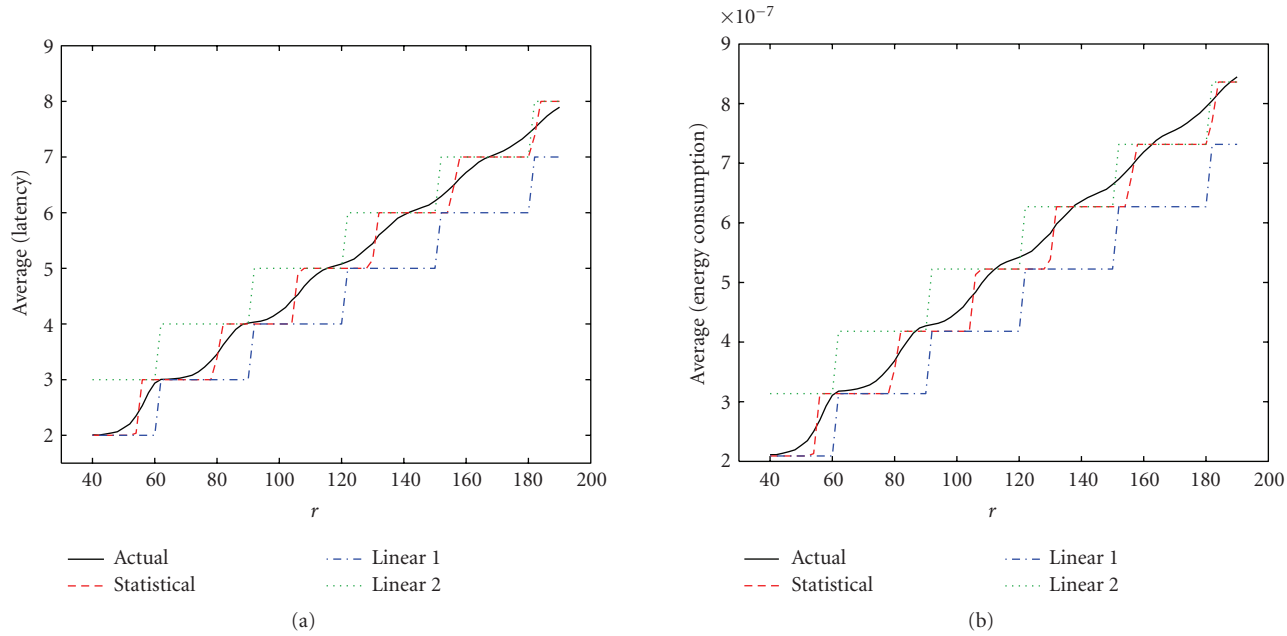


Figure 5: Estimation average: (a) latency; (b) energy consumption.

where $\hat{n}$ is the estimated number of hops for given r and r_1 is the single-hop distance because the message is relayed hop by hop.

On the average,

$$\begin{aligned}\overline{E}_{\text{total}}(l,r) &= \hat{n}l(E_{\text{elec}} + \epsilon_{fs}E[r_1^2] + E_{\text{elec}}) \\ &= \hat{n}l(2E_{\text{elec}} + \epsilon_{fs}(m_1^2 + \sigma_1^2)).\end{aligned} \tag{26}$$

3.3. Simulation

We used the same scenario described in Section 2.1 and varied the node density λ and transmission range R. In each simulation, the number of hops is estimated for each node using (11) and (13), and then the latency and energy consumption are estimated using (22) and (26), respectively. As comparison to our proposed statistic-based estimator, we choose a widely used linear estimator,

$$\begin{aligned}\text{linear estimator 1 } \hat{n} &= \left[\frac{r}{R}\right] + 1, \\ \text{linear estimator 2 } \hat{n} &= \left[\frac{r}{R}\right] + 2,\end{aligned} \tag{27}$$

where r is the given distance, R, the transmission range, and $[r/R]$ is the maximum integer less than r/R. We plot the average of latency and energy consumption in Figures 5(a) and 5(b) and the RMSE in Figures 6(a) and 6(b), respectively. The latency is plotted in units of T_{hop} while the energy consumption in units of joules. The ripple shape of RMSE is due to the fact that decision errors occur more often in the overlapping zones of neighboring $f(r \mid H_i)$. Figure 5 shows that the linear estimator 1 performs well at the shorter range but suffers visibly at larger range, while the linear estimator does the opposite. The linear estimators, no matter what value their parameters take, may significantly underestimate or overestimate the latency and energy consumption as already pointed out in Section 2.1, while our statistic-based model keeps close to the actual latency and energy consumption at all ranges except for the border. This is also verified by Figure 6, which also shows that our model can reduce RMSE to at least half for both latency and energy consumption. These results show that linear models cannot identify network behavior accurately, as also confirmed by our extensive simulations for different settings of node density and transmission range, which is not shown here due to space constraints.

4. CONCLUSION

To address the fundamental problem "how many hops does it take for a packet to be relayed for a given distance," we make both probabilistic and statistical studies. We proposed a Bayesian decision based on the conditional pdf of $f(r \mid H_i)$. Since $f(r \mid H_i)$ is computationally complex, we also proposed an attenuated Gaussian approximation for the conditional pdf, which visibly simplifies the decision process and the error analysis. This error analysis based on Gaussian approximation is also applicable to other estimators, including the linear ones. We also show that several linear models, though intuitively sound and widely used, may give significant bias error. Given as application examples, our approximation is also applied in the latency and energy consumption estimation in dense WSN. Simulations show that our approximation model can predict the latency and energy

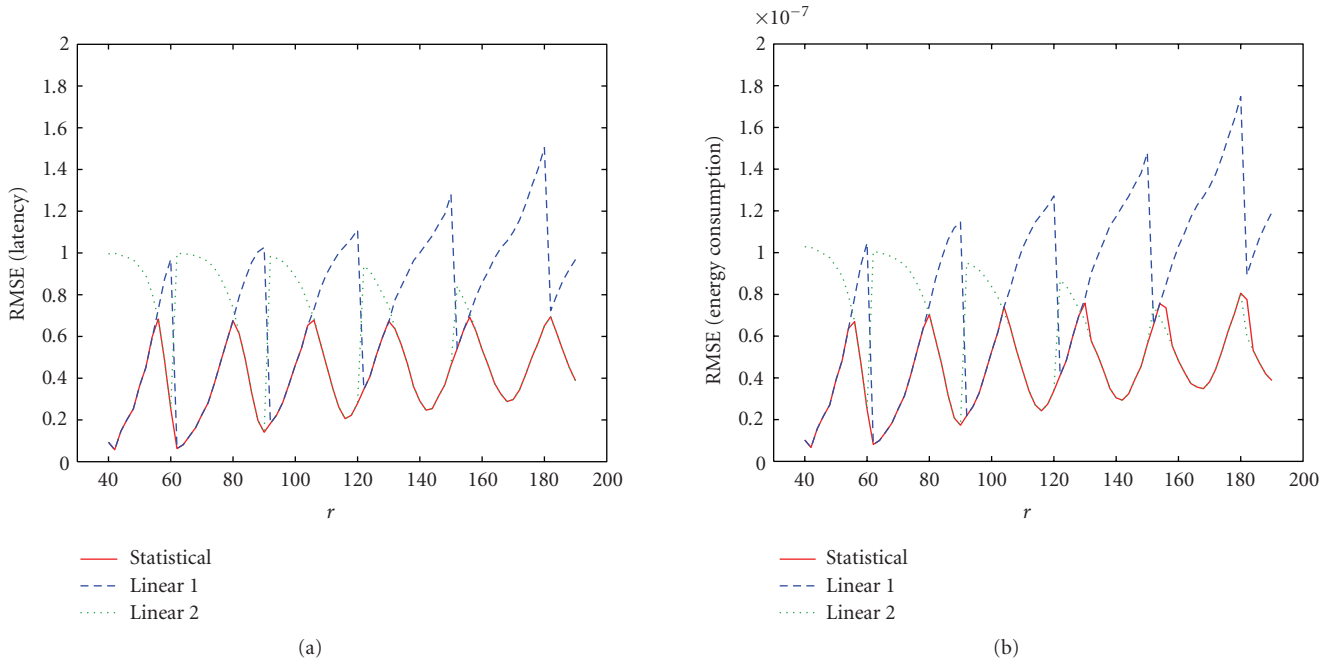


Figure 6: Estimation RMSE: (a) latency; (b) energy consumption.

consumption with less than half RMSE, compared to the aforementioned linear models.

ACKNOWLEDGMENT

This work was supported by the US Office of Naval Research (ONR) Young Investigator Award under Grant N00014-03-1-0466.

REFERENCES

[1] I. F. Akyildiz, W. Su, Y. Sankarasubramaniam, and E. Cayirci, "A survey on sensor networks," *IEEE Communications Magazine*, vol. 40, no. 8, pp. 102–114, 2002.

[2] H. Lim and J. C. Hou, "Localization for anisotropic sensor networks," in *Proceedings of the 24th Annual Joint Conference of the IEEE Computer and Communications Societies (INFOCOM '05)*, vol. 1, pp. 138–149, Miami, Fla, USA, March 2005.

[3] A. Caruso, S. Chessa, S. De, and A. Urpi, "GPS free coordinate assignment and routing in wireless sensor networks," in *Proceedings of the 24th Annual Joint Conference of the IEEE Computer and Communications Societies (INFOCOM '05)*, vol. 1, pp. 150–160, Miami, Fla, USA, March 2005.

[4] L. Fang, W. Du, and P. Ning, "A beacon-less location discovery scheme for wireless sensor networks," in *Proceedings of the 24th Annual Joint Conference of the IEEE Computer and Communications Societies (INFOCOM '05)*, vol. 1, pp. 161–171, Miami, Fla, USA, March 2005.

[5] N. B. Priyantha, H. Balakrishnan, E. D. Demaine, and S. Teller, "Mobile-assisted localization in wireless sensor networks," in *Proceedings of the 24th Annual Joint Conference of the IEEE Computer and Communications Societies (INFOCOM '05)*, vol. 1, pp. 172–183, Miami, Fla, USA, March 2005.

[6] R. Jain, A. Puri, and R. Sengupta, "Geographical routing using partial information for wireless ad hoc networks," *IEEE Personal Communications*, vol. 8, no. 1, pp. 48–57, 2001.

[7] Y. Xu, J. Heidemann, and D. Estrin, "Geography-informed energy conservation for ad hoc routing," in *Proceedings of the 7th Annual International Conference on Mobile Computing and Networking (MOBICOM '01)*, pp. 70–84, ACM Press, Rome, Italy, July 2001.

[8] M. Zorzi and R. R. Rao, "Geographic random forwarding (GeRaF) for ad hoc and sensor networks: multihop performance," *IEEE Transactions on Mobile Computing*, vol. 2, no. 4, pp. 337–348, 2003.

[9] Q. Huang, C. Lu, and G.-C. Roman, "Spatiotemporal multicast in sensor networks," in *Proceedings of the 1st International Conference on Embedded Networked Sensor Systems (SenSys '03)*, pp. 205–217, ACM Press, Los Angeles, Calif, USA, November 2003.

[10] T.-C. Hou and V. O. K. Li, "Transmission range control in multihop packet radio networks," *IEEE Transactions on Communications*, vol. 34, no. 1, pp. 38–44, 1986.

[11] Y.-C. Cheng and T. G. Robertazzi, "Critical connectivity phenomena in multihop radio models," *IEEE Transactions on Communications*, vol. 37, no. 7, pp. 770–777, 1989.

[12] S. Vural and E. Ekici, "Analysis of hop-distance relationship in spatially random sensor networks," in *Proceedings of the 6th ACM International Symposium on Mobile Ad Hoc Networking and Computing (MOBIHOC '05)*, pp. 320–331, ACM Press, Urbana-Champaign, Ill, USA, May 2005.

[13] S. A. G. Chandler, "Calculation of number of relay hops required in randomly located radio network," *Electronics Letters*, vol. 25, no. 24, pp. 1669–1671, 1989.

[14] S. Mukherjee and D. Avidor, "On the probability distribution of the minimal number of hops between any pair of nodes in a bounded wireless ad-hoc network subject to fading," in

Proceedings of the 2nd International Workshop on Wireless Ad-Hoc Networks (IWWAN '05), London, UK, May 2005.

[15] G. Snedecor and W. Cochran, *Statistical Methods*, Iowa State University Press, Ames, Iowa, USA, 1989.

[16] M. Zorzi and R. R. Rao, "Geographic random forwarding (GeRaF) for ad hoc and sensor networks: energy and latency performance," *IEEE Transactions on Mobile Computing*, vol. 2, no. 4, pp. 349–365, 2003.

[17] H. M. Ammari and S. K. Das, "Trade-off between energy savings and source-to-sink delay in data dissemination for wireless sensor networks," in *Proceedings of the 8th ACM Symposium on Modeling, Analysis and Simulation of Wireless and Mobile Systems (MSWiM '05)*, pp. 126–133, ACM Press, Montreal, Quebec, Canada, October 2006.

[18] W. Ye, J. Heidemann, and D. Estrin, "Medium access control with coordinated adaptive sleeping for wireless sensor networks," *IEEE/ACM Transactions on Networking*, vol. 12, no. 3, pp. 493–506, 2004.

[19] W. B. Heinzelman, A. P. Chandrakasan, and H. Balakrishnan, "An application-specific protocol architecture for wireless microsensor networks," *IEEE Transactions on Wireless Communications*, vol. 1, no. 4, pp. 660–670, 2002.

International Journal of Wireless Information Networks, Vol. 14, No. 3, September 2007 (© 2007)
DOI: 10.1007/s10776-007-0060-7

Distributed Sensor Networks Deployment Using Fuzzy Logic Systems

Haining Shu[1,3], Qilian Liang[1], and Jean Gao[2]

The effectiveness of distributed wireless sensor networks highly depends on the sensor deployment scheme. Given a finite number of sensors, optimizing the sensor deployment will provide sufficient sensor coverage and ameliorate the quality of communications. In this paper, we apply fuzzy logic systems to optimize the sensor placement after an initial random deployment. We use the outage probability due to co-channel interference to evaluate the communication quality. Fenton–Wilkinson method is applied to approximate the sum of log-normal random variables. Our algorithm is compared against the existing distributed self-spreading algorithm. Simulation results show that our approach achieves faster and stabler deployment and maximizes the sensor coverage with less energy consumption. Outage probability, as a measure of communication quality gets effectively decreased in our algorithm but it was not taken into consideration in the distributed self-spreading algorithm.

KEY WORDS: wireless sensor networks; sensor deployment; fuzzy logic system; Fenton–Wilkson method; outage probability

1. INTRODUCTION

Wireless sensor networks consist of certain amount of small and energy constrained nodes. Sensor nodes are deployed in support of various missions such as environment and habitat monitoring, industrial process control, infrastructure security [1] and automation in the transportation. One networked sensing experiment on Great Duck Island [2] provides a small lens into an expansive future of such applications. The experiment was conducted by a team of computer engineers from the University of California, Berkeley. Up to date, 190 wireless sensors have been deployed on a small island 10 miles off the coast of Maine to study the nesting behaviors of petrels. Biologists are now monitoring the petrels on the island from their offices, browsing data from sensors linked by satellite.

[1] Electrical Engineering, University of Texas at Arlington, Arlington, TX, 76019, USA
[2] Computer Science and Engineering, University of Texas at Arlington, Arlington, TX, 76019, USA
[3] E-mail: shu@wcn.uta.edu

The deployment of sensors varies with different applications. A number of applications require the placement of sensors at desired locations like data collection [3] and infrastructure security [1], where critical area, buildings and facilities are monitored by a network of sensors placed adequately. For such placement-friendly applications, sufficient knowledge of the environment is assumed to be available before deployment is carried out.

In other applications where prior knowledge of the environment can not be obtained, sensors may have to be randomly air-dropped and human intervention after deployment to recharge or replace node batteries may not be feasible. Mobile sensors are practically desirable in this situation because they have the capability to move around and re-adjust their positions for high quality communication and better coverage and surveillance [4]. However mobile sensor deployment itself is an energy consuming process because of the motion and communication between sensors. An efficient sensor re-deployment scheme is a necessity to save energy resources and improve the quality of communications.

1068-9605/07/0900-0163/0 © 2007 Springer Science+Business Media, LLC

Some prior research proposed sensor deployment strategies based on virtual forces for target localization [5–7]. One example of virtual force concept was presented in [7]. The pair-wise interaction between sensor nodes is governed by two kinds of virtual forces – one causes the nodes to repel each other to improve their coverage and the other is an attractive force that prevents the nodes from losing connectivity. Later Cheng et al. [8] formulated a constrained multivariable nonlinear programming problem to determine both the locations of the sensor nodes and data transmission pattern. In [9, 10], Heo and Varshney developed a distributed self-spreading algorithm (DSSA) and an intelligent deployment and clustering algorithm (IDCA) for sensor deployment. Recently, a voronoi diagram (VD)-based deployment algorithm was included in [11]. All the above algorithms have made lots of efforts to formulate the virtual forces, however none of which can well handle the uncertainties with the random move and unpredictable oscillation in sensor deployment. For the purpose of stability and convergence, various parameters or constraints such as oscillation limit, stable status [9–11], and number of neighbors [7] have to be imposed to avoid excessive sensor oscillation.

In this paper, we apply fuzzy logic systems (FLSs) to handle these uncertainties in distributed sensor deployment. Instead of attempting to formulate the virtual forces, we propose to apply FLSs to re-deploy the sensors. Each individual mobile sensor uses a FLS to self-adjust its location. For a single sensor node, neighboring nodes' location is the only information needed to make the movement decision. Therefore the deployment scheme based on FLSs is a fully distributed approach. After applying FLSs, exhaustive move and unpredictable oscillation is efficiently avoided and fast deployment is achieved. As a result, the entire sensor network survives for longer lifetime and the quality of communication in terms of outage probability is greatly ameliorated. A concept of coherence time is introduced for the purpose of synchronization among sensors.

The rest of this paper is organized as follows. In Section 2, we briefly review the basic concept of FLSs. Section 3 details the FLSs design for distributed sensor deployment. Simulation and discussion are presented in Section 4. Section 5 concludes this paper with a summary. Fenton–Wilkinson method to tackle the outage problem is expatiated in Appendix.

2. OVERVIEW OF FLSS

Figure 1 shows the structure of a rule-based type-1 FLS [12]. It contains four components: fuzzifier, rules, inference engine and defuzzifier. When an input is applied to a FLS, the inference engine computes the output set corresponding to each rule. The defuzzifer then computes a crisp output from these rule output sets.

Rules are the heart of a FLS and may be provided by experts or can be extracted from numerical data. In either case, the rules that we are interested in can expressed as a collection of IF-THEN statements, e.g. [13]

IF the total average input rate of real-time voice and video traffic is a *moderate amount*, and the total average input rate of the non-real-time data traffic is *some*, THEN the confidence of accepting the telephone call is a *large amount*.

The IF-part of a rule is its *antecedent* and the THEN-part of a rule is its *consequent*.

The process of making a crisp input fuzzy is called *fuzzification*. The most widely used

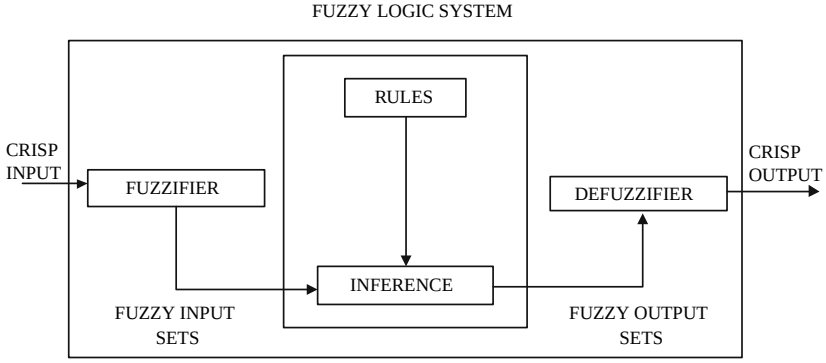


Fig. 1. The structure of a fuzzy logic system.

fuzzification is the *singleton fuzzification*. All fuzziness for a particular fuzzy set is essentially characterized by the *membership functions* (MFs). The shapes used to describe the fuzziness have very few restrictions but with the help of mathematical structure, some standard terms related to the shape of MFs have been developed over the years [14]. The most common forms of MFs are those that are normal and convex.

Consider a type-1 FLS having p inputs and one output. Let us suppose that it has M rules, there the lth rule has the form:

R^l: IF x_1 is F_1^l *and* x_2 is F_2^l *and* $\cdots$ *and* x_p is F_p^l, *THEN* y is G^l. $l = 1, \ldots, M$

Assuming singleton fuzzification is used, when an input $x' = \{x'_1, \ldots, x'_p\}$ is applied, the degree of firing corresponding to the lth rule is computed as

$$\mu_{F_1^l}(x'_1) \star \mu_{F_2^l}(x'_2) \star \cdots \star \mu_{F_p^l}(x'_p) = \mathcal{T}_{i=1}^{p} \mu_{F_i^l}(x'_i) \quad (1)$$

where $\star$ and $\mathcal{T}$ both indicate the chosen t-norm.

The last but not the least process in a FLS is called *defuzzification*. Defuzzification is the conversion of fuzzy output sets to crisp output sets. There are many defuzzification methods including maximum, mean-of-maxima, centroid, center-of-sums, height, modified height and center-of-sets. In this paper, we focus, for illustrative purposes, on the center-of-sets defuzzifier [13]. It computes a crisp output for the FLS by first computing the centroid, c_{G^l}, of every consequent set G^l, and, then computing a weighted average of these centroids. The weight corresponding to the lth rule consequent centroid is the degree of firing associated with the lth rule, $\mathcal{T}_{i=1}^{p} \mu_{F_i^l}(x'_i)$, so that

$$y_{cos}(x') = \frac{\sum_{l=1}^{M} c_G^l \mathcal{T}_{i=1}^{p} \mu_{F_i^l}(x'_i)}{\sum_{l=1}^{M} \mathcal{T}_{\rangle=\infty}{}^{p} \mu_{F_i^l}(x'_i)} \quad (2)$$

where M is the number of rules in the FLS.

In the next section, we will detail the design of the rule-based type-1 FLSs for distributed sensor deployment issue.

3. DESIGN OF FLSS FOR DISTRIBUTED SENSOR DEPLOYMENT

3.1. Assumptions and Notations

In this research, we make several assumptions:

- Sensor field is denoted by a two-dimensional grid. Sensing and communication is modeled as a circle on this grid.
- Coverage discussed in this paper is grid coverage. A grid point is covered when at least one sensor covers this point.
- A sensor can detect or sense any event within its sensing range, denoted by *Rs*. Coverage is determined based on Rs.
- Two sensors within their communication range, denoted by Rc can communicate with each other. Neighbors of a sensor are defined as nodes within its communication range.
- All sensor nodes are assumed peer to peer.
- Sensor nodes have certain mobility and are capable of computing, detection and communication.
- Sensor node can obtain the knowledge of its location.
- Sensors are synchronized by coherence time. One-time move is made within each coherence period.

3.2. FLSs Design for Distributed Sensor Deployment

FLS is well known to be able to handle uncertainty and ambiguity. Practically not all uncertainty is random. Some forms of uncertainty are non-random and hence not suited to treatment or modeling by probability theory. Fuzzy set theory is a marvelous tool for modeling uncertainty associated with vagueness, or with a lack of information regarding a particular element of the problem at hand. Upon concerning the distributed sensor deployment, the moving distance and direction of each sensor are distributed and full of uncertainty which can barely be described by some random distribution. FLS is well known as model free. Their MFs are not based on statistical distributions. Therefore we propose to apply FLS to the distributed sensor deployment problem. Each sensor makes fully distributed decision on its movement based on FLS.

Our algorithm starts with random deployment. Assume a two-dimensional sensor field is the target area of surveillance. In the initial condition, a given number of sensors are randomly deployed such as air-dropping. Because of the randomness in initial deployment, very likely the sensor field will not be fully covered. Part of the sensor field might be over crowded with the sensors. Such unbalanced deployment brings difficulty in target detection and tracking, and increases the interference during communications. Figure 2 gives an example of randomly deployed field. As shown in Figure 2, targets in the

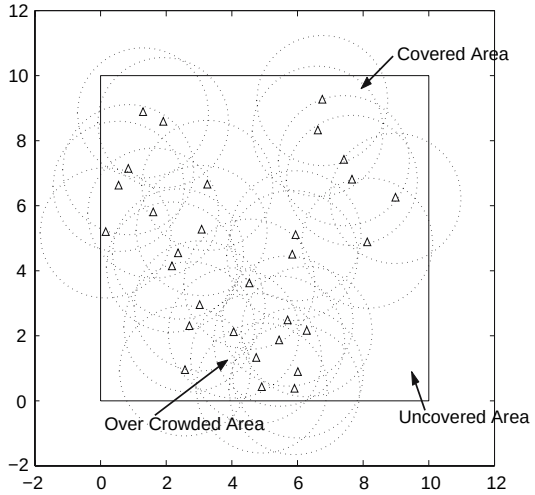


Fig. 2. An example of random deployment: targets in the uncovered area can not be detected; In the over crowded area communication between sensors has lots of interference.

uncovered area can not be detected while in the over crowded area, communication between sensors is corrupted by the interference from neighboring nodes.

Our algorithm then intends to re-deploy the sensors such that maximum field coverage and high quality communication could be achieved. Each individual sensor in the network needs to fine-tune its location such that densely deployed sensors can be evenly spreaded in the field. Two critical procedures are considered in our algorithm:

- Determine the next-step move distance for each sensor.
- Determine the next-step move direction for each sensor.

The next-step move distance is hard to determine. Too small or big move distance each step consumes the network more time and energy to get stable deployment. Excessive move and oscillation is unavoidable in previous work with no fuzzy system. In this paper, we design a FLS to determine the next-step move distance for each sensor.

An ideal sensor deployment will have uniform distribution for better coverage. But in random deployment, coverage uniformity is hardly to achieve initially. In sensor network composed of mobile sensors, each sensor detects the number and location of its neighbors and decides its *neighborhood density*. If the sensor has a high density of neighboring nodes, it makes decision using FLSs to shift a certain distance away from the high density area. If the neighborhood density is low, the sensor might stand still or shift a little distance away from the current location.

As illustrated in Figure 2, the *neighborhood density* of a sensor node is determined by two factors: the number of neighbors and the distance between sensor node and its neighbors. The more the neighboring nodes, the higher the neighborhood density. The closer the neighboring nodes, the higher the neighborhood density. Based on this knowledge, we choose two antecedents as follows:

Antecedent 1. Number of neighbors of each sensor.
Antecedent 2. Average Euclidean distance between sensor node and its neighbors.

The linguistic variables to represent the number of neighbors for each sensor are divided into three levels: *high*, *moderate* and *low*; and those to represent the average Euclidean distance between sensor node and its neighbors are divided into three levels: *far*, *moderate* and *near*. The consequent – the shift distance normalized by sensing range *Rs* is divided into three levels: *far*, *moderate* and *near*. Table 1 summaries the rules and consequents.

One example of rules is as follows:

IF the number of neighbors of sensor *i* is *high* and average Euclidean distance between sensor *i* and its neighbors is *moderate*, THEN the normalized shift distance of sensor *i* should be *moderate*.

We setup 9 rules for this FLS because every antecedent has 3 fuzzy sub-sets and there are 2 antecedents. Trapezoidal MFs are used to represent *high*, *low*, *far* and *near* and triangle MFs to represent *moderate*. Two antecedents are normalized to the range [0,10]. We show these MFs in Figures 2 and 3.

Table 1. Fuzzy rules and consequent

Antecedent 1	Antecedent 2	Consequent
Low	Near	Moderate
Low	Moderate	Near
Low	Far	Near
Moderate	Near	Far
Moderate	Moderate	Moderate
Moderate	Far	Near
High	Near	Far
High	Moderate	Moderate
High	Far	Moderate

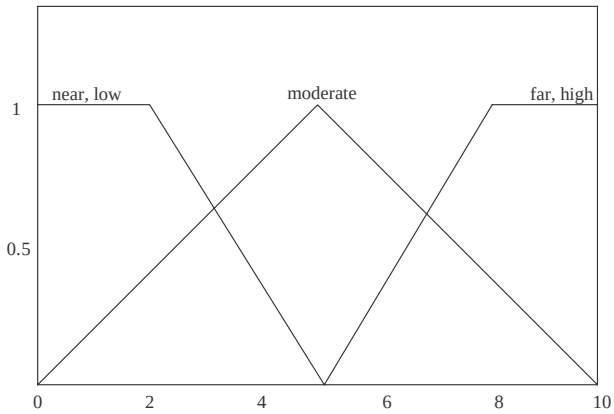


Fig. 3. Antecedent membership functions.

Applying center-of-sets defuzzification [7], for every input (x_1, x_2), the output is computed using

$$y_{(x_1,x_2)} = \frac{\sum_{l=1}^{9} c_G^l \mu_{F_1^l}(x_1)\mu_{F_2^l(x_2)}}{\sum_{l=1}^{9} \mu_{F_1^l}(x_1)\mu_{F_2^l}(x_2)} \tag{3}$$

Repeating these calculations for $\forall x_i \in [0, 10]$,we obtain a decision surface $y(x_1, x_2)$ as shown in Figure 4.

Generally, the decision surface is time-varying and nonlinear. From Figure 4, we can see that although the number of neighbors for a particular sensor is high, the move distance can be smaller than some sensor with fewer "crowded" neighbors, i.e. very close average Euclidean distance between the sensor and its neighbors. With the assist of decision surface, the next-step move distance can be determined.

Comparing to move distance, the next-step move direction is much easier to decide. Coulomb's law in physics becomes a useful tool to tackle the problem. For instance, assume sensor i has 2 neighbors in its communication range as shown in Figure 5.

The coordinate of sensor i is denoted as $C_i = (X_i, Y_i)$.

The next-step move direction of sensor i could be represented as follows:

$$\vec{v} = \sum_{j=1}^{2} \frac{\vec{C}_j - \vec{C}_i}{|\vec{C}_j - \vec{C}_i|^2} \tag{4}$$

$$tan(\alpha) = \frac{Y_{(\vec{v})}}{X_{(\vec{v})}} \tag{5}$$

After getting distance and direction (angle α) , sensor i clearly knows his next-step move information. In order to prolong the battery life of each individual sensor, we introduce a coherence time as the duty cycle during which the changes of two antecedents can be ignored. Sensors are put into idle or sleep mode if within the coherence time, the information of neighbors remains unchanged.

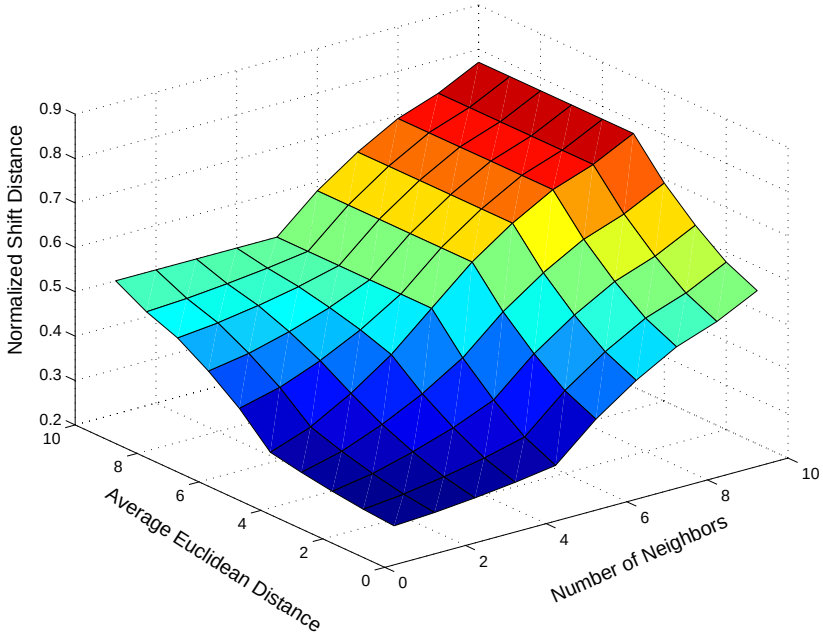


Fig. 4. Control surface of shift distance.

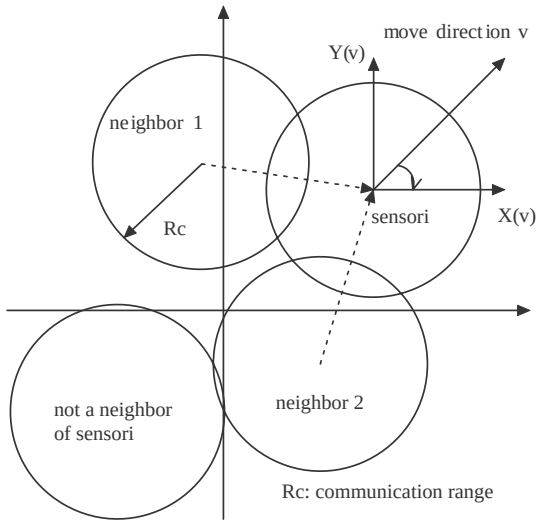


Fig. 5. Example of next step move direction for sensor having two neighbors.

4. SIMULATION AND DISCUSSION

We investigate various number of sensors deployed in a field of 250 × 250 m^2 area. We assume each sensor is equipped with an omni-directional antenna to carry out the task of detection and communication. Evaluation of our scheme follows three criteria: field coverage, converging speed, mean travel distance per node and outage probability. Results are averaged over 200 Monte Carlo simulations.

We compare the performance of our algorithm with the Distributed Self Spreading Algorithm (DSSA) proposed in [9]. DSSA is known as a good solution in the self-deployment of mobile sensor nodes. The main idea of DSSA is to define a partial force for the movement of sensors during the deployment process. The force a node receives from a closer neighbor node is greater than that from a farther neighbor. For N sensor nodes deployed in a square field with area A, DSSA formulates the partial force sensor node i receives from neighbor node j as:

$$f_n^{i,j} = \frac{D}{\mu^2}(R_c - |p_n^i - p_n^j|)\frac{p_n^i - p_n^j}{|p_n^i - p_n^j|} \qquad (6)$$

where R_c stands for communication range, $\mu = N \cdot \pi \cdot R_c^2/A$ is called the expected density while D is the local density, and p_n^i stands for the location of node i at time step n. Each node makes decision to move by adding up all partial forces from its neighboring nodes. DSSA sets up two criteria: stable status limit ($S_{\lim}$) and oscillation limit ($O_{\lim}$) to stop a sensor's movement.

Figure 6 shows at 50 m sensing range (R_s = 50 m) and 100 m communication range (R_c = 100 m), the coverage of the initial random deployment, the coverage after DSSA is implemented and the coverage after using FLSs. We ran three iterations for all three schemes. When 20 sensors are deployed, the coverage after random deployment was initially around 85% and the DSSA increased it to 93%. After FLSs were used, the coverage reached approximate 98% after three iterations.

Figure 7 gives the results when 10 iterations are completed for the three deployment schemes. We observe that the performance of DSSA gets closer to our FLSs after 10 iterations. Both FLSs and DSSA can dramatically increase the network coverage in the low density network. Figures 6 and 7 also indicates that instead of deploying large amount of sensors, the desired field coverage could be achieved with fewer sensors. Comparing Figures 6 and 7, we noticed that our FLSs increases the network coverage faster than DSSA in terms of iteration times.

Figures 8–10 are the real pictures of 20 sensors from random deployment, after implementing FLS and DSSA respectively. Both FLS and DSSA can spread the densely deployed sensors but the deployment after using FLS demonstrates more uniformity than the one using DSSA.

We then simulated two cases when 30 sensor nodes and 60 sensor nodes are deployed respectively. Network coverage according to these two cases are presented in Figurs 11 and 12.

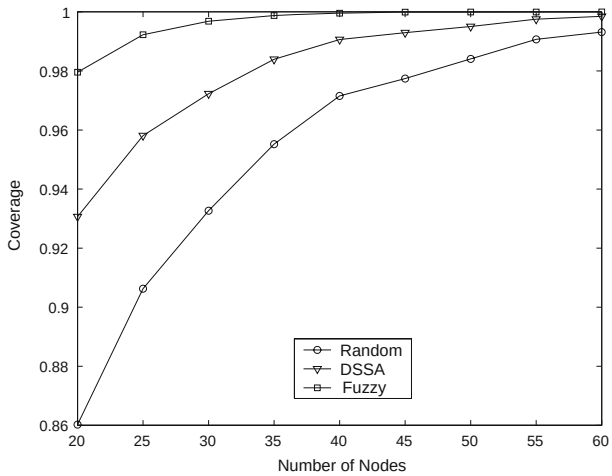


Fig. 6. Coverage vs. number of sensors deployed (after three iterations, Rc = 100 m).

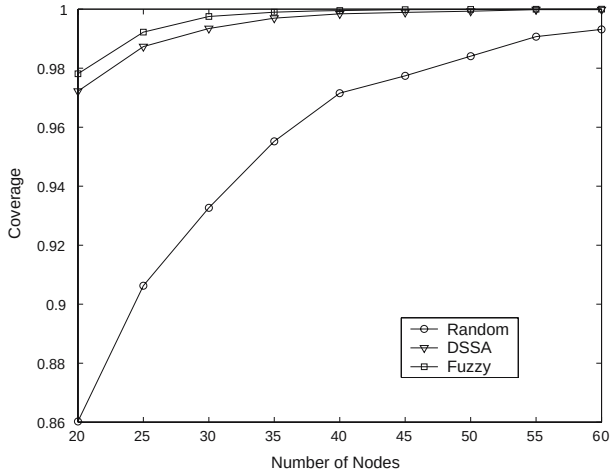


Fig. 7. Coverage vs. number of sensors deployed (after 10 iterations, Rc = 100 m).

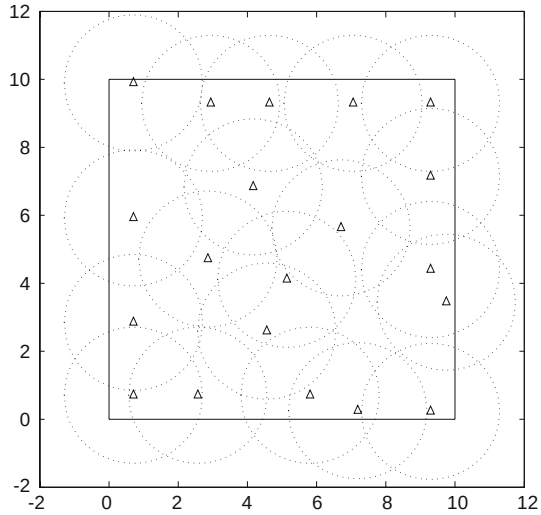


Fig. 9. Deployment with 20 sensors after implementing FLS (after three iterations, Rc = 100 m).

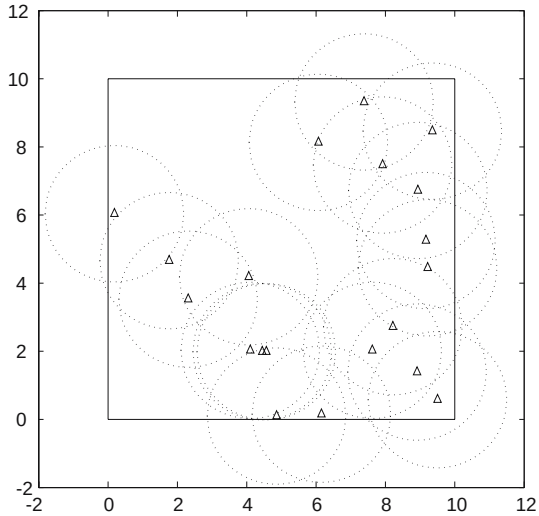


Fig. 8. Random deployment with 20 sensors (Rc = 100 m).

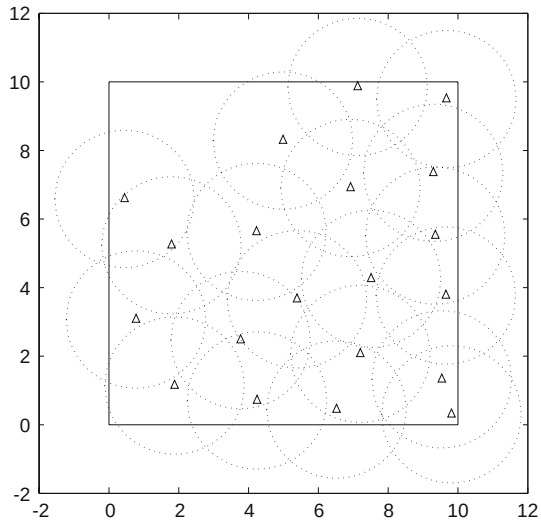


Fig. 10. Deployment with 20 sensors after implementing DSSA (after three iterations, Rc = 100 m).

It is fairly clear in Figures 11 and 12 that our FLSs increase the network coverage much faster than the DSSA. For instance, when 30 sensor nodes were deployed, our FLSs boost the network coverage from initial 93% to around 98.5% in only 1 iteration whereas the DSSA takes 6 iterations to reach the same coverage.

The average distance traveled by each sensor node is also important in energy saving problem. For energy constrained wireless sensor nodes, less travel distance leads to less energy consumption. Our goal is to adjust sensors' positions appropriately such that the maximum coverage is achieved with minimum energy dissipation in deployment. We calculated the average distance traveled by each sensor node for our FLS and compared it against the DSSA as both reach the same network coverage. Results in Figure 13 indicate that for the FLS scheme, each sensor node travels less average distance than that in DSSA. Furthermore, in FLS scheme, the average travel distance by each node varies little when the number of sensors changes which implies that the energy consumed in deployment is nearly independent of network density.

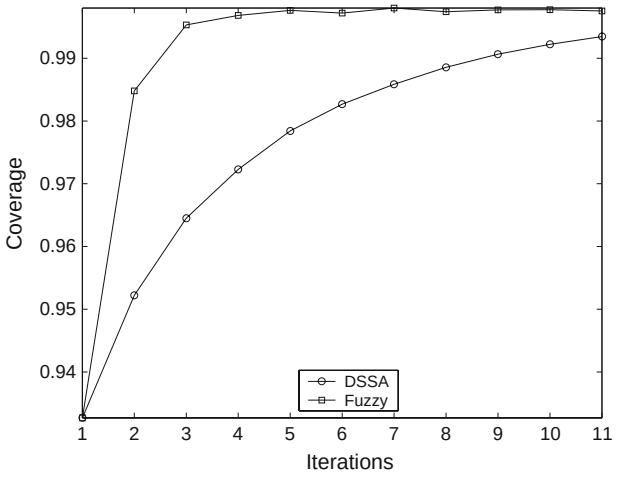


Fig. 11. Coverage vs. number of iterations (30 nodes deployed, Rc = 100 m).

In wireless sensor networks, the radio link performance is usually limited by interference rather than noise, therefore, the probability of outage due to co-channel interference is of primary concern. Measurements [16] have shown that at any value of $d_{i,j}$ (the Euclidean distance between sensor i and sensor j), the path loss $PL(d_{i,j})$ is random and distributed log-normally (normal in dB) about the mean distance dependent value. That is:

$$PL(d_{i,j})[\mathrm{dB}] = \overline{PL}(d_{i,j}) + X_\sigma = \overline{PL}(d_0) + 10n\log\left(\frac{d_{i,j}}{d_0}\right) + X_\sigma \tag{7}$$

and

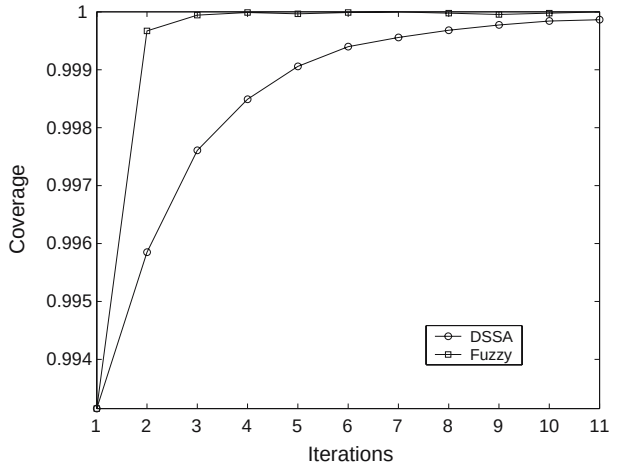


Fig. 12. Coverage vs. number of iterations (60 nodes deployed, Rc = 100 m).

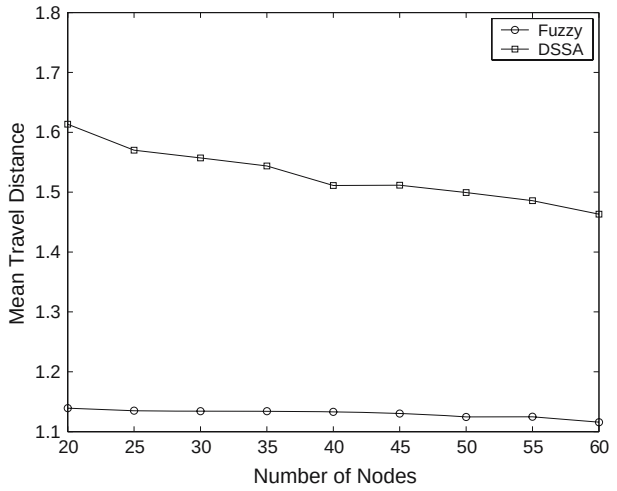


Fig. 13. Travel distance vs. number of sensors deployed (10 iterations).

$$P_r(d_{i,j})[\mathrm{dB}m] = P_t[\mathrm{dB}m] - PL(d_{i,j})[\mathrm{dB}] \tag{8}$$

where X_σ is a zero-mean Gaussian distribution random variable (in dB) with standard deviation σ (also in dB).

The log-normal distribution describes the random *shadowing* effects on the propagation path which implies that measured signal levels at certain distance have a Gaussian (normal) distribution about the distance-dependent mean and standard deviation σ. Since $PL(d_{i,j})$ follows normal distribution, so is $P_r(d_{i,j})$, and the Q function may be used to determine the probability that the received signal level will exceed (or fall below) a particular level.

The probability that the received signal level will exceed a certain value γ can be calculated from the cumulative density function as

$$P_r[P_r(d_{i,j}) > \gamma] = Q\left(\frac{\gamma - \overline{P_r}(d_{i,j})}{\sigma}\right) \tag{9}$$

For sensor i with N neighbors, if sensor i acts as the destination node during one communication, the signal to interference ratio (SIR) is represented as:

$$\mathrm{SIR}(i) = \frac{P_r(d_{i,j})}{\sum_{k=1}^{N} P_r(d_{i,k})}, k \neq j \tag{10}$$

The denominator denoting the effect of co-channel interference is a sum of $N-1$ log-normal signals. Evaluating the outage probability requires the probability distribution of the interference power. There is no known exact expression for the probability distribution for the sum of log-normal random variables, but various authors have derived several approaches

which approximate the sum of log-normal random variables by another log-normal random variable.

In this paper, we used Fenton–Wilkinson method [17]. The co-channel interference can now be approximated by one log-normal random variable. SIR(in dB) as a result follows log-normal distribution as well. We expatiate the Fenton–Wilkinson method in the Appendix. Results of outage probability are presented in Figure 14.

Observe Figure 14, the FLSs scheme successfully reduced the outage probability by nearly 15% comparing to DSSA when the number of sensors is 60, which implies a higher probability that the received signal level will exceed the SIR threshold using our FLSs scheme. The DSSA did not perform well considering the outage probability because it did not take the outage probability into performance evaluation [9].

We have introduced earlier that DSSA stops a sensor's movement by two criteria: stable status limit ($S_{\lim}$) and oscillation limit ($O_{\lim}$). Ref. [9] shows that it takes more than 10 times iteration to termination. Our fuzzy approach gains a distinct advantage over DSSA by converging in around three iterations. Thus stop criteria is not required in our fuzzy approach. These facts indicate that our FLS scheme is much faster and simpler to implement comparing to DSSA and more significantly, the FLS scheme maximizes the network coverage with less energy consumption in deployment.

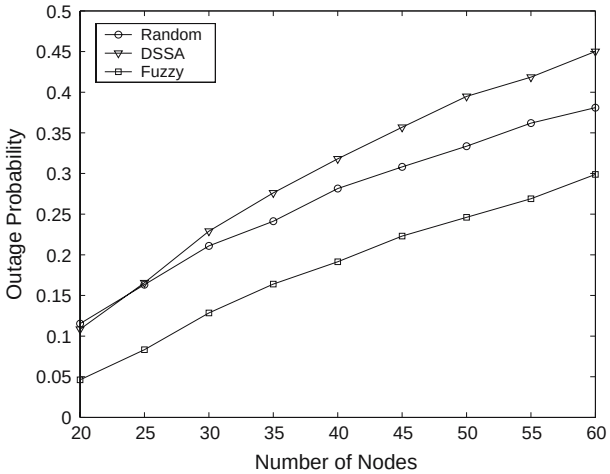


Fig. 14. Outage probability vs. number of sensors (Rc = 100 m).

5. CONCLUSIONS

In this paper, we proposed a sensor deployment strategy based on FLS. Our approach has a great advantage to deal with the uncertainty in distributed sensor deployment which is particularly useful when emergency rescue or redeployment over hostile situation is needed. We believe that in an energy constrained wireless sensor network, fast and efficient deployment strategy is a necessity to save energy and extend network lifetime. Our FLSs scheme is capable to model all distributed sensor deployment with a FLS. The network coverage and quality of communication in term of outage probability are greatly improved as a result. Moreover, the FLSs scheme brings the whole network to a stable and optimal deployment very soon which will significantly reduce the energy consumption. Our future work will focus on modeling the random deployment with some existing pattern so that the energy consumption can be further studied in the deployment problem.

Acknowledgments This work was supported by the Office of Naval Research (ONR) Young Investigator Award under Grant N00014-03-1-0466, "Energy Efficient Wireless Sensor Networks for Future Combat System Using Fuzzy Logic".

Appendix Multiple Log-Normal Interferers Consider the sum of N_I log-normal random variables

$$I = \sum_{k=1}^{N_I} \Omega_k = \sum_{k=1}^{N_I} 10^{\Omega_{k(\mathrm{dBm})}/10} \tag{11}$$

where the $\Omega_{k(\mathrm{dBm})}$ are Gaussian random variables with mean $\mu_{\Omega_{k(\mathrm{dBm})}}$ and variance $\sigma^2_{\Omega_k}$, and the $\Omega_k = 10^{\Omega_{k(\mathrm{dBm})}/10}$ are the log-normal random variables. Unfortunately, there is no known closed form expression for the probability density function (pdf) of the sum of multiple ($N_I \geq 2$) log-normal random variables. However, there is a general consensus that the sum of independent log-normal random variables can be approximated by another log-normal random variable with appropriately chosen parameters. That is,

$$I = \sum_{k=1}^{N_I} 10^{\Omega_{k(\mathrm{dBm})}/10} \approx 10^{Z_{(\mathrm{dBm})}/10} = \hat{I} \tag{12}$$

where $Z_{(\mathrm{dBm})}$ is a Gaussian random variable with mean $\mu_{Z(\mathrm{dBm})}$ and variance σ^2_Z. The problem is to

determine $\mu_{Z(\mathrm{dBm})}$ and variance σ_Z^2 in terms of the $\mu_{\Omega_{k(\mathrm{dBm})}}$ and variance $\sigma_{\Omega_k}^2$, $k = 1, \ldots, N_I$. Several methods have been suggested in the literature to solve this problem including those by Fenton, Schwartz and Yen, and Farley. Each of these methods provides varying degrees of accuracy over specified ranges of the shadow standard deviation σ_Ω, the sum I, and the number of interferes N_I.

Fenton–Wilkinson Method With the Fenton–Wilkinson method, the mean $\mu_{Z(\mathrm{dBm})}$ and variance σ_Z^2 of $Z_{(\mathrm{dBm})}$ are obtained by matching the first two moments of the sum I with the first two moments of the approximation $\hat{I}$. To derive the appropriate moments, it is convenient to use natural logarithms. We write

$$\Omega_k = 10^{\Omega_{k(\mathrm{dBm})}/10} = e^{\epsilon\Omega_{k(\mathrm{dBm})}} = e^{\hat{\Omega}_k} \tag{13}$$

where $\epsilon = (\ln 10)/10 = 0.23026$ and $\hat{\Omega}_k = \epsilon\Omega_{k(\mathrm{dBm})}$. Note that $\mu_{\hat{\Omega}_k} = \epsilon\mu_{\Omega_{k(\mathrm{dBm})}}$ and $\sigma_{\hat{\Omega}_k}^2 = \epsilon^2\sigma_{\Omega_k}^2$. The nth moment of the log-normal random variable Ω_k can be obtained from the moment generating function of the Gaussian random variables $\hat{\Omega}_k$ as

$$E[\Omega_k^n] = E[e^{n\hat{\Omega}_k}] = e^{n\mu_{\hat{\Omega}_k} + (1/2)n^2\sigma_{\hat{\Omega}_k}^2} \tag{14}$$

To find the appropriate moments for the log-normal approximation we can use (14) and equate the first two moments on both sides of the equation

$$I = \sum_{k=1}^{N_I} e^{\hat{\Omega}_k} \approx e^{\hat{Z}} = \hat{I} \tag{15}$$

where $\hat{Z} = \epsilon Z_{(\mathrm{dBm})}$. For example, suppose that $\hat{\Omega}_k$, $k = 1, \ldots, N_I$ have mean $\mu_{\hat{\Omega}_k}$, $k = 1, \ldots N_I$ and identical variances $\sigma_{\hat{\Omega}}^2$. Identical variances are often assumed because the standard deviation of log-normal shadowing is largely independent of the radio path length. Equating the means on both sides of (15)

$$\mu_I = E[I] = \sum_{k=1}^{N_I} E[e^{\hat{\Omega}_k}] = E[e^{\hat{Z}}] = E[\hat{I}] = \mu_{\hat{I}} \tag{16}$$

gives the result

$$\left(\sum_{k=1}^{N_I} e^{\mu_{\hat{\Omega}_k}}\right) e^{(1/2)\sigma_{\hat{\Omega}}^2} = e^{\mu_{\hat{Z}} + (1/2)\sigma_{\hat{Z}}^2} \tag{17}$$

Likewise, we can equate the variances on both sides of (15) under the assumption that the $\hat{\Omega}_k$, $k = 1, \ldots, N_I$ are independent

$$\sigma_I^2 = E[I^2] - \mu_I^2 = E[\hat{I}^2] = \sigma_{\hat{I}}^2 \tag{18}$$

giving the result

$$\left(\sum_{k=1}^{N_I} e^{2\mu_{\hat{\Omega}_k}}\right) e^{\sigma_{\hat{\Omega}}^2}(e^{\sigma_{\hat{\Omega}}^2} - 1) = e^{2\mu_{\hat{Z}}} e^{\sigma_{\hat{Z}}^2}(e^{\sigma_{\hat{Z}}^2} - 1) \tag{19}$$

By squaring each side of (17) and dividing each side of resulting equation by the respective side of (19) We can solve for $\sigma_{\hat{Z}}^2$ in terms of the known values of $\mu_{\hat{\Omega}_k}$, $k = 1, \ldots, N_I$ and $\sigma_{\hat{\Omega}}^2$. Afterwards, $\mu_{\hat{Z}}$ can be obtained from (17). This procedure yields the following solution:

$$\mu_{\hat{Z}} = \frac{\sigma_{\hat{\Omega}}^2 - \sigma_{\hat{Z}}^2}{2} + \ln\left(\sum_{k=1}^{N_I} e^{\mu_{\hat{\Omega}_k}}\right) \tag{20}$$

$$\sigma_{\hat{Z}}^2 = \ln\left((e^{\sigma_{\hat{\Omega}}^2} - 1)\frac{\sum_{k=1}^{N_I} e^{2\mu_{\hat{\Omega}_k}}}{(\sum_{k=1}^{N_I} e^{\mu_{\hat{\Omega}_k}})^2} + 1\right) \tag{21}$$

Finally, $\mu_{Z(\mathrm{dBm})} = \epsilon^{-1}\mu_{\hat{Z}}$ and $\sigma_Z^2 = \epsilon^{-2}\sigma_{\hat{Z}}^2$.
The accuracy of this log-normal approximation can be measured in terms of how accurately the first two moments of $I_{(dB)} = 10\log_{10} I$ are estimated, and how well the cumulative distribution function (cdf) of $I_{(\mathrm{dB})}$ is described by a Gaussian cdf. In problems relating to the co-channel interference outage in cellular radio systems, we are usually interested in the tails of both the complementary distribution function (cdfc) $F_I^C = P(I \geq x)$ and the cdf $F_I(x) = 1 - F_I^C = P(I < x)$. In this case, we are interested in the accuracy of the approximation

$$F_I(x) \approx P(e^{\hat{Z}} \geq x) = Q\left(\frac{\ln x - \mu_{\hat{Z}}}{\sigma_{\hat{Z}}}\right) \tag{22}$$

for large and small values of x. It will be shown later that the Fenton–Wilkinson method can approximate the tails of the cdf and cdfc functions with good accuracy.

REFERENCES

1. C. Y. Chong, and S. P Kumar, Sensor networks: evolution, opportunities, and challenges, *Proceedings of the IEEE,* Vol. 91, No. 8, pp. 1247–1256, 2003.
2. A. Mainwaring, J. Polastre, R. Szewczyk, D. Culler and J. Anderson, Wireless sensor networks for habitat monitoring, *Proceedings of the WSNA*'02, Atlanta, Georgia, Sep 28, 2002.
3. E. Biagioni and G. Sasaki, Wireless sensor placement for reliable and efficient data collection. *Proc. Hawaii Int. Conf. Syst. Sci.*, Jan., 2003.

4. H. Qi, S. S. Iyengar, and K. Chakrabarty, Distributed sensor fusion – a review of recent research, *Journal of the Franklin Institute,* Vol. 338, pp. 655–668, 2001.
5. Y. Zhou, and K. Chakrabarty, Sensor deployment and target localization based on virtual forces, *IEEE Twenty-Second Annual Joint Conference of the Computer and Communications Societies,* Vol. 2, pp. 1293–1303, 2003.
6. T. Wong, T. Tsuchiya, and T. Kikuno, A self-organizing technique for sensor placement in wireless micro-sensor networks, *18th International Conference on Advanced Information Networking and Applications,* Vol. 1, pp. 78–83, AINA 2004.
7. S. Poduri, and G. S. Sukhatme, Constrained coverage for mobile sensor networks, *IEEE International Conference on Robotics and Automation,* Vol. 1, pp. 165–171, 2004.
8. P. Cheng, C. Chuah, and X. Liu, Energy-aware node placement in wireless sensor networks, *IEEE Global Telecommunications Conference,* Vol. 5, pp. 3210–3214, 2004.
9. N. Heo, and P. K. Varshney, A distributed self spreading algorithm for mobile wireless sensor networks, *IEEE International Conference on Wireless Communications and Networking,* Vol. 3, pp. 1597–1602, New Orleans, LA 2003.
10. N. Heo, and P. K. Varshney, An intelligent deployment and clustering algorithm for a distributed mobile sensor network, *IEEE International Conference on Systems, Man and Cybernetics,* Vol. 5, pp. 4576–4581, 2003.
11. N. Heo, and P. K. Varshney, Energy-efficient deployment of Intelligent Mobile sensor networks, *IEEE Transactions on Systems, Man and Cybernetics, Part A,* Vol. 35, No. 1, pp. 78–92, 2005.
12. J. M. Mendel, Fuzzy logic systems for engeneering: a tutorial. *Proceedings of the IEEE*, Vol. 83, No. 3, pp. 345–377, 1995.
13. J. M. Mendel, *Uncertain Rule-Based Fuzzy Logic Systems*,Prentice-Hall, Upper Saddle River, NJ, 2001.
14. T. J. Ross, *Fuzzy Logic with Engineering Applications*,McGraw-Hill International Editions, Singapore, 1997.
15. E. H. Mamdani, Applications of fuzzy logic to approximate reasoning using linguistic systems, *IEEE Transactions on Systems, Man, and Cybernetics,* Vol. 26, No. 12, pp. 1182–1191, 1977.
16. T. S. Rappaport, *Wireless Communications: Principles and Practice*,Prentice-Hall, Upper Saddle River, NJ, 2001.
17. G. L. Stuber, *Principles of Mobile Communication*,Kluwer Academic Publishers, Boston, 2001.



Haining Shu received the B.S. degree in Electronics and Information Systems from Peking University, China in 1996 and M.S. degree in Electrical Engineering from the University of Texas at Dallas in 2002. Prior to the master program, she was a System Engineer at Telecom Planning and Research Institute in Beijing, China. She is currently working toward the Ph.D degree in Electrical Engineering at the University of Texas at Arlington. Her research interests include fuzzy logic systems and applications, distributed source coding, sensor networks and collaborative radar system.



Qilian Liang received the B.S. degree from Wuhan University, China, in 1993, M.S. degree from Beijing University of Posts and Telecommunications in 1996, and Ph.D degree from University of Southern California (USC) in May 2000, all in Electrical Engineering.Dr. Liang joined the faculty of the University of Texas at Arlington in August 2002. Prior to that he was a Member of Technical Staff in Hughes Network Systems Inc at San Diego, California. His research interests include Sensor networks (energy efficiency, cross layer design, optimal sensor deployment, etc), wireless communications, wireless networks, communication system and communication theory, signal processing for communications, fuzzy logic systems and applications, multimedia network traffic modeling and classification, collaborative and distributed signal processing.

Dr. Liang has published more than 100 journal and conference papers, 5 book chapters, and has 6 U.S. patents pending. He received 2002 IEEE Transactions on Fuzzy Systems Outstanding Paper Award, 2003 Office of Naval Research (ONR) Young Investigator Award and 2005 UTA College of Engineering Outstanding Young Faculty Award.



Jean Gao is an Assitant Professor in the Computer Science and Engineering Department at University of Texas at Arlington. She is the recipient of prestigious CAREER Award from National Science Foundation. She received her Ph.D. in electrical engineering from Purdue University, and her M.S. and B.S. in biomedical engineering from Rose-Hulman Institute of Technology and Shanghai Medical University, respectively. Her research interests in computer vision and pattern recognition are object motion estimation, shape classification, multi-dimensional multi-object tracking, and reconstruction.

Medium-Contention Based Energy-Efficient Distributed Clustering (MEDIC) For Wireless Sensor Networks

Liang Zhao and Qilian Liang
Department of Electrical Engineering
University of Texas at Arlington
Arlington, TX 76010, USA
Email: zhao@wcn.uta.edu, liang@uta.edu

Abstract

In this paper, we utilize clustering to organize wireless sensors into an energy-efficient hierarchy. We propose a Medium-contention based Energy-efficient DIstributed Clustering (MEDIC) scheme, through which sensors self-organize themselves into energy-efficient clusters by bidding for cluster headship. This scheme is based on a new criterion that can be used by each sensor node to make a distributed decision on whether electing to be a cluster head or a non-head member, which is a fully distributed approach. Although MEDIC uses only local information, it achieves better performance in terms of effective lifetime and its Data/Energy Ratio is 25% higher than native LEACH (Low-Energy Adaptive Clustering Hierarchy), which relies on other routing algorithms to access global information. A complementary exponential data correlation model is also introduced to simulate different data aggregation effect.

Index Terms

Wireless sensor networks, energy-aware systems, clustering, distributed applications

I. Introduction

A wireless sensor network (WSN) can be thought of as an *ad hoc* network consisting of sensors linked by a wireless medium to perform distributed sensing tasks. Thanks to recent

advances in semiconductor technology, the sensors nodes can be made small in size and cheap for mass production. Due to their low-power antenna and limited energy reserves in form of chemical battery, the sensor nodes can communicate with each other in a short range and work for a relatively short duration.

WSNs share many communication technologies with *ad hoc* networks, but there are some vital differences such as dense deployment and energy constraint [1], thus the protocols developed for traditional wireless ad hoc networks are not necessarily well suited to the unique features of WSNs. When a wireless sensor may have to operate for a relatively long duration on a tiny battery, energy efficiency becomes a major concern.

A variety of “power-aware” routing protocols have been proposed to address this problem. In one school of thoughts [2]–[4], the traditional Shortest Path First strategy is replaced by Least Energy First routing, i.e., a multihop route is preferred to a single-hop one if only multiple short-distance relays cost less energy than a single long-distance transmission. For example, “Minimum Transmission Energy”(MTE) routing [3], [4] was proposed in place of traditional “minimum hops routing”. Another school of thoughts is that nodes are clustered so that a hierarchy is formed [5]–[7]. Based on the observations on cellular networks [8], it would be advisable to partition nodes into clusters for the reasons such as spatial reuse, less update cost, less routing information and less data transmission.

Another dispute in clustering research is whether a cluster head be elected within each cluster. Some researchers [6], [7], [9] argue that it is unreasonable to have a cluster head because every node has similar energy constraint and the cluster head will consume energy much faster. Their methodology breaks the information exchange into two parts; cluster members proactively perform the intracluster exchange, and intercluster information exchange is achieved by demand-based operations. This approach does have some advantage when the traffic is mostly within the cluster, however, when the major traffic in WSN is directed from sensor nodes to the base station, i.e., of intercluster type, headless structure suffers from cumbersome intercluster information exchange.

On the other hand, the extra burden of cluster head can be mitigated by rotating the headship among the members. The rotation can also take advantage of the relaxation effect [10], which indicates frequently reducing the current drawn from the battery enables the battery to recover a portion of its lost capacity and hence lengthens the battery lifetime. In addition, the cluster head

can perform data fusion and reduce the data sent back to the base station. LEACH (Low-Energy Adaptive Clustering Hierarchy) [11], an example of the latter school, can extend network lifetime by an order of magnitude compared with general-purpose multihop approaches. In conclusion, the characteristics of WSN prefer hierarchical structure with cluster heads.

However, the cluster formation in LEACH is based on global information. To access such information, other routing schemes are required. In this sense, LEACH is only a semi-distributed protocol for WSN. Another problem with LEACH is the random head election that cannot guarantee that the desired number of cluster heads be elected or the elected heads evenly positioned. In this paper, we are concerned to optimize the cluster formation using only local information. The intuition behind the proposed Medium-contention based Energy-efficient DIstributed Clustering (MEDIC) is using medium contention to keep the cluster size within an ideal range. By exploiting medium contention to simulate an auction for the cluster headship, we also eliminate the need for location information.

The problems of LEACH are also addressed by other researchers. HEED [12] corrects the problem that no or not enough cluster heads are elected by doubling the probability of electing to be a cluster head for those nodes that are not covered by any cluster heads. In [13], Qin and Zimmermann proposed a voting-based clustering algorithm (VCA) for energy-efficient data dissemination in quasi-stationary sensor networks. Their approach lets sensors vote for their neighbors to elect suitable cluster heads. Connectivity based k-hop clustering [14] proposed to combine two known approaches into a single clustering algorithm which considers connectivity as a primary criterion and lower ID as secondary criterion for selecting cluster heads. Their clustering goal is to minimize the number of clusters, which results in dominating sets of smaller sizes (this is important for applications in broadcasting and Bluetooth formation). Bandyopadhyay and Coyle in [15] extend clustering to multiple levels, generating a hierarchy of clusterheads and observed that the energy savings increase with the number of levels in the hierarchy. They also used stochastic geometry to derive solutions for the values of parameters of our algorithm that minimize the total energy spent in the network when all sensors report data through the cluster heads to the processing center. Weighted Clustering Algorithm (WCA) [16] took into consideration the ideal degree, transmission power, mobility and battery power of a mobile node and tried to keep the number of nodes in a cluster around a pre-defined threshold to facilitate the optimal operation of the medium access control (MAC) protocol, The on-demand execution

of WCA aimed to maintain the stability of the network, thus lowering the computation and communication costs associated with it. In [17], Two-Phase Clustering (TPC) partitions the network into clusters in phase I, each with a cluster head, forming a direct link between cluster member and cluster head. In phase II, each cluster member searches for a neighbor closer than the cluster head within the cluster to set up an energy-saving data relay link. The sensors use either the direct link or the data relay link for their sensed data forwarding depending on the requirements specified by the users or applications. Other work on clustering also tries to distribute the clustering formation [18], [19]. Our approach is independent and orthogonal to these advances in clustering and thus may be used to further improve the energy efficiency.

This paper builds on the work described in [20] by giving a detailed description and analysis of Medium-contention based Energy-efficient DIstributed Clustering (MEDIC). The rest of this paper is organized as follows. Section II reviews LEACH and wireless medium access. Section IV-A introduces the data correlation model that our research is based on. In section IV, we make data-centric analysis of energy consumption in WSN and propose a new criterion that MEDIC bases the self-electing decision on. MEDIC is described in Section V and simulations are given in Section VI. Section VII concludes this paper.

II. Related Work

In this section, we provide some preliminaries needed for further discussion.

A. LEACH

LEACH uses CDMA-TDMA hybrid communication scheme. Each cluster has its own Spread Spectrum code so that the interference between clusters is minimized. For intracluster communications, TDMA slots are assigned for each member to minimize media contention. The operation of LEACH is divided into rounds. At the beginning of each round, cluster heads are elected and other nodes join them as members so that N nodes are partitioned into c clusters. When a cluster is formed, the cluster head creates and broadcasts a time schedule to its members. As shown in Fig.1, each member is assigned a time slot per frame to send its data to its cluster head, and then the cluster head performs data aggregation and sends the resulting data back to the base station. Compared with multihop routing schemes, LEACH shows an outstanding energy efficiency, which is referred to as clustering energy gain in the following.

B. Review of Wireless Medium Access

In this paper, we consider a generic MAC that is compatible with the basic access mechanism described in 802.11 DCF [21]. As illustrated in Fig. 3, after the channel is sensed idle for greater than or equal to a DIFS (Distributed InterFrame Spacing) period, the transmitting node generates a random backoff timer chosen uniformly from the range $[0, w-1]$, where w is the size of contention window. In a binary exponential backoff scheme, the value of w is reset to CW_{min} after each successful transmission, and doubled after each unsuccessful transmission, up to CW_{max} (maximum contention window). The backoff timer is decremented as long as the channel is sensed idle, stopped when a transmission is detected, and reactivated when the channel is sensed idled again for a DIFS period. After the backoff timer reaches zero, the node starts transmission.

The collisions of packets in the contention-based MAC generally degrade channel utilization and increase energy consumption, which motivates establishing transmission schedules to allow nodes to communicate without collisions. In NAMA (Node Activation Multiple Access) [22] and TRAMA (Traffic-Adaptive Medium Access protocol) [23], a distributed election scheme is used to determine which node can transmit at a particular time slot. From this point of view, LEACH is also a schedule-based scheme, in which cluster formation is a random-access period to establish a scheduled-access period collision-free (Fig. 1).

C. Auction Theory

Auctions are heavily studied as a market clearing mechanism to equate demand and supply [24]. In WSN, the cluster headship is a scarce resource, and hence, it would help to view the process of electing a cluster head among nodes in WSNs as an auction for the headship. Auctions can be classified according to several distinct criteria. For example, they can be classified into open and sealed-bid auctions, based on whether all bids are publicly observable. Open auctions can be further classified into ascending and descending price auction. The ascending auction, also called English auction, starts at a low price and bids have to be increasing. The auction stops when no bidder is willing to increase his bid above the highest standing bid. The bidder with the highest bidder wins the auction and pays the highest bid. The English auction is the best-known format of auctions, its drawback is a bidder can take a dominating strategy to win the bid, that is, as long as his bid is higher than the second highest bid, this bidder can win the

bid, even when the highest bid is still much lower than the true value of the auctioned object. As comparison, the descending price auction, also known as Dutch auctions, starts at a high price that continuously decreases on an automated clock. The auction ends when one of the bidders stops the clock. This bidder wins the object and pays the price at which the clock stopped. The aforementioned dominating strategy can't be used in Dutch auctions, therefore, the highest bid in the Dutch auction tends to reflect the true value of the resource. However, our interest in the Dutch auction is for another advantage - its time efficiency. Note that in the Dutch auction, the highest bidder always speaks first, and the auction ends right after its bid. On the other hand, the English auction could start with a lower bid, and when this does happen, it might take several rounds before a bidder dominates. Therefore, we design MEDIC based on the Dutch auction.

D. Radio Energy Consumption

The following model is adopted from [11] where perfect power control is assumed. To transmit l bits over distance d, the sender's radio expends

$$E_{TX}(l,d) = \begin{cases} lE_{elec} + l\epsilon_{fs}d^2 & d < d_0 \\ lE_{elec} + l\epsilon_{mp}d^4 & d \geq d_0 \end{cases} \tag{1}$$

and the receiver's radio expends

$$E_{RX}(l,d) = lE_{elec}. \tag{2}$$

E_{elec} is the unit energy consumed by the electronics to process one bit of message, ϵ_{fs} and ϵ_{mp} are the amplifier factor for free-space and multi-path models, respectively, and d_0 is the reference distance to determine which model to use. The values of these communication energy parameters are set as in Table I.

III. Problems and Motivations

Random election has been widely used in algorithms for wireless sensor networks for its simplicity and convenience [11]. However, there are two fundamental drawbacks in random election:

a. **Dependence on Global Information** In LEACH, each node i elects itself to be a cluster head at the beginning of round $r + 1$(which starts at time t) with probability $P_i(t)$. Two

ways were used to determine the self-electing probability $P_i(t)$ in [11]. If all nodes are assumed to start with an equal amount of energy, $P_i(t)$ is given by

$$P_i(t) = \begin{cases} \frac{c}{N - c*(r mod \frac{N}{c})} & : C_i(t) = 1 \\ 0 & : C_i(t) = 0 \end{cases}, \tag{3}$$

where c is the desired number of clusters and $C_i(t)$ is the indicator function determining whether or not node i has been a cluster head in the most recent $(r \ mod \ (N/c))$ rounds. The more general estimate of $P_i(t)$ is given by

$$P_i(t) = min\{\frac{E_i(t)}{E_{total}(t)}c, 1\}, \tag{4}$$

where $E_i(t)$ is the current energy(i.e. remaining battery capacity) of node i and

$$E_{total}(t) = \sum_{i=1}^{N} E_i(t). \tag{5}$$

Essentially, N in (3) and E_{total} in (4) are global information, which is only accessible via other routing schemes.

b. **High Variation** Although random decision generally strengthens the robustness by avoiding sticking to a single choice, high variation in decision may shift the decision too far away from the optimal range. For example, suppose (4) is used and all nodes have equal amount of energy, if N nodes want to elect c heads among them, then the self-electing probability for each node is

$$p = \frac{c}{N} \tag{6}$$

Then the probability of "n heads are elected" is

$$Pr(n \text{ elected heads}) = \binom{N}{n} p^n (1-p)^{(N-n)} \tag{7}$$

The distribution of the number of elected heads is listed in Table II. Obviously, too few (Fig. 2(c)) and too many (Fig. 2(d)) elected heads would damage the energy efficiency. Moreover, in the case of "no elected head" whose probability listed in row 1, all the nodes have to communicate directly with the base station, in which case all the clustering energy gain is lost. When the number of elected heads is too few, for example, only one head is elected, the head may be exhausted by the tremendous data sent to it. In such cases, the energy efficiency is tremendously compromised.

Another problem introduced by the random head selection is that the sensor locations are not taken into consideration. Obviously, the even layout of heads would favor energy efficiency (Fig. 2(a)). When heads are randomly selected as in LEACH, elected heads sometimes clump together as shown in Fig. 2(b), which leads to unnecessary energy waste.

IV. Optimal Clustering

In this section, we first introduce a data correlation model, and then based on this model, make data-centric analysis of energy consumption in WSN. A new criterion is proposed for clustering, which is the theoretical basis of Medium-contention based Energy-efficient DIstributed Clustering (MEDIC).

A. Data Correlation Model

The data collected by neighboring sensors have a lot of redundancy, thus, [11] assumes perfect data correlation that all individual signals from members of the same cluster can be combined into a single representative signal. Nevertheless, this assumption cannot hold when the cluster size increases to some extent. Therefore, we develop a complementary exponential data correlation model based on the observations in distributed data compression [25], [26].

Considering the phenomenon of interest as a random process, the correlation between data collected by two sensors is generally a decreasing function of the distance r between them. After the data aggregation removes most of the redundancy, the residue can be assumed to be an increasing function of r. Based on the above observation, the data aggregation effect is modeled as below.

Suppose there are M_k non-head members in cluster k ($k = 1, 2, 3, ..., c$), the ith member ($i = 1, 2, 3, ..., M_k$) collects l bits and sends them back to its head k at distance r_{ki}, the head expends $2lE_{DA}$ Joules on the data aggregation of the $2l$ bits (l bits collected by itself and another l bits by its ith member), where E_{DA} is set as $5nJ/bit$ as in [11] and listed in Table I. The resulting data is assumed of $l(1 + \eta_{ki})$ bits, where η_{ki} is data aggregation residue ratio and assumed to be complementary exponential, specifically,

$$\eta_{ki} = 1 - e^{-\alpha r_{ki}}, 0 < \alpha < 1, \tag{8}$$

where α is a small positive real number whose magnitude depends on specific phenomenon of interest. For example, the light, acoustic, seismic and thermal signals often show a strong

correlation at short distance, and thus, α will have smaller values for such data. Since η is a monotonically decreasing function of α and r, η approaches zero for smaller α and r. This model can approach the perfect-data-correlation assumption in [11] by decreasing α or approach the no-data-aggregation assumption in [3], [4] by increasing α, thus, different scenarios can easily be set up by varying α.

B. Problem Formulation

Clustering has been widely used in pattern recognition, and we use it to obtain the energy-efficient organization for WSN. From the data-centric view, the data collected by a node can be sent back directly to the base station or relayed by a cluster head. The first case occurs if this node is a cluster head; the data collected by head k is data-aggregated (with the data collected by its members) and sent back to the base station. Thus, the energy cost for each bit of data collected by head k is

$$J_{CH(k)} = E_{DA} + E_{elec} + \epsilon_{mp} d_k^4, \tag{9}$$

where d_k is the distance between head k and the base station.

For the second case, consider non-head member ki, the ith sensor in cluster k, with distance r_{ki} to its cluster head, member ki sends its data to head k, and then head k performs data aggregation on the data and sends the resulting data to the base station. Thus, the energy cost for each bit of data collected by non-head member ki is

$$J_{CM(ki)} = E_{elec} + \epsilon_{fs} r_{ki}^2 + E_{elec} + E_{DA} + \eta(r_{ki})(E_{elec} + \epsilon_{mp} d_k^4), \tag{10}$$

where $\eta(r_{ki})$ is the data aggregation residue ratio introduced in Section IV-A.

Considering all c clusters, the overall cost is

$$J_{total} = \sum_{k=1}^{c} \{ J_{CH(k)} + \sum_{i=1}^{M_k} J_{CM(ki)} \}, \tag{11}$$

where M_k is the number of non-head members in cluster k.

Taking $E[J_{total}]$ the expected value of the overall energy cost as the objective function, the original problem is translated into an objective function clustering. If a central control scheme is possible, an iterative algorithm can be run at the base station to minimized $E[J_{total}]$. For example, Fuzzy c-Means is utilized in [27] to minimize a Euclidean-distance-based functional representing the energy cost in Wireless Personal Area Networks. However, since WSNs are

working in *ad hoc* mode, clustering decision must be distributed to each sensor node. Thus, our goal is using only local information to achieve energy-efficient clustering.

C. Influence Range

When a node finds no cluster head around, it should naturally elect to be a cluster head. However, if a node is close to a cluster head, there could be some energy gain or loss if it joins that cluster. In the following, we will discuss how a node decided to be a cluster head when it finds a cluster head in its communication range. The energy gain diminishes when the distance between the non-head member and the head increases. Consequently, the energy gain approaches zero at some critical distance, termed as influence range. To determine the influence range, consider a node i with a head k at distance r. The node could choose to be a non-head member or a head, which would consequently cost J_{CM} or J_{CH} as in (10) and (9). Naturally, the decision should be based on the comparison of J_{CM} and J_{CH} as

$$J_{CM} \underset{CM}{\overset{CH}{\gtrless}} J_{CH}, \tag{12}$$

i.e., the decision rule for each sensor is:

$$\text{Node } i \text{ elects to be } \begin{cases} \text{a non-head member} & \text{if } J_{CM} < J_{CH} \\ \text{a cluster head} & \text{if } J_{CM} > J_{CH} \end{cases} \tag{13}$$

We call this criterion as local energy efficiency criterion, because it is based on only the local information. Substituting (9) and (10) into (12), we obtain

$$\begin{aligned} E_{elec} + \epsilon_{fs} r_{ik}^2 + E_{elec} + E_{DA} + \eta(r_{ik})(E_{elec} + \epsilon_{mp} d_k^4) \\ \underset{CM}{\overset{CH}{\gtrless}} E_{DA} + E_{elec} + \epsilon_{mp} d_i^4. \end{aligned} \tag{14}$$

The influence range can be obtained by equating two sides though a closed form may be unavailable. Obviously, the cluster radius R_c has to be much smaller than the influence range because the energy gain is so low at the outer ring that a new cluster be formed. Although this criterion is too complex to be used in real applications, it promotes using R_c instead of c as the clustering objective parameter to guide the election. Denote the areas occupied by the whole WSN and the cluster by S_N and S_c respectively,

$$c \approx \frac{S_N}{S_c}. \tag{15}$$

Assume S_N and S_c are both circular, R_c is related to c by

$$c = \frac{\pi R^2}{\pi R_c^2} = (\frac{R}{R_c})^2, \tag{16}$$

where R is the radius of S_N. Although it is mathematically equivalent to partition nodes into c clusters or to organize nodes into clusters with radius R_c, the former is definitely a global approach, which leads to dependence on the global information. Thus, the latter is more suitable for a distributed algorithm.

D. Optimal Cluster Size

As indicated in (16), it is equivalent to determine c or R_c. Here, we try to analytically determine the optimal value of c using the introduced models. LEACH can only determine a rough range $c_{opt} \in [1, 6]$ for a similar 100-node network [11], while our analysis predicts the optimal value of R_c in simulation with satisfying accuracy.

The typical scenario is that N nodes are distributed uniformly in a circular region with radius R. There are c clusters with one cluster head and $n-1$ non-head members within each cluster. n is the average number of cluster members and related to c by

$$n \approx N/c. \tag{17}$$

Based on (11), the average total energy cost can be approximated by

$$\begin{aligned} \bar{J}_{total} &= c(\bar{J}_{CH} + (n-1)\bar{J}_{CM}) \\ &= c\bar{J}_{CH} + (N-c)\bar{J}_{CM} \end{aligned} \tag{18}$$

where $\bar{J}_{CH}$ and $\bar{J}_{CM}$ are the average energy cost for the cluster head and non-head member respectively.

Following (9) and (10),

$$\bar{J}_{CH} = E_{DA} + E_{elec} + \epsilon_{mp} E[d^4], \tag{19}$$

$$\bar{J}_{CM} = E_{elec} + \epsilon_{fs} E[r^2] + E_{elec} + E_{DA} + E[\eta(r)(E_{elec} + \epsilon_{mp} d^4)]. \tag{20}$$

Since all nodes are independently deployed, r and d are independent, thus, (20) can be written as

$$\bar{J}_{CM} = E_{elec} + \epsilon_{fs} E[r^2] + E_{elec} + E_{DA} + E[\eta(r)](E_{elec} + \epsilon_{mp} E[d^4]). \tag{21}$$

We estimate the expected values in (19) and (21) as follows. Assuming the cluster head is at the center of mass of the cluster,

$$\begin{aligned} E[r^2] &= \int\int_{S_c} r^2 \rho_c(r,\theta) r dr d\theta \\ &= \int_0^{2\pi}\int_0^{R_c} r^2 \rho_c(r,\theta) r dr d\theta \end{aligned} \tag{22}$$

where $\rho_c(r,\theta)$ is the node distribution density. Since the nodes are assumed to be uniformly distributed, $\rho_c(r,\theta)$ is a constant given by

$$\rho_c = 1/\pi R_c^2 = c/(\pi R^2). \tag{23}$$

Substituting (23) and (16) into (22),

$$\begin{aligned} E[r^2] &= \frac{\pi \rho_c R_c^4}{2} \\ &= \frac{R^2}{2c} \end{aligned} \tag{24}$$

Similarly,

$$\begin{aligned} E[\eta(r)] &= \int\int_{S_c} (1-e^{-\alpha r}) \rho_c(r,\theta) r dr d\theta \\ &= \frac{c}{\pi R^2}\int_0^{2\pi}\int_0^{R_c} (1-e^{-\alpha r}) r dr d\theta \\ &= \frac{2c}{R^2}\int_0^{R_c} (1-e^{-\alpha r}) r dr \qquad (25) \\ &= 1 + \frac{2c}{\alpha^2 R^2}(e^{-\frac{\alpha R}{\sqrt{c}}}(\frac{\alpha R}{\sqrt{c}}+1)-1) \qquad (26) \end{aligned}$$

$$\begin{aligned} E[d^4] &= \int\int_{S_N} |r - r_{BS}|^4 \rho_N(r,\theta) r dr d\theta \\ &= \frac{1}{\pi R^2}\int_0^{2\pi}\int_0^{R} (r^2 + r_{BS}^2 - 2 r r_{BS} cos(\theta - \theta_{BS}))^2 r dr d\theta \end{aligned} \tag{27}$$

Since $E[d^4]$ is a function of R and irrelevant to c, we keep it in the further derivation.

The optimal value of c can be obtained by setting $\frac{\partial \bar{J}_{total}}{\partial c}$ to zero.

$$\begin{aligned} \frac{\partial \bar{J}_{total}}{\partial c} &= \bar{J}_{CH} - \bar{J}_{CM} + (N-c)\frac{\partial \bar{J}_{CM}}{\partial c} \\ &= \epsilon_{mp} E[d^4] - E_{elec} - \epsilon_{fs}\frac{R^2}{2c} - E[\eta(r)](E_{elec} + \epsilon_{mp} E[d^4]) \\ &\quad + (N-c)(-\frac{\epsilon_{fs} R^2}{2c^2} + \frac{\partial E[\eta(r)]}{\partial c}(E_{elec} + \epsilon_{mp} E[d^4])), \end{aligned} \tag{28}$$

$$\begin{aligned}\frac{\partial^2 \bar{J}_{total}}{\partial c^2} &= \frac{\epsilon_{fs}R^2}{2c^2} - \frac{\partial E[\eta(r)]}{\partial c}(E_{elec} + \epsilon_{mp}E[d^4]) \\ &\quad -(-\frac{\epsilon_{fs}R^2}{2c^2} + \frac{\partial E[\eta(r)]}{\partial c}(E_{elec} + \epsilon_{mp}E[d^4])) \\ &\quad +(N-c)(\frac{\epsilon_{fs}R^2}{c^3} + \frac{\partial^2 E[\eta(r)]}{\partial c^2}(E_{elec} + \epsilon_{mp}E[d^4])) \\ &= \frac{\epsilon_{fs}R^2}{c^2} + (N-c)\frac{\epsilon_{fs}R^2}{c^3} \\ &\quad -2\frac{\partial E[\eta(r)]}{\partial c}(E_{elec} + \epsilon_{mp}E[d^4]) \\ &\quad +(N-c)\frac{\partial^2 E[\eta(r)]}{\partial c^2}(E_{elec} + \epsilon_{mp}E[d^4]) \end{aligned} \tag{29}$$

where $\frac{\partial E[\eta(r)]}{\partial c}$, $\frac{\partial^2 E[\eta(r)]}{\partial c^2}$ can be computed based on (26).

$$\frac{\partial E[\eta(r)]}{\partial c} = \frac{2}{\alpha^2 R^2}(e^{-\frac{\alpha R}{\sqrt{c}}}(\frac{\alpha R}{\sqrt{c}} + 1) - 1) + \frac{e^{-\frac{\alpha R}{\sqrt{c}}}}{c} \tag{30}$$

$$\frac{\partial^2 E[\eta(r)]}{\partial c^2} = \frac{\alpha R e^{-\frac{\alpha R}{\sqrt{c}}}}{2c^{5/2}} \tag{31}$$

Since it is impossible to solve (28) algebraically, we turn to the numerical solution. For example, the base station is located at $(r_{BS}, \theta_{BS}) = (125, 0)$ and $N = 100$, $R = 50m$ in our experiments, we can evaluate (27) as

$$E[d^4] = 5.8997e + 008. \tag{32}$$

In Fig. 4(a)(b), we plot $\frac{\partial \bar{J}_{total}}{\partial c}$ over c for $\alpha = 0.001$ and $\alpha = 0.05$ respectively. The corresponding c_{opt} can be easily obtained by setting $\frac{\partial \bar{J}_{total}}{\partial c} = 0$.

$$c_{opt} = \begin{cases} 1.6569, & \text{for } \alpha = 0.001 \\ 20.2600, & \text{for } \alpha = 0.05 \end{cases} \tag{33}$$

Note that $\frac{\partial^2 \bar{J}_{total}}{\partial c^2} \mid_{c_{opt}=1.6569} = 2.98E-7 > 0$ and $\frac{\partial^2 \bar{J}_{total}}{\partial c^2} \mid_{c_{opt}=20.26} = 2.51E-9 > 0$, which indicates $\bar{J}_{total}$ is minimized at these c_{opt}'s. According to (16), the corresponding R_c is

$$R_c = \begin{cases} 38m, & \text{for } \alpha = 0.001 \\ 11m, & \text{for } \alpha = 0.05 \end{cases} \tag{34}$$

We are also interested in the relation of N to c_{opt}. In Fig. 5(a)(b), we plot c_{opt} over N for $\alpha = 0.001$ and $\alpha = 0.05$ respectively. These figures show that c_{opt} is an increasing function of N, which indicates the clustering objective parameter (c or R_c) should be adjusted adaptively if N varies.

V. MEDIUM-CONTENTION BASED ENERGY-EFFICIENT DISTRIBUTED CLUSTERING

Medium-contention based Energy-efficient DIstributed Clustering (MEDIC) is designed to replace the cluster formation occurring at the beginning of each round in LEACH. We design MEDIC based on the Dutch auction for its time efficiency. Note that in the Dutch auction, the highest bidder always speaks first, and the auction ends right after its bid. On the other hand, the English auction could start with a lower bid, and when this does happen, it might take several rounds before a bidder dominates.

In MEDIC, there is no global broadcast. As shown in Fig. 6, each node firstly broadcasts its vital information at the maximum radio power level so that the knowledge is spread as widely as possible. Such "maximum-power" broadcasts are not frequent in MEDIC, which helps saving energy. The vital information may include nodes' energy, location, etc., though only energy information is needed by MEDIC. Then, each node counts its neighbors and broadcasts the number of its neighbors at an adjusted power level corresponding to the cluster radius R_c. The cluster radius R_c is an important system parameter for energy efficiency. As shown in Section IV-D, given a specific type of application, R_c is mainly determined by the node density. In MEDIC, each node should choose an appropriate R_c according the neighbor count in its transmission range, which is a good estimator of the local density.

If a node's headship potential *qualifies* as a head compared to its neighbors', it will try to claim the headship by broadcasting locally, which can be viewed as placing a bid for the headship. A node's "neighbors" are defined as the nearby nodes within distance R_c from that node. Due to the possible contention for the headship, such bids could fail, which is indicated by the collision of "headship claims". Using the modified MAC described below, the bidders will contend with each other until a node with satisfactory potential wins. By doing so, the head-to-be expels other possible heads in its neighborhood, and in consequence, the clusters with desired size are formed.

The headship potential is an important parameter, which replaces the self-electing probability used in native LEACH. As discussed in [11], the node's energy is important to determine its potential because the headship can be rotated among nodes by assigning more potential to the nodes with higher energy. In addition, we propose taking the number of neighbors into consideration, because the energy gain is prominent only in the neighborhood of the head as

shown in Section IV-C and thus it is energy-efficient to let the node with more neighbors win the headship.

Based on these considerations, the qualification conditions are set as below. For any node, let $\mathcal{N}$ denote the set of its neighbors, $E(i)$ and $B(i)$ be the energy and the number of neighbors of the ith neighbor respectively, $i \in \mathcal{N}$. The thresholds are set as the linear combination of the maximum and mean value of corresponding parameters as in (35) and (36) so that the thresholds are adapted to the current distribution of parameters and take values between the maximum and mean.

$$E_{Th} \triangleq \gamma_1 \max_{i \in \mathcal{N}} E(i) + (1-\gamma_1) \operatorname{mean}_{i \in \mathcal{N}} E(i) \tag{35}$$

$$B_{Th} \triangleq \gamma_2 \max_{i \in \mathcal{N}} B(i) + (1-\gamma_2) \operatorname{mean}_{i \in \mathcal{N}} B(i) \tag{36}$$

The conditions can be relaxed by decreasing γ_1, γ_2, where $\gamma_1, \gamma_2 \in [0, 1]$. Since there is no closed-form objective function, it is difficult to determine optimal γ_1, γ_2 analytically. Fortunately, our experiments show that the performance is not sensitive to the setting of γ_1, γ_2. Thus, we simply choose a smaller value for γ_1 and a larger value for γ_2 as $\gamma_1 = 0$, $\gamma_2 = 0.8$, because we want to emphasize the position condition in order to achieve energy efficiency and relax the energy condition in order to accept more nodes into the headship auction.

Depending on their conditions, the nodes classify themselves into three categories shown in Fig. 7. Each node can classify itself into one of the three categories by comparing itself to its neighbors. The nodes meeting both conditions consider themselves in Category-A, meeting one of the conditions indicates Category-B, and Category-C for the rest which fail both conditions. Note that $DIFS_B = DIFS_A + CW_{min}$ in Fig. 8, Category-B bidders have to wait CW_{min} longer than Category-A to ascertain there are no Category-A bidders in their neighborhoods. That is, no matter which slot Category-A nodes randomly choose to send out the claim, there is no chance for a Category-B node to access the channel if there is one Category-A node in its neighborhood. The extreme case that no heads are elected is avoided by permitting Category-B bidders into the headship auction because it is impossible that there are only Category-C nodes in the neighborhood.

Once a node successfully sends out the “headship claim”, its neighbors must join it by sending “Request to join”. Since these requests can be eavesdropped by their neighbors, their neighbors can correspondingly correct their numbers of unclustered neighbors. If a node finds all its

neighbors are clustered, it can elect to be a cluster head by sending out a "headship claim". Those nodes outside the neighborhood of existing cluster heads cannot join any clusters. When the public channel is idle again, which indicates there is no node in its neighborhood trying to join existing clusters, another round of auction will begin until all nodes are clustered.

VI. Simulations

In this section, we compare the performance of MEDIC and LEACH using computer simulations. 100 nodes with 2J initial energy were evenly distributed in a circular region with diameter $100m$, and the base station was located at $(125m, 0)$. We ran LEACH and MEDIC over 1000 random network topologies for each c or R_c and took average of collected data. Since the steady state is much longer than the cluster formation phase, the time and energy used in the cluster formation is generally two orders of magnitude less than in the steady state, whose effect is safe to neglect.

A. MEDIC vs. LEACH

In this case, MEDIC is compared to native LEACH for nearly perfect data correlation (α = 0.001). Fig.9(a)(b) plot the received data in the base station over time and the energy dissipated, respectively, and Fig.9(c)(d) plot the number of survival nodes whose batteries are not completely exhausted over time and per given amount of received data in the base station, respectively. The results show that the *maximum transportation*, the total data delivered back to the base station during a simulation, was maximized at $c \approx 7$ for LEACH and $R_c \approx 40m$ for MEDIC (See Fig. 12 and Fig. 13).

At first glance, LEACH seems have longer lifetime than MEDIC as shown in Fig. 9(a). However, a further study of Fig. 10 reveals that LEACH cannot guarantee the data delivery during the later phase. The reason is that the ill result of random election (e.g. too few heads are elected) often puts tremendous burden on the heads whose energy is already low during the later phase. After the heads are exhausted quickly, the cluster members remain idle during the rest of that round, which seems to extend the lifetime. Therefore, we define the effective lifetime as when the data loss remains below 10 percent. Fig. 10 shows that MEDIC extends the effective lifetime by about $3200s$.

Another good measurement of energy efficiency is the ratio of data transportation over energy consumption, termed as Data/Energy Ratio (DER), which is indicated by the slope in Fig. 9(b). Higher slope implies the corresponding scheme can transport more data with given amount of energy dissipation. Fig. 9(b) shows MEDIC increased DER by about 25%. The energy efficiency improvement is achieved by successfully electing required number of cluster heads and evenly distributing them among the whole sensor networks. In MEDIC, once a node successfully wins the bid for cluster headship, it also elimininate all its neighbor's possibility to be a cluster head. And the nodes outside its influence range still have chance to be a cluster head. In this way, MEDIC avoids electing too many or too few cluster heads in the simulation, and the elected cluster heads are evenly laid out. The mean and std of cluster heads are plotted in Fig.11. The higher variation in the head election of LEACH indicates the clustering in the LEACH led to worse result, which is the the main reason for its damaged energy efficency.

The analysis in section IV-D indicates that R_c should be adapted to the decreasing node density. Since the death of nodes decreases the node density, we expect the optimal R_c to decrease accordingly. However, since MEDIC remarkably extends the effective lifetime, the number of survival nodes does not decrease visibly during most of the network lifetime. Therefore, we need not adapt R_c to keep energy efficiency.

B. Optimal R_c at Varying Data Aggregation Effect

In this case, MEDIC is evaluated at different α. We ran 1000 simulations at different R_c with $\alpha = 0.05$ to determine optimal R_c. Fig.14 shows that the performance of MEDIC is optimal at around $R_c = 10m$, which is far from $R_c = 40m$ with $\alpha = 0.001$. The reason that the smaller clusters are formed is that the influence range shrinks when the data correlation decreases. These values of R_c agree well with the analysis in section IV-D for both values of α. This shows the advantage of MEDIC over original LEACH; the clusters resulting from MEDIC conform to the energy-efficient expectation. This also shows the advantage of our data correlation model; we can easily fit the simulation scenarios for the phenomena of interest by varying α.

VII. CONCLUSION

The previous clustering researches often take a global approach, which is appropriate for global optimization. However, when a distributed clustering is desired, the already-answered questions

such as “How many clusters should the nodes be partitioned into?” have to be translated into a distributed version, that is, ’‘What’s the appropriate cluster size?”, because it is easier for a node to know its cluster size than the number of clusters in the whole network. In this paper, we take a fully distributed approach to energy efficiency for WSN. Motivated by the local energy efficiency criterion, we propose using the cluster size instead of the number of clusters as the clustering objective parameter in clustering. Furthermore, we utilize the medium contention to implement the headship auction to keep the cluster size within an ideal range. As shown by the simulations, although the proposed MEDIC uses only local information, it achieves better energy efficiency than native LEACH in terms of Data/Energy Ratio and effective lifetime. The simulations also show that the optimal cluster radius obtained from the experiments agrees well with the analysis of optimal clustering, which indicates the performance of our distributed clustering is close to that of the global optimal one.

ACKNOWLEDGMENT

This work was supported by the U.S. Office of Naval Research (ONR) Young Investigator Program Award under Grant N00014-03-1-0466.

The second author would like to thank his Research Assistant Mr. Xiang Hong for helping with part of the simulations.

REFERENCES

[1] I. F. Akyildiz, W. Su, Y. Sankarasubramaniam, and E. Cayirci, “A survey on sensor networks,” *IEEE Commun. Mag.*, vol. 20, pp. 102–114, Aug. 2002.

[2] R. Min, M. Bhardwaj, S.-H. Cho, N. Ickes, E. Shih, A. Sinha, A. Wang, and A. Chandrakasan, “Energy-centric enabling technologies for wireless sensor networks,” *IEEE Wireless Communications*, vol. 9, no. 4, pp. 28 – 39, Aug. 2002.

[3] T. Shepard, “A channel access scheme for large dense packet radio networks,” in *Proc. ACM SIGCOMM*, Stanford, CA, Aug. 1996, pp. 219–230.

[4] M. Ettus, “System capacity, latency and power consumption in multihop-routed ss-cdma wireless networks,” in *Proc. Radio and Wireless Conf. (RAWCON’98)*, Colorado Springs, CO, Aug. 1998, pp. 55–58.

[5] R. Ramanathan and M. Steenstrup, “Hierarchically-organized, multihop mobile wireless networks for quality-of-service support,” *Mobile Networks Appl.*, vol. 3, no. 1, pp. 101–119, 1998.

[6] A. B. McDonald and T. F. Znati, “A mobility-based framework for adaptive clustering in wireless ad hoc networks,” *IEEE J. Select. Areas Commun.*, vol. 17, pp. 1466–1487, Aug 1999.

[7] P. Krishna, N. H. Vaidya, M. Chatterjee, and D. K. Pradhan, “A cluster-based approach for routing in dynamic networks,” *ACM Comput. Commun. Rev.*, vol. 17, no. 2, pp. 49 – 64, Apr. 1997.

[8] T. S. Rappaport, *Wireless Communications:Principles and Practice*. Upper Saddle River, NJ: Prentice-Hall, 2002.

[9] C. R. Lin and M. Gerla, "Adaptive clustering for mobile wireless networks," *IEEE J. Select. Areas Commun.*, vol. 15, pp. 1265–1275, Sept. 1997.

[10] C. F. Chiasserinia and R. R. Rao, "Pulsed battery discharge in communication devices," in *Proc. Mobicom*, 1999, pp. 88–95.

[11] W. B. Heinzelman, A. P. Chandrakasan, and H. Balakrishnan, "An application-specific protocol architecture for wireless microsensor networks," *IEEE Trans. Wireless Commun.*, vol. 1, no. 4, pp. 660 – 670, Oct. 2002.

[12] O. Younis and S. Fahmy, "Distributed clustering in ad-hoc sensor networks: a hybrid, energy-efficient approach," in *Twenty-third Annual Joint Conference of the IEEE Computer and Communications Societies (INFOCOM 2004)*, vol. 1, 2004, pp. –640.

[13] M. Qin and R. Zimmermann, "An energy-efficient voting-based clustering algorithm for sensor networks," in *Sixth International Conference on Software Engineering, Artificial Intelligence, Networking and Parallel/Distributed Computing, 2005 and First ACIS International Workshop on Self-Assembling Wireless Networks. SNPD/SAWN 2005.*, 2005, pp. 444–451.

[14] G. Chen, F. Nocetti, J. Gonzalez, and I. Stojmenovic, "Connectivity based k-hop clustering in wireless networks," in *Proceedings of the 35th Annual Hawaii International Conference on System Sciences (HICSS'02).*, 2002, pp. 2450–2459.

[15] S. Bandyopadhyay and E. Coyle, "An energy efficient hierarchical clustering algorithm for wireless sensor networks," in *Twenty-Second Annual Joint Conference of the IEEE Computer and Communications Societies (INFOCOM'03)*, vol. 3, 2003, pp. 1713–1723 vol.3.

[16] M. Chatterjee, S. Sas, and D. Turgut, "An on-demand weighted clustering algorithm (wca) for ad hocnetworks," in *IEEE Global Telecommunications Conference (GLOBECOM '00)*, vol. 3, 2000, pp. 1697–1701 vol.3.

[17] W. Choi, P. Shah, and S. Das, "A framework for energy-saving data gathering using two-phase clustering in wireless sensor networks," in *The First Annual International Conference on Mobile and Ubiquitous Systems: Networking and Services (MOBIQUITOUS'04)*, 2004, pp. 203–212.

[18] K. Chowdhury, P. Chanda, D. P. Agrawal, and Q.-A. Zeng, "Dca: A distributed channel allocation scheme for wireless sensor networks," in *16th International Symposium on Personal Indoor and Mobile Radio Communications (PIMRC'05)*, Berlin, Germany, September 2005.

[19] V. Shah, H. Deng, and D. Agrawal, "Parallel cluster formation for secured communication in wireless ad hoc networks," in *Proceedings. 12th IEEE International Conference on Networks (ICON 2004)*, vol. 2, 2004.

[20] L. Zhao, X. Hong, and Q. Liang, "Energy-efficient self-organization for wireless sensor networks: A fully distributed approach," in *IEEE Globecom'04*. Dallas, TX: IEEE, Dec 2004.

[21] *Wireless LAN Medium Access Control(MAC) and Physical Layer(PHY) Specifications*, 1997.

[22] L. Bao and J. Garcia-Luna-Aceves, "Hybrid channel access scheduling in ad hoc networks," in *Proc. IEEE Tenth Int'l Conf on Network Protocols (ICNP)*, November 2002.

[23] W. Rajendran, K. Obraczka, and J. Garcia-Luna-Aceves, "Energy-efficient, collision-free medium access control for wireless sensor networks," in *Proc. First Int'l Conf on Embedded Networked Sensor Systems*, November 2003.

[24] F. Menezes and P. Monteiro, *An Introduction To Auction Theory*. Oxford University Press Inc., 2005.

[25] S. Pradhan, J. Kusuma, and K. Ramchandran, "Distributed compression in a dense microsensor network," *IEEE Signal Processing Mag.*, vol. 19, no. 2, pp. 51–60, Mar 2002.

[26] A. Boulis, S. Ganeriwal, and M. Srivastava, “Aggregation in sensor networks: an energy-accuracy trade-off,” in *Proceedings of the First IEEE International Workshop on Sensor Network Protocols and Applications*, May 2003, pp. 128–138.

[27] Q. Liang, “A design methodology for wireless personal area networks with power efficiency,” in *IEEE Wireless Communications and Networking 2003(WCNC’03)*, vol. 3, 2003, pp. 16–20.

List of Tables

I Communication Energy Parameters 21
II Outcome of 100 nodes electing 5 heads. 21

TABLE I

COMMUNICATION ENERGY PARAMETERS

Name	Value
d_0	86.2m
E_{elec}	$50nJ/bit$
E_{DA}	$5nJ/bit$
ϵ_{fs}	$10pJ/bit/m^2$
ϵ_{mp}	$0.0013pJ/bit/m^4$

TABLE II

OUTCOME OF 100 NODES ELECTING 5 HEADS.

n: number of elected heads	$Pr(n$ elected heads$)$
0	0.0059
1	0.0312
2	0.0812
3	0.1396
4	0.1781
5	0.1800
6	0.1500
7	0.1060
8	0.0649
9	0.0349
≥ 10	0.0341

LIST OF FIGURES

1 Time line showing LEACH's frame structure. 21
2 100 nodes elect 5 heads. 21
3 A generic MAC. 22
4 Plot of $\frac{\partial \bar{J}_{total}}{\partial c}$ for $N = 100$, $R = 50m$ and $(r_{BS}, \theta_{BS}) = (125, 0)$.(a)$\alpha = 0.001$. (b)$\alpha = 0.05$. 22
5 Plot of c_{opt} vs. N for $R = 50m$ and $(r_{BS}, \theta_{BS}) = (125, 0)$.(a)$\alpha = 0.001$. (b)$\alpha = 0.05$. 22
6 Flow chart of a node in MEDIC. 23
7 Categories of bidders. 23
8 The Medium Access Control used in MEDIC. 24
9 MEDIC vs. LEACH. (a) Amount of data received at the base station over time. (b) Amount of data received at the base station per given amount of energy. (c) Number of survival nodes over time. (d) Number of survival nodes per amount of data received in the base station. 24
10 MEDIC vs. LEACH. Node-to-basestation throughput over time. 25
11 The elected number of heads (Average and std). 25
12 Data of LEACH. 26
13 Data of MEDIC at $\alpha = 0.001$. 26
14 Data of MEDIC at $\alpha = 0.05$. 27

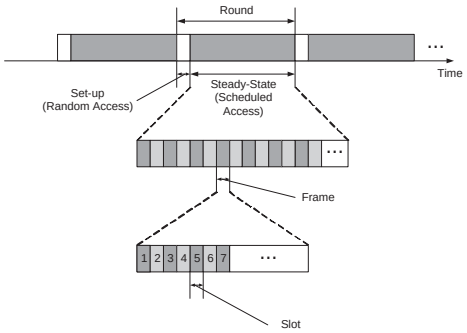


Fig. 1. Time line showing LEACH's frame structure.

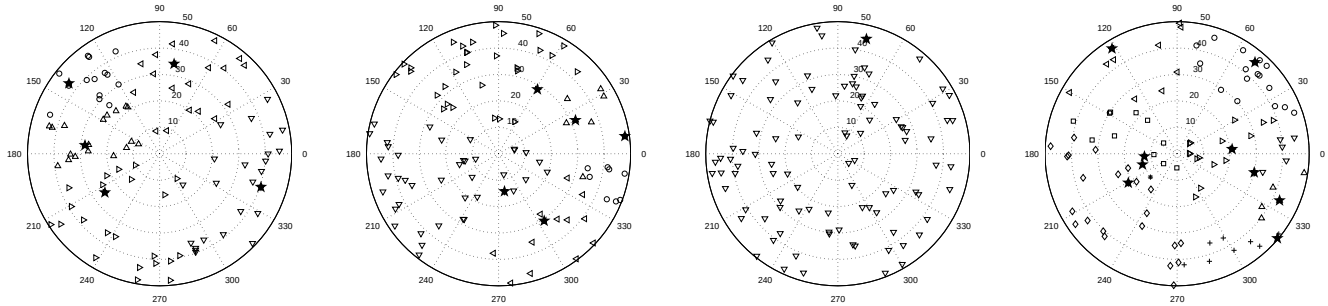


Fig. 2. 100 nodes elect 5 heads (Heads marked by pentagrams).(a) Five heads are elected and evenly distributed. (b) Five heads are elected and clump in the right semicircle. (c) Only one head is elected. (d) Nine heads are elected.

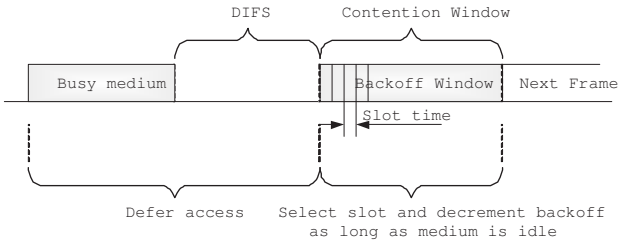
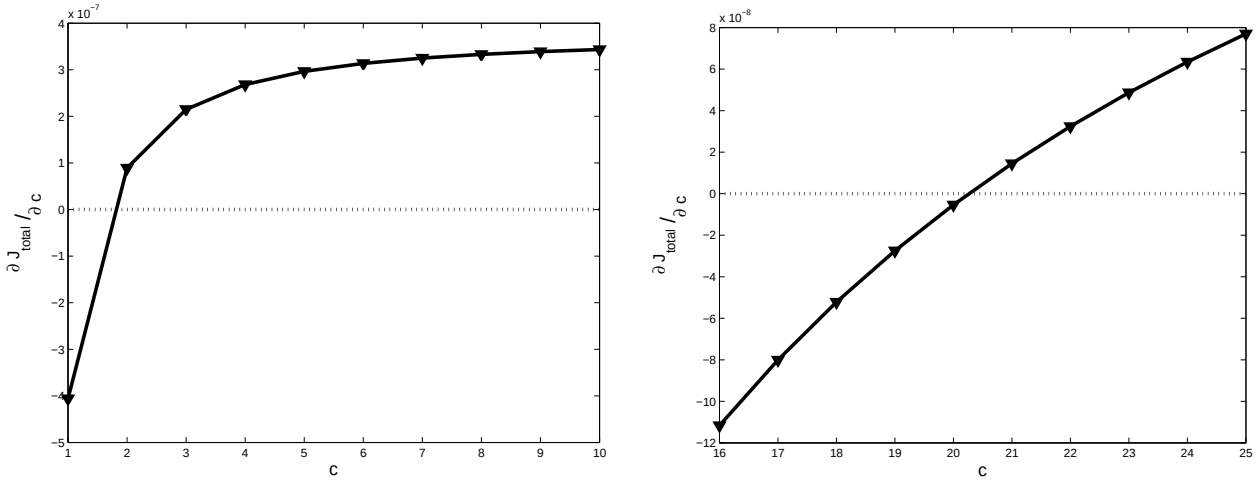
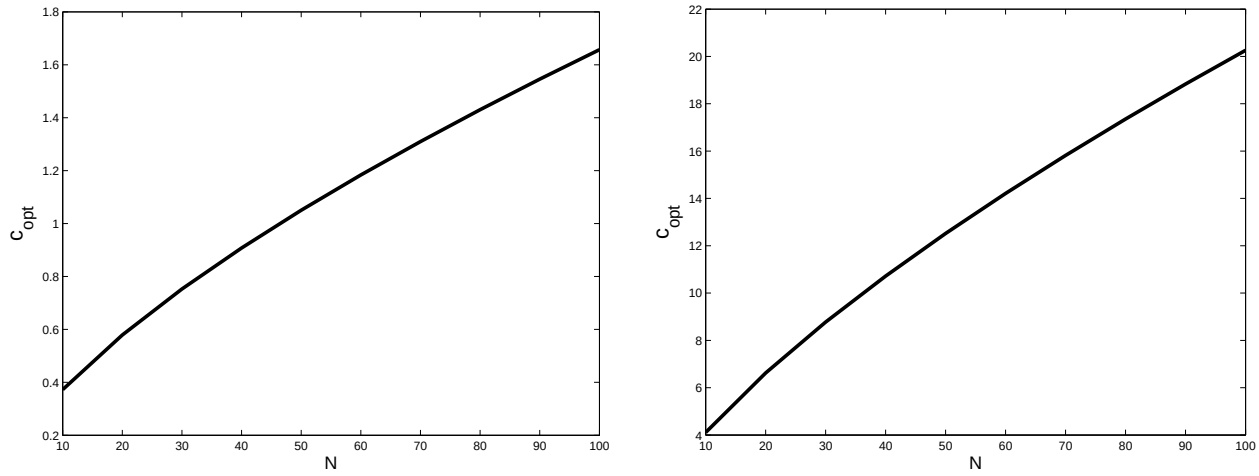


Fig. 3. A generic MAC.



(a) (b)

Fig. 4. Plot of $\frac{\partial \bar{J}_{total}}{\partial c}$ for $N = 100$, $R = 50m$ and $(r_{BS}, \theta_{BS}) = (125, 0)$.(a)$\alpha = 0.001$. (b)$\alpha = 0.05$.



(a) (b)

Fig. 5. Plot of c_{opt} vs. N for $R = 50m$ and $(r_{BS}, \theta_{BS}) = (125, 0)$.(a)$\alpha = 0.001$. (b)$\alpha = 0.05$.

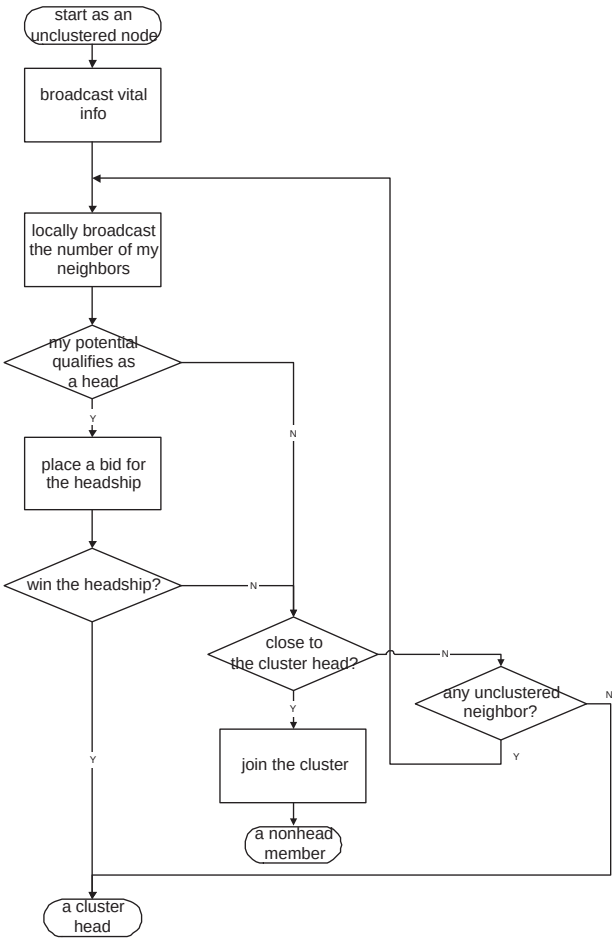


Fig. 6. Flow chart of a node in MEDIC.

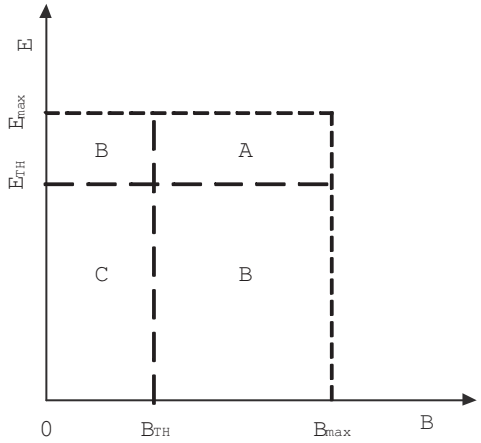


Fig. 7. Categories of bidders.

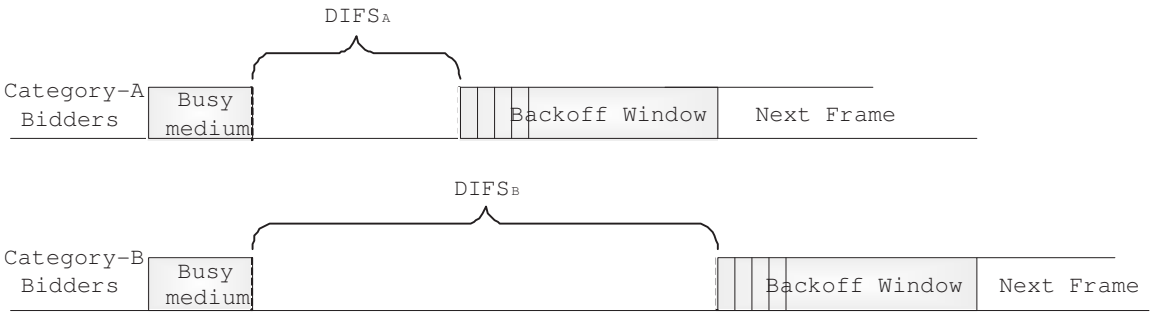


Fig. 8. The Medium Access Control used in MEDIC.

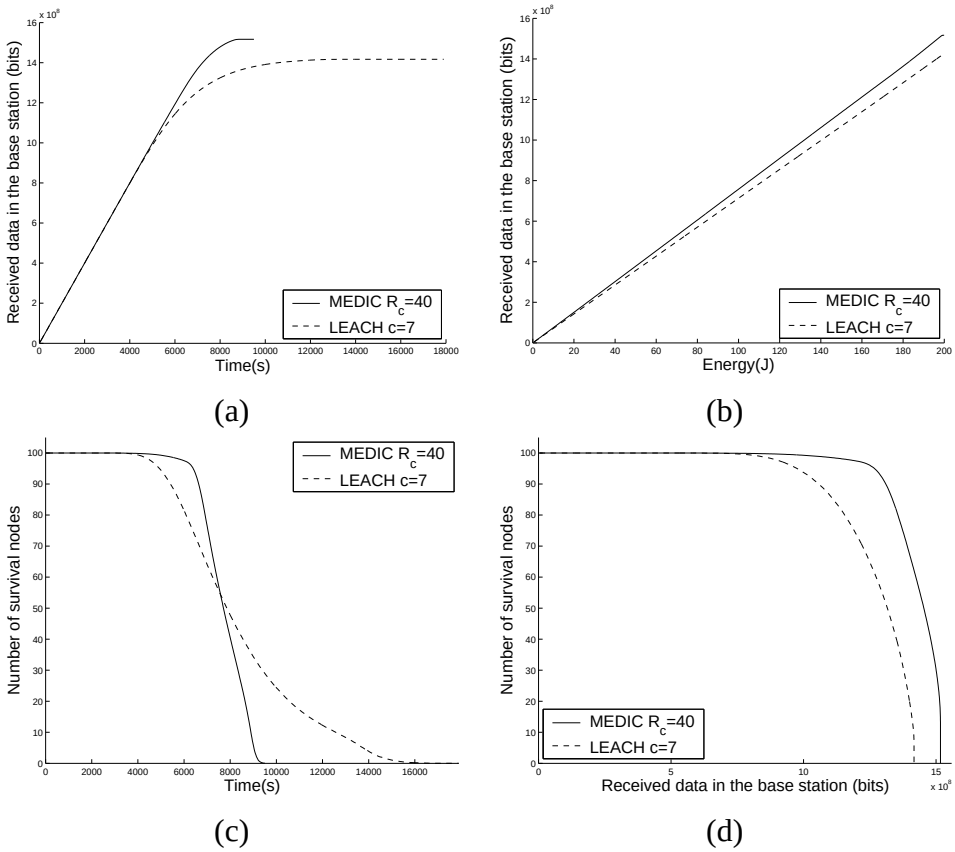


Fig. 9. MEDIC vs. LEACH. (a) Amount of data received at the base station over time. (b) Amount of data received at the base station per given amount of energy. (c) Number of survival nodes over time. (d) Number of survival nodes per amount of data received in the base station.

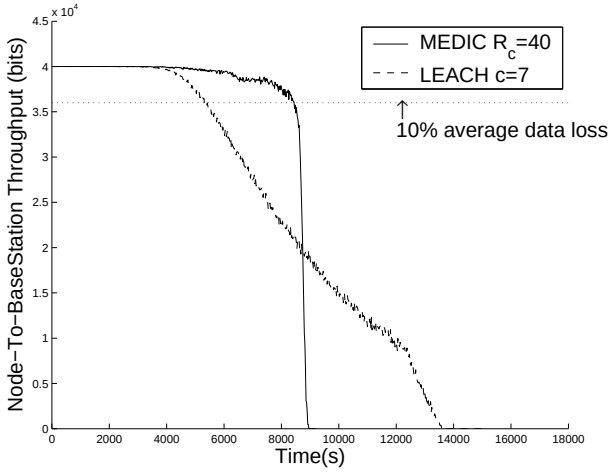


Fig. 10. MEDIC vs. LEACH. Node-to-basestation throughput over time.

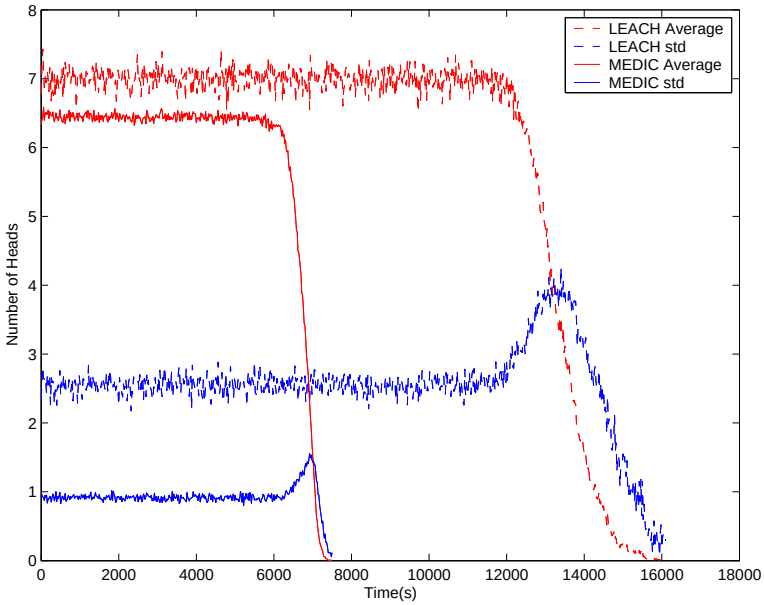


Fig. 11. The elected number of heads (Average and std).

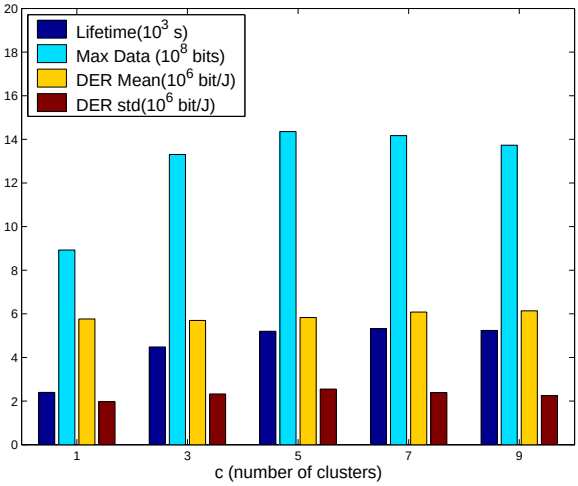


Fig. 12. Data of LEACH.

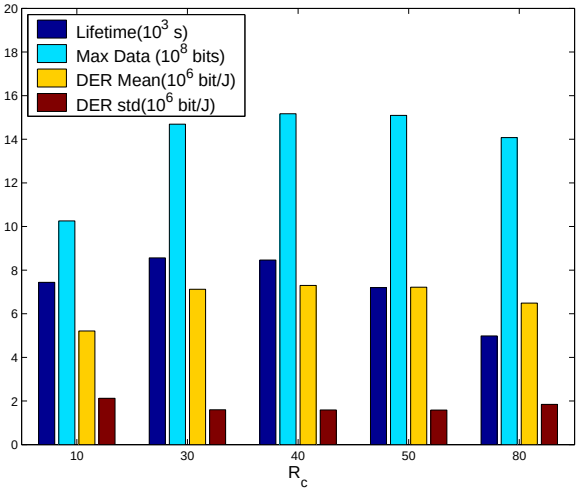


Fig. 13. Data of MEDIC at $\alpha = 0.001$.

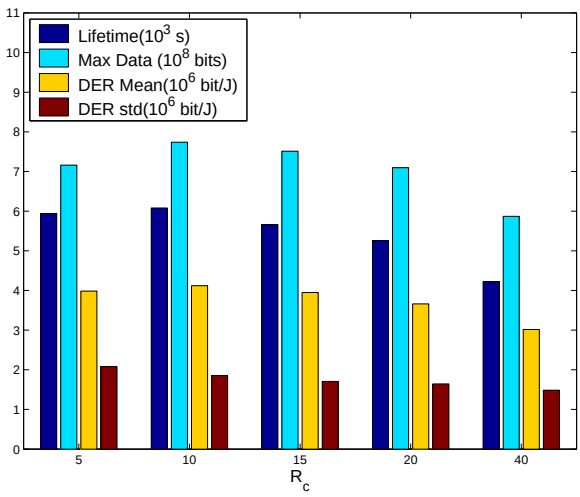


Fig. 14. Data of MEDIC at $\alpha = 0.05$.

Available online at www.sciencedirect.com
ScienceDirect
Information Sciences 177 (2007) 2188–2205
INFORMATION SCIENCES
AN INTERNATIONAL JOURNAL
www.elsevier.com/locate/ins

Energy and quality aware query processing in wireless sensor database systems

Qingchun Ren *, Qilian Liang

Department of Electrical Engineering, University of Texas at Arlington, Arlington, TX 76019-0016, USA

Received 7 February 2006; received in revised form 23 October 2006; accepted 20 December 2006

Abstract

Query processing has been studied extensively in traditional database systems. However, few existing methods can be directly applied to wireless sensor database systems (WSDSs) due to their characteristics, such as decentralized nature, limited computational power, imperfect information recorded, and energy scarcity in individual sensor nodes. This paper proposes a quality-guaranteed and energy-efficient (QGEE) algorithm. QGEE utilizes in-network query processing method to task WSDSs through declarative queries, and confidence interval strategy to determine the accuracy of query answers. In QGEE, the correlation between a query and a node is calculated by vector space model (VSM), and a query correlation indicator (QCI) is designed to quantify the priority of becoming active for individual nodes. Given a query, the QGEE algorithm will adaptively form an optimal query plan in terms of energy efficiency and quality awareness. This approach can reduce disturbance from measurements with extreme error and minimize energy consumption, while providing satisfying service for various applications. Simulation results demonstrate that QGEE can reduce resource usage by about 50% and frame loss rate by about 20%. Moreover, the confidence of query answers is always higher than, or equal to, the users' pre-specified precision.
© 2007 Elsevier Inc. All rights reserved.

Keywords: Wireless sensor database system; Query processing; Energy-efficiency; Space vector model; Imagine chain; *k*-Partial cover set problem; Energy reservation; Query optimization; Multipath routing

1. Introduction

Recent developments in integrated circuit technology have allowed the construction of low-cost sensor nodes that are generally equipped with sensing capability, wireless communication, as well as limited power supply and memory. Embedded those devices into environment, an emerging new type of network is created: wireless sensor network (WSN) [34]. Moreover, most of high-level tasks of WSNs, such as monitoring specific events, collecting and processing information, are accomplished by cooperation of multiple sensor nodes.

* Corresponding author. Tel.: +1 8172723488.
E-mail addresses: ren@wcn.uta.edu (Q. Ren), liang@uta.edu (Q. Liang).

0020-0255/$ - see front matter © 2007 Elsevier Inc. All rights reserved.
doi:10.1016/j.ins.2006.12.017

WSNs are being intended for a broad range of environmental sensing applications from weather data collection to vehicle tracking to habitat monitoring [44,8].

In WSNs, the widespread deployment of sensor nodes is transforming the physical world into a computing platform. Sensor nodes not only respond to physical signals for producing data, but also are equipped with computing and communicating capabilities. They are thus able to store, process locally, and transfer data produced. From data storage and process point of view, a WSN can be regarded as a kind of database – distributed wireless sensor database system (WSDS). Compared with traditional database systems, WSDSs store data within system and allow queries to be injected anywhere through query processing operators.

In a WSDS, the query execution usually starts from front-end nodes that issue queries into the system. Sensor nodes are viewed as data sources that provide relevant information for query processing operators. Generally, queries in a WSDS can be classified into three categories depending on the type of data (past, present, or future) requested:

- Historical queries
  This type of query is mainly used for the analysis of historical data stored at front-end nodes. For example, "what was the temperature two hours ago in the northwest quadrant?"
- One-time queries
  This type of query gives a snapshot view of a system. For example, "what is the temperature in the northwest quadrant?"
- Persistent queries
  This type of query is mainly used to monitor a system over a time interval with respect to some parameters. For example, "report the temperature in the northwest quadrant for next two hours".

Warehousing and on-demand approaches are two conventional ways of handling queries [25]. In the warehousing approach, base stations collect and store data, periodically, depending on a set of predefined parameters. There are two specific limitations for this approach: users can only query base stations, and query processing is very expensive as it utilizes valuable resources like channel bandwidth and energy. In the on-demand way, data is collected based on users' requests. However the drawbacks are that the delay for queries is unacceptable for time critical data, and the flooding of the entire system might be wasteful for one-time queries.

Lessons learned from developing network protocols for WSNs in the last couple of years show that using traditional layered networking approach has several drawbacks in system performance and efficiency. Quite often, significant improvements are possible for network protocols, but they require a great amount of information to be passed along the layers of system. Although this approach, in principle, allows independence among various protocols, it incurs significant overhead in parameter transfer. Moreover, improvements performed in a specific layer can cause impairments, or even be counterproductive for other layers. Therefore, optimization can be more effective when taking into account overall system and using all available knowledge. In other words, cross-layer design approach is a viable approach for WSNs' energy and quality problems.

The goal of monitoring through sensor nodes is to infer information about objects from measurements made from remote locations. Moreover, inference processes are always less than perfect. Consequently, the problem of uncertainty, which stands for the quality of query answer, is central to monitoring applications. Hence, to build useful information systems, it is necessary to learn how to represent and reason with imperfect information [43]. As a result, Motro [28] is interested in how imperfect information may be represented in a database system. In [42] and [31], they proposed methods of dealing with the uncertainty of moving objective databases. In [41], they presented a unified fuzzy-probabilistic framework for modelling processes of medical diagnosis. In their work, the belief computation is related to diagnostic inference. The final conclusion of inference is the diagnosis with the greatest belief value. It is also shown how their membership functions and basic probability assignments are estimated on the basis of experimental data.

In general, imperfect information is typically handled by attaching a number to it, which represents a subjective measure of the certainty according to the observer. The way, in which the number is manipulated, depends upon the theory that underlies the number. There are possibilistic databases [35] and probabilistic databases [7,32,33]. Probabilistic approach has begun to be used by WSDSs to process query with limited information [2]. In [38], they discussed how to handle aggregate operations in probabilistic databases. They

devised a formal linear programming method, analyzed its complexity, and introduced several families of approximation algorithm that run in polynomial time. In [12], a new semantics for database queries is introduced, which supports uncertain matches and ranked results through combining probabilistic relational algebras and models for belief. However, those existing works do not consider the energy constraint problem, nor how to reason and represent the uncertainty introduced by network natures.

Most algorithms for determining query processing strategy for WSDSs are static in nature. In [3], Bodorik proposed the aborted join last (AJL) method to substitute static mechanisms with an adaptive one that owns low overhead and delay to decide when to correct a strategy. In AJL, the decision to correct is computationally simple and, moreover, a corrective strategy is already existed when it is decided to correct. In [14], the phases of adaptive query processing (AQP) is decoupled, and generic framework is constructed. Their work advocated an approach based on self-monitoring algebraic operators. This approach is shown to be generic, independent of any specific adaptation mechanism, easily implementable, and portable.

Considering energy constraint issues, some energy efficient solutions are proposed. Query processing based on random walk technique [1] is an alternative scheme to implement failure recovery in dynamic environments. The robustness of this approach under dynamic situation follows the simplicity of processing, which only requires the connectivity of moving neighbors. In [11] and [21], they proposed an indexing method that supports content-based retrieval queries on a wireless data stream and a tree-structured index to increase the energy efficiency of query processing. To reduce network traffic when accessing and manipulating data, in-network query processing requires placing not only a tree of query processing operators such as filters and aggregations, but also the correlation of nodes. In [4], an adaptive and decentralized algorithm is proposed. This algorithm progressively refines the placement of query processing operators by walking through neighbors. Thus, an initial arbitrary placement of query processing operators can be progressively refined toward an optimal placement.

Existing query processing systems for WSDSs, including Directed Diffusion [19], TinyDB [24], U-DBMS [9] and Cougar [47], provide high-level interfaces that allow users to collect and process such continuous streams. Note that they are especially attractive as ways to efficiently implement monitoring applications without forcing users to write complex, low-level codes for managing multihop network topology and acquiring samples from sensor nodes. TinyDB, Directed Diffusion and Cougar are relatively mature research prototypes that give some ideas on how future query processing system will function for WSDSs.

In this paper, we propose a quality-guaranteed and energy-efficient (QGEE) query processing algorithm for distributed and heterogeneous WSDSs. In the following sections, we outline the QGEE algorithm, explain its key features, and describe the details using a particular example of environmental temperature monitoring. The local rules are specified to select desired sensor nodes and the strategies are stated to acquire bounded query answers. Moreover, leveraging cross-layer designing idea, we combine the application layer, network layer and physical layer to implement this quality-guaranteed and energy-efficient algorithm. In doing so, we show how QGEE differs from existing query processing algorithms, and qualitatively argue that this paradigm offering scaling, robustness and energy efficiency benefits. We quantify some of these benefits through detailed packet-level simulations on QGEE.

The remainder of this paper is organized as follows: Some preliminaries are provided in Sections 2; 3 formulates problems we considered; Section 4 presents the QGEE algorithm; Simulation results are given in Sections 5; 6 concludes this paper.

2. Preliminaries

2.1. Vector space model

Vector space model (VSM) [10,46] is a way to represent documents through words that they contain. VSM has been widely used in traditional information retrieval (IR) field [15,17]. Most search engines also use similarity measures based on this model to rank Web documents. VSM creates a space in which both documents and queries are represented by vectors. For a fixed collection of documents, an m-dimensional vector is generated for each document and query from sets of terms with associated weights. Then, a vector similarity function such as the inner product can be used to compute the similarity between a document and a query.

In VSM, weights associated with the terms are calculated based on the following two numbers:

- term frequency, f_{ij}, the number of occurrence of term y_i in document x_i; and
- inverse document frequency, $g_i = \log(N/d_j)$, where N is the total number of documents in a collection and d_j is the number of documents containing term y_i.

The similarity $sim_{vs}(q,x_i)$ between a query q and a document x_i can be defined as an inner product of query vector Q and document vector X_i:

$$sim_{vs}(q,x_i) = Q \cdot X_i = \frac{\sum_{j=1}^{m} v_j \cdot w_{ij}}{\sqrt{\sum_{j=1}^{m}(v_j^2) \cdot \sum_{j=1}^{m}(w_{ij}^2)}} \tag{1}$$

where m is the number of unique terms in a document collection. Document weight $w_{i,j}$ and query weight v_j are

$$\begin{aligned} &w_{ij} = f_{ij} w_{ij} = f_{ij} log(N/d_j) \quad \text{and} \\ &\begin{cases} v_j = \log(N/d_j) & y_j \text{ is a term in } q \\ 0 & \text{otherwise.} \end{cases} \end{aligned} \tag{2}$$

2.2. k-Partial set cover problem

Covering problems are widely studied in discrete optimization. Basically, these problems involve picking a least-cost collection of sets to cover elements. Classical problems in this framework include general set cover problem and partial covering problem. k-Partial set cover problem [13] as a partial covering problem is about how to choose a minimum number of sets to cover at least n elements, and which k elements should be chosen. k-Partial set cover problem can be formulated as an integer program as following:

$$\text{MINIMIZE:} \quad \sum_{j=1}^{m} c(S_j) \cdot x_j \tag{3}$$

$$\begin{aligned} \text{SUBJECT TO:} \quad & y_i + \sum_{j:t_i \in S_j} x_j \geqslant 1 \\ & \sum_{i=1}^{n} y_i \leqslant n - k \\ & x_j \geqslant 0, \quad j = 1,2,\ldots,m, \quad \text{and} \quad y_i \geqslant 0, \quad i = 1,2,\ldots,n, \end{aligned} \tag{4}$$

where $x_i \in \{0,1\}$ corresponds to each $S_j \in S$. Iff set S_j belongs to the cover, then $x_j = 1$. Iff set t_j is not covered, then $y_i = 1$. $t_i \in \Gamma$.

3. Problem statement

As a motivation for the quality-guaranteed and energy-efficient query processing algorithm, we describe a scenario:

- A great multitude of temperature sensor nodes are randomly deployed in an interested region. Individual sensor nodes (or in short, nodes) are connected to other nodes in their vicinity through wireless communication interface, and use a multihop routing protocol to communicate with nodes that are spatially distant. All nodes are interconnected to at least one gateway directly or through intermedial nodes. Gateways are in charge of relaying data to a powered PC (front-end node) and, on the opposite direction, disseminating queries to related nodes. Within this WSDS, each node owns equal computing and sensing capability, but measurement quality for sensor parts might not be identical.
  This scenario involves such a kind of region-based query:

```
SELECT          AVG(temp)
FROM            sensors
WHERE           loc in (a,b,c,d) AND PROB ≥ p
SAMPLE PERIOD   100 seconds;
```

Fig. 1. Average temperature query in SQL form.

- *Environmental Temperature Monitoring:* With p confidence, tell the average temperature of nodes in the region defined by a rectangle (a, b, c, d).

Written in SQL-like language [16] or MeshSQL [22], this query is shown in Fig. 1.

3.1. Source of imperfect information

Imperfect information is ubiquitous (almost all information that we have about the real world is not certain, complete or precise). In most occasions, there are four types of imperfection in an information system: uncertainty, incompleteness, ambiguity and imprecision [5,6]. Incompleteness arises from the absence of values, imprecision is caused by the existence of values that cannot be measured with suitable precision, ambiguity is introduced by vague statements, and uncertainty arises from the fact that an agent has constructed a subjective opinion on the truth of a fact that it does not know for certain.

In the context of analyzing and understanding the uncertainty of query answer, one significant challenge is how to correctly understand the nature and source of uncertainty of the information derived from remote sensing. Image chain approach [39] is one of the most important and useful models for describing remote sensing process. It can identify steps in remote sensing process (or links in chain) completely and illustrate the interrelation nature of those steps.

Analyzing the working process of this temperature monitoring application, there are three main kinds of imperfect information source: measurement quality, point spread function (PSF) and link quality. Fig. 2 illustrates the image chain model we exploit. Links in the chain represent various steps from nodes collecting related information (Input), to flowing data records back to related front-end nodes (Collection) at run-time, to obtaining query answers through processing all collected information at front-end nodes (Output).

- *Measurement quality*
  As we know, the quality of nodes' sensing part usually boils down to their measurement stability and accuracy. In general, as measurement stability and accuracy increase, so do their power requirement and cost, which are all troublesome for general nodes. Therefore, inaccurate measurements generated by sensing parts are very common. Measurement quality of nodes introduces uncertainty and imprecise information into query answers.
- *Point spread function (PSF)*
  Temperature monitoring application is interested in the temperature over a region instead of one point in space. However considering the operation feasibility, as well as the cost on hardware and time, sampling method is widely used rather than completely measuring. In this aspect, another imperfect information source – PSF is raised. PSF is caused by nodes' nonuniform sensitivity within their monitoring space. In

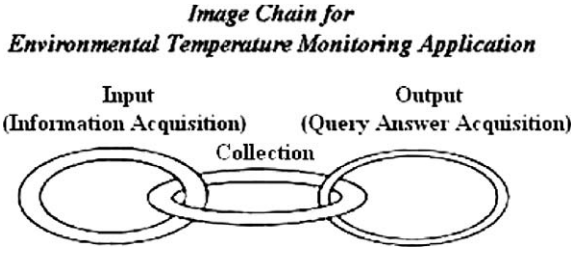


Fig. 2. Image chain model.

general, nodes exhibit sensitivity variation following Gaussian distribution. That is, nodes are more sensitive to the center than toward the edge of their regions. PSF of nodes introduces ambiguity into query answers.

- *Link quality*
  The dynamic and lossy nature of wireless communication pose the major challenge to reliable, self-organized WNSs. Failure transmissions may happen during data transmission because of collision, node dying out (no battery), node being busy, or node's mobility. Moreover, in physical layer, sensor node's mobility generates channel fading during data transmission, which degrades the performance in terms of bit error rate (BER) and frame error rate (FER). Packet loss due to poor link quality introduces incompleteness into query answers.

In a set of temperature monitoring experiments, such as finding the highest temperature, the lowest temperature and the average temperature over a region, we vary measurement quality, PSF and link quality respectively to check the impact of those imperfect information sources on the confidence of query answers. During those experiments, we fix other parameters, such as the number of nodes, node density, communication range, sensing range and network coverage. Assuming true results are known beforehand. Experiment results are shown in Table 1. We observe the following:

- *Measure quality*
  When employing nodes with poor measurement quality, whose measurements have 0.1 standard deviation, the error of query answers is much larger (around ten times) than the one when using nodes whose measurements just have 0.01 standard deviation.
- *PSF*
  When using large disks to cover a monitoring region, i.e., the radius r of disks is 1.96 meter, query answers deviate from the true values much more than those, in which disks with 1.65 meter radius are used. Note that, more information is missed since less nodes are employed, thus large error is introduced into query answers.
- *Link quality*
  When using more reliable links to forward collected data, in which there is only 0.1 percentage of links broken during information transmission, more data reach query processing operators. Thus, the more missing information is caused by link broken, the more the difference between the true values and the acquired values becomes.

In conclusion, with measurement errors, misrepresent errors, and/or missing information increased, the error introduced into query answers is obviously increased, consequently the confidence of query answers is reduced. Even though those conclusions are derived from the temperature monitoring application, they are still valuable for other remote sensing applications, such as humidity monitoring, hurt gas monitoring, etc.

3.2. Source of energy consumption

Sensor nodes are very limited in their processing, computation, communication, storage and power supply. For example, a typical Crossbow MICA mote MPR300CB [36] has a low-speed 4 MHz processor equipped

Table 1
Using root mean square of error (RMSE) to quantify the error of query answers

RMSE	Measure quality		PSF ($\sigma^2 = 1$)		Link quality	
	$\sigma = 0.01$	$\sigma = 0.1$	$r = 1.65$ m	$r = 1.96$ m	LBR = 0.14	LBR = 0.5
MAXIMUM	0.2537	2.5618	22.882	25.17	0.2069	0.7132
MINIMUM	0.2541	2.5416	22.905	25.195	0.1291	0.5895
AVERAGE	0.0102	0.0944	3.0802	3.5202	0.0936	0.3127

σ is the standard deviation of nodes' measurements. r is the radius utilized for modelling nodes' sensing space. LBR stands for link break rate.

with only 128 KB flash, 4 KB SRAM and 4 KB EEPROM. It has a maximal data rate of 40 kbps, a transmission range of about 100 feet, and is powered by two AA batteries. However, communication, not only transmitting, but also receiving, or merely scanning channel, can use up to half energy [40]. Therefore wireless transmitting and receiving are the most energy consuming operations inside nodes. Recently, some researchers have begun studying the problem of reducing power consumption on wireless interface. One approach is reducing energy consumption for transmitting/receiving each bit [37], the other is reducing the amount of information exchanged over networks.

Low cost on devices makes it feasible to generate high density network. This kind of dense deployment can help to improve a WSDS's reliability. Somehow, within a WSDS, not all available nodes provide useful/related information that improves the accuracy of query answers. For example, if nodes are far away from the interested region, the information collected by those nodes is less useful/lower correlative. Furthermore, some information might be redundant because nodes closing to each other would have similar data. From those prospects, collecting raw readings from all nodes involves large amounts of readings, which will lead to shorter network lifetime.

For example, there is a WSDS with n nodes. Assuming that the power for all nodes is P_{init}, each query consumes same energy P_{ea} for processing a query, and queries submitted to the network are processed sequently. If there are ω queries (i.e., A_1, A_2, …, and A_ω) relating to certain regions in this network, γ_1 nodes participate query A_1 relating to area S_{A_1}, γ_2 nodes participate query A_2 relating area S_{A_2}, …, and γ_ω nodes participate query A_ω relating to area $S_{A_\omega}(\gamma_1+\gamma_2+\cdots+\gamma_\omega=n)$. In this case, the node density is $\frac{n}{\sum_{i=1}^{\omega} S_{A_i}}$ and the network lifetime is $L_{t,w}=\omega\frac{P_{\text{init}}}{P_{\text{ea}}}$. Note that with node density decreasing (i.e., $\frac{n}{S_{A_1}}>\frac{n}{S_{A_1}+S_{A_2}}>\frac{n}{\sum_{i=1}^{\omega} S_{A_i}}$), the network lifetime is increased (i.e., $L_{t,1}<L_{t,2}<L_{t,\omega}$).

For the energy reservation issue on data collection, previous networking researches approach data aggregation [48] as an application specific technique to reduce the amount of data sent over a network. But where the aggregation should be carried out is a very essential and tough problem, which relates to the correctness and effectiveness of operations.

4. Description and discussion on quality-guaranteed and energy-efficient (QGEE) query processing algorithm

Keeping those two primary problems: quality-required and energy-constraint in mind, we propose a quality-guaranteed and energy-efficient (QGEE) query processing algorithm for WSDSs. Acquisitional query processing (ACQP) [24] is employed to task network through declarative queries. Compared with typical methods, QGEE focuses on betaking the significantly new opportunity risen in WSDSs: smart sensor nodes have the capability to control over where, when, and how often data is physically acquired (i.e., sampled) and delivered to query processing operators.

In QGEE, only a subset of nodes will be chosen to acquire readings or samplings corresponding to the fields or attributes referenced in queries. During data's forwarding, nodes' mobility, link quality and battery level are considered to establish multiple paths. The overall goals of this approach are reducing disturbance from measurements with extreme error, decreasing information loss from link failure and minimizing energy consumption, but still providing satisfying service for various applications. Furthermore, according to the analysis and classification on the sources of imperfect information, probabilistic method is employed to formulate their distributions. Finally probabilistic query answers are acquired on uncertain data. The probability corresponding with query answers can be used to determine the amount of confidence the users should have.

4.1. Confidence control for query answer

4.1.1. Query vector space model (VSM) design and active node selection

In information retrieval, VSM is one of efficient methods to quantify the correlation between a query and all candidate documents. If treating sensor nodes as candidate documents for a query, the correlation between a query and a node can be quantified by utilizing the same principle. However, redesign on the VSM vector is needed to implement quality and energy control. Based on the study mentioned above, following factors are considered:

- Location
  Given a piece of space, number and location of nodes determine the monitoring coverage. In order to employ as few as possible nodes to cover as large as possible area, those nodes, located at some special locations called optimal locations, should be selected. The detail on determining optimal locations is presented in Section 4.1.2.
- Measurement quality
  Since the cost and measurement quality of sensor node are related to each other, sensor nodes owning a variety of qualities are always deployed simultaneously in a WSN for economical reasons. Moreover, through a query, database users supply not only what information they are interested in, but also the expectation on answers' quality, i.e., the confidence of answers. In this case, suitable nodes should be selected to response queries rather than all of them.
- Battery
  Remaining battery capacity of sensor nodes is the third factor, but not the least important one. When the battery of a node is used up, the uncertainty of answers, at some degree, will increase caused by missing data. It inspires us to select those nodes with high remaining battery capacity, so that all expected data could be collected with best effort.

In the QGEE algorithm, VSM is employed to incorporate above all factors for electing the most related nodes (called active nodes) for query processing. Query vector is designed as $= [R_l, A_d, B_m]$.

- R_l stands for location relativity. It is the indicator of the distance between the location of a sensor node at (x, y) and the optimal location at (x_0, y_0).

$$R_l = 1 - \frac{\sqrt{(x - x_0)^2 + (y - y_0)^2}}{L} \tag{5}$$

  where L is the factor to ensure R_l to be a positive numeric value. For instance, L can be equal to the maximum distance of two nodes within a network. Small value of R_l indicates a node closing to an optimum location.
- A_d stands for measurement quality. A_d is equal to the confidence of measurement bias. For example, for speed detecting sensor nodes, CXM539 [36], the bias is ± 1 m Gauss and owns 0.95 confidence. In this case, $A_d = 0.95$.
- B_m stands for remaining battery capacity.

When a query is submitted, the related top-end node fixes the optimal locations, and translates this query into a query VSM vector $_0 = [1, A_{d,0}, B_{m,0}]$. For instance, $_0 = [1, p, 5]$ according to the query given in Fig. 1. Assuming the maximum battery capacity for nodes is $5J$. $_0$ and information on optimal locations will be flooded over the network. Then, nodes update their query VSM vectors ($_i = [R_{l,i}, A_{d,i}, B_{m,i}]$ $(i = 1, 2, \ldots, n)$). Assuming there are n nodes in this network. For node i the node location $R_{l,i}$ is defined as:

$$R_{l,i} = \max_j \{r_{l,i,j}\} \tag{6}$$

where $r_{l,i,j} = 1 - \frac{\sqrt{(x_i - x_{0,j})^2 + (y_i - y_{0,j})^2}}{L}$, (x_i, y_i) is the position of node i, and $(x_{0,j}, y_{0,j})$ is the position of the jth optimal location.

A query correlation indicator (QCI) is designed, which is referred as ζ, to represent the correlation between individual nodes and a query. ζ is formulated as follows.

$$\zeta_{\Upsilon_0, \Upsilon_i} = \mathrm{sim}_{vs}(\Upsilon_0, \Upsilon_i) = \Upsilon_0 \cdot \Upsilon_i = \frac{1 \times R_{l,i} + A_{d,0} \times A_{d,i} + B_{m,0} \times B_{m,i}}{\sqrt{(1 + A_{d,0}^2 + B_{m,0}^2)(R_{l,i}^2 + A_{d,i}^2 + B_{m,i}^2)}} \tag{7}$$

Observe that, QCI $\zeta_{\Upsilon_0, \Upsilon_i}$ is a function of query quality $A_{d,o}$, node's energy $B_{m,i}$, measurement quality $A_{d,i}$ and node location $R_{l,i}$. Moreover, $\zeta_{\Upsilon_0, \Upsilon_i}$ is computed by nodes through a distributed way.

ζ directly indicates the similarity between a query and a node. Inspired by this, the criterion for active node choosing is formed: the decision – which nodes are active to respond queries – is based on nodes' QCIs. That is, nodes with highest QCI among their one-hop neighbors are chosen to participate in related query processing. In QGEE, active nodes are chosen locally leveraging cooperation among nodes. Assuming that each node knows QCIs of its one-hop neighbors, which can be achieved by requiring each node to broadcast its QCI initially. This distributed calculation balances the working load for QCIs over the entire network so that the overhead introduced by VSM for each node is extremely reduced. Furthermore, according to (7), the computing complexity is only around O (16). Therefore, it is safe to claim that the overhead caused by VSM is minor, even though the processing capability for general nodes is limited (i.e., 4 MIPS for Berkeley MICA Mote [48]).

4.1.2. Optimal location determination

Modelling the problem – determining optimal locations for a query – as a k-partial set cover problem. This problem is defined as follows: Let n be the number of all sensor nodes, n' be a given positive integer so that $n' \leqslant n$. If we have k disks with radius r, the k-partial set cover problem tries to solve whether and which k disks can cover at least n' nodes. In this paper, sensor nodes on a plane (the dimension is 2) are only considered.

Unfortunately, this kind of k-partial set cover problem is a NP problem. At present, all known algorithms for NP problem require time that is exponential to the problem size. It is unknown whether there is any faster algorithm. Therefore, to solve a NP problem for any nontrivial problem size, one of approaches is approximation algorithm, which can acquire solution during polynomial time. The SETCOVER algorithm [13] is a good approximation method to determine the value of k and locations of those disks on a plane. QGEE chooses the centers of those k disks as the optimal locations, and lets $n' = n$. Therefore, for QGEE, nodes locating at the centers of those disks can monitor the entire interested region.

According to users' requirements, QGEE, considering the impact of PSF on the uncertainty of query answers, adaptively adjusts the radius r instead of fixing it. Assuming PSF $g(d)$ of nodes in a WSDS is defined by (8) and the confidence of query answer is required to be at least equal to p as shown in the example in Fig. 1. Here d is the distance between a point and the center on a disk.

$$g(d) = \mathrm{e}^{-\pi d^2} \tag{8}$$

It is obviously that, among various locations on a disk, measurements own the lowest sensitivity/confidence when they stand for the situation at a disk's edge. This nature inspires us to design a criterion to calculate suitable value for r. That is, if the sensitivity/confidence is equal to or higher than p at the edge of disks, it is ensure that the measurements of all active nodes can represent the situation within their disks, at least, with p confidence. Deriving (9) from (8) to determine the suitable value for r.

$$r = -\sqrt{\frac{1}{\pi} lnp} \tag{9}$$

Note that, r is a function of standard deviation σ of PSF and quality requirement p. If fixing σ, r will decrease with the increase of p. That means, with higher query quality, smaller disks should be used to search the optimum locations and more active nodes are needed for a query.

4.1.3. Sample size determination and semi-manufactured query answer acquisition

A set of nodes has been chosen to respond a query. While, "How many measurements should be included in one sample (any subset of a population)?" is the question that will be answered in this Section. Sample size determination refers to the process of determining exactly how many samples should be measured/observed in order that the sampling distribution of estimators meets users' pre-specified precision [27].

As a matter of fact, nodes' readings are subject to errors caused by limitations of devices' hardware and environmental noise. Consequently, uncertainty is inherent regarding a true value. In this paper, the formula for a node's reading x is:

$$x = v + e_m + \eta \tag{10}$$

where v is the true value, e_m is the measurement error introduced by limitations of device's hardware, and η is the environmental noise considered as white Gaussian noise in this paper and $\eta \sim N(0, \frac{N_0}{2})$. Based on central

limit theorem [30], the probability distribution of measurement errors complies with a normal distribution. That is, $e_m \sim N(0, \sigma_e^2)$. Generally, in product's technical datasheet, manufactories supply the information on measurement errors. For example, as mentioned above, the bias for CXM539 is ±1Gauss with 0.95 confidence. In this case, $\sigma_e^2 = 0.1302$. For general cases, if knowing the maximum bias Δx and its confidence p, the general expression of σ_e^2 can be obtained. That is

$$\sigma_e^2 = \frac{\Delta x^2}{\left[Q^{-1}\left(\frac{1-p}{2}\right)\right]^2} \tag{11}$$

where $Q(x)$ stands for Q-function, defined as $Q(x) \triangleq \frac{1}{\sqrt{2\pi}} \int_x^\infty e^{-\frac{y^2}{2}} dy$.

Moreover, e_m and n_o are independent. Therefore, node reading also complies with a Gaussian distribution with μ_x-mean and σ_x-standard deviation given as follows:

$$\mu_x = v \qquad \text{and} \qquad \sigma_x = \sqrt{\sigma_e^2 + \frac{N_0}{2}} \tag{12}$$

Therefore the PDF of node reading x is

$$f_X(x) = \frac{1}{\sqrt{2\pi(\sigma_e^2 + \frac{N_0}{2})^2}} e^{-\frac{(x-v)^2}{2(\sigma_e^2+\frac{N_0}{2})^2}} \tag{13}$$

Using sample mean to estimate the mean of a random variable is an unbiased estimation, in which the estimator aims at the true value or the correct average [29]. Thus, an unbiased estimation on the true value v is done when choosing sample mean as the estimator, i.e. $\hat{v}_n = \frac{1}{n}\sum_{j=1}^n x_j$. Here n is sample size. In this case, the probability density function of $\hat{v}_n(f_{\widehat{V_n}}(\hat{v}_n))$ is similar to $f_X(x)$ with $\mu_{\hat{v}_n} = \mu_x$ and $\sigma_{\hat{v}_n}^2 = \frac{1}{n}\sigma_x^2$. That is

$$f_{\widehat{V_n}}(\hat{v}_n) = \frac{\sqrt{n}}{\sqrt{2\pi(\sigma_e^2 + \frac{N_0}{2})}} e^{-\frac{n(\hat{v}_n - v)^2}{2(\sigma_e^2+\frac{N_0}{2})}} \tag{14}$$

QGEE lets Δx as the error margin between the estimator $\hat{v}_n$ and the true value v to reflect the target precision of query answers, and specifies the capability for ensuring this error not to be smaller than p. The criterion for sample size determination is simply stated as:

$$P_r\{|\hat{v}_n - v| \leqslant \Delta x\} \geqslant p \tag{15}$$

The probability of the estimation error not larger than Δx is

$$P_r\{|\hat{v}_n - v| \leqslant \Delta x\} = 1 - 2Q\left(\frac{\Delta x}{\sqrt{\frac{\sigma_e^2+\frac{N_0}{2}}{n}}}\right) \tag{16}$$

Solving (15) and (16) for sample size n, we obtain

$$n \geqslant \frac{(\sigma_e^2 + \frac{N_0}{2})[Q^{-1}(\frac{1-p}{2})]^2}{\Delta x^2} \tag{17}$$

Since a statistic measurement on samples can rarely, if ever, be expected to be exactly equal to a parameter, it is important for estimations to be accompanied by statements that describe their precision. Confidence interval [45] provides a method of stating both how close the value of a statistic being likely to be value of a parameter and the chance of being close. A confidence interval of an attribute denoted by U_i is a interval $[l_i, h_i]$ such that l_i and h_i are real-valued, and the condition $h_i \geqslant l_i$ holds. Note that (15) is the same statement made when defining a $100 \times p\%$ confidence interval, and Δx is about half of the width of this confidence interval. Using the sample size computed by (17) to estimate the true value (v), we have

$$P_r\{\hat{v}_n - \Delta x < v < \hat{v}_n + \Delta x\} \geqslant p \tag{18}$$

With (18), a bounded value: $v \in [\hat{v}_n - \Delta x, \hat{v}_n + \Delta x]$ is obtained, which is called "semi-manufactured" query answer.

Since heterogeneity is one of natures of general WSDSs, that is, measurement quality p_i, sample size n_i and confidence interval U_i for individual nodes might vary. For node i, accompanying confidence p_i, n_i and U_i are given as follows:

$$n_i = \left\lfloor \frac{\left(\sigma_{e,i}^2 + \frac{N_0}{2}\right)\left[Q^{-1}\left(\frac{1-p_i}{2}\right)\right]^2}{\Delta x_i^2} \right\rfloor \quad \text{and} \quad v_i \in [\hat{v}_{n_i} - \Delta x_i, \hat{v}_{n_i} + \Delta x_i] \tag{19}$$

4.1.4. Data collection

After active nodes being chosen, a data centric routing algorithm, EM-GMR [23] is employed, which is a multipath, power-aware and mobility-aware routing scheme. It is used to establish route-tree from active nodes to front-end nodes for query answers' return. EM-GMR uses reactive networking approach, in which a route is found only when a message is to be delivered from a source to a destination.

In EM-GMR, *distance to the destination*, *remaining battery capacity*, and *mobility* of each sensor node are considered. The geographical locations of destination node are known to source nodes (as in [20]), and the physical location of each node can be estimated easily if the locations of three nodes (within a communication range) are known in a WSN. This scheme is a fully distributed approach where each sensor only needs the above three parameters, and fuzzy logic systems (FLS) are utilized to handle those three parameters. The EM-GMR scheme consists of route discovery phase, route reconstruction phase and route deletion phase.

- *Route discovery phase*
  The source node uses a fuzzy logic system (FLS) [26] to evaluate all eligible nodes (closer to the destination location) based on the parameters of each node: distance to the destination, remaining battery capacity, and degree of mobility. It chooses the top M nodes based on the degree of the possibility (output of FLS). The source node sends a Route Notification (RN) packet to each desired node, and each desired node would reply using a REPLY packet if it is available. After a certain period of time, if the source node does not receive REPLY from some desired nodes, it will pick the node with the $M+1$st degree of selection possibility. In the second hop, selected nodes in each path will choose its next hop node using a FLS.
- *Route reconstruction phase*
  Because each node is mobile, it may be possible that some nodes move out of the communication range or some nodes die out, which will lead to link failure. Then a route reconstruction phase is started. The last-hop of the failure node in the routing path will apply FLS to determine the selection possibility for all of its eligible neighbor nodes, and choose the top one degree node (via RNREPLAY procedure). The new node will determine its next node accordingly.
- *Route deletion phase*
  Energy, mobility and physical location of each node are changing. It may be possible that a node (in path) observes that its next node is not the optimal after a while, and then this node will initiate a route deletion phase. This node will send an RN packet to the optimal node via common control channel, and this RN packet will also be received by the original relay node, which will notice that the original path is deleted.

In EM-GMR for M-path routing, the source node selects M nodes in its communication range for the first hop relay. Assume there are N ($N > M$) nodes in its communication range, nodes who are further to the destination node than the source node are not considered. Choosing M nodes from remaining eligible nodes is based on a FLS. Starting the second hop, each node in the M-path selects its next hop node also using a FLS. For example, as illustrated in Fig. 3, node B needs to choose one node from eligible nodes C, D, E, F, H based on their three parameters, and sends RN packet to the selected node and waits for REPLY. If the top one node is unavailable (selected by another path or busy), then the top second node will be selected. By this means, M paths can be set up.

Note that EM-GMR considers distance, remaining battery capacity, and mobility of each node during route path setting up. This scheme could tremendously reduce frame loss rate and link failure rate since mobility is considered, so that incompleteness information caused by poor link quality can be reduced at certain degree.

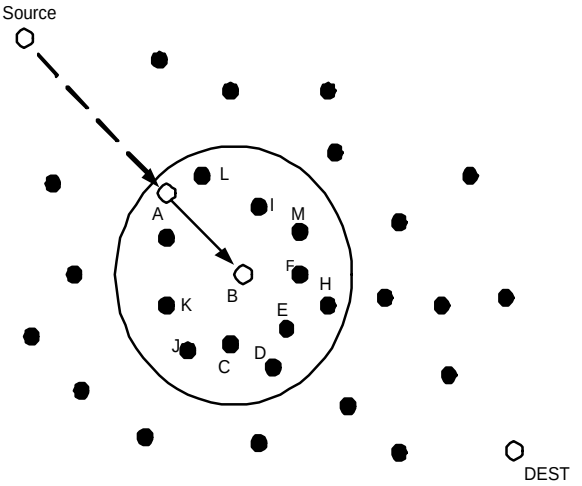


Fig. 3. Illustration of node selection.

4.2. Energy consumption control for query processing

In energy consumption control, three strategies are employed. There are active node number control, sample size control and link quality control.

Firstly, in query SVM design, nodes' location is considered besides measurement quality and remaining battery capacity, since it is directly related to the number of active nodes. Through solving optimal location problem, as few as possible nodes can be employed to cover as large as possible monitoring space so as to carry out energy reservation task.

However, too large sample size implies a waste of resources, and too small sample size will diminish the utility of results. QGEE achieves (19) to specify the value of sample size during information sensing, so that it can acquire enough samples to meet users' pre-specified precision, and reduce energy consumption for data sensing.

Third, frame loss rate and link failure rate are tremendously reduced through choosing more suitable nodes to set up route-tree for queries. With this improvement, energy consumption is reduced for route-tree maintenance and information retransmission.

4.3. Final query answer acquisition

Once query processing strategies have been optimized, disseminated, and semi-manufactured query answers have been acquired from active nodes, query processing operators continue to acquire final query answers. Aggregations are required in many database applications. Common functions applied to collections of numeric value include SUM, AVERAGE, MAXIMUM, and MINIMUM. This paper will specifically discuss how to obtain final query answers, as examples, which focus on those most often used aggregation operations: MAXIMUM, MINIMUM, and AVERAGE.

Returned semi-manufactured answers have a confidence interval form, i.e. $[\hat{v}_{n_i} - \Delta x_i, \hat{v}_{n_i} + \Delta x_i]$ with confidence $p_i\,(i = 1, 2 \ldots, \psi)$. For simplified reason, letting $l_i = \hat{v}_{n_i} - \Delta x_i, h_i = \hat{v}_{n_i} + \Delta x_i$. Assuming there are ψ active nodes for a query.

4.3.1. MAXIMUM/MINIMUM aggregation

The cumulative distribution function (CDF) of $\hat{v}_{n_i}$ is given as follows according to (14).

$$F_{\widehat{V}_{n_i}}(\hat{v}_{n_i}) = Q\left(\frac{\sqrt{n_i}(\hat{v}_{n_i} - \mu_{x_i})}{\sigma_{x_i}}\right) \tag{20}$$

Since measurements from individual active nodes are independent with each other, the CDFs for $Z_{\max} \triangleq \max_i(\hat{v}_{n_i})$ and $Z_{\min} \triangleq \min_i(\hat{v}_{n_i})$ $(i = 1, 2, \ldots, \psi)$ are given as follows for MAXIMUM and MINIMUM.

$$F_{Z_{\max}}(z) = \prod_{i=1}^{\psi} F_{\widehat{V}_{n_i}}(z) = \prod_{i=1}^{\psi} Q\left(\frac{\sqrt{n_i}(z-\mu_{x_i})}{\sigma_{x_i}}\right) \tag{21}$$

and

$$F_{Z_{\min}}(z) = 1 - \prod_{i=1}^{\psi}\{1 - F_{\widehat{V}_{n_i}}(z)\} = 1 - \prod_{i=1}^{\psi}\left\{1 - Q\left(\frac{\sqrt{n_i}(z-\mu_{x_i})}{\sigma_{x_i}}\right)\right\} \tag{22}$$

For the MAXIMUM aggregation, the final query answer is $Z_{\max} \in [l_{\max}, h_{\max}]$ with $p_{\max}$ confidence in bounded probability form. Here

$$l_{\max} = \arg\max_i\{l_i\} \quad \text{and} \quad h_{\max} = \arg\max_i\{h_i\}, \quad p_{\max} = \frac{1}{\psi}\sum_{i=1}^{\psi} p_i \tag{23}$$

For MINIMUM aggregation, the final query answer is $Z_{\min} \in [l_{\min}, h_{\min}]$ with $p_{\min}$ confidence in bounded probability form. Where

$$l_{\min} = \arg\min_i\{l_i\} \quad \text{and} \quad h_{\min} = \arg\min_i\{h_i\}, \quad p_{\min} = \frac{1}{\psi}\sum_{i=1}^{\psi} p_i \tag{24}$$

4.3.2. AVERAGE aggregation

In this aggregation operation, a derivative value over a group of active nodes' data is returned. The PDF for $Z_{\text{avg}} \triangleq \frac{1}{\psi}\sum_{j=1}^{\psi}\hat{x}_{n_j,j}(f_{Z_{\text{avg}}(z)})$ has the similar distribution to $f_{\hat{X}_n}(\hat{x}_n)$. But the mean and variance are $\frac{1}{\psi}\Sigma_{j=1}^{\psi}\hat{\mu}_{n_j,j}$ and $\frac{1}{n\psi^2}\sum_{j=1}^{\psi}\hat{\sigma}^2_{n_j,j}$ individually.

For AVG aggregation, the final query answer is $Z_{\text{avg}} \in [l_{\text{avg}}, h_{\text{avg}}]$ with p_{avg} confidence in bounded probability form. Where

$$l_{\text{avg}} = \frac{1}{\psi}\sum_{j=1}^{\psi} l_i \quad \text{and} \quad h_{\text{avg}} = \frac{1}{\psi}\sum_{j=1}^{\psi} h_i, \quad p_{\text{avg}} = \frac{1}{\psi}\sum_{i=1}^{\psi} p_i \tag{25}$$

5. Simulation and performance evaluation

In the simulations, nodes are randomly deployed in an area $10 \times 10\ \text{m}^2$, and sensing range for individual nodes is 1 m. Initial energy of nodes uniformly distributes within $[0, 5]$ J. Monte Carlo simulations are run to remove the randomicity of simulation results. We compare QGEE against the query processing method without any query optimization.

The energy consumption model for data sensing is shown as follows:

$$E_q = E_{\text{se}} * S_t \tag{26}$$

where E_q is the total energy consumed by sensing, E_{se} is the energy consumed by sensing unit sample, S_t is the sample period. In this simulation, $E_{\text{se}} = 5$ nJ/sample.

Same energy consumption model is used as in [18] for radio hardware. To transmit an l-symbol message for a distance d, the radio expends:

$$E_{\text{Tx}}(l, d) = E_{\text{Tx-elec}(l)} + T_{\text{Tx-amp}(l,d)} = l \times E_{\text{elec}} + l \times e_{\text{fs}} \times d^2 \tag{27}$$

and to receive this message, the radio expends:

$$E_{\text{Rx}} = l \times E_{\text{elec}} \tag{28}$$

The electronics energy, E_{elec}, as described in [18], depends on factors such as coding, modulation, pulse-shaping and matched filtering. The amplifier energy, $e_{fs} \times d^2$ depends on the distance to the receiver and the acceptable bit error rate. In this paper, $E_{elec} = 50$ nJ/syn and $e_{fs} = 10$ pJ/sym/m^2.

5.1. Energy reservation performance

In this simulation, before active nodes selection, nodes individually update their VSM vectors, i.e., determining latest values for R_l, A_d and B_m. Based on this query VSM vector, its OCI ζ can be determined. Through collaboration among nodes, each node can acquire their neighbors' OCIs. Then active nodes can be distributedly selected according to those OCIs. Data Sensing, packet transmitting and receiving are considered for energy consumption. Except for active nodes, other nodes in a network will enter energy saving mode – sleeping mode. Assuming that in sleep mode there is no data sensing nor communication. Moreover, a node is excluded from experiments when its power is used up. Same number of nodes is used for different algorithms and queries are submitted to the network until all nodes are dead.

In Fig. 4, we plot query index versus nodes dead time. We can see that after processing about 20 queries, all nodes, without query optimization, use up their energy. But for QGEE, the whole network is not down until 53 queries are completed. Therefore, QGEE can reserve 50% of energy on processing same number of queries.

In Fig. 5, we compare the coverage of these two schemes. Observed that, QGEE employs $70 - 45 = 25$ less nodes to cover 90% area interested. This simulation result illustrates the reason why QGEE can implement

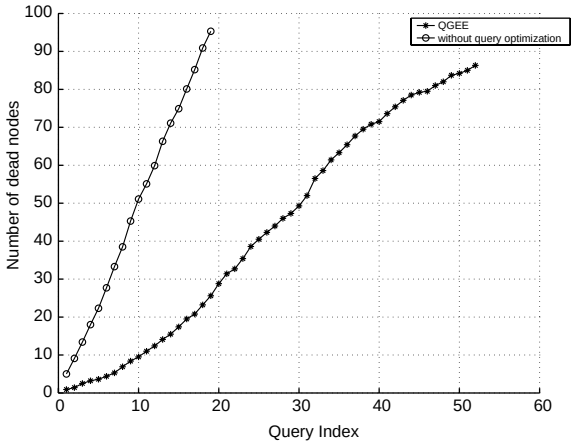


Fig. 4. Nodes dead time.

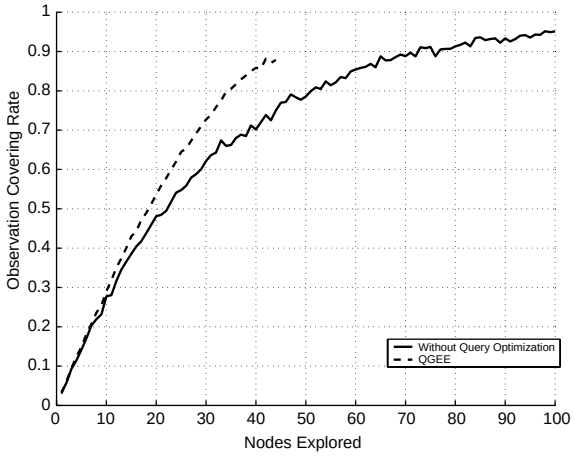


Fig. 5. Observation coverage rate.

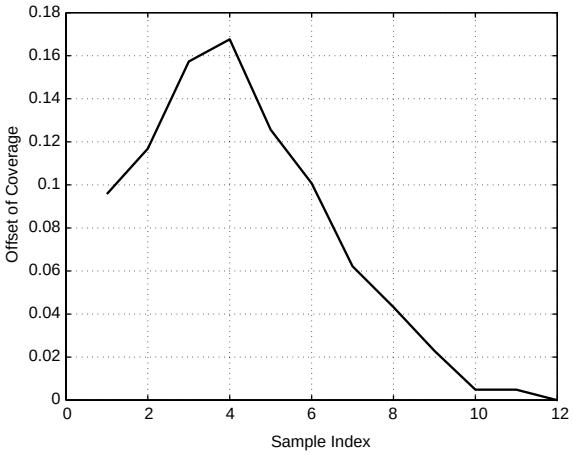


Fig. 6. Decrease of coverage.

energy reservation. That is, about $\frac{25}{70} \times 100 = 35.71\%$ nodes switch to energy saving model during query processing.

By employing QGEE, the energy is saved and the network lifetime is extended. But the cost to achieve this improvement is the decrease of coverage. Fig. 6 shows that the biggest decrease of monitoring coverage is 16.6% for QGEE.

5.2. Quality guarantee performance

In this simulation, various requirements on query answers' confidence are given (i.e., various value for p). To simplify the simulation scenarios, enough nodes are set up to satisfy measurement quality requirements. For MAXIMUM, MINIMUM and AVERAGE aggregation operation, we check the probability of true values locating within the confidence intervals acquired at front-end nodes (see Table 2). Note that QGEE can successfully obtain suitable confidence intervals to guarantee the true value located within them with a probability p_2, which is equal to or larger than the pre-specified probability p_1. In reality, maybe, all available nodes do not own enough measurement quality to satisfy users' requirement. Then, even using QGEE, expected results still cannot be acquired. However, QGEE processes query with best effort.

5.3. EM-GMR performance

We compare EM-GMR against the geographical multipath routing (GMR) [20] scheme where only distance to the destination is considered. We run the simulations using OPNET. 60 nodes in total are deployed initially. There are 5 couples of source and destination nodes communicating at the same time in this network.

Table 2
Confidence for query answers

p_1	MAXIMUM	MINIMUM	AVERAGE
	p_2	p_2	p_2
0.8	0.8133	0.8133	0.8112
0.9	0.9139	0.9151	0.9144
0.9050	0.912	0.9122	0.9144
0.9246	0.93	0.9318	0.9301
0.9334	0.948	0.942	0.9428
0.95	0.958	0.9561	0.9551
0.99	0.9939	0.9924	0.9938

p_1 is the pre-specified value for p. p_2 is the acquired value for p using QGEE.

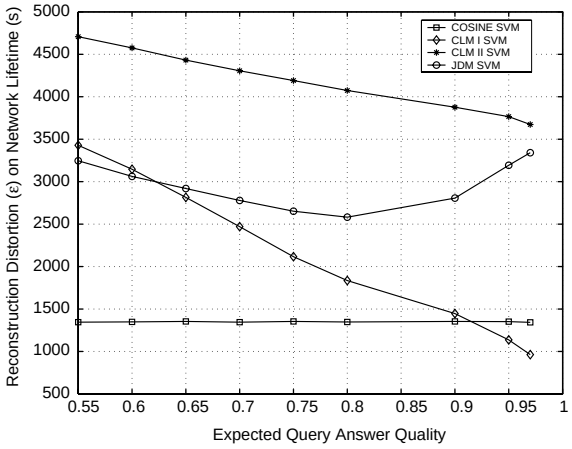


Fig. 7. Simulation time versus number of nodes dead.

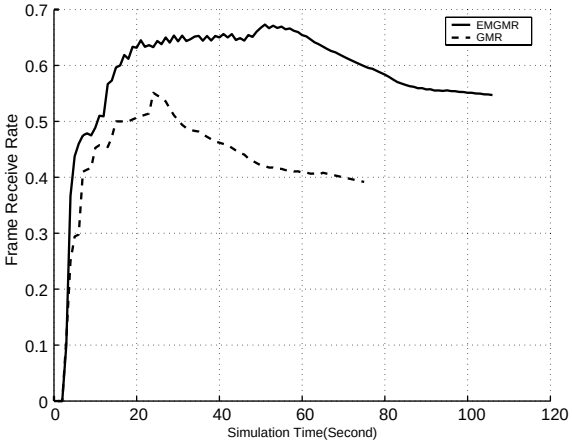


Fig. 8. Simulation time versus frame loss rate.

Each node (including source and destination nodes) has moving speed ranging from 0 to 10 m/s, and its moving speed changes in every 10 s. The frame length is 512 symbols and symbol rate is 9.6 ksym/s in this simulation. Each sensor locally broadcasts a beacon message in every 2 s to keep link alive, so that neighbor table can be updated (including new neighbor joins in, and old neighbors expire). That information is used for route discovery, reconstruction, and deletion. The coherence time is set as 10 s.

In Fig. 7, we plot the simulation time versus the number of nodes dead. Observe that when 50% nodes (30 nodes) die out, the network lifetime for EM-GMR has been extended about $\frac{175-125}{125} = 40\%$. In Fig. 8, we compare the frame loss rate of these two scheme. Observe that EM-GMR outperforms GMR by about 20% on frame loss. The average latency during transmission (end-to-end) is 419.68 ms for EM-GMR and 407.5 ms for GMR, and link failure rate for EM-GMR is 5.68%, but for GMR it is 10.42%.

6. Conclusions

This paper proposes a quality-guaranteed and energy-efficient (QGEE) algorithm for WSDSs. It employs an in-network query processing method to task WSDSs through declarative queries, and uses confidence interval strategy to determine the accuracy of a query answer. In QGEE, the correlation between a query and a node is calculated by vector space model (VSM), and a query correlation indicator (QCI) is designed to

quantify the priority of becoming active for individual nodes. Given a query, QGEE will adaptively form an optimal query plan in terms of energy efficiency and quality awareness. This approach can reduce the disturbance from measurements with extreme error and minimize energy consumption, while providing satisfying service for various applications. Furthermore, probabilistic method is employed to formulate the distribution of imperfect information and the accuracy of each query answer. The probability corresponding with each query answer can be used to determine the amount of confidence the users should have.

Simulation results demonstrate that QGEE can reduce resource usage by about 50% and frame loss rate by about 20%. Moreover, the confidence of acquired query answers is always higher than, or equal to, users' pre-specified precision.

Acknowledgement

This work was supported by the US Office of Naval Research (ONR) Young Investigator Program Award under Grant N00014-03-1-0466.

References

[1] C. Avin, C. Brito, Efficient and robust query processing in dynamic environments using random walk techniques, in: Proceedings of the 3rd International Symposium on Information Processing in Sensor Networks (IPSN'04), Berkeley, CA, Apr. 2004, pp. 277–286.
[2] R. Biswas, S. Thrun, L.J. Guibas, A probabilistic approach to inference with limited information in sensor networks, in: Proceedings of the 3rd International Symposium on Information Processing in Sensor Networks (IPSN'04), Berkeley, CA, Apr. 2004, pp. 269–276.
[3] P. Bodorik, J.S. Riordon, J.S. Pyra, Deciding to correct distributed query processing, IEEE Transaction on Knowledge Data Engineering 5 (3) (1992) 253–265.
[4] B.J. Bonfils, P. Bonnet, Adaptive and decentralized operator placement for in-network query processing, in: Proceedings of the 2nd International Symposium on Information Processing in Sensor Networks (IPSN'03), Palo Alto, CA, Apr. 2003, pp. 47–62.
[5] P.P. Bonissone, R.M. Tong, Editorial: reasoning with uncertainty in expert systems, IEEE Transaction on Man-Machine Systems 22 (3) (1985) 241–250.
[6] P. Bosc, H. Prade, An introduction to the fuzzy set and possibility theory-based treatment of flexible queries and uncertain or imprecise databases, in: Proceedings of the Workshop on Uncertainty Management in Information Systems: From Needs to Solutions, Dec. 1996, pp. 285–324.
[7] R. Cavallo, M. Pittarelli, The theory of probabilistic databases, in: Proceedings of the 13th Very Large Database Conference, Brighton, England, Sep. 1987, pp. 71–81.
[8] A. Cerpa, J. Elson, M. Hamilton, J. Zhao, Habitat monitoring: application driver for wireless communications technology, in: Proceedings of the 1st ACM SIGCOMM Workshop on Data Communications in Latin America and the Caribbean, San Jose, CR, Apr. 2001, pp. 20–41.
[9] R. Cheng, S. Singh, S, Prabhakar, U-DBMS: a database system for managing constantly-evolving data, in: Proceedings of the 31st VLDB Conference, Trondheim, Norway, Aug. 2005, pp. 1271–1274.
[10] D. Chow, C.T. Yu, On the construction of feedback queries, Journal of the ACM 29 (1) (1982) 27–151.
[11] Y.D. Chung, An indexing scheme for energy-efficient processing of content-based retrieval queries on a wireless data stream, Information Sciences, Available online May 2006.
[12] N. Dalvi, D. Suciu, Efficient query evaluation on probabilistic databases, International Journal of Very Large Data Bases, Published online Jun. 2006.
[13] R. Gandhi, S. Khuller, A. Srinivasan, Approximation algorithm for partial covering problems, Journal of Algorithms 53 (1) (2004) 55–84.
[14] A. Gounaris, N.W. Paton, A.A.A. Fernandes, R. Sakellariou, Self-monitoring query execution for adaptive query processing, Data & Knowledge Engineering 51 (3) (2004) 325–348.
[15] L. Gravano, H. Garcia-Molina, A. Tomasic, Gloss: Text-source discovery over the internet, ACM Transaction on Database Systems 24 (2) (1999) 229–264.
[16] J.R. Groff, P.N. Weinber, L. Wald, SQL: The Complete Reference, Osborne/McGraw-Hill, Berkeley, CA, 2002.
[17] D. Grossman, O. Frieder, D. Holmes, D. Roberts, Integrating structured data and text: a relational approach, Journal of the American Society for Information Science 48 (2) (1997) 122–132.
[18] W.B. Heinzelman, A.P. Chandrakasan, H. Balakrishnan, An application-specific protocol architecture for wireless microsensor networks, IEEE Transaction on Wireless Communication 1 (4) (2002) 660–670.
[19] C. Intanagonwiwat, R. Govindan, D. Estrin, Directed diffusion: a scalable and robust communication paradigm for sensor networks, in: Proceedings of the 6th Annual International Conference on Mobile Computing and Networking (MobiCOM 2001), Cologne, Germany, Aug. 2000, pp. 56–67.
[20] R. Jain, A. Puri, R. Sengupta, Geographical routing using partial information for wireless ad hoc networks, IEEE Personal Communications 8 (1) (2001) 48–57.
[21] J. Kim, Advanced structural joins using element distribution, Information Sciences 176 (22) (2006) 3300–3331.

[22] B.S. Lee, R. Musick, MeshSQL: the query language for simulation mesh data, Information Sciences 159 (3-4) (2004) 177–202.
[23] Q. Liang, Q. Ren, Energy and mobility aware geographical multipath routing for wireless sensor networks, in: Proceedings of IEEE Wireless Communications and Networking Conference 2005 (WCNC 2005), New Orleans, LA, Mar. 2005, pp. 1867–1871.
[24] S.R. Madden, M.J. Franklin, J.M. Hellerstein, W. Hong, TinyDB: an acquisitional query processing system for sensor networks, ACM Transaction on Database Systems 30 (1) (2005) 122–173.
[25] A. Manjeshwar, Z. Qing-An, D.P. Agrawal, An analytical model for information retrieval in wireless sensor networks using enhanced APTEEN protocol, IEEE Transaction on Parallel Distributed Systems 13 (12) (2002) 1290–1302.
[26] J.M. Mendel, Uncertain Rule-Based Fuzzy Logic Systems: Introduction and New Directions, Prentice-Hall, Englewood Cliffs, NJ, 2001.
[27] J.M. Mendel, Lessons in Estimation Theory for Signal Processing Communications, and Control, Prentice Hall, Englewood Cliffs, NJ, 1995.
[28] A. Motro, Sources of uncertainty in information systems, in: Proceedings of the 2nd Workshop on Uncertainty Management and Information Systems: From Needs to Solutions, Santa Catalina, CA, Sep. 1992, pp. 1–18.
[29] P. Olofsson, Probability, Statistics and Stochastic Processes, Wiley Interscience, Hoboken, NJ, 2005.
[30] A. Papoulis, Probability, Random Variables, and Stochastic Processes, McGraw-Hill, Boston, NY, 2002.
[31] H.K. Park, J.H. Son, M.H. Kim, Dynamic histograms for future spatiotemporal range predicates, Information Sciences 172 (1-2) (2005) 195–214.
[32] M. Pittarelli, An algebra for probabilistic databases, IEEE Transaction on Knowledge Data Engineering 6 (2) (1994) 293–303.
[33] M. Pittarelli, Probabilistic databases for decision analysis, International Journal of Intelligent Systems 5 (4) (1990) 209–236.
[34] G.J. Pottie, W.J. Kaiser, Wireless integrated network sensors, Communication of the ACM 43 (5) (2000) 551–558.
[35] H. Prade, C. Testemal, Generalizing database relational algebra for the treatment of incomplete or uncertain information and vague queries, Information Sciences 34 (2) (1984) 115–143.
[36] Products Description, Available from: <http://xbow.com>.
[37] Q. Ren, Q. Liang, An energy-efficient MAC protocol for wireless sensor networks, in: Proceedings of IEEE Global Telecommunications Conference 2005 (GLOBECOM'2005), St. Louis, MO, Dec. 2005, pp. 157–161.
[38] R. Ross, V.S. Subrahmanian, J. Grant, Aggregate operators in probabilistic databases, Journal of the ACM 52 (1) (2005) 54–101.
[39] J.R. Schott, Remote Sensing: The Image Chain Approach, Oxford University Press, New York, NY, 1997.
[40] M. Stemm, R.H. Katz, Measuring and reducing energy consumption of network modules in hand-held devices, IEICE Transaction on Communication E80-B (8) (1997) 1125–1131.
[41] E. Straszecka, Combining uncertainty and imprecision in models of medical diagnosis, Information Sciences 176 (20) (2006) 3026–3059.
[42] G. Trajcevski, K. Hinrichs, S. Chamberlain, Managing uncertainty in moving objects databases, ACM Transactions on Database Systems 29 (3) (2004) 463–507.
[43] H.R. Turtle, W.B. Corft, Uncertainty in information retrieval systems, in: Proceedings of the 2nd Workshop on Uncertainty Management and Information Systems: From Needs to Solutions, Santa Catalina, CA, Sep. 1992, pp. 93–111.
[44] J. Warrior, Smart sensor networks of the future, Sensors Magazine, Mar. 1997.
[45] J.D. Wilfrid, J.M.J. Frank, Introduction to Statistical Analysis, McGraw-Hill, New York, NY, 1983.
[46] S.K.M. Wong, W. Ziarko, V.V. Raghavan, P.C.N. Wong, On modeling of information retrieval concepts in vector spaces, ACM Transaction on Database Systems 12 (2) (1987) 299–321.
[47] Y. Yao, J. Gehrke, Query processing in sensor networks, in: Proceedings of the 1st Biennial Conference on Innovative Data Systems Research, Monterey, CA, Jan. 2003, pp. 1–12.
[48] F. Zhao, L. Guibas, Wireless Sensor Networks: An Information Processing Approach, Morgan Kaufman, San Francisco, CA, 2004.

A Propagation Environment Modeling in Foliage

Jing Liang and Qilian Liang, *Senior Member, IEEE*
Department of Electrical Engineering
University of Texas at Arlington
Arlington, TX 76019-0016, USA
E-mail: jliang@wcn.uta.edu, liang@uta.edu

Sherwood W. Samn
Air Force Research Laboratory/HEX
Brooks City Base
San Antonio, TX 78235, USA
Sherwood.samn@brooks.af.mil

Abstract

Foliage clutter, generally much larger than receiver noise, is a crucial factor that degrades the target detection performance. Conventional research have investigated land clutter or sea clutter but not much work on foliage clutter beforehand. In this paper, we propose a new statistical model using log-logistic distribution. On a basis of pragmatic ultra-wideband (UWB) radar measurement, we analyze two different data sets by maximum likelihood (ML) parameter estimation as well as the root mean square error (RMSE) calculation. We not only investigate log-logistic model, but compare it with other popular clutter models, namely log-normal, Weibull and Nakagami. It shows that the log-logistic model not only achieves the smallest standard divination (STD) error on estimated model parameters, but also the best goodness-of-fit and smallest RMSE for both poor and good clutter signals.

Index Terms : foliage clutter, log-logistic, log-normal, Weibull, Nakagami, goodness-of-fit

1 Introduction and Motivation

Detection and identification of military equipment in a strong clutter background, such as foliage, soil cover or building has been a long-standing subject of intensive study. It is believed that solving the target detection through foliage environment will significantly benefit sense-

through-wall and many other subsurface sensing problems. However, to this date, the detection of foliage-covered military targets with the required probability of detection and false alarm still remains a challenging issue. Recent investigations on environment behavior of tree canopies have shown that both signal backscattering and attenuation are significantly influenced by tree architecture [11]. Therefore use the return signal from foliage to establish the clutter model that accounts for environment effects is crucial for the sense-through-foliage radar detection.

Clutter is a term used to define all unwanted echoes from natural environment [26]. The nature of clutter may necessarily vary on a basis of different applications and radar parameters. Most previous studies have investigated land clutter or sea clutter, and some conclusions have been reached. For example, log-normal, Weibull, and K-distributions have been proven to be better suited for the clutter description other than Rayleigh and Rician models in high resolution radar systems. Fred [19] did statistical comparisons and found that sea clutter at low grazing angles and high range resolution is spiky based on the data measured from various sites in Kauai and Hawaii. David generalized radar clutter models using noncentral chi-square density by allowing the noncentrality parameter to fluctuate according to the gamma distribution [4]. Furthermore, Henry *et al.* used a Neural-Network-based approach to predict sea clutter model [9] [34].

However, as far as clutter modeling in forest is concerned, it is still of great interest and will be likely to take some time to reach any agreement. A team of researchers from MIT [7] and U. S. Army Research Laboratory (ARL) [14] [22] have measured ultra-wideband (UWB) backscatter signals in foliage for different polarizations and frequency ranges. The measurements show that the foliage clutter is impulsively corrupted with multipath fading, which leads to inaccuracy of the K-distributions description [32]. The Air Force Office of Scientific Research (AFOSR) has conducted field measurement experiment concerning foliage penetration radar since 2004 and noted that metallic targets may be more easily identified with wideband than with narrowband signals

In this investigation, we will apply ultra-wide band (UWB) radar to model the foliage

clutter. UWB radar emissions are at a relatively low frequency-typically between 100 MHz and 3 GHz. Additionally, the fractional bandwidth of the signal is very large (greater than 0.2). Such a radar sensor has exceptional range resolution that also has an ability to penetrate many common materials (e.g., walls). Law enforcement personnel have used UWB ground penetrating radars (GPRs) for at least a decade. Like the GPR, sense-through-foliage radar takes advantage of UWB's very fine resolution (time gating) as well as low frequency of operation.

In our present work, we investigate the use of the log-logistic distribution to model foliage clutter and illustrate the goodness-of-fit to real UWB clutter data conducted by AFOSR. Additionally, we compare the goodness-of-fit with existing popular models namely log-normal, Weibull, and Nakagami by means of maximum likelihood estimation (MLE) and the root mean square error (RMSE). The result shows that log-logistic model provides the best fit to the foliage clutter. Our contribution is not only the new proposal on the foliage clutter model with estimated concrete parameters, but also provide the criteria and approaches based on which the statistical analysis is deduced. Further, the theoretical study about the probability of detection as well as the probability of false alarm is discussed.

The rest of this paper is organized as follows. Section 2 provides a statistical model review on log-logistic, log-normal, Weibull and Nakagami distributions and discuss their properties and applicability as models for foliage clutter. Section 3 summarizes the measurement and the 2 sets of clutter data that we used in this paper. Section 4 discusses estimation on parameters and the goodness-of-fit for log-logistic, log-normal, Weibull and Nakagami models respectively. Section 5 analyzes the performance of radar detection at presence of foliage clutter. Finally, section 6 concludes this paper and describes some future research topics.

2 Clutter Models

Many radar clutter models have been proposed in terms of distinct statistical distributions, most of which describe the characteristics of clutter amplitude or power. Before detailed

analysis, first we would like to discuss the properties and applicability of log-logistic, log-normal, Weibull, and Nakagami statistic distributions, which are designated as "curve fit" models in section 4, since they are more likely to provide good fit to our collections of pragmatic clutter data in general. Detailed explanations would be given in following subsections.

2.1 Log-logistic Model

Recently Log-logistic model has been applied in hydrological analysis. This distribution is a special case of Burr's type-XII distribution [1] as well as a special case of the kappa distribution proposed by Mielke and Jonson [15]. Lee *et al.* employed the LLD for frequency analysis of multiyear drought durations [13], whereas Shoukri *et al.* employed LLD to analyse extensive Canadian precipitation data [27], and Narda & Malik used LLD to develop a model of root growth and water uptake in wheat [17]. In spite of its intensive application in precipitation and stream-flow data, the log-logistic distribution (LLD) [8] statistical model, to the best of our knowledge, has never been applied to radar foliage clutter. The motivation for considering log-logistic model is based on its higher kurtosis and longer tails, as well as its PDF curve similarity to log-normal and Weibull distributions. It is intended to be employed to estimate how well the model matches our collected foliage clutter statistics.

Here we apply the two-parameter distribution with parameters μ and σ. The PDF for this distribution is given by

$$f(x) = \frac{e^{\frac{\ln x-\mu}{\sigma}}}{\sigma x(1+e^{\frac{\ln x-\mu}{\sigma}})^2}, \quad x>0,\ \sigma>0 \tag{1}$$

where μ is scale parameter and σ is shape parameter. The mean of the the LLD is

$$E\{x\} = e^{\mu}\Gamma(1+\sigma)\Gamma(1-\sigma) \tag{2}$$

The variance is given by

$$Var\{x\} = e^{2\mu}\{\Gamma(1+2\sigma)\Gamma(1-2\sigma) - [\Gamma(1+\sigma)\Gamma(1-\sigma)]^2\} \tag{3}$$

while the moment of order k is

$$E\{x^k\} = \sigma e^{\mu} B(k\sigma, 1 - k\sigma),\ k < \frac{1}{\sigma} \tag{4}$$

where

$$B(m, n) = \int_0^1 x^{m-1}(1-x)^{n-1} dx \tag{5}$$

PDFs for LLD for selected μ's and σ's are illustrated in Fig. 1.

2.2 Log-normal Model

Most previous experimental data have resulted in clutter being modeled using a log-normal distribution, which is most frequently used when the radar sees land clutter [31] or sea clutter [29] at low grazing angles (≤ 5 degrees) since log-normal has a long tail. However, it has been reported that the log-normal model tends to overestimate the dynamic range of the real clutter distribution [21]. Furthermore, most previous research applies log-normal model to land and sea clutter, but how accurately it models foliage clutter requires detailed analysis.

The log-normal distribution [12] is also a two-parameter distribution with parameters μ and σ. The PDF for this distribution is given by

$$f(x) = \frac{1}{x\sigma\sqrt{2\pi}} e^{-\frac{(\ln x - \mu)^2}{2\sigma^2}},\quad x > 0, \sigma > 0 \tag{6}$$

where μ is the scale parameter and σ is the shape parameter. The mean, variance and the moment of order k are given respectively by

$$E\{x\} = e^{\mu + \frac{\sigma^2}{2}} \tag{7}$$

$$Var\{x\} = (e^{\sigma^2} - 1)e^{2\mu + \sigma^2} \tag{8}$$

$$E\{x^k\} = e^{k\mu + \frac{k^2\sigma^2}{2}} \tag{9}$$

PDFs for selected μ's and σ's for log-normal distribution are shown in Fig. 2.

2.3 Weibull Model

The Weibull distribution, which is named after Waloddi Weibull, can be made to fit clutter measurements that lie between the Rayleigh and log-normal distribution [33]. It has been applied to land clutter [3] [24], sea clutter [6] [25] and weather clutter [23]. However, in very spiky sea and foliage clutter, the description of the clutter statistics provided by Weibull distributions may not always be sufficiently accurate [30].

The Weibull distribution is also a two-parameter distribution with parameters a and b. The PDF for this distribution is given by

$$f(x) = ba^{-b}x^{b-1}e^{-(x/a)^b}, \quad x > 0, a > 0, \ b > 0 \tag{10}$$

where b is the shape parameter and a is the scale parameter. The mean, variance and the moment of order k are given respectively by

$$E\{x\} = a\Gamma(1 + \frac{1}{b}) \tag{11}$$

$$Var\{x\} = a^2\{\Gamma(1 + \frac{2}{b}) - [\Gamma(1 + \frac{1}{b})]^2\} \tag{12}$$

$$E\{x^k\} = a^k\Gamma(1 + \frac{k}{b}) \tag{13}$$

PDFs for selected a's and b's for Weibull distribution are shown in Fig. 3.

2.4 Nakagami Model

In the foliage penetration setting, the target returns suffer from multipath effects corrupted with fading. As Nakagami distribution is used to model scattered fading signals that reach a receiver by multiple paths, it is natural to investigate how well it fits the foliage clutter statistics.

The PDF for Nakagami distribution is given by

$$f(x) = 2(\frac{\mu}{\omega})^{\mu} \frac{1}{\Gamma(\mu)} x^{(2\mu-1)} e^{-\frac{\mu}{\omega}x^2}, \quad x > 0, \omega > 0 \tag{14}$$

where μ is the shape parameter and ω is the scale parameter. The mean, variance and the moment of order k of Nakagami distribution are given respectively by

$$E\{x\} = \frac{\Gamma(\mu + \frac{1}{2})}{\Gamma(\mu)}(\frac{\omega}{\mu})^{\frac{1}{2}} \tag{15}$$

$$Var\{x\} = \omega[1 - \frac{1}{\mu}(\frac{\Gamma(\mu + \frac{1}{2})}{\Gamma(\mu)})^2] \tag{16}$$

$$E\{x^k\} = \frac{\Gamma(\mu + \frac{k}{2})}{\Gamma(\mu)}(\frac{\omega}{\mu})^{\frac{k}{2}} \tag{17}$$

The PDFs for selected μ's and ω's for the Nakagami distribution are illustrated in Fig. 4.

3 Experiment Setup and Data Collection

The foliage penetration measurement effort began in August 2005 and continued through December 2005. Working in August through the fall of 2005, the foliage measured included late summer foliage and fall and early winter foliage. Late summer foliage, because of the limited rainfall, involved foliage with decreased water content. Late fall and winter measurements involved largely defoliated but dense forest. A picture of experiment site is shown in Fig.5.

The principle pieces of equipment are:

- Dual antenna mounting stand
- Two antennas
- A trihedral reflector target
- Barth pulse source (Barth Electronics, Inc. model 732 GL) for UWB
- Tektronix model 7704 B oscilloscope
- Rack system
- HP signal Generator
- IBM laptop

- Custom RF switch and power supply
- Weather shield (small hut)

A bistatic UWB radar (individual transmit and receive antennas) was used (see Fig. 6) as it was believed that circulators did not exist for wideband signals at that time. The foliage clutter was a round trip distance of 600 feet from the bistatic antennas (300 feet one way).

An 18 foot distance between antennas was chosen to reduce the signal coupling between transmitter and the receiver [10]. The radar was constructed on a seven-ton man lift, which had a total lifting capacity of 450 kg. The limit of the lifting capacity was reached during the experiment as essentially the entire measuring apparatus was placed on the lift (as shown in Fig. 7). Throughout this work, a Barth pulse source (Barth Electronics, Inc. model 732 GL) was used. The pulse generator uses a coaxial reed switch to discharge a charge line for a very fast rise time pulse outputs. The model 732 pulse generator provides pulses of less than 50 picoseconds (ps) rise time, with amplitude from 150 V to greater than 2 KV into any load impedance through a 50 ohm coaxial line. The generator is capable of producing pulses with a minimum width of 750 ps and a maximum of 1 microsecond. This output pulse width is determined by charge line length for rectangular pulses, or by capacitors for 1/e decay pulses.

For the return data we used in this paper, each sample is spaced at 50 picoseconds interval, and 16,000 samples were collected for each collection for a total time duration of 0.8 microseconds at a rate of approximately 20 Hz. We considered two sets of data from this experiment. Initially, the Barth pulse source was operated at lower amplitude and 35 pulses of clutter signals were obtained at each site but different time. These pulses have been averaged to remove the random noise. Data have been collected from 10 different sites. one collection of transmitted pulse and received backscattering are shown in Fig. 8(a) and (b) respectively. The unit of clutter amplitude in this paper is "V". Although pulse-to-pulse variability was noted for collections of received echoes, the fading tendency of different returned signals are the same. These data is referred to as data set I.

Later, additional improvements were made in the measurement procedure, include the improved isolation of transmit and receive antennas, the addition of a log-periodic antenna (Antenna Research Associates LPC-2010-C) as a transmit antenna, and the EMCO ridged waveguide horn (Microwave horn, EMCO 3106). Echoes for data set II were collected using this higher amplitude transmitted pulses. 2 collections at different site with 100 pulsese average have been obtained, one of which is shown in Fig. 8(c). To make them clearer to readers, we provide expanded views of received traces from sample 10,000 to 12,000 in Fig. 9.

4 Statistical Analysis of the Foliage Clutter Data

4.1 Maximum Likelihood Estimation

Using the collected clutter data mentioned above, we apply Maximum Likelihood Estimation (MLE) approach to estimate the parameters of the log-logistic, log-normal, Weibull, and Nakagami models. MLE is often used when the sample data are known and parameters of the underlying probability distribution are to be estimated [5] [2]. It is generalized as follows:

Let y_1, y_2, $\cdots$, y_N be N independent samples drawn from a random variable $\mathbf{Y}$ with m parameters θ_1, θ_2, $\cdots$, θ_m, where $\theta_i \in \theta$, then the likelihood function expressed as a function of θ conditional on $\mathbf{Y}$ is

$$L_N(\mathbf{Y}|\theta) = \prod_{k=1}^{N} f_{Y|\theta}(y_k|\theta_1, \theta_2, \cdots, \theta_m) \tag{18}$$

The maximum likelihood estimate of θ_1, θ_2, $\cdots$, θ_m is the set of values $\hat{\theta}_1$, $\hat{\theta}_2$, $\cdots$, $\hat{\theta}_m$ that maximize the likelihood function $L_N(\mathbf{Y}|\theta)$.

As the logarithmic function is monotonically increasing, maximizing $L_N(\mathbf{Y}|\theta)$ is equivalent to maximizing $\ln(L_N(\mathbf{Y}|\theta))$. Hence, it can be shown that a necessary but not sufficient condition to obtain the ML estimate $\hat{\theta}$ is to solve the likelihood equation

$$\frac{\partial}{\partial\theta} \ln(L_N(\mathbf{Y}|\theta)) = 0 \tag{19}$$

Note that the amplitude of foliage clutter faded with the increase of sample time. Even At the same sample, it varies for different collections. In order to better analyze its randomness, we studied each collection. Using the collected clutter radar mentioned above, we apply MLE to obtain $\hat{\mu}$ and $\hat{\sigma}$ for log-logistic, $\hat{\mu}$ and $\hat{\sigma}$ for the log-normal, $\hat{a}$ and $\hat{b}$ for the Weibull, and $\hat{\mu}$ and $\hat{\omega}$ for the Nakagami. The estimation results for data set I are listed in table 1. We also explore the standard deviation (STD) error of each parameter. These descriptions are shown in table 1 in the form of ε_x, where x denotes different parameter for each model. We also calculate the average values of estimated parameters and their STD errors in table 2.

From table 1 and 2 we can see STD error for log-logistic and log-normal parameters are less than 0.02 and their estimated parameters vary little from data to data compared to Weibull and Nakagami. It is obvious that log-logistic model provides the smallest STD error for all the 10 collections compared to log-normal. It is obvious that apply both Weibull and Nakagami models, accurate shape parameter estimation can be achieved but the result of scale parameter estimations are not acceptable.

The estimation results for data set II are shown in table 3. Due to the improvement on this set of signal, STD error for log-logistic and log-normal parameters have been reduced compared those of data set I. However, for Weibull and Nakagami, it is a different case, which implies log-logistic and log-normal are much more accurate to model foliage clutter.

In the view of error on parameter estimation, log-logistic model fits the collected data best compared to log-normal, Weibull, and Nakagami. Log-normal is also acceptable.

4.2 Goodness-of-fit in curve and RMSE

We may also observe the extend to which the PDF curve of the statistic model matches that of clutter data by calculating the averaged root mean square error (RMSE) for each data set. Let i (i=1, 2, $\cdots$, n) be the sample index of clutter amplitude, c_i is the corresponding PDF value whereas $\hat{c}_i$ is the PDF value of the statistical model with estimated parameters by means of MSE. The RMSE is obtained through

$$\texttt{RMSE} = \frac{1}{k}\sum_{k}\sqrt{\frac{1}{n}\sum_{i=1}^{n}(c_i - \hat{c}_i)^2} \tag{20}$$

Here we apply n=100 for each model and k is the number of data collections for each set.

In Fig. 10 and 11, we use one collection from data set I and II respectively to illustrate the goodness-of-fit in curve. Also, we calculate the averaged RMSE of each model for both collected data set I and II. The PDF of absolute amplitude of one collection of clutter data is presented by means of histogram bars. In Fig. 10, it can be seen obviously that log-logistic model with MLE parameters provides the best goodness-of-fit compared to the other models, since it provides the most suitable kurtosis, slope and tail. As for the maximum PDF value, the log-logistic is about 1×10^{-3}, while that of other models are over 1.2×10^{-3}. For the slope part, which connects the kurtosis and the tail and which is in the range from 0.1×10^{4} to 0.5×10^{4} in view of x axes, the log-logistic provides the smallest skewness whereas Nakagami provides the largest. Examination of the tails show that log-logistic and log-normal provide very similar-valued tails, while tails of the Weibull and the Nakagami are lager than the collected data. Meanwhile, we obtain that $\texttt{RMSE}_{log-logistic} = 2.5425\times10^{-5}$, $\texttt{RMSE}_{log-normal} = 3.2704\times10^{-5}$, $\texttt{RMSE}_{Weibull} = 3.7234\times10^{-5}$, $\texttt{RMSE}_{Nakagami} = 5.4326\times10^{-5}$. This also shows that the log-logistic model is more accurate than the other three models.

Similarly, in Fig. 11 histogram bars denote the PDF of the absolute amplitude of one collection of clutter data from set II. Compared to Fig 10, the log-logistic and the log-normal provide more similar extend of goodness-of-fit. Weibull is worse since it cannot fit well in either kurtosis or tail, while Nakagami is the worst and unacceptable. Also, we obtain $\texttt{RMSE}_{log-logistic} = 2.739\times10^{-5}$, $\texttt{RMSE}_{log-normal} = 3.1866\times10^{-5}$, $\texttt{RMSE}_{Weibull} = 3.6361\times10^{-5}$, $\texttt{RMSE}_{Nakagami} = 4.4045\times10^{-5}$. This illustrates that for clutter backscattering data set II, the log-logistic model still fits the best.

5 Target Detection Performance

As we have mentioned previously, one of the primary goal to be carried out by a radar is target detection. On a basis of the clutter model that have been just studied, we may apply a special case of the Bayesian criterion named Neyman-Person criterion to analyze the target detection performance in the foliage environment.

If the received sample signal to be tested is R, then the two hypotheses are shown as follows:

$$\begin{aligned} H_0 &: R = C + n \\ H_1 &: R = S + C + n \end{aligned} \tag{21}$$

where C and n represent the random variable of clutter and noise respectively. C follows log-logistic model with both parameters μ and σ, and n is gaussian noise with zero mean and variance ν^2. S is the target signal, which assumes to be a constant for simplicity.

Therefore $f(R|H_0)$ and $f(R|H_1)$ mean:

$f(R|H_0) = \ PDF\ of\ R\ given\ that\ a\ target\ was\ not\ present$

$f(R|H_1) = \ PDF\ of\ R\ given\ that\ a\ target\ was\ present$

They can be denoted as follows:

$$f(R|H_0) = \int_0^\infty \frac{e^{\frac{lnr-\mu}{\sigma}}}{\sigma r(1+e^{\frac{lnr-\mu}{\sigma}})^2} \times \frac{1}{\sqrt{2\pi}\nu} e^{-\frac{(R-r)^2}{2\nu^2}} dr \tag{22}$$

$$f(R|H_1) = \int_0^\infty \frac{e^{\frac{ln(r-s)-\mu}{\sigma}}}{\sigma(r-s)(1+e^{\frac{ln(r-s)-\mu}{\sigma}})^2} \times \frac{1}{\sqrt{2\pi}\nu} e^{-\frac{(R-s-r)^2}{2\nu^2}} dr \tag{23}$$

If the probability that a target was not present is $P(H_0)$ whereas that of a target was present is $P(H_1)$, then PDF of R is

$$f(R) = P(H_0)f(R|H_0) + P(H_1)f(R|H_1) \tag{24}$$

To decide whether there is a target or not, Neyman-Pearson detection rule is shown as

$$\frac{f(R|H_0)}{f(R|H_1)} \underset{H_1}{\overset{H_0}{\gtrless}} \frac{P(H_1)}{P(H_0)} \tag{25}$$

In case of $P(H_1) = P(H_0)$, (26) is simplified as

$$f(R|H_0) \underset{H_1}{\overset{H_0}{\gtrless}} f(R|H_1) \tag{26}$$

which actually is

$$\frac{e^{[\frac{s^2-2s(R-r)}{2\nu^2}+\frac{ln(\frac{r}{r-s})}{\sigma}]}}{\frac{r}{r-s}[\frac{1+e^{\frac{lnr-\mu}{\sigma}}}{1+e^{\frac{ln(r-s)-\mu}{\sigma}}}]^2} \underset{H_1}{\overset{H_0}{\gtrless}} 1 \tag{27}$$

It is easy to obtain the decision threshold T in terms of the above function

$$T = -\frac{\nu^2}{s} ln[\frac{1+e^{\frac{lnr-\mu}{\sigma}}}{1+e^{\frac{ln(r-s)-\mu}{\sigma}}}]^2 + \frac{\nu^2[ln(\frac{r}{r-s})-\sigma]}{s\sigma} + \frac{s}{2} + r \tag{28}$$

Under hypothesis H_0, a false alarm occurs anytime $R > T$, therefore the probability of false alarm is

$$\begin{aligned} P_{FA} &= \int_T^\infty f(R|H_0)dR \\ &= \frac{1}{\sqrt{2\pi}\sigma\nu}\int_T^\infty \int_0^\infty \frac{e^{[-\frac{(R-r)^2}{2\nu^2}+\frac{lnr-\mu}{\sigma}]}}{(1+e^{\frac{lnr-\mu}{\sigma}})^2 r} drdR \end{aligned} \tag{29}$$

Similarly, Under hypothesis H_1, when $R > T$, the target is detectable. Therefore the probability of detection is

$$\begin{aligned} P_D &= \int_T^\infty f(R|H_1)dR \\ &= \frac{1}{\sqrt{2\pi}\sigma\nu}\int_T^\infty \int_0^\infty \frac{e^{[-\frac{(R-r-s)^2}{2\nu^2}+\frac{ln(r-s)-\mu}{\sigma}]}}{(1+e^{\frac{ln(r-s)-\mu}{\sigma}})^2 (r-s)} drdR \end{aligned} \tag{30}$$

Fig. 12 shows the probability of detection for a fluctuating radar target using Monte Carlo simulation. The "no clutter" curve describes the situation when there are only radar echoes and noise. Swerling II model is applied for the detection [20]. "SCR" stands for signal to clutter ratio, where log-logistic clutter model is used, and "SNR" is the signal to noise ratio. These curves show that no matter what SCR is, the clutter generally reduces the probability of detection. The higher SNR, the less reduction compared to the case without clutter. When SCR increases, the probability of detection will become more close to the value of "no clutter" case along with the increase of SNR. Similarly, Fig. 13 illustrates the probability of false alarm, which shows that the clutter tremendously increase the probability of false alarm.

6 Conclusion

On a basis of two sets of foliage clutter data using UWB radar, we show that it is more accurate to describe the amplitude of foliage clutter using log-logistic statistic model other than log-normal, Weibull, or Nakagami. Log-normal is also acceptable. The goodness-of-fit for Weibull is worse whereas that of Nakagami is the worst. Our contribution is not only the new proposal on the foliage clutter model with estimated parameters, but also provide the criteria and approaches based on which the statistical analysis is deduced. Further, the theoretical study on the probability of detection and the probability of false alarm at the presence of foliage clutter is discussed. Future research will investigate the characteristics of targets and the design of radar receiver under this clutter to improve the target detection, tracking and imaging.

Acknowledgement

This work was supported in part by Office of Naval Research (ONR) under Grant N00014-07-1-0395, N00014-07-1-1024, and National Science Foundation (NSF) under Grant CNS-0721515.

References

[1] Burr, I. W.,"Cumulative frequency functions" *Ann. Math. Statist.*, 13, 215-232, 1942.

[2] Barkat, M., *Signal Deteciton and Estimation* 2nd, London: Artech house, 2005.

[3] Boothe, R. R., "The Weibull distribution applied to the ground clutter backscatter coefficient", U.S. Army Missile Command Report No. RE-TR-69-15, June, 1969.

[4] David, A. Shnidman, "Generalized radar clutter model", *IEEE Trans. on Aerosp. Electron. Syst*, vol. 35, no. 3, July 1999.

[5] Devore, Jay L., *Probability and Statistics for Engineering and the Sciences*, Monterey, CA: BrooksiCole, 1982.

[6] Fay, F. A., Clarke, J. and Peters, R. S, "Weibull distributed applied to sea clutter", *Radar 77, IEE Conf. Publ.*, 155, pp. 101-104, 1977.

[7] Fleischman, J. G., Ayasli, S., Adams, E. M., and Gosselin, D. R., Foliage penetration experiment: Part I: Foliage attenuation and backscatter analysis of SAR imagery, *IEEE Trans. on Aerosp. Electron. Syst.*, 32, 1, part 1 of 3 (1996), 134-144.

[8] Gupta, R. C., Akman, O. and Lvin, S., "A study of log-logistic model in survival analysis", *Biometrical Journal*, 41, pp. 431-443, 1999.

[9] Hennessey, G. and Leung, H., "Sea-clutter modeling using a radial-basis-function neural network", *IEEE Journal of Oceanic Engineering*, vol. 26, no. 3, pp. 358-372, July, 2001.

[10] Henning, J. A., Design and Performance of An Ultra-Wideband Foliage Penetrating Noise Radar, Masters Thesis, University of Nebraska, May 2001.

[11] Imhoff, M. L., "A theoretical analysis of the effect of forest structure on SAR backscatter and the remote sensing of biomass," *IEEE Trans. Geosci. Remote Sensing*, vol. 33, pp. 341C352, Mar. 1995.

[12] Limpert, E., Stahel, W. and Abbt, M., "Log-normal Distributions across the Sciences: Keys and Clues.", *BioScience*, 51 (5), pp. 341C352, 2001.

[13] Lee, K. S., Sadeghipour, J. and Dracup, J. A., "An approach for frequency analysis of multiyear dought duration.", *Wat. Resour. Res.* 22(5), 655-662, 1986.

[14] Mccorkle, J. W., "Early results from the ARL UWB Foliage attenuation (FOPEN) SAR", Presented at the SPIE International Symposium on Optical Engineering and Photonics in Aerospace and Remote Sensing, Conference 1942, Underground and Obscured Object Detection, Apr. 1993.

[15] Mielke, P. W. and Johnson. E. S.,"Three-parameter kappa distribution maximum likelihood estimates and likelihood ratio tests," *Monthly Weather Rev.*, 101, 701-709, 1973.

[16] M. Nakagami, "The m-Distribution, a general formula of intensity of rapid fading". In W. G. Hoffman, editor, *Statistical Methods in Radio Wave Propagation: Proceedings of a Symposium held at the University of California*, pp 3-36. Permagon Press, 1960.

[17] Narda, N. K. and Malik, R. K., "Dynamic model of root growth and water uptake in wheat.", *Indian J. Agric. Engng* 3(3&4), 147-155, 1993.

[18] ONR BAA 07-009, "Electronic Warfare Discovery and Invention (D&I)," http://www.onr.navy.mil/02/baa/.

[19] Posner, F. L., *IEEE Trans. on Aerosp. Electron. Syst.*, vol. 38, no. 1, pp. 58-73, Jan 2002.

[20] Richards, M. A., *Fundamentals of Radar Signal Processing*, McGraw- Hill Companies, New York, 2005.

[21] Schleher, D. C., "Radar Detection in Weibull Clutter", *IEEE Trans. on Aerosp. Electron. Syst.*, vol. AES-12, No. 6, Nov. 1976.

[22] Sheen, D. R., Malinas, N. P., Kletzli, D. W., Lewis, T. B., and Roman, J. F., "Foliage transmission meassurement using a ground-based ultra-wideband (UWB) (300-1300MHz) SAR system", *IEEE Trans. on Geoscience and Remote Sensing*, 32, 1(1994).

[23] Sekine, M., *et al*, "On Weibull distributed weather clutter.", *IEEE Trans. on Aerosp. Electron. Syst.*, AES-15, pp. 824-830, 1979.

[24] Sekine, M., *et al*, "Weibull distributed ground clutter.", *IEEE Trans. on Aerosp. Electron. Syst.*, AES-17 pp. 596-598, July 1981.

[25] Sekine, M., *et al*, "Weibull distributed sea clutter.", *IEE Proceedings, Part F - Communications, Radar and Signal Processing*, vol. 130, no. 5, Aug. 1983.

[26] Skolnik, M. I., *Introduction to Radar Systems*, 3rd ed, New York, McGraw Hill, 2001.

[27] Shoukri, M. M., Mian, I. U. H. and Tracy, D. S., " Sampling properties of estimators of the log-logistic distribution with application to Canadian precipitation data.", *Can. J. Statist.* 16(3), 223-236, 1988.

[28] Singh, V. P., Guo, H. and Yu, F. X., "Parameter estimation for 3-parameter log-logistic distribution (LLD3) by Pome", *Parameter estimation for 3-parameter log-logistic distribution (LLD3) by Pome*, vol.7, no.3, pp. 163-177, 2005.

[29] Trunk, G. and George, S., "Detection of targets in non-Gaussian sea clutter", *IEEE Trans. on Aerosp. Electron. Syst.*, vol. AES-6, Sept. 1970.

[30] Tsihrintzis, G. A. and Nikias, C. L., "Evaluation of fractional lower-order statistics-based detection algorithms on real sea-clutter data.", *IEE Proc-Radar, Sonar Navig.*, vol. 144, no.1, Feb., pp. 29-37, 1997.

[31] Warden, M., "An experimental study of some clutter characteristics.", in *AGARD Conf. Proc. 66-Advanced Radar Systems*, May 1970.

[32] Watts, S., "Radar detection prediction in K-distribution sea clutter and thermal noise", *IEEE Trans. on Aerosp. Electron. Syst.*, AES-23, pp. 40-45, 1987.

[33] Weibull, W. "A statistical distribution function of wide applicability", J. Appl. Mech.-Trans. ASME 18(3), 293-297, 1951.

[34] Xie, N. and Leung, H., "A Multiple-Model Prediction Approach for Sea Clutter Modeling", *IEEE Trans. on Geoscience and Remote Sensing*, vol. 41, no. 6, pp. 1491-1502, June, 2003.

List of Tables

1 Estimated Parameters for Data Set I 18

2 Averaged Estimated Parameters for Data Set I 19

3 Estimated and Averaged Parameters for Data Set II 19

Table 1: Estimated Parameters for Data Set I

PDF	Log-Logistic	Log-normal	Weibull	Nakagami
data 1	$\hat{\mu} = 7.24161$ $\hat{\sigma} = 1.06483$ $\varepsilon_\mu = 0.0141212$ $\varepsilon_\sigma = 0.00724181$	$\hat{\mu} = 7.0455$ $\hat{\sigma} = 2.20761$ $\varepsilon_\mu = 0.0174527$ $\varepsilon_\sigma = 0.0123415$	$\hat{a} = 2975.33$ $\hat{b} = 0.594979$ $\varepsilon_a = 41.6157$ $\varepsilon_b = 0.00356925$	$\hat{\mu} = 0.177062$ $\hat{\omega} = 9.09663e+007$ $\varepsilon_\mu = 0.00150615$ $\varepsilon_\omega = 1.70907e+006$
data 2	$\hat{\mu} = 6.9716$ $\hat{\sigma} = 1.2126$ $\varepsilon_\mu = 0.014747$ $\varepsilon_\sigma = 0.00773723$	$\hat{\mu} = 6.72573$ $\hat{\sigma} = 2.33617$ $\varepsilon_\mu = 0.0184691$ $\varepsilon_\sigma = 0.0130602$	$\hat{a} = 2285.13$ $\hat{b} = 0.563747$ $\varepsilon_a = 33.7127$ $\varepsilon_b = 0.00337485$	$\hat{\mu} = 0.162375$ $\hat{\omega} = 7.4776e+007$ $\varepsilon_\mu = 0.00137422$ $\varepsilon_\omega = 1.46679e+006$
data 3	$\hat{\mu} = 7.00554$ $\hat{\sigma} = 1.10741$ $\varepsilon_\mu = 0.0145728$ $\varepsilon_\sigma = 0.0076303$	$\hat{\mu} = 6.76262$ $\hat{\sigma} = 2.31258$ $\varepsilon_\mu = 0.0182825$ $\varepsilon_\sigma = 0.0129283$	$\hat{a} = 2341.52$ $\hat{b} = 0.57073$ $\varepsilon_a = 34.1207$ $\varepsilon_b = 0.00341448$	$\hat{\mu} = 0.164695$ $\hat{\omega} = 7.46366e+007$ $\varepsilon_\mu = 0.001395$ $\varepsilon_\omega = 1.45459e+006$
data 4	$\hat{\mu} = 7.03055$ $\hat{\sigma} = 1.07858$ $\varepsilon_\mu = 0.0142027$ $\varepsilon_\sigma = 0.00741556$	$\hat{\mu} = 6.80711$ $\hat{\sigma} = 2.25973$ $\varepsilon_\mu = 0.0178647$ $\varepsilon_\sigma = 0.0126329$	$\hat{a} = 2395.85$ $\hat{b} = 0.579381$ $\varepsilon_a = 34.4066$ $\varepsilon_b = 0.00345156$	$\hat{\mu} = 0.167391$ $\hat{\omega} = 7.4926e+007$ $\varepsilon_\mu = 0.0014916$ $\varepsilon_\omega = 1.44727e+006$
data 5	$\hat{\mu} = 7.16226$ $\hat{\sigma} = 1.10132$ $\varepsilon_\mu = 0.014605$ $\varepsilon_\sigma = 0.00750067$	$\hat{\mu} = 6.95712$ $\hat{\sigma} = 2.26592$ $\varepsilon_\mu = 0.0179137$ $\varepsilon_\sigma = 0.0126675$	$\hat{a} = 2806.76$ $\hat{b} = 0.577823$ $\varepsilon_a = 40.4226$ $\varepsilon_b = 0.00347389$	$\hat{\mu} = 0.17112$ $\hat{\omega} = 9.03298e+007$ $\varepsilon_\mu = 0.00145265$ $\varepsilon_\omega = 1.72749e+006$
data 6	$\hat{\mu} = 7.01527$ $\hat{\sigma} = 1.10123$ $\varepsilon_\mu = 0.0144902$ $\varepsilon_\sigma = 0.00758568$	$\hat{\mu} = 6.77515$ $\hat{\sigma} = 2.30286$ $\varepsilon_\mu = 0.0182057$ $\varepsilon_\sigma = 0.012874$	$\hat{a} = 2360.33$ $\hat{b} = 0.572749$ $\varepsilon_a = 34.2753$ $\varepsilon_b = 0.00342376$	$\hat{\mu} = 0.165292$ $\hat{\omega} = 7.50824e+007$ $\varepsilon_\mu = 0.00140035$ $\varepsilon_\omega = 1.46145e+006$
data 7	$\hat{\mu} = 7.14523$ $\hat{\sigma} = 1.09486$ $\varepsilon_\mu = 0.0145132$ $\varepsilon_\sigma = 0.00745994$	$\hat{\mu} = 6.94201$ $\hat{\sigma} = 2.25621$ $\varepsilon_\mu = 0.0178369$ $\varepsilon_\sigma = 0.0126132$	$\hat{a} = 2753.69$ $\hat{b} = 0.578948$ $\varepsilon_a = 39.585$ $\varepsilon_b = 0.00347442$	$\hat{\mu} = 0.170964$ $\hat{\omega} = 8.80474e+007$ $\varepsilon_\mu = 0.00145125$ $\varepsilon_\omega = 1.68382e+006$
data 8	$\hat{\mu} = 6.95411$ $\hat{\sigma} = 1.11486$ $\varepsilon_\mu = 0.0146774$ $\varepsilon_\sigma = 0.00768003$	$\hat{\mu} = 6.71591$ $\hat{\sigma} = 2.31898$ $\varepsilon_\mu = 0.0183331$ $\varepsilon_\sigma = 0.0129641$	$\hat{a} = 2250.66$ $\hat{b} = 0.564989$ $\varepsilon_a = 33.1387$ $\varepsilon_b = 0.0033763$	$\hat{\mu} = 0.162448$ $\hat{\omega} = 7.31436e+007$ $\varepsilon_\mu = 0.00137488$ $\varepsilon_\omega = 1.4338e+006$
data 9	$\hat{\mu} = 7.18561$ $\hat{\sigma} = 1.09854$ $\varepsilon_\mu = 0.0145483$ $\varepsilon_\sigma = 0.00749265$	$\hat{\mu} = 6.9715$ $\hat{\sigma} = 2.27088$ $\varepsilon_\mu = 0.0179529$ $\varepsilon_\sigma = 0.0126952$	$\hat{a} = 2840.72$ $\hat{b} = 0.581219$ $\varepsilon_a = 40.6593$ $\varepsilon_b = 0.0034984$	$\hat{\mu} = 0.172324$ $\hat{\omega} = 8.97304e+007$ $\varepsilon_\mu = 0.00146348$ $\varepsilon_\omega = 1.70923e+006$
data 10	$\hat{\mu} = 7.192$ $\hat{\sigma} = 1.0866$ $\varepsilon_\mu = 0.0144166$ $\varepsilon_\sigma = 0.0073916$	$\hat{\mu} = 6.99196$ $\hat{\sigma} = 2.23975$ $\varepsilon_\mu = 0.0177067$ $\varepsilon_\sigma = 0.0125211$	$\hat{a} = 2869.65$ $\hat{b} = 0.584803$ $\varepsilon_a = 40.837$ $\varepsilon_b = 0.00351294$	$\hat{\mu} = 0.173572$ $\hat{\omega} = 9.01631e+007$ $\varepsilon_\mu = 0.0014747$ $\varepsilon_\omega = 1.71142e+006$

Table 2: Averaged Estimated Parameters for Data Set I

PDF	Log-Logistic	Log-normal	Weibull	Nakagami
average	$\hat{\mu} = 7.0904$ $\hat{\sigma} = 1.1061$ $\varepsilon_\mu = 0.0145$ $\varepsilon_\sigma = 0.0075$	$\hat{\mu} = 6.8695$ $\hat{\sigma} = 2.2771$ $\varepsilon_\mu = 0.0180$ $\varepsilon_\sigma = 0.0127$	$\hat{a} = 2588$ $\hat{b} = 0.5769$ $\varepsilon_a = 37.4316$ $\varepsilon_b = 0.0035$	$\hat{\mu} = 0.1687$ $\hat{\omega} = 8.218e + 007$ $\varepsilon_\mu = 0.0014$ $\varepsilon_\omega = 1.4905e + 006$

Table 3: Estimated and Averaged Parameters for Data Set II

PDF	Log-Logistic	Log-normal	Weibull	Nakagami
data 1	$\hat{\mu} = 7.76868$ $\hat{\sigma} = 0.786511$ $\varepsilon_\mu = 0.0107792$ $\varepsilon_\sigma = 0.00521601$	$\hat{\mu} = 7.79566$ $\hat{\sigma} = 1.41771$ $\varepsilon_\mu = 0.011208$ $\varepsilon_\sigma = 0.00792559$	$\hat{a} = 4901.07$ $\hat{b} = 0.743223$ $\varepsilon_a = 55.3011$ $\varepsilon_b = 0.00434465$	$\hat{\mu} = 0.239587$ $\hat{\omega} = 1.16839e + 008$ $\varepsilon_\mu = 0.00207912$ $\varepsilon_\omega = 1.88719e + 006$
data 2	$\hat{\mu} = 7.78096$ $\hat{\sigma} = 0.787426$ $\varepsilon_\mu = 0.0107917$ $\varepsilon_\sigma = 0.0052213$	$\hat{\mu} = 7.8046$ $\hat{\sigma} = 1.41855$ $\varepsilon_\mu = 0.0112147$ $\varepsilon_\sigma = 0.00793033$	$\hat{a} = 4942.48$ $\hat{b} = 0.745233$ $\varepsilon_a = 55.6114$ $\varepsilon_b = 0.0043612$	$\hat{\mu} = 0.240593$ $\hat{\omega} = 1.17237e + 008$ $\varepsilon_\mu = 0.00208848$ $\varepsilon_\omega = 1.88953e + 006$
average	$\hat{\mu} = 7.7748$ $\hat{\sigma} = 0.7870$ $\varepsilon_\mu = 0.0108$ $\varepsilon_\sigma = 0.0052$	$\hat{\mu} = 7.7881$ $\hat{\sigma} = 1.4181$ $\varepsilon_\mu = 0.0112$ $\varepsilon_\sigma = 0.0079$	$\hat{a} = 4921.8$ $\hat{b} = 0.7442$ $\varepsilon_a = 55.4565$ $\varepsilon_b = 0.0044$	$\hat{\mu} = 0.2401$ $\hat{\omega} = 1.1704 + 008$ $\varepsilon_\mu = 0.0021$ $\varepsilon_\omega = 1.8884 + 006$

List of Figures

1 Log-logistic distribution PDF for $\mu = 0.5$ and $\sigma = 0.5$, $\mu = 0.5$ and $\sigma = 1$, $\mu = 2$ and $\sigma = 0.5$, $\mu = 2$ and $\sigma = 1$ 20

2 Log-normal distribution PDF for $\mu = 0.5$ and $\sigma = 0.5$, $\mu = 0.5$ and $\sigma = 1$, $\mu = 2$ and $\sigma = 0.5$, $\mu = 2$ and $\sigma = 1$ 20

3 Weibull distribution PDF for $a = 2$ and $b = 1$, $a = 4$ and $b = 1$, $a = 2$ and $b = 4$, $a = 4$ and $b = 4$ 21

4 Nakagami distribution PDF for $\mu = 0.5$ and $\omega = 0.5$, $\mu = 0.5$ and $\omega = 4$, $\mu = 2$ and $\omega = 0.5$, $\mu = 2$ and $\omega = 4$ 21

5 A picture of foliage 22

6 Illustration for the experimental radar antennas 22

7 This figure shows the lift with the experiment. The antennas are at the far end of the lift from the viewer under the roof that was built to shield the equipment from the elements. This picture was taken in September with the foliage largely still present. The cables coming from the lift are a ground cable to an earth ground and one of 4 tethers used in windy conditions. 23

8 Clutter data (a)transmitted pulse before antenna amplification (b) an example of received echoes from data set I, and (c) an example of received echoes from data set II 24

9 Expanded view from clutter samples 10,000 to 12,000 (a) from data set I, and (b) from data set II 25

10 Clutter model comparison from data set I (a) log-logistic vs. log-normal, and (b) log-logistic vs. Weibull (c) log-logistic vs. Nakagami. $\texttt{RMSE}_{log-logistic} = 2.5425 \times 10^{-5}$, $\texttt{RMSE}_{log-normal} = 3.2704 \times 10^{-5}$, $\texttt{RMSE}_{Weibull} = 3.7234 \times 10^{-5}$, $\texttt{RMSE}_{Nakagami} = 5.4326 \times 10^{-5}$. 26

11 Clutter model comparison from data set II (a) log-Logistic vs. log-normal, and (b) log-logistic vs. Weibull (c) log-logistic vs. Nakagami. $\texttt{RMSE}_{log-logistic} = 2.739 \times 10^{-5}$, $\texttt{RMSE}_{log-normal} = 3.1866 \times 10^{-5}$, $\texttt{RMSE}_{Weibull} = 3.6361 \times 10^{-5}$, $\texttt{RMSE}_{Nakagami} = 4.4045 \times 10^{-5}$. 27
12 Probability of detection 28
13 Probability of false alarm 28

List of Figures : 2

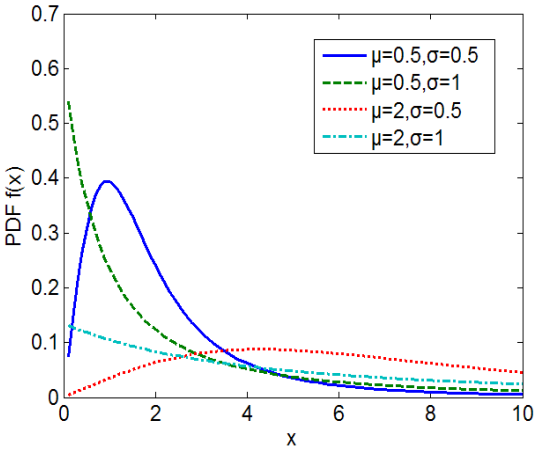


Figure 1: Log-logistic distribution PDF for $\mu = 0.5$ and $\sigma = 0.5$, $\mu = 0.5$ and $\sigma = 1$, $\mu = 2$ and $\sigma = 0.5$, $\mu = 2$ and $\sigma = 1$

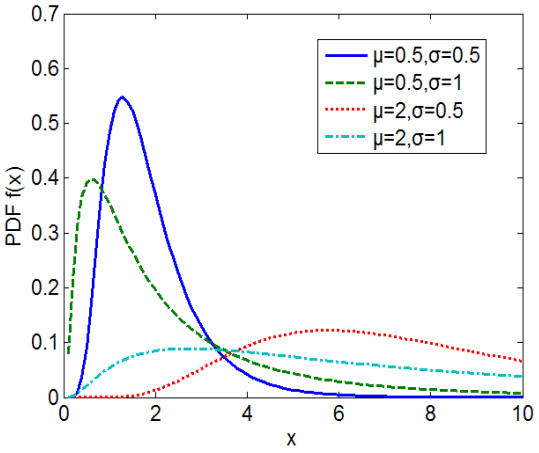


Figure 2: Log-normal distribution PDF for $\mu = 0.5$ and $\sigma = 0.5$, $\mu = 0.5$ and $\sigma = 1$, $\mu = 2$ and $\sigma = 0.5$, $\mu = 2$ and $\sigma = 1$

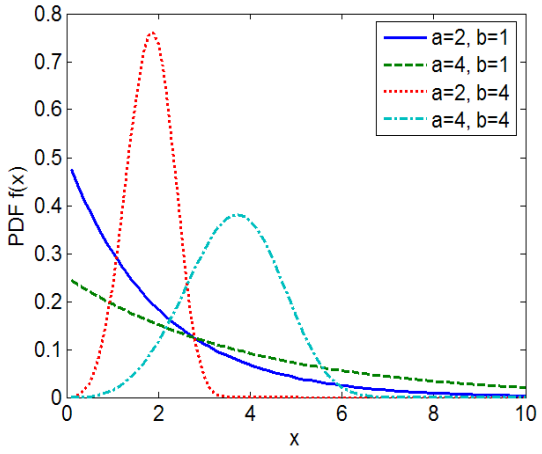


Figure 3: Weibull distribution PDF for $a = 2$ and $b = 1$, $a = 4$ and $b = 1$, $a = 2$ and $b = 4$, $a = 4$ and $b = 4$

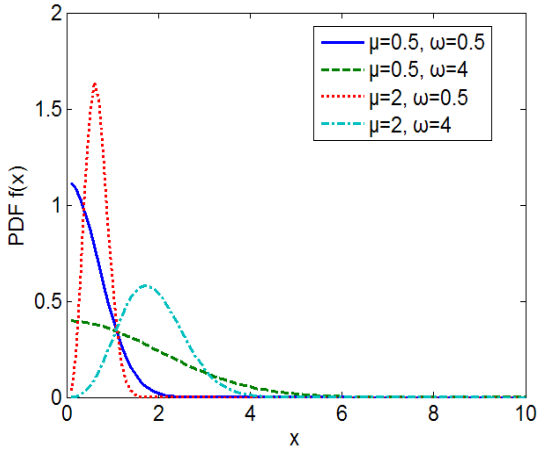


Figure 4: Nakagami distribution PDF for $\mu = 0.5$ and $\omega = 0.5$, $\mu = 0.5$ and $\omega = 4$, $\mu = 2$ and $\omega = 0.5$, $\mu = 2$ and $\omega = 4$



Figure 5: A picture of foliage

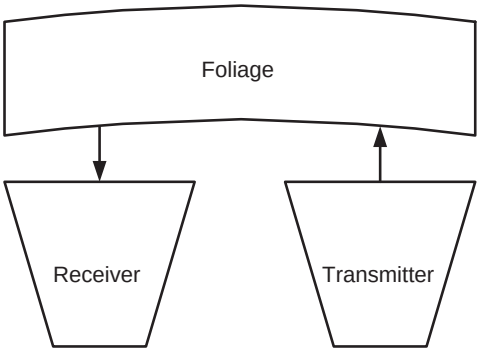
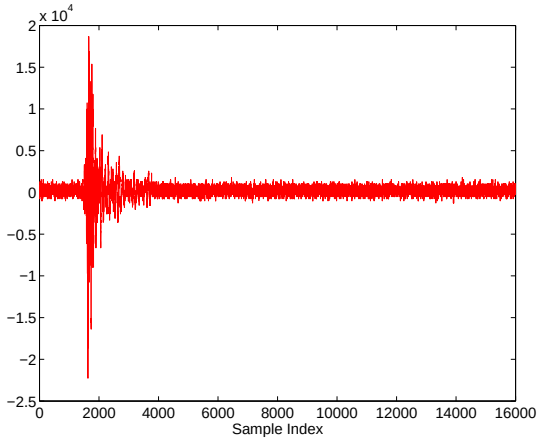


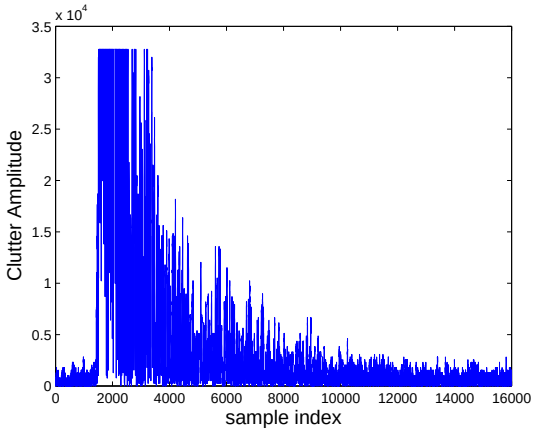
Figure 6: Illustration for the experimental radar antennas



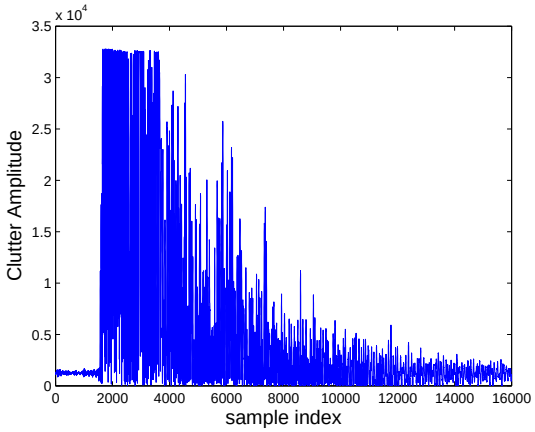
Figure 7: This figure shows the lift with the experiment. The antennas are at the far end of the lift from the viewer under the roof that was built to shield the equipment from the elements. This picture was taken in September with the foliage largely still present. The cables coming from the lift are a ground cable to an earth ground and one of 4 tethers used in windy conditions.



(a)

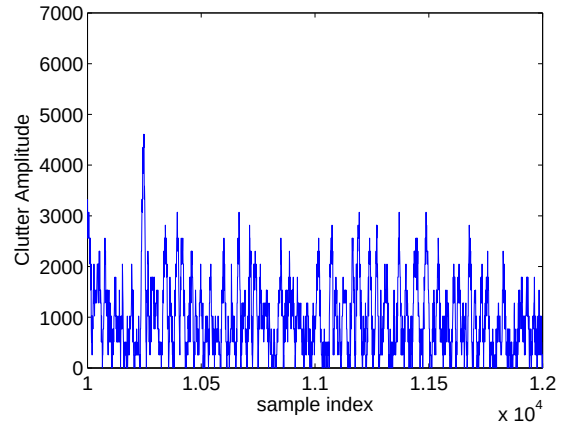


(b)

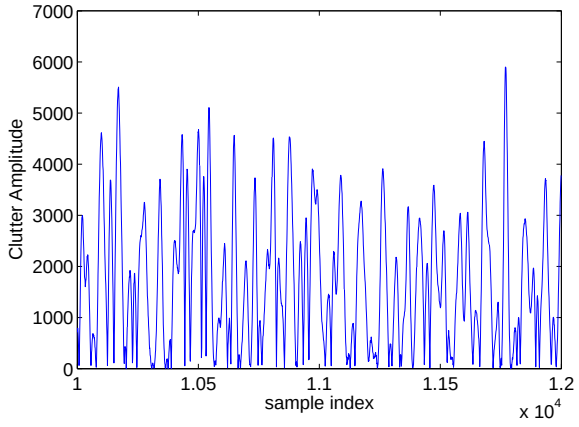


(c)

Figure 8: Clutter data (a)transmitted pulse before antenna amplification (b) an example of received echoes from data set I, and (c) an example of received echoes from data set II

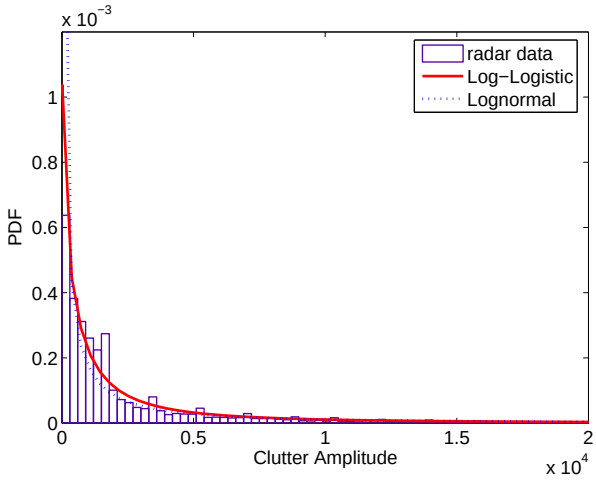


(a)

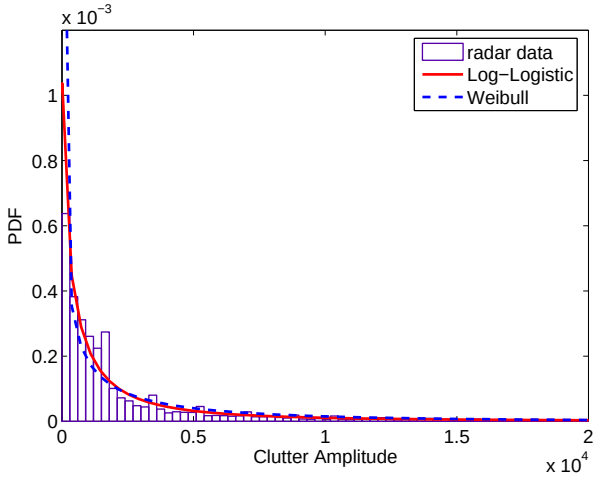


(b)

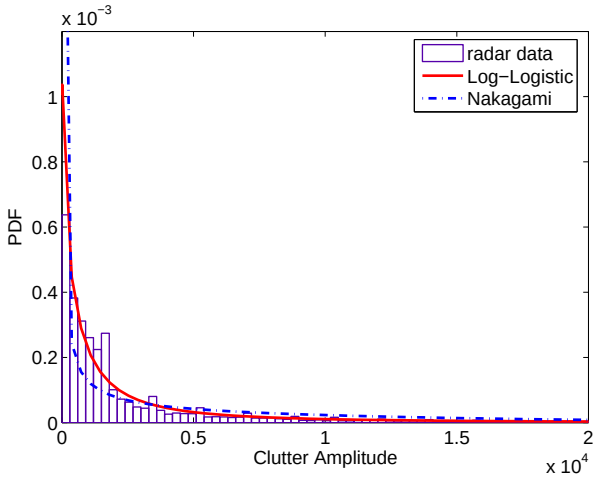
Figure 9: Expanded view from clutter samples 10,000 to 12,000 (a) from data set I, and (b) from data set II



(a)

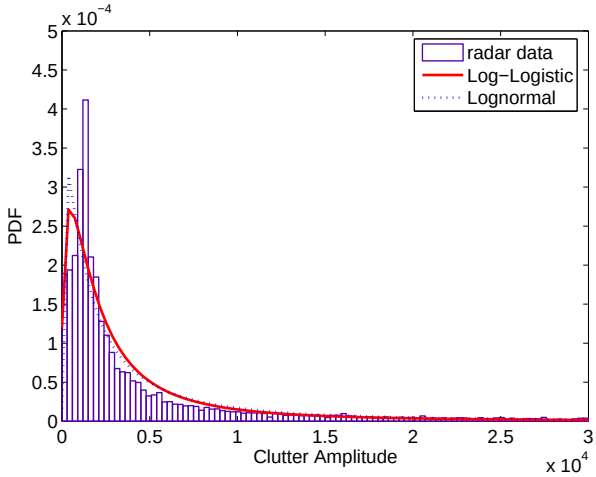


(b)

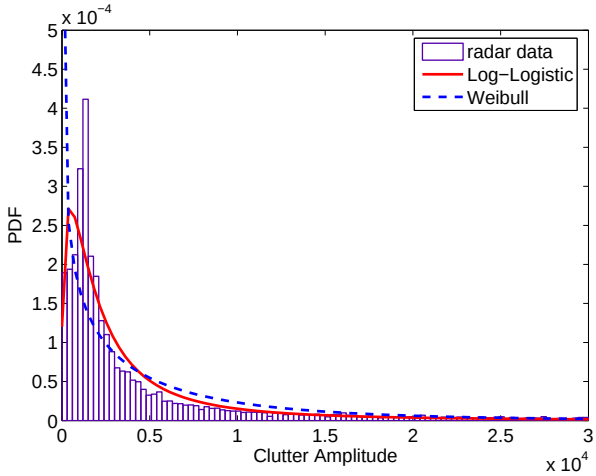


(c)

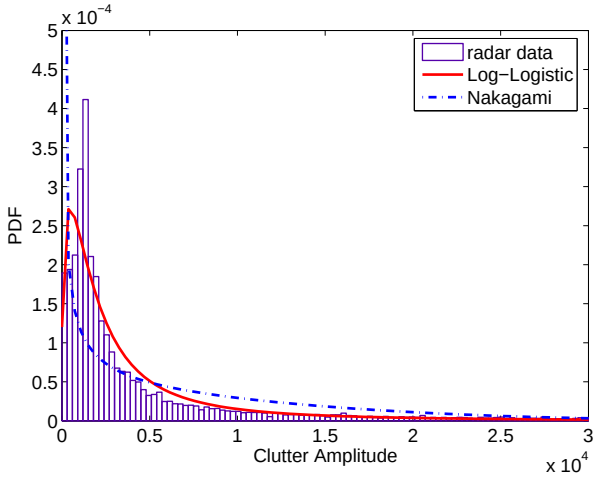
Figure 10: Clutter model comparison from data set I (a) log-logistic vs. log-normal, and (b) log-logistic vs. Weibull (c) log-logistic vs. Nakagami. $\texttt{RMSE}_{log-logistic} = 2.5425 \times 10^{-5}$, $\texttt{RMSE}_{log-normal} = 3.2704 \times 10^{-5}$, $\texttt{RMSE}_{Weibull} = 3.7234 \times 10^{-5}$, $\texttt{RMSE}_{Nakagami} = 5.4326 \times 10^{-5}$.



(a)



(b)



(c)

Figure 11: Clutter model comparison from data set II (a) log-Logistic vs. log-normal, and (b) log-logistic vs. Weibull (c) log-logistic vs. Nakagami. $\texttt{RMSE}_{log-logistic} = 2.739 \times 10^{-5}$, $\texttt{RMSE}_{log-normal} = 3.1866 \times 10^{-5}$, $\texttt{RMSE}_{Weibull} = 3.6361 \times 10^{-5}$, $\texttt{RMSE}_{Nakagami} = 4.4045 \times 10^{-5}$.

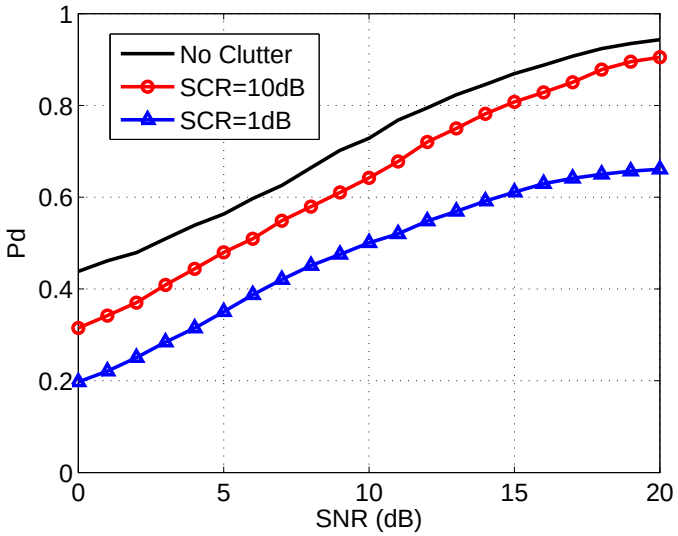


Figure 12: Probability of detection

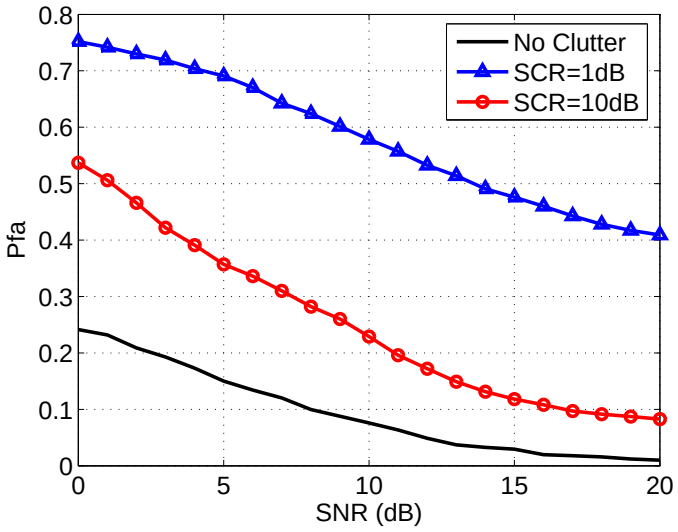


Figure 13: Probability of false alarm

LATENCY-AWARE AND ENERGY EFFICIENCY TRADEOFFS FOR WIRELESS SENSOR NETWORKS

Xinsheng Xia*
Department of Electrical Engineering,
University of Texas at Arlington, USA
E-mail: xia@wcn.uta.edu
*Corresponding author

Qilian Liang
Department of Electrical Engineering,
University of Texas at Arlington, USA
E-mail: liang@uta.edu

Abstract: Latency and energy efficiency are two important parameters to evaluate the Wireless Sensor Networks (WSN). To reduce delays in the WSN, the sensor node will send out redundant packets. Suppose the WSN has a cell-partitioned structure and the two-hop relay algorithm is adopted, the relay/destination nodes selection will determine the networks performance. The FLS is applied to the nodes selection. In contrast with the cases that only consider one descriptor, the FLS application can manage the delay/energy tradeoffs to meet the network performance requirements. Another work discussed is packets transmission in wireless sensor networks. We proposed FLS in the optimization of SIR threshold selection. Average delay and distance of a node to the source node are selected as antecedents for the FLS. The output of FLS provided adjusting factors for the SIR threshold. Simulation results showed the fuzzy optimization could achieve a better network efficiency, reduce the average delay, and extend the network lifetime.

Keywords: Wireless Sensor Networks, Fuzzy Logic System, Energy, Latency

Biographical notes:

Xinsheng Xia is a Senior Network Engineer at Tellabs Inc. He completed his PhD degree from University of Texas at Arlington in 2007. His research interests include cross-layer design, fuzzy logic systems and applications, energy efficiency and QoS provision in wireless Ad Hoc and sensor networks.

Qilian Liang is an Associate Professor at University of Texas at Arlington. He completed his PhD degree from University of Southern California in 2000. His Areas of Expertise include Sensor networks (energy efficiency, cross layer design, optimal sensor deployment, etc), wireless communications, wireless networks, communication system and communication theory, signal processing for communications, fuzzy logic systems and applications, multimedia network traffic modeling and classification, collaborative and distributed signal processing.

1 INTRODUCTION

WSNs are likely to be widely deployed in commercial and military applications. However, several obstacles need to be overcome, such as latency-aware and energy efficiency (Akyildiz et al., 2002; Heinzelman et al., 2002). Latency-aware means to transfer the packets among sensors as quickly as possible. Energy efficiency means to the net-

Copyright © 200x Inderscience Enterprises Ltd.

works should function for as long as possible (Xia and Liang, 2008).

The cell-partitioned model is adopted in this chapter (Fig.1). We can assume that the network is divided into non-overlapping cells, each cell is of equal size (Neely et al., 2002).

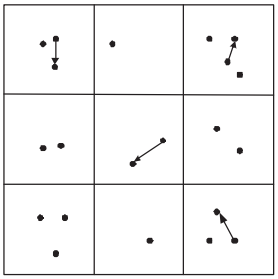


Figure 1: A Cell-partitioning Wireless Sensor Network

The sensor nodes are roaming independently from one cell to another. If two sensor nodes are in the same cell, they can transfer packets with each other, and sensor nodes within different cells cannot communicate with each other. The sensor nodes have a variable mobility speed and the actual mobility can be described by one-step Markov path model (Hou and Tsai, 1998). Each sensor node can generate packets with a Poisson distribution and each sensor node can reserve original and relay packets. Each packet enters its subqueue according to its destination node ID. This model can simplify the scheduling complexity and facilitates analysis. It can also conceal the detail of global network topology from the individual sensor node (Nakano and Olariu, 2000).

In this chapter, we consider the tradeoffs between the delay performance and the energy efficiency offered by the cell partitioned wireless model. The contributions are twofold: First, we classified the sensor service into two priorities: high and low. The higher priority, the better delay performance and more energy consumption. We realized it with the two-hop relay algorithm, and we establish energy/delay tradeoffs curve for the performance of the two-hop relay algorithm. Second, The FLS is used to elect the three relay nodes. When there are several pairs within one cell, we use the FLS to elect the destination node.

Generally, a node with the maximum remaining energy capacity or a node with the nearest distance to the source node or a node with the highest degree of mobility is elected as the relay/destination node.

The remainder of this chapter is structured as following. In Section 2, we introduced the energy, delay, and the two-hop relay algorithm. In Section 3, we applied the FLS into the two-hop relay algorithm. Simulation results and discussions were presented in Section 4. In Section 5, we concluded the chapter.

In this chapter, we designed a FLS for relay/destination nodes election. The rules were designed to be based on the knowledge from a group of network experts.

2 Energy And The 2-Hop Relay Algorithm

2.1 Energy

A sensor node consumes significant power when it either transmits a packet or when it receives a packet. It will also consume energy when the sensor node is idle because the sensor node keeps moving. The energy consumption ratio of Transmit: Receive: Idle is approximately 40:20:1 (Raghavendra et al., 2002).

2.2 The Two-hop Relay Algorithm

This relay algorithm restricts packets to 2-hop paths, and the relay packet is inserted into the subqueue of the relay sensors until a source encounters its destination.

We summarize the two-hop relay algorithm as follows (Grossglauser and Tse, 2002):

1)If there exists source-destination pairs within a cell, there are two options:

- If there exists one source-destination pair within a cell and if the source contains a new packet intended for that destination, transmit.
- If there exists more than one source-destination pair within a cell, choose the sensor with the longest subsequeue as the source and choose the sensor with the energy most as the destination and transmit it.

2)If there is no source-destination pair in a cell, there are two options:

- Send a relay packet to its destination: if the designated transmitter has a packet destined for the designated receiver, send the packets to the receiver.
- Send a new relay packet:
    1. For high priority sensor: if the designated transmitter has a new packet that has never before been transmitted, conserve the packet in its own subqueue according to its destination. Choose the three energy most sensors as the relay destinations and transmit three copies to them.
    2. For low priority sensor: conserve the packet in its own subqueue according to its destination.

This algorithm restricts all routes to 2-hop while the relay packets are only allowed to transmit to their destinations. We pick up the packet reserved in the subqueue with the longest queuing length to keep the queuing length in balance among the sensors in order to reduce the time jitter. We chose the sensors with most energy as the destination to keep the energy in balance among sensors.

2.3 Cell Location Algorithm

Each sensor node knows its location (X position, Y position). As all the cells are of equal size, each sensor node can determine the cell serial number it belongs to.

For example, the network size is $N \times N$ and it is partitioned into $C = S^2$ cells:

$$C_{sn} = [\frac{X \cdot S}{N}] + [\frac{Y \cdot S}{N}] \cdot S + 1 \quad (1)$$

Where [ ] refers to the round function and it will round the value of the float argument to the nearest integer value.

Every sensor node will send a "Hello" message with its cell serial number C_{sn} and other information to other sensor nodes between a constant time interval. When a sensor node with ID number A receives a "Hello" message sent by sensor node B, sensor node A compares its cell serial number C_{sna} with the cell serial number C_{snb} of sensor node B.

- If C_{sna} is equal to C_{snb}, which means sensor node A and sensor node B are in the same cell and if the information of sensor node B is already in the database of sensor node A, update the information of sensor node B.
- If C_{sna} is equal to C_{snb}, which means sensor node A and sensor node B are in the same cell and if the information of sensor node B is not in the database of sensor node A, record the information of sensor node B.
- If C_{sna} is not equal to C_{snb}, which means sensor node A and sensor node B are not in the same cell and if the information of sensor node B is in the database of sensor node A, delete the information of sensor node B.
- If C_{sna} is not euqal to C_{snb}, which means sensor node A and sensor node B are not in the same cell and if the information of sensor node B is not in the database of sensor node A, remain idle.

Notice that a sensor node only keeps the information of the sensor nodes that in the same cell and keeps updating it. The sensor node can reduce the memory usage and keep the latest information.

2.4 In-cell Feedback Algorithm

As there is redundancy in the network, when a packet has been delivered to its destination, its remnant versions of this packet should be ignored by the network. We assume all packets have a sending serials number P_{sn}. P_{sn} combining with the source node ID is unique in the network. When sensor node A receives a packet, it will send out a "notice" message with its sending serials number P_{sn}, source sensor ID B and destination sensor node ID A.

When a sensor node receives the "notice" message, it will search packet in its A subqueue. If there is a packet with sending serials number P_{sn} and source node ID B, remove it from its subqueue. Otherwise, remain idle.

Notice that, no packet will be transmitted to its destination twice. We can reduce the energy consumption and shorten average delay.

3 The FLS application for the two-hop relay algorithm

The effect of transmitting redundant packets will consume more energy, however, it will also increase the chance that the nodes which hold the original or relay packets to reach their destination node. How to elect the relay/destination nodes will determine the energy and latency performance.

We collect the knowledge for node election based on the following three descriptors:

1. distance of a node to the source node,
2. its remaining energy, and
3. its degree of mobility.

The linguistic variables used to represent the distance of a node to the source node were divided into three levels: *near*, *moderate*, and *far*; and those to represent its remaining energy and degree of mobility were divided into three levels: *low*, *moderate*, and *high*. The consequent – the possibility that this node will be elected as a relay/destination nodes – was divided into 5 levels, *Very Strong, Strong, Medium, Weak, Very Weak*.

We designed questions such as:

IF *distance of a node to the source node* is *near*, and *its remaining energy* is *low*, and *its degree of mobility* is *moderate*, THEN the possibility that this node will be elected as a relay/destination nodes is _____.

so we need to set up $3^3 = 27$ (because every antecedent has 3 fuzzy sub-sets, and there are 3 antecedents) rules for this FLS.

We created one survey for the network experts. We used rules obtained from the knowledge of 6 network experts. These experts were requested to choose a consequent using one of the five linguistic variables. Different experts gave different answers to the questions in the survey. Table 1 summarizes the questions used in this survey, and Table 2 captures the results from the completed survey.

We used trapezoidal membership functions (MFs) to represent *near*, *low*, *far*, and *high*, and triangle MFs to represent *moderate*. We show these MFs in Fig.2.

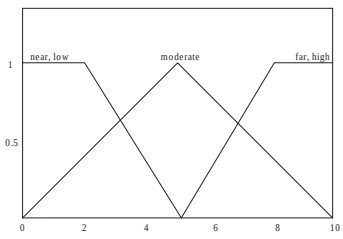


Figure 2: MFs for antecedents

In our approach to form a rule base, we chose a single consequent for each rule. To do this, we averaged the centroids of all the responses for each rule and used this

average in place of the rule consequent centroid. Doing this leads to rules that have the following form:

R^l : IF *distance of a node to the source node* (x_1) is F_l^1, and *its remaining energy* (x_2) is F_l^2, and *its degree of mobility* (x_3) is F_l^3, THEN the possibility that this node will be elected as a relay/destination node (y) is c_{avg}^l.

where $l = 1, \ldots, 27$. c_{avg}^l is defined as

$$c_{avg}^l = \frac{\sum_{i=1}^{5} w_i^l c^i}{\sum_{i=1}^{5} w_i^l} \tag{2}$$

in which w_i^l is the number of people choosing linguistic label i for the consequent of rule l ($i = 1, \cdots, 5; l = 1, \ldots, 27$) (see Table 2); and, c^i is the centroid of the ith consequent set ($i = 1, 2, \cdots, 5$). The centroids of the three fuzzy sets depicted in Fig.3 are $c^1 = 1.0561$, $c^2 = 3$, $c^3 = 5$, $c^4 = 7$, and $c^5 = 8.9439$.

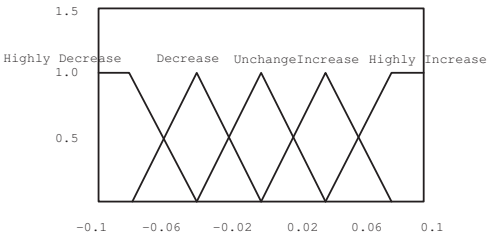


Figure 3: MFs for consequent

To illustrate the use of (2), note, for example, that

$$c_{avg}^{11} = \frac{3c^1 + 2c^2 + c^3}{3 + 2 + 1} = 2.3614 \tag{3}$$

All 27 c_{avg}^l values are listed in Table 2.

For every input (x_1, x_2, x_3), the output is computed using

$$y(x_1, x_2, x_3) = \frac{\sum_{l=1}^{27} \mu_{\mathrm{F}_l^1}(x_1)\mu_{\mathrm{F}_l^2}(x_2)\mu_{\mathrm{F}_l^3}(x_3)c_{avg}^l}{\sum_{l=1}^{27} \mu_{\mathrm{F}_l^1}(x_1)\mu_{\mathrm{F}_l^2}(x_2)\mu_{\mathrm{F}_l^3}(x_3)} \tag{4}$$

4 Simulation

We implemented the simulation model using the OPNET modeler. The simulation region is 180×180 meters, and it is divided into 9 non-overlapping cells. Each cell is of equal size, that is 60×60 meters. In the previous section, we know that the energy consumption ratio is 40:20:1. So we can assume that the sensor node consumes approximately 3×10^{-5} watts when idle, 1.2×10^{-3} watts during transmissions and 6×10^{-4} watts during reception.

There were 80 sensor nodes in the simulation model, and the sensor nodes were roaming independently with the ground speed from 1 m/s to 9 m/s. The mobility model is called one-step Markov path model. The probability of moving in the same direction as the previous move is higher than other directions in this model; That means this model has memory.

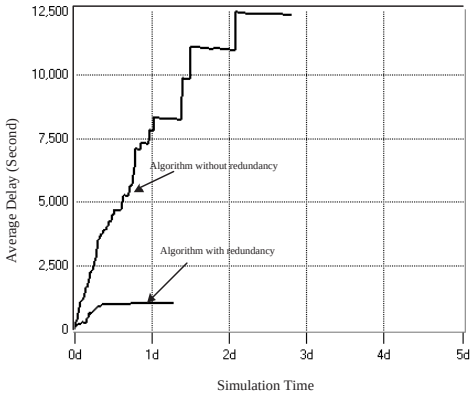


Figure 4: Average latency performance of the two algorithms

4.1 Average Latency

We use the average latency to evaluate the network performance. It is the average transmission delay of the entire received packet, which is in the same priority. Each packet is labeled a timestamp when it was generated by the source sensor node. When its destination sensor node receives it, the time interval is the transmission delay.

$$Average\,Latency = \frac{\sum_{i=1}^{K} D_i}{K} \tag{5}$$

Observe Fig.4 the latency performance of the algorithm with redundancy for high priority packets is much better than that of the algorithm without redundancy for the low priory packets. Not only the average delay of high priority packets is much smaller than that of the low priority packets, but also the time jitter is much better. Time jitter refers to short-term variation or instability in the duration of a specified time interval. We can draw a conclusion: if the service is time-sensitive, such as video or audio service, we can adopt the scheduling algorithm with redundancy to improve their delay performance.

4.2 Energy Efficiency

The algorithm for high priority packets uses the multicast technique to transmit redundant packets to improve the latency performance, however, transmitting redundant packets will consume more energy. The algorithm with redundancy will make its energy efficiency worse than that of the algorithm without redundancy. In the wireless sensor networks, we use two parameters: the number of sensor nodes alive and the remaining energy to describe the energy efficiency.

When the remaining energy of a sensor node is lower than a certain threshold, the sensor is considered as "dead". In this simulation, we choose 1.2×10^{-3} as the threshold. This threshold is the minimum energy to transfer a lK bits packets in a 1K bps bandwidth wireless channel. A sensor is "dead" means it cannot transmit/receive

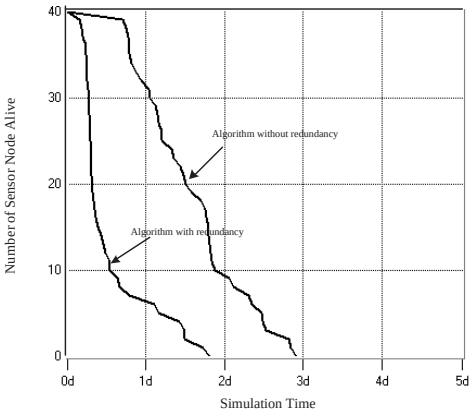


Figure 5: Sensor nodes alive of the two algorithms

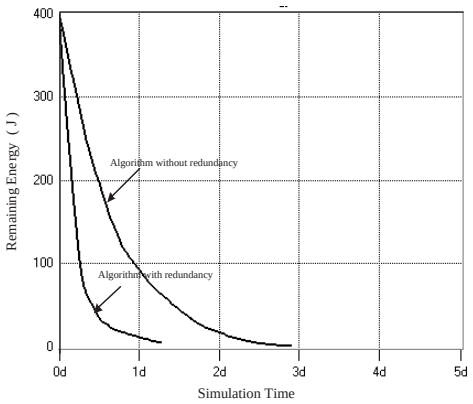


Figure 6: Remaining energy of the two algorithms

packets any longer, so it will be removed from the sensor network. Sensors are used to collect data and transmit the packets. The number of sensors of wireless sensor networks, which is below a certain threshold, means this network does not work. As Fig.5 showed, the remaining sensor nodes alive of the algorithm with redundancy for high priority packets were decreasing much quicker that of the algorithm without redundancy. As descried in the 2-Hop relay algorithm, we chose the sensors with most energy as the destination; we could keep the energy consumption balance among sensors. We could observe from Fig.5 that the curve was dropping sharply. Comparing with the average delay performance, we could find it was a tradeoff between network life and delay performance. The simulation result could be a reference when we design the WSNs.

Fig.6 showed the remaining energy of the two scheduling algorithm. We assumed that the energy of each sensor was 10J and the packet size was 125 bytes (1K bits), and the channel transmission rate is 1K bps. So when the sensor transmitted or received a packet, it would cost 1 second. And we adopt CSMA/CA protocol to solve the packets collision problem. If a sensor node transmitted N_s packets (each packet cost 1 second) and received N_r packets (each packets also cost 1 second) and it was roaming in the network for T_m, we could get the remaining energy E_i of this sensor node:

$$E_i = 10 - (3 \times 10^{-5} \times T_m + 1.2 \times 10^{-3} \times N_s + 6 \times 10^{-4} \times N_r) \quad (6)$$

The remaining energy E_w of the whole networks is described as:

$$E_w = \sum_{i=1}^{40} E_i \quad (7)$$

Fig.6 showed the remaining energy of the algorithm without redundancy is not dropping as sharply as that of the algorithm without redundancy. It illustrated that the algorithm without redundancy cost less energy.

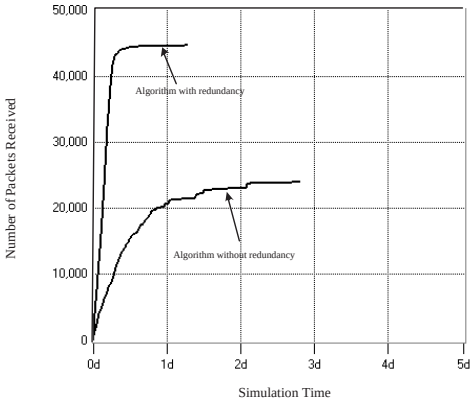
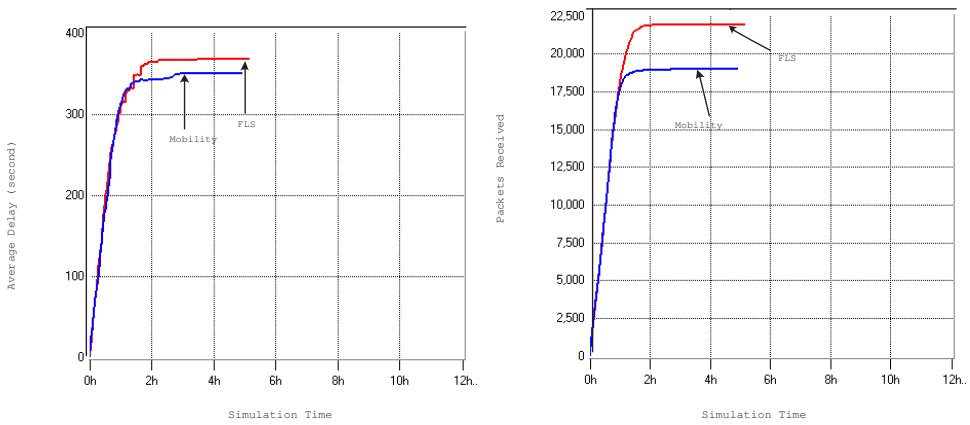


Figure 7: Packets received of the two algorithms

4.3 Network Quality

The role of the wireless sensor network in the real world is to collect data and transmit packets. In our simulation, we assumed the collecting data distribution of the sensor node is Poisson distribution and the arriving interval was 1 second. Observing from Fig.7, although the lifetime of the algorithm with redundancy was shorter than that of the algorithm without redundancy, but it could collect and transmit more packets. One of the main reasons was that the sensors in the networks were keeping moving, that meant it kept consuming energy. For the algorithm without redundancy, the sensor node consumed more energy under idle condition, although the sensor node of the algorithm with redundancy consumed more energy when it transmitted or received packets.

From Fig.4 to Fig.7, we could observe that the simulation time of the algorithm with redundancy was shorter than that of the algorithm without redundancy, which meant the networks lifetime of the algorithm with redundancy was shorter.



(a) (b)

Figure 8: The FLS application vs the degree of mobility. (a) average delay, (b) packets received

4.4 FLS vs Mobility

We obtained the simulation result of FLS application, which considered three antecedents. If we only considered one antecedent: the degree of mobility, the performance of average delay would be better. As plotted in Fig.8(a), the performance of average delay which only considered the degree of mobility was about 6% better than that of FLS application. However, the FLS application could achieve a better performance for packets received, about 18%, as plotted in Fig.8(b).

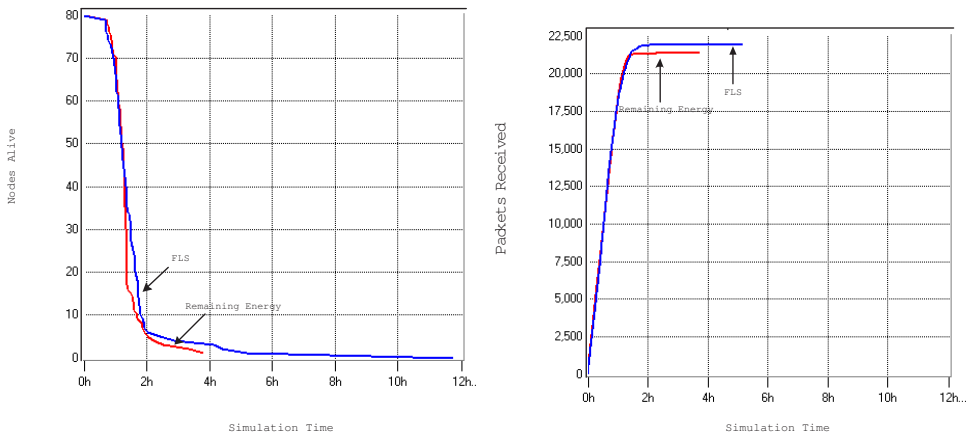
4.5 FLS vs the Remaining Energy

Similarly, we considered only one antecedent: the remaining energy, the performance of first "dead" node would be better. As plotted in Fig.9(a), the life time of the first "dead" node was 3 minutes longer than that of FLS application. However, the FLS application achieved a better performance for the network life, about 8 hours longer. The reason was that we adopted the path loss model in the simulation and the FLS had considered another antecedent: the distance to the source node. The nearer distance, the less energy consumed. At the same time, the FLS application also achieved a better performance for the packets received, about 5%, as plotted in Fig.9(b).

Simulation results showed that the FLS application could manage the delay/energy tradeoffs to meet the networks performance requirement.

5 Conclusion

In order to meet different performance requirement of the service, we classified the services into high priority and low priority. Considering the effect of transmitting redundant packets, the 2-Hop relay algorithm was introduced. The algorithm with redundancy could improve the delay performance, but cost more energy to reduce the system life. In the two-hop relay algorithm, the relay/destination nodes election would determine the network performance. The simulation result showed that the two-Hop relay algorithm with/without redundancy could establish the delay/energy tradeoffs to meet different performance requirement of the services in WSN. We applied FLS to the relay/destination nodes selection. Three descriptors were used: the distance to the source node, the remaining energy and the degree of mobility. We obtained the linguistic knowledge from a group of experts. Based on the linguistic knowledge, we set up 27 rules. The nodes possibility was the output of FLS. We elected the nodes with the highest three possibilities as the relay nodes and we elected the node with the highest possibility as the destination node. Further more, simulation results suggested that if we designed different FLS for the two-hop relay algorithm, we could meet different performance requirement in WSN.



(a) (b)

Figure 9: The FLS application vs the remaining energy. (a) nodes alive, (b) packets received

ACKNOWLEDGMENT

This work was supported by the U.S. Office of Naval Research (ONR) Young Investigator Award under Grant N00014-03-1-0466.

REFERENCES

Akyildiz, I. *et al.* (2002) 'A survey on sensor networks ', *IEEE Coummun. Magazine*, August, pp.102–114.

Heinzelman, W.B., Chandrakasan, A.P. and Balakrishnan, H. (2002) 'An application-specific protocol architecture for wireless microsensor networks', *IIEEE Transactions on Wireless Communications*, October, Vol. 1, No. 4.

Xia, X., and Liang, Q. and Oz, G. (2008) 'A Fuzzy-based Latency-aware and Energy Efficiency Tradeoffs in Wireless Sensor Networks', *Submitted to IEEE International Conference on Communications 2008.*

Neely, M.J. and Modiano, E. (2002) 'Capacity and delay tradeoffs for Ad-Hoc mobile networks', *Procedding of IEEE Transactions on Information theory.*

Hou, T.C. and Tsai, T.J. (1998) 'Adaptive clustering in a hierarchical ad hoc network', *Proc. Int. Computer Symp.,Tainan, Taiwan,R.O.C.*, December, pp.171–176.

Nakano, K. and Olariu S. (2000) 'Randomized initializtion protocols for Ad Hoc networks', *IEEE Transactions on Parallel and distributed systems*, July, Vol. 11, No. 7.

Raghavendra, C.S. and Tse, D. (2002) 'PAMAS-Power aware multi-acess protocol with signalling for Ad-Hoc networks', *Proceeding of the eighth IEEE real-time and embedded technology and applications Symposium.*

Grossglauser, M. and Tse, D. (2002) 'Mobility increases the capacity of Ad-hoc wireless networks', *IEEE/ACM Transactions on Networking*, August, Vol. 10, No. 4, pp.477–486.

Table 1: The questions for Nodes Election for the two-Hop Relay Algorithm

Antecedent 1 is *distance of a node to the source node*, Antecedent 2 is *its remaining energy*, Antecedent 3 is *its degree of mobility*, and Consequent is *the possibility that this node will be elected.* The experts were asked to fill in the blank for the Consequent using one of five linguistic labels (very weak, weak, medium, strong, very strong).

Q #	Ant 1	Ant 2	Ant 3	Cont
1	near	low	high	
2	near	low	moderate	
3	near	low	low	
4	near	moderate	high	
5	near	moderate	moderate	
6	near	moderate	low	
7	near	high	high	
8	near	high	moderate	
9	near	high	low	
10	moderate	low	high	
11	moderate	low	moderate	
12	moderate	low	low	
13	moderate	moderate	high	
14	moderate	moderate	moderate	
15	moderate	moderate	low	
16	moderate	high	high	
17	moderate	high	moderate	
18	moderate	high	low	
19	far	low	high	
20	far	low	moderate	
21	far	low	low	
22	far	moderate	high	
23	far	moderate	moderate	
24	far	moderate	low	
25	far	high	high	
26	far	high	moderate	
27	far	high	low	

Table 2: Histograms of expert responses about Nodes Election for the Two-Hop Relay Algorithm.

6 network experts answered the questions. The entries in the second – sixth columns correspond to the weights w_1^l, w_2^l, w_3^l, w_4^l, and w_5^l, respectively.

R # (l)	VW	W	M	S	VS	c_{avg}^l
1	0	3	3	0	0	4.0
2	1	5	0	0	0	2.676
3	3	1	2	0	0	2.6947
4	0	0	3	3	0	6.0
5	0	0	0	5	1	7.3240
6	0	4	1	1	0	4.0
7	0	0	0	1	5	8.6199
8	0	0	1	5	0	6.6667
9	0	1	4	1	0	5.0
10	0	4	2	0	0	3.6667
11	3	2	1	0	0	2.3614
12	4	1	1	0	0	2.0374
13	0	1	3	2	0	5.3333
14	1	1	4	0	0	4.0093
15	2	3	0	1	0	3.0187
16	0	0	2	3	1	6.6573
17	0	1	2	3	0	5.6667
18	0	3	2	1	0	4.3333
19	2	4	0	0	0	2.3520
20	5	1	0	0	0	1.3801
21	5	1	0	0	0	1.3801
22	1	4	1	0	0	3.0093
23	1	4	1	0	0	3.0093
24	5	0	1	0	0	1.7134
25	0	2	2	2	0	5.0
26	0	0	2	3	1	6.6573
27	0	2	2	1	1	5.3240

Radar Sensor Network Using A Set of New Ternary Codes: Theory and Application

Lei Xu and Qilian Liang, Senior Member, IEEE

Department of Electrical Engineering

University of Texas at Arlington

Arlington, TX 76010-0016 USA

Email: xu@wcn.uta.edu, liang@uta.edu

Abstract

In radar sensor network (RSN), the interferences among radars can be effectively reduced when waveforms are properly designed. In this paper, we perform some theoretical studies on co-existence of phase coded waveforms in RSN, then we give the definition of a new kind of ternary codes–optimized punctured Zero Correlation Zone sequence-Pair Set (ZCZPS) and analyze their properties. Besides, we apply our newly provided ternary codes and equal gain combination technique to RSN and study the detection performance versus different number of radars in RSN under the condition of either Doppler shift or time delay among transmitting sensors. Simulation results show that no matter whether the target is moving in the system, detection performances of RSN using our optimized punctured ZCZPS are superior to those of single radar using the traditional compression codes.

Index Terms : zero correlation zone, optimized punctured ZCZ sequence-pair, radar sensor network, Doppler shift

1 Introduction

Recently, the idea of networking radar sensors has attracted considerable interest. A network of multiple radar sensors can be introduced to overcome performance degradation of single radar along with waveform optimization. In the existing works on radar waveform design, Bell [2] who introduced information theory to radar waveform design, concluded that distributing energy is a good choice to better detect targets. Sowelam and Tewfik [18] applied a sequential experiment design procedure to select signal for radar target classification. In their work, each waveform selected maximizes the Kullback/Leibler information number that measures the dissimilarity between the observed target and the alternative targets in order to minimize the decision time. All the above researches only focused on the waveform design for a single active radar. Nevertheless, in [11], Liang studied constant frequency (CF) pulse waveform design and proposed maximum-likelihood (ML) automatic target recognition (ATR) approach for both nonfluctuating and fluctuating targets in a network of multiple radar sensors. Furthermore, RSN design based on linear frequency modulation (LFM) waveform was studied and LFM waveform design was applied to RSN with application to ATR with delay-Doppler uncertainty by Liang [12] as well. In addition, binary coded pulses using simulated annealing in RSN are highlighted in [4].

In addition to the above radar waveform design work, phase coded waveform design is one of the widely used waveform design methods for pulse compression technique which allows a radar to simultaneously achieve the energy of a long pulse and the resolution of a short pulse without the high peak power which is required by a high energy short duration pulse [2]. Since high range sidelobes could mask returns from targets in radar system, there has been considerable interest in study of reducing range sidelobe of corresponding codes in radar system. In addition to the well-known Barker code, by suffering a small S/N loss, the authors [16] present several binary pulse compression codes to greatly reduce sidelobes. In [17], pulse compression using a digital-

analog hybrid technique is studied to achieve very low range sidelobes for potential application to spaceborne rain radar. Tanner et al.[21] uses time-domain weighting of the transmitted pulse to achieve a range sidelobe level of -55 dB or better in flight tests. Nevertheless, the range sidelobes in the above work could hardly reach as low as zero in the previous work.

In this paper, we theoretically study RSN design based on phase coded waveforms: the conditions of waveforms co-existence. Then we apply our newly proposed ternary code–optimized punctured ZCZ sequence-Pair Set (ZCZPS) as the phase coded waveforms to RSN. The newly proposed codes could reach zero autocorrelation sidelobe and zero mutual cross correlation values during zero correlation zone. We perform studies on the codes' properties, especially the cross correlation property and analyze the performance of optimized punctured ZCZPS in RSN system under the environment of Doppler shift and time delay among transmitting radar sensors. Monte Carlo simulation results show that RSN based on our optimized punctured ZCZ sequence-pairs performs much better than that of single radar, in terms of probability of miss and false alarm detection.

The rest of the paper is organized as follows. In Section 2, we study the co-existence of phase coded waveforms. Section 3 introduces the definition and properties of our newly provided ternary coded waveform–optimized punctured ZCZ sequence-pair set, especially the outstanding autocorrelation and cross correlation property. In Section 4, we study the performance versus different number of radars in RSN either under the condition of Doppler shift or not, by applying our ternary codes and equal gain combination technique to the system simulation. In Section 5, conclusions are drawn on radar sensor network using our optimized punctured ZCZPS.

2 CO-EXISTENCE OF PHASE CODED WAVEFORMS IN RSN

In RSN, it is easy to see that radar sensors are likely to interfere with each other and the performances may degrade if their waveforms are not properly designed.

The phase coded waveform can be defined as

$$x(t) = \sum_{n=0}^{M-1} x^{(n)}(t - nt_b) \tag{1}$$

Here, $0 < t \leq t_b$. M is the period of the modulation signal, each bit of duration t_b and $T = Mt_b$.

The bits are phase modulated by the phase sequence $\beta^{(n)}$ of length M:

$$x^{(n)}(t) = \begin{cases} exp(j2\pi\beta^{(n)}t) & 0 \leq t \leq t_b \\ 0 & \text{elsewhere} \end{cases} \tag{2}$$

For $t > T$ or $t < 0$, within the duration of the signal, the periodicity implies that the complex envelope of the transmitted signal $x(t)$ obeys

$$x(t) = x(t + iT), \quad i = 0, \pm 1, \pm 2, ... \tag{3}$$

We assume there are N radars networking together in a self-organizing fashion in our RSN. The radar i transmits a waveform as

$$x_i(t) = \sum_{n=0}^{M-1} x_i^{(n)}(t - nt_b) = \sum_{n=0}^{M-1} exp(j2\pi\beta_i^{(n)}(t - nt_b)) \tag{4}$$

Here, $0 < t \leq t_b$.

The cross correlation between $x_i(t)$ and $x_j(t)$ could be expressed as:

$$R(\tau) = R(mt_b) = \frac{1}{T}\int_{-T/2}^{T/2} x_i(t)x_j^*(t-\tau)dt \tag{5}$$

$$= \sum_{n=0}^{N-1} \int_{-T/2+nt_b}^{-T/2+(n+1)t_b} exp[j2\pi\beta_i^{(n+1)}(t - (n+1)t_b)]exp^*[j2\pi\beta_j^{(M-m+n+1)}(t - (M-m+n+1)t_b)]dt$$

$$= \frac{1}{M}\sum_{n=0}^{M-1} exp[j2\pi[\beta_j^{(M-m+n+1)}(Mt_b - mt_b + \frac{T}{2} + \frac{t_b}{2}) + \beta_i^{(n+1)}(-\frac{T}{2} - \frac{t_b}{2})]]$$

$$sinc[t_b(\beta_i^{(n+1)} - \beta_j^{(M-m+n+1)})]$$

In order to reduce the interference of different waveforms, we would like to achieve that when $i \neq j$, $R(\tau)$ should be as small as possible. According to equation (5), if $\pi t_b(\beta_i^{(n+1)} - \beta_j^{(M-m+n+1)}) = k\pi, k = 1, 2, 3...$, then $R(\tau) = 0$. This result is used later in the paper. Observing the equation (5), when $i = j$ and $m = 0$, then $sinc[t_b(\beta_i^{(n+1)} - \beta_j^{(M-m+n+1)})] = 1$ and $R(\tau)$ could be normalized as 1. It is obvious that this is desirable in a radar sensor network.

It is known that orthogonal waveforms could provide optimized correlation property as

$$\frac{1}{T}\int_{-T/2}^{T/2} x_i(t)x_j^*(t-\tau)dt = \begin{cases} 1 & i = j \text{ and } m = 0 \\ 0 & i \neq j \text{ or } m \neq 0 \end{cases} \tag{6}$$

As a result, orthogonal waveforms, which could minimize or remove the interference from one waveform to the other, can work well simultaneously in Radar Sensor Network.

Nevertheless, there are time delay and Doppler shift ambiguity that will introduce interference to waveforms in RSN. Ambiguity function (AF) [15] generally identified with Woodward [23][24] is usually used to succinctly characterize the behavior of a waveform paired with its matched filter. So it is an analytical tool for waveform design especially there are time delay and Doppler shift ambiguity.

PAF (Periodic Ambiguity Function) is introduced by Levanon [3] as an extension of the periodic autocorrelation for Doppler shift. And the single-periodic complex envelope would be:

$$A(\tau, F_D) \equiv |\frac{1}{T}\int_{-T/2}^{T/2} x(t+\frac{\tau}{2})e^{j2\pi F_D t}x^*(t-\frac{\tau}{2})dt| \equiv |\hat{A}(\tau, F_D)| \tag{7}$$

Where τ is the time delay, T is one period of the signal and F_D is the Doppler shift.

Accordingly, the single-periodic ambiguity function of phase coded waveform here can be

$$
\begin{aligned}
& A(\tau, F_D) \qquad (8)\\
= \; & |\frac{1}{T}\int_{-\frac{T}{2}}^{\frac{T}{2}} x(t)exp(j2\pi F_D t)x^*(t-\tau)dt| \\
= \; & |\frac{1}{T}\sum_{n=0}^{M-1}\int_{-\frac{T}{2}+nt_b}^{-\frac{T}{2}+(n+1)t_b} exp[j2\pi\beta^{(n+1)}(t-(n+1)t_b)]exp^*[j2\pi\beta^{(M-m+n+1)}(t-(M-m+n+1))] \\
& exp(j2\pi F_D t)dt| \\
= \; & |\frac{1}{M}\sum_{n=0}^{M-1} exp[j2\pi[\beta^{(M-m+n+1)}[(M-m)t_b+\frac{t_b}{2}+\frac{T}{2}]+\beta^{(n+1)}(-\frac{t_b}{2}-\frac{T}{2})+F_D(-\frac{T}{2}+(n+1)t_b)] \\
& sinc[t_b(\beta^{(n)}-\beta^{(n-m)}+F_D)]|
\end{aligned}
$$

When it is satisfied that

$$\pi t_b(\beta^{(n)}-\beta^{(n-m)}+F_D)=k\pi, \quad k=1,2,3... \qquad (9)$$

The amplitude of ambiguity function turns to be zero. Stating differently, based on the result that when $\pi t_b(\beta_i^{(n+1)}-\beta_j^{(M-m+n+1)})=k\pi, k=1,2,3...$, then $R(\tau)=0$, it is achieved that $A(\tau,F_D)=0$, when $F_D=\frac{k}{t_b}, k=0,1,2...$

The ambiguity function of MIMO radar systems have been analyzed in [19]. We extend the ideas of single-periodic ambiguity to RSN in this paper. In the RSN, all the radar sensors are transmitting signals, the radar i not only receives its own back-scattered waveform, but also scattered signals generated by other radars which caused interference to radar i. Assuming it is well synchronized that there are no time delay among the transmitting radars $t_1=t_2=...=t_N=0$, we study the interferences from all the other $N-1$ radars ($j\neq i$). Also assuming time delay $\tau=mt_b$ for

receiving radar i, the ambiguity function of radar i with phase coded waveform can be

$$
\begin{aligned}
& A_i(\tau, F_{D_1}, ..., F_{D_N}) \qquad (10)\\
= \; & |\sum_{j=1}^{N} \frac{1}{T} \int_{-\frac{T}{2}}^{\frac{T}{2}} x_j(t) exp(j2\pi F_{D_i} t) x_i^*(t-\tau) dt| \\
= \; & |\frac{1}{M} \sum_{j=1}^{N} \sum_{n=0}^{M-1} exp[j2\pi[\beta_i^{(M-m+n+1)}[(M-m+\frac{1}{2})t_b + \frac{T}{2}] + \beta_j^{(n+1)}(-\frac{t_b}{2}+\frac{T}{2}) + F_{D_j}[-\frac{T}{2}+(n+1)t_b]]] \\
& sinc[t_b(\beta_j^{(n+1)} - \beta_i^{(M-m+n+1)} + F_{D_j})]|
\end{aligned}
$$

Here, $0 < i \leq N$. (10) consists of two parts: useful signal(reflected signal from the transmitting radar i waveform), $j = i$ part in the (10); and interferences from other $N-1$ radar waveforms, $j \neq i$ parts in (10).

3 Optimized Punctured ZCZ Sequence-Pair Set

Zero correlation zone (ZCZ) is a new concept provided by Fan [5][6] [7] [8] in which both auto-correlation and cross correlation sidelobes are zero while the time delay is kept within the Zero Correlation Zone instead of the whole period of time domain.

Matsufuji and Torii have provided some methods of constructing ZCZ sequences in [14] [22]. In this section, we apply optimized punctured sequence-pair [9] to zero correlation zone to construct a new kind of ternary codes–optimized punctured ZCZ sequence-pair set, and prove that the newly provided ternary code which has good autocorrelation and cross correlation properties in ZCZ can be good candidates for phase coded waveforms in RSN.

3.1 The Definition of Optimized Punctured ZCZ Sequence-Pair Set

We introduce some useful definitions first.

Definition 3-1 Assume $(x_i^{(n)}, y_i^{(n)})$ is a sequence-pair set that consists of K sequence-pairs of length N, where $n = 1, 2, 3, ..., M-1, i = 0, 1, 2, ..., K-1$, if all the sequences in the set satisfy the

following equation:

$$R_{x_i y_j}(\tau) = \sum_{n=0}^{M-1} x_i^{(n)} y_j^{*(n+m) \mod M} = \begin{cases} \lambda M, & \text{for } \tau = 0 \text{ and } i = j \\ 0, & \text{for } \tau = 0 \text{ and } i \neq j \\ 0, & \text{for } 0 < |\tau| \leq Z_0 t_b \end{cases} \tag{11}$$

where t_b is the duration of each bit, $\tau = mt_b$ and $0 < \lambda \leq 1$, then $(x_i^{(n)}, y_i^{(n)})$ is called ZCZ sequence-pair set. $0 < |\tau| \leq Z_0 t_b$ is the Zero Correlation Zone during which the autocorrelation and cross correlation values could be kept zero. $ZCZPS(M, K, Z_0)$ is an abbreviation.

Definition 3-2 [9] Sequence $\mathbf{u} = (u^{(0)}, u^{(1)}, ..., u^{(M-1)})$ is the punctured sequence for $\mathbf{v} = (v^{(0)}, v^{(1)}, ..., v^{(M-1)})$,

$$u^{(n)} = \begin{cases} 0, & \text{if } n \in p \text{ punctured bits} \\ v^{(n)}, & \text{if } n \in \text{Non-punctured bits} \end{cases} \tag{12}$$

Where p is the number of punctured bits in sequence $\mathbf{v}$, suppose $v^{(n)} \epsilon (-1, 1)$ and $u^{(n)} \epsilon (-1, 0, 1)$, $\mathbf{u}$ is p-punctured binary sequence, $(\mathbf{u}, \mathbf{v})$ is called a punctured binary sequence-pair.

Definition 3-3 [9] The autocorrelation of punctured sequence-pair $(\mathbf{u}, \mathbf{v})$ is defined

$$R_{uv}(\tau) = R_{uv}(mt_b) = \sum_{n=0}^{M-1} u^{(n)} v^{*(n+m) \mod M}, 0 \leq \tau \leq M-1 \tag{13}$$

If the punctured sequence-pair has the following autocorrelation property:

$$R_{uv}(\tau) = \begin{cases} E, & \text{if } \tau \equiv 0 \text{mod} M \\ 0, & \text{others} \end{cases} \tag{14}$$

the punctured sequence-pair is called optimized punctured sequence-pair [9]. Where,

$E = \sum_{n=0}^{M-1} u^{(n)} v^{*(n+m) \mod M} = M - p$, is the energy of the punctured sequence-pair.

The properties, Fourier transform characteristics, existing necessary conditions and some construction methods with help of already known sequences of punctured sequence-pairs have been

studied by Jiang [9]. An amount of optimized punctured sequence-pairs have been found of length from 3 to 31 so far.

Definition 3-4 If $(x_i^{(n)}, y_i^{(n)})$ in Definition 3-1 is constructed by optimized punctured sequence-pair and a certain matrix, such as Hadamard matrix or an orthogonal matrix, where

$$x_i^{(n)} \in (-1, 1), \quad i = 0, 1, 2, ..., M-1$$

$$y_i^{(n)} \in (-1, 0, 1), \quad i = 0, 1, 2, ..., M-1$$

$$R_{x_i y_j}(\tau) = \sum_{n=0}^{M-1} x_i^{(n)} y_j^{*(n+m)} \mod M = \begin{cases} \lambda M, & \text{for } \tau = 0 \text{ and } i = j \\ 0, & \text{for } \tau = 0 \text{ and } i \neq j \\ 0, & \text{for } 0 < |\tau| \leq Z_0 t_b \end{cases} \tag{15}$$

where $\tau = mt_b$ and $0 < \lambda \leq 1$, then $(x_i^{(n)}, y_i^{(n)})$ can be called optimized punctured ZCZ sequence-pair set, and we use $OPZCZPS(M, K, Z_0)$ as its abbreviation.

3.2 Design for Optimized Punctured ZCZ Sequence-pair Set

Based on odd length optimized punctured binary sequence pairs and a Hadamard matrix, we provide a method to construct an optimized punctured ZCZ sequence-pair set.

Step 1: Considering an odd length optimized punctured binary sequence-pair $(\mathbf{u}, \mathbf{v})$, the length of each sequence is M_1

$$\mathbf{u} = u^{(0)}, u^{(1)}, ..., u^{(M_1-1)}, u^{(n)} \in (-1, 1),$$

$$\mathbf{v} = v^{(0)}, v^{(1)}, ..., v^{(M_1-1)}, v^{(n)} \in (-1, 0, 1),$$

$$n = 0, 1, 2, ..., M_1 - 1, M_1$$

Step 2: Considering a Hadamard matrix $\mathbf{B}$ of order M_2, the length of each sequence in $\mathbf{B}$ equals to the number of the sequences as M_2. Here, any Hadamard matrix order is possible and $\mathbf{b}_i$

is the row vector.

$$\mathbf{B} = [\mathbf{b}_0; \mathbf{b}_1; ...; \mathbf{b}_{M_2-1})],$$

$$\mathbf{b}_i = (b_i^{(0)}, b_i^{(1)}, ..., b_i^{(M_2-1)}),$$

$$R_{\mathbf{b}_i\mathbf{b}_j} = \begin{cases} M_2, & \text{if } i = j \\ 0, & \text{if } i \neq j \end{cases}$$

Step 3: Doing bit-multiplication on the optimized punctured binary sequence-pair and each row of Hadamard matrix $\mathbf{B}$, then sequence-pair set $(\mathbf{X}, \mathbf{Y})$ is obtained,

$$\mathbf{b}_i = (b_i^{(0)}, b_i^{(1)}, ..., b_i^{(M_2-1)}), i = 0, 1, ..., M_2 - 1,$$

$$x_i^{(n)} = u^{(n \mod M_1)} b_i^{(n \mod M_2)}, 0 \leq i \leq M_2 - 1, 0 \leq n \leq M - 1,$$

$$\mathbf{X} = (\mathbf{x}_0; \mathbf{x}_1; ...; \mathbf{x}_{M_2-1}),$$

$$y_i^{(n)} = v^{(n \mod M_1)} b_i^{(n \mod M_2)}, 0 \leq i \leq M_2 - 1, 0 \leq n \leq M - 1,$$

$$\mathbf{Y} = (\mathbf{y}_0; \mathbf{y}_1; ...; \mathbf{y}_{M_2-1})$$

Since the optimized punctured binary sequence-pairs used here are of odd lengths and the length of Walsh sequence in Hadamard matrix is $2^k, k = 1, 2, ...$, it is easy to see that $GCD(M_1, M_2) = 1$ (greatest common divisor of M_1 and M_2 is 1) and $M = M_1 * M_2$.

To sum up, the sequence-pair set $(\mathbf{X}, \mathbf{Y})$ is optimized punctured ZCZPS and $M_1 - 1$ is the Zero Correlation Zone coefficient Z_0. The length of each sequence in optimized punctured ZCZ sequence-pair set is $M = M_1 * M_2$ that depends on the product of length of optimized punctured sequence-pair and the length of Walsh sequence each row in Hadamard matrix. The number of sequence-pairs in optimized punctured ZCZ sequence-pair set rests on the order of the Hadamard matrix. The sequence $\mathbf{x}_i$ in sequence set $\mathbf{X}$ and the corresponding sequence $\mathbf{y}_i$ in sequence set Y construct an optimized punctured ZCZ sequence-pair $(\mathbf{x}_i, \mathbf{y}_i)$ that can be used as a pulse compression code. The

correlation property of the sequence-pairs in optimized punctured ZCZ sequence-pair set is:

$$R_{x_iy_j}(\tau) = R_{uv}((m \mod M_1)t_b)R_{b_ib_j}((m \mod M_2)t_b) = \begin{cases} EN_2, & \text{if } m = 0 \text{ and } i = j \\ 0, & \text{if } 0 < |m| \leq M_1 - 1 \text{ and } i = j \\ 0, & \text{if } i \neq j \end{cases} \quad (16)$$

where $\tau = mt_b$ is the time delay and t_b is one bit duration.

Proof:

1) When $i = j$,

$m = 0$,

$R_{uv}(0) = E, R_{b_ib_j}(0) = M_2, R_{x_iy_j}(0) = R_{uv}(0)R_{b_ib_j}(0) = EM_2$;

$0 < |m| \leq M_1 - 1$,

$R_{uv}(mt_b) = 0, R_{x_iy_j}(mt_b) = R_{uv}((m \mod M_1)t_b)R_{b_ib_j}((m \mod M_2)t_b) = 0$;

2) When $i \neq j$,

$m = 0$,

$R_{b_ib_j}(0) = 0, R_{x_iy_j}(0) = R_{x_jy_i}(0) = R_{uv}((m \mod M_1)t_b)R_{b_ib_j}((m \mod M_2)t_b) = 0$;

$0 < |m| \leq M_1 - 1$,

$R_{uv}(mt_b) = 0, R_{x_iy_j}(mt_b) = R_{uv}((m \mod M_1)t_b)R_{b_ib_j}((m \mod M_2)t_b) = 0$.

According to **Definition 3-1** and **Definition 3-4**, it is obvious that the sequence-pair set constructed by the above method is an optimized punctured ZCZ sequence-pair set.

3.3 Properties of Optimized Punctured ZCZ Sequence-pair set

Constructed by the above method, the autocorrelation and cross correlation properties of OPZCZPS can be simulated and analyzed. For example, the 124-bit long optimized punctured ZCZPS $(\mathbf{X}, \mathbf{Y})$

is constructed by 31-bit long optimized punctured binary sequence-pair $(\mathbf{u}, \mathbf{v}), \mathbf{u} = [+++{+}{-}{-}{-}{+}$
$-{+}{-}{+}{+}{+}{-}{-}{-}{-}{+}{-}{-}{+}{-}{-}{+}{+}{+}{-}{+}{+}{-}], \mathbf{v} = [+++{+}000{+}0{+}0{+}{+}{+}0000{+}00{+}00{+}{+}{+}0{+}{+}0]$
(using $'+'$ and $'-'$ symbols for $'1'$ and $'-1'$) and Hadamard matrix $\mathbf{H}$ of order 4. The number of sequence-pairs here is 4, and the length of each sequence is $31 * 4 = 124$. The first row of each matrix $\mathbf{X} = [\mathbf{x}_1; \mathbf{x}_2; \mathbf{x}_3; \mathbf{x}_4]$ and $\mathbf{Y} = [\mathbf{y}_1; \mathbf{y}_2; \mathbf{y}_3; \mathbf{y}_4]$ constitute a certain optimized punctured ZCZP $(\mathbf{x}_1, \mathbf{y}_1)$. Similarly, the second row of each matrix $\mathbf{X}$ and $\mathbf{Y}$ constitute another optimized punctured ZCZ sequence-pair $(\mathbf{x}_2, \mathbf{y}_2)$ and so on.

$$
\begin{aligned}
\mathbf{x}_1 &= [+++{+}{-}{-}{-}{+}{-}{+}{-}{+}{+}{+}{-}{-}{-}{-}{+}{-}{-}{+}{-}{-}{+}{+}{+}{-}{+}{+}{-}{+}{+}{+}{+}{-}{-}{-}{+} \\
&\quad -{+}{-}{+}{+}{+}{-}{-}{-}{-}{+}{-}{-}{+}{-}{-}{+}{+}{+}{-}{+}{+}{-}{+}{+}{+}{+}{-}{-}{-}{+}{-}{+}{-}{+}{+}{+}{-}{-}{-} \\
&\quad -{+}{-}{-}{+}{-}{-}{+}{+}{+}{-}{+}{+}{-}{+}{+}{+}{+}{-}{-}{-}{+}{-}{+}{-}{+}{+}{+}{-}{-}{-}{+}{-}{+}{-}{+}{+}{-}{+} \\
&\quad -{+}{+}{+}{+}{-}{+}{+}{+}{-}{+}], \\
\mathbf{y}_1 &= [+++{+}000{+}0{+}0{+}{+}{+}0000{+}00{+}00{+}{+}{+}0{+}{+}0{+}{+}{+}{+}000{+}0{+}0{+}{+}{+}000 \\
&\quad 0{+}00{+}00{+}{+}{+}0{+}{+}0{+}{+}{+}{+}000{+}0{+}0{+}{+}{+}0000{+}00{+}00{+}{+}{+}0{+}{+}0{+}{+}{+} \\
&\quad {+}000{+}0{+}0{+}{+}{+}0000{+}00{+}00{+}{+}{+}0{+}{+}0], \\
\mathbf{x}_2 &= [+{-}{+}{-}{-}{+}{-}{-}{-}{-}{-}{-}{-}{+}{-}{-}{+}{-}{+}{+}{+}{-}{-}{-}{+}{+}{-}{+}{+}{+}{-}{-}{-}{+}{-}{+}{+}{-}{+} \\
&\quad {+}{+}{+}{-}{+}{+}{-}{+}{-}{-}{-}{+}{+}{+}{-}{-}{+}{-}{-}{-}{+}{+}{+}{-}{+}{-}{-}{+}{-}{-}{-}{-}{-}{-}{-}{+}{-}{-}{+}{-} \\
&\quad {+}{+}{+}{-}{-}{-}{+}{+}{-}{+}{+}{+}{-}{-}{-}{+}{-}{+}{+}{-}{+}{+}{+}{+}{+}{+}{+}{-}{+}{+}{-}{+}{-}{-}{-}{+}{+}{+}{-}{-} \\
&\quad {+}{-}{-}{-}{+}{+}], \\
\mathbf{y}_2 &= [+{-}{+}{-}000{-}0{-}0{-}{+}{-}0000{+}00{-}00{+}{-}{+}0{+}{-}0{-}{+}{-}{+}000{+}0{+}0{+}{-}{+}00 \\
&\quad 00{-}00{+}00{-}{+}{-}0{-}{+}0{+}{-}{+}{-}000{-}0{-}0{-}{+}{-}0000{+}00{-}{+}00{+}{-}{+}{+}0{+}{-}{+} \\
&\quad 0{-}{+}{+}{-}{+}{+}000{+}0{+}0{+}{-}{+}0000{-}00{+}00{-}{+}{-}0{-}{+}0].
\end{aligned}
$$

Optimized punctured ZCZ sequence-pairs $(\mathbf{x}_1, \mathbf{y}_1)$ and $(\mathbf{x}_2, \mathbf{y}_2)$ are simulated and studied in the following parts.

3.3.1 Autocorrelation and Cross Correlation Properties

The autocorrelation property and cross correlation property of 124-bit long optimized punctured ZCZ sequence-pair set $(\mathbf{X}, \mathbf{Y})$ are shown in Figs. 1 and 2.

From the Figs. 1 and 2, the autocorrelation function (ACF) sidelobe of optimized punctured ZCZPS and the cross correlation function (CCF) can be kept as low as 0 when the time delay is kept within $Z_0 = N_1 - 1 = 30$ (Zero Correlation Zone).

It is known that a traditional criterion for evaluating code of length M is the signal peak to sidelobe ratio (PSR) of their aperiodic ACF, which can be bounded by [20]

$$[PSR]_{dB} \leq 20logM = [PSR_{max}]_{dB} \tag{17}$$

The only uniform aperiodic phase codes that can reach the PSR_{max} are the Barker codes whose length is equal or less than 13. Considering the periodic sequences, the m-sequences or Legendre sequences could achieve the lowest periodic ACF of $|R_i(\tau \neq 0) = 1|$. For non-binary sequences, it is possible to find perfect sequences of ideal ACF. Golomb codes are a kind of two-valued (biphase) perfect codes which obtain zero periodic ACF but result in large mismatch power loss. The Ipatov code shows a way of designing code pairs with perfect periodic autocorrelation (the cross correlation of the code pair) and minimal mismatch loss. In addition, zero periodic autocorrelation function for all nonzero shifts could be obtained by polyphase codes, such as Frank and Zadoff codes. However, for both binary and non-binary sequences, it is not possible for the sequences to have perfect ACF and CCF simultaneously although ideal CCFs could be achieved alone. According to Figs. 1 and 2, both of ACF and CCF sidelobe of the new code could reach as low as 0. Stating differently, the signal peak to sidelobes can be as large as infinite. In addition, the reference sequence of our

proposed codes is made of -1,0,1 which is much less complicated than some other perfect ternary codes such as Ipatvo code. The reference code for Ipatov code is of a three-element alphabet which might not always be integer.

Nevertheless, there might be the concern that multiple peaks of the autocorrelation function would lead to ambiguity in ranging. Since we are studying the single target system in this research, well controlled the PRF (pulse repetition frequency), the only concern is that multiple peaks of single transmitting signal reflected from one target may affect determining the main peak of ACF. As a matter of fact, the matched filter here could shift at the period of ZCZ length to track each peak instead of shifting bit by bit after the first peak is acquired. Hence, in this way could it be working more efficiently. Alike the tracking technology in synchronization of CDMA system, checking several peaks instead of only one peak guarantee the precision of P_D and avoidance of P_{FA}. In addition, those obtained peaks could be averaged before the detection in order to reduce the effect of random noise in the channel so that the detection performance could be improved.

3.3.2 Ambiguity Function

When the transmitted impulse is reflected by a moving target, the reflected echo signal includes a linear phase shift which corresponds to a Doppler shift F_D [15]. As a result of the Doppler shift F_D, the main peak of the autocorrelation function is reduced and so as to the SNR degradation shown as following:

$$[d]_{dB} = 10log\frac{\int_{-T/2}^{T/2} x(t)x^*(t)dt}{\int_{-T/2}^{T/2} x(t)e^{j2\pi F_D t}x^*(t)dt} \tag{18}$$

The sidelobe structure is also changed because of the Doppler shift.

Considering the sequence-pair $(\mathbf{x}, \mathbf{y})$ and the periodic correlation property of the sequence-pair,

we use the single-periodic ambiguity function [3] and rewrite it as

$$A(\tau, F_D) = |\frac{1}{T}\int_{-T/2}^{T/2} x(t)exp(j2\pi F_D t)y^*(t-\tau)dt| \tag{19}$$

Equation (19) can be used to analyze the autocorrelation performance within Doppler shift, and is plotted in Fig. 3 in a three-dimensional surface plot to analyze the time-Doppler performance of the OPZCZPS. Here, maximal time delay is 1 unit (normalized to length of the code, in units of Mt_b) and maximal Doppler shift is 3 units for ACF (normalized to the inverse of the length of the code, in units of $1/(Mt_b)$). From Fig. 3, it is easy to see that there is relative uniform plateau suggesting low and uninform sidelobes, minimizing target masking effect in zero correlation zone of time domain, where $Z_0 = 30$, $-31 < \tau < 31, \tau \neq 0$.

3.4 Co-existence of Optimized Punctured ZCZ Sequence-Pairs

Considering interference from another radar j, if there are time delay between two transmitting radars and Doppler shift, the ambiguity function of radar i can be expressed as

$$A_i(\tau, F_{D_i}, F_{D_j}) = |\frac{1}{T}\int_{-T/2}^{T/2} (x_i(t)exp(j2\pi F_{D_i} t) + x_j(t)exp(j2\pi F_{D_j} t))y_i^*(t-\tau)dt| \tag{20}$$

Where τ is the time delay for ith receiving radar, F_{D_i} and F_{D_j} are the Doppler shift for signals transmitting from ith and jth radar antennas respectively.

Fig. 4 is three-dimensional surface plot to analyze the ambiguity function of radar i (considering interference from radar j). Generally speaking, Fig. 4 closely resembles Fig. 3. There is relative uniform plateau suggesting low and uninform sidelobes, minimizing target masking effect in zero correlation zone of time domain, where $Z_0 = 30$, $-31 < \tau < 31, \tau \neq 0$. It is obvious that even considering the interference from another radar j, the radar i may work as well as there is no interference.

The output of matched filter of radar i (considering interference from radar j) is illustrated in

Fig. 5 under the condition of no Doppler shift. Figs. 1 and 5 are similar. There are regular high peaks on multiples of period 31 that is the length of the optimized punctured sequence-pair used in the constructing method. And the sidelobe can be as low as 0 when the time delay is kept among zero correlation zone $-31 < \tau < 31, \tau \neq 0$. The high peak on zero time delay point can be used to detect targets.

Assuming that precise synchronization could be obtained between the reflected signal and the matched filter on the receiving side, the output of matched filter of radar i (considering interference from radar j) with no time delay, is illustrated in Fig. 6. Here, the Doppler shift is kept among 5 units (normalized to the inverse of the length of the code, in units of $1/Mt_b$). Fig. 6 shows that while the Doppler shift is less than 1 unit (normalized to length of the code, in units of Mt_b), the amplitude decreases sharply. The amplitude has a downward trend on the whole frequency domain. For some traditional phase coded waveforms, such as the Barker code, when Doppler frequencies equal to multiples of the pulse repetition frequency ($PRF = 1/PRI = 1/t_b$) the ambiguity value turns to be zero. Because of these zeros, such multiples of the pulse repetition frequency will render the radar blind [1] to their velocities. However, in Fig. 6, ambiguity values are zero only when Doppler frequencies are equal to odd multiples of the PRF. Therefore, using the optimized punctured ZCZ sequence-pair in the RSN system could, to some extent, improves the blind speed problem in moving target detection system.

4 System Simulation in Radar Sensor Network

In RSN of N radars, the combined signal for ith receiving radar is

$$r_i(u,t) = \sum_{j=1}^{N} x_j(t - t_j) exp(j2\pi F_{D_j} t) + n(u,t) \tag{21}$$

Where F_{D_j} and t_j are Doppler shift and time delay of reflected signal of jth transmitting radar respectively. $x_j(t)$ is radar transmitting waveform and $n(u,t)$ is additive white Gaussian noise (AWGN).

According to the structure illustrated in Fig. 7, the combined received signal $r_i(u,t)$ is processed by its corresponding matched filter $y_i(t)$ and the output of branch i is $Z_i(u)$. Each $Z_i(u)$ can be equal gain combined to construct the final output $Z(u)$.

The output of branch i is

$$|Z_i(u)| = |\int_{-T/2}^{T/2}[\sum_{j=1}^{N} x_j(t-t_j)exp(j2\pi F_{D_j}t) + n(u,t)]y_i^*(t-t_i)dt| \tag{22}$$

Where t_i is the time delay of matched filter $y_i(t)$ on ith receiving radar. $n(u) = \int_{-T/2}^{T/2} n(u,t)y_i^*(t-t_i)dt$ can be easily proved to be an AWGN.

We investigate the three special cases for $|Z_i(u)|$:

1) If all the radar sensors transmit the signals synchronously and the target is not moving, stating differently, there is no time delay for each radar sensor nor Doppler shift, $t_1 = t_2 = ... = t_N = 0$ and $F_{D_1} = F_{D_2} = ... = F_{D_N} = 0$, then

$$|Z_i(u)| = |\int_{-T/2}^{T/2}[\sum_{j=1}^{N} x_j(t) + n(u,t)]y_i^*(t)dt| = |E + 0 + n(u)| \tag{23}$$

2) Considering Doppler shift but no time delay for each transmitting signal, $t_1 = t_2 = ... = t_N = 0$, then

$$|Z_i(u)| = |\int_{-T/2}^{T/2}[\sum_{j=1}^{N} x_j(t)exp(j2\pi F_{D_j}) + n(u,t)]y_i^*(t)dt| \tag{24}$$

In our work, we assume the Doppler shift could be estimated in the receiving radar sensor, so the Doppler shift compensation factor $exp^*(j2\pi F_D)$ is introduced and F_D is the estimated Doppler

shift on the receiving radar here. The equation can be modified as:

$$\begin{aligned} |Z_i(u)| &= |\int_{-T/2}^{T/2}[\sum_{j=1}^{N} x_j(t)exp(j2\pi F_{D_j}) + n(u,t)]y_i^*(t)exp^*(j2\pi F_{D_i}t)dt| \\ &\leq |E| + |\int_{-T/2}^{T/2}[\sum_{j=1}^{N} x_j(t)exp(j2\pi(F_{D_j} - F_{D_i}))y_i^*(t)| + |\int_{-T/2}^{T/2} n(u,t)y_i^*(t)exp^*(j2\pi F_{D_i}t)dt| \end{aligned} \quad (25)$$

According to the the third part of the equation (25), the magnitude of noise is reduced because of the Doppler shift compensation factor.

Since we are studying the single moving target system and assuming that the Doppler shift could be precisely estimated on the receiving antenna, it is reasonable to have $F_{D_1} = F_{D_2} = ... = F_{D_j} = F_D$, the equation (24) can be further simplified as

$$|Z_i(u)| \leq |E| + 0 + |\int_{-T/2}^{T/2} n(u,t)y_i^*(t)exp^*(j2\pi F_{D_i}t)dt| \quad (26)$$

3) Considering both time delay and Doppler shift in the RSN, the Doppler shift compensation factor is also introduced in the receiving sensor,

$$\begin{aligned} & |Z_i(u)| \quad (27) \\ = & |\int_{-T/2}^{T/2}[\sum_{j=1}^{N} x_j(t-t_j)exp(j2\pi F_{D_j}t) + n(u,t)]y_i^*(t-t_i)exp^*(j2\pi F_{D_i}t)dt| \\ \leq & |\int_{-T/2}^{T/2}[\sum_{j=1}^{N} x_j(t-t_j)exp(j2\pi(F_{D_j} - F_{D_i}))]y_i^*(t-t_i)| + |\int_{-T/2}^{T/2} n(u,t)y_i^*(t-t_i)exp^*(j2\pi F_{D_i}t)dt| \end{aligned}$$

Similarly, we assume that $F_{D_1} = F_{D_2} = ... = F_D$,

$$|Z_i(u)| \leq |E| + |\int_{-T/2}^{T/2}[\sum_{j\neq i}^{N} x_j(t-t_j)]y_i^*(t-t_i)dt| + |\int_{-T/2}^{T/2} n(u,t)y_i^*(t-t_i)exp^*(j2\pi F_{D_i}t)dt| \quad (28)$$

Because of the good periodic ACF and CCF of our codes, we modify the frame of receiving data before the matched filter to improve the RSN performance. The frame of received data is illustrated in Fig. 8. The data from bit $M+1$ to bit $max(t_j)+M$ are added to data from bit 1 to bit M bit by bit. It is easy to obtain that $|\int_{-T/2}^{T/2}[\sum_{j\neq i}^{N} x_j(t-t_j)]y_i^*(t-t_i)dt| = 0$.

Therefore, equation (28) is

$$|Z_i(u)| \leq |E| + 0 + |\int_{-T/2}^{T/2} n(u,t) y_i^*(t) exp^*(j2\pi F_{D_i} t) dt| \tag{29}$$

Based on (26) and (29), it is obvious that using frame modification before the matched filter, the performance of case 2) and 3) can be theoretically comparable. In other words, using our provided codes and frame modification, the RSN under the condition of time delay for each transmitting radar can, to some extent, work as well as the RSN where all the radar sensors transmit signal synchronously.

We apply optimized punctured ZCZPS as a bank of phase coded waveforms together with equal gain combination technique to RSN. We simulate and study the performance versus different number of radars in RSN under the condition of either Doppler shift or not. According to [15], P_D(Probability of Detection), P_{FA}(Probability of False Alarm) and P_M(Probability of Miss) are three probabilities of most interest in the radar system. Note that $P_M = 1 - P_D$, thus, P_D and P_{FA} suffice to specify all of the probabilities of interest in radar system. Hence, we respectively simulated the above two probabilities of different number of radars using different number of optimized punctured ZCZ sequence-pairs in single radar system, 4-radar system and 8-radar system. We also compare its performance with single radar system using the Barker code respectively in this section. Three special cases of performances have been simulated. They are detection performance under the condition of transmitting signals synchronously and immovable target, under the condition of transmitting signals synchronously and moving target and under the condition of transmitting signals non-synchronously and moving target. 10^6 times of Monte-Carlo simulation has been run for each SNR value. When multiple radars are working in RSN to detect a single moving target, we assume that the Doppler shift are supposed to be precisely estimated in the receiving radar sensor and the compensating factors are introduced in the receiving radars.

The probability of miss detection of the envelope detector in single radar, 4-radar, 8-radar and

the single radar system using Barker code under the above three conditions are compared in Figs. 9(a), 9(b) and 9(c) respectively. According to the Fig. 9(a), to achieve the same $P_M = 10^{-3}$, single radar system using Barker code requires about $2dB$ more SNR than that of 4-radars under the environment of transmitting signals synchronously and moving target. Fig. 9(b) also illustrates that when $P_M = 10^{-3}$, SNR of 8-radars are $2.2dB$ smaller than that of single radar system using Barker code when the target is moving in the system. If we consider time delay among transmitting radars, the system should at lease consist of two radars. Hence, we only simulate P_M of 4-radar and 8-radar system in Fig. 9(c). From Fig. 9(c), SNR of 8-radar RSN can gain $1.7dB$ smaller than 4-radar SNR to achieve the same $P_M = 10^{-3}$.

The probability of false alarm of envelope detector of different number of radars under the three conditions are shown in Figs. 10(a), 10(b) and 10(c) respectively. Fig. 10(a) shows that the SNR of single radar system using Barker code requires about $5dB$ greater than that of 8-radars to obtain the same $P_{FA} = 10^{-2}$ under the condition of transmitting signals synchronously and immovable target. When the target is moving in the system, it is illustrated in Fig. 10(b) that the SNR of 8-radars can be nearly $3.8dB$ smaller than that of single radar system using Barker code in order to achieve the same $P_{FA} = 10^{-2}$. From Fig. 10(c), 4-radar system requires $1.7dB$ more than that of 8-radar RSN under the condition of transmitting signals non-synchronously and one single moving target.

It is clear to see that, no matter how many radars have been exploited in the RSN, the performances of system without Doppler shift are worse than that under Doppler shift condition. It is of the reason that Doppler shift is precisely estimated and well compensated on the receiving radar in the system. According to the equation (26),the Doppler shift compensating factor $exp(j2\pi F_D t)$ in receiving radar also, to some extent, reduces the magnitude of Gaussian noise of the channel. The above figures also clearly illustrate that no matter whether considering a moving target or

an immovable one, performance of detection of multiradars (applying our optimized punctured ZCZPS and equal gain combination) are superior to that of single radar. In addition, because of the superior cross correlation property of our codes and the modified frame, the performances of 4-radar and 8-radar RSN under the condition of transmitting signals non-synchronously can be comparable to those under the condition of transmitting synchronously.

Therefore, according to the above results, applying our optimized punctured ZCZPS in RSN, the detection performances are much better than those of applying traditional phase coded waveforms in a single radar system.

5 Conclusions

We have studied phase coded waveform design and spatial diversity under the condition of one single moving target in radar sensor networks (RSN). We provided a new kind of ternary codes– optimized punctured ZCZPS which could be used as phase coded waveforms in RSN. The significant advantage of the optimized punctured ZCZPS is the considerably reduced sidelobe as low as zero and zero mutual cross correlation value in the zero correlation zone. Because of the orthogonal property of any two optimized punctured ZCZ sequence-pairs among one optimized punctured ZCZPS, they can co-exist in RSN and achieve better detection performance than that of a single radar. Consequently, the general conclusion can be drawn from the results presented in this paper that the optimized punctured ZCZPS can effectively satisfy higher demands criterion for detection accuracy of RSN in the modern military and security affairs. Since we are investigating the single target radar system in this research, we will study the application of our codes in multiple-target system especially the range resolution in the future work.

Acknowledgement

This work was supported by the Office of Naval Research (ONR) Grant N00014-07-1-0395, N00014-07-1-1024, and N00014-03-1-0466.

References

[1] S. Ariyavisitakul, N. Sollenberger, and L. Greenstein, *Introduction to Radar System,* Tata McGraw-Hill, 2001.

[2] M. R. Bell, "Information theory and radar waveform design," *IEEE Trans on Information Theory,* vol. 39, no. 5, pp. 1578-1597, Sept. 1993.

[3] L. W. Couch, "Effects of modulation nonlinearity on the range response of FM radars," *IEEE Trans on Aerospace and Electronic systems,* vol. 9, no. 4, pp. 598-606, Jul. 1973.

[4] H. Deng, "Synthesis of binary sequences with good correlation and cross-correlation properties by simulated annealing," *IEEE Trans on Aerospace and Electronic systems,* vol. 32, no. 1, Jan 1996.

[5] P. Z. Fan and M. Darnell, *Sequence design for communications applications,* Research Studies Press, John Wiley & Sons Ltd, London, 1996.

[6] P. Z. Fan, N. Suehiro, N. Kuroyanagi and X. M. Deng, "A class of binary sequences with zero correlation zone," *IEE Electron.Letter*, 35 (10): 777-779, 1999.

[7] P. Z. Fan and L. Hao, "Generalized Orthogonal Sequences and Their Applications in Synchronous CDMA Systems," *IEICE Trans.Fundamentals*, E832A(11): 1 16, 2000.

[8] P. Z. Fan, "New Direction in Spreading Sequence Design and the Related Theoretical Bounds," *International Conference of Communications , Circuits and Systems*, Jun. 29-Jul. 1, 2002, PRC.

[9] T. Jiang, *Research on Quasi-Perfect Binary Signal Pair and Perfect Punctured Binary Signal Pair Theory,* Ph.D Dissertation: Yanshan University, 2003.

[10] H. Levanon and A. Freedman, "Periodic ambiguity function of CW signals with perfect periodic autocorrelation," *IEEE Trans on Aerospace and Electronic systems,* vol. 28, no. 2, pp. 387-395, Apr. 1992.

[11] Q. Liang, "Waveform Design and Diversity in Radar Sensor Networks: Theoretical Analysis and Application to Automatic Target Recognition," *IEEE Sensor and Ad Hoc Communications and Networks Conference,* vol. 2, no. 28, pp. 684-689, Sep. 2006.

[12] Q. Liang, "Radar Sensor Networks for Automatic Target Recognition with Delay-Doppler Uncertainty," *IEEE Military Communications Conference,* 23-25, pp. 1-7, Oct. 2006.

[13] J. Liang and Q. Liang, "Orthogonal Waveform Design and Performance Analysis in Radar Sensor Networks," *IEEE Military Communications Conference,* 23-25, pp. 1-6, Oct. 2006.

[14] S. Matsufuji, N Suehiro , N Kuroyanagi and P Z Fan, "Two types of polyphase sequence set for approximately synchronized CDMA systems," *IEICE Trans. Fundamentals*, E862A(1): 229-234, Jan. 2003.

[15] M. A. Richards, *Fundamentals of Radar Signal Processing,* McGraw-Hill, 2005.

[16] R. Sato and M. Shinrhu, "Simple mismatched filter for binary pulse compression code with small PSL and small S/N loss [radar]", *IEEE Transactions on Aerospace and Electronic Systems,* AES-39(2), pp. 711-718, April 2003.

[17] K. Sato, H. Horie, H. Hanado and H. Kumagai, "A digital-analog hybrid technique for low range sidelobe pulse compression", *IEEE Transactions on Aerospace and Electronic Systems,* AES-39(7), pp. 1612-1615, July 2001.

[18] S. Sowelam and A. Tewfik, "Waveform selection in radar target classification," *IEEE Trans on Information Theory,* vol. 46, no. 3, pp. 1014-1029, 2000.

[19] G. San Antonio, D. R. Fuhrmann and F. C. Robey, "MIMO radar ambiguity functions," *IEEE Select. Signal Process,* vol. 1, no. 1, pp. 167-177, Jun. 2007.

[20] M. I. Skolnik, *Radar Handbook,* New York: McGraw-Hill, 1970.

[21] A. Tanner, S. L. Durden, R. Denning, E. Im, F. K. Li, W. Ricketts and W. Wilson, "Pulse compression with very low sidelobes in an airborne rain mapping radar", *IEEE Transactions on Aerospace and Electronic Systems,* AES-32(1), pp. 211-213, Jan. 2004.

[22] H. Torii, M. Nakamura and N. Suehiro, "A new class of zero correlation zone sequences," *IEEE Tran. Inform.Theory*, 50: 559-565, Mar. 2004.

[23] P. Woodward, *Probability and Information Theory, with applications to Radar.* New York: Pergamon, 1957.

[24] P. Woodward, Radar ambiguity analysis Tech. Rep. RRE Technical Note No. 731, Feb. 1967

List of Figures

1 Periodic autocorrelation property of optimized punctured ZCZPS 2

2 Periodic cross correlation property of optimized punctured ZCZPS 2

3 Amplitude of ACFs of several transmitting signals 3

4 Ambiguity function of 124-length ZCZPS: autocorrelation 3

5 Ambiguity function of radar i (considering interference from radar j) 4

6 Output of matched filter of radar i (considering interference from radar j) with no Doppler shift 4

7 Output of matched filter of radar i (considering interference from radar j) with no time delay 5

8 Waveform diversity combining in RSN 5

9 Received Signal Frame 6

10 Probability of miss detection in RSN under the condition of: (a)No time delay nor Doppler shift (b)No time delay but Doppler shift (c)Time delay and Doppler shift . 7

11 Probability of false alarm in RSN under the condition of: (a)No time delay nor Doppler shift (b)No time delay but Doppler shift (c)Time delay and Doppler shift . 8

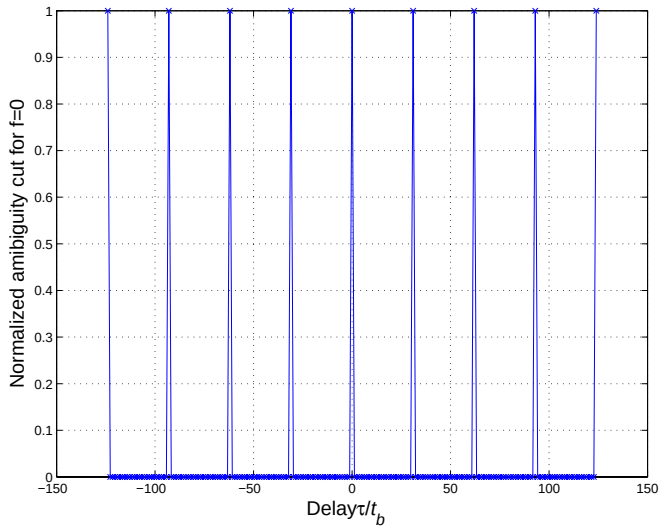


Figure 1: Periodic autocorrelation property of optimized punctured ZCZPS

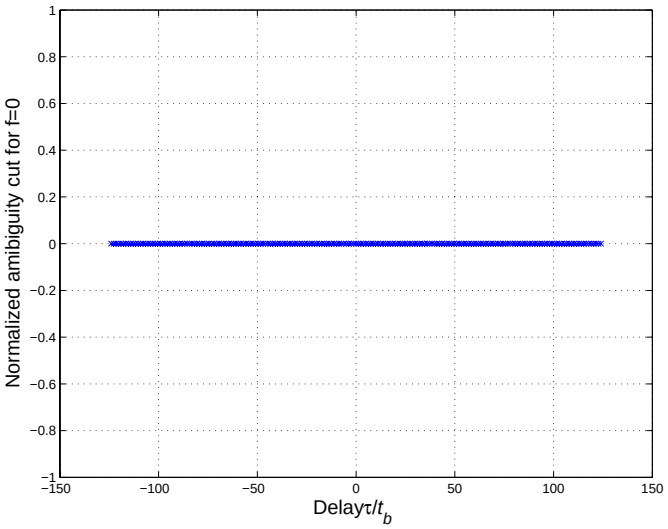


Figure 2: Periodic cross correlation property of optimized punctured ZCZPS

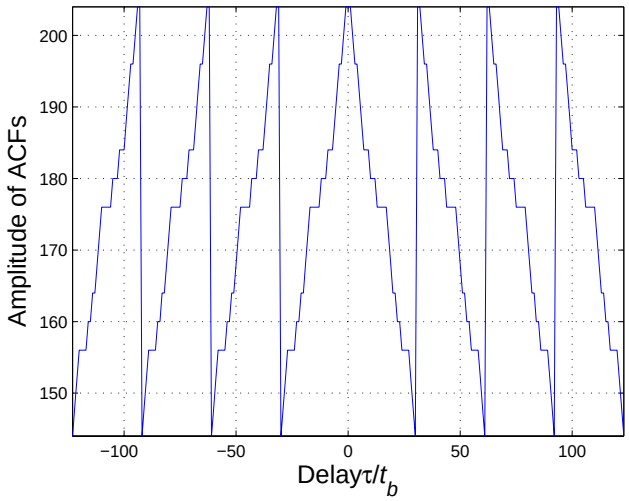


Figure 3: Amplitude of ACFs of several transmitting signals

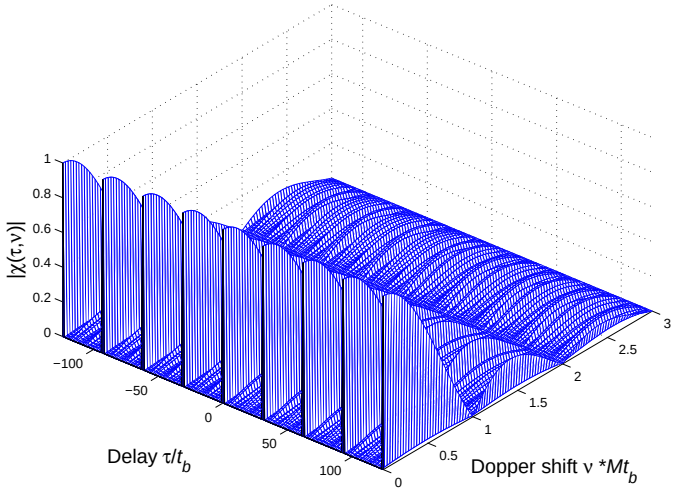


Figure 4: Ambiguity function of 124-length ZCZPS: autocorrelation

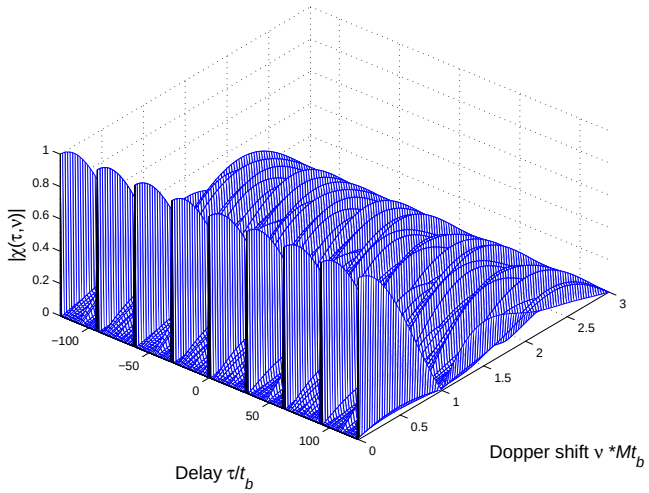


Figure 5: Ambiguity function of radar i (considering interference from radar j)

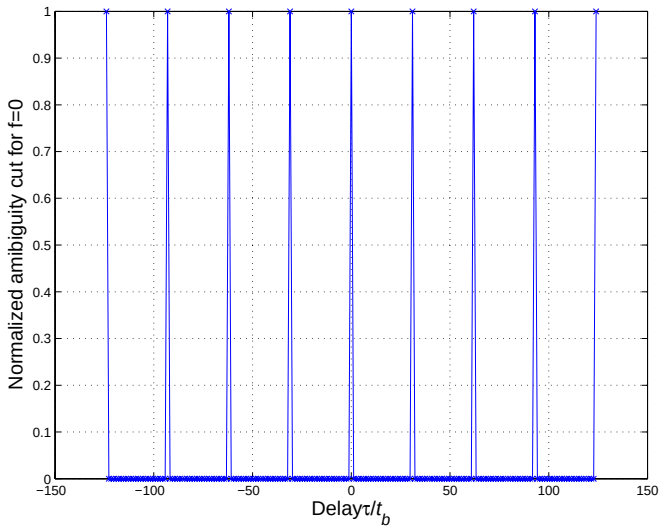


Figure 6: Output of matched filter of radar i (considering interference from radar j) with no Doppler shift

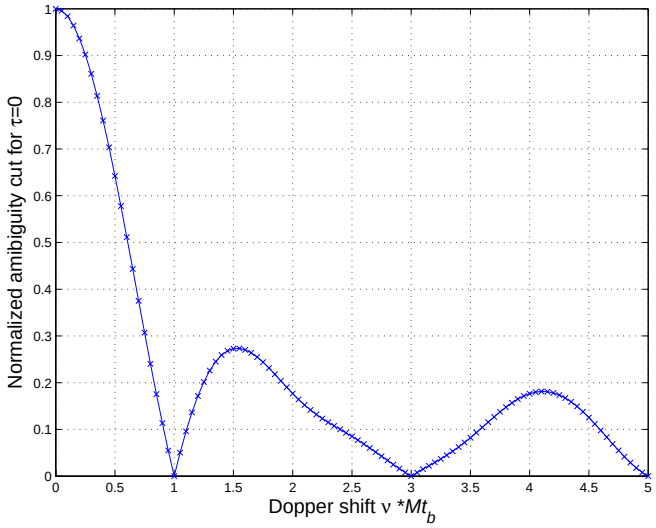


Figure 7: Output of matched filter of radar i (considering interference from radar j) with no time delay

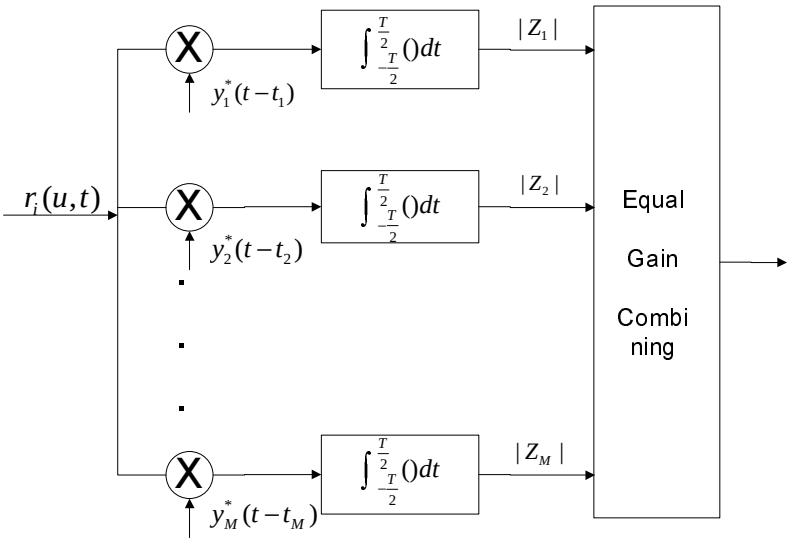
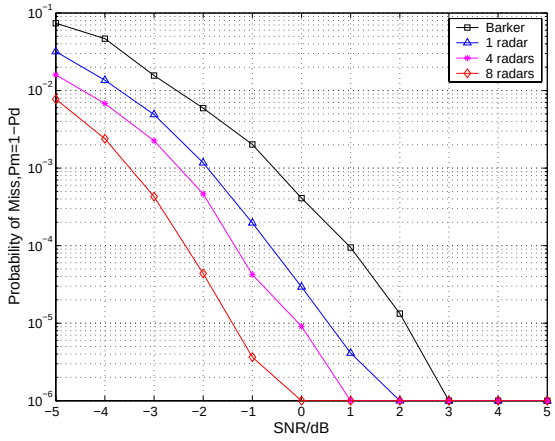


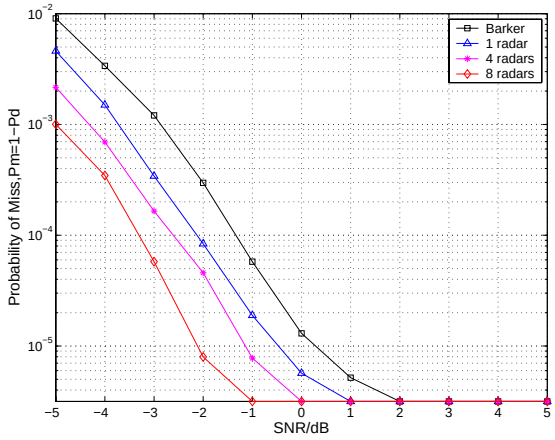
Figure 8: Waveform diversity combining in RSN



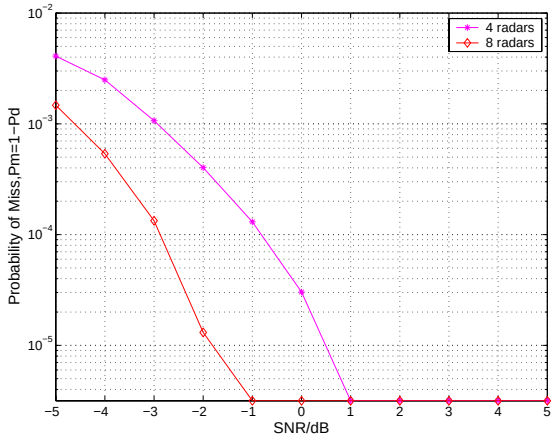
Figure 9: Received Signal Frame



(a)

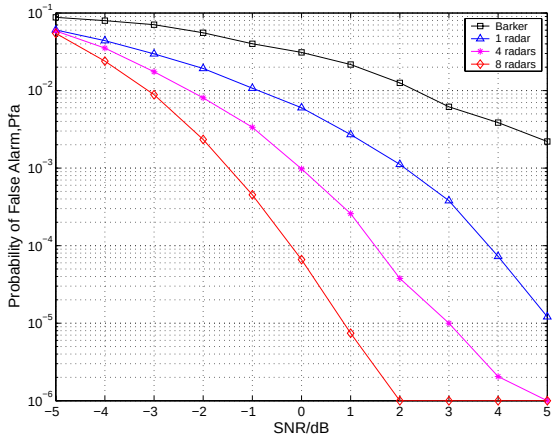


(b)

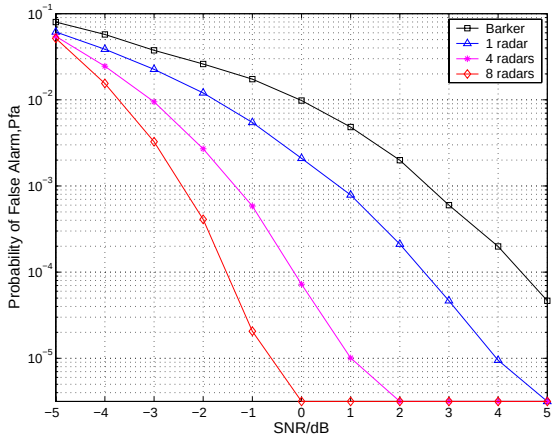


(c)

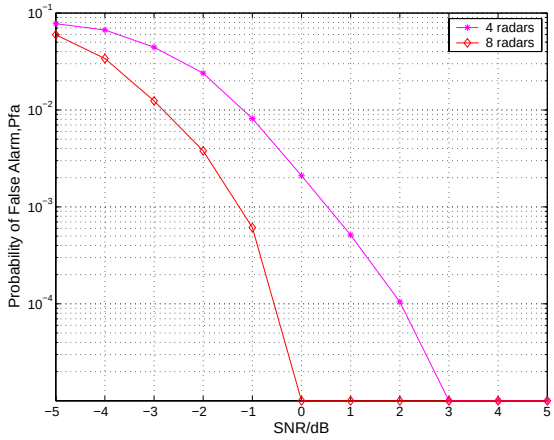
Figure 10: Probability of miss detection in RSN under the condition of: (a)No time delay nor Doppler shift (b)No time delay but Doppler shift (c)Time delay and Doppler shift



(a)



(b)



(c)

Figure 11: Probability of false alarm in RSN under the condition of: (a)No time delay nor Doppler shift (b)No time delay but Doppler shift (c)Time delay and Doppler shift

Orthogonal Pulse Compression Codes for MIMO Radar System

Lei Xu and Qilian Liang, *Senior Member, IEEE*

Department of Electrical Engineering

University of Texas at Arlington

Arlington, TX 76010-0016 USA

Email: xu@wcn.uta.edu, liang@uta.edu

Abstract

Inspired by recent advances in MIMO radar, we introduce orthogonal pulse compression codes to MIMO radar system in order to gain better range resolution and target direction finding performance. We investigate the MIMO radar ambiguity function of the system using phase coded waveforms. We also present and study a generalized MIMO radar system model using orthogonal phase coded waveforms. Accordingly, we propose the concept and the design methodology for a set of ternary phase coded waveforms that is the optimized punctured Zero correlation Zone (ZCZ) sequence-Pair Set (ZCZPS). The method is to use the optimized punctured sequence-pair along with Hadamard matrix in the ZCZ. We analyze the properties of our proposed phase coded waveforms and show that better range resolution could be achieved. In the end, we apply our proposed codes to MIMO radar system and simulate its target direction finding performance. The simulation results show that diversity gain could be obtained by using our orthogonal pulse compression codes in the MIMO radar system. The more receiving antennas used, the better target direction finding performance provided.

Index Terms : MIMO radar, ambiguity function, orthogonal, optimized punctured ZCZ sequence-pair, phase coded waveform

1 Introduction

It has been showed that processing data from a radar network with spatially distributed nodes could offer significant performance improvement, as a result, there has been considerable interest in MIMO radars which employ multiple antennas both at the transmitter and at the receiver.

On one hand, for the single radar system, there has been a lot of work on waveforms design. In [1], stochastic waveforms, such as random noise or chaotic signals are studied and used in the theoretical aspects of radar imaging. In addition, Y. Zhang [2] *et al.* studied the theory and technique of angle-of -arrival (AOA) estimation using random-noise or other stochastic transmit waveforms. And the experimental results also validate the theoretical predictions of random-noise monopulse characteristics and suggest its potential applications. The authors in [3] proposed a new technique for UWB random noise radar which combines median and anodization filtering so that the high range sidelobes could be suppressed and the special merits of UWB random noise radars could be still achieved at the same time. On the other hand, MIMO radars, unlike single radar or phased array radars, transmit different waveforms on the different antennas of the transmitter, which makes it necessary to do the waveform design for the system. The researchers have also done some work on the MIMO radar using orthogonal waveforms [4], partial correlation waveforms [5] or the more general non-orthogonal set of waveforms [6][7][8].

Ambiguity function [9], which is the response to a point target in the matched filter output, determines the range resolution and Doppler resolution of the system. As a result, in the traditional radar system, several waveform design methods [9] are based on optimization of the ambiguity function in the traditional single radar system. Also in [10], generalized wideband ambiguity function is proposed and investigated to study the performance of a coherent UWB random noise radar. Recently, the radar ambiguity function has also been extended to the MIMO radar system by San Antonio *et al.* [11]. In addition, pulse compression, known as a technique to raise the signal

to maximum sidelobe (signal-to-sidelobe) ratio to improve the target detection and range resolution abilities of the radar system, allows a radar to simultaneously achieve the energy of a long pulse and the resolution of a short pulse without the high peak power [12]. In this paper, applying the pulse compression technique to the MIMO radar system, we study and derive the MIMO radar ambiguity function of the system using a set of phase coded waveforms. Later, we would use this function to study the resolution of the MIMO radar system using our proposed codes as the phase coded waveforms.

Apart from the MIMO radar ambiguity function, direction finding [13] [14] is another important technology in MIMO radar system that a well known waveform is transmitted by an omnidirectional antenna, and a target reflects some of the transmitted energy toward an array of sensors that is used to estimate some unknown parameters, e.g. bearing, range, or speed. Also, beamforming [15] is a process generally used in direction finding process that an array of receivers can steer a beam toward any direction in space. The advantages of using an array of closely spaced sensors at the receiver are the lack of any mechanical elements in the system, the ability to use advanced signal processing techniques for improving performance, and the ability to steer multiple beams at once.

In this paper, we design a set of new orthogonal ternary codes for the MIMO radar system using the pulse compression technology. To the best of our knowledge, it is the first time to introduce phase coded waveforms to MIMO radar system to improve the range resolution and direction finding performance. A generalized MIMO radar signal model using our orthogonal phase coded waveforms is analyzed and the simulation results show that better performance could be obtained.

The rest of the paper is organized as follows. In Section 2, we study and derive the MIMO radar ambiguity function within phase coded waveforms. Section 3 presents and analyzes a generalized MIMO radar system using orthogonal phase coded waveforms. Section 4 introduces the definition and properties of ZCZPS as well as a set of specific ZCZPS which is the optimized punctured

ZCZPS. A method using optimized punctured sequence-pair and Hadamard matrix to construct ZCZPS is also given and proved. In section 5, some simulation results are provided by using specific examples with different number of uniform linear antennas at the transmitter and receiver of MIMO radar system. In Section 6, conclusions are drawn on our newly provided orthogonal pulse compression codes and their applications in the MIMO radar system.

2 MIMO Radar Ambiguity Functions

In this paper, we introduce the pulse compression technique to the MIMO radar system. In this section, we derive the MIMO radar ambiguity function for the case that the pulse waveform consists of the phase coded waveforms.

We write the phase coded waveforms as following:

$$u(t) = \frac{1}{\sqrt{Nt_b}} \sum_{n=1}^{N} u^{(n)} rect[\frac{t-(n-1)t_b}{t_b}] \tag{1}$$

where $u^{(n)} = exp(j\phi^{(n)})$ and the set of N phases $\phi^{(1)}, \phi^{(2)}, ..., \phi^{(n)}$ is the phase code associated with $u(t)$. Nt_b is the duration of waveform $u(t)$.

As the **MIMO radar ambiguity function** is defined [16]

$$\chi(\tau, v, f, f') \cong \sum_{m=0}^{M-1} \sum_{m'=0}^{M-1} \chi_{m,m'}(\tau, v) e^{j2\pi(fm - f'm')r} \tag{2}$$

where

$$\chi_{m,m'}(\tau, v) \cong \int_{-\infty}^{\infty} u_m(t) v_{m'}^*(t+\tau) e^{j2\pi vt} dt \tag{3}$$

Here, the target spatial frequency f and the assumed spatial frequency f' represent the spatial mismatch. τ is the delay corresponding to the target range, and ν is the Doppler frequency of the target. $r \cong d_t/d_r$ where the spacing between the transmitting elements is d_t and the spacing

between the receiving elements is d_r. M is the number of transmitting antennas and the function $\chi_{m,m'}(\tau,\nu)$ is called the **cross ambiguity function**.

The cross ambiguity function of phase coded waveforms could be expressed as

$$\begin{aligned}
\chi_{m,m'}(\tau,\nu) &= \int_0^{Nt_b} u_m(t)u_{m'}^*[(t+\tau) \mod Nt_b]e^{j2\pi\nu t}dt \qquad (4)\\
&= \int_0^{Nt_b} \frac{1}{\sqrt{Nt_b}}\sum_{n=1}^{N} u_m^{(n)} rect[\frac{t-(n-1)t_b}{t_b}]\frac{1}{\sqrt{Nt_b}}\sum_{n'=1}^{N} u_{m'}^{(n')*} rect([\frac{t-(n'-1)t_b}{t_b}] \mod N)e^{j2\pi\nu t}dt\\
&= \frac{1}{Nt_b}\sum_{n=1}^{N}\sum_{n'=1}^{N}\int_0^{t_b} rect[\frac{t-(n-1)t_b}{t_b}]rect([\frac{t-(n'-1)t_b}{t_b}] \mod N)e^{j2\pi\nu t}dt\\
&= \begin{cases} \frac{t_b}{N}\sum_{n=1}^{N}\sum_{n'=1}^{N} u_m^{(n)}u_{m'}^{(n')*}e^{j\pi\nu t_b}sinc(\pi\nu t_b), & [k-(n'-n)] \bmod N = 0\\ 0, & [k-(n'-n)] \bmod N \neq 0 \end{cases}
\end{aligned}$$

Where delay $\tau = kt_b$.

Using equation (2) in the definition of MIMO ambiguity function, we get

$$\chi(\tau,\nu,f,f') = \begin{cases} \frac{t_b}{N}\sum_{m=0}^{M-1}\sum_{m'=0}^{M-1}\sum_{n=1}^{N}\sum_{n'=1}^{N} u_m^{(n)}v_{m'}^{(n')*}e^{j2\pi(fm-f'm')r}e^{j\pi\nu t_b}sinc(\pi\nu t_b), & S=0\\ 0, & S\neq 0 \end{cases} \qquad (5)$$

where $S = ([k-(n'-n)] \bmod N)$ and $\tau = kt_b$.

According to equation (5), it is easy to see that pulses $u_m(t)$ or sequence u_m only affect the range and spatial resolution. This implies that the choice of the waveforms $u_m(t)$ does not affect the Doppler resolution. Therefore, we extract a function $\Omega(\tau,f,f')$ from MIMO radar ambiguity function to study the range resolution as

$$\Omega(\tau,f,f') = \begin{cases} \frac{t_b}{N}\sum_{m=0}^{M-1}\sum_{m'=0}^{M-1}\sum_{n=1}^{N}\sum_{n'=1}^{N} u_m^{(n)}u_{m'}^{(n')*}e^{j2\pi(fm-f'm')r}, & S=0\\ 0, & S\neq 0 \end{cases} \qquad (6)$$

where $S = [k-(n'-n)] \bmod N$, and $\tau = kt_b$.

The value $|\Omega(0,f,f)|$ represents the partial of matched filter output without mismatch. To obtain better system range resolution, the function $\Omega(\tau,f,f')$ should be sharp around the line $\{(\tau,f,f')|\tau=0, f=f'\}$.

For $M = 1$, the equation (6) reduces to

$$\Omega_0(\tau, f, f) = \begin{cases} \frac{t_b}{N} \sum_{n=1}^{N} \sum_{n'=1}^{N} u^{(n)} u^{(n')*}, & [k - (n' - n)] \bmod N = 0 \\ 0, & [k - (n' - n)] \bmod N \neq 0 \end{cases} \tag{7}$$

where $S = ([k - (n' - n)] \bmod N)$, and $\tau = kt_b$.

It is easy to see that equation (7) resembles the autocorrelation function of sequence u_m. For the MIMO radar case that $M > 1$, the cross correlation function between pulses has also to be taken into account in addition to the autocorrelation functions in order to have a sharp $\Omega(\tau, f, f')$.

Observing the equation (6), if the waveforms are orthogonal, the waveforms have high peak mainlobe, zero sidelobes of the autocorrelation function and have zero cross correlation values.

$$\sum_{n=0}^{N-1} u_m^{(n)} u_{m'}^{*(n+k) \mod N} = \begin{cases} E_s, & \text{for } m = m', k = 0 \\ 0, & \text{for } m = m', k \neq 0 \\ 0, & \text{for } m \neq m' \end{cases} \tag{8}$$

The MIMO ambiguity function turns to be

$$\chi(\tau, \nu, f, f') = \begin{cases} \frac{t_b}{N} E_s \sum_{m=1}^{M} e^{j2\pi(f-f')mr} e^{j\pi\nu t_b} sinc(\pi\nu t_b), & \text{for } \tau = 0 \\ 0, & \text{for } \tau = kt_{b,k=1,2,\ldots,N-1} \end{cases} \tag{9}$$

where $E_s = \sum_{n=0}^{N-1} u_m^{(n)} u_m^{(n)*}$ is the energy of the sequence u_m.

Assuming there exists no mismatch in range and Doppler domain and $f = f'$, the function becomes

$$\chi(0, 0, f, f) = \sum_{m=1}^{M} \frac{t_b}{N} E_s = M \frac{t_b}{N} E_s \tag{10}$$

It is obvious that the ambiguity function is a constant along the line $(0, 0, f, f)$ which is independent of the waveform design of $u_m(t)$. It implies that when there exists no mismatch in range and Doppler domain, the output of matched filter is independent of the waveform design but only relating to the length of waveform. However, if considering the mismatch, the waveforms design

should be taken into account so that the range resolution could be improved. Besides, comparing equation (10) with (7), a diversity gain of M could be achieved here.

On the another hand, observing the right part of equation (9), Doppler resolution of the MIMO radar ambiguity function is affected by $e^{j\pi\nu t_b} sinc(\pi\nu t_b)$. According to the property of $sinc(\pi\nu t_b)$, when Doppler frequencies equal to multiples of the pulse repetition frequency ($PRF = 1/PRI = 1/t_b$), all the ambiguity values turn to zero. That is the same as the single radar system widely using the pulse compression technology. Overall, the Doppler resolution of MIMO radar ambiguity function could keep the characteristics of the single radar system.

3 MIMO Radar Signal Model

In this section, we describe a signal model for the MIMO radar system using orthogonal pulse compression codes to improve the direction finding performance. Assume a radar system that utilizes an array with M antennas at the transmitter, and N antennas at the receiver. For simplicity, we assume that the target scatters are laid out as a linear array, and the arrays at the transmitter and receiver are parallel. A transmitting linear array made up of M elements equally spaced a distance d_t apart. The elements are assumed to be isotropic radiators in that they have uniform response for signals from all directions. The first antenna will be taken as the reference with zero phase. The signal radiated by the transmit antenna impinges at angle θ which is the angle of arrival (AOA). From simple geometry, the difference in path length between adjacent elements for signals transmitting at an angle θ with respect to the normal to the antenna, is $d_t sin\theta$. This gives a phase difference between adjacent elements of $\phi = 2\pi(d_t/\lambda)sin\theta$, where λ is wavelength of the received signal. And the phase difference for m-th transmit antenna is $\phi_m = 2\pi((m-1)d_t/\lambda)sin\theta$. For convenience, we take the amplitude of the signal at each element to be unity. A pulse compression code $C_m = \sum_{p=0}^{P-1} C_m^{(p)}(t - p\tau_c)$ is applied to m-th transmit antenna, and the signal vector induced

by the m-th transmit antenna is given by

$$C_m = [C_m^{(0)}, C_m^{(1)}, C_m^{(2)}, ..., C_m^{(P-1)}]; \tag{11}$$

$$g_m = e^{-j\phi_m}[C_m^{(0)}, C_m^{(1)}, C_m^{(2)}, ..., C_m^{(P-1)}], 1 \leq m \leq M;$$

The signal vectors are organized in the $M \times P$ transmit matrix $\mathbf{G} = [g_1, g_2, ..., g_M]^T$. The transmitted waveforms are listed as a $M \times 1$ matrix $\mathbf{S} = [s_1, s_2, ..., s_M]^T$. The transmitted waveforms could be normalized such that $|s_i|^2 = 1/M$. The normalizing method ensures that transmitted power is not dependent of the number of antennas.

Similar to the transmitter, the model for the array at the receiver could be developed, resulting in an $N \times P$ channel matrix K. Similarly, the first antenna on the receiving part will be taken as the reference with zero phase. The signal radiated by the n-th receive antenna impinges at angle θ_0. The phase difference for n-th transmit antenna is $\varphi_n = 2\pi((n-1)d_r/\lambda)sin\theta_0$. For phase-modulated pulse compression waveforms, the sum of the corresponding pulse compression codes $\sum_{m=1}^{M} C'_m = \sum_{m=1}^{M}\sum_{p=0}^{P-1} C_m'^{(p)}(t - p\tau_c)$ have to be applied to each receive antenna to implement the matched filter. The signal vector arrived at the n-th receive antenna could be given by

$$C'_m = [C_m'^{(0)}, C_m'^{(1)}, C_m'^{(2)}, ..., C_m'^{(P-1)}]; \tag{12}$$

$$k_n = e^{-j\varphi_n}\sum_{m=1}^{M} C'_m;$$

$$\mathbf{K} = [k_1, k_2, ..., k_N]^T$$

Assume there is a far field complex (multiple scatters) target and it is known that small changes in the aspect angle of complex targets can cause major changes in the radar cross section (RCS). Here, RCS for each receiver antenna is assumed to have isotropic reflectivity modeled by zero-mean, unit-variance, independent and identically distributed (i.i.d.) Gaussian complex random variables λ_i. The target is then modeled by the diagonal matrix

$$\Sigma = \frac{1}{\sqrt{2M}} \begin{bmatrix} \lambda_1 & 0 & \cdots & 0 \\ 0 & \lambda_2 & \ddots & \vdots \\ \vdots & \ddots & \ddots & 0 \\ 0 & ... & 0 & \lambda_M \end{bmatrix} \tag{13}$$

where the normalization factor makes the target average RCS= $\sum_{i=1}^{M} |\lambda_i|^2 = 1$ independent of the number of transmitting antennas in the model. The nonfluctuating target modeled using non-zero constants for λ_i is identified as "$Swerling0$" or "$Swerling5$" model. For the fluctuating target, if $|\lambda_i|$ is drawn from the Rayleigh pdf and vary independently from path to path, the target model represents a classical "$Swerling2$" model.

Processing the transmit RCS matrix, the target matrix and the receive matrix together, the MIMO radar channel model is given by $N \times M$ matrix shown in (14).

$$\begin{aligned} \mathbf{H} = \mathbf{K}[\mathbf{G}^{\mathbf{H}}\Sigma] &= \begin{bmatrix} k_1 \\ k_2 \\ \vdots \\ k_N \end{bmatrix} \left[g_1^H, g_2^H, \ldots, g_M^H\right] \begin{bmatrix} \lambda_1 & 0 & \cdots & 0 \\ 0 & \lambda_2 & \ddots & \vdots \\ \vdots & \ddots & \ddots & 0 \\ 0 & ... & 0 & \lambda_M \end{bmatrix} \\ &= \begin{bmatrix} \lambda_1 k_1 g_1^H & \lambda_2 k_1 g_2^H & \ldots & \lambda_M k_1 g_M^H \\ \lambda_1 k_2 g_1^H & \lambda_2 k_2 g_2^H & \ldots & \lambda_M k_2 g_M^H \\ \vdots & \vdots & \vdots & \vdots \\ \lambda_1 k_N g_1^H & \lambda_2 k_N g_2^H & \ldots & \lambda_M k_N g_M^H \end{bmatrix} \end{aligned} \tag{14}$$

According to (14), it is easy to notice that each entry of the matrix could be expressed as

$$\lambda_m k_n g_m^H = \lambda_m [e^{-j\varphi_n} \sum_{m'=1}^{M} C'_{m'}][e^{-j\phi_m} C_m]^H = \lambda_m e^{j(\phi_m - \varphi_n)} \sum_{m'=1}^{M} C'_{m'} C_m^H \tag{15}$$

If we select orthogonal pulse compression codes for transmit and receive antennas, it is satisfied that

$$\sum_{p=0}^{P-1} C_m^{(p)} C_{m'}^{(p)'} = \begin{cases} E_s, & m = m' \\ 0, & m \neq m' \end{cases} \tag{16}$$

$\lambda_m k_n g_m^H = \lambda_m e^{j(\phi_m - \varphi_n)} E_s$ and the $\mathbf{H}$ matrix turns to be shown as (17).

$$\mathbf{H} = \begin{bmatrix} \lambda_1 e^{j(\phi_1-\varphi_1)} E_s & \lambda_2 e^{j(\phi_2-\varphi_1)} E_s & \cdots & \lambda_M e^{j(\phi_M-\varphi_1)} E_s \\ \lambda_1 e^{j(\phi_1-\varphi_2)} E_s & \lambda_2 e^{j(\phi_2-\varphi_2)} E_s & \cdots & \lambda_M e^{j(\phi_M-\varphi_2)} E_s \\ \vdots & \vdots & \vdots & \vdots \\ \lambda_1 e^{j(\phi_1-\varphi_N)} E_s & \lambda_2 e^{j(\phi_2-\varphi_N)} E_s & \cdots & \lambda_M e^{j(\phi_M-\varphi_N)} E_s \end{bmatrix} \tag{17}$$

As a result, the signal vector received by the MIMO radar is given by

$$r = \mathbf{HS} + n = \begin{bmatrix} E_s \sum_{m=1}^{M} \lambda_m e^{j(\phi_m-\varphi_1)} s_m \\ E_s \sum_{m=1}^{M} \lambda_m e^{j(\phi_m-\varphi_2)} s_m \\ \vdots \\ E_s \sum_{m=1}^{M} \lambda_m e^{j(\phi_m-\varphi_N)} s_m \end{bmatrix} + n \tag{18}$$

Where the additive white Gaussian noise vector n consists of i.i.d, zero-mean complex normal distributed random variables. The transmitted waveforms are normalized. The normalizing factor ensures that the transmitted power is independent of the number of transmit antennas. In this case that the antennas transmit signals which are organized in the vector $\mathbf{S} = [s_0, s_1, ..., s_M]^T$.

If receiver antenna uses a beamformer to steer towards direction $\theta_0^{'}$, $\varphi_n^{'} = 2\pi((n-1)d_r/\lambda)sin\theta_0^{'}$. The beamformer is modeled by a vector

$$\beta(\theta_0') = [e^{-j\varphi_1^{'}}, e^{-j\varphi_2^{'}}, \cdots, e^{-j\varphi_M^{'}}]^T \tag{19}$$

The following expression is evaluated:

$$\begin{aligned} \mathbf{y} &= \beta^H(\theta_0^{'})r = \beta^H(\theta_0^{'})(\mathbf{HS}) + n^{'} \\ &= E_s \sum_{n=1}^{N} \sum_{m=1}^{M} \lambda_m e^{j(\phi_m - \varphi_n + \varphi_n^{'})} s_m + n^{'} \end{aligned} \tag{20}$$

where $E_s >> \sigma^2(n')$.

In MIMO radar for direction finding (DF) purpose, the transmit antennas are sufficiently separated, so the phase shifts at the transmitter are set to zero. It is easy to see that when $\theta = 0$, $\phi_m = 2\pi(d/\lambda)sin\theta = 0$ and $\mathbf{g}_m = [C_m^{(0)}, C_m^{(1)}, C_m^{(2)}, ..., C_m^{(P-1)}]^T$.

The output turns to be

$$\mathbf{y}' = E_s(\sum_{m=1}^{M} \lambda_m s_m)(\sum_{n=1}^{N} e^{j(\varphi_n' - \varphi_n)}) + n^{'} \tag{21}$$

The angle of arrival is estimated as the $\theta^{'}$ which maximizes $|\mathbf{y}'|^2$. To prevent the effect that signal components s_m might destructively interfere with each other, orthogonal waveforms could be employed here.

$$|\mathbf{y}'|^2 \approx E_s^2(\sum_{m=1}^{M} |\lambda_m s_m|^2)(|\sum_{n=1}^{N} e^{j(\varphi_n' - \varphi_n)}|^2) + n^{''} \tag{22}$$

It is easy to see that if the beamformer can well estimate the direction θ_0 at the receiver antenna, $\theta_0^{'} \cong \theta_0$ and $\varphi_n = \varphi_n'$, a diversity gain of N^2 which is square of the number of receiving antennas could be obtained.

4 Orthogonal Pulse Compression Codes

According to the previous sections, orthogonal pulse compression codes could be introduced to the MIMO radar system to improve the range resolution and direction finding performance. It is also known that it is impossible to have perfect autocorrelation function (ACF) and cross correlation function (CCF) simultaneously, since the corresponding parameters have to be limited by certain

bounds, such as Welch bound [18], Sidelnikov bound [19] and Sarwate bound [20]. As a result, based on the Zero Correlation Zone (ZCZ) [21][22][23], we propose a set of ternary codes, analyze the concept and design the methodology of them which could be applied to MIMO radar system.

4.1 The Definition and Properties of ZCZ sequence-Pair Set

Here, we introduce sequence-pair into the ZCZ concept to construct ZCZPS. We consider ZCZPS $(\mathbf{X}, \mathbf{Y})$, $\mathbf{X}$ to be a set of K sequences of length N and $\mathbf{Y}$ to be a set of K sequences of the same length N:

$$\mathbf{x}_p \in \mathbf{X} \quad p = 0, 1, 2, ..., K-1 \tag{23}$$

$$\mathbf{y}_q \in \mathbf{Y} \quad q = 0, 1, 2, ..., K-1 \tag{24}$$

The autocorrelation function for sequence-pair $(\mathbf{x}_p, \mathbf{y}_p)$ is defined by:

$$R_{\mathbf{x}_p\mathbf{y}_p}(\tau) = \sum_{i=0}^{N-1} x_p^{(i)} y_p^{(i+\tau)modN}, 0 \leq \tau \leq N-1 \tag{25}$$

The cross correlation function for sequence-pair $(\mathbf{x}_p, \mathbf{y}_p)$ and $(\mathbf{x}_q, \mathbf{y}_q), p \neq q$ is defined by:

$$C_{\mathbf{x}_p\mathbf{y}_q}(\tau) = \sum_{i=0}^{N-1} x_p^{(i)} y_q^{*(i+\tau)modN}, 0 \leq \tau \leq N-1 \tag{26}$$

$$C_{\mathbf{x}_q\mathbf{y}_p}(\tau) = \sum_{i=0}^{N-1} x_q^{(i)} y_p^{*(i+\tau)modN}, 0 \leq \tau \leq N-1 \tag{27}$$

For pulse compression sequences, some properties are of particular concern in the optimization for any design in engineering. They are the peak sidelobe level, the energy of autocorrelation sidelobes and the energy of their mutual cross correlation [24]. Therefore, the peak sidelobe level which represents a source of mutual interference and obscures weaker targets can be presented as $\max_K |R_{x_p y_p}(\tau)|, \tau \in Z_0$ (zero correlation zone) for ZCZPS. Another optimization criterion for the set of sequence-pair is the energy of autocorrelation sidelobes joined together with the energy of cross

correlation. By minimizing the energy, it can be distributed evenly, and the peak autocorrelation level can be minimized as well [24]. Here, the energy of ZCZPS can be employed as:

$$E = \sum_{p=0}^{K-1} \sum_{\tau=1}^{Z_0} R^2_{\mathbf{x}_p \mathbf{y}_p}(\tau) + \sum_{p=0}^{K-1} \sum_{q=0}^{K-1} \sum_{\tau=0}^{N-1} C_{\mathbf{x}_p \mathbf{y}_q}(\tau) \qquad (p \neq q) \tag{28}$$

According to (28), it is obvious to see that the energy can be kept low while minimizing the autocorrelation sidelobes and cross correlation of the sequence-pair set.

Then, the ZCZPS can be constructed to minimize the autocorrelation and cross correlation of the sequence-pair set and the definition of ZCZPS can be expressed:

Definition 4-1: Assume $(\mathbf{x}_p^{(i)}, \mathbf{y}_p^{(i)})$ to be sequence-pair set of length N and the number of sequence-pair K, where $p = 1, 2, 3, ..., K-1, i = 0, 1, 2, ..., N-1$, if all the sequences in the set satisfy the following equation:

$$R_{\mathbf{x}_p \mathbf{y}_q}(\tau) = \sum_{i=0}^{N-1} x_p^{(i)} y_q^{*(i+\tau) mod(N)} = \sum_{i=0}^{N-1} y_p^{(i)} x_q^{*(i+\tau) mod(N)}$$

$$= \begin{cases} \lambda N, & \text{for } \tau = 0, p = q \\ 0, & \text{for } \tau = 0, p \neq q \\ 0, & \text{for } 0 < |\tau| \leq Z_0 \end{cases} \tag{29}$$

where $0 < \lambda \leq 1$, then $(x_p^{(i)}, y_p^{(i)})$ is called a ZCZ sequence-Pair, $ZCZP(N, K, Z_0)$ is an abbreviation, and $(\mathbf{X}, \mathbf{Y})$ is called a ZCZ sequence-Pair Set, $ZCZPS(N, K, Z_0)$ is an abbreviation.

4.2 Definition and Design for Optimized Punctured ZCZ Sequence-Pair Set

Matsufuji and Torii have provided some methods of constructing ZCZ sequences in [27] [28]. In this section, a set of novel ternary codes, namely the optimized punctured ZCZ sequence-pair set, is constructed through applying the optimized punctured sequence-pair [29] to the zero correlation zone. In some other words, optimized punctured ZCZPS is a specific kind of ZCZPS.

Definition 4-2 [29] Sequence $\mathbf{u} = (u^{(0)}, u^{(1)}, ..., u^{(N-1)})$ is the punctured sequence for $\mathbf{v} = (v^{(0)}, v^{(1)}, ..., v^{(N-1)})$,

$$u^{(j)} = \begin{cases} 0, & \text{if bit } u^{(j)} \text{ is punctured} \\ v^{(j)}, & \text{if bit } u^{(j)} \text{ is Non-punctured} \end{cases} \tag{30}$$

Here P is the number of punctured bits in sequence $\mathbf{v}$, suppose $v^{(j)} \in (-1, 1)$, $u^{(j)} \in (-1, 0, 1)$, $\mathbf{u}$ is P-punctured binary sequence, $(\mathbf{u}, \mathbf{v})$ is called a punctured binary sequence-pair.

Definition 4-3 [29] The autocorrelation of punctured sequence-pair $(\mathbf{u}, \mathbf{v})$ is defined

$$R_{\mathbf{uv}}(\tau) = \sum_{i=0}^{N-1} u^{(i)} v^{*(i+\tau) mod N}, 0 \leq \tau \leq N-1 \tag{31}$$

If the punctured sequence-pair has the following autocorrelation property:

$$R_{\mathbf{uv}}(\tau) = \begin{cases} E, & \text{if } \tau \equiv 0 \text{mod} N \\ 0, & \text{otherwise} \end{cases} \tag{32}$$

the punctured sequence-pair is called optimized punctured sequence-pair [29]. Where, $E = \sum_{i=0}^{N-1} u^{(i)} v^{*(i+\tau) mod N} = N - P$, is the energy of punctured sequence-pair.

If $(x_p^{(i)}, y_p^{(i)})$ in Definition 4-1 is constructed by optimized punctured sequence-pair and a certain matrix, such as Hadamard matrix or an orthogonal matrix, where

$$x_p^{(i)} \in (-1, 1), \quad i = 0, 1, 2, ..., N-1$$

$$y_q^{(i)} \in (-1, 0, 1), \quad i = 0, 1, 2, ..., N-1$$

$$R_{\mathbf{x}_p \mathbf{y}_q}(\tau) = \sum_{i=0}^{N-1} x_p^{(i)} y_q^{*(i+\tau) mod N} = \sum_{i=0}^{N-1} y_p^{(i)} x_q^{*(i+\tau) mod N}$$

$$= \begin{cases} \lambda N, & \text{for } \tau = 0, p = q \\ 0, & \text{for } \tau = 0, p \neq q \\ 0, & \text{for } 0 < |\tau| \leq Z_0 \end{cases} \tag{33}$$

where $0 < \lambda \leq 1$, then $(x_p^{(i)}, y_p^{(i)})$ can be called optimized punctured ZCZ sequence-pair set. Based on odd length optimized punctured binary sequence pairs and a Hadamard matrix, an optimized punctured ZCZPS can be constructed on following steps:

Step 1: Considering an odd length optimized punctured binary sequence-pair $(\mathbf{u}, \mathbf{v})$, the length of each sequence is N_1

$$\mathbf{u} = u^{(0)}, u^{(1)}, ..., u^{(N_1-1)}, u^{(i)} \in (-1, 1),$$

$$\mathbf{v} = v^{(0)}, v^{(1)}, ..., v^{(N_1-1)}, v^{(i)} \in (-1, 0, 1),$$

$$i = 0, 1, 2, ..., N_1 - 1, N_1 \ odd$$

Step 2: A Hadamard matrix B of order N_2 is considered. The length of the sequence of the matrix is N_2 which is equal to the number of the sequences. Here, any Hadamard matrix order is possible and $\mathbf{b}_i$ is the row vector.

$$\mathbf{B} = [\mathbf{b}_0, \mathbf{b}_1, ..., \mathbf{b}_{N_2-1}]^T,$$

$$\mathbf{b}_i = (b_i^{(0)}, b_i^{(1)}, ..., b_i^{(N_2-1)}),$$

$$R_{\mathbf{b}_i\mathbf{b}_j} = \begin{cases} N_2, & \text{if } i = j \\ 0, & \text{if } i \neq j \end{cases}$$

Step 3: Perform bit-multiplication on the optimized punctured binary sequence-pair and each line of Walsh sequences set B (Hadamard matrix), then sequence-pair set **(X,Y)** is obtained,

$$\mathbf{b}_i = (b_i^{(0)}, b_i^{(1)}, ..., b_i^{(N_2-1)}), i = 0, 1, ..., N_2 - 1,$$

$$x_i^{(j)} = u^{(jmodN_1)} b_i^{(jmodN_2)}, 0 \leq i \leq N_2 - 1, 0 \leq j \leq N - 1,$$

$$\mathbf{X} = (\mathbf{x}_0, \mathbf{x}_1, ..., \mathbf{x}_{N_2-1})^T,$$

$$y_i^{(j)} = v^{(jmodN_1)} b_i^{(jmodN_2)}, 0 \leq i \leq N_2 - 1, 0 \leq j \leq N - 1,$$

$$\mathbf{Y} = (\mathbf{y}_0, \mathbf{y}_1, ..., \mathbf{y}_{N_2-1})^T$$

Since we use the optimized punctured binary sequence-pairs of odd lengths here and the lengths of Walsh sequence are $2^n, n = 1, 2, ..., GCD(N_1, N_2) = 1$, common divisor of N_1 and N_2 is 1, $N = N_1 * N_2$. The sequence-pair set $(\mathbf{X}, \mathbf{Y})$ is optimized punctured ZCZPS and $N_1 - 1$ is the zero correlation zone Z_0. The length of each sequence in optimized punctured ZCZPS is $N = N_1 * N_2$ that depends on the product of length of optimized punctured sequence-pair and the length of Walsh sequence in Hadamard matrix. The number of sequence-pair in optimized punctured ZCZPS rests on the order of the Hadamard matrix. The sequence $\mathbf{x}_i$ in sequence set $\mathbf{X}$ and the corresponding sequence $\mathbf{y}_i$ in sequence set $\mathbf{Y}$ construct a sequence-pair $(\mathbf{x}_i, \mathbf{y}_i)$ that can be used as a pulse compression code.

The correlation property of the sequence-pair in optimized punctured ZCZPS is:

$$\begin{aligned} R_{\mathbf{x}_i\mathbf{y}_j}(\tau) &= R_{\mathbf{x}_j\mathbf{y}_i}(\tau) = R_{\mathbf{uv}}(\tau mod N_1) R_{\mathbf{b}_i\mathbf{b}_j}(\tau mod N_2) \\ &= R_{\mathbf{uv}}(\tau mod N_1) R_{\mathbf{b}_j\mathbf{b}_i}(\tau mod N_2) \\ &= \begin{cases} EN_2, & \text{if } \tau = 0, i = j \\ 0, & \text{if } 0 < |\tau| \leq N_1 - 1, i = j \\ 0, & \text{if } i \neq j \end{cases} \end{aligned} \tag{34}$$

where $N_1 - 1$ is the zero correlation zone Z_0.

Proof:

1) When $i = j$,

$$\tau = 0,$$

$$R_{\mathbf{uv}}(0) = E, R_{\mathbf{b}_i\mathbf{b}_j}(0) = N_2,$$

$$R_{\mathbf{x}_i\mathbf{y}_j}(0) = R_{uv}(0)R_{b_ib_j}(0) = EN_2;$$

$$0 < |\tau| \leq N_1 - 1,$$

$$R_{\mathbf{uv}}(\tau) = 0,$$

$$R_{\mathbf{x}_i\mathbf{y}_j}(\tau) = R_{\mathbf{uv}}(\tau mod N_1)R_{\mathbf{b}_i\mathbf{b}_j}(\tau mod N_2) = 0;$$

2) When $i \neq j$,

$$\tau = 0,$$

$$R_{\mathbf{b}_i\mathbf{b}_j}(0) = 0,$$

$$R_{\mathbf{x}_i\mathbf{y}_j}(0) = R_{\mathbf{x}_j\mathbf{y}_i}(0)$$

$$= R_{\mathbf{uv}}(\tau mod N_1)R_{b_ib_j}(\tau mod N_2) = 0;$$

$$0 < |\tau| \leq N_1 - 1,$$

$$R_{\mathbf{uv}}(\tau) = 0,$$

$$R_{\mathbf{x}_i\mathbf{y}_j}(\tau) = R_{\mathbf{x}_j\mathbf{y}_i}(\tau)$$

$$= R_{\mathbf{uv}}(\tau mod N_1)R_{b_ib_j}(\tau mod N_2) = 0.$$

According to Definition 4-1, the sequence-pair set constructed by the above method is ZCZPS.

4.3 Properties of Optimized Punctured ZCZ Sequence-pair Set

Considering the optimized punctured ZCZPS that is constructed by the method mentioned in the last part, the autocorrelation and cross correlation properties can be simulated and analyzed with MATLAB. For example, the optimized punctured ZCZPS $(\mathbf{X}, \mathbf{Y})$ is constructed by 5-bit length

optimized punctured binary sequence-pair $(\mathbf{u}, \mathbf{v}), \mathbf{u} = [++-+-], \mathbf{v} = [++000]$ (using $'+'$ and $'-'$ symbols for $'1'$ and $'-1'$) and Hadamard matrix H of order 4. We follow the three steps presented in the previous section to construct the 20-bit length optimized punctured ZCZPS. The number of sequence-pairs here is 4, and the length of each sequence is $5 * 4 = 20$. The first row of each matrix $\mathbf{X} = [\mathbf{x}_1; \mathbf{x}_2; \mathbf{x}_3; \mathbf{x}_4]$ and $\mathbf{Y} = [\mathbf{y}_1; \mathbf{y}_2; \mathbf{y}_3; \mathbf{y}_4]$ constitute a certain optimized punctured ZCZP $(\mathbf{x}_1, \mathbf{y}_1)$. Similarly, the second row of each matrix X and Y constitute another optimized punctured ZCZ sequence-pair $(\mathbf{x}_2, \mathbf{y}_2)$ and so on.

$$\mathbf{X} = \begin{bmatrix} ++-+-++-+-++-+-++-+- \\ +-----++++-----++++ \\ +++--+-++---+-+--+ \\ +-++----+-+--++++-- \end{bmatrix};$$

$$\mathbf{Y} = \begin{bmatrix} ++000++000++000++000 \\ +-000-+000+-000-+000 \\ ++000+-000--000-+000 \\ +-000--000-+000++000 \end{bmatrix}.$$

The autocorrelation property and cross correlation property of 20-bit length optimized punctured ZCZ sequence pair set $(\mathbf{X}, \mathbf{Y})$ are shown in Figs. 1 and 2.

From the Figs. 1 and 2, the sidelobe of autocorrelation of ZCZPS can be as low as 0 when the time delay is kept within $Z_0 = N_1 = 5$ (zero correlation zone) and the cross correlation value is kept as low as 0 during the whole time domain.

It is known that a suitable criterion for evaluating code of length N is the ratio of the peak signal divided by the peak signal sidelobe (PSR) of their autocorrelation function, which can be bounded by [30]

$$[PSR]_{dB} \leq 20logN = [PSR_{max}]_{dB} \tag{35}$$

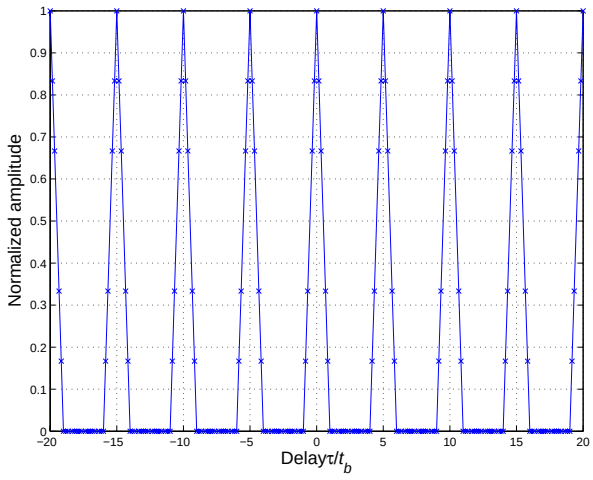


Figure 1: Periodic autocorrelation property of optimized punctured ZCZPS

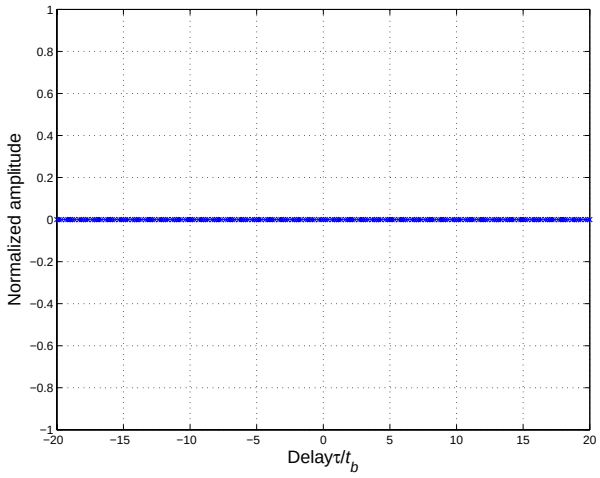


Figure 2: Periodic cross correlation property of optimized punctured ZCZPS

The only uniform phase codes that can reach the PSR_{max} are the Barker codes whose length is equal or less than 13. The sidelobe of the new code shown in Fig. 1 can be as low as 0, so the peak signal divided by the peak signal sidelobe can be as high as infinite. Besides, the length of the new code is various and much longer than the length of the Barker code.

Referring to the MIMO ambiguity function of Section 2, the MIMO ambiguity function of the system using our proposed codes is

$$\chi(\tau,\nu,f,f') = \begin{cases} \frac{t_b}{N}E_s \sum_{m=1}^{M} e^{j2\pi(f-f')mr} e^{j\pi\nu t_b} sinc(\pi\nu t_b), & \text{for } \tau = 0 \\ 0, & \text{for } \tau = kt_b, k = 1,2,...,N_1-1 \end{cases} \tag{36}$$

where $E_s = \sum_{n=0}^{N-1} u_m^{(n)} v_m^{(n)*}$ is the energy of the sequence-pair and N_1 is the ZCZ. Only the range resolution is affected by the waveform design, so we would study the range resolution of proposed codes. The function is

$$\Omega(\tau,f,f') = \begin{cases} \frac{t_b}{N}E_s \sum_{m=1}^{M} e^{j2\pi(f-f')mr}, & \text{for } \tau = 0 \\ 0, & \text{for } \tau = kt_b, k = 1,2,...,N_1-1 \end{cases} \tag{37}$$

Assuming the estimated parameter equals the normalized spatial frequency of the target, $f = f'$, we get the function

$$\Omega(\tau,f,f) = \begin{cases} \frac{Mt_b}{N}E_s, & \text{for } \tau = 0 \\ 0, & \text{for } \tau = kt_b, k = 1,2,...,N_1-1 \end{cases} \tag{38}$$

Take the same example of our proposed codes in this section into account. Here, $E_s = 8, M = 4, N_1 = 5$ and $N = 20$. We can easily get the range resolution shown as following

$$\Omega(\tau,f,f) = \begin{cases} 1.6t_b, & \text{for } \tau = 0 \\ 0, & \text{for } \tau = kt_b, k = 1,2,...,4 \end{cases} \tag{39}$$

Accordingly, it is easy to draw the conclusion that the MIMO radar system using our proposed set of orthogonal codes could improve the range resolution to $\frac{1}{N}$ (N is the length of the corresponding sequence) of the original one. And the peak value is increased from t_b of single radar system without

using pulse compression technique to $1.6t_b$ in the above case. However, the time delay should be limited to the value of ZCZ of the codes here.

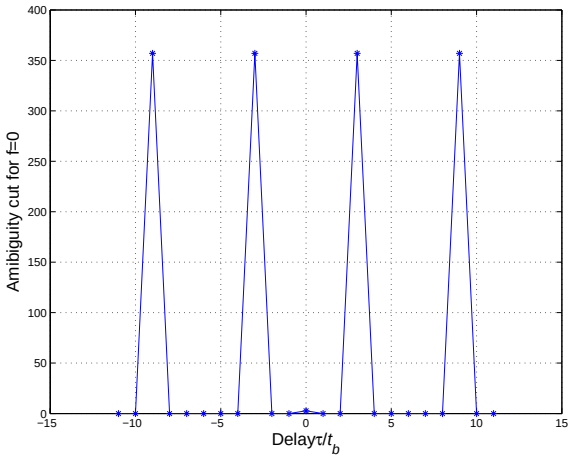
Nevertheless, if there is no limit to the time delay, the range resolution would be interfered. We use the matlab to simulate the performance of three examples, such as 12x4 length ZCZ codes, 20x4 length ZCZ codes and 28x4 length ZCZ codes in Fig. 3.

The above figures show that the ambiguity function has high peaks at the period of the ZCZ expect for a short sharp at zero time delay. However, there might be the concern that multiple peaks of the autocorrelation function would lead to ambiguity in ranging. Since the periodic correlation function is used in this paper, the peaks from other targets would not be high enough to mask the peak of the target under the study. In addition, we are studying the single target system in this research and well controlling the PRF (pulse repetition frequency), the only concern is that multiple peaks of the transmitting signal reflected from one target may affect determining the main peak of ACF. As a matter of fact, the matched filter here could shift at the period of ZCZ length to track each peak instead of shifting bit by bit after the first peak is acquired, which could make the system work more efficiently. Alike the tracking technology in synchronization of CDMA system, checking several peaks instead of only one peak guarantee the precision of P_D and avoidance of P_{FA}. And the range could be determined by obtaining the the middle point of time range of the first and the last high peaks where we could achieve a short sharp.

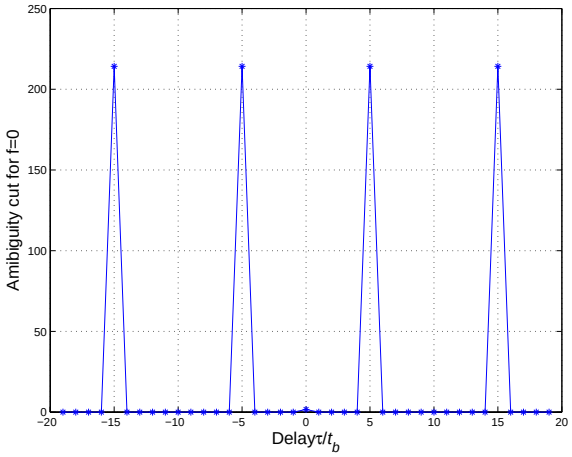
5 Simulations and Analysis

In this section, we are running MATLAB simulations of the MIMO radar system using different number of transmitting antennas and receiving antennas to see the direction finding performance. The transmit antennas are spaced sufficiently and the antenna array is used in the receiving part. The target fluctuating model in which the channel fluctuated according to a Rayleigh distribution

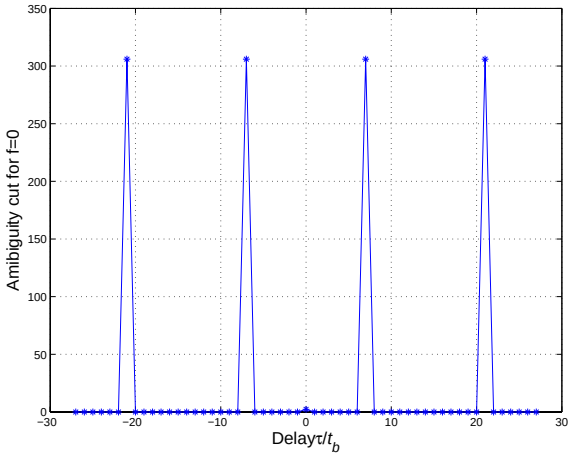
Figure 3: Range Resolution



(a) 12x4 ZCZ codes



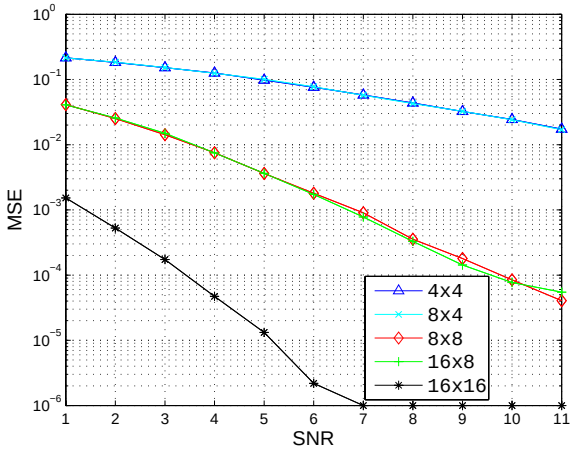
(b) 20x4 ZCZ codes



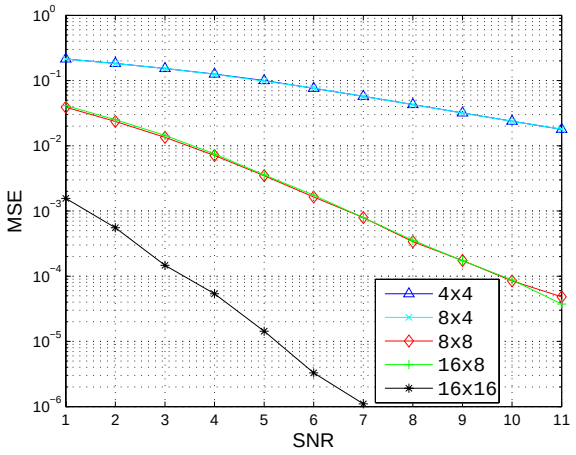
(c) 28x4 ZCZ codes

is considered besides the nonfluctuating model. Estimation MSE is used as the common figure of merit for comparing the performance. Using nonfluctuating and fluctuating target model, the MIMO radar systems of different antennas are illustrated in Fig. 4.

Figure 4: MSE of beamforming at the receiver



(a) nonfluctuating model



(b) fluctuating model

From the Fig. 4, it is easy to see that under the situation of both nonfluctuating and fluctuating models the system of more receiving antennas could always achieve better MSE than the system of less receiving antennas. However, the system of the same number of receiving antennas

could achieve similar performance though different number of transmitting antennas are used, so the number of transmitting antennas seems not to have great effect on the direction finding performance. Observing the equation (22), we can see that $\sum|_{m=1}^{M}\lambda_m s_m|^2$ determines how the number of transmitting antennas affects the direction finding performance. Since we introduce normalization factor to make the target average RCS independent of the number of scatters in the model, the value of $\sum_{m=1}^{M}|\lambda_m s_m|^2$ is as small as around 1 so that the number of transmitting antennas will not affect the final result much. Therefore, according to the equation (22), if the the target average RCS is large enough, the more transmitting antennas we have, the better performance could be obtained for sure. Comparing the Fig. 4(a) and 4(b), the performance of our system for fluctuating modeal is not severely degraded because of the Rayleigh fading. So we can see that the model using our proposed codes could work well both under fluctuating and nonfluctuating conditions. As a result, a general conclusion could be drawn that the more antennas MIMO radar system utilized the better direction finding performance could achieved in both models.

6 Conclusions

In this paper, we introduced the orthogonal phase coded waveforms to the MIMO radar system to improve the radar range resolution and direction finding performance. The MIMO radar ambiguity function of the system within phase coded waveforms are investigated and used to study the range resolution of our proposed codes. We presented and analyzed a generalized MIMO radar system model for our provided framework, in which Beamforming and estimate MSE are also used to find the direction of the target at receive part. We provided a set of new ternary pulse compression codes, gave a specific example and analyzed the codes' correlation properties and range resolution by using the MIMO radar ambiguity function. Simulation results showed that significant diversity gain could be obtained in MIMO radar system using orthogonal phase coded waveforms. The MIMO

radar system using more receiving antennas outperforms the one having less receiving antennas. The paper is only to introduce the basic concept of our newly provided MIMO radar system with orthogonal pulse compression codes to find the direction of a single fixed target. In the subsequent work, we may consider the Doppler shift effect for moving targets and some complicate radar channel models for the new approach.

Acknowledgement

This work was supported by the Office of Naval Research (ONR) under Grant N00014-07-1-0395, N00014-07-1-1024, and N00014-03-1-0466.

References

[1] D.C. Bell and R.M. Narayanan, "Theoretical aspects of radar imaging using stochastic waveforms", *IEEE Trans. on Signal Processing*, 49(2): pp. 394-400, 2001.

[2] Y. Zhang and R.M. Narayanan, "Design considerations for a real-time random-noise tracking radar", *IEEE Trans. Aerosp. Electron. syst.*, 40(2): pp. 434-445, 2004.

[3] X. Xu and R.M. Narayanan, "Range sidelobe suppression technique for coherent ultra wideband random noise radar imaging", *IEEE Trans. on Antennas and propagation*, 49(12): pp. 1836-1842, 2001.

[4] E. Fishler, A. Haimovich, R. S. Blum, L. J. Cimini, D. Chizhik and R. A. Valenzuela, "Spatial diversity in radars-models and detection performance", *IEEE Trans. on Signal Processing*, 54(3): pp. 823-838, 2006.

[5] D. R. Furhrmann and G. San Antonio, "Transmit beamforming for MIMO radar systems using partial signal correlation", *the 38th Asilomar Conference on Signal, Systems and Computers*, pp. 295-299, Nov. 2004.

[6] B. Friedlander, "Adaptive waveform design for a multi-antenna radar system", *Proceedings of the Asilomar Conference on Sginal, Systems and Computers,*, Oct.29-Nov.1, 2006, Pacific Grove, CA.

[7] B. Friedlander, "Waveform design for MIMO radars", *IEEE Trans. on Aero. Electr. Systems.*, Oct, 2007.

[8] B. Friedlander, "On data-adaptive waveform desgin for MIMO radar", *Proceedings of the Asilomar Conference on Sginal, Systems and Computers,*, Nov.4-Nov.7, 2007, Pacific Grove, CA.

[9] N. Levanon and E. Mozeson, *Radar Signals*, Wiley-IEEE Press, New York, 2004.

[10] M. Dawood and R.M. Narayanan, "Generalised wideband ambiguity function of a coherent ultrawideband random noise radar", *Radar, Sonar and Navigation, IEE Proceedings*, Vol.150, no.5, pp. 379-389, Oct. 2003.

[11] G. San Antonio, D. R. Furhrmann and C. R. Frank, "MIMO radar ambiguity functions", *IEEE Journal of Selected Topics in Signal Processing,* 1(1), pp. 167-177, 2007.

[12] S. Ariyavisitakul, N. Sollenberger, and L. Greenstein, *Introduction to Radar System*, Tata McGraw-Hill, 2001.

[13] A. Dogandzic and A. Nehorai, "Cramer-Rrao bounds for estimating range, velocity ,and direction with an active array," *IEEE Transactions on Signal Processing*, vol.49, no.6, pp. 1122-1137, June 2001.

[14] S. Pasupathy and A. N. Venetsanopoulos, "Optimum active array processing structure and space-time factorability," *IEEE Trans. Aerosp. Electron. syst.*, vol.10, pp. 770-778, 1974.

[15] S. Haykin, J. Litva and T. J. Shepherd, *Radar Array Processing*, Springer-Verlag, New York, 1st edition, 1993.

[16] C. Chen, and P.P. Vaidyanathan "MIMO Radar Ambiguity Properties and Optimization Using Frequency-Hopping Waveforms," *IEEE Transactions on Signal Processing*, 56(13), 6, pp. 5926-5936, Dec.2008.

[17] L. Xu, J. Li and P. Stoica, "Target Detection and Parameter Estimation for MIMO Radar Systems", *IEEE Transactions on Aerospace and Electronic Systems*, Vol.44, no.3, pp. 927-939, July 2008.

[18] L. R. Welch, "Lower bounds on the maximum cross correlation of signals," *IEEE Trans. Inform. Theory*, IT-20, (3), pp. 397-399, 1974.

[19] V. M. Sidelnikov, "On mutual correlation of sequences," *Soviet Math doklady*, 12,pp. 197-201, 1971.

[20] D. V. Sarwate and M .B. Pursley, "Crosscorrelation properties of pseudorandom and related sequences," *Proc. IEEE*, 68, (3), pp. 593-620, 1980.

[21] P. Z. Fan and M. Darnell, *Sequence design for communications applications,* Research Studies Press, John Wiley & Sons Ltd, London, 1996.

[22] P. Z. Fan and M. Darnell, "On the construction and comparison of period digital sequences sets," *IEE Proc. Commun.*, 144, (6), pp. 111-117, 1997.

[23] P. Z. Fan, N. Suehiro, N. Kuroyanagi and X. M. Deng, "A class of binary sequences with zero correlation zone," *IEE Electron.Letter*, Vol.35, no.10: pp. 777-779, 1999.

[24] U. Somaini, "Bianry sequences with good autocorrelation and cross correlation properties," *IEEE Transactions on Aerospace and Electronic Systems*, AES-11, 6, pp. 1226-1231, Nov.1975.

[25] H. Godrich, A. M. Haimovich and R. S. Blum, " Target Localization Techniques and Tools for MIMO Radar", *IEEE Radar Conference, 2008*, pp. 1-6, May. 26-30 2008.

[26] P. Z. Fan and L. Hao, "Generalized Orthogonal Sequences and Their Applications in Synchronous CDMA Systems," *IEICE Trans.Fundamentals*, E832A(11): 1 16, 2000.

[27] S. Matsufuji, N. Suehiro, N. Kuroyanagi and P.Z. Fan, "Two types of polyphase sequence set for approximately synchronized CDMA systems," *IEICE Trans. Fundamentals*, E862A(1): pp. 229-234, Jan. 2003.

[28] H. Torii, M. Nakamura and N. Suehiro, "A new class of zero correlation zone sequences," *IEEE Tran. Inform.Theory*, Vol.50: pp. 559-565, Mar. 2004.

[29] T. Jiang, *Research on Quasi-Optimized Binary Signal Pair and Perfect Punctured Binary Signal Pair Theory,* Ph.D Dissertation: Yanshan University, 2003.

[30] M.A. Richards, *Fundamentals of Radar Signal Processing,* McGraw-Hill, 2005.

Wireless Channel Modeling Using Radar in Foliage Environment: UWB versus Narrowband*

Qilian Liang, *Senior Member, IEEE*

Dept of Electrical Engineering

University of Texas at Arlington

Arlington, TX 76019-0016, USA

Abstract

In this paper, we study the wireless channel modeling in foliage environment, a rich scattering and time-varying environment, based on extensive data collected using UWB and narrowband (200MHz and 400MHz) radars. We apply two approaches to the wireless channel modeling: Saleh and Valenzuela (S-V) method for UWB channel modeling and CLEAN method for narrowband and UWB channel modeling. We validated that UWB echo signals (within a burst) don't hold self-similarity, which means the future signals can't be forecasted based on the received signals and channel modeling is necessary from statistical point of view. Based on the S-V method for UWB channel modeling, in foliage UWB channel, the multi-path contributions arriving at the receiver are grouped into clusters. The time of arrival of clusters can be modeled as a Poisson arrival process, while within each cluster, subsequent multipath contributions or rays also arrive according to a Poisson process. At different distance (near distance, medium distance, and far distance), we observe that the Poisson process parameters are quite different. We also observe that the amplitude of channel coefficient at each path follows Rician distrib-

*Partial material in this paper was presented at IEEE Military Communication Conference, November 2008, San Diego, CA.

ution for medium and far distance, and it's non-stationary for paths from short distance (one of two Rician distributions), and these observations are quite different with the IEEE indoor UWB channel model and S-V indoor channel model. Based on the CLEAN method, the narrowband (200MHz and 400MHz) and UWB channel impulse responses have many similarities: both can be modeled as linear time-variant filter channel. We also studied the large-scale fading using path-loss and log-normal shadowing model for foliage enviroment, and observed that the path-loss exponent is very high because it has rich scattering.

Index Terms : Channel modeling, radar, UWB channel, narrowband channel, CLEAN method, self-similarity, Rician distribution.

1 Introduction and Motivation

The true challenge for new communication technologies is to "make the thing work" in real-world wireless channels. System designers classically focus on the impact of the radio channel on the received signals and use propagation models for testing and evaluation of receiver designs and transmission schemes. Yet, the needs for such models evolve as new applications emerge with different bandwidths, terminal mobility, higher carrier frequencies, new antennas, and so forth. Furthermore, channel characterization also yields the fundamental ties to classical electromagnetics and physics, as well as the answers to some crucial questions in communication and information theory. While many efforts have been spent on indoor channel modeling as well as outdoor open space (or less scattering) environment, wireless channel modeling in foliage (forest) environment has not been studied. In Vietnam, Bosnia, Kosovo, and in the jungles of Columbia, air to ground communnications have been thwarded by the presence of foliage that protects and hides the enemy. In this paper, we study UWB and narrowband channel modeling in foliage environment.

In July 2003, the Channel Modeling sub-committee of study group IEEE 802.15.SG3a pub-

lished the final report regarding the UWB indoor multipath channel model [11]. It is a modified version of the indoor Saleh and Valenzuela (S-V) channel model [17]. The S-V model was developped for NLOS channel, and it has also been applied to LOS channels where it is perhaps less valid, unless LOS components are specifically added [16]. In [12], the aircraft cabin UWB channel modeling based on a measurement campaign conducted on board an Airbus A319 cabin in the frequency range from 3 - 8 GHz was reported. Besides path loss and time dispersion parameters, RMS delay spread, a modified S-V model was derived for this new environment in [12]. In [1], a high-order finite-difference time-domain technique was applied to indoor microwave ultrawideband channel modeling. In [7], an indoor UWB propagation model was studied, which includes the time-ofarrival, angle-of-arrival, and level distributions of a collection of received signals. In [19], an analysis of the joint antenna-channel problem in ultrawideband communications was carried out in order to provide tools for the performance evaluation of antennas while taking into account the system architecture and the radio link scenarios. In [14], a comprehensive statistical model is described for UWB propagation channels that is valid for a frequency range from 310 GHz. It was based on measurements and simulations in the following environments: residential indoor, office indoor, builtup outdoor, industrial indoor, farm environments, and body area networks. The IEEE suggested an initial set of values for the indoor UWB channel model which has a range of less than 10 meters. However, lots of applications of UWB are for outdoor activities such as sense-through-foliage target detection. Forests favor asymmetric threats because the warfighter has a limited sensing capability. Forests provide excellent concealment from observation, ambush, and escape, as well as provide secure bases for enemy Command & Control (C2), weapons caches, and Improvised Explosive Device (IED)/ Weapon of Mass Destruction (WMD) assembly. These have become “the high ground” in fourth-generation warfare, providing a significant strategic advantage. However, no work has been done on the comparison of UWB and narrowband channels in foliage environment.

Very recently, some preliminary works on outdoor UWB channel modeling was reported in [13].

In this paper, we will model the UWB and narrowband channels using UWB and narrowband radars in foliage environment which is a rich scattering and time-varying environment. UWB radar emissions are at a relatively low frequency-typically between 100 MHz and 3 GHz. Additionally, the fractional bandwidth of the signal is very large (greater than 0.2). Such radar sensor has exceptional range resolution that also has an ability to penetrate many common materials (e.g., walls). Law enforcement personnel have used UWB ground penetrating radars (GPRs) for at least a decade. Like the GPR, sense-through-foliage radar takes advantage of UWB's very fine resolution (time gating) and low frequency of operation.

The rest of this paper is organized as follows. In Section 2, we summarize the measurement and collection of data we used in this paper. In Section 3, we demonstrate that the UWB reflected signal in foliage environment does not hold self-similarity and validate that outdoor channel modeling is necessary. In Section 4, we present our outdoor UWB channel model in rich scattering and time-varying environment. In Section 5, we study the channel impulse response based on CLEAN method for narrowband and UWB channels. In Section 6, large scale fading in foliage environment is modeled. We conclude this paper in Section 7.

2 Experiment Setup and Data Collection

Our work is based on the data collected in UWB radar-based sense-through-foliage experiment in late summer and fall, so it's a rich scattering environment. Because of wind or different temperature in dense forest, it's also a time-varying environment. The foliage experiment was constructed on a seven-ton man lift, which had a total lifting capacity of 450 kg. The limit of the lifting capacity was reached during the experiment as essentially the entire measuring apparatus was placed on the lift. The principle pieces of equipment secured on the lift are listed below:

- Dual Antenna mounting stand
- Two antennas
- Rack system (2)
- Barth pulser
- Tektronix model 7704 B oscilloscope
- IBM laptop
- HP signal Generator
- Custom RF switch and power supply
- Weather shield (small hut)

Figure 1 shows the experiment under a weather shield that was constructed on the lift. The weather shield was needed to protect the equipment hoisted up with the lift. A negative side effect of this weather shield was to provide a significant sail area at the maximum lever arm relative to the lift stabilizing jacks on the ground. Lift stabilization was achieved using cables and anchor points. A system of 4 tethers was used under gusty conditions. The transmit and receive rotating platform systems were built using heavy gauge Unistruts, thrust bearings, and roller bearings for the multiple axes of freedom. The importance of the rigidity of the antenna mounts the and axis of rotation was in the establishment and maintenance of the antenna alignment during the measurement. See Figure 2, for a photographic side view of the equipment platform on the lift.

Throughout this work, a Barth pulse source (Barth Electronics, Inc. model 732 GL) was used. The pulse generator uses a coaxial reed switch to discharge a charge line for a very fast rise time pulse outputs. The model 732 pulse generator provides pulses of less than 50 picoseconds (ps) rise

time, with amplitude from 150 V to greater than 2 KV into any load impedance through a 50 ohm coaxial line. The generator is capable of producing pulses with a minimum width of 750 ps and a maximum of 1 microsecond. This output pulse width is determined by charge line length for rectangular pulses, or by capacitors for 1/e decay pulses. The data collections were extensive. 20 different positions were used, and 35 independent collections were performed at each position.

For the UWB data we used in this paper, each sample is spaced at 50 picosecond interval, and 16,000 samples were collected for each collection for a total time duration of 0.8 microseconds at a rate of approximately 20 Hz. The Barth pulse source was operated at low amplitude (1 KW peak power) and 35 pulses reflected signal were averaged for each collection. Significant pulse-to-pulse variability was noted for these collections. We plot the transmitted pulse (one realization) in Fig. 3a) and the received echos in one collection in Fig. 3b (averaged over 35 pulses).

For comparison, we also studied narrowband (200MHz and 400MHz) radar signal propagation. Henry Radio preamplifiers were model 50B-200 and 50B-400 for 200MHz and 400MHz respectively. The Henry Radio power amplifiers were TEMPO-2002A and TEMPO-2400A for 1 KW pulsed at 200MHz and 400MHz respectively. The amplifier was speced at a minimum bandwidth of 2 MHz around it center frequency. The source for 200MHz and 400MHz narrow band wave signal was an Agilent 8648A signal generator. For the data we used in this paper, each sample is space at 50 picosecond interval, and 16,000 samples were collected for each collection for a total time duration of 0.8 microseconds at a rate of approximately 20 Hz. Fig. 4a shows the transmitted signal and Fig. 4b shows the received echos (averaged over 35 pulses) for 200MHz narrowband radar. Fig. 5a shows the transmitted signal and Fig. 5b shows the received echos (averaged over 35 pulses) for 400MHz narrowband radar. The data collections were extensive. Twenty different positions were used, and thirty-five collections were performed at each position for UWB, 200MHZ, and 400MHz radars.

3 Self-Similarity Properties of UWB Reflected Signals

It has been observed that ethernet video/voice/data traffic have self-similarity [21] [20]. But the self-similarity of UWB signals has not been studied. Here we briefly present its definition [8]. Given a zero-mean, stationary time-series $X = (X_t; t = 1, 2, 3, \cdots)$, we define the m-aggregated series $X^{(m)} = (X_k^{(m)}; k = 1, 2, 3, \cdots)$ by summing the original series X over nonoverlapping blocks of size m. Then it's said that X is H-self-similar, if, for all positive m, $X^{(m)}$ has the same distribution as X rescaled by m^H. That is,

$$X_t \stackrel{\triangle}{=} m^{-H} \sum_{i=(t-1)m+1}^{tm} X_i \quad \forall m \in N \tag{1}$$

If X is H-self-similar, it has the same autocorrelation function $r(k) = E[(X_t - \mu)(X_{t+k} - \mu)]/\sigma^2$ as the series $X^{(m)}$ for all m, which means that the series is distributionally self-similar: the distribution of the aggregated series is the same as that of the original.

Self-similar processes can show *long-range dependence*. A process with long-range dependence has an autocorrelation function $r(k) \sim k^{-\beta}$ as $k \to \infty$, where $0 < \beta < 1$. The degree of self-similarity can be expressed using *Hurst* parameter $H = 1 - \beta/2$. For self-similar series with long-range dependence, $1/2 < H < 1$. As $H \to 1$, the degree of both self-similarity and long-range depence increases.

One method that has been widely used to verify self-similarity is the *variance-time plot*, which relies on the slowly decaying variance of a self-similar series. The variance of $X^{(m)}$ is plotted against m on a log-log plot, and a straight line with slope $(-\beta)$ greater than -1 is indicative of self-similarity, and the parameter H is given by $H = 1 - \beta/2$. We use this method in this paper. In Fig. 6, we plot the variance of $X^{(m)}$ against m on a log-log plot for 10 different UWB data collections. From this figure, it's very clear that **the UWB signal does not have self-similarity** because its trace has slope lower than -1. This conclusion means that we can't use current received signals

to forecast future reflected signals within one collection, so channel modeling is very important to UWB outdoor channel because the charateristics of the future reflected signal could be known in advance if its channel can be modelled.

4 UWB Channel Modeling Based on S-V Approaches

4.1 Introduction to Channel Modeling for Indoor UWB Channel

In the S-V model [17], the arrival of clusters is modelled as a Poisson arrival process with a rate Λ, while within each cluster, subsequent multipath contributions or rays also arrive according to a Poisson process with a rate λ (see Fig. 7). In the S-V model, the magnitude of the k-th path within the l-th cluster follows a Rayleigh distribution, and the phase of each path is assumed to be a statistically independent random variable over $[0, 2\pi)$. Besides, the average Power Decay Profile (PDP) is characterized by an exponential decay of the amplitude of the clusters, and a different exponential decay for the amplitude of the received pulses within each cluster, as shown in Fig. 8. In the IEEE UWB indoor channel model [11], the cluster approach was adopted (same as S-V model), but a log-normal distribution was suggested for characterizing the multi-path gain amplitude, and an additional log-normal variable was introbuced for representing the fluctuations of the total multipath gain. Besides, the phase of each path is assumed to be either 0 or π with equal probability.

4.2 Outdoor UWB Channel Modeling

4.2.1 Cluster Arrival and Power Decay Profile

We study the outdoor UWB signal propagation in three cases: short distance (less than $55m$), medium distance ($55m$–$85m$), and far distance (above $85m$ and up to $120m$ in this study). In the

data collection, each sample is spaced at 50 picosecond interval, so these cases are corresponding to samples 1–7333 for short distance, samples 7333–11333 for medium distance, and samples 11334–16000 for far distance. In Fig. 9, we plot the power profile of the received echos (averaged over 30 collections to eliminate the effect of random noise and each collection was averaged based on 35 pulses) for the three different cases. Since the transmitted pulse (as plotted in Fig. 3a) is a very narrow impulse pulse (like a delta function in time domain), we analyzed the channel property based on the received echos power profile plotted in Fig. 9, and similar methodology was also used in S-V model studies [17].

Observe Fig. 9, multi-path contributions arrive at the receiver grouped into clusters. The time of arrival of clusters can be modeled as a Poisson arrival process with a rate Λ, while within each cluster, subsequent multipath contributions or rays also arrive according to a Poisson process with a rate λ (see Fig. 7). We define:

- T_l = the arrival time of the first path of the l-th cluster;
- $\tau_{k,l}$ = the delay of the k-th path within the l-th cluster relative to the first path arrival time T_l;
- Λ = the cluster arrival rate;
- λ = the ray arrival rate, i.e., the arrival rate of the paths within each cluster.

By definition, we have $\tau_{0l} = T_l$. The distributions of the cluster arrival time and the ray arrival time are given by

$$p(T_l|T_{l-1}) = \Lambda \exp\left(-\Lambda(T_l - T_{l-1}), l > 0\right)$$
$$p(\tau_{k,l}|\tau_{(k-1),l}) = \lambda \exp\left(-\lambda(\tau_{k,l} - \tau_{(k-1),l})\right), k > 0 \quad (2)$$

The above observations are very similar as that for the indoor UWB channel. Specifically, we also

observed the Λ and λ are quite different for three different cases.

- Observe Fig. 9a for short distance, Λ (1/ns) is around 0.02 (one cluster in every $50ns$ or 1000 samples), and λ (1/ns) is around 0.4 (one path in every $2.5ns$ or 50 samples). Perhaps it's because some major scatters in short distance (such as tree stems) reflected signals, so some paths are quite dominant.

- Observe Fig. 9b for medium distance, clusters arrive quite often. Λ (1/ns) is around 0.05 (one cluster in every $20ns$ or 400 samples), and λ (1/ns) is around 1 (one path in every $1ns$ or 20 samples).

- Observe Fig. 9c for far distance, clusters almost always arrive (because of rich scattering), so Λ (1/ns) is around 0.5 (one cluster in every $2ns$ or 20 samples), and λ (1/ns) is around 4 (one path in every $250ps$ or 5 samples). Perhaps it's because of rich scattering, every path has very similar power level.

Besides, the average PDP can be represented by an exponential decay of the amplitude of the clusters, and a different exponential decay for the amplitude of the received pulses within each cluster, as shown in Fig. 8.

4.2.2 Statistical Distribution of Channel Coefficients

We also study the statistical distributions of each given path. We plot the histogram for some sample values of the above three cases based on 30 collections and each collection is averaged over 35 pulses. Short distance samples are based on samples 5001–6000; medium distance samples are based on samples 8001–9000; and far distance samples are based on samples 12001–13000. Since the samples are very close (within 7.5m distance), so their path-loss effect can be ignored. For each case, we have 30000 samples, and we plot their histogram in Fig. 10.

First, observe Fig. 10c for far distance, the histogram can be almost perfectly modelled by a non-zero-mean Gaussian distribution, which means the amplitude of the channel coefficient follows a Rician distribution,

$$p_\alpha(x) = \frac{x}{\sigma^2}\exp\{-\frac{x^2+s^2}{2\sigma^2}\}I_0(\frac{xs}{\sigma^2}) \quad x \geq 0 \tag{3}$$

where s is the mean value of Gaussian and $I_0(\cdot)$ is the zero order modified Bessel function. This kind of channel is known as Rician fading channel. A Rician channel is characterized by two parameters, Rician factor K which is the ratio of the direct path power to that of the multipath, i.e., $K = s^2/2\sigma^2$, and the Doppler spread (or single-sided fading bandwidth) f_d. Similarly, Fig. 10b for medium distance, the histogram can be approximately modelled by a non-zero-mean Gaussian distribution, which means the amplitude of the channel coefficient follows a Rician distribution. Observe Fig. 10a for short distance, the histogram can be approximately modelled by two non-zero-mean Gaussian distributions, which means it's non-stationary, and the amplitude of the channel coefficient follows one of two Rician distributions. We analyzed the collected data and observed that K is in the range of -5dB to 5dB, which means the direct path energy and scattered paths energy are very similar. Our observations are different with the observations made in [2] for forest environment where K is in the range of 8dB-24dB. In [2], the transmitter and receiver in [2] are not co-located, i.e., it's an one-way communication, so direct LoS has much higher energy than the scattered paths.

The above observations are quite different with the indoor UWB channel model (log-normal distribution) and S-V model (Rayleigh distribution). The sign of channel coefficient is either +1 or -1, i.e., its phase is either 0 or π, which matches the IEEE indoor UWB channel model. The major reason why our observations are different from the S-V model and IEEE indoor UWB channel model is because our foliage environment is time-varying and has rich scattering. The S-V model and IEEE indoor UWB channel model were obtained in indoor

enviroment, where the number of scatters is much less, and most scatters are time-invariant.

5 Wireless Channel Modeling Based on CLEAN Method

We apply the CLEAN algorithm to obtain the UWB channel model based on the transmitted pulses and received echos. The CLEAN algorithm was first introduced in [10] and has been applied to UWB measurements [6][18] and it assumes that the channel is a series of impulses which is consistent with the tapped-delay line channel model. This algorithm searches the received echos iteratively with the template to find the maximum correlation [3]. The steps are [16]:

1. Calculate the autocorrelation of the template $r_{ss}(t)$ and the cross-correlation of the template with the received waveform $r_{sy}(t)$.

2. Find the largest correlation peak in $r_{sy}(t)$, record the normalized amplitudes α_k and relative time delay τ_k of the correlation peak.

3. Subtract $r_{ss}(t)$ scaled by α_k from $r_{sy}(t)$ at the time delay τ_k.

4. If a stopping criterion (e.g., a minimum threshold on the peak correlation) is not met, go to step 2. Otherwise stop.

Based on the CLEAN method, we successfully obtained the channel impulse responses for all transmit waveforms and receive echoes. For illustration purposes, in Figs. 11, 12, and 13, we plot the channel impulse responses for 200MHz, 400MHz, and UWB channels using CLEAN method in two experiments. Observe that for all channels, channel impulse responses have many similarities: all can be modeled as linear time-variant filter channel, which is a more general case of the S-V model. The channel gains from UWB channel is much higher (e.g., 10^7 to 10^8 level) than that from narrowband channels. In $400MHz$ narrowband channel, the channel gains are in a range of 10^4 to

10^5 level, and in $200MHz$ narrowband channel, the channel gains are in a range of 10^6 to 10^7 level. Such differences between UWB channel and narrowband channel are because UWB signals could penetrate through the foliage, so more energy is kept during the propagation. Most paths of the linear time-invariant channel have gains zero, which means the intersymbol interferences because of the channel memory are very low.

6 Large Scale Fading Channel Modeling

It is well known that path-loss and log-normal shadowing model model can be represented as [15],

$$PL(d)[dB] = \bar{PL}(d_0) + 10n\log(\frac{d}{d_0}) + X_\sigma \tag{4}$$

where n is the path-loss exponent which indicates the rate at which the path loss increases with distance; d_0 is the close-in reference distance which is determined from measurements close to the transmitter, and d is the distance to the transmitter; X_sigma is a zero-mean Gaussian distributed random variable (in dB) with standard deviation σ (also in dB). The log-normal distribution describe the random shadowing effects which occur over a large number of measurement locations which have the same T-R separations, but have different levels of clutter on the propagation path. Large-scale fading and time dispersion parameters of UWB channel in underground mines were studied in [5][4], and it was reported that the path loss modeling can be simplified by assuming that the frequency dependence and the distance dependence can be treated independently of each other. In this paper, we focus on path-loss and log-normal shadowing in foliage environment where high level of clutter exists.

Based on all the data, i.e., 20 different positions were used, and 35 independent collections were performed at each position, we obtained that the path-loss exponent $n = 5.1$ for UWB, and $n = 14.1$ for narrowband (200MHz). The log-normal shadowing std $\sigma = 8.7dB$ for UWB and $\sigma = 3.3dB$

for narrowband (200MHz). The path-loss exponent in foliage is much higher than that in other enviroments such as free space ($n = 2$) or obstructed in factories ($n = 2to3$) [15] because foliage is a rich scattering enviroment. In Fig. 14, we plot the measured signal power versus the distance to the transmitter. Observe Fig. 14, the signals fade much more quickly in narrowband than that in UWB because UWB signals can panetrate through the foliage, so more echos are collected. But UWB signal has more log-normal shadowing effects because of different foliage environment, and the narrowband signals are less sensitive to the foliage environment change. Observe Fig. 14b, in the closer distance to the narrowband radar, the signal power is even lower than that in a further distance. For example, the signal power is about 70dB at distance $d = 31m$ (i.e., $\log(d) = 1.5$), and the signal power is about 80dB at distance $d = 63m$ (i.e., $\log(d) = 1.8$), which is because there is no much major scatters (e.g., trunck) in the closer area of the narrowband radar, but UWB radar could get enough scattering from the foliage (see Fig. 1). In contrast, the path loss exponents were found to range from 2.2-4.3 in [2]. It is because transmitters and receivers were separated by distances ranging from 4 to 50 meters in [2], where the transmitter and receiver are co-located, so two-way transmissions happened in our experiment.

7 Conclusions

In this paper, we studied the statistical modeling for outdoor wireless channels (200MHz, 400MHz, and UWB) in rich scattering and time-varying environment based on extensive data collected using narrowband and UWB radars. We validated that UWB echo signals (within a burst) don't hold self-similarity, which means the future signals can't be forecasted based on the received signals and channel modeling is necessary from statistical point of view. In outdoor UWB channel, the multi-path contributions arrive at the receiver are grouped into clusters. The time of arrival of clusters can be modeled as a Poisson arrival process, while within each cluster, subsequent multipath con-

tributions or rays also arrive according to a Poisson process. At different distance (short distance, medium distance, and far distance), we observed that the Poisson process parameters are quite different. We also observed that the amplitude of channel coefficient at each path follows Rician distribution for medium and far distance, and it's non-stationary for paths from short distance (one of two Rician distributions), and these observations are quite different with the IEEE indoor UWB channel model and S-V model. Using CLEAN method, we observed that for all channels, channel impulse responses have many similarities: all can be modeled as linear time-variant filter channel, which is a more general case of the S-V model. We also studied the large-scale fading using path-loss and log-normal shadowing model, and observed that the path-loss exponent is very high in foliage environment because it has rich scattering. Narrowband signal fades more quickly than UWB signal in foliage environment and UWB signal has higher path-loss shadowing effects than narrowband signal in foliage environment.

References

[1] A. Alighanbari, and C. D. Sarris, "Parallel Time-Domain Full-Wave Analysis and System-Level Modeling of Ultrawideband Indoor Communication Systems," *IEEE Transactions on Antennas and Propagation*, vol 57, no. 1, Jan. 2009, pp. 231 - 240.

[2] C. R. Anderson, H. I. Volos, W. C. Headley, F.C.B. Muller, R. M. Buehrer, "Low Antenna Ultra Wideband Propagation Measurements and Modeling in a Forest Environment," *IEEE Wireless Communications and Networking Conference*, 2008, pp.1229-1234, March 2008.

[3] R. M. Buehrer, et al, "Characterization of the UWB channel," *IEEE Conf on Ultra Wideband Systems and Technologies*, pp. 26-31, Reston, VA, Nov 2003.

[4] A. Chehri, P. Fortier, H. Aniss, and P. M. Tardif, "UWB spatial fading and small scale characterization in underground mines," *Proceedings of the 23rd Biennial Symposium on Communications*, pp. 213218, Kingston, Canada, May-June 2006.

[5] A. Chehri, P. Fortier, and P. M. Tardif, "Large-Scale Fading and Time Dispersion Parameters of UWB Channel in Underground Mines," *International Journal of Antennas and Propagation*, vol. 2008, Article ID 806326, 10 pages, 2008.

[6] R. J.-M. Cramer, *An Evaluation of Ultrawideband Propagation Channels*, Ph.D Dissertation, USC, 2000.

[7] R. J.-M Cramer, R. A. Scholtz, and M. Z. Win, "Evaluation of an ultra-wide-band propagation channel," *IEEE Transactions on Antennas and Propagation*, vol 50, no. 5, May 2002, pp. 561 - 570.

[8] M. E. Crovella and A. Bestavros, "Self-similarity in world wide web traffic: evidence and possible causes," *IEEE Trans. on Networking*, vol. 5, no. 6, pp. 835-846, Dec 1997.

[9] M. W. Garrett and W. Willinger, "Analysis, modeling and generation of self-similar VBR video traffic," *SIGCOMM'94*, pp. 269-280, Aug. 1994, London, UK.

[10] J. A. Hogbom, "Aperture synthesis with a non-regular distribution of interferometer baseline," *Atronomy and Astrophysics Supplement Ser.*, vol. 15, 1974.

[11] IEEE 802.15.SG3a, "Channel modeling sub-committee report final," *IEEE P802.15-02/490r1-SG3a*, Feb 2003.

[12] J. Jemai, R. Piesiewicz, R. Geise, I. Schmidt, M. Schwark, M. Schirrmacher, T. Kurner, "UWB channel modeling within an aircraft cabin," *IEEE International Conference on Ultra-Wideband*, vol. 2, pp. 5-8, Sept 2008.

[13] Q. Liang, X. Cheng, "Wireless Channel Modeling in Foliage Environment: UWB versus Narrowband," *IEEE Military Communication Conference*, November 2008, San Diego, CA.

[14] A. F. Molisch, et al, "A Comprehensive Standardized Model for Ultrawideband Propagation Channels," *IEEE Transactions on Antennas and Propagation*, vol 54, no. 11, Part 1, Nov. 2006, pp. 3151 - 3166.

[15] T. S. Rappaport, *Wireless Communications: Principles and Practice*, Prentice Hall, Upper Saddle River, NJ, 2002.

[16] J. H. Reed, *An Introduction to Ultra Wideband Communication Systems*, Prentice Hall, Upper Saddler River, NJ, 2005.

[17] A. A. Saleh and R. A. Valenzuela, "A statistical model for indoor multipath propagation," *IEEE J. on Selected Areas in Communications*, vol. 5, no. 2, pp. 128-137, Feb 1987.

[18] R. A. Scholtz, M. Z. Win, and J. M. Cramer, "Evaluation of the Characteristics of the ultra-wideband propagation channel," *Proc of Antenna and Propagation Symposium*, vol. 2, no. 626-630, 1998.

[19] A. Sibille, C. Roblin, S. Bories, and A. C. Lepage, "A Channel-Based Statistical Approach to Antenna Performance in UWB Communications," *IEEE Transactions on Antennas and Propagation*, vol 54, no. 11, Part 1, Nov. 2006 pp. 3207 - 3215.

[20] W. Stallings, *High-Speed Networks: TCP/IP and ATM Design Principles*, Upper Saddle River, NJ, 1998.

[21] W. Willinger, M. S. Taqqu, R. Sherman, and D. V. Wilson, "Self-similarity through high-variability: statistical analysis of ethernet LAN traffic at the source level," *IEEE Trans. on Networking*, vol. 5, no. 1, pp. 71-86, Feb 1997.

List of Figures

1 This figure shows the lift with the experiment. The antennas are at the far end of the lift from the viewer under the roof that was built to shield the equipment from the elements. This picture was taken in September with the foliage largely still present. The cables coming from the lift are a ground cable to an earth ground and one of 4 tethers used in windy conditions. 18

2 This figure shows the experiment on top of the lift under the hut built for weather protection. The black box in the foreground is a weather resistant box that held the oscilloscope and Barth pulser during the testing. 19

3 UWB radar Transmitted pulse and received echos in one experiment. (a) Transmitted pulse. (b) Received echos. 20

4 Narrowband radar (200MHz) transmitted pulse and received echos in one experiment. (a) Transmitted pulse. (b) Received echos. 21

5 Narrowband radar (400MHz) transmitted pulse and received echos in one experiment. (a) Transmitted pulse. (b) Received echos. 22

6 The *variance-time* plot of 10 UWB data collections, which demonstrates that UWB reflected signals are not self-similar within each collection. 23

7 An illustration of the channel impulse response in S-V model. 23

8 An illustration of the double exponential decay of the mean cluster power and the ray power within clusters in S-V model. 23

9 The power profile for three different cases: (a) short distance, (b) medium distance, and (c) far distance. 24

10 The histograms and their approximation using Gaussian distributions (dashed lines). The histograms are based on 30 collections and each collection is averaged over 35 pulses. (a) short distance samples, (b) medium distance samples, and (c) far distance samples. 25

11 The channel impulse responses for 200MHz channel using CLEAN method in two experiments. 26

12 The channel impulse responses for 400MHz channels using CLEAN method in two experiments. 27

13 The channel impulse responses for UWB channels using CLEAN method in two experiments. 28

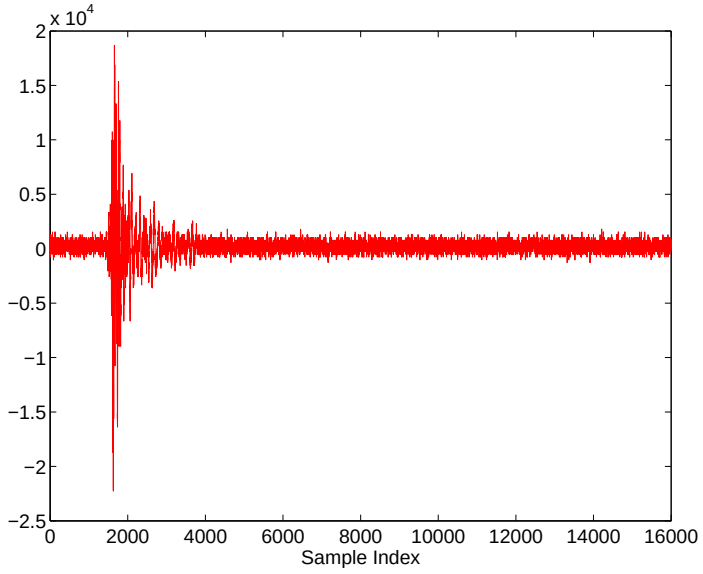
14 The measured signal power versus the distance to the transmitter. (a) UWB signal, and (b) 200MHz narrowband signal. 29



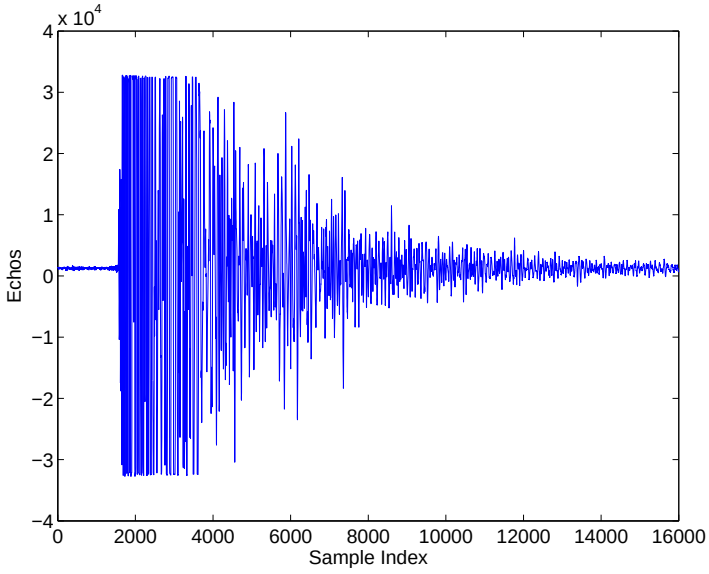
Figure 1: This figure shows the lift with the experiment. The antennas are at the far end of the lift from the viewer under the roof that was built to shield the equipment from the elements. This picture was taken in September with the foliage largely still present. The cables coming from the lift are a ground cable to an earth ground and one of 4 tethers used in windy conditions.



Figure 2: This figure shows the experiment on top of the lift under the hut built for weather protection. The black box in the foreground is a weather resistant box that held the oscilloscope and Barth pulser during the testing.



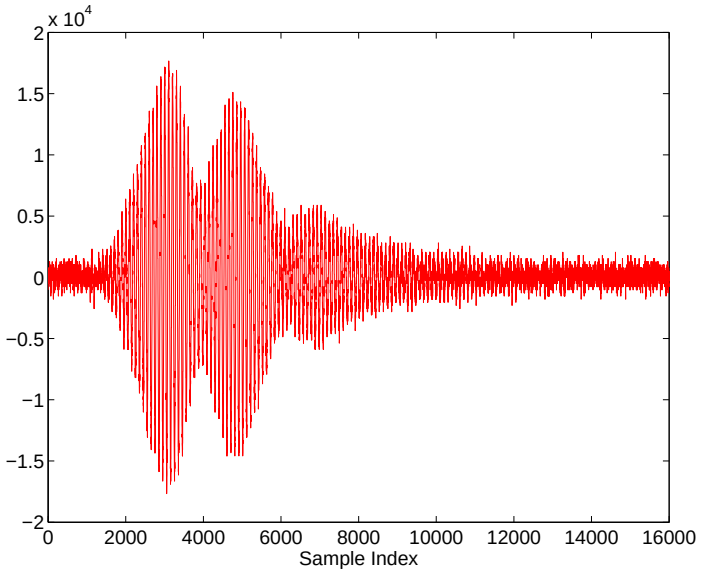
(a)



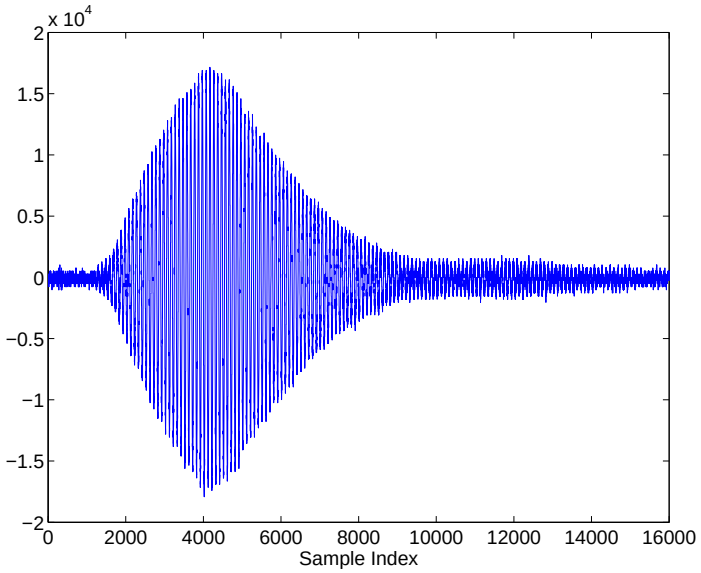
(b)

Figure 3: UWB radar Transmitted pulse and received echos in one experiment. (a) Transmitted pulse. (b) Received echos.

.

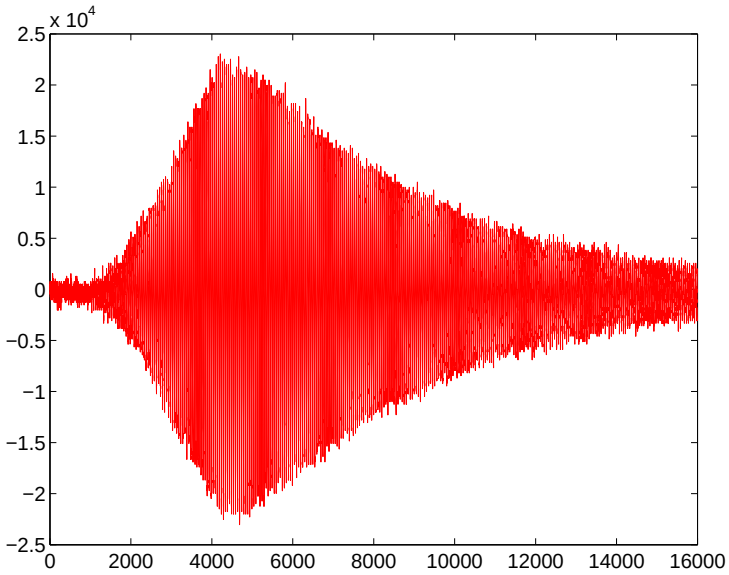


(a)

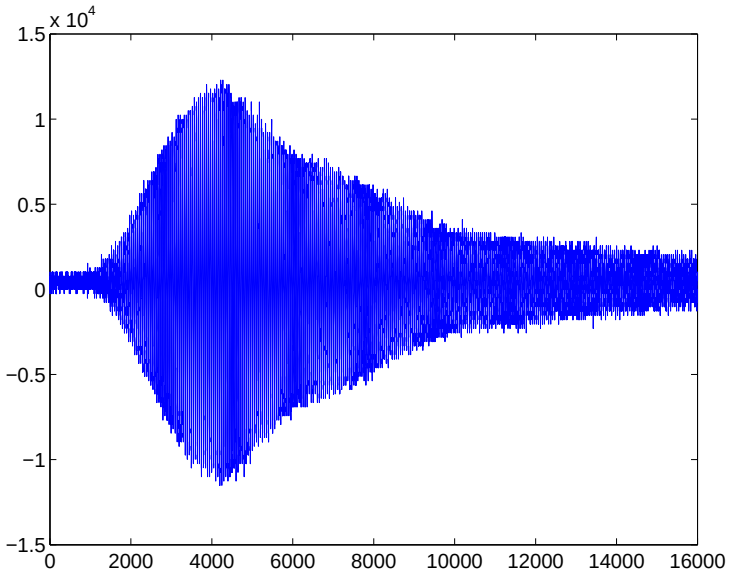


(b)

Figure 4: Narrowband radar (200MHz) transmitted pulse and received echos in one experiment. (a) Transmitted pulse. (b) Received echos.



(a)



(b)

Figure 5: Narrowband radar (400MHz) transmitted pulse and received echos in one experiment. (a) Transmitted pulse. (b) Received echos.

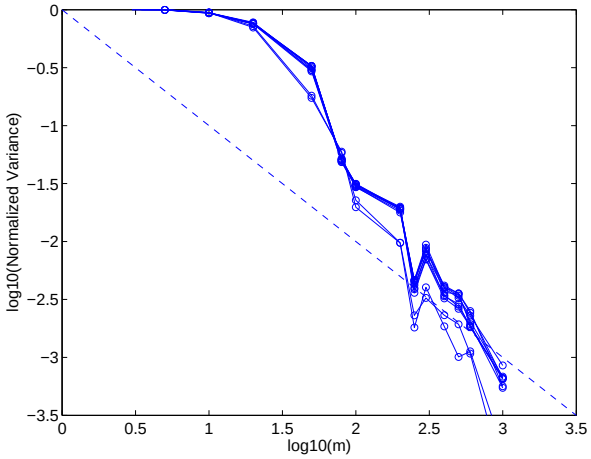


Figure 6: The *variance-time* plot of 10 UWB data collections, which demonstrates that UWB reflected signals are not self-similar within each collection.

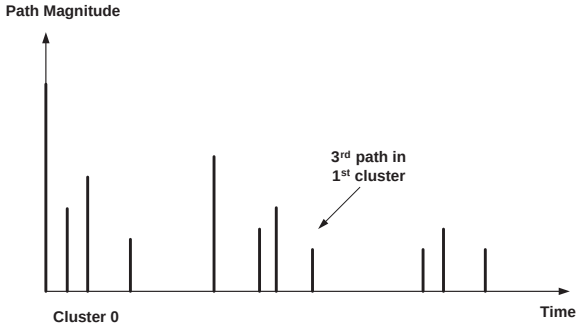


Figure 7: An illustration of the channel impulse response in S-V model.

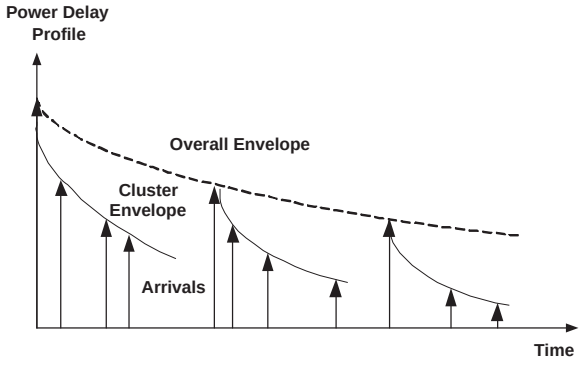
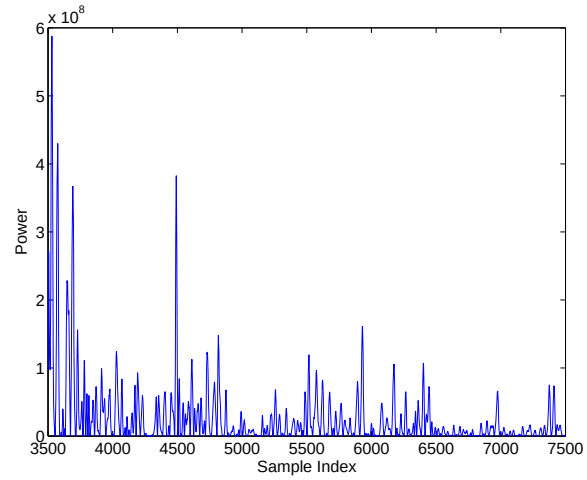
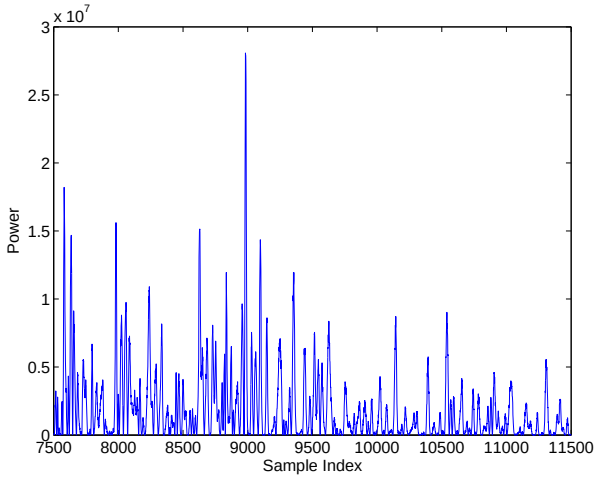


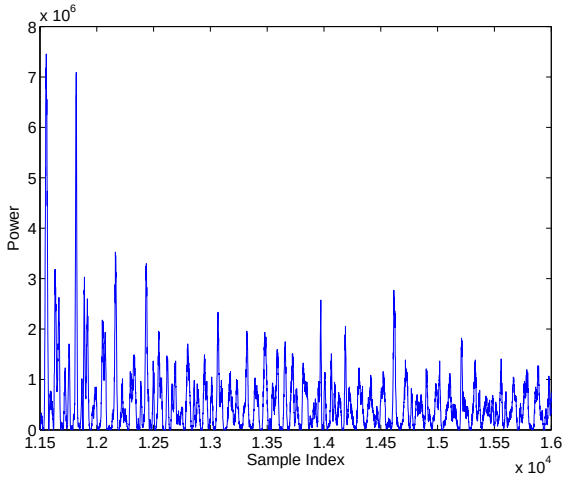
Figure 8: An illustration of the double exponential decay of the mean cluster power and the ray power within clusters in S-V model.



(a)

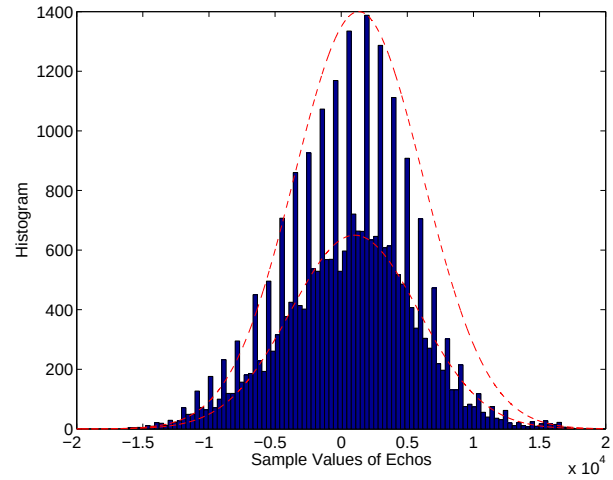


(b)

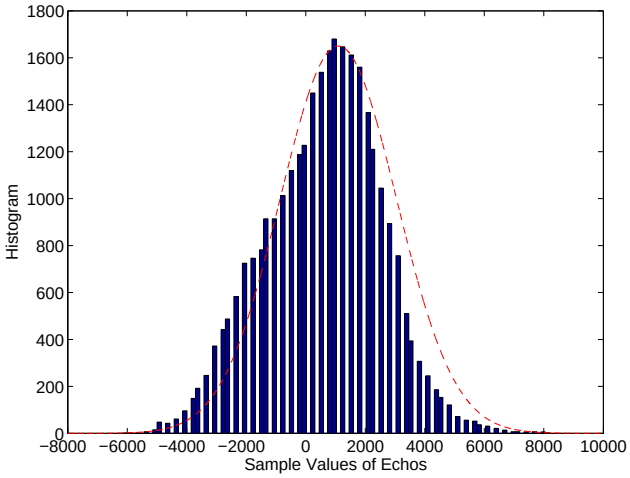


(c)

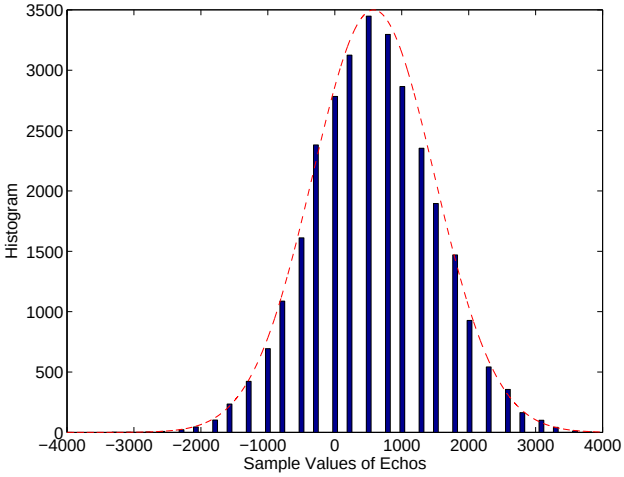
Figure 9: The power profile for three different cases: (a) short distance, (b) medium distance, and (c) far distance.



(a)

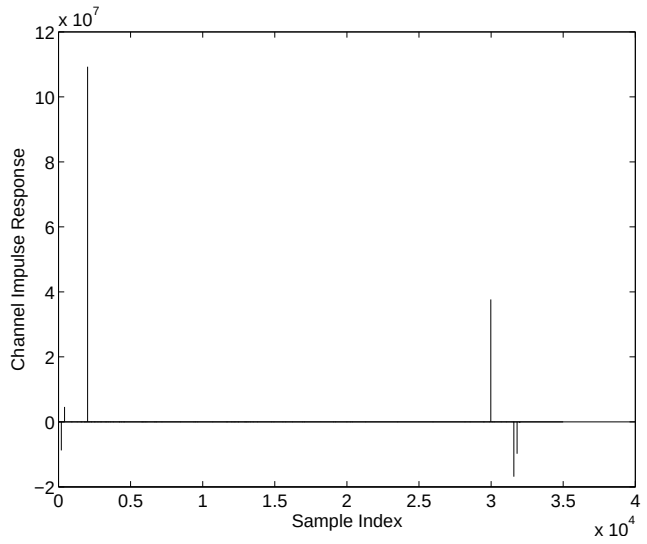


(b)

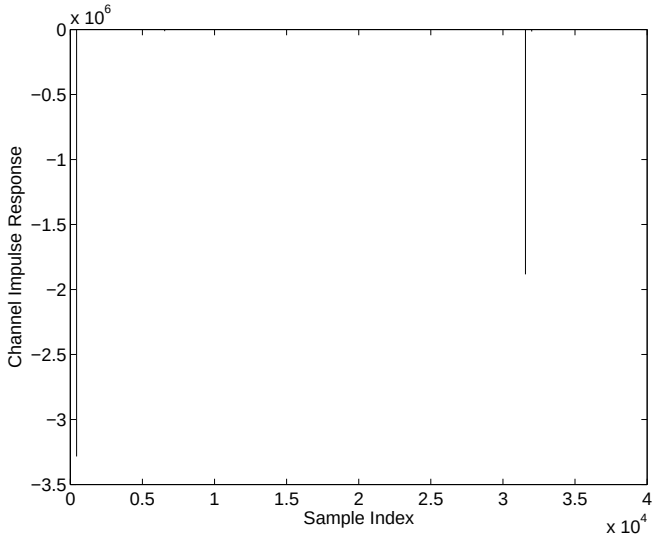


(c)

Figure 10: The histograms and their approximation using Gaussian distributions (dashed lines). The histograms are based on 30 collections and each collection is averaged over 35 pulses. (a) short distance samples, (b) medium distance samples, and (c) far distance samples.

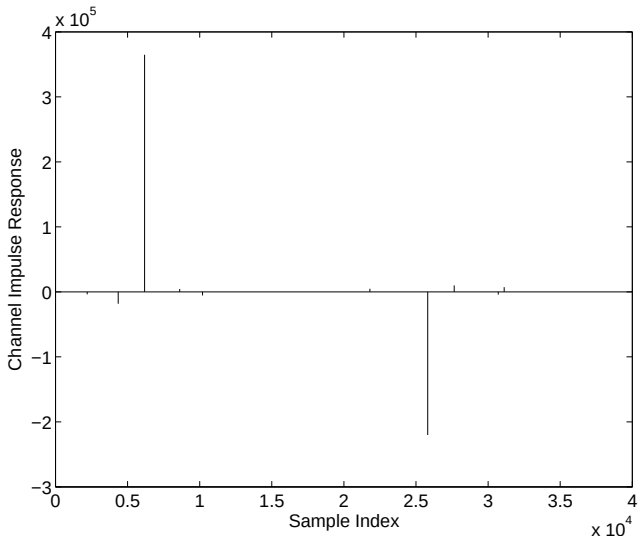


(a)

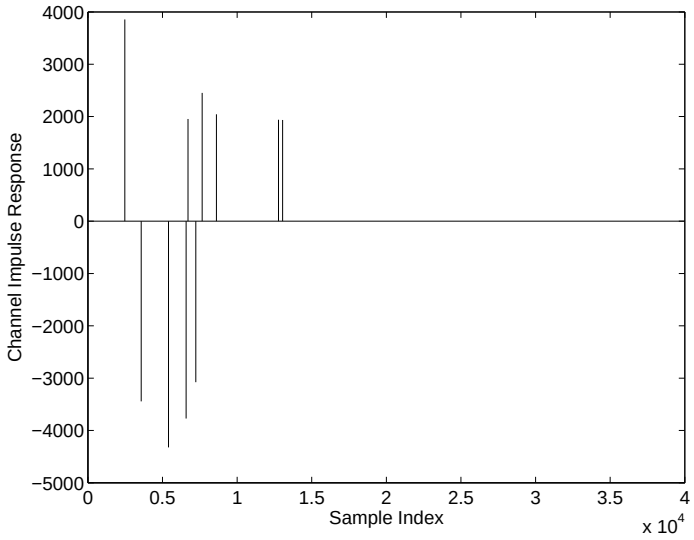


(b)

Figure 11: The channel impulse responses for 200MHz channel using CLEAN method in two experiments.

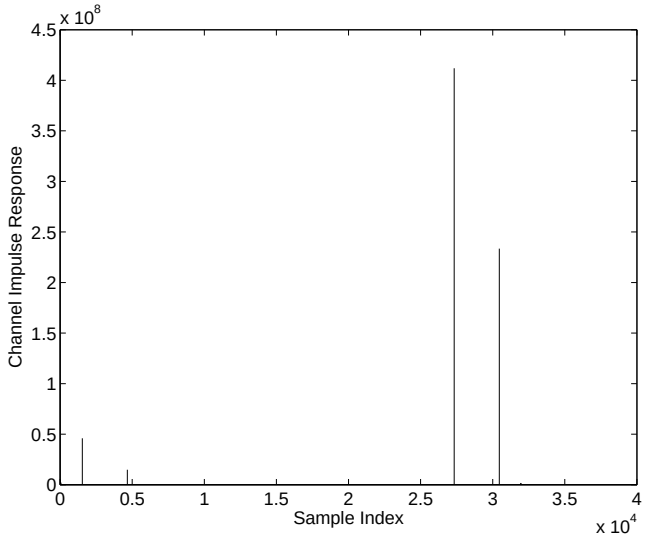


(a)

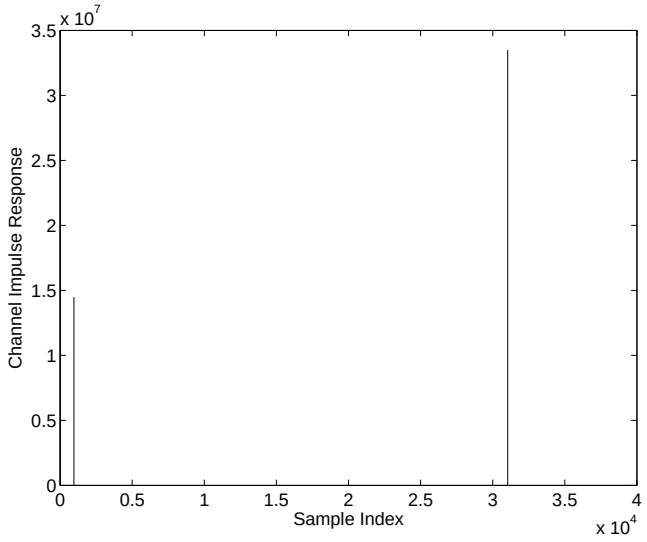


(b)

Figure 12: The channel impulse responses for 400MHz channels using CLEAN method in two experiments.

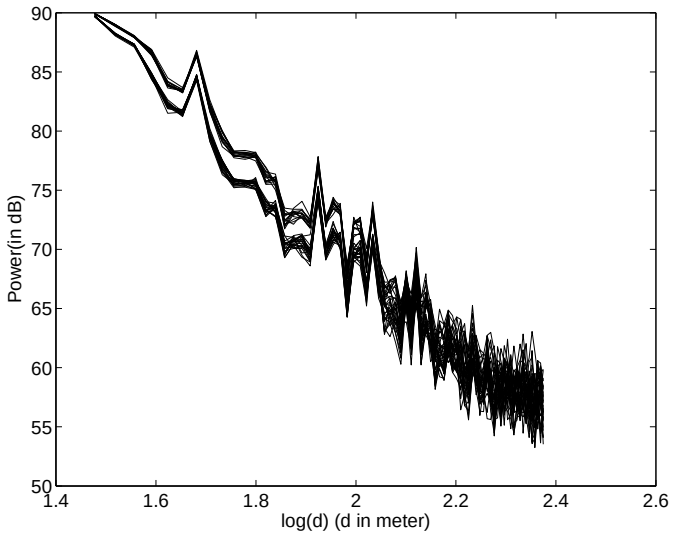


(a)

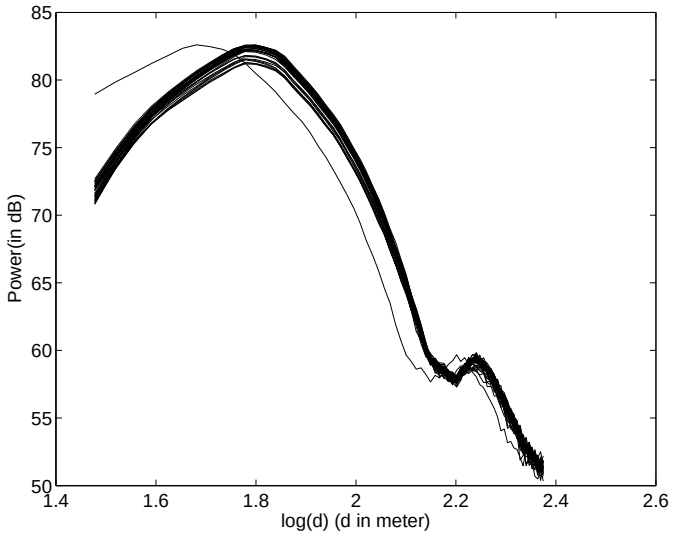


(b)

Figure 13: The channel impulse responses for UWB channels using CLEAN method in two experiments.



(a)



(b)

Figure 14: The measured signal power versus the distance to the transmitter. (a) UWB signal, and (b) 200MHz narrowband signal.

Collaborative Multi-Target Detection in Radar Sensor Networks

Hung D. Ly
Department of Electrical and Computer Engineering
Texas A&M University
College Station, TX 77843, USA
Email: hungly@tamu.edu

Qilian Liang
Dept of Electrical Engineering
University of Texas at Arlington
Arlington, TX 76019-0016, USA
E-mail: liang@uta.edu

Abstract

In many military and civilian applications, estimating the number of targets in a region of interest plays a primary role in performing important tasks such as target localization, classification, recognition, tracking, etc. Such an estimation problem is however very challenging since the number of targets is time-varying, targets' state is fluctuating, and various kinds of targets might appear at the same time in the field of interest. In this paper, we develop a framework for estimating the number of targets in a sensing area using Radar Sensor Networks (RSNs). Specifically, the multi-target detection problem is first formulated. Models of signals, interference (e.g., clutter, jamming, and interference between radars), and noise at radar sensors are studied. A Maximum Likelihood Multi-Target Detection (ML-MTD) algorithm to combine received measurements and estimate the number of targets present in the sensing area is then proposed. We evaluate multi-target detection performance using RSNs in terms of the probability of miss detection P_{MD} and the root mean square error (RMSE). Simulation results show that multi-target detection performance of the RSNs is much better than that of single radar systems.

Index Terms : waveform design, diversity, target detection, radar sensor networks.

1 Introduction and Motivations

Radar sensor networks (RSNs) are networks of distributed radar sensors which collaboratively operate and are deployed ubiquitously on airborne, surface, and unmanned vehicles in a large geographical area. Radar sensors have capabilities for radar sensing, signal processing, and wireless communications. In RSNs, radar sensors are networked together in an ad-hoc fashion, i.e., they do not depend on any preexisting infrastructure. In fact, they are self-organizing entities that are deployed on demand to perform various tasks such as surveillance, search and rescue, disaster relief, etc. RSNs have advantages compared to single radar systems in improving the system sensitivity, reducing obscuration effects and vulnerability, and increasing the detection performance [Kadambe 2001], [Baker 2002].

An RSN is organized into clusters, which are independently controlled and dynamically reconfigured as sensors move, to observe targets such as tactical weapons, missiles, aircraft, ships, etc. in the surveillance area. In a cluster, sensors receive the signals backscattered by targets in the presence of interference (e.g., clutter, jamming, interference between radar sensors), and noise. Then, the observed signals from all radar sensors are forwarded to a clusterhead where received data set will be combined to perform important tasks such as detection, localization, identification, classification, and tracking. For target detection problem, there are two primary levels: single target detection and multi-target detection. In the single target scenario, we proposed a diversity scheme in [Ly and Liang 2006] to improve detection performance of RSNs in the presence of strong interference, especially clutters, and noise. We are now interested in using RSNs to estimate the number of targets present in the surveillance area. In practice, various moving targets might appear in the sensing area, the number of targets is time-varying, and targets' state is fluctuating. The multi-target detection is therefore more challenging and difficult to solve than the single target detection.

Among the existing work on multi-target detection, Yung and Mourad [Huang 1989] used frequency diversity signaling to estimate the number of moving targets. Kaveh *et al.* applied

the information theoretic criteria to detect the number of targets [Kaveh et al 1987]. However, both work only studied the performance of their proposals for the case of two closely spaced targets. A performance analysis for a general case was provided in [Xu and Kaveh 1995] and [Zhang 1989]. In [Gini 2003], multiple target detection and estimation by exploiting the amplitude modulation induced by antenna scanning was proposed and a sequential hypothesis test was examined to determine the number of targets. However, all above work studied multi-target detection problem using a single radar. For the sensor network scenario, Wang *et al.* [Wang2003] applied Bayesian source number estimation to solve the distributed multiple target detection in sensor networks. Based on their approach, each cluster computed the posterior probability corresponding to each hypothesis on the number of sources and a central processor fused posterior probabilities using Bayes' theorem to select the best hypothesis. Their proposal however did not consider Doppler shifts of the targets and was not suitable for the multi-target detection in RSNs. In [Ly and Liang 2007], some preliminary works on estimating the number of targets in RSN were reported. In [Liang 2008], waveform design and diversity for single target recognition was proposed.

In this paper, we develop a framework for estimating the number of targets in the field of interest using RSNs. At the ith sensor, we deploy a receiver with an K element-ULA (Uniform Linear Array) whose spacing between elements is d_i. During the observation time, P pulses are transmitted to track targets. The useful signals backscattered from targets include spatial-temporal snapshots of targets and parameters representing radar cross section of targets. Then, a RSN-clusterhead collects measurements from all radar sensors and combines them to perform detection procedures. To fuse received measurements and estimate the unknown number of targets in the area of interest, at the RSN-clusterhead, we propose a multi-target detection algorithm which is Maximum Likelihood Multi-Target Detection (ML-MTD) algorithm. We use the probability of miss detection P_{MD} and the root mean square error (RMSE) as metrics to evaluate multi-target detection performance using RSN. Simulation results show that detection performance of the RSN is much better than that of a single radar system.

The rest of this paper is organized as follows. In Section 2, we state our multi-target detection problem. In Section 3, we model signals, interference, and noise at radar sensors. In Section 4, we propose an ML-MTD algorithm to estimate the number of targets present in the sensing field. Multi-target detection performance of RSN is discussed in Section 5 while conclusions and open directions are given in Section 6.

2 Multi-Target Detection Problem Statement

In this paper, we address a realistic situation in which the number of targets in the region of interest is generally unknown and has to be estimated. To handle our problem, an RSN consisting of N radar sensors is deployed. Radar sensors receive signals embedded in interference and forward them to a central processor, e.g., a clusterhead to perform detection tasks. At the RSN-clusterhead, we propose a detection algorithm to estimate the number of targets. To support the rest of the paper, we make some assumptions as follows:

- Targets evolve along independent trajectories and do not leave the surveillance area during the entire observation time of P consecutive pulses.
- Targets are modeled as Swerling II target models whose magnitudes fluctuate independently from pulse to pulse according to a chi-square probability density function.
- The locations of targets are unknown. Besides, Doppler frequencies when targets are moving relatively to radar platforms are uncertain.
- The measurements from radar sensors either originate from true targets or clutters.

The estimated number of targets present in the surveillance area is determined as

$$[\hat{\tau}_1, \hat{\tau}_2, ..., \hat{\tau}_N] = \arg \min_{\tau_1, \tau_2, ..., \tau_N} \Lambda(\tau), \tag{1}$$

where $\hat{\tau}_i$ is the estimated number of targets at sensor i, $\tau = [\tau_1, \tau_2, ..., \tau_N]$, and $\Lambda(\tau)$ is an utility function derived in Section 4. Hence, the possible number of targets $\widehat{M}$ that RSN can

detect is the average value of $\hat{\tau}_1, \hat{\tau}_2, ...,$ and $\hat{\tau}_N$, i.e.,

$$\widehat{M} = \left\lceil \frac{1}{N} \sum_{i=1}^{N} \hat{\tau}_i \right\rceil, \tag{2}$$

where $\lceil x \rceil$ returns the smallest integer not less than x.

3 Signal and Interference Models

3.1 Signal Models

At radar sensor i, we deploy a receiver with an K-element ULA whose spacing between elements is d_i. If P pulses are processed in a coherent pulse interval, the snapshot of target m is a $KP \times 1$ spatial-temporal steering vector with the following form [Melvin 2004], [Guerci 2003]:

$$\mathbf{e}(\theta_{im}, f_{im}) = \mathbf{b}_t(f_{im}) \otimes \mathbf{a}_s(\theta_{im}), \tag{3}$$

where f_{im} and θ_{im} are the normalized Doppler shift and normalized angle for the target m, respectively. The notation $\otimes$ denotes the Kronecker product, $\mathbf{b}_t(f_{im}) \in \mathbb{C}^{P \times 1}$ is a Doppler steering vector, and $\mathbf{a}_s(\theta_{im}) \in \mathbb{C}^{K \times 1}$ is a spatial steering vector. $\mathbf{b}_t(f_{im})$ and $\mathbf{a}_s(\theta_{im})$ are defined as follows:

$$\mathbf{b}_t(f_{im}) = [1 \quad e^{j2\pi f_{im}} \quad ... \quad e^{j2\pi(P-1)f_{im}}]^T, \tag{4}$$

$$\mathbf{a}_s(\theta_{im}) = [1 \quad e^{-j2\pi\theta_{im}} \quad ... \quad e^{-j2\pi(K-1)\theta_{im}}]^T. \tag{5}$$

where T denotes the transpose operation. Let ϕ_{im} be an angle that sensor i observes the mth target, f_m be the maximum Doppler frequency for target m, and T_p be the pulse duration. The normalized angle θ_{im} for target m and the normalized Doppler shift f_{im} when target m is moving relatively to sensor platform i are computed as [Guerci 2003]

$$\theta_{im} = \frac{d_i \sin\phi_{im}}{\lambda_i}, \tag{6}$$

$$f_{im} = 4 f_m T_p \theta_{im}. \tag{7}$$

We now assume that radar sensor i can detect M_i targets during the observation time. The received signal vector $\mathbf{z}_i(u,t)$ at sensor i is the superposition of signals reflected from M_i targets, interference, and noise.

$$\begin{aligned}\mathbf{z}_i(u,t) &= \sum_{m=1}^{M_i} \mathbf{e}(\theta_{im}, f_{im})\alpha_m(u)s_{mi}(t) + \mathbf{w}_i, \\ &= \mathbf{A}(\theta_i, f_i)\mathbf{s}_i(u,t) + \mathbf{w}_i, \quad i = 1, 2, ..., N \end{aligned} \tag{8}$$

where

- $\mathbf{A}(\theta_i, f_i) = [\mathbf{e}(\theta_{i1}, f_{i1}), \mathbf{e}(\theta_{i2}, f_{i2}), ..., \mathbf{e}(\theta_{iM_i}, f_{iM_i})] \in \mathbb{C}^{PK \times M_i}$ is the target response matrix. $\mathbf{e}(\theta_{im}, f_{im})$ is a spatial-temporal steering vector that models the mth target return at angle θ_{im} and Doppler shift f_{im}.

- $\mathbf{s}_i(u,t) = [\alpha_1(u)s_{1i}(t), \alpha_2(u)s_{2i}(t), ..., \alpha_{M_i}(u)s_{M_i i}(t)]^T \in \mathbb{C}^{M_i \times 1}$ is the target signal vector with a random variable $\alpha_m(u)$ that models the radar cross section (RCS) of the target m and $s_{mi}(t)$ is the waveform reflected from target m.

- $\mathbf{w}_i = \mathbf{w}_{ci} + \mathbf{w}_{ji} + \mathbf{w}_{si} + \mathbf{n}_i$ represents the overall interference and noise: a clutter vector $\mathbf{w}_{ci}$, a jamming vector $\mathbf{w}_{ji}$, an interference vector between radar sensors $\mathbf{w}_{si}$, and thermal noise $\mathbf{n}_i$.

Received signals from radar sensors are forwarded to a central controller, e.g., clusterhead. Then, these received signal vectors $\mathbf{z}_i(u,t)$ are fused to make estimation operations. Since $\mathbf{z}_i(u,t)$ is a zero-mean Gaussian vector, the probability density function of $\mathbf{z}_i(u,t)$ can be presented as

$$f(\mathbf{z}_i(u,t)) = \frac{\exp\left(-\frac{1}{2}\mathbf{z}_i^H \left[\mathbf{R}_{z,i}^{(\tau_i)}\right]^{-1} \mathbf{z}_i\right)}{(2\pi)^{\frac{KP}{2}} \left|\mathbf{R}_{z,i}^{(\tau_i)}\right|^{\frac{1}{2}}}, \tag{9}$$

where $\mathbf{R}_{z,i}^{(\tau_i)}$ is the covariance matrix of $\mathbf{z}_i(u,t)$, τ_i is the rank of $\mathbf{R}_{z,i}$, and $|\cdot|$ denotes the determinant of the matrix.

3.2 Interference and Noise Models

As pointed out, at the ith radar sensor, the interference vector $\mathbf{w}_i$ is the sum of clutter $\mathbf{w}_{ci}$, jamming $\mathbf{w}_{ji}$, and interference between sensors $\mathbf{w}_{si}$. We apply the waveform design algorithm proposed in [Liang 2007] to have waveforms at sensors be orthogonal. By doing so, interference between sensors can be canceled, i.e., $\mathbf{w}_{si} = \mathbf{0}$. Following are characteristics and models of clutter, jamming, and thermal noise at radar sensor i.

3.2.1 Clutter

Clutter generates undesired radar returns that may interfere with the desired signal. In RSNs, the signal-to-clutter ratio (SCR) is often more important than the signal-to-noise ratio (SNR). The integrated clutter can be generally approximated as the sum of N_{ci} clutter patches. For clutter patch k, the space-time data vector is modeled as [Guerci 2003]

$$\begin{aligned} \mathbf{p}_{ki} &= \xi_{ki}\mathbf{b}_t(f_{ki}) \otimes \mathbf{a}_s(\theta_{ki}) \\ &= \xi_{ki}\mathbf{u}_{ki}, \quad k = 1, 2, ..., N_{ci} \end{aligned} \tag{10}$$

where ξ_{ki} is a complex random variable that accounts for the amplitude and phase of clutter patch k. $\mathbf{u}_{ki} = \mathbf{b}_t(f_{ki}) \otimes \mathbf{a}_s(\theta_{ki})$ where $\mathbf{b}_t(f_{ki})$ and $\mathbf{a}_s(\theta_{ki})$ are temporal vector and spatial vector of clutter patch k, respectively. f_{ki} and θ_{ki} are the normalized Doppler shift and angle of arrival of the kth clutter patch, respectively. Total clutter vector, $\mathbf{w}_{ci}$, equals to

$$\begin{aligned} \mathbf{w}_{ci} &= \sum_{k=1}^{N_{ci}} \xi_{ki}\mathbf{b}_t(f_{ki}) \otimes \mathbf{a}_s(\theta_{ki}), \\ &= \sum_{k=1}^{N_{ci}} \xi_{ki}\mathbf{u}_{ki}. \end{aligned} \tag{11}$$

The covariance matrix of the clutter, $\mathbf{R}_{ci} \in \mathbb{C}^{KP \times KP}$, at the ith radar is given by

$$\begin{aligned} \mathbf{R}_{ci} &= \mathrm{E}\{\mathbf{w}_{ci}\mathbf{w}_{ci}^H\}, \\ &= \sum_{k=1}^{N_{ci}}\sum_{j=1}^{N_{ci}} \mathrm{E}\{\xi_i\xi_j^H\}\mathbf{u}_{ki}\mathbf{u}_{ji}^H, \\ &= \sigma_{ci}^2\mathbf{M}_{ci}, \end{aligned} \tag{12}$$

where H denotes the Hermitian operation, $\mathrm{E}\{\cdot\}$ denotes the expectation, and $\mathbf{M}_{ci}$ is the normalized covariance matrix, i.e., all diagonal entries of $\mathbf{M}_{ci}$ are ones.

3.2.2 Jamming

Jamming signals are generated by hostile interfering signal sources that seek to degrade the performance of radar sensors by mechanisms such as degrading signal-to-interference-plus-noise ratio (SINR) by increasing the noise level, or generating false detections to overwhelm RSNs with false targets. A model for N_{ji} jamming signals is commonly presented as [Melvin 2004]

$$\mathbf{w}_{ji} = \sum_{l=1}^{N_{ji}} \beta_l \otimes a_{ji}(\theta_l), \quad i = 1, 2, ..., N \tag{13}$$

where β_l contains voltage samples of the lth jamming waveform and $a_{ji}(\theta_l)$ is the jamming signal waveform at an angle θ_l. The different jamming waveforms are uncorrelated with each other.

3.2.3 Thermal Noise

Among noise existing in RSNs, thermal noise due to ohmic losses at the radar receiver is normally dominant. We model the thermal noise vector $\mathbf{n}_i$ at radar sensor i as a complex white Gaussian vector with zero-mean and covariance σ_{ni}^2. The covariance matrix of noise $\mathbf{R}_{ni} = \sigma_{ni}^2\mathbf{I}$ where $\mathbf{I} \in \mathbb{R}^{KP\times KP}$ is the identity matrix.

In RSNs, detection performance is largely affected by clutters. So we will consider the disturbance at the ith radar as a sum of thermal noise and clutter. The disturbance covariance matrix $\mathbf{R}_{wi}$ is given by

$$\begin{aligned} \mathbf{R}_{wi} &= E\{\mathbf{w}_i\mathbf{w}_i^H\}, \\ &= \mathbf{R}_{ni} + \varepsilon_{ci}(h)\mathbf{R}_{ci}, \end{aligned} \tag{14}$$

where $\mathbf{R}_{ni}$ and $\mathbf{R}_{ci}$ are the covariance matrices of noise and clutter, respectively. $\varepsilon_{ci}(h)$ is a random variable used to model the clutter power of the hth range cell. $\varepsilon_{ci}(h)$ often follows

Weibull distribution for ground clutter or gamma distribution for sea and/or weather clutter [Nitzberg 1990][Melvin 2000]. In homogeneous environments, the average clutter power does not depend on h, i.e., $\varepsilon_{ci}(h)$ is constant. Therefore, the disturbance covariance matrix is rewritten as

$$\begin{aligned} \mathbf{R}_{wi} &= \sigma_{wi}^2 \mathbf{M}_{wi}, \\ &= \sigma_{ni}^2 \mathbf{I} + \varepsilon_c \sigma_{ci}^2 \mathbf{M}_{ci}, \end{aligned} \tag{15}$$

where σ_{wi}^2 is the total disturbance power and $\mathbf{M}_{wi}$ is the normalized disturbance covariance matrix.

$$\mathbf{M}_{wi} = \frac{1}{\mathrm{CNR}_i + 1}\mathbf{I} + \frac{\mathrm{CNR}_i}{\mathrm{CNR}_i + 1}\mathbf{M}_{ci} \tag{16}$$

with $\mathrm{CNR}_i = \frac{\varepsilon_c \sigma_{ci}^2}{\sigma_{ni}^2}$ is the clutter-to-noise power ratio. Then, total interference and noise can be modeled as a complex zero-mean white Gaussian vector with the covariance matrix $\sigma_{wi}^2 \mathbf{M}_{wi}$, i.e., $\mathbf{w}_i \sim \mathcal{CN}(0, \sigma_{wi}^2 \mathbf{M}_{wi})$.

4 Maximum Likelihood Multi-Target Detection (ML-MTD) Algorithm

In this section, we develop an algorithm to detect the number of targets in the sensing region. We assume that signals backscattered from targets and interference are uncorrelated. From the signal model in (8), the covariance matrix of received signal $\mathbf{z}_i(u,t)$ at radar sensor i is given by

$$\begin{aligned} \mathbf{R}_{z,i}^{(\tau_i)} &= \mathrm{E}\{\mathbf{z}_i(u,t)\mathbf{z}_i^H(u,t)\}, \\ &= \mathbf{A}(\theta_i, f_i)\mathbf{R}_{s,i}\mathbf{A}^H(\theta_i, f_i) + \sigma_{wi}^2 \mathbf{M}_{wi}, \\ &= \mathbf{\Phi}_i^{(\tau_i)} + \sigma_{wi}^2 \mathbf{M}_{wi}, \end{aligned} \tag{17}$$

where $\mathbf{R}_{s,i} \in \mathbb{C}^{M_i \times M_i}$ is a positive definite matrix which represents the covariance matrix of the signal $\mathbf{s}_i(u,t)$, σ_{wi}^2 is the disturbance power, and $\mathbf{M}_{wi}$ is the normalized disturbance covariance

matrix at radar sensor i. $\mathbf{R}_{s,i}$ and $\mathbf{\Phi}_i^{(\tau_i)}$ are defined:

$$\mathbf{R}_{s,i} = E\{\mathbf{s}_i(u,t)\mathbf{s}_i^H(u,t)\}, \tag{18}$$

$$\mathbf{\Phi}_i^{(\tau_i)} = \mathbf{A}(\theta_i, f_i)\mathbf{R}_{s,i}\mathbf{A}^H(\theta_i, f_i). \tag{19}$$

The random variables $\alpha_m(u)$ $(i = 1, 2, ..., M_i)$ in $\mathbf{s}_i(u,t)$ models the RCS of the mth target. In [Swerling 1960], Swerling proposed five target models called Swerling models where Swerling V model is for non-fluctuating targets and Swerling I-IV models are for fluctuating targets. In this paper, we focus our studies on the Swerling II target models. We know that magnitude of the RCS $|\alpha(u)|$ for Swerling II targets fluctuates independently from pulse to pulse according to a chi-square probability density function with two degree of freedom, i.e., a Rayleigh probability density function. Therefore, the RCS of target m can be modeled as a Gaussian random variables. That is,

$$\alpha_m(u) = \alpha_{Im}(u) + j\alpha_{Qm}(u), \tag{20}$$

where $\alpha_{Im}(u)$ and $\alpha_{Qm}(u)$ follow Gaussian distribution with zero mean and variance $\rho_m^2/2$ for each branch I, Q.

From (17), it follows that the rank of matrix $\mathbf{R}_{z,i}^{(\tau_i)}$ is τ_i, which is equal to the number of targets M_i present in the surveillance region, and the smallest $(KP - \tau_i)$ of its eigenvalues are zero, i.e., the received signal contains interference and noise only. Sorting the eigenvalues of $\mathbf{R}_{z,i}^{(\tau_i)}$ in a decreasing order, we obtain

$$\lambda_1 \geq \lambda_2 \geq ... \geq \lambda_{\tau_i} \geq \lambda_{\tau_i+1}. \tag{21}$$

$$\lambda_{\tau_i+1} = \lambda_{\tau_i+2} = ... = \lambda_{KP} = \sigma_{wi}^2. \tag{22}$$

Assume that measurements $\mathbf{z}_i(u,t)$, at the clusterhead, are statistically independent complex Gaussian random vectors with zero mean. The joint probability density function of these

random vectors has the form:

$$\begin{aligned} f(\mathbf{z}(u,t)) &= \prod_{i=1}^{N} f(\mathbf{z}_i(u,t)), \\ &= \prod_{i=1}^{N} \frac{\exp\{-\frac{1}{2}\mathbf{z}_i^H[\mathbf{R}_{z,i}^{(\tau_i)}]^{-1}\mathbf{z}_i\}}{(2\pi)^{\frac{KP}{2}}|\mathbf{R}_{z,i}^{(\tau_i)}|^{\frac{1}{2}}}. \end{aligned} \tag{23}$$

Basically, we have to estimate $\hat{\tau}_i$ such that the joint probability density function $f(\mathbf{z}(u,t))$ is maximized. We now define a log-likelihood function $\Gamma(\tau)$ where $\tau = [\tau_1, \tau_2, ..., \tau_N]$ in (24). Hence, our mission is to find $\hat{\tau}_i$ such that $\Gamma(\tau)$ is minimized.

$$\begin{aligned} \Gamma(\tau) &= -\ln f(\mathbf{z}(u,t)), \\ &= \frac{N \times KP}{2}\ln(2\pi) + \frac{1}{2}\sum_{i=1}^{N}\log\left|\mathbf{R}_{z,i}^{(\tau_i)}\right| + \frac{1}{2}\sum_{i=1}^{N}\mathbf{z}_i^H\left[\mathbf{R}_{z,i}^{(\tau_i)}\right]^{-1}\mathbf{z}_i. \end{aligned} \tag{24}$$

Omitting terms that are independent of τ_i, we find the log-likelihood function $\Gamma(\tau)$.

$$\Gamma(\tau) = \sum_{i=1}^{N}\log\left|\mathbf{R}_{z,i}^{(\tau_i)}\right| + \sum_{i=1}^{N}\mathbf{z}_i^H\left[\mathbf{R}_{z,i}^{(\tau_i)}\right]^{-1}\mathbf{z}_i. \tag{25}$$

From [Akaike 1974], [Rissanen 1983], and [Schwartz 1978], the utility function $\Lambda(\tau)$ takes the form:

$$\Lambda(\tau) = \Gamma(\tau) + P(N), \tag{26}$$

where $P(N) = \wp(N)[\tau_a(2KP - \tau_a)]$ is a bias correction term or penalty function to make estimate unbiased. τ_a is an average value of $\{\tau_i | i = 1, 2, ..., N\}$ and $\wp(N)$ is a penalty coefficient which is a constant function of N. For example, $\wp(N) = 1$ for the Akaike information criterion (AIC) and $\wp(N) = \frac{1}{2}\ln N$ for the minimum description length (MDL). $\Lambda(\tau)$ then can be rewritten as

$$\Lambda(\tau) = \sum_{i=1}^{N}\log\left|\mathbf{R}_{z,i}^{(\tau_i)}\right| + \sum_{i=1}^{N}\mathbf{z}_i^H\left[\mathbf{R}_{z,i}^{(\tau_i)}\right]^{-1}\mathbf{z}_i + \wp(N)(\tau_a(2KP - \tau_a)). \tag{27}$$

Our ML-MTD algorithm to detect the number of targets $\widehat{M}$ present in the sensing field now can be expressed as

$$\widehat{M} = \left\lceil \frac{1}{N}\sum_{i=1}^{N}\hat{\tau}_i \right\rceil, \tag{28}$$

where $\hat{\tau} = \{\hat{\tau}_1, \hat{\tau}_2, ..., \hat{\tau}_N\}$ is computed as

$$\{\hat{\tau}_1, \hat{\tau}_2, ..., \hat{\tau}_N\} = \arg \min_{\tau_1, \tau_2, ..., \tau_N} \Lambda(\tau). \tag{29}$$

In practice, sensors can observe the different numbers of targets may not be equal since targets might not be exposed to all sensors. However, for the sake of simplicity, we assume that all radar sensors can observe the same number of targets, i.e., $\tau_1 = \tau_2 = ... = \tau_N = \tau$ and energy backscattered from targets is similar at radar sensors. Furthermore, we assume that the environment is homogeneous, that is, the average clutter power is a constant. These assumptions imply that $\mathbf{R}_{z,1}^{(\tau)} = \mathbf{R}_{z,2}^{(\tau)} = \mathbf{R}_{z,N}^{(\tau)} = \mathbf{R}_{z}^{(\tau)}$. For those reasons, our ultimate purpose is to evaluate detection performance improvement achievable by exploiting the networking of multiple radar sensors. Under our assumptions, the utility function $\Lambda(\tau)$ can be simplified as

$$\Lambda(\tau) = N \log \left| \mathbf{R}_{z}^{(\tau)} \right| + N \mathbf{tr} \left(\left[\mathbf{R}_{z}^{(\tau)} \right]^{-1} \mathbf{Y} \right) + \wp(N)(\tau(2KP - \tau)), \tag{30}$$

where $\mathbf{tr}(\cdot)$ denotes the trace of a matrix and $\mathbf{Y}$ is the sample covariance matrix of $\mathbf{z}_1, \mathbf{z}_2, ..., \mathbf{z}_N$.

$$\mathbf{Y} = \frac{1}{N} \sum_{i=1}^{N} \mathbf{z}_i \mathbf{z}_i^T. \tag{31}$$

Based on (30) and (31), we can observe that the utility function $\Lambda(\tau)$ depends on the number of radar sensors N. Our ML-MTD algorithm is used to determine any non-negative integer τ to minimize the utility function $\Lambda(\tau)$ when the number of radars is changed. Achieved results are analyzed to evaluate the multi-target detection performance in Section 5.

5 Multi-Target Detection Performance Analysis

We denote the true number of targets appearing in the observation area and the number of targets we can estimate from received signals as M and $\widehat{M}$, respectively. The probability of miss detection P_{MD} and the root mean square error (RMSE) are used as metrics to evaluate detection performance of the RSN using our proposed algorithm. We define P_{MD} and RMSE as follows:

- P_{MD} is the probability that the estimated number of targets is smaller than the true number of targets. Suppose that ω_{md} is the number of estimations in which the estimated number of targets is smaller than the true number of targets and ω_t is the total number of estimations. P_{MD} is given as

$$\begin{aligned} P_{MD} &= P(\widehat{M} < M) \\ &= \frac{\omega_{md}}{\omega_t}. \end{aligned} \tag{32}$$

- RMSE is used to determine the vibration of the estimated number of targets $\widehat{M}$ around the true number of targets M.

$$RMSE = \sqrt{\frac{1}{\omega_t}\sum_{g=1}^{\omega_t}(M - \widehat{M}_g)^2}. \tag{33}$$

To study the MTD performance, we setup parameters for the RSN and targets as follows.

1. Spacing d_i between elements of the K-element ULA at radar sensor i is chosen to be a half of the wavelength λ_i, i.e., $d_i = \frac{\lambda_i}{2}$.

2. The pulse duration (T_p) is 1 ms.

3. The number of elements (K) in ULA is 5.

4. The number of pulses (P) in a coherent pulse interval is 4.

5. To observe targets, we assume that θ_{im} is a random variable which follows a uniform distribution in an interval [-0.5, 0.5].

6. The maximum Doppler frequencies for targets are similar, e.g., f_{max} = 5000Hz. The normalized Doppler shift f_{im} only depends on the random variable θ_{im}.

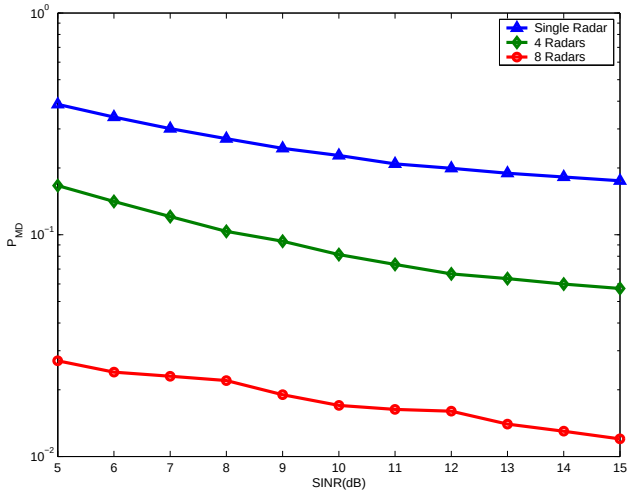
7. Average Signal-to-Interference-plus-Noise Ratio (SINR) refers to average SINR of all radars in RSN. We examine detection performance of RSN with average SINR in an interval [5dB, 15dB].

8. The MDL criterion is used for the penalty function.

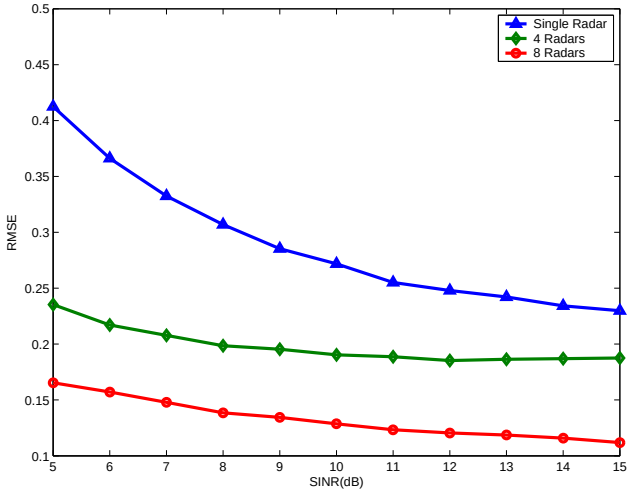
9. 10^5 estimations are performed, i.e., $\omega_t = 10^5$.

We first examine the case in which there are three targets in surveillance region, i.e., $M = 3$. Single radar system, 4-radar RSN, and 8-radar RSN are employed to detect these targets. At each average SINR, the estimated number of targets is compared to the true number of targets to compute P_{MD} and RMSE which are drawn in Fig. 1 for this case. After that, we increase the number of targets into four, i.e., $M = 4$. Using the same RSNs as the previous case, we can get P_{MD} and RMSE as plotted in Fig. 2. Based on achieved results in Fig. 1a and Fig. 2a, we can realize that miss detection probability of 4-radar RSN and 8-radar RSN is much smaller than that of single radar system. This implies that detection performance of 4-radar RSN and 8-radar RSN is improved. For example, to achieve the same $P_{MD} = 10\%$ which is good enough according to Skolnik [Skolnik 2001], the average SINR required for 4-radar RSN to detect three targets is about 9dB while the average SINR required for the single radar system is greater than 15dB. This means that detection performance gain of the 4-radar RSN is greater than 6dB. In both cases, moreover, the probability of miss detection is vastly reduced when the 8-radar RSN is used.

Furthermore, we observe that the higher average SINR, the smaller probability of miss detection. The reason is that, at high average SINR, radar sensors radiate signals at a high power level, so the coverage area of radar sensors is large. However, radiating signals at high power levels is costly. Thus tradeoff between cost and detection performance is necessary. We also observe that when we increase the number of targets, the detection performance is slightly reduced. For example, to achieve the same $P_{MD} = 10\%$, the 4-radar RSN to detect four targets requires average SINR around 4dB higher than that to detect three targets. This means that we need increase the transmit power for radar sensors. If the number of sensor radars is however large, e.g. $N = 8$, the detection performance of the RSN does not change much.

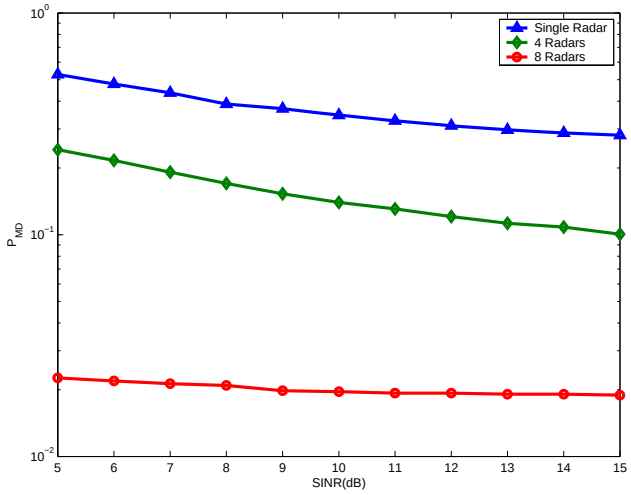


(a)

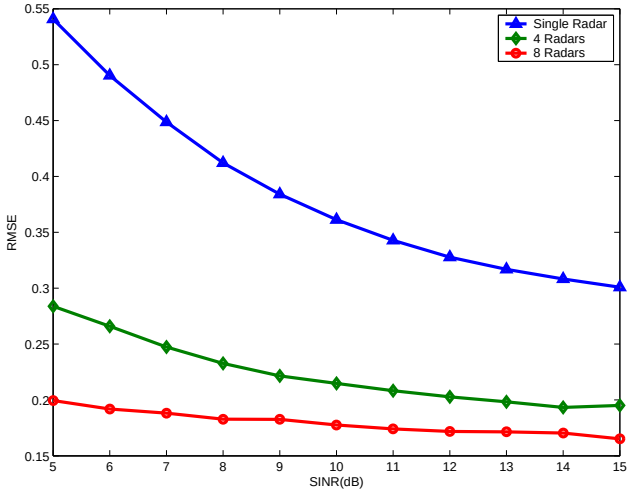


(b)

Figure 1: P_{MD} and RMSE vs. Average SINR, M=3



(a)



(b)

Figure 2: P_{MD} and RMSE vs. Average SINR, M=4

Besides the miss detection probability, RMSE is the other metric to examine the detection performance of the RSN. RMSE helps us evaluate the variability of the estimated number of targets around the true number of targets present in the sensing field. From Fig. 1b and Fig. 2b, we note that, to estimate three or four targets, RMSE of a single radar system is very high while RMSE of RSNs is reduced tremendously. For example, at SINR = 9dB, compared to a single radar system, the 4-radar RSN can reduce RMSE by 31.52% for three target case and 42.32% for four target case. Moreover, we can see that RMSE is reduced when we increase the number of sensors and/or average SINR.

6 Conclusions

We investigate a multi-target detection problem in Radar Sensor Networks. Signal, interference, and noise models at radar sensors are presented and analyzed. We also propose a Maximum Likelihood Multi-Target Detection algorithm to estimate the possible number of targets in a surveillance area. RSN-clusterhead utilizes our algorithm to combine measurements from radar sensors and make decision. Achieved results show that detection performance of our RSN is much better than that of a single radar system in terms of the miss detection probability and the root mean square error. Besides scenarios presented in our work, one can extend our proposal in several directions as follows:

1. For the sake of simplicity, we assumed clutter environment which affects largely the performance of RSNs is homogeneous. Multi-target detection therefore can be examined when heterogeneous clutter environment is considered.

2. We only consider target models as small moving point-like targets. Thus dynamic and state space-based models might be further studied.

3. We only examine the case in which Swerling II target models are present in the sensing area. Naturally, multiple target model types can appear during the observation time, so

multi-target detection problem when multiple target models coexist in the sensing region is worth looking into.

4. Our proposal is a primary state for important tasks such as target recognition, classification, tracking, etc. A joint algorithm to combine multi-target detection and one of above tasks can be investigated.

Acknowledgement

This work was supported by the U.S. Office of Naval Research (ONR) under Grant N00014-07-1-0395, N00014-07-1-1024, and N00014-03-1-0466.

References

[Akaike 1974] Akaike H., "A new look at the statistical model identification," *IEEE Transactions on Automatic Control,* vol 19, pp. 716-723, Dec. 1974.

[Baker 2002] Baker C. J., A.L.Hume, "Netted Radar Sensing," *IEEE A&E Systems Magazine,* Feb. 2002.

[Guerci 2003] Guerci J. R., *Space-Time Adaptive Processing for Radar*, Artech House, 2003.

[Gini 2003] Gini F., *et al.*, "Multiple target detection and estimation by exploiting the amplitude modulation induced by antenna scanning. Part II: Detection," IEEE ICASSP, pp. 533-536, 2003.

[Huang 1989] Huang Y. D., and M. Barkat, "On estimation of number of moving targets via frequency-diversity signaling," *Proceedings of the 32nd Midwest Symposium on Circuits and Systems,* vol.2, pp. 1170-1173, Aug. 1989.

[Kadambe 2001] Kadambe S., "Feature discovery and sensor discrimination in a network of distributed radar sensors for target tracking," HRL Laboratories, LLC, 2001.

[Kaveh et al 1987] Kaveh M. *et al.*, "On the theoretical performance of a class of estimators of the number of narrow-band sources," *IEEE Trans. on Acoustics, speech, and signal processing,* no.9, Sept. 1987.

[Liang 2008] Liang Q., "Automatic Target Recognition Using Waveform Diversity in Radar Sensor Networks," *Pattern Recognition Letters (Elsevier)*, vol. 29, no. 2, pp. 377-381, 2008.

[Liang 2007] Liang Q, "Radar Sensor Networks: Algorithms for Waveform Design and Diversity with Application to ATR with Delay-Doppler Uncertainty," *EURASIP Journal on Wireless Communications and Networking,* Vol 2007, 2007.

[Ly and Liang 2006] Ly H. D., and Q. Liang, "Spatial-Temporal-Frequency Diversity in Radar Sensor Networks," *Military Communications Conference (MILCOM 2006),* Oct. 2006, Washington, DC.

[Ly and Liang 2007] Ly H. D., and Q. Liang, "Collaborative Multi-Target Detection in Radar Sensor Networks," *Military Communications Conference (MILCOM 2007),* Oct. 2007, Orlando, FL.

[Melvin 2000] Melvin W. L., "Space-time adaptive radar performance in heterogeneous clutter," *IEEE Transaction on Aerospace and Electronic Systems,* vol 36, no.2, pp. 621-633, Apr. 2000.

[Melvin 2004] Melvin W. L., "A STAP Overview," *IEEE A&E Systems Magazine*, vol 19, no. 1, pp. 19-35, Jan. 2004.

[Nitzberg 1990] Nitzbergm R., "An effect of range-heterogeneous clutter on adaptive doppler filters," *IEEE Transaction on Aerospace and Electronic Systems,* vol 26, no.3, pp. 475-480, May 1990.

[Rissanen 1983] Rissanen J., "A universal prior for intergers and estimation by minimum description length," *Annals of Statistics,* vol. 11, no. 2, pp. 431-466, 1983.

[Richards 2005] Richards M. A., *Fundamentals of Radar Signal Processing*, McGraw-Hill Companies, New York 2005.

[Swerling 1960] Swerling, P., "Probability of Detection for Fluctuating Targets," *IRE Transactions on Information Theory,* vol IT-6, pp. 269-308, April 1960.

[Schwartz 1978] Schwartz G., "Estimating the dimension of a model," *Annals of Statistics,* vol. 6, pp. 497-511, 1978.

[Skolnik 2001] Skolnik M. I., *Introduction to Radar Systems*, 3rd ed, McGraw Hill, 2001.

[Wax and Kailath 1985] Wax M. and T. Kailath, "Detection of signals by information theoretic criteria," *IEEE Transactions on Acoustics, Speech, and Signal Processing,* vol 33, no.2, pp. 387-392, Apr. 1985.

[Wang2003] Wang X, H. Qi, H. Du, "Distributed source number estimation for multiple target detection in sensor networks," *IEEE Workshop on Statistical Signal Processing,* pp. 395-398, MO, Sept. 2003.

[Xu and Kaveh 1995] Xu W. and M. Kaveh, "Analysis of the performance and sensitivity of Eigendecomposition-based detectors," *IEEE Trans. on signal processing,* vol. 43, no.6, Jun. 1995.

[Zhang 1989] Zhang Q. T.,*et al.*, "Statistical Analysis of the performance of Information Theoretic Criteria in the detection of the number of signals in array processing," *IEEE Trans. on Acoustics, speech, and signal processing,* pp. 1557-1565, vol. 37, no.10, Oct. 1989.

Design and Analysis of Distributed Radar Sensor Networks

Jing Liang and Qilian Liang, *Senior Member*, IEEE

Abstract—In this paper, we design a network of distributed radar sensors that work in an ad hoc fashion, but are grouped together by an intelligent clusterhead. This system is named *Radar Sensor Network* (RSN). RSN not only provide spatial resilience for target detection and tracking compared to traditional radar sensors, but also alleviate inherent radar sensor defects such as the blind speed problem. This interdisciplinary area offers a new paradigm for parallel and distributed sensor research. We propose both coherent and noncoherent RSN detection systems applying selection combination algorithm (SCA) performed by clusterhead to take the advantage of spatial diversity. Monte Carlo simulations show that proposed RSN can provide much better detection performance than that of single radar sensor for fluctuating targets, in terms of probability of false alarm and miss detection. The proposed system design and combination algorithm can also be applied to an active RFID sensor networks and underwater acoustic sensor networks.

Index Terms—Distributed sensor, radar sensor networks, system design, selection combination algorithm, performance analysis

1 Introduction

Advances in hardware design and computational intelligence have led to recent evolution of sensor networks. A distributed radar sensor, is a small independent system that transmits a waveform of known shape and receives the echoes returned by targets and various obstacles [1]. Networks of multiple distributed radar sensors, namely radar sensor networks (RSN), can be utilized to combat the performance degradation of a single radar sensor [2] - [5]. They are arranged to survey a large area, while targets are observed from a number of different aspect angles. These networks will be include in the future tactical combat systems that are deployed on airborne, surface, and sub-surface unmanned vehicles in order to protect critical infrastructure from terrorist activities. Realistic RSN are documented in the literature [4].

The investigations on topologies of distributed wireless sensor networks is very extensive. [6] studied cluster-based sensor network, sensor network with a fusion center, and concatenated sensor network, to show the impact of topology on the performance and energy efficiency. [7] showed that geographical cluster-based routing performs best in sensing-covered networks. Therefore, cluster-based topologies will be applied in our design. Distributed radar sensor nodes can be efficiently grouped into clusters by means of [8]-[12] while cluster-heads [13] offer centralized control over each member. Additionally, the joint scheduling approach proposed in [14] can be adopted in RSN to provide both sensing coverage and network connectivity with efficient energy consumption.

There is also work pertaining to the radar systems with more than one transmitting or receiving element. These solutions can be divided into two groups. One is the array radar system and another is the multiple-input multiple-output (MIMO) radar system. Phased array radars have been intensively studied since the mid-1960s. Each radar array is composed of a number of individual antenna elements that are electronically combined to point the radar beam in a particular direction [15]. Its advantage mainly lies in the rapid steering of the beam from one direction to another without the necessity for mechanically positioning a large and heavy antenna, whereas its disadvantage is great cost and complexity [16].

Recently, the concept of MIMO radar have been proposed in [17]-[24], motivated by the development in communication theory. Unlike the standard phased array radar that transmits scaled version of a single waveform, a MIMO radar can overcome target radar cross section (RCS) scintillations by transmitting different signals due to the large spacing between the transmitting or receiving elements. However, for clarity and mathematical tractability, these studies are based on a simple model that ignores Doppler effects and clutter, thus more realistic models are left to subsequent work. Further, the cost and the complexity to fabricate a MIMO radar hinder the system from its pragmatical application.

Unlike the phased-array or the MIMO radar, each radar sensor in RSN is monostatic and contains only one transmitting and receiving element. Although every member work independently, they are managed by the clusterhead that combines waveform diversity in order to satisfy the common goals of the network. The cost and complexity can be tremendously reduced using RSN compared to using a phased-array or MIMO radar. In

- *Jing Liang is with the Department of Electrical Engineering, University of Texas at Arlington, Arlington, TX, 76019. E-mail: jliang@wcn.uta.edu*
- *Qilian Liang is with the Department of Electrical Engineering, University of Texas at Arlington, Arlington, TX, 76019. E-mail: liang@uta.edu*

addition, RSN offers to alleviate the blind speed problem. The radar's blind speed occurs when the Doppler shift is equal to the same or a multiple of the pulse repetition frequency (PRF). Under these circumstances, target return is suppressed so that a zero signal is obtained [25]. As for RSN, if PRF of each member are properly designed, for instance, co-prime to each other, the probability of blind speed occurrence for the entire system will be tremendously reduced [26]. It is worth mentioning that the price for improvements in radar sensitivity and data fusion is wider bandwidth and the increased resource consumption.

In [27], Liang has performed theoretical studies on constant frequency (CF) pulse waveform design and proposed maximum-likelihood (ML) automatic target recognition (ATR) approach for both nonfluctuaing and fluctuating targets. In [28], Shu and Liang have studied the decision fusion rules of multiple fluctuating targets in RSN. Nevertheless these studies also assumed no Doppler shift.

In this paper, we propose an orthogonal CF pulse waveform model for RSN, which eliminates interference between radar sensors in the absence of Doppler shift. Interference among network members is analyzed in detail in the presence of Doppler effect. We design both coherent and noncoherent RSN detection systems applying selection combination algorithm (SCA) [29] performed by clusterhead to take the advantage of spatial diversity. Assume the existence of clutter and noise, we analyze the detection performance versus SNR, as well as the performance versus Doppler shift. Moreover, multi-target performance has also been investigated. Monte Carlo simulation shows to what extent RSN outperforms single radar sensor , in terms of probability of false alarm and probability of miss detection. It also illustrates how the performance become worse along with the increase of Doppler shift.

The rest of this paper is organized as follows. Section 2 describes the distributed model of RSN. Section 3 and 4 focus on coherent and noncoherent system respectively. Section 5 illustrates the simulation result. Finally, section 6 concludes this paper and proposes future work.

2 Distributed Model and Problem Formulation

A RSN incorporates N radar sensors working in a self-organizing fashion. Each radar can detect targets and provide the detected waveform to their clusterhead radar, which combines these waveforms and makes final decision of target detection. We assume there is no information loss when transmitting signals to the clusterhead. The propagation and target model of RSN is illustrated in Fig.1. Complex target signals are constructed from distinct scatterers. The radar cross section (RCS) fluctuates when the target changes relatively to the radar antenna [30]. In this case, RCS is usually presented by Rayleigh PDF [31]. As the amplitude of each pulse is statistically independent, "Swerling II" model can be applied for a pulse-to-pulse fluctuating target.

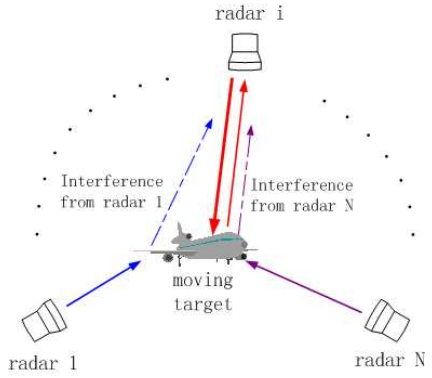


Fig. 1. Propagation and target model for RSN

To the best of our knowledge, this is the first time to study detection performance of RSN in the presence of Doppler shift. For clarity and simplicity, we apply CF impulse with the same pulse duration to each radar. Every impulse consists of a sinusoidal waveform that typically expressed as

$$\tilde{S}_i(t) = A_{ti} \cdot \sqrt{\frac{2}{T_p}} \cos[2\pi(f_c + \Delta_i)(t + t_i)] \tag{1}$$

where tilde on S_i denotes that the signal has been modulated. A_{ti} is the constant amplitude of the radar pulse. T_p is the time duration for radar pulses. $\sqrt{\frac{2}{T_p}}$ is a normalization factor to ensure that

$$\int_0^{T_p} \left\{ \sqrt{\frac{2}{T_p}} \cdot \cos[2\pi(f_c + \Delta_i)t] \right\}^2 dt = 1 \tag{2}$$

Here each oscillator of radar sensor works at a different frequency: $f_i = f_c + \Delta_i, f_c \gg \Delta_i$, where f_c is the system carrier frequency.

If Δ_i satisfies the following equation:

$$\Delta_{i+1} - \Delta_i = \frac{n_i}{T_p} \tag{3}$$

where n_i is a nonzero integer, then the cross-correlation between any two nonidentical waveforms become

$$\begin{aligned} & \frac{2}{T_p} \int_0^{T_p} \{\cos[2\pi(f_c + \Delta_m)t] \cos[2\pi(f_c + \Delta_n)t]\} dt \\ = \; & \text{sinc}[2\pi(\Delta_m - \Delta_n)T_p] \\ = \; & 0 \end{aligned} \tag{4}$$

(3) and (4) demonstrate the orthogonality between the transmitted waveform of each radar sensor. This implies that in case of stationary targets, the useful backscattered radar sensor signals are also orthogonal.

For mathematical tractability, in this section we assume there is only one target moving at an instant range. Multi-target situation will be discussed in section 5.3. Assume t_i second after transmitting the pulse, the

received combined back-scattered signal can be modeled as

$$\tilde{R}_i(t) = \tilde{S_{ri}}(t) + \tilde{I}_i(t) + \tilde{C}_i(t) + n_{ri}(t) \quad (5)$$

where $\tilde{S_{ri}}(t)$ is the expected back-scattered radiation from the target, which is corrupted with the scattered interference signal $\tilde{I}_i(t)$ introduced by other radar sensors, as well as clutter $\tilde{C}_i(t)$ and noise $n_{ri}(t)$.

$$\tilde{S_{ri}}(t) = A_i \cdot \sqrt{\frac{2}{T_p}} \cos[2\pi(f_c + \Delta_i + f_{di})t] \quad (6)$$

A_i represents the amplitude of the returned radar waveform and f_{di} denotes the Doppler shift in the returned signal compared to the transmitted waveform.

As Swerling II model is applied, $|A_i|$ is a random variable that follows Rayleigh distribution, which can be denoted as $A_i = A_i^I + jA_i^Q$ and both I and Q subchannels of A_i follow zero-mean Gaussian distribution with corresponding variance $\frac{\gamma^2}{2}$.

Assume the target is moving at a speed v, as each radar provides a unique carrier frequency and location to the same target, f_{di} can be given as

$$f_{di} = 2 \cdot \frac{v(f_c + \Delta_i)}{c} \cdot \cos\phi = f_{di_{max}} \cdot \cos\phi \quad (7)$$

where c is the speed of light, and ϕ is the elevation angle between each radar and the target. Normally, RSN can be deployed on high mountains or lower ground, therefore target can be above or below RSN. We may consider RSN uniformly distributed around the target, and thus ϕ is a random variable that follows uniform distribution within $[0, 2\pi]$, owning to the uncertainty of this angle.

When all of radar sensors are working, radar i not only receives its own back-scattered waveform, but also scattered signals generated by other radars. These interference waveforms received by radar i can be modeled as

$$\tilde{I}_i(t) = \sum_{k=1, k\neq i}^{N} B_k \cdot \sqrt{\frac{2}{T_p}} \cos[2\pi(f_c + \Delta_k + f_{dk})t] \quad (8)$$

where $B_k = B_k^I + jB_k^Q$ is the amplitude of interference from radar k assumed to be independent. The estimation uncertainty of B_k^I and B_k^Q can be effectively approximated by a Gaussian distribution with corresponding variance $\frac{\rho^2}{2}$, thus similar to $|A_i|$, $|B_k|$ also follows Rayleigh distribution. f_{dk} is the Doppler shift based on carrier frequency of radar k and geometric configuration of radar i, k and the target.

As far as the clutter is concerned, $\tilde{C}_i(t)$ can be given as

$$\tilde{C}_i(t) = M_i \cdot \sqrt{\frac{2}{T_p}} \cos[2\pi(f_c + \Delta_i)t] \quad (9)$$

Similarly, $C_i = C_i^I + jC_i^Q$ where I and Q subchannels follow zero-mean Gaussian distribution with variance $\frac{\eta^2}{2}$. Apart from clutter, the radar i also receives additive white Gaussian noise (AWGN) $n_{ri}(t) = n_{ri}^I(t) + jn_{ri}^Q(t)$, where I and Q subchannels follow zero-mean Gaussian distribution with variance $\frac{\sigma^2}{2}$. After introducing our propagation and target model, further analysis on coherent and noncoherent RSN are carried out respectively.

3 Coherent Detection

In coherent RSN, radar members are smart enough to obtain the knowledge of the exact Doppler shift introduced by moving targets. For example, the police radar sensor employs a focused high power beam to detect vehicle speed. Hence based on the *a-priori* information, the demodulator of each radar can be constructed as shown in Fig. 2.

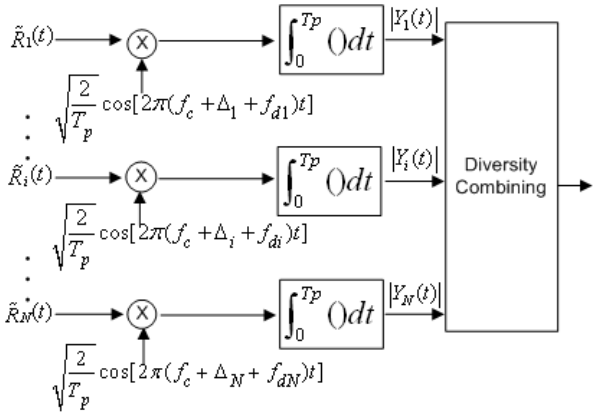


Fig. 2. Coherent RSN demodulation and waveform combining

According to this structure, the combined received waveform $\tilde{R}_i(t)$ is processed by its corresponding matched filter. The output of the ith branch $Y_i(t)$ is

$$Y_i = \int_0^{T_p} \tilde{R}_i(t) \cdot \sqrt{\frac{2}{T_p}} \cos[2\pi(f_c + \Delta_i + f_{di})t]dt \quad (10)$$

It can also be represented as

$$Y_i = S_i + I_i + C_i + n_i \quad (11)$$

where S_i, I_i, C_i, n_i denote the output of useful signal, interference, clutter and noise respectively

$$S_i = \int_0^{T_p} \tilde{S_{ri}}(t) \cdot \sqrt{\frac{2}{T_p}} \cos[2\pi(f_c + \Delta_i + f_{di})t]dt \quad (12)$$

$\tilde{S_{ri}}(t)$ has been given in (6). It can be easily derived that

$$S_i = A_i \quad (13)$$

Similarly, I_i is

$$I_i = \int_0^{T_p} \tilde{I}_i(t) \cdot \sqrt{\frac{2}{T_p}} \cos[2\pi(f_c + \Delta_i + f_{di})t]dt \quad (14)$$

where $\tilde{I}_i(t)$ has been given by (8). Simplifies the above equation, we can obtain that

$$I_i = \sum_{k=1,k\neq i}^{N} \frac{B_k \sin[2\pi(f_{dk}-f_{di})T_p]}{2\pi\left[(k-i)+(f_{dk}-f_{di})T_p\right]} \tag{15}$$

Also C_i is

$$C_i = \int_0^{T_p} \tilde{C}_i(t)\cdot\sqrt{\frac{2}{T_p}}\cos[2\pi(f_c+\Delta_i+f_{di})t]dt \tag{16}$$

It can be easily derived that

$$C_i \approx M_i \tag{17}$$

As for noise, it can be easily proved that subchannels of n_i still follow Gaussian distribution with variance $\frac{\sigma^2}{2}$, therefore the output envelope of radar i is

$$|Y_i| \approx |A_i + \sum_{k=1,k\neq i}^{N} \frac{B_k \sin[2\pi(f_{dk}-f_{di})T_p]}{2\pi\left[(k-i)+(f_{dk}-f_{di})T_p\right]} + M_i + n_i| \tag{18}$$

To simplify the expression, we define

$$e = E\{\frac{\sin[2\pi(f_{dk}-f_{di})T_p]}{2\pi\left[(k-i)+(f_{dk}-f_{di})T_p\right]}\} \tag{19}$$

Here $E\{\}$ denotes the expectation, therefore (18) becomes

$$|Y_i| \approx |A_i + \sum_{k=1,k\neq i}^{N} eB_k + M_i + n_i| \tag{20}$$

$$\sum_{k=1,k\neq i}^{N} eB_k = \sum_{k=1,k\neq i}^{N} eB_k^I + j\sum_{k=1,k\neq i}^{N} eB_k^Q \tag{21}$$

As gaussian random variable plus gaussian random variable still results in random variable, $\sum_{k=1,k\neq i}^{N} eB_k^I$ and $\sum_{k=1,k\neq i}^{N} eB_k^Q$ follow gaussian distribution with variance $\frac{\beta^2}{2} = (N-1)\frac{e^2\rho^2}{2}$, therefore $|\sum_{k=1,k\neq i}^{N} eB_k|$ follows Rayleigh distribution. Since $|A_i|$, M_i and $|n_i|$ are also Rayleigh random variables, $|Y_i|$ follows Rayleigh distribution with the parameter

$$\alpha = \sqrt{\gamma^2+\beta^2+\eta^2+\sigma^2} \tag{22}$$

To this end when there is a moving target, the pdf for $|Y_i|$ is

$$f_s(y_i) = \frac{y_i}{\alpha^2}\exp(-\frac{y_i^2}{2\alpha^2}) \tag{23}$$

The mean value of y_i is $\alpha\sqrt{\frac{\pi}{2}}$, and the variance is $(2-\frac{\pi}{2})\alpha^2$. The variance of useful radar signal, clutter and noise are $(2-\frac{\pi}{2})\gamma^2$, $(2-\frac{\pi}{2})\eta^2$ and $(2-\frac{\pi}{2})\sigma^2$ respectively. Therefore, signal-to-noise ratio (SNR) is $\frac{\gamma^2}{\sigma^2}$ and signal-to-clutter ratio (SCR) is $\frac{\gamma^2}{\eta^2}$.

Before making a final decision, the RSN clusterhead applies SCA to take the advantage of spatial diversity. The combiner selects the branch with the maximum envelope. This is equivalent to choosing the radar with the highest $\frac{\gamma^2}{\sigma^2}$ and $\frac{\gamma^2}{\eta^2}$.

On account of independence of each $|Y_i|$, the pdf of output from diversity combiner is

$$f_s(\mathbf{y}) = \prod_{i=1}^{N}\frac{y_i}{\alpha^2}\exp(-\frac{y^2}{2\alpha^2}) \tag{24}$$

In case of no target, i.e., there exits only clutter and noise, and hence the pdf of $|Y_i(t)|$ becomes

$$f_{cn}(y_i) = \frac{y_i}{\varsigma^2}\exp(-\frac{y_i^2}{2\varsigma^2}) \tag{25}$$

where $\varsigma = \sqrt{\eta^2+\sigma^2}$.

Accordingly pdf of output from diversity combiner becomes

$$f_{cn}(\mathbf{y}) = \prod_{i=1}^{N}\frac{y_i}{\varsigma^2}\exp(-\frac{y_i^2}{2\varsigma^2}) \tag{26}$$

In light of pdf for the above two cases, we may apply Bayesian's rule to decide the existence of targets based on $\mathbf{y}$

$$\frac{f_s(\mathbf{y})}{f_{cn}(\mathbf{y})} \underset{no\ target}{\overset{target\ exists}{\gtrless}} \frac{P_{cn}}{P_s} \tag{27}$$

where P_{cn} denotes the probability of no target but noise and P_s represents the probability of target occurrence.

4 Noncoherent Detection

As far as noncoherent RSN is concerned, its difference from the above system is that radar sensors have no knowledge of exact Doppler shift in back-scattered signals, so each matched filter applies the same frequency as that of transmitted waveforms, and finally lead to more ambiguity in target detection. In spite of its complexity, this system is more practical. Our construction of RSN demodulators is shown in Fig.3.

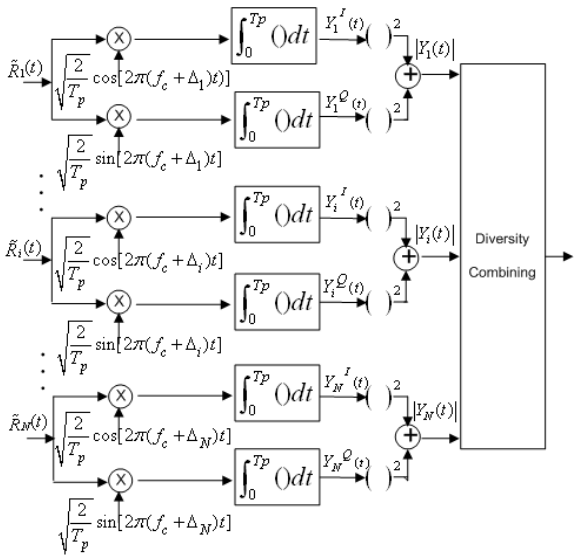


Fig. 3. Noncoherent RSN demodulation and waveform combining

In terms of this structure, the received signal of the radar i is first multiplied by cosine and sine waveforms generated by the local oscillator with the same frequency. The receiver then sums of the sine and cosine correlations, extracts its envelope, and then transmits the result to RSN cluterhead, which would make final decision based on the combined information collected by each radar member. However, it is obvious that because of not knowing the Doppler shift, this system involves nonlinear operations, a major difference from the coherent system.

Consider the radar i, the output of inphase branch is

$$Y_i^I = \int_0^{T_p} \tilde{R}_i(t) \cdot \sqrt{\frac{2}{T_p}} \cos[2\pi(f_c + \Delta_i)t]dt \tag{28}$$

where $\tilde{R}_i(t)$ is given in (5). Similar to (11), Y_i^I can also be represented as

$$Y_i^I = S_i^I + I_i^I + C_i^I + n_i^I \tag{29}$$

Through some simple computation, one can easily deduce that

$$S_i^I = A_i \cdot \mathtt{sinc}(2\pi f_{di} T_p) \tag{30}$$

$$I_i^I = \sum_{k=1,k\neq i}^{N} B_k \mathtt{sinc}\left[2\pi(\Delta_k - \Delta_i + f_{dk})T_p\right] \tag{31}$$

$$C_i^I = M_i^I \tag{32}$$

and n_i^I is the noise in inphase branch.

In the same way, the output of quadrature branch is

$$Y_i^Q = \int_0^{T_p} \tilde{R}_i(t) \cdot \sqrt{\frac{2}{T_p}} \sin[2\pi(f_c + \Delta_i)t]dt \tag{33}$$

which can also be given as

$$Y_i^Q = S_i^Q + I_i^Q + C_i^Q + n_i^Q \tag{34}$$

where

$$S_i^Q = \frac{A_i\left[\cos(2\pi f_{di} T_p) - 1\right]}{2\pi f_{di} T_p} \tag{35}$$

$$I_i^Q = \sum_{k=1,k\neq i}^{N} \frac{B_k\left\{\cos[2\pi(\Delta_k - \Delta_i + f_{dk})T_p] - 1\right\}}{2\pi(\Delta_k - \Delta_i + f_{dk})T_p} \tag{36}$$

$$C_i^Q = M_i^Q \tag{37}$$

and n_i^Q is the noise in quadrature branch.

To simplify the computation, we define

$$\theta_i \triangleq \pi f_{di} T_p \tag{38}$$

so (30)(31)(35)(36) become following expressions respectively

$$S_i^I = \frac{A_i(t)\sin\theta_i\cos\theta_i}{\theta_i} \tag{39}$$

$$I_i^I = \sum_{k=1,k\neq i}^{N} \frac{B_k \sin\theta_k \cos\theta_k}{\pi(k-i)+\theta_k} \tag{40}$$

$$S_i^Q = -\frac{A_i \sin^2\theta_i}{\theta_i} \tag{41}$$

$$I_i^Q = \sum_{k=1,k\neq i}^{N} -\frac{B_k \sin^2\theta_k}{\pi(k-i)+\theta_k} \tag{42}$$

Based on the above equations and the construction in Fig.3

$$|Y_i| = \sqrt{(S_i^I + I_i^I + C_i^I + n_i^I)^2 + (S_i^Q + I_i^Q + C_i^Q + n_i^Q)^2} \tag{43}$$

Apply (39)(40)(41) and (42) into (43), the final result becomes

$$|Y_i| = \sqrt{\frac{A_i^2(t)\sin^2\theta_i}{\theta_i^2} + \sum_{k=1,k\neq i}^{N} \frac{2A_i(t)B_k(t)\sin\theta_i\sin\theta_k\cos(\theta_i-\theta_k)}{[\pi(k-i)+\theta_k]\theta_i} + \left(\sum_{k=1,k\neq i}^{N} \frac{B_k(t)\sin\theta_k\cos\theta_k}{\pi(k-i)+\theta_k}\right)^2 + \left(\sum_{k=1,k\neq i}^{N} \frac{-B_k(t)\sin^2\theta_k}{\pi(k-i)+\theta_k}\right)^2 + M_i^2 + n_i^2} \tag{44}$$

There are two special cases as follows:

1) If there is no Doppler shift, then $f_{di} = f_{dk} = \theta_i = \theta_k = \sin\theta_i = \sin\theta_k = 0$ and $\frac{\sin^2\theta_i}{\theta_i^2}$=1, and thus (44) is simplified to

$$|Y_i(t)| = \sqrt{A_i^2 + M_i^2 + n_i^2} \tag{45}$$

This is easy to understand, because our RSN waveforms provide orthogonality under the circumstances of zero Doppler effect, so all interferences between any radars are eliminated.

2) If there is only one radar, interferences no longer exists, then (44) becomes

$$|Y_i| = \sqrt{A_i^2 \mathtt{sinc}^2(\theta_i) + M_i^2 + n_i^2} \tag{46}$$

From the definition of θ_i (see (38)), we know that if $f_{di}T_p = k$, where $k = \pm1, \pm2, \pm3\cdots$, then Y_i is totally clutter and noise. In this case the performance of single noncoherent radar is severely terrible.

To simplify (44), we define

$$\xi = E\{\frac{\sin\theta_i}{\theta_i}\} \tag{47}$$

$$\psi = E\{\frac{\sin\theta_k\cos\theta_k}{\pi(k-i)+\theta_k}\} \tag{48}$$

$$\omega = E\{-\frac{\sin^2\theta_k}{\pi(k-i)+\theta_k}\} \tag{49}$$

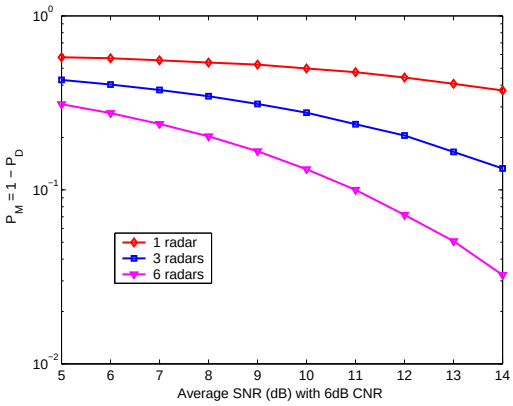
Then (44) can be approximate to

$$|Y_i| \cong |A_i\xi + \sum_{k=1,k\neq i}^{N} B_k\psi + \sum_{k=1,k\neq i}^{N} B_k\omega + n_i| \tag{50}$$

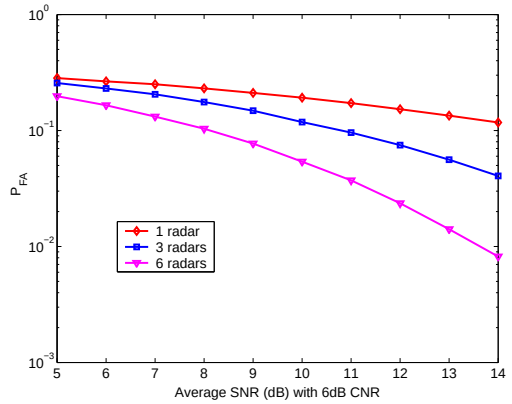
$|Y_i|$ approximately follows Rayleigh distribution with the parameter

$$\alpha = \sqrt{\gamma^2\xi^2 + (N-1)\rho^2(\psi^2+\omega^2) + \eta^2 + \sigma^2} \tag{51}$$

Similarly, we apply the SCA diversity scheme and (23)-(27) to analyze the detection performance in noncoherent RSN.

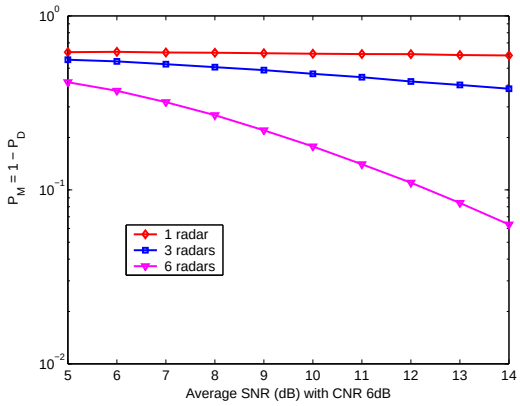


(a)

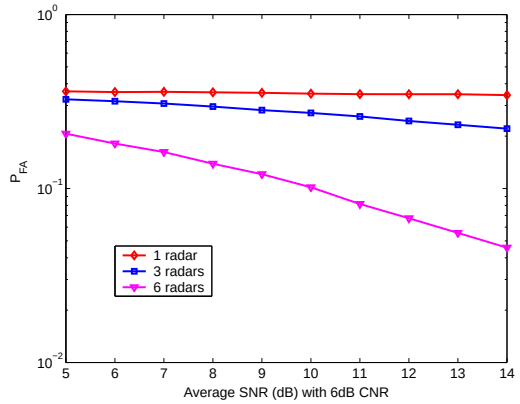


(b)

Fig. 4. Performance versus SNR and SCR for coherent RSN $f_{di_{max}}$=5KHz, (a) Probability of miss detection, and (b) Probability of false alarm.



(a)



(b)

Fig. 5. Performance versus SNR and SCR for noncoherent RSN $f_{di_{max}}$=5KHz, (a) Probability of miss detection, and (b) Probability of false alarm.

5 Simulations and Performance Analysis

In this section, we analyze the detection performance versus SNR and the detection performance versus Doppler shift respectively of both coherent and noncoherent RSN by means of Monte-Carlo simulations. Notice that in (7), $f_c \gg \Delta_i$, in order to simply the simulation, we assume each $f_{di_{max}}$ is the same for different i. Other parameters are:

1) $T_p = 1ms$
2) $P_n = P_s$
3) The mean value and variance of B_k are equal to those of A_i
4) Clutter-to-noise ratio (CNR) is 6dB
5) 10^6 times Monte-Carlo simulations

5.1 Performance versus SNR and SCR

Fig. 4 and Fig. 5 compare the probability of false alarm and the probability of miss detection between 1/3/6 radar sensors at each averaged SNR value when $f_{di_{max}}$ is at 5KHz. Notice that CNR is 6dB, so average SCR ranges from -1 dB to 8 dB, which corresponds to 5dB to 14dB SNR. The averaged SNR value refers to the averaged SNR of all radars in RSN.

Fig. 4 demonstrates that our coherent RSN could provide superior detection performance to that of single radar. Observe Fig. 4(a), we can see that P_M of single radar is much larger than 0.1 even SNR reaches 14dB. However, to meet the requirement of $P_M = 0.1$, the performance which is required according to [30], 6-member RSN only demand 11dB SNR . Fig. 4(b) illustrates that in order to achieve the same $P_{FA} = 0.1$, 3-radar and 6-radar requires at least 11dB SNR and 8.2dB SNR respectively while single radar can not successfully carry out this task even if SNR reaches 14dB. This pair of figures illustrate that to fulfil the same detection performance, coherent RSN demand tremendously less average SNR than a single radar.

Compare Fig. 5 with Fig. 4, it clearly shows that both the probability of false alarm and the probability of miss detection of noncoherent 1/3/6 radar(s) are much worse than that of the coherent system. In other words, noncoherent RSN requires higher power in order to achieve the same performance, owing to the ambiguity of its Doppler shift. For the single radar, P_M of noncoherent radar at 14dB SNR is only slightly smaller than that of 5dB SNR. As P_M is much larger than 0.1, noncoherent single radar can not work properly even at

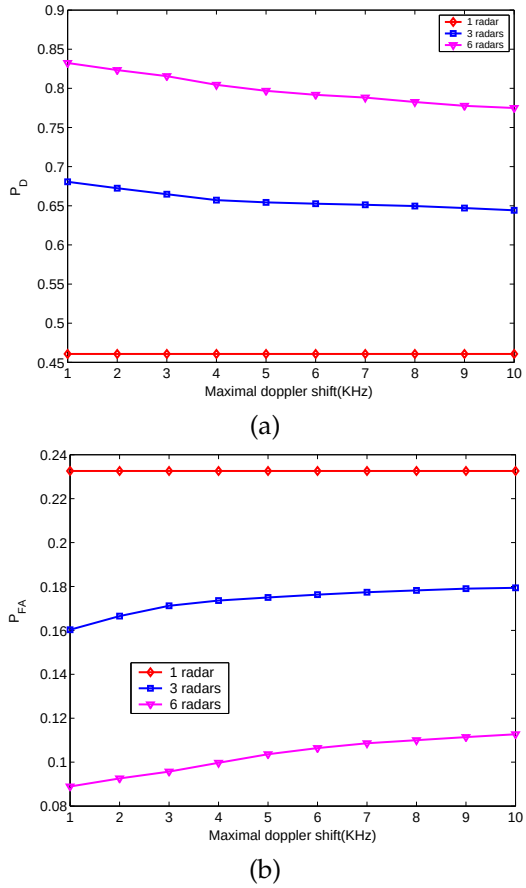


Fig. 6. Performance versus doppler shift for coherent RSN when SNR=1dB, (a) Probability of detection, and (b) Probability of false alarm.

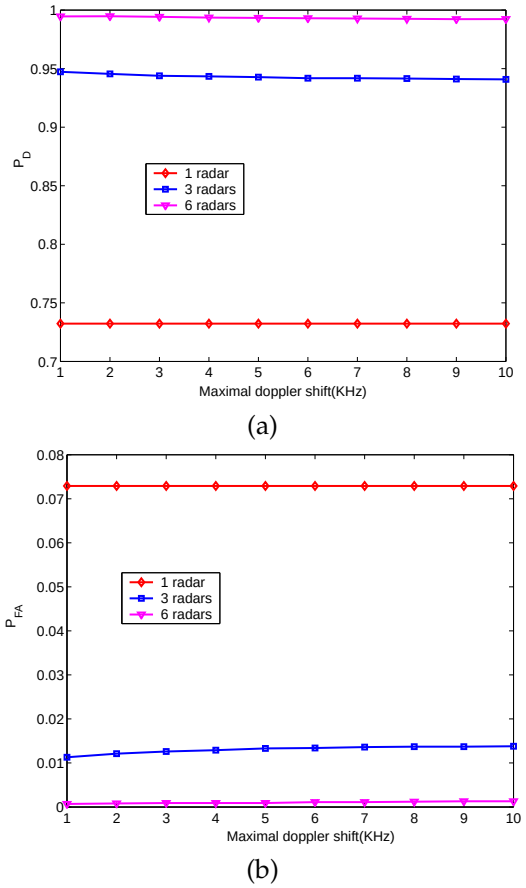


Fig. 7. Performance versus doppler shift for coherent RSN when SNR=10dB, (a) Probability of detection, and (b) Probability of false alarm.

14dB SNR. Apparently, P_M of 3-radar noncoherent RSN is still greater than 0.1 at 14dB SNR and it would not provide enough performance improvement. Applying 6-radar nocherent RSN, performance has been improved a lot compared to 1 and 3 radar systems. In this case $P_M = 0.1$ can be achieved at around 12.2dB SNR with $P_{FA} = 0.1$ at about 9.9dB.

5.2 Performance versus Doppler shift

Fig. 6$\sim$ Fig. 9 illustrate detection performances at different maximal Doppler shifts that range from 1KHz to 10kHz for both systems when SNR is fixed. Fig. 6 and Fig. 7 are for coherent RSN at SNR = 1dB and 10dB respectively while Fig.8 and Fig.9 are for noncoherent system with SNR = 1dB and 10dB respectively.

These 4 pairs of figures reveal a general tendency, that is in the same RSN, at the same SNR, the larger Doppler shift, the worse detection performance, i.e, the smaller probability of detection and the larger probability of false alarm and vice versa. The single coherent radar is an exception because the exact Doppler shift is known to the demodulation system, and thus the performance is exact the same in spite of different Doppler shift.

Compare Fig. 6 with Fig. 7, we may see that at lower SNR, Doppler uncertainty results in larger variance in performance. When SNR increases to higher value, it would better combat Doppler uncertainty.

As for noncoherent cases, although it is the same tendency that the larger Doppler shift, the worse detection performance, the variance of performances are much larger than those of coherent system. Also, the degradation of RSN performance is larger than single radar as the Doppler shift increases. For example, in Fig. 8 at SNR =1 dB and the maximal Doppler shift at 1kHz, P_D of 3-radar and 6-radar are about 0.24 and 0.4 greater than that of single radar respectively. However, when the maximal Doppler shift reaches 10KHz, P_D of 3-radar and 6-radar become 0.07 and 0.13 greater than that of single radar respectively. Similar situations occur in P_{FA}. This implies that for nocoherent RSN, more radars are needed to combat the Doppler shift ambiguity.

5.3 Multi-target Performance

Previous study in this paper has provided a methodology to obtain P_D^N and P_{FA}^N for both coherent and noncoherent RSN systems that consist of N radars under the assumption of one moving target. In this subsection,

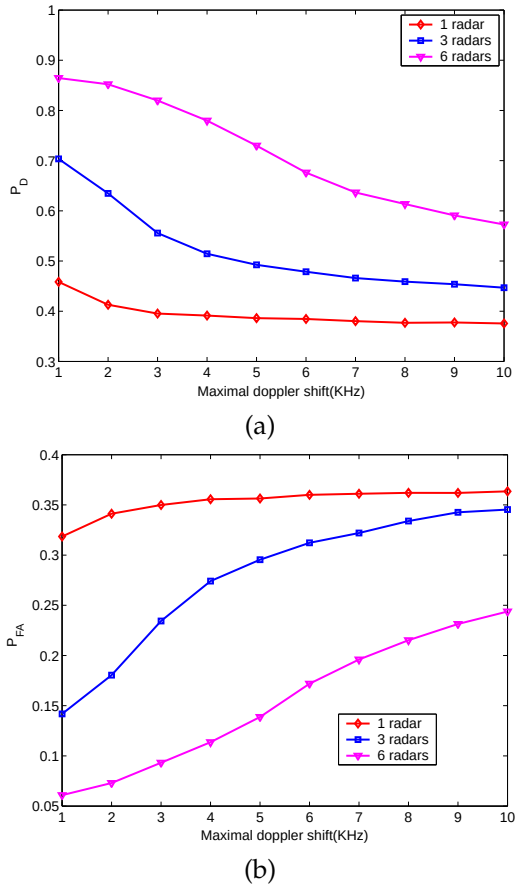


Fig. 8. Performance versus doppler shift for noncoherent RSN when SNR=1dB, (a) Probability of detection, and (b) Probability of false alarm.

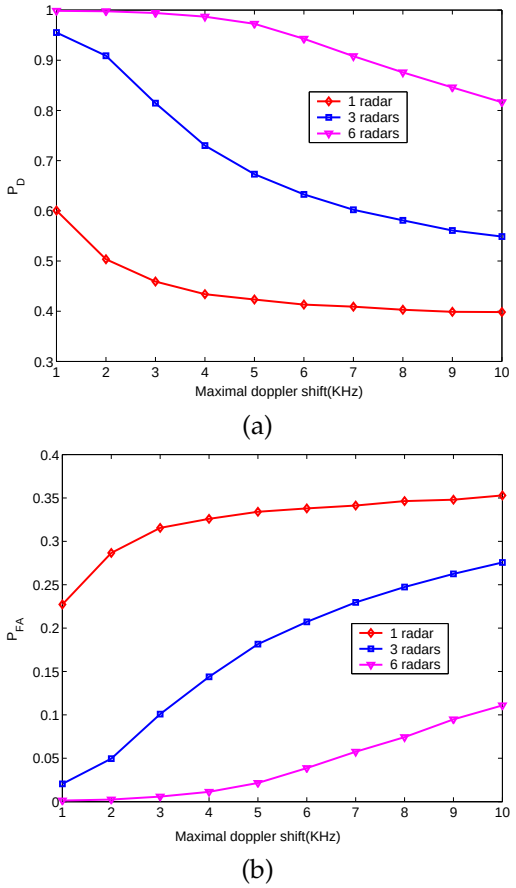


Fig. 9. Performance versus doppler shift for noncoherent RSN when SNR=10dB, (a) Probability of detection, and (b) Probability of false alarm.

we will discuss the multi-target performance in respect of statistics.

In [33], we have investigated how to estimate the number of targets in a region of interest. So we may assume RSN know there are m targets within the range. To make the problem tractable, we assume these m targets are independent, then the probability that all targets can be detected turns out to be $(P_D^N)^m$. Also, the probability that at least one target has been false alarmed is $1-(1-P_D^N)^m$. The performance are illustrated in Fig. 10 and 11 respectively.

6 Conclusions and Future Work

We have studied orthogonal waveforms and spatial diversity under the condition of the Doppler shift in both coherent and noncoherent RSN. In case of no Doppler shift, our orthogonal waveforms eliminate interference between each radar member. However, when there is Doppler shift, there exists interference that can not be avoided. In a word, the analysis of the simulation shows that

1) The larger number of radars in RSN, the better detection performance at the same SNR and the Doppler shift
2) The larger Doppler shift, the worse detection performance at the same SNR within the same RSN
3) Coherent RSN provide better performance than nocoherent RSN at the same SNR and the Doppler shift.

This design not only satisfies higher demanding criterion for detection accuracy in modern military and security affairs, but also offers advantages to combat the blind speed problem.

One can extend the above procedure in several directions:

1) In this paper we have only considered constant frequency (CF) pulse design. Naturally, we would like to extend our results to other waveforms, such as linear LFM and binary phase-coded pulse, and analyze their performances.
2) This paper is very much of a first foray into the resilience of netted radars to the Doppler shift, so only physical layer has been taken into account. One may apply cross layer design to better improve the RSN performances.

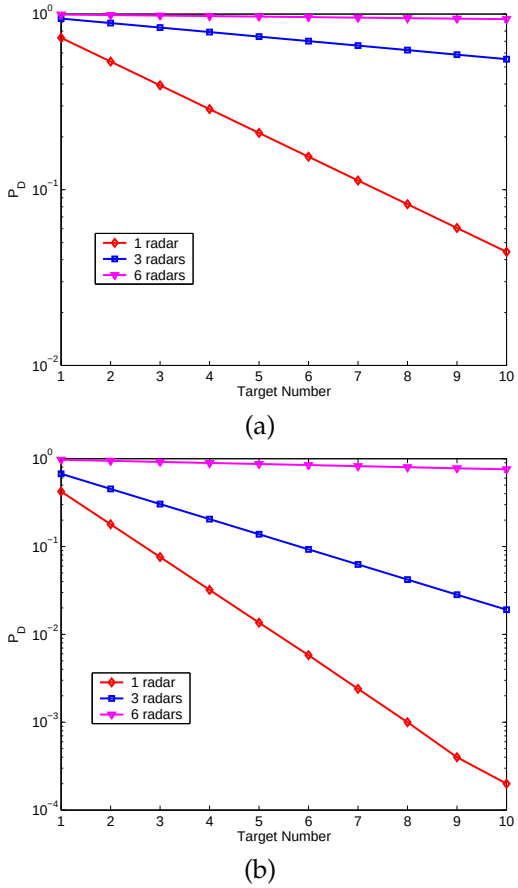


Fig. 10. Probability that all targets can be detected versus radar numbers, (a) Coherent system and (b) Noncoherent system.

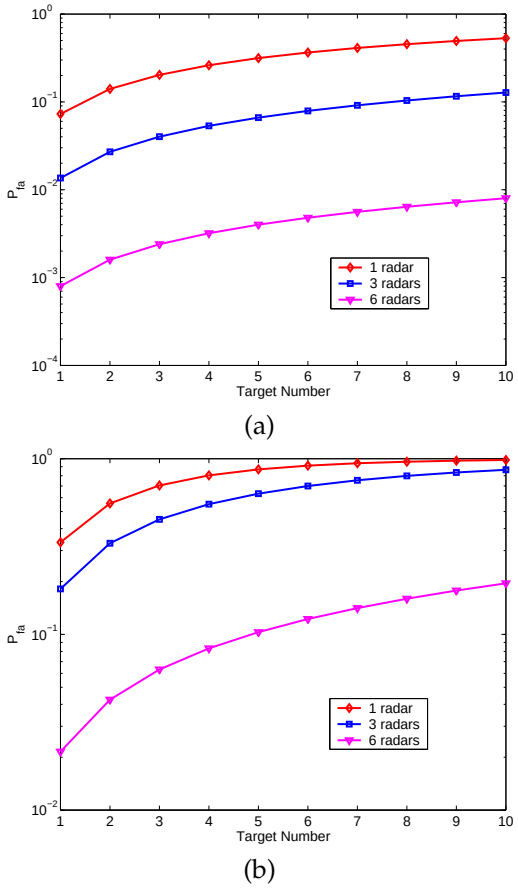


Fig. 11. Probability that at least one target is false alarmed versus radar numbers, (a) Coherent system and (b) Noncoherent system.

ACKNOWLEDGEMENT

This work was supported in part by Office of Naval Research (ONR) under Grant N00014-07-1-0395, N00014-07-1-1024, and National Science Foundation (NSF) under Grant CNS-0721515.

REFERENCES

[1] F. L. Chevalier, *P*rinciples of Radar and Sonar Signal Processing MA: Artech house, 2002.

[2] A. L. Hume and C. J. Baker, "Netted Radar Sensing", *Proceedings of the 2001 IEEE Radar Conference*, May 2001, pp. 23 - 26.

[3] S. Haykin, "Cognitive radar networks" , *2005 1st IEEE International Workshop on Computational Advances in Multi-Sensor Adaptive Processing*, Dec 2005, pp. 1-3.

[4] P. K. Dutta, A. K. Arora, S. B. Bibyk, "Towards radar-enabled sensor networks", *The Fifth International Conference on Information Processing in Sensor Networks, 2006*, April 2006, pp. 467 - 474.

[5] P. Withington, H. Fluhler and S. Nag, "Enhancing Homeland Security with Advanced Radar Sensors", *IEEE Microwave Magazine*, Spet. 2003, pp. 51-58.

[6] H. Chen, C. K. Tse and J. Feng, "Impact of Topology on Performance and Energy Efficiency in Wireless Sensor Networks for Source Extraction", *IEEE Transactions on Parallel and Distributed Systems*, vol. 20, no.6, June 2009, pp. 886-897.

[7] H. Frey and D. Görgen, "Geographical Cluster-Based Routing in Sensing-Covered Networks", *IEEE Transactions on Parallel and Distributed Systems*, vol. 17, no.9, Sept. 2006, pp. 899-911.

[8] O. Younis and S. Fahmy, "Distributed clustering in ad hoc sensornetworks: a hybrid, energy-efficient approach", in *Proc. IEEE Conference on Computer Communications (INFOCOM)*, Hong-Kong, China, Mar. 2004, pp. 629 - 640.

[9] T.J. Kwon and M. Gerla, "Clustering with power control" , in *Proc. Military Communications Conference*, Atlantic City, NJ, USA, Nov. 1999, pp. 1424 - 1428.

[10] S. Bandyopadhyay and E. Coyle, "An energy-efficient hierarchical clustering algorithm for wireless sensor networks", in *Proc. IEEE Conference on Computer Communications (INFOCOM)*, San Francisco, CA, USA, Apr. 2003, pp. 1713 - 1723.

[11] A.D. Amis, R. Prakash, T.H.P. Voung, and D.T. Huynh, "Max-min d-cluster formation in wireless ad hoc networks" , in *Proc. IEEE Conference on Computer Communications (INFOCOM)*, Tel-Aviv, Israel, Mar. 2000, pp. 32 - 41.

[12] L. Ramaswamy, B. Gedik and L. Liu, "A Distributed Approach to Node Clustering in Decentralized Peer-to-Peer Networks", *IEEE Transactions on Parallel and Distributed Systems*, vol. 16, no.9, Sept. 2005, pp. 814-829.

[13] Q. Liang, "Clusterhead election for mobile ad hoc wireless network", *IEEE International Symposium on Personal, Indoor and Mobile Radio Communications (PIMRC2003)*, Beijing, Sept 2003.

[14] C. Liu, K. Wu, Y. Xiao and B. Sun, "Random Coverage with Guaranteed Connectivity: Joint Scheduling for Wireless Sensor Networks Chong Liu,", *IEEE Transactions on Parallel and Distributed Systems*, vol. 17, no.6, June 2006, pp. 562-575.

[15] S. Haykin, J. Litva, and T. J. Shepherd, ed. New York: *Radar Array Processing*, 1st ed. New York: Springer-Verlag, 1993.

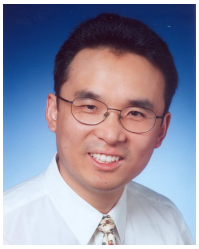
[16] R. C. Hansen, *Radar Array Antennas*, New York: John Wiley, 1998.

[17] E. Fishler, A. Haimovich, R. S. Blum, L. J. Cimini, D. Chizhik, A. Valenzuela, "Spatial Diversity in Radars - Models and Detection

Performance" , *IEEE Transactions on Sigal Processing*, vol. 54, no. 3, pp. 823-838, March 2006.
[18] E. Fishler, A. Haimovich, R. S. Blum, L. J. Cimini, D. Chizhik, A. Valenzuela, "MIMO radar: An idea whose time has come", in *Processings of the 2004 IEEE radar conference*, pp. 71 - 78, 26-29 April 2004.
[19] F. C. Robey, S. Coutts, D. Weikle, J. C. McHarg and K. Cuomo, "MIMO radar theory and experimental results", in *Processings of the Thirty-Eighth Asilomar Conference on Signals, Systems and Computers*, vol. 1, pp. 300 - 304, 7-10, Nov. 2004.
[20] K. Forsythe, D. Bliss and G. Fawcett, "Multiple-input multiple-output (MIMO) radar: Performance issues", in *Processings of the Thirty-Eighth Asilomar Conference on Signals, Systems and Computers*, vol. 1, pp. 310 - 315, 7-10, Nov. 2004.
[21] J. Li and P. Stoica, "MIMO radar-diversity means superiority", *The Fourteenth Annual Workshop on Adaptive Sensor Array Processing*, MIT Lincoln Laboratory, Lexington, MA, June 2006.
[22] L. Xu, J. Li and P. Stoica, "Adaptive techniques for MIMO radar", *4th IEEE Workshop on Sensor Array and Multi-channel Processing*, Waltham, MA, July 2006.
[23] L. Xu, J. Li, P. Stoica, K. W. Forsythe and D. W. Bliss, "Waveform optimization for MIMO radar: A Cramer-Rao bound based study", *2007 IEEE International Conference on Acoustics, Speech, and Signal Processing*, Honolulu, Hawaii, April 2007.
[24] Y. Yang and R. S. Blum, "MIMO Radar Waveform Design Based on Mutual Information and Minimum Mean-Square Error Estimation", *IEEE Transactions on Aerospace and Electronic Systems*, vol. 43, no. 1, pp. 330 - 342, Jan. 2007.
[25] M. A. Richards, *Fundamentals of Radar Signal Processing* , McGraw-Hill Companies, New York, 2005.
[26] Jing Liang, Qilian Liang and Zheng Zhou, "Radar Sensor Network Design and Optimization for Blind Speed Alleviation " , *Wireless Communications and Networking Conference 2007*, pp. 2643 - 2647, 11-15 March 2007.
[27] Q. Liang, "Waveform Design and Diversity in Radar Sensor Networks: Theoretical Analysis and Application to Automatic Target Recognitionc *2006 3rd Annual IEEE Communications Society on Sensor and Ad Hoc Communications and Networks*, SECON '06. vol. 2, 28-28, pp. 684 - 689, Sept. 2006.
[28] Haining Shu and Qilian Liang, "Data Fusion in a Multi-Target Radar Sensor Network", *2007 IEEE Radio and Wireless Symposium*, pp. 129 - 132, 9-11 Jan. 2007
[29] D. G. Brennan, " Linear Diversity Combining Techniques", *Proc. of IEEE*, pp. 331 - 356, Vol. 91, No. 2, Feb. 2003.
[30] M. I. Skolnik, *Introduction to Radar Systems* , 3rd ed, New York, McGraw Hill, 2001.
[31] N. Levanon, *Radar Principles*, New York, Wiley, 1988.
[32] Joseph T. Schaefer, "The Critical Success Index as an Indicator of Warning Skill" , *Weather and Forecasting*, vol. 5, pp. 570 - 575, Dec. 1990.
[33] Hung D. Ly and Qilian Liang, "Collaborative Multi-Target Detection in Radar Sensor Networks" , *Military Communications Conference, 2007*, pp.1-7 29-31, Oct. 2007



Jing Liang (S'06) received the B.S. and M.S. degrees from Beijing University of Posts and Telecommunications, China, both in Electrical Engineering in 2003 and 2005 respectively. She is currently working toward the Ph.D. degree in Electrical Engineering at the University of Texas at Arlington. Her current research interests include radar sensor networks, collaborative and distributed signal processing, wireless communications, wireless networks and fuzzy logic systems.



Qilian Liang (M'01-SM'05) received the B.S. degree from Wuhan University in 1993, M.S. degree from Beijing University of Posts and Telecommunications in 1996, and Ph.D degree from University of Southern California (USC) in May 2000, all in Electrical Engineering. Dr. Liang is currently an Associate Professor in the Department of Electrical Engineering, University of Texas at Arlington, where he has been since August 2002. Prior to that he was a Member of Technical Staff in Hughes Network Systems Inc at San Diego, California. His research interests include sensor networks, wireless communications, wireless networks, communication system and communication theory, signal processing for communications, fuzzy logic systems and applications, collaborative and distributed signal processing.

Dr. Liang has published more than 130 journal and conference papers, 6 book chapters, and has 6 U.S. patents pending. He received 2002 IEEE Transactions on Fuzzy Systems Outstanding Paper Award, 2003 U.S. Office of Naval Research (ONR) Young Investigator Award, 2005 UTA College of Engineering Outstanding Young Faculty Award, and 2007 U.S. Air Force Summer Faculty Fellowship Program Award.

Passive Geolocation of RF Emitters by A Netcentric Small Unmanned Aerial System

Jing Liang and Qilian Liang, *Senior Member, IEEE*

Department of Electrical Engineering

University of Texas at Arlington

Arlington, TX 76019-0016 USA

E-mail: jliang@wcn.uta.edu, liang@uta.edu

Abstract

In this paper, we design a netcentric Small Unmanned Aerial System (SUAS) for passive geolocation of RF emitters. Each small UAV is equipped with multiple Electronic Surveillance (ES) sensors to provide local mean distance estimation based on received signal strength indicator (RSSI). Fusion center will determine the location of the target through UAV triangulation. Different with previous existing studies, our method is on a basis of an empirical path loss and log-normal shadowing model, from a wireless communication and signal processing vision to offer an effective solution. The performance degradation between UAVs and fusion center has been taken into consideration other than assuming lossless communication. We analyze the geolocation error and the error probability of distance based on the proposed system. The result shows that this approach provides robust performance for high frequency RF emitters.

Index Terms : fading, geolocation, path-loss, log-normal shadowing, UAV

1 Introduction and Motivation

Determining the location of an emitting target is one of the fundamental functions of wireless communication systems [1]. The precision geolocation will assist targeting military invaders and rescuing airplanes or ships sunk at sea. Among the traditional work of target detection and location,

care has been taken on a basis of bearing-only measurements from the aspect of geometry [2]-[6] to determine the position, velocity and direction. There is no doubt that this bearing-based methodology such as Angel of Arrival (AOA) can be adopted in RF emitter geolocation, since RF emitter is in essence a target. On the other hand, RF emitters stand out from conventional targets as they are capable of sending out electromagnetic signals, which suggests the wireless communication and signal processing vision to offer the effective solution.

Conventionally, synthetic aperture radar (SAR), inverse synthetic aperture radar (ISAR) and moving target indicator (MTI) radar have been employed to provide situational awareness picture, such as localization of targets. Due to the principle that radars operate by radiating energy into space and detecting the echo signal reflected from the target [7], the vulnerability of active radars are obvious:

- Given transmitter and receiver, a radar systems is generally bulky, expensive and not easily portable
- Transmitter is easily detectable while in operation, thus draws unwanted attention of adversary
- Detection range is limited by the power of transmitter
- The transmission energy highly reduce the life of battery for MTI radars

Therefore, passive geolocation approaches are preferred.

Currently, there is a developing trend to use unmanned aerial vehicles (UAVs) for geolocation of RF emitters owing to better grazing angles closer to the target than large dedicated manned surveillance platforms [8]. In addition, UAVs are capable of continuous 24-hour surveillance coverage. As a result, they had been developed for battlefield reconnaissance beginning in the 1950s. During the 1980s, all the major military powers and many of the minor ones acquired a battlefield UAV capability, and they are now an essential component of any modern army. Till now, UAV is not only limited to an unpiloted aircraft, but unmanned aerial systems (UAS) including ground stations and other elements as well.

Small unmanned aerial systems (SUAS) are rapidly gaining popularity due to the miniaturization of RF components and processors. In particular, given the cutting-edge technology in modern remote sensing (RS), SUAS can be equipped with Electronic Surveillance (ES) sensors in place of bulky active radars, which result in smaller, lighter and lower-cost counterparts. These types of SUAS are generally classified as having a wing-span of less than 4 meters [9] and a gross vehicle weight less than 15 pounds [10]. A number of UAV manufacturers have developed low-cost TDMA data links that support the cooperative team work of multiple UAVs, which provides higher mobility, survivability and closer proximity to the targeting emitters.

In the present work, [10] and [11] are based on a team of UAVs working cooperatively with on-board camera systems. The location of an object is determined by the fusion of camera images. However, the visual feature can become vulnerable in the following cases: 1)when telemetry and image streams are not synchronized, the target coordinates read by UAV can be particularly misleading; 2)when weather is severe and visibility is low, the image based geolocation may not provide day-or-night, all-weather surveillance; 3)target is well protected and hidden, such as deeply beneath the foliage.

Besides visual feature, the time difference of arrival (TDOA) technique has been adopted in the current work [12]-[16]. In these work, a network of at least three UAVs has been employed with on-board ES sensors, a global positioning system (GPS) receiver and a precision clock. When the target is detected by the sensor, the time of arrival would be transmitted to a fusion center, which would finally estimate the emitter location based on their TDOA. Also, Kalman filters is used to track the object. However, TDOA, like other methods including Angle of Arrival (AOA), Frequency of Arrival (FOA), Frequency Difference of Arrival (FDOA) and Phase Difference of Arrival (PDOA) etc., is well known for difficult synchronization issues, such as fine synchronization for geolocation algorithms and coarse synchronization for the coordinating data collected within the area of interest at a common time.

In this paper, we apply netcentric SUAS with on-board multiple ES sensors for RF emitter geolocation. Different from previous work described above, our work describes about a complete system design and analyze the performance in detail. Our method is on a basis of an empirical

pass loss and log-normal shadowing model, which has been adopted for reliable high-speed wireless communications for moving users in dynamic environment, but has never been used in the SUAS before, to the best of our knowledge. Also, the performance of multiple ES sensors will be considered for the system as a whole. In addition, we will provide a confidence assessment through error bounding, which has not been seen in the existing approaches.

The rest of paper is organized as follows. Section 2 describes about the system design including the emitter detection, path loss and log-normal shadowing approach and netcentric decision. Section 3 presents simulation results and performance analysis. Finally, section 4 draws the conclusion.

2 System Design Based on Path loss and Log-normal shadowing

2.1 Target Detection

Before UAVs cooperatively locating the RF emitter, it is necessary for them to understand whether targets are present in the range or not. Due to the randomness of dynamic environment, statistical model can be used to characterize the signal fluctuation. Herein threshold detection based on Bayesian's rule is adopted.

The Rayleigh distribution has been generally applied to describe the fluctuations of the amplitude over a short period of time or travel distance [17]. when there is no any RF emitter, moving UAVs will obtain scattered noise that reach the receiver by multipath, which can be denoted as

$$g(u) = g_I(u) + jg_Q(u) \tag{1}$$

where the envelope of received signal $r = \sqrt{g_I^2(u) + g_Q^2(u)}$ obeys a Rayleigh distribution. $g_I(u)$ and $g_Q(u)$ are two independent quadrature Gaussian random variables with zero mean and variance ϕ^2. The probability density function (PDF) of the amplitude is

$$f(r) = \frac{r}{\phi^2} e^{-\frac{r^2}{2\phi^2}}, \quad \phi > 0 \tag{2}$$

When a RF emitter is present, its dominant signal component will contribute to a line-of-sight (LOS) propagation path, consequently the envelope in this case follows Rician distribution with

PDF

$$f(r) = \frac{r}{\phi^2} e^{-\frac{r^2+s^2}{2\phi^2}} I_0(\frac{rs}{\phi^2}), \quad \phi > 0 \tag{3}$$

where $I_0(\cdot)$ is the zero-order modified Bessel function and it is monotonically increasing for positive argument; s is the averaged RF signal amplitude.

Assume the presence of RF emitter is with probability $0 < p < 1$, then Bayesian's decision rule can be designed as

$$\frac{\frac{r}{\phi^2} e^{-\frac{r^2+s^2}{2\phi^2}} I_0(\frac{rs}{\phi^2})}{\frac{r}{\phi^2} e^{-\frac{r^2}{2\phi^2}}} \underset{no\ emitter}{\overset{emitter\ exists}{\gtrless}} \frac{1-p}{p} \tag{4}$$

Based on 4, the detection threshold turns out to be

$$T = \frac{\phi}{s} I_0^{-1}(\frac{1-p}{p}) e^{\frac{s^2}{2\phi}} \tag{5}$$

Therefore the probability of detection, i.e., the probability that the RF emitter be detected at its real presence can be expressed as

$$P_d = p\{r \geq T\} = \int_T^\infty \frac{r}{\phi^2} e^{-\frac{r^2+s^2}{2\phi^2}} I_0(\frac{rs}{\phi^2}) dr \tag{6}$$

The probability of false alarm can be denoted by

$$P_{fa} = p\{r \geq T\} = \int_T^\infty \frac{r}{\phi^2} e^{-\frac{r^2}{2\phi}} dr = e^{-\frac{T^2}{2\phi^2}} \tag{7}$$

2.2 Path Loss and Log-normal shadowing Approach

In our work, we assume the SUAS is composed of $R(R \geq 3)$ small UAVs. Each UAV is equipped with $N(N \geq 1)$ ES sensors, whose task is to provide Received Signal Strength Indicator (RSSI) of RF emitters. A processor is also on-board to compute the current distance from the RF emitter to the sensors based on RSSI. Notice that even though the computation can be achieved in a very fast time on a basis of detected RSSI, estimated distance poses drifts from the real distance due to the relative motion between the UAV and the RF emitter as well as wind gusts during the moment of computation. Thus multiple sensors are employed to provide the receiver diversity. Later we will show that multiple sensors help reduce the distance error and improve the geolocation performance. The processor also applies Equal Gain Combining (EGC) to average out local spatial variations

within a UAV. EGC is adopted due to its simplicity and fast computation. Additionally, each UAV works independently and knows its own position either by a GPS receiver or pre-planned paths. Also, it is capable of communicating with a fusion center, which makes a final geolocation decision based on the information given by multiple UAVs.

Assume an emitter is sending out RF signal and a UAV d distance away from it detected the signal at this moment. The signal propagating between these two points with no attenuation or reflection follows the free-space propagation law [18]. This commonly adopted path loss model as a function of distance is expressed as

$$\frac{P(d)}{P(d_0)} = \gamma(\frac{d}{d_0})^{-\beta} \tag{8}$$

where d_0 is a close-in distance used as a known received power reference point; β is the path-loss exponent depending on the propagation environment. γ is a unitless constant that depends on the antenna characteristics and the average channel attenuation, which can be defined as

$$\gamma dB = 20\ lg\frac{C}{4\pi f d_0} \qquad (lg = log_{10}) \tag{9}$$

where C is the speed of light and f denotes the frequency. This definition is supported by empirical data for free-space path loss at a transmission distance of 100m [19]. Based on this free-space model, the power in dB form is linearly decreasing with the increase of $log(d)$, as illustrated by the straight dash line in Fig. 1.

However, in practice, the reflecting surfaces and scattering objects will typically contribute to the random variation of RF signal transmission. The most common model for this additional attenuation is log-normal shadowing, which has been empirically confirmed to model accurately the variation in received power in both outdoor [20] and indoor [21] environments. In this case, the difference between the value predicted by the path loss model and the actual power is a log-normal random variable, i.e., normally distributed in dB, which is denoted by

$$[\frac{P(d)}{P(d_0)}]_{dB} = [\frac{\hat{P}(d)}{P(d_0)}]_{dB} + X \tag{10}$$

where X is a Gaussian random variable, with mean m and variance σ^2.

We will use the combined path loss and log-normal shadowing model to estimate the distance between RF emitter and a UAV through RSSI. This model is illustrated in Fig. 1 with a dotted curve. The power in dB is given by

$$[\frac{P_{ri}}{P(d_0)}]_{dB} = 10lg\gamma - 10\beta lg(\frac{\hat{d}_i}{d_0}) + X \tag{11}$$

where P_{ri} is the RSSI of ES sensor i. Based on (11), when P_{ri} is detected, the processor can easily compute $\hat{d}_i$ in a dB form, which is

$$\hat{d}_{idB} = \frac{1}{\beta}\{\gamma_{dB} + \beta d_{0dB} - [\frac{P_{ri}}{P(d_0)}]_{dB}\} + \frac{X}{\beta} \tag{12}$$

Notice that $d_{idB} = \frac{1}{\beta}\{\gamma_{dB} + \beta d_{0dB} - [\frac{P_{ri}}{P(d_0)}]_{dB}\}$, therefore

$$\hat{d}_{idB} - d_{idB} = \frac{X}{\beta} \tag{13}$$

Then it is obvious that the expectation of distance mean square error based on sensor i is

$$E\{(\hat{d}_{idB} - d_{idB})^2\} = \frac{m^2 + \sigma^2}{\beta^2} \tag{14}$$

N sensors equipped on a UAV are applied to compute the local mean distance that average the local spatial variations. The estimated local mean distance is

$$\hat{D} = \frac{1}{N}\sum_{i=1}^{N} \hat{d}_{idB} \tag{15}$$

This value is obtained based on dB measurement due to the smaller estimation error compared to the linear form [22].

Notice that $D = d_{dB}$. At the detection moment, UAV is d distance away from the RF target, i.e., $d_{idB} = d_{dB}$. Also, each sensor independently obtains the $\hat{d}_{idB}$, i.e., $\hat{d}_{idB} - d_{idB}$ can be considered independent for different i, thus the expectation of *distance mean square error* for each UAV can be expressed as

$$E\{(\hat{D} - D)^2\} = \frac{m^2 + \sigma^2}{N^2\beta^2} \tag{16}$$

This shows that based on path loss and log-normal model, the larger number of sensor N, the smaller distance mean square error will be achieved for each UAV.

As each UAV geolocates RF emitter only based on RSSI and there is no any information about phase, in this situation the current detected area at the moment can be denoted by $a = \pi d^2$. If a is denoted by dB form, then $A = 10lg\pi + 2D$, therefore the expectation of *area mean square error* for each UAV is

$$P_A = E\{(A - \hat{A})^2\} = 4E\{(D - \hat{D})^2\} = \frac{4(m^2 + \sigma^2)}{N^2\beta^2} \tag{17}$$

Finally the upper bound of *geolocation area mean square error* of a UAV network can be denoted by

$$P_e = P(\bigcup_{i=1}^{R} A_i) \leq \sum_{i=1}^{R} P_{Ai} = \frac{4R(m^2 + \sigma^2)}{N^2\beta^2} \tag{18}$$

We show this upper bound in Fig. 2, where $R = 3, m = 0, \beta = 2$ are used for illustration.

Apart from geolocation performance, we also define *distance range probability* as the probability that the estimated local mean distance $\hat{D}$ falls within $D_1 \leq \hat{D} \leq D_2$, where $D_1 < D_2$ and D_1, D_2 are also in dB form. The corresponding linear form of $\hat{D}, D_1$ and D_2 are $\hat{d}, d_1$ and d_2 respectively.

In order to simplify the expression, we would like to denote

$$S_i = \frac{1}{\sigma}\{\gamma_{dB} + [\frac{P(d_0)}{P_r}]_{dB} - \beta D_i + \beta d_{0dB}\}, \quad i = 1, 2 \tag{19}$$

It's obvious that $S_2 < S_1$. Therefore the distance range probability turns out to be

$$P(D_1 \leq \hat{D} \leq D_2) = \begin{cases} Q(S_2) - Q(-S_1) = Q(S_2) + Q(S_1) - 1 & \text{if (a)} S_1 \leq 0 \text{ or (b)} 0 < S_1 < -S_2 \\ Q(-S_1) - Q(S_2) = 1 - Q(S_1) - Q(S_2) & \text{if (c)} 0 \leq -S_2 < S_1 \text{ or (d) } S_2 > 0 \end{cases} \tag{20}$$

where the Q-function is defined as the probability that a Gaussian random Z is greater than x:

$$Q(x) = p(Z > x) = \int_x^{\infty} \frac{1}{\sqrt{2\pi}} e^{-\frac{y^2}{2}} dy \tag{21}$$

The (a)-(d) situations are illustrated in the Fig. 3. It's worth mentioning that $P(D_1 \leq \hat{D} \leq D_2) = P(d_1 \leq \hat{d} \leq d_2)$. When D_1 and D_2 are set to be values pretty close to D, (20) turns out to be the probability of correct distance range.

Based on our previous analysis, it's obvious that

$$\hat{D} = D + \frac{X}{N\beta} \tag{22}$$

When the relative motion between UAV and the emitter is very slow, the mean of $\frac{X}{N\beta}$, i.e., $l = \frac{m}{N\beta}$ can be considered zero because the mean may be considered to describe the average discrepancies in real and estimated distance between the RF emitter and the UAV during the moment of computation. Also, for simplicity and clarity, we use η to denote the variance of $\frac{X}{N\beta}$, which is $\frac{\sigma^2}{N^2\beta^2}$. Therefore, the probability of estimation that RF emitter locate in the range $[D_1, D_2]$ by a single UAV becomes

$$\begin{aligned} P_{cs}(D_1, D_2) &= \int_{D_1}^{D_2} P(D_1 \leq \hat{D} \leq D_2) f_N(u) du \\ &= \int_{D_1}^{D_2} P(D_1 \leq \hat{D} \leq D_2) \frac{1}{\sqrt{2\pi}\eta} e^{\frac{-(u-D)^2}{2\eta^2}} d\hat{D} \\ &= P(D_1 \leq \hat{D} \leq D_2)[Q(\frac{D_1 - D}{\eta}) - Q(\frac{D_2 - D}{\eta})] \end{aligned} \tag{23}$$

When the relative motion between the UAV and the RF emitter is obvious, due to the random variation, even the mean can be considered as a variable which follows uniform distribution in the range $[L_1, L_2]$(in dB form), where $L_1 < D_1 - D$ and $L_2 > D_2 - D$. In this case, the probability of RF emitter locating in the range $[D_1, D_2]$ by a single UAV becomes

$$\begin{aligned} P_{cm}(D_1, D_2) &= \int_{D_1}^{D_2} P(D_1 \leq \hat{D} \leq D_2) \int_{L_1}^{L_2} \frac{1}{\sqrt{2\pi}\eta} e^{\frac{-(u-D-v)^2}{2\eta^2}} \cdot \frac{1}{L_2 - L_1} dv du \\ &= \frac{P(D_1 \leq \hat{D} \leq D_2)}{L_2 - L_1} [\int_{L_1}^{L_2} Q(\frac{D_1 - D - v}{\eta}) - \int_{L_1}^{L_2} Q(\frac{D_2 - D - v}{\eta})] dv \end{aligned} \tag{24}$$

2.3 Netcentric Decision

As soon as each UAV obtains its distance from the RF emitter, this data will immediately be sent to a fusion center through TDMA data links. The fusion center can be a ground station or even mounted on one of the UAVs. Due to the shadowing and multiparth, the signal sent by a UAV will encounter fading before arriving at the fusion center. Assume the instantaneous signal-to-noise ratio (SNR) is y, the statistical averaging probability of error over the fading distribution [23] is

$$P_{e_m_f} = \int_0^\infty P_m(y) p_f(y) dy \tag{25}$$

where $P_m(y)$ is the probability of symbol error in AWGN based on a certain modulation scheme and $p_f(y)$ denotes the PDF of the fading amplitude.

Apply the moment generating function (MGF) $M_f(s) = \int_0^\infty p_f(y)e^{sy}dy$ and alternate Q-function $Q(x) = \frac{1}{\pi}\int_0^{\pi/2} e^{\frac{-x^2}{2\sin^2\varphi}}d\varphi$, we derive the probability of symbol error for the UAV network using 4 most common modulation schemes: phase-shift keying (MPSK), pulse amplitude modulation (MPAM), quadrature amplitude modulation (MQAM) and noncoherent frequent-shit keying (MFSK) respectively as follows:

$$P_{e_MPSK_f} = \frac{1}{\pi}\int_0^{\frac{(M-1)\pi}{M}} M_f(-\frac{\sin^2(\pi/M)}{\sin^2\varphi})d\varphi \tag{26}$$

$$P_{e_MPAM_f} = \frac{2(M-1)}{\pi M}\int_0^{\frac{\pi}{2}} M_f(\frac{-3}{\sin^2\varphi(M^2-1)})d\varphi \tag{27}$$

$$\begin{aligned} P_{e_MQAM_f} &= \frac{4}{\pi}(\frac{\sqrt{M}-1}{\sqrt{M}})\int_0^{\frac{\pi}{2}} M_f(-\frac{3}{2(M-1)\sin^2\varphi})d\varphi \\ &\quad -\frac{4}{\pi}(\frac{\sqrt{M}-1}{\sqrt{M}})^2\int_0^{\frac{\pi}{4}} M_f(-\frac{3}{2(M-1)\sin^2\varphi})d\varphi \end{aligned} \tag{28}$$

$$P_{e_MFSK_f} = \sum_{n=1}^{M-1}\binom{M-1}{n}\frac{1}{n+1}M_f(-\frac{n}{n+1}) \tag{29}$$

When the channel is Rician fading with factor K, after derivation the detailed expression of (26)-(29) are as follows respectively:

$$P_{e_MPSK_Rician} = \frac{1+K}{\pi}\int_0^{\frac{(M-1)\pi}{M}} \frac{\sin^2\varphi\cdot\exp[-\frac{yK\sin^2(\pi/M)}{y\sin^2(\pi/M)+(1+K)\sin^2\varphi}]}{y\sin^2(\pi/M)+(1+K)\sin^2\varphi}d\varphi \tag{30}$$

$$P_{e_MPAM_Rician} = \frac{2(1+K)(M-1)}{\pi M}\int_0^{\pi/2} \frac{\sin^2\varphi\cdot\exp\{-\frac{3Ky}{(M^2-1)[\frac{3y}{M^2-1}+(1+K)\sin^2\varphi]}\}}{\frac{3y}{M^2-1}+(1+K)\sin^2\varphi}d\varphi \tag{31}$$

$$\begin{aligned} P_{e_MQAM_Rician} &= \frac{4(\sqrt{M}-1)(1+K)}{\pi\sqrt{M}}\int_0^{\frac{\pi}{2}} \frac{\sin^2\varphi\cdot\exp\{-\frac{3Ky}{2(M-1)[\frac{3y}{M^2-1)}+(1+K)\sin^2\varphi]}\}}{\frac{3y}{2(M-1)}+(1+K)\sin^2\varphi}d\varphi \\ &\quad -\frac{4(1+K)}{\pi}(\frac{\sqrt{M}-1}{\sqrt{M}})^2\int_0^{\frac{\pi}{4}} \frac{\sin^2\varphi\cdot\exp\{-\frac{3Ky}{2(M-1)[\frac{3y}{M^2-1)}+(1+K)\sin^2\varphi]}\}}{\frac{3y}{2(M-1)}+(1+K)\sin^2\varphi}d\varphi \end{aligned} \tag{32}$$

$$P_{e_MFSK_Rician} = \sum_{n=1}^{M}(-1)^{n+1}\binom{M-1}{n}\frac{1}{n+1}\cdot\frac{1+K}{1+K+\frac{ny}{n+1}}\exp\{\frac{-K\frac{ny}{n+1}}{1+K+\frac{ny}{n+1}}\} \tag{33}$$

To simplify the (30)-(33), two extreme cases are taken into account. When the Rician fading factor $K \to 0$, it becomes Rayleigh distribution, therefore (30)-(33) can be denoted using following expressions in this case:

$$P_{e_MPSK_Ray} = 1 - \sqrt{\frac{y\sin^2(\frac{\pi}{M})}{1+y\sin^2(\frac{\pi}{M})}} \tag{34}$$

$$P_{e_MPAM_Ray} = \frac{M-1}{M}\cdot(1-\sqrt{\frac{\frac{3y}{M^2-1}}{1+\frac{3y}{M^2-1}}}) \tag{35}$$

$$\begin{aligned} P_{e_MQAM_Ray} &= \frac{2(\sqrt{M}-1)}{\sqrt{M}}(1-\sqrt{\frac{\frac{3y}{2(M-1)}}{1+\frac{3y}{2(M-1)}}}) - 4(\frac{\sqrt{M}-1}{\sqrt{M}})^2 \\ &\cdot[\frac{1}{4}-\frac{1}{\pi}\sqrt{\frac{\frac{3y}{2(M-1)}}{1+\frac{3y}{2(M-1)}}}arctg\sqrt{\frac{1+\frac{3y}{2(M-1)}}{\frac{3y}{2(M-1)}}}] \end{aligned} \tag{36}$$

$$P_{e_MFSK_Ray} = \sum_{n=1}^{M-1}(-1)^{n+1}\binom{M-1}{n}\frac{1}{n+1}(1+\frac{n}{n+1}y)^{-1} \tag{37}$$

When $K \to \infty$, the Rician fading channel becomes AWGN channel. In this situation, the probability of symbol error based on above modulation schemes have been well studied and the result is provided in [18], Table 6.1.

According to these performance, the best modulation scheme can be chosen to reduce the probability of error. This will be further illustrated in Section 3 by simulations.

For simplicity and clarity, we assume the RF emitter is on the ground surface. In the case that the relative motion between the RF emitter and UAVs are quite slow, the UAV a is able to be aware that the RF emitter is somewhere on a circle, of which the center is itself and the radius is d_a, as illustrated in Fig. 4(a). Another UAV b can also identify that there is a RF emitter on a circumference with radius d_b. After combining the information from both a and b, the fusion center will be aware that the target either locates at the position A or B. With the help of a third UAV

c, the fusion center will have the knowledge that the RF emitter is at the position A. Therefore with the triangulation, 3 UAVs are able to locate the RF emitter on the ground. In the case that the target is above the ground, 4 UAVs are necessary with one more member providing altitude geolocation information.

When the relative movement between the target and UAVs are obvious, a and b will aware that the RF emitter is moving within a ring area, and the fusion system will understand that the the target is within the intersection of 2 rings. Suppose the intersection area is $\widehat{abc}$ (the intersection can also be 2 independent areas, here we use one case for illustration without loss of generality), shown in Fig. 4(b). When the data from c is obtained, its detected range ring will intersect with $\widehat{abc}$ in a line $\overline{DE}$. Therefore, the trace of the RF emitter DE will be successfully obtained. After a few numbers of measurement, the motion speed, acceleration of the target can be calculated based on range and time difference.

Due to the independence of the distance estimation by each UAV and the transmission of data to the fusion center, the probability that a single UAV accurately provides the geolocation information to the fusion center is $P_{cs}(D_1, D_2) \cdot (1 - P_{e_MPSK_f})$ or $P_{cm}(d_1, d_2) \cdot (1 - P_{e_MPSK_f})$ for different relative motion situations, where D_1, D_2 and d_1, d_2 are close to D and d respectively. Therefore, the probability of error for the netcentric SUAS made up of 3 UAVs can be denoted as

$$P_{es} \leq 1 - [P_{cs}(D_1, D_2) \cdot (1 - P_{e_MPSK_f})]^3 \tag{38}$$

$$P_{em} \leq 1 - [P_{cm}(d_1, d_2) \cdot (1 - P_{e_MPSK_f})]^3 \tag{39}$$

The above expressions are error upper bound, this is because the netcentric decision provides much more resilience than a single UAV. For example, in Fig. 4(a) assume UAV a and b accurately geolocate the target while c has a large location error and believes the target is far away from the pint A and B, the whole system may still provide accurate estimation if c determines that the target is closer to A compared with B. Demanding every UAV to provide accurate information to fusion center is a stringent rule, therefore (38) and (39) are upper bounds.

3 Simulation Results and Performance Analysis

Simulations on a basis of mathematical expressions in Section 2 are presented in this Section for better analysis and illustration about SUAS performance. In the simulation, we assume $d = 100m$, $d_0 = 0.1d$ and $\beta = 2$.

Fig. 5 describes about error probability of distance range vs. frequency for a single UAV, where $d_1 = 0.99d$ and $d_2 = 1.01d$ have been used. The curves show that given the same σ (see (10)), the error probability of distance range will be reduced as the frequency increases. However, when the frequency is higher than a certain threshold value, such as 10^8 for $\sigma = 10$, the error probability becomes a constant. This phenomenon is the result of nonlinearity of the Q function. Therefore, this UAV system is more appropriate for geolocate an emitter with higher frequency.

Fig. 6 shows the contribution of another important factor power-rate-to-noise ratio (PRNR) to the correct probability of distance range for a single UAV. We define PRNR as $\frac{P(d_0)}{\sigma P_r}$. It is easy to observe that similar to Fig. 5, there is also a threshold value in correct probability of distance range. The larger the η (see (22)), the smaller the threshold value as well as the probability correctness.

Fig. 7-10 illustrate upper bound error probability for netcentric UAVs based on (38) and (39). Fig. 7 and 8 are in the environment of AWGN while Fig. 9 and 10 are for Rayleigh fading. In the case that relative motion between the RF emitter and UAVs are slow, $d_1 = 0.99d$, $d_2 = 1.01d$ and $\eta = 1$; when the relative motion is obvious we apply $l_1 = -0.1d$, $l_2 = 0.1d$ and $\eta = 1$, therefore $P_{cs}(D_1, D_2) = 0.9876$ and $P_{cm}(D_1, D_2) = 0.94$. In Figs. 7 and 9, modulation schemes MFSK, MPAM, MPSK and MQAM with $M = 4$ are applied for illustration. This does not mean $M = 2$ can not be used. Actually, the smaller M, the smaller probability of symbol error rate for the same modulation scheme. That partially contributes to the smaller probability of error in Fig. 8. Moreover, the resilience of netcentric design makes the probability of error using BFSK and BPSK much smaller compared to that of 4-FSK and QPSK. This is the same situation while comparing Fig. 10 with 9.

These figures show that no matter the wireless radio channel between UAVS and fusion center is AWGN or Rayleigh, MQAM will provide the smallest probability of error at low SNR while MPSK will provide the smallest probability of error at moderate to high SNR. Therefore MQAM

and MPSK can be applied for adaptive modulation for data fusion depending on how large is the SNR at the receiver of fusion center.

4 Conclusions

In this work, we propose a passive geolocation approach to geolocate RF emitter using a netcentric small UAV systems (SUAS) equipped with ES sensors. This approach is based on log-normal shadowing model, which has been empirically confirmed to model accurately the variation in received power in propagation environments. We show that the geolocation error is essentially a log-normal random variable. The larger number of ES sensors, the smaller geolocation area upper bound error. We also analyze the error probability of distance range for the system. We demonstrate that when the emitter frequency is higher than a certain threshold value, the error probability becomes a constant. The situation is similar for power-rate-to-noise ratio (PRNR). Regardless what the wireless radio channel between UAVS and fusion center is, for example AWGN, Rayleigh or Rician, at low SNR MQAM modulation is applied while MPSK will be chosen at moderate to high SNR due to the smallest performance error of the whole system.

Acknowledgement

This work was supported in part by Office of Naval Research (ONR) under Grant N00014-07-1-0395, N00014-07-1-1024, and National Science Foundation (NSF) under Grant CNS-0721515.

References

[1] R. Poisel, *Electronic Warfare Target Location Method*, Artech House, Boston, 2005.

[2] A. G. Lindgren and K. F. Gong, "Position and velocity estimation via bearing-only observations", *IEEE Trans. Aerosp. Electron. Syst.*, vol. 14, pp. 564-577, July 1978.

[3] S. C. Nardone, A.G. Lindgren and K.F. Gong, "Fundamental properties and performance of conventional bearing-only target motion analysis", *IEEE Trans. Automat. Contr.*, vol. 29, pp. 775-787, Sept. 1984.

[4] M. Gavish and A. J. Weiss, "Performance analysis of bearing-only target location algorithm", *IEEE Trans. Aerosp. Electron. Syst.*, vol. 26, pp. 22-26, Oct. 1992.

[5] V. J. Aidala and S. E. Hammel, "Utilization of modified polar coordinates for bearing-only tracking", *IEEE Trans. Automat. Contr.*, vol. 28, pp. 283-294, March 1983.

[6] J. P. Le Cadre and C. Jauffret, "On the convergence of iterative methods for bearing-only tracking", *IEEE Trans. Aerosp. Electron. Syst.*, vol. 34, pp. 179-193, Jan. 1998.

[7] M. I. Skolnik, *Introduction to Radar Systems* , 3rd ed, New York, McGraw Hill, 2001.

[8] K. C. Overman, K. A. Leahy, T. W. Lawrence and R. J. Fritsch, "The future of surface surveillance - revolutionizing the view of the battlefield", *IEEE International Radar Conf.*, pp.1-6, May 2000.

[9] D. Ledger, "Electronic warfare capabilities of mini UAVs", http://aerosonde.com.au/downloads/electronic_warfare_ledger.doc

[10] R. Madison, P. DeBitetto, A. R. Olean and M. Peebles, "Target Geolocation from a Small Unmanned Aircraft System", *2008 IEEE Aerospace Conference*, pp. 1-19, March 2008.

[11] M. Wheeler, B. Schrick, W. Whitacre, M. Campbell, R. Rysdyk and R. Wise, "Cooperative Tracking of Moving Targets by a Team of Autonomous UAVs", *2006 IEEE/AIAA 25th Digital Avionics Systems Conference*, pp. 1-9, Oct. 2006.

[12] N. Okello, "Emitter Geolocation with Multiple UAVs", *2006 9th International Conference on Information Fusion*, pp. 1-8, July, 2006.

[13] N. Okello and D. Musicki, "Measurement Association for emitter geolocation with two UAVs", *2007 10th International Conference on Information Fusion*, pp. 1-8, July 2007.

[14] L. Marsh, D. Gossink, S. P. Drake and G. Calbert, "UAV Team Formation for Emitter Geolocation", *Information, Decision and Control, 2007, IDC'07*, pp. 176-181, Feb. 2007.

[15] A. Mikhalev and R. F. Ormondroyd, "comparison of hough transform and particle filter methods of emitter geolocation using fusion of TDOA Data", *4th Workshop on Positioning, Navigation and Communication 2007, WPNC'07*, pp.121-127.

[16] F. Fletcher, B. Ristic, D. Musicki, "Recursive estimation of emitter location using TDOA measurements from two UAVs", *2007 10th International Conference on Information Fusion*, pp. 1-8, July 2007.

[17] T. S. Rappaport, *Wireless Communications: Principles and Practice*, 2nd ed., Upper Saddle River, NJ: Prentice-Hall, 2002.

[18] A. Goldsmith, *Wireless Communications*, Cambridge University Press, NJ 2001.

[19] V. Erceg, L. J. Greenstein, S. Y. Tjandra, S. R. Parkoff, A. Gupta, B. Kulic, A. A. Julius, and R. Bianchi, "An empirically based path loss model for wireless channels in suburban environments", *IEEE J. Sel. Areas Commun.*, pp. 1205-11, July 1999.

[20] V. Erceg, L. J. Greenstein, S. Y. Tiandra, S. R. Parkoff, A. Gupta, B. Kulic, A. A. Julius, and R. Bianchi, "An empirically based path loss model for wireless channels in suburban environments", *IEEE J. Sel. Aresas Commun.*, pp. 1205-1211, July 1999.

[21] S. S. Ghassemzadeh, L. J. Greenstein, A. Kavcic, T. Sveinsson, and V. Tarokh, "Indoor path loss model for residential and commercial buildings", *Proc. IEEE Veh. Tech, Conf.*, pp. 3115-3119, Oct. 2003.

[22] A. J. Goldsmith, L. J. Greenstein and G. J. Foschini, "Error statistics of real-time power measurements in cellular channels with multipath and shadowing", *IEEE Trans. Veh. Tech.*, pp. 439-446, August, 1994.

[23] M. K. Simon and M.-S. Alouini, *Digital Communication over Fading Channels*, 2nd, Wiley, New Jersy, 2005.

List of Figures

1 Path loss, shadowing vs. distance. 17

2 Upper bound of geolocation area mean square error for a UAV network. 17

3 Distance range probability illustration based on Q function: (a)$S_1 \leq 0$ (b)$0 < S_1 < -S_2$ (c)$0 \leq -S_2 < S_1$ (d) $S_2 > 0$. 18

4 RF emitter Geolocation by SUAS (a) Relative movement between RF emitter and UAVs are slow (b) Relative movement between RF emitter and mini UAVs are obvious. 18

5 Error probability of distance range vs. frequency for a single UAV. 19

6 Correct probability of distance range vs. power-rate-to-noise ratio (PRNR) for a single UAV. 19

7 Upper error bound of the netcentric UAVs in AWGN when relative movement between the RF emitter and UAVs are slow. 20

8 Upper error bound of the netcentric UAVs in AWGN when relative movement between the RF emitter and UAVs are obvious. 20

9 Upper error bound of the netcentric UAVs in Rayleigh fading when relative movement between the RF emitter and UAVs are slow. 21

10 Upper error bound of the netcentric UAVs in Rayleigh fading when relative movement between the RF emitter and UAVs are obvious. 21

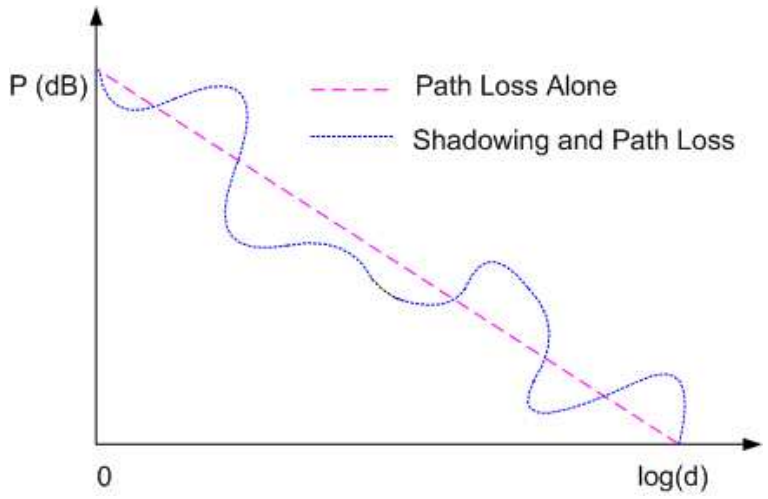


Figure 1: Path loss, shadowing vs. distance.

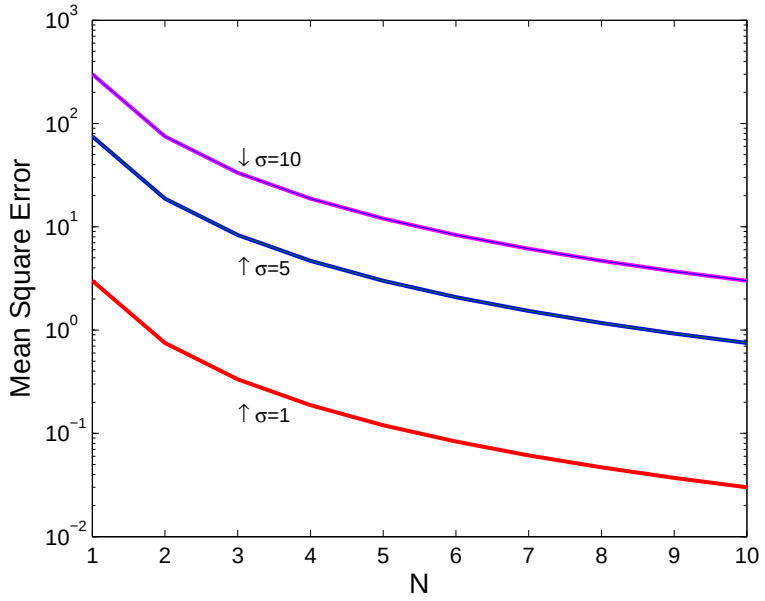


Figure 2: Upper bound of geolocation area mean square error for a UAV network.

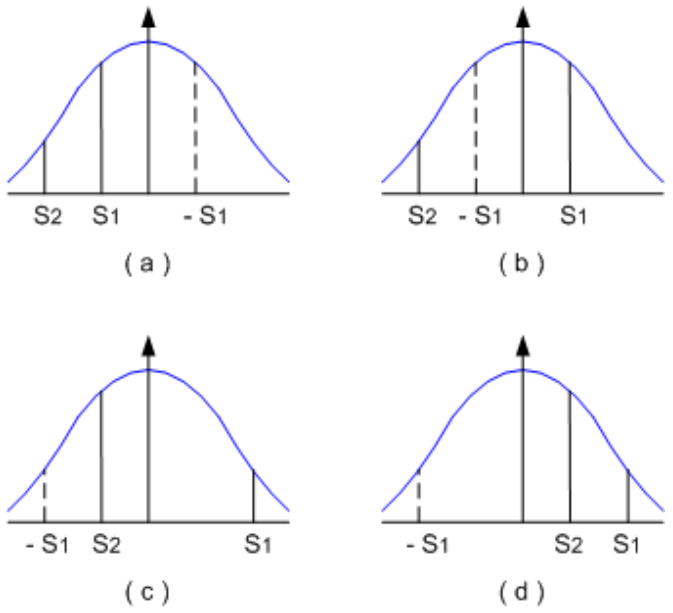
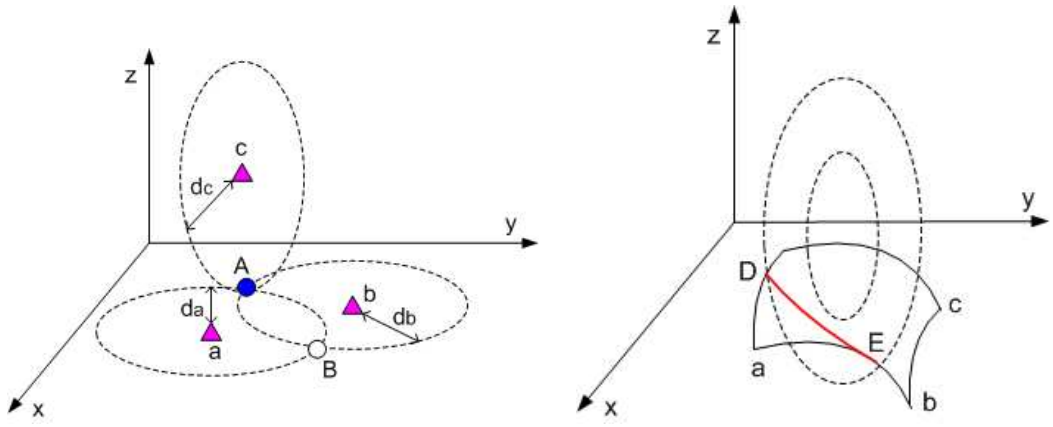


Figure 3: Distance range probability illustration based on Q function: (a)$S_1 \leq 0$ (b)$0 < S_1 < -S_2$ (c)$0 \leq -S_2 < S_1$ (d) $S_2 > 0$.



(a) (b)

Figure 4: RF emitter Geolocation by SUAS (a) Relative movement between RF emitter and UAVs are slow (b) Relative movement between RF emitter and mini UAVs are obvious.

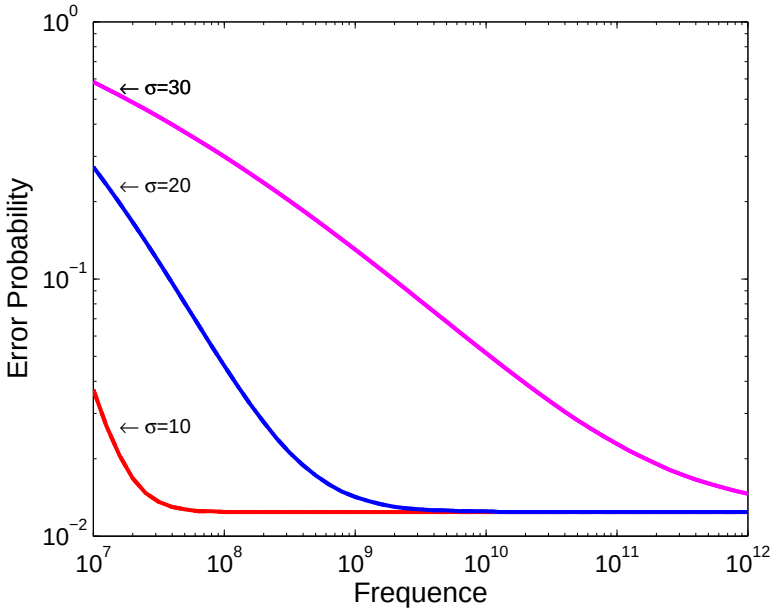


Figure 5: Error probability of distance range vs. frequency for a single UAV.

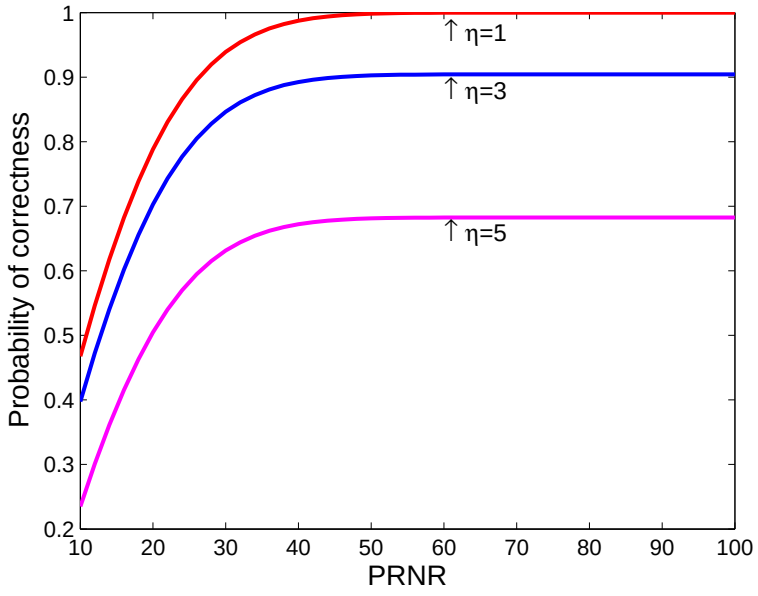


Figure 6: Correct probability of distance range vs. power-rate-to-noise ratio (PRNR) for a single UAV.

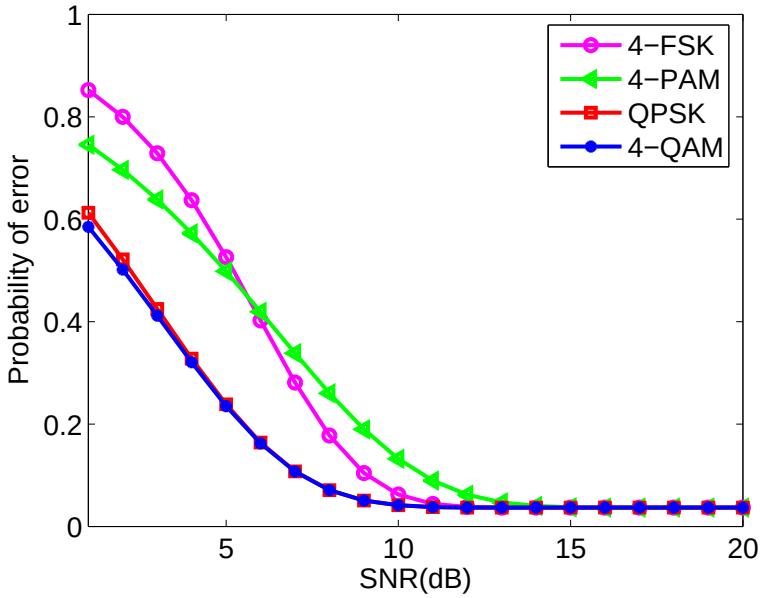


Figure 7: Upper error bound of the netcentric UAVs in AWGN when relative movement between the RF emitter and UAVs are slow.

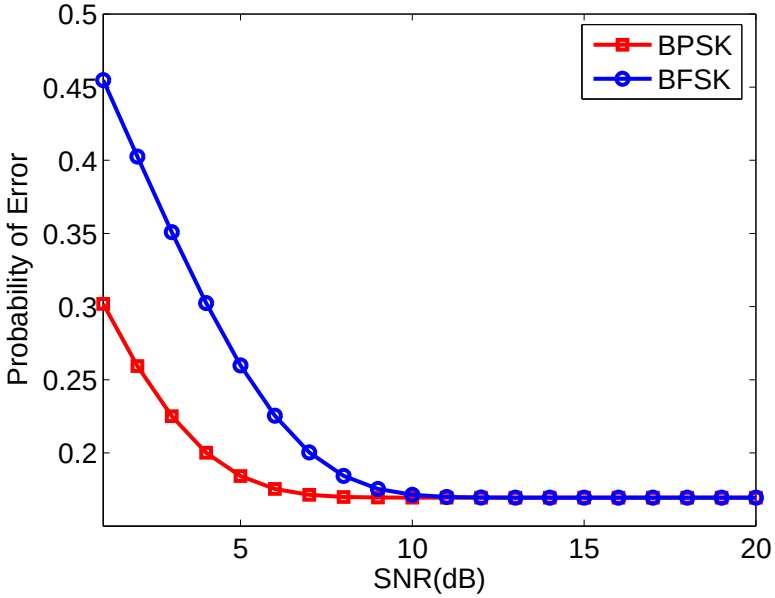


Figure 8: Upper error bound of the netcentric UAVs in AWGN when relative movement between the RF emitter and UAVs are obvious.

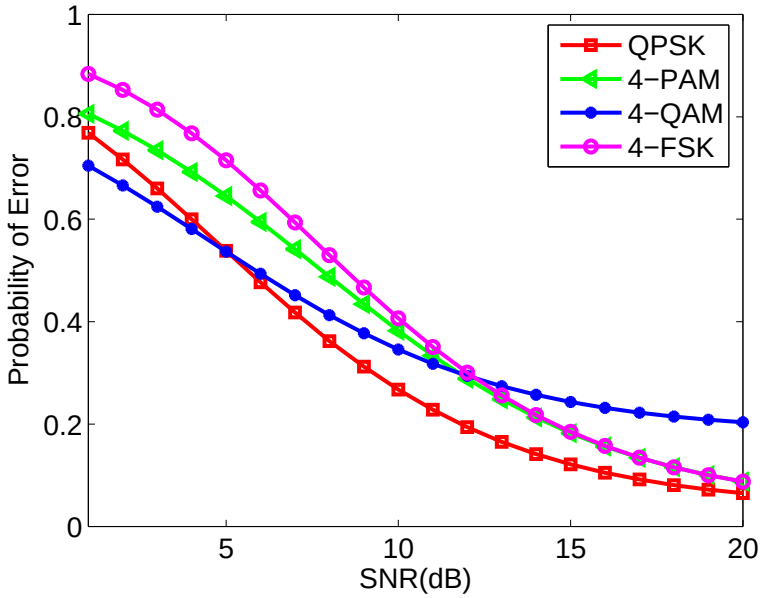


Figure 9: Upper error bound of the netcentric UAVs in Rayleigh fading when relative movement between the RF emitter and UAVs are slow.

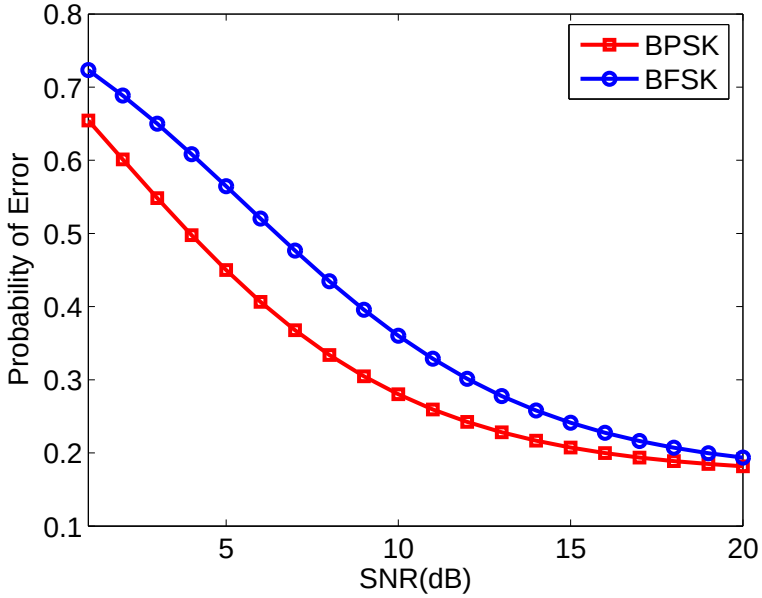


Figure 10: Upper error bound of the netcentric UAVs in Rayleigh fading when relative movement between the RF emitter and UAVs are obvious.

Human-Inspired Favor-Weak Fuzzy Logic Systems: Theory and Applications

Qilian Liang, *Senior Member, IEEE*

Department of Electrical Engineering

University of Texas at Arlington

Arlington, TX 76019-0016 USA

E-mail: liang@uta.edu

Abstract

Humans use multiple sources of sensory information to estimate environmental properties and has innate ability to integrate information from heterogeneous data sources. How the multi-sensory and multimodal information are integrated in human brain? There is consensus that it depends on the prefrontal cortex (PFC). The PFC has top-down control (favor weak) and rule-based mechanisms, and we propose to incorporate the favor weak mechanism into rule-based fuzzy logic systems (FLS) via using upper and lower membership functions. The inference engine of favor weak fuzzzy logic system is proposed under three different categories based on fuzzifiers. We observe that the favor weak FLS is a special type-1 FLS which is embeded in an interval type-2 FLS, so it's much simpler in computing than an interval type-2 FLS. We apply the favor weak FLS to situation understanding based on heterogeneous sensor network, and it shows that our favor weak fuzzy logic system has clear advantage comparing to the type-1 FLS. The favor weak FLS can increase the probability of threat detection, and provides timely indication & warning (I&W).

Index Terms : Fuzzy logic systems, prefrontal cortex (PFC), favor weak, upper and lower membership functions, situation understanding, heterogeneous sensor networks.

1 Introduction and Motivation

Humans use multiple sources of sensory information to estimate environmental properties. For example, the eyes and hands both provide relevant information about an objects shape. The eyes estimate shape using binocular disparity, perspective projection, etc. The hands supply haptic shape information by means of tactile and proprioceptive cues. **Combining information across cues can improve estimation of object properties** but may come at a cost: loss of single-cue information. Recent studies [14] showed that single-cue information is indeed lost when cues from within the same sensory modality (e.g., disparity and texture gradients in vision) are combined, **but not when different modalities (vision and haptics) are combined**. In another study on human [8], gaze shifts are coordinated movements of the eyes (eyes-re-head) and head (head-re-space) that rapidly reorient the visual axis (eyes-re-space) to a target of interest. Reaction latencies for gaze shifts to combined auditory and visual stimuli presented in close spatial and temporal register are **less than those to either stimulus presented alone**, suggesting that the integration of multisensory information may play an important role in forming appropriate motor behaviors. These studies demonstrate that human has innate ability to integrate information from heterogeneous data sources and multi-sensory and multimodal information integration has clear advantage.

In this paper, as a product of multidisciplinary collaborative research, we incorporate human brain mechanisms to a new fuzzy logic system design and apply it to situation understanding based on heterogeneous sensor network. A heterogeneous sensor network consists of multiple networked sensors with different modality (video, audio, acoustic, radar, etc), and such networks are necessary in different applications. For example, in an emergency natural disaster scenario, information integration for first responders is critical for search and rescue. Besides, the first responders need to be situation-aware. Danger may appear anywhere at any time, therefore, first responders must monitor a large area continuously in order to iden-

tify potential danger and take actions. Due to the dynamic and complex nature of natural disaster, some victims may not be found with a single type of sensor modality, for example, image/video sensors can't be used to find a buried/foleage victim, UWB radar sensors need to be used for penetrating the ground or sense-through-wall, and acoustic sensors are needed to collect the voice from victims. Similarly, some potential dangers may not be identified using a single modality sensor. More modalities are required to search victims and identify potential dangers and that means large-scale Heterogeneous Sensor Networks (HSN) are needed for search, rescue, and situation awareness. However, information integration algorithms (especially for situation awareness) for heterogeneous sensor networks don't exist. Motivated by the above challenges, we study human-inspired information integration for heterogeneous sensor networks.

The remaining of the paper is organized as follows. In Section 2, we present the heterogeneous information integration in Human brain and challenges to fuzzy logic system design. In Section 3, we give an overview on upper and lower membership design and describe how it can be used to the new fuzzy logic system design. In Section 4, we present the inference engine for favor weak fuzzy logic system, and its relations with the interval type-2 fuzzy logic systems are described in Section 5. The application to situation understanding based on heterogeneous sensor network is presented in Section 6. Section 7 concludes this paper.

2 Heterogeneous Information Integration in Human Brain and Challenges to Fuzzy Logic System Design

One of the great mysteries of the brain is cognitive control. How can the interactions between millions of neurons result in behavior that is coordinated and appears willful and voluntary? There is consensus that it depends on the prefrontal cortex (PFC) [35][39]. A schematic diagram of some of the extrinsic and intrinsic connections of the PFC is depicted in Fig. 1 [35].

Many PFC areas receive converging inputs from at least two sensory modalities [5][18]. For example, the dorsolateral (DL) (areas 8, 9, and 46) and ventrolateral (12 and 45) PFC both receive projections from visual, auditory, and somatosensory cortex. Furthermore, the PFC is connected with other cortical regions that are themselves sites of multimodal convergence. Many PFC areas (9, 12, 46, and 45) receive inputs from the rostral superior temporal sulcus, which has neurons with bimodal or trimodal (visual, auditory, and somatosensory) responses [1][40]. The arcuate sulcus region (areas 8 and 45) and area 12 seem to be particularly multimodal. They contain zones that receive overlapping inputs from three sensory modalities [40]. Observe, for example, that mid-dorsal area 9 directly processes and integrates visual, auditory, and multimodal information.

2.1 PFC Top-Down Control (Favor Weak) and Rule-Based Mechanisms

According to [35][39], the PFC is modulatory rather than transmissive. That is, the pathway from input to output does not "run through" the PFC. Instead, the PFC guides activity flow along task-relevant pathways in more posterior and/or subcortical areas. The PFC is important when "top-down" processing is needed; that is, when behavior must be guided by internal states or intentions. The PFC is critical in situations when the mappings between sensory inputs, thoughts, and actions either are *weakly established* relative to other existing ones or are *rapidly changing*. This is when we need to use the "*rules* of the game," internal representations of goals and the means to achieve them [35]. Several investigators have argued that this is a cardinal function of the PFC [7][41][12][46][34]. The top-down control and favor weak mechanism can be illustrated using the Stroop task Wisconsin card sort task (WCST).

In the Stroop task [44][31], subjects either read words or name the color in which they are written. To perform this task, subjects must selectively attend to one attribute. This is especially so when naming the color of a conflict stimulus (e.g. the word GREEN displayed in red), because there is a strong prepotent tendency to read the word ("green"), which competes

with the response to the color ("red"). This illustrates one of the most fundamental aspects of cognitive control and goal-directed behavior: the ability to select a weaker, task-relevant response (or source of information) in the face of competition from an otherwise stronger, but task-irrelevant one. Patients with frontal impairment have difficulty with this task, especially when the instructions vary frequently, which suggests that they have difficulty adhering to the goal of the task or its rules in the face of a competing stronger (i.e. more salient or habitual) response [35]. Similar findings are evident in the WCST [36]. Subjects are instructed to sort cards according to the shape, color, or number of symbols appearing on them and the sorting rule varies periodically. Thus, any given card can be associated with several possible actions, no single stimulus-response mapping will work, and the correct one changes and is dictated by whichever rule is currently in effect. Humans with PFC damage show stereotyped deficits in the WCST. They are able to acquire the initial mapping without much difficulty but are unable to adapt their behavior when the rule varies [36]. Monkeys with PFC lesions are impaired in an analog of this task and in others when they must switch between different rules [35].

The Stroop task, naming the color of a conflict stimulus, and WCST [36] are variously described as tapping the cognitive functions of either **selective attention, behavioral inhibition, top-down control, working memory, or rule-based or goal-directed behavior** [35]. As suggested by Desimone and Duncan [10], selective attention and behavioral inhibition are two sides of the same coin: attention is the effect of biasing competition in favor of task-relevant information, and inhibition is the consequence that this has for the irrelevant information. In this project, we will study human brain top-down control and rule-based mechanisms inspired information integration. In current HSN design, the clusterhead only serves a "transmissive" (data collection and relay to gateway) function. In this project, the HSN clusterhead will also provide a "modulatory" function, i.e., multimodal information integration. In natural disaster or terrorist attack recovery, the most dangerous potential threat factors (stimuli) are weak or hidden but are highly correlated with the situation understanding

task, and of course, they are time sensitive (rapidly changing), which indicates that the PFC "top-down" control mechanism can be applied to HSN-based situation understanding.

The PFC top-down control signals *favor weak (but task-relevant) stimulus-response mappings* when they are in competition with more habitual, stronger ones (as in the Stroop task, where the word GREEN is stronger and the color red is weak), especially when flexibility is needed (such as in the WCST) [35]. Moreover, all of the PFC neural mechanisms depend on the representation of goals and *rules* in the form of patterns of activity in the PFC, which configure processing in other parts of the brain in accordance with current task demands [35][39]. Such mechanisms motivate us to heavily revisit a rule-based approach: fuzzy logic systems (FLS), mimicking the rule-based PFC neural mechanism, and subsequently applying it to HSN-based situation awareness.

2.2 Overview of Fuzzy Logic Systems and Its Shortfall

The current type-1 FLS designs doesn't have "favor strong or favor weak control". In a type-1 FLS with a rule base of M rules, in which each rule has p antecedents, let the lth rule be denoted by R^l, where R^l: IF x_1 is F_1^l, and x_2 is F_2^l, and, ..., and x_p is F_p^l THEN y is G^l. The membership function, $\mu_{\mathrm{B}^l}(y)$, of a fired rule can be expressed by the following sup-star composition [33]:

$$\mu_{\mathrm{B}^l}(y) = \sup_{\mathbf{x}\in \mathrm{A}^*}[\mu_{\mathrm{A}^*}(\mathbf{x}) \star \mu_{\mathrm{A}^l \to \mathrm{B}^l}(\mathbf{x}, y)] \tag{1}$$

where A^* is a p-dimensional Cartesian product space, $\mathrm{A}^* = \mathrm{A}_1^* \times \cdots \times \mathrm{A}_p^*$, A_k^* is the measurement domain of input x_k, $(k = 1, \cdots, p)$; and, A^* is given by

$$\mu_{\mathrm{A}^*}(\mathbf{x}) = \mu_{\mathrm{A}_1^* \times \cdots \times \mathrm{A}_p^*}(\mathbf{x}) = \mu_{\mathrm{X}_1}(x_1) \star \cdots \star \mu_{\mathrm{X}_p}(x_p) \tag{2}$$

In the current type-1 FLS design,

$$\mu_{\mathrm{A}^l \to \tilde{\mathrm{B}}^l}(\mathbf{x}, y) = \mu_{\mathrm{F}_1^l}(x_1) \star \mu_{\mathrm{F}_2^l}(x_2) \star \cdots \star \mu_{\mathrm{F}_p^l}(x_p) \star \mu_{\mathrm{G}^l}(y) \tag{3}$$

For the Stroop task, to name the color of a conflict stimulus (e.g. the word GREEN displayed in red), needs the favor weak mechanism because there is a strong prepotent tendency to read the word ("green"), which competes with the response to the color ("red"). In Fig. 2, we illustrate the schematic of the Stroop model using the example to name the color when the word GREEN displayed in red [35].

So in the FLS design, the firing degree for "red" should be boosted to reflect the "favor weak" mechanism if a conflict stimulus presents, but no control should be taken if no conflict stimulus presents (e.g., name the word when the word GREEN displayed in red). This motivates us to use different membership degrees under different scenarios. We propose to use interval type-2 fuzzy membership function for this favor weak (using upper membership function) or no control (using lower membership function) mechanism.

3 Upper and Lower Membership Functions

An upper MF and a lower MF are two type-1 MFs which are bounds for the footprint of uncertainty of an interval type-2 MF. The upper MF is a subset which has the maximum membership grade of the footprint of uncertainty; and, the lower MF is a subset which has the minimum membership grade of the footprint of uncertainty [21].

Same as that in [21], we use an overbar (underbar) to denote the upper (lower) MF. For example, the upper and lower MFs of $\mu_{\tilde{\text{A}}_k^l}(x_k)$ are $\overline{\mu}_{\tilde{\text{A}}_k^l}(x_k)$ and $\underline{\mu}_{\tilde{\text{A}}_k^l}(x_k)$, respectively, so that

$$\mu_{\tilde{\text{A}}_k^l}(x_k) = \int_{q^l \in [\underline{\mu}_{\tilde{\text{A}}_k^l}(x_k), \overline{\mu}_{\tilde{\text{A}}_k^l}(x_k)]} 1/q^l \tag{4}$$

Example 1: Gaussian Primary MF with Uncertain Standard Deviation

Consider the case of a Gaussian primary MF having a fixed mean, m_k^l, and an uncertain standard deviation that takes on values in $[\sigma_{k1}^l, \sigma_{k2}^l]$, i.e.,

$$\mu_k^l(x_k) = \exp\left[-\frac{1}{2}(\frac{x_k - m_k^l}{\sigma_k^l})^2\right], \ \ \sigma_k^l \in [\sigma_{k1}^l, \sigma_{k2}^l] \tag{5}$$

where: $k = 1, \ldots, p$; p is the number of antecedents; $l = 1, \ldots, M$; and, M is the number of rules. The upper MF, $\overline{\mu}_k^l(x_k)$, is (see Fig. 3b)

$$\overline{\mu}_k^l(x_k) = \mathcal{N}(m_k^l, \sigma_{k2}^l; x_k), \tag{6}$$

and the lower MF, $\underline{\mu}_k^l(x_k)$, is (see Fig. 3)

$$\underline{\mu}_k^l(x_k) = \mathcal{N}(m_k^l, \sigma_{k1}^l; x_k) \tag{7}$$

□

This example illustrates how to define $\overline{\mu}$ and $\underline{\mu}$, so that it is clear how to define these membership functions for other situations (e.g., triangular, trapezoidal, bell MFs). In [50], different membership functions and approximation accuracy were studied.

4 The Inference Engine for Favor Weak FLSs

In a favor weak FLS with a rule base of M rules, in which each rule has p antecedents, let the lth rule be denoted by R^l, where R^l: IF x_1 is $\tilde{\mathrm{F}}_1^l$, and x_2 is $\tilde{\mathrm{F}}_2^l$, and, ..., and x_p is $\tilde{\mathrm{F}}_p^l$ THEN y is G^l. Although the rule may look the same as that of the interval type-2 FLS, but the inference engine is different.

In a favor weak FLS with p antecedents, without loss of generality, assume the first w ($w < p$) antecedents are weak and should be favored, and all other antecedents $(w+1, i_{w+2}, \cdots, i_p)$ should be in no control. If the antecedents are not in this order, they can be re-orderred. Then we can obtain the following Theorem. Our major result for favor weak FLSs is given in:

Theorem 1 *In a favor weak nonsingleton FLS (the first w antecedents are weak and should be favored) with type-2 fuzzification and meet under minimum or product t-norm: (a) the firing degree for rule l, i.e., the result of the input and antecedent operations, is*

$$f^l = \sup_{\mathbf{x} \in X} \int_{X_1} \cdots \int_{X_p} [\overline{\mu}_{\tilde{X}_1}(x_1) \star \overline{\mu}_{\tilde{F}_1^l}(x_1)] \star \cdots \star [\overline{\mu}_{\tilde{X}_w}(x_w) \star \overline{\mu}_{\tilde{F}_w^l}(x_w)] \tag{8}$$

$$\star [\underline{\mu}_{\tilde{X}_w+1}(x_{w+1}) \star \underline{\mu}_{\tilde{F}_{w+1}^l}(x_{w+1})] \star \cdots \star [\underline{\mu}_{\tilde{X}_p}(x_p) \star \underline{\mu}_{\tilde{F}_p^l}(x_p)] / \mathbf{x}\,; \tag{9}$$

the supremum is attained when each term in brackets attains its supremum;

(b) the rule R^l *fired output consequent set,* $\mu_{B^l}(y)$*, is*

$$\mu_{B^l}(y) = f^l \star \mu_{G^l}(y) \tag{10}$$

where $\underline{\mu}_{\tilde{G}^l}(y)$ *and* $\overline{\mu}_{\tilde{G}^l}(y)$ *are the lower and upper membership grades of* $\mu_{\tilde{G}^l}(y)$*; and,*

(c) the output fuzzy set, $\mu_B(y)$*, is*

$$\mu_{\tilde{B}}(y) = \bigcup_{l=1}^{M} \mu_{B^l}(y) \tag{11}$$

When the input is fuzzified to a type-1 fuzzy set, so that $\mu_{\tilde{\mathrm{X}}_k} \to \mu_{\mathrm{X}_k}$ $(k = 1, \ldots, p)$, the upper and lower MFs of $\mu_{\tilde{\mathrm{X}}_k}$ merge into one MF, $\mu_{\mathrm{X}_k}(x_k)$, in which case Theorem 1 simplifies to:

Corollary 1 *In a favor weak FLS (the first* w *antecedents are weak and should be favored) with* nonsingleton type-1 fuzzification *and meet under minimum or product t-norm,* f^l *in (9) simplifies to: the firing degree for rule* l *is*

$$f^l = \sup_{\mathbf{x} \in X} \int_{X_1} \cdots \int_{X_p} [\mu_{X_1}(x_1) \star \overline{\mu}_{\tilde{F}_1^l}(x_1)] \star \cdots \star [\mu_{X_w}(x_w) \star \overline{\mu}_{\tilde{F}_w^l}(x_w)] \tag{12}$$

$$\star [\mu_{X_{w+1}}(x_{w+1}) \star \underline{\mu}_{\tilde{F}_{w+1}^l}(x_{w+1})] \star \cdots \star [\mu_{X_p}(x_p) \star \underline{\mu}_{\tilde{F}_p^l}(x_p)] / \mathbf{x}\,; \tag{13}$$

the supremum is attained when each term in brackets attains its supremum.

When a singleton fuzzifier is used, the upper and lower MFs of $\mu_{\tilde{\mathrm{X}}_k}(x_k)$ merge into one crisp value, namely 1, in which case Theorem 1 simplifies further to:

Corollary 2 *In a favor weak FLS (the first* w *antecedents are weak and should be favored) with* singleton fuzzification *and meet under minimum or product t-norm,* f^l *in (9) simplifies to: the firing degree for rule* l*, i.e., the result of the input and antecedent operations,*

$$f^l = \overline{\mu}_{\tilde{F}_1^l}(x_1) \star \cdots \star \overline{\mu}_{\tilde{F}_w^l}(x_w) \star \underline{\mu}_{\tilde{F}_{w+1}^l}(x_{w+1}) \star \cdots \star \underline{\mu}_{\tilde{F}_p^l}(x_p) \tag{14}$$

where x_i $(i = 1, \ldots, p)$ *denotes the location of the singleton.*

5 Relations between Favor Weak FLS and Interval Type-2 FLS

In decision theory, *ambiguity* about probabilities should not affect choices. However, recent experiments [15] showed that many people are more willing to bet on risky outcomes (e.g., gambling on a roulette wheel) than on an ambiguous one (e.g., chance of a terrorist attack based on meager or conflicting evidence), holding the judged probability of outcomes constant. So, the confidence in judged probability can vary widely for "risky" and "ambiguous". Using functional brain imaging, Hsu et al [15] showed that the *level of ambiguity* in choices correlates positively with activation in the amygdala and orbitofrontal cortex, and negatively with a striatal system. This suggests that *degree of uncertainty* should be considered in decision making, contrary to traditional decision theory. In [13], a new model was proposed for group decision making in which experts preferences can be expressed as incomplete fuzzy preference relations. Type-2 fuzzy sets and FLSs are successful in handling the uncertainties [21]. Type-2 fuzzy sets have grades of membership that are themselves fuzzy. A type-2 membership grade can be any subset in $[0, 1]$ – the *primary membership*; and, corresponding to each primary membership, there is a *secondary membership* (which can also be in $[0, 1]$) that defines the possibilities for the primary membership. Figure 4 shows an example of a type-2 set. The domain of the membership grade corresponding to $x = 4$ is also shown.

In [21][24][26][27][28], Liang and Mendel proposed the theory and design of interval type-2 FLS. With their pioneering works, people are able to efficiently handle uncertainties. They applied interval type-2 FLS to a number of very important applications where uncertainties abound, such as fading channel equalization [22] and co-channel interference elimination [23], network video traffic modeling and classification [25], connection admission control for ATM network [20]. Recently, Liang and his students applied interval type-2 FLSs to sensor network lifetime estimation[43][42], event forecasting in wireless sensor networks[29][30], and cross-layer optimization in ad hoc networks[48][47].

Recently, Juang and Tsao [17] proposed a type-2 self-organizing neural fuzzy system (T2SONFS), of which the antecedent parts in fuzzy rule are interval type-2 fuzzy sets, and the consequent part is of Mamdani type. Using interval type-2 fuzzy sets in T2SONFS enables it to be more robust than type-1 fuzzy systems. A type-2 fuzzy logic system (FLS) cascaded with neural network, type-2 fuzzy neural network (T2FNN), was presented in [45] to handle uncertainty with dynamical optimal learning In [19], the interval type-2 fuzzy-model stability was analyzed. In [3], a type-2 fuzzy function system for uncertainty modeling using evolutionary algorithms (ET2FF) was proposed.

In this paper, PFC's "top-down control (favor weak)", "rule-based", and "brain handling ambiguity" mechanisms are incorporated into the favor weak FLS design to mimic human brain learning and decision making for associating, integrating and understanding/inferencing discovered knowledge from disparate sources. The favor weak FLS we proposed in this paper is a type-1 FLS which is embeded in the interval type-2 FLS.

6 Application to Situation Understanding Based on Heterogeneous Sensor Network

Some valuable work has been reported on situation understanding (situation awareness and threat assessment). In [11], an intelligent threat assessment processor using genetic algorithms and fuzzy logic was proposed. In [37], threat assessment was studied in tactical airborne environments. In [16], a neural network was applied to threat assessment for automated visual surveillance. In [9], an intelligent assistant was proposed to provide automatic situation and threat advice in the Air Defence Ground Environment. In [2], a situation and threat assessment model based on group analysis was proposed. A situation/threat assessment fusion system was proposed in [6]. Other approaches that have appeared include multiple attribute decision making [4], bayesian networks [38], etc. Unfortunately, none of these approaches is appropriate

for the multimodal sensor network scenario and none of them have used models derived from human or biological system mechanisms, although some computational intelligence models (such as neural networks and fuzzy logic) were used.

In situation awareness, the "weak" can be interprated as, for example, 1) a target (or entity) rarely appears in the sensor field; or 2) the behavior pattern of this target (or entity) has low match with the existing ones in database; or 3) space/time correlation of data/entities to events is low, etc. All the above information can be obtained based on the assumption that high quality information about objects and events is available as a contributor to situation awareness. In general, however, such information is insufficient to provide adequate situation awareness. Actually, some lessons gained from terrorist attacks have already demonstrated that the above "weaks" should be favored in situation awareness. Situation awareness needs the "favor weak" and rule-based mechanisms from PFC.

The new favor weak FLS can be used for level 2/3 fusion (situation awareness and threat assessment) for inferring activities, relationships, and intentions of objects and people in the battlespace based on retrieved knowledge consisting of behavioral patterns, new activities, and anticipated behavior, and also taking into account contextual information (terrain, roads, weather, etc). The level 1 data fusion results (traditional automatic target recognition and pattern recognition) from multimodal sensors will be used as antecedents. For example, considering a heterogeneous sensor network with radar, image/video sensors, and GPS sensor, we can choose the following three antecedents:

1. The number of switches from non-maneuvering set (constant behavior in speed, acceleration, and direction, etc) to the maneuvering set (varying behavior in speed, acceleration, and direction, etc). When a target is beginning a maneuver from a non-maneuvering class, the tracking system can switch the algorithms applied to the problem from a non-maneuvering set to the maneuvering set. The errors in distance from where the tracker

estimates the position of a target between the actual position can be very large when the incorrect motion models are applied to the problem. Additionally, when the tracker does finally catch up to the target after the maneuver, the track will "jump" across the operator's scope giving a very unrealistic and unreliable picture of what that target is actually doing. So a threat target will quite often switch from a non-maneuvering set to the maneuvering set, and vice versa, to avoid being tracked all the time. This knowledge can be used as an antecedent for situation awareness.

2. The frequency of appearance of such type of target based on some a priori knowledge such as archival radar data. Generally threat targets are new comparing to archival radar data.

3. The importance of geolocation of this target based on the geographical information systems (GISs). Examples of important geolocations include large metroplex, landmarks, military bases, airport, etc. Threats happen quite often in such areas.

Of the above three antecedents, *the frequency of appearance of such type of target* is weak stimulus and should be favored. A typical rule using the above three antecedents can be

IF the number of switches from non-maneuvering set to the maneuvering set is *High*, and the frequency of appearance of such target is *Low*, and the importance of geolocation of such type of target is *High*, THEN the possibility that an I&W needs to be issued is *Very Strong*.

The linguistic variables used to represent each antecedent are divided into three levels: *Low*, *Moderate*, and *High*. The consequent – the possibility that an indication and warning (I&W) needs to be issued – is divided into 5 levels, *Very Strong, Strong, Medium, Weak, Very Weak*. So we need to set up $3^3 = 27$ (because every antecedent has 3 fuzzy sub-sets, and there are 3 antecedents) rules for this FLS. Table 1 summarizes the fuzzy rules we use in this paper. We show these MFs in Fig. 5.

For input (x_1, x_2, x_3), the output is computed using

$$y(x_1, x_2, x_3) = \frac{\sum_{l=1}^{27} \underline{\mu}_{\tilde{\mathrm{F}}_l^1}(x_1)\overline{\mu}_{\tilde{\mathrm{F}}_l^2}(x_2)\underline{\mu}_{\tilde{\mathrm{F}}_l^3}(x_3)c_{avg}^l}{\sum_{l=1}^{27} \underline{\mu}_{\tilde{\mathrm{F}}_l^1}(x_1)\overline{\mu}_{\tilde{\mathrm{F}}_l^2}(x_2)\underline{\mu}_{\tilde{\mathrm{F}}_l^3}(x_3)} \tag{15}$$

By repeating these calculations for $\forall x_i \in [0, 10]$, we obtain a hypersurface $y(x_1, x_2, x_3)$. This equation represents the nonlinear mapping between three inputs and one output of the FLS. Since it's a 4-D surface (x_1, x_2, x_3, y), it's impossible to be plotted visually.

If we have $x_3 = 8$, and two other antecedents, x_1 and x_2 are variables, we obtain a hypersurface $y(x_1, x_2, 8)$ based on the favor weak FLS, as plotted in Fig. 6(a). In contrast, we use a type-1 FLS where the antecedent membership functions are the lower membership functions in Fig. 5a since favor weak mechanism is not used, and its output hypersurface $y(x_1, x_2, 8)$ is plotted in Fig. 6(b). Observe that from Fig. 6, the favor weak FLS provides a higher possibility that this target is a threat, which makes sense because the weak factor, frequency of appearance of such type of target, has been favored. So our proposed favor weak FLS can increase the probability of threat detection, and provides timely I&W.

7 Conclusions

Humans use multiple sources of sensory information to estimate environmental properties and has innate ability to integrate information from heterogeneous data sources. There is consensus that it depends on the brain PFC. The PFC has top-down control (favor weak) and rule-based mechanisms, which can be illustrated using the Stroop model. In this paper, we proposed to incorporate the favor weak mechanism into rule-based fuzzy logic systems (FLS) via using upper and lower membership functions. The inference engine of favor weak fuzzzy logic system was proposed under three different categories based on fuzzifiers. We analyzed that the favor weak FLS is a special type-1 FLS which is embeded in an interval type-2 FLS, so it's much simpler in computing than an interval type-2 FLS. We apply the favor weak FLS to situation understanding based on heterogeneous sensor network, and it shows that our favor weak fuzzy

logic system has clear advantage comparing to the type-1 FLS. The favor weak FLS can increase the probability of threat detection, and provides timely indication & warning (I&W).

Acknowledgement

This work was supported in part by U.S. Office of Naval Research (ONR) under Grant N00014-07-1-0395, N00014-07-1-1024, N00014-03-1-0466, and National Science Foundation (NSF) under Grant CNS-0721515.

References

[1] C. Bruce C, R. Desimone, C. G. Gross, "Visual properties of neurons in a polysensory area in superior temporal sulcus of the macaque," *J. Neurophysiol.*, vol. 46 369- 84, 1981.

[2] Y. Cai, et al, "A Situation and Threat Assessment Model Based on Group Analysis," *Proceedings of 2005 International Conference on Machine Learning and Cybernetics*, Aug. 2005, pp. 356 - 361.

[3] A. Celikyilmaz, I. B. Turksen, "Uncertainty Modeling of Improved Fuzzy Functions With Evolutionary Systems," *IEEE Trans. on Systems, Man, and Cybernetics - Part B*, vol. 38, no. 4, Aug. 2008, pp. 1098 - 1110.

[4] Q. Changwen, H. You, "A method of threat assessment using multiple attribute decision making," *6th International Conference on Signal Processing*, Aug. 2002, pp. 1091 - 1095.

[5] D. A. Chavis, D. N. Pandya, "Further observations on cortico-frontal connections in the rhesus monkey," *Brain Res.*, vol. 117, pp. 369-386, 1976.

[6] J. W. Choi; J. W. Joo; D. L. Cho, "Situation/Threat Assessment Fusion System (STAFS)," *Proceedings of the Fifth International Conference on Information Fusion*, July 2002, pp. 1374 - 1380.

[7] J. D. Cohen, D. Servan-Schreiber, "Context, cortex and dopamine: a connectionist approach to behavior and biology in schizophrenia," *Psychol. Rev.*, vol. 99, pp. 45-77.

[8] B. D. Corneil, and D. P. Munoz, "The Influence of Auditory and Visual Distractors on Human Orienting Gaze Shifts," *The Journal of Neuroscience*, vol. 16, no. 24, pp. 8193-8207, December 15, 1996.

[9] I. W. Dall, "Threat assessment without situation assessment," *Proc of Information, Decision and Control*, Feb. 1999, pp. 365 - 370.

[10] R. Desimone, J. Duncan, "Neural mechanisms of selective visual attention," *Annu. Rev. Neurosci.*, vol. 18, pp. 193–222, 1995.

[11] P. Gonsalves, et al, "Intelligent threat assessment processor (ITAP) using genetic algorithms and fuzzy logic," *Proceedings of the Third International Conference on Information Fusion*, 2000.

[12] J. Grafman, "Alternative frameworks for the conceptualization of prefrontal functions," *Handbook of Neuropsychology*, ed. F Boller, J Grafman, pp. 187. Amsterdam: Elsevier.

[13] E. Herrera-Viedma, F. Chiclana, F. Herrera, S. Alonso, "Group Decision-Making Model With Incomplete Fuzzy Preference Relations Based on Additive Consistency," *IEEE Trans. on Systems, Man, and Cybernetics - Part B*, vol. 37, no. 1, Feb. 2007, pp. 176 - 189.

[14] J. M. Hillis, M. O. Ernst, M. S. Banks, and M. S. Landy, "Combining sensory information: Mandatory fusion within, but not between, senses," *Science*, vol. 298, No. 5598, pp. 1627-1630, 2002.

[15] M. Hsu, et al, "Neural systems responding to degrees of uncertainty in human decision making," *Science*, vol. 310, pp. 1680-1683, Dec 2005.

[16] T. Jan, "Neural network based threat assessment for automated visual surveillance," *IEEE International Joint Conference on Neural Networks*, vol. 2, July 2004, pp. 1309 - 1312.

[17] C.-F. Juang, Y.-W. Tsao, "A Type-2 Self-Organizing Neural Fuzzy System and Its FPGA Implementation," *IEEE Trans. on Systems, Man, and Cybernetics - Part B*, vol. 38, no. 6, Dec. 2008, pp. 1537 - 1548.

[18] E. G. Jones, T. P. S. Powell, "An anatomical study of converging sensory pathways within the cerebral cortex of the monkey," *Brain*, vol. 93, pp. 793–820, 1970.

[19] H. K. Lam, L. D. Seneviratne, "Stability Analysis of Interval Type-2 Fuzzy-Model-Based Control Systems," *IEEE Trans. on Systems, Man, and Cybernetics - Part B*, vol. 38, no. 3, June 2008, pp. 617 - 628.

[20] Q. Liang, N. Karnik, and J. M. Mendel, " Connection admission control in ATM network using survey-based type-2 fuzzy logic systems," *IEEE Transactions on Systems, Man, and Cybernetics, Part C*, vol. 30, no. 3, pp. 529-539, August 2000.

[21] Q. Liang and J. M. Mendel, "Interval type-2 fuzzy logic systems: theory and design," *IEEE Transactions on Fuzzy Systems*, vol. 8, no. 5, pp. 535-550, Oct 2000.

[22] Q. Liang and J. M. Mendel, "Equalization of time-varying nonlinear channels using type-2 fuzzy adaptive filters," *IEEE Trans. on Fuzzy Systems*, vol. 8, no. 5, pp. 551-563, Oct 2000.

[23] Q. Liang and J. M. Mendel, " Overcoming time-varying co-channel interference using type-2 fuzzy adaptive filters", *IEEE Transactions on Circuits and Systems, II*, vol. 47, no. 12, pp. 1419-1428, Dec 2000.

[24] Q. Liang, J. M. Mendel, "Design interval type-2 fuzzy logic systems using SVD-QR method: rule reduction," *International Journal of Intelligent Systems*, vol. 15, no. 10, pp. 939957, Oct 2000.

[25] Q. Liang and J. M. Mendel, " MPEG VBR video traffic modeling and classification using fuzzy techniques," *IEEE Transactions on Fuzzy Systems*, vol. 9, no. 1, pp.183-193, Feb 2001.

[26] Q. Liang, J. M. Mendel, "Chapter 13: TSK fuzzy logic systems," *Uncertain Rule-Based Fuzzy Logic Systems,* pp. 421-453, Prentice-Hall, Upper Saddle River, NJ, Dec 2000.

[27] Q. Liang, J. M. Mendel, "Introduction to type-2 TSK fuzzy logic systems," *IEEE International Conference on Fuzzy Systems,* August 1999, Seoul, Korea.

[28] Q. Liang, J. M. Mendel, "Interval type-2 fuzzy logic systems," *IEEE International Conference on Fuzzy Systems,* May 2000, San Antonio, TX.

[29] Q. Liang, L. Wang, "Event Forecasting for Wireless Sensor Networks Using Interval Type-2 Fuzzy Logic System," submitted to *IEEE Transactions on Systems, Man, and Cybernetics, Part B.*

[30] Q. Liang, L. Wang, "Sensed signal strength forecasting for wireless sensors using interval type-2 fuzzy logic systems," *IEEE Intl Conference on Fuzzy Systems*, Reno, NV, May 2005.

[31] C. M. MacLeod, "Half a century of research on the Stroop effect: an integrative review," *Psychol. Bull.*, vol. 109, 163-203, 1991.

[32] K. Matsumoto and K. Tanaka, Conflict and Cognitive Control, *Science*, vol. 303, pp. 969-970, Feb 2004.

[33] J. M. Mendel, " Fuzzy logic systems for engineering: a tutorial ," *Proc. of the IEEE*, vol. 83, no. 3, pp. 345-377, March 1995.

[34] E. K. Miller, "The prefrontal cortex: complex neural properties for complex behavior," *Neuron*, vol. 22, pp. 15-17, 1999.

[35] E. K. Miller, J. D. Cohen, "An Integrative Theory of Prefrontal cortex function," *Annu. Rev. Neurosci.*, vol. 24, pp. 167, 2001.

[36] B. Milner, "Effects of different brain lesions on card sorting," *Arch. Neurol.*, vol. 9, pp. 90, 1963.

[37] X. T. Nguyen, "Threat assessment in tactical airborne environments," *Proceedings of the Fifth International Conference on Information Fusion*, July 2002.

[38] N. Okello, G. Thorns, "Threat assessment using bayesian networks," *Proceedings of the Sixth International Conference of Information Fusion*, vol. 2, pp. 1102 - 1109, 2003.

[39] R. C. O'Reilly, "Biologically Based Computational Models of High-Level Cognition," *Science*, Oct 2006.

[40] D. N. Pandya, C. Barnes, "Architecture and connections of the frontal lobe," *The Frontal Lobes Revisited*, ed. E Perecman, pp. 41- 72. New York: IRBN, 1987.

[41] R. Passingham, *The Frontal Lobes and Voluntary Action*, Oxford, UK: Oxford Univ. Press.

[42] H. Shu, Q. Liang, "Wireless Sensor Network Lifetime Analysis Using Interval Type-2 Fuzzy Logic Systems," *IEEE Intl Conference on Fuzzy Systems*, Reno, NV, May 2005.

[43] H. Shu, Q. Liang, "Wireless Sensor Network Lifetime Analysis Using Interval Type-2 Fuzzy Logic Systems," *IEEE Transactions on Fuzzy Systems*, vol. 16, no. 2, April 2008.

[44] J. R. Stroop, "Studies of interference in serial verbal reactions," *J. Exp. Psychol.* vol. 18, pp. 643- 62, 1935.

[45] C.-H. Wang; C.-S. Cheng; T.-T. Lee; "Dynamical optimal training for interval type-2 fuzzy neural network (T2FNN)," *IEEE Trans. on Systems, Man, and Cybernetics - Part B*, vol. 34, no. 3, June 2004, pp. 1462 - 1477.

[46] S. P. Wise, et al, "The frontal-basal ganglia system in primates," *Crit. Rev. Neurobiol.*, vol. 10, pp. 317-356.

[47] X. Xia and Q. Liang, "Cross-Layer Optimization for Mobile Ad Hoc Networks Using Fuzzy Logic Systems," *International Journal of Uncertainty, Fuzziness and Knowledge-Based Systems*, vol. 16, no. 3, pp. 391-407, June 2008.

[48] X. Xia and Q. Liang, "Cross-Layer Optimization for Mobile Ad Hoc Networks Using Interval Type-2 Fuzzy Logic Systems," *IEEE GLOBECOM*, Nov 2006, San Francisco, CA.

[49] L. A. Zadeh, " The concept of a linguistic variable and its application to approximate reasoning - I," *Information Sciences*, vol. 8, pp. 199-249, 1975.

[50] X.-J. Zeng and M. G. Singh, "A relationship between membership functions and approximation accuracy," *IEEE Trans. on Systems, Man, and Cybernetics - Part B*, vol. 26, no. 1, pp. 176 - 180, 1996.

List of Tables

1 Fuzzy rules used in the application. Ante 1 is the number of switches from non-maneuvering set to the maneuvering set or vice versa; Ante 2 the frequency of appearance of such type of target; Ante 3 is the importance of geolocation of this target; and Consequent is the possibility that this target is a threat. 21

Table 1: Fuzzy rules used in the application. Ante 1 is the number of switches from non-maneuvering set to the maneuvering set or vice versa; Ante 2 the frequency of appearance of such type of target; Ante 3 is the importance of geolocation of this target; and Consequent is the possibility that this target is a threat.

Rule #	Ante 1	Ante 2	Ante 3	Consequent
1	low	low	low	Weak
2	low	low	moderate	Medium
3	low	low	high	Strong
4	low	moderate	low	Very Weak
5	low	moderate	moderate	Weak
6	low	moderate	high	Medium
7	low	high	low	Very Weak
8	low	high	moderate	Weak
9	low	high	high	Medium
10	moderate	low	low	Medium
11	moderate	low	moderate	Strong
12	moderate	low	high	Very Strong
13	moderate	moderate	low	Weak
14	moderate	moderate	moderate	Medium
15	moderate	moderate	high	Strong
16	moderate	high	low	Very Weak
17	moderate	high	moderate	Weak
18	moderate	high	high	Medium
19	high	low	low	Medium
20	high	low	moderate	Strong
21	high	low	high	Very Strong
22	high	moderate	low	Weak
23	high	moderate	moderate	Medium
24	high	moderate	high	Strong
25	high	high	low	Very Weak
26	high	high	moderate	Weak
27	high	high	high	Moderate

List of Figures

1 Schematic diagram of some of the extrinsic and intrinsic connections of the PFC. Most connections are reciprocal; the exceptions are indicated by arrows. The frontal eye field (FEF) has variously been considered either adjacent to, or part of, the PFC. 22

2 Schematic of the Stroop model. (a) No control. Activation of conflicting inputs in the two pathways produces a response associated with the word, due to the stronger connections in the word reading pathway. (b) Presentation of a conflict stimulus. The color unit is activated (indicated by the orange fill), representing the current intent to name the color. This passes activation to the intermediate units in the color naming pathway (indicated by arrows), which primes those units (indicated by larger size), and biases processing in favor of activity flowing along this pathway. This biasing effect favors activation of the response unit corresponding to the color input, even though the connection weights in this pathway are weaker than in the word pathway. 23

3 The type-2 MFs for Example 1. The thick solid lines denote upper MFs, and the thick dashed lines denote lower MFs. The shaded regions are the footprints of uncertainty for interval secondaries. The center of the Gaussian MFs is 5, and the variance varies from 1.0 to 2.0. 24

4 (a) Pictorial representation of a type-2 fuzzy set. The secondary memberships are shown in (b) to represent the confidence of the primary memberships. . . . 25

5 The MFs used to represent the linguistic labels. (a) MFs for antecedents, and (b) MFs for consequent. 26

6 The threat assessment surface for different FLSs when $x_3 = 8$. (a) Favor weak FLS, and (b) Traditional type-1 FLS. 27

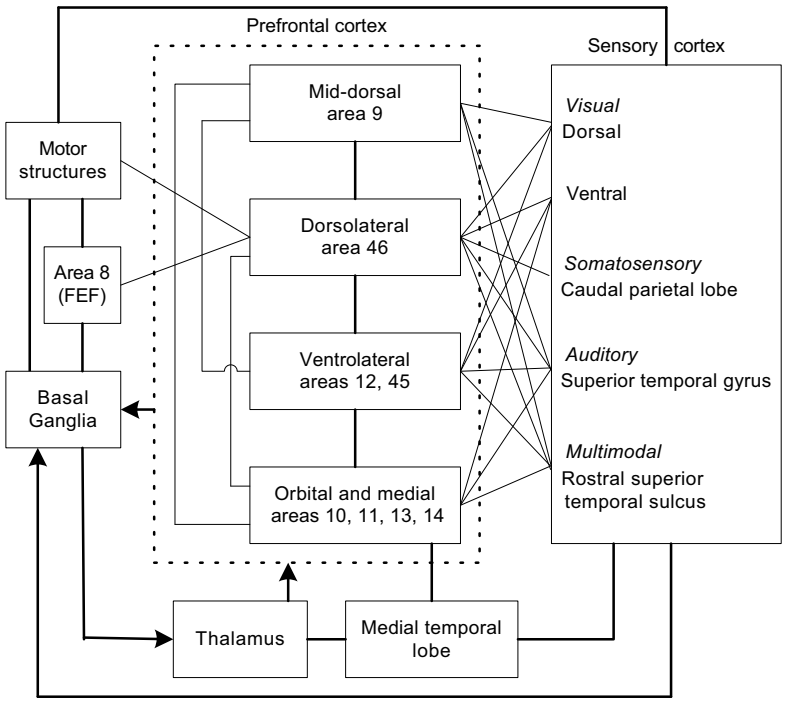
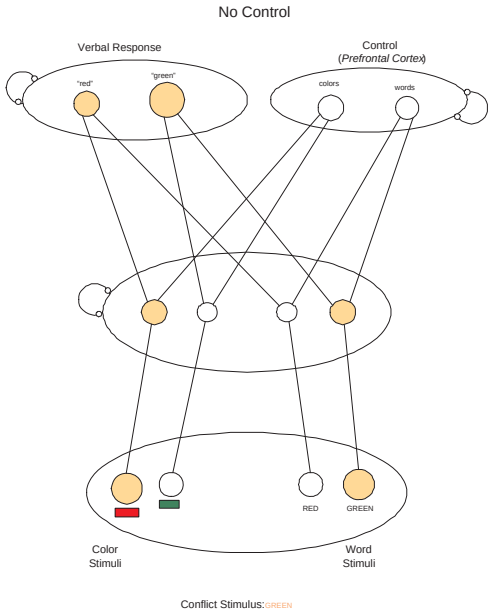
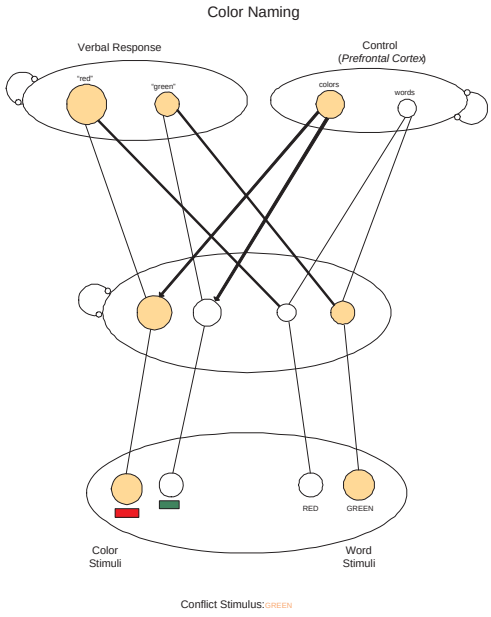


Figure 1: Schematic diagram of some of the extrinsic and intrinsic connections of the PFC. Most connections are reciprocal; the exceptions are indicated by arrows. The frontal eye field (FEF) has variously been considered either adjacent to, or part of, the PFC.



(a)



(b)

Figure 2: Schematic of the Stroop model. (a) No control. Activation of conflicting inputs in the two pathways produces a response associated with the word, due to the stronger connections in the word reading pathway. (b) Presentation of a conflict stimulus. The color unit is activated (indicated by the orange fill), representing the current intent to name the color. This passes activation to the intermediate units in the color naming pathway (indicated by arrows), which primes those units (indicated by larger size), and biases processing in favor of activity flowing along this pathway. This biasing effect favors activation of the response unit corresponding to the color input, even though the connection weights in this pathway are weaker than in the word pathway.

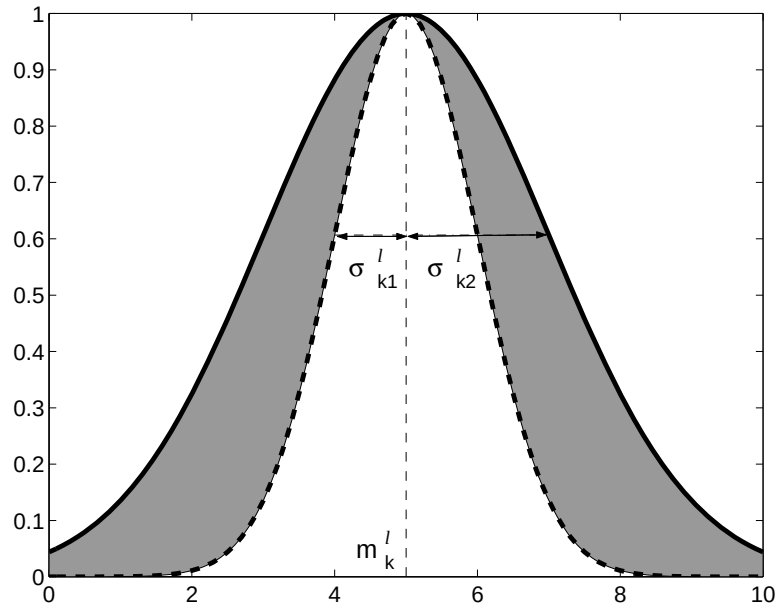


Figure 3: The type-2 MFs for Example 1. The thick solid lines denote upper MFs, and the thick dashed lines denote lower MFs. The shaded regions are the footprints of uncertainty for interval secondaries. The center of the Gaussian MFs is 5, and the variance varies from 1.0 to 2.0.

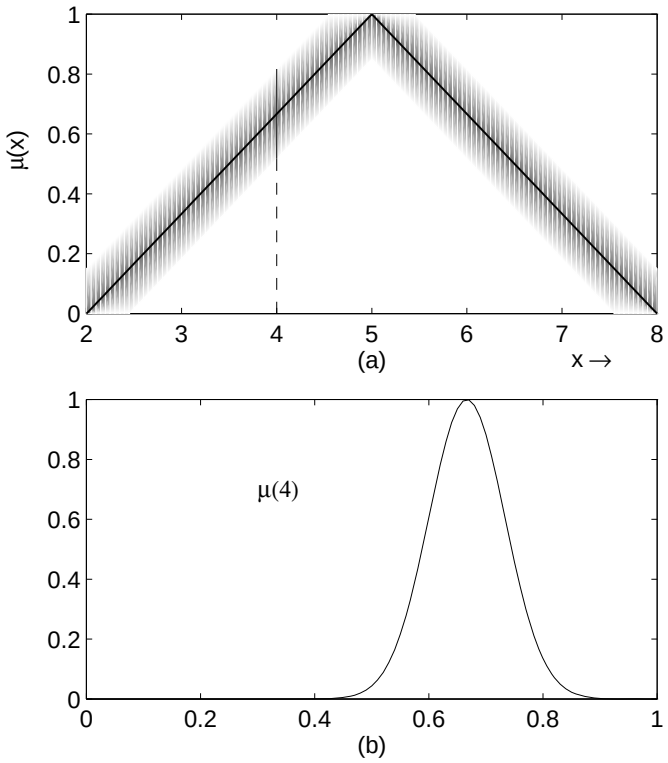
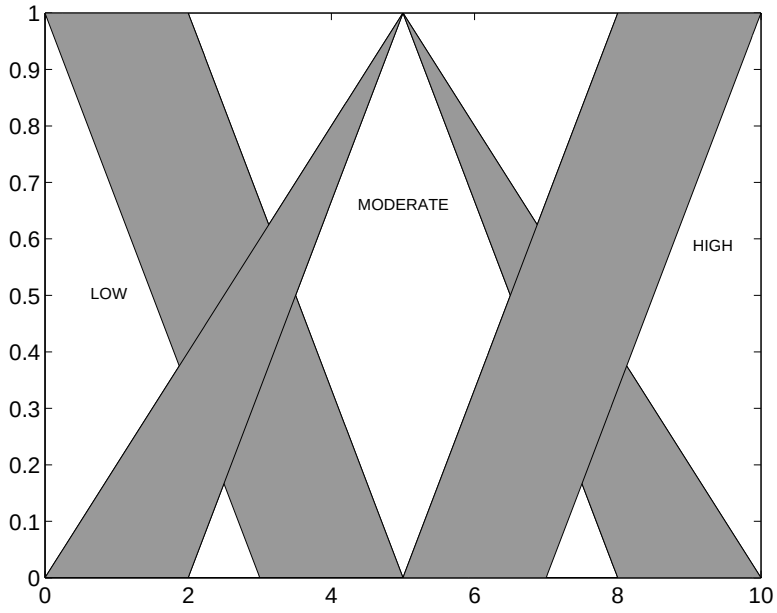
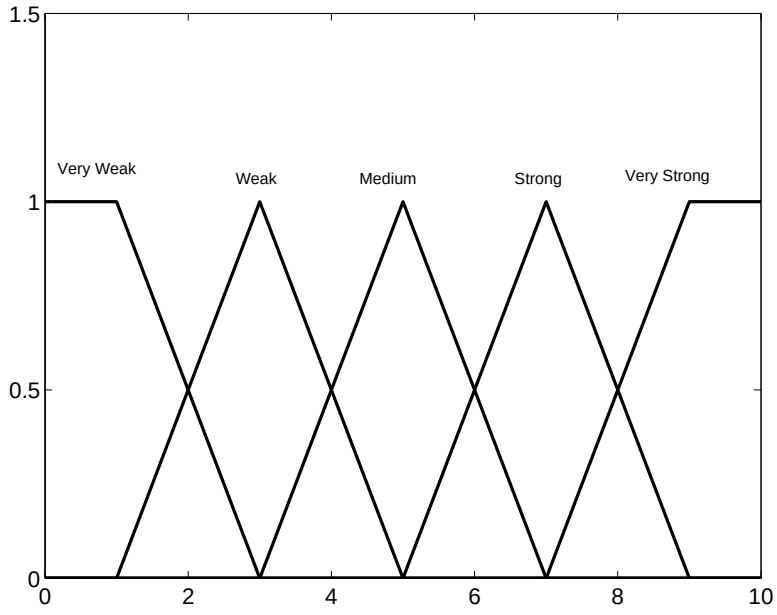


Figure 4: (a) Pictorial representation of a type-2 fuzzy set. The secondary memberships are shown in (b) to represent the confidence of the primary memberships.

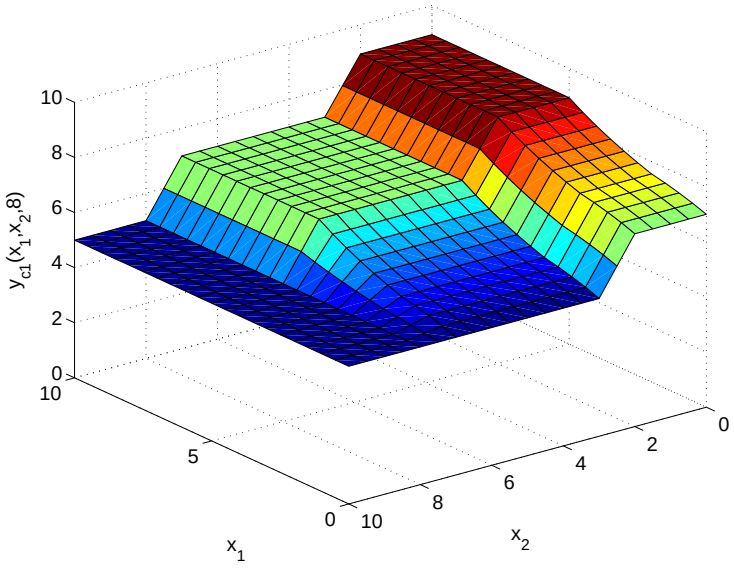


(a)

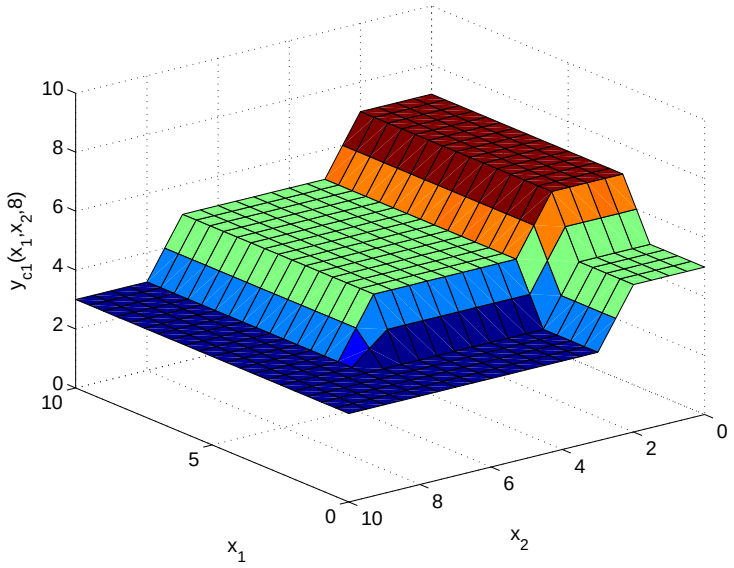


(b)

Figure 5: The MFs used to represent the linguistic labels. (a) MFs for antecedents, and (b) MFs for consequent.



(a)



(b)

Figure 6: The threat assessment surface for different FLSs when $x_3 = 8$. (a) Favor weak FLS, and (b) Traditional type-1 FLS.

Joint Multi-target Identification and Classification in Cognitive Radar Sensor Networks

Hong-Sam T. Le and Qilian Liang
Department of Electrical Engineering
The University of Texas at Arlington
Arlington, TX 76019, USA
E-mail: le@wcn.uta.edu, liang@uta.edu

Abstract

We investigate the problem of jointly classifying and identifying multiple targets in radar sensor networks where the maximum number of categories and the maximum number of targets in each category are obtained a priori based on statistical data. However, the actual number of targets in each category and the actual number of target categories being present at any given time are assumed unknown. It is assumed that a given target only belongs to one category and one identification number. The target signals are moreover modeled as zero-mean complex Gaussian processes. In this paper, we propose a joint multi-target identification and classification (JMIC) algorithm for radar surveillance using the cognitive radar network. The existing target categories are first classified and then the targets in each category are accordingly identified. Simulation results are presented to evaluate the feasibility and effectiveness of the proposed JMIC algorithm in a query surveillance region.

Index Terms : Radar sensor networks, multiple target identification and classification, Gaussian process.

I. Introduction

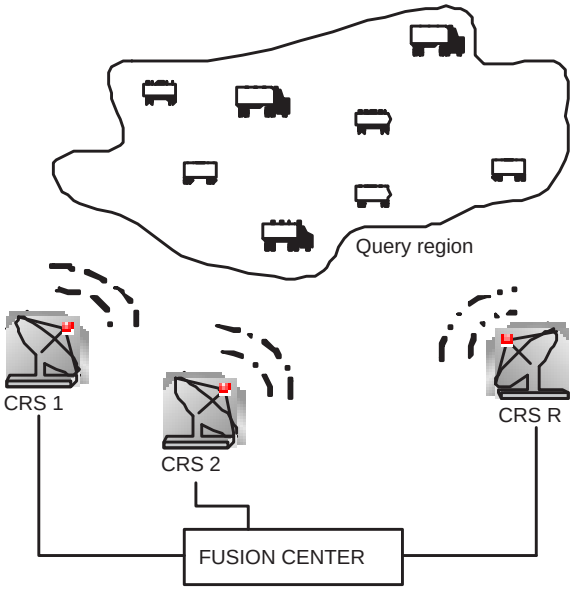
The importance of providing multiple target identification and classification (MTIC) capability for military applications is widely recognized nowadays. When the total number of targets being present in tactical battlefields is increased, classifying as well as identifying these targets will become a very challenging task. Measurements received from multiple radar sensors should be collected and processed in an efficient and robust manner to obtain the most meaningful information for identification and classification. Therefore, collaborative processing algorithms at the fusion center are in urgent need to successfully achieve this ultimate goal. For example, in [6], Liang proposed a collaborative waveform design and diversity approach for single target detection in radar sensor networks.

Many algorithms have been suggested in literature to handle the task of multiple target identification and classification. A Gaussian Mixture Model (GMM) classifier was proposed in [9] to distinct target categories in

a semi-structured outdoor environment. For radar target identification, a multi-feature decision space approach was discussed in [10]. Other approaches to the problem of target identification were presented in [5] applying two statistical-based techniques, namely Bayesian and Dempster-Shafer, to develop radar target identification algorithms. Distributed multi-class classification with fault-tolerance capability was studied in [11]. Collaborative classification algorithms [7] were applied to single target scenarios and then extended to more complex scenarios of multiple targets.

Multiple target identification and classification have become major concerns in radar surveillance applications. This task is usually implemented based on wideband radars or imaging radars [8]. In this paper, we address the problem of MTIC for radar surveillance using a network of R cognitive radar sensors. Cognitive radars, as presented in [2] and [3], continuously interact with the environment, intelligently collect data and thereby efficiently adapt to statistical variations in the environment in real-time so as to achieve reliable surveillance where the likelihood of the presence of targets is high. Particularly, in [3], Haykin stated that *"Cognitive Radar is an intelligent system that is aware of its surrounding environment (i.e., outside world), uses prior knowledge as well as learning through continuing interactions with the environment, and thereby adapts both its receiver and transmitter in response to statistical variations in the environment in real-time so as to meet specific remote-sensing objectives in an efficient, reliable, and robust manner.*" Here, we emphasize that radars in our radar sensor network can observe activities of radars in other radar networks which are called primary networks (i.e., radar sensors are aware of its surrounding environment and can learn through continuing interactions with the environment). They then determine whether frequency bands assigned to those primary networks are available or not. If these frequency bands are available, they can utilize these frequencies without generating any interference to the primary networks by sending this information to the controller center to activate the waveform design algorithms proposed in [Liang2008] (i.e., radars adapt both their receivers and transmitters in response to statistical variations in the environment). Since the price of frequency license to employ any sensor network is very expensive, taking advantage of available frequencies is an important step to make radar sensor networks feasible in terms of installation cost and efficient spectrum usage. Cognitive radars therefore show promise in home health care, rescue and homeland security applications [3], [1].

In this paper, we consider the scenario in which the total number of targets K is unknown in a region of interest and a query regarding to the classification of these targets and the identification of the targets in each category is inquired. This generalizes the surveillance scenario considered in [4] wherein each target belonging to one distinct category was considered. In this work, some targets now share the same target category but possess different identification numbers. In order to perform this higher complexity version of surveillance scenario, we assume that each given target only belongs to one distinct pair of one target category and one identification number. Based on statistical data, we then reasonably assume that the maximum number of target categories M and the maximum



1: System architecture for JMIC algorithm

number of targets N in each category are a priori known parameters. However, the actual number of existing target categories and the actual number of targets being present in each category at any given time will be estimated. To achieve this goal, we propose a joint multi-target identification and classification (JMIC) algorithm for radar surveillance. The existing target categories are first classified based on 2^M hypotheses which correspond to all possibilities we may have regarding to the presence or absence of each category. Based on the result obtained from classification specifying which target categories exist, we then identify targets belonging to each detected category. Targets in a category are identified based on their identification numbers or identification indices. Therefore, $2^N - 1$ hypotheses are set up corresponding to all scenarios of presence or absence of each target identification index. Numerical results based on simulated data are finally presented to demonstrate the feasibility and effectiveness of the proposed JMIC algorithm in a query surveillance region.

The rest of the paper is organized as follows. In Section II, we provide a framework and formulate the multi-target classification and identification problem in a cognitive radar network. In Section III, we propose the joint multi-target identification and classification algorithm. Simulation results are presented in Section IV. Finally, Section V concludes the paper.

II. System description and problem formulation

The general system architecture for MTIC problem, shown in Fig. 1, accommodates the deployment of R cognitive radar sensors (CRSs) which will collect and then send all the target signals to the fusion center. It is assumed that there are K targets in the region of interest. Each target is moreover considered as a point source and target signals can be modeled as zero-mean complex Gaussian processes [4]. The Gaussian assumption is reasonable since the

signals reflected from the target may experience many different paths to the receiver due to the reflection and diffraction of wave transmission environment. At the receiver, the received signal is the combination of all signals bearing the information about target. Therefore, following the Central Limit Theorem, the received signal tends to be Gaussian. The assumption of zero-mean just helps our analysis tractable. In addition, all measurements from sensors are combined at the fusion center to reduce the impact of target signal variability. At any given time, the measurements in distinct cognitive radar sensors are approximately independent.

We assume that at most M distinct target categories and N targets in each category are present in the surveillance region in the observation duration. However, the actual existing number of target categories is unknown. Therefore, we set up 2^M hypotheses corresponding to all possible scenarios of presence or absence of each target category. We denote these hypotheses by H_k (k = 0, 1, ..., $2^M - 1$). Target categories are denoted by i (i = 1, 2, ..., M) and in each ith category, targets are identified by the identification indices j (j = 1, 2, ..., N). We use the parameter $b_{ij} \in \{0, 1\}$ to denote the event in which target of category i and index j is absent or present. Specifically,

$$b_{ij} = \begin{cases} 0 & \text{if target of category } i \text{ and index } j \text{ is absent} \\ 1 & \text{if target of category } i \text{ and index } j \text{ is present} \end{cases}$$

Classification and identification parameters are given in Table I in which each row represents one target category and each column represents one target index. The probability of target of category i and index j being absent $P(b_{ij} = 0)$ is denoted by p_{ij}, i.e., $P(b_{ij} = 0) = p_{ij}$. Hence, the probability of presence of this target $P(b_{ij} = 1) = 1 - p_{ij}$.

We employ hypothesis H_0 for scenario of no category being present, hypothesis H_1 for scenario of category 1 being present,..., and hypothesis H_{2^M-1} for scenario of all M categories being present. We assume that the total number of targets K in the region of interest is unknown. If K = 0, there is no target in the surveillance region and hypothesis H_0 is chosen. The prior probability of hypothesis H_0 can be computed as

$$\begin{aligned} P(H_0) &= \text{P } \{\text{no category present}\} \\ &= P(\forall b_{1j} = 0; \forall b_{2j} = 0; ...; \forall b_{Mj} = 0), \quad j = 1, 2, ..., N \end{aligned} \tag{1}$$

Since the possibilities for presence or absence of targets are independent, we have

$$\begin{aligned} P(H_0) &= P(\forall b_{1j} = 0).P(\forall b_{2j} = 0)...P(\forall b_{Mj} = 0) \\ &= (p_{11}.p_{12}...p_{1N})(p_{21}.p_{22}...p_{2N})...(p_{M1}...p_{MN}) \\ &= \prod_{i=1}^{M}\prod_{j=1}^{N} p_{ij} \end{aligned} \tag{2}$$

I: Classification and Identification Parameters

	Index 1	Index 2	Index 3	...	Index N
Category 1	b_{11}	b_{12}	b_{13}	...	b_{1N}
Category 2	b_{21}	b_{22}	b_{23}	...	b_{2N}
Category 3	b_{31}	b_{32}	b_{33}	...	b_{3N}
⋮	⋮	⋮	⋮	⋮	⋮
Category M	b_{M1}	b_{M2}	b_{M3}	...	b_{MN}

Similarly, the prior probability of H_1 is given by:

$$\begin{aligned} P(H_1) &= \mathrm{P}\left\{\text{category 1 present}\right\} \\ &= P(\textit{at least one } b_{1j} = 1; \forall b_{2j} = 0; ...; \forall b_{Mj} = 0) \\ &= P(\exists \textit{ one } b_{1j} = 1).P(\forall b_{2j} = 0)...P(\forall b_{Mj} = 0) \\ &= \left(1 - \prod_{j=1}^{N} p_{1j}\right) \prod_{i=2}^{M} \prod_{j=1}^{N} p_{ij} \end{aligned} \tag{3}$$

Generally, we obtain the prior probability of hypothesis H_k in the form as follows:

$$P(H_k) = \prod_{i=1}^{M} \left[b_i^{(k)} \left(1 - \prod_{j=1}^{N} p_{ij}\right) + \left(1 - b_i^{(k)}\right) \prod_{j=1}^{N} p_{ij} \right] \tag{4}$$

where $b_i^{(k)}$ takes the value of 0 when category i is absent, otherwise $b_i^{(k)}$ takes the value of 1 when category i is present under hypothesis H_k.

III. Joint multi-target identification and classification algorithm

Joint multi-target identification and classification algorithm consists of two steps. In the first step, multiple target classification is implemented to investigate which target categories are present within the entire surveillance region. Then, in the second step, based on classification results, targets in each detected category are identified using identification indices. Our JMIC algorithm relies on the framework previously presented in Section II.

A. Multiple Target Classification

The 2^M-ary hypothesis testing problem is formulated as

$$H_k : \mathbf{z}_l = \mathbf{s}_l + \mathbf{n}_l, \qquad k = 0, 1, ..., 2^M - 1 \tag{5}$$

where $\mathbf{z}_l$ is a D-dimensional vector of measurements collected by the lth (l = 1,2,..., R) radar sensor and target signals are modeled as zero-mean complex Gaussian vectors with the same covariance matrices $\mathbf{\Sigma}_m$. Thus, $\mathbf{s}_l \sim \mathcal{CN}(0, \mathbf{\Sigma}_{s_{lk}})$

and $\mathbf{\Sigma}_{s_{lk}}$ is given by

$$\begin{aligned}\mathbf{\Sigma}_{s_{lk}} &= \mathbb{E}\left[\sum_{i=1(i\in H_k)}^{M}\sum_{j=1}^{N} b_{ij}\mathbf{\Sigma}_m\right] \\ &= \sum_{i=1(i\in H_k)}^{M}\sum_{j=1}^{N}\mathbb{E}\left[b_{ij}\right]\mathbf{\Sigma}_m \end{aligned} \tag{6}$$

where $\mathbb{E}[x]$ denotes the expectation of a random variable x and (6) follows from the independence of b_{ij}. Moreover, signals are corrupted by zero-mean complex white Gaussian noise $\mathbf{n}_l$, that is

$$\mathbf{n}_l \sim \mathcal{CN}(0, \sigma_n^2\mathbf{I}). \tag{7}$$

Under hypothesis H_k, the probability density function of the feature vector $\mathbf{z}_l$ is

$$\begin{aligned}P(\mathbf{z}_l|H_k) &= p_k(\mathbf{z}_l) \\ &= \frac{1}{\pi^D|\mathbf{\Sigma}_{z_{lk}}|}\exp\left(-\mathbf{z}_l^H\mathbf{\Sigma}_{z_{lk}}^{-1}\mathbf{z}_l\right)\end{aligned} \tag{8}$$

where $\mathbf{\Sigma}_{z_{lk}} = \mathbf{\Sigma}_{s_{lk}} + \sigma_n^2\mathbf{I}$. Let δ_k denote $P(H_k)$. The decision rule for the multiple target classifier therefore becomes

$$\hat{k} = \arg\max_{k=0,1,...,2^M-1} p_k(\mathbf{z}_1, \mathbf{z}_2, ..., \mathbf{z}_R)\delta_k \tag{9}$$

Due to the conditional independence of $\mathbf{z}_l$, (9) can be expressed as

$$\hat{k} = \arg\max_{k=0,1,...,2^M-1}\prod_{l=1}^{R} p_k(\mathbf{z}_l)\delta_k \tag{10}$$

In term of log-likelihood, we have

$$\begin{aligned}\Delta_k(\mathbf{z}_1, \mathbf{z}_2, ..., \mathbf{z}_R) &= \log\prod_{l=1}^{R} p_k(\mathbf{z}_l)\delta_k \\ &= \sum_{l=1}^{R}\log p_k(\mathbf{z}_l) + \log\delta_k\end{aligned} \tag{11}$$

By substituting $p_k(\mathbf{z}_l)$ from (8) to (11) and omitting constants that do not depend on categories, we obtain Δ_k in the following form

$$\Delta_k(\mathbf{z}_1, \mathbf{z}_2, ..., \mathbf{z}_R) = -R\log|\mathbf{\Sigma}_{z_{lk}}| - \sum_{l=1}^{R}\mathbf{z}_l^H\mathbf{\Sigma}_{z_{lk}}^{-1}\mathbf{z}_l + \log\delta_k \tag{12}$$

The information about $\mathbf{z}_l$ is then sent from the lth (l = 1, 2,..., R) cognitive radar sensor to the fusion center. The classifier at the fusion center then makes the final classification decision in the following manner:

$$\begin{aligned}\hat{k} &= \arg \max_{k=0,1,...,2^M-1} \Delta_k(\mathbf{z}_1, \mathbf{z}_2, ..., \mathbf{z}_R) \\ &= \arg \min_{k=0,1,...,2^M-1} \left(R \log |\mathbf{\Sigma}_{z_{lk}}| + \sum_{l=1}^{R} \mathbf{z}_l^H \mathbf{\Sigma}_{z_{lk}}^{-1} \mathbf{z}_l - \log \delta_k \right) \end{aligned} \quad (13)$$

From (13), we map the integer value of $\hat{k}$ to binary value to obtain a category vector $\mathbf{c}$ = [c_1, c_2, ..., c_M] where c_i (i = 1, 2, ..., M) takes value of 1 corresponding to category i being present or takes value of 0 corresponding to category i being absent in the area of interest. The total number of target categories being present in the surveillance region is computed by

$$N_C = \sum_{i=1}^{M} c_i \quad (14)$$

For example, if $\hat{k}$ = 5, then we get $\mathbf{c}$ = [1, 0, 1, 0, ...,0], i.e., only categories 1 and 3 are present within the surveillance region. Therefore, the total number of target categories being present N_C is 2.

B. Multiple Target Identification

Based on the estimated value $\hat{k}$, we realize which target categories have shown up in the surveillance region. However, we still have no information about the number of targets belonging to each category. Therefore, the second step of the JMIC algorithm is repeatedly applied to each detected category to identify targets in the surveillance region. We aim at searching all the targets using their jth indices. For each category i, we denote $H^i_{h,\hat{k}}$ to represent the hypothesis h (h = 0, 1, ..., 2^N - 1), given category $i \in \mathbf{S}$ being present under hypothesis $H_{\hat{k}}$. Note that $\mathbf{S}$ is a set of all categories i being present in hypothesis $H_{\hat{k}}$, i.e., $\mathbf{S} = \{i \text{ present in } H_{\hat{k}}\}$.

Since category i is estimated to be present, i.e, at least one target index j shows up in this category, the scenario of no target index of category i being present is eliminated, i.e., P($H^i_{0,\hat{k}}$) = 0. As a sequence, we only have $N^\star$ = 2^N - 1 hypotheses corresponding to h = 1, 2, ..., $N^\star$. We now choose $H^i_{1,\hat{k}}$ to represent the hypothesis of target index $\sharp 1$ of category $i \in \mathbf{S}$ being present, $H^i_{2,\hat{k}}$ to represent the hypothesis of target index $\sharp 2$ of category $i \in \mathbf{S}$ being present, ..., $H^i_{N^\star,\hat{k}}$ to represent the hypothesis of all targets index $\sharp 1$, $\sharp 2$, ..., $\sharp N$ of category $i \in \mathbf{S}$ being present. $P(H^i_{h,\hat{k}})$ is calculated as

$$\begin{aligned} P(H^i_{h,\hat{k}}) &= P(H^i_h, H_{\hat{k}}) \\ &= P(H^i_h | H_{\hat{k}}) P(H_{\hat{k}}) \end{aligned} \quad (15)$$

The conditional probability of hypothesis $H^i_{1,\hat{k}}$ is given by

$$\begin{aligned} P(H^i_1|H_{\hat{k}}) &= \mathrm{P}\ \{\text{target index } \sharp 1 \text{ category } i \text{ present}\} \\ &= P(b_{i1}=1; b_{i2}=0; ...; b_{iN}=0) \end{aligned} \tag{16}$$

Because the possibilities for presence or absence of targets are independent, we have

$$\begin{aligned} P(H^i_1|H_{\hat{k}}) &= P(b_{i1}=1).P(b_{i2}=0)...P(b_{iN}=0) \\ &= (1-p_{i1}).p_{i2}...p_{iN} \end{aligned} \tag{17}$$

Similarly, the conditional probability of hypothesis $H^i_{2,\hat{k}}$ is

$$\begin{aligned} P(H^i_2|H_{\hat{k}}) &= \mathrm{P}\ \{\text{target index } \sharp 2 \text{ category } i \text{ present}\} \\ &= P(b_{i1}=0; b_{i2}=1; ...; b_{iN}=0) \\ &= P(b_{i1}=0).P(b_{i2}=1)...P(b_{iN}=0) \\ &= p_{i1}.(1-p_{i2})...p_{iN} \end{aligned} \tag{18}$$

In general, we obtain the conditional probability of hypothesis $H^i_{h,\hat{k}}$ as follows:

$$P(H^i_h|H_{\hat{k}}) = \prod_{j=1}^{N} \left[b^{(h)}_{ij}(1-p_{ij}) + \left(1-b^{(h)}_{ij}\right) p_{ij} \right] \tag{19}$$

where $b^{(h)}_{ij}$ takes the value of 0 when target index j of category i is absent, otherwise $b^{(h)}_{ij}$ takes the value of 1 when target index j of category i is present under hypothesis H^i_h given hypothesis $H_{\hat{k}}$.

We now set up $N^\star$ hypotheses:

$$H^i_{h,\hat{k}} : \mathbf{z}^i_l = \mathbf{s}^i_l + \mathbf{n}^i_l, \qquad h = 1, 2, ..., N^\star \tag{20}$$

where $\mathbf{z}^i_l$ is collected by lth (l = 1, 2, ..., R) cognitive radar sensor regarding to ith category. Target signals of ith category are modeled as $\mathbf{s}^i_l \sim \mathcal{CN}(0, \mathbf{\Sigma}_{s^i_{l,h}})$ in which $\mathbf{\Sigma}_{s^i_{l,h}}$ is given by

$$\begin{aligned} \mathbf{\Sigma}_{s^i_{l,h}} &= \mathbb{E}\left[\sum_{j=1(j\in H^i_{h,\hat{k}})}^{N} b_{ij}\mathbf{\Sigma}_m \right] \\ &= \sum_{j=1(j\in H^i_{h,\hat{k}})}^{N} \mathbb{E}[b_{ij}]\mathbf{\Sigma}_m \end{aligned} \tag{21}$$

where $\mathbb{E}[x]$ denotes the expectation of a random variable x and (21) follows from the independence of b_{ij}. Signals

are moreover corrupted by zero-mean complex white Gaussian noise $\mathbf{n}_l^i$, that is

$$\mathbf{n}_l^i \sim \mathcal{CN}(0, \sigma_n^2 \mathbf{I}) \tag{22}$$

Under hypothesis $H_{h,\hat{k}}^i$, the probability density function of the feature vector $\mathbf{z}_l^i$ of category i can be written as

$$\begin{aligned} P(\mathbf{z}_l^i | H_{h,\hat{k}}^i) &= p_{h,\hat{k}}(\mathbf{z}_l^i) \\ &= \frac{1}{\pi^D |\mathbf{\Sigma}_{z_{l,h}^i}|} \exp\left\{-(\mathbf{z}_l^i)^H \mathbf{\Sigma}_{z_{l,h}^i}^{-1} \mathbf{z}_l^i\right\} \end{aligned} \tag{23}$$

where $\mathbf{\Sigma}_{z_{l,h}^i} = \mathbf{\Sigma}_{s_{l,h}^i} + \sigma_n^2 \mathbf{I}$. Let α_h^i denote $P(H_h^i | H_{\hat{k}})$. From (15) and due to the conditional independence of $\mathbf{z}_l^i$, the identification decision rule hence can be expressed as

$$\hat{h} = \arg \max_{h=1,2,...,N^\star} \prod_{l=1}^{R} p_{h,\hat{k}}(\mathbf{z}_l^i) \alpha_h^i \delta_{\hat{k}} \tag{24}$$

In term of log-likelihood, we have

$$\begin{aligned} \Delta_k^i &= \log \prod_{l=1}^{R} p_{h,\hat{k}}(\mathbf{z}_l^i) \alpha_h^i \delta_{\hat{k}} \\ &= \sum_{l=1}^{R} \log p_{h,\hat{k}}(\mathbf{z}_l^i) + \log \alpha_h^i + \log \delta_{\hat{k}} \end{aligned} \tag{25}$$

By substituting $p_{h,\hat{k}}(\mathbf{z}_l^i)$ from (23) to (25) and omitting constants that do not depend on target indices in each category, we have Δ_k^i in the following form:

$$\Delta_k^i = -R \log |\mathbf{\Sigma}_{z_{l,h}^i}| - \sum_{l=1}^{R} (\mathbf{z}_l^i)^H \mathbf{\Sigma}_{z_{l,h}^i}^{-1} \mathbf{z}_l^i + \log \alpha_h^i + \log \delta_{\hat{k}} \tag{26}$$

The information about $\mathbf{z}_l^i$ is sent from the lth cognitive radar sensor to the fusion center. The identifier at the fusion center then makes the final identification decision:

$$\begin{aligned} \hat{h} &= \arg \max_{h=1,2,...,N^\star} \Delta_k^i \\ &= \arg \min_{h=1,2,...,N^\star} \left(R \log |\mathbf{\Sigma}_{z_{l,h}^i}| + \sum_{l=1}^{R} (\mathbf{z}_l^i)^H \mathbf{\Sigma}_{z_{l,h}^i}^{-1} \mathbf{z}_l^i - \log \alpha_h^i - \log \delta_{\hat{k}} \right) \end{aligned} \tag{27}$$

From (27), we map the integer value of $\hat{h}$ to binary value to obtain a index vector $\mathbf{b}_i = [b_{i1}, b_{i2}, ..., b_{iN}]$ where every component of $\mathbf{b}_i$ takes the value of 1 or 0. Component $\sharp j$ takes value of 1 corresponding to the scenario of target index $\sharp j$ of category i being present. The total number of targets N_i in each category i is calculated by

$$N_i = \sum_{j=1}^{N} b_{ij} \tag{28}$$

II: Classification and Identification Example

	Index 1	Index 2	Index 3	Index 4
Category 1	0	1	0	1
Category 2	1	1	0	1
Category 3	1	1	0	0

Following the example previously described in classification step, for i = 1, if $\hat{h}$ = 7, then we get $\mathbf{b}_1$ = [1, 1, 1, 0, ...,0]. Therefore, only targets with indices 1, 2 and 3 of category 1 are present within the surveillance region. The total number of targets of category 1 being present N_1 is 3. Repeatedly implementing this step, for i = 3, if $\hat{h}$ = 3, we obtain $\mathbf{b}_3$ = [1, 1, 0, 0, ..., 0]. So, targets with indices 1 and 2 of category 3 are present. The total number of targets of category 3 being present N_3 is 2.

The total number of targets K in the surveillance region finally can be written as

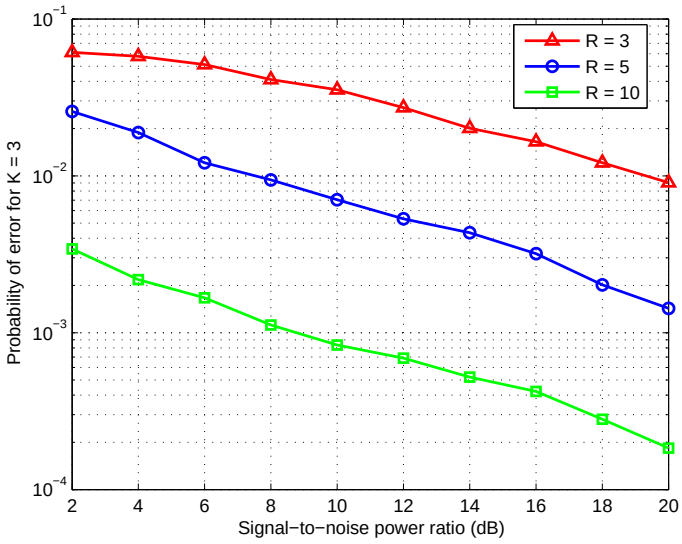
$$K = \sum_{i=1}^{M} N_i = \sum_{i=1}^{M} \sum_{j=1}^{N} b_{ij} \tag{29}$$

In the example, the total number of targets within the surveillance region K is 5.

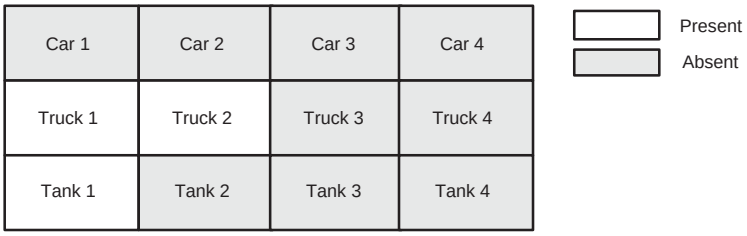
IV. Simulation results

We perform simulations to illustrate the performance of the proposed JMIC algorithm using a network of R cognitive radar sensors which may detect more than one target at any given time. Therefore, a more accurate estimation about target categories and the total number of targets being present in each category can be obtained by fusion of several radar sensors. The maximum number of categories M = 3 and the maximum number of targets in each category N = 4 were assumed in this region of interest. An example using JMIC for K = 7 targets in the interest area is given in Table II. We use JMIC algorithm to obtain $\hat{k}$ = 7 which specifies that categories 1, 2, 3 are present and thus N_c = 3. The number of targets of category 1 is 2 (target index ♯2 and ♯4) corresponding to $\hat{h}$ = 10. The number of targets of category 2 is 3 (target index ♯1, ♯2, and ♯4) corresponding to $\hat{h}$ = 11. The total number of targets of category 3 is 2 (target index ♯1 and ♯2) corresponding to $\hat{h}$ = 3.

To evaluate the performance of the proposed JMIC algorithm, we conduct a Monte-Carlo simulation of 10^5 runs. We assume that R = 3, 5 and 10 cognitive radar sensors were employed in simulations. The probabilities of joint classification and identification error of the proposed JMIC algorithm for $K = 3, 6, 8$, which are expressed as functions of signal-to-noise power ratios, are depicted in Fig. 2a, Fig. 3a, and Fig. 4a, respectively. From Fig. 2a, we realize that a sufficiently low probability of error can be obtained with a small number of cognitive radar sensors, e.g. $R = 5$, in the surveillance scenario of $K = 3$ targets as shown in Fig. 2b. Comparison of probabilities of error for the different number of cognitive radar sensors in the scenario of $K = 3$ targets was shown in Fig. 2a. The



(a)



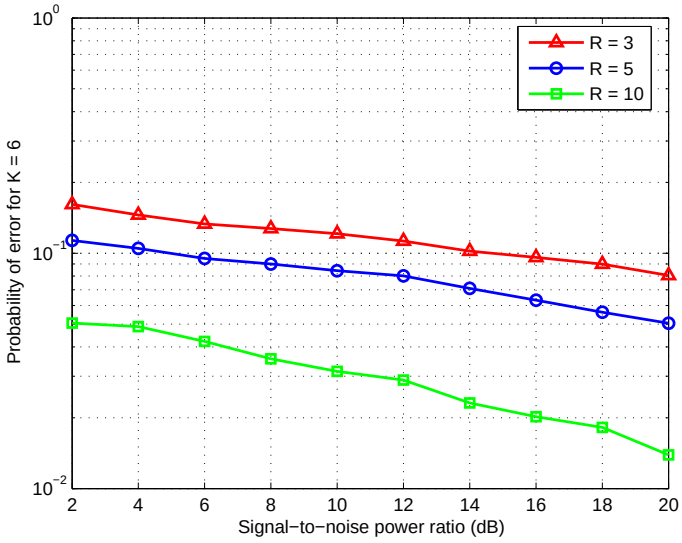
(b)

2: Probability of error using JMIC algorithm and surveillance scenario for K = 3: (a) Probability of error (b) Surveillance scenario.

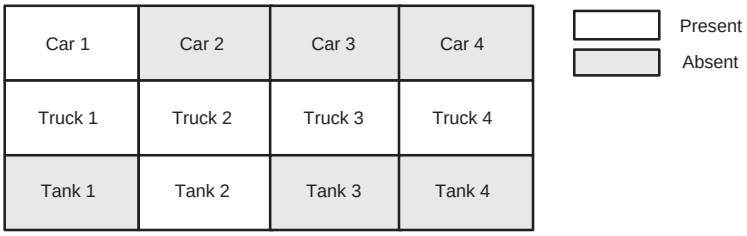
simulation results demonstrate our algorithm in the surveillance scenarios of $K = 6$ as described in Fig. 3b and $K = 8$ as in Fig. 4b are, correspondingly, given in Fig. 3a and Fig. 4a. We also observe that for a given number of targets K in the surveillance region, the performance of JMIC using $R = 5$ or $R = 10$ radar sensors is better than that using $R = 3$ radar sensors. Besides, for a given number of R radar sensors, the identification and classification performance is reduced when we notice an increasing number of targets in the surveillance region. The probability of JMIC error is inversely proportional to signal-to-noise power ratio. At high SNR, the probability of error is rather small. The simulation results validate the robustness and effectiveness of our proposed JMIC algorithm.

V. Conclusion

We have demonstrated that K targets in a query region can be classified and identified efficiently by a network of R cognitive radar sensors using our JMIC algorithm. A computer simulation with simulated radar data was used to investigate the accuracy of a joint classification and identification algorithm in the variations of the target signals in the network. Using JMIC algorithm, we show that a sufficiently low probability of error can be achieved with a fairly small number of radar sensors for a given common number of targets. The unprecedented desire of knowing



(a)



(b)

3: Probability of error using JMIC algorithm and surveillance scenario for K = 6: (a) Probability of error (b) Surveillance scenario.

not only the number of target categories, but also the total number of targets in each category in a surveillance region is making JMIC algorithm an attractive choice in practice for military applications.

ACKNOWLEDGEMENT

This work was supported by the U.S. Office of Naval Research (ONR) under Grant N00014-07-1-0395, N00014-07-1-1024, and N00014-03-1-0466.

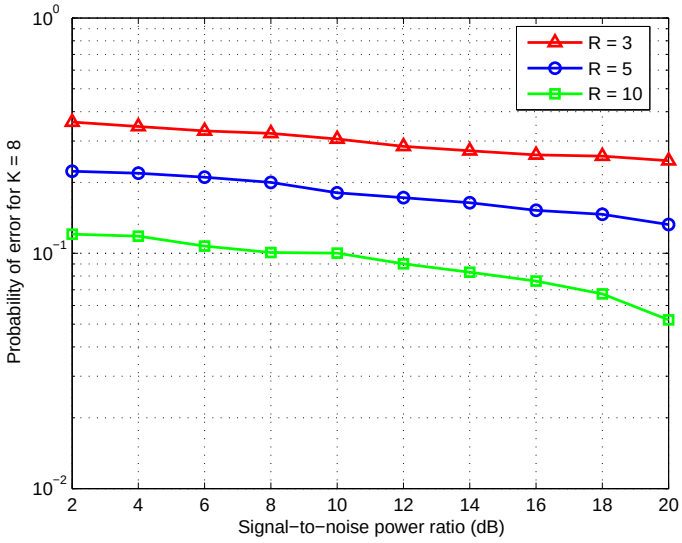
REFERENCES

[1] Chen, Y., E. Gunawan, K. S. Low, Y. Kim, C. B. Soh, A. R. Leyman, and L. L. Thi, "Non-invasive respiration rate estimation using ultra-wideband distributed cognitive radar system," in *Proc. of the 28th IEEE Engineering in Medicine and Biology Society Annual International Conference, New York City, USA*, pp. 920-923, Aug. 2006.

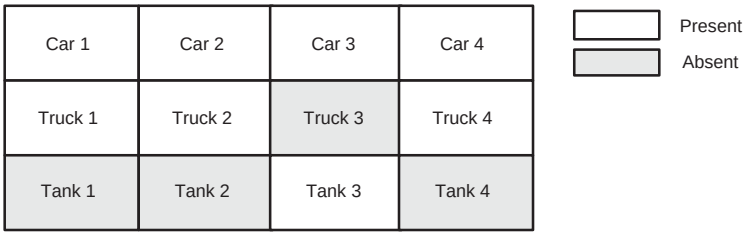
[2] Haykin S., "Cognitive radar: A way of the future," *IEEE Signal Processing Mag.*, vol. 23, no. 1, pp. 30-40, Jan. 2006.

[3] Haykin S., "Cognitive radar networks," *Fourth IEEE Workshop on Sensor Array and Multichannel Processing, 2006*, pp. 1-24, Jul. 2006.

[4] Kotecha J. H., V. Ramachandran, and A. M. Sayeed, "Distributed multitarget classification in wireless sensor networks," *IEEE Journal on Selected Areas in Communications*, vol. 23, no. 4 , pp. 703-713, Apr. 2005.



(a)



(b)

4: Probability of error using JMIC algorithm and surveillance scenario for K = 8: (a) Probability of error (b) Surveillance scenario.

[5] Leung H. and J. Wu, "Bayesian and Dempster-Shafer target identification for radar surveillance," *IEEE Trans. on Aerospace and Electronic Systems*, vol. 36, no. 2, pp. 432-447, Apr. 2000.

[6] Liang Q., "Automatic Target Recognition Using Waveform Diversity in Radar Sensor Networks," *Pattern Recognition Letters (Elsevier)*, vol. 29, no. 2, pp. 377-381, 2008.

[7] Meesookho C., S. Narayanan, C. S. Raghavendra, "Collaborative classification applications in sensor networks," *Sensor Array and Multichannel Signal Processing Workshop Proceedings, 2002*, pp. 370-374, Aug. 2002.

[8] Nebabin V. G., *Methods and techniques of radar recognition*, Artech House, 1994.

[9] Premebida, C. "A multi-target tracking and GMM-classifier for intelligent vehicles," in *2006 IEEE Proc. Intelligent Transportation Systems, Toronto, Cananda*, pp. 313-318, Sept. 2006.

[10] Teti J. G., R. P. Gorman, and W. A. Berger, "A multifeature decision space approach to radar target identification," *IEEE Trans. on Aerospace and Electronic Systems*, vol. 32, no. 1, pp. 480-487, Jan. 1996.

[11] Wang T-Y., Y. S. Han, Pramod K. Varshney, and Po-Ning Chen, "Distributed fault-tolerant classification in wireless sensor networks," *IEEE Journal on Selected Areas in Communications*, vol. 23, no. 4 , pp. 724-734, Apr. 2005.

Sense-Through-Foliage Target Detection Using UWB Radar Sensor Networks

Jing Liang and Qilian Liang, *Senior Member, IEEE*
Department of Electrical Engineering
University of Texas at Arlington
Arlington, TX 76019-0016 USA
E-mail: jliang@wcn.uta.edu, liang@uta.edu

Abstract

In this paper, we propose two signal processing approaches to detect the target obscured by foliage based on real data collected by an Ultra-wide band (UWB) radar sensor. One is a differential-based four-step signal processing approach that estimates and offsets the impulsive clutter; the other approach employs short-time Fourier transform (STFT) to distinguish the target from foliage clutter. Both of these approaches provide better detection performance compared to the common 2-D image algorithm used for UWB radar. From time to time, due to the significant pulse-to-pulse variability of the foliage clutter, neither differential-based nor STFT approach can detect the target. In this case, we propose radar sensor network (RSN) and a RAKE structure in addition to the previous signal processing approaches for data fusion. The result shows that accurate detection can be achieved. Numerical performances have been analyzed for both cases in terms of probability of detection and probability of false alarm.

Index Terms : Target detection, radar sensor networks, foliage, short-time Fourier transform (STFT), differential-based approach

1 Introduction

Detection and identification of objects that are embedded in a strong clutter (e.g., foliage, soil cover and buildings) is of interest to both military and civilian research. The efficient

and accurate detection provides a broad range of applications, such as locating weapon caches during military operations and rescuing people from natural diasters. Currently the detection of targets, such as human, vehicles and weapons that are hidden in foliage is still a challenging issue due to the low detection and high false alarm rate. This is mainly due to the following facts:

1. Given multipath propagation effects of rough surfaces, scattering from trees and ground tend to overwhelm the weak backscattering of targets.

2. Target is an object, so are trees. When both of them appear to have similar dielectric and frequency properties, it's hard to make a clear distinction between foliage clutter and desired targets.

3. Due to the changes in atmosphere and ground conditions, foliage is more likely to be a time-variant channel environment. For example, wind results in moving branches and leaves, therefore the foliage clutter is quite impulsive in nature.

There have been many efforts undertaken to investigate foliage penetration (FOPEN). They can be categorized into two groups. One direction is to pursue the foliage clutter modeling and analysis in order to gain better understanding of the clutter and improve the detection performance. [1] measured one-way transmission properties of foliage using a bistatic and coherent wide-band system over the band from 300 to 1300 MHz. [2] made measurements of two-way foliage attenuation by synthetic aperture radar (SAR) and discussed probability dependency for frequency, polarization and depression angle. Other than SAR, Millimeter-Wave (MMW) radars also have been applied in measurements of foliage attenuation and ground reflectivity [3]-[5]. These studies have showed the strong spatial and angular fluctuations of foliage. The clutter contains many spikes and is very "impulsive", therefore it's difficult to achieve effective and accurate target detection. Although K-distribution has been favored for statistic model of radar clutter [6], [7] demonstrated that in very spiky and impulsive foliage clutter, K-distribution is inaccurate. Based on a Ultra-wide band (UWB) radar, [8] proposed an alpha-stable model while [9]presented a log-logistic model for foliage clutter. However, to what extent can the detection performance be improved has not been further analyzed in these studies.

The second group centers on advanced signal processing approaches to support better image formation for target detection. [10] described the on-going development of a test bed system including real-time UHF FOPEN SAR image formation and Automatic Target Detection and Cueing (ATD/C) processing that was based on Bayesian neural network (BNN) algorithm. However, the BNN discriminator requires an elaborate and extensive training process. Alternative approaches, based on the application of a set of filters, have been proposed. As nonlinear filters have demonstrated good noise suppression characteristics in many environments with "spiky" noise characteristics, [11] presented a number of simple rank-order filters (Alpha-Trimmed, Modified Nearest Neighbor, Inner-Sigma Filter etc.) for UWB SAR image processing. This work has analyzed that the inner-sigma filter can generate good target detection performance with respect to many of the other filters. Nevertheless, this is very preliminary investigation and further performance estimation is needed. Other interesting filter schemes include adaptive Windrow Least Mean Squares (LMS) filter design [12] and a sequence of directional filters using a hidden Markov model (HMM) [13]. Notice that all these approaches are employed for SAR image. Other than SAR, a whitening/dewhitening (WD) transform has been proposed in [14] to help correct target spectral signatures under varying conditions for general multispectral image, but this transform can not be directly applied to colored noise, which also occurs in foliage detection.

Three types of waveforms are commonly seen in the literature dealing with the practical FOPEN measurements. The first type is multiwavelengths. [15] used multiwavelength Light Detection and Ranging (lidar) to detect a vehicle hidden inside a vegetated area. Due to the fact that a laser beam is generally considered not being able to penetrating vegetation foliage, when the vegetation is dense and the target is completely covered, it is not possible to detect the hidden targets using a lidar sensor. The second type is Millimeter-Wave (MMW) [16], that falls in the class of microwave. Compared to the lidar, the wavelength of microwave is much longer. Microwave and millimeter-wave (MMW) frequencies penetrate through foliage with higher attenuations, and thus this type of radar requires numbers of openings through most foliage covers. Relatively low frequency UWB signals between 100 MHZ and 3 GHz are frequently employed in recent years owning to the following characteristics: 1) high resolutions 2) very good ability of penetration, such as penetrating walls and ground [17]-[19] 3) low power

cost. Despite comparatively short detection range, UWB signal would have advantages over a narrowband signal with limited frequency content.

In this paper, we propose two approaches to detect the target obscured by foliage based on the "good" data (the detail will be provided in Section 2) collected by a UWB radar. One is a differential-based four-step signal processing approach: estimate the clutter decay profile, offset the impulsive clutter, compute the derivative power and finally make a detection decision according to the threshold. The other approach employs short-time Fourier transform (STFT) to distinguish the target from foliage clutter. Both of these approaches provide better detection performance compared to the 2-D image algorithm employed in [19]. As far as "poor" data is concerned, neither differential-based nor STFT approach can detect the target due to the significant pulse-to-pulse variability. In this case, we propose radar sensor network (RSN) and a RAKE structure in addition to the previous signal schemes for data fusion. The numerical performance have been analyzed for both "good" and "poor" data in terms of probability of detection (P_d) and probability of false alarm (P_{fa}).

The remainder of this paper is organized as follows. Section 2 summarizes the measurement of data used in this work. Section 3 proposes differential-based approach and STFT for target detection when the signal quality is "good". Section 4 proposes RSN and RAKE structure when the signal quality is "poor". Section 5 concludes our work and discusses future research.

2 Sense-Through-Foliage Data Measurement and Collection

The sense-through-foliage measurement effort began in August 2005 and continued through December 2005. The data used in this paper were measured in November, involved largely defoliated but dense forest.

The principle pieces of equipment are:

- dual antenna mounting stand
- two antennas
- a trihedral reflector target mounted on an artist easel stand
- Barth pulse source (Barth Electronics, Inc. model 732 GL) for UWB

- Tektronix model 7704 B oscilloscope
- rack system
- HP signal Generator
- IBM laptop
- Custom RF switch and power supply
- weather shield (small hut)

A bistatic system (individual transmit and receive antennas) have been used as it was believed that circulators did not exist for wideband signals in 2005. An 18 foot distance between antennas was chosen to reduce the signal coupling between transmitter and the receiver [20]. The triangular-shaped target, which was shown in Fig. 1, was a round trip distance of 600 feet from the bistatic antennas (300 feet one way). The UWB pulse generator uses a coaxial reed switch to discharge a charge line for a very fast rise time pulse outputs. The model 732 pulse generator provides pulses of less than 50 picoseconds (ps) rise time, with amplitude from 150 V to greater than 2 KV into any load impedance through a 50 ohm coaxial line. The generator is capable of producing pulses with a minimum width of 750 ps and a maximum of 1 microsecond. This output pulse width is determined by charge line length for rectangular pulses, or by capacitors for 1/e decay pulses.

The radar experiment was constructed on a seven-ton man lift, which had a total lifting capacity of 450 kg. The limit of the lifting capacity was reached during the experiment as essentially the entire measuring apparatus was placed on the lift. It was a 4-wheel drive diesel platform that was driven up and down a graded track 25 meters long. The measurement system was moved to different positions on the track. The illustration of the lift was shown in Fig. 2. This picture was taken in September with the foliage largely still present.

For the data we used in this paper, each sample is spaced at 50 picosecond interval, and 16,000 samples were collected for each collection for a total time duration of 0.8 microseconds at a rate of approximately 20 Hz. There are two sets of data. Initially, the Barth pulse source was operated at lower amplitude and 35 pulses of signals were obtained. The unit of amplitude is “V”. This collection is referred to as “poor” data, which means signal quality is poor. Later,

additional improvements were made in the measurement procedure, including the improved isolation of transmit and receive antennas, the addition of a log-periodic antenna (Antenna Research Associates LPC-2010-C) as a transmit antenna, and the EMCO ridged waveguide horn (Microwave horn, EMCO 3106). 100 pulses at different sites were collected using the new transmitted signal with higher amplitude. The integration of these 100 pulses is referred to as "good" data.

3 Target Detection for Good Data: A Differential-Based Approach and Short-Time Fourier Transform

3.1 Target Detection Problem

In Fig. 3, we plot two received collections for "good" data. Fig. 3a shows the situation that there is not a target on range and Fig. 3b shows the opposite case. The target appears around samples from 13,900 to 14,000. In order to further analyze the discrepancy between these two collections, we provide expanded views of traces from sample 13,001 to 15,000 in Figs. 4a and 4b. Since there is no target in Fig. 4a, it can be considered that this collection represents the backscattering of foliage clutter. Therefore, it's quite straightforward that the target response will be the difference between Fig. 4b and Fig. 4a, which is plotted in Fig. 4c. Nevertheless, in practice we either obtain Fig. 4a (clutter echoes without target) or Fig. 4b (combined echoes of both target and clutter) without the priori knowledge about the presence of a target. The challenge is how can we make target detection simply based on Fig. 4a (with target) or Fig. 4b (no target)?

To solve this problem, we applied the algorithm proposed in [19], where 2-D image (range and azimuth) was created via adding voltages with the appropriate time offset. In Figs. 5(a) and 5(b), we plot the 2-D image created based on the above two data sets (from samples 13,800 to 14,200). Since the measurement was made with one radar, the bright spot should represent reflections from an object or objects. Unfortunately, from these two figures, we may declare there are several targets in each image. Therefore, the simple 2-D image algorithm provided very high false alarm rate for current radar data.

3.2 A Differential-Based Approach

In order to improve the detection performance, we consider removing the clutter signal first [21]. Of course, since the foliage is very impulsive and time-variant in nature, it is very challenging to generate real-time clutter data. Also, notice that in Fig. 4b, for samples where target appears (around sample from 13900 to 14,000), the waveform changes much abruptly than that in Fig. 4a. As derivative represents the changing rate of a function, it is quite intuitively that the derivatives of amplitude value at around samples 13900 to 14,000 should be larger than those without target. Therefore, we decide to combine the clutter offset with the differentiation computation to test the detection performance. The block diagram of this approach is illustrated in Fig.6.

1. *Step1.* According to UWB indoor multi-path channel model (IEEE 802.15.SG3a, 2003), the average power decay profile (PDP) is characterized by an exponential decay of the amplitude of the clusters [22]. Therefore, we may roughly consider the foliage decay profile as

$$\hat{y} = \begin{cases} Ae^{-Bx} & y > 0 \\ -Ae^{-Bx} & \text{otherwise} \end{cases} \tag{1}$$

   where $\hat{y}$ is the amplitude of estimated clutter echo, x is sample index and y is the amplitude of original measured data. A and B are constants. These two parameters should be carefully chosen so that $\hat{y}$ is as close to y as possible.

   We apply trust-region algorithm [23] [24] and robust least-squares fitting by minimizing the least absolute residuals (LAR). We use LAR criteria instead of the commonly used least squares fitting because the LAR is more robust than least squares in cases where the statistical properties and distribution of the noise are unknown [25]. Fig. 7 illustrates the goodness-of-fit for foliage clutter decay profile for "good" data. Although the figure for "poor" data is not provided due to the similarity and conciseness, Table 1 shows the estimated parameters A and B for both "good" and "poor" data.

2. *Step2.* By offsetting the clutter signal, we get

$$S_1 = y - \hat{y} \tag{2}$$

3. *Step3.* Apply derivation and compute power

$$S_2 = \frac{dS_1}{dx} \tag{3}$$

$$S_3 = {S_2}^2 \tag{4}$$

4. *Step4.* Finally apply threshold detection to conclude whether there is a target or not.

We plot the power of clutter-accounted and differentiated echoes in Fig. 8. It is quite straightforward to see there is no target in Fig. 8a and there is target in Fig. 8b at samples from 13,900 to 14,000.

3.3 Short-Time Fourier Transform Approach

Another way to understand the abrupt change where target appears is that the signal contains more AC values when there is target. Therefore we also consider employing the short-time Fourier transform (STFT) approach, which uses a slide window to determine the sinusoidal frequency and phase content of a signal as it changes over time [26]. This form of the Fourier transform, also known as time-dependent fourier transform, has numbers of applications in sonar and radar processing.

For the continuous-time signal, the function to be transformed is multiplied by a nonzero window sliding along the time axis, therefore a two-dimensional expression can be defined as:

$$F(m, w) = \int_{-\infty}^{\infty} x(t)w(t - m)e^{-jwt}dt \tag{5}$$

where $x(t)$ is the function to be transformed and $w(t)$ is the window function. $F(m, w)$ represents sinusoidal values at the center of the window. m is the starting time position of window $w(t)$.

The discrete STFT can be expressed as

$$F(m, w) = \sum_{n=0}^{N-1} r(n)w(n - m)e^{-jwn} \tag{6}$$

where $r(n)$ is UWB radar measurement and $w(n)$ is the window function.

We apply a rectangular window, with its length $L = 30$ and step size $M = 16$.

$$w(n) = \begin{cases} 1 & \text{if } 0 \leq n \leq 29 \\ 0 & \text{otherwise} \end{cases} \tag{7}$$

Then the cumulated power of AC values ($m \geq 4$) can be obtained by

$$P(m) = \sum_{w=4}^{L-1} \mid F(m,w) \mid^2 \tag{8}$$

We plot the power of AC values $P(m)$ versus time domain sample index in Fig. 9a and 9b for the data collection in Figs. 3a and 3b respectively. We can see that at the samples where there is a target, the curve of the power signal looks like a Gaussian probability density function (PDF) other than chaotic impulses. And thus it is quite straightforward to see that there is no target on range in Fig. 9a.

It's worth mentioning that for better visual inspection, window length and step size may change for radar data collected in a different environment.

3.4 Performance Analysis

We analyzed the detection performance in terms of probability of detection (P_d) and probability of false alarm (P_{fa}) for both differential-based approach and STFT approach. Fig. 10 shows the relationship between the performance and the threshold for differential-based approach. The unit of the threshold illustrated by X axis is "10^5 W". The decision of the threshold has been intensively studied [27] therefore it's out of the scope of this paper. It can be clearly seen that the higher the threshold, the higher the P_{fa}, but the lower the P_d. In order to achieve accurate target detection (100% P_d and 0% P_{fa}), the threshold should be set in the range of $[1.346 \times 10^5, 1.716 \times 10^5]$.

As for STFT approach, since the Gaussian curves are not as numerically intuitive as the threshold detection, we first analyze all the segments of curves that are similar to Gaussian PDF, then design the decision criteria. The general Gaussian model for these curves is defined as

$$f(x) = \sum_{i=1}^{n} a \times e^{-(\frac{x-b}{c})^2} \tag{9}$$

where a is the amplitude, b is the centroid (location), c is related to the peak width and n is the number of peaks to fit. For simplicity we choose $n = 1$, therefore c is the standard deviation (STD). Notice that the detection decision is determined by the shape of the Gaussian curve, i.e., related with factors a and c, not decided by b. The larger a and c, the higher probability

that the target exists. Since the detection depends on both a and c, we normalize them respectively and set the product of these normalized factors as a decision criteria. These parameters are shown in Table 2. Fig. 11 illustrates the performance for STFT. When the product of normalized factor is in the range [0.3439, 0.8876] the accurate target detection (100% P_d and 0% P_{fa}) can be achieved.

Compare STFT approach with differential-based approach, both of them are able to detect target effectively. Meanwhile, each of them has inherited defects. For differential-based approach, the major disadvantage is that it requires clutter estimation. If the clutter signal is not removed, the performance of detection is not acceptable. Therefore when the Target-to-Clutter ratio (TCR) is weak, this approach may not work well, which is exactly the case for "poor" data. The drawback of STFT approach is that the detection is not numerically intuitive, therefore it requires extra training and computing for setting up the decision boundary.

4 Target Detection for Poor Data: Radar Sensor Networks and RAKE Structure

As mentioned in Section 2, when the Barth pulse source was operated at low amplitude, significant pulse-to-pulse variability was noted and the return signal quality is poor. Fig. 12 illustrate the received echoes in this situation. Even with the application of our proposed differential-based scheme or STFT approach, it is difficult to detect the target. Since pulse-to-pulse variability exists in the echoes at different time or different site, the spatial and time diversity can be explored by using Radar Sensor Networks (RSN).

In nature, a network of multiple radar sensors can be utilized to combat performance degradation of single radar [28]. These radar sensors are managed by an intelligent clusterhead that combines waveform diversity in order to satisfy the common goals of the network other than each radar operate substantively. As radar sensors are environment dependent [29], it may provide better signal quality if uncorrelated radars work collaboratively to perform data fusion. For example, consider a system of two radars. If they are spaced sufficiently far apart, it is not likely that both of them experience deep fading at the same time. By selecting better waveform from the two candidates, the more accurate detection will be achieved compared to

using single radar.

In our work, we assume the radar sensors are synchronized and RAKE structure is employed to combine the diversity of received signals. The detailed processing diagrams are illustrated in Fig. 13 and Fig. 14 for differential-based approach and STFT approach respectively. The echo, i.e., the backscattering received by each radar sensor, is combined by the clusterhead using a weighted average, and the weight w_i is determined by the power of each echo $x_i(m)$ (m is the sample index),

$$w_i = \frac{E_i}{\sum_{i=1}^{n} E_i} \tag{10}$$

and

$$E_i = \text{var}(x_i(m)) + [\text{mean}(x_i(m))]^2 \tag{11}$$

As for STFT, we apply window length $L = 25$ and step size $M = 15$. We ran simulations for n = 35. Fig. 15 and Fig. 16 show the results. For RSN with differential-based approach, it is obvious that there is a target around sample 13,950 in Fig. 15b and no target appears in Fig. 15a. Also, for RSN with STFT approach, around samples 13,900 to 14,000, Gaussian curve appears. The related parameters for "poor" data are shown in Table 1 and Table 3 respectively. Fig. 17 and Fig. 18 illustrate the analyzed detection performance. For differential-based approach, accurate detection is obtained when the threshold lies in $[0.843, 1.173]$. For STFT, the decision boundary should be within [0.3155, 0.7120].

5 Conclusion and Future Works

In this paper, we propose two signal processing approaches to improve sense-through-foliage target detection. Additionally, we employ Radar Sensor Networks (RSN) and RAKE structure to improve the robustness of the detection performance. However, as each approach has its own advantage and drawback, it's hard to conclude which is superior. Detecting targets obscured by foliage will be an on-going research that may include future works listed as follows:

1. Investigate the time-variant properties of foliage clutter. The foliage is not a static environment due to the changes in temperature and ground conditions. Although many previous studies have assume the clutter to be time-invariant, the future analysis on the

noncoherent and variant properties will help better understand the impulsiveness nature of the foliage.

2. As more sensing-through-foliage data will be collected, we may optimize the proposed approaches and improve their robustness.

3. Apply proposed approaches and structures to targets obscured by other clutters, such as walls, soil cover, etc.

Acknowledgement

This work was supported in part by Office of Naval Research (ONR) under Grant N00014-07-1-0395 and N00014-07-1-1024, and National Science Foundation (NSF) under Grant CNS-0721515 and CNS-0831902.

References

[1] D. R. Sheen, N. P. Malinas, D. W. Kletzli, T. B. Lewis, and J. F. Roman, "Foliage transsmission measurementsusing a ground-based ultrawideband (UWB) (3001300 Mhz) SAR system", *IEEE Transactions on Geoscience and Remote Sensing*, vol. 32, pp. 118-130, Jan. 1994.

[2] J. G. Fleischman; S. Ayasli; E. M. Adams; D. R. Gosselin, "Foliage penetration experiment: Part I: Foliage attenuation and backscatter analysis of SAR imagery", *IEEE Transactions on Aerospace and Electronic Systmes*, vol. 32, pp. 135-144, Jan. 1996.

[3] F. K. Schwering, E. J. Violette and R. H. Espeland, "Millimeter-wave propagation in vegetation: Experiments and theory", *IEEE Trans. Geosci. Remote Sensing,* vol.26, pp. 355-367, May 1988.

[4] F. T. Ulaby, T. E. Van Deventer, J. R. East, T. F. Haddock and M. E. Coluzzi, "Millimeter-wave bistatic scaterring from ground and vegetation targets" , *IEEE Trans. Geosci. Remote Sensing,* vol.26, pp. 229-243, May 1988.

[5] A. Y. Nashashibi, k. Sarabandi, S. Oveisgharan *et al.*, "Millimeter-Wave Measurement of Foliage Attenuation and Ground Reflectivity of Tree Stands at Nadir Incidence", *IEEE Trans. Antennas Propagat.,* vol.52, pp. 1211-2004, May 2004.

[6] T. Nohara and S. Haykin, "Canadian east coast radar trials and the K-distribution", *IEE Proc.-F*, vol. 138, pp. 80-88, April 1991.

[7] S. Watts, "Radar detection prediction in K-distribution sea clutter and thermal noise", *IEEE Transactions on Aerospace and Electronic Systmes*, vol. 23, pp. 40-45, Jan. 1987.

[8] R. Kapoor, G. A. Tsihrintzis, N. Nandhakumar, "Detection of obscured targets in heavy-tailed radar clutter usingan ultra-wideband (UWB) radar and alpha-stable clutter models", *In proceedings of the Thirtieth Asilomar Conference on Signals, Systems and Computers*, vol.2, pp. 863-867, Nov. 1996.

[9] J. Liang, Q. Liang, and S. W. Samn, "Foliage Clutter Modeling Using the UWB Radar", *IEEE International Conference on Communications 2008 (ICC '08) Rec.*, pp. 1937-1941.

[10] D. MacDonald, J. Isenman, and J. Roman, "Radar detection of hidden targets", *Aerospace and Electronics Conference 1997 (NAECON '97)*, vol.2, pp. 846-855.

[11] A. K. Mitra, T. L. Lewis, and A. K. Shaw, "Rank-order filters for FOPEN target detection", *IEEE Signal Processing Letters*, vol. 11, Part 1, Feb. 2004, pp. 93-96.

[12] J. G. Nanis, S. D. Halversen, G. J. Owirka and L. M. Novak, "Adaptive filters for detection of targets in foliage", *IEEE Aerospace and Electronic Systems Magazine*, vol. 10, pp. 34-36, Aug. 1995.

[13] P. Runkle, L. H. Nguyen, J. H. McClellan and L. Carin, "Multi-aspect target detection for SAR imagery using hidden Markov models", *IEEE Transactions on Geoscience and Remote Sensing*, vol. 39, pp. 46-55, Jan. 2001.

[14] R. Mayer, F. Bucholtz, and D. Scribner, "Object detection by using whitening/dewhitening to transform target signatures in multitemporal hyperspectral and multispectral imagery", *IEEE Transactions on Geoscience and Remote Sensing*, vol. 41, Part 2, pp. 1136-1142, May 2003.

[15] S. Tan, S. Greenlee, and J. Stoker, "Detection of foliage-obscured vehicle using a multi-wavelength polarimetric lidar", *IEEE International Geoscience and Remote Sensing Symposium 2007 (IGARSS '07)*, pp. 2503-2506.

[16] A. Y. Nashashibi, F. T. Ulaby, "Detection of stationary foliage-obscured targets by polarimetric millimeter-wave Radar", *IEEE Transactions on Geoscience and Remote Sensing*, vol. 43, pp. 13-23, Jan. 2005.

[17] B. Ferrell "Ultrawideband foliage penetration measurement", in *Proc. IEEE Nation Radar Conf 1994,* pp. 80-84.

[18] X. Xu; R. M. Narayanan, "FOPEN SAR imaging using UWB step-frequency and random noise waveforms ", *IEEE Trans. Aerospace and Electronic Systems*, vol.37, pp. 1287-1300, Oct. 2001.

[19] P. Withington , H. Fluhler, and S. Nag, "Enhancing homeland security with advanced UWB sensors," *IEEE Microwave Magazine*, Sept. 2003.

[20] J. A. Henning, "Design and Performance of An Ultra-Wideband Foliage Penetrating Noise Radar", Masters Thesis, University of Nebraska, May 2001.

[21] J. Liang, Q. Liang, and S. W. Samn, "A Differential Based Approach for Sense-Through-Foliage Target Detection Using UWB Radar Sensor Networks", *IEEE International Conference on Communications 2008 (ICC '08) Rec.*, pp. 1952-1956.

[22] Benedetto M. D and Giancola G., *Understanding Ultra Wide Band Radio Fundamentals*, Person Education, 2004.

[23] T. Liu and H. Chen., "Real-time tracking using trust-region methods", *IEEE Trans. on Pattern Anal. and Machine Intell.* vol. 26 pp. 397C402, 2004.

[24] L. Xiao and P. Li, "Improvement on Mean Shift based tracking using second-order information", *19th International Conference on Pattern Recognition 2008 (ICPR '08)*, pp. 1-4.

[25] J. Ke, C. Zhang and Y. Qiao, "Modified Evolution Strategy Based Identification of Multi-input Single-Output Wiener-Hammerstein Model", *Third International Conference on Natural Computation 2007. (ICNC '07)*, pp. 251-255.

[26] D. Gabor, "Theory of communication", *Journal of the IEE*, vol. 93, no. 3, pp. 429-457, 1946.

[27] M. I. Skolnik, *Introduction to Radar Systems* , 3rd ed, New York, McGraw Hill, 2001.

[28] S. Haykin, "Cognitive radar networks" , *2005 1st IEEE International Workshop on Computational Advances in Multi-Sensor Adaptive Processing*, pp. 1-3, Dec 2005.

[29] R. A. Johnson and E. L. Titlebaum, "Range Doppler Uncoupling in the Doppler Tolerant Bat Signal", *Proc. of IEEE Ultrasonics Symposium* , New York, pp. 64-67, 1972.

List of Tables

1 Estimated Clutter Decay Parameters 16
2 Gaussian Parameters and Normalized Product for Good Data using STFT . . . 16
3 Gaussian Parameters and Normalized Product for Poor Data using STFT . . . 16

Table 1: Estimated Clutter Decay Parameters

Data Set	A (with 95% confidence bounds)	B (with 95% confidence bounds)
Good Data	1.317×10^4 (1.301×10^4, 1.332×10^4)	0.0002628 (0.0002664, 0.0002592)
Poor Data	6881 (6779, 6983)	0.0002506 (0.0002549, 0.0002463)

Table 2: Gaussian Parameters and Normalized Product for Good Data using STFT

Data	Gaussian Parameter a	Gaussian Parameter c	Product of the normalized factors
Target	6.02×10^8	2.82	0.8876
False Alarm 1	4.071×10^8	1.615	0.3438
False Alarm 2	1.353×10^8	0.9674	0.0684
False Alarm 3	3.563×10^8	1.52	0.2832
False Alarm 4	2.904×10^8	1.091	0.1657

Table 3: Gaussian Parameters and Normalized Product for Poor Data using STFT

Data	Gaussian Parameter a	Gaussian Parameter c	Product of the normalized factors
Target	6.068×10^7	3.177	0.7120
False Alarm 1	3.795×10^7	1.649	0.2311
False Alarm 2	3.267×10^7	1.567	0.1891
False Alarm 3	8.523×10^7	1.002	0.3154
False Alarm 4	2.511×10^7	1.509	0.1399

List of Figures

1 The target (a trihedral reflector) is shown on the stand at 300 feet from the lift. 17

2 This figure shows the lift with the experiment. The antennas are at the far end of the lift from the viewer under the roof that was built to shield the equipment from the elements. This picture was taken in September with the foliage largely still present. The cables coming from the lift are a ground cable to an earth ground and one of 4 tethers used in windy conditions. 18

3 Measurement with very good signal quality and 100 pulses integration. (a) no target on range (b) with target on range (target appears at around sample 13900 to 14000) 19

4 Measurement with good signal quality and 100 pulses integration (a) Expanded view of traces (no target) from samples 13001 to 15000 (b) Expanded view of traces (with target) from samples 13001 to 15000 (c) Expanded view of traces difference between with and without target 20

5 2-D image created via adding voltages with the appropriate time offset (a) no target (b) with target in the field 21

6 Block diagram of differential-based approach for single radar 21

7 Curve fit for foliage clutter decay profile 22

8 The power of processed waveforms with differential-based approach for good data (a) no target (b) with target in the field 23

9 The power of AC values versus sample index using STFT for good data. (a) no target (b) with target in the field 24

10 Performance of differential-based approach based on good data. (a) Probability of detection (b) Probability of false alarm 25

11 Performance of STFT approach based on good data. (a) Probability of detection (b) Probability of false alarm 26

12 Measurement with poor signal quality (a) Expanded view of traces (no target) from samples 13001 to 15000 (b) Expanded view of traces (with target) from samples 13001 to 15000 (c) Expanded view of traces difference between with and without target 27

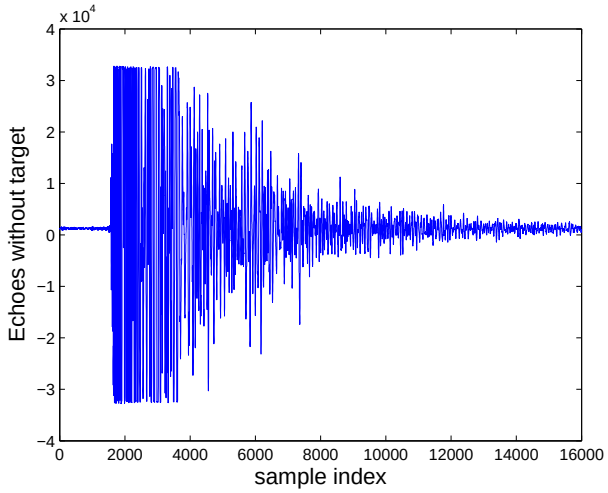
13 Block diagram of differential based approach and diversity combination in RSN 28
14 Block diagram of STFT based approach and diversity combination in RSN . . 28
15 The power of processed waveforms with differential-based approach and RSN for poor data (a) no target (b) with target in the field 29
16 The power of AC values versus sample index using STFT and RSN for poor data. (a) no target (b) with target in the field 30
17 Performance of differential-based approach based on poor data. (a) Probability of detection (b) Probability of false alarm 31
18 Performance of STFT approach based on poor data. (a) Probability of detection (b) Probability of false alarm 32



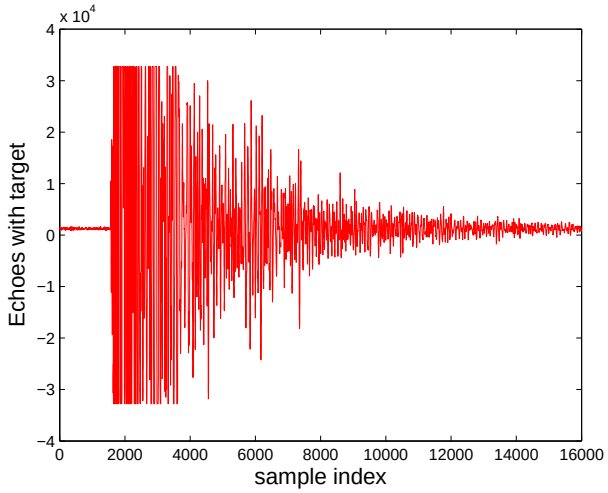
Figure 1: The target (a trihedral reflector) is shown on the stand at 300 feet from the lift.



Figure 2: This figure shows the lift with the experiment. The antennas are at the far end of the lift from the viewer under the roof that was built to shield the equipment from the elements. This picture was taken in September with the foliage largely still present. The cables coming from the lift are a ground cable to an earth ground and one of 4 tethers used in windy conditions.

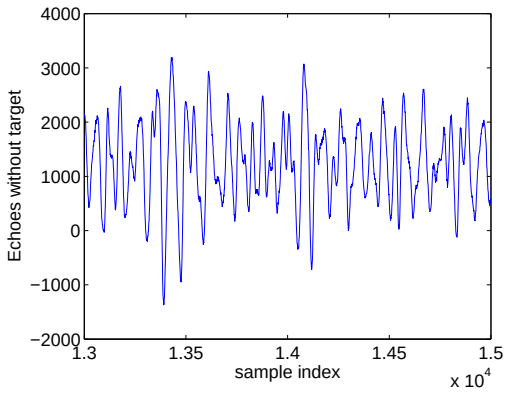


(a)

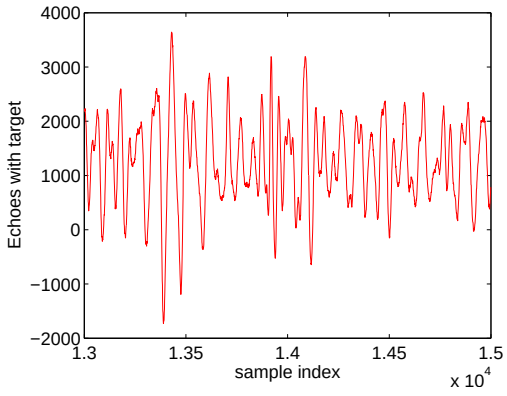


(b)

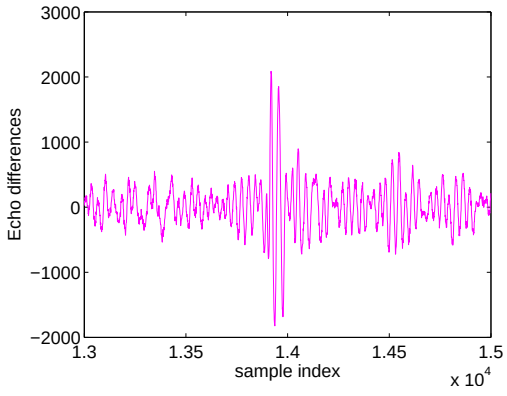
Figure 3: Measurement with very good signal quality and 100 pulses integration. (a) no target on range (b) with target on range (target appears at around sample 13900 to 14000)



(a)

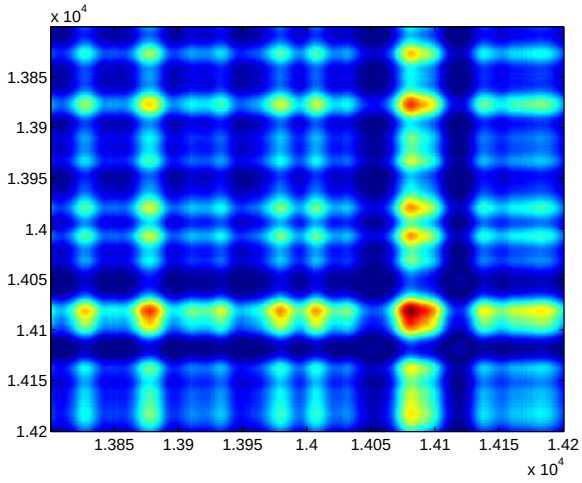


(b)

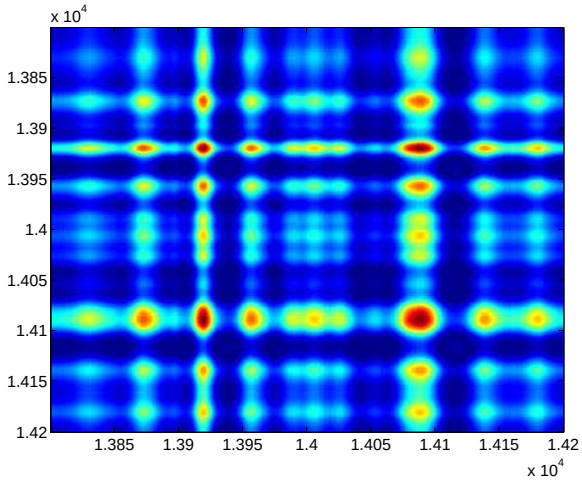


(c)

Figure 4: Measurement with good signal quality and 100 pulses integration (a) Expanded view of traces (no target) from samples 13001 to 15000 (b) Expanded view of traces (with target) from samples 13001 to 15000 (c) Expanded view of traces difference between with and without target



(a)



(b)

Figure 5: 2-D image created via adding voltages with the appropriate time offset (a) no target (b) with target in the field

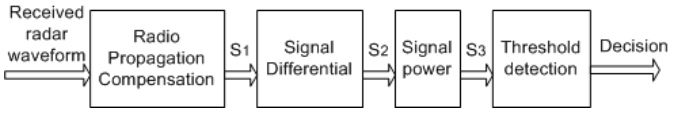


Figure 6: Block diagram of differential-based approach for single radar

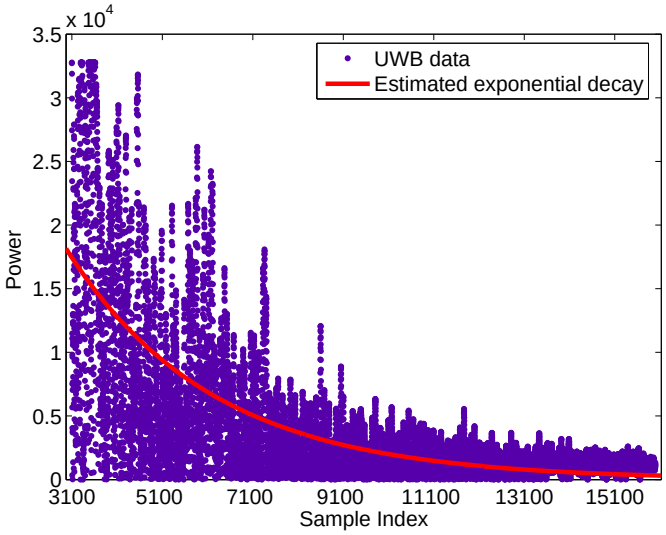
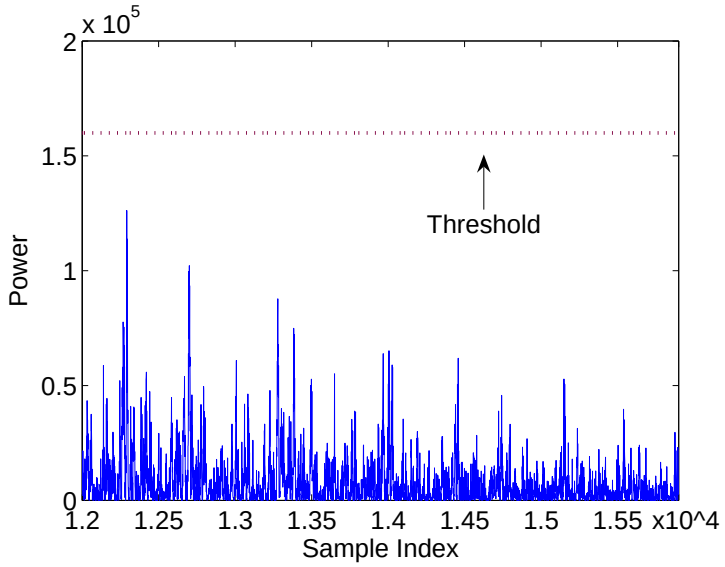
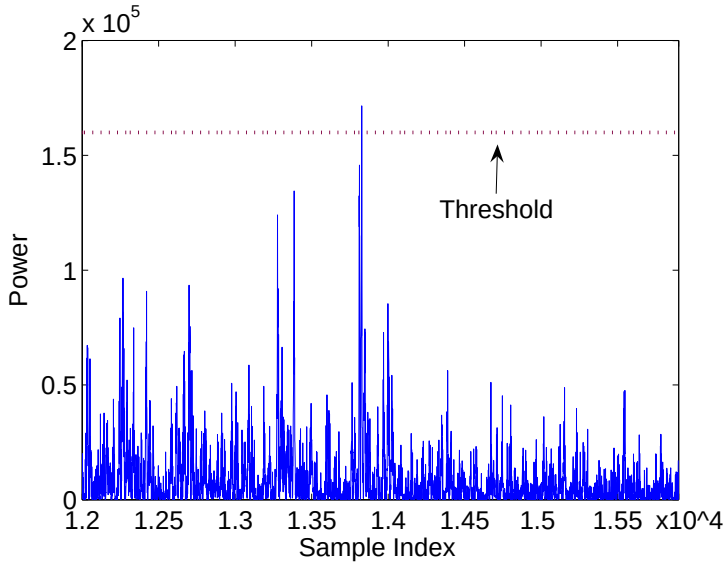


Figure 7: Curve fit for foliage clutter decay profile

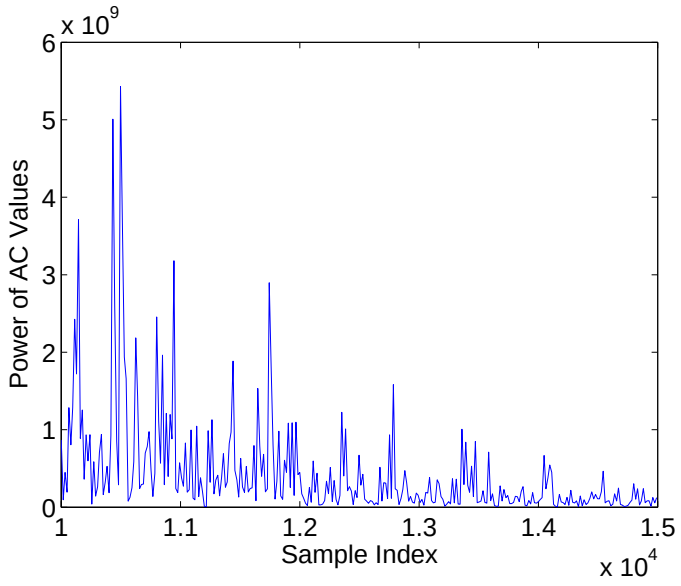


(a)

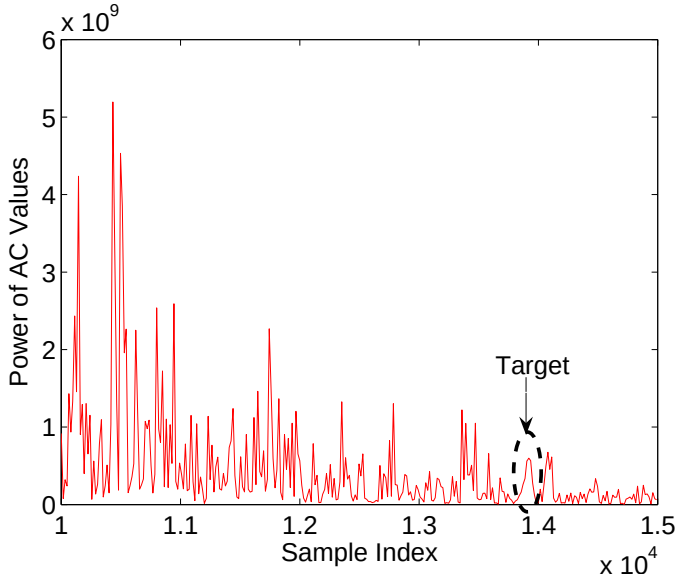


(b)

Figure 8: The power of processed waveforms with differential-based approach for good data (a) no target (b) with target in the field

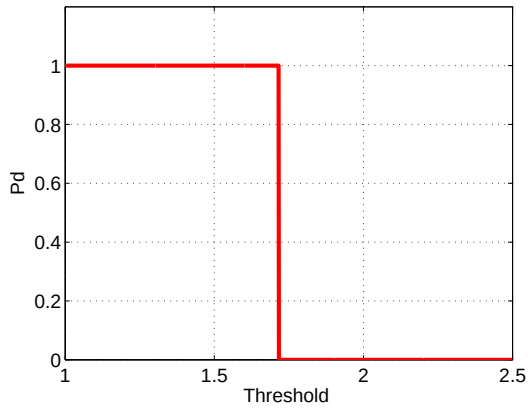


(a)

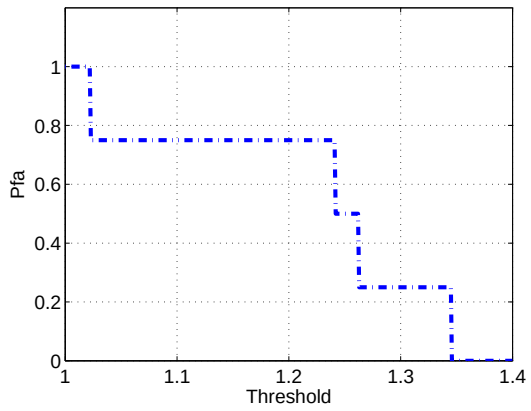


(b)

Figure 9: The power of AC values versus sample index using STFT for good data. (a) no target (b) with target in the field

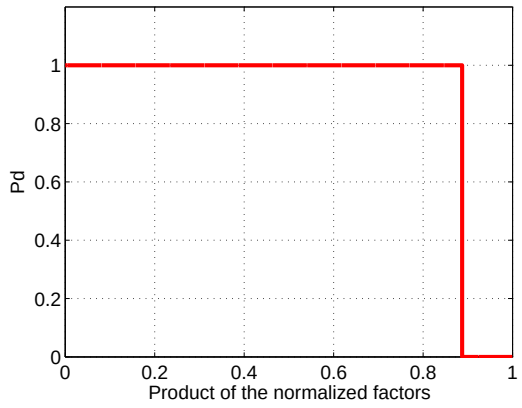


(a)

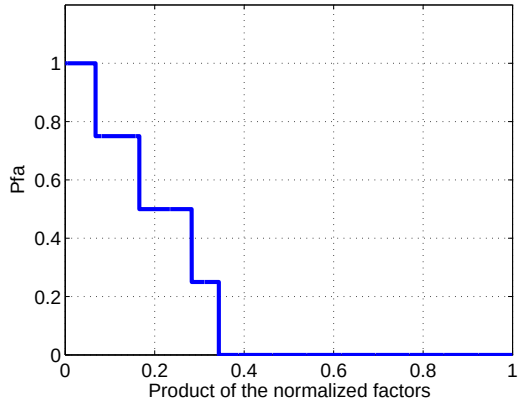


(b)

Figure 10: Performance of differential-based approach based on good data. (a) Probability of detection (b) Probability of false alarm

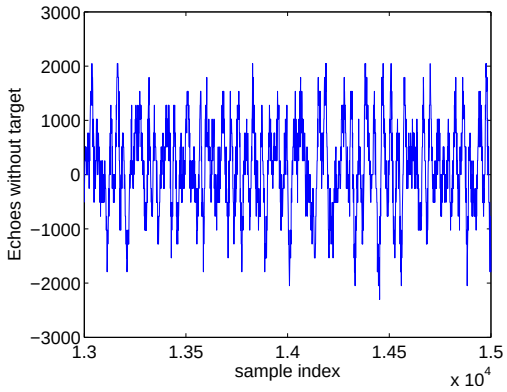


(a)

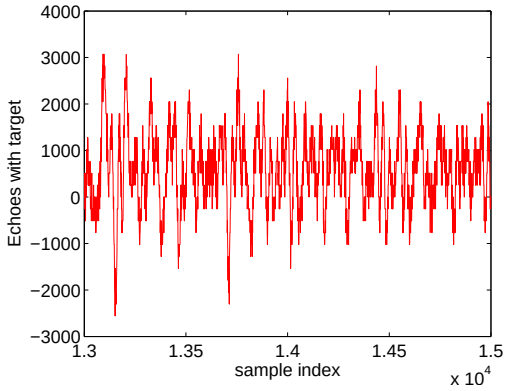


(b)

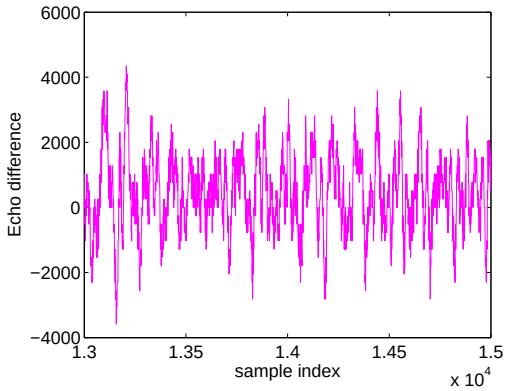
Figure 11: Performance of STFT approach based on good data. (a) Probability of detection (b) Probability of false alarm



(a)



(b)



(c)

Figure 12: Measurement with poor signal quality (a) Expanded view of traces (no target) from samples 13001 to 15000 (b) Expanded view of traces (with target) from samples 13001 to 15000 (c) Expanded view of traces difference between with and without target

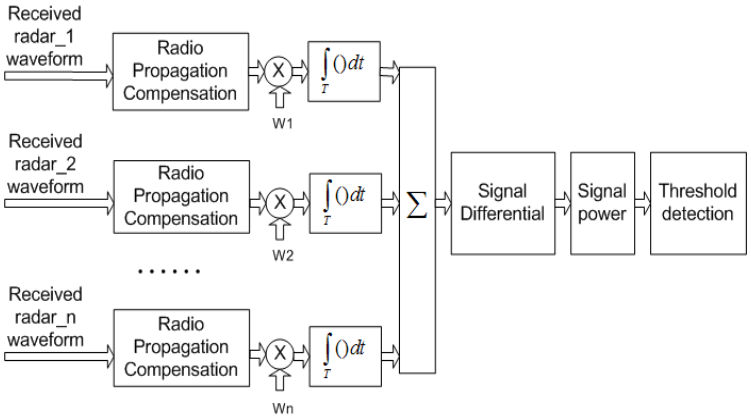


Figure 13: Block diagram of differential based approach and diversity combination in RSN

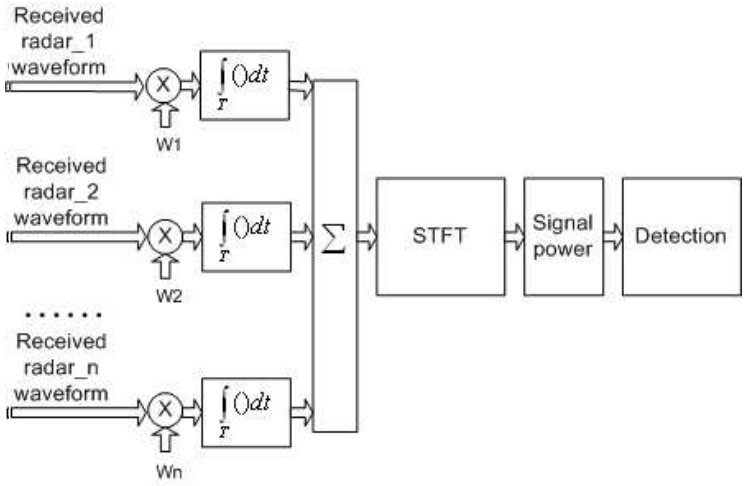
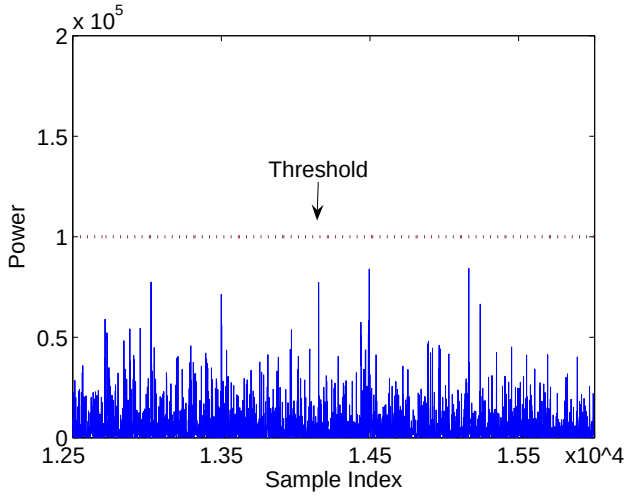
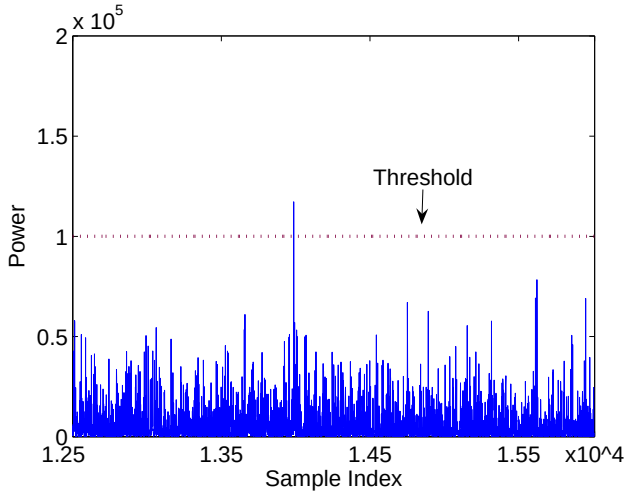


Figure 14: Block diagram of STFT based approach and diversity combination in RSN

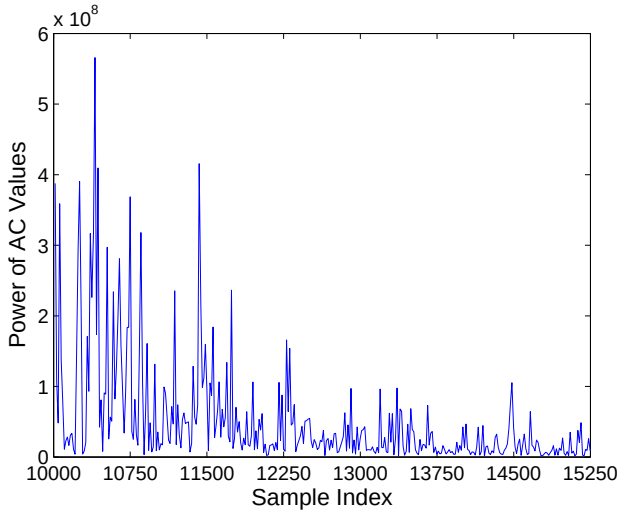


(a)

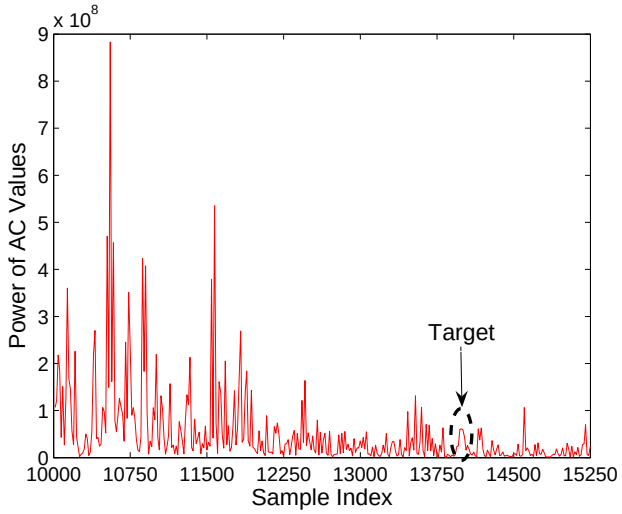


(b)

Figure 15: The power of processed waveforms with differential-based approach and RSN for poor data (a) no target (b) with target in the field

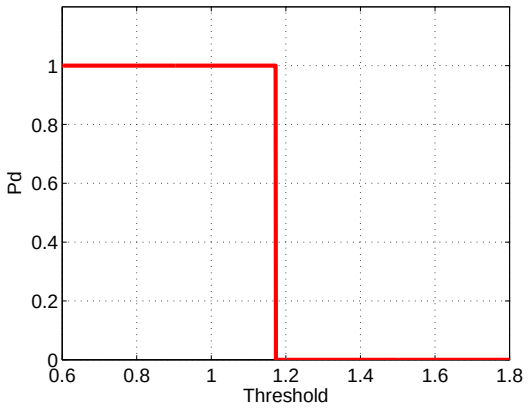


(a)

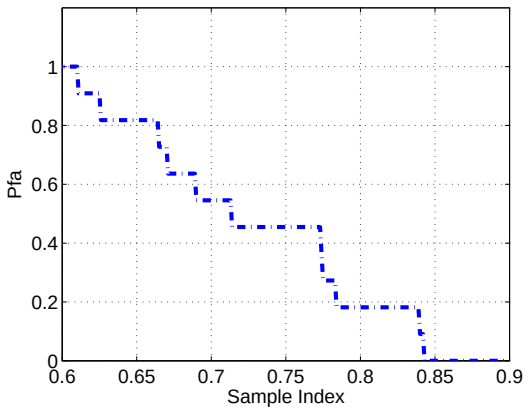


(b)

Figure 16: The power of AC values versus sample index using STFT and RSN for poor data. (a) no target (b) with target in the field

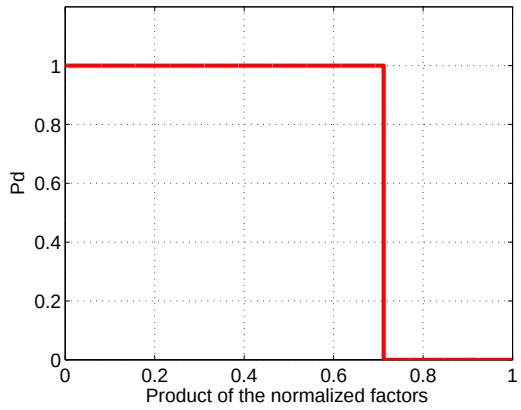


(a)

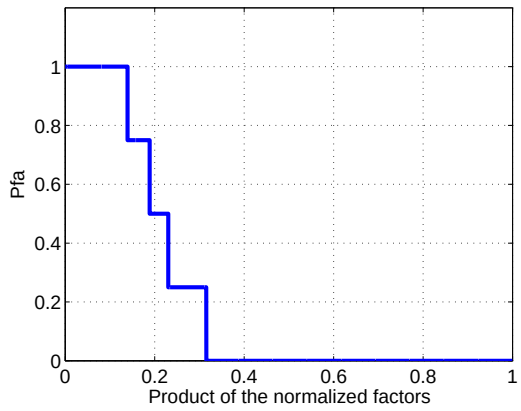


(b)

Figure 17: Performance of differential-based approach based on poor data. (a) Probability of detection (b) Probability of false alarm



(a)



(b)

Figure 18: Performance of STFT approach based on poor data. (a) Probability of detection (b) Probability of false alarm

Passive Geolocation Based on Wireless Channel Estimation

Qilian Liang
Department of Electrical Engineering
University of Texas at Arlington
Arlington, TX 76019-0016, USA
E-mail: liang@uta.edu

Sherwood W. Samn
Air Force Research Laboratory/711 HPW
Brooks City Base
San Antonio, TX 78235, USA
E-mail: Sherwood.samn@brooks.af.mil

Abstract

Determining the location of an emitting target is one of the fundamental functions of communication Electronic Warfare systems. In this paper, we propose a Time Difference of Arrival (TDoA) algorithm for passive geolocation based on delay estimation of two correlated wireless channels. It's assumed that the passive receiver is carried by a small flying UAV in the sky, and the transmitter is located on the ground (static or mobile), so Rician flat fading model should be used. To estimate the delay of two correlated channels, Block Phase Estimation (BPE) is used for each wireless channel estimation, and then the two estimated channels are compared to get the best time delay. We also compare it against a cross-correlation-based TDoA algorithm. Simulation results show that our TDoA algorithm performs much better than the cross-correlation-based TDoA algorithm with a lower level of magnitude in terms of average TDoA error and Root-Mean-Square-Error (RMSE). Four different Rician fading channel groups are evaluated, and conclusions are drawn for our TDoA algorithm and the cross-correlation-based TDoA algorithm.

Index Terms : Electronic warfare, passive geolocation, time difference of arrival, block phase estimation, Rician fading.

1 Introduction

Determining the location of an emitting target is one of the fundamental functions of communication *Electronic Warfare* (EW) systems [9]. The U.S. military has a urgent need to pinpoint an enemy based purely on the reception of radio signals, without the need for using radar. In contrast, locating an enemy actively with radar is to be avoided, since it draws unwanted attention to the platform operating the radar. The measurement of an emitter's position using electronic support (ES) sensors is termed **passive geolocation**, and plays an important part both in electronic support and electronic attack. Existing systems and technology for the precision geolocation of non-cooperative RF emitters are costly and time consuming to develop and deploy, and lack the flexibility to make cost-effective enhancements once deployed. Additionally, existing systems also rely on Global Positioning System (GPS), which is susceptible to jamming. Because a variety of operational scenarios are required, RF emitters will experience impairments that hamper reception. These impairments include obscuration, multi-path, foliage attenuation, RF interference from a dense RF signal environment having multiple RF emitters sharing common RF spectrum. Thus, the ability of large standoff intelligence gathering systems is severely hampered, and the use of passive sensors on appropriate airborne platforms provides the most effective solution.

Several techniques of passive geolocation were presented in [9], which includes triangulation, Time of Arrival (ToA), Time Difference of Arrival (TDoA), Angle of Arrival (AoA), etc. In this paper, we are interested in studying passive geolocation from wireless communication point of view and propose a TDoA algorithm for passive geolocation based on wireless channels delay estimation. Some related works in this direction have already been reported. In [7], a TDoA location scheme for the orthogonal frequency division multiplexing (OFDM) based wireless metropolitan area networks (WMANs) was presented. The TDoA algorithm enhances the location performance by utilizing the information in the time and frequency domains obtained from the received location

OFDM signals. In [1], a TDoA estimation is carried out for narrowband multipath system using a correlation technique and a super-resolution method - root multiple signal classification (MUSIC). In [2], ultra-wideband (UWB) radio for positioning techniques were overviewed, which include the angle of arrival (AOA), the signal strength (SS), or time delay information, etc. In order to achieve timing error reduction in TDoA, a high-resolution first arriving path detector from propagation channel estimates is derived based on the minimum variance (MV) estimates and normalized minimum variance (NMV) of the power delay profile in [13]. In [8], a received signal phase-based TDoA approach was proposed in [8]. The least squares range difference location problem has been investigated by Schmidt [11] and others. Schmidt showed that the TDoA averaging process produced the geolocation that was the closest feasible one in a lest squared sense based on the measured ranging differences.

Besides RF-based signal geolocation, some other signals such as acoustic-based geolocation were also studied. In [10], a TDoA for multiple acoustic sources in reverberant environments was proposed, and the ambiguities in TDoA estimation caused by multipath propagation and multiple sources were resolved by exploiting two TDoA constraints, the raster condition and the zero cyclic sum condition. In [15], a near-optimal procedure to localize a single stationary source in a two-path underwater acoustic environment was proposed, where the range and depth estimators were developed using a linear least-squares technique when a set of auto- and cross-correlators is used for TDoA estimates.

In this paper, we propose a TDoA algorithm via wireless channel estimation. The rest of this paper is organized as follows. In Section 2, propagation channel modeling in passsive geolocation scenario is overviewed. In Section 3, we propose a blind channel phase estimation approach named Block Phase Estimation (BPE) without knowing the unique words. In Section 4, we propose our TDoA algorithm based on the estimated phase differences of the two wireless channels. In Section

5, we present our simulation results on our TDoA algorithm and compare it against an existing TDoA approach. Section 6 concludes this paper.

2 Propagation Channel Modeling

In passive geolocation applications, the passive receiver is carried by a small flying UAV in the sky, and the transmitter is located on the ground (static or mobile). Two parallel antennas with distance d are equipped under the UAV. When $d < 0.38\lambda$ [3], where λ is the wavelength of the RF signal, the two wireless channels are correlated, and one is the delayed version of the other.

In this paper, vertical polarization of the transmitter is assumed. The n-th plane wave arrives at the UAV antenna 1 (closer to the transmitter) with an elevation angle θ_n. The UAV movement introduces a Doppler shift, which is given by

$$f_{D,n} = f_m \cos\theta_n \quad Hz \tag{1}$$

where $f_m = \upsilon/\lambda_c$ and λ_c is the wavelength of the arriving plane wave, and f_m is the maximum Doppler frequency occurring when $\theta_n = 0$. Plane waves arriving from the direction of motion will experience a positive Doppler shift, while those arriving opposite the direction of motion will experience a negative Doppler shift.

Consider the transmission of the band-pass signal from the RF emitter

$$s(t) = Re[\tilde{s}(t)e^{j2\pi f_c t}] \tag{2}$$

where $\tilde{s}(t)$ is the complex envelope of the transmitted signal, f_c is the carrier frequency, and $Re[z]$ denotes the real part of z. If the channel is comprised of N propagation paths, then the noiseless received band-pass waveform is [12]

$$r(t) = Re\left[\sum_{n=1}^{N} C_n e^{j2\pi[(f_c+f_{D,n})(t-\tau_n)]}\tilde{s}(t-\tau_n)\right] \tag{3}$$

where C_n and τ_n are the amplitude and time delay, respectively, associated with the nth propagation path. The magnitude C_n depends on the cross sectional area of the nth reflecting surface or the length of the nth diffracting edge.

Similar to (2), the received band-pass signal $r(t)$ has the form [12]

$$r(t) = Re[\tilde{r}(t)e^{j2\pi f_c t}] \tag{4}$$

where the received complex envelope is

$$\tilde{r}(t) = \sum_{n=1}^{N} C_n e^{-j\phi_n(t)} \tilde{s}(t - \tau_n) \tag{5}$$

and

$$\phi_n(t) = 2\pi\{(f_c + f_{D,n})\tau_n - f_{D,n}t\} \tag{6}$$

is the phase associated with the nth path. From (5), the channel can be modeled by a linear time-variant filter having the complex low-pass impulse response [12]

$$g(t, \tau) = \sum_{n=1}^{N} C_n e^{-j\phi_n(t)} \delta(t - \tau_n) \tag{7}$$

where $g(\tau, t)$ is the channel response at time t due to an impulse applied at time $t - \tau$, and $\delta(\cdot)$ is the dirac delta function.

For frequency non-selective channel (flat fading channel), the arrival time of each scatter n ($n = 1, 2, \cdots, N$), τ_n, can be approximated as the same, τ, so (7) can be represented as [12]

$$g(t, \tau) = \sum_{n=1}^{N} C_n e^{-j\phi_n(t)} \delta(t - \hat{\tau}) = g(t)\delta(t - \hat{\tau}) \tag{8}$$

So

$$g(t) = \sum_{n=1}^{N} C_n e^{-j\phi_n(t)} \tag{9}$$

For the second antenna under the UAV, since it's further to the transmitter, each scatter will have time delay ζ, so the channel impulse response from the RF emitter to the second antenna is $g(t-\zeta)$. In this paper, we estimate TDoA, ζ, based on the time delay of the two Rician fading channels.

There exists a Line of Sight (LoS) between transmitter and receiver, and Rician flat fading model should be used. Rician fading occurs when there is a strong specular (direct path or line of sight component) signal in addition to the scatter (multipath) components. The channel gain,

$$g(t) = g_I(t) + jg_Q(t) \tag{10}$$

can be treated as a wide-sense stationary complex Gaussian random process, and $g_I(t)$ and $g_Q(t)$ are Gaussian random processes with non-zero means $m_I(t)$ and $m_Q(t)$, respectively; and they have same variance σ_g^2, then the magnitude of the received complex envelop has a Rician distribution,

$$p_\alpha(x) = \frac{x}{\sigma^2}\exp\{-\frac{x^2+s^2}{2\sigma^2}\}I_0(\frac{xs}{\sigma^2}) \quad x \geq 0 \tag{11}$$

where

$$s^2 = m_I^2(t) + m_Q^2(t) \tag{12}$$

and $I_0(\cdot)$ is the zero order modified Bessel function. This kind of channel is known as Rician fading channel. A Rician channel is characterized by two parameters, Rician factor K which is the ratio of the direct path power to that of the multipath, i.e., $K = s^2/2\sigma^2$, and the Doppler spread (or single-sided fading bandwidth) f_d. We simulate the Rician fading using a direct path added by a Rayleigh fading generator. The Rayleigh fade generator is based on Jakes' model [4] in which an ensemble of sinusoidal waveforms are added together to simulate the coherent sum of scattered rays with Doppler spread f_d arriving from different directions to the receiver. The amplitude of the Rayleigh fade generator is controlled by the Rician factor K. The number of oscillators to simulate the Rayleigh fading is 60.

In military applications, modulation classification is already a very mature technology, so we assume that the modulation used by the transmitter could be classified by the passive receiver successfully. In this paper, we assume QPSK modulation (a very popular modulation used by various communication systems) is used.

3 Block Phase Estimation for Wireless Channel

The general structure of the phase estimator is illustrated in Fig. 1. We are supposed to estimate the phase at the midpoint of the estimation period which is denoted as T_E, it encompass N_E m-ary symbols, and we let $N_E = 2N + 1$, where N is the number of samples before and after the sample whose phase is to be estimated. In this context and in the presence of additive white Gaussian noise(AWGN) and zero frequency uncertainty, Fig. 1 with the dotted box eliminated (so that $x_n^{'} = x_n$, $y_n^{'} = y_n$)represents the optimal (maximum likelihood) estimator for $m = 1$, $\Delta f = 0$ which corresponds to an unmodulated carrier. For m-PSK modulated waveform, the phase of each successive symbol should take a different value. Obviously, the above estimator is useless. To solve it, a two-dimentional (complex) nonlinear function is inserted in the dotted box

$$x_n' + iy_n' = F(\rho_n)e^{im\phi_n} \tag{13}$$

where $\rho_n = \sqrt{x_n^2 + y_n^2}$ and $\phi_n = tan^{-1}(y_n/x_n)$. This is a rectangular-to-polar transformation. Multiply phase ϕ_n by m and perform an arbitrary nonlinear transformation on ρ_n; and finally perform a polar-to-rectangular transformation on the result. Obviously by using the preceding and succeeding N symbols to estimate each symbol phase, all but the first and last N symbol estimates can be made unbiased by overlapping estimation periods. For $F(\rho) = \rho^k$, k even,

$$\begin{aligned}
&E(\frac{\rho^{2k}}{\sigma^{2k}}cos2\epsilon') = \gamma^k \sum_{n=0}^{m+k} n!\binom{m+k}{n}\binom{m-k+n+1}{n}(\frac{-2}{\gamma})^n \\
&+(-1)^{m+k+1}2^k e^{-\gamma/2}(\frac{2}{\gamma})^{k+1} \\
&\cdot \sum_{n=0}^{m-k-1} \binom{m+k+n}{n}\frac{(m+k)!}{(m-k-n-1)!}(\frac{2}{\gamma})^n, \\
&k \leq m-2,
\end{aligned} \tag{14}$$

$$E\left(\frac{\rho^{2k}}{\sigma^{2k}}\right) = \sum_{n=0}^{k}\binom{k}{n}^2 \gamma^{k-n}2^n n!, \;\; k = m, \tag{15}$$

where σ^2 is the variance of the real and the imaginary part of each sample. From the above equation, it is shown in [14], for QPSK ($m = 4$), by choosing $F(\rho) = 0, \rho^2$, and ρ^4, the estimator can performs nearly as well as the linear estimator for unmudulated carries with moderate degradation.

To implement the nonlinear transformation, we need to first multiply the phase by m, along with the final operation of dividing the tan^{-1} function by m, thus gives rise to an m-fold ambiguity in the phase estimate. Liang and Wang applied Unique Words (UW) to remove the ambiguity in wireless channel estimation [5], however the receive antennas don't know any UW in the passive geolocation application. Fortunately, we only need the phase differences of the two correlated wireless channels, so ambiguity is not a problem in our applicaation, and it's automatically canceled by each other of the two wireless channels. After the nonlinear transformation, for each block, we got

$$\hat{\theta}(m) = \frac{1}{m} tan^{-1}(\frac{y}{x}), \tag{16}$$

without considering the phase ambiguity, where $x = \frac{1}{2N+1} \sum_{n=-N}^{N} x_n^{'}$ and $y = \frac{1}{2N+1} \sum_{n=-N}^{N} y_n^{'}$. Using the preceding and succeeding N symbols to estimate each symbol phase individually, so that make the estimation unbiased. That is, approximately $(2N + 1)$ as many operations as performing a single estimate are required for all the $(2N + 1)$ symbols in the interval [14]. In our scheme, we set up a parameter s denoted as step. For each s symbols, we only do the estimation once, and get the phase of the other $s - 1$ symbols by interpolation. Thus, we only need $(2N + 1)/s$ operations. It is shown in the simulation result that there is hardly any degradation in terms of the BER.

4 TDoA Finding Algorithm and Comparison with Existing Approach

Based on the BPE algorithm in Section 3, we could be able to obtain two channels $g_1(t)$ and $g_2(t)$. Since the two channels are highly correlated, and ideally one is the delay of the other. We construct

a cost function,

$$J(\zeta) = \frac{1}{T}\int_0^T [g_1(t-\zeta) - g_2(t)]^2 dt \tag{17}$$

where T is the burst length, and the ζ value that can minimize the cost function is the TDoA value, i.e.,

$$\hat{\zeta} = \inf_{\zeta\in[0,T]} J(\zeta) \tag{18}$$

$$= \arg\inf_{\zeta\in[0,T]} \frac{1}{T}\int_0^T [g_1(t-\zeta) - g_2(t)]^2 dt \tag{19}$$

For discrete case, our TDoA finding algorithm can be represented as

$$\hat{\zeta} = \arg\min_{\zeta\in\{1,2,\cdots,L\}} \frac{1}{L}\sum_{n=0}^{L} [g_1(n-\zeta) - g_2(n)]^2 \tag{20}$$

where L is the total number of symbols of a burst.

Our approach is a channel estimation-based TDoA approach based on the received signals. In the existing approach, a cross-correlation of the received signals based TDoA approach was proposed in [9]. We summarize this approach and will compare with our TDoA algorithm. The received signals from two parallell antennas j and k are

$$r_j(t) = s(t) + n_j(t) \tag{21}$$

$$r_k(t) = As(t-\tau_{jk}) + n_k(t) \tag{22}$$

where A is an attentuation factor and τ_{jk} is the relative time delay between the antennas. The cross correlation of these two received signals is given by

$$C_{jk}(\tau) = \mathcal{E}\{r_j(k) r_k(t-\tau)\} \tag{23}$$

$$= A\mathcal{E}[s(t)s(t-\tau-\tau_{jk})] \tag{24}$$

$$= AC_{ss}(\tau-\tau_{jk}) \tag{25}$$

where $C_{ss}(\tau)$ is the autocorrelation function of $s(t)$. $|C_{jk}(\tau)| \leq 1$ and its maximum value is 1 when $tau = \tau_{jk}$, so the delay τ_{jk} could be estimated based on the cross-correlation of the received signals.

5 Simulations

We evaluated our TDoA algorithm for different time delays betwen the two wireless channels, and compared it against the cross-correlation-based approach. The burst length is 936 symbols and transmitting 1 burst needs 10ms, so the symbol rate is 93,600 symbols/s. We totally ran two sets of simulations with time delay 10 symbols (i.e., $0.107ms$), and 100 symbols (i.e., $1.07ms$) for the two algorithms. We studied four groups of Rician fading channels and each group has two channels (one is the delayed version of the other): the first group with Rician factor $K = 12dB$, doppler shift $f_d = 200Hz$; the second group of channels $K = 12dB$, $d_d = 500Hz$; the third group of channels $K = 9dB$, $f_d = 200Hz$; and the fourth group of channels $K = 9dB$, $f_d = 500Hz$.

For channel simulation, we chose $N = 60$ (number of scatters), and ran our simulations for different SNR values. At each SNR values, we ran the Monte-Carlo simulations for $MC = 50,000$ bursts, and obtained the average TDoA estimation errors for the two TDoA algorithms which are plotted in Fig. 2(a)(b) for the 100-symbol delay, and Fig. 3(a)(b) for the 10-symbol delay. Observe these figures, the average TDoA errors are not zero, which means both TDoA algorithms are not unbiased, so Cramer-Rao bound can't be used for the TDoA error variance analysis.

We evaluated the estimation variance via the Monte-Carlo simulations based on $MC = 50,000$ bursts. We used the root-mean-square-error (RMSE) of the TDoA estimation, which is defined as

$$RMSE = \sqrt{\frac{1}{MC}\sum_{i=1}^{MC}(\hat{\zeta}_i - \zeta_i)^2} \tag{26}$$

where i is the index of bursts in Monte-Carlo simulations. The RMSE for the two TDoA algorithms were plotted in Fig. 4(a)(b) for the 100-symbol delay, and Fig. 5(a)(b) for the 10-symbol delay.

Observe these figures for average TDoA error and RMSE (Figs. 2 to 5),

1. Our TDoA algorithm performs much better than the cross-correlation-based TDoA algorithm with different magnitude level. In terms of average TDoA error as well as RMSE, our

TDoA algorithm performs more than 10 times lower than the cross-correlation-based TDoA algorithm. Why the cross-correlation-based TDoA algorithm couldn't perform well? It's because it ignores the channel fading phase distortion, but channel fading happens in all mobile communications.

2. Our TDoA algorithm performs very well with very low average TDoA error, for example, the average TDoA error is 0.57 symbol time, and RMSE is 16.7 symbol time for channel $K = 12dB$, $f_d = 200Hz$, at $SNR = 10dB$ when the delay is 100-symbol time.

3. The TDoA algorithm performance is related to channel fading condition. According to our simulations, our TDoA algorithm performs in the following order (from the best to the worst):

   - $K = 12dB$, $f_d = 200Hz$;
   - $K = 9dB$, $f_d = 200Hz$;
   - $K = 12dB$, $d_d = 500Hz$;
   - $K = 9dB$, $f_d = 500Hz$.

   It's very clear that larger Doppler shift f_d and lower fading factor K cause TDoA performance degradation. But surprisingly, the cross-correlation-based TDoA algorithm doesn't perform in a consistent order for the four channels because channel fading was not considered in this algorithm.

4. The TDoA performance is sensitive to the time delay. The performance is better for larger time delay case than for smaller time delay. It's because for larger time delay, the time delay finding algorithm will easily locate the delay with less error.

6 Conclusions

We have proposed a Time Difference of Arrival (TDoA) algorithm for passive geolocation based on delay estimation of two correlated wireless channels. It's assumed that the passive receiver is carried by a small flying UAV in the sky, and the transmitter is located on the ground (static or mobile), so Rician flat fading model should be used. To estimate the delay of two correlated channels, Block Phase Estimation (BPE) was used for each wireless channel estimation, and then the two estimated channels are compared to get the best time delay. We also compared our TDoA algorithm against a cross-correlation-based TDoA algorithm. Simulation results showed that our TDoA algorithm performs much better than the cross-correlation-based TDoA algorithm with a lower level of maganitude in terms of average TDoA error and Root-Mean-Square-Error (RMSE).

References

[1] C. R. Comsa, J. Luo; A. Haimovich, S. Schwartz, "Wireless Localization using Time Difference of Arrival in Narrow-Band Multipath Systems," *International Symposium on Signals, Circuits and Systems*, vol. 2, July 2007, pp. 1-4.

[2] S. Gezici, Z. Tian, G. B. Giannakis, H. Kobayashi, A. F. Molisch, H. V. Poor, Z. Sahinoglu, "Localization via ultra-wideband radios: a look at positioning aspects for future sensor networks," *IEEE Signal Processing Magazine*, vol. 22, no. 4, July 2005, pp. 70 - 84.

[3] A. Goldsmith, *Wireless Communications*, Cambridge University Press, New York, NY, 2005.

[4] W. C. Jakes, *Microwave Mobile Communication*, New York, NY: IEEE Press, 1993.

[5] Q. Liang and L. Wang, "Block Phase Estimation with Decision Feedback Demodulator for Satellite-Based Wireless ATM Networks," *62nd IEEE Vehicular Technology Conference*, Dallas,

TX, Sept 2005.

[6] J. M. Mendel, *Lessons in Estimation Theory for Signal Processing, Communications, and Control*, Englewood Cliffs, NJ: Prentice Hall, 1995.

[7] H. Ni, G. Ren; Y. Chang; "A TDOA location scheme in OFDM based WMANs," *IEEE Trans on Consumer Electronics*, vol. 54, no. 3, August 2008, pp. 1017 - 1021.

[8] A. G. Piersol, "Time delay estimation using phase data," *IEEE Trans on Acoustic, Speech, and Signal Processing*, vol 29, no. 3, June 1981, pp. 471-477.

[9] R. Poisel, *Electronic Warfare Target Location Method*, Artech House, Boston, 2005.

[10] J. Scheuing and B. Yang, "Disambiguation of TDOA Estimation for Multiple Sources in Reverberant Environments," *IEEE Trans on Audio, Speech, and Language Processing*, vol. 16, no. 8, Nov. 2008, pp. 1479 - 1489.

[11] R. O. Schmidt, "Least squares range difference location," *IEEE Trans on Aerospace and Electronic Systems*, vol. 32, no. 1, Jan 1996, pp. 234-242.

[12] G. L. Stuber, *Principles of Mobile Communication*, 2nd Ed, Kluwer Academic Publishers, Boston, MA, 2001.

[13] J. Vidal, M. Najar, R. Jativa, "High resolution time-of-arrival detection for wireless positioning systems," *IEEE Vehicular Technology Conference*, 2002, vol. 4, Sept. 2002, pp. 2283 - 2287.

[14] A. J. Viterbi, and A. M. Viterbi, "Nonlinear estimation of PSK modulated carrier phase with application to burst digital transmission," *IEEE Trans. Information Theory*, vol. 32, pp. 432-451, July 1983.

[15] Y. X. Yuan, C. Carter, J. E. Salt, "Near-optimal range and depth estimation using a vertical array in a correlated multipath environment," *IEEE Trans on Signal Processing*, vol. 48, no. 2, Feb. 2000, pp. 317 - 330.

List of Figures

1 Block phase estimator for m-PSK carriers 15

2 The average TDoA error versus SNR for four different Rician fading channels with $1.07ms$ (100-symbol) time delay. (a) Our TDoA Algorithm, (b) Cross-correlation-based TDoA algorithm [9]. 16

3 The average TDoA error versus SNR for four different Rician fading channels with $0.107ms$ (10-symbol) time delay. (a) Our TDoA Algorithm, (b) Cross-correlation-based TDoA algorithm [9]. 17

4 The TDoA RMSE versus SNR for four different Rician fading channels with $1.07ms$ (100-symbol) time delay. (a) Our TDoA Algorithm, (b) Cross-correlation-based TDoA algorithm [9]. 18

5 The TDoA RMSE versus SNR for four different Rician fading channels with $0.107ms$ (10-symbol) time delay. (a) Our TDoA Algorithm, (b) Cross-correlation-based TDoA algorithm [9]. 19

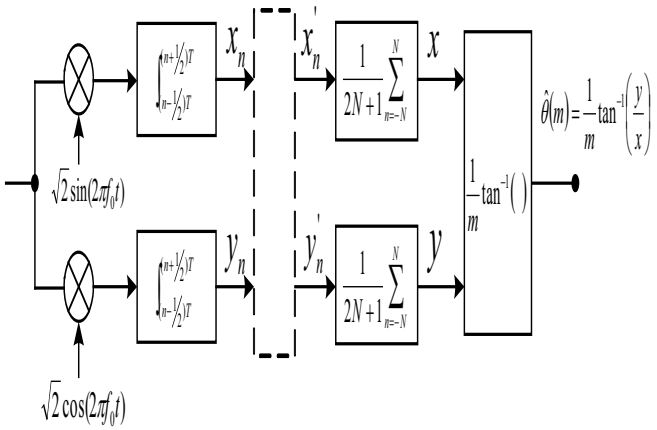
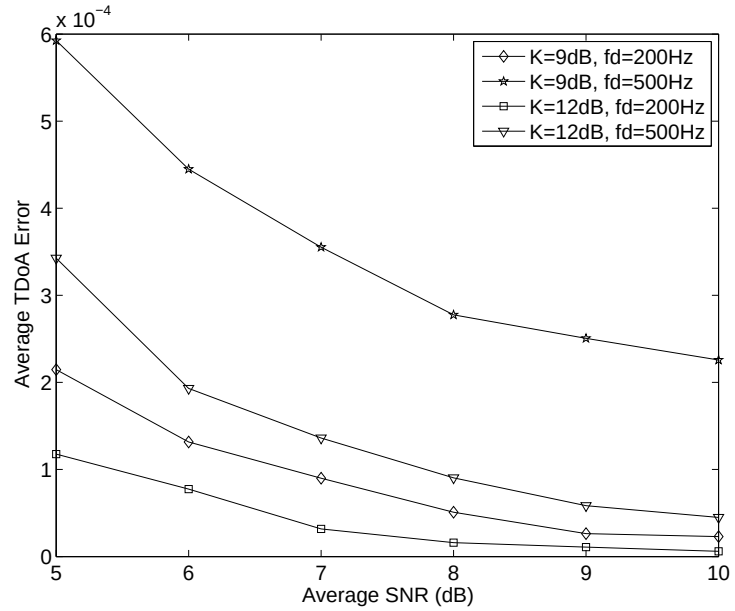
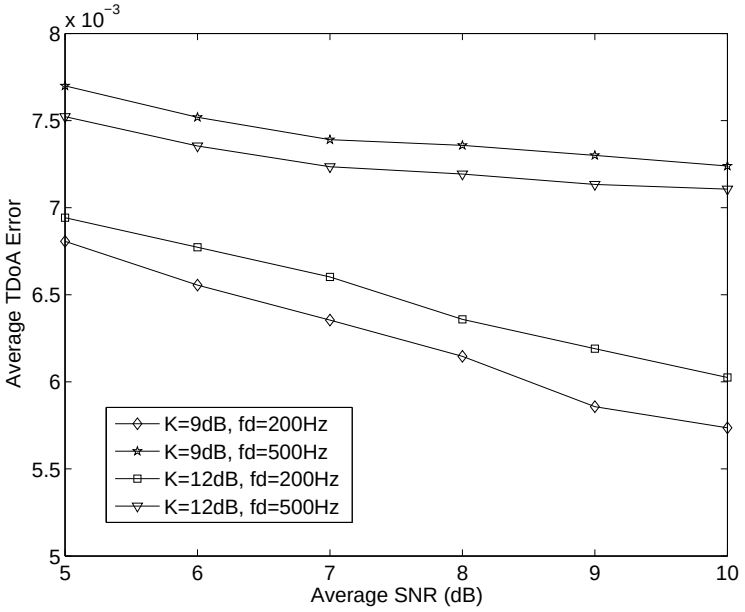


Figure 1: Block phase estimator for m-PSK carriers

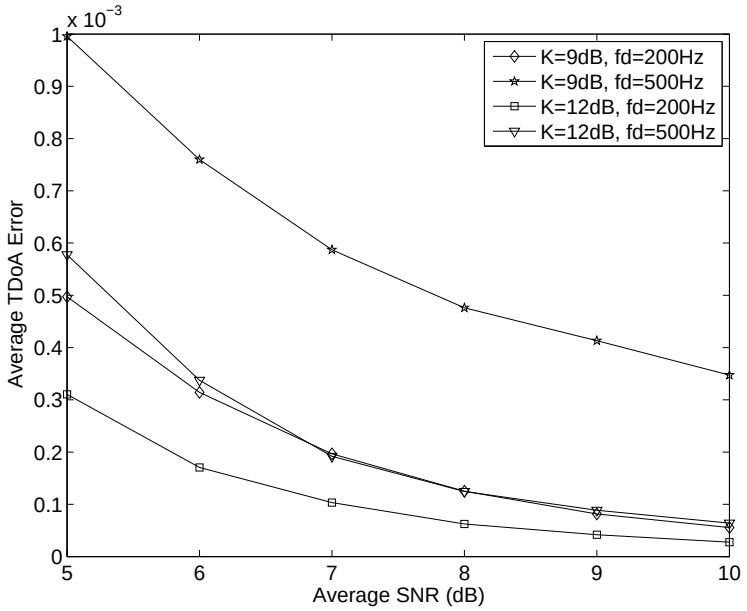


(a)

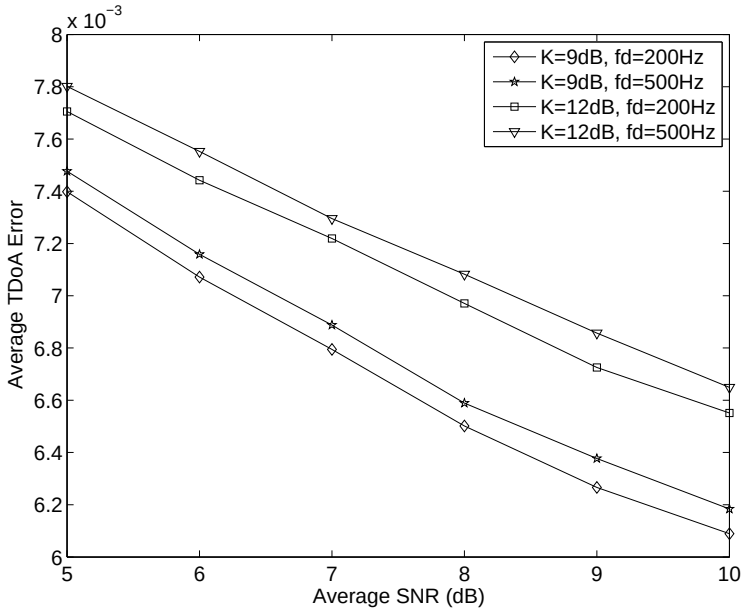


(b)

Figure 2: The average TDoA error versus SNR for four different Rician fading channels with $1.07ms$ (100-symbol) time delay. (a) Our TDoA Algorithm, (b) Cross-correlation-based TDoA algorithm [9].

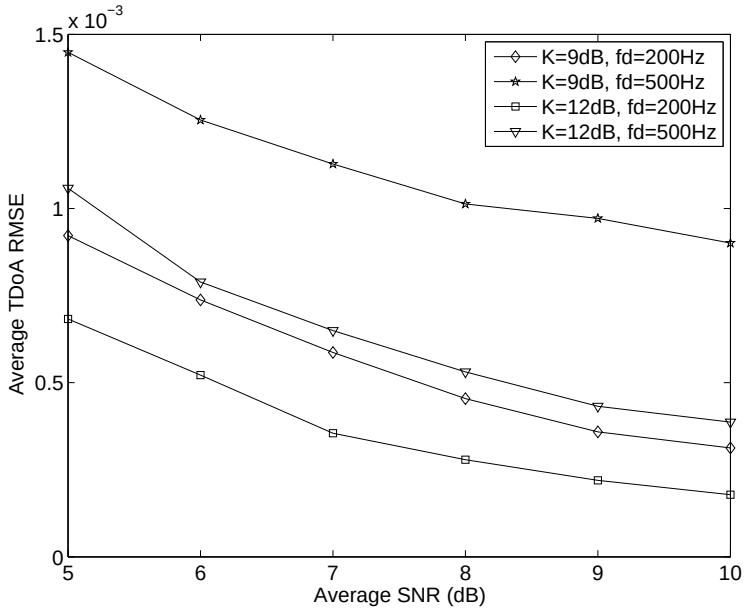


(a)

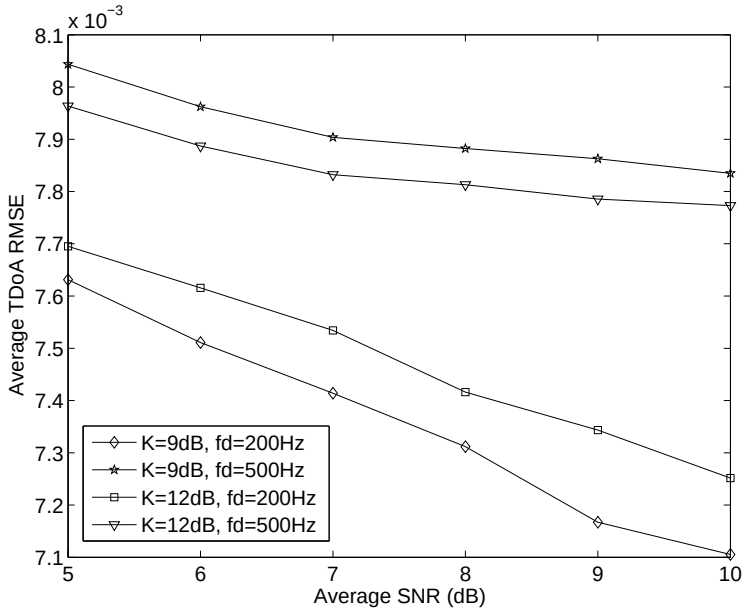


(b)

Figure 3: The average TDoA error versus SNR for four different Rician fading channels with $0.107ms$ (10-symbol) time delay. (a) Our TDoA Algorithm, (b) Cross-correlation-based TDoA algorithm [9].

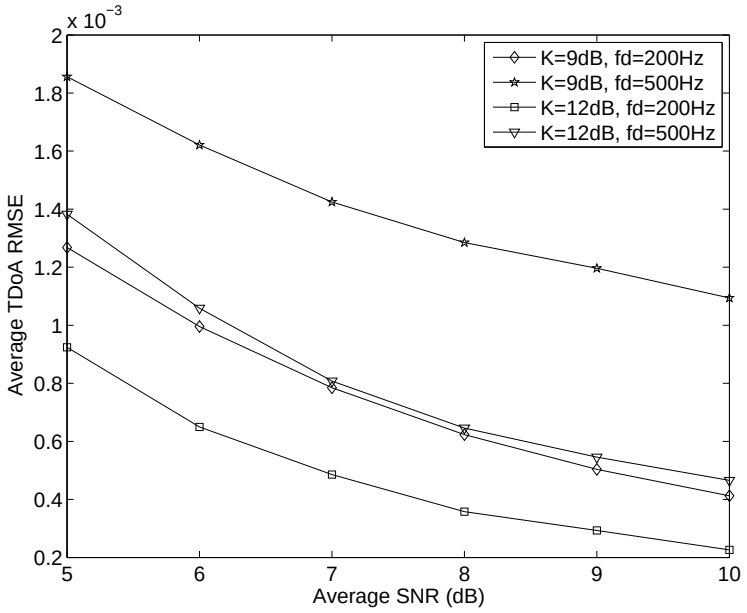


(a)

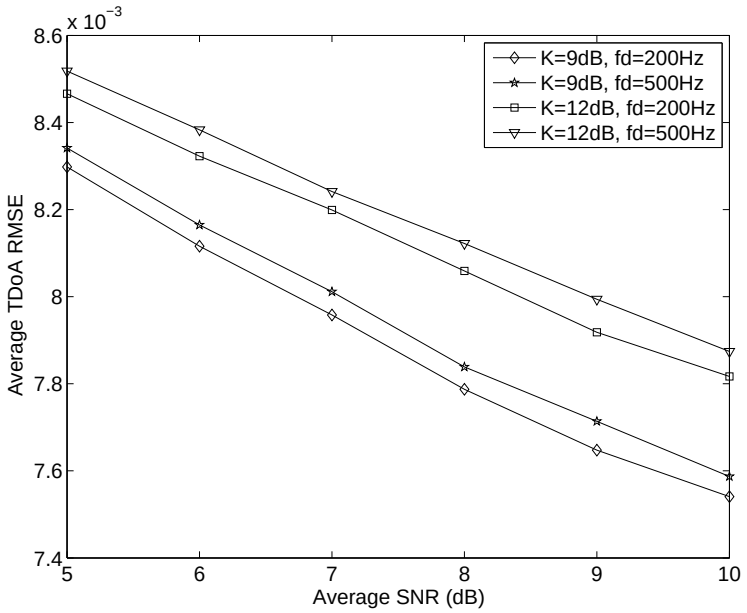


(b)

Figure 4: The TDoA RMSE versus SNR for four different Rician fading channels with $1.07ms$ (100-symbol) time delay. (a) Our TDoA Algorithm, (b) Cross-correlation-based TDoA algorithm [9].



(a)



(b)

Figure 5: The TDoA RMSE versus SNR for four different Rician fading channels with $0.107ms$ (10-symbol) time delay. (a) Our TDoA Algorithm, (b) Cross-correlation-based TDoA algorithm [9].

UWB Radars for Sense-through-Foliage Target Detection*

Qilian Liang, *Senior Member, IEEE*

Dept of Electrical Engineering

University of Texas at Arlington

Arlington, TX 76019-0016, USA

E-mail: liang@uta.edu

Abstract

In this paper, we study sense-through-foliage target detection using ultra-wideband (UWB) radars. We propose a Discrete-Cosine-Transform (DCT)-based approach for sense-through-foliage target detection using a single UWB radar when the echo signal quality is good, and a Radar Sensor Network (RSN) and DCT-based approach when the echo signal quality is poor. A RAKE structure which can combine the echos from different cluster-members is proposed for clusterhead in the RSN. We compared our approach with the ideal case when both echos are available, i.e., echos with target and without target. We also compared our approach against the scheme in which 2-D image was created via adding voltages with the appropriate time offset as well as the matched filter-based approach. We observed that the matched filter-based couldn't work well because the UWB channel has memory. Simulation results show that our DCT-based scheme works much better than the existing approaches, and our RSN and DCT-based approach can be used for target detection successfully while even the ideal case fails to do it.

Key Words : UWB radars, sense-through-foliage, target detection, Discrete-Cosine-Transform (DCT), matched filter, radar sensor networks.

*Partial material in this paper was presented at the IEEE International Conference on Communications, Beijing, China, 2008.

1 Introduction and Motivation

UWB radars are used nowadays for different applications such as subsurface sensing, classification of aircrafts, collision avoidance, etc. In all of these applications the ultra-high resolution of UWB radars is essentially used [35]. UWB radar emissions are at a relatively low frequency-typically between 100 MHz and 3 GHz. Additionally, the fractional bandwidth of the signal is very large (greater than 0.25). In this definition, bandwidth means the difference between the highest and lowest frequencies of interest and contains about 95% of the signal power [29][30]. Such radar sensor has exceptional range resolution that also has an ability to penetrate many common materials (e.g., walls). Law enforcement personnel have used UWB ground penetrating radars (GPRs) for at least a decade. In 1995, James D. Taylor's [30] Introduction to Ultra-Wideband Radar Systems introduced engineers to the theory behind a promising new concept for remote sensing. Since then, the field has undergone enormous growth with new applications realized and more applications conceptualized at a remarkable pace [29]. In [14], Immoreev gave an overview on new practical applications of UWB radars. In [4], through-wall UWB radar operating within FCC's mask was studied for heart beat and breathing rate. In [35][36][37], UWB radar for detection and positioning of human beings in a complex environment was studied. In the existing works on UWB radar/sensor based target detection, Some algorithms for sense-through-wall target detection were overviewed in [33], which are mainly based on target response signal strength (1-D) and different copies of signals to construct 2-D features. In [18], UWB radar for human being detection behind the wall was studied based on the spectrum of breathing human. The Adaptive Polarization-Difference Imaging (APDI) algorithm and PDI technique [26][31] were originally developed for optical imaging and in many situations can provide significant enhancements in target detection and feature extraction over conventional methods. In [38], these two techniques were applied to transient time-domain microwave signals with particular applications in through-wall microwave imaging (TWMI). In

[32], a chaos-based high-resolution imaging technique was applied to through-the-wall imaging, but no detection algorithm was presented. In [17], the problem of locating two straight and parallel road edges in radar images that are acquired from a stationary millimeter-wave radar platform positioned near ground-level was addressed. In [22], two new online clustering algorithms are developed for radar emitter classification: one is model-based using the minimum description length (MDL) criterion and the other is based on competitive learning. A maximum a posteriori (MAP) probability estimation framework for shape-from-shading (SFS) from synthetic aperture radar (SAR) images was developped in [3]. In [8], Fuzzy reasoning was used to improve the accuracy of the automatic detection of aircraft in Synthetic Aperture Radar (SAR) images. A unified theory of pixel processing based on a Bayesian framework was presented in [11] for the Lidar radar signals with multiple returns. In [39], an image segmentation method named iterative region growing using semantics (IRGS) was proposed, and the algorithm has been successfully tested on several artificial images and synthetic aperture radar (SAR) images. A matched-filter-bank-based 3-D imaging algorithm for rapidly spinning targets using ISAR radar was proposed in [34]. An adaptive and fast CFAR algorithm based on automatic censoring for target detection in high-resolution SAR images was proposed in [10]. In [6], alternate transmission and receiver switching was applied to improve space-based moving target indication. An appropriate data fusion rule was derived to to generate a composite SAR image containing enhanced target shape characteristics for improved target recognition [19]. Four-dimensional SAR imaging for height estimation and monitoring of single and double scatterers was proposed in [9]. All the above target detection approaches were based on 2-D or more dimensional radar images. Recently, we presented some preliminary results on UWB radar target detection using discrete cosine transform in [20], which was based on 1-D radar signals.

In this paper, we will perform studies sense-through-foliage target detection using UWB radar

and UWB radar sensor networks in more details, and will compare against some other existing approaches. Like the GPR, sense-through-foliage radar takes advantage of UWB's very fine resolution (time gating) and low frequency of operation. Sheen, et al. [28] have measured ultrawideband (UWB) backscatter from foliage, as has a team of researchers from MIT [7] and from the U.S. Army Research Laboratory (ARL) [23], for different polarizations and frequency ranges. In [16], Kapoor et al studied the detection of targets obscured by a forest canopy using a UWB radar. They observed that the forest clutter observed in the radar imagery is a highly impulsive random process that is more accurately modeled with the alpha-stable processes as compared with Gaussian, Weibull, and K-distribution models. With this more accurate model, segmentation was performed on the imagery into forest and clear regions. Further, a region-adaptive symmetric alpha stable (SαS) constant false-alarm rate (CFAR) detector was introduced and its performance is compared with the Weibull and Gaussian CFAR detectors. The approach in [16] is a statistical model based approach. In this paper, we are interested in a non-statistical model-based approach for UWB sense-through-foliage target detection, and we will apply our expertise in signal processing, data fusion, sensor networks, etc to achieve effective sense-through-foliage technology. We are interested in investigating more features from sense through foliage signals and extracting as much information as possible for data fusion.

The rest of this paper is organized as follows. In Section 2, we summarize the measurement and collection of data we used in this paper. In Section 3, we propose a discrete-cosine-transform (DCT) based approach for sense-through-foliage target detection with good signal quality. In Section 4, we propose a radar sensor network (RSN) and DCT-based approach for sense-through-foliage target detection when the signal quality is poor. We conclude this paper and discuss some future research topics in Section 5.

2 Sense-through-Foliage Data Measurement and Collection

The foliage penetration measurement effort was conducted in late summer and fall. Late summer foliage, because of the limited rainfall, involved foliage with decreased water content. Late fall and winter measurements involved largely defoliated but dense forest. The foliage experiment was constructed on a seven-ton man lift, which had a total lifting capacity of 450 kg. The limit of the lifting capacity was reached during the experiment as essentially the entire measuring apparatus was placed on the lift. The principle pieces of equipment secured on the lift are listed below:

- Dual Antenna mounting stand
- Two antennas
- Rack system (2)
- Barth pulser
- Tektronix model 7704 B oscilloscope
- IBM laptop
- HP signal Generator
- Custom RF switch and power supply
- Weather shield (small hut)

Figure 1 shows the experiment under a weather shield that was constructed on the lift. The weather shield was needed to protect the equipment hoisted up with the lift. A negative side effect of this weather shield was to provide a significant sail area at the maximum lever arm relative to the lift stabilizing jacks on the ground. Lift stabilization was achieved using cables and anchor points. A system of 4 tethers was used under gusty conditions. The transmit and receive rotating platform

systems were built using heavy gauge Unistruts, thrust bearings, and roller bearings for the multiple axes of freedom. The importance of the rigidity of the antenna mounts the and axis of rotation was in the establishment and maintenance of the antenna alignment during the measurement. See Figure 2, for a photographic side view of the equipment platform on the lift.



Figure 1: This figure shows the lift with the experiment. The antennas are at the far end of the lift from the viewer under the roof that was built to shield the equipment from the elements. This picture was taken in September with the foliage largely still present. The cables coming from the lift are a ground cable to an earth ground and one of 4 tethers used in windy conditions.

The experimental target was a trihedral reflector with a slant length of 1.5 meters (as shown in Fig. 3). Throughout this work, a Barth pulse source (Barth Electronics, Inc. model 732 GL) was used. The pulse generator uses a coaxial reed switch to discharge a charge line for a very fast rise time pulse outputs. The model 732 pulse generator provides pulses of less than 50 picoseconds



Figure 2: This figure shows the experiment on top of the lift under the hut built for weather protection. The black box in the foreground is a weather resistant box that held the oscilloscope and Barth pulser during the testing.

(ps) rise time, with amplitude from 150 V to greater than 2 KV into any load impedance through a 50 ohm coaxial line. The generator is capable of producing pulses with a minimum width of 750 ps and a maximum of 1 microsecond. This output pulse width is determined by charge line length for rectangular pulses, or by capacitors for 1/e decay pulses. The data collections were extensive. 20 different positions were used, and 35 independent collections were performed at each position.

For the data we used in this paper, each sample is spaced at 50 picosecond interval, and 16,000 samples were collected for each collection for a total time duration of 0.8 microseconds at a rate of approximately 20 Hz. We considered two sets of data from this experiment. Initially, the Barth pulse source was operated at only 1 KW peak power and the system was not sufficiently loaded for repeatable charge control pulse-to-pulse. In Fig. 4, a Barth pulse captured on TEK7704 oscilloscope is plotted. Significant pulse-to-pulse variability was noted for these collections. In this set of experiments, 35 pulses reflected signal were averaged for each collection. The scheme for the sense-through-foliage target detection with "poor" signal quality will be presented in Section 4.



Figure 3: The target (a trihedral reflector) is shown on the stand at 300 feet from the lift.

This problem was remedied by running the pulser at higher power while protecting the radiating antenna using a non-distorting attenuator Barth 3dB attenuator model number 142-NMFP-3. Pulse production stability was very important to this measurement effort. Pulse-to-pulse differences, if any were observed, should be due to changes in the foliage or changes in the transmitter-receiver positions relative to the foliage and target. When operated at the higher amplitudes it was noted that the pulse source was very stable. Fig. 5 shows a series of ten pulses. In this graph only the peak, the most variable portion of the pulse, is shown. The measured pulse-to-pulse variation was found to be less than 7% at the peak. In this set of experiments, 100 pulses reflected signals were averaged for each collection to average the variation because of the movement of foliage. The scheme for target detection with "good" signal quality will be presented in Section 3.

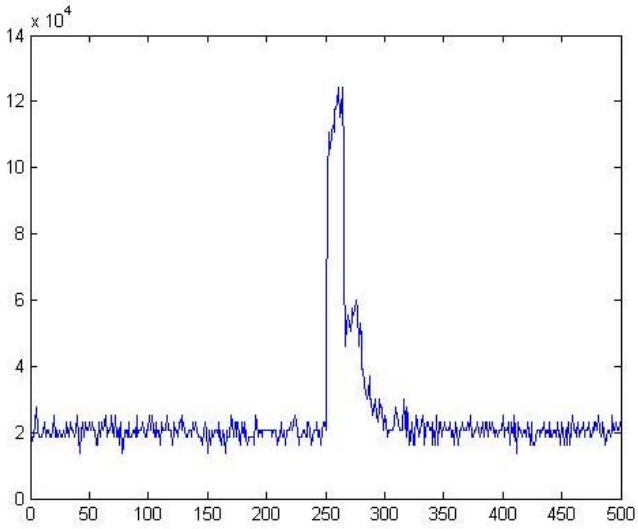


Figure 4: Barth Pulse captured on TEK7704 oscilloscope.

3 Sense-through-Foliage Target Detection with Good Signal Quality: A DCT-based Approach

In Fig. 6, we plot two collections with good signal quality, one without target on range (Fig. 6a) and the other one with target on range (Fig. 6b and target appears at around sample 13,900). To make it more clear to the readers, we provide expanded views of traces (with target) from sample 13,001 to 15,000 for the above two collections in Figs. 7a and 7b. Since there is no target in Fig. 7a, it can be treated as the response of foliage clutter. It's quite straightfoward that the target response will be the echo difference between Fig. 7b and Fig. 7a, which is plotted in Fig. 7c. However, it's impossible to obtain Fig. 7a (clutter echo) in practical situation if there is target on range. The challenge is how to make target detection based on Fig. 7b (with target) or Fig. 7a (no target) only?

Observe Fig. 7b, for samples where target appears (around sample 13,900), the sample strength changes much abruptly than that in Fig. 7a, which means echo from target contains more AC values

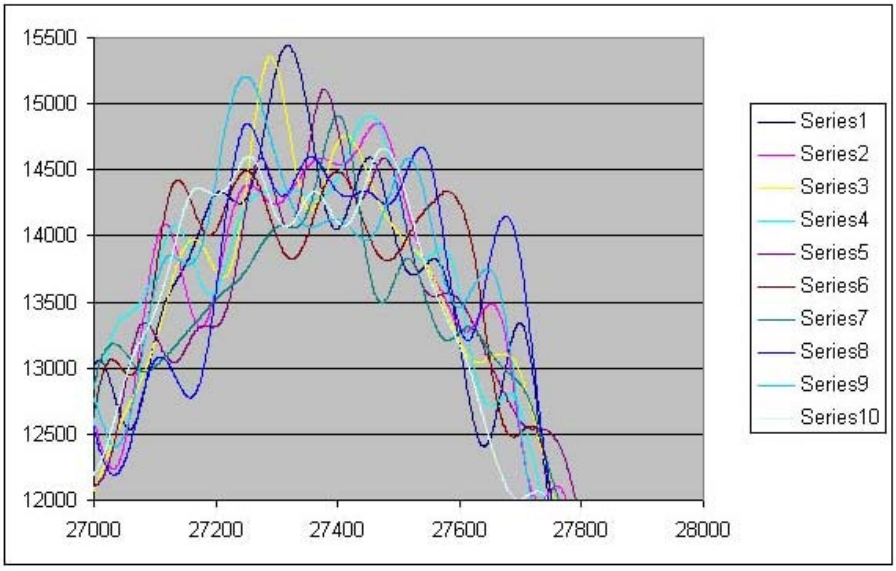


Figure 5: Barth pulse output peaks captured by a TEK7704 oscilloscope when operated at higher power. Only the peak of the ten traces are shown and the reference level is 0. Ten traces are overlaid and display a peak pulse-to-pulse variability of less than 7%.

than that without target. Motivated by this, we applied Discrete Cosine Transform (DCT) to the echos $x(iM+n)$ $(n = 0, 1, 2, \cdots, N-1)$ where N is the DCT window length, M is the step size of each DCT window, and i is the window index. Let $x(n,i) \stackrel{\triangle}{=} x(iM+n)$

$$X(K,i) = \sum_{n=0}^{N-1} x(n,i)\cos(\frac{2\pi}{N}nK) \tag{1}$$

then we cumulate the power of AC values (for $K > 2$)

$$P(i) = \sum_{K=3}^{N-1} X(K,i)^2 \tag{2}$$

For $N = 100$ and $M = 10$, we plot the power of AC values $P(i)$ versus iM (time domain sample index) in Figs. 8a and 8b for the above data sets in Figs. 7a and 7b respectively. Observe that in Fig. 8b, the power of AC values (around sample 13,900) where the target is located is non-fluctuating (monotonically increase then decrease). Although some other samples also have very high AC power values, it is very clear that they are quite fluctuating and the power of AC values

behave like random noise because generally the clutter has Gaussian distribution in the frequency domain [2]. Based on our simulations, the window length N in DCT affects the performance of the target detection. The appropriate N should be the length of target impulse response with strong signal strength (see Fig. 7c). This depends on target size, UWB signal resolution, and propagation environment.

We compared our DCT-based approach to the scheme proposed in [33]. In [33], 2-D image was created via adding voltages with the appropriate time offset. In Figs. 9a and 9b, we plot the 2-D image created based on the above two data sets (from samples 13,800 to 14,200). However, it's not clear which image shows there is target on range.

We also compared our approach to the matched filter approach. The matched filter is by definition a filter in the radar receiver designed to maximize the SNR at its output. The impulse response of the filter having this property turns out to be a replica of the transmitted waveform's modulation function that has been reversed in time and conjugated [25]. Assume the transmitted waveform is $s(t)$, then the matched filter impulse response $h(t) = s^*(T_M - t)$ The time T_M at which the SNR is maximized is arbitrary, however, $T_M \geq t$ is required for $h(t)$ to be causal. Given the received echo $x(t)$ consisting of clutter, target, and noise components, the output $y(t)$ of the matched filter is given by the convolution between $x(t)$ and $h(t)$

$$y(t) = \int_{-\infty}^{\infty} x(\tau)h(t-\tau)d\tau \quad (3)$$

$$= \int_{-\infty}^{\infty} x(\tau)s^*(\tau + T_M - t)d\tau \quad (4)$$

In this paper, we choose $T_M = 16001$, and the matched filter outputs for received signal in Fig. 6a (without target) and signal in Fig. 6b (with target) are plotted in Figs. 10a and 10b respectively. Since the received echoes plotted in Fig. 6a and b are averaged over 100 pulses, the transmitted pulse $s(t)$ in (4) is obtained via averaging corresponding 100 transmission pulses and is plotted in Fig. 11. Observe Figs. 10ab, it's impossible to perform target detection based on the matched

filter output.

Why the matched filter approach doesn't work for UWB radar-based target detection? We further studied the UWB channel using CLEAN algorithm [12][5][27]. Based on the transmit pulse in Fig. 11 and received echo in Fig. 7a, we applied CLEAN algorithm and obtained the UWB channel (plotted in Fig. 12). Observe Fig. 12, the UWB channel has memory because it's a linear filter. However, the matched filter is derived based on the assumption that the radar channel has no memory. The memory in UWB radar channel causes intersymbol interference of transmit pulse and makes the matched filter approach perform poor.

4 Sense-through-Foliage Target Detection with Poor Signal Quality: A Sensor Network and DCT-based Approach

As mentioned in Section 2, when the Barth pulse source was operated at low amplitude and the sample values are not obtained based on sufficient pulse response averaging (averaged over 35 pulses for each collection), significant pulse-to-pulse variability was noted and the return signal quality is poor. In Figs. 13a and 13b, we plot two collections with poor signal quality. Fig. 13a has no target on range, and Fig. 13b has target at samples around 13,900. We plot the echo differences between Figs. 13a and 13b in Fig. 13c. However, it is impossible to identify whether there is any target and where there is target based on Fig. 13c. We observed the DCT-based approach failed to detect target based on one collection. Since significant pulse-to-pulse variability exists in the echos, this motivate us to explore the spatial and time diversity using Radar Sensor Networks (RSN).

In RSN, the radar sensors are networked together in an ad hoc fashion. They do not rely on a preexisting fixed infrastructure, such as a wireline backbone network or a base station. They are self-organizing entities that are deployed on demand in support of various events surveillance, battlefield,

disaster relief, search and rescue, etc. Scalability concern suggests a hierarchical organization of radar sensor networks with the lowest level in the hierarchy being a cluster. As argued in [21] [15] [13] [24], in addition to helping with scalability and robustness, aggregating sensor nodes into clusters has additional benefits:

1. conserving radio resources such as bandwidth;
2. promoting spatial code reuse and frequency reuse;
3. simplifying the topology, e.g., when a mobile radar changes its location, it is sufficient for only the nodes in attended clusters to update their topology information;
4. reducing the generation and propagation of routing information; and,
5. concealing the details of global network topology from individual nodes.

In RSN, each radar can provide their pulse parameters such as timing to their clusterhead radar, and the clusterhead radar can combine the echos (RF returns) from the target and clutter. In this paper, we propose a RAKE structure for combining echos, as illustrated by Fig. 14. The RAKE structure is so named because it reminds the function of a garden rake, each finger collecting echo signals similarly to how tines on a rake collect leaves. The integration means time-average for a sample duration T and it's for general case when the echos are not in discrete values. It is quite often assumed that the radar sensor platform will have access to Global Positioning Service (GPS) and Inertial Navigation Unit (INU) timing and navigation data [1]. In this paper, we assume the radar sensors are synchronized in RSN. In Fig. 14, the echo, i.e., RF response by the pulse of each cluster-member sensor, will be combined by the clusterhead using a weighted average, and the weight w_i is determined by the power of each echo $x_i(n)$ (n is the sample index),

$$w_i = \frac{E_i}{\sum_{i=1}^{M} E_i} \tag{5}$$

and

$$E_i = \text{var}(x_i(n)) + [\text{mean}(x_i(n))]^2 \tag{6}$$

We ran simulations for $M = 30$, and plot the power of AC values in Figs. 15a and 15b for the two cases (with target and without target) respectively. Observe that in Fig. 8b, the power of AC values (around sample 13,900) where the target is located is non-fluctuating (monotonically increase then decrease). Although some other samples also have very high AC power values, it is very clear that they are quite fluctuating and the power of AC values behaves like random noise because generally the clutter has Gaussian distribution in the frequency domain.

5 Conclusions and Future Works

In this paper, we proposed a DCT-based approach for sense-through-foliage target detection when the echo signal quality is good, and a sensor network and DCT-based approach when the echo signal quality is poor. A RAKE structure which can combine the echos from different cluster-members is proposed for clusterhead in the RSN. We compared our approach with ideal case when both echos are available, i.e., echos with target and without target. We also compared our approach against the scheme in which 2-D image was created via adding voltages with the appropriate time offset as well as the matched filter-based approach. We observed that the matched filter-based couldn't work well because the UWB channel has memory. Simulation results show that our DCT-based scheme works much better than the existing approach, and our RSN and DCT-based approach can be used for target detection successfully while the ideal case fails to do it. For future works, we will collect more data with different targets and perform automatic target recognition besides target detection.

Acknowledgement

This work was supported by U.S. Office of Naval Research (ONR) under Grant N00014-07-1-0395, N00014-07-1-1024, N00014-03-1-0466 and Air Force Office of Scientific Research (AFOSR) Summer Faculty Fellowship Program Award.

References

[1] ONR BAA 07-017, "NET-SENTRIC Surveillance," http://www.onr.navy.mil/02/baa/.

[2] D. K. Barton, *Radar System Analysis and Modeling*, Artech House, Boston, MA, 2006.

[3] A. G. Bors, E. R. Hancock, R. Wilson, "Terrain analysis using radar shape-from-shading," *IEEE Trans on Pattern Analysis and Machine Intelligence*, vol. 25, no. 8, Aug. 2003, pp. 974 - 992

[4] M. Y. W. Chia, et. al, "Through-wall UWB radar operating within FCC's mask for sensing heart beat and breathing rate," *2005 European Radar Conference*, Oct. 2005, pp. 267 - 270.

[5] R. J.-M. Cramer, *An Evaluation of Ultrawideband Propagation Channels*, Ph.D Dissertation, USC, 2000.

[6] J. H. G. Ender, C. H. Gierull, D. Cerutti-Maori, "Improved Space-Based Moving Target Indication via Alternate Transmission and Receiver Switching," *IEEE Trans on Geoscience and Remote Sensing*, vol. 46, no. 12, Dec. 2008, pp. 3960 - 3974.

[7] J. G. Fleischman, et al, "Foliage penetration experiment: Part I: Foliage attenuation and backscatter analysis of SAR imagery," *IEEE Transactions on Aerospace and Electronic Systems*, vol. 32, no. 1, part 1 of 3, 134144, 1996.

[8] A. Filippidis, L. C. Jain, N. Martin, "Fusion of intelligent agents for the detection of aircraft in SAR images," *IEEE Trans on Pattern Analysis and Machine Intelligence*, vol. 22, no. 4, April 2000, pp. 378 - 384.

[9] G. Fornaro, D. Reale, F. Serafino, "Four-Dimensional SAR Imaging for Height Estimation and Monitoring of Single and Double Scatterers," *IEEE Trans Geoscience and Remote Sensing*, vol. 47, no. 1, Part 2, Jan. 2009, pp. 224 - 237.

[10] G. Gao, L. Liu, L. Zhao, G. Shi; G. Kuang, "An Adaptive and Fast CFAR Algorithm Based on Automatic Censoring for Target Detection in High-Resolution SAR Images," *IEEE Trans on Geoscience and Remote Sensing*, vol. 47, no. 6, June 2009, pp. 1685 - 1697.

[11] S. Hernandez-Marin, A. M. Wallace, G. J. Gibson, "Bayesian Analysis of Lidar Signals with Multiple Returns," *IEEE Trans on Pattern Analysis and Machine Intelligence*, vol. 29, no. 12, Dec. 2007, pp. 2170 - 2180.

[12] J. A. Hogbom, "Aperture synthesis with a non-regular distribution of interferometer baseline," *Atronomy and Astrophysics Supplement Ser.*, vol. 15, 1974.

[13] T.-C. Hou and T-J. Tsai, " An access-based clustering protocol for multihop wireless ad hoc networks," *IEEE J. Selected Areas in Communications*, vol. 19, no. 7, pp. 1201-1210, July 2001.

[14] I. Y. Immoreev, "New practical application of ultra-wideband radars," *2007 European Radar Conference, 2007*, Oct. 2007, pp. 216 - 219.

[15] A. Iwata, C. C. Chiang, G. Pei, M. Gerla, and T. W. Chen, " Scalable routing strategies for ad hoc networks," *IEEE J. Selected Areas in Communications*, vol. 17, pp. 1369-1379, 1999.

[16] R. Kapoor, et al, "UWB radar detection of targets in foliage using alpha-stable clutter models," *IEEE Trans on Aerospace and Electronic Systems*, vol. 35, no. 3, July 1999, pp. 819 - 834.

[17] S. Lakshmanan, D. Grimmer, "A deformable template approach to detecting straight edges in radar images," *IEEE Trans on Pattern Analysis and Machine Intelligence*, vol. 18, no. 4, April 1996, pp. 438 - 443

[18] B. Levitas, J. Matuzas, "UWB Radar for Human Being Detection Behind the Wall," *Proc. of 2006 Intl Radar Symposium*, May 2006, pp. 1 - 3.

[19] Z. Li, S. Papson, R. M. Narayanan, "Data-Level Fusion of Multilook Inverse Synthetic Aperture Radar Images," *IEEE Trans on Geoscience and Remote Sensing*, vol. 46, no. 5, May 2008, pp. 1394 - 1406.

[20] Q. Liang, S. Samn, X. Cheng, "UWB Radar Sensor Networks for Sense-through-Foliage Target Detection," *IEEE International Conference on Communications*, May 2008, Beijing, China.

[21] C. R. Lin and M. Gerla, "Adaptive clustering in mobile wireless networks," *IEEE J. Selected Areas in Communications*, vol. 16, pp. 1265-1275, 1997.

[22] J. Liu, J.P.Y. Lee, L. Li, Z.-Q. Luo, K. M. Wong, "Online clustering algorithms for radar emitter classification," *IEEE Trans on Pattern Analysis and Machine Intelligence*, vol. 27, no. 8, Aug. 2005, pp. 1185 - 1196.

[23] J. W. McCorkle, "Early results from the ARL UWB Foliage Penetration (FOPEN) SAR," *SPIE International Symposium on Optical Engineering and Photonics in Aerospace and Remote Sensing, Underground and Obscured Object Detection*, Apr. 1993.

[24] C. E. Perkins, "Chapter 4, Cluster-Based Networks," *Ad Hoc Networking*, Edited by C. E. Perkins, pp. 75-138, Addison-Wesley, 2001.

[25] M. A. Richards, *Fundamentals of Radar Signal Processing*, McGraw-Hill Companies, New York, 2005.

[26] M. P. Rowe, E. N. Pugh, Jr., J. S. Tyo, and N. Engheta, "Polarization-difference imaging: a biologically inspired technique for observation through scattering media," *Optics Letters*, Vol. 20, pp. 608-610, 1995.

[27] R. A. Scholtz, M. Z. Win, and J. M. Cramer, "Evaluation of the Characteristics of the ultra-wideband propagation channel," *Proc of Antenna and Propagation Symposium*, vol. 2, no. 626-630, 1998.

[28] D. R. Sheen, et al, "Foliage transsmission measurements using a ground-based ultrawideband (UWB) (3001300 Mhz) SAR system," *IEEE Transactions on Geoscience and Remote Sensing*, vol. 32, no. 1, 1994.

[29] J. D. Taylor, *Ultra-wideband radar technology*, CRC Press, 2001.

[30] J. D. Taylor, *Introduction to Ultra-Wideband Radar Systems*, CRC Press, 1995.

[31] J. S. Tyo, M. P. Rowe, E. N. Pugh, Jr., N. Engheta, "Target detection in optically scattering media by polarization difference imaging," *Applied Optics*, Vol. 35, pp. 1855-1870, 1996.

[32] V. Venkatasubramanian and Henry Leung, "A Novel Chaos-Based High-Resolution Imaging Technique and Its Application to Through-the-Wall Imaging," *IEEE Signal Proc Letters*, Vol. 12, No. 7, July 2005.

[33] P. Withington , H. Fluhler, and S. Nag , "Enhancing homeland security with advanced UWB sensors," *IEEE Microwave Magazine*, Sept 2003.

[34] M. Xing, Q. Wang, G. Wang, Z. Bao, "A Matched-Filter-Bank-Based 3-D Imaging Algorithm for Rapidly Spinning Targets," *IEEE Trans on Geoscience and Remote Sensing*, vol. 47, no. 7, Part 2, July 2009, pp. 2106 - 2113.

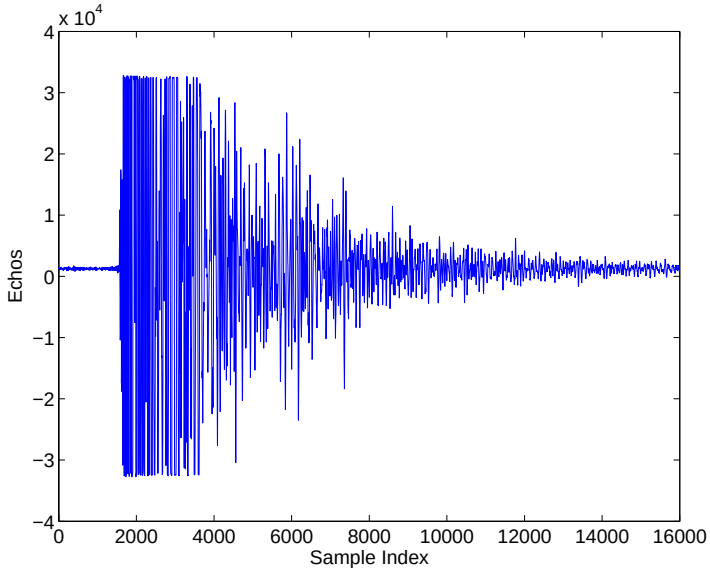
[35] A. G. Yarovoy, et. al, "UWB Radar for Human Being Detection," *IEEE Aerospace and Electronic Systems Magazine*, vol. 23, no. 5, May 2008, pp. 36 - 40.

[36] A. G. Yarovoy, et. al, "UWB Radar for Human Being Detection," *IEEE Aerospace and Electronic Systems Magazine*, vol. 21, no. 11, Nov 2006, pp. 22 - 26.

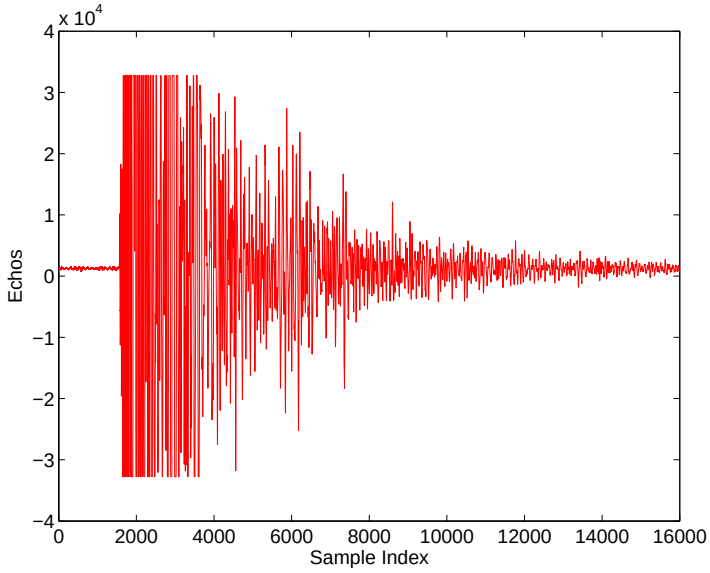
[37] A. G. Yarovoy, et. al, "UWB Radar for Human Being Detection," *IEEE Aerospace and Electronic Systems Magazine*, vol. 21, no. 3, March 2006, pp. 10 - 14.

[38] K. M. Yemelyanov, J. A. McVay, N. Engheta, A. Hoorfar, "Adaptive Polarization-Difference Imaging Algorithms for Through-the-Wall Microwave Imaging Scenarios," *Proc. IEEE AP-S Int. Symposium and USNC/URSI National Radio Science Meeting*, July 3-6, 2005, Washington DC, USA.

[39] Q. Yu, D. A. Clausi, "IRGS: Image Segmentation Using Edge Penalties and Region Growing," *IEEE Trans on Pattern Analysis and Machine Intelligence*, vol. 30, no. 12, Dec. 2008, pp. 2126 - 2139.

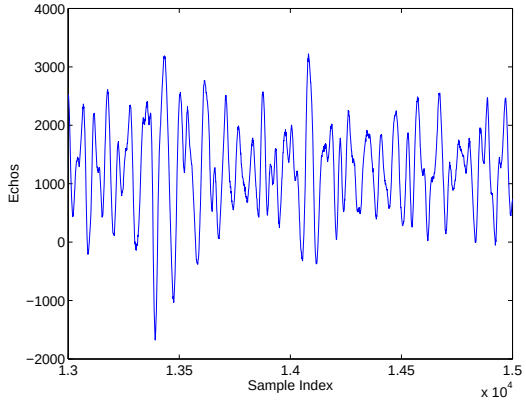


(a)

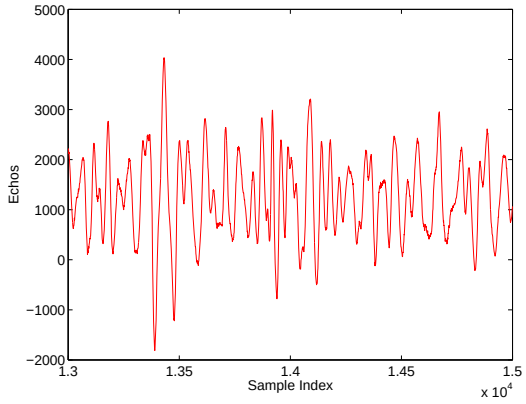


(b)

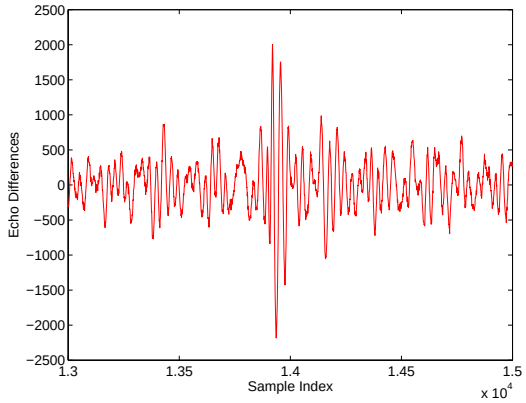
Figure 6: Measurement with very good signal quality and 100 pulses average. (a) No target on range, (b) with target on range (target appears at around sample 13,900).



(a)

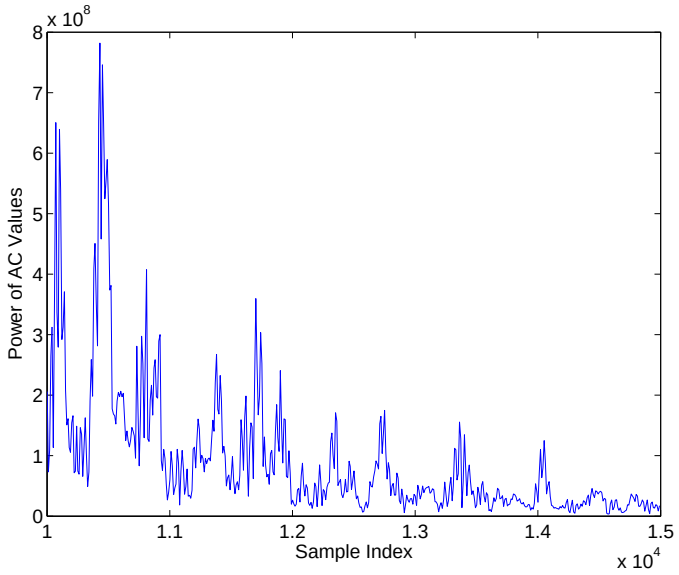


(b)

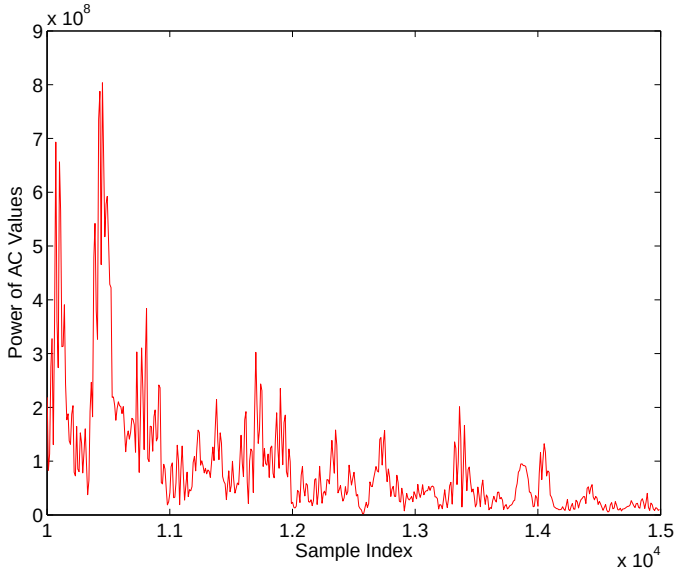


(c)

Figure 7: Measurement with very good signal quality and 100 pulses average. (a) Expanded view of traces (with target) from samples 13,001 to 15,000. (b) Expanded view of traces (without target) from samples 13,001 to 15,000. (c) Echo differences between (a) and (b).

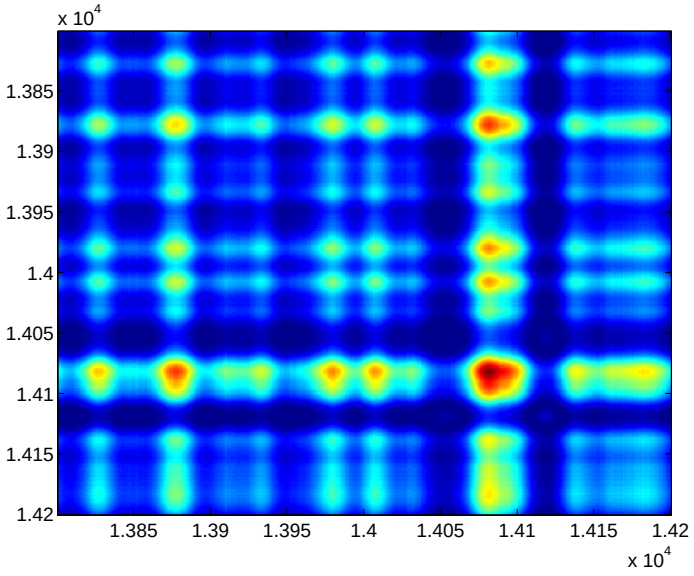


(a)

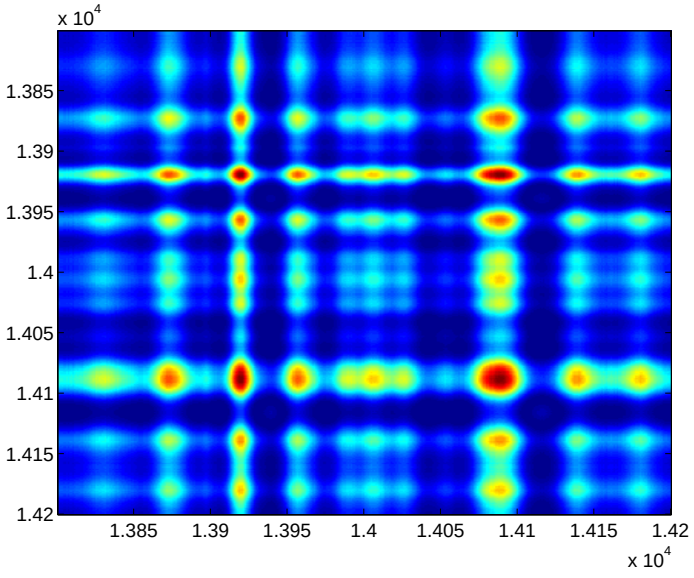


(b)

Figure 8: The power of AC values versus sample index. (a) No target (b) With target in the field.

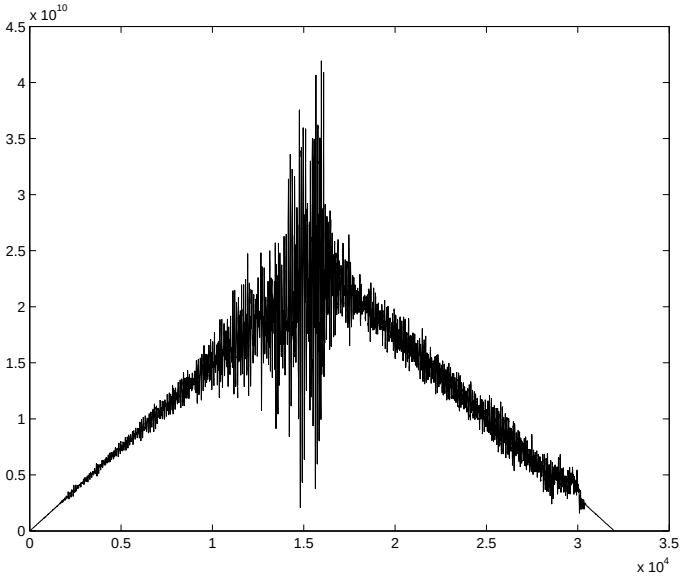


(a)

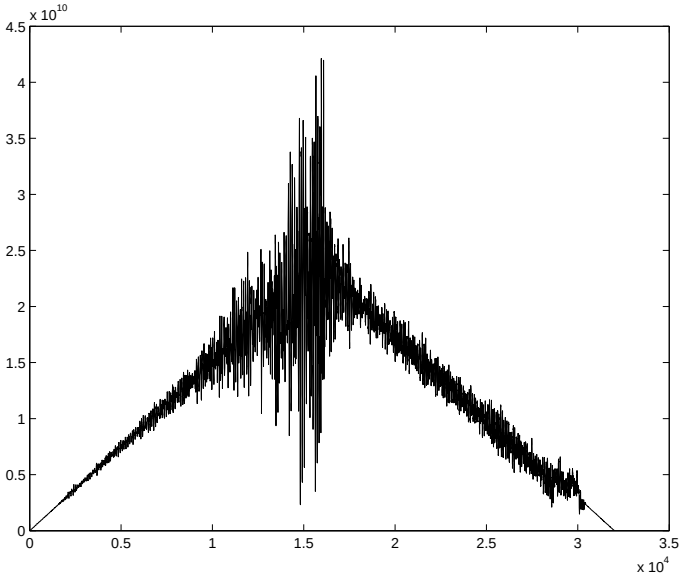


(b)

Figure 9: 2-D image created via adding voltages with the appropriate time offset. (a) No target (b) With target in the field.



(a)



(b)

Figure 10: The matched filter output (a) no target, and (b) with target.

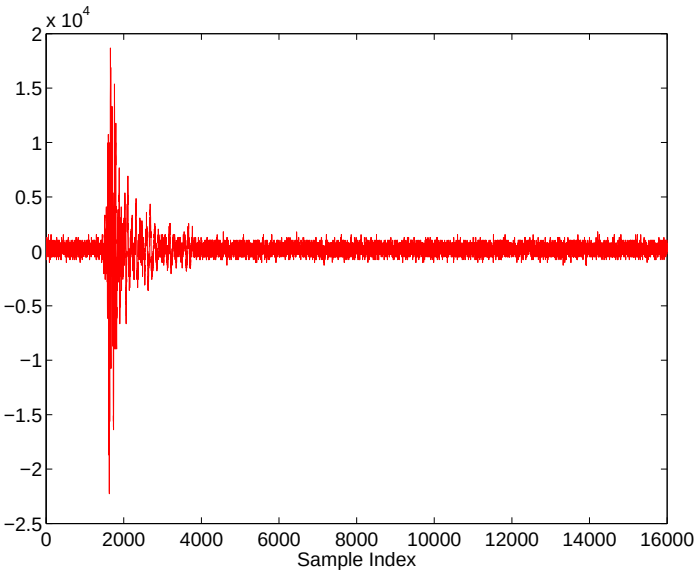


Figure 11: UWB radar transmitted pulse (averaged over 100 pulses).

.

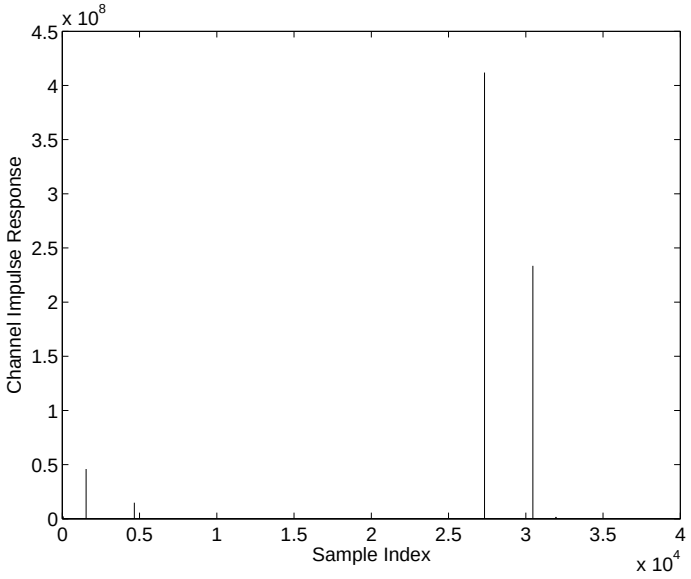
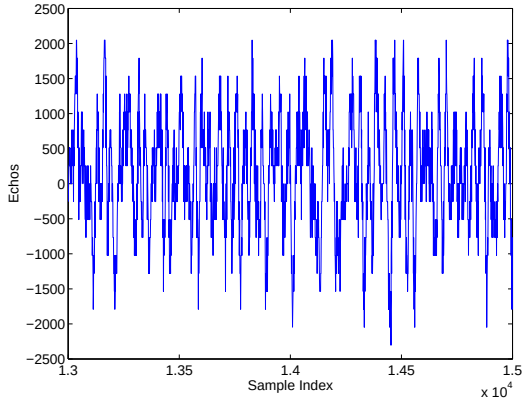
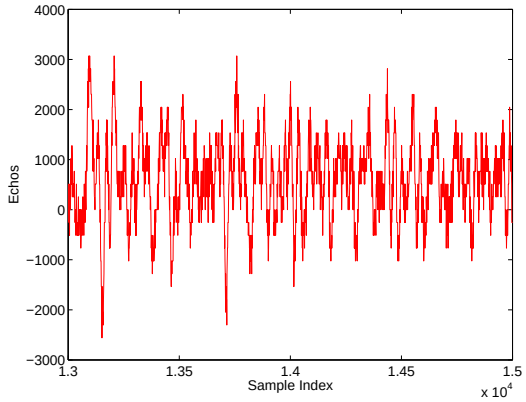


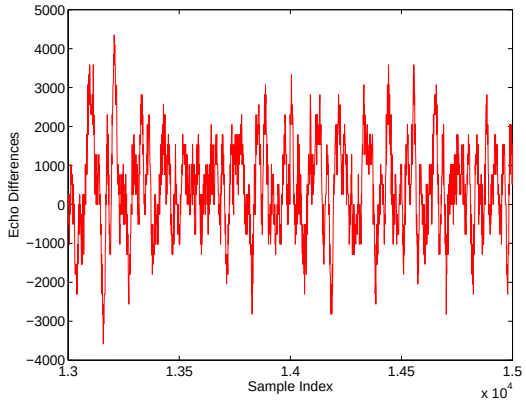
Figure 12: The channel impulse responses for UWB channel using CLEAN method.



(a)



(b)



(c)

Figure 13: Measurement with poor signal quality and 35 pulses average. (a) Expanded view of traces (no target) from sample 13,001 to 15,000. (b) Expanded view of traces (with target) from sample 13,001 to 15,000. (c) The differences between (a) and (b).

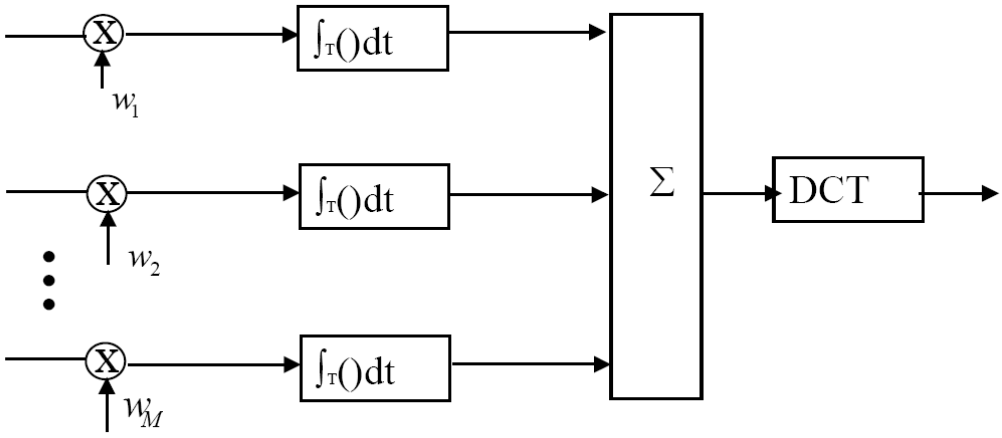
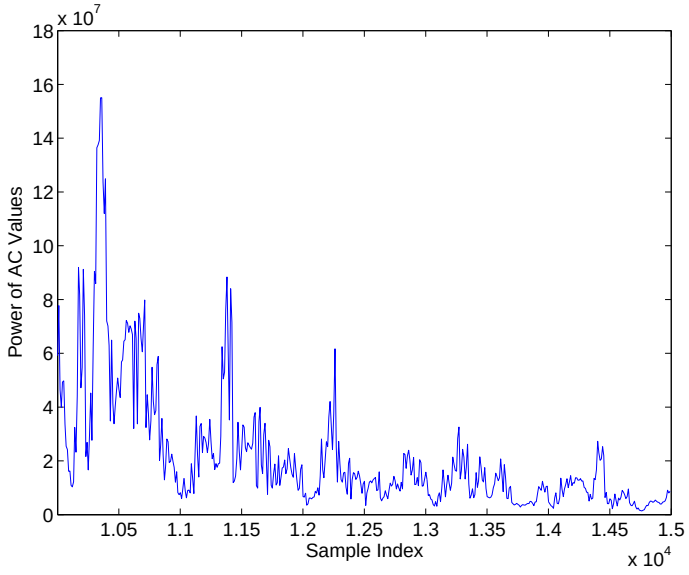
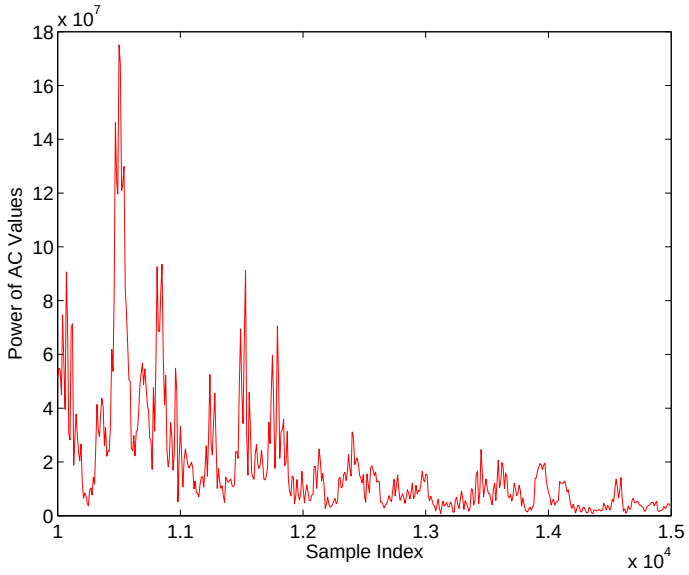


Figure 14: Echo combining by clusterhead in RSN.



(a)



(b)

Figure 15: Power of AC values based on UWB radar sensor networks and DCT based approach. (a) No target (b) With target in the field.

A TENARY PULSE COMPRESSION CODE: DESIGN AND APPLICATION TO RADAR SYSTEM

Lei Xu and Qilian Liang

Department of Electrical Engineering
University of Texas at Arlington
Arlington, TX 76010

Ting Jiang

School of Telecommunications Engineering
Beijing University of Posts and Telecommunication
Beijing 100876, China

ABSTRACT

In this paper, we present new developed tenary code – punctured binary sequence-pair, give its definitions and the autocorrelation properties. We also investigate Doppler shift performance of the proposed code. The significant advantages of this tenary codes over conventional pulse compression codes, such as the widely used Barker codes, are zero autocorrelation sidelobes and the longer length of the code which can be as long as 31 so far. We apply our new tenary codes to radar system for target detection and observe that our codes outperform some other conventional pulse compression codes.

Index Terms— Tenary, Phase coded waveform, Pulse compression, Radar system.

1. INTRODUCTION

Pulse compression, which allows a radar to simultaneously achieve the energy of a long pulse and the resolution of a short pulse without the high peak power required by a high energy short duration pulse [1], is generally used in modern radar system. The main purpose of this technique is to raise the signal to maximum sidelobe (signal-to-sidelobe) ratio to improve the target detection and range resolution abilities of the radar system. The lower the sidelobes, relative to the mainlobe peak, the better the main peak can be distinguished.

One of the basic waveform designs suitable for pulse compression is the phase-coded waveform, a long pulse of duration *T* is divided into *N* subpulses each of width T_s. Each subpulse has a particular phase, which is selected in accordance with a given code sequence. The pulse compression ratio equals to the number of subpulses $N = T/T_s$.

The criterion for selecting the subpulse phases is that all the time-sidelobe of the compressed pulse should be equal and as low as possible. One family of binary phase code widely used as a form of phase coding nowadays that can produce compressed waveforms with constant sidelobe levels equal to unity is the Barker code. It has special features with which its sidelobe structure contains the minimum energy which is theoretically possible for binary codes, and the energy is uniformly distributed among the sidelobes (the sidelobe level of the Barker codes is $1/N^2$ that of the peak signal) [2]. Unfortunately, the length *N* of known binary and complex Barker codes is limited to 13 and 25, respectively [3], which may not be sufficient for the desired radar applications. In [4] [5], polyphase codes, with better Doppler tolerance and lower range sidelobes such as the Frank and P1 codes, the Butler-matrix derived P2 code and the linear-frequency derived P3 and P4 codes were intensively analyzed. However, the low range sidelobe of the polyphase codes can not reach the level zero either, what is more, the structure of polyphase codes is more complicated and is not easy to generate comparing with binary codes. Therefore, we propose and analyze a new tenary code–punctured binary sequence-pair, whose sidelobe level is as low as zero and the longest length of which is found 31 so far, and subsequently apply it to radar system as pulse compression waveform. The results show that the new code can be a good alternative for the current used pulse compression codes in radar system.

The rest of the paper is organized as following. Section 2 introduces the basic concept and properties of our proposed code. In Section 3, examples of punctured binary sequence-pair are given and the properties are investigated. In Section 4, the performance of our proposed code is also simulated and analyzed in radar targets detection system. In Section 5, some conclusions are drawn about our tenary code.

2. DESIGN OF PUNCTURED BINARY SEQUENCE-PAIR

A CW sequence is made up of N bits of duration T_s. The complex envelope during one period is given by

$$x(t) = \sum_{i=1}^{N} x_i[t-(i-1)T_s], 0 \le t \le NT_s \tag{1}$$

Definition 1: A sequence-pair $(\mathbf{x}, \mathbf{y})$ is made up of two *N*-length sequences $\mathbf{x} = (x_0, x_1, \cdots, x_{N-1})$ and $\mathbf{y} = (y_0, y_1, \cdots, y_{N-1})$.

$$R_{\mathbf{xy}}(\tau) = R_{\mathbf{xy}}(rT_s) = \sum_{j=0}^{N-1} x_j y^*_{(j+\tau)modN}, \tag{2}$$
$$0 \le r \le N-1, 0 \le \tau \le (N-1)T_s$$

is called the periodic autocorrelation function of the sequence pair, while $\mathbf{x} = \mathbf{y}$, the sequence-pair $(\mathbf{x}, \mathbf{y})$ turns to be a one-sequence code.

Definition 2 [6]: Sequence $\mathbf{y} = (y_0, y_1, \cdots, y_{N-1})$ is the punctured sequence for $\mathbf{x} = (x_0, x_1, \cdots, x_{N-1})$,

$$y_j = \begin{cases} 0 & \text{if } y_j \text{ is punctured} \\ x_j & \text{if } y_j \text{ is Non-punctured} \end{cases} \tag{3}$$

Where p is the number of punctured bits in sequence $\mathbf{x}$, suppose $x_j \in [-1, 1]$, $y_j \in [-1, 0, 1]$, $(\mathbf{x}, \mathbf{y})$ is called a punctured binary sequence-pair.

Definition 3: The periodic autocorrelation of punctured sequence-pair $(\mathbf{x}, \mathbf{y})$ is defined

$$R_{\mathbf{xy}}(\tau) = R_{\mathbf{xy}}(rT_s) = \sum_{j=0}^{N-1} x_j y^*_{(j+r)modN}, 0 \le r \le N-1$$

If

$$R_{\mathbf{xy}}(\tau) = \begin{cases} E & \tau \equiv 0 \bmod \mathrm{N} \\ 0 & \text{otherwise} \end{cases} \quad (4)$$

$(\mathbf{x}, \mathbf{y})$ is called optimized punctured sequence-pair [6]. Here, $E = \sum_{j=0}^{N-1} x_i y_i = N - p$, is the energy of punctured sequence-pair. Then binary sequence-pair $(\mathbf{x}, \mathbf{y})$ is called a p-punctured sequence-pair.

Definition 4: The balance of the sequence $\mathbf{x}$ is defined as $I = \sum_{j=0}^{N-1} x_j = n_p - n_n$, while n_p, n_n are the number of $'+1'$ and $'-1'$ in $\mathbf{x}$ separately.

Assume $(\mathbf{x}, \mathbf{y})$ to be an optimized punctured binary sequence-pair. Several Theorems are deduced to construct more optimized punctured sequence-pairs easily.

Theorem 1: Mapping property, if $x_i^{'} = x_{-i}, y_i^{'} = y_{-i}$, then $(\mathbf{x}^{'}, \mathbf{y}^{'})$ is optimized punctured binary sequence-pair.

Theorem 2: Opposite to element symbol property, if $x_i^{'} = -x_i, y_i^{'} = -y_i$,then $(\mathbf{x}^{'}, \mathbf{y}^{'})$ is optimized punctured binary sequence-pair.

Theorem 3: Cyclic shift property, if $x_i^{'} = -x_{(i+u)}, y_i^{'} = -y_{(i+u)}$,then $(\mathbf{x}^{'}, \mathbf{y}^{'})$ is optimized punctured binary sequence-pair.

Theorem 4: Periodically sampling property, if $x_i^{'} = -x_{ki}, y_i^{'} = -y_{ki}, k$ and N are relatively prime, then $(\mathbf{x}^{'}, \mathbf{y}^{'})$ is optimized punctured binary sequence-pair.

In [6], the properties, existing necessary conditions and some constructing methods have been well studied and examples of length from 3 to 31 are presented there.

3. PROPERTIES

3.1. Autocorrelation Properties

The autocorrelation function is one of the most important properties that represent the compressed pulse in an ideal pulse compression system, since it is proportional to the matched filter response in the noise-free condition.

EXAMPLE 1

The autocorrelation property of 31-length punctured binary sequence-pair ($\mathbf{x}_{31} = [+++-----+-+-++++----+--+---++++-+++-]$ and $\mathbf{y}_{31} = [+++000+0+0++++0000+00+00+++0++0]$) $('+' for '1' and '-' for '-1')$ shown in Fig. 1.

As it is known that a suitable criterion for evaluating code of length N is the peak signal to peak signal sidelobe ratio (PSR)[7] of their autocorrelation function. The only aperiodic uniform phase codes that can reach the PSR_{max} are the Barker codes whose length is equal or less than 13. However, the sidelobe of the new code shown in Fig. 1 could be as low as 0. Thus, the peak signal to peak signal sidelobe ratio can be as large as infinite. The length of the new code can expand at least to 31 that is much longer than the length of the Barker code.

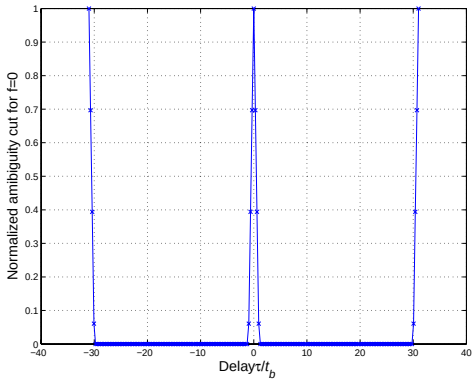


Fig. 1. Periodic autocorrelation property of 31-length punctured binary sequence-pair

3.2. Ambiguity Function

When the transmitted impulse is reflected by a moving target, the reflected echo signal includes a linear phase shift which corresponds to a Doppler shift F_D [8]. As a result of the Doppler shift F_D, the main peak of the autocorrelation function is reduced as well as SNR. And the sidelobe structure is also changed thanks to the Doppler shift.

We use different codes for the transmitter and the receiver, so the single period ambiguity function of sequence-pair can be defined as:

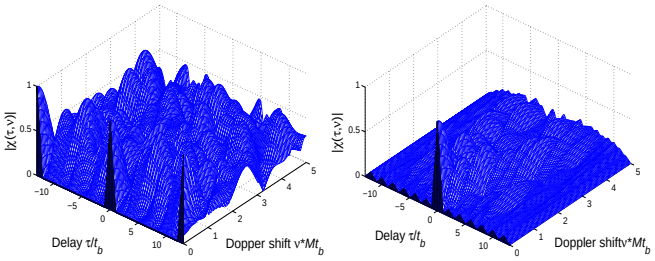
$$A_{T-pair}(\tau, F_D) \cong |\frac{1}{T}\int_0^T x(t+\frac{\tau}{2}) e^{j2\pi F_D t} y^*(t-\frac{\tau}{2}) dt| \quad (5)$$

When the signal is of duration MT, the response of the correlation receiver is the PAF (periodic ambiguity function) for M periods. After normalization and splitting it into M sections,

$$\begin{aligned} A_{MT-pair}(\tau, F_D) &\cong |\frac{1}{MT}\int_0^{MT} x(t+\frac{\tau}{2}) e^{j2\pi F_D t} y^*(t-\frac{\tau}{2}) dt| \\ &= A_{T-pair}(\tau, F_D) |\frac{sin(\pi F_D MT)}{M sin(\pi F_D T)}| \end{aligned} \quad (6)$$

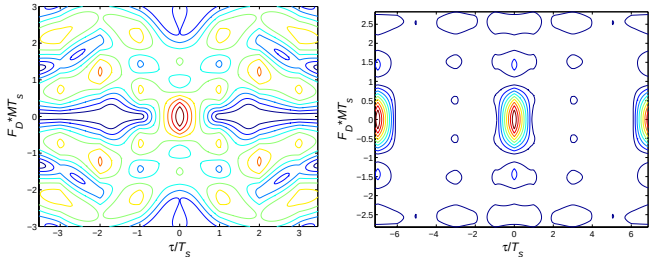
EXAMPLE 2

Ambiguity functions of our ternary code of length 13 ($\mathbf{x}_{13} = [+++--+-+----++-]$, $\mathbf{y}_{13} = [+0+0++0000++0]$) is studied, where maximal time delay is 1 unit (normalized to length of the code, in units of NT_s) and maximal Doppler shift is 5 units (normalized to the inverse of the length of the code, in units of $1/NT_s$). The ambiguity function of 13-bit long Barker code is also presented in Fig. 2 in order to compare with our ternary code of the same length. According to Fig. 2, the sidelobe of our ternary code can reach as low as zero. Nevertheless, when there are Doppler shift and time delay, the ambiguity functions of our code is not as flat as those of Barker code. Our ternary code is less tolerant of Doppler shifts than Barker code. The reasons



(a) Punctured binary sequence-pair (b) Barker code

Fig. 2. Ambiguity function of 13-length codes



(a) $M = 1$ (b) $M = 4$

Fig. 3. Contour plot of sequence-pair

why our code is not tolerant of large Doppler shift could be that the periodic correlation property of our code is studied instead of the aperiodic correlation property.

EXAMPLE 3

In order to improve the tolerance of Doppler shift of our proposed code, we repeat the sequence-pair M times to construct the signal of duration of MT. We study the performance of the sequence-pair of M periods in this section. The optimized punctured binary sequence-pair of length 7 ($x_7 = [+++--+-], y_7 = [++ +00+0]$) is used here.

Figs. 3 presents contour plots of the absolute amplitude of the ambiguity function, for the two cases $M = 1, 4$. The scales are normalized with respect to the bit duration of T_s. Namely, the delay axis is of τ/T_s, and the Doppler shift axis is of $F_D T_s$. Since the single period is $T = NT_s$, the ambiguity function repeats itself every N normalization delay units. The pronounced strips, parallel to the Doppler shift axis, appear at N normalized delay units.

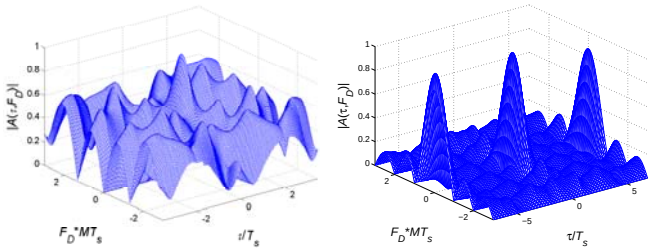
The corresponding 3-D plots are given in Figs. 4. The prominent feature of the ambiguity function, when $M > 1$, the strips get narrower as M increases. The cuts of periodic ambiguity function at $\tau/T_s = nN$ are independent of the number of periods M.

3.3. Doppler Shift Performance Without Time Delay

According to the previous work [8], the cut along Doppler axis is obtained as, namely, when the time delay is zero,

$$A_T(0, F_D) = |\frac{sin(\pi F_D T)}{\pi F_D T}| \tag{7}$$

It is easy to see that $F_D = n/T$ for all but $n = 0, (n = \pm 1, \pm 2, ...)$, the amplitude must get a zero. It is known that



(a) $M = 1$ (b) $M = 4$

Fig. 4. 3-D view of ambiguity function of sequence-pair (x_7, y_7)

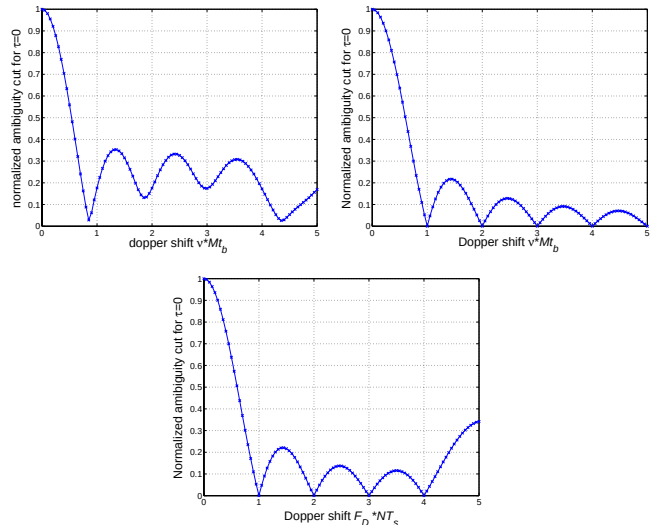


Fig. 5. Doppler shift of codes(time delay=0): (a) 31-length Punctured binary sequence-pair (b) P4 code (c) 7x5-length Punctured binary sequence-pair

Doppler frequency F_D is given by

$$F_D = 2\frac{vf_c}{c} \tag{8}$$

where v is the speed of moving target, f_c is the carrier frequency of radar and c is the speed of light. This states that Doppler shifts which equal to multiples of the PRF (pulse repetition frequency) will render the radar blind to the velocities of the targets. However, the optimized punctured sequence-pairs used here are in a different case which would be studied in this section.

The ambiguity function of single period can be simplified when there is no time delay:

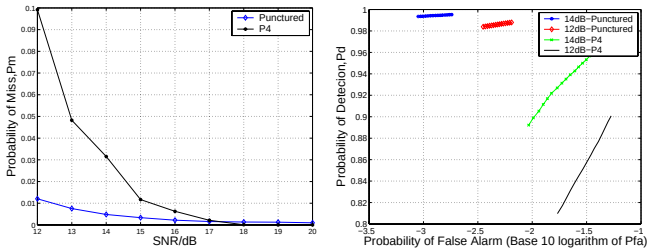
$$A_{T-pair}(0, F_D) = |\frac{1}{T}\int_0^T x(t)y^*(t)e^{(j2\pi F_D t)}dt| \tag{9}$$

According to the equation (8), the ambiguity function of duration of M periods could be expressed as:

$$A_{MT-pair}(0, F_D) = A_{T-pair}(0, F_D)|\frac{sin(\pi F_D MT)}{Msin(\pi F_D T)}| \tag{10}$$

Where M is the number of the periods.

The Doppler shift performance without time delay is presented in Fig. 5. Without time delay, while the Doppler shift



(a) P_m (b) $P_d versus P_{fa}$

Fig. 6. 31-length Punctured binary sequence-pair VS. 31-length P4 code

is less than 1 unit, the amplitude of our 31-length code has a sharp downward trend and decreases more quickly than P4 code. However, when the Doppler shift is larger than 1 unit, the performances of these codes are distinguished. On one hand, the trend presented by our 31-length code is not as regular as the other two codes. On the other hand, for P4 code, its multiples of the pulse repetition frequency will render the radar blind[1] to the velocities. Nevertheless, ambiguity values of 31-length punctured binary sequence-pair do not go to zero when Doppler frequencies are equal to multiples of the PRF. According to Fig. 5(c), 7x5-length punctured binary sequence-pair which generally resembles the 31-length P4 code is more tolerant of Doppler shift than the punctured binary sequence-pair of correspongding length 31, but it has more amiguity values go to zero when Doppler shift equals to some multiples of the PRF. Therefore, using the our ternary code as the compression code could, to some extent, improve the blind speed problem in moving target detection system. Using several periods of punctured binary sequence-pair could improve the tolerance of Doppler shift when Doppler shift is larger than 1 unit.

4. APPLICATION TO RADAR SYSTEM

According to [8], P_D (Probability of Detection), P_{FA} (Probability of False Alarm) and P_M (Probability of Miss) suffice to specify all of the probabilities of interest in radar system. Therefore, the above three probabilities of our newly provided ternary code in radar system are simulated, as shown in Fig. 6(a) and Fig. 6(b). The performance of 13-length Barker code and 31-length P4 code are also provided in order to compare with the performance of our ternary codes of corresponding lengths. In the simulation model, we ran Monte-Carlo simulation for 10^5 times at each SNR value, the Doppler shift frequency which is kept less than 1 unit (normalized to the inverse of the length of the code, in units of $1/NT_s$) is randomly given by Matlab.

In Fig. 6(a), we plotted the probabilities of miss targets detection of our 31-length ternary code and those of the same length P4 code. The probability of miss targets detection of the system using our 31-length ternary code is less than 31-length P4 code especially when the SNR is not large. When SNR is larger than 17 dB, both probabilities of miss targets detection of the system approach zero. However, the probability of miss targets of P4 code is a little lower than our ternary code.

In addition, we also plotted the probability of detection versus probability of false alarm of the coherent receiver in Fig. 6(b). Fig. 6(b) illustrates performance of our 31-length ternary codes and the same length P4 code when the SNR is 12dB and 14dB. Having the same SNR value such as 12dB or 14dB in the figure, the P_D of our 31-length ternary code is larger than P_D of our 31-length P4 code while the P_{FA} of the first code is also smaller than P_{FA} of the latter code. In some other words, our 31-length ternary code has much higher target detection probability while keeping a lower false alarm probability. Furthermore, observe Fig. 6(b), our 31-length ternary code even has much better performance at 10dB SNR than 31-length P4 code at 14dB SNR.

5. CONCLUSION

A new ternary code and its properties have been investigated in this paper. The significant advantage of punctured binary sequence-pair over conventional phase compression code is the considerably reduced sidelobe as low as zero and correspondingly the significantly improved PSR. We apply the new code to the target detection in the radar system and obtain better performance. In conclusion, the punctured binary sequence-pair, which has much longer code length and better autocorrelation sidelobe property than the biphase code such as Barker code, and simpler structure than those polyphase codes such as P4 code, effectively increases the variety of candidates for pulse compression codes especially for long code.

6. REFERENCES

[1] S. Ariyavisitakul, N. Sollenberger, and L. Greenstein, *Introduction to Radar System*, Tata McGraw-Hill, 2001.

[2] J.L. Eaves and E.K. Reedy, *Principles of Modern Radar*, Van Nostrand Reinhold, 1987.

[3] L. Bomer and M. Antweiler, "Polyphase barker sequences," in *Electronics Letters*, December 1989, pp. 1577–1579.

[4] R.L. Frank, "Polyphase codes with good nonperiodic correlation properties," *IEEE Transactions on Information Theory*, pp. 43–45, January 1963.

[5] B.L. Lewis and F.F. Kretschuner, "Linear frequency modulation derived polyphase pulse compression codes," *IEEE Transactions on Aerospace and Electronic Systems*, vol. 18, pp. 637–641, Sep. 1982.

[6] T. Jiang, *Research on Quasi-Perfect Binary Signal Pair and Perfect Punctured Binary Signal Pair Theory*, Ph.D. thesis, Yanshan University, Qing Huangdao, 2003.

[7] M. I. Skolnik, *Radar Handbook*, McGraw-Hill, New York, NY, 1970.

[8] M. A. Richards, *Fundamentals of Radar Signal Processing*, McGraw-Hill, New York, NY, 2005.

Sense-Through-Wall Channel Modeling Using UWB Noise Radar

Jing Liang, Qilian Liang
Department of Electrical Engineering
University of Texas at Arlington
Arlington, TX 76019-0016, USA
Email: jliang@wcn.uta.edu, liang@uta.edu

Sherwood W. Samn
Air Force Research Laboratory/HEX
Brooks City Base
San Antonio, TX 78235, USA
Email: Sherwood.samn@brooks.af.mil

Ram M. Narayanan
Department of Electrical Engineering
The Pennsylvania State University
University Park, PA 16802, USA
Email: ram@engr.psu.edu

***Abstract*— Sensing-through-wall will benefit various applications such as emergence rescues and military operations. In order to add more signal processing functionality, it is vital to understand the characterization of sense-through-wall channel. In this paper, we propose a statistical channel model on a basis of real experimental data using UWB noise radar. We employ CLEAN algorithm to obtain the multipath channel impulse response (CIR) and observe that the channel amplitude at each path can be accurately characterized as T location-scale distribution. We also analyze that the multipath contributions arrive at the receiver are grouped into clusters. The time of arrival of clusters can be modeled as a Poisson arrival process, while within each cluster, subsequent multipath contributions or rays also arrive according to a Poisson process. However, these arrival rates are much smaller than those of indoor UWB channels.**

I. Introduction

Sensing-through-wall techniques have attracted great interest due to a broad range of military and civilian applications. During detection, it is more likely that signal processing occurs at one side of the wall and the interior space to be exploited is on the other and it can not be seen through conventional measures. Therefore it is desirable that the wall penetration sensing provide following information: building layouts like rooms and inner objects; identification of humans and their positions; the composition and structure of the wall. These characterizations will be of great use in locating weapon caches during military operations, searching and rescuing people from natural diasters such as earthquakes and providing sustainability assessment of bridges and buildings.

In recent years UWB waveforms are frequently employed for indoor wireless propagation systems due to the exceptional range resolution and strong penetrating capability. There has been a great amount of research on statistical modeling of UWB indoor multipath channels [1]-[3] and IEEE [4] has standardized it on a basis of Saleh and Valenzuela (S-V) channel model [5]. There have been some efforts investigating sensing-through-wall using UWB waveforms. [6] uses finite difference time-domain (FDTD) method to simulate reflected UWB pulses for three different types of walls. [7] proposes UWB transmission pulses for walls with different thickness and conductivity. However, these reports only describe about transmitted or reflected waveforms based on simulation, sense-through-wall channel has not yet been touched on. Imaging techniques have also been employed to show objects behind the wall in [8] and [9]. [8] uses wideband synthetic aperture radar and incorporates wall thickness and dielectric constant to generate the indoor scene through image fusion. [9] discusses the advantages of using thermally generated noise as a probing signal and analyzes the basic concepts of synthetic aperture radar image formation using noise waveforms. Nevertheless these studies haven't provide any insight into any property of through-wall radio channel.

In this paper, we propose a statistical multipath model of through-wall radio channel based on real measurement. The UWB noise waveform presented in [9] has been adopted in our work. This is due to the inherently low probability of intercept (LPI) and low probability of detection (LPD). These characterizations provide immunity from detection, jamming, and interference. We investigate the model based on channel impulse response (CIR) obtained through CLEAN processing method. It is observed that the amplitude of channel coefficient at each path can be accurately characterized by T location-scale distribution. It is also observed that the multipath contributions arrive at the receiver are grouped into clusters. The time of arrival of clusters can be modeled as a Poisson arrival process, while within each cluster, subsequent multipath contributions or rays also arrive according to a Poisson process.

The rest of this paper is organized as follows. In Section II, we summarize the measurement and collection of the data. In Section III, we apply CLEAN algorithm to extract CIR. Section IV presents the channel model in terms of amplitude and temporal parameters. Conclusion and future work is given in Section V.

II. Measurement Setup

A UWB noise radar system was set up in the Radar Imaging Lab at Villanova University. Fig. 1 illustrates the layout of the experiment room. The wall segment, constructed utilizing solid concrete blocks with a dielectric constant of 7.66, is 0.14m thick 2.8m long and 2.3m high. The room behind this wall is empty.

A horn antenna, model ETS-Lindgren 3164-04, with an operational bandwidth from 0.7 to 6 GHz, was used as the transceiver. The antenna was placed only 1cm to the front

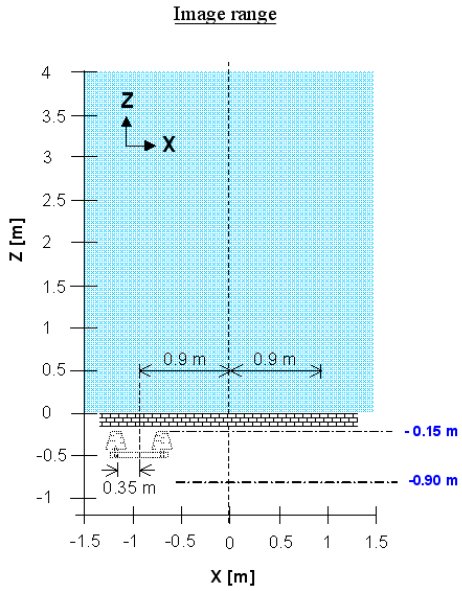


Fig. 1. Experiment Setup

wall, which is illustrated in Fig. 2. Therefore the propagation length from antenna front edge to the backside of the wall is 15cm. 37 times of measurements are collected at different but equally spaced positions along the wall with step size 5cm. An Agilent network analyzer, model ENA 5071B, was used for signal synthesis and data collection.

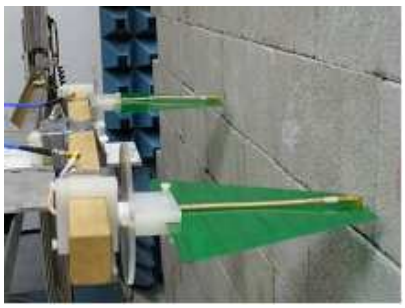


Fig. 2. Radar antenna and wall in the experiment

III. Channel Impulse Response Based on the Measured Data and CLEAN Algorithm

The transmitted noise waveform and received echoes of one measurement are plotted in Fig. 3. It shows that UWB noise waveform has a very good sensing-through-wall capability. During 37 experiments, the frequency of the transmitted signal is $400 - 720$ MHz and sampling rate is 1.5GHz/s. The tremendously large amplitude at around sample 100 is due to the antenna coupling [10]. Note that at a different position the measurement result will be slightly different but the characterization of the signals are quite similar. Thus the illustration of pulses collected at one position is sufficient to describe the property.

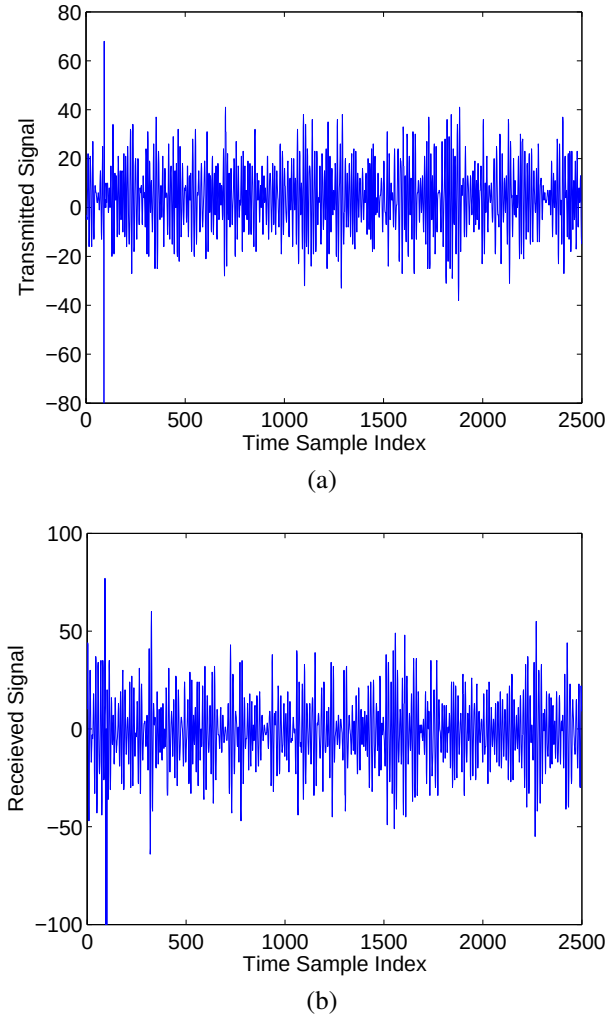


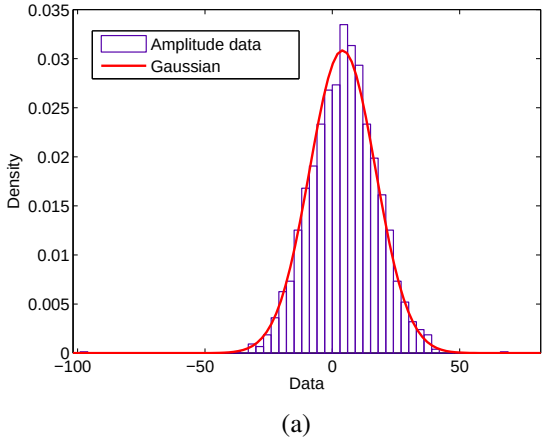
Fig. 3. UWB noise waveforms: (a) transmitted pulse (b) received echoes

Fig. 4 shows the histogram of transmitted and received waveform amplitude. It is very interesting to see that after sensing-through-the wall, the back scattered signal still roughly follows Gaussian distribution. This conclusion applies to all other 36 measurements. Assume the Gaussian mean and variance are μ and σ^2 respectively, Table I shows the detail of these parameters.

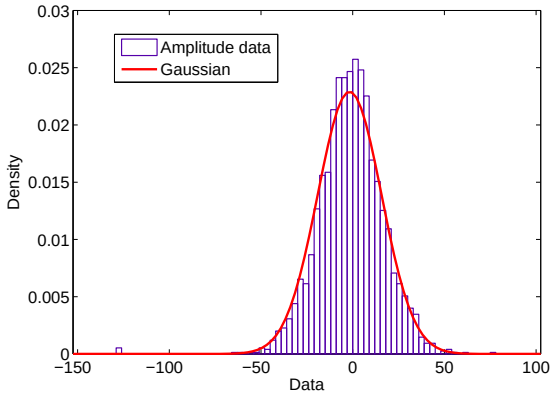
Since the transmitted and received signals have been known, the CLEAN algorithm can be used to extract channel impulse response (CIR). This method was initially introduced in [11] to enhance radio astronomical maps of the sky, and has been frequently employed in UWB channel characterization problems [12]-[14]. The CLEAN algorithm is an iterative, high-resolution, subtractive deconvolution procedure that is capable resolving dense multipath components which are usually irresolvable by conventional inverse filtering [16].

Our steps involved [15] are:

1) Calculate the autocorrelation of the transmitted signal $R_{ss}(t)$ and the cross-correlation of the transmitted with the received waveform $R_{sy}(t)$.



(a)



(b)

Fig. 4. Amplitude density: (a) transmitted pulse (b) received echoes

TABLE I

ESTIMATED STATISTICAL PARAMETERS OF TRANSMITTED AND RECEIVED SIGNALS

parameter	transmitted signal	received signal
μ	4.0512	-1.6756
STD Error of μ	0.258655	0.348318
σ	12.9328	17.4159
STD Error of σ	0.182952	0.246372

2) Find the largest correlation peak in $R_{sy}(t)$, record the normalized amplitudes α_k and the relative time delay τ_k of the correlation peak.
3) Subtract $R_{ss}(t)$ scaled by α_k from $R_{sy}(t)$ at the time delay τ_k.
4) If a stopping criterion (a minimum threshold) on the peak correlation is not met, go step 2. otherwise stop.

Fig. 5 illustrated the absolute value of through-wall CIR at one measurement position by CLEAN algorithm. We can see that the channel consists of multipaths that arrive in clusters. Each cluster is made up of subsequent rays. This is very similar to the multipath rays in S-V channel model. However, in S-V model, the largest scattering, i.e., the highest magnitude always appears at the first path. It is obvious to see this is not

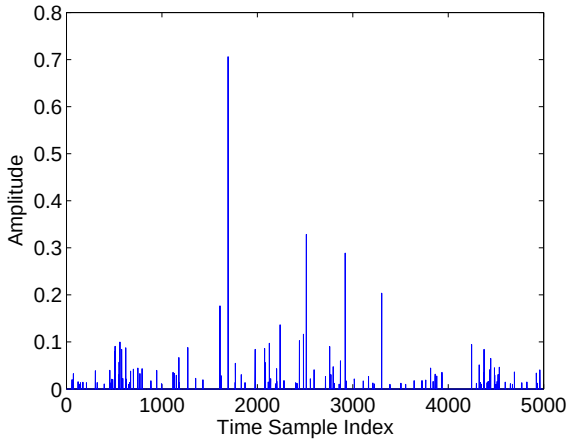


Fig. 5. Normalized CIR by CLEAN algorithm

the general case in the through-wall channel. On a basis of CIR, the channel can be represented as

$$r(t) \approx \sum_n a_n p_n(t - \tau_n) \tag{1}$$

where a_n and τ_n is referred to as the amplitude and delay of the n^{th} propagation path. In the next Section we shall analyze them in detail.

IV. SENSE-THROUGH-WALL CHANNEL MODELING

A. Temporal Characterization

Like in S-V model, multipath contributions arrive at the receiver grouped into clusters and therefore similar methodology used in S-V model studies may be also applied to sensing-through-wall CIR. The time of arrival of clusters can be modeled as a Poisson arrival process with a rate Λ, while within each cluster, subsequent multipath contributions or rays also arrive according to a Poisson process with a rate λ.

We define:

- T_l : the arrival time of the first path of the l-th cluster;
- $\tau_{k,l}$: the delay of the k-th path within the l-th cluster relative to the first path arrival time T_l;
- Λ : the cluster arrival rate;
- λ : the ray arrival rate, i.e., the arrival rate of the paths within each cluster;
- $\bar{\tau}$: the mean excess delay;
- σ_τ : the rms delay spread

By definition, we have $\tau_{0l} = T_l$. The distributions of the cluster arrival time and the ray arrival time are given by

$$\begin{aligned} p(T_l|T_{l-1}) &= \Lambda \exp\left(-\Lambda(T_l - T_{l-1}), l > 0\right) \\ p(\tau_{k,l}|\tau_{(k-1),l}) &= \lambda \exp\left(-\lambda(\tau_{k,l} - \tau_{(k-1),l})\right), k > 0 \end{aligned} \tag{2}$$

$\bar{\tau}$, σ_τ are defined by

$$\bar{\tau} \equiv \frac{\sum_n a_n^2 \tau_n}{\sum_n a_n^2} \tag{3}$$

$$\sigma_\tau \equiv \sqrt{\bar{\tau^2} - \bar{\tau}^2} \tag{4}$$

where

$$\bar{\tau^2} \equiv \frac{\sum_n a_n^2 \tau_n^2}{\sum_n a_n^2} \quad (5)$$

We analyze these parameters based on 37 experiments and show the result in Table II.

TABLE II
TEMPORAL PARAMETERS FOR SENSE-THROUGH-WALL CHANNEL MODEL

parameter	$\Lambda(1/ns)$	$\lambda(1/ns)$	$\bar{\tau}(\mu s)$	σ_τ
value	0.002	0.0224	1.8153	0.0827

We may compare the Λ and λ in Table II with the same parameters for indoor UWB, which are 0.0667 and 2.1 respectively with unit $1/ns$ [17]. The parameters for through-wall channel is much smaller due to the resistance of wireless propagation in wall.

B. Statistical Distribution of Channel Amplitude

In the S-V model, the amplitude follows rayleigh distribution. In the IEEE UWB indoor channel model [4], log-normal distribution was introduced for representing the fluctuations of the total multipath gain. In this Section we propose that the amplitude of sensing-through-wall channel follows T location-scale distribution. Its probability density function (PDF) is

$$f(x) = \frac{\Gamma(\frac{\nu+1}{2})}{\phi\sqrt{\nu\pi}\cdot\Gamma(\frac{\nu}{2})}[\frac{\nu+(\frac{x-\delta}{\phi})^2}{\nu}]^{-(\frac{\nu+1}{2})}, \phi>0, \nu>0 \quad (6)$$

where δ is the location parameter, ϕ is scale parameter, ν is shape parameter and $\Gamma(\cdot)$ denotes gamma function. Note that if define $y \equiv \frac{x-\delta}{\phi}$, then y follows student's T distribution with ν degrees of freedom. As v goes to infinity, the T location-scale distribution approaches the standard Gaussian distribution.

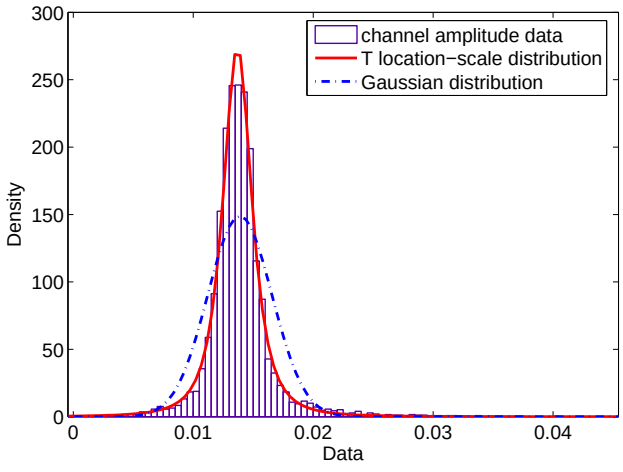


Fig. 6. Goodness-of-fit

Fig. 6 clearly illustrates to what extend does the CIR amplitude match the PDF curve of the statistic model. The absolute amplitude values of CIR have been plotted in terms of histogram. We compare T location-scale distribution with Gaussian distribution. Although the transmitted and received signal amplitude follows Gaussian model, this is not the case for the channel. It can be easily seen that T location-scale model provides perfect goodness-of-fit.

On a basis of CIR amplitudes from 37 different positions, we apply Maximum Likelihood Estimation (MLE) approach to estimate the parameters [18] [19]. It is generalized as follows:

Let $y_1, y_2, \cdots, y_N$ be N independent samples drawn from a random variable $\mathbf{Y}$ with m parameters $\theta_1, \theta_2, \cdots, \theta_m$, where $\theta_i \in \theta$, then the joint PDF of $y_1, y_2, \cdots, y_N$ is

$$L_N(\mathbf{Y}|\theta) = f_{Y|\theta}(y_1|\theta_1, \cdots, \theta_m) \ldots f_{Y|\theta}(y_n|\theta_1, \cdots, \theta_m) \quad (7)$$

When expressed as the conditional function of $\mathbf{Y}$ depends on the parameter θ, the likelihood function is

$$L_N(\mathbf{Y}|\theta) = \prod_{k=1}^{N} f_{Y|\theta}(y_k|\theta_1, \theta_2, \cdots, \theta_m) \quad (8)$$

The maximum likelihood estimate of $\theta_1, \theta_2, \cdots, \theta_m$ is the set of values $\hat{\theta}_1, \hat{\theta}_2, \cdots, \hat{\theta}_m$ that maximize the likelihood function $L_N(\mathbf{Y}|\theta)$.

As the logarithmic function is monotonically increasing, maximizing $L_N(\mathbf{Y}|\theta)$ is equivalent to maximizing $\ln(L_N(\mathbf{Y}|\theta))$. Hence, it can be shown that a necessary but not sufficient condition to obtain the ML estimate $\hat{\theta}$ is to solve the likelihood equation

$$\frac{\partial}{\partial\theta}\ln(L_N(\mathbf{Y}|\theta)) = 0 \quad (9)$$

We obtain $\hat{\delta}$, $\hat{\phi}$ and $\hat{\nu}$ for T location-scale distribution, $\hat{\mu}$ and $\hat{\sigma}$ for Gaussian distribution. These are shown in table III. We also explore the standard deviation (STD) error of each parameter. These descriptions are also shown in table III in the form of ε_x, where x denotes different parameter for each model. It can be seen that T location-scale provides smaller STD errors than those of Gaussian distribution.

TABLE III
STATISTICAL AMPLITUDE PARAMETERS FOR SENSE-THROUGH-WALL CHANNEL MODEL

PDF	T location-scale	Gaussian
Parameters	$\hat{\delta} = 0.0136836$ $\hat{\phi} = 0.00129967$ $\hat{\nu} = 2.18286$ $\varepsilon_\delta = 2.35418e^{-005}$ $\varepsilon_\phi = 2.50893e^{-005}$ $\varepsilon_\nu = 0.0821753$	$\hat{\mu} = -0.0138875$ $\hat{\sigma} = 0.00267908$ $\varepsilon_\mu = 3.78917e^{-005}$ $\varepsilon_\sigma = 2.67975e^{-005}$
RMSE	9.8983	25.5854

We may also observe the goodness-of-fit by root mean square error (RMSE). Let i (i=1, 2, $\cdots$, n) be the sample index of CIR amplitude in Fig. 6. c_i is the corresponding density value of CIR amplitude and $\hat{c}_i$ is the density value of the statistical model with estimated parameters by means of MLE. RMSE is obtained through

$$\mathtt{RMSE} = \sqrt{\frac{1}{n}\sum_{i=1}^{n}(c_i - \hat{c}_i)^2} \qquad (10)$$

where n is the total amount of sample index. The RMSE for T location-scale and Gaussian distributions have been listed in Table III also. It demonstrates that T location-scale is the model that fits the channel amplitude data very well.

V. Conclusion

From our investigation, we would draw following conclusions: 1)UWB noise waveform may have a very good sensing-through-wall capability for walls composed of solid concrete blocks. 2)Sense-through-wall channels are made up of multipath components and the highest magnitude does not always appear at the first path. 3)The multipath contributions arrive at the receiver are grouped into clusters. The time of arrival of clusters can be modeled as a Poisson arrival process, while within each cluster, subsequent multipath contributions or rays also arrive according to a Poisson process. However, these arrival rates are much smaller than those of indoor UWB channels. 4) The amplitude of channel coefficient at each path can be more accurately characterized as T location-scale distribution other than Gaussian distribution due to better goodness-of-fit and smaller root-mean-square-error (RMSE).

Acknowledgement

This work was supported in part by Office of Naval Research (ONR) under Grant N00014-07-1-0395 and N00014-07-1-1024, and National Science Foundation (NSF) under Grant CNS-0721515 and CNS-0831902.

References

[1] D. Cassioli, M. Z. Win, and A. F. Molisch, "The ultra-wide bandwidth indoor channel: From statistical study to simulations", *IEEE J. Select. Areas Commun.*, vol. 20, pp. 1247-1257, Aug. 2002.

[2] S. S. Ghassemzadeh, R. Jana, C. W. Rice, W. Turin, and V. Tarokh, "Measurement and modeling of an ultra-wide bandwidth indoor channel", *IEEE Trans. Commun.*, vol. 52, pp. 1786-1796, Oct. 2004.

[3] B. M. Donlan, D. R. McKinstry and R. M. Buehrer, "The UWB Indoor Channel: Large and Small Scale Modeling", *IEEE Trans. on Wireless Commun.*, vol. 5, pp. 2863-2873, Oct. 2006.

[4] IEEE 802.15.SG3a, "Channel modeling sub-committee report final", *IEEE P802.15-02/490r1-SG3a*, Feb. 2003.

[5] A. A. Saleh and R. A. Valenzuela, "A statistical model for indoor multipath propagation", *IEEE Journal on Selected Areas in Communications*, vol. 5, no.2, pp. 128-137, Feb. 1987.

[6] Z. Yun and M. F. Iskander, "UWB Pulse Propagation through Complex Walls in Indoor Wireless Communications Environments", *International Conference on Wireless Networks, Communications and Mobile Computing, 2005*, vol.2, pp. 1358-1361, June 2005.

[7] N. Noori, A. Abolghasemi and M. Fardis, "Modeling of ultra wideband transmission through building walls", *International Conference on Microwave and Millimeter Wave Technology, 2008, ICMMT 2008*, vol.2, pp. 982-985.

[8] F. Ahmad and M.G.Amin, "Multi-location wideband synthetic aperture imaging for urban sensing applications", *Journal of the Franklin Institute*, 345 (6), pp.618-639, Sep 2008.

[9] R. M. Narayanan, "Through-wall radar imaging using UWB noise waveforms", *Journal of the Franklin Institute*, 345 (6), pp.659-678, Sep 2008.

[10] J. A. Henning, "Design and Performance of An Ultra-Wideband Foliage Penetrating Noise Radar", Masters Thesis, University of Nebraska, May 2001.

[11] J. A. Högbom, "Aperture Synthesis with a non-regular distribution of interferometer baselines", *Astronomy and Astrophysics Supplement Ser.*, vol. 15, pp. 417-426, 1974.

[12] R. J. -M. Cramer, R. A. Scholtz and M. Z. Win, "Evaluation of an ultra-wide-band propagation channel", *IEEE Transactions on Antennas and Propagation*, vol. 50, pp. 561-570, May 2002.

[13] P. C. Richardson, W. Xiang and W. Stark, "Modeling of ultra-wideband channels within vehicles", *IEEE Journal on selected areas in communications*, vol. 24, pp. 906-912, Apr. 2006.

[14] W. Yang and Z. Naitong, "A new multi-template CLEAN algorithm for UWB channel impulse response characterization", in *Proc. Int. Conf. Coommun. Technol.*, Nov. 2006, pp. 1-4.

[15] J. H. Reed, *An introduction to Ultra Wideband Communication Systems*, Prentice Hall, 2005.

[16] A. F. Molisch, "Ultrawideband propagtion channels: Theory, measurement and modeling", *IEEE Transactions on Vehicular Technology*, vol. 54, Sept. 2005, pp. 1528-1545.

[17] M. -G. Di Benedetto and G. Giancola, *Understanding ultra wideband Radio Fundamentals*, Prentice Hall, 2004.

[18] Devore, *Probability and Statistics for Engineering and the Sciences*, Monterey, CA: BrooksiCole, 1982.

[19] M. Barkat, *Signal deteciton and estimation*, 2nd, London: Artech house, 2005.

A SET OF TRIPHASE CODED WAVEFORMS: DESIGN, ANALYSIS AND APPLICATION TO RADAR SYSTEM

Lei Xu and Qilian Liang
Department of Electrical Engineering
University of Texas at Arlington
Arlington, TX 76019-0016
Email: xu@wcn.uta.edu, liang@uta.edu

ABSTRACT

Based on the Zero Correlation Zone (ZCZ) concept, we present the definition and properties of a set of new triphase coded waveforms –ZCZ sequence-pair set (ZCZPS) in this paper and propose a method to use the optimized punctured sequence-pair along with Hadamard matrix construct the optimized punctured ZCZ sequence-pair set (optimized punctured ZCZPS). According to property analysis under the Doppler shift condition, the optimized punctured ZCZPS has good autocorrelation and cross correlation properties when Doppler shift is not large. We apply it to radar target detection. The simulation results show that optimized punctured ZCZ sequence-pairs (optimized punctured ZCZPs) outperform other conventional pulse compression codes, such as the well known polyphase code–P4 code.

Keywords: Triphase; Zero correlation zone; Optimized punctured ZCZ sequence-pair; Phase coded waveform.

INTRODUCTION

Pulse compression allows a radar to simultaneously achieve the energy of a long pulse and the resolution of a short pulse without the high peak power which is required by a high energy short duration pulse [1]. One of the waveform designs suitable for pulse compression is phase-coded waveform design, which is a long pulse of duration *T* divided into *N* subpulses each of width T_s. Each subpulse has a particular phase, which is selected in accordance with a given code sequence. The pulse compression ratio equals the number of subpulses $N = T/T_s$. In general, a phase-coded waveform with longer code word, in other words, higher pulse compression ratio, can have lower sidelobe of autocorrelation, relative to the mainlobe peak, allowing its main peak to be better distinguished. Moreover, the cross correlation property of the pulse compression codes should be considered in order to reduce the interference among radars when we choose a set of pulse compression codes, because in the real world, a radar may not work alone, such as in the RSN (Radar Sensor Network).

Much time and effort was put in the waveform design. However, the most popular biphase coded waveform is Barker code, which is only found at the maximum length of 13. It is also known that for most good binary sequences of length $N(N > 13)$, the attainable autocorrelation sidelobe levels are approximately $\sqrt{N}$ [2] [3], and the mutual cross correlation peaks of sequences of the same length are larger and usually in the order of $2\sqrt(N)$ to $3\sqrt(N)$. Set of binary sequences of length N with autocorrelation sidelobes and cross-correlation peak values both of approximately $\sqrt(N)$ are only achieved in paper [4]. In addition to binary sequences, other sources [5] [6] [7] provided and intensively analyzed polyphase codes with better Doppler tolerance and lower range sidelobes (such as the Frank and P1 codes, the Butler-matrix derived P2 code and the linear-frequency derived P3 and P4 codes). However, the sidelobe's range of the polyphase codes can not be as low as zero either. The structure of polyphase codes is more complicated and is not easy to generate comparing with binary codes. On the other hand, for the periodic sequences, the lowest periodic autocorrelation function (ACF) that could be achieved for binary sequences, as in the case of m-sequences [8] or Legendre sequences, is $|R_i(\tau \neq 0) = 1|$. GMW [9] has the same periodic ACF properties, but posses larger linear complexity. Considering the non-binary case, it is possible to find perfect sequences, such as two valued Golomb sequences, Ipatov ternary sequences, Frank sequences, Chu sequences, and modulatable sequences. It should be noted that for both binary and non-binary cases, it is impossible for the sequences to have perfect ACF and cross correlation function (CCF) simultaneously although ideal CCFs could be achieved alone. One can synthesize a set of non-binary sequences with impulsive ACF and the lower bound of CCF: $R_{ij} = \sqrt{N}, \forall \tau, i \neq j$ [10][11], which is governed by Welch bound and Sidelnikov bound.

In a word, so far in the previous work, range sidelobes could hardly reach as low as zero. In addition, it has also been well proven that it is impossible to design a set of codes with ideal impulsive autocorrelation function and ideal zero cross-correlation functions, since the corresponding parameters have to be limited by certain bounds, such as Welch bound [10],

978-1-4244-5239-2/09/$26.00 ©2009 IEEE

Sidelnikov bound [11], Sarwate bound [12], Levenshtein bound [13], etc. To overcome these difficulties, the new concepts, generalized orthogonality (GO), also called Zero Correlation Zone (ZCZ) is introduced. Therefore, based on the ZCZ [14] concept, we propose triphase coded waveforms called ZCZ sequence-pair set (ZCZPS), which can reach zero autocorrelation sidelobe during ZCZ and zero mutual cross correlation value during the whole period. We also propose and analyze a method that optimized punctured sequence-pair joins together with Hadamard matrix to construct the triphase coded waveforms called optimized punctured ZCZ sequence-pairs set (optimized punctured ZCZPS), and subsequently apply them to a radar detection system. For the performance evaluation of the proposed triphase coded waveforms, an example is presented and investigated in the radar targets detection simulation system. According to the simulation performances, our proposed new codes can be effective candidates for pulse compression application.

The rest of the paper is organized as follows. Section 2 introduces the definition and properties of ZCZPS. In Section 3, the optimized punctured ZCZPS is introduced, and a method using optimized punctured sequence-pair and Hadamard matrix to construct ZCZPS is given and proved. In Section 4, the properties and ambiguity function of optimized punctured ZCZPS are simulated and analyzed. In section 5, the performance of optimized punctured ZCZPS is investigated in radar targets detection simulation system comparing with P4 code. In Section 6, final conclusions are made on optimized punctured ZCZPS.

DEFINITIONS OF ZCZ SEQUENCE-PAIR SET

Zero Correlation Zone is a new concept provided by Fan [14] in which the autocorrelation and cross correlation sidelobes are zero while the time delay is kept within the value Z_0 instead of the whole period of time domain, and Z_0 is called the ZCZ.

We consider ZCZPS $(\mathbf{X}, \mathbf{Y})$, $\mathbf{X}$ is a set of K sequences of length N and $\mathbf{Y}$ is a set of K sequences of the same length N:

$$\mathbf{x}^{(p)} \in \mathbf{X} \quad p = 0, 1, 2, ..., K-1 \tag{1}$$

$$\mathbf{y}^{(q)} \in \mathbf{Y} \quad q = 0, 1, 2, ..., K-1 \tag{2}$$

The periodic autocorrelation function for sequence-pair $(\mathbf{x}^{(p)}, \mathbf{y}^{(p)})$is defined by:

$$R_{\mathbf{x}^{(p)}\mathbf{y}^{(p)}}(\tau) = \sum_{i=0}^{N-1} \mathbf{x}_i^{(p)} \mathbf{y}_{(i+\tau)modN}^{(p)*}, 0 \le \tau \le N-1 \tag{3}$$

The periodic cross correlation function for sequence-pair $(\mathbf{x}^{(p)}, \mathbf{y}^{(p)})$ and $(\mathbf{x}^{(q)}, \mathbf{y}^{(q)}), p \ne q$ is defined by:

$$C_{\mathbf{x}^{(p)}\mathbf{y}^{(q)}}(\tau) = \sum_{i=0}^{N-1} x_i^{(p)} y_{(i+\tau)modN}^{(q)*}, 0 \le \tau \le N-1 \tag{4}$$

$$C_{\mathbf{x}^{(q)}\mathbf{y}^{(p)}}(\tau) = \sum_{i=0}^{N-1} x_i^{(q)} y_{(i+\tau)modN}^{(p)*}, 0 \le \tau \le N-1 \tag{5}$$

For pulse compression sequences, some properties are of particular concern in the optimization for any design in engineering field. They are the peak sidelobe level, the energy of autocorrelation sidelobes and the energy of their mutual cross correlation [4]. Therefore, the peak sidelobe level which represents a source of mutual interference and obscures weaker targets can be presented as $\max_K |R_{\mathbf{x}^{(p)}\mathbf{y}^{(p)}}(\tau)|, \tau \in Z_0$(zero correlation zone) for ZCZPS. Another optimization criterion for the set of sequence-pairs is the energy of autocorrelation sidelobes joined together with the energy of cross correlation. By minimizing the energy, it can be distributed evenly, and the peak autocorrelation level can be minimized as well [4]. Here, the energy of ZCZPS can be employed as:

$$E = \sum_{p=0}^{K-1} \sum_{\tau=1}^{Z_0} R_{\mathbf{x}^{(p)}\mathbf{y}^{(p)}}^2(\tau) + \sum_{p=0}^{K-1} \sum_{q=0}^{K-1} \sum_{\tau=0}^{N-1} C_{\mathbf{x}^{(p)}\mathbf{y}^{(q)}}(\tau) \quad (p \ne q) \tag{6}$$

According to (6), it is obvious to see that the energy can be kept low while minimizing the autocorrelation sidelobes and cross correlation of the sequence-pair set.

As a result, the ZCZPS could be constructed to minimize the autocorrelation sidelobes and cross correlation of the sequence-pair set, and the definition of ZCZPS can be expressed:

Definition 2-1 Assume $(\mathbf{x}^{(p)}, \mathbf{y}^{(p)})$ to be a sequence-pair of set $(\mathbf{X}, \mathbf{Y})$ of length N and the number of sequence-pairs K, where $p = 0, 1, ..., K-1$. If sequences in the set satisfy the following equation:

$$\begin{aligned} R_{\mathbf{x}^{(p)}\mathbf{y}^{(q)}}(\tau) &= \sum_{i=0}^{N-1} x_i^{(p)} y_{(i+m)mod(N)}^{(q)*} \\ &= \begin{cases} \lambda N, & \text{for } \tau = 0, p = q \\ 0, & \text{for } \tau = 0, p \ne q \\ 0, & \text{for } 0 < |\tau| \le Z_0 \end{cases} \end{aligned} \tag{7}$$

where $0 < \lambda \le 1$, $\tau = m\tau_c$ and $i = 0, 1, ..., N-1$, then $(\mathbf{x}^{(p)}, \mathbf{y}^{(p)})$ is called a ZCZ sequence-pair, $ZCZP(N, K, Z_0)$ is an abbreviation, and $(\mathbf{X}, \mathbf{Y})$ is called a ZCZ sequence-pair set, $ZCZPS(N, K, Z_0)$ is an abbreviation.

OPTIMIZED PUNCTURED ZCZ SEQUENCE-PAIR SET

A. Definition of Optimized Punctured ZCZ Sequence-pair Set

Matsufuji and Torii have provided some methods of constructing ZCZ sequences in [15] [16]. In this section, we apply optimized punctured sequence-pair [17] to Zero Correlation Zone to construct our newly provided triphase coded waveform–optimized punctured ZCZ sequence-pair set (optimized punctured ZCZPS). In other words, optimized punctured ZCZPS is a specific kind of ZCZPS.

Definition 3-1 [17] Sequence $\mathbf{u} = (u_0, u_1, ..., u_{N-1})$ is the punctured sequence for $\mathbf{v} = (v_0, v_1, ..., v_{N-1})$,

$$u_j = \begin{cases} 0, & \text{if } u_j \text{ is punctured} \\ v_j, & \text{if } u_j \text{ is Non-punctured} \end{cases} \tag{8}$$

where P is the number of punctured bits in sequence **v**. Then, suppose $v_j = (-1, 1)$, **u** is P-punctured binary sequence, $(\mathbf{u}, \mathbf{v})$ is called a punctured binary sequence-pair.

Theorem 3-1 [17] The autocorrelation of punctured sequence-pair $(\mathbf{u}, \mathbf{v})$ is defined as

$$R_{\mathbf{uv}}(\tau) = \sum_{i=0}^{N-1} u_i v_{(i+m) mod N}, 0 \le m \le N-1 \tag{9}$$

where $\tau = m\tau_c$. If the punctured sequence-pair has the following autocorrelation property:

$$R_{\mathbf{uv}}(\tau) = \begin{cases} E, & \text{if } m \equiv 0 \text{mod} N \\ 0, & \text{others} \end{cases} \tag{10}$$

the punctured sequence-pair is called optimized punctured sequence-pair [17]. Where, $E = \sum_{i=0}^{N-1} u_i v_{(i+m) mod N} = N - p$, is the energy of punctured sequence-pair.

Definition 3-2 If $(\mathbf{X}, \mathbf{Y})$ in Definition 2-1 is constructed by optimized punctured sequence-pair and a certain matrix, such as Hadamard matrix or an orthogonal matrix, where

$$x_i^{(p)} \in (-1, 1), \quad i = 0, 1, 2, ..., N-1$$
$$y_i^{(q)} \in (-1, 0, 1), \quad i = 0, 1, 2, ..., N-1$$

$$\begin{aligned} R_{\mathbf{x}^{(p)}\mathbf{y}^{(q)}}(\tau) &= \sum_{i=0}^{N-1} x_i^{(p)} y_{(i+m) mod N}^{(q)*} \\ &= \begin{cases} \lambda N, & \text{for } \tau = 0, p = q \\ 0, & \text{for } \tau = 0, p \ne q \\ 0, & \text{for } 0 < |\tau| \le Z_0 \end{cases} \end{aligned} \tag{11}$$

where $0 < \lambda \le 1$ and $\tau = m\tau_c$, then $(\mathbf{X}, \mathbf{Y})$ can be called optimized punctured ZCZ sequence-pair set.

B. Design For Optimized Punctured ZCZ Sequence-pair Set

Based on odd length optimized punctured binary sequence pairs and a Hadamard matrix, an optimized punctured ZCZPS can be constructed from the following steps:

Step 1: Given an odd length optimized punctured binary sequence-pair $(\mathbf{u}, \mathbf{v})$, the length of each sequence is N_1

$$\mathbf{u} = u_0, u_1, ..., u_{N_1-1}, u_i \in (-1, 1),$$
$$\mathbf{v} = v_0, v_1, ..., v_{N_1-1}, v_i \in (-1, 0, 1),$$

Step 2: Given Hadamard matrix **B**(consists of N_2 Walsh sequences), the length of the sequence is N_2 which is equal to the number of the sequences.

$$\mathbf{B} = (\mathbf{b}^{(0)}; \mathbf{b}^{(1)}; ...; \mathbf{b}^{(N_2-1)}), \mathbf{b}^{(p)} = (b_0^{(p)}, b_1^{(p)}, ..., b_{N_2-1}^{(p)})$$

Step 3: Doing bit-multiplication of optimized punctured binary sequence-pair and each row of Hadamard matrix B,

$$x_j^{(p)} = u_{j \ modN_1} b_{j \ modN_2}^{(p)}, 0 \le p \le N_2 - 1, 0 \le j \le N - 1,$$
$$\mathbf{X} = (\mathbf{x}^{(0)}; \mathbf{x}^{(1)}; ...; \mathbf{x}^{(N_2-1)}), \mathbf{x}^{(p)} = (x_0^{(p)}, x_1^{(p)}, ..., x_{N-1}^{(p)})$$
$$y_j^{(p)} = v_{j \ modN_1} b_{j \ modN_2}^{(p)}, 0 \le p \le N_2 - 1, 0 \le j \le N - 1,$$
$$\mathbf{Y} = (\mathbf{y}^{(0)}, \mathbf{y}^{(1)}, ..., \mathbf{y}^{(N_2-1)}), \mathbf{y}^{(p)} = (y_0^{(p)}, y_1^{(p)}, ..., y_{N-1}^{(p)})$$

Since the optimized punctured binary sequence-pairs are of odd lengths and the lengths of Walsh sequence are $2^n, n = 1, 2, ...$, it is easy to see that $gcd(N_1, N_2) = 1$, common divisor of N_1 and N_2 is 1, $N = N_1 * N_2$. The three steps make the sequence-pair set $(\mathbf{X}, \mathbf{Y})$ an optimized punctured ZCZPS, where ZCZ $Z_0 = N_1 - 1$. The length of each sequence in optimized punctured ZCZPS is $N = N_1 * N_2$ that depends on the product of length of optimized punctured sequence-pair and the length of a row in Hadamard matrix. The number of sequence-pairs in optimized punctured ZCZPS rests on the order of the Hadamard matrix. The sequence $\mathbf{x}^{(p)}$ in $\mathbf{X}$ and the corresponding sequence $\mathbf{y}^{(p)}$ in $\mathbf{Y}$ construct an optimized punctured ZCZP $(\mathbf{x}^{(p)}, \mathbf{y}^{(p)})$ that can be used as a phase coded waveform, such as $\mathbf{x}^{(p)}$ for radar transmitter and $\mathbf{y}^{(p)}$ for radar receiver. The phase states for any sequence-pair among $(\mathbf{x}^{(p)}, \mathbf{y}^{(p)})$ are only of three options, so our newly provided optimized punctured ZCZPS is a new set of triphase codes.

The correlation property of the sequence-pair in optimized punctured ZCZPS is:

$$\begin{aligned} R_{\mathbf{x}^{(p)}\mathbf{y}^{(q)}}(\tau) &= R_{\mathbf{uv}}(\tau \ modN_1) R_{\mathbf{b}^{(p)}\mathbf{b}^{(q)}}(\tau \ modN_2) \\ &= \begin{cases} EN_2, & \text{if } m = 0, p = q \\ 0, & \text{if } 0 < |m| \le N_1 - 1, p = q \\ 0, & \text{if } 0 \le |m| \le N_1 - 1 \text{ and } p \ne q \end{cases} \end{aligned}$$

where $N_1 - 1$ is the Zero Correlation Zone Z_0 and $\tau = m\tau_c$.

Proof:

1) When $p = q$,

$$\tau = 0, R_{\mathbf{uv}}(0) = E, R_{\mathbf{b}^{(p)}\mathbf{b}^{(q)}}(0) = N_2,$$
$$R_{\mathbf{x}^{(p)}\mathbf{y}^{(q)}}(0) = R_{uv}(0) R_{\mathbf{b}^{(p)}\mathbf{b}^{(q)}}(0) = EN_2;$$
$$0 < |\tau| \le N_1 - 1, R_{\mathbf{uv}}(\tau) = 0,$$
$$R_{\mathbf{x}^{(p)}\mathbf{y}^{(q)}}(\tau) = R_{\mathbf{uv}}(m \ modN_1) R_{\mathbf{b}^{(p)}\mathbf{b}^{(q)}}(m \ modN_2) = 0;$$

2) When $p \ne q$,

$$\tau = 0, R_{\mathbf{b}^{(p)}\mathbf{b}^{(q)}}(0) = 0,$$
$$R_{\mathbf{x}^{(p)}\mathbf{y}^{(q)}}(0) = R_{\mathbf{uv}}(m \ modN_1) R_{b^{(p)}b^{(q)}}(m \ modN_2) = 0;$$
$$0 < |\tau| \le N_1 - 1, R_{\mathbf{uv}}(\tau) = 0,$$
$$R_{\mathbf{x}^{(p)}\mathbf{y}^{(q)}}(\tau) = R_{\mathbf{uv}}(m \ modN_1) R_{\mathbf{b}^{(p)}\mathbf{b}^{(q)}}(m \ modN_2) = 0.$$

According to Definition 2-1, the sequence-pair set constructed by the above method is a ZCZPS.

PROPERTIES OF OPTIMIZED PUNCTURED ZCZ SEQUENCE-PAIR SET

Considering the optimized punctured ZCZPS that is constructed by the method mentioned in the last part, the auto-correlation and cross correlation properties can be simulated and analyzed with Matlab. For example, the optimized punctured ZCZPS $(\mathbf{X}, \mathbf{Y})$ is constructed by 31-length optimized punctured binary sequence-pair $(\mathbf{u}, \mathbf{v})$, $\mathbf{u} = [+++-----+-+-++++--------+--+-----+++-++-+-]$, $\mathbf{v} = [+++000+0+0+++0000+00+00+++0++0]$ (using $'+'$ and $'-'$ symbols for $'1'$ and $'-1'$) and Hadamard matrix **H** of order 4. We follow the three steps presented in Section **B** to construct the 124-length optimized punctured ZCZPS.

The number of sequence-pairs here is 4, and the length of each sequence is $31 * 4 = 124$. The first row of each matrix $\mathbf{X} = [\mathbf{x}_1; \mathbf{x}_2; \mathbf{x}_3; \mathbf{x}_4]$ and $\mathbf{Y} = [\mathbf{y}_1; \mathbf{y}_2; \mathbf{y}_3; \mathbf{y}_4]$ constitute a certain optimized punctured ZCZP $(\mathbf{x}_1, \mathbf{y}_1)$. Similarly, the second row of each matrix $\mathbf{X}$ and $\mathbf{Y}$ constitute another optimized punctured ZCZ sequence-pair $(\mathbf{x}_2, \mathbf{y}_2)$ and so on.

$$
\begin{aligned}
\mathbf{x}_1 &= [+++-----+-+-++++----+--\\
&\quad +--+++-+-+-++++---+-+-\\
&\quad +++---+--+--+-+++-+-+\\
&\quad +++---+-+-+++----+--+\\
&\quad --+++-+-+-++++---+-+-\\
&\quad ++---+--+--+-+++-+-+],\\
\mathbf{y}_1 &= [+++000+0+0+++0000+00\\
&\quad +00+++0++0+++000+0+0+++00\\
&\quad 00+00+00+++0++0+++000+0+0\\
&\quad ++0000+00+00+++0++0+++00\\
&\quad 0+0+0+++0000+00+00+++0++0];\\
\mathbf{x}_2 &= [+-+--+---------+--+-+++-\\
&\quad --++-+++--+-+-+++++++\\
&\quad +-+++-+---++++--+---++++\\
&\quad -+--+---------+--+-+-++--\\
&\quad -++-+++---+-+-+++++++++\\
&\quad -++-+---++++--+---++++],\\
\mathbf{y}_2 &= [+--+000-0-0--+-0000+00\\
&\quad -00+-+0+-0-++-+000+0+0+-+00\\
&\quad 00-00+00--+-0-+0+-+-000-0-0\\
&\quad -+-0000+00-00+-+0+-0-+-+00\\
&\quad 0+0+0+-+0000-00+00-+-0-+0].
\end{aligned}
$$

A. Autocorrelation and Cross Correlation Properties

The autocorrelation property $R(\mathbf{x}_1, \mathbf{y}_1)$ and cross correlation property $R(\mathbf{x}_1, \mathbf{y}_2) = R(\mathbf{y}_1, \mathbf{x}_2)$ of 124-length optimized punctured ZCZPS $(\mathbf{X}, \mathbf{Y})$, are shown in Fig.1.

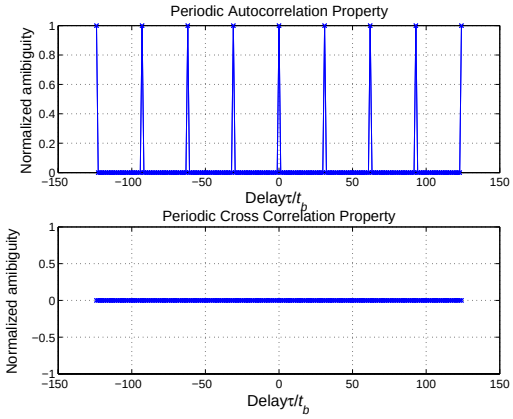


Fig. 1. Periodic autocorrelation property of optimized punctured ZCZPS

From the Fig.1, the sidelobe of autocorrelation of ZCZPS can be as low as 0 when the time delay is kept within $Z_0 = N_1 - 1 = 30$ and the cross correlation value is 0 during the whole time domain.

It is known that a suitable criterion for evaluating code of length N is the ratio of the peak signal divided by the peak signal sidelobe (PSR) of their autocorrelation function, which can be bounded by [18]

$$[PSR]_{dB} \leq 20logN = [PSR_{max}]_{dB} \tag{12}$$

The only uniform phase codes that can reach the PSR_{max} are the Barker codes whose length is equal or less than 13. The sidelobe of the new code shown in Fig.1 can be as low as 0, and the peak signal divided by the peak signal sidelobe can be as large as infinite. Besides, the length of the new code is various and much longer than the length of the Barker code.

B. Ambiguity function

When the transmitted impulse is reflected by a moving target, the reflected echo signal includes a linear phase shift, which comes from the Doppler shift F_d [18]. As a result of the Doppler shift F_d, the main peak of the autocorrelation function is reduced. At the same time, SNR degradation occurs as well.

The ambiguity function, which is commonly used to analyze the radar performance within Doppler shift can be found in [18] shown as following:

$$A(\tau, F_D) = |\int_{-\infty}^{\infty} x(s) e^{j2\pi F_D s} x^*(s-\tau) ds| \equiv |\hat{A}(t, F_D)| \tag{13}$$

where t is the time delay and F_D is the Doppler shift.

In [19], PAF (Periodic Ambiguity Function) is introduced by Levanon as an extension of the periodic autocorrelation for Doppler shift. And the single-periodic complex envelope is [20]:

$$
\begin{aligned}
A_{periodic}(\tau, F_D) &\equiv |\frac{1}{T}\int_0^T x(s+\frac{\tau}{2}) e^{j2\pi F_D s} x^*(s-\frac{\tau}{2}) ds| \\
&\equiv |\hat{A}_{periodic}(\tau, F_D)|
\end{aligned} \tag{14}
$$

where T is one period of the signal.

We are studying sequence-pairs in this research, so we use different codes for transmitting part and receiving part. The single-period ambiguity function for ZCZPS can be rewritten as

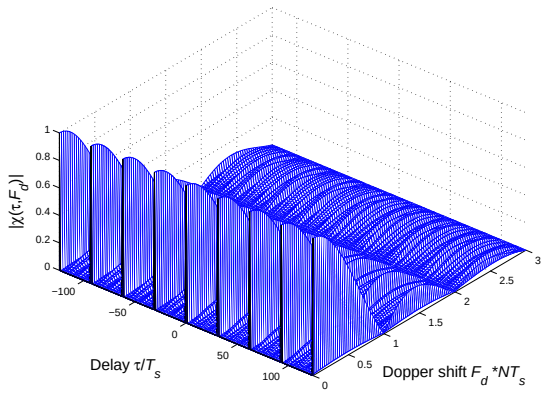
$$A_{pair}(\tau, F_D) \equiv |\hat{A}_{pair}(\tau, F_D)| \tag{15}$$

The $\hat{A}_{pair}(\tau, F_D)$ in one period of length $T = N\tau_c$ can be expressed as:

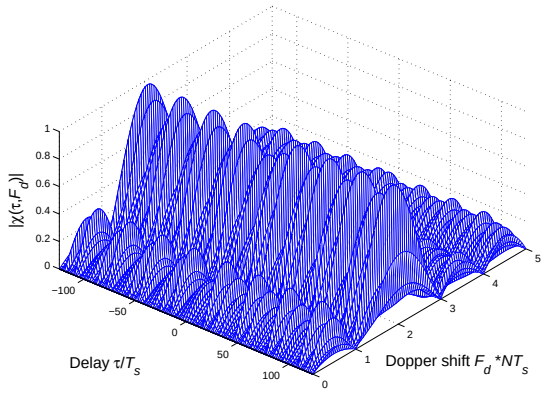
$$\hat{A}_{pair}(\tau, F_D) = \frac{1}{T}\int_0^T x^{(p)}(s+\frac{\tau}{2}) e^{j2\pi F_D s} y^{(p)*}(s-\frac{\tau}{2}) ds \tag{16}$$

where $p, q = 0, 1, 2..., K-1$, $T = N\tau_c$ is one period of the signal and τ_c is one bit duration. At the same time, when $p = q$, equation (16) can be used to analyze the autocorrelation performance within the Doppler shift, and when $q \neq p$, equation (16) can be used to analyze the cross correlation performance within the Doppler shift. Equation (16) is plotted

in Fig.2 in a three-dimensional surface plot to analyze the radar performance of optimized punctured ZCZPS within the Doppler shift. Here, maximal time delay is 1 unit (normalized to length of the code, in units of NT_s) and the maximal doppler shift is 5 units for cross correlation and 3 units for autocorrelation (normalized to the inverse of the length of the code, in units of $1/NT_s$).



(a)



(b)

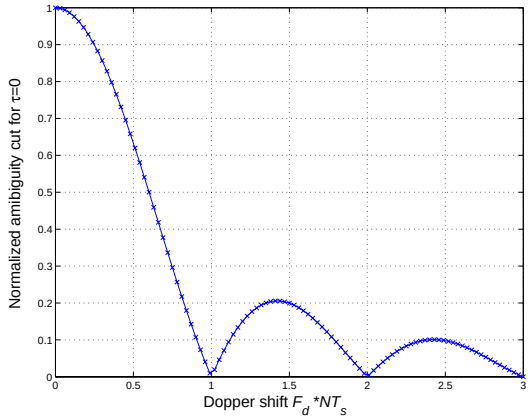
Fig. 2. Ambiguity function of 124-length ZCZPS: (a) autocorrelation (b) cross correlation

In Fig.2(a), there is a relative uniform plateau suggesting low and uninform sidelobes. This low and uniform sidelobes minimizes target masking effect in ZCZ of time domain, where $Z_0 = 30$, $-30 \leq \tau \leq 30$. From Fig.2(b), we can consider a cross correlation property between any two optimized punctured ZCZ sequence-pairs in the ZCZ sequence-pair set such as $R(\mathbf{x}_1, \mathbf{y}_2)$ or $R(\mathbf{y}_1, \mathbf{x}_2)$ where $(\mathbf{x}_1, \mathbf{y}_1)$ and $(\mathbf{x}_2, \mathbf{y}_2)$ are two pairs of optimized punctured ZCZP. A 124-length optimized punctured ZCZP is tolerant of Doppler shift when the Doppler shift is not large. When the Doppler shift is zero, the range sidelobe of cross correlation of our proposed code is zero in the whole time domain.

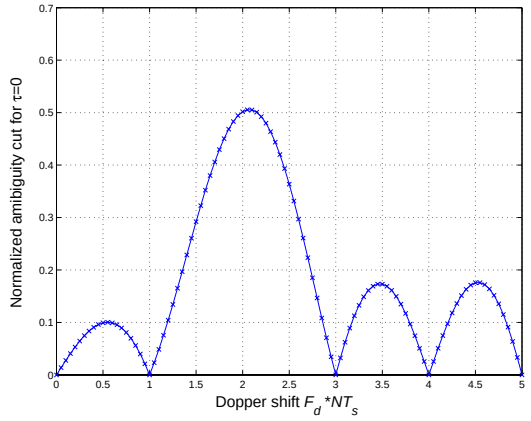
As synchronization technology develops exponentially in the industrial world, time delay can, to some extent, be well controlled. Therefore, it is necessary to investigate the performance of our proposed code without time delay. When $t = 0$, the ambiguity function can be expressed as:

$$\hat{A}_{pair}(0, F_D) = \int_0^{(N-1)T_s} x^{(p)}(s) y^{(q)*}(s) e^{(j2\pi F_D s)} ds \quad (17)$$

And this kind of Doppler shift performance with no time delay is presented in the Fig.3.



(a)



(b)

Fig. 3. Doppler shift of 124-length ZCZPS(time delay=0): (a) autocorrelation (b) cross correlation

Fig.3(a) illustrates that without a time delay and having the Doppler shift less than 1 unit, the autocorrelation value of optimized punctured ZCZPS falls sharply during one unit, and the trend of the amplitude over the whole frequency domain decreases as well. Fig.3(b) shows that there are some convex surfaces in the cross correlation performance. One should observe Fig.3(a) and Fig.3(b), when Doppler frequencies equal to multiples of the pulse repetition frequency ($PRF = 1/PRI = 1/Ts$), all the ambiguity value turns to zero except when Doppler frequency is equal to 2 PRF for cross correlation. That is the same as many widely used pulse compression binary code such as the Barker code. Overall, the amibuguity function performances of optimized punctured ZCZP can be as efficient as conventional pulse compression binary code.

SYSTEM SIMULATION IN RADAR SYSTEM

According to [18], P_D (Probability of Detection), P_{FA} (Probability of False Alarm) and P_M (Probability of Miss) suffice to specify all of the probabilities of interest in a radar system. Therefore, we simulated the above three probabilities of optimized punctured ZCZP to a radar system in this section. The performance of the 124-length P4 code is also studied in order to compare with the performance of the optimized punctured ZCZP of corresponding length. In the simulation model, 10^5 times of Monte-Carlo simulation has been run for each SNR value. The Doppler shift frequency that is kept less than 1 unit (normalized to the inverse of the length of the code, in units of $1/NT_s$) is a random variable, and the time delay is assumed to be zero. Also, threshold detection is used in this coherent system where the threshold is adaptively adjusted.

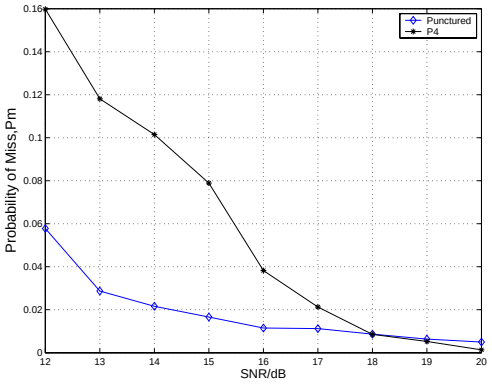


Fig. 4. Probability of miss targets detection (No time delay, Doppler shift less than 1): 124-length optimized punctured ZCZP VS. 124-length P4 code

In Fig.4, the probabilities of a miss target detection P_M of the system using the 124-length optimized punctured ZCZP are lower than the 124-length P4 code especially when the SNR is not large. When SNR is larger than 18 dB, both probabilities of the system's miss targets approach zero.

We plotted the probability of detection P_D versus probability of false alarm P_{FA} of the coherent receiver in Fig.5.

Fig.5 shows the performance of the 124-length optimized punctured ZCZP and the same length P4 code when the SNR is 12dB and 14dB. Within the same SNR value either 12dB or 14dB, the probabilities of detection of optimized punctured ZCZP are much larger than the detection probabilities of P4 code. While this is all happening, the false alarm probabilities of the first code are also smaller than that of the latter code. In other words, the 124-length optimized punctured ZCZP has higher target detection probability while keeping a lower false alarm probability. Furthermore, from observing Fig.5, the 124-length optimized punctured ZCZP has a much better performance at 12dB SNR than the 124-length P4 code at 14dB SNR.

CONCLUSION

The definition and properties of a set of our newly provided triphase coded waveforms–ZCZ sequence-pair set were discussed in this paper. Based on optimized punctured sequence-pair and Hadamard matrix, we have investigated a constructing method for the triphase coded waveform–optimized punctured ZCZPS made up of a set of optimized punctured ZCZPs along with studying its properties. The significant advantage of the optimized punctured ZCZPS is that it considerably reduces the sidelobe as low as zero in the ZCZ, and also zero mutual cross correlation value in the whole time domain. The disadvantage of our proposed code is that the number of the sequences in the set depends on the order of Hadamard matrix that is limited by $2^k, (k = 0, 1, ...)$. However, 124-length optimized punctured ZCZPS has better performance than 124-length P4 code when the Doppler shift is kept less than 1 unit. A general conclusion can be drawn that the optimized punctured ZCZPs in an optimized punctured ZCZPS can effectively increase the variety of candidates for pulse compression codes if and only if optimized punctured ZCZPS has much better autocorrelation and cross correlation properties than the optimum biphase codes (longer than 13), whose autocorrelation sidelobes and cross correlation peak value have been found to be both approximately $\sqrt{N}$. Because of the ideal cross correlation properties of optimized punctured ZCZPS, future work should focus on the application of the optimized punctured ZCZPS in a multiple radar system such as a radar sensor network.

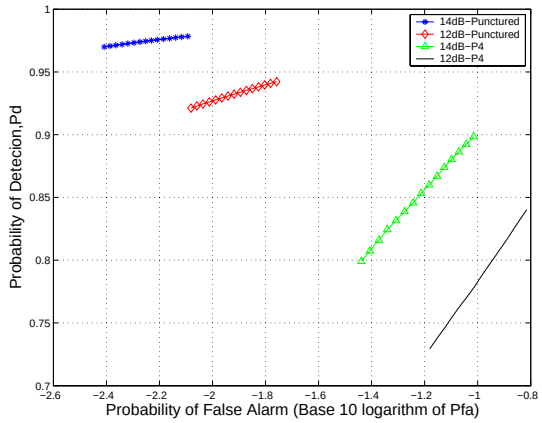


Fig. 5. Probability of detection versus probability of false alarm of the coherent receiver(No time delay, Doppler shift less than 1) : 124-length optimized punctured ZCZ sequence-pair VS. 124-length P4 code

ACKNOWLEDGEMENT

This work was supported in part by Office of Naval Research (ONR) under Grant N00014-07-1-0395 and N00014-07-1-1024, and National Science Foundation (NSF) under Grant CNS-0721515 and CNS-0831902.

REFERENCES

[1] S. Ariyavisitakul, N. Sollenberger, and L. Greenstein, *Introduction to Radar System*, Tata McGraw-Hill, 2001.

[2] A. M. Boehmer, "Binary pulse compression codes," *IEEE Trans.Informaion Theory*, vol.IT-13, pp.156-167, April 1967.

[3] R. Turyn, "On Barker codes of event length," *Proc.IEEE*, vol.51,9.1256, September 1963.

[4] U. Somaini, "Bianry sequences with good autocorrelation and cross correlation properties," *IEEE Transactions on Aerospace and Electronic Systems*, AES-11, 6, 1226-1231, Nov.1975.
[5] R. L. Frank, "Polyphase codes with good nonperiodic correlation properties", *IEEE Transactions on Information Theory*, IT. -9, pp. 43-45, Jan. 1963.
[6] B. L. Lewis and F. F. Kretschuner, "A new class of polyphase pulse compression codes and techniques", *IEEE Transactions on Aerospace and Electronic Systems*, AES-17, pp. 364-372, May. 1981.
[7] B. L. Lewis and F. F. Kretschuner, "Linear frequency modulation derived polyphase pulse compression codes", *IEEE Transactions on Aerospace and Electronic Systems*, AES-18, pp. 637-641, Sep. 1982.
[8] S. W. Golomb, *Shift register sequences*, Holden-Day, 1967, Revised edn: Aegean Park Press, Laguna Hills, CA, 1982.
[9] R. A. Scholtz and L. R. Welch, "GMW sequences", *IEEE Transactions on Information Theory*, IT. -30, pp. 548-553, Jan. 1984.
[10] L. R. Welch, "Lower bounds on the maximum cross correlation of signals," *IEEE Trans. Inform. Theory*, IT-20, (3), pp. 397-399, 1974.
[11] V. M. Sidelnikov, "On mutual correlation of sequences," *Soviet Math doklady*, 12,pp. 197-201, 1971.
[12] D. V. Sarwate and M .B. Pursley, "Crosscorrelation properties of pseudorandom and related sequences," *Proc. IEEE*, 68, (3), pp. 593-620, 1980.
[13] P. G. Boyvalenkov, D. P. Danev and S.P. Bumova, "Upper bounds on the minimum distance of spherical codes," *IEEE Trans. Inform. Theory*, 42, (5), pp. 1576-1581, 2002.
[14] P. Z. Fan, N. Suehiro, N. Kuroyanagi and X. M. Deng, "A class of binary sequences with zero correlation zone," *IEE Electron.Letter*, 35 (10): 777-779, 1999.
[15] S. Matsufuji, N Suehiro , N Kuroyanagi and P Z Fan, "Two types of polyphase sequence set for approximately synchronized CDMA systems," *IEICE Trans. Fundamentals*, E862A(1): 229-234, Jan. 2003.
[16] H. Torii, M. Nakamura and N. Suehiro, "A new class of zero correlation zone sequences," *Tran. Inform.Theory*, 50: 559-565, Mar. 2004.
[17] T. Jiang, *Research on Quasi-Optimized Binary Signal Pair and Perfect Punctured Binary Signal Pair Theory*, Ph.D Dissertation: Yanshan University, 2003.
[18] M.A.Richards, *Fundamentals of Radar Signal Processing*, McGraw-Hill, 2005.
[19] N. Levanon and A. Freedman, "Periodic ambiguity function of CW signals with perfect periodic autocorrelation", *IEEE Transactions on Aerospace and Electronic Systems*, AES-28(2), pp. 387-395, Apr. 1992.
[20] L. W. Couch, "Effects of modulation nonlinearity on the range response of FM radars", *IEEE Transactions on Aerospace and Electronic Systems*, AES-9(4), pp. 598-606, Jul. 1973.

Situation Assessment via Multi-Target Identification and Classification in Radar Sensor Networks

Hong-Sam T. Le and Qilian Liang
Department of Electrical Engineering
The University of Texas at Arlington
Arlington, TX 76019, USA
E-mail: le@wcn.uta.edu, liang@uta.edu

***Abstract*— DoD has defined three levels of data fusion for Network Centric Warfare (NCW). Level 1 data fusion combines data from single or multiple sensors and sources to provide the best estimate of objects and events in the battlespace. Level 2 data fusion focuses on situation assessment. Level 3 data fusion is threat assessment. To facilitate situation assessment, we investigate the problem of jointly classifying and identifying multiple targets in radar sensor networks where the maximum number of categories and the maximum number of targets in each category are obtained a priori based on statistical data. However, the actual number of targets in each category and the actual number of target categories being present at any given time are assumed unknown. It is assumed that a given target belongs to one category and one identification number. The target signals are modeled as zero-mean complex Gaussian processes. We propose a joint multi-target identification and classification (JMIC) algorithm for radar surveillance using cognitive radars. The existing target categories are first classified and then the targets in each category are accordingly identified. Simulation results are presented to evaluate the feasibility and effectiveness of the proposed JMIC algorithm in a query surveillance region.**

Index Terms : Situation assessment, radar sensor networks, multiple target identification and classification, Gaussian process.

I. Introduction

In current and future military operational environments, such as Global War on Terrorism (GWOT) and Maritime Domain Awareness (MDA), warfighters require technologies evolved to support information needs regardless of location and consistent with the users level of command or responsibility and operational situation. To support this need, the U.S. Department of Defense (DoD) has developed the concept of Network Centric Warfare (NCW), defined as "*military operations that exploit state-of-the-art information and networking technology to integrate widely dispersed human decision makers, situational and targeting sensors, and forces and weapons into a highly adaptive, comprehensive system to achieve unprecedented mission effectiveness*" [1]. DoD has defined three levels of data fusion for NCW. Level 1 data fusion combines data from single or multiple sensors and sources to provide the best estimate of objects and events in the battlespace in terms of their position, kinematics (e.g. tracks), identity, or identification features. Level 2 data fusion focuses on situation assessment. This requires recognition of objects/entities in the regions of interest, as well as recognizing activities of these objects, and inferring their relationships. Level 3 data fusion is threat assessment which requires inferring intent of objects/entities, or groups of objects, in the regions of interest. Situation assessment needs lower level data fusion results such as multi-target Identification and Classification.

Many algorithms have been suggested to handle the task of multiple target identification and classification. In [7], a Gaussian Mixture Model (GMM) classifier was proposed to distinct target categories in a semi-structured outdoor environment. For radar target identification, a multi-feature decision space approach was discussed in detail in [8]. In [4], complex Gaussian distribution was applied to cognitive radar sensor network target recognition. Collaborative classification algorithms [6] were applied to single target scenarios and then extended to more complex scenarios of multiple targets.

We consider the scenario wherein the total number of targets K is unknown in a region of interest and a query regarding to the classification of these targets and the identification of the targets in each category is inquired. This is the general surveillance scenario since each target belonging to one distinct category as in [3] is no longer considered. In this work, some targets now share the same target category but possess different identification numbers. In order to perform this higher complexity version of surveillance scenario, we assume that each given target belongs to one distinct pair of one target category and one

978-1-4244-5239-2/09/$26.00 ©2009 IEEE

identification number. Based on statistical data, we then reasonably assume that the maximum number of target categories M and the maximum number of targets N in each category are a priori known parameters. However, the actual number of existing target categories and the actual number of targets being present in each category at any given time are unknown. It is assumed that there are R cognitive radar sensors in the query region.

Within the above-described framework, we propose a joint multi-target identification and classification (JMIC) algorithm for radar surveillance. Firstly, the existing target categories are classified based on $M^\star$-ary hypothesis testing where $M^\star = 2^M$. Note that, $M^\star$ hypotheses correspond to all possibilities we may have regarding to the presence or absence of each category. Thereafter, based on the result obtained from classification specifying which target categories exist, we identify targets belonging to each detected category. Targets in a category are identified based on their identification numbers or identification indices. Therefore, $N^\star$ ($N^\star$ = 2^N - 1) hypotheses are set up corresponding to all scenarios of presence or absence of each target identification index. Numerical results based on simulated data are finally presented to demonstrate the feasibility and effectiveness of the proposed JMIC algorithm in a query surveillance region.

The rest of the paper is organized as follows. In section II, we provide a framework and formulate the multi-target classification and identification problem in a cognitive radar network. In section III, we propose the joint multi-target identification and classification algorithm. Simulation results are presented in section IV. Finally, section V concludes the paper.

II. System description and problem formulation

The general system architecture for MTIC problem used in this work is shown in Fig. 1. This architecture accommodates the deployment of R cognitive radar sensors (CRSs). These sensors will collect and then send all the target signals to the fusion center. It is assumed that there are K targets in the region of interest. Each target is considered as a point source and target signals are modeled as zero-mean complex Gaussian processes [3]. All measurements from sensors are combined to reduce the impact of target signal variability. At any given time, the measurements in distinct cognitive radar sensors are approximately independent.

We assume that at most M distinct target categories and N targets in each category are present in the surveillance region in the observation duration. However, the actual existing number of target categories is unknown. Therefore, we set up 2^M hypotheses corresponding to all possible scenarios of presence or absence of each target category. We denote these hypotheses by H_k (k = 0, 1, ..., $2^M - 1$).

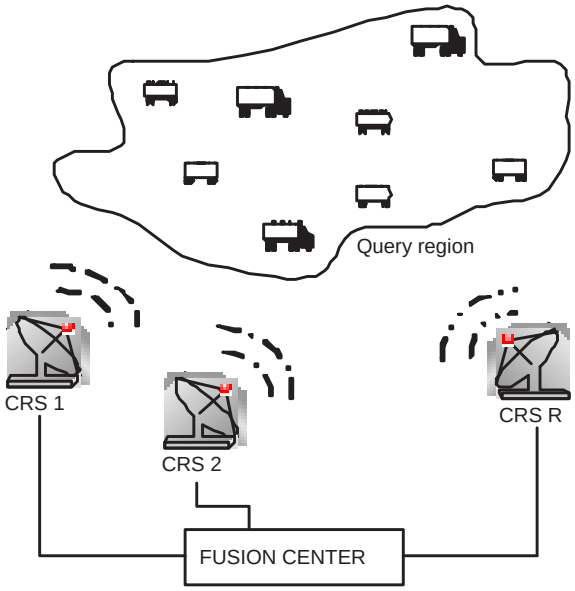


Fig. 1. System architecture for JMIC algorithm

Target categories are denoted by i (i = 1, 2, ..., M) and in each ith category, targets are identified by the identification indices j (j = 1, 2, ..., N). We use the parameter $b_{ij} \in \{0, 1\}$ to denote the event in which target of category i, index j is absent or present. Specifically,

$$b_{ij} = \begin{cases} 0 & \text{if target of category } i\text{, index } j \text{ is absent} \\ 1 & \text{if target of category } i\text{, index } j \text{ is present} \end{cases}$$

Classification and identification parameters are given in Table I wherein each row represents one target category and each column represents one target index. The probability of target of category i, index j being absent $P(b_{ij} = 0)$ is denoted by p_{ij}, i.e., $P(b_{ij} = 0) = p_{ij}$. Hence, the probability of presence of this target $P(b_{ij} = 1)$ is: $P(b_{ij} = 1)$ = 1- p_{ij}.

We employ hypothesis H_0 for scenario of no category being present, hypothesis H_1 for scenario of category 1 being present,..., and hypothesis H_{2^M-1} for scenario of all M categories being present. We assume that the total number of targets K in the region of interest is unknown. In the case of K = 0, i.e., there is no target in the surveillance region, hypothesis H_0 is chosen. The prior probability of hypothesis H_0 is given by:

$$\begin{aligned} P(H_0) &= \text{P } \{\text{no category present}\} \\ &= P(\forall b_{1j} = 0; \forall b_{2j} = 0; ...; \forall b_{Mj} = 0), \\ &\qquad \text{for } j = 1, 2, ..., N \end{aligned} \tag{1}$$

Since the possibilities for presence or absence of targets

are independent, we have

$$\begin{aligned} P(H_0) &= P(\forall b_{1j}=0).P(\forall b_{2j}=0)...P(\forall b_{Mj}=0) \\ &= (p_{11}.p_{12}...p_{1N})(p_{21}.p_{22}...p_{2N})...(p_{M1}...p_{MN}) \\ &= \prod_{j=1}^{N} p_{1j} \cdot \prod_{j=1}^{N} p_{2j} \cdots \prod_{j=1}^{N} p_{Mj} \end{aligned} \quad (2)$$

Similarly, the prior probability of H_1 is given by:

$$\begin{aligned} P(H_1) &= \text{P}\{\text{category 1 present}\} \\ &= P(\textit{at least one } b_{1j} = 1; \forall b_{2j}=0; ...; \forall b_{Mj}=0) \\ &= P(\exists \textit{ one } b_{1j} = 1).P(\forall b_{2j}=0)...P(\forall b_{Mj}=0) \\ &= (1-\prod_{j=1}^{N} p_{1j}) \cdot \prod_{j=1}^{N} p_{2j} \cdots \prod_{j=1}^{N} p_{Mj} \end{aligned} \quad (3)$$

Generally, we obtain the prior probability of hypothesis H_k in the form as follows:

$$P(H_k) = \prod_{i=1}^{M} [b_i^{(k)}(1-\prod_{j=1}^{N} p_{ij}) + (1-b_i^{(k)}) \prod_{j=1}^{N} p_{ij}] \quad (4)$$

where $b_i^{(k)}$ takes the value of 0 when category i is absent, otherwise $b_i^{(k)}$ takes the value of 1 when category i is present under hypothesis H_k.

III. Joint multi-target identification and classification algorithm

Joint multi-target identification and classification algorithm consists of two steps. In the first step, multiple target classification is implemented to investigate which target categories are present within the entire surveillance region. Then, in the second step, based on classification results, targets in each detected category are identified using identification indices. Our JMIC algorithm relies on the framework previously presented in section II.

A. Multiple Target Classification

The $M^\star$-ary hypothesis testing problem is given by:

$$H_k : \mathbf{z}_l = \mathbf{s}_l + \mathbf{n}_l, \qquad k = 0, 1, ..., 2^M - 1 \quad (5)$$

where $\mathbf{z}_l$ is a feature vector of dimension D collected by the lth (l = 1,2,..., R) cognitive radar sensor. We assume that target signals have the same energy, i.e., these signals are modeled as zero-mean complex Gaussian vectors with covariance matrix $\mathbf{\Sigma}_m$. Thus,

$$\mathbf{s}_l \sim \mathcal{CN}(0, \mathbf{\Sigma}_{s_{lk}}), \quad \text{where} \quad \mathbf{\Sigma}_{s_{lk}} = \sum_{i=1(i\in H_k)}^{M} \sum_{j=1}^{N} b_{ij} \mathbf{\Sigma}_m \quad (6)$$

Signals are corrupted by zero-mean complex white Gaussian noise.

$$\mathbf{n}_l \sim \mathcal{CN}(0, \sigma_n^2 \mathbf{I}). \quad (7)$$

TABLE I
Classification and Identification Parameters

	Index 1	Index 2	Index 3	...	Index N
Category 1	b_{11}	b_{12}	b_{13}	...	b_{1N}
Category 2	b_{21}	b_{22}	b_{23}	...	b_{2N}
Category 3	b_{31}	b_{32}	b_{33}	...	b_{3N}
⋮	⋮	⋮	⋮	⋮	⋮
Category M	b_{M1}	b_{M2}	b_{M3}	...	b_{MN}

Under hypothesis H_k, the probability density function of the feature vector $\mathbf{z}_l$ is given by:

$$\begin{aligned} P(\mathbf{z}_l|H_k) &= p_k(\mathbf{z}_l) \\ &= \frac{1}{\pi^D |\mathbf{\Sigma}_{z_{lk}}|} \exp\{-\mathbf{z}_l^H \mathbf{\Sigma}_{z_{lk}}^{-1} \mathbf{z}_l\} \end{aligned} \quad (8)$$

where $\mathbf{\Sigma}_{z_{lk}} = \mathbf{\Sigma}_{s_{lk}} + \sigma_n^2 \mathbf{I}$

We denote $P(H_k)$ by δ_k. The decision rule for the multiple target classifier is therefore given by:

$$\hat{k} = \arg \max_{k=0,1,...,M^\star-1} p_k(\mathbf{z}_1, \mathbf{z}_2, ..., \mathbf{z}_R)\delta_k \quad (9)$$

Due to the conditional independence of $\mathbf{z}_l$, (9) can be expressed as:

$$\hat{k} = \arg \max_{k=0,1,...,M^\star-1} \prod_{l=1}^{R} p_k(\mathbf{z}_l)\delta_k \quad (10)$$

In term of log-likelihood, we have

$$\begin{aligned} \Delta_k(\mathbf{z}_1, \mathbf{z}_2, ..., \mathbf{z}_R) &= \log \prod_{l=1}^{R} p_k(\mathbf{z}_l)\delta_k \\ &= \sum_{l=1}^{R} \log p_k(\mathbf{z}_l) + \log \delta_k \end{aligned} \quad (11)$$

By substituting $p_k(\mathbf{z}_l)$ from (8) to (11) and omitting constants that do not depend on categories, we then obtain Δ_k in the following form, :

$$\Delta_k(\mathbf{z}_1, \mathbf{z}_2, ..., \mathbf{z}_R) = -R \log |\mathbf{\Sigma}_{z_{lk}}| - \sum_{l=1}^{R} \mathbf{z}_l^H \mathbf{\Sigma}_{z_{lk}}^{-1} \mathbf{z}_l + \log \delta_k \quad (12)$$

The information about $\mathbf{z}_l$ is then sent from the lth (l = 1, 2,..., R) cognitive radar sensor to the fusion center. The classifier at the fusion center then makes the final classification decision in the form:

$$\begin{aligned} \hat{k} &= \arg \max_{k=0,1,...,M^\star-1} \Delta_k(\mathbf{z}_1, \mathbf{z}_2, ..., \mathbf{z}_R) \\ &= \arg \min_k \{R \log |\mathbf{\Sigma}_{z_{lk}}| + \sum_{l=1}^{R} \mathbf{z}_l^H \mathbf{\Sigma}_{z_{lk}}^{-1} \mathbf{z}_l - \log \delta_k\} \end{aligned} \quad (13)$$

From (13), we map the integer value of $\hat{k}$ to binary value to obtain a category vector $\mathbf{c}$ = [c_1, c_2, ..., c_M] where c_i (i = 1, 2, ..., M) takes value of 1 corresponding to category i being present or takes value of 0 corresponding to category i being absent in the area of interest. The total number of target categories being present in the surveillance region is given by:

$$N_C = \sum_{i=1}^{M} c_i \tag{14}$$

For example, if $\hat{k}$ = 5, then we get $\mathbf{c}$ = [1, 0, 1, 0, ...,0], i.e., only categories 1 and 3 are present within the surveillance region. Therefore, the total number of target categories being present N_C is 2.

B. Multiple Target Identification

Based on the estimated value $\hat{k}$, we realize which target categories have shown up in the surveillance region. However, we still have no information about the number of targets belonging to each category. Therefore, the second step of the JMIC algorithm is repeatedly applied to each detected category to identify targets in the surveillance region. We aim at searching all the targets using their jth indices. For each category i, we denote $H^i_{h,\hat{k}}$ to represent the hypothesis h (h = 0, 1, ..., 2^N - 1), given category i $\in$ $\mathbf{S}$ being present under hypothesis $H_{\hat{k}}$. Note that, $\mathbf{S}$ is a set of all categories i being present in hypothesis $H_{\hat{k}}$.

$$\mathbf{S} = \{i \text{ present in } H_{\hat{k}}\} \tag{15}$$

Since category i is estimated to be present, i.e, at least one target index j shows up in this category, thus, the scenario of no target index of category i being present is eliminated, i.e., P($H^i_{0,\hat{k}}$) = 0. Thus, we only have $N^\star$ = 2^N - 1 hypotheses corresponding to h = 1, 2, ..., $N^\star$. We choose $H^i_{1,\hat{k}}$ to represent the hypothesis of target index $\sharp$1 of category $i \in \mathbf{S}$ being present, $H^i_{2,\hat{k}}$ to represent the hypothesis of target index $\sharp$2 of category $i \in \mathbf{S}$ being present, ..., $H^i_{N^\star,\hat{k}}$ to represent the hypothesis of all targets index $\sharp$1, $\sharp$2, ..., $\sharp N$ of category $i \in \mathbf{S}$ being present.

We have

$$\begin{aligned} P(H^i_{h,\hat{k}}) &= P(H^i_h, H_{\hat{k}}) \\ &= P(H^i_h|H_{\hat{k}})P(H_{\hat{k}}) \end{aligned} \tag{16}$$

The conditional probability of hypothesis $H^i_{1,\hat{k}}$ is given by:

$$\begin{aligned} P(H^i_1|H_{\hat{k}}) &= \text{P}\ \{\text{target index } \sharp 1 \text{ category } i \text{ present}\} \\ &= P(b_{i1} = 1; b_{i2} = 0; ...; b_{iN} = 0) \end{aligned} \tag{17}$$

TABLE II
CLASSIFICATION AND IDENTIFICATION EXAMPLE

	Index 1	Index 2	Index 3	Index 4
Category 1	0	1	0	1
Category 2	1	1	0	1
Category 3	1	1	0	0

Because the possibilities for presence or absence of targets are independent, we have

$$\begin{aligned} P(H^i_1|H_{\hat{k}}) &= P(b_{i1} = 1).P(b_{i2} = 0)...P(b_{iN} = 0) \\ &= (1 - p_{i1}).p_{i2}...p_{iN} \end{aligned} \tag{18}$$

Similarly, the conditional probability of hypothesis $H^i_{2,\hat{k}}$ is:

$$\begin{aligned} P(H^i_2|H_{\hat{k}}) &= \text{P}\ \{\text{target index } \sharp 2 \text{ category } i \text{ present}\} \\ &= P(b_{i1} = 0; b_{i2} = 1; ...; b_{iN} = 0) \\ &= P(b_{i1} = 0).P(b_{i2} = 1)...P(b_{iN} = 0) \\ &= p_{i1}.(1 - p_{i2})...p_{iN} \end{aligned} \tag{19}$$

In general, we obtain the conditional probability of hypothesis $H^i_{h,\hat{k}}$ as follows:

$$P(H^i_h|H_{\hat{k}}) = \prod_{j=1}^{N} [b^{(h)}_{ij}(1 - p_{ij}) + (1 - b^{(h)}_{ij})p_{ij}] \tag{20}$$

where $b^{(h)}_{ij}$ takes the value of 0 when target index j of category i is absent, otherwise $b^{(h)}_{ij}$ takes the value of 1 when target index j of category i is present under hypothesis H^i_h given hypothesis $H_{\hat{k}}$.

We now set up $N^\star$ hypotheses:

$$H^i_{h,\hat{k}} : \mathbf{z}^i_l = \mathbf{s}^i_l + \mathbf{n}^i_l, \qquad h = 1, 2, ..., N^\star \tag{21}$$

where $\mathbf{z}^i_l$ is collected by lth (l = 1, 2, ..., R) cognitive radar sensor regarding to ith category. Target signals of ith category are given by:

$$\mathbf{s}^i_l \sim \mathcal{CN}(0, \mathbf{\Sigma}_{s^i_{l,h}}), \quad \text{where} \quad \mathbf{\Sigma}_{s^i_{l,h}} = \sum_{j=1(j \in H^i_{h,\hat{k}})}^{N} b_{ij}\mathbf{\Sigma}_m \tag{22}$$

Signals are corrupted by zero-mean complex white Gaussian noise.

$$\mathbf{n}^i_l \sim \mathcal{CN}(0, \sigma^2_n\mathbf{I}) \tag{23}$$

Under hypothesis $H^i_{h,\hat{k}}$, the probability density function of the feature vector $\mathbf{z}^i_l$ of category i is given by:

$$\begin{aligned} P(\mathbf{z}^i_l|H^i_{h,\hat{k}}) &= p_{h,\hat{k}}(\mathbf{z}^i_l) \\ &= \frac{1}{\pi^D|\mathbf{\Sigma}_{z^i_{l,h}}|} \exp\{-(\mathbf{z}^i_l)^H \mathbf{\Sigma}^{-1}_{z^i_{l,h}} \mathbf{z}^i_l\} \end{aligned} \tag{24}$$

where $\mathbf{\Sigma}_{z^i_{l,h}} = \mathbf{\Sigma}_{s^i_{l,h}} + \sigma_n^2\mathbf{I}$.

We denote $P(H^i_h|H_{\hat{k}})$ by α^i_h. From (16) and due to the conditional independence of $\mathbf{z}^i_l$, the identification decision rule is hence given by:

$$\hat{h} = \arg \max_{h=1,2,...,N^\star} \prod_{l=1}^{R} p_{h,\hat{k}}(\mathbf{z}^i_l)\alpha^i_h\delta_{\hat{k}} \tag{25}$$

In term of log-likelihood, we have

$$\begin{aligned}\Delta^i_k &= \log \prod_{l=1}^{R} p_{h,\hat{k}}(\mathbf{z}^i_l)\alpha^i_h\delta_{\hat{k}} \\ &= \sum_{l=1}^{R} \log p_{h,\hat{k}}(\mathbf{z}^i_l) + \log \alpha^i_h + \log \delta_{\hat{k}}\end{aligned} \tag{26}$$

By substituting $p_{h,\hat{k}}(\mathbf{z}^i_l)$ from (24) to (26) and omitting constants that do not depend on target indices in each category, we have Δ^i_k in the following form:

$$\Delta^i_k = -R\log|\mathbf{\Sigma}_{z^i_{l,h}}| - \sum_{l=1}^{R}(\mathbf{z}^i_l)^H\mathbf{\Sigma}^{-1}_{z^i_{l,h}}\mathbf{z}^i_l + \log\alpha^i_h + \log\delta_{\hat{k}} \tag{27}$$

The information about $\mathbf{z}^i_l$ is sent from the lth cognitive radar sensor to the fusion center. The identifier at the fusion center then makes the final identification decision:

$$\begin{aligned}\hat{h} &= \arg \max_{h=1,2,...,N^\star} \Delta^i_k \\ &= \arg\min_h\{R\log|\mathbf{\Sigma}_{z^i_{l,h}}| + \sum_{l=1}^{R}(\mathbf{z}^i_l)^H\mathbf{\Sigma}^{-1}_{z^i_{l,h}}\mathbf{z}^i_l - \log\alpha^i_h \\ &\qquad - \log\delta_{\hat{k}}\}\end{aligned} \tag{28}$$

From (28), we map the integer value of $\hat{h}$ to binary value to obtain a index vector $\mathbf{b}_i = [b_{i1}, b_{i2}, ..., b_{iN}]$ where every component of $\mathbf{b}_i$ takes the value of 1 or 0. Component $\sharp j$ takes value of 1 corresponding to the scenario of target index $\sharp j$ of category i being present. The total number of targets N_i in each category i is calculated by:

$$N_i = \sum_{j=1}^{N} b_{ij} \tag{29}$$

Following the example previously described in classification step, for i = 1, if $\hat{h}$ = 7, then we get $\mathbf{b}_1$ = [1, 1, 1, 0, ...,0]. Therefore, only targets with indices 1, 2 and 3 of category 1 are present within the surveillance region. The total number of targets of category 1 being present N_1 is 3. Repeatedly implementing this step, for i = 3, if $\hat{h}$ = 3, we obtain $\mathbf{b}_3$ = [1, 1, 0, 0, ..., 0]. So, targets with indices 1 and 2 of category 3 are present. The total number of targets of category 3 being present N_3 is 2.

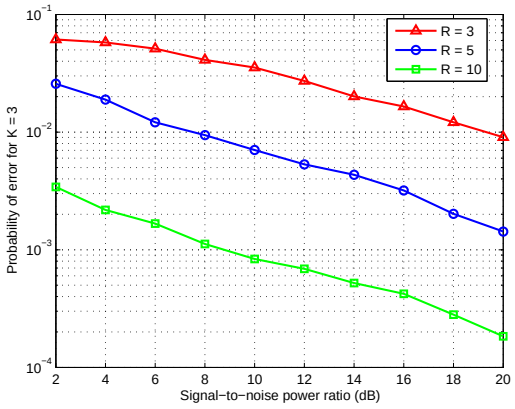


Fig. 2. Probability of error using JMIC algorithm for K = 3

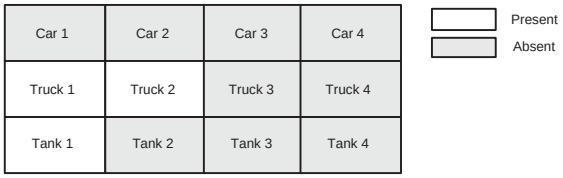


Fig. 3. Surveillance scenario of K = 3

The total number of targets K in the surveillance region is finally given by:

$$K = \sum_{i=1}^{M} N_i = \sum_{i=1}^{M}\sum_{j=1}^{N} b_{ij} \tag{30}$$

In the example, the total number of targets within the surveillance region K is 5.

IV. Simulation Results

We perform simulations to illustrate the performance of the proposed JMIC algorithm. An encounter of unknown K targets in the region of query was simulated. A set of R cognitive radar sensors was deployed. A cognitive radar sensor may detect more than one target at any given time. Therefore, a more accurate estimation about target categories and the total number of targets being present in each category can be obtained by fusion of several radar sensors. The maximum number of categories M = 3 and the maximum number of targets in each category N = 4 were assumed in this region of interest.

An example using JMIC for K = 7 targets in the region of interest is given in Table II. We use JMIC algorithm to obtain $\hat{k}$ = 7 which specifies that categories 1, 2, 3 are present and thus N_c = 3. The number of targets of category 1 is 2 (target index $\sharp 2$ and $\sharp 4$) corresponding to $\hat{h}$ = 10. The number of targets of category 2 is 3 (target

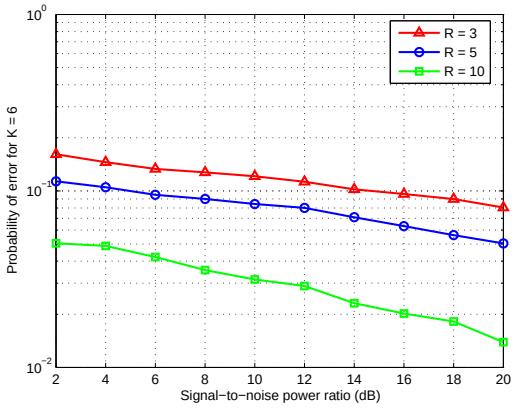


Fig. 4. Probability of error using JMIC algorithm for K = 6

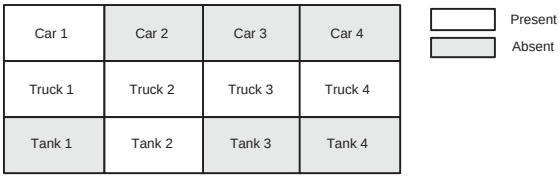


Fig. 5. Surveillance scenario of K = 6

index ♯1, ♯2, and ♯4) corresponding to $\hat{h}$ = 11. The total number of targets of category 3 is 2 (target index ♯1 and ♯2) corresponding to $\hat{h}$ = 3.

To evaluate the performance of the proposed JMIC algorithm, we conduct a Monte-Carlo simulation of 10^5 runs. The probability of error of the proposed JMIC algorithm given in the form of function of signal-to-noise power ratio is shown in Fig. 2 and Fig. 4. The scenarios of R = 3, 5 and 10 cognitive radar sensors were used in the simulations. From Fig. 2, we realize that a sufficiently low probability of error can be obtained with a small number of cognitive radar sensors R = 5 in the surveillance scenario of K = 3 targets as shown in Fig. 3. Comparison of probability of error for the different number of cognitive radar sensors in the scenario of K = 3 targets was shown in Fig. 2. The simulation results demonstrate our algorithm in the surveillance scenarios of K = 6 as described in Fig. 5 is given in Fig. 4. From Fig. 2 and Fig. 4, we also observe that for a given number of targets K in the surveillance region, the performance of JMIC using R = 5 or R = 10 radar sensors is better than that using R = 3 radar sensors. Besides, for a given number of R radar sensors, the identification and classification performance is reduced when we notice an increasing number of targets in the surveillance region. The probability of JMIC error is inversely proportional to signal-to-noise power ratio. At high SNR, the probability of error is rather small. The simulation results validate the robustness and effectiveness of our proposed JMIC algorithm.

V. Conclusion

We have demonstrated that K targets in a query region can be classified and identified efficiently by a network of R cognitive radar sensors using our JMIC algorithm. A computer simulation with simulated radar data was used to investigate the accuracy of classification and identification algorithm in the variations of the target signals in the network. Using JMIC algorithm, we show that a sufficiently low probability of error can be achieved with a fairly small number of radar sensors for a given common number of targets. The unprecedented desire of knowing not only the number of target categories, but also the total number of targets in each category in a surveillance region is making JMIC algorithm an attractive choice in practice for military applications.

Acknowledgement

This work was supported in part by Office of Naval Research (ONR) under Grant N00014-07-1-0395 and N00014-07-1-1024, and National Science Foundation (NSF) under Grant CNS-0721515 and CNS-0831902.

References

[1] "Command and Control and Combat Systems (C2 and CS)", ONR BAA 06-016.
[2] Kay S. M., *Fundamentals of Statistical Signal Processing: Detection Theory*, PTR Prentice-Hall Inc., vol. 2, 1993.
[3] Kotecha J. H., V. Ramachandran, and A. M. Sayeed, "Distributed multitarget classification in wireless sensor networks", *IEEE Journal on Selected Areas in Communications*, vol. 23, no. 4 , pp. 703-713, Apr. 2005.
[4] Le H. and Q. Liang, "Joint multi-target identification and classification in cognitive radar sensor networks," submitted to *Pattern Recognition Letters*.
[5] Liang Q., "Automatic Target Recognition Using Waveform Diversity in Radar Sensor Networks," *Pattern Recognition Letters (Elsevier)*, vol. 29, no. 2, pp. 377-381, 2008.
[6] Meesookho C., S. Narayanan, C. S. Raghavendra, "Collaborative classification applications in sensor networks", *Sensor Array and Multichannel Signal Processing Workshop Proceedings, 2002*, pp. 370-374, Aug. 2002.
[7] Premebida, C. "A multi-target tracking and GMM-classifier for intelligent vehicles", in *2006 IEEE Proc. Intelligent Transportation Systems, Toronto, Cananda*, pp. 313-318, Sept. 2006.
[8] Teti J. G., R. P. Gorman, and W. A. Berger, "A multifeature decision space approach to radar target identification", *IEEE Trans. on Aerospace and Electronic Systems*, vol. 32, no. 1, pp. 480-487, Jan. 1996.
[9] Vercauteren T., D. Guo, and X. Wang, "Joint multiple target tracking and classification in collaborative sensor networks", *IEEE Journal on Selected Areas in Communications*, vol. 23, no. 4 , pp. 714-723, Apr. 2005.

Biologically-Inspired Target Recognition in Radar Sensor Networks

Qilian Liang

Department of Electrical Engineering
University of Texas at Arlington
Arlington, TX 76019-0016, USA
liang@uta.edu
http://www3.uta.edu/faculty/liang

Abstract. Inspired by biological systems' (such as human's) innate ability to process and integrate information from disparate, network-based sources, we apply biologically-inspired information integration mechanisms to target detection in cognitive radar sensor network. Humans' information integration mechanisms have been modelled using maximum-likelihood estimation (MLE) or soft-max approaches. In this paper, we apply these two algorithms to radar sensor networks target detection. Discrete-cosine-transform (DCT) is used to process the integrated data from MLE or soft-max. We apply fuzzy logic system (FLS) to automatic target detection based on the AC power values from DCT. Simulation results show that our MLE-DCT-FLS and soft-max-DCT-FLS approaches perform very well in the radar sensor network target detection, whereas the existing 2-D construction algorithm doesn't work in this study.

1 Introduction and Motivation

A radar sensor network consists of multiple networked radar sensors and radar sensors sense and communicate with each other collaboratively to complete a mission. In real world, radar sensor network information integration is necessary in different applications. For example, in an emergency natural disaster scenario, such as Utah Mine Collapse in August 2007 or West Virginia Sago mine disaster in January 2006, radar sensor network-based information integration for first responders is critical for search and rescue. Danger may appear anywhere at any time, therefore, first responders must monitor a large area continuously in order to identify potential danger and take actions. Due to the dynamic and complex nature of natural disaster, some buried/foleage victims may not be found with image/video sensors, and UWB radar sensors are needed for penetrating the ground or sense-through-wall. Unfortunately, the radar data acquired are often limited and noisy. Unlike medical imaging or synthetic aperture radar imaging where abundance of data is generally available through multiple looks and where processing time may not be crucial, practical radar sensor networks are typically the opposite: availability of data is limited and required processing time is short. This need is also motivated by the fact that biological systems

B. Liu et al. (Eds.): WASA 2009, LNCS 5682, pp. 115–124, 2009.
© Springer-Verlag Berlin Heidelberg 2009

such as humans display a remarkable capability to quickly perform target recognition despite noisy sensory signals and conflicting inputs. Humans are adept at network visualization, and at understanding subtle implications among the network connections. To date, however, human's innate ability to process and integrate information from disparate, network-based sources for situational understanding has not translated well to automated systems. In this paper, we apply biologically-inspired information integration mechanisms to information fusion in radar sensor network.

2 Sense-through-Foliage Radar Sensor Networks Data Measurement and Collection

Our work is based on the sense-through-foliage UWB radar sensor networks. The foliage experiment was constructed on a seven-ton man lift, which had a total lifting capacity of 450 kg. The limit of the lifting capacity was reached during the experiment as essentially the entire measuring apparatus was placed on the lift. The principle pieces of equipment secured on the lift are: Barth pulser, Tektronix model 7704 B oscilloscope, dual antenna mounting stand, two antennas, rack system, IBM laptop, HP signal Generator, Custom RF switch and power supply and Weather shield (small hut). The target is a trihedral reflector (as shown in Fig. 1). Throughout this work, a Barth pulse source (Barth Electronics, Inc. model 732 GL) was used. The pulse generator uses a coaxial reed switch to discharge a charge line for a very fast rise time pulse outputs. The model 732 pulse generator provides pulses of less than 50 picoseconds (ps) rise time, with amplitude from 150 V to greater than 2 KV into any load impedance through a 50 ohm coaxial line. The generator is capable of producing pulses with a minimum width of 750 ps and a maximum of 1 microsecond. This output pulse width is determined by charge line length for rectangular pulses, or by capacitors for 1/e decay pulses.

For the data we used in this paper, each sample is spaced at 50 picosecond interval, and 16,000 samples were collected for each collection for a total time duration of 0.8 microseconds at a rate of approximately 20 Hz. We plot the transmitted pulse (one realization) in Fig. 2a) and the received echos in one collection in Fig. 2b (averaged over 35 pulses).

3 Human Information Integration Mechanisms

Recently, a maximum-likelihood estimation (MLE) approach was proposed for multi-sensory data fusion in human [4]. In the MLE approach [4], sensory estimates of an environmental property can be represented by $\hat{S}_j = f_i(S)$ where S is the physical property being estimated, f is the operation the nervous system performs to derive the estimate, and $\hat{S}$ is the perceptual estimate. Sensory estimates are subject to two types of error: random measurement error and bias. Thus, estimates of the same object property from different cues usually differ. To



Fig. 1. The target (a trihedral reflector) is shown on the stand at 300 feet from the lift

reconcile the discrepancy, the nervous system must either combine estimates or choose one, thereby ignoring the other cues. Assuming that each single-cue estimate is unbiased but corrupted by independent Gaussian noise, the statistically optimal strategy for cue combination is a weighted average [4]

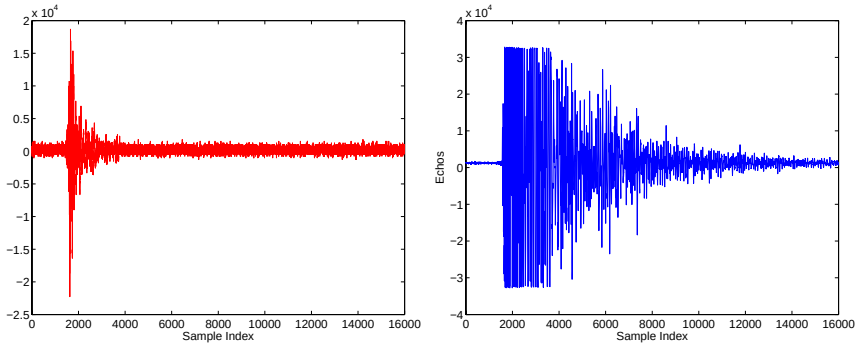
$$\hat{S}_c = \sum_{i=1}^{M} w_i \hat{S}_i \tag{1}$$

where $w_i = \frac{1/\sigma_i^2}{\sum_j 1/\sigma_j^2}$ and is the weight given to the ith single-cue estimate, σ_i^2 is that estimates variance, and M is the total number of cues. Combining estimates by this MLE rule yields the least variable estimate of S and thus more precise estimates of object properties.

Besides, some other summation rules have been proposed in perception and cognition such as soft-max rule: $y = (\sum_{i=1}^{M} x_i^n)^{\frac{1}{n}}$ [3] where x_i denotes the input from an input source i, and M is the total number of sources. In this paper, we will apply MLE and soft-max human brain information integration mechanisms to cognitive radar sensor network information integration.

4 Human-Inspired Sense-through-Foliage Target Detection

In Figs. 3a and 3b, we plot two collections of UWB radars. Fig. 3a has no target on range, and Fig. 3b has target at samples around 13,900. We plot the echo differences between Figs. 3a and 3b in Fig. 3c. However, it is impossible to identify whether there is any target and where there is target based on Fig. 3c. Since significant pulse-to-pulse variability exists in the echos, this motivate us to explore the spatial and time diversity using Radar Sensor Networks (RSN).



(a) (b)

Fig. 2. Transmitted pulse and received echos in one experiment. (a) Transmitted pulse. (b) Received echos.

In RSN, each radar can provide their pulse parameters such as timing to their clusterhead radar, and the clusterhead radar can combine the echos (RF returns) from the target and clutter. In this paper, we propose a RAKE structure for combining echos, as illustrated by Fig. 4. The integration means time-average for a sample duration T and it's for general case when the echos are not in discrete values. It is quite often assumed that the radar sensor platform will have access to Global Positioning Service (GPS) and Inertial Navigation Unit (INU) timing and navigation data [1]. In this paper, we assume the radar sensors are synchronized in RSN. In Fig. 4, the echo, i.e., RF response by the pulse of each cluster-member sensor, will be combined by the clusterhead using a weighted average, and the weight w_i is determined by the two human-inspired mechanisms.

We applied the human-inspired MLE algorithm to combine the sensed echo collection from $M = 30$ UWB radars, and then the combined data are processed using discrete-cosine transform (DCT) to obtain the AC values. Based on our experiences, echo with a target generally has high and nonfluctuating AC values and the AC values can be obtained using DCT. We plot the power of AC values in Figs. 5a and 5b using MLE and DCT algorithms for the two cases (with target and without target) respectively. Observe that in Fig. 5b, the power of AC values (around sample 13,900) where the target is located is non-fluctuating (somehow monotonically increase then decrease). Although some other samples also have very high AC power values, it is very clear that they are quite fluctuating and the power of AC values behaves like random noise because generally the clutter has Gaussian distribution in the frequency domain.

Similarly, we applied the soft-max algorithm ($n = 2$) to combine the sensed echo collection from $M = 30$ UWB radars, and then used DCT to obtain the AC values. We plot the power of AC values in Figs. 5a and 5b using soft-max and DCT algorithms for the two cases (with target and without target) respectively. Observe that in Fig. 6b, the power of AC values (around sample 13,900) where the target is located is non-fluctuating (somehow monotonically increase then decrease).

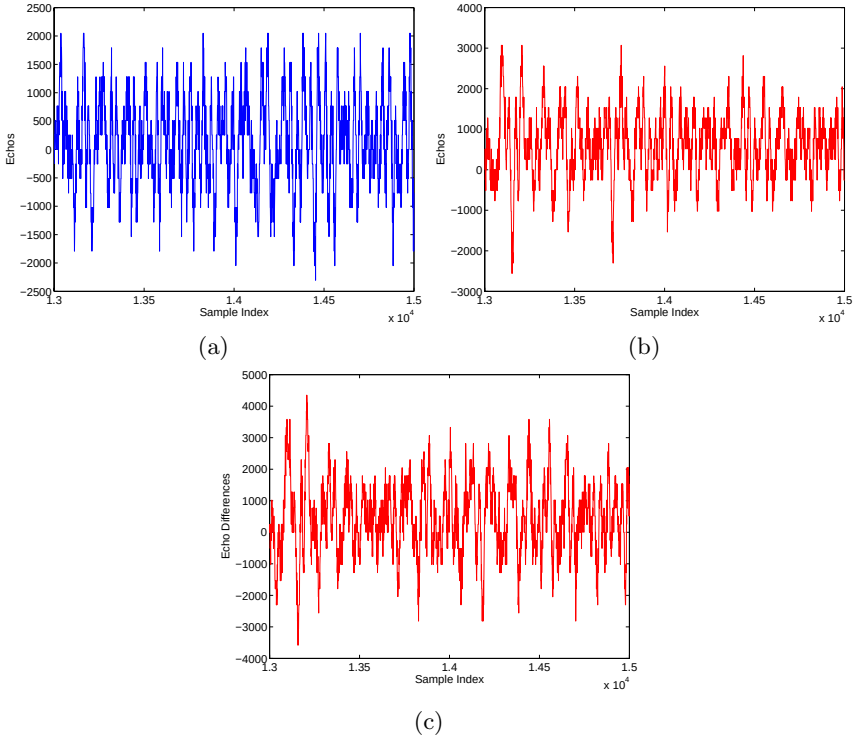


Fig. 3. Measurement with poor signal quality and 35 pulses average. (a) Expanded view of traces (no target) from sample 13,001 to 15,000. (b) Expanded view of traces (with target) from samples 13,001 to 15,000. (c) The differences between (a) and (b).

We made the above observations. However, in real world application, automatic target detection is necessary to ensure that our algorithms could be performed in real time. In Section 5, we apply fuzzy logic systems to automatic target detection based on the power of AC values (obtained via MLE-DCT or soft-max-DCT).

We compared our approaches to the scheme proposed in [6]. In [6], 2-D image was created via adding voltages with the appropriate time offset. In Figs. 7a and 7b, we plot the 2-D image created based on the above two data sets (from samples 13,800 to 14,200). The sensed data from 30 radars are averaged first, then plotted in 2-D [6]. However, it's not clear which image shows there is target on range.

5 Fuzzy Logic System for Automatic Target Detection

5.1 Overview of Fuzzy Logic Systems

Figure 8 shows the structure of a fuzzy logic system (FLS) [5]. When an input is applied to a FLS, the inference engine computes the output set corresponding

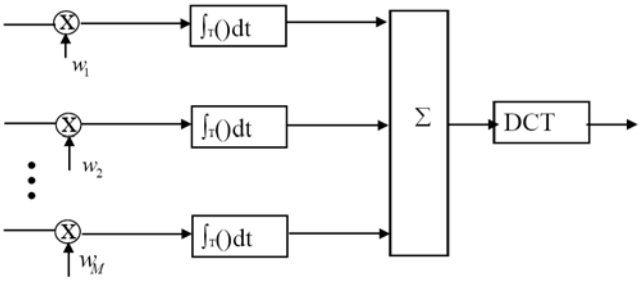


Fig. 4. Echo combining by clusterhead in RSN

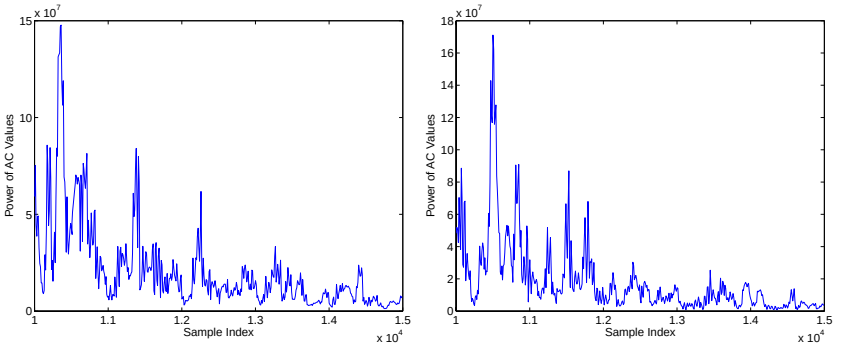


Fig. 5. Power of AC values using MLE-based information integration and DCT. (a) No target (b) With target in the field.

to each rule. The defuzzifer then computes a crisp output from these rule output sets. Consider a p-input 1-output FLS, using singleton fuzzification, *center-of-sets* defuzzification [5] and "IF-THEN" rules of the form

$$R^l : \text{IF } x_1 \text{ is } \mathrm{F}_1^l \text{ and } x_2 \text{ is } \mathrm{F}_2^l \text{ and } \cdots \text{ and } x_p \text{ is } \mathrm{F}_p^l, \text{ THEN } y \text{ is } \mathrm{G}^l.$$

Assuming singleton fuzzification, when an input $\mathbf{x}' = \{x_1', \ldots, x_p'\}$ is applied, the degree of firing corresponding to the lth rule is computed as

$$\mu_{\mathrm{F}_1^l}(x_1') \star \mu_{\mathrm{F}_2^l}(x_2') \star \cdots \star \mu_{\mathrm{F}_p^l}(x_p') = \mathcal{T}_{i=1}^{p} \mu_{\mathrm{F}_i^l}(x_i') \tag{2}$$

where $\star$ and $\mathcal{T}$ both indicate the chosen t-norm. There are many kinds of defuzzifiers. In this paper, we focus, for illustrative purposes, on the center-of-sets defuzzifier [5]. It computes a crisp output for the FLS by first computing the centroid, c_{G^l}, of every consequent set G^l, and, then computing a weighted average of these centroids. The weight corresponding to the lth rule consequent centroid is the degree of firing associated with the lth rule, $\mathcal{T}_{i=1}^{p} \mu_{\mathrm{F}_i^l}(x_i')$, so that

$$y_{cos}(\mathbf{x}') = \frac{\sum_{l=1}^{M} c_{\mathrm{G}^l} \mathcal{T}_{i=1}^{p} \mu_{\mathrm{F}_i^l}(x_i')}{\sum_{l=1}^{M} \mathcal{T}_{i=1}^{p} \mu_{\mathrm{F}_i^l}(x_i')} \tag{3}$$

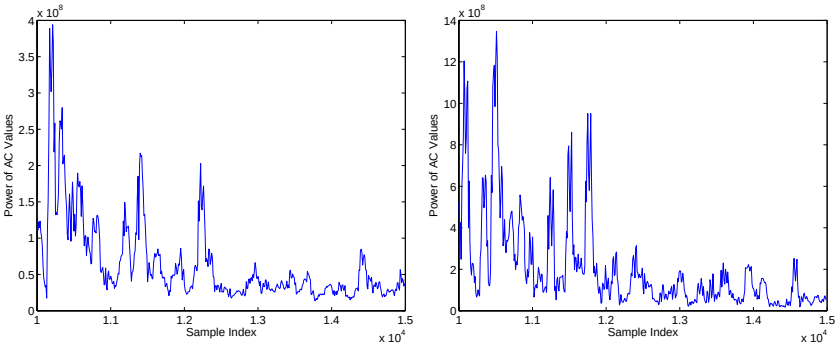


Fig. 6. Power of AC values using soft-max based information integration and DCT. (a) No target (b) With target in the field.

where M is the number of rules in the FLS. In this paper, we design a FLS for automatic target recognition based on the AC values obtained using MLE-DCT or soft-max-DCT.

5.2 FLS for Automatic Target Detection

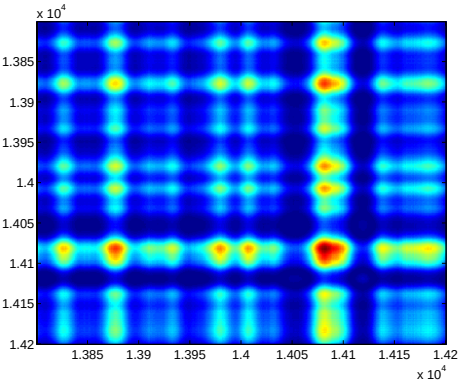
Observe that in Figs. 5 and 6, the power of AC values are quite fluctuating and have lots of uncertainties. FLS is well known to handle the uncertainties. For convenience in describing the FLS design for Automatic Target Detection (ATD), we first give the definition of *footprint of uncertainty* of AC power values and *region of interest* in the footprint of uncertainty.

Definition 1 (Footprint of Uncertainty). *Uncertainty in the AC power values and time index consists of a bounded region, that we call the* footprint of uncertainty *of AC power values. It is the union of all AC power values.*

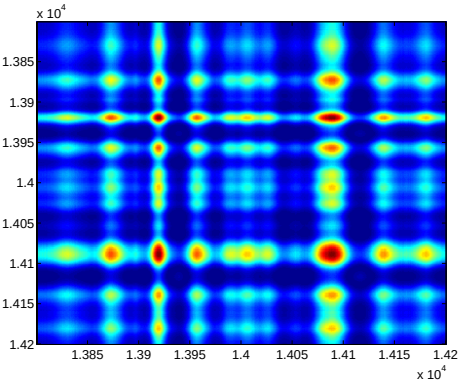
Definition 2 (Region of Interest (RoI)). *An RoI in the footprint of uncertainty is a contour consisting of a large number (greater than 50) of AC power values where AC power values increase then decrease.*

Definition 3 (Fluctuating Point in RoI). $P(i)$ *is called a* fluctuating point *in the RoI if* $P(i-1), P(i), P(i+1)$ *are non-monotonically increasing or decreasing.*

Our FLS for automatic target detection will classify each ROI (with target or no target) based on two antecedents: *the centroid of the ROI* and *the number of fluctuating points in the ROI*. The linguistic variables used to represent these two antecedents were divided into three levels: *low*, *moderate*, and *high*. The consequent – the possibility that there is a target at this RoI – was divided into 5 levels, *Very Strong, Strong, Medium, Weak, Very Weak*. We used trapezoidal membership functions (MFs) to represent *low*, *high*, *very strong*, and *very weak*;



(a)



(b)

Fig. 7. 2-D image created via adding voltages with the appropriate time offset. (a) No target (b) With target in the field.

and triangle MFs to represent *moderate*, *strong*, *medium*, and *weak*. All inputs to the antecedents are normalized to 0–10.

Based on the fact the AC power value of target is non-fluctuating (somehow monotonically increase then decrease), and the AC power value of clutter behaves like random noise because generally the clutter has Gaussian distribution in the frequency domain, we design a fuzzy logic system using rules such as:

R^l : IF *centroid of a RoI* (x_1) is F_l^1, and *the number of fluctuating points in the ROI* (x_2) is F_l^2, THEN the possibility that there is a target at this RoI (y) is G^l.

where $l = 1, \ldots, 9$. We summarize all the rules in Table 1. For every input (x_1, x_2), the output is computed using

$$y(x_1, x_2) = \frac{\sum_{l=1}^{9} \mu_{\mathrm{F}_l^1}(x_1)\mu_{\mathrm{F}_l^2}(x_2)c_{avg}^l}{\sum_{l=1}^{9} \mu_{\mathrm{F}_l^1}(x_1)\mu_{\mathrm{F}_l^2}(x_2)} \tag{4}$$

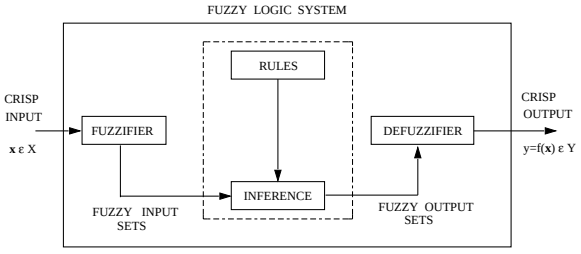


Fig. 8. The structure of a fuzzy logic system

We ran simulations to 1000 collections in the real world sense-through-foliage experiment, and found that our FLS performs very well in the automatic target detection based on the AC power values obtained from MLE-DCT or soft-max-DCT, and achieve probability of detection $p_d = 100\%$ and false alarm rate $p_{fa} = 0$.

Table 1. The rules for target detection. Antecedent 1 is *centroid of a RoI*, Antecedent 2 is *the number of fluctuating points in the ROI*, and Consequent is *the possibility that there is a target at this RoI*.

Rule #	Antecedent 1	Antecedent 2	Consequent
1	low	low	medium
2	low	moderate	weak
3	low	high	very weak
4	moderate	low	strong
5	moderate	moderate	medium
6	moderate	high	weak
7	high	low	very strong
8	high	moderate	strong
9	high	high	medium

6 Conclusions

Inspired by biological systems' (such as humans) innate ability to process and integrate information from disparate, network-based sources, we applied biologically-inspired information integration mechanisms to target detection in radar sensor network. Humans' information integration mechanisms have been modelled using maximum-likelihood estimation (MLE) or soft-max approaches. In this paper, we applied these two algorithms to cognitive radar sensor networks target detection. Discrete-cosine-transform (DCT) was used to process the integrated data from MLE or soft-max. We applied fuzzy logic system (FLS) to automatic target detection based on the AC power values from DCT. Simulation results showed that our MLE-DCT-FLS and soft-max-DCT-FLS approaches performed very well in the radar sensor network target detection, whereas the existing 2-D construction algorithm couldn't work in this study.

Acknowledgement

This work was supported in part by U.S. Office of Naval Research (ONR) under Grant N00014-07-1-0395, N00014-07-1-1024, and National Science Foundation (NSF) under Grant CNS-0721515 and CNS-0831902.

References

1. ONR BAA 07-017, NET-SENTRIC Surveillance, `http://www.onr.navy.mil`
2. Barton, D.K.: Radar System Analysis and Modeling. Artech House, Boston (2006)
3. Graham, N.V.S.: Visual pattern analyzers, pp. xvi, 646. Oxford University Press, New York (1989)
4. Hillis, J.M., Ernst, M.O., Banks, M.S., Landy, M.S.: Combining sensory information: Mandatory fusion within, but not between, senses. Science 298(5598), 1627–1630 (2002)
5. Mendel, J.M.: Uncertain Rule-Based Fuzzy Logic Systems. Prentice-Hall, Upper Saddle River (2001)
6. Withington, P., Fluhler, H., Nag, S.: Enhancing homeland security with advanced UWB sensors. IEEE Microwave Magazine (September 2003)

This full text paper was peer reviewed at the direction of IEEE Communications Society subject matter experts for publication in the IEEE ICC 2009 proceedings

Situation Understanding Based on Heterogeneous Sensor Networks and Human-Inspired Favor Weak Fuzzy Logic System

Qilian Liang,
Department of Electrical Engineering
University of Texas at Arlington
Arlington, TX 76019-0016 USA
E-mail: liang@uta.edu

***Abstract*— Humans use multiple sources of sensory information to estimate environmental properties and has innate ability to integrate information from heterogeneous data sources. How the multi-sensory and multimodal information are integrated in human brain? There is consensus that it depends on the prefrontal cortex (PFC). The PFC has top-down control (favor weak) and rule-based mechanisms, and we incorporate the favor weak mechanism into rule-based fuzzy logic systems (FLS) via using upper and lower membership functions. The inference engine of favor weak fuzzzy logic system is proposed under three different categories based on fuzzifiers. We apply the favor weak FLS to situation understanding based on heterogeneous sensor network, and it shows that our favor weak fuzzy logic system has clear advantage comparing to the type-1 FLS. The favor weak FLS can increase the probability of threat detection, and provides timely indication & warning (I&W).**

I. Introduction and Motivation

Humans use multiple sources of sensory information to estimate environmental properties. For example, the eyes and hands both provide relevant information about an objects shape. The eyes estimate shape using binocular disparity, perspective projection, etc. The hands supply haptic shape information by means of tactile and proprioceptive cues. **Combining information across cues can improve estimation of object properties** but may come at a cost: loss of single-cue information. Recent studies [7] showed that single-cue information is indeed lost when cues from within the same sensory modality (e.g., disparity and texture gradients in vision) are combined, **but not when different modalities (vision and haptics) are combined**. In another study on human [4], gaze shifts are coordinated movements of the eyes (eyes-re-head) and head (head-re-space) that rapidly reorient the visual axis (eyes-re-space) to a target of interest. Reaction latencies for gaze shifts to combined auditory and visual stimuli presented in close spatial and temporal register are **less than those to either stimulus presented alone**, suggesting that the integration of multisensory information may play an important role in forming appropriate motor behaviors. These studies demonstrate that human has innate ability to integrate information from heterogeneous data sources and multi-sensory and multimodal information integration has clear advantage.

In this paper, we incorporate human brain mechanisms to a new fuzzy logic system design and apply it to situation understanding based on heterogeneous sensor network. A heterogeneous sensor network consists of multiple networked sensors with different modality (video, audio, acoustic, radar, etc), and such networks are necessary in different applications. For example, in an emergency natural disaster scenario, information integration for first responders is critical for search and rescue. Besides, the first responders need to be situation-aware. Danger may appear anywhere at any time, therefore, first responders must monitor a large area continuously in order to identify potential danger and take actions. Due to the dynamic and complex nature of natural disaster, some victims may not be found with a single type of sensor modality, for example, image/video sensors can't be used to find a buried/foleage victim, UWB radar sensors need to be used for penetrating the ground or sense-through-wall, and acoustic sensors are needed to collect the voice from victims. Similarly, some potential dangers may not be identified using a single modality sensor. More modalities are required to search victims and identify potential dangers and that means large-scale Heterogeneous Sensor Networks (HSN) are needed for search, rescue, and situation awareness. However, information integration algorithms (especially for situation awareness) for heterogeneous sensor networks don't exist. Motivated by the above challenges, we study human-inspired information integration for heterogeneous sensor networks.

The remaining of the paper is organized as follows. In Section II, we present the heterogeneous information integration in Human brain and challenges to fuzzy logic system design. In Section III, we present the inference engine for favor weak fuzzy logic system. The application to situation

978-1-4244-3435-0/09/$25.00 ©2009 IEEE

Authorized licensed use limited to: University of Texas at Arlington. Downloaded on December 18, 2009 at 14:35 from IEEE Xplore. Restrictions apply.

understanding based on heterogeneous sensor network is presented in Section IV. Section V concludes this paper.

II. Heterogeneous Information Integration in Human Brain and Challenges to Fuzzy Logic System Design

One of the great mysteries of the brain is cognitive control. How can the interactions between millions of neurons result in behavior that is coordinated and appears willful and voluntary? There is consensus that it depends on the prefrontal cortex (PFC) [14][16]. A schematic diagram of some of the extrinsic and intrinsic connections of the PFC is depicted in Fig. 1 [14]. Many PFC areas receive converging inputs from at least two sensory modalities [2][9]. For example, the dorsolateral (DL) (areas 8, 9, and 46) and ventrolateral (12 and 45) PFC both receive projections from visual, auditory, and somatosensory cortex. Furthermore, the PFC is connected with other cortical regions that are themselves sites of multimodal convergence. Many PFC areas (9, 12, 46, and 45) receive inputs from the rostral superior temporal sulcus, which has neurons with bimodal or trimodal (visual, auditory, and somatosensory) responses [1][17]. The arcuate sulcus region (areas 8 and 45) and area 12 seem to be particularly multimodal. They contain zones that receive overlapping inputs from three sensory modalities [17]. Observe, for example, that mid-dorsal area 9 directly processes and integrates visual, auditory, and multimodal information.

A. PFC Top-Down Control (Favor Weak) and Rule-Based Mechanisms

According to [14][16], the PFC is modulatory rather than transmissive. That is, the pathway from input to output does not "run through" the PFC. Instead, the PFC guides activity flow along task-relevant pathways in more posterior and/or subcortical areas. The PFC is important when "top-down" processing is needed; that is, when behavior must be guided by internal states or intentions. The PFC is critical in situations when the mappings between sensory inputs, thoughts, and actions either are *weakly established* relative to other existing ones or are *rapidly changing*. This is when we need to use the "*rules* of the game," internal representations of goals and the means to achieve them [14]. Several investigators have argued that this is a cardinal function of the PFC [3][18][6][20][13]. The top-down control and favor weak mechanism can be illustrated using the Stroop task.

In the Stroop task [19], subjects either read words or name the color in which they are written. To perform this task, subjects must selectively attend to one attribute. This is especially so when naming the color of a conflict stimulus (e.g. the word GREEN displayed in red), because there is a strong prepotent tendency to read the word ("green"), which competes with the response to the color ("red"). This illustrates one of the most fundamental aspects of cognitive control and goal-directed behavior: the ability to select a weaker, task-relevant response (or source of information) in the face of competition from an otherwise stronger, but task-irrelevant one. Patients with frontal impairment have difficulty with this task, especially when the instructions vary frequently, which suggests that they have difficulty adhering to the goal of the task or its rules in the face of a competing stronger (i.e. more salient or habitual) response [14].

The Stroop task, naming the color of a conflict stimulus, is variously described as tapping the cognitive functions of either **selective attention, behavioral inhibition, top-down control, working memory, or rule-based or goal-directed behavior** [14]. In this paper, we will study human brain top-down control and rule-based mechanisms inspired information integration. In current HSN design, the clusterhead only serves a "transmissive" (data collection and relay to gateway) function. In this project, the HSN clusterhead will also provide a "modulatory" function, i.e., multimodal information integration. In natural disaster or terrorist attack recovery, the most dangerous potential threat factors (stimuli) are weak or hidden but are highly correlated with the situation understanding task, and of course, they are time sensitive (rapidly changing), which indicates that the PFC "top-down" control mechanism can be applied to HSN-based situation understanding.

The PFC top-down control signals *favor weak (but task-relevant) stimulus-response mappings* when they are in competition with more habitual, stronger ones (as in the Stroop task, where the word GREEN is stronger and the color red is weak). Moreover, all of the PFC neural mechanisms depend on the representation of goals and *rules* in the form of patterns of activity in the PFC, which configure processing in other parts of the brain in accordance with current task demands [14][16]. Such mechanisms motivate us to heavily revisit a rule-based approach: fuzzy logic systems (FLS), mimicking the rule-based PFC neural mechanism, and subsequently applying it to HSN-based situation awareness.

B. Overview of Fuzzy Logic Systems and Its Shortfall

The current type-1 FLS designs doesn't have "favor strong or favor weak control". In a type-1 FLS with a rule base of M rules, in which each rule has p antecedents, let the lth rule be denoted by R^l, where R^l: IF x_1 is F_1^l, and x_2 is F_2^l, and, ..., and x_p is F_p^l THEN y is G^l. The membership function, $\mu_{\mathrm{B}^l}(y)$, of a fired rule can be expressed by the following sup-star composition [12]:

$$\mu_{\mathrm{B}^l}(y) = \sup_{\mathbf{x}\in\mathrm{A}^*}[\mu_{\mathrm{A}^*}(\mathbf{x}) \star \mu_{\mathrm{A}^l\to\mathrm{B}^l}(\mathbf{x}, y)] \qquad (1)$$

where A^* is a p-dimensional Cartesian product space, $\mathrm{A}^* = \mathrm{A}_1^* \times \cdots \times \mathrm{A}_p^*$, A_k^* is the measurement domain of input x_k, $(k = 1, \cdots, p)$; and, A^* is given by

$$\mu_{\mathrm{A}^*}(\mathbf{x}) = \mu_{\mathrm{A}_1^*\times\cdots\times\mathrm{A}_p^*}(\mathbf{x}) = \mu_{\mathrm{X}_1}(x_1) \star \cdots \star \mu_{\mathrm{X}_p}(x_p) \qquad (2)$$

Authorized licensed use limited to: University of Texas at Arlington. Downloaded on December 18, 2009 at 14:35 from IEEE Xplore. Restrictions apply.

In the current type-1 FLS design,

$$\mu_{\mathrm{A}^l \to \tilde{\mathrm{B}}^l}(\mathbf{x}, y) = \mu_{\mathrm{F}_1^l}(x_1) \star \mu_{\mathrm{F}_2^l}(x_2) \star \cdots \star \mu_{\mathrm{F}_p^l}(x_p) \star \mu_{\mathrm{G}^l}(y) \tag{3}$$

For the Stroop task, to name the color of a conflict stimulus (e.g. the word GREEN displayed in red), needs the favor weak mechanism because there is a strong prepotent tendency to read the word ("green"), which competes with the response to the color ("red").

So in the FLS design, the firing degree for "red" should be boosted to reflect the "favor weak" mechanism if a conflict stimulus presents, but no control should be taken if no conflict stimulus presents (e.g., name the word when the word GREEN displayed in red). This motivates us to use different membership degrees under different scenarios. We propose to use interval type-2 fuzzy membership function for this favor weak (using upper membership function) or no control (using lower membership function) mechanism.

III. The Inference Engine for Favor Weak FLSs

In a favor weak FLS with a rule base of M rules, in which each rule has p antecedents, let the lth rule be denoted by R^l, where R^l: IF x_1 is $\tilde{\mathrm{F}}_1^l$, and x_2 is $\tilde{\mathrm{F}}_2^l$, and, ..., and x_p is $\tilde{\mathrm{F}}_p^l$ THEN y is G^l. Although the rule may look the same as that of the interval type-2 FLS, but the inference engine is different.

In a favor weak FLS with p antecedents, without loss of generality, assume the first w ($w < p$) antecedents are weak and should be favored, and all other antecedents ($w+1, i_{w+2}, \cdots, i_p$) should be in no control. If the antecedents are not in this order, they can be re-orderred. Then we can obtain the following Theorem. Our major result for favor weak FLSs is given in:

Theorem 1: In a favor weak nonsingleton FLS (the first w antecedents are weak and should be favored) with type-2 fuzzification and meet under minimum or product t-norm: (a) the firing degree for rule l, i.e., the result of the input and antecedent operations, is

$$\begin{aligned} f^l \;=\; & \sup_{\mathbf{x}\in X} \int_{X_1} \cdots \int_{X_p} [\overline{\mu}_{\tilde{\mathrm{X}}_1}(x_1) \star \overline{\mu}_{\tilde{\mathrm{F}}_1^l}(x_1)] \star \cdots \star \\ & \star [\overline{\mu}_{\tilde{\mathrm{X}}_w}(x_w) \star \overline{\mu}_{\tilde{\mathrm{F}}_w^l}(x_w)] \star [\underline{\mu}_{\tilde{\mathrm{X}}_{w+1}}(x_{w+1}) \\ & \star \underline{\mu}_{\tilde{\mathrm{F}}_{w+1}^l}(x_{w+1})] \star \cdots \star [\underline{\mu}_{\tilde{\mathrm{X}}_p}(x_p) \star \underline{\mu}_{\tilde{\mathrm{F}}_p^l}(x_p)] / \mathbf{x} \end{aligned} \tag{4}$$

the supremum is attained when each term in brackets attains its supremum;

(b) the rule R^l fired output consequent set, $\mu_{\mathrm{B}^l}(y)$, is

$$\mu_{\mathrm{B}^l}(y) = f^l \star \mu_{\mathrm{G}^l}(y) \tag{5}$$

where $\underline{\mu}_{\tilde{\mathrm{G}}^l}(y)$ and $\overline{\mu}_{\tilde{\mathrm{G}}^l}(y)$ are the lower and upper membership grades of $\mu_{\tilde{\mathrm{G}}^l}(y)$; and,

(c) the output fuzzy set, $\mu_{\mathrm{B}}(y)$, is

$$\mu_{\tilde{\mathrm{B}}}(y) = \bigcup_{l=1}^{M} \mu_{\mathrm{B}^l}(y) \tag{6}$$

When the input is fuzzified to a type-1 fuzzy set, so that $\mu_{\tilde{\mathrm{X}}_k} \to \mu_{\mathrm{X}_k}$ ($k = 1, \ldots, p$), the upper and lower MFs of $\mu_{\tilde{\mathrm{X}}_k}$ merge into one MF, $\mu_{\mathrm{X}_k}(x_k)$, in which case Theorem 1 simplifies to:

Corollary 1: In a favor weak FLS (the first w antecedents are weak and should be favored) with *nonsingleton type-1 fuzzification* and meet under minimum or product t-norm, f^l in (4) simplifies to: the firing degree for rule l is

$$\begin{aligned} f^l \;=\; & \sup_{\mathbf{x}\in X} \int_{X_1} \cdots \int_{X_p} [\mu_{X_1}(x_1) \star \overline{\mu}_{\tilde{\mathrm{F}}_1^l}(x_1)] \\ & \star \cdots \star [\mu_{X_w}(x_w) \star \overline{\mu}_{\tilde{\mathrm{F}}_w^l}(x_w)] \star [\mu_{X_{w+1}}(x_{w+1}) \\ & \star \underline{\mu}_{\tilde{\mathrm{F}}_{w+1}^l}(x_{w+1})] \star \cdots \star [\mu_{X_p}(x_p) \star \underline{\mu}_{\tilde{\mathrm{F}}_p^l}(x_p)] / \mathbf{x} \end{aligned} \tag{7}$$

the supremum is attained when each term in brackets attains its supremum;

When a singleton fuzzifier is used, the upper and lower MFs of $\mu_{\tilde{\mathrm{X}}_k}(x_k)$ merge into one crisp value, namely 1, in which case Theorem 1 simplifies further to:

Corollary 2: In a favor weak FLS (the first w antecedents are weak and should be favored) with *singleton fuzzification* and meet under minimum or product t-norm, f^l in (4) simplifies to: the firing degree for rule l, i.e., the result of the input and antecedent operations,

$$f^l = \overline{\mu}_{\tilde{\mathrm{F}}_1^l}(x_1) \star \cdots \star \overline{\mu}_{\tilde{\mathrm{F}}_w^l}(x_w) \star \underline{\mu}_{\tilde{\mathrm{F}}_{w+1}^l}(x_{w+1}) \star \cdots \star \underline{\mu}_{\tilde{\mathrm{F}}_p^l}(x_p) \tag{8}$$

where x_i ($i = 1, \ldots, p$) denotes the location of the singleton.

IV. Application to Situation Understanding Based on Heterogeneous Sensor Network

In situation awareness, the "weak" can be interprated as, for example, 1) a target (or entity) rarely appears in the sensor field; or 2) the behavior pattern of this target (or entity) has low match with the existing ones in database; or 3) space/time correlation of data/entities to events is low, etc. All the above information can be obtained based on the assumption that high quality information about objects and events is available as a contributor to situation awareness. In general, however, such information is insufficient to provide adequate situation awareness. Actually, some lessons gained from terrorist attacks have already demonstrated that the above "weaks" should be favored in situation awareness. Situation awareness needs the "favor weak" and rule-based mechanisms from PFC.

The new favor weak FLS can be used for level 2/3 fusion (situation awareness and threat assessment) for inferring activities, relationships, and intentions of objects and people in the battlespace based on retrieved knowledge consisting of behavioral patterns, new activities, and anticipated behavior, and also taking into account contextual information (terrain, roads, weather, etc). The level 1 data fusion results (traditional automatic target recognition and pattern recognition) from multimodal sensors will be used as antecedents. For example, considering a heterogeneous sensor network with

Authorized licensed use limited to: University of Texas at Arlington. Downloaded on December 18, 2009 at 14:35 from IEEE Xplore. Restrictions apply.

radar, image/video sensors, and GPS sensor, we can choose the following three antecedents:

1) The number of switches from non-maneuvering set (constant behavior in speed, acceleration, and direction, etc) to the maneuvering set (varying behavior in speed, acceleration, and direction, etc). When a target is beginning a maneuver from a non-maneuvering class, the tracking system can switch the algorithms applied to the problem from a non-maneuvering set to the maneuvering set. The errors in distance from where the tracker estimates the position of a target between the actual position can be very large when the incorrect motion models are applied to the problem. Additionally, when the tracker does finally catch up to the target after the maneuver, the track will "jump" across the operator's scope giving a very unrealistic and unreliable picture of what that target is actually doing. So a threat target will quite often switch from a non-maneuvering set to the maneuvering set, and vice versa, to avoid being tracked all the time. This knowledge can be used as an antecedent for situation awareness.
2) The frequency of appearance of such type of target based on some a priori knowledge such as archival radar data. Generally threat targets are new comparing to archival radar data.
3) The importance of geolocation of this target based on the geographical information systems (GISs). Examples of important geolocations include large metroplex, landmarks, military bases, airport, etc. Threats happen quite often in such areas.

Of the above three antecedents, *the frequency of appearance of such type of target* is weak stimulus and should be favored. A typical rule using the above three antecedents can be

IF the number of switches from non-maneuvering set to the maneuvering set is *High*, and the frequency of appearance of such target is *Low*, and the importance of geolocation of such type of target is *High*, THEN the possibility that an I&W needs to be issued is *Very Strong*.

The linguistic variables used to represent each antecedent are divided into three levels: *Low*, *Moderate*, and *High*. The consequent – the possibility that an indication and warning (I&W) needs to be issued – is divided into 5 levels, *Very Strong, Strong, Medium, Weak, Very Weak*. So we need to set up $3^3 = 27$ (because every antecedent has 3 fuzzy subsets, and there are 3 antecedents) rules for this FLS. Table I summarizes the fuzzy rules we use in this paper.

For input (x_1, x_2, x_3), the output is computed using

$$y(x_1, x_2, x_3) = \frac{\sum_{l=1}^{27} \underline{\mu}_{\tilde{\mathrm{F}}_l^1}(x_1)\overline{\mu}_{\tilde{\mathrm{F}}_l^2}(x_2)\underline{\mu}_{\tilde{\mathrm{F}}_l^3}(x_3)c_{avg}^l}{\sum_{l=1}^{27} \underline{\mu}_{\tilde{\mathrm{F}}_l^1}(x_1)\overline{\mu}_{\tilde{\mathrm{F}}_l^2}(x_2)\underline{\mu}_{\tilde{\mathrm{F}}_l^3}(x_3)} \quad (9)$$

By repeating these calculations for $\forall x_i \in [0, 10]$, we obtain a hypersurface $y(x_1, x_2, x_3)$. This equation represents the nonlinear mapping between three inputs and one output of the FLS. Since it's a 4-D surface (x_1, x_2, x_3, y), it's impossible to be plotted visually.

If we have $x_3 = 8$, and two other antecedents, x_1 and x_2 are variables, we obtain a hypersurface $y(x_1, x_2, 8)$ based on the favor weak FLS, as plotted in Fig. 2(a). In contrast, we use a type-1 FLS where the antecedent membership functions are the lower membership functions since favor weak mechanism is not used, and its output hypersurface $y(x_1, x_2, 8)$ is plotted in Fig. 2(b). Observe that from Fig. 2, the favor weak FLS provides a higher possibility that this target is a threat, which makes sense because the weak factor, frequency of appearance of such type of target, has been favored. So our proposed favor weak FLS can increase the probability of threat detection, and provides timely I&W.

V. Conclusions

Humans use multiple sources of sensory information to estimate environmental properties and has innate ability to integrate information from heterogeneous data sources. There is consensus that it depends on the brain PFC. The PFC has top-down control (favor weak) and rule-based mechanisms, which can be illustrated using the Stroop model. In this paper, we proposed to incorporate the favor weak mechanism into rule-based fuzzy logic systems (FLS) via using upper and lower membership functions. The inference engine of favor weak fuzzzy logic system was proposed under three different categories based on fuzzifiers. We analyzed that the favor weak FLS is a special type-1 FLS which is embeded in an interval type-2 FLS, so it's much simpler in computing than an interval type-2 FLS. We apply the favor weak FLS to situation understanding based on heterogeneous sensor network, and it shows that our favor weak fuzzy logic system has clear advantage comparing to the type-1 FLS. The favor weak FLS can increase the probability of threat detection, and provides timely indication & warning (I&W).

References

[1] C. Bruce C, R. Desimone, C. G. Gross, "Visual properties of neurons in a polysensory area in superior temporal sulcus of the macaque," *J. Neurophysiol.*, vol. 46 369- 84, 1981.
[2] D. A. Chavis, D. N. Pandya, "Further observations on cortico-frontal connections in the rhesus monkey," *Brain Res.*, vol. 117, pp. 369-386, 1976.
[3] J. D. Cohen, D. Servan-Schreiber, "Context, cortex and dopamine: a connectionist approach to behavior and biology in schizophrenia," *Psychol. Rev.*, vol. 99, pp. 45-77.
[4] B. D. Corneil, and D. P. Munoz, "The Influence of Auditory and Visual Distractors on Human Orienting Gaze Shifts," *The Journal of Neuroscience*, vol. 16, no. 24, pp. 8193-8207, December 15, 1996.
[5] R. Desimone, J. Duncan, "Neural mechanisms of selective visual attention," *Annu. Rev. Neurosci.*, vol. 18, pp. 193–222, 1995.
[6] J. Grafman, "Alternative frameworks for the conceptualization of prefrontal functions," *Handbook of Neuropsychology*, ed. F Boller, J Grafman, pp. 187. Amsterdam: Elsevier.
[7] J. M. Hillis, M. O. Ernst, M. S. Banks, and M. S. Landy, "Combining sensory information: Mandatory fusion within, but not between, senses," *Science*, vol. 298, No. 5598, pp. 1627-1630, 2002.

Authorized licensed use limited to: University of Texas at Arlington. Downloaded on December 18, 2009 at 14:35 from IEEE Xplore. Restrictions apply.

[8] M. Hsu, et al, "Neural systems responding to degrees of uncertainty in human decision making," *Science*, vol. 310, pp. 1680-1683, Dec 2005.
[9] E. G. Jones, T. P. S. Powell, An anatomical study of converging sensory pathways within the cerebral cortex of the monkey," *Brain*, vol. 93, pp. 793–820, 1970.
[10] Q. Liang and J. M. Mendel, "Interval type-2 fuzzy logic systems: theory and design," *IEEE Transactions on Fuzzy Systems*, vol. 8, no. 5, pp. 535-550, Oct 2000.
[11] K. Matsumoto and K. Tanaka, Conflict and Cognitive Control, *Science*, vol. 303, pp. 969-970, Feb 2004.
[12] J. M. Mendel, " Fuzzy logic systems for engineering: a tutorial ," *Proc. of the IEEE*, vol. 83, no. 3, pp. 345-377, March 1995.
[13] E. K. Miller, "The prefrontal cortex: complex neural properties for complex behavior," *Neuron*, vol. 22, pp. 15-17, 1999.
[14] E. K. Miller, J. D. Cohen, "An Integrative Theory of Prefrontal cortex function," *Annu. Rev. Neurosci.*, vol. 24, pp. 167, 2001.
[15] B. Milner, "Effects of different brain lesions on card sorting," *Arch. Neurol.*, vol. 9, pp. 90, 1963.
[16] R. C. O'Reilly, "Biologically Based Computational Models of High-Level Cognition," *Science*, Oct 2006.
[17] D. N. Pandya, C. Barnes, "Architecture and connections of the frontal lobe," *The Frontal Lobes Revisited*, ed. E Perecman, pp. 41- 72. New York: IRBN, 1987.
[18] R. Passingham, *The Frontal Lobes and Voluntary Action*, Oxford, UK: Oxford Univ. Press.
[19] J. R. Stroop, "Studies of interference in serial verbal reactions," *J. Exp. Psychol.* vol. 18, pp. 643- 62, 1935.
[20] S. P. Wise, et al, "The frontal-basal ganglia system in primates," *Crit. Rev. Neurobiol.*, vol. 10, pp. 317-356.

TABLE I

FUZZY RULES USED IN THE APPLICATION. ANTE 1 IS THE NUMBER OF SWITCHES FROM NON-MANEUVERING SET TO THE MANEUVERING SET OR VICE VERSA; ANTE 2 THE FREQUENCY OF APPEARANCE OF SUCH TYPE OF TARGET; ANTE 3 IS THE IMPORTANCE OF GEOLOCATION OF THIS TARGET; AND CONSEQUENT IS THE POSSIBILITY THAT THIS TARGET IS A THREAT.

Rule #	Ante 1	Ante 2	Ante 3	Consequent
1	low	low	low	Weak
2	low	low	moderate	Medium
3	low	low	high	Strong
4	low	moderate	low	Very Weak
5	low	moderate	moderate	Weak
6	low	moderate	high	Medium
7	low	high	low	Very Weak
8	low	high	moderate	Weak
9	low	high	high	Medium
10	moderate	low	low	Medium
11	moderate	low	moderate	Strong
12	moderate	low	high	Very Strong
13	moderate	moderate	low	Weak
14	moderate	moderate	moderate	Medium
15	moderate	moderate	high	Strong
16	moderate	high	low	Very Weak
17	moderate	high	moderate	Weak
18	moderate	high	high	Medium
19	high	low	low	Medium
20	high	low	moderate	Strong
21	high	low	high	Very Strong
22	high	moderate	low	Weak
23	high	moderate	moderate	Medium
24	high	moderate	high	Strong
25	high	high	low	Very Weak
26	high	high	moderate	Weak
27	high	high	high	Moderate

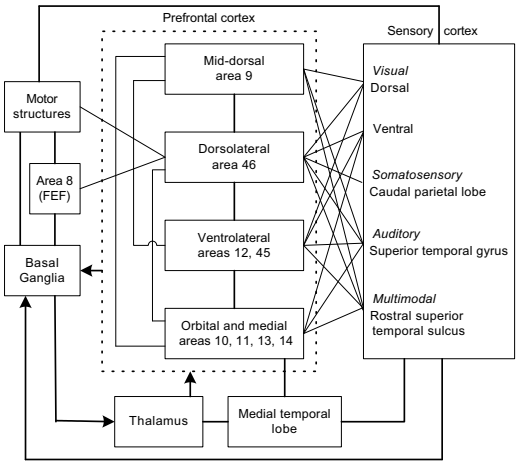


Fig. 1. Schematic diagram of some of the extrinsic and intrinsic connections of the PFC. Most connections are reciprocal; the exceptions are indicated by arrows. The frontal eye field (FEF) has variously been considered either adjacent to, or part of, the PFC.

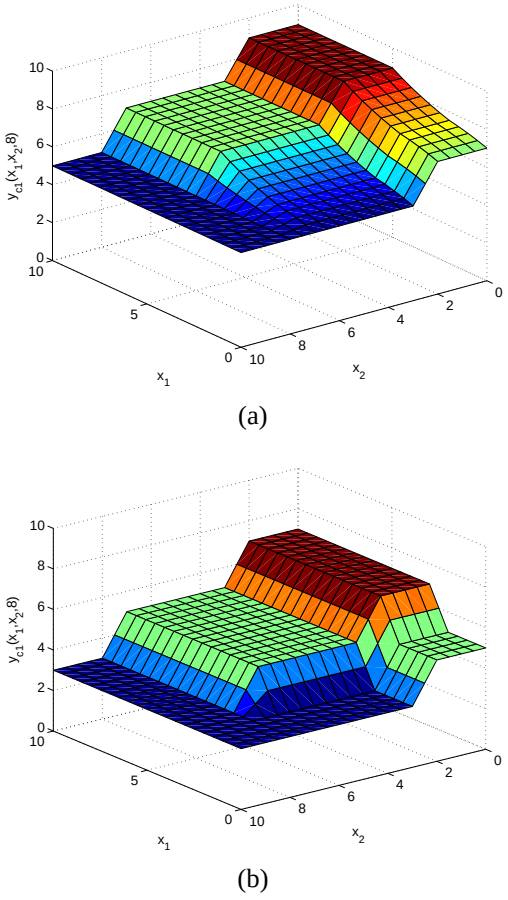


Fig. 2. The threat assessment surface for different FLSs when $x_3 = 8$. (a) Favor weak FLS, and (b) Traditional type-1 FLS.

Authorized licensed use limited to: University of Texas at Arlington. Downloaded on December 18, 2009 at 14:35 from IEEE Xplore. Restrictions apply.

This full text paper was peer reviewed at the direction of IEEE Communications Society subject matter experts for publication in the IEEE ICC 2009 proceedings

Radar Sensor Network Using a New Triphase Coded Waveform: Theory and Application

Lei Xu and Qilian Liang
Department of Electrical Engineering
University of Texas at Arlington
Arlington, TX 76019-0016
Email: xu@wcn.uta.edu, liang@uta.edu

ABSTRACT

In radar sensor network (RSN), interference with each radar can be effectively reduced when waveforms are properly designed. In this paper, we firstly perform some theoretical studies on co-existence of phase coded waveforms in RSN. Then we give the definition of a new set of triphase coded waveforms called optimized punctured Zero Correlation Zone sequence-pair set (optimized punctured ZCZPS) and analyze their properties especially their optimized cross correlation property of any two sequence-pairs in the set. Furthermore, we apply our newly provided triphase coded waveforms and equal gain combination technique to the system simulation, and study the performances versus different number of radars in RSN, with Doppler shift or not. Simulation results show that detection performances of multiradars (utilizing our optimized punctured ZCZPS and equal gain combination), either under the Doppler shift condition or not, are superior to those of singler radar.

Keywords: Zero correlation zone; Opimized punctured ZCZ sequence-pair; Radar sensor network.

I. INTRODUCTION

With recent rapid development in information fusion technology, much time and effort have been put in radar waveform design for a single active radar [1] [2]. However, multiple radar sensors can be combined to form a multiradar system to overcome performance degradation of single radar along with waveform optimization. In [3], Liang studied constant frequency (CF) pulse waveform design and proposed maximum-likelihood (ML) automatic target recognition (ATR) approach for both nonfluctuaing and fluctuating targets in a network of multiple radar sensors. In [4], RSN design based on linear frequency modulation (LFM) waveform was studied and LFM waveform design was applied to RSN with application to ATR with delay-Doppler uncertainty by Liang as well. J.Liang [5] provided an orthogonal waveform model for RSN, which eliminates interference when there is no Doppler shift.

Nevertheless, the radar sensor network using phase coded waveforms has not been well studied so far. Phase coded waveform design is one of the widely used waveform design methods for pulse compression which allows a radar to simultaneously achieve the energy of a long pulse and the resolution of a short pulse without the high peak power which is required by a high enery short duration pulse [1]. In this paper, we firstly theoretically study RSN design based on phase coded waveforms: the conditions for waveforms co-existence. We perform studies on the codes' properties, especially the cross correlation property and analyze the performance of optimized punctured ZCZ sequence-pairs in RSN system with Doppler shift. Then we apply our newly proposed triphase codes called optimized punctured ZCZ sequence-pair set (optimized punctured ZCZPS) to RSN. The simulation results show that RSN based on a set of optimized punctured ZCZ sequence-pairs provides promising detection performance much better than that of single radar.

The rest of the paper is organized as follows. In Section 2, we study the co-existence of phase coded waveforms. Section 3 introduces the definition and properties of our newly provided triphase coded waveform–optimized punctured ZCZ sequence-pair set. In Section 4, we study the performance versus the number of radars in RSN with Doppler shift. In Section 5, conclusions are drawn on a RSN using our optimized punctured ZCZPS.

II. CO-EXISTENCE OF PHASE CODED WAVEFORMS IN RSN

We assume there are N radars networking together in a self-organizing fashion in our RSN. The radar i transmits a waveform as

$$x_i(t) = \sum_{n=0}^{N-1} x_i^{(n)}(t - n\tau_c) = \sum_{n=0}^{N-1} exp(j2\pi\beta_i^{(n)}(t - n\tau_c)) \quad (1)$$

Here, $0 < t <= \tau_c$.

When the phase coded waveforms are orthogonal to each other, the interference from one waveform to the another can be minimized or even removed. The cross correlation between $x_i(t)$ and $x_j(t)$ could be

$$\int_{-T/2}^{T/2} x_i(t)x_j^*(t)dt = \tau_c \sum_{n=0}^{N-1} exp[j2\pi(-\frac{N}{2} + \frac{1}{2})\tau_c(\beta_i^{(n)} - \beta_j^{(n)}]$$

$$sinc[\tau_c(\beta_i^{(n)} - \beta_j^{(n)})] \quad (2)$$

978-1-4244-3435-0/09/$25.00 ©2009 IEEE

Authorized licensed use limited to: University of Texas at Arlington. Downloaded on December 18, 2009 at 14:37 from IEEE Xplore. Restrictions apply.

The optimized cross correlation is that of orthogonal waveforms

$$\int_{-T/2}^{T/2} x_i(t)x_j^*(t)dt = \begin{cases} N\tau_c & i=j \\ 0 & i\neq j \end{cases} \quad (3)$$

It is easy to see that when $\sum_{n=0}^{N-1}\pi\tau_c(\beta_i^{(n)}-\beta_j^{(n)}) = k\pi, k = 1,2,3...$, it satisfies the equation (3). In this way can phase coded waveforms be orthogonal to each other and work well simultaneously in Radar Sensor Network.

Nevertheless, there are time delay and Doppler shift ambiguity that will introduce interference to waveforms in RSN. Ambiguity function (AF) [6] is usually used to succinctly characterize the behavior of a waveform paired with its matched filter. In the RSN of M radars, the radar i not only receives its own back-scattered waveform, but also scattered signals generated by other $M-1$ radars which caused interference to radar i.

Assuming each radar transmits signal synchronously, $t_1 = t_2 = t_M = 0$. Considering time delay $\tau = m\tau_c$ for receiving radar i and interferences from all the other $M-1$ radars, the ambiguity function of radar i could be

$$\begin{aligned} & A_i(\tau, F_{D_1}, ..., F_{D_M}) \quad (4) \\ = \; & |\tau_c \sum_{j=1}^{M}\sum_{n=m}^{N-1} exp[j2\pi[\beta_i^{(n-m)}(\frac{N}{2}+m-1)\tau_c \\ & +\beta_j^{(n)}(-\frac{N}{2}+1)\tau_c + F_{D_j}(-\frac{N}{2}+n+1)\tau_c]] \\ & sinc[\tau_c(\beta_j^{(n)}-\beta_i^{(n-m)}+F_{D_j})]| \end{aligned}$$

Here, $0 < i <= M$. (4) consists of two parts: useful signal $j = i$ part in the (4); and interferences from other $M-1$ radar waveforms, $j \neq i$ parts in (4). Since $\sum_{n=0}^{N-1}\pi\tau_c(\beta^{(n)} - \beta^{(n-m)}+F_D) = k\pi, k = 1,2...$, it satisfies that $A(\tau, F_D) = 0$, when $F_D = \frac{k}{\tau_c}, k = 0,1,....$

III. Optimized Punctured ZCZ Sequence-Pair set

Zero correlation zone (ZCZ) is a new concept provided by Fan [7] in which both autocorrelation and cross correlation sidelobes are zero while the time delay is kept within the ZCZ instead of the whole period of time domain.

Matsufuji and Torii have provided some methods of constructing ZCZ sequences in [8] [9]. In this section, we apply optimized punctured sequence-pair [10] in ZCZ to construct optimized punctured ZCZ sequence-pair set.

A. The Definition of Optimized Punctured ZCZ Sequence-Pair Set

Definition 3-1 Assume $(x^{(p)}, y^{(p)})$ to be a sequence-pair of set (X, Y) of length N and the number of sequence-pairs K, where $p = 0,1,...,N-1, i = 0,1,...,K-1$, if sequences in the set satisfy the following equation:

$$R_{x^{(p)}y^{(q)}}(\tau) = \sum_{i=0}^{N-1} x_i^{(p)} y_{(i+\tau)mod(N)}^{(q)*} = \sum_{i=0}^{N-1} y_i^{(p)} x_{(i+\tau)mod(N)}^{(q)*}$$

$$= \begin{cases} \lambda N, & \text{for } \tau = 0, p = q \\ 0, & \text{for } \tau = 0, p \neq q \\ 0, & \text{for } 0 < |\tau| \leq Z_0 \end{cases} \quad (5)$$

where $0 < \lambda \leq 1$, $(x^{(p)}, y^{(p)})$ is called a ZCZ sequence-pair, $ZCZP(N, K, Z_0)$ is an abbreviation. (X, Y) is called a ZCZ sequence-pair set, $ZCZPS(N, K, Z_0)$ is an abbreviation.

Definition 3-2 [10] Sequence $u = (u_0, u_1, ..., u_{N-1})$ is the punctured sequence for $v = (v_0, v_1, ..., v_{N-1})$,

$$u_j = \begin{cases} 0, & \text{if } j \in p \text{ punctured bits} \\ v_j, & \text{if } j \in \text{Non-punctured bits} \end{cases} \quad (6)$$

Here, p is the number of punctured bits in sequence v. Suppose $v_j \in (-1, 1)$, u is p-punctured binary sequence that $u_j \in (-1, 0, 1)$, (u, v) is called a punctured binary sequence-pair.

Theorem 3-1 [10] The autocorrelation of punctured sequence-pair (u, v) is defined

$$R_{uv}(\tau) = \sum_{i=0}^{N-1} u_i v_{(i+\tau)modN}, 0 \leq \tau \leq N-1 \quad (7)$$

If the punctured sequence-pair has the following autocorrelation property:

$$R_{uv}(\tau) = \begin{cases} E, & \text{if } \tau \equiv 0 \text{mod} N \\ 0, & \text{others} \end{cases} \quad (8)$$

the punctured sequence-pair is called optimized punctured sequence-pair [10]. Where, $E = \sum_{i=0}^{N-1} u_i v_{(i+\tau)modN} = N - p$, is the energy of punctured sequence-pair.

The properties, existing necessary conditions and some construction methods of punctured binary sequence-pair have been well studied by Jiang [10]. Many optimized punctured sequence-pairs have been found of length from 7 to 31 so far.

Definition 3-3 If $(x^{(p)}, y^{(p)})$ in Definition 3-1 is constructed by optimized punctured sequence-pair and a certain matrix, such as Hadamard matrix or an orthogonal matrix, where

$$x_i^{(p)} \in (-1, 1), \quad i = 0,1,2,...,N-1$$
$$y_i^{(q)} \in (-1, 0, 1), \quad i = 0,1,2,...,N-1$$

$$R_{x^{(p)}y^{(q)}}(\tau) = \sum_{i=0}^{N-1} x_i^{(p)} y_{(i+\tau)modN}^{(q)*} = \sum_{i=0}^{N-1} y_i^{(p)} x_{(i+\tau)modN}^{(q)*}$$

$$= \begin{cases} \lambda N, & \text{for } \tau = 0, p = q \\ 0, & \text{for } \tau = 0, p \neq q \\ 0, & \text{for } 0 < |\tau| \leq Z_0 \end{cases} \quad (9)$$

where $0 < \lambda \leq 1$, then $(x^{(p)}, y^{(p)})$ can be called an optimized punctured ZCZP.

B. Design for Optimized Punctured ZCZ Sequence-pair Set

An optimized punctured ZCZ sequence-pair set can be constructed from the following steps:

Step 1: Given an odd length optimized punctured binary sequence-pair (u, v), the length of each sequence is N_1

$$u = u_0, u_1, ..., u_{N_1-1}, u_i \in (-1, 1),$$
$$v = v_0, v_1, ..., v_{N_1-1}, v_i \in (-1, 0, 1),$$

Authorized licensed use limited to: University of Texas at Arlington. Downloaded on December 18, 2009 at 14:37 from IEEE Xplore. Restrictions apply.

Step 2: Given Hadamard matrix B, the length of the sequence is N_2 which is equal to the number of the sequences.

$$B = (b^0; b^1; ..., b^{N_2-1}), b^i = (b_0^i, b_1^i, ..., b_{N_2-1}^i)$$

Step 3: Process bit-multiplication of optimized punctured binary sequence-pair and each row of Hadamard matrix B,

$$\begin{aligned}
&x_j^i = u_{jmodN_1} b_{jmodN_2}^i, 0 \le i \le N_2 - 1, 0 \le j \le N - 1,\\
&X = (x^0; x^1; ...; x^{N_2-1}), x^i = (x_0^i, x_1^i, ..., x_{N-1}^i,)\\
&y_j^i = v_{jmodN_1} b_{jmodN_2}^i, 0 \le i \le N_2 - 1, 0 \le j \le N - 1,\\
&Y = (y^0, y^1, ..., y^{N_2-1}), y^i = (y_0^i, y_1^i, ..., y_{N-1}^i,)
\end{aligned}$$

Where $GCD(N_1, N_2) = 1$ and $N = N_1 * N_2$. The three steps make the sequence-pair set (X, Y) an optimized punctured ZCZPS, where ZCZ $Z_0 = N_1 - 1$. The length of each sequence in optimized punctured ZCZPS is $N = N_1 * N_2$ that depends on the product of length of optimized punctured sequence-pair and the length of a row in Hadamard matrix. The number of sequence-pairs in optimized punctured ZCZPS rests on the order of the Hadamard matrix. The sequence x^i in X and the corresponding sequence y^i in Y construct an optimized punctured ZCZP (x^i, y^i) that can be used as a phase coded waveform, such as x^i for radar transmitter and y^i for radar receiver. The phase states for any sequence-pair among (x^i, y^i) are only of three options, so our newly provided optimized punctured ZCZPS is a new set of triphase codes.

It is easy to prove that the correlation property of the sequence-pairs in the set is:

$$\begin{aligned}
R_{x^i y^j}(\tau) &= R_{x^j y^i}(\tau) = R_{uv}(\tau mod N_1) R_{b^i b^j}(\tau mod N_2)\\
&= \begin{cases} EN_2, & \text{if } \tau = 0, i = j \\ 0, & \text{if } 0 < |\tau| \le N_1 - 1, i = j \\ 0, & \text{if } i \ne j \end{cases}
\end{aligned}$$

According to Definition 3-1, the sequence-pair set constructed by the above method is a ZCZPS.

C. Properties of Optimized Punctured ZCZ Sequence-pair set

An example is given to analyze the autocorrelation and cross correlation properties of the optimized punctured ZCZPS constructed by the method mentioned above. The 124-length optimized punctured ZCZPS (X, Y) is constructed by 31-length optimized punctured binary sequence-pair $(u, v), u = [+++-----+-+-+++-----+--+--+++-++-]$, $v = [++++000+0+0+++0000+00+00+++0++0]$ (using $'+'$ and $'-'$ symbols for $'1'$ and $'-1'$) and Hadamard matrix H of order 4. Each row of matrix $X = [x_1; x_2; x_3; x_4]$ and $Y = [y_1; y_2; y_3; y_4]$ constitute a certain optimized punctured ZCZP (x_i, y_i).

1) Autocorrelation and Cross Correlation Properties: The autocorrelation property $R(x_1, y_1)$ and cross correlation property $R(x_1, y_2) = R(y_1, x_2)$ of 124-length optimized punctured ZCZPS (X, Y), are shown in Fig.1.

According to Fig.1, the sidelobe of autocorrelation of ZCZPS can be as low as 0 when the time delay is kept within $Z_0 = N_1 = 31$ and the cross correlation value is 0 during the whole time domain. The only uniform phase codes that can reach the maximum peak signal sidelobe ratio (PSR) [6] are the Barker codes whose length is equal or less than 13. The sidelobe of the new code shown in Fig.1 can be as low as 0, and the PSR can be as large as infinite. Besides, the length of the new code is various and much longer than the length of the Barker code.

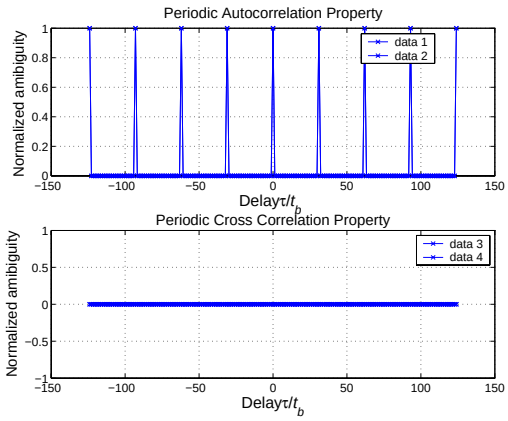


Fig. 1. Periodic autocorrelation property of optimized punctured ZCZ sequence-pair set

2) Ambiguity function: Because of the Doppler shift f_d [6], the main peak of the autocorrelation function is reduced and so as to the SNR degradation. Focusing on the sequence-pair (x, y) here, the receiving sequence in ambiguity function is different from the echo signal and the periodic correlation is used instead of aperiodic correlation here. The ambiguity function can be rewritten as

$$\begin{aligned}
A(\tau, F_D) = |&\int_{-\frac{T}{2}}^{-\frac{T}{2}+\tau} x(t) exp(j2\pi F_D t) y^*(t + T - \tau)) dt\\
&+ \int_{-\frac{t}{2}+\tau}^{\frac{T}{2}} x(t) exp(j2\pi F_D t) y^*(t - \tau) dt| \qquad (10)
\end{aligned}$$

In order to analyze the autocorrelation performance of an optimized punctured ZCZP with delay-Doppler shift, Equation (10) is plotted in Fig.2(a) in a three-dimensional surface plot. In Fig.2(a), there is relative uniform plateau suggesting low and uninform sidelobes. This low and uniform sidelobes minimize target masking effect in ZCZ of time domain, where $Z_0 = 31$, $-31 < \tau < 31, \tau \ne 0$.

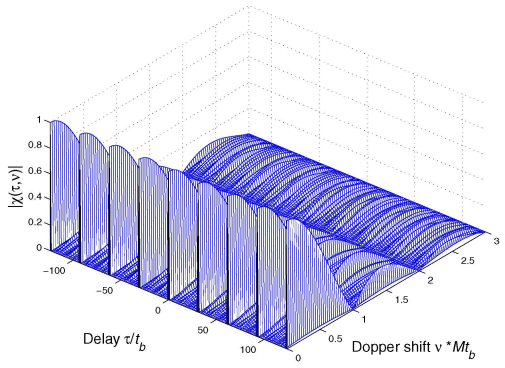
D. Co-existence of Optimized Punctured ZCZ Sequence-pairs

Considering interference from other radars $j \ne i$, with delay-Doppler shift, the ambiguity function of radar i is

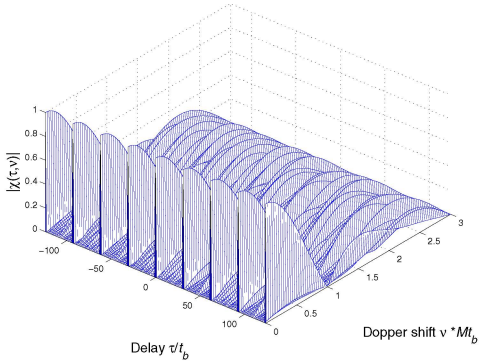
$$\begin{aligned}
&A(\tau, F_{D_1}, ...F_{D_M})\\
&= |\int_{-\infty}^{\infty} \sum_{j}^{M} (x_j(t) exp(j2\pi F_{D_i} t) y_i^*(t - \tau) dt| \qquad (11)
\end{aligned}$$

Fig.2(b) is three-dimensional surface plot to analyze the ambiguity function of radar i (considering interference from other radars). Fig.2(b) closely resembles Fig.2(a). Without Doppler shift, there are regular high peaks on multipliers of

Authorized licensed use limited to: University of Texas at Arlington. Downloaded on December 18, 2009 at 14:37 from IEEE Xplore. Restrictions apply.



(a)



(b)

Fig. 2. (a)Ambiguity function of a 124-length ZCZ sequence-pair(x_i, y_i) (b)Ambiguity function of radar i (considering interference from other radars)

period of 31 which is the length of ZCZ. And the high peak on zero time delay point can be used to detect targets. Hence, even considering the interference from other $M-1$ radars, the radar i may work as well as there is no interference.

IV. System Simulation in Radar Sensor Network

In RSN of M radars, the combined received signal for the radar i is

$$r_i(u,t) = \sum_{j=1}^{M} x_j(t-t_j)exp(j2\pi F_{D_j}t) + n(u,t) \qquad (12)$$

F_{D_j} and t_j are Doppler shift of target and time delay relative to waveform j, and $n(u,t)$ is additive white Gaussian noise (AWGN). The structure can be constructed as Fig.3.

According to this structure, the combined received signal $r_i(u,t)$ is processed by its corresponding matched filter i and the output of branch i is $Z_i(u,t)$. Each $Z_i(u,t)$ can be equal gain combined to construct the final output $Z(u,t)$.

The output $|Z_i(u)|$ of branch i is

$$|\int_{-\frac{T}{2}}^{-\frac{T}{2}} [\sum_{j=1}^{M} x_j(t-t_j)exp(j2\pi F_{D_j}t) + n(u,t)]y_i^*(t-t_i)dt| \qquad (13)$$

Where $n(u) = \int_{-\frac{T}{2}}^{-\frac{T}{2}} n(u,t)y_i^*(t-t_i)dt$ can be easily proved to be still an AWGN.

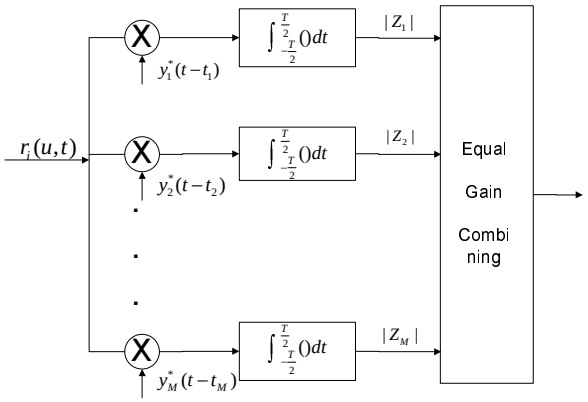


Fig. 3. Waveform diversity combining in RSN

We can also have two special cases for $|Z_i(u)|$:
1)If there is Dopper shift but no time delay, all the radar sensors transmit signals synchronously, $|Z_i(u)|$ turns to be:

$$|\int_{-\frac{T}{2}}^{-\frac{T}{2}} [\sum_{j=1}^{M} x_j(t)exp(j2\pi F_{D_j}) + n(u,t)]y_i^*(t)dt| \qquad (14)$$

Assuming that the Doppler shift can be well estimated in the receiving radar sensor, so the Doppler shift compensation factor $exp^*(j2\pi F_{D_j})$ is introduced here.

$$|Z_i(u)| \le |E| + |\int_{-\frac{T}{2}}^{-\frac{T}{2}} [\sum_{j=1}^{M} x_j(t)exp(j2\pi(F_{D_j} - F_{D_i}))y_i^*(t)|$$
$$+|\int_{-\frac{T}{2}}^{-\frac{T}{2}} n(u,t)y_i^*(t)exp^*(j2\pi F_{D_i}t)dt| \qquad (15)$$

If $F_{D_1} = F_{D_2} = ... = F_{D_j} = F_D$, further simlified as

$$|Z_i(u)| \le |E| + 0 + |\int_{-\frac{T}{2}}^{-\frac{T}{2}} n(u,t)y_i^*(t)exp^*(j2\pi F_{D_i}t)dt| \qquad (16)$$

2) If both time delay and Doppler shift exist in the RSN, assuming $F_{D_1} = F_{D_2} = ... = F_{D_j} = F_D$, considering the Doppler shift compensation factor in the receiving sensor,

$$|Z_i(u)| \le |E| + |\int_{-\frac{T}{2}}^{-\frac{T}{2}} [\sum_{j\neq i}^{M} x_j(t-t_j)]y_i^*(t-t_i)dt|$$
$$+|\int_{-\frac{T}{2}}^{-\frac{T}{2}} n(u,t)y_i^*(t-t_j)exp^*(j2\pi F_{D_i}t)dt| \qquad (17)$$

Because of the good properties of our proposed codes, we modify the frame of receiving data before the matched filter on the receiver to improve the RSN performance. The data from $N+1$ to $max(t_j)+N$ are added to data from 1 to $max(t_j)$, bit by bit, where N is the original data length and t_j is the time delay for jth transmitting radar sensor. In this way can we get the output of the matched filter

$$|Z_i(u)| \le |E| + 0 + |\int_{-\frac{T}{2}}^{-\frac{T}{2}} n(u,t)y_i^*(t)exp^*(j2\pi F_{D_i}t)dt| \qquad (18)$$

Authorized licensed use limited to: University of Texas at Arlington. Downloaded on December 18, 2009 at 14:37 from IEEE Xplore. Restrictions apply.

According to (16) and (18), it is easy to see that using our provided codes and frame modification the RSN under the condition of time delay for each radar sensor can, to some extent, work as well as the RSN where all the radar sensors transmit signals synchronously.

We apply optimized punctured ZCZPS as a bank of phase coded waveforms together with equal gain combination technique in the simulation in order to study the performance versus different number of radars in RSN with Doppler shift. We respectively simulated P_M (Probability of Miss Detection) and P_{FA} (Probability of False Alarm) of different number of radars using different number of optimized punctured ZCZ sequence-pairs. Two special cases of performances have been simulated. They are performances under the condition of no time delay but Doppler shift, and under the condition of time delay for each radar sensor and having Doppler shift.

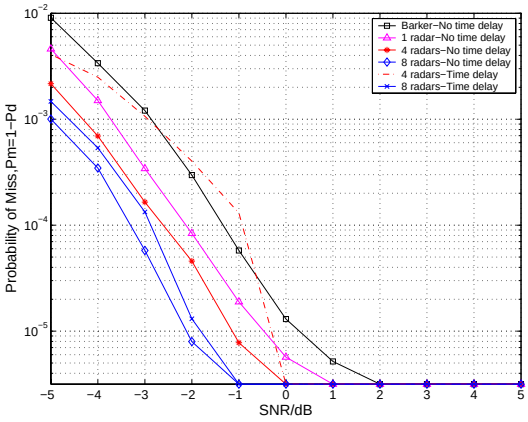


Fig. 4. Probability of miss detection in RSN under the condition of no time delay but Doppler shift or time delay and Doppler shift

Fig.4 illustrates that when $P_M = 10^{-3}$, SNR of 8-radars are $2.2dB$ smaller than that of single radar system using Barker code with Doppler shift. Considering time delay for each radar in Fig.4, SNR of 8-radar RSN can gain $1.7dB$ smaller than 4-radar SNR to acheive the same $P_M = 10^{-3}$.

According to Fig.5, the SNR of 8-radars can be nearly $3.8dB$ smaller than that of single radar system using Barker code in order to achieve the same $P_{FA} = 10^{-2}$. In addition, 4-radar system requires $1.7dB$ more than that of 8-radar RSN under the condition of both time delay and Doppler shift.

The above figures distinctly illustrate that performances of detection of multiradars are superior to that of singler radar. The performances of 4-radar and 8-radar RSN considering time delay for each radar transimtting sensor can be comparable to those under the condition of no time delay, when large amount of radars are used in the RSN.

V. Conclusion

We have studied phase coded waveform design and spatial diversity under the condition of Doppler shift in RSN. In this paper, we also investigate the definition and properties of

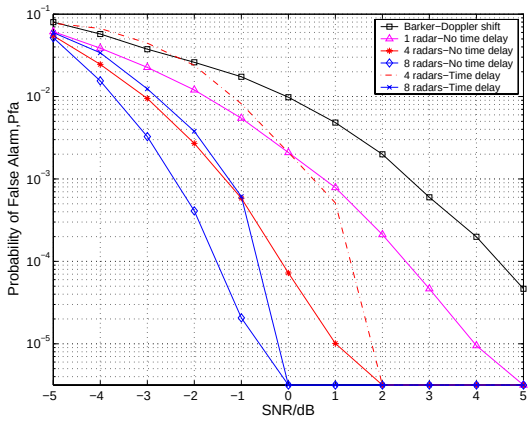


Fig. 5. Probability of false alarm in RSN under the condition of no time delay but Doppler shift or time delay and Doppler shift

optimized punctured ZCZPS. The significant advantage of the optimized punctured ZCZ sequence-pair set is a considerably reduced autocorrelation sidelobe as low as zero in ZCZ and zero mutual cross correlation value in the whole time domain. The general conclusion can be drawn that applying our optimized punctured ZCZPS as a bank of phase coded waveforms to a RSN can effectively satisfy higher demands criterion for detection accuracy in modern military and security affairs.

Acknowledgement

This work was supported by the Office of Naval Research (ONR) Grant N00014-07-1-0395, N00014-07-1-1024, and N00014-03-1-0466.

References

[1] M. R. Bell, "Information theory and radar waveform design," *IEEE Trans on Information Theory,* vol. 39, no. 5, pp. 1578-1597, Sept. 1993.

[2] S. Sowelam and A. Tewfik, "Waveform selection in radar target classification," *IEEE Trans on Information Theory,* vol. 46, no. 3, pp. 1014-1029, 2000.

[3] Q. Liang, "Waveform Design and Diversity in Radar Sensor Networks: Theoretical Analysis and Application to Automatic Target Recognition," *Sensor and Ad Hoc Communications and Networks,* vol. 2, no. 28, pp. 684-689, Sep. 2006.

[4] Q. Liang, "Radar Sensor Networks for Automatic Target Recognition with Delay-Doppler Uncertainty," *Military Communications Conference, 2006. MILCOM 2006* 23-25, pp. 1-7, Oct. 2006.

[5] J. Liang, and Q. Liang, "Orthogonal Waveform Design and Performance Analysis in Radar Sensor Networks," *Military Communications Conference, 2006. MILCOM 2006* 23-25, pp. 1-6, Oct. 2006.

[6] M. A. Richards, *Fundamentals of Radar Signal Processing,* McGraw-Hill, 2005.

[7] P. Z. Fan, N. Suehiro, N. Kuroyanagi and X. M. Deng, "A class of binary sequences with zero correlation zone," *IEE Electron.Letter,* 35 (10): 777-779, 1999.

[8] S. Matsufuji, N Suehiro , N Kuroyanagi and P Z Fan, "Two types of polyphase sequence set for approximately synchronized CDMA systems," *IEICE Trans. Fundamentals,* E862A(1): 229-234, Jan. 2003.

[9] H. Torii, M. Nakamura and N. Suehiro, "A new class of zero correlation zone sequences," *Tran. Inform.Theory,* 50: 559-565, Mar. 2004.

[10] T. Jiang, *Research on Quasi-Perfect Binary Signal Pair and Perfect Punctured Binary Signal Pair Theory,* Ph.D Dissertation: Yanshan University, 2003.

Authorized licensed use limited to: University of Texas at Arlington. Downloaded on December 18, 2009 at 14:37 from IEEE Xplore. Restrictions apply.

This full text paper was peer reviewed at the direction of IEEE Communications Society subject matter experts for publication in the IEEE ICC 2009 proceedings

UWB Radar Sensor Networks Detection of Targets in Foliage Using Short-Time Fourier Transform

Jing Liang, Qilian Liang
Department of Electrical Engineering
University of Texas at Arlington
Arlington, TX 76019-0016, USA
Email: jliang@wcn.uta.edu, liang@uta.edu

***Abstract*— In this paper, we study target detection in foliage environment. When radar echoes are in good quality, the detection of target can be achieved by applying short time Fourier transform (STFT) to the received UWB radar waveform. We compare our approach in case of no target as well as with target against the scheme in which 2-D image was created via adding voltages with the appropriate time offset. Results show that our approach can detect target more easily. When radar echoes are in poor condition and single radar is unable to carry out the detection, we employ both Radar Sensor Networks (RSN) and RAKE structure to combine the echoes from different radar members and finally detect the target.**

I. Introduction

Forest has been an asymmetric threat environment due to a limited sensing capability of a warfighter. It provides excellent concealment from observation, ambush, and escape, as well as secure bases for enemy command & control (C2), weapons caches, and improvised explosive device (IED)/ weapon of mass destruction (WMD) assembly. Detecting targets beneath foliage has been a long-standing problem for both military and civilian communities. In addition, it will benefit other sensing problems such as detection and recognition of targets obscured by soil or building structures.

There have been many efforts undertaken to investigate foliage penetration. [1] measured one-way transmission properties of foliage using a bistatic and coherent wide-band system over the band from 300 to 1300 MHz. [2] made measurements of two-way foliage attenuation by synthetic aperture radar (SAR) and discussed probability dependency for frequency, polarization and depression angle. These studies has shown that foliage contains many spikes and is very "impulsive", which makes target detection difficult to achieve. Some other works are based on foliage clutter modeling. Although K-distribution has been favored for statistic model of radar clutter [3], [4] demonstrated that in very spiky and impulsive foliage clutter, K-distribution is inaccurate. Afterwards, an alpha-stable foliage clutter model has been proposed in [5]. However, all the above efforts are focusing on the analysis of foliage characterization. The pragmatic target detection measurements in foliage has not been available previously in the literature.

A new foliage penetration measurement effort began in August 2005 and continued through December 2005. The foliage measured included late summer foliage and fall and early winter foliage. Late summer foliage, because of the limited rainfall, involved foliage with decreased water content. Late fall and winter measurements involved largely defoliated but dense forest. Ultra-wide band (UWB) radars have been employed due to the exceptional range resolution coupled with penetrating capability and low power [6] [7]. The triangular-shaped target, which was shown in Fig. 1, was a round trip distance of 600 feet from the bistatic antennas (300 feet one way). The collected data is illustrated in Fig. 2.



Fig. 1. The target (a trihedral reflector) is shown on the stand.

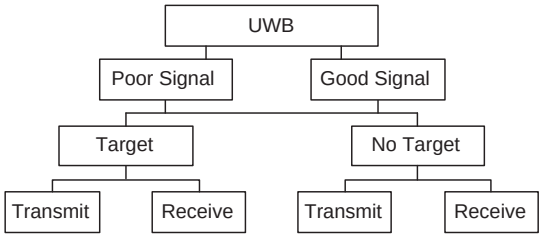


Fig. 2. Data file structure.

For further detailed measurement, please refer to [8]. In [8], we applied differential based technology to received UWB radar waveforms in order to detect the target. Although it can work well for good quality echoes and poor ones with the help of radar sensor networks (RSN), actually a threshold is needed to separate false-alarm signal from real target echoes. This will be further illustrated in Section III.

978-1-4244-3435-0/09/$25.00 ©2009 IEEE

Authorized licensed use limited to: University of Texas at Arlington. Downloaded on December 18, 2009 at 14:38 from IEEE Xplore. Restrictions apply.

In this paper we propose a short-time Fourier transform (STFT) based approach to detect the target obscured by foliage canopy. Compared with the differential based technology, this new approach is more accurate and intuitive. The organization of the paper is as follows: Section II elaborates the target detection problem. Section III proposes a STFT based approach for through-foliage target detection when the signal quality is good. Section IV applies RSN and RAKE structure for through-foliage target detection when the signal quality is poor. Section V concludes this paper.

II. Target Detection Problem

We considered two sets of data from this experiment: "good" and "poor". Good signal quality data were collected using high amplitude pulses and 100 pulses reflected signals were averaged for each collection. When the Barth pulse source was operated at low amplitude and significant pulse-to-pulse variability was noted for these collections. We refer this set of collections as "poor" signal. Fig. 3 shows the received UWB waveforms with and without target for good signal. Poor echoes look similar on the whole. In order to further analyze their difference as well as the discrepancy between no target and with target, we provide expanded views from sample 13001 to 15000 in Fig.4 and 5. Each sample is spaced at 50 picosecond interval, and 16,000 samples were collected for each collection for a total time duration of 0.8 microseconds.

The target response for good and poor signals will be the echo differences, plotted in Fig. 4c and 5c respectively. However, in a practical situation we either obtain clutter echo without target or waveforms with target on range without the knowledge about the presence of it. The challenge is how can we make target detection only based on Fig. 4b and Fig. 5b (with target)? How can we tell the absence of target only based on Fig. 4a or Fig. 5a (no target)?

III. Target Detection with Good Signal Quality

Although Fig. 4a and 4b look quite similar at first sight, after careful observation, it is not difficult to find that the sample strength change more abruptly where target appears (around sample 14000), which implies that echo from target contains more AC values than that without target. This phenomenon inspires the application of short time Fourier transform (STFT) [9].

STFT uses a slide window to determine the sinusoidal frequency and phase content of a signal as it changes over time. This form of the Fourier transform, also known as time-dependent fourier transform, has a great many applications in sonar and radar processing. We will show that STFT - based approach is able to make target detection more intuitively and easily.

For the continuous-time signal, the function to be transformed is multiplied by a nonzero window sliding along the time axis, therefore a two-dimensional expression can be defined as:

$$F(m,w) = \int_{-\infty}^{\infty} x(t)w(t-m)e^{-jwt}dt \qquad (1)$$

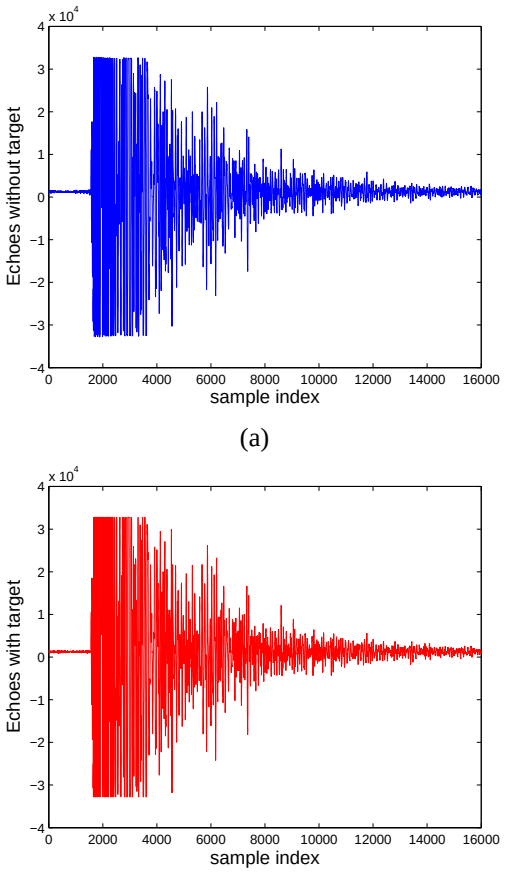


Fig. 3. Measurement with very good signal quality and 100 pulses integration. (a) no target on range (b) with target on range (target appears at around sample 14000)

where $x(t)$ is the function to be transformed and $w(t)$ is the window function. $F(m,w)$ represents sinusoidal values at the center of the window $w(t)$ that starts at time position m.

The discrete STFT can be expressed as

$$F(m,w) = \sum_{n=0}^{N-1} r(n)w(n-m)e^{-jwn} \qquad (2)$$

where $r(n)$ is radar measurement and $w(n)$ is the window function.

We apply a rectangular window, with its length $L = 30$ and step size $M = 16$.

$$w(n) = \begin{cases} 1 & \text{if } 0 \le n \le 29 \\ 0 & \text{otherwise} \end{cases} \qquad (3)$$

Then the cumulated power of AC values ($m \ge 4$) can be obtained by

$$P(m) = \mid \sum_{w=4}^{L-1} F(m,w)^2 \mid \qquad (4)$$

We plot the power of AC values $P(m)$ versus time domain sample index in Fig. 6a and 6b for the data sets in Fig. 3a

Authorized licensed use limited to: University of Texas at Arlington. Downloaded on December 18, 2009 at 14:38 from IEEE Xplore. Restrictions apply.

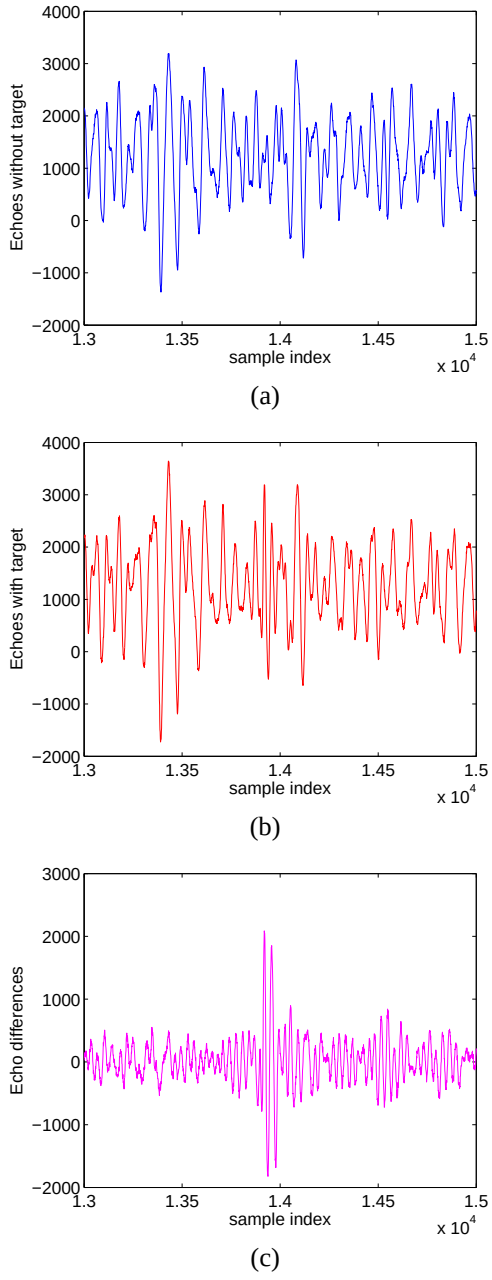


Fig. 4. Measurement with good signal quality and 100 pulses integration (a) Expanded view of traces (no target) from samples 13001 to 15000 (b) Expanded view of traces (with target) from samples 13001 to 15000 (c) Expanded view of traces difference between with and without target

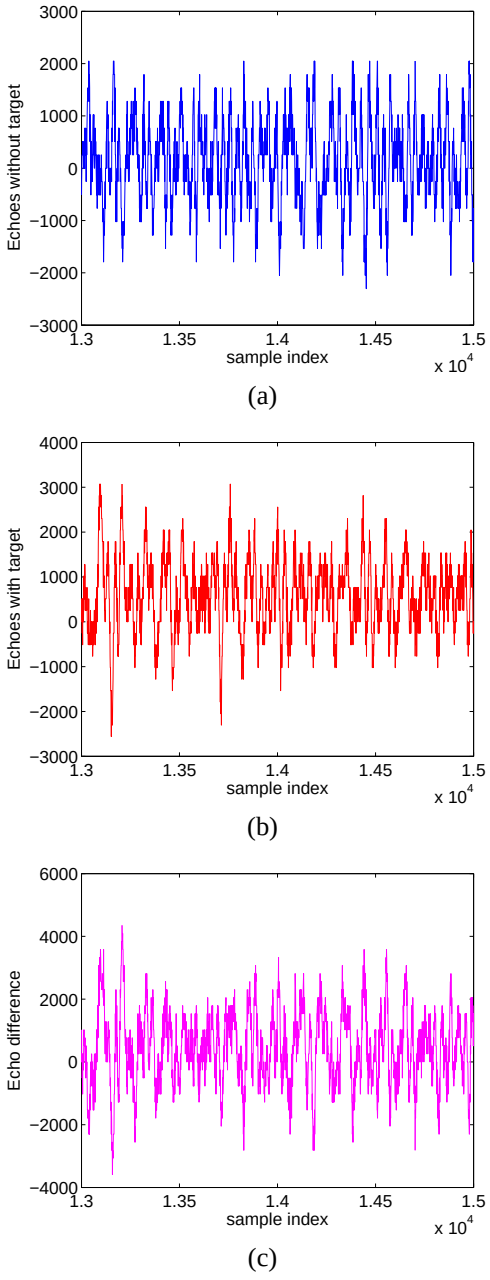


Fig. 5. Measurement with poor signal quality (a) Expanded view of traces (no target) from samples 13001 to 15000 (b) Expanded view of traces (with target) from samples 13001 to 15000 (c) Expanded view of traces difference between with and without target

and 3b respectively. We can see that at the samples where there is a target, the curve of the power signal looks like a Gaussian pdf rather than chaotic impulses. And thus it is quite straightforward to see that there is no target on range in Fig. 6a.

It's worth mentioning that for better visual inspection, window length and step size may change on a basis of different radar data.

Based on the approach in [8], the power of clutter-accounted and differentiated echoes in Fig. 7. If no thereshold is applied, one may claim that the high impulses occurred around sample 13400 and 13500 indicate the presence of targets. Therefore, a threshold comparison is indefensible to reduce false alarm for the differential-based target detection approach. However, this step will increase computing complexity and system cost. The new STFT based technology does not demand the threshold detection at all. Therefore without a threshold, STFT based approach will lead to smaller false alarm compared to the

Authorized licensed use limited to: University of Texas at Arlington. Downloaded on December 18, 2009 at 14:38 from IEEE Xplore. Restrictions apply.

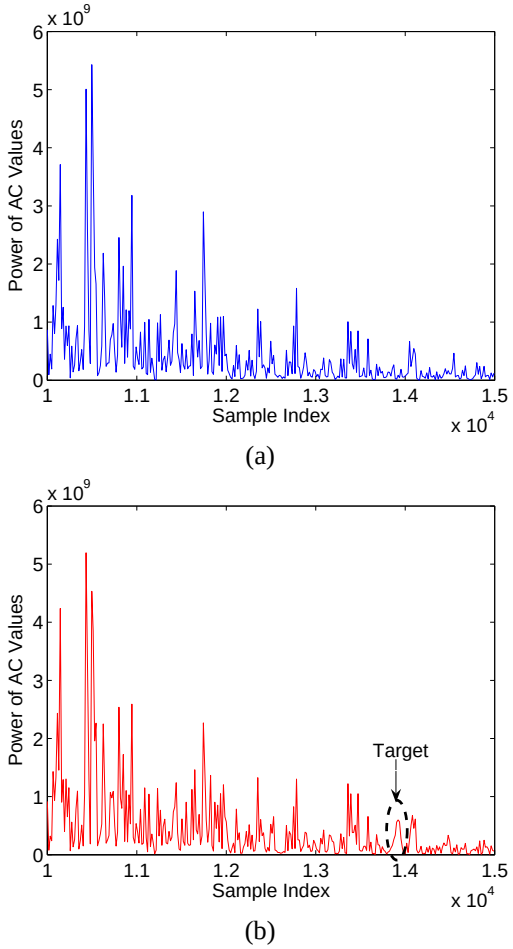


Fig. 6. The power of AC values versus sample index. (a) no target (b) with target in the field

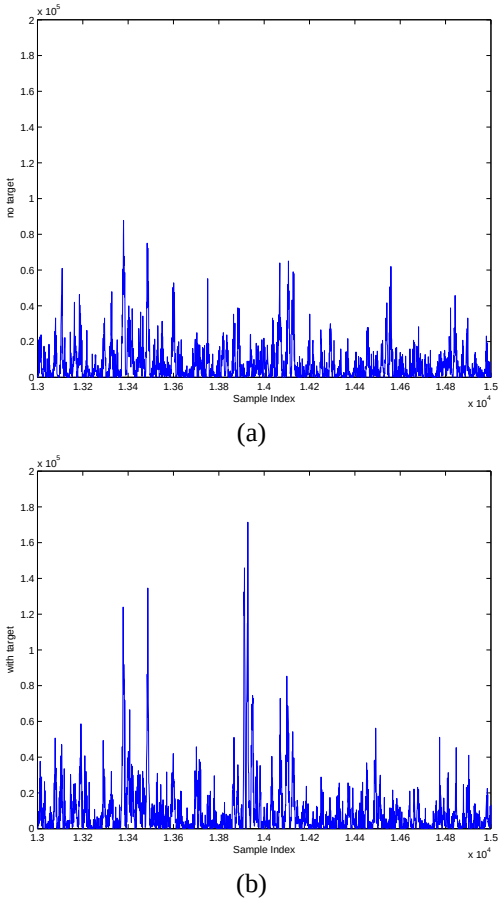


Fig. 7. The power of processed waveforms (a) no target (b) with target in the field

differential based one.

IV. Target Detection with Poor Signal Quality

As mentioned in Section II, when the Barth pulse source was operated at low amplitude and the sample values are obtained based on insufficient pulse response averaging (averaged over 35 pulses for each collection), significant pulse-to-pulse variability was noted and the return signal quality is poor. Fig. 5 illustrate the received echoes in this situation. Even with the application of the STFT - based scheme proposed above, we can not tell whether there is a target or not in the range. Since pulse-to-pulse variability exists in the echoes at different time or different site, this motivate us to explore the spatial and time diversity using Radar Sensor Networks (RSN).

In nature, a network of multiple radar sensors can been utilized to combat performance degradation of single radar [12]. These radar sensors are managed by an intelligent clusterhead that combines waveform diversity in order to satisfy the common goals of the network other than each radar operate substantively. As radar sensors are environment dependent [13], it may provide better signal quality if different radars work collaboratively to perform data fusion. For example, consider a system of two radars. When the signal of either radar unfortunately experience a severe fading, if two radars are spaced sufficiently far apart, it is not likely that both of the radars experience deep fade at the same time. By selecting better waveform from the two radars, the useful data is less likely to be lost.

In this paper, we assume the radar sensors are synchronized in RSN and we employed RAKE structure to combine received information for RSN. The detailed process is shown in Fig. 9. The echo, i.e., RF response by the pulse of each cluster-member radar sensor, will be combined by the clusterhead using a weighted average, and the weight A_i is determined by the power of each echo $x_i(m)$ (m is the sample index),

$$A_i = \frac{E_i}{\sum_{i=1}^{n} E_i} \tag{5}$$

and

$$E_i = \text{var}(x_i(m)) + [\text{mean}(x_i(m))]^2 \tag{6}$$

As for STFT, we apply window length $L = 25$ and step size $M = 15$. We ran simulations for n = 35 and plot the power of combined signal obtained through STFT - based approach in Fig. 8. Compare this figure with Fig. 5a and Fig. 5b, it is quite obvious to see that there is a target around sample 14,000.

Authorized licensed use limited to: University of Texas at Arlington. Downloaded on December 18, 2009 at 14:38 from IEEE Xplore. Restrictions apply.

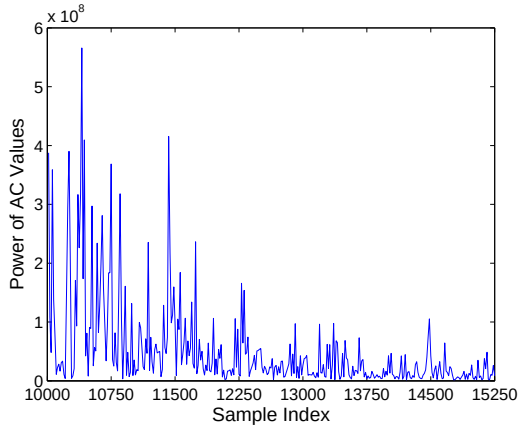


Fig. 8. The power of AC values versus sample index. (a) no target (b) with target in the field

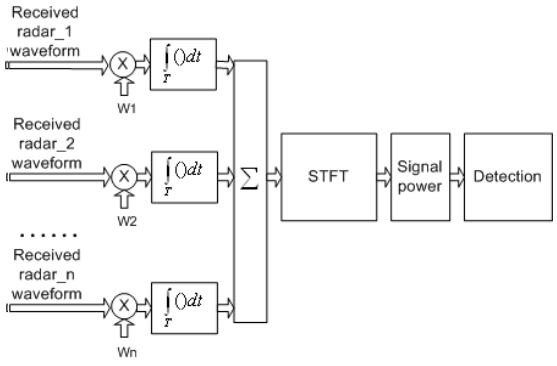


Fig. 9. Block diagram of STFT - based approach and diversity combination in RSN

V. Conclusion

In this paper, we propose a short time Fourier transform (STFT) - based signal processing approach on received UWB Radar waveforms to improve through-foliage target detection. The foliage penetration measurements were taken in Holliston, Massachusetts. When radar echoes are in good quality, the detection of target can be achieved by applying STFT-based technology to single radar. We compared our approach in case of no target as well as with target against the scheme in which 2-D image was created via adding voltages with the appropriate time offset. Results show that our approach can detect target more intuitively. When radar echoes are in poor condition and single radar is unable to carry out detection, we employe both Radar Sensor Networks (RSN) and RAKE structure to combine the echoes from different radar members and finally successfully detect the target.

Acknowledgement

This work was supported in part by Office of Naval Research (ONR) under Grant N00014-07-1-0395, N00014-07-1-1024, and National Science Foundation (NSF) under Grant CNS-0721515.

References

[1] D. R. Sheen, N. P. Malinas, D. W. Kletzli, T. B. Lewis, and J. F. Roman, “Foliage transsmission measurementsusing a ground-based ultrawideband (UWB) (300ł1300 Mhz) SAR system”, *IEEE Transactions on Geoscience and Remote Sensing*, vol. 32, pp. 118- 130, Jan. 1994.

[2] J. G. Fleischman; S. Ayasli; E. M. Adams; D. R. Gosselin, “Foliage penetration experiment: Part I: Foliage attenuation and backscatter analysis of SAR imagery”, *IEEE Transactions on Aerospace and Electronic Systmes*, vol. 32, pp: 135-144, Jan 1996.

[3] T. Nohara and S. Haykin, “Canadian east coast radar trials and the K-distribution”, *IEE Proc.-F*, vol. 138, pp: 80-88, April 1991.

[4] S. Watts, “Radar detection prediction in K-distribution sea clutter and thermal noise”, *IEEE Transactions on Aerospace and Electronic Systmes*, vol. 23, pp: 40-45, Jan 1987.

[5] R. Kapoor, G. A. Tsihrintzis, N. Nandhakumar, “Detection of obscured targets in heavy-tailed radar clutter usingan ultra-wideband (UWB) radar and alpha-stable clutter models”, *In proceedings of the Thirtieth Asilomar Conference on Signals, Systems and Computers*, vol.2, pp: 863-867, Nov 1996.

[6] B. Ferrell “Ultrawideband foliage penetration measurement”, in *Proc. IEEE Nation Radar Conf.*, Mar. 29-31, pp.80-84, 1994

[7] X. Xu; R. M. Narayanan, “FOPEN SAR imaging using UWB step-frequency and random noise waveforms ”, *IEEE Trans. Aerospace and Electronic Systems*, vol.37, pp.1287-1300, Oct. 2001

[8] Jing Liang and Qilian Liang, “A Differential Based Approach for Sense-Through-Foliage Target Detection Using UWB Radar Sensor Networks Communications”, *IEEE International Conference on communications, 2008. ICC ’08*, pp: 1952-1956, May 2008.

[9] D. Gabor, “Theory of communication”, *Journal of the IEE*, vol. 93, no. 3, pp: 429C457, 1946.

[10] P. Withington , H. Fluhler, and S. Nag, “Enhancing homeland security with advanced UWB sensors,” *IEEE Microwave Magazine*, Sept 2003.

[11] Benedetto M. D and Giancola G., *Understanding Ultra Wide Band Radio Fundamentals*, Person Education, 2004

[12] S. Haykin, “Cognitive radar networks” , *2005 1st IEEE International Workshop on Computational Advances in Multi-Sensor Adaptive Processing*, pp.1-3, Dec 2005.

[13] R. A. Johnson and E. L. Titlebaum, “Range Doppler Uncoupling in the Doppler Tolerant Bat Signal”, *Proc. of IEEE Ultrasonics Symposium* , New York, pp.64-67, 1972.

Authorized licensed use limited to: University of Texas at Arlington. Downloaded on December 18, 2009 at 14:38 from IEEE Xplore. Restrictions apply.

Wireless Channel Modeling in Foliage Environment: UWB versus Narrowband

Qilian Liang
Department of Electrical Engineering
University of Texas at Arlington
Arlington, TX 76019-0016, USA
E-mail: liang@uta.edu

Xiuzhen Cheng
Dept of Computer Science
George Washington University
Washington, DC 20052
E-mail: cheng@gwu.edu

***Abstract*— In this paper, we study the wireless channel modeling in foliage environment, a rich scattering and time-varying environment, based on extensive data collected using UWB and narrowband (200MHz and 400MHz) radars. We apply two approaches to the wireless channel modeling: Saleh and Valenzuela (S-V) method for UWB channel modeling and CLEAN method for narrowband and UWB channel modeling. We validated that UWB echo signals (within a burst) don't hold self-similarity, which means the future signals can't be forecasted based on the received signals and channel modeling is necessary from statistical point of view. Based on the S-V method for UWB channel modeling, in foliage UWB channel, the multi-path contributions arrive at the receiver are grouped into clusters. The time of arrival of clusters can be modeled as a Poisson arrival process, while within each cluster, subsequent multipath contributions or rays also arrive according to a Poisson process. At different field (near field, medium field, and far field), we observe that the Poisson process parameters are quite different. We also observe that the amplitude of channel coefficient at each path follows Rician distribution for medium and far field, and it's non-stationary for paths from near field (one of two Rician distributions), and these observations are quite different with the IEEE indoor UWB channel model and S-V indoor channel model. Based on the CLEAN method, the narrowband (200MHz and 400MHz) and UWB channel impulse responses have many similarities: both can be modeled as linear time-variant filter channel.**

I. Introduction and Motivation

In July 2003, the Channel Modeling sub-committee of study group IEEE 802.15.SG3a published the final report regarding the UWB indoor multipath channel model [4]. It is a modified version of the indoor Saleh and Valenzuela (S-V) channel model [6]. The S-V model was developped for NLOS channel, and it has also been applied to LOS channels where it is perhaps less valid, unless LOS components are specifically added [5] The IEEE suggested an initial set of values for the indoor UWB channel model which has range less than 10 meters. However, lots of applications of UWB are for outdoor activities such as sense-through-foliage target detection. Forests favor asymmetric threats because the warfighter has a limited sensing capability. Forests provide excellent concealment from observation, ambush, and escape, as well as provide secure bases for enemy Command & Control (C2), weapons caches, and Improvised Explosive Device (IED)/ Weapon of Mass Destruction (WMD) assembly. These have become "the high ground" in fourth-generation warfare, providing a significant strategic advantage. Unfortunately, no work has been done on the outdoor UWB channel modeling.

In this paper, we will model the UWB and narrowband channels using UWB and narrowband radars in foliage environment which is a rich scattering and time-varying environment. UWB radar emissions are at a relatively low frequency-typically between 100 MHz and 3 GHz. Additionally, the fractional bandwidth of the signal is very large (greater than 0.2). Such radar sensor has exceptional range resolution that also has an ability to penetrate many common materials (e.g., walls). Law enforcement personnel have used UWB ground penetrating radars (GPRs) for at least a decade. Like the GPR, sense-through-foliage radar takes advantage of UWB's very fine resolution (time gating) and low frequency of operation.

The rest of this paper is organized as follows. In Section II, we summarize the measurement and collection of data we used in this paper. In Section III, we present our outdoor UWB channel model in rich scattering and time-varying environment. In Section IV, we study the channel impulse response based on CLEAN method for narrowband and UWB channels. We conclude this paper in Section V.

II. Experiment Setup and Data Collection

Our work is based on the data collected in UWB radar-based sense-through-foliage experiment in late summer and fall. Late summer foliage, because of the limited rainfall, involved foliage with decreased water content. Late fall and winter measurements involved largely defoliated but dense forest, so it's a rich scattering environment. Because of wind or different temperature in dense forest, it's also a time-varying environment. The UWB radar-based

Authorized licensed use limited to: University of Texas at Arlington. Downloaded on December 18, 2009 at 14:39 from IEEE Xplore. Restrictions apply.

experiment was constructed on a seven-ton man lift, which had a total lifting capacity of 450 kg. The limit of the lifting capacity was reached during the experiment as essentially the entire measuring apparatus was placed on the lift (as shown in Fig. 1). For the UWB data we used in this paper, each sample is spaced at 50 picosecond interval, and 16,000 samples were collected for each collection for a total time duration of 0.8 microseconds at a rate of approximately 20 Hz. The Barth pulse source was operated at low amplitude and 35 pulses reflected signal were averaged for each collection. Significant pulse-to-pulse variability was noted for these collections. We plot the transmitted pulse (one realization) in Fig. 2a) and the received echos in one collection in Fig. 2b (averaged over 35 pulses).



Fig. 1. This figure shows the lift with the experiment. The antennas are at the far end of the lift from the viewer under the roof that was built to shield the equipment from the elements. This picture was taken in September with the foliage largely still present. The cables coming from the lift are a ground cable to an earth ground and one of 4 tethers used in windy conditions.

For comparison, we also studied narrowband (200MHz and 400MHz) radar signal propagation. For the data we used in this paper, each sample is spaced at 50 picosecond interval, and 16,000 samples were collected for each collection for a total time duration of 0.8 microseconds at a rate of approximately 20 Hz. Fig. 3a shows the transmitted signal and Fig. 3b shows the received echos (averaged over 35 pulses) for 200MHz narrowband radar. Fig. 4a shows the transmitted signal and Fig. 4b shows the received echos (averaged over 35 pulses) for 400MHz narrowband radar. The data collections were extensive. 20 different positions were used, and 35 collections were performed at each position for UWB, 200MHZ, and 400MHz radars.

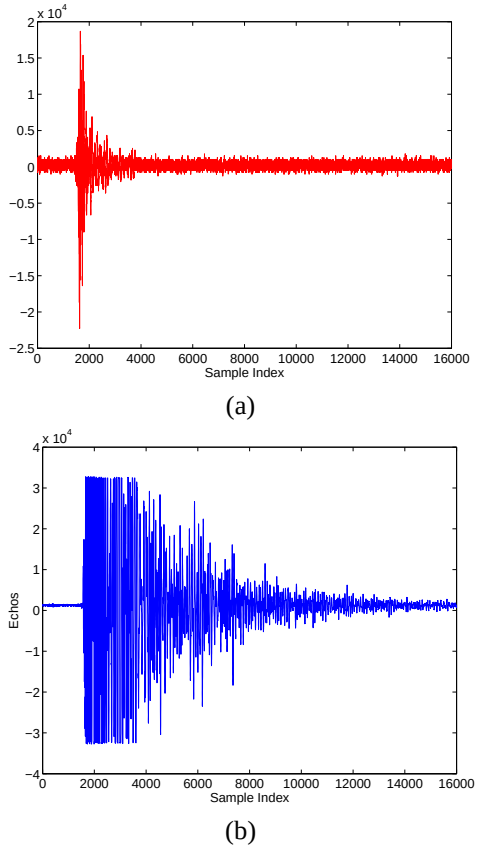


Fig. 2. UWB radar transmitted pulse and received echos in one experiment. (a) Transmitted pulse. (b) Received echos.

III. UWB Channel Modeling Based on S-V Approaches

A. Introduction to Channel Modeling for Indoor UWB Channel

In the S-V model [6], the arrival of clusters is modelled as a Poisson arrival process with a rate Λ, while within each cluster, subsequent multipath contributions or rays also arrive according to a Poisson process with a rate λ (see Fig. 5). In the S-V model, the magnitude of the k-th path within the l-th cluster follows a Rayleigh distribution, and the phase of each path is assumed to be a statistically independent random variable over $[0, 2\pi)$. Besides, the average Power Decay Profile (PDP) is characterized by an exponential decay of the amplitude of the clusters, and a different exponential decay for the amplitude of the received pulses within each cluster, as shown in Fig. 6. In the IEEE UWB indoor channel model [4], the cluster approach was adopted (same as S-V model), but a log-normal distribution was suggested for characterizing the multi-path gain amplitude, and an additional log-normal variable was introbuced for representing the fluctuations of the total multipath gain. Besides, the phase of each path is

Authorized licensed use limited to: University of Texas at Arlington. Downloaded on December 18, 2009 at 14:39 from IEEE Xplore. Restrictions apply.

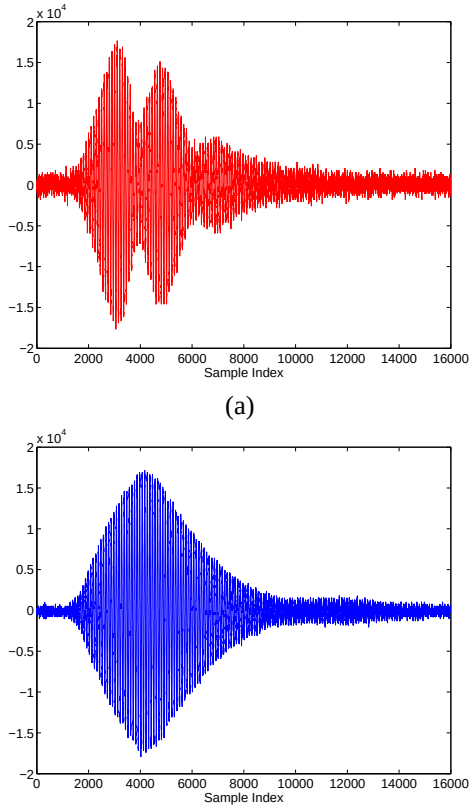


Fig. 3. Narrowband radar (200MHz) transmitted pulse and received echos in one experiment. (a) Transmitted pulse. (b) Received echos.

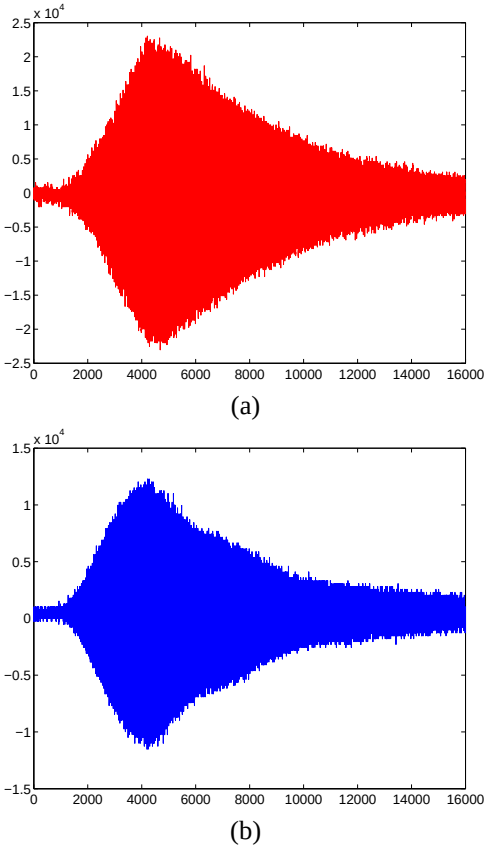


Fig. 4. Narrowband radar (400MHz) transmitted pulse and received echos in one experiment. (a) Transmitted pulse. (b) Received echos.

assumed to be either 0 or π with equal probability.

B. Outdoor UWB Channel Modeling

1) Cluster Arrival and Power Decay Profile: We study the outdoor UWB signal propagation in three cases: near field (less than $55m$), medium field ($55m$–$85m$), and far field (above $85m$ and up to $120m$ in this study). In the data collection, each sample is spaced at 50 picosecond interval, so these cases are corresponding to samples 1–7333 for near field, samples 7333–11333 for medium field, and samples 11334–16000 for far field. In Fig. 7, we plot the power profile of the received echos (averaged over 30 collections to eliminate the effect of random noise and each collection was averaged based on 35 pulses) for the three different cases. Since the transmitted pulse (as plotted in Fig. 2a) is a very narrow impulse pulse (like a delta function in time domain), we analyzed the channel property based on the received echos power profile plotted in Fig. 7, and similar methodology was also used in S-V model studies [6].

Observe Fig. 7, multi-path contributions arrive at the receiver grouped into clusters. The time of arrival of

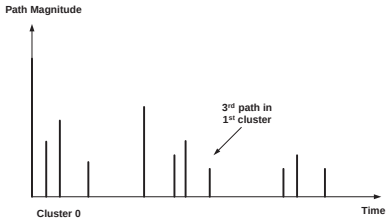


Fig. 5. An illustration of the channel impulse response in S-V model.

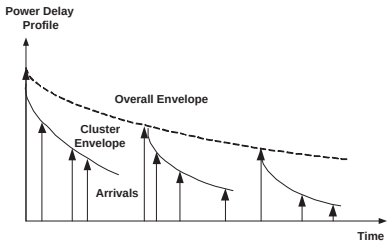


Fig. 6. An illustration of the double exponential decay of the mean cluster power and the ray power within clusters in S-V model.

clusters can be modeled as a Poisson arrival process with a rate Λ, while within each cluster, subsequent multipath

Authorized licensed use limited to: University of Texas at Arlington. Downloaded on December 18, 2009 at 14:39 from IEEE Xplore. Restrictions apply.

contributions or rays also arrive according to a Poisson process with a rate λ (see Fig. 5). We define:

- T_l = the arrival time of the first path of the l-th cluster;
- $\tau_{k,l}$ = the delay of the k-th path within the l-th cluster relative to the first path arrival time T_l;
- Λ = the cluster arrival rate;
- λ = the ray arrival rate, i.e., the arrival rate of the paths within each cluster.

By definition, we have $\tau_{0l} = T_l$. The distributions of the cluster arrival time and the ray arrival time are given by

$$p(T_l|T_{l-1}) = \Lambda \exp\left(-\Lambda(T_l - T_{l-1}), l > 0\right)$$
$$p(\tau_{k,l}|\tau_{(k-1),l}) = \lambda \exp\left(-\lambda(\tau_{k,l} - \tau_{(k-1),l})\right), k > 0 \quad (1)$$

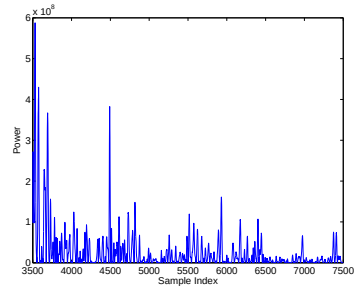
The above observations are very similar as that for the indoor UWB channel. Specifically, we also observed the Λ and λ are quite different for three different cases.

- Observe Fig. 7a for near field, Λ (1/ns) is around 0.02 (one cluster in every $50ns$ or 1000 samples), and λ (1/ns) is around 0.4 (one path in every $2.5ns$ or 50 samples). Perhaps it's because some major scatters in near field (such as tree stems) reflected signals, so some paths are quite dominant.
- Observe Fig. 7b for medium field, clusters arrive quite often. Λ (1/ns) is around 0.05 (one cluster in every $20ns$ or 400 samples), and λ (1/ns) is around 1 (one path in every $1ns$ or 20 samples).
- Observe Fig. 7c for far field, clusters almost always arrive (because of rich scattering), so Λ (1/ns) is around 0.5 (one cluster in every $2ns$ or 20 samples), and λ (1/ns) is around 4 (one path in every $250ps$ or 5 samples). Perhaps it's because of rich scattering, every path has very similar power level.

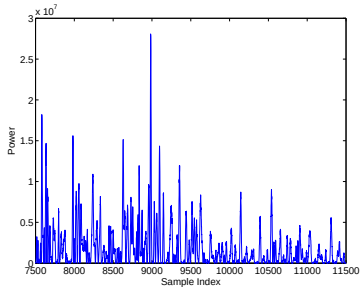
Besides, the average PDP can be represented by an exponential decay of the amplitude of the clusters, and a different exponential decay for the amplitude of the received pulses within each cluster, as shown in Fig. 6.

2) Statistical Distribution of Channel Coefficients: We also study the statistical distributions of each given path. We plot the histogram for some sample values of the above three cases based on 30 collections and each collection is averaged over 35 pulses. Near field samples are based on samples 5001–6000; medium field samples are based on samples 8001–9000; and far field samples are based on samples 12001–13000. Since the samples are very close (within 7.5m distance), so their path-loss effect can be ignored. For each case, we have 30000 samples, and we plot their histogram in Fig. 8.

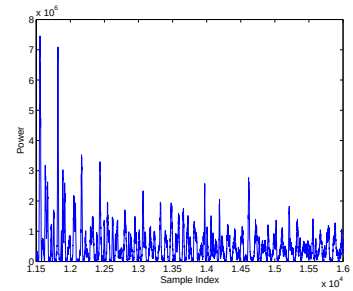
First, observe Fig. 8c for far field, the histogram can be almost perfectly modelled by a non-zero-mean Gaussian distribution, which means the amplitude of the channel



(a)



(b)



(c)

Fig. 7. The power profile for three different cases: (a) near field, (b) medium field, and (c) far field.

coefficient follows a Rician distribution,

$$p_\alpha(x) = \frac{x}{\sigma^2} \exp\{-\frac{x^2 + s^2}{2\sigma^2}\} I_0(\frac{xs}{\sigma^2}) \quad x \geq 0 \quad (2)$$

where s is the mean value of Gaussian and $I_0(\cdot)$ is the zero order modified Bessel function. This kind of channel is known as Rician fading channel. A Rician channel is characterized by two parameters, Rician factor K which is the ratio of the direct path power to that of the multipath, i.e., $K = s^2/2\sigma^2$, and the Doppler spread (or single-sided fading bandwidth) f_d. Similarly, Fig. 8b for medium field, the histogram can be approximately modelled by a non-zero-mean Gaussian distribution, which means the amplitude of the channel coefficient follows a Rician distribution. Observe Fig. 8a for near field, the histogram can be approximately modelled by two non-zero-mean Gaussian distributions, which means it's non-stationary, and the amplitude of the channel coefficient follows one of two Rician distributions. **The above observations are**

Authorized licensed use limited to: University of Texas at Arlington. Downloaded on December 18, 2009 at 14:39 from IEEE Xplore. Restrictions apply.

quite different with the indoor UWB channel model (log-normal distribution) and S-V model (Rayleigh distribution). The sign of channel coefficient is either +1 or -1, i.e., its phase is either 0 or π, which matches the IEEE indoor UWB channel model.

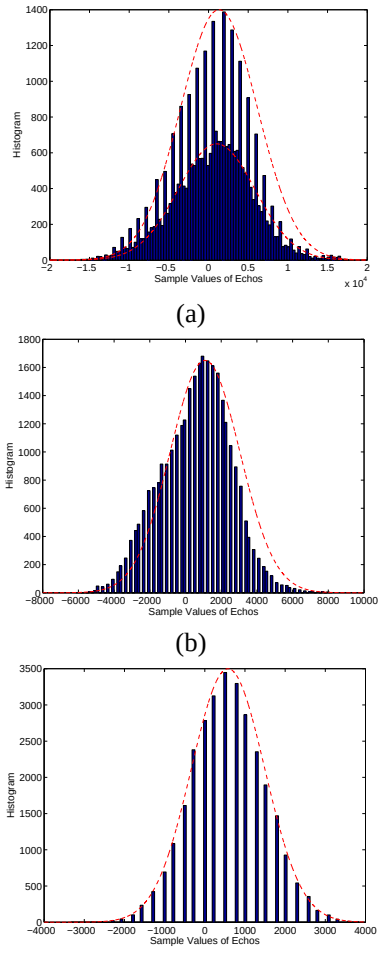


Fig. 8. The histograms and their approximation using Gaussian distributions (dashed lines). The histograms are based on 30 collections and each collection is averaged over 35 pulses. (a) near field samples, (b) medium field samples, and (c) far field samples.

IV. Wireless Channel Modeling Based on CLEAN Method

We apply the CLEAN algorithm to obtain the UWB channel model based on the transmitted pulses and received echos. The CLEAN algorithm was first introduced in [3] and has been applied to UWB measurements [2][7] and it assumes that the channel is a series of impulses which is consistent with the tapped-delay line channel model. This algorithm searches the received echos iteratively with the template to find the maximum correlation [1]. The steps are [5]:

1) Calculate the autocorrelation of the template $r_{ss}(t)$ and the cross-correlation of the template with the received waveform $r_{sy}(t)$.
2) Find the largest correlation peak in $r_{sy}(t)$, record the normalized amplitudes α_k and relative time delay τ_k of the correlation peak.
3) Subtract $r_{ss}(t)$ scaled by α_k from $r_{sy}(t)$ at the time delay τ_k.
4) If a stopping criterion (e.g., a minimum threshold on the peak correlation) is not met, go to step 2. Otherwise stop.

Based on the CLEAN method, we successfully obtained the channel impulse responses for all transmit waveforms and receive echoes. For illustration purposes, in Figs. 9, 10, and 11, we plot the channel impulse responses for 200MHz, 400MHz, and UWB channels using CLEAN method in two experiments. Observe that for all channels, channel impulse responses have many similarities: all can be modeled as linear time-variant filter channel, which is a more general case of the S-V model.

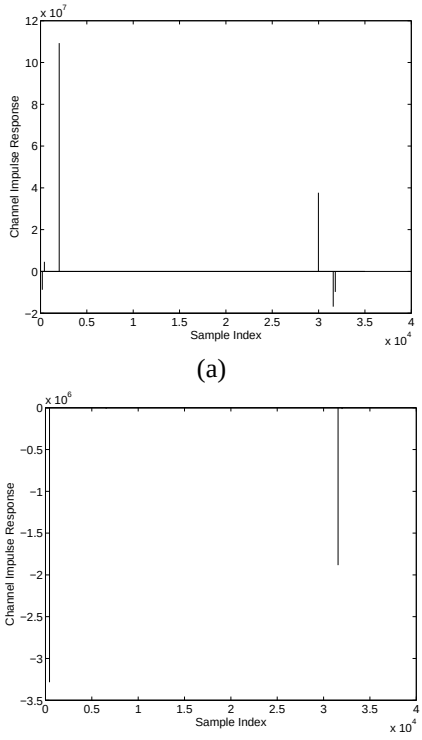


Fig. 9. The channel impulse responses for 200MHz channel using CLEAN method in two experiments.

V. Conclusions

In this paper, we studied the statistical modeling for outdoor wireless channels (200MHz, 400MHz, and UWB) in

Authorized licensed use limited to: University of Texas at Arlington. Downloaded on December 18, 2009 at 14:39 from IEEE Xplore. Restrictions apply.

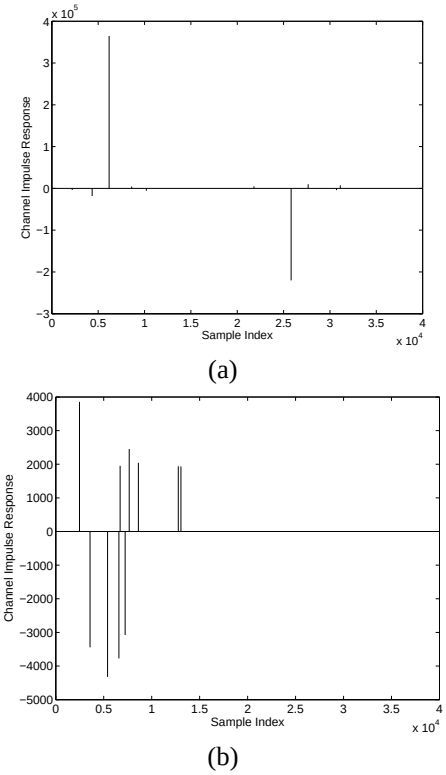


Fig. 10. The channel impulse responses for 400MHz channels using CLEAN method in two experiments.

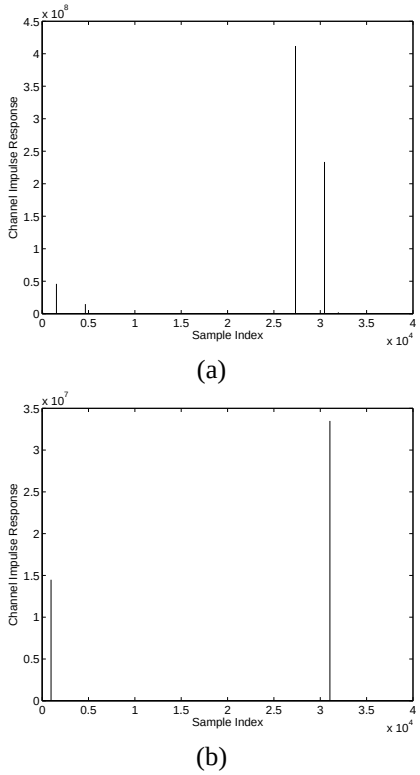


Fig. 11. The channel impulse responses for UWB channels using CLEAN method in two experiments.

rich scattering and time-varying environment based on extensive data collected using narrowband and UWB radars. We validated that UWB echo signals (within a burst) don't hold self-similarity, which means the future signals can't be forecasted based on the received signals and channel modeling is necessary from statistical point of view. In outdoor UWB channel, the multi-path contributions arrive at the receiver are grouped into clusters. The time of arrival of clusters can be modeled as a Poisson arrival process, while within each cluster, subsequent multipath contributions or rays also arrive according to a Poisson process. At different field (near field, medium field, and far field), we observed that the Poisson process parameters are quite different. We also observed that the amplitude of channel coefficient at each path follows Rician distribution for medium and far field, and it's non-stationary for paths from near field (one of two Rician distributions), and these observations are quite different with the IEEE indoor UWB channel model and S-V model. Using CLEAN method, we observed that for all channels, channel impulse responses have many similarities: all can be modeled as linear time-variant filter channel, which is a more general case of the S-V model.

ACKNOWLEDGEMENT

The authors would like to thank Dr. Sherwood Samn in AFRL/RHX for providing the radar data.

The research of Liang was supported in part by Office of Naval Research (ONR) under Grant N00014-07-1-0395 and N00014-07-1-1024, and National Science Foundation (NSF) under Grant CNS-0721515 and CNS-0831902. The research of Cheng was supported in part by NSF under Grant CNS-0721669 and CNS-0831852.

REFERENCES

[1] R. M. Buehrer, et al, "Characterization of the UWB channel," *IEEE Conf on Ultra Wideband Systems and Technologies*, pp. 26-31, Reston, VA, Nov 2003.

[2] R. J.-M. Cramer, *An Evaluation of Ultrawideband Propagation Channels*, Ph.D Dissertation, USC, 2000.

[3] J. A. Hogbom, "Aperture synthesis with a non-regular distribution of interferometer baseline," *Atronomy and Astrophysics Supplement Ser.*, vol. 15, 1974.

[4] IEEE 802.15.SG3a, "Channel modeling sub-committee report final," *IEEE P802.15-02/490r1-SG3a*, Feb 2003.

[5] J. H. Reed, *An Introduction to Ultra Wideband Communication Systems*, Prentice Hall, Upper Saddler River, NJ, 2005.

[6] A. A. Saleh and R. A. Valenzuela, "A statistical model for indoor multipath propagation," *IEEE J. on Selected Areas in Communications*, vol. 5, no. 2, pp. 128-137, Feb 1987.

[7] R. A. Scholtz, M. Z. Win, and J. M. Cramer, "Evaluation of the Characteristics of the ultra-wideband propagation channel," *Proc of Antenna and Propagation Symposium*, vol. 2, no. 626-630, 1998.

Authorized licensed use limited to: University of Texas at Arlington. Downloaded on December 18, 2009 at 14:39 from IEEE Xplore. Restrictions apply.

A Graph Theoretical Algorithm for Virtual MIMO Channel Selection in Wireless Sensor Networks

Jing Liang and Qilian Liang, Senior Member, IEEE
Department of Electrical Engineering
University of Texas at Arlington
Arlington, TX 76019-0016 USA
E-mail: jliang@wcn.uta.edu, liang@uta.edu

***Abstract*—In this paper we investigate a methodology named *channel selection* with the aim of balancing the multiple input multiple output (MIMO) advantage and the complexity of node cooperations for wireless sensor networks (WSN). In respect of cross-layer design, we propose the Maximum Spanning Tree Searching (MASTS) algorithm to select a set of subchannels that always provide a path connecting all sensors. The performances are analyzed through Monte Carlo simulation in terms of capacity, diversity gain, bit error rate (BER) and multiplexing gain. It is shown that MASTS channel selection can achieve satisfying performances compared to those of full virtual MIMO with reduced resource consumption.**

I. Introduction and Motivation

Virtual multiple-input-multiple-output (MIMO) has been studied intensively in recent years in order to improve the energy-efficiency in wireless sensor networks (WSN) [1][2]. Constrained by its physical size and limited battery, individual sensor is allowed to contain only one antenna. Numerical results show that if these sensors can be constructed into cooperative MIMO systems, over certain distance ranges they may outperform single-input-sinlge-output (SISO) systems in energy consumption.

In order to encompass both wireless and networking communications, virtual MIMO based WSN have so far been extended by incorporating the multi-hop routings and hop-by-hop recovery schemes. [3][4]. This model is illustrated in Fig. 1. Assume the multi-hop WSN are made up of n clusters. Here cluster refers to a group of closely gathered wireless sensors that have been cooperated as multiple transmitters or receivers. If each cluster consists of c_i $i = 1, 2, ..., n$ sensor nodes respectively, then the RF chains for this virtual MIMO WSN system will turn out to be $\prod_{i=1}^{n} c_i$, which implies tremendous circuit energy consumption along with the increase of n. Provided that the energy and delay cost associated with the local information exchange have to be taken into account, cooperative virtual MIMO WSN may not always guarantee to be effective.

In this paper we investigate a methodology named *channel selection* with the aim of balancing the MIMO advantage and the complexity of sensor cooperations. This channel selection based virtual MIMO WSN model is illustrated in Fig. 2. It

978-1-4244-2677-5/08/25.00 (c)2008 *IEEE*

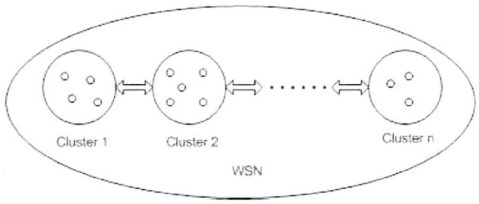


Fig. 1. Cooperative clusters in multi-hop wireless sensor networks

is a common scenario that sensor nodes (denoted by circles) are efficiently grouped into clusters while cluster-heads (denoted by triangles) offer centralized control over cooperative virtual MIMO channels. These cluster-heads are not subject to strict energy constrains but others are [2]. At first, channel side information (CSI) may be obtained by various channel estimation techniques such as the reciprocity principle or a feedback channel [5]. Then channel selection may be applied through subset selection algorithms by switches either at a transmitting or receiving cluster-head, or jointly working at both ends. Therefore the best set of channels are selected to be active while remaining ones are not employed. Since at some hops transmissions are turned off, energy will be saved during the virtual MIMO communications. If the same total transmitting power is allocated to the best subset of channels, performances after channel selection, such as capacity, BER may even be better compared to those before channel selection.

It is worth mentioning that the energy consumption introduced by collecting CSI information is indispensable for the proper operation of virtual MIMO. In [1], MIMO fading channels is presented as a scalar matrix, which implies that CSI is assumed to be known, however the the overhead computation for CSI is ignored. [2] takes into account this extra training energy to provide a fair comparison and demonstrates that if the system is designed with judicious parameters, significant energy efficiency can be achieved after all.

Among the existing research on conventional MIMO channel selection, the following criteria have been used:

1) Capacity Maximization: In the previous work of [6] [7] [8], channel capacity is used as the optimality criterion, i.e., antennas that achieve the largest capacity are active.

Authorized licensed use limited to: University of Texas at Arlington. Downloaded on December 18, 2009 at 14:40 from IEEE Xplore. Restrictions apply.

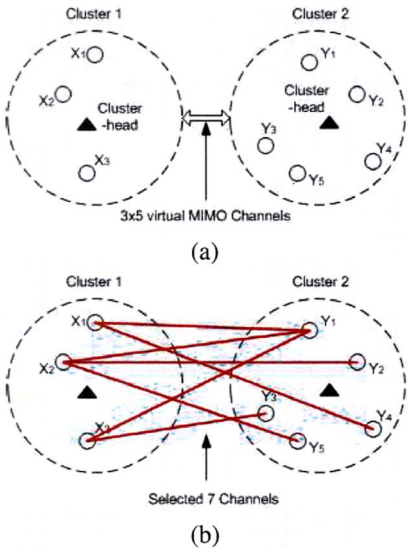


Fig. 2. System illustration for virtual MIMO channel selection (a) before channel selection (b) after channel selection

In [6], it is demonstrated that in case of no CSIT but CSIR, close capacity to that of the full-MIMO system can be achieved as far as the number of selected receivers is no less than the number of transmitters. [7] and [8] considered CSIT and proposed an exhaustive search algorithm.

2) Minimum Error rate: Apart from maximization of capacity based on Shannon theory, [9] derived another criteria from the respect of minimum error rate when coherent receivers, either maximum likelihood (ML), zero-forcing (ZF) or the minimum mean-square error (MMSE) linear receiver is employed.
3) Cross-layer optimal scheduling: Besides physical layer, some related works have adopted graph theory approach to consider cross-layer design. [10] performed the optimal antenna assignment for spatial multiplexing by Hungarian algorithm using weighted bipartite matching graph, and [11] took into account users' QoS requirement with clique-searching algorithm for antenna selection.

Although the above have provided dazzling mathematical standards, one problem is how to accommodate them to WSN rather than traditional communications; the other problem is how to encompass inter-cluster multi-hop connectivity so as to better support networking capability and QoS requirement.

In this paper, under the assumption of quasi-static channels and both CSIT and CSIR, we propose Maximum Spanning Tree Searching (MASTS) algorithm on a basis of Kruskal's theory [13] to perform channel selection. The idea behind the scheme is that selected channels not only provide better channel gain, but also act as a connected path between two arbitrary sensor nodes to perfectly serve the upper layer routing and networking. Take Fig. 2(b) as an example, these channels denoted by red lines have been selected based on MASTS. It is obvious that between any two nodes $X_iY_j, i = 1,2,3, j = 1,\cdots,5$; $X_iX_j, i = 1,2,3, j = 1,2,3, i \neq j$ or $Y_iY_j, i = 1,\cdots,5, y = 1,\cdots,5, i \neq j$, there is a path connecting them through single hop or multi-hop. Due to the inherent link layer connectivity, MASTS can be referred to as a cross-layer design.

In our investigation, concrete example is presented to illustrate each step. We also analyze its performance by means of Monte Carlo simulations to estimate capacity, diversity gain, bit error rate (BER) and multiplexing gain. The result shows that at high SNR, MASTS can achieve higher capacity than that of full virtual MIMO.

We organize the remainder of this paper as follows. In Section II, we introduce virtual MIMO channel model. Section III proposes MASTS algorithm step by step. Section IV compares the performances of MASTS with that of full virtual MIMO and Section V draws the conclusion.

II. Channel Model

Based on CSIT and CSIR, the estimated virtual MIMO channel model with M_t transmitters and M_r receivers ($M_t + M_r$ sensors) is illustrated in Fig. 3, where each receiver observes a superposition of the M_t transmitted signals corrupted by flat fading and additive white gaussian noise. Each h_{ji}, $i = 1,2,\cdots,Mr$ and $j = 1,2,\cdots,Mt$ represents the transmission channel gain from transmitter i to receiver j [14], which is assumed to be independent and identically distributed (i.i.d.). The additive noise also has i.i.d entries $n_j \sim \mathcal{CN}(0,\sigma^2)$.

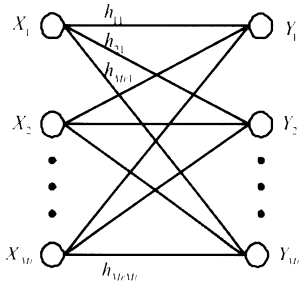


Fig. 3. Channel Graph for virtual MIMO

We may denote this virtual MIMO channels with discrete time model:

$$\begin{bmatrix} Y_1 \\ Y_2 \\ \vdots \\ Y_{Mr} \end{bmatrix} = \begin{bmatrix} h_{11} & h_{12}\cdots h_{1Mt} \\ h_{21} & h_{22}\cdots h_{2Mt} \\ \vdots & \vdots \\ h_{Mr1} & h_{Mr2}\cdots h_{MrMt} \end{bmatrix} \begin{bmatrix} X_1 \\ X_2 \\ \vdots \\ X_{Mt} \end{bmatrix} + \begin{bmatrix} n_1 \\ n_2 \\ \vdots \\ n_{Mr} \end{bmatrix} \quad (1)$$

We may simplify the above equation as $\mathbf{Y} = \mathbf{HX} + \mathbf{n}$, where $\mathbf{H}$ is a $Mr \times Mt$ independent zero mean random matrix and $\mathbf{n}$ denotes random noise.

Authorized licensed use limited to: University of Texas at Arlington. Downloaded on December 18, 2009 at 14:40 from IEEE Xplore. Restrictions apply.

From the respect of graph theory, Fig. 3 is a connected graph [15], i.e., there is an edge connecting any two vertex with sensors and transmission channels forming vertex set and edge set respectively, h_{ji} denoting edge weight. This gives rise to the graph theoretical approach to virtual MIMO study. However, the integration of graph theory into communication systems is still neonatal and deserves more attention and development.

Our purpose is to replace $\mathbf{H}$ with an approximate matrix $\hat{\mathbf{H}}$ with lower dimensions but satisfying performances and basic network layer connections.

III. MASTS Virtual MIMO

A. Introduction of MASTS

As mentioned in section II, we may use a graph of vertices and edges to represent the virtual MIMO communication scenario. From this aspect, essentially channel selection is to remove some of vertices and edges while keep those remaining. Spanning tree [15] suggests such an algorithm that in an arbitrary graph, all the vertices are connected with the minimum necessary edges, i.e., there is no isolated vertices under the condition of the least possible edge number. For example, when $Mt = 3$ and $Mr = 5$, some of the possible spanning trees are drawn in Fig. 4.

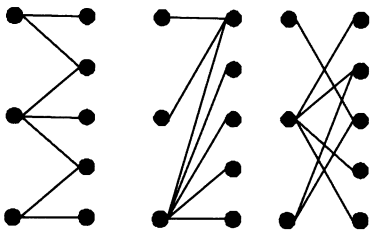


Fig. 4. Examples of spanning trees for 5×3 MIMO

In general, MASTS algorithm is to compute a spanning tree with the maximum sum of weight of edge, i.e., to select the maximum sum of channel gain while realizing the connectivity of all the sensors on a basis of maximum spanning tree algorithm. Our contribution is to apply the graph theoretical concept on maximum spanning tree into virtual MIMO channel selection and program the algorithm.

Note that for an arbitrary graph of n vertices, its spanning tree is of n vertices and $n-1$ edges [15]. Since there are $Mt + Mr$ vertices, the number of edges to be selected by MASTS algorithm is a fixed $Mt + Mr - 1$, which means MASTS always chooses $Mt + Mr - 1$ channels.

B. MASTS in virtual MIMO channel selection

MASTS algorithm is:

1) *Step 1*: Select 3 edges with the largest weight at first (including their vertices).
2) *Step 2*: Enlarge the subgraph by edges with large weight in decreasing manner and make sure no cycles are formed.

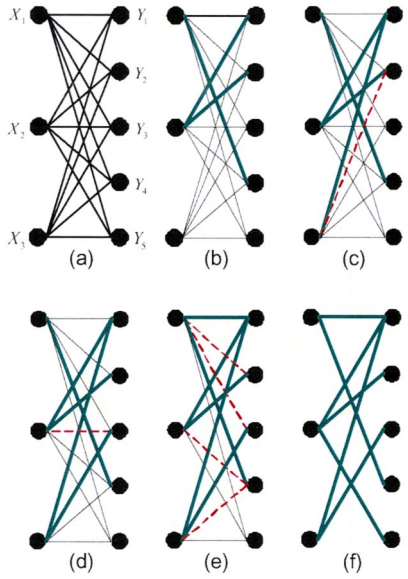


Fig. 5. MASTS algorithm

3) *Step 3*: Continue *Step 2* until the edge number of enlarged subgraph is equal to $Mt + Mr - 1$. This final subgraph is the spanning tree with the maximum sum of weight.

As virtual MIMO graph contains the same information as that of channel gain matrix $\mathbf{H}$, we illustrate MASTS algorithm by matrix entry selection procedure using Fig. 5 and matrix $\mathbf{H}_b$ $\mathbf{H}_c$ $\mathbf{H}_d$ $\mathbf{H}_e$ $\hat{\mathbf{H}}$.

Fig. 5 (a) is the original virtual MIMO graph. Fig. 5 (b) shows the subgraph with 3 largest weight. These edges are denoted by $\langle\rangle$ in matrix $\mathbf{H}_b$. This is *Step 1*.

$$\mathbf{H}_b = \begin{bmatrix} 0.6211 & \langle 0.7536\rangle & 0.6595 \\ 0.5602 & \langle 0.6596\rangle & 0.1834 \\ 0.2440 & 0.2141 & 0.6365 \\ \langle 0.8220\rangle & 0.6021 & 0.1703 \\ 0.2632 & 0.6049 & 0.5396 \end{bmatrix}$$

Note that among the selected 3 entries, 0.8220 have the different row index either with 0.7536 or 0.6595, so enlarging this subgraph with any of the remaining edges will absolutely not form a cycle.

Thus, the second step starts with selecting the edge with the fourth largest weight, which is shown in Fig. 5 (c) and Matrix $\mathbf{H}_c$.

$$\mathbf{H}_c = \begin{bmatrix} 0.6211 & \langle 0.7536\rangle & \langle 0.6595\rangle \\ 0.5602 & \langle 0.6596\rangle & 0.1834\times \\ 0.2440 & 0.2141 & 0.6365 \\ \langle 0.8220\rangle & 0.6021 & 0.1703 \\ 0.2632 & 0.6049 & 0.5396 \end{bmatrix}$$

Note that after selection of entry 0.6595, the entry 0.1834 will no longer be selected, or there is going to form a cycle $X_2Y_1X_3Y_2$, so we note the entry 0.1834 with "$\times$" and use

Authorized licensed use limited to: University of Texas at Arlington. Downloaded on December 18, 2009 at 14:40 from IEEE Xplore. Restrictions apply.

dash line to represent the unavailability of corresponding edge in Fig. 5(c). This implies following criteria:

Any four entries with index (i,j) (i,q) (p,j) (p,q), where $i, p \leq Mr$, $i \neq p; j, q \leq Mt$, $j \neq q$ form a cycle. If any three have been selected, the remaining one should be eliminated.

Based on this criteria, we continuously select entries as shown in Fig. 5 (d) (e) (f) and matrix $\mathbf{H}_d$ $\mathbf{H}_e$ $\mathbf{H}_f$. As we only have to select $3 + 5 - 1 = 7$ edges. Edges in graph (f) represented by none-zero entries in matrix $\hat{\mathbf{H}}$ are the channels finally selected.

$$\mathbf{H}_d = \begin{bmatrix} 0.6211 & \langle 0.7536 \rangle & \langle 0.6595 \rangle \\ 0.5602 & \langle 0.6596 \rangle & 0 \\ 0.2440 & 0.2141\times & \langle 0.6365 \rangle \\ \langle 0.8220 \rangle & 0.6021 & 0.1703 \\ 0.2632 & 0.6049 & 0.5396 \end{bmatrix}$$

$$\mathbf{H}_e = \begin{bmatrix} \langle 0.6211 \rangle & \langle 0.7536 \rangle & \langle 0.6595 \rangle \\ 0.5602\times & \langle 0.6596 \rangle & 0 \\ 0.2440\times & 0 & \langle 0.6365 \rangle \\ \langle 0.8220 \rangle & 0.6021\times & 0.1703\times \\ 0.2632 & 0.6049 & 0.5396 \end{bmatrix}$$

$$\hat{\mathbf{H}} = \begin{bmatrix} 0.6211 & 0.7536 & 0.6595 \\ 0 & 0.6596 & 0 \\ 0 & 0 & 0.6365 \\ 0.8220 & 0 & 0 \\ 0 & 0.6049 & 0 \end{bmatrix}$$

IV. Performance Analysis

A. Capacity

When the channel matrix $\mathbf{H}$ / $\hat{\mathbf{H}}$ is known at both transmitters and receivers, water-filling technique can be utilized to optimally allocate power P_i at independent parallel channel i. The sum of capacities on each of these independent parallel channels is the maximal capacity of virtual MIMO [14]. The capacity on full virtual MIMO can be expressed as

$$C = \max_{\sum P_i \leq P} \sum_{i=1}^{r} B \log_2(1 + \frac{P_i}{\sigma^2}\lambda_i) \tag{2}$$

where P is total power constraint for transmitters, r is the rank of $\mathbf{H}$ and λ_i is the eigenvalue of $\mathbf{H}\mathbf{H}^T$. Since the SNR at the ith channel at full power is $SNR_i = \lambda_i P/\sigma^2$, the capacity (2) can also be given in terms of the power allocation P_i as

$$C = \max_{\sum P_i \leq P} \sum_{i=1}^{r} B \log_2(1 + \frac{P_i}{P} SNR_i) \tag{3}$$

where

$$\frac{P_i}{P} = \begin{cases} 1/SNR_0 - 1/SNR_i & SNR_i \geq SNR_0 \\ 0 & SNR_i < SNR_0 \end{cases} \tag{4}$$

for some cutoff value SNR_0. The final capacity is given as

$$C = \sum_{SNR_i \geq SNR_0} B \log_2(\frac{SNR_i}{SNR_0}) \tag{5}$$

The value of SNR_0 must be found numerically, owning to no existence of closed-form solution for continues distributions of SNR [22]. This results in Monte Carlo simulation to analyze the capacity performance on MASTS virtual MIMO. We take following steps to do each experiment:

1) For simplicity, we apply Matlab "rand" to generate channel gain matrix $\mathbf{H}$.
2) Follow the MASTS channel selection algorithm to obtain the new channel gain matrix $\hat{\mathbf{H}}$.
3) Employ "svd" to obtain $\hat{\lambda}_i$ and its rank $\hat{r}$ for $\hat{\mathbf{H}}$. Note that $\hat{\lambda}_i$ is different with λ_i of $\mathbf{H}$.
4) Use water-filling power allocation to find out the cutoff value SNR_0 and the resulting capacity for MASTS virtual MIMO based on (3) (4) and (5). Here we assume $B = 1Hz$.

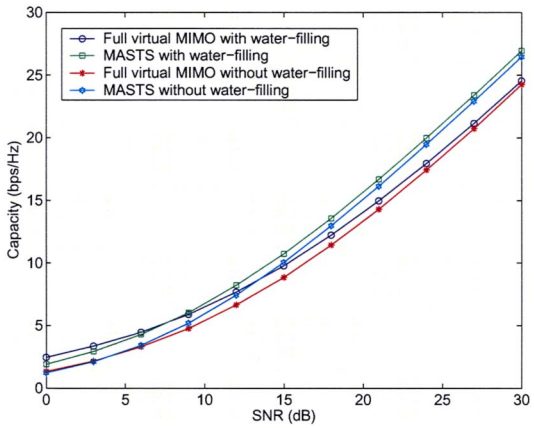


Fig. 6. Capacity for full / MASTS 4×4 virtual MIMO

Due to the randomness, 10000 times Monte Carlo simulation are applied to obtain the expectation of capacity for both MASTS and full 4×4 virtual MIMO at different SNR, which are plotted in Fig. 6. It shows when SNR is larger than 8dB, MASTS achieves larger capacity than that of full virtual MIMO. This is because the same total power have been optimally allocated to the best set of channels in spite of less channel number.

Sometimes in order to reduce the cost and complexity, instead of using water-filling power optimization, people simply allocate equal power to each transmitters. In that case, the capacity becomes

$$C = \sum_{i=1}^{r} B \log_2(1 + \frac{SNR_i}{M_t}) \tag{6}$$

Here we also apply 10000 time Monte Carlo simulation to obtain the expectation of capacities, which are also plotted in Fig. 6. It shows when SNR is larger than 5dB, MASTS achieves larger capacity than that of full virtual MIMO.

B. Diversity Gain and Multiplexing Gain

Intuitively, diversity gain corresponds to the number of independently faded paths that a symbol passes through [23].

Authorized licensed use limited to: University of Texas at Arlington. Downloaded on December 18, 2009 at 14:40 from IEEE Xplore. Restrictions apply.

In general, based our assumption of independent fading channel model, if finally M channels are selected, the maximal diversity gain provided is M. Since MASTS select M_t+M_r-1 channels, its maximal diversity gain is M_t+M_r-1, compared to that of M_tM_r on full virtual MIMO. Therefore, MASTS can not provide as much as full virtual MIMO on maximal diversity gain. This is illustrated in Fig. 7.

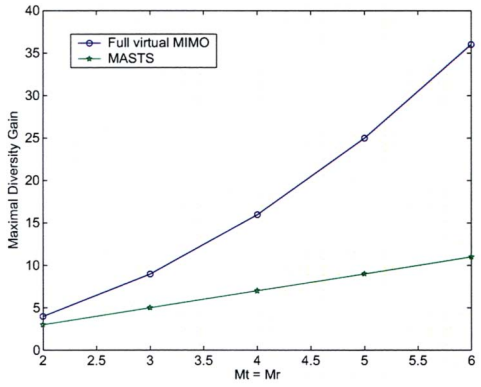


Fig. 7. Maximal diversity comparison

If BPSK and maximal ratio combining (MRC) are employed at maximal diversity gain, then the bit error rate (BER) is [24]

$$P_b = (\frac{1-\mu}{2})^L \sum_{k=0}^{L-1} \binom{L-1+k}{k} \binom{1+\mu}{2}^k \quad (7)$$

where

$$\mu = \sqrt{\frac{\frac{P}{\sigma^2}}{1+\frac{P}{\sigma^2}}} \quad (8)$$

and L is the diversity gain. Based on (7) (8), we get Fig. 8 for 2×2 virtual MIMO.

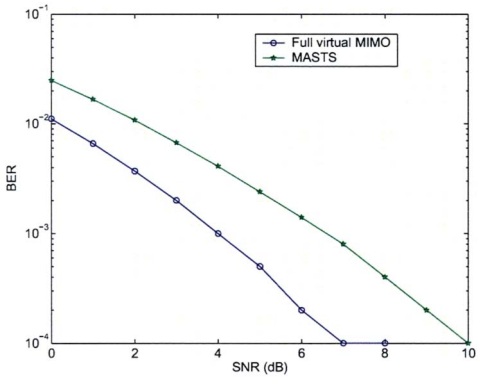


Fig. 8. BER for Full / MASTS 2×2 virtual MIMO

Normally, in order to increase the data rate, different transmitters simultaneously transmit different symbols, so in this case diversity for full and MASTS virtual MIMO are M_r and $(M_t + M_r - 1)/M_t$ respectively.

As for maximal multiplexing gain, it is the number of equivalent multiple parallel spatial channels [25], and also it is referred to as degrees of freedom to communicate [23], which is related with the row and column number of $\mathbf{H}$ and $\hat{\mathbf{H}}$. It has been derived in [23] that the maximal multiplexing gain provided by $M_t \times M_r$ MIMO is $\min(M_t, M_r)$. However, the accurate multiplexing gain is $r = rank(\mathbf{H})$ since it is possible that $\mathbf{H}$ is not full rank. The maximal multiplexing gain offered by MASTS is $\hat{r} = rank(\hat{\mathbf{H}})$. Under the premise that $\mathbf{H}$ is full rank, we ran 10000 times Monte Carlo simulation to obtain the multiplexing gain On MASTS in Fig. 9.

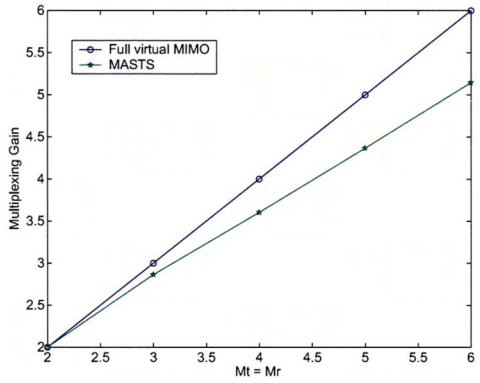


Fig. 9. Multiplexing Gain full / MASTS virtual MIMO

It shows when $Mt = Mr \leq 6$, the difference of Multiplexing Gain between full and MASTS virtual MIM can be less than 1.

In general, MASTS provide satisfying performances compared to that of full virtual MIMO.

V. Conclusion and Future Work

This paper is a preliminary work on practical virtual MIMO channel selection algorithm. MASTS approach with a concrete example is proposed from respect of cross-layer design. By means of Monte Carlo simulation, we approve that MASTS virtual MIMO can achieve even better capacity with/without water-filling, less diversity gain and similar multiplexing gain as those of full virtual MIMO. We not only propose the channel selection algorithm in practice, but also provide the detailed approach on performance analysis with Monte Carlo simulation. Future research tracks might concern the extension of the proposed algorithm to integrate with space time coding (STC) so as to further optimize the system performance.

Acknowledgement

This work was supported in part by National Science Foundation (NSF) under Grant CNS-0721515 and CNS-0831902, and Office of Naval Research (ONR) under Grant N00014-07-1-0395 and N00014-07-1-1024.

Authorized licensed use limited to: University of Texas at Arlington. Downloaded on December 18, 2009 at 14:40 from IEEE Xplore. Restrictions apply.

REFERENCES

[1] S. Cui and A. Goldsmith "Energy-efficiency of MIMO and Cooperative MIMO Techniques in Sensor Networks" , *IEEE Journal on selected areas in communications*, vol. 22, Aug 2004, pp. 1089 - 1098

[2] S. K. Jayaweera "Virtual MIMO-based cooperative communication for energy-constrained wireless sensor networks" , *IEEE Transactions on Wireless Communications*, vol. 5, May 2006, pp. 984 - 989

[3] A. del Coso, U. Spagnolini and C. Ibars, "Cooperative Distributed MIMO Channels in Wireless Sensor Networks" , *IEEE Journal on Selected Areas in Communications*, vol. 25, Feb. 2007, pp. 402 - 414.

[4] Y. Yuan; Z. He and M. Chen "Virtual MIMO-based cross-layer design forwireless sensor networks" , *IEEE Transactions on Vehicular Technology*, vol. 55, May 2006, pp. 856 - 864

[5] M. Bengtsson and B. Ottersten, "Optimal and suboptimal transmit beamforming", *Handbook of Antennas in Wireless Communications*, L. C. Godara, Ed. Boca Raton, Fl, CRC, 2001

[6] A. F. Molisch, M. Z. Win and J. H. Winters, "Capacity of MIMO systems with antenna selection", in *Proc. Int. Conf. Communications*, 2001, pp. 570-574

[7] "Selecting an optimal set of transmit antennas for a low rank matrix channel", in *Proc. Int. Conf. Acoustics, Speech, and Signal Processing*, 2000, pp. 2785-2788

[8] "Near optimal antenna selection of transmit antennas for a MIMO channel based on Shannon capacity", in Proc. 34th Asilomar Conf., Nov. 1999, pp. 567-571

[9] "Antenna Selection for spatial multiplexing systems based on minimum error rate", in *Proc. IEEE Int. Control Conf.*, 2001, pp. 2276-2280

[10] Y. J. Choi, J. Kim and S. Bahk, "Downlink scheduling with fairness and optimal antenna assignment for MIMO cellular systems", *Global Telecommunications Conference, 2004*, Vol. 5, 2004 Page(s):3165 - 3169

[11] Y. J. Choi, J. Kim and S. Bahk, "Optimal antenna assignment considering QoS under MIMO environments", *IEEE International Conference on Communications, 2004*, Vol.7, June 2004, pp. 4216 - 4221

[12] S. Sanayei and A. Nosratinia, "Antenna selection in MIMO systems", *IEEE Communications Magazine*, vol. 42, Oct. 2004

[13] J. B. Kruskal "On the shortest spanning subtree and the traveling salesman problem", *Proceedings of the American Mathematical Society*, vol. 7, 1956, pp. 48C50.

[14] A. Goldsmith, *Wireless Communications*, Cambridge University Press, NJ 2001.

[15] D. B. West, *Introduction to Graph Theory (2 Ed.)*, Prentice-Hall of India, NY 2005.

[16] Chen, S., S. A. Billings and W. Luo, "Orthogonal Least Squares Methods and their Application to Nonlinear System Identification," *Int. J. Control*, vol. 50, 1989, pp. 1873-1896.

[17] G. H. Golub, and C. F. Van Loan, *Matrix Computations*, Johns Hopkins University Press, MD 1983.

[18] G. C. Mouzouris and J. M. Mendel, "Designing fuzzy logic systems for uncertain environments using a singular-value-QR decomposition method" , *Proc of IEEE 5th Intl. Conf. on Fuzzy Systems*, pp.295-301, 1996, New Orleans, LA.

[19] G. C. Mouzouris and J. M. Mendel, "A singular-value-QR decomposition based method for training fuzzy logic systems in uncertain environments", *J Intell Fuzzy Systems*, vol. 5, 1997, pp.367-374.

[20] Q. Liang and J. M. Mendal, "Designing interval type-2 fuzzy logic systems using an SVD-QR method: Rule reduction" , *International Journal of Intelligent Systems*, vol. 15, 2000, pp.939-957.

[21] Q. Liang and L. Wang, "Redundancy Reduction in Wireless Sensor Networks Using Singular-Value-QR Decomposition" , *IEEE Military Communication Conference*, Oct. 2005, Atlantic City, NJ.

[22] M.-S. Alouini and A. J. Goldsmith, " Capacity of Rayleigh fading channels under different adaptive transmission and diversity combining techniques", *IEEE Trans. Veh. Tech*, pp. 1165-1181, July. 1999

[23] L. Zheng, D. N. C. Tse, "Diversity and multiplexing: a fundamental tradeoff in multiple-antenna channels", *IEEE Trans. on Information Theory*, vol. 49, pp. 1073-1096, May 2003

[24] G. L. Stuber, *Principles of Mobile Communication*, 2nd ed., Kluwer Academic Publishers, 2001

[25] Jr. R. Heath and A. Paulraj, "Switching between multiplexing and diversity based on constellation distance", in *Proc. Allerton Conf. Communication, Contril and Computing*, Oct 2000.

Authorized licensed use limited to: University of Texas at Arlington. Downloaded on December 18, 2009 at 14:40 from IEEE Xplore. Restrictions apply.

This full text paper was peer reviewed at the direction of IEEE Communications Society subject matter experts for publication in the ICC 2008 proceedings.

UWB Radar Sensor Networks for Sense-through-Foliage Target Detection

Qilian Liang
Department of Electrical Engineering
University of Texas at Arlington
Arlington, TX 76019-0016, USA
E-mail: liang@uta.edu

Sherwood W. Samn
Air Force Research Laboratory/HEX
Brooks City Base
San Antonio, TX 78235, USA
E-mail: Sherwood.samn@brooks.af.mil

Xiuzhen Cheng
Dept of Computer Science
George Washington University
Washington, DC 20052
E-mail: cheng@gwu.edu

***Abstract*— In this paper, we propose a Discrete-Cosine-Transform (DCT)-based approach for sense-through-foliage target detection when the echo signal quality is good, and a Radar Sensor Network (RSN) and DCT-based approach when the echo signal quality is poor. A RAKE structure which can combine the echos from different cluster-members is proposed for clusterhead in the RSN. We compared our approach with the ideal case when both echos are available, i.e., echos with target and without target. We also compared our approach against the scheme in which 2-D image was created via adding voltages with the appropriate time offset. Simulation results show that our DCT-based scheme works much better than the existing approach, and our RSN and DCT-based approach can be used for target detection successfully while even the ideal case fails to do it.**

I. Introduction and Motivation

Forests and buildings favor asymmetric threats because the warfighter has a limited sensing capability. Forest and buildings provide excellent concealment from observation, ambush, and escape, as well as provide secure bases for enemy Command & Control (C2), weapons caches, and Improvised Explosive Device (IED)/ Weapon of Mass Destruction (WMD) assembly. These have become "the high ground" in fourth-generation warfare, providing a significant strategic advantage. We believe that solving the sense-through-foliage target detection will significantly benefit sense-through-wall and other subsurface sensing problems. The objective of this paper is to develop measurable advances in improving the understanding of intelligence for the forest conflict using UWB radar. The key focus of this study is to develop advanced technologies that make foliage transparent, thereby eliminating the safe harbor that forest provides to hostile forces and their malicious activities. Sense-through-foliage target detection resulting from this research will benefit emerging Department of Defense (DoD) net-centric warfare programs.

In this paper, we will apply our expertise in signal processing, data fusion, sensor networks, etc to achieve effective sense-through-foliage technology using ultra-wideband (UWB) radar. UWB radar emissions are at a relatively low frequency-typically between 100 MHz and 3 GHz. Additionally, the fractional bandwidth of the signal is very large (greater than 0.2). Such radar sensor has exceptional range resolution that also has an ability to penetrate many common materials (e.g., walls). Law enforcement personnel have used UWB ground penetrating radars (GPRs) for at least a decade. Like the GPR, sense-through-foliage radar takes advantage of UWB's very fine resolution (time gating) and low frequency of operation. In the existing works on UWB radar/sensor based target detection, Time Domain Inc has invented UWB radars, and some algorithms for target detection were overviewed in [5]; these are mainly based on target response signal strength (1-D) and different copies of signals to construct 2-D features. The Adaptive Polarization-Difference Imaging (APDI) algorithm and PDI technique [3][4] were originally developed for optical imaging and in many situations can provide significant enhancements in target detection and feature extraction over conventional methods. The rest of this paper is organized as follows. In Section II, we summarize the measurement and collection of data we used in this paper. In Section III, we propose a discrete-cosine-transform (DCT) based approach for sense-through-foliage target detection with good signal quality. In Section IV, we propose a radar sensor network (RSN) and DCT-based approach for sense-through-foliage target detection when the signal quality is poor. We conclude this paper and discuss some future research topics in Section V.

II. Sense-through-Foliage Data Measurement and Collection

Our work is based on the sense-through-foliage data from Air Force Research Lab. The foliage penetration measurement effort began in August 2005 and continued through December 2005. Working in August through the fall of 2005, the foliage measured included late summer foliage and fall and early winter foliage. Late summer foliage, because of the limited rainfall, involved foliage with decreased water content. Late fall and winter measurements involved largely defoliated but dense forest.

The foliage experiment was constructed on a seven-ton man lift, which had a total lifting capacity of 450 kg. The limit of the lifting capacity was reached during the experiment as essentially the entire measuring apparatus

978-1-4244-2075-9/08/$25.00 ©2008 IEEE

Authorized licensed use limited to: University of Texas at Arlington. Downloaded on December 18, 2009 at 14:40 from IEEE Xplore. Restrictions apply.

was placed on the lift. The principle pieces of equipment secured on the lift are: Barth pulser, Tektronix model 7704 B oscilloscope, dual antenna mounting stand, two antennas, rack system, IBM laptop, HP signal Generator, Custom RF switch and power supply and Weather shield (small hut). The target is a trihedral reflector (as shown in Fig. 1). Throughout this work, a Barth pulse source (Barth Electronics, Inc. model 732 GL) was used. The pulse generator uses a coaxial reed switch to discharge a charge line for a very fast rise time pulse outputs. The model 732 pulse generator provides pulses of less than 50 picoseconds (ps) rise time, with amplitude from 150 V to greater than 2 KV into any load impedance through a 50 ohm coaxial line. The generator is capable of producing pulses with a minimum width of 750 ps and a maximum of 1 microsecond. This output pulse width is determined by charge line length for rectangular pulses, or by capacitors for 1/e decay pulses.



Fig. 1. The target (a trihedral reflector) is shown on the stand at 300 feet from the lift.

For the data we used in this paper, each sample is spaced at 50 picosecond interval, and 16,000 samples were collected for each collection for a total time duration of 0.8 microseconds at a rate of approximately 20 Hz. We considered two sets of data from this experiment. Initially, the Barth pulse source was operated at low amplitude and 35 pulses reflected signal were averaged for each collection. Significant pulse-to-pulse variability was noted for these collections. The scheme for the sense-through-foliage target detection with "poor" signal quality will be presented in Section IV. Later, good signal quality data were collected using higher amplitude pulses and 100 pulses reflected signals were averaged for each collection. The scheme for target detection with "good" signal quality will be presented in Section III.

III. Sense-through-Foliage Target Detection with Good Signal Quality: A DCT-based Approach

In Fig. 2, we plot two collections with good signal quality, one without target on range (Fig. 2a) and the other one

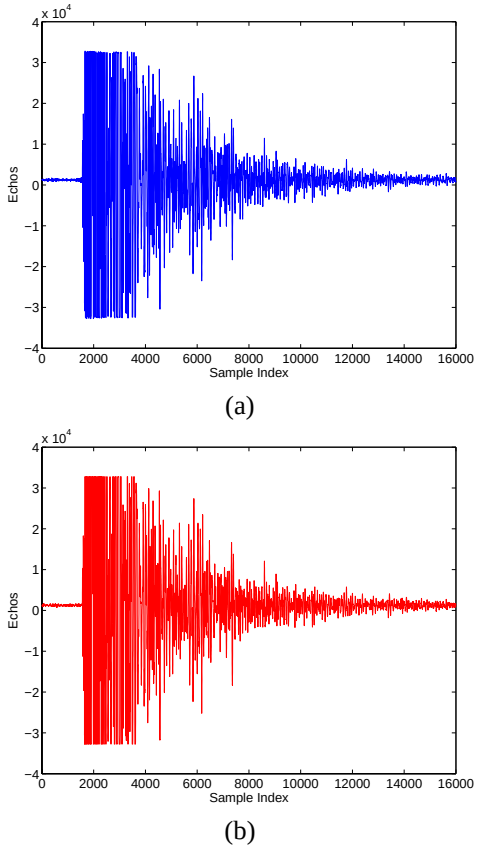


Fig. 2. Measurement with very good signal quality and 100 pulses average. (a) No target on range, (b) with target on range (target appears at around sample 14,000).

with target on range (Fig. 2b and target appears at around sample 14,000). To make it more clear to the readers, we provide expanded views of traces (with target) from sample 13,001 to 15,000 for the above two collections in Figs. 3a and 3b. Since there is no target in Fig. 3a, it can be treated as the response of foliage clutter. It's quite straightfoward that the target response will be the echo difference between Fig. 3b and Fig. 3a, which is plotted in Fig. 3c. However, it's impossible to obtain Fig. 3a (clutter echo) in practical situation if there is target on range. The challenge is how to make target detection based on Fig. 3b (with target) or Fig. 3a (no target) only?

Observe Fig. 3b, for samples where target appears (around sample 14,000), the sample strength changes much abruptly than that in Fig. 3a, which means echo from target contains more AC values than that without target. Motivated by this, we applied Discrete Cosine Transform (DCT) to the echos $x(iM+n)$ $(n = 0, 1, 2, \cdots, N-1)$ where N is the DCT window length, M is the step size of each DCT window, and i is the window index. Let $x(n,i) \triangleq x(iM+n)$

$$X(K,i) = \sum_{n=0}^{N-1} x(n,i)\cos(\frac{2\pi}{N}nK) \qquad (1)$$

Authorized licensed use limited to: University of Texas at Arlington. Downloaded on December 18, 2009 at 14:40 from IEEE Xplore. Restrictions apply.

then we cumulate the power of AC values (for $K > 2$)

$$P(i) = \sum_{K=3}^{N-1} X(K,i)^2 \quad (2)$$

For $N = 100$ and $M = 10$, we plot the power of AC values $P(i)$ versus iM (time domain sample index) in Figs. 4a and 4b for the above data sets in Figs. 3a and 3b respectively. Observe that in Fig. 4b, the power of AC values (around sample 14,000) where the target is located is non-fluctuating (monotonically increase then decrease). Although some other samples also have very high AC power values, it is very clear that they are quite fluctuating and the power of AC values behave like random noise because generally the clutter has Gaussian distribution in the frequency domain [2].

We compared our DCT-based approach to the scheme proposed in [5]. In [5], 2-D image was created via adding voltages with the appropriate time offset. In Figs. 5a and 5b, we plot the 2-D image created based on the above two data sets (from samples 13,800 to 14,200). However, it's not clear which image shows there is target on range.

IV. Sense-through-Foliage Target Detection with Poor Signal Quality: A Sensor Network and DCT-based Approach

As mentioned in Section II, when the Barth pulse source was operated at low amplitude and the sample values are not obtained based on sufficient pulse response averaging (averaged over 35 pulses for each collection), significant pulse-to-pulse variability was noted and the return signal quality is poor. In Figs. 6a and 6b, we plot two collections with poor signal quality. Fig. 6a has no target on range, and Fig. 6b has target at samples around 14,000. We plot the echo differences between Figs. 6a and 6b in Fig. 6c. However, it is impossible to identify whether there is any target and where there is target based on Fig. 6c. We observed the DCT-based approach failed to detect target based on one collection. Since significant pulse-to-pulse variability exists in the echos, this motivate us to explore the spatial and time diversity using Radar Sensor Networks (RSN).

In RSN, each radar can provide their pulse parameters such as timing to their clusterhead radar, and the clusterhead radar can combine the echos (RF returns) from the target and clutter. In this paper, we propose a RAKE structure for combining echos, as illustrated by Fig. 7. The integration means time-average for a sample duration T and it's for general case when the echos are not in discrete values. It is quite often assumed that the radar sensor platform will have access to Global Positioning Service (GPS) and Inertial Navigation Unit (INU) timing and navigation data [1]. In this paper, we assume the radar sensors are synchronized in RSN. In Fig. 7, the echo, i.e., RF response by the pulse of each cluster-member sensor, will be combined by the clusterhead using a weighted average, and the weight w_i is determined by the power of each echo $x_i(n)$ (n is the sample index),

$$w_i = \frac{E_i}{\sum_{i=1}^{M} E_i} \quad (3)$$

and

$$E_i = \text{var}(x_i(n)) + [\text{mean}(x_i(n))]^2 \quad (4)$$

We ran simulations for $M = 30$, and plot the power of AC values in Figs. 8a and 8b for the two cases (with target and without target) respectively. Observe that in Fig. 4b, the power of AC values (around sample 14,000) where the target is located is non-fluctuating (monotonically increase then decrease). Although some other samples also have very high AC power values, it is very clear that they are quite fluctuating and the power of AC values behaves like random noise because generally the clutter has Gaussian distribution in the frequency domain.

V. Conclusions and Future Works

In this paper, we proposed a DCT-based approach for sense-through-foliage target detection when the echo signal quality is good, and a sensor network and DCT-based approach when the echo signal quality is poor. A RAKE structure which can combine the echos from different cluster-members is proposed for clusterhead in the RSN. We compared our approach with ideal case when both echos are available, i.e., echos with target and without target. We also compared our approach against the scheme in which 2-D image was created via adding voltages with the appropriate time offset. Simulation results show that our DCT-based scheme works much better than the existing approach, and our RSN and DCT-based approach can be used for target detection successfully while the ideal case fails to do it. For future works, we will collect more data with different targets and perform automatic target recognition besides target detection.

Acknowledgement

This work was supported in part by ONR under Grant N00014-07-1-0395, N00014-03-1-0466, N00014-07-1-1024, NSF under Grant CNS-0721515, and AFOSR Summer Faculty Fellowship Program Award.

References

[1] ONR BAA 07-017, "NET-SENTRIC Surveillance," http://www.onr.navy.mil/02/baa/.

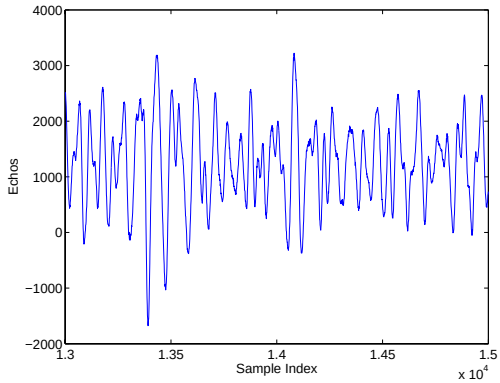
[2] D. K. Barton, *Radar System Analysis and Modeling*, Artech House, Boston, MA, 2006.

[3] M. P. Rowe, E. N. Pugh, Jr., J. S. Tyo, and N. Engheta, "Polarization-difference imaging: a biologically inspired technique for observation through scattering media," *Optics Letters*, Vol. 20, pp. 608-610, 1995.

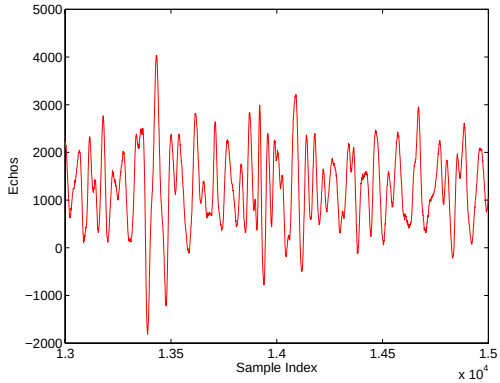
[4] J. S. Tyo, M. P. Rowe, E. N. Pugh, Jr., N. Engheta, "Target detection in optically scattering media by polarization difference imaging," *Applied Optics*, Vol. 35, pp. 1855-1870, 1996.

[5] P. Withington , H. Fluhler, and S. Nag , "Enhancing homeland security with advanced UWB sensors," *IEEE Microwave Magazine*, Sept 2003.

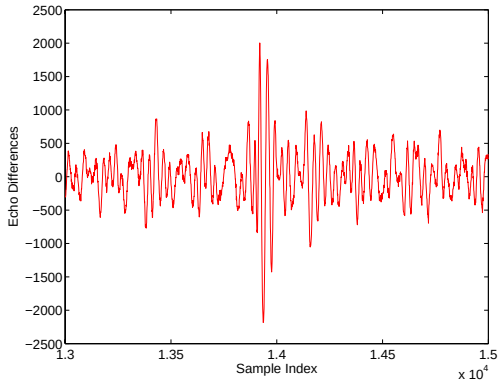
Authorized licensed use limited to: University of Texas at Arlington. Downloaded on December 18, 2009 at 14:40 from IEEE Xplore. Restrictions apply.



(a)

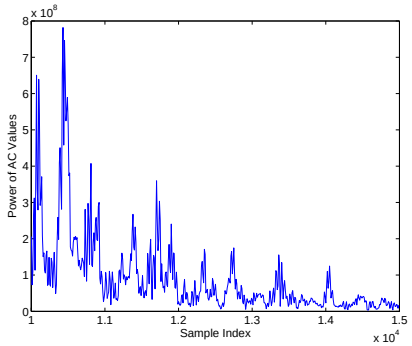


(b)

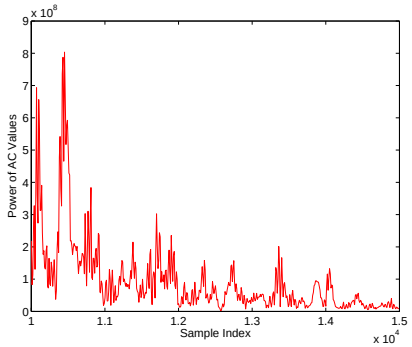


(c)

Fig. 3. Measurement with very good signal quality and 100 pulses average. (a) Expanded view of traces (with target) from samples 13,001 to 15,000. (b) Expanded view of traces (without target) from samples 13,001 to 15,000. (c) The differences between (a) and (b).

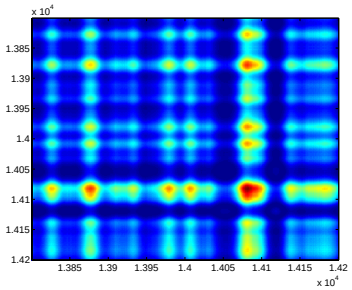


(a)

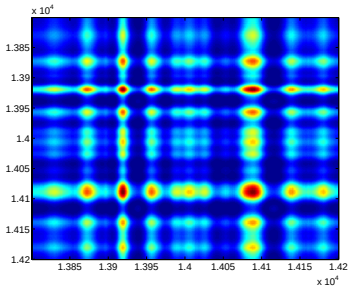


(b)

Fig. 4. The power of AC values versus sample index. (a) No target (b) With target in the field.



(a)



(b)

Fig. 5. 2-D image created via adding voltages with the appropriate time offset. (a) No target (b) With target in the field.

Authorized licensed use limited to: University of Texas at Arlington. Downloaded on December 18, 2009 at 14:40 from IEEE Xplore. Restrictions apply.

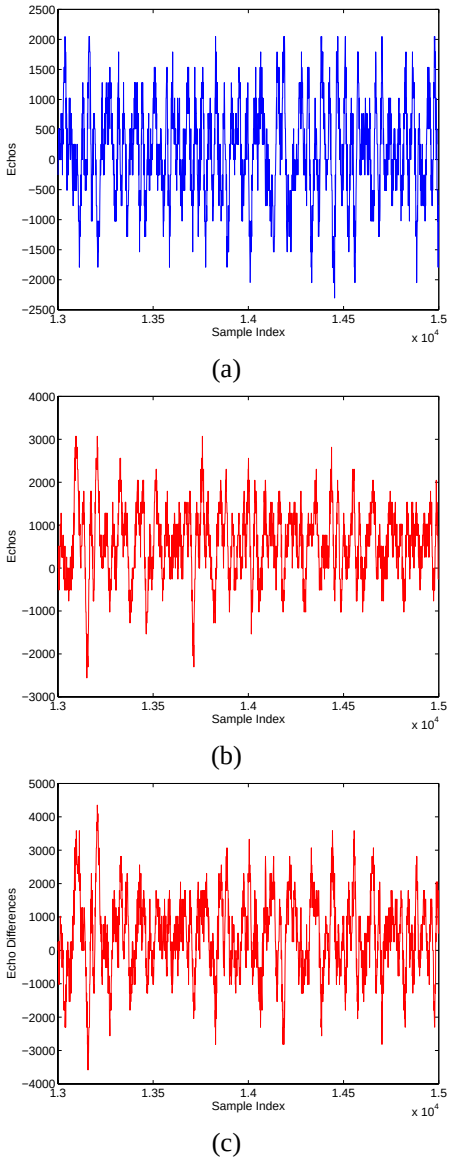


Fig. 6. Measurement with poor signal quality and 35 pulses average. (a) Expanded view of traces (no target) from sample 13,001 to 15,000. (b) Expanded view of traces (with target) from sample 13,001 to 15,000. (c) The differences between (a) and (b).

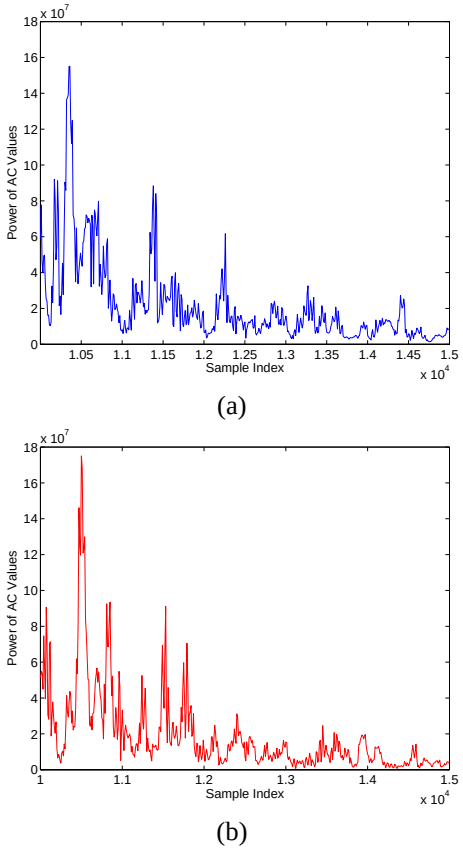


Fig. 8. Power of AC values based on UWB radar sensor networks and DCT based approach. (a) No target (b) With target in the field.

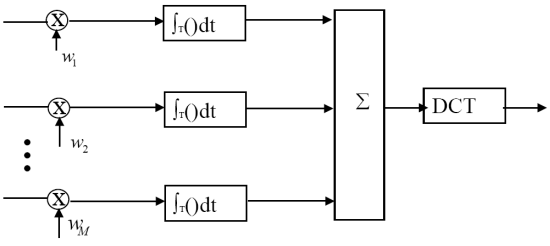


Fig. 7. Echo combining by clusterhead in RSN.

Authorized licensed use limited to: University of Texas at Arlington. Downloaded on December 18, 2009 at 14:40 from IEEE Xplore. Restrictions apply.

This full text paper was peer reviewed at the direction of IEEE Communications Society subject matter experts for publication in the ICC 2008 proceedings.

A Differential Based Approach for Sense-Through-Foliage Target Detection using UWB Radar Sensor Networks

Jing Liang, Qilian Liang
Department of Electrical Engineering
University of Texas at Arlington
Arlington, TX 76019-0016, USA
Email: jliang@wcn.uta.edu, liang@uta.edu

Sherwood W. Samn
Air Force Research Laboratory/HEX
Brooks City Base
San Antonio, TX 78235, USA
Email: Sherwood.samn@brooks.af.mil

***Abstract*— In this paper, the foliage penetration measurement data is provided by Air Force Office of Scientific Research (AFOSR). When radar echoes are in good quality, the detection of target can be achieved by applying our differential based technology on received single UWB radar waveform. We compared our approach in case of no target as well as with target against the scheme in which 2-D image was created via adding voltages with the appropriate time offset. Results show that our approach can work much better. When radar echoes are in poor condition and single radar is unable to carry out the detection, we employ both Radar Sensor Networks (RSN) and RAKE structure to combine the echoes from different radar members and successfully detect the target.**

I. Introduction

Detection and identification of military equipment in a strong clutter background, such as foliage, soil cover or building leads has been a long-standing subject of intensive study. It is believed that solving the target detection through foliage will significantly benefit sense-through-wall and many other subsurface sensing problems. However, to this date, the detection of foliage-covered military targets, such as artillery, tanks, trucks and other weapons with the required probability of detection and false alarm still remains a challenging issue. This is due to the following facts:

1) Given certain low radar cross section(RCS), scattering from tree trunk and ground reflectivity may overwhelm the returned target signals of interest.
2) Very high multiple fading severely corrupt the amplitude and phase of the echoes.
3) Even if target is stationery, tree leaves and branches are likely to swing in result of gust, which will result in doppler shift of clutter and difficulty of target detection.

Therefore, our main goal is to account for the above effects and better analyze the "defoliated" signal and thus improve the probability of target detection.

Over the past two decades, following 3 types of signals have been mainly studied to examine the performance on target detection in foliage:

1) Traditional sinusoidal waveforms at VHF through UHF bands [1], as the lower the radar frequency, the lower the attenuation and scattering from branches and trees, and thus better penetration through foliage. However, these approaches result in low resolution and low RCS.
2) Millimeter-Wave (MMW) radars are used in [2] [3] and [4]. Results demonstrate the potential for satisfying performance but need further investigation.
3) Relatively low frequency Ultra-wide band (UWB) radars between 100 MHZ and 3 GHz are frequently employed in recent years owning to the characteristics provided by their high resolutions as well as the very good ability of penetration, such as penetrating walls [5] [6]. Despite comparatively short detection range, UWB signal would have advantages over a narrowband signal with limited frequency content.

In this paper, we will apply our expertise in signal processing, data fusion, radar sensor networks (RSN) etc. to achieve effective through-foliage technology using ultra-wideband (UWB) radar and extracting as much information as possible to improve the probability of target detection.

The remainder of this paper is organized as follows. In Section II, we summarize the measurement and collection of data we used in this paper. In Section III, we propose a differential based approach for through-foliage target detection when the signal quality is good. In Section IV, we propose RSN and RAKE structure for through-foliage target detection when the signal quality is poor. We conclude this paper and discuss some future research topics in Section V.

II. Sense-Through-Foliage Data Measurement and Collection

Our work is based on the sense-through-foliage data from Air Force Research Lab [7]. The foliage penetration measurement effort began in August 2005 and continued through December 2005. Working in August through the fall of 2005, the foliage measured included late summer foliage and fall and early winter foliage. Late summer foliage, because of the limited rainfall, involved foliage with decreased water content. Late fall and winter measurements involved largely defoliated but dense forest.

978-1-4244-2075-9/08/$25.00 ©2008 IEEE

Authorized licensed use limited to: University of Texas at Arlington. Downloaded on December 18, 2009 at 14:41 from IEEE Xplore. Restrictions apply.

The foliage experiment was constructed on a seven-ton man lift, which had a total lifting capacity of 450 kg. The limit of the lifting capacity was reached during the experiment as essentially the entire measuring apparatus was placed on the lift. The principle pieces of equipment secured on the lift are: Barth pulser, Tektronix model 7704 B oscilloscope, dual antenna mounting stand, two antennas, rack system, IBM laptop, HP signal Generator, Custom RF switch and power supply and Weather shield (small hut). The target is a trihedral reflector (as shown in Fig. 1). Throughout this work, a Barth pulse source (Barth Electronics, Inc. model 732 GL) was used. The pulse generator uses a coaxial reed switch to discharge a charge line for a very fast rise time pulse outputs. The model 732 pulse generator provides pulses of less than 50 picoseconds (ps) rise time, with amplitude from 150 V to greater than 2 KV into any load impedance through a 50 ohm coaxial line. The generator is capable of producing pulses with a minimum width of 750 ps and a maximum of 1 microsecond. This output pulse width is determined by charge line length for rectangular pulses, or by capacitors for 1/e decay pulses.

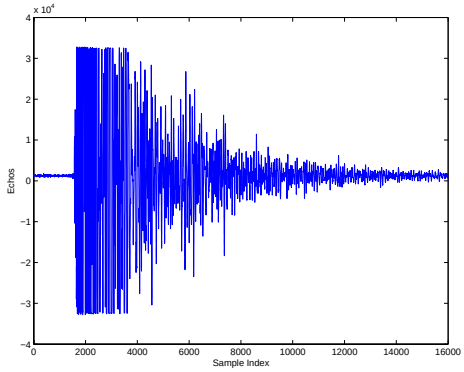


Fig. 1. The target (a trihedral reflector) is shown on the stand at 300 feet from the lift.

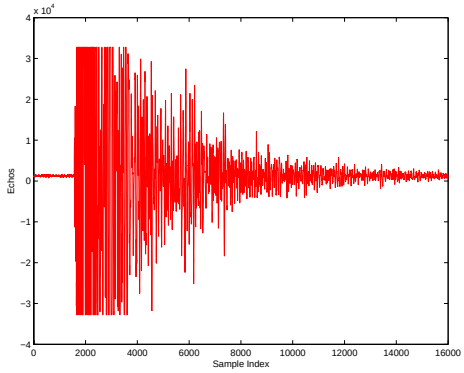
For the data we used in this paper, each sample is spaced at 50 picosecond interval, and 16,000 samples were collected for each collection for a total time duration of 0.8 microseconds at a rate of approximately 20 Hz. We considered two sets of data from this experiment. Initially, the Barth pulse source was operated at low amplitude and 35 pulses reflected signal were averaged for each collection. these collectionsThe scheme for the sense-through-foliage target detection with "poor" signal quality will be presented in Section IV. Later, good signal quality data were collected using higher amplitude pulses and 100 pulses reflected signals were averaged for each collection. The scheme for target detection with "good" signal quality will be presented in Section III.

III. Target Detection with Good Signal Quality: A Differential-Based Approach

In Fig. 2, we plot two collections with good signal quality, one without a target on range (Fig. 2a) and the other one with a target on range (Fig. 2b and target appears at around sample 14,000). To make it more clear to the readers, we provide expanded views of traces (with target) from sample 13,001 to 15,000 for the above two collections in Figs. 3a and 3b. Since there is no target in Fig. 3a, it can be treated as the response of foliage clutter. It's quite straightforward that the target response will be the echo difference between Fig. 3b and Fig. 3a, which is plotted in Fig. 3c. However, in practical situation we either obtain Fig. 3a (clutter echo without target) or Fig. 3b (target on range) without the knowledge about the presence of a target. The challenge is how can certain artificial intelligence make target detection only based on Fig. 3b (with target) or Fig. 3a (no target)?



(a)



(b)

Fig. 2. Measurement with very good signal quality and 100 pulses average. (a) no target on range (b) with target on range (target appears at around sample 14000)

To solve this problem, a scheme is previously proposed in [8], where 2-D image was created via adding voltages with the appropriate time offset. In Figs. 4(a) and 4(b), we plot the 2-D image created based on the above two data sets (from samples 13,800 to 14,200) using the approach in [8]. However, from these two figures, we can not clearly tell which image shows there is target on range.

The block diagram of our approach is generalized in Fig.5.

Actually, the waveforms in Fig. 2a and 2b result from the synthesized effect of large-scale path loss and small-scale fading. We believe if UWB propagation channel at foliage can be accurately estimated based on transmitted signals and

Authorized licensed use limited to: University of Texas at Arlington. Downloaded on December 18, 2009 at 14:41 from IEEE Xplore. Restrictions apply.

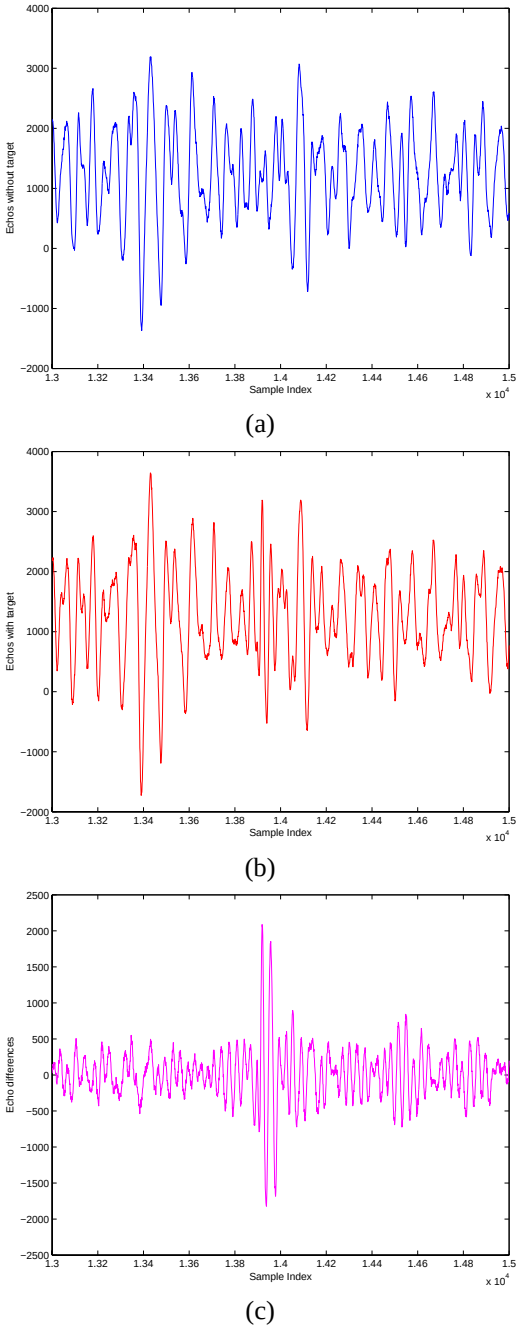


Fig. 3. Measurement with good signal quality and 100 pulses integration (a) Expanded view of traces (no target) from samples 13001 to 15000 (b) Expanded view of traces (with target) from samples 13001 to 15000 (c) Expanded view of traces difference between with and without target

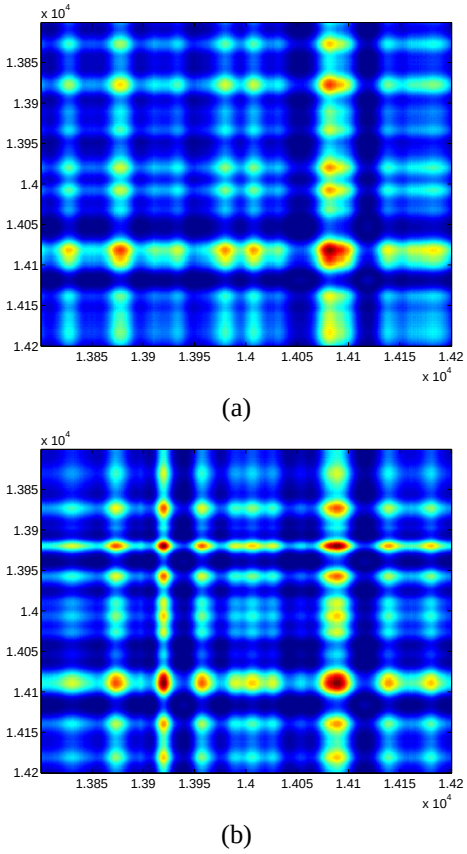


Fig. 4. 2-D image created via adding voltages with the appropriate time offset (a) no target (b) with target in the field

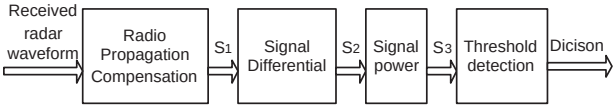


Fig. 5. Block diagram of differential based approach for single radar

received echoes with good quality, we may compensate the "foliage-based" UWB channel effect on received waveforms and the target under foliage will be more detectable. However, to this date, the outdoor channel model for UWB radars is still an open problem.

According to UWB indoor multi-path channel model (IEEE 802.15.SG3a, 2003), the average power delay profile (PDP) is characterized by an exponential decay of the amplitude of the clusters [9]. Therefore, we may roughly consider the foliage channel gain model as

$$\hat{y} = \begin{cases} Ae^{-Bx} & y > 0 \\ -Ae^{-Bx} & \text{otherwise} \end{cases} \quad (1)$$

where $\hat{y}$ is the amplitude of estimated clutter echo, x is sample index and y is the amplitude of original measured data. A and B are constants. These two parameters should be carefully chosen so that $\hat{y}$ is as close to y as possible. Here we use $A = 35000$ and $B = 0.00025$. Although it deserves much

Authorized licensed use limited to: University of Texas at Arlington. Downloaded on December 18, 2009 at 14:41 from IEEE Xplore. Restrictions apply.

further study on the estimation problem, we shall see later that as the target appears at a tail part, this simple estimation is applicable, therefore we get the processed signal:

$$S_1 = y - \hat{y} \tag{2}$$

Observe Fig. 3b, for samples where target appears (around sample 14,000), the waveform changes much abruptly than that in Fig. 3a. As differential value represents the changing rate of a function, it is quite intuitively that the amplitude of differential value at around sample 14,000 should be large. Apply differentiator and power ordinally,

$$S_2 = \frac{dS_1}{dx} \tag{3}$$

$$S_3 = {S_2}^2 \tag{4}$$

We plot the power of clutter-accounted and differentiated echoes in Fig. 6. It is quite straightforward to see there is no target in Fig. 6a and there is target in Fig. 6b.

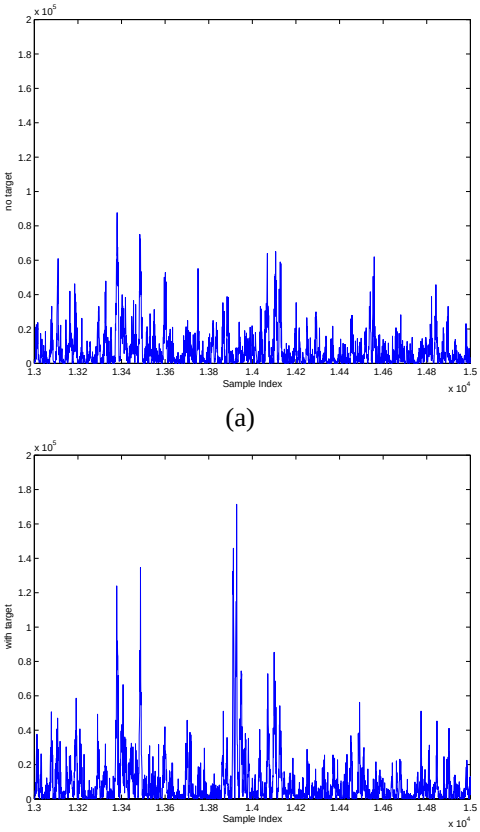


Fig. 6. The power of processed waveforms (a) no target (b) with target in the field

IV. Target Detection with Poor Signal Quality: Radar Sensor Network and Differential-Based Approach

As mentioned in Section II, when the Barth pulse source was operated at low amplitude and the sample values are not obtained based on sufficient pulse response averaging (averaged over 35 pulses for each collection), significant pulse-to-pulse variability was noted and the return signal quality is poor. Fig. 8a illustrate the received echoes in this situation. Even with the application of our proposed differential-based scheme, we can not tell whether there is target or not in the range based on Fig. 8b. Since pulse-to-pulse variability exists in the echos at different time or different site, this motivate us to explore the spatial and time diversity using Radar Sensor Networks (RSN).

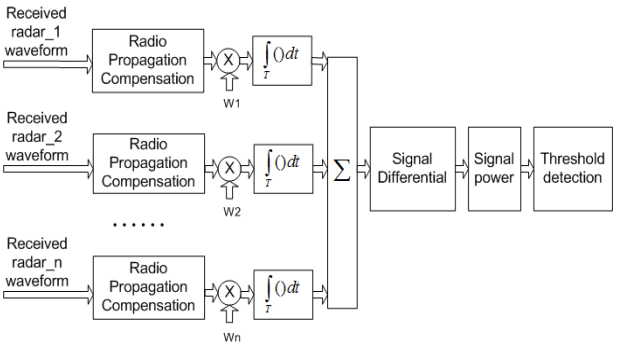


Fig. 7. Block diagram of differential based approach and diversity combination in RSN

In nature, a network of multiple radar sensors can been utilized to combat performance degradation of single radar [10]. These radar sensors are managed by an intelligent clusterhead that combines waveform diversity in order to satisfy the common goals of the network other than each radar operate substantively. As radar sensors are environment dependent [11], it may provide better signal quality if different neighboring radars work collaboratively to perform data fusion. For example, consider a system of two radars. When the signal of either radar unfortunately experience a severe fading, if two radars are spaced sufficiently far apart, it is not likely that both of the radars experience deep fade at the same time. By selecting better waveform from the two radar waveforms, the data is less likely to be lost.

In this paper, we assume the radar sensors are synchronized in RSN and we employed RAKE structure to combine received information for RSN. The detailed process is shown in Fig. 7. The echo, i.e., RF response by the pulse of each cluster-member radar sensor, will be combined by the clusterhead using a weighted average, and the weight w_i is determined by the power of each echo $x_i(m)$ (m is the sample index),

$$w_i = \frac{E_i}{\sum_{i=1}^{n} E_i} \tag{5}$$

and

$$E_i = \text{var}(x_i(m)) + [\text{mean}(x_i(m))]^2 \tag{6}$$

We ran simulations for n = 35 and plot the power of combined signal obtained through differential based approach in Fig. 8c. Compare this figure with Fig. 8a and Fig. 8b, it is quite obvious to see that there is a target around sample 14,000.

Authorized licensed use limited to: University of Texas at Arlington. Downloaded on December 18, 2009 at 14:41 from IEEE Xplore. Restrictions apply.

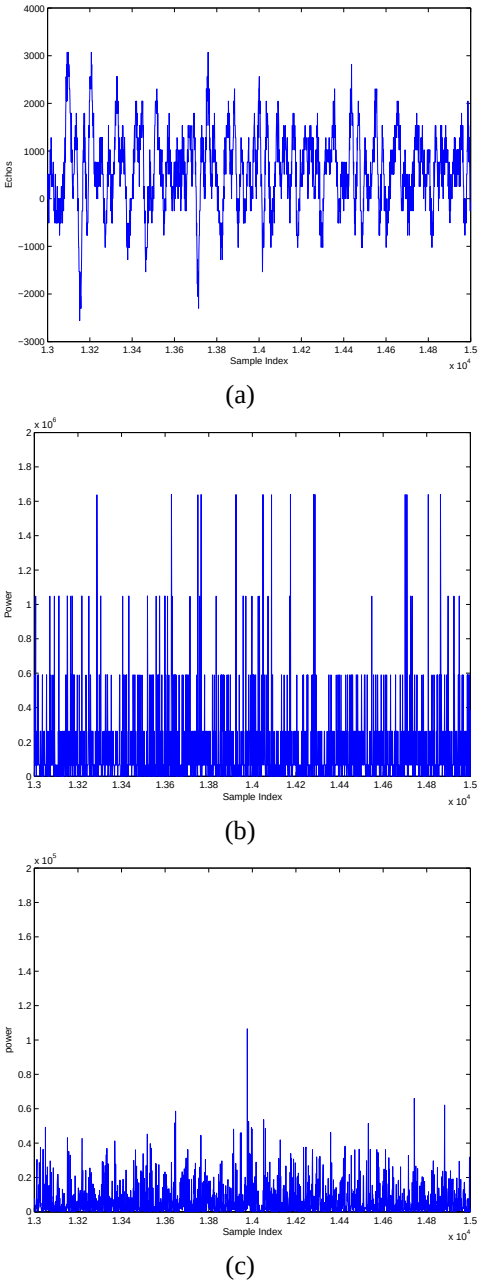


Fig. 8. Measurement with poor signal quality (with target) and 35 pulses integration (a) Expanded view of traces with target from samples 13001 to 15000 (b) Power of single radar after differential based approach (c) Power after both differential based approach and echoes combination in RSN

V. Conclusion and Future Works

In this paper, we propose a differential-based signal processing approach on received UWB Radar waveforms to improve through-foliage target detection. The foliage penetration measurements were taken in Holliston, Massachusetts. When radar echoes are in good quality, the detection of target can be achieved by applying differential-based technology to single radar waveform. We compared our approach in case of no target as well as with target against the scheme in which 2-D image was created via adding voltages with the appropriate time offset. Results show that our approach can work much better. When radar echoes are in poor condition and single radar is unable to carry out detection, we employe both Radar Sensor Networks (RSN) and RAKE structure to combine the echoes from different radar members and finally successfully detect the target. For future works, we will collect more data with different targets and perform automatic target recognition besides target detection.

Acknowledgement

This work was supported in part by Office of Naval Research (ONR) under Grant N00014-07-1-0395, N00014-07-1-1024, and National Science Foundation (NSF) under Grant CNS-0721515.

References

[1] S. Ayasli and L. Bessette, " UHF & VHF SAR phenomenology, presented at the Proc. PIERS, Workshop on Advances in Radar Mathods, Baveno, Italy, July 20-22, 1998"

[2] F. K. Schwering, E. J. Violette and R. H. Espeland, "Millimeter-wave propagation in vegetation: Experiments and theory", *IEEE Trans. Geosci. Remote Sensing*, vol.26, pp. 355-367, May 1988

[3] F. T. Ulaby, T. E. Van Deventer, J. R. East, T. F. Haddock and M. E. Coluzzi, "Millimeter-wave bistatic scaterring from ground and vegetation targets" , *IEEE Trans. Geosci. Remote Sensing*, vol.26, pp. 229-243, May 1988

[4] A. Y. Nashashibi, k. Sarabandi, S. Oveisgharan *et al.*, "Millimeter-Wave Measurement of Foliage Attenuation and Ground Reflectivity of Tree Stands at Nadir Incidence", *IEEE Trans. Antennas Propagat.*, vol.52, pp.1211-2004, May, 2004

[5] B. Ferrell "Ultrawideband foliage penetration measurement", in *Proc. IEEE Nation Radar Conf.*, Mar. 29-31, pp.80-84, 1994

[6] X. Xu; R. M. Narayanan, "FOPEN SAR imaging using UWB step-frequency and random noise waveforms ", *IEEE Trans. Aerospace and Electronic Systems*, vol.37, pp.1287-1300, Oct. 2001

[7] C. Dill, "Foliage Penetration (Phase II) Field Test: Narrowband versus Wideband Foliage Penetration," *Final Report of Contract Number F41624-03-D-7001/04*, July 2005 to Feb 2006.

[8] P. Withington , H. Fluhler, and S. Nag, "Enhancing homeland security with advanced UWB sensors," *IEEE Microwave Magazine*, Sept 2003.

[9] Benedetto M. D and Giancola G., *Understanding Ultra Wide Band Radio Fundamentals*, Person Education, 2004

[10] S. Haykin, "Cognitive radar networks" , *2005 1st IEEE International Workshop on Computational Advances in Multi-Sensor Adaptive Processing*, pp.1-3, Dec 2005.

[11] R. A. Johnson and E. L. Titlebaum, "Range Doppler Uncoupling in the Doppler Tolerant Bat Signal", *Proc. of IEEE Ultrasonics Symposium* , New York, pp.64-67, 1972.

Authorized licensed use limited to: University of Texas at Arlington. Downloaded on December 18, 2009 at 14:41 from IEEE Xplore. Restrictions apply.

This full text paper was peer reviewed at the direction of IEEE Communications Society subject matter experts for publication in the ICC 2008 proceedings.

Foliage Clutter modeling Using the UWB Radar

Jing Liang, Qilian Liang
Department of Electrical Engineering
University of Texas at Arlington
Arlington, TX 76019-0016, USA
Email: jliang@wcn.uta.edu, liang@uta.edu

Sherwood W. Samn
Air Force Research Laboratory/HEX
Brooks City Base
San Antonio, TX 78235, USA
Email: Sherwood.samn@brooks.af.mil

***Abstract*— In this paper, we propose that the foliage clutter follows log-logistic model using maximum likelihood (ML) parameter estimation as well as the root mean square error (RMSE) on PDF curves between original clutter and statistical model data. The measured clutter data is provided by Air Force Office of Scientific Research (AFOSR). In addition to investigating the log-logistic model, we also compare it with other popular clutter models, namely log-normal, Weibull and Nakagami. We show that the log-logistic model not only achieves the smallest standard deviation (STD) error on estimated model parameters, but also has the best goodness-of-fit and smallest RMSE. Further, the performance of detection at presence of foliage clutter is theoretically analyzed.**

I. Introduction and Motivation

Clutter is a term used to define all unwanted echoes from natural environment [1]. The nature of clutter may necessarily vary on a basis of different applications and radar parameters. Most previous studies have investigated land clutter and sea clutter. As far as clutter modeling in forest is concerned, it is still of great interest and is likely to take some time to reach any agreement. A team of researchers from MIT [2] and U. S. Army Research Laboratory (ARL) [3] [4] have measured ultra-wideband (UWB) backscatter signals in foliage for different polarizations and frequency ranges. The measurements show that the foliage clutter is impulsively corrupted with multipath fading, which leads to inaccuracy of the K-distributions description [5]. The Air Force Office of Scientific Research (AFOSR) has conducted field measurement experiment concerning foliage penetration radar since 2004 and noted that metallic targets may be more easily identified with wideband than with narrowband signals [6].

In this investigation, we will apply ultra-wide band (UWB) radar to model the foliage clutter. UWB radar emissions are at a relatively low frequency-typically between 100 MHz and 3 GHz. Additionally, the fractional bandwidth of the signal is very large (greater than 0.2). Such radar sensors have exceptional range resolution that also has an ability to penetrate many common materials (e.g., walls). Law enforcement personnel have used UWB ground penetrating radars (GPRs) for at least a decade. Like the GPR, sense-through-foliage radar takes advantage of UWB's very fine resolution (time gating) as well as low frequency of operation.

In our present work, we investigate the use of the log-logistic distribution to model foliage clutter and illustrate the goodness-of-fit to real UWB clutter data conducted by AFOSR. Additionally, we compare the goodness-of-fit with existing popular models namely log-normal, Weibull, and Nakagami by means of maximum likelihood estimation (MLE) and the root mean square error (RMSE). The result shows that log-logistic model provides the best fit to the foliage clutter.

The rest of this paper is organized as follows. In Section II we discuss the properties and applicability of log-logistic as a statistical model for foliage clutter. The measurement and collection of clutter data we used in this paper are summarized in Section III. Section IV discusses the estimation of model parameters and the goodness-of-fit. section V analyzes the performance of radar detection at presence of foliage clutter. Finally, section VI concludes this paper and describes some future work.

II. Log-logistic Model

Log-logistic has been applied recently in hydrological analysis. In spite of its intensive application in precipitation and stream-flow data, the log-logistic distribution (LLD) [7] statistical model, to the best of our knowledge, has never been applied to radar foliage clutter. The motivation for considering log-logistic model is based on its higher kurtosis and longer tails, as well as its shape similarity to log-normal and Weibull distributions. Thus it is intended to be employed to estimate how well the model matches our collected foliage clutter statistics.

Here we employ the two-parameter distribution with parameters μ and σ. The PDF for this distribution is given by

$$f(x) = \frac{e^{\frac{\ln x-\mu}{\sigma}}}{\sigma x(1+e^{\frac{\ln x-\mu}{\sigma}})^2}, \quad x>0,\ \sigma>0 \qquad (1)$$

where μ is scale parameter and σ is shape parameter.

III. Experiment Setup and Data Collection

Our work is based on the sense-through-foliage data from Air Force Research Lab [6]. The foliage penetration measurement effort began in August 2005 and continued through December 2005. Working in August through the fall of 2005, the foliage measured included late summer foliage and fall and early winter foliage. Late summer foliage, because of the limited rainfall, involved foliage with decreased water content. Late fall and winter measurements involved largely defoliated but dense forest.

978-1-4244-2075-9/08/$25.00 ©2008 IEEE

Authorized licensed use limited to: University of Texas at Arlington. Downloaded on December 18, 2009 at 14:41 from IEEE Xplore. Restrictions apply.



Fig. 1. This figure shows the lift with the experiment. The antennas are at the far end of the lift from the viewer under the roof that was built to shield the equipment from the elements. This picture was taken in September with the foliage largely still present. The cables coming from the lift are a ground cable to an earth ground and one of 4 tethers used in windy conditions.

The UWB radar-based experiment was constructed on a seven-ton man lift, which had a total lifting capacity of 450 kg. The limit of the lifting capacity was reached during the experiment as essentially the entire measuring apparatus was placed on the lift (as shown in Fig. 1). The principle pieces of equipment secured on the lift are: Barth pulser, Tektronix model 7704 B oscilloscope, dual antenna mounting stand, two antennas, rack system, IBM laptop, HP signal Generator, Custom RF switch and power supply and Weather shield (small hut). Throughout this work, a Barth pulse source (Barth Electronics, Inc. model 732 GL) was used. The pulse generator uses a coaxial reed switch to discharge a charge line for a very fast rise time pulse outputs. The model 732 pulse generator provides pulses of less than 50 picoseconds (ps) rise time, with amplitude from 150 V to greater than 2 KV into any load impedance through a 50 ohm coaxial line. The generator is capable of producing pulses with a minimum width of 750 ps and a maximum of 1 microsecond. This output pulse width is determined by charge line length for rectangular pulses, or by capacitors for 1/e decay pulses.

For the data we used in this paper, each sample is spaced at 50 picoseconds interval, and 16,000 samples were collected for each collection for a total time duration of 0.8 microseconds at a rate of approximately 20 Hz. The Barth pulse source was operated at low amplitude and 10 pulses reflected clutter signal were obtained for each collection at the same site but different time, one example of transmitted pulse and received backscattering are shown in Fig. 2(a) and (b) respectively. To make them clearer to readers, we provide expanded views of received traces from sample 10,000 to 12,000 in (c).

IV. Statistical Analysis of the Foliage Clutter Data

A. Maximum Likelihood Estimation

Using the collected clutter data mentioned above, we apply Maximum Likelihood Estimation (MLE) approach to estimate the parameters of the log-logistic, log-normal, Weibull, and

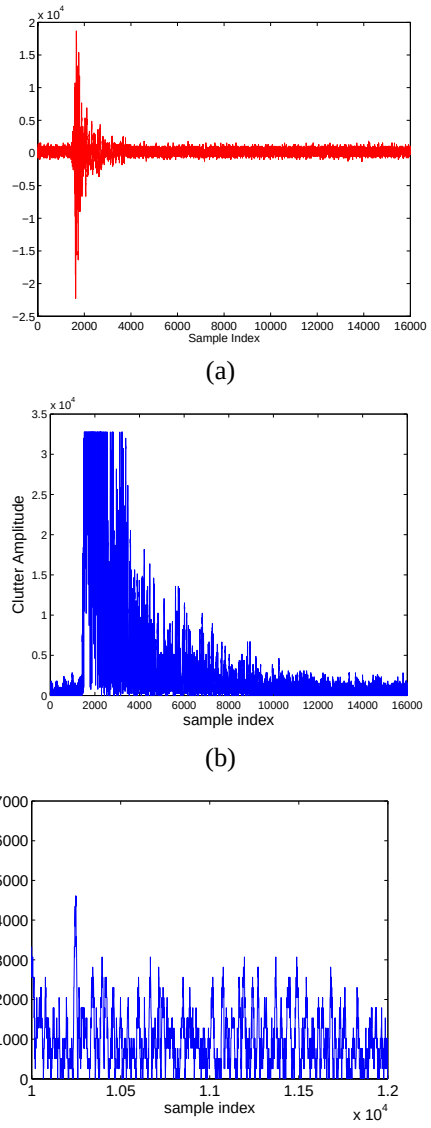


Fig. 2. Clutter data (a)transmitted pulse before antenna amplification (b)received echoes (c) Expanded view from clutter samples 10,000 to 12,000

Nakagami models. MLE is often used when the sample data are known and parameters of the underlying probability distribution are to be estimated [8] [9]. It is generalized as follows:

Let $y_1, y_2, \cdots, y_N$ be N independent samples drawn from a random variable $\mathbf{Y}$ with m parameters $\theta_1, \theta_2, \cdots, \theta_m$, where $\theta_i \in \theta$, then the likelihood function expressed as a function of θ conditional on $\mathbf{Y}$ is

$$L_N(\mathbf{Y}|\theta) = \prod_{k=1}^{N} f_{Y|\theta}(y_k|\theta_1, \theta_2, \cdots, \theta_m) \qquad (2)$$

The maximum likelihood estimate of $\theta_1, \theta_2, \cdots, \theta_m$ is the set of values $\hat{\theta}_1, \hat{\theta}_2, \cdots, \hat{\theta}_m$ that maximize the likelihood function $L_N(\mathbf{Y}|\theta)$.

As the logarithmic function is monotonically increasing, maximizing $L_N(\mathbf{Y}|\theta)$ is equivalent to maximizing

Authorized licensed use limited to: University of Texas at Arlington. Downloaded on December 18, 2009 at 14:41 from IEEE Xplore. Restrictions apply.

$\ln(L_N(\mathbf{Y}|\theta))$. Hence, it can be shown that a necessary but not sufficient condition to obtain the ML estimate $\hat{\theta}$ is to solve the likelihood equation

$$\frac{\partial}{\partial\theta}\ln(L_N(\mathbf{Y}|\theta)) = 0 \tag{3}$$

Using the collected clutter radar mentioned above, we apply MLE to obtain $\hat{\mu}$ and $\hat{\sigma}$ for log-logistic, $\hat{\mu}$ and $\hat{\sigma}$ for the log-normal, $\hat{a}$ and $\hat{b}$ for the Weibull, and $\hat{\mu}$ and $\hat{\omega}$ for the Nakagami. The results are shown in Table I. We also explore the standard deviation (STD) error of each parameter. These descriptions are shown in table I in the form of ε_x, where x denotes different parameter for each model. As there are 10 data sets for poor clutter signal, we also calculate the average values of estimated parameters and their STD error.

From Table II, we can see STD error for log-logistic and log-normal parameters are less than 0.02 and their estimated parameters vary little from data to data compared to Weibull and Nakagami. It is obvious that log-logistic model provides the smallest STD error and Nakagami the largest. Therefore, in the view of statistics, log-logistic model fits the collected data best compared to log-normal, Weibull, and Nakagami.

B. Goodness-of-fit in curve and RMSE

We may also observe the extend to which the PDF curve of the statistic model matches that of clutter data by calculating the root mean square error (RMSE). Let i (i=$1, 2, \cdots, n$) be the sample index of clutter amplitude, c_i is the corresponding PDF value whereas $\hat{c}_i$ is the PDF value of the statistical model with estimated parameters by means of MSE. The RMSE is obtained through following equation:

$$\mathsf{RMSE} = \sqrt{\frac{1}{n}\sum_{i=1}^{n}(c_i - \hat{c}_i)^2} \tag{4}$$

Here we apply n=101 for each model.

The goodness-of-fit in curve and the RMSE of each model are illustrated in Fig. 3. The PDF of absolute amplitude of one-time poor data is presented by means of histogram bars. In Fig. 3, it can be seen obviously that log-logistic model with MLE parameters provides the best goodness-of-fit compared to the other models, since it provides the most suitable kurtosis, slope and tail. As for the maximum PDF value, the log-logistic is about 1×10^{-3}, while that of other models are over 1.2×10^{-3}. For the slope part, which connects the kurtosis and the tail and which is in the range from 0.1×10^4 to 0.5×10^4 in view of x axes, the log-logistic provides the smallest skewness whereas Nakagami provides the largest. Examination of the tails show that log-logistic and log-normal provide very close-valued tails, while tails of the Weibull and the Nakagami are lager than the collected data. Meanwhile, we obtain that $\mathsf{RMSE}_{log-logistic} = 2.5425 \times 10^{-5}$, $\mathsf{RMSE}_{log-normal} = 3.2704 \times 10^{-5}$, $\mathsf{RMSE}_{weibull} = 3.7234 \times 10^{-5}$, $\mathsf{RMSE}_{nakagami} = 5.4326 \times 10^{-5}$. This shows that the log-logistic model is more accurate than the other three models.

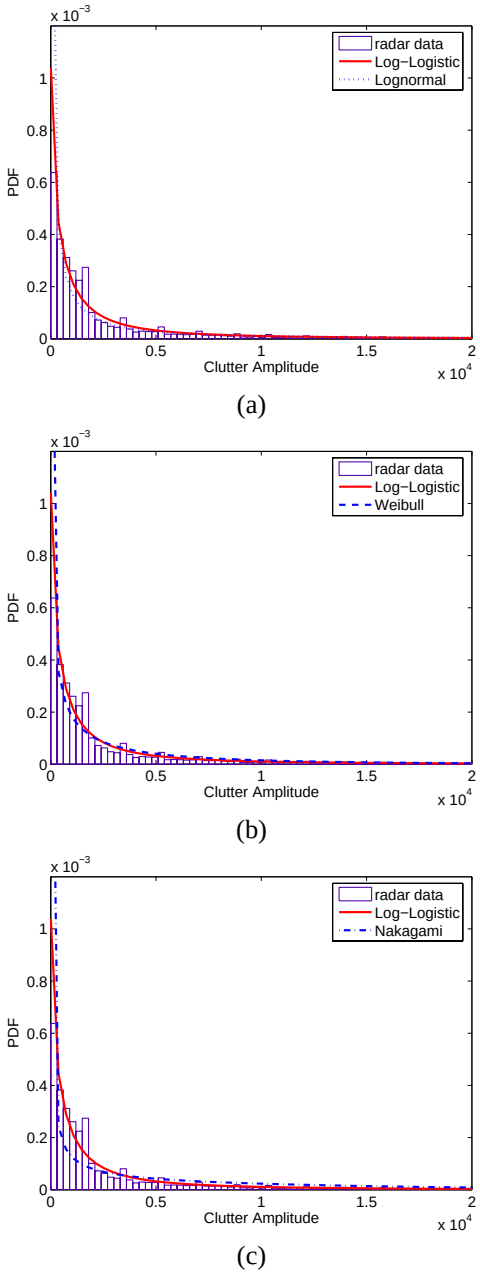


Fig. 3. Clutter model comparison (a) log-logistic vs. log-normal, and (b) log-logistic vs. weibull (c) log-logistic vs. nakagami. $\mathsf{RMSE}_{log-logistic} = 2.5425 \times 10^{-5}$, $\mathsf{RMSE}_{log-normal} = 3.2704 \times 10^{-5}$, $\mathsf{RMSE}_{weibull} = 3.7234 \times 10^{-5}$, $\mathsf{RMSE}_{nakagami} = 5.4326 \times 10^{-5}$.

V. Target Detection Performance

One of the primary goal to be carried out by a radar is target detection. On a basis of the clutter model that have been just studied, we may apply a special case of the Bayesian criterion named Neyman-Person criterion to analyze the target detection performance in the foliage environment.

If the received sample signal to be tested is R, then the two

Authorized licensed use limited to: University of Texas at Arlington. Downloaded on December 18, 2009 at 14:41 from IEEE Xplore. Restrictions apply.

hypotheses are shown as follows:

$$\begin{aligned} H_0 &: R = C + n \\ H_1 &: R = S + C + n \end{aligned} \tag{5}$$

where C and n represent the random variable of clutter and noise respectively. C follows log-logistic model with both parameters μ and σ, and n is gaussian noise with zero mean and variance ν^2. S is the target signal, which assumes to be a constant for simplicity.

Therefore $f(R|H_0)$ means PDF of R given that a target was not present while $f(R|H_1)$ means PDF of R given that a target was present.

They can be denoted as follows:

$$f(R|H_0) = \int_0^\infty \frac{e^{\frac{lnr-\mu}{\sigma}}}{\sigma r(1+e^{\frac{lnr-\mu}{\sigma}})^2} \times \frac{1}{\sqrt{2\pi}\nu} e^{-\frac{(R-r)^2}{2\nu^2}} dr \tag{6}$$

$$f(R|H_1) = \int_0^\infty \frac{e^{\frac{ln(r-s)-\mu}{\sigma}}}{\sigma(r-s)(1+e^{\frac{ln(r-s)-\mu}{\sigma}})^2} \times \frac{1}{\sqrt{2\pi}\nu} e^{-\frac{(R-s-r)^2}{2\nu^2}} dr \tag{7}$$

If the probability that a target was not present is $P(H_0)$ whereas that of a target was present is $P(H_1)$, then PDF of R is

$$f(R) = P(H_0)f(R|H_0) + P(H_1)f(R|H_1) \tag{8}$$

To decide whether there is a target or not, Neyman-Pearson detection rule is shown as

$$\frac{f(R|H_0)}{f(R|H_1)} \underset{H_1}{\overset{H_0}{\gtrless}} \frac{P(H_1)}{P(H_0)} \tag{9}$$

In case of $P(H_1) = P(H_0)$, (26) is simplified as

$$f(R|H_0) \underset{H_1}{\overset{H_0}{\gtrless}} f(R|H_1) \tag{10}$$

which actually is

$$\frac{e^{[\frac{s^2-2s(R-r)}{2\nu^2} + \frac{ln(\frac{r}{r-s})}{\sigma}]}}{\frac{r}{r-s}[\frac{1+e^{\frac{lnr-\mu}{\sigma}}}{1+e^{\frac{ln(r-s)-\mu}{\sigma}}}]^2} \underset{H_1}{\overset{H_0}{\gtrless}} 1 \tag{11}$$

It is easy to obtain the decision threshold T in terms of the above function

$$T = -\frac{\nu^2}{s} ln[\frac{1+e^{\frac{lnr-\mu}{\sigma}}}{1+e^{\frac{ln(r-s)-\mu}{\sigma}}}]^2 + \frac{\nu^2[ln(\frac{r}{r-s}) - \sigma]}{s\sigma} + \frac{s}{2} + r \tag{12}$$

Under hypothesis H_0, a false alarm occurs anytime $R > T$, therefore the probability of false alarm is

$$\begin{aligned} P_{FA} &= \int_T^\infty f(R|H_0)dR \\ &= \frac{\int_T^\infty \int_0^\infty \frac{e^{[-\frac{(R-r)^2}{2\nu^2} + \frac{lnr-\mu}{\sigma}]}}{(1+e^{\frac{lnr-\mu}{\sigma}})^2 r} drdR}{\sqrt{2\pi}\sigma\nu} \end{aligned} \tag{13}$$

Similarly, Under hypothesis H_1, when $R > T$, the target is detectable. Therefore the probability of detection is

$$\begin{aligned} P_D &= \int_T^\infty f(R|H_1)dR \\ &= \frac{\int_T^\infty \int_0^\infty \frac{e^{[-\frac{(R-r-s)^2}{2\nu^2} + \frac{ln(r-s)-\mu}{\sigma}]}}{(1+e^{\frac{ln(r-s)-\mu}{\sigma}})^2 (r-s)} drdR}{\sqrt{2\pi}\sigma\nu} \end{aligned} \tag{14}$$

As mentioned in section IV, $\mu \approx 7.1$ and $\sigma \approx 1.1$ by means of MLE. If $\nu = 1$, then (13) and (14) become

$$P_{FA} = 0.362675 \int_T^\infty \int_0^\infty \frac{e^{-0.5(R-r)^2 + 0.91(lnr-7.1)}}{[1+e^{0.91(lnr-7.1)}]^2 r} drdR \tag{15}$$

$$P_D = 0.362675 \int_T^\infty \int_0^\infty \frac{e^{-0.5(R-r-s)^2 + 0.91[ln(r-s)-7.1]}}{\{1+e^{0.91[ln(r-s)-7.1]}\}^2 (r-s)} drdR \tag{16}$$

VI. Conclusion

On a basis of foliage clutter data measured by the UWB radar, we show that it is more accurate to describe foliage clutter using log-logistic statistic model rather than log-normal, Weibull, or Nakagami. Future research will investigate the characteristics of target to better achieve the target detection, tracking and imaging.

Acknowledgement

This work was supported in part by Office of Naval Research (ONR) under Grant N00014-07-1-0395, N00014-07-1-1024, and National Science Foundation (NSF) under Grant CNS-0721515.

References

[1] Skolnik, M. I.,*Introduction to Radar Systems*, 3rd ed, New York, McGraw Hill, 2001.

[2] Fleischman, J. G., Ayasli, S., Adams, E. M., and Gosselin, D. R., Foliage penetration experiment: Part I: Foliage attenuation and backscatter analysis of SAR imagery, *IEEE Trans. on Aerosp. Electron. Syst.*, 32, 1, part 1 of 3 (1996), 134-144.

[3] Mccorkle, J. W., "Early results from the ARL UWB Foliage attenuation (FOPEN) SAR", Presented at the SPIE International Symposium on Optical Engineering and Photonics in Aerospace and Remote Sensing, Conference 1942, Underground and Obscured Object Detection, Apr. 1993.

[4] Sheen, D. R., Malinas, N. P., Kletzli, D. W., Lewis, T. B., and Roman, J. F., "Foliage transmission meassurement using a ground-based ultra-wideband (UWB) (300-1300MHz) SAR system", *IEEE Trans. on Geoscience and Remote Sensing*, 32, 1(1994).

[5] Watts, S., "Radar detection prediction in K-distribution sea clutter and thermal noise", *IEEE Trans. on Aerosp. Electron. Syst.*, AES-23, 1, 1987, pp. 40-45.

[6] Dill, C., "Foliage Penetration (Phase II) Field Test: Narrowband versus Wideband Foliage Penetration," Final Report of Contract Number F41624-03-D-7001/04, July 2005 to Feb 2006.

[7] Gupta, R. C., Akman, O. and Lvin, S., "A Study of Log-Logistic Model in Survival Analysis", *Biometrical Journal*, 41, pp. 431-443, 1999

[8] Devore, Probability and Statistics for Engineering and the Sciences. Monterey, CA: BrooksiCole, 1982.

[9] Barkat, M., Signal deteciton and estimation, 2nd, London: Artech house, 2005.

Authorized licensed use limited to: University of Texas at Arlington. Downloaded on December 18, 2009 at 14:41 from IEEE Xplore. Restrictions apply.

TABLE I

ESTIMATED PARAMETERS AND STD ERROR

PDF	Log-Logistic	Log-normal	Weibull	Nakagami
data 1	$\hat{\mu} = 7.24161$ $\hat{\sigma} = 1.06483$ $\varepsilon_\mu = 0.0141212$ $\varepsilon_\sigma = 0.00724181$	$\hat{\mu} = 7.0455$ $\hat{\sigma} = 2.20761$ $\varepsilon_\mu = 0.0174527$ $\varepsilon_\sigma = 0.0123415$	$\hat{a} = 2975.33$ $\hat{b} = 0.594979$ $\varepsilon_a = 41.6157$ $\varepsilon_b = 0.00356925$	$\hat{\mu} = 0.177062$ $\hat{\omega} = 9.09663e+007$ $\varepsilon_\mu = 0.00150615$ $\varepsilon_\omega = 1.70907e+006$
data 2	$\hat{\mu} = 6.9716$ $\hat{\sigma} = 1.2126$ $\varepsilon_\mu = 0.014747$ $\varepsilon_\sigma = 0.00773723$	$\hat{\mu} = 6.72573$ $\hat{\sigma} = 2.33617$ $\varepsilon_\mu = 0.0184691$ $\varepsilon_\sigma = 0.0130602$	$\hat{a} = 2285.13$ $\hat{b} = 0.563747$ $\varepsilon_a = 33.7127$ $\varepsilon_b = 0.00337485$	$\hat{\mu} = 0.162375$ $\hat{\omega} = 7.4776e+007$ $\varepsilon_\mu = 0.00137422$ $\varepsilon_\omega = 1.46679e+006$
data 3	$\hat{\mu} = 7.00554$ $\hat{\sigma} = 1.10741$ $\varepsilon_\mu = 0.0145728$ $\varepsilon_\sigma = 0.0076303$	$\hat{\mu} = 6.76262$ $\hat{\sigma} = 2.31258$ $\varepsilon_\mu = 0.0182825$ $\varepsilon_\sigma = 0.0129283$	$\hat{a} = 2341.52$ $\hat{b} = 0.57073$ $\varepsilon_a = 34.1207$ $\varepsilon_b = 0.00341448$	$\hat{\mu} = 0.164695$ $\hat{\omega} = 7.46366e+007$ $\varepsilon_\mu = 0.001395$ $\varepsilon_\omega = 1.45459e+006$
data 4	$\hat{\mu} = 7.03055$ $\hat{\sigma} = 1.07858$ $\varepsilon_\mu = 0.0142027$ $\varepsilon_\sigma = 0.00741556$	$\hat{\mu} = 6.80711$ $\hat{\sigma} = 2.25973$ $\varepsilon_\mu = 0.0178647$ $\varepsilon_\sigma = 0.0126329$	$\hat{a} = 2395.85$ $\hat{b} = 0.579381$ $\varepsilon_a = 34.4066$ $\varepsilon_b = 0.00345156$	$\hat{\mu} = 0.167391$ $\hat{\omega} = 7.4926e+007$ $\varepsilon_\mu = 0.0014916$ $\varepsilon_\omega = 1.44727e+006$
data 5	$\hat{\mu} = 7.16226$ $\hat{\sigma} = 1.10132$ $\varepsilon_\mu = 0.014605$ $\varepsilon_\sigma = 0.00750067$	$\hat{\mu} = 6.95712$ $\hat{\sigma} = 2.26592$ $\varepsilon_\mu = 0.0179137$ $\varepsilon_\sigma = 0.0126675$	$\hat{a} = 2806.76$ $\hat{b} = 0.577823$ $\varepsilon_a = 40.4226$ $\varepsilon_b = 0.00347389$	$\hat{\mu} = 0.17112$ $\hat{\omega} = 9.03298e+007$ $\varepsilon_\mu = 0.00145265$ $\varepsilon_\omega = 1.72749e+006$
data 6	$\hat{\mu} = 7.01527$ $\hat{\sigma} = 1.10123$ $\varepsilon_\mu = 0.0144902$ $\varepsilon_\sigma = 0.00758568$	$\hat{\mu} = 6.77515$ $\hat{\sigma} = 2.30286$ $\varepsilon_\mu = 0.0182057$ $\varepsilon_\sigma = 0.012874$	$\hat{a} = 2360.33$ $\hat{b} = 0.572749$ $\varepsilon_a = 34.2753$ $\varepsilon_b = 0.00342376$	$\hat{\mu} = 0.165292$ $\hat{\omega} = 7.50824e+007$ $\varepsilon_\mu = 0.00140035$ $\varepsilon_\omega = 1.46145e+006$
data 7	$\hat{\mu} = 7.14523$ $\hat{\sigma} = 1.09486$ $\varepsilon_\mu = 0.0145132$ $\varepsilon_\sigma = 0.00745994$	$\hat{\mu} = 6.94201$ $\hat{\sigma} = 2.25621$ $\varepsilon_\mu = 0.0178369$ $\varepsilon_\sigma = 0.0126132$	$\hat{a} = 2753.69$ $\hat{b} = 0.578948$ $\varepsilon_a = 39.585$ $\varepsilon_b = 0.00347442$	$\hat{\mu} = 0.170964$ $\hat{\omega} = 8.80474e+007$ $\varepsilon_\mu = 0.00145125$ $\varepsilon_\omega = 1.68382e+006$
data 8	$\hat{\mu} = 6.95411$ $\hat{\sigma} = 1.11486$ $\varepsilon_\mu = 0.0146774$ $\varepsilon_\sigma = 0.00768003$	$\hat{\mu} = 6.71591$ $\hat{\sigma} = 2.31898$ $\varepsilon_\mu = 0.0183331$ $\varepsilon_\sigma = 0.0129641$	$\hat{a} = 2250.66$ $\hat{b} = 0.564989$ $\varepsilon_a = 33.1387$ $\varepsilon_b = 0.0033763$	$\hat{\mu} = 0.162448$ $\hat{\omega} = 7.31436e+007$ $\varepsilon_\mu = 0.00137488$ $\varepsilon_\omega = 1.4338e+006$
data 9	$\hat{\mu} = 7.18561$ $\hat{\sigma} = 1.09854$ $\varepsilon_\mu = 0.0145483$ $\varepsilon_\sigma = 0.00749265$	$\hat{\mu} = 6.9715$ $\hat{\sigma} = 2.27088$ $\varepsilon_\mu = 0.0179529$ $\varepsilon_\sigma = 0.0126952$	$\hat{a} = 2840.72$ $\hat{b} = 0.581219$ $\varepsilon_a = 40.6593$ $\varepsilon_b = 0.0034984$	$\hat{\mu} = 0.172324$ $\hat{\omega} = 8.97304e+007$ $\varepsilon_\mu = 0.00146348$ $\varepsilon_\omega = 1.70923e+006$
data 10	$\hat{\mu} = 7.192$ $\hat{\sigma} = 1.0866$ $\varepsilon_\mu = 0.0144166$ $\varepsilon_\sigma = 0.0073916$	$\hat{\mu} = 6.99196$ $\hat{\sigma} = 2.23975$ $\varepsilon_\mu = 0.0177067$ $\varepsilon_\sigma = 0.0125211$	$\hat{a} = 2869.65$ $\hat{b} = 0.584803$ $\varepsilon_a = 40.837$ $\varepsilon_b = 0.00351294$	$\hat{\mu} = 0.173572$ $\hat{\omega} = 9.01631e+007$ $\varepsilon_\mu = 0.0014747$ $\varepsilon_\omega = 1.71142e+006$

TABLE II

AVERAGED ESTIMATED PARAMETERS

PDF	Log-Logistic	Log-normal	Weibull	Nakagami
average	$\hat{\mu} = 7.0904$ $\hat{\sigma} = 1.1061$ $\varepsilon_\mu = 0.0145$ $\varepsilon_\sigma = 0.0075$	$\hat{\mu} = 6.8695$ $\hat{\sigma} = 2.2771$ $\varepsilon_\mu = 0.0180$ $\varepsilon_\sigma = 0.0127$	$\hat{a} = 2588$ $\hat{b} = 0.5769$ $\varepsilon_a = 37.4316$ $\varepsilon_b = 0.0035$	$\hat{\mu} = 0.1687$ $\hat{\omega} = 8.218e+007$ $\varepsilon_\mu = 0.0014$ $\varepsilon_\omega = 1.4905e+006$

Authorized licensed use limited to: University of Texas at Arlington. Downloaded on December 18, 2009 at 14:41 from IEEE Xplore. Restrictions apply.

Channel Selection Algorithms in Virtual MIMO Sensor Networks

Jing Liang
University of Texas at Arlington
jliang@wcn.uta.edu

Qilian Liang
University of Texas at Arlington
liang@uta.edu

ABSTRACT

In this paper, we present two practical algorithms to select a subset of channels in virtual MIMO wireless sensor networks (WSN). One is the Singular-Value Decomposition-QR with Threshold (SVD-QR-T) approach that selects the best subset of transmitters while keeping all receivers active. The threshold is adaptive by means of Fuzzy C-Mean (FCM). The other is the Maximum Spanning Tree Searching (MASTS) algorithm on a basis of graph theory in respect of cross-layer design, which potentially provides a path connecting all sensors that benefits routing and QoS of networks. The MASTS algorithm keeps all sensors active but selects $M_t + M_r - 1$ subchannels, where M_t and M_r are the number of transmitters and receivers, respectively. These two approaches are compared against the case without channel selection in terms of capacity, bit error rate (BER), and multiplexing gain in the presence of water-filling as well as the circumstance of without water-filling under the same total transmission power constraint. Despite less multiplexing gain, when water-filling is applied, MASTS achieves higher capacity and lower BER than that of virtual MIMO without channel selection at moderate to high SNR while SVD-QR-T FCM provides the lowest BER at high SNR; in case of no water-filling and equal transmission power allocation, MASTS still offers the highest capacity at moderate to high SNR but SVD-QR-T FCM achieves the lowest BER. Both algorithms provide satisfying performances with reduced cost and resources compared to the case without channel selection.

Categories and Subject Descriptors

D.2.8 [**Software Engineering**]: Metrics—*performance measures*

General Terms

Algorithms

Permission to make digital or hard copies of all or part of this work for personal or classroom use is granted without fee provided that copies are not made or distributed for profit or commercial advantage and that copies bear this notice and the full citation on the first page. To copy otherwise, to republish, to post on servers or to redistribute to lists, requires prior specific permission and/or a fee.
HeterSANET'08, May 30, 2008, Hong Kong SAR, China.
Copyright 2008 ACM 978-1-60558-113-2/08/05 ...$5.00.

1. INTRODUCTION AND MOTIVATION

1.1 Channel selection in virtual MIMO

Virtual multiple-input-multiple-output (MIMO) has been studied intensively in recent years in order to improve the energy-efficiency in wireless sensor networks (WSN) [1][2][3]. Constrained by its physical size and limited battery, an individual sensor is allowed to contain only one antenna. Numerical results show that if these individual sensors jointly form a MIMO system, tremendous energy will be saved while satisfying the required performance. However, a natural drawback of the virtual MIMO is the increased complexity and the cost of multiple radio frequency (RF) chains. One technique to reduce the complexity and cost while providing similar capacity and performance is channel selection.

The knowledge of channels can be obtained by various channel estimation techniques such as the reciprocity principle and feedback channel [4]. When channel side information (CSI) is known to transmitters or receivers, antenna selection can be applied through subset selection algorithms by switches either at transmitters or receivers, or jointly working at both ends. Therefore the best set of channels are selected to be active while remaining ones are not employed. These switches typically cost much less than RF chains so that low-cost and low-complexity can be achieved with the benefits of multiple antennas [5] [6]. This system is illustrated in Fig. 1.

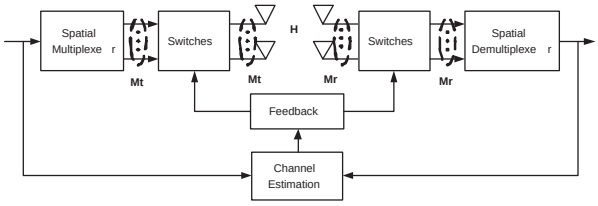


Figure 1: System diagram for virtual MIMO channel selection

Recent years have seen an explosion of interest in MIMO antenna selection and various criteria have been used:

1. Capacity Maximization: In the previous work of [7], channel capacity is used as the optimality criterion, i.e., antennas that achieve the largest capacity are active. [7] demonstrated that in case of no CSI at transmitters (CSIT) but receivers (CSIR), similar capacity to that of the MIMO system can be achieved as far

as the number of selected receivers is no less than the number of transmitters.

2. Minimum Error Rate: Apart from maximization of capacity based on Shannon theory, [8] derived another criteria from the respect of minimum error rate when coherent receivers, either maximum likelihood (ML), zero-forcing (ZF), or the minimum mean-square error (MMSE) linear receiver is employed.

3. SNR Maximization: In [9], antenna selection is performed only at the receiver on a basis of largest instantaneous SNR using space-time coding. It is analytically shown that full diversity advantage promised by MIMO can be fully exploited using this criteria as long as the space-time code employed has full spatial diversity.

4. Cross-layer Optimal Scheduling: Besides physical layer, some related works have adopted graph theory approach to consider cross-layer design. [10] performed the optimal antenna assignment for spatial multiplexing by Hungarian algorithm using weighted bipartite matching graph, and [11] took into account users' QoS requirement with clique-searching algorithm for antenna selection.

Although there have been dazzling mathematical studies on antenna selection criteria, practical algorithms of joint transmit and receive antenna selection, i.e., *channel selection* is still open and the problem of corresponding performance analysis requires more investigations.

1.2 Contributions and Organization of Paper

In this paper, under the assumption of the quasi-static Rayleigh fading, we propose two practical algorithms to perform channel selection. One is the singular-value decomposition-QR with threshold (SVD-QR-T) employing Fuzzy C-Mean (FCM) to virtually provide adaptive threshold ; the other approach is the Maximum Spanning Tree Searching (MASTS) algorithm on a basis of Kruskal's theory [12] in respect of graph theory, which potentially offers route connectivity of all sensors for network layer. The former is pure physical layer design, which selects rt (see Section 3) best subset of transmitters while keeping all receivers active. The latter is a cross-layer method, which selects $M_t + Mr - 1$ subsets of channels while keeping all transmitters and receivers active. Examples are presented to illustrate each step. Their performances are estimated in terms of capacity, BER, and multiplexing gain by means of Monte Carlo simulations, which is an efficient approach to illustrate the tendency of practical results. In general, it is shown that in spite of less multiplexing gain, when water-filling is applied, MASTS achieves higher capacity and lower BER than virtual MIMO without channel selection at moderate to high SNR while SVD-QR-T FCM provides the lowest BER at high SNR; in case of no water-filling and equal transmission power allocation, MASTS still offers the highest capacity at moderate to high SNR but SVD-QR-T FCM achieves the lowest BER. Both algorithms provide satisfying performances with reduced cost and resource compared to the case without channel selection .

We organize the remainder of this paper as follows. In Section 2, we introduce the virtual MIMO channel model in respect of matrix as well as graph theory. Section 3 and 4 propose SVD-QR-T FCM and MASTS algorithms respectively. Section 5 compares the performance of these two algorithms with virtual MIMO and Section 6 draws the conclusion and presents future work.

2. CHANNEL MODEL

Virtual MIMO channel model with M_t transmitters and M_r receivers (M_t+M_r sensors) is illustrated in Fig. 2, where each receiver observes a superposition of the M_t transmitted signals corrupted by the Rayleigh flat fading and additive white gaussian noise. Each h_{ij}, $i = 1, 2, \cdots, M_r$ and $j = 1, 2, \cdots, M_t$ represents the channel gain from transmitter j to receiver i [13], which is assumed to be Rayleigh independent and identically distributed (i.i.d.). The additive noise also has i.i.d entries $n_j \sim \mathcal{CN}(0, \sigma^2)$.

We may denote this virtual MIMO channel graph with a discrete time model:

$$\begin{bmatrix} Y_1 \\ Y_2 \\ \vdots \\ Y_{Mr} \end{bmatrix} = \begin{bmatrix} h_{11} & h_{12} \cdots h_{1Mt} \\ h_{21} & h_{22} \cdots h_{2Mt} \\ \vdots & \vdots \\ h_{Mr1} & h_{Mr2} \cdots h_{MrMt} \end{bmatrix} \begin{bmatrix} X_1 \\ X_2 \\ \vdots \\ X_{Mt} \end{bmatrix} + \begin{bmatrix} n_1 \\ n_2 \\ \vdots \\ n_{Mr} \end{bmatrix} \quad (1)$$

The above equation can be simplified as $\mathbf{Y} = \mathbf{HX} + \mathbf{n}$, where $\mathbf{H}$ is a $Mr \times Mt$ independent Rayleigh random matrix and $\mathbf{n}$ denotes the random noise.

From the respect of graph theory, Fig. 2 is a connected graph [14], i.e., there is a path connecting any two sensors with antennas and channels making up vertex set and edge set respectively. h_{ij} denotes its edge weight. This gives rise to the graph theoretical approach on virtual MIMO study. However, integration of graph theory into wireless communication systems is still neonatal and deserves much more attention and development.

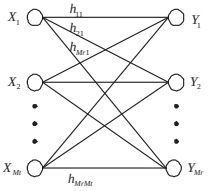


Figure 2: Graphic channel model for virtual MIMO

3. SINGULAR-VALUE DECOMPOSITION-QR WITH THRESHOLD (SVD-QR-T)

3.1 SVD-QR-T in channel selection

SVD has been applied to MIMO channel decomposition in [13], [15], and sensor node selection in [16]. However, these studies are theoretical analysis only and no algorithm has been proposed about which channels will be physically selected in practice.

We propose SVD-QR-T as follows:

1. Given the channel gain matrix $\mathbf{H} \in R^{Mr \times Mt}$ and $r = rank(\mathbf{H}) \leq \min(Mt, Mr)$, determine a numerical estimate rt of the rank r by calculating the singular value decomposition

$$\mathbf{H} = \mathbf{U}\Sigma\mathbf{V}^T, \tag{2}$$

where $\mathbf{U}$ is an $Mr \times Mr$ matrix of orthonormalized eigenvectors of $\mathbf{H}\mathbf{H}^T$, $\mathbf{V}$ is an $Mt \times Mt$ matrix of orthonormalized eigenvectors of $\mathbf{H}^T\mathbf{H}$, and Σ is the diagonal matrix $\Sigma = diag(\sigma_1, \sigma_2, \ldots, \sigma_i, \ldots, \sigma_r)$, where $\sigma_i = \sqrt{\lambda_i}$. λ_i is the ith eigenvalue of $\mathbf{H}\mathbf{H}^T$ while σ_i is the singular value of $\mathbf{H}$ and $\sigma_1 \geq \sigma_2 \geq \cdots \geq \sigma_r > 0$. In many practical cases, σ_1, σ_1, $\cdots$, σ_{rt} are much larger than $\sigma_{rt+1}, \cdots, \sigma_r$; thus we may set threshold to pick up valuable $\sigma_i, i = 1, 2, \cdots, \sigma_{rt}$ and discard those trivial singular values in order to save resource but maintain satisfying performance. Sometimes rt can be much smaller than the rank r, e.g., even 1. In this paper, we propose to use fuzzy c-means (FCM) to determine rt. Details will be discussed in section 3.2.

2. Partition

$$\mathbf{V} = \begin{matrix} \mathbf{V}_{11} & \mathbf{V}_{12} \\ \mathbf{V}_{21} & \mathbf{V}_{22} \end{matrix} \tag{3}$$

where $\mathbf{V}_{11} \in R^{rt \times rt}$, $\mathbf{V}_{12} \in R^{rt \times (Mt-rt)}$, $\mathbf{V}_{21} \in R^{(Mt-rt) \times rt}$, and $\mathbf{V}_{22} \in R^{(Mt-rt) \times (Mt-rt)}$.

3. Using QR decomposition with column pivoting, determine $\mathbf{E}$ such that

$$[\mathbf{V}_{11}^T, \mathbf{V}_{21}^T]\mathbf{E} = \mathbf{Q}\mathbf{R}, \tag{4}$$

where $\mathbf{Q}$ is a unitary matrix, and $\mathbf{R} \in R^{rt \times Mt}$ forms an upper triangular matrix with decreasing diagonal elements; and $\mathbf{E}$ is the permutation matrix. The positions of 1 in the first rt columns of $\mathbf{E}$ correspond to the rt ordered *most-significant* transmitters.

3.2 Fuzzy C-Means – Unsupervised Clustering for Adaptive Threshold

In order to keep the balance between performances and cost, we propose FCM clustering approach to divide singular values $(\sigma_1, \sigma_2, \ldots, \sigma_r)$ into two clusters, and thus provides virtual adaptive threshold, so the cluster with higher center would remain for active channels.

FCM clustering is a data clustering technique where each data point belongs to a cluster to certain degree specified by a membership grade. This technique was originally introduced by Bezdek [17] as an improvement on earlier clustering methods. Here we briefly summarize it.

Definition 1 (Fuzzy c-Partition). *Let $\mathbf{X} = x_1, x_2, \cdots, x_n$ be any finite set, $\mathbf{V}_{cn}$ be the set of real $c \times n$ matrices, and c be an integer, where $2 \leq c < n$. The* Fuzzy c-partition space *for $\mathbf{X}$ is the set*

$$M_{fc} = U \in V_{cn} | u_{ik} \in [0, 1] \ \forall i, k; \tag{5}$$

where $\sum_{i=1}^{c} u_{ik} = 1 \ \forall k$ and $0 < \sum_{k=1}^{n} u_{ik} < n \ \forall i$. The row i of matrix $U \in M_{fc}$ contains values of the ith membership function, u_i, in the fuzzy c-partition U of $\mathbf{X}$.

Definition 2 (Fuzzy c-Means Functionals). *[17] Let $J_m : M_{fc} \times \mathcal{R}^{cp} \rightarrow \mathcal{R}^+$ be*

$$J_m(\mathbf{U}, \mathbf{v}) = \sum_{k=1}^{n} \sum_{i=1}^{c} (u_{ik})^m (d_{ik})^2 \tag{6}$$

where $\mathbf{U} \in M_{fc}$ is a fuzzy c-partition of X; $\mathbf{v} = (\mathbf{v}_1, \mathbf{v}_2, \cdots, \mathbf{v}_c) \in \mathcal{R}^{cp}$, where $\mathbf{v}_i \in \mathcal{R}^p$, is the cluster center of prototype u_i, $1 \leq i \leq c$;

$$(d_{ik})^2 = ||\mathbf{x}_k - \mathbf{v}_i||^2 \tag{7}$$

where $||\cdot||$ is any inner product induced norm on $\mathcal{R}^p$; weighting exponential $m \in [1, \infty)$; and, u_{ik} is the membership of $\mathbf{x}_k$ in fuzzy cluster u_i. $J_m(\mathbf{U}, \mathbf{v})$ represents the distance from any given data point to a cluster weighted by that point's membership grade.

The solutions of

$$\min_{\mathbf{U} \in M_{fc}, \mathbf{v} \in \mathcal{R}^{cp}} J_m(\mathbf{U}, \mathbf{v}) \tag{8}$$

are least-squared error stationary points of J_m. An infinite family of fuzzy clustering algorithms — one for each $m \in (1, \infty)$ — is obtained using the necessary conditions for solutions of (8), as summarized in the following:

Theorem 1. *[17] Assume $||\cdot||$ to be an inner product induced norm: fix $m \in (1, \infty)$, let $\mathbf{X}$ have at least $c < n$ distinct points, and define the sets ($\forall k$)*

$$I_k = \{i | 1 \leq i \leq c; d_{ik} = ||\mathbf{x}_k - \mathbf{v}_i|| = 0\} \tag{9}$$

$$\tilde{I}_k = \{1, 2, \cdots, c\} - I_k \tag{10}$$

Then $(\mathbf{U}, \mathbf{v}) \in M_{fc} \times \mathcal{R}^{cp}$ is globally minimal for J_m only if (ϕ denotes an empty set)

$$I_k = \phi \Rightarrow u_{ik} = 1 \Big/ [\sum_{j=1}^{c} (\frac{d_{ik}}{d_{jk}})^{2/(m-1)}] \tag{11}$$

or

$$I_k \neq \phi \Rightarrow u_{ik} = 0 \ \forall i \in \tilde{I}_k \text{ and } \sum_{i \in I_k} u_{ik} = 1, \tag{12}$$

and

$$\mathbf{v}_i = \sum_{k=1}^{n} (u_{ik})^m \mathbf{x}_k \Big/ \sum_{k=1}^{n} (u_{ik})^m \ \forall i \tag{13}$$

Bezdek proposed the following iterative method [17] to minimize $J_m(\mathbf{U}, \mathbf{v})$:

1. Fix c, $2 \leq c < n$; choose any inner product norm metric for $\mathcal{R}^p$; and fix m, $1 \leq m < \infty$. Initialize $\mathbf{U}^{(0)} \in M_{fc}$ (e.g., choose its elements randomly from the values between 0 and 1). Then at step l ($l = 1, 2, \cdots$):

2. Calculate the c fuzzy cluster centers $\mathbf{v}_i^{(l)}$ using (13) and $\mathbf{U}^{(l)}$.

3. Update $\mathbf{U}^{(l)}$ using (11) or (12).

4. Compare $\mathbf{U}^{(l)}$ to $\mathbf{U}^{(l-1)}$ using a convenient matrix norm, i.e., if $||\mathbf{U}^{(l)} - \mathbf{U}^{(l-1)}|| \leq \varepsilon_L$ stop; otherwise, return to step 2.

3.3 An Example of SVD-QR-T with FCM in virtual MIMO channel selection

We use the following example to illustrate the SVD-QR-T with FCM application in MIMO-WSN channel selection.

1. *Step 1.* Assume the estimated channel gain is

$$\mathbf{H} = \begin{bmatrix} 0.6211 & 0.7536 & 0.6595 \\ 0.5602 & 0.6596 & 0.1834 \\ 0.2440 & 0.2141 & 0.6365 \\ 0.8220 & 0.6021 & 0.1703 \\ 0.2632 & 0.6049 & 0.5396 \end{bmatrix}$$

By matrix computation, we get:

$$\mathbf{V} = \begin{bmatrix} -0.5856 & -0.5075 & -0.6321 \\ -0.6574 & -0.1589 & 0.7366 \\ -0.4743 & 0.8469 & -0.2406 \end{bmatrix}$$

$diag(\Sigma) = (2.0017, 0.6347, 0.2572)$. Use FCM to divide $diag(\Sigma)$ into 2 clusters, we get

$$\mathbf{v} = \begin{matrix} 2.0010 \\ 0.4445 \end{matrix}$$

$$\mathbf{U} = \begin{matrix} 1.0000 & 0.0190 & 0.0114 \\ 0.0000 & 0.9810 & 0.9886 \end{matrix}$$

The entry 1.0000 at $\mathbf{U}$ means that the membership degree of 2.0017 belonging to the cluster with center 2.0010 is 1.0000. Therefore, the cluster with higher center is composed of only 2.0017, then 2.0017 is chosen and $rt = 1$.

2. *Step 2.* Obtain $\mathbf{V}_{11}$ and $\mathbf{V}_{21}$ from $\mathbf{V}$:

$$\mathbf{V}_{11} = -0.5856$$

$$\mathbf{V}_{21} = \begin{matrix} -0.6574 \\ -0.4743 \end{matrix}$$

Based on $[\mathbf{V}_{11}^T \mathbf{V}_{21}^T]$ get $\mathbf{E}$ by QR:

$$\mathbf{E} = \begin{bmatrix} 0 & 1 & 0 \\ 1 & 0 & 0 \\ 0 & 0 & 1 \end{bmatrix}$$

As $rt = 1$, choose the first column of $\mathbf{E}$

$$\mathbf{E}(:, rt) = \begin{bmatrix} 0 \\ 1 \\ 0 \end{bmatrix}$$

3. *Step 3.* Analyze $\mathbf{E}(:, rt)$, 1 appears on the $2nd$ row, and thus the $2nd$ column of $\mathbf{H}$ is selected to construct $\mathbf{H}_s$, which is:

$$\mathbf{H}_s = \begin{bmatrix} 0 & 0.7536 & 0 \\ 0 & 0.6596 & 0 \\ 0 & 0.2141 & 0 \\ 0 & 0.6021 & 0 \\ 0 & 0.6049 & 0 \end{bmatrix}$$

This implies that the channel to be selected are those that connect the $2nd$ transmitter and all receivers, i.e., transmitter 2 and all the receivers are selected to be active while other transmitters are not employed to save their battery.

As we may see, the row index in which 1 appears in $\mathbf{E}(:, rt)$ particularly determines which transmitters to be selected, so with regard to SVD-QR-T, $rt \times M_r$ channels are selected to be active.

4. THE MAXIMUM SPANNING TREE SEARCHING (MASTS)

4.1 Introduction of MASTS

As mentioned in Section 2, we may use a graph of vertices and edges to represent the virtual MIMO communication scenario. From this aspect, essentially channel selection is to remove some edges while keep those remaining. However, global connectivity is usually required for WSN [18][19]. Spanning tree [14] suggests such an algorithm that in an arbitrary graph, all the vertices are connected with the minimum necessary edges, i.e., there is no isolated vertice under the condition of the least possible edge number. For example, when $Mt = 3$ and $Mr = 5$, some of the possible spanning trees are drawn in Fig. 3.

Note that for an arbitrary graph of n vertices, its spanning tree is of n vertices and $n - 1$ edges [14]. Since there are $Mt + Mr$ vertices, the number of edges to be selected by MASTS algorithm is a fixed $Mt + Mr - 1$, which means MASTS always chooses $Mt + Mr - 1$ channels.

Given Mt and Mr, the ways to construct a spanning tree (not necessarily with maximum sum of weight) is $Mt^{Mr-1} \times Mr^{Mt-1}$. We prove this conclusion by Matrix Tree Theorem [14] as follows:

1. The adjacency matrix of the virtual MIMO graph shown in Fig. 2 is

$$\begin{array}{c} \\ X_1 \\ X_2 \\ \vdots \\ X_{Mt} \\ Y_1 \\ Y_2 \\ \vdots \\ Y_{Mr} \end{array} \begin{array}{c} \begin{array}{cccccccc} X_1 & X_2 & \cdots & X_{Mt} & Y_1 & Y_2 & \cdots & Y_{Mr} \end{array} \\ \begin{bmatrix} 0 & 0 & \cdots & 0 & 1 & 1 & \cdots & 1 \\ 0 & 0 & \cdots & 0 & 1 & 1 & \cdots & 1 \\ \vdots & \vdots & \vdots & \vdots & \vdots & \vdots & \vdots & \vdots \\ 0 & 0 & \cdots & 0 & 1 & 1 & \cdots & 1 \\ 1 & 1 & \cdots & 1 & 0 & 0 & \cdots & 0 \\ 1 & 1 & \cdots & 1 & 0 & 0 & \cdots & 0 \\ \vdots & \vdots & \vdots & \vdots & \vdots & \vdots & \vdots & \vdots \\ 1 & 1 & \cdots & 1 & 0 & 0 & \cdots & 0 \end{bmatrix} \end{array}$$

2. The degree matrix of the above MIMO graph is:

$$\begin{array}{c} \\ X_1 \\ X_2 \\ \vdots \\ X_{Mt} \\ Y_1 \\ Y_2 \\ \vdots \\ Y_{Mr} \end{array} \begin{array}{c} \begin{array}{cccccccc} X_1 & X_2 & \cdots & X_{Mt} & Y_1 & Y_2 & \cdots & Y_{Mr} \end{array} \\ \begin{bmatrix} Mr & 0 & \cdots 0 & 0 & 0 & \cdots & 0 \\ 0 & Mr & \cdots 0 & 0 & 0 & \cdots & 0 \\ \vdots & \vdots & \vdots & \vdots & \vdots & \vdots & \vdots \\ 0 & 0 & \cdots Mr & 0 & 0 & \cdots & 0 \\ 0 & 0 & \cdots 0 & Mt & 0 & \cdots & 0 \\ 0 & 0 & \cdots 0 & 0 & Mt & \cdots & 0 \\ \vdots & \vdots & \vdots & \vdots & \vdots & \vdots & \vdots \\ 0 & 0 & \cdots 0 & 0 & 0 & \cdots & Mt \end{bmatrix} \end{array}$$

3. The degree matrix minus the adjacency matrix, we get

the matrix $\mathbf{D}$ which is:

$$\mathbf{D} = \begin{bmatrix} Mr & 0 & \cdots 0 & -1 & -1 & \cdots & -1 \\ 0 & Mr & \cdots 0 & -1 & -1 & \cdots & -1 \\ \vdots & \vdots & \vdots & \vdots & \vdots & \vdots & \vdots \\ 0 & 0 & \cdots Mr & -1 & -1 & \cdots & -1 \\ -1 & -1 & \cdots -1 & Mt & 0 & \cdots & 0 \\ -1 & -1 & \cdots -1 & 0 & Mt & \cdots & 0 \\ \vdots & \vdots & \vdots & \vdots & \vdots & \vdots & \vdots \\ -1 & -1 & \cdots -1 & 0 & 0 & \cdots & Mt \end{bmatrix} \quad (14)$$

4. Delete both an arbitrary row and an arbitrary column of $\mathbf{D}$ and take the determinant of remaining matrix, the result comes to $Mt^{Mr-1} \times Mr^{Mt-1}$, which is the number of ways to form a spanning tree on a basis of a MIMO graph.

In general, MASTS algorithm is to compute a spanning tree with the maximum sum of weight of edge, i.e., to select the maximum sum of channel gain while realizing the connectivity of all the sensors. Our contributions mainly lie in applying the graph theoretical concept on maximum spanning tree into virtual MIMO channel selection and program the algorithm.

The MASTS algorithm is:

1. *Step 1*: Select 3 edges with the highest weight including their vertices at first.
2. *Step 2*: Enlarge the subgraph by edges with high weight in decreasing manner and make sure no cycles are formed.
3. *Step 3*: Continue *step 2* until the edge number of enlarged subgraph is equal to $Mt + Mr - 1$. This final subgraph is the spanning tree with the maximum sum of weight.

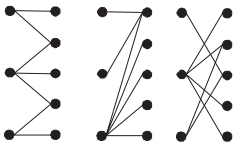


Figure 3: Examples of spanning trees for 3×5 MIMO

4.2 An Example of MASTS in virtual MIMO channel selection

As a virtual MIMO graph contains the same information as that of channel gain matrix $\mathbf{H}$, we illustrate MASTS algorithm by matrix entry selection procedure using Fig. 4 and matrix $\mathbf{H}_b$ $\mathbf{H}_c$ $\mathbf{H}_d$ $\mathbf{H}_e$ $\mathbf{H}_g$.

Fig. 4 (a) is the original virtual MIMO graph. Here we assume $\mathbf{H}$ is the same as that in SVD-QR example. Fig. 4 (b) shows the subgraph with 3 highest weight. These edges are denoted by $\langle\rangle$ in matrix $\mathbf{H}_b$. This is the *step 1*.

$$\mathbf{H}_b = \begin{bmatrix} 0.6211 & \langle 0.7536\rangle & 0.6595 \\ 0.5602 & \langle 0.6596\rangle & 0.1834 \\ 0.2440 & 0.2141 & 0.6365 \\ \langle 0.8220\rangle & 0.6021 & 0.1703 \\ 0.2632 & 0.6049 & 0.5396 \end{bmatrix}$$

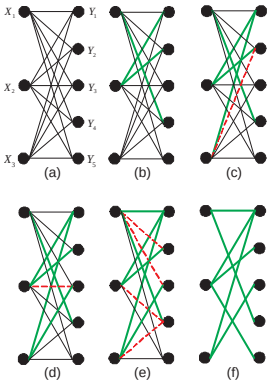


Figure 4: The MASTS algorithm

Note that among the selected 3 entries, 0.8220 has the different row index either with that of 0.7536 or 0.6595, so enlarging this subgraph with any of the remaining edges will absolutely not form a cycle.

Thus, the second step starts with selecting the edge with the fourth highest weight, which is shown in Fig. 4 (c) and Matrix $\mathbf{H}_c$.

$$\mathbf{H}_c = \begin{bmatrix} 0.6211 & \langle 0.7536\rangle & \langle 0.6595\rangle \\ 0.5602 & \langle 0.6596\rangle & 0.1834\times \\ 0.2440 & 0.2141 & 0.6365 \\ \langle 0.8220\rangle & 0.6021 & 0.1703 \\ 0.2632 & 0.6049 & 0.5396 \end{bmatrix}$$

Note that after the selection of entry 0.6595, the entry 0.1834 will no longer be selected, or there is going to form a cycle $X_2Y_1X_3Y_2$, so we note the entry 0.1834 with "$\times$" and use a dash line to represent the unavailability of the corresponding edge in Fig. 4(c). This implies the following criteria:

Criteria *Any four entries with index (i,j) (i,q) (p,j) (p,q), where $i, p \le Mr$, $i \ne p; j, q \le Mt$, $j \ne q$ form a cycle. If any three have been selected, the remaining one should be eliminated.*

Based on this condition, we continually select entries as shown in Fig. 4 (d) (e) (f) and matrix $\mathbf{H}_d$ $\mathbf{H}_e$ $\mathbf{H}_f$. As we only have to select $3 + 5 - 1 = 7$ edges, edges in graph (f) represented by none-zero entries in matrix $\mathbf{H}_g$ are the channels finally selected.

$$\mathbf{H}_d = \begin{bmatrix} 0.6211 & \langle 0.7536\rangle & \langle 0.6595\rangle \\ 0.5602 & \langle 0.6596\rangle & 0 \\ 0.2440 & 0.2141\times & \langle 0.6365\rangle \\ \langle 0.8220\rangle & 0.6021 & 0.1703 \\ 0.2632 & 0.6049 & 0.5396 \end{bmatrix}$$

$$\mathbf{H}_e = \begin{bmatrix} \langle 0.6211\rangle & \langle 0.7536\rangle & \langle 0.6595\rangle \\ 0.5602\times & \langle 0.6596\rangle & 0 \\ 0.2440\times & 0 & \langle 0.6365\rangle \\ \langle 0.8220\rangle & 0.6021\times & 0.1703\times \\ 0.2632 & 0.6049 & 0.5396 \end{bmatrix}$$

$$\mathbf{H}_g = \begin{bmatrix} 0.6211 & 0.7536 & 0.6595 \\ 0 & 0.6596 & 0 \\ 0 & 0 & 0.6365 \\ 0.8220 & 0 & 0 \\ 0 & 0.6049 & 0 \end{bmatrix}$$

It is worth mentioning that $\mathbf{H}_g$ obtained through MASTS is different from $\mathbf{H}_s$ derived by SVD-QR-T.

5. PERFORMANCE ANALYSIS

Due to the randomness of the channel gain matrix, we employ Monte Carlo simulations to analyze the performances of our algorithms in terms of capacity, multiplexing gain and bit error rate (BER). Following steps are applied:

1. Use Jake's Model [20] to randomly generate independent a $M_t \times M_r$ Rayleigh channel model.

2. Follow the SVD-QR-T FCM and MASTS channel selection algorithms respectively to select channels.

3. Obtain eigenvalue λ_{is} and its rank r_s for $\mathbf{H}_s$. Note that λ_{is} is totally different from λ_i of $\mathbf{H}$. Similarly, we can obtain λ_{ig}, r_g for $\mathbf{H}_g$.

4. Here we assume $B = 1Hz$. Through 10,000 times Monte Carlo simulations to obtain capacity, BER for QPSK modulation, and multiplexing gain with and without water-filling.

5.1 Channel Known At the Transmitter: Water-Filling

When both of CSIT and CSIR are known, the water-filling technique can be utilized to optimally allocate power P_i at the independent parallel channel i. The sum of capacities on each of these independent parallel channels is the maximal capacity of the virtual MIMO [13]. This capacity can be expressed as

$$C = \max_{\sum P_i \le P} \sum_{i=1}^{r} B \log_2(1 + \frac{P_i}{\sigma^2}\lambda_i) \qquad (15)$$

where P is the total power constraint for transmitters, r is the rank of $\mathbf{H}$ and λ_i is the eigenvalue of $\mathbf{H}\mathbf{H}^T$. Since the SNR at the ith channel at full power is $SNR_i = \lambda_i P/\sigma^2$, the capacity (15) can also be given in terms of the power allocation P_i as

$$C = \max_{\sum P_i \le P} \sum_{i=1}^{r} B \log_2(1 + \frac{P_i}{P} SNR_i) \qquad (16)$$

where

$$\frac{P_i}{P} = \begin{array}{ll} 1/SNR_0 - 1/SNR_i & SNR_i \ge SNR_0 \\ 0 & SNR_i < SNR_0 \end{array} \qquad (17)$$

for some cutoff value SNR_0. The final capacity is given as

$$C = \sum_{SNR_i \ge SNR_0} B \log_2(\frac{SNR_i}{SNR_0}) \qquad (18)$$

The value of SNR_0 must be found numerically, owning to that there is no existence of closed-form solution for continuous distributions of SNR [21]. This results in Monte Carlo simulations to analyze the capacity performances on SVD-QR-T FCM and MASTS virtual MIMO, which is illustrated in Fig. 5. When SNR is lower than 5dB, SVD-QR-T FCM provides a larger capacity than that of MASTS. However, MASTS grows larger than a virtual MIMO when SNR reaches around 8.5 dB. It clearly shows that MASTS can offer the largest capacity at high SNR, due to the feature on singular value of $\mathbf{H}_g$. We shall illustrate this using following example:

Suppose

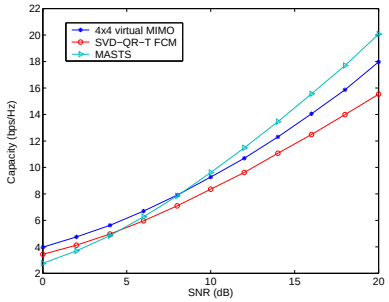


Figure 5: Capacity of SVD-QR-T FCM / MASTS / virtual MIMO with water-filling

$$\mathbf{H} = \begin{bmatrix} 0.7733 & 1.3614 & 1.2254 & 0.3695 \\ 0.6867 & 0.2879 & 1.2014 & 1.7755 \\ 1.2381 & 0.5776 & 1.5719 & 0.2469 \\ 0.6749 & 1.4501 & 0.4248 & 0.6060 \end{bmatrix}$$

We can get $\lambda = [13.4770\ 2.0235\ 1.1696\ 0.0743]$; $\lambda_g = [7.7490\ 3.7149\ 2.3701\ 0.2236]$; $\lambda_s = [10.6485\ 2.0002\ 1.0406]$. With the increase of P/σ^2, MASTS capacity in (18) will increase faster then that of the virtual MIMO without channel selection.

Although SVD-QR-T FCM does not seem to provide any advantage in the above figure, it offers lower BER than virtual MIMO without channel selection when SNR is higher than about 7dB as well as lowest BER after SNR grows to 13dB, which is shown in Fig. 6. This is because SVD-QR-T FCM chooses the best subset of equivalent parallel channels so that SNR allocated at each parallel is larger than that of MASTS and virtual MIMO as P/σ^2 grows larger. Here we employ QPSK modulation with multiplexing but no space-time coding (STC) is adopted. Since no diversity gain is obtained, maximal multiplexing does exist.

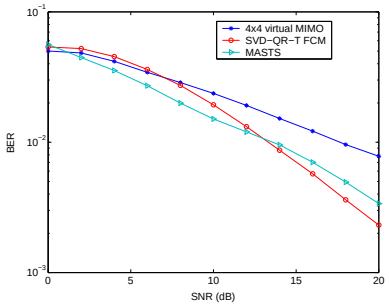


Figure 6: BER of SVD-QR-T / MASTS / 4×4 virtual MIMO with water-filling

Maximal multiplexing gain is the number of equivalent multiple parallel spatial channels [22]. It is also referred to as degrees of freedom to communicate [23], which is related to the row and column numbers of $\mathbf{H}$, $\mathbf{H}_s$ and $\mathbf{H}_g$. It has been derived in [23] that the maximal multiplexing gain provided by $M_r \times M_t$ MIMO is $\min(M_t, M_r)$. However, the accurate multiplexing gain is $r = rank(\mathbf{H})$ since it is possible that $\mathbf{H}$ is not full rank. As SVD-QR-T FCM selects rt transmitters and all receivers, the maximal multiplexing

gain offered by SVD-QR-T FCM is $\min(rt, M_r)$. Note that $rt \leq r \leq M_r$, therefore the accurate multiplexing gain for SVD-QR-T FCM is rt. Concerning MASTS, all transmitters and receivers are active and the maximal multiplexing gain is $rank(\mathbf{H}_g)$. If water-filling are applied, less multiplexing gain will be offered as some singular values with SNR lower than SNR_0 will be cut off.

Under the premise that $\mathbf{H}$ is full rank, we obtain the multiplexing gain on SVD-QR-T FCM and MASTS in Fig. 7 and Fig. 8 respectively. When $M_t = M_r = 10$, multiplexing gain for SVD-QR-T FCM and MASTS are 3.5 and 4 respectively if SNR is 0dB while they grow to 5 and 8.2 if SNR becomes 20dB. Note that although along the increase of SNR, the multiplexing gain of both algorithms grow larger, this characteristic is more obvious for MASTS.

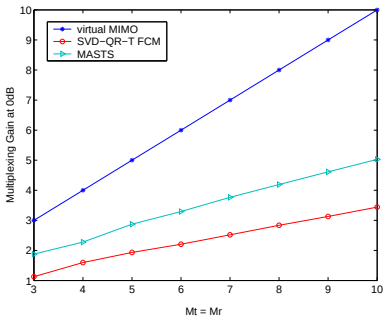


Figure 7: Multiplexing gain of SVD-QR-T FCM/ MASTS / virtual MIMO with water-filling at SNR=0dB

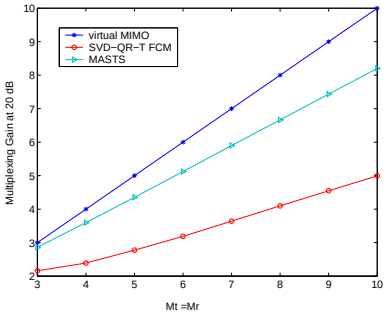


Figure 8: Multiplexing gain of SVD-QR-T FCM/ MASTS / virtual MIMO with water-filling at SNR=20dB

Figs. 5∼8 imply that MASTS generally outweighs SVD-QR-T FCM on performances under the circumstances of water-filling, nevertheless it is worth mentioning that less multiplexing gain implies less transmitters are applied for SVD-QR-T FCM, so less resources are consumed. As for MASTS, it always employs all transmitters and receivers, which costs more resources than those of SVD-QR-T FCM.

5.2 Channel Unknown At Transmitter: Uniform Power Allocation

it is not always the case that both CSIT and CSIR are known. In the case of only CSIR, water-filling power optimization can not be applied and people simply allocate equal power to each transmitters, therefore its capacity becomes

$$C = \sum_{i=1}^{r} B \log_2(1 + \frac{SNR_i}{M_t}) \tag{19}$$

Here we also apply 10,000 times of Monte Carlo simulations to obtain the expectation of capacity for SVD-QR-T FCM / MASTS and a 4×4 virtual MIMO at a different SNR in Fig. 9.

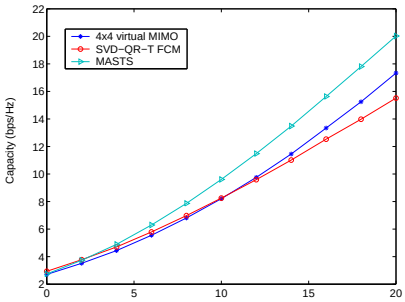


Figure 9: Capacity of SVD-QR-T FCM / MASTS / virtual MIMO without water-filling

It is shown that SVD-QR-T FCM provides a higher capacity than that of a virtual MIMO without channel selection if SNR is less than 10dB and a higher capacity than that of MASTS if SNR is less than 2.5dB. MASTS outweighs virtual MIMO without channel selection in capacity from 0dB and this advantage is more obvious along the increase of SNR.

However, MASTS can not provide better performance in BER while SVD-QR-T FCM performs best, which is illustrated in Fig. 10. This is because SNR allocated at each equivalent parallel channel by means of SVD-QR-T FCM is larger than that of MASTS and virtual MIMO from 0dB.

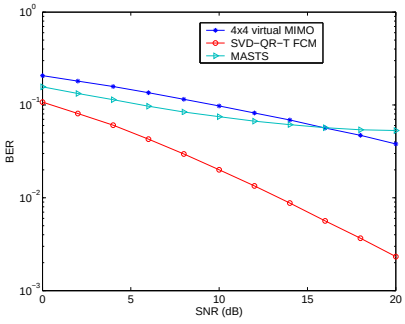


Figure 10: BER of SVD-QR-T / MASTS / 4×4 virtual MIMO without water-filling

In the mean time, Fig. 11 illustrates that MASTS can achieve larger multiplexing gain than that of SVD-QR-T FCM but that means more resource consumption, which is the same situation as in the case of water-filling. When no-water-filling is used, multiplexing gain is not associate with SNR.

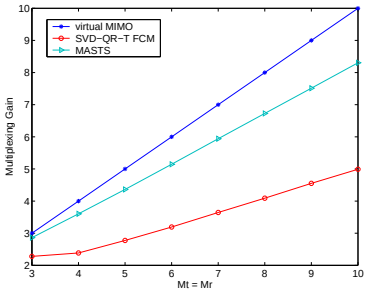


Figure 11: Multiplexing gain of SVD-QR-T FCM/ MASTS / virtual MIMO without water-filling

6. CONCLUSION

This paper is a preliminary work on the virtual MIMO channel selection problem in practice. Two approaches with concrete examples are proposed from respect of pure physical design and cross-layer consideration respectively. We not only present the channel selection algorithms, but also provide the detailed approach on performance analysis with Monte Carlo simulations. We demonstrate that with the same total transmission power constraint, the MASTS can offer the highest capacity (either with water-filling or without) than that of virtual MIMO while SVD-QR-T FCM can provide the best BER performance. Future research tracks might concern the extension of the proposed algorithm to integrate with space time coding (STC) so as to further optimize the system performances.

Acknowledgement

This work was supported in part by Office of Naval Research (ONR) under Grant N00014-07-1-0395, N00014-07-1-1024, and National Science Foundation (NSF) under Grant CNS-0721515.

7. REFERENCES

[1] S. Cui and A. Goldsmith, "Energy-efficiency of MIMO and Cooperative MIMO Techniques in Sensor Networks" , *IEEE Journal on selected areas in communications*, vol. 22, Aug 2004, pp. 1089-1098.

[2] S. K. Jayaweera, "Virtual MIMO-based cooperative communication for energy-constrained wireless sensor networks" , *IEEE Transactions on Wireless Communications*, vol. 5, May 2006, pp. 984 - 989.

[3] Y. Yuan; Z. He and M. Chen, "Virtual MIMO-based cross-layer design forwireless sensor networks" , *IEEE Transactions on Vehicular Technology*, vol. 55, May 2006, pp. 856 - 864.

[4] M. Bengtsson and B. Ottersten, "Optimal and suboptimal transmit beamforming", *Handbook of Antennas in Wireless Communications*, L. C. Godara, Ed. Boca Raton, Fl, CRC, 2001.

[5] D. A. Gore and A. J. Paulraj, "MIMO antenna subset selection with space-time coding", *IEEE Transactions on Signal Processing*, vol. 50, Oct. 2002.

[6] A. Gorokhov, D. A. Gore and A. J. Paulraj, "Receive antenna selection for MIMO flat-fading channels: theory and algorithms", *IEEE Transactions on Information Theory*, vol. 49, Oct. 2003.

[7] A. F. Molisch, M. Z. Win and J. H. Winters, "Capacity of MIMO systems with antenna selection", in *Proc. Int. Conf. Communications*, 2001, pp. 570-574.

[8] R. W. Heath Jr. and A. Paulraj, "Antenna Selection for spatial multiplexing systems based on minimum error rate", in *Proc. IEEE Int. Control Conf.*, 2001, pp. 2276-2280.

[9] I. Bahceci, T. M. Duman and Y. Altunbasak, "Antenna Selection for Multiple-Antenna Transmission Systems: Performance Analysis and Code Construction", *IEEE Transctions on Information Theory*, vol. 49, oct. 2003.

[10] Y. J. Choi, J. Kim and S. Bahk, "Downlink scheduling with fairness and optimal antenna assignment for MIMO cellular systems", *Global Telecommunications Conference, 2004*, Vol. 5, 2004 Page(s):3165-3169.

[11] Y. J. Choi, J. Kim and S. Bahk, "Optimal antenna assignment considering QoS under MIMO environments", *IEEE International Conference on Communications, 2004*, Vol.7, June 2004, pp. 4216-4221.

[12] J. B. Kruskal, "On the shortest spanning subtree and the traveling salesman problem", *Proceedings of the American Mathematical Society*, vol. 7, 1956, pp. 48-50.

[13] A. Goldsmith, *Wireless Communications*, Cambridge University Press, NJ 2001.

[14] D. B. West, *Introduction to Graph Theory (2 Ed.)*, Prentice-Hall of India, NY 2005.

[15] Chen, S., S. A. Billings and W. Luo, "Orthogonal Least Squares Methods and their Application to Nonlinear System Identification," *Int. J. Control*, vol. 50, 1989, pp. 1873-1896.

[16] Q. Liang and L. Wang, "Redundancy Reduction in Wireless Sensor Networks Using Singular-Value-QR Decomposition" , *IEEE Military Communication Conference*, Oct. 2005, Atlantic City, NJ.

[17] J. C. Bezdek, *Pattern Recognition with Fuzzy Objective Function Algorithms*, Plenum Press, New York, 1981.

[18] Xiuzhen Cheng, et al, "Strong Minimum Energy Topology: NP-Completeness and Heuristics" , *IEEE Transaction on Mobile Computing*, Vol. 2, No. 3, pp. 248-256, July-September 2003.

[19] Xiuzhen Cheng, et al, "Polynomial-Time Approximation Scheme for Minimum Connected Dominating Set in Ad Hoc Wireless Networks", Networks, Vol. 42, No. 4, pp. 202-208, 2003.

[20] G. Stüber, *Mobile Communications*, 2nd ed., Kluwer Academic Publishers, 2001.

[21] M.-S. Alouini and A. J. Goldsmith, " Capacity of Rayleigh fading channels under different adaptive transmission and diversity combining techniques", *IEEE Trans. Veh. Tech*, pp. 1165-1181, July. 1999.

[22] Jr. R. Heath and A. Paulraj, "Switching between multiplexing and diversity based on constellation distance", in *Proc. Allerton Conf. Communication, Contril and Computing*, Oct 2000.

[23] L. Zheng, D. N. C. Tse, "Diversity and multiplexing: a fundamental tradeoff in multiple-antenna channels", *IEEE Trans. on Information Theory*, vol. 49, pp. 1073-1096, May 2003.

Image Fusion on Radar Sensor Networks

Jing Liang and Qilian Liang
Department of Electrical Engineering
University of Texas at Arlington
416 Yates Street
Nedderman Hall, Rm 518
Arlington, TX 76019
Email: jliang@wcn.uta.edu, liang@uta.edu

***Abstract*— Owning to Rician fading and white gaussian noise, the scattered back image signal of radar sensors would be distorted to some extend. In this paper, we apply two schemes named Equal Gain Combination (EGC) and Maximal Ration Combination (MRC) respectively for RSN image fusion. Simulation results show that image fusion by means of MRC can provide much better image quality based on both minimum mean squared error (MMSE) and the mean of structural similarity (MSSIM) index if the channel estimation offers satisfying channel side information at receiver (CSIR). However, EGC itself does not require any channel estimation scheme and thus more simple to implement.**

I. Introduction

Enhancing homeland security demands challenging accuracy to detect unauthorized intrusion. For some applications, information provided by single radar may be imprecise or incomplete [1] [2]. A network of multiple radar sensors can been utilized to combat performance degradation of single radar [3]. By employing Radar Sensor Networks (RSN), we are able to protect critical infrastructure from terrorist activities [4].

Image fusion on RSN is that radars are managed by an intelligent clusterhead which combines image diversity in order to satisfy the common goals of the network other than each radar operates independently.

There have been intensive study on radar image fusion, which can be mainly categorized into 3 applications. The first application uses a pair of antennas to obtain an elevation map of the observed scene to resolve the problem of Synthetic Aperture Radar (SAR) Interferometry [5]; the second considers fusion of multisensor images of the same site at different time by means of neural networks [6] [7]; the third refers to a processor to fuse multifrequency, multipolarization and multiresolution images on a basis of wavelet transform and multiscale Kalman filter [8] [9]. However, to this date, the concept of RSN have rarely been employed during the exiting research on radar image fusion. Instead, attention has been mainly given to image fusion on the same single radar. Furthermore, in the previous studies, image processing and physical layer characteristics are usually studied mutually independently to each other. The joint study on both fields demands further exploration besides joint source-channel coding [10] [11].

In this paper, we apply two schemes named Equal Gain Combination (EGC) and Maximal Ration Combination (MRC) respectively for RSN image fusion. Simulation results show that image fusion by means of MRC can provide much better image quality based on both minimum mean squared error (MMSE) and the mean of structural similarity (MSSIM) index if the channel estimation offers satisfying channel side information at receiver (CSIR). However, EGC itself does not require any channel estimation scheme and thus more simple to implement.

The remainder of this paper will be organized as follows: Section II describes EGC and MRC image fusion schemes respectively. Section III shows image fusion result and Section IV draws conclusion and future work.

II. Theory Of Operation

Radar operates by radiating energy into space and detecting echo signals reflected back from a target [12]. When the non-fluctuating target is constructed from many independently positioned scatterers, the probability density function (PDF) of its radar cross section (RCS) can usually be described by Rician PDF [13] and thus the channel through which the signal is scattered back is usually described by corruption of Rician fading.

As radar sensors are environment dependent [14], it may provide better image quality if different neighboring radars work collaboratively to perform image fusion. For example, consider a system of two radars. When the signal of either radar unfortunately experience a severe fading, if two radars are spaced sufficiently far apart, it is not likely that both of the radars experience deep fade at the same time. By selecting better image pixel from the two radar image candidates, it is unlikely that the image information will be lost as much as that of single radar image. Fig.1 illustrates this scenario. The solid line represents the transmitted signal of radar member while the dash line represents the echo signal which is corrupted with Rician fading and noise.

Fig. 2 shows the diagram of image fusion we have applied to RSN. As the fine details that accurately describes target is critical for reliable detection and classification of targets, before image fusion, the processing for resolution enhancement is required [15]. $\underline{R_1}$, $\underline{R_2}$, $\cdots$, $\underline{R_n}$ represent pixel matrices of images obtained from radar sensor 1, radar sensor

2, $\cdots$, sensor n respectively. a_1, a_2, $\cdots$, a_n is pixel weighting employed by image fusion. The main purpose of EGC and MRC image fusion schemes is to coherently combine the independent faded images so that the effects of fading and noise are mitigated.

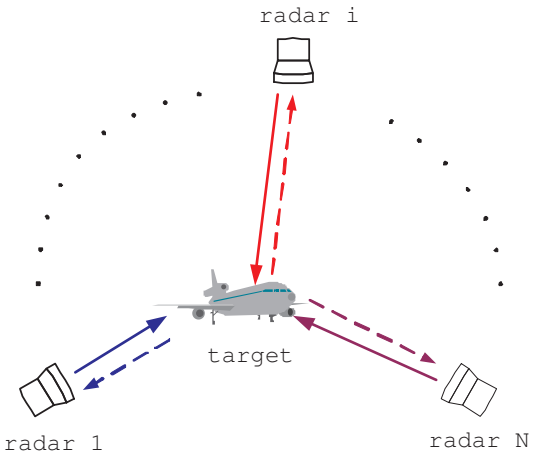


Fig. 1. Radar Sensor Network (RSN)

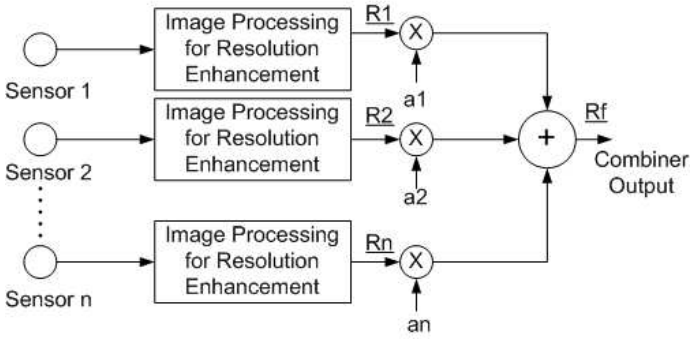


Fig. 2. Diagram of Image Fusion for RSN

EGC is a simple technique which co-phases the image signals on each radar sensor and then combines them using equal weighting, therefore each a_1, a_2, $\cdots$, a_n equals to the same 1. The pixel matrix after EGC image fusion is

$$\underline{R_f} = (\underline{R_1} + \underline{R_2} + \cdots + \underline{R_n})/n \tag{1}$$

In this case, the output equals to the average of each radar image.

In MRC, the output image is a weighted sum of all radars, the pixel matrix after MRC image fusion is

$$\underline{R_f} = \frac{(\sum_{i=1}^{n} a_i \underline{R_i})^2}{\sum_{i=1}^{n} a_i^2} \tag{2}$$

We can find a_i that maximize $\underline{R_f}$ by taking partial derivatives of (2) or employing the Cauchy-Schwartz inequality [16]. The optimal weights yields $a_i^2 = \underline{R_i}^2$. This implies that radar with good image quality should be weighted more. MRC requires knowledge of time-varying Rician channel fading on each radar, i.e., channel side information at receiver (CSIR) is necessary. CSIR can be obtained through various channel estimation techniques, which are out of the scope of this paper. However, EGC does not have this requirement and thus is more simple to be implemented.

III. Simulation

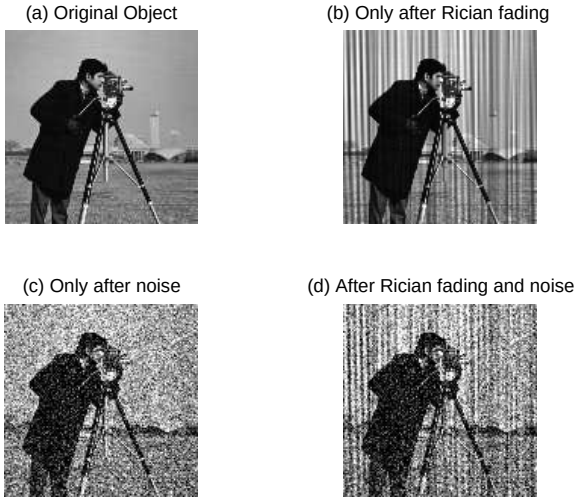


Fig. 3. radar images illustration: (a) Original Object, (b) Only corrupted by Rician fading without noise, (c) Only corrupted by noise without Rician fading, (d) Corrupted by both Rician fading and noise

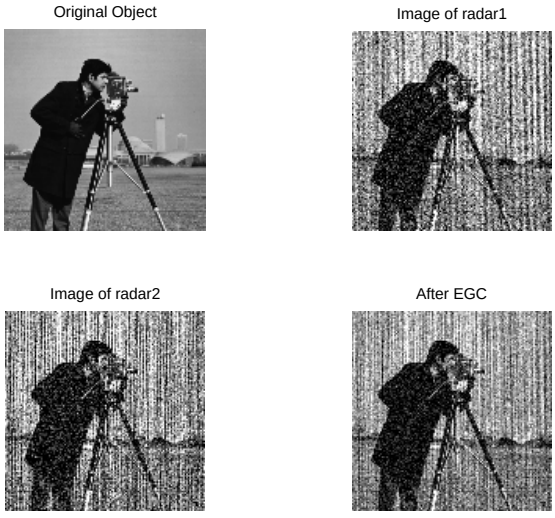


Fig. 4. EGC image fusion: (a) Original Object, (b) image obtained by radar sensor 1, (c) image obtained by radar sensor 2, (d) image obtained by means of EGC

For simplicity, we assume the RSN consist of 2 radars. Of course, the situation of larger number of radar members can be easily extended from this simple case. Jake's Model [17] is

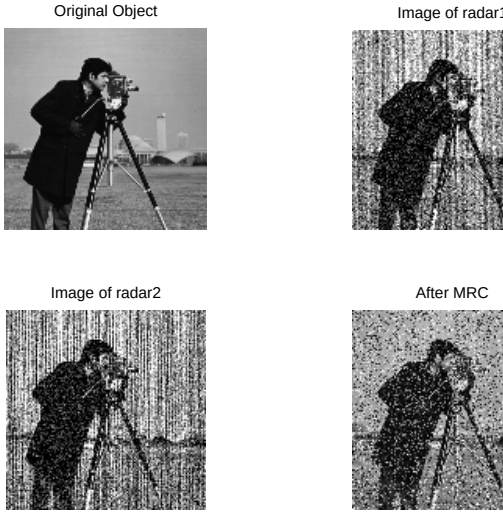


Fig. 5. MRC image fusion: (a) Original Object, (b) image obtained by radar sensor 1, (c)image obtained by radar sensor 2, (d) image obtained by means of MRC with poorer channel estimation

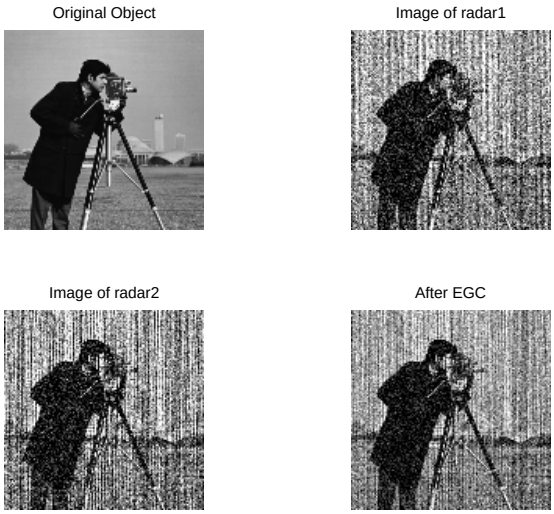


Fig. 6. EGC image fusion: (a) Original Object, (b) image obtained by radar sensor 1, (c) image obtained by radar sensor 2, (d) image obtained by means of EGC

applied to generate Rician fading channel by means of Matlab. As mentioned before, EGC is simply average all images, so no channel estimation technique is required by EGC. However, MRC is on a basis of CSI and thus different channel estimation performance would result in different quality of image fusion. we employ block phase estimation (BPE) raised by Viterbi [18] to estimate Rician channel. This estimation is only used in MRC simulation.

Fig. 3 illustrate image distortion result from Rician fading and white gaussian noise. Fig. (a) is the image of the original object. Fig. (b) is the image corrupted only by Rician fading channels without white gaussian noise. Fig. (c) is the image corrupted only by noise without rician fading. (d) is the image corrupted by both Rician fading and noise, which is practical, as in the real world, fading and noise always coexist. Note that if fading and noise become more inclement, the quality of image can be drastically reduced.

Fig. 4 illustrates the EGC image fusion result compared with the original object and images obtained by independent sensors. Fig (b) and (c) are images obtained by radar sensor 1 and sensor 2 respectively, both are corrupted by white gaussian noise and Rician fading with different fading factor $K = 10$ and $K = 5$, doppler shift $f_d = 100Hz$ and $f_d = 200Hz$ and variance of noise = 0.04 (double size). It is shown that quality of EGC infused image (d) is better than both (b) and (c), this can be particularly analyzed through the jacket of cameraman. However, the improvement on background is not easy to tell by human eyes. The Minimum Mean Squared Error (MMSE) of image (b) and (c) are 0.0541 and 0.0706 respectively, while the MMSE of EGC fused image is 0.0316. Besides MMSE, we also calculate the mean of structural similarity (MSSIM) index [19] by comparing (b)(c)(d) with (a) respectively and get

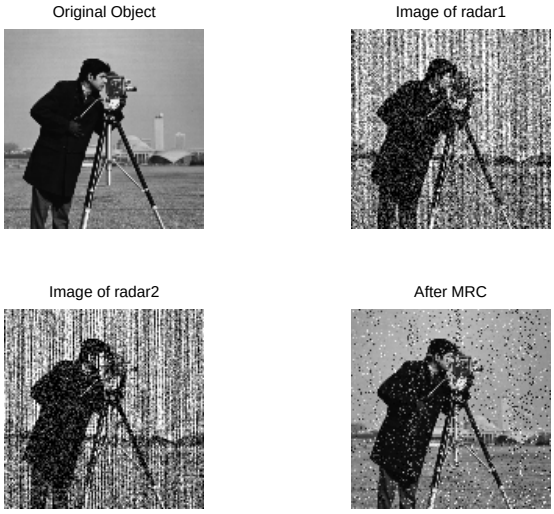


Fig. 7. MRC image fusion: (a) Original Object, (b) image obtained by radar sensor 1, (c)image obtained by radar sensor 2, (d) image obtained by means of MRC with better channel estimation

0.9979, 0.9972 and 0.9988. All MMSE and MSSIM employ "double" size. Both MMSE and MSSIM illustrate that the image obtained through EGC offers better quality then that obtained by independent member.

Similarly, MRC image fusion result is shown in Fig. 5. Fig (b) and (c) are the same images in Fig. 4 (b) and (c). Fig. 5 (d) is the fused image obtained by means of MRC when the performance of channel estimation is bad. Due to the large error in the channel knowledge, we can see that MRC could

not provide good quality of fused image, even the fused image look worse than (b) and (c) to some extend in this case. The MMSE and MSSIM of (d) is 0.0406 and 0.9984 respectively, compared to 0.0316 and 0.9988 of EGC.

Under the condition that the performance of channel estimation is good, we obtain a new group of images in Fig. 6 and 7 with the same fading factor, doppler shift and variance of noise. Note that Fig. 6 is different with Fig. 4. Although channel estimation would not result in the difference between performances of EGC, as EGC itself does not require any knowledge of channel, for better comparison, Fig. 6 is generated in the way that (b) an (c) are the same as those in Fig. 7 with MMSE 0.0510 and 0.0691, MSSIM 0.998 and 0.9973. MMSE of Fig. 6 (d) and Fig. 7 (d) are 0.0298 and 0.0153 respectively while their MSSIM are 0.9988 and 0.9994. These values further illustrate that MRC under good channel estimation can definitely offer better quality of fused image than that of EGC.

IV. Conclusion and Future Works

This paper is a preliminary work on image fusion on RSN. We applied EGC and MRC to fuse images and the result shows that both EGC and MRC are capable of offering better image quality than that of single radar.

Acknowledgement

This work was supported by the Office of Naval Research (ONR) Young Investigator Award under Grant N00014-03-1-0466, and ONR Award under Grant N00014-07-1-0395.

References

[1] P. K. Varshney, "Multisensor data fusion" , *Electronics & Communication Engineering Journal*, pp.245-263Dec. 1997.

[2] D. L. Hall and J. Llinas, "An Introduction to Multisensor Data Fusion", *Proceedings of the IEEE* vol. 85, No. 1, pp.6-23, Jan. 1997

[3] S. Haykin, "Cognitive radar networks" , *2005 1st IEEE International Workshop on Computational Advances in Multi-Sensor Adaptive Processing*, pp.1-3, Dec 2005.

[4] S. Haykin, "Towards Radar-Enabled Sensor Network" , *ISPN'06* , April 19-21, 2006.

[5] M. Costantini, A. Farina and F. Zirilli "A Fast Phase Unwrapping Algorithm for SAR Interferometry" , *IEEE Transactions on Geoscience and Remote Sesning*, vol. 37, No.1 pp.452-469, Jan. 1999

[6] S. B. Serpico and F. Roli, "Classification of Multisensor Remote Sensing Images by Structured Neural Networks", *IEEE Transactions on Geoscience and Remote Sensing*, vol. 33, No.3, pp.562-578, May 1995

[7] L. Bruzzone, D. F. Prieto and S. B. Serpico, "A Neural Statistical Approach to Multitemporal and Multisensor and Multisource Remote Sensing Image Classification", *IEEE Transactions on Geoscience and Remote Sensing*, vol. 37, No. 3, pp. 1350-1359, May 1999

[8] A. M. Signorini, A. Farina and G. Zappa, "Application of multiscale estimation algorithm to SAR images fusion", *International Symposium on Radar* IRS98, Munich, pp. 1341-1352, Sept. 15-17, 1998

[9] P. W. Feieguth et al, "Multiresolution Optimal Interpolation and Statistical Analysis of TOPEX/POSEIDON Statellite Altimetry", *IEEE Transactions on Geoscience and Remote Sensing*, vol. 33. No.2, pp. 280-292, March 1995

[10] J. Cai and C. W. Chen "Robust joint source-channel coding for image transmission over wireless channels", *IEEE Transactions on Circuits and Systems for Video Technology*, vol. 10. No.2, pp. 962-996, Sept. 2000

[11] E. Arikan and N. Merhav "Joint source-channel coding and guessing with application to sequential decoding " *IEEE Transactions on Information Theory* vol. 44, pp. 1756-1759, Sept. 1998

[12] M. I. Skolnik, *Introduction to Radar Systems* , 3rd ed, New York, McGraw Hill, 2001.

[13] N. Levanon, *Radar Principles*, New York, Wiley, 1988.

[14] R. A. Johnson and E. L. Titlebaum, "Range Doppler Uncoupling in the Doppler Tolerant Bat Signal", *Proc. of IEEE Ultrasonics Symposium* , New York, pp.64-67, 1972.

[15] M. K. Sundareshan and S. Bhatacharjee, "Super-Resolution of Tractical Surveillance and Tracking Data for Fusion of Images" *Data fusion for Situation Monitoring, Incident Detection, Alert and Response Management* pp.448-463, IOS Press 2005

[16] A. Goldsmith, *Wireless Communications*, Cambridge University Press, NJ 2001.

[17] G. Stüber, *Mobile Communications*, 2nd ed., Kluwer Academic Publishers, 2001

[18] A. J. Viterbi and A. M. Viterbi "Nonlinear Estimation of PSK-Modulated Carrier Phase with Application to Burst Digital Transmission" *IEEE Transcations on Information Theory* no.4, pp. 543-551, July 1983

[19] Z. Wang, A. C. Bovik, H. R. Sheikh and E. P. Simoncelli, "Image quality assessment: From error visibility to structural simalrity" *IEEE Transactions on Image Processing* vol.13, no.4, pp. 600-612, April, 2004

NEW-CATR: Network-enabled Electronic Warfare for Collaborative Automatic Target Recognition

Qilian Liang
Department of Electrical Engineering
University of Texas at Arlington
Arlington, TX 76019-0016, USA
E-mail: liang@uta.edu

Sherwood W. Samn
Air Force Research Laboratory/HEX
Brooks City Base
San Antonio, TX 78235, USA
E-mail: Sherwood.samn@brooks.af.mil

***Abstract*— Network-enabled Electronic Warfare (NEW) is to develop modeling and simulation efforts to explore the advantages and limitations of network-enabled electronic warfare concepts. The advantages of linking multiple electronic support measures (ESM) and electronic attack (EA) assets to achieve improved capabilities across a networked battleforce have yet to be quantified. In this paper, we will use radar sensors as ESM and EA assets to demonstrate the advantages of NEW in Collaborative Automatic Target Recognition (CATR). We apply the NEW to CATR via waveform diversity combining and and propose maximum-likehood (ML)-ATR algorithms for nonfluctuating target as well as fluctuating target. Simulation results show that our NEW-CATR performs much better than single sensor-based ATR algorithm for nonfluctuating targets or fluctuating targets. Conclusions are drawn based on our analysis and simulations and future research works on this research topic are discussed.**[1]

Index Terms : Network-enabled electronic warfare, radar sensor networks, waveform diversity, collaborative automatic target recognition, maximum-likelihood, interferences.

I. Introduction and Motivation

In current and future military operational environments, such as Global War on Terrorism (GWOT) and Maritime Domain Awareness (MDA), warfighters require technologies evolved to support information needs regardless of location and consistent with the users level of command or responsibility and operational situation. To support this need, the U.S. Department of Defense (DoD) has developed the concept of Network Centric Warfare (NCW), defined as "*military operations that exploit state-of-the-art information and networking technology to integrate widely dispersed human decision makers, situational and targeting sensors, and forces and weapons into a highly adaptive, comprehensive system to achieve unprecedented mission effectiveness*" [1]. The goal of electronic warfare is to control the electromagnetic (EM) spectrum by exploiting, disrupting, or denying enemy use of the spectrum while ensuring its use by friendly forces [2].

[1]1-4244-1513-06/07/$25.00 ©2007 IEEE

Network-enabled Electronic Warfare (NEW) is to develop modeling and simulation efforts to explore the advantages and limitations of network-enabled electronic warfare concepts. The advantages of linking multiple electronic support measures (ESM) and electronic attack (EA) assets to achieve improved capabilities across a networked battleforce have yet to be quantified [2]. In this paper, we will use radar sensors as ESM and EA assets to demonstrate the advantages of NEW in Collaborative Automatic Target Recognition (CATR). The network of radar sensors should operate with multiple goals managed by an intelligent platform network that can manage the dynamics of each radar to meet the common goals of the platform, rather than each radar to operate as an independent system. Therefore, it is significant to perform signal design and processing and networking cooperatively within and between platforms of radar sensors and their communication modules. This need is also testified by recent solicitations from U.S. Office of Naval Research [2][3]. For example, in [3], it is stated that "Algorithms are sought for fused, and or, coherent cross-platform Radio Frequency (RF) sensing. The focus of this effort is to improve surveillance utilizing a network, not fusion of disparate sensor products. The algorithms should be capable of utilizing RF returns from multiple aspects in a time-coordinated sensor network." In this paper, we will study waveform design and diversity algorithms for radar sensor networks. Waveform diversity is the technology that will allow one or more sensors on board a platform to automatically change operating parameters, e.g., frequency, gain pattern, and pulse repetition frequency (PRF) to meet the varying environments. It has long been recognized that judicious use of properly designed waveforms, coupled with advanced receiver strategies, is fundamental to fully utilizing the capacity of the electromagnetic spectrum. However, it is only relatively recent advances in hardware technology that are enabling a much wider range of design freedoms to be explored. As a result, there are emerging and compelling changes in system requirements such as more efficient spectrum usage, higher sensitivities, greater information content, improved robustness to errors,

Authorized licensed use limited to: University of Texas at Arlington. Downloaded on December 18, 2009 at 14:46 from IEEE Xplore. Restrictions apply.

reduced interference emissions, etc. The combination of these is fuelling a worldwide interest in the subject of waveform design and the use of waveform diversity techniques.

In the existing works on waveform design and selection, Fitzgerald [8] demonstrated the inappropriateness of selection of waveform based on measurement quality alone: the interaction between the measurement and the track can be indirect, but must be accounted for. Bell [6] used information theory to design radar waveform for the measurement of extended radar targets exhibiting resonance phenomena. In [5], singularity expansion method was used to design some discriminant waveforms such as K-pulse, E-pulse, and S-pulse. Sowelam and Tewfik [24] developed a signal selection strategy for radar target classification, and a sequential classification procedure was proposed to minimize the average number of necessary signal transmissions. Intelligent waveform selection was studied in [4][12], but the effect of doppler shift was not considered. In [15], the performance of constant frequency (CF) and linear frequency modulated (LFM) waveform fusion from the standpoint of the whole system was studied, but the effects of clutter was not considered. In [23], CF and LFM waveforms were studied for sonar system, but it was assumed that the sensor is nonintelligent (i.e., waveform can't be selected adaptively). All the above studies and design methods were focused on the waveform design or selection for a single active radar or sensor. In [21], cross-correlation properties of two radars are briefly mentioned and the binary coded pulses using simulated annealing [7] are highlighted. However, the cross-correlation of two binary sequences such as binary coded pulses (e.g. Barker sequence) are much easier to study than that of two analog radar waveforms. In this paper, we will focus on the waveform diversity and design for radar sensor networks using constant frequency (CF) pulse waveform.

The rest of this paper is organized as follows. In Section II we propose a RAKE structure for waveform diversity combining and propose maximum-likelihood (ML) algorithms for CATR. In Section II we propose another RAKE structure for UWB radar diversity combining. In Section IV, we conclude this paper and provide some future works.

II. NEW FOR COLLABORATIVE AUTOMATIC TARGET RECOGNITION

In NEW, the radar sensors are networked together in an ad hoc fashion. They do not rely on a preexisting fixed infrastructure, such as a wireline backbone network or a base station. They are self-organizing entities that are deployed on demand in support of various events surveillance, battlefield, disaster relief, search and rescue, etc. Scalability concern suggests a hierarchical organization of radar sensor networks with the lowest level in the hierarchy being a cluster. As argued in [14] [10] [9] [17], in addition to helping with scalability and robustness, aggregating sensor nodes into clusters has additional benefits:

1) conserving radio resources such as bandwidth;
2) promoting spatial code reuse and frequency reuse;
3) simplifying the topology, e.g., when a mobile radar changes its location, it is sufficient for only the nodes in attended clusters to update their topology information;
4) reducing the generation and propagation of routing information; and,
5) concealing the details of global network topology from individual nodes.

In Radar Sensor Network (RSN), each radar can provide their waveform parameters such as δ_i to their clusterhead radar, and the clusterhead radar can combine the waveforms from its cluster members. In this paper, we propose a RAKE structure for waveform diversity combining, as illustrated by Fig. 1. According to this structure, the received $r_1(u,t)$ is processed by a bank of matched filters.

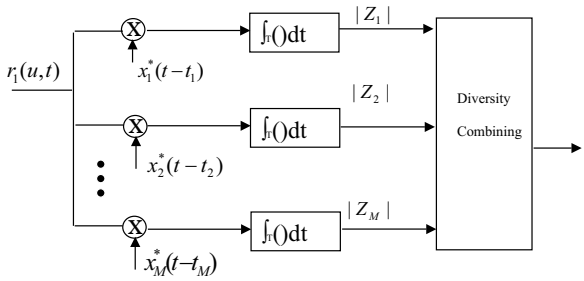


Fig. 1. Waveform diversity combining by clusterhead in RSN.

How to combine all the Z_m's ($m = 1, 2, \cdots, M$) are very similar to the diversity combining in communations to combat channel fading, and the combination schemes may be different for different applications. In this paper, we are interested in applying RSN waveform diversity to CATR, e.g., recognition that the echo on a radar display is that of an aircraft, ship, motor vehicle, bird, person, rain, chaff, clear-air turbulence, land clutter, sea clutter, bare montains, forested areas, meteors, aurora, ionized media, or other natural phenomena via collaborations among different radars. Early radars were "blob" detectors in that they detected the presence of a target and gave its location in range and angle, and radar began to be more than a blob detector and could provide recognition of one type of target from another[21]. It is known that small changes in the aspect angle of complex (multiple scatter) targets can cause major changes in the radar cross section (RCS). This has been considered in the past as a means of target recognition,

Authorized licensed use limited to: University of Texas at Arlington. Downloaded on December 18, 2009 at 14:46 from IEEE Xplore. Restrictions apply.

and is called *fluctuation of radar cross section with aspect angle*, but it has not had much success[21]. In this paper, we propose a maximum likelihood collaborative automatic target recognition (ML-CATR) algorithm for RSN. We will study non-fluctuating target as well as fluctuating target.

A. ML-CATR for Non-fluctuating Targets

In some sources, the non-fluctuating target is identified as "Swerling 0" or "Swerling 5" model [22]. For non-fluctuating target, the RCS $\alpha_m(u)$ is just a constant α for a given target. Noise $n(u,\tau)$ is a zero-mean Gaussian random variable for given τ, so $|Z_m|$ follows Rician distribution because signal $E\alpha(u)$ is a positive constant $E\alpha$ for non-fluctuating target. Let $y_m \stackrel{\triangle}{=} |Z_m|$, then the probability density function (pdf) of y_m is

$$f(y_m) = \frac{2y_m}{\sigma^2}\exp[-\frac{(y_m^2+\lambda^2)}{\sigma^2}]I_0(\frac{2\lambda y_m}{\sigma^2}) \quad (1)$$

where

$$\lambda = E\alpha, \quad (2)$$

σ^2 is the noise power (with I and Q sub-channel power $\sigma^2/2$), and $I_0(\cdot)$ is the zero-order modified Bessel function of the first kind. Let $\mathbf{y} \stackrel{\triangle}{=} [y_1, y_2, \cdots, y_M]$, then the pdf of $\mathbf{y}$ is

$$f(\mathbf{y}) = \prod_{m=1}^{M} f(y_m) \quad (3)$$

Our CATR is a multiple-category hypothesis testing problem, i.e., to decide a target category (e.g. aircraft, ship, motor vehicle, bird, etc) based on $r_1(u,t)$. Assume there are totally N categories and category n target has RCS α_n, so the ML-CATR algorithm to decide a target category C can be expressed as,

$$\begin{aligned} C &= \arg\max_{n=1}^{N} f(\mathbf{y}|\lambda = E\alpha_n) \quad (4)\\ &= \arg\max_{n=1}^{N} \prod_{m=1}^{M} \frac{2y_m}{\sigma^2}\exp[-\frac{(y_m^2+E^2\alpha_n^2)}{\sigma^2}] \\ &\quad I_0(\frac{2E\alpha_n y_m}{\sigma^2}) \quad (5)\end{aligned}$$

B. ML-CATR for Fluctuating Targets

Fluctuating target modeling is more realistic in which the target RCS is drawn from either the Rayleigh or chi-square of degree four pdf. The Rayleigh model describes the behavior of a complex target consisting of many scatters, none of which is dominant. The fourth-degree chi-square models targets having many scatters of similar strength with one dominant scatter. Based on different combinations of pdf and decorrelation characteristics (scan-to-scan or pulse-to-pulse decorrelation), four Swerling models are used[19]. In this paper, we will focus on "Swerling 2" model which is Rayleigh distribution with pulse-to-pulse decorrelation. The pulse-to-pulse decorrelation implies that each individual pulse results in an independent value for RCS α.

For Swerling 2 model, the RCS $|\alpha(u)|$ follows Rayleigh distribution and its I and Q subchannels follow zero-mean Gaussian distributions with variance γ^2. Assume

$$\alpha(u) = \alpha_I(u) + j\alpha_Q(u) \quad (6)$$

and $n(u) = n_I(u) + jn_Q(u)$ follows zero-mean complex Gausian distribution with variance σ^2 for the I and Q subchannels. Z_m is a zero-mean Gaussian random variable with variance $E^2\gamma^2 + \sigma^2$ for the I and Q subchannels, which means $y_m \stackrel{\triangle}{=} |Z_m|$ follows Rayleigh distribution with parameter $\sqrt{E^2\gamma^2+\sigma^2}$,

$$f(y_m) = \frac{y_m}{E^2\gamma^2+\sigma^2}\exp(-\frac{y_m^2}{E^2\gamma^2+\sigma^2}) \quad (7)$$

The mean value of y_m is $\sqrt{\frac{\pi(E^2\gamma^2+\sigma^2)}{2}}$, and variance is $\frac{(4-\pi)(E^2\gamma^2+\sigma^2)}{2}$. The variance of signal is $\frac{(4-\pi)E^2\gamma^2}{2}$ and the variance of noise is $\frac{(4-\pi)\sigma^2}{2}$.

Let $\mathbf{y} \stackrel{\triangle}{=} [y_1, y_2, \cdots, y_M]$, then the pdf of $\mathbf{y}$ is

$$f(\mathbf{y}) = \prod_{m=1}^{M} f(y_m) \quad (8)$$

Assume there are totally N categories and category n target has RCS $\alpha_n(u)$ (with variance γ_n^2), so the ML-ATR algorithm to decide a target category C can be expressed as,

$$\begin{aligned} C &= \arg\max_{n=1}^{N} f(\mathbf{y}|\gamma = \gamma_n) \quad (9)\\ &= \arg\max_{n=1}^{N} \prod_{m=1}^{M} \frac{y_m}{E^2\gamma_n^2+\sigma^2}\exp(-\frac{y_m^2}{E^2\gamma_n^2+\sigma^2})\end{aligned}$$

C. Simulations

Radar sensor networks will be required to detect a broad range of target classes. Too often, the characteristics of objects that are not of interest (e.g., bird) will be similar to those of threat objects (e.g., missile). Therefore, new techniques to discriminate threat against undesired detections (e.g. birds, etc.) are needed. We applied our ML-CATR to this important application, to recognize a target from many target classes. We assume that the domain of target classes is known a priori (N in Sections II-A and II-B), and that the RSN is confined to work only on the known domain.

For non-fluctuating target recognition, our targets have 5 classes with different RCS values, which are summarized in Table I[21]. We applied the ML-CATR algorithms in Section II-A (for nonfluctuating target case) to classify an unknown target as one of these 5 target classes. At each average SNR value, we ran Monte-Carlo simulations

Authorized licensed use limited to: University of Texas at Arlington. Downloaded on December 18, 2009 at 14:46 from IEEE Xplore. Restrictions apply.

for 10^5 times for each target. The average SNR value is based on the average power from all targets (signal variance), so the actual SNRs for bird and missile are much lower than the average SNR value. For example, at the average SNR=16dB, the bird target SNR=-33.1646dB, and missile target SNR=0.8149dB; and at average SNR=20dB, the bird target SNR=-29.1646dB, and missile target SNR=4.8149dB. In Fig. 2(a)(b), we plotted the probability of ATR error in bird and missile recognition when they are assumed as nonfluctuating targets. Observe both figures, single radar system can't perform well in both recognitions, and their probability of ATR error is above 10%, which can't be used for real-world ATR. However, the 5-radar RSN and 10-radar RSN can maintain very low ATR errors. In Fig. 2(c), we plotted the average probability of ATR error for all 5 targets recognition. Since the other 3 targets (different aircrafts) have much higher SNRs, so their ATR error is lower, which makes the average probability of ATR error lower.

For fluctuating target recognition, we assume the fluctuating targets follow "Swerling 2" model (Rayleigh with pulse-to-pulse decorrelation), and assume the RCS value listed in Table I to be the standard deviation (std) γ_n of RCS $\alpha_n(u)$ for target n. We applied the ML-CATR algorithm in Section II-B (for fluctuating target case) for target recognition within the 5 targets domain. Similarly we ran Monte-Carlo simulations at each SNR value. In Fig. 3(a)(b)(c), we plot the ATR performance for fluctuating targets and compared the performances of single radar system, 5-radar RSN, and 10-radar RSN. Observe that the two RSNs perform much better than the single radar system. The ATR error for missile is higher than that of bird because Rayleigh distribution of missile has lots of overlap with its neighbor targets (aircrafts). Comparing Fig. 2(a)(b)(c) to Fig. 3(a)(b)(c), it is clear that higher SNRs are needed for fluctuating target recognition comparing to nonfluctuating target recognition. According to Skolnik[21], radar performance with probability of recognition error (p_e) less than 10% is good enough. Our RSN with waveform-diversity can have probability of ATR error much less than 10% for each target ATR as well as the average ATR for all targets. However, the single radar system has probability of ATR error much higher than 10%. Observe Fig. 3(c), the average probability of ATR error of single-radar is impossible to be less than 10% even at extreme high SNR. Our RSN with waveform diversity is very promising to be used for real-world ATR.

III. Sense-through-Foliage Target Detection Using Radar Sensor Network

In Figs. 4a and 4b, we plot two collections using UWB radars. Fig. 4a has no target on range, and Fig. 4b has target at samples around 14,000. We plot the echo differences between Figs. 4a and 4b in Fig. 4c. However, it is impossible to identify whether there is any target and where there is target based on Fig. 4c. Since significant pulse-to-pulse variability exists in the echos, this motivate us to explore the spatial and time diversity using Radar Sensor Networks (RSN).

TABLE I

RCS values at microwave frequency for 5 targets.

Index n	Target	RCS
1	Bird	0.01
2	Conventional unmanned winged missile	0.5
3	Small single-engine aircraft	1
4	Small flighter aircraft or 4 passenger jet	2
5	Large flighter aircraft	6

In Fig. 5, the echo, i.e., RF response by the pulse of each cluster-member sensor, will be combined by the clusterhead using a weighted average, and the weight w_i is determined by the power of each echo $x_i(n)$ (n is the sample index),

$$w_i = \frac{E_i}{\sum_{i=1}^{M} E_i} \tag{10}$$

and

$$E_i = \text{var}(x_i(n)) + [\text{mean}(x_i(n))]^2 \tag{11}$$

We ran simulations for $M = 30$, and plot the power of AC values in Figs. 6a and 6b for the two cases (with target and without target) respectively. Observe that in Fig. 6b, the power of AC values (around sample 14,000) where the target is located is non-fluctuating (monotonically increase then decrease). Although some other samples also have very high AC power values, it is very clear that they are quite fluctuating and the power of AC values behaves like random noise because generally the clutter has Gaussian distribution in the frequency domain.

IV. Conclusions and Future Works

We have studied constant frequency pulse waveform design and diversity in radar sensor networks. We proposed a RAKE structure for waveform diversity combining in RSN. As an application example, we applied the waveform design and diversity to CATR in RSN and proposed ML-CATR algorithms for nonfluctuating target as well as fluctuating target. Simulation results show that RSN using our waveform diversity-based ML-ATR algorithm performs much better than single radar system for nonfluctuating targets and fluctuating targets recognition.

In our future works, we will investigate the CATR when multiple targets co-exist in RSN, and the number of targets are time-varying. In this paper, we used spatial diversity combining. For multi-target ATR, we will further investigate spatial-temporal-frequency combining for waveform diversity in RSN.

Authorized licensed use limited to: University of Texas at Arlington. Downloaded on December 18, 2009 at 14:46 from IEEE Xplore. Restrictions apply.

ACKNOWLEDGEMENT

This work was supported in part by ONR under Grant N00014-07-1-0395, N00014-03-1-0466, N00014-07-1-1024, NSF under Grant CNS-0721515, and AFOSR Summer Faculty Fellowship Program Award.

REFERENCES

[1] ONR BAA 06-016, "Command and Control and Combat Systems (C2 and CS)", http://www.onr.navy.mil/02/baa/expired.asp.

[2] ONR BAA 07-009, "Electronic Warfare Discovery and Invention (D&I)," http://www.onr.navy.mil/02/baa/.

[3] ONR BAA 07-017, "NET-SENTRIC Surveillance," http://www.onr.navy.mil/02/baa/.

[4] P. Baggenstoss, "Adaptive pulselength correction (APLECORR): a strategy for waveform optimization in ultrawideband active sonar," *IEEE Trans on Oceanic Engineering*, vol. 23, no. 1, pp. 1-11, 1998.

[5] C. E. Baum, et al, "The singularity expansion method and its application to target identification", *Proc. of the IEEE*, vol 79, no. 10, Oct 1991.

[6] M. R. Bell, "Information theory and radar waveform design", *IEEE Trans on Information Theory*, vol. 39, no. 5, pp. 1578-1597, Sept 1993.

[7] H. Deng, "Synthesis of binary sequences with good correlation and cross-correlation properties by simulated annealing," *IEEE Trans on Aerospace and Electronic Systems*, vol. 32, no. 1, Jan 1996.

[8] R. Fitzgerald, "Effects of range-doppler coupling on chirp radar tracking acuracy," *IEEE Trans on Aerospace and Eletronic Systems*, vol. 10, pp. 528-532, July 1974.

[9] T.-C. Hou and T-J. Tsai, " An access-based clustering protocol for multihop wireless ad hoc networks," *IEEE J. Selected Areas in Communications*, vol. 19, no. 7, pp. 1201-1210, July 2001.

[10] A. Iwata, C. C. Chiang, G. Pei, M. Gerla, and T. W. Chen, " Scalable routing strategies for ad hoc networks," *IEEE J. Selected Areas in Communications*, vol. 17, pp. 1369-1379, 1999.

[11] R. A. Johnson and E. L. Titlebaum, "Range Doppler Uncoupling in the Doppler Tolerant Bat Signal", *Proc. of IEEE Ultrasonics Symposium*, New York, pp. 64-67, 1972.

[12] D. Kershaw and R. Evans, "Optimal waveform selection for tracking system", *IEEE Trans on Information Theory*, vol. 40, no. 5, pp. 1536-1550, 1994.

[13] Q. Liang, X. Cheng, " KUPS: Knowledge-based Ubiquitous and Persistent Sensor Networks for Threat Assessment", submitted to *IEEE Trans on Aerospace and Electronic Systems*.

[14] C. R. Lin and M. Gerla, "Adaptive clustering in mobile wireless networks," *IEEE J. Selected Areas in Communications*, vol. 16, pp. 1265-1275, 1997.

[15] R. Niu, P. Willett, and Y. Bar-Shalom, "Tracking consideration in selection of radar waveform for range and range-rate measurements", *IEEE Transactions on Aerospace and Electronic Systems*, Vol. 38, No. 2, 2002.

[16] A. Papandreou, G. F. Boudreaux-Bartels, and S. M. Kay, "Detection and estimation of generalized chirps using time-frequency representations", *Twenty-Eighth Asilomar Conference on Signals, Systems and Computers*, vol. 1, pp. 50-54, Oct. 1994.

[17] C. E. Perkins, "Chapter 4, Cluster-Based Networks," *Ad Hoc Networking*, Edited by C. E. Perkins, pp. 75-138, Addison-Wesley, 2001.

[18] J. Roman, M. Rangaswamy, D. Davis, Q. Zhang, B. Himed, and J. Michels, "Parametric adaptive matched filter for airborne radar applications," *IEEE Trans. Aerosp. Electron. Syst.*, vol. 36, no. 2, pp. 677-692, 2000.

[19] M. A. Richards, *Fundamentals of Radar Signal Processing*, McGraw-Hill Companies, New York, 2005.

[20] T.K. Sarkar and N. Sangruji, "An adaptive nulling system for a narrow-band signal with a look-direction constraint utilizing the conjugate gradient method," *IEEE Trans. Antennas Propagat.*, vol. 37, no. 7, pp. 940-944, July 1989.

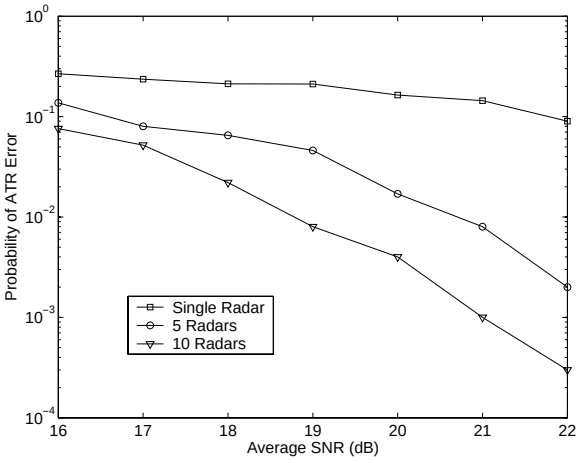
[21] M. I. Skolnik, *Introduction to Radar Systems*, 3rd ed, New York, McGraw Hill, 2001.

[22] P. Swerling, "Probability of detection for fluctuating targets", *IRE Trans on Information Theory*, vol. 6, pp. 269-308, April 1960.

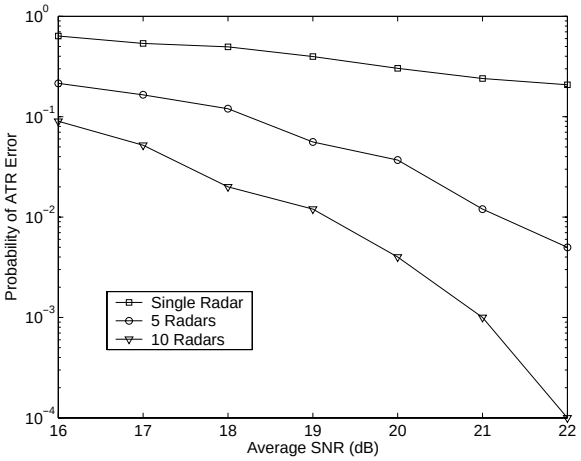
[23] Y. Sun, P. Willett, and R. Lynch, "Waveform fusion in sonar signal processing", *IEEE Transactions on Aerospace and Electronic Systems*, Vol. 40, No. 2, 2004

[24] S. Sowelam and A. Tewfik, "Waveform selection in radar target classification," *IEEE Trans on Information Theory*, vol. 46, no. 3, pp. 1014-1029, 2000.

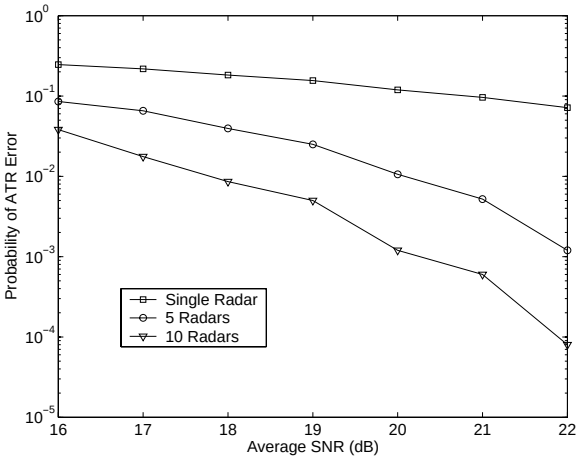
Authorized licensed use limited to: University of Texas at Arlington. Downloaded on December 18, 2009 at 14:46 from IEEE Xplore. Restrictions apply.



(a)

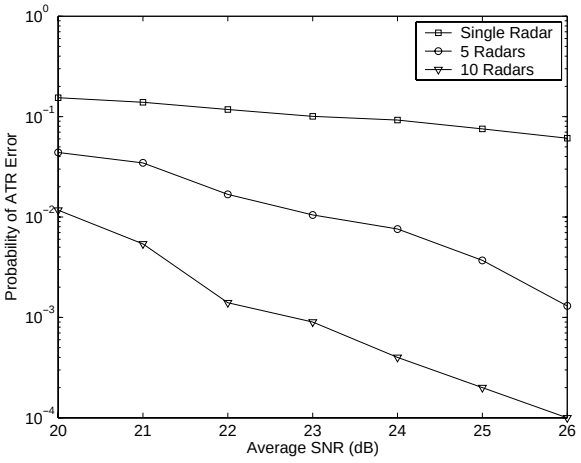


(b)

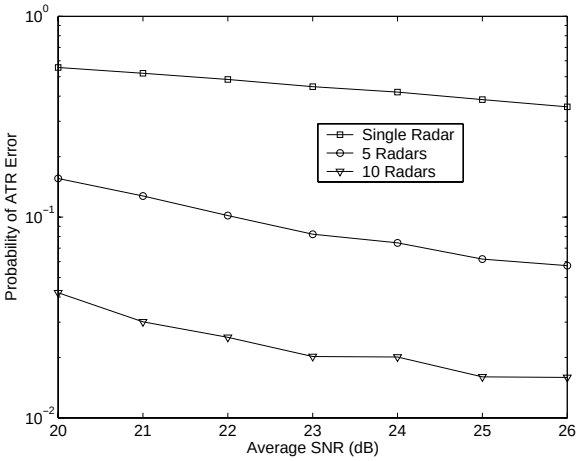


(c)

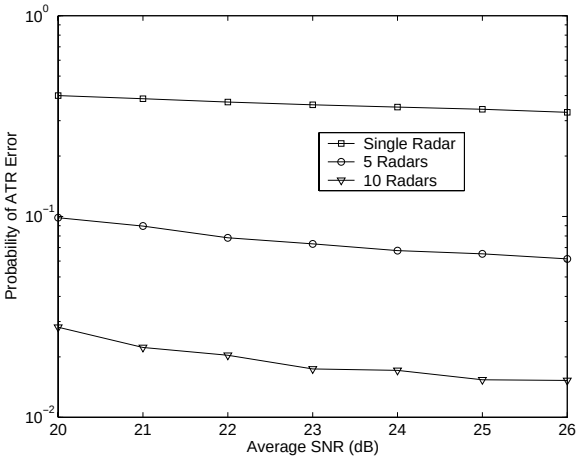
Fig. 2. Probability of ATR error for *nonfluctuating* targets at different average SNR (dB) values. (a) bird, (b) missile, (c) the average probability of ATR error for 5 targets.



(a)



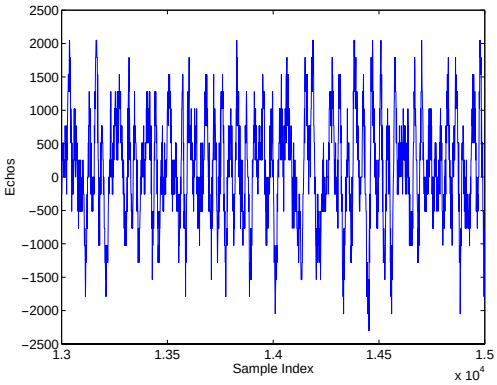
(b)



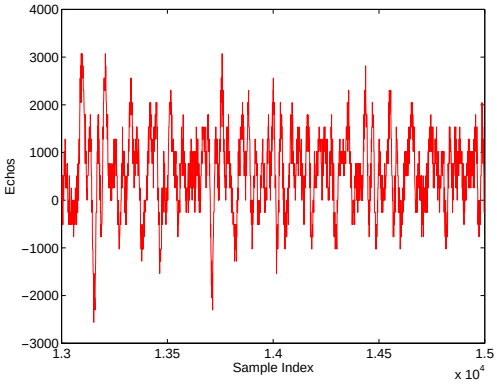
(c)

Fig. 3. Probability of ATR error for *fluctuating* targets at different average SNR (dB) values. (a) bird, (b) missile, (c) the average probability of ATR error for 5 targets.

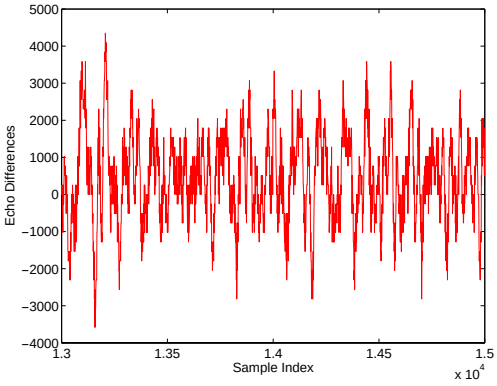
Authorized licensed use limited to: University of Texas at Arlington. Downloaded on December 18, 2009 at 14:46 from IEEE Xplore. Restrictions apply.



(a)



(b)



(c)

Fig. 4. Measurement with poor signal quality and 35 pulses average. (a) Expanded view of traces (no target) from sample 13,001 to 15,000. (b) Expanded view of traces (with target) from sample 13,001 to 15,000. (c) The differences between (a) and (b).

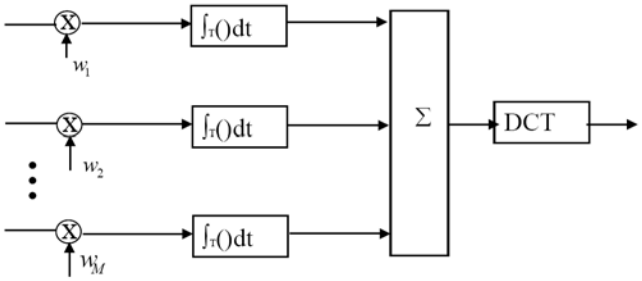
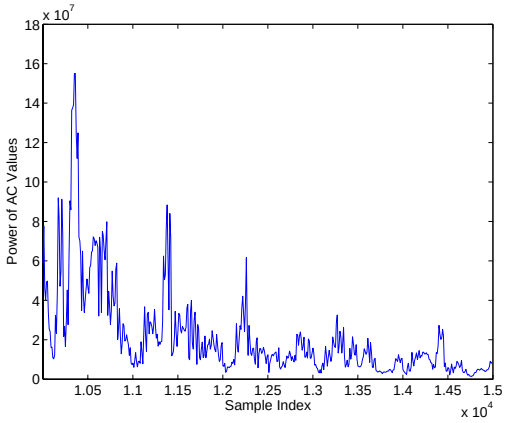
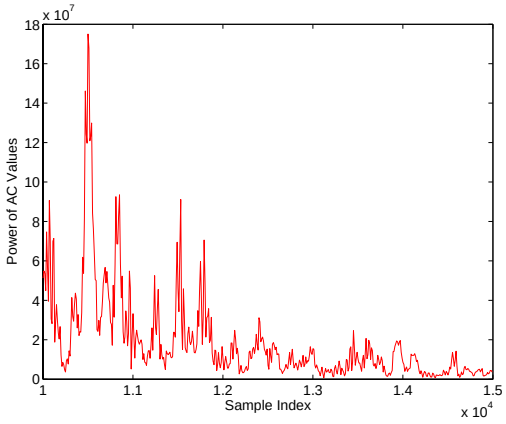


Fig. 5. Echo combining by clusterhead in RSN.



(a)



(b)

Fig. 6. Power of AC values based on UWB radar sensor networks and DCT based approach. (a) No target (b) With target in the field.

Authorized licensed use limited to: University of Texas at Arlington. Downloaded on December 18, 2009 at 14:46 from IEEE Xplore. Restrictions apply.

Collaborative Multi-Target Detection in Radar Sensor Networks

Hung D. Ly and Qilian Liang
Department of Electrical Engineering
The University of Texas at Arlington
Arlington, TX 76019-0016, USA
E-mail: ly@wcn.uta.edu, liang@uta.edu

***Abstract*— In many military and civilian applications, estimating the number of targets in a region of interest plays a primary role in performing important tasks such as target localization, classification, recognition, tracking, etc. Such an estimation problem is however very challenging since the number of targets is time-varying, targets' states are fluctuating, and various kinds of targets might appear in the field of interest. In this paper, we develop a framework for estimating the number of targets in a sensing area using Radar Sensor Networks (RSN): (1) the multi-target detection problem is formulated; (2) signals, interference (e.g., clutter, jamming, and interference between radars), and noise at radar sensors are modeled; and (3) a Maximum Likelihood Multi-Target Detection (ML-MTD) algorithm is proposed to combine received measurements and estimate the number of targets present in the sensing area. We evaluate multi-target detection performance using RSN in terms of the probability of miss-detection P_{MD} and the root mean square error (RMSE). Simulation results show that multi-target detection performance of the RSN is much better than that of single radar systems.**

I. Introduction and Motivations

Radar sensor networks (RSN) are networks of distributed radar sensors which collaboratively operate and are deployed ubiquitously on airborne, surface, and unmanned vehicles in a large geographical area. Radar sensors have capabilities for radar sensing, signal processing, and wireless communications. In RSN, radar sensors are networked together in an ad-hoc fashion, i.e., they do not depend on any preexisting infrastructure. In fact, they are self-organizing entities that are deployed on demand to perform various tasks such as surveillance, search and rescue, disaster relief, etc. RSN have advantages compared to single radar systems in improving the system sensitivity, reducing obscuration effects and vulnerability, and increasing the detection performance [2], [3].

An RSN is organized into clusters, which are independently controlled and dynamically reconfigured as sensors move, to observe targets such as tactical weapons, missiles, aircraft, ships, etc. in the surveillance area. In a cluster, sensors receive the signals backscattered by targets in the presence of interference (e.g., clutter, jamming, interference between radar sensors), and noise. Then, the observed signals from all radar sensors are forwarded to a clusterhead where received data set will be combined to perform fundamental tasks such as detection, localization, identification, classification, and tracking. For target detection problem, there are two primary levels: single target detection and multi-target detection. In the single target scenario, we proposed a diversity scheme in [13] to improve detection performance of RSN in the presence of strong interference, especially clutters, and noise. We are now interested in using RSN to estimate the number of targets present in the surveillance area. In practice, multiple moving targets might appear in the sensing area, the number of targets is time-varying, and targets' states are fluctuating. Therefore, the multi-target detection is more challenging and difficult to solve than the single target detection.

Among the existing work on multi-target detection, Yung and Mourad [16] used frequency diversity signaling to estimate the number of moving targets while Kaveh *et al.* [20] applied the information theoretic criteria to detect the number of targets. However, both work only studied the performance of their proposals for the case of two closely spaced targets. A performance analysis for a general case was provided in [19] and [18]. In [15], multiple target detection and estimation by exploiting the amplitude modulation induced by antenna scanning was proposed and a sequential hypothesis test was examined to determine the number of targets. However, all above work studied multi-target detection problem using a single radar. For the sensor network scenario, Wang *et al.* [17] applied Bayesian source number estimation to solve the distributed multiple target detection in sensor networks. Based on their approach, each cluster computed the posterior probability corresponding to each hypothesis on the number of sources and a central processor fused posterior probabilities using Bayes' theorem to select the best hypothesis. Their proposal however did not consider Doppler shifts of the targets and was not suitable for the multi-target detection in RSN.

In this paper, we develop a framework for estimating the number of targets in the field of interest using RSNs. At the ith sensor, we deploy a receiver with an K element-ULA (Uniform Linear Array) whose spacing between elements is d_i. During the observation time, P pulses are transmitted to track targets. The useful signals backscattered from targets include spatial-temporal snapshots of targets and parameters representing radar cross section of targets. Then, a RSN-clusterhead collects measurements from all radar sensors and combines them to perform detection procedures. To fuse

1-4244-1513-06/07/$25.00 ©2007 IEEE

Authorized licensed use limited to: University of Texas at Arlington. Downloaded on December 18, 2009 at 14:47 from IEEE Xplore. Restrictions apply.

received measurements and estimate the unknown number of targets in the area of interest, at the RSN-clusterhead, we propose a multi-target detection algorithm which is Maximum Likelihood Multi-Target Detection (ML-MTD) algorithm. We use the probability of miss-detection P_{MD} and the root mean square error (RMSE) as metrics to evaluate multi-target detection performance using RSN. Simulation results show that detection performance of the RSN is much better than that of a single radar system.

The rest of this paper is organized as follows. In Section II, we state our multi-target detection problem. In Section III, we model signals, interference, and noise at radar sensors. In Section IV, an ML-MTD algorithm to estimate the number of targets present in the sensing field is proposed. Multi-target detection performance of RSN is discussed in Section V while conclusions and open directions are given in Section VI.

II. Multi-Target Detection Problem Statement

In this paper, we address a realistic situation in which the number of targets to be detected is generally unknown and has to be estimated. To handle our problem, an RSN consisting of N radar sensors is deployed. Radar sensors receive signals embedded in interference and forward them to a central processor, e.g., a clusterhead to perform detection tasks. At the RSN-clusterhead, we propose a detection algorithm to estimate the number of targets. To support the rest of the paper, we make some assumptions as follows:

- Targets evolve along independent trajectories and do not leave the surveillance area during the entire observation time of P consecutive pulses.
- Targets are modeled as Swerling II target models whose magnitudes fluctuate independently from pulse to pulse according to a chi-square probability density function.
- The locations of targets are unknown. Besides, Doppler frequencies when targets are moving relatively to radar platforms are uncertain.
- Observation data or measurements from radar sensors, at the RSN-clusterhead, are statistically independent. The measurements furthermore either originate from true targets or clutters.

The estimated number of targets present in the surveillance area is determined as

$$\{\hat{\tau}_1, \hat{\tau}_2, ..., \hat{\tau}_N\} = \arg \min_{\tau_1, \tau_2, ..., \tau_N} \Lambda(\tau). \quad (1)$$

where $\hat{\tau}_i$ is the estimated number of targets at sensor i and $\Lambda(\tau)$ is an utility function derived in IV. Hence, the possible number of targets $\widehat{M}$ that RSN can detect is the average value of $\hat{\tau}_1, \hat{\tau}_2, ...,$ and $\hat{\tau}_N$, i.e.,

$$\widehat{M} = \lceil \frac{1}{N} \sum_{i=1}^{N} \hat{\tau}_i \rceil. \quad (2)$$

where $\lceil \cdot \rceil$ denotes a ceil operation.

III. Signal and Interference Models

A. Signal Models

At radar sensor i, we deploy a receiver with an K-element ULA whose spacing between elements is d_i. If P pulses are processed in a coherent pulse interval, the snapshot of target m is a $KP \times 1$ spatial-temporal steering vector with the following form [1], [9]:

$$\mathbf{e}(\theta_{im}, f_{im}) = \mathbf{b}_t(f_{im}) \otimes \mathbf{a}_s(\theta_{im}). \quad (3)$$

where f_{im} and θ_{im} are the normalized Doppler shift and normalized angle for the target m, respectively. The notation $\otimes$ denotes the Kronecker product, $\mathbf{b}_t(f_{im})$ is a $P \times 1$ Doppler steering vector, and $\mathbf{a}_s(\theta_{im})$ is a $K \times 1$ spatial steering vector. $\mathbf{b}_t(f_{im})$ and $\mathbf{a}_s(\theta_{im})$ are defined as follows:

$$\mathbf{b}_t(f_{im}) = [1 \quad e^{j2\pi f_{im}} \quad ... \quad e^{j2\pi(P-1)f_{im}}]^T. \quad (4)$$

$$\mathbf{a}_s(\theta_{im}) = [1 \quad e^{-j2\pi\theta_{im}} \quad ... \quad e^{-j2\pi(K-1)\theta_{im}}]^T. \quad (5)$$

where T denotes the transpose operation. Let ϕ_{im} be an angle that sensor i observes the mth target, $f_{max,m}$ be the maximum Doppler frequency for target m, and T_p be the pulse duration. The normalized angle θ_{im} for target m and the normalized Doppler shift f_{im} when target m is moving relatively to sensor platform i are computed as [9]

$$\theta_{im} = \frac{d_i \sin\phi_{im}}{\lambda_i} \quad (6)$$

$$f_{im} = 4 f_{max,m} T_p \theta_{im} \quad (7)$$

We now assume that radar sensor i can detect M_i targets during the observation time. The received signal vector $\mathbf{z}_i(u,t)$ at sensor i is the superposition of signals reflected from M_i targets, interference, and noise.

$$\begin{aligned} \mathbf{z}_i(u,t) &= \sum_{m=1}^{M_i} \mathbf{e}(\theta_{im}, f_{im}) \alpha_m(u) s_{mi}(t) + \mathbf{w}_i, \\ &= \mathbf{A}(\theta_i, f_i)\mathbf{s}_i(u,t) + \mathbf{w}_i, \quad i = 1, 2, ..., N. \end{aligned} \quad (8)$$

where

- $\mathbf{A}(\theta_i, f_i) = [\mathbf{e}(\theta_{i1}, f_{i1}), \mathbf{e}(\theta_{i2}, f_{i2}), ..., \mathbf{e}(\theta_{iM_i}, f_{iM_i})]$ is the $PK \times M_i$ target response matrix. $\mathbf{e}(\theta_{im}, f_{im})$ is a spatial-temporal steering vector that models the mth target return at angle θ_{im} and Doppler shift f_{im}.
- $\mathbf{s}_i(u,t) = [\alpha_1(u)s_{1i}(t), \alpha_2(u)s_{2i}(t), ..., \alpha_{M_i}(u)s_{M_i i}(t)]^T$ is the $M_i \times 1$ target signal vector with a random variable $\alpha_m(u)$ that models the radar cross section (RCS) of the target m and $s_{mi}(t)$ is the waveform reflected from target m.
- $\mathbf{w}_i = \mathbf{w}_{ci} + \mathbf{w}_{ji} + \mathbf{w}_{si} + \mathbf{n}_i$ represents the overall interference and noise: a clutter vector $\mathbf{w}_{ci}$, a jamming vector $\mathbf{w}_{ji}$, an interference vector between radar sensors $\mathbf{w}_{si}$, and thermal noise $\mathbf{n}_i$.

Authorized licensed use limited to: University of Texas at Arlington. Downloaded on December 18, 2009 at 14:47 from IEEE Xplore. Restrictions apply.

Received signals from radar sensors are forwarded to a central controller, e.g., clusterhead. Then, these received signal vectors $\mathbf{z}_i(u,t)$ are fused to make estimation operations. Since $\mathbf{z}_i(u,t)$ is a zero-mean Gaussian vector, the probability density function of $\mathbf{z}_i(u,t)$ can be presented as

$$f(\mathbf{z}_i(u,t)) = \frac{\exp\{-\frac{1}{2}\mathbf{z}_i^H[\mathbf{R}_{z,i}^{(\tau_i)}]^{-1}\mathbf{z}_i\}}{(2\pi)^{\frac{KP}{2}}|\mathbf{R}_{z,i}^{(\tau_i)}|^{\frac{1}{2}}}. \quad (9)$$

where $\mathbf{R}_{z,i}^{(\tau_i)}$ is the covariance matrix of $\mathbf{z}_i(u,t)$, τ_i is the rank of $\mathbf{R}_{z,i}$, and $|\cdot|$ denotes the determinant of the matrix.

B. Interference and Noise Models

As pointed out, at the ith radar sensor, the interference vector $\mathbf{w}_i$ is the sum of clutter $\mathbf{w}_{ci}$, jamming $\mathbf{w}_{ji}$, and interference between sensors $\mathbf{w}_{si}$. We apply the waveform design algorithm proposed in [12] to have waveforms at sensors be orthogonal. By doing so, interference between sensors is insignificant, i.e., $\mathbf{w}_{si} \simeq \mathbf{0}$. Following are characteristics and models of clutter, jamming, and thermal noise at radar sensor i.

1) Clutter: Clutter generates undesired radar returns that may interfere with the desired signal. In RSN, the signal-to-clutter ratio (SCR) is often more important than the signal-to-noise ratio (SNR). The integrated clutter can be generally approximated as the sum of N_{ci} clutter patches. For clutter patch k, the space-time data vector is modeled as [9]

$$\begin{aligned}\mathbf{p}_{ki} &= \xi_{ki}\mathbf{b}_t(f_{ki}) \otimes \mathbf{a}_s(\theta_{ki}) \\ &= \xi_{ki}\mathbf{u}_{ki}, \quad k = 1,2,...,N_{ci}. \end{aligned} \quad (10)$$

where ξ_{ki} is a complex random variable that accounts for the amplitude and phase of clutter patch k. $\mathbf{u}_{ki} = \mathbf{b}_t(f_{ki}) \otimes \mathbf{a}_s(\theta_{ki})$ where $\mathbf{b}_t(f_{ki})$ and $\mathbf{a}_s(\theta_{ki})$ are temporal vector and spatial vector of clutter patch k, respectively. f_{ki} and θ_{ki} are the normalized Doppler shift and angle of arrival of the kth clutter patch, respectively. Total clutter vector $\mathbf{w}_{ci}$ equals to

$$\begin{aligned}\mathbf{w}_{ci} &= \sum_{k=1}^{N_{ci}} \xi_{ki}\mathbf{b}_t(f_{ki}) \otimes \mathbf{a}_s(\theta_{ki}) \\ &= \sum_{k=1}^{N_{ci}} \xi_{ki}\mathbf{u}_{ki}. \end{aligned} \quad (11)$$

The $KP \times KP$ covariance matrix of the clutter $\mathbf{R}_{ci}$ at the ith radar is given by

$$\begin{aligned}\mathbf{R}_{ci} &= E\{\mathbf{w}_{ci}\mathbf{w}_{ci}^H\} \\ &= \sum_{k=1}^{N_{ci}}\sum_{j=1}^{N_{ci}} E\{\xi_i\xi_j^H\}\mathbf{u}_{ki}\mathbf{u}_{ji}^H, \\ &= \sigma_{ci}^2\mathbf{M}_{ci}. \end{aligned} \quad (12)$$

where H denotes the Hermitian operation, $E\{\cdot\}$ denotes the expectation, and $\mathbf{M}_{ci}$ is the normalized covariance matrix, i.e., all diagonal entries of $\mathbf{M}_{ci}$ are ones.

2) Jamming: Jamming signals are generated by hostile interfering signal sources that seek to degrade the performance of radar sensors by mechanisms such as degrading signal-to-interference-plus-noise ratio (SINR) by increasing the noise level, or generating false detections to overwhelm RSN with false targets. A model for N_{ji} jamming signals is commonly presented as [1]

$$\mathbf{w}_{ji} = \sum_{l=1}^{N_{ji}} \beta_l \otimes a_{ji}(\theta_l), \quad i = 1,2,...,N. \quad (13)$$

where β_l contains voltage samples of the lth jamming waveform and $a_{ji}(\theta_l)$ is the jamming signal waveform at an angle θ_l. The different jamming waveforms are uncorrelated with each other.

3) Thermal Noise: Among noise existing in RSN, thermal noise due to ohmic losses at the radar receiver is normally dominant. We model the thermal noise vector $\mathbf{n}_i$ at radar sensor i as a complex white Gaussian vector with zero-mean and covariance σ_{ni}^2. The covariance matrix of noise $\mathbf{R}_{ni} = \sigma_{ni}^2\mathbf{I}$ where $\mathbf{I}$ is the $KP \times KP$ identity matrix.

In RSN, detection performance is largely affected by clutters. So we will consider the disturbance at the ith radar as a sum of thermal noise and clutter. The disturbance covariance matrix $\mathbf{R}_{wi}$ is given by

$$\begin{aligned}\mathbf{R}_{wi} &= E\{\mathbf{w}_i\mathbf{w}_i^H\} \\ &= \mathbf{R}_{ni} + \varepsilon_{ci}(h)\mathbf{R}_{ci}. \end{aligned} \quad (14)$$

where $\mathbf{R}_{ni}$ and $\mathbf{R}_{ci}$ are the covariance matrices of noise and clutter, respectively. $\varepsilon_{ci}(h)$ is a random variable used to model the clutter power of the hth range cell. $\varepsilon_{ci}(h)$ often follows Weibull distribution for ground clutter or gamma distribution for sea and/or weather clutter [14][21]. In homogeneous environments, the average clutter power does not depend on h, i.e., $\varepsilon_{ci}(h)$ is constant. Therefore, the disturbance covariance matrix is rewritten as

$$\begin{aligned}\mathbf{R}_{wi} &= \sigma_{wi}^2\mathbf{M}_{wi} \\ &= \sigma_{ni}^2\mathbf{I} + \varepsilon_c\sigma_{ci}^2\mathbf{M}_{ci}. \end{aligned} \quad (15)$$

where σ_{wi}^2 is the total disturbance power and $\mathbf{M}_{wi}$ is the normalized disturbance covariance matrix.

$$\mathbf{M}_{wi} = \frac{1}{CNR_i + 1}\mathbf{I} + \frac{CNR_i}{CNR_i + 1}\mathbf{M}_{ci}. \quad (16)$$

with $CNR_i = \frac{\varepsilon_c\sigma_{ci}^2}{\sigma_{ni}^2}$ is the clutter-to-noise power ratio. Then, total interference and noise can be modeled as a complex zero-mean white Gaussian vector with the covariance matrix $\sigma_{wi}^2\mathbf{M}_{wi}$, i.e., $\mathbf{w}_i \sim \mathcal{CN}(0, \sigma_{wi}^2\mathbf{M}_{wi})$.

IV. Maximum Likelihood Multi-Target Detection (ML-MTD) Algorithm

In this section, we develop an algorithm to detect the number of targets in the sensing region. We assume that signals

Authorized licensed use limited to: University of Texas at Arlington. Downloaded on December 18, 2009 at 14:47 from IEEE Xplore. Restrictions apply.

backscattered from targets and interference are uncorrelated. From the signal model in (8), the covariance matrix of received signal $\mathbf{z}_i(u,t)$ at radar sensor i is given by

$$\begin{aligned}\mathbf{R}_{z,i}^{(\tau_i)} &= E\{\mathbf{z}_i(u,t)\mathbf{z}_i^H(u,t)\},\\ &= \mathbf{A}(\theta_i,f_i)\mathbf{R}_{s,i}\mathbf{A}^H(\theta_i,f_i)+\sigma_{wi}^2\mathbf{M}_{wi},\\ &= \mathbf{\Phi}_i^{(\tau_i)}+\sigma_{wi}^2\mathbf{M}_{wi}. \end{aligned} \quad (17)$$

where $\mathbf{R}_{s,i}$ is a $M_i \times M_i$ positive definite matrix which represents the covariance matrix of the signal $\mathbf{s}_i(u,t)$, σ_{wi}^2 is the disturbance power, and $\mathbf{M}_{wi}$ is the normalized disturbance covariance matrix at radar sensor i. $\mathbf{R}_{s,i}$ and $\mathbf{\Phi}_i^{(\tau_i)}$ are defined:

$$\mathbf{R}_{s,i} = E\{\mathbf{s}_i(u,t)\mathbf{s}_i^H(u,t)\} \quad (18)$$

$$\mathbf{\Phi}_i^{(\tau_i)} = \mathbf{A}(\theta_i,f_i)\mathbf{R}_{s,i}\mathbf{A}^H(\theta_i,f_i) \quad (19)$$

The random variables $\alpha_m(u)$ $(i=1,2,...,M_i)$ in $\mathbf{s}_i(u,t)$ models the RCS of the mth target. In [11], Swerling proposed five target models called Swerling models where Swerling V model is for non-fluctuating targets and Swerling I-IV models are for fluctuating targets. In this paper, we focus our studies on the Swerling II target models. We know that magnitude of the RCS $|\alpha(u)|$ for Swerling II targets fluctuates independently from pulse to pulse according to a chi-square probability density function with two degree of freedom, i.e., a Rayleigh probability density function. Therefore, the RCS of target m can be modeled as a Gaussian random variables. That is,

$$\alpha_m(u) = \alpha_{Im}(u) + j\alpha_{Qm}(u). \quad (20)$$

where $\alpha_{Im}(u)$ and $\alpha_{Qm}(u)$ follow Gaussian distribution with zero mean and variance $\rho_m^2/2$ for each branch I, Q.

From (17), it follows that the rank of matrix $\mathbf{R}_{z,i}^{(\tau_i)}$ is τ_i, which is equal to the number of targets M_i present in the surveillance region, and the smallest $(KP-\tau_i)$ of its eigenvalues are zero, i.e., the received signal contains interference and noise only. Sorting the eigenvalues of $\mathbf{R}_{z,i}^{(\tau_i)}$ in a decreasing order, we obtain

$$\lambda_1 \geq \lambda_2 \geq ... \geq \lambda_{\tau_i} \geq \lambda_{\tau_i+1}. \quad (21)$$

$$\lambda_{\tau_i+1} = \lambda_{\tau_i+2} = ... = \lambda_{KP} = \sigma_{wi}^2. \quad (22)$$

Assume that measurements $\mathbf{z}_i(u,t)$, at the clusterhead, are statistically independent complex Gaussian random vectors with zero mean. The joint probability density function of these random vectors has the form:

$$\begin{aligned} f(\mathbf{z}(u,t)) &= \prod_{i=1}^{N} f(\mathbf{z}_i(u,t)),\\ &= \prod_{i=1}^{N} \frac{\exp\{-\frac{1}{2}\mathbf{z}_i^H[\mathbf{R}_{z,i}^{(\tau_i)}]^{-1}\mathbf{z}_i\}}{(2\pi)^{\frac{KP}{2}}|\mathbf{R}_{z,i}^{(\tau_i)}|^{\frac{1}{2}}}. \end{aligned} \quad (23)$$

Basically, we have to estimate $\hat{\tau}_i$ such that the joint probability density function $f(\mathbf{z}(u,t))$ is maximized. We now define a log-likelihood function $\Gamma(\tau)$ $\{\tau=[\tau_1,\tau_2,...,\tau_N]\}$ in (24). Hence, our mission is to find $\hat{\tau}_i$ such that $\Gamma(\tau)$ is minimized.

$$\begin{aligned}\Gamma(\tau) &= -\ln f(\mathbf{z}(u,t)),\\ &= \frac{N\times KP}{2}\ln(2\pi)+\frac{1}{2}\sum_{i=1}^{N}\log|\mathbf{R}_{z,i}^{(\tau_i)}|+\\ &+ \frac{1}{2}\sum_{i=1}^{N}\mathbf{z}_i^H[\mathbf{R}_{z,i}^{(\tau_i)}]^{-1}\mathbf{z}_i. \end{aligned} \quad (24)$$

Omitting terms that are independent of τ_i, we find the log-likelihood function $\Gamma(\tau)$.

$$\Gamma(\tau) = \sum_{i=1}^{N}\log|\mathbf{R}_{z,i}^{(\tau_i)}| + \sum_{i=1}^{N}\mathbf{z}_i^H[\mathbf{R}_{z,i}^{(\tau_i)}]^{-1}\mathbf{z}_i. \quad (25)$$

From [6], [8], and [7], the utility function $\Lambda(\tau)$ takes the form:

$$\Lambda(\tau) = \Gamma(\tau) + P(N). \quad (26)$$

where $P(N) = \wp(N)[\tau_{avg}(2KP-\tau_{avg})]$ is a bias correction term or penalty function to make estimate unbiased. τ_{avg} is an average value of $\{\tau_i | i=1,2,...,N\}$ and $\wp(N)$ is a penalty coefficient which is a constant function of N. For example, $\wp(N)=1$ for the Akaike information criterion (AIC) and $\wp(N)=\frac{1}{2}\ln N$ for the minimum description length (MDL). $\Lambda(\tau)$ then can be rewritten as

$$\begin{aligned}\Lambda(\tau) &= \sum_{i=1}^{N}\log|\mathbf{R}_{z,i}^{(\tau_i)}| + \sum_{i=1}^{N}\mathbf{z}_i^H[\mathbf{R}_{z,i}^{(\tau_i)}]^{-1}\mathbf{z}_i +\\ &+ \wp(N)\{\tau_{avg}(2KP-\tau_{avg})\}. \end{aligned} \quad (27)$$

Our ML-MTD algorithm to detect the number of targets $\widehat{M}$ present in the sensing field now can be expressed as

$$\widehat{M} = \lceil \frac{1}{N}\sum_{i=1}^{N}\hat{\tau}_i \rceil. \quad (28)$$

where $\hat{\tau} = \{\hat{\tau}_1,\hat{\tau}_2,...,\hat{\tau}_N\}$ is computed as

$$\{\hat{\tau}_1,\hat{\tau}_2,...,\hat{\tau}_N\} = \arg\min_{\tau_1,\tau_2,...,\tau_N}\Lambda(\tau). \quad (29)$$

In practice, sensors can observe the different numbers of targets, i.e., τ_is may not be equal, since targets might not be exposed to all sensors. However, for the sake of simplicity, we assume that all radar sensors can observe the same number of targets, i.e., $\tau_1=\tau_2=...=\tau_N=\tau$ and energy backscattered from targets is similar at radar sensors. Furthermore, we assume that the environment is homogeneous, that is, the average clutter power is a constant. These assumptions imply that $\mathbf{R}_{z,1}^{(\tau)}=\mathbf{R}_{z,2}^{(\tau)}=\mathbf{R}_{z,N}^{(\tau)}=\mathbf{R}_z^{(\tau)}$. For those reasons, our ultimate purpose is to evaluate detection performance improvement achievable by exploiting the networking of multiple radar sensors. Under our assumptions, the utility function $\Lambda(\tau)$ can be simplified as

Authorized licensed use limited to: University of Texas at Arlington. Downloaded on December 18, 2009 at 14:47 from IEEE Xplore. Restrictions apply.

$$\Lambda(\tau) = N \log |\mathbf{R}_z^{(\tau)}| + N\mathbf{tr}([\mathbf{R}_z^{(\tau)}]^{-1}\mathbf{Y}) + \wp(N)\{\tau(2KP-\tau)\}. \quad (30)$$

where $\mathbf{tr}(\cdot)$ denotes the trace of a matrix and $\mathbf{Y}$ is the sample covariance matrix of $\mathbf{z}_1, \mathbf{z}_2, ..., \mathbf{z}_N$.

$$\mathbf{Y} = \frac{1}{N}\sum_{i=1}^{N} \mathbf{z}_i \mathbf{z}_i^T. \quad (31)$$

Based on (30) and (31), we can observe that the utility function $\Lambda(\tau)$ depends on the number of radar sensors N. Our ML-MTD algorithm is used to determine any non-negative integer τ to minimize the utility function $\Lambda(\tau)$ when the number of radars is changed. Achieved results are analyzed to evaluate the multi-target detection performance in Section V.

V. Multi-Target Detection Performance Analysis

We denote the true number of targets appearing in the observation area and the number of targets we can estimate from received signals as M and $\widehat{M}$, respectively. The probability of miss detection P_{MD} and the root mean square error (RMSE) are used as metrics to evaluate detection performance of the RSN using our proposed algorithm. We define P_{MD} and RMSE as follows:

- P_{MD} is the probability that the estimated number of targets is smaller than the true number of targets. Suppose that ω_{md} is the number of estimations in which the estimated number of targets is smaller than the true number of targets and ω_t is the total number of estimations. P_{MD} is given as

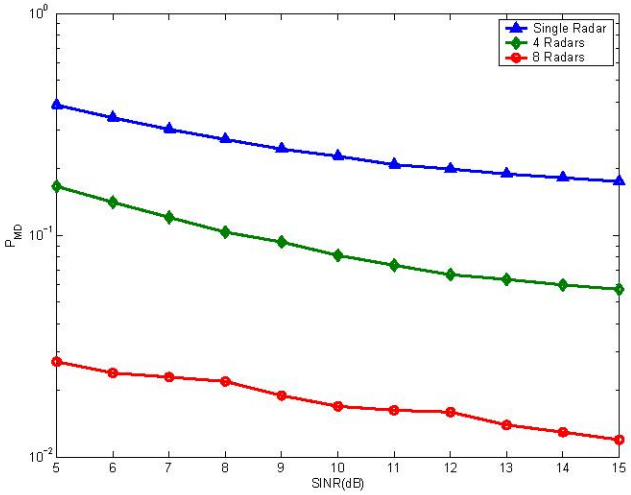
$$P_{MD} = P(\widehat{M} < M) = \frac{\omega_{md}}{\omega_t}. \quad (32)$$

- RMSE is used to determine the vibration of the estimated number of targets $\widehat{M}$ around the true number of targets M.

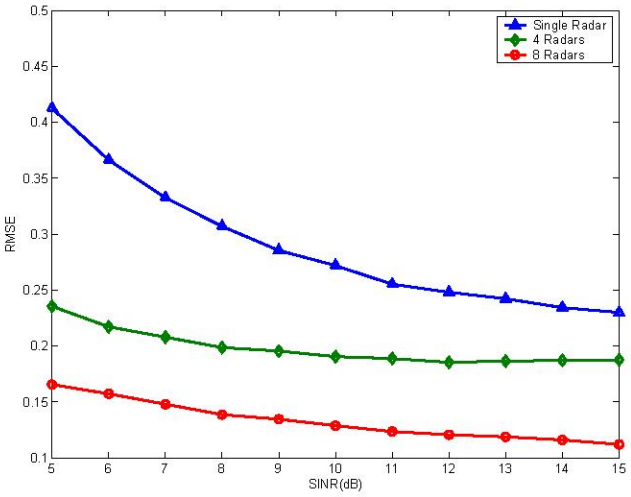
$$RMSE = \sqrt{\frac{1}{\omega_t}\sum_{g=1}^{\omega_t}(M - \widehat{M}_g)^2}. \quad (33)$$

To study the MTD performance, we setup parameters for the RSN and targets as follows.

1) Spacing d_i between elements of the K-element ULA at radar sensor i is chosen to be a half of the wavelength λ_i, i.e., $d_i = \frac{\lambda_i}{2}$.
2) The pulse duration (T_p) is 1 ms.
3) The number of elements (K) in ULA is 5.
4) The number of pulses (P) in a coherent pulse interval is 4.
5) To observe targets, we assume that θ_{im} is a random variable which follows a uniform distribution in an interval [-0.5, 0.5].
6) The maximum Doppler frequencies for targets are similar, e.g., $f_{max} = 5000$Hz. The normalized Doppler shift f_{im} only depends on the random variable θ_{im}.



(a)



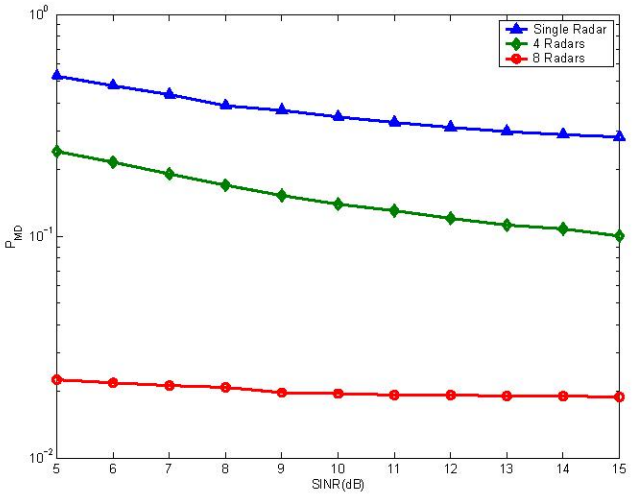
(b)

Fig. 1: P_{MD} and RMSE vs. Average SINR, M=3

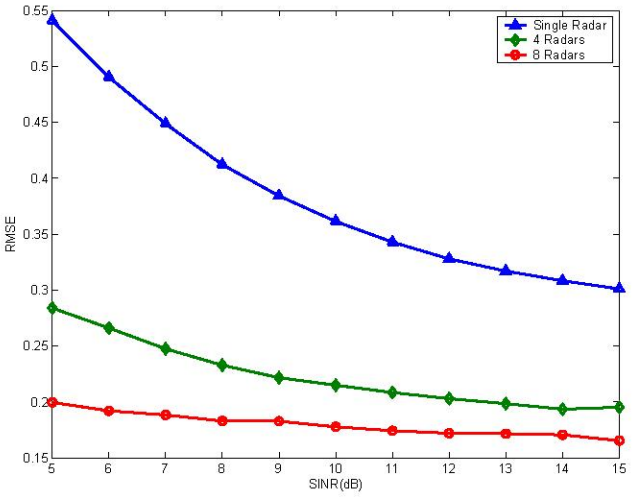
7) Average Signal-to-Interference-plus-Noise Ratio (SINR) refers to average SINR of all radars in RSN. We examine detection performance of RSN with average SINR in an interval [5dB, 15dB].
8) The MDL criterion is used for the penalty function.
9) 10^5 estimations are performed, i.e., $\omega_t = 10^5$.

We first examine the case in which there are three targets in surveillance region, i.e., $M = 3$. Single radar system, 4-radar RSN, and 8-radar RSN are employed to detect these targets. At each average SINR, the estimated number of targets is compared to the true number of targets to compute P_{MD} and RMSE which are drawn in Fig. 1 for this case. After that, we increase the number of targets into four, i.e., $M = 4$. Using the same RSN as the previous case, we can get P_{MD} and RMSE as plotted in Fig. 2. Based on achieved results in Fig. 1a and Fig. 2a, we can realize that miss-detection probability of 4-radar RSN and 8-radar RSN is much smaller than that of single radar system. This implies that detection

Authorized licensed use limited to: University of Texas at Arlington. Downloaded on December 18, 2009 at 14:47 from IEEE Xplore. Restrictions apply.



(a)



(b)

Fig. 2: P_{MD} and RMSE vs. Average SINR, M=4

performance of 4-radar RSN and 8-radar RSN is improved. For example, to achieve the same $P_{MD} = 10\%$ which is good enough according to Skolnik [4], the average SINR required for 4-radar RSN to detect three targets is about 9dB while the average SINR required for the single radar system is greater than 15dB. This means that detection performance gain of the 4-radar RSN is greater than 6dB. In both cases, moreover, the probability of miss-detection is vastly reduced when the 8-radar RSN is used.

Furthermore, we observe that the higher average SINR, the smaller probability of miss-detection. The reason is that, at high average SINR, radar sensors radiate signals at a high power level, so the coverage area of radar sensors is large. However, radiating signals at high power levels is costly. Thus tradeoff between cost and detection performance is necessary. We also observe that when we increase the number of targets, the detection performance is slightly reduced. For example, to achieve the same $P_{MD} = 10\%$, the 4-radar RSN to detect four targets requires average SINR around 4dB higher than that to detect three targets. This means that we need increase the transmit power for radar sensors. If the number of sensor radars is however large, e.g. $N = 8$, the detection performance of the RSN does not change much.

Besides the miss-detection probability, RMSE is the other metric to examine the detection performance of the RSN. RMSE helps us evaluate the variability of the estimated number of targets around the true number of targets present in the sensing field. From Fig. 1b and Fig. 2b, we note that, to estimate three or four targets, RMSE of a single radar system is very high while RMSE of RSN is reduced tremendously. For example, at SINR = 9dB, compared to a single radar system, the 4-radar RSN can reduce RMSE by 31.52% for three target case and 42.32% for four target case. Moreover, we can see that RMSE is reduced when we increase the number of sensors and/or average SINR.

VI. Conclusions

We investigate a multi-target detection problem in Radar Sensor Networks. Signal, interference, and noise models at radar sensors are presented and analyzed. We also propose a Maximum Likelihood Multi-Target Detection algorithm to estimate the possible number of targets in a surveillance area. RSN-clusterhead utilizes our algorithm to combine measurements from radar sensors and make decision. Achieved results show that detection performance of our RSN is much better than that of a single radar system in terms of the miss-detection probability and the root mean square error. Besides scenarios presented in our work, one can extend our proposal in several directions as follows:

1) For the sake of simplicity, we assumed clutter environment which affects largely the performance of RSN is homogeneous. Multi-target detection therefore can be examined when heterogeneous clutter environment is considered.
2) We only consider target models as small moving point-like targets. Thus dynamic and state space-based models might be further studied.
3) We only examine the case in which Swerling II target models are present in the sensing area. Naturally, multiple target model types can appear during the observation time, so multi-target detection problem when multiple target models coexist in the sensing region is worth looking into.
4) Our proposal is a primary state for important tasks such as target recognition, classification, tracking, etc. A joint algorithm to combine multi-target detection and one of above tasks can be investigated.

Acknowledgement

This work was supported by the U.S. Office of Naval Research (ONR) Young Investigator Program Award under Grant N00014-03-1-0466 and ONR Award under Grant N00014-07-1-0395.

Authorized licensed use limited to: University of Texas at Arlington. Downloaded on December 18, 2009 at 14:47 from IEEE Xplore. Restrictions apply.

REFERENCES

[1] William L. Melvin, "A STAP Overview," *IEEE A&E Systems Magazine*, vol 19, no. 1, pp. 19-35, Jan. 2004.

[2] S. Kadambe, "Feature discovery and sensor discrimination in a network of distributed radar sensors for target tracking," HRL Laboratories, LLC, 2001.

[3] C.J. Baker, A.L.Hume, "Netted Radar Sensing," *IEEE A&E Systems Magazine,* Feb. 2002.

[4] Skolnik, *Introduction to Radar Systems*, 3rd ed, McGraw Hill, 2001.

[5] M. Wax and T. Kailath, "Detection of signals by information theoretic criteria," *IEEE Transactions on Acoustics, Speech, and Signal Processing,* vol 33, no.2, pp 387-392, April 1985.

[6] H. Akaike, "A new look at the statistical model identification," *IEEE Transactions on Automatic Control,* vol 19, pp 716-723, Dec. 1974.

[7] G. Schwartz, "Estimating the dimension of a model," *Annals of Statistics,* vol. 6, pp. 497-511, 1978.

[8] J. Rissanen, "A universal prior for intergers and estimation by minimum description length," *Annals of Statistics,* vol. 11, no. 2, pp. 431-466, 1983.

[9] J.R Guerci, *Space-Time Adaptive Processing for Radar*, Artech House, 2003.

[10] Mark A. Richards, *Fundamentals of Radar Signal Processing*, McGraw-Hill Companies, New York 2005.

[11] Swerling, P., "Probability of Detection for Fluctuating Targets," *IRE Transactions on Information Theory,* vol IT-6, pp. 269-308, April 1960.

[12] Q. Liang, "Radar Sensor Networks: Algorithms for Waveform Design and Diversity with Application to ATR with Delay-Doppler Uncertainty," *EURASIP Journal on Wireless Communications and Networking,* Volume 2007, 2007.

[13] Hung D. Ly and Q. Liang, "Spatial-Temporal-Frequency Diversity in Radar Sensor Networks," *Military Communications Conference (MILCOM 2006),* Oct. 2006, Washington, DC.

[14] R. Nitzberg, "An effect of range-heterogeneous clutter on adaptive doppler filters," *IEEE Transaction on Aerospace and Electronic Systems,* vol 26, no.3, pp 475-480, May 1990.

[15] Fulvio Gini *et al.*, "Multiple target detection and estimation by exploiting the amplitude modulation induced by antenna scanning. Part II: Detection," IEEE ICASSP, pp 533-536, 2003.

[16] Y. D. Huang and M. Barkat, "On estimation of number of moving targets via frequency-diversity signaling," *Proceedings of the 32nd Midwest Symposium on Circuits and Systems,* vol.2, pp 1170-1173, Aug. 1989.

[17] X. Wang, H. Qi, H. Du, "Distributed source number estimation for multiple target detection in sensor networks," *IEEE Workshop on Statistical Signal Processing,* pp 395-398, MO, Sept. 2003.

[18] Q. T. Zhang *et al.*, "Statistical Analysis of the performance of Information Theoretic Criteria in the detection of the number of signals in array processing," *IEEE Trans. on Acoustics, speech, and signal processing,* pp 1557-1565, vol. 37, no.10, Oct. 1989.

[19] W. Xu and M. Kaveh, "Analysis of the performance and sensitivity of Eigendecomposition-based detectors," *IEEE Trans. on signal processing,* vol. 43, no.6, Jun. 1995.

[20] M. Kaveh *et al.*, "On the theoretical performance of a class of estimators of the number of narrow-band sources," *IEEE Trans. on Acoustics, speech, and signal processing,* no.9, Sept. 1987.

[21] William L. Melvin, "Space-time adaptive radar performance in heterogeneous clutter," *IEEE Transaction on Aerospace and Electronic Systems,* vol 36, no.2, pp 621-633, April 2000.

Authorized licensed use limited to: University of Texas at Arlington. Downloaded on December 18, 2009 at 14:47 from IEEE Xplore. Restrictions apply.

EXPERIMENTAL PATH LOSS MODELS FOR WIRELESS SENSOR NETWORKS

Rahul P. Sawant[†], Qilian Liang[†], Dan O. Popa[†*] and Frank L. Lewis[†*]
[†]Department of Electrical Engineering; [*]Automation & Robotics Research Institute
University of Texas at Arlington
Arlington, TX 76019 – 0016 U.S.A.
E – Mail: liang@uta.edu

ABSTRACT

Energy conservation is critical in Wireless Sensor Networks. Replacing or recharging batteries is not an option for sensors deployed in hostile environments. Generally communication electronics in the sensor utilizes most energy. This paper studies the effect of changing the transmission power and baud rate on transmission distance. Using Shannon channel capacity formula and Log – Distance Path Loss Model, transmission distance is shown to be related to transmit power and baud rate. Extensive empirical readings are taken to confirm the above relation. The path loss exponent got as a result of data fitting is within the acceptable range for wireless environment. Using the equation derived in this paper, the distance between neighboring motes and traffic density it will be possible for sensors to adjust their transmit power and baud rate so as to use only the required amount of energy to maintain the wireless link to the neighbor and conserve power.

I. INTRODUCTION

Wireless Sensor Networks (WSN) are comprised of small, inexpensive sensors with wireless communication capabilities, called motes. They are deployed in ad – hoc networks and are powered by limited power supplies. These motes are deployed in large numbers and provide unprecedented opportunities for instrumenting and controlling homes, cities and the environment. They find applications in different fields like military sensing, physical security, air traffic control, traffic monitoring, video surveillance, industrial automation etc. Each poses different challenges for these motes but one common challenge faced in all fields is power conservation. This is because motes are sometimes deployed in difficult to reach regions and this makes it difficult to replace the batteries. Hence power conservation becomes an important factor for these motes. One of the main reasons for deploying these motes in ad – hoc is power conservation. Power is consumed during data processing and RF communication, but communication electronics uses far more power than processing. Hence a lot of effort goes into designing energy efficient routing algorithms [1, 2, 3], directed diffusion algorithms [4, 5], clustering algorithms [6, 7, 8], data aggregation [9] and MAC protocols [10, 11, 12]. Many of these algorithms assume fixed transmit power and baud rate.

In this paper we study the effect of changing the transmit power and baud rate on transmission distance. This study is particularly useful for WSN's which are mobile, such as in applications involving robotic swarms [19]. We experimentally determine a relation between distance, transmit power and baud rate for Crossbow's Mica2 motes deployed in indoor environment. This can be incorporated along with the above algorithms and with knowledge of the distance to neighboring mote and the traffic density can be used to adjust the transmit power and baud rate so that packets can be forwarded to the neighboring mote with the least energy and maximum reliability. Adjusting the transmit power the neighboring mote will fall within the transmission range and neither will be out of range nor will be the transmission range much bigger than the desired distance. This will also help to keep packet exchange to the desired mote and not to any distant mote, which can itself start some other packet exchange and so will help keep interference to a minimum. This study along with the energy efficient algorithms will further increase energy efficiency in real time when deployed on Mica2 motes.

This paper is organized as follows. In section II we briefly describe the factors affecting transmission distance. Section III gives the details of our experiment and the empirical data plots obtained. In section IV curve and surface fitting is described and lastly in section V we provide a conclusion of our study.

II. TRANSMISSION DISTANCE

The study of Transmission Distance, Transmit Power and Baud Rate done for this paper is related to Energy Conservation in Wireless Sensor Network. Transmit Power and Baud Rate together affect the Transmission Distance. In a wireless channel there is some power loss called Path Loss. This path loss is inversely proportional to the distance between the transmitter and receiver. With the knowledge of distance and path loss we can find the exact transmit power required to maintain a good link to the receiver without wasting any energy.

1-4244-1513-06/07/$25.00 ©2007 IEEE

Authorized licensed use limited to: University of Texas at Arlington. Downloaded on December 18, 2009 at 14:48 from IEEE Xplore. Restrictions apply.

Another factor that affects the transmission distance is the antenna sensitivity. Baud rate of the data affects the receiver antenna sensitivity. This is because at the higher baud rate, there is less energy and a fewer number of actual radio waves in each bit of information transmitted. The lower baud rates have more energy per bit and more actual radio waves per bit transmitted. The more radio waves received per bit makes it much easier to establish the correct waveform. Thus, lower baud rates mean more energy per bit; better receive signals and longer transmission distances [13]. The advantage is by keeping the transmit power constant and only decreasing the baud rate we can increase the transmission distance of the radio.

III. EXPERIMENT DETAILS

The following hardware was used for the experiment

1. MIB510 Programming board manufactured by Crossbow Technology.
2. Mica2 motes 2 nos. manufactured by Crossbow Technology
   For the radio communications Mica2 uses the CC1000 Chip which works in the 433 MHz band. The usual antenna chosen is a length of insulated wire called the monopole whip antenna one – quarter wavelength long. This happens to be 6.8 inches for the 433 MHz Mica2 [14]. Mica2 is powered by two AA batteries and requires a voltage between 2.7 – 3.3 Volts for successful operation.

A. CC1000 transceiver details

CC1000 uses the Binary Frequency Shift Keying (BFSK) modulation in the physical layer. Its transmit power and the baud rate are completely programmable. The crystal oscillator connected has a frequency of 14.7456 MHz. There are 22 inbuilt 8 – bit registers which can be used to program the operating parameters. A few relevant parameters are as follows.

Frequency Control Word A which sets the local oscillator frequency in receive mode and Frequency Control Word B which sets the transmitting frequency, f_0 in the transmit mode, together operate the frequency synthesizer (PLL). In the experiment Word A had a value of 0x580000 and B had a value of 0x57F685. Two registers FSEP0 and 1 are used to set the frequency separation and they hold a value of 0x355. Transmit and receive frequencies can be calculated using the following formula [15].

$$f_{VCO} = f_{ref} \times \frac{FREQ + (FSEP \times TXDATA) + 8192}{16384} \quad (1)$$

Here f_{VCO} gives the Local Oscillator (LO) frequency in receive mode and the f_0 and f_1 frequency in transmit mode (lower and upper FSK frequency). f_{ref} is the reference frequency calculated using the formula given below. *FREQ* is the value in frequency control word A or B according to whether the formula is used to calculate receive or transmit frequency. *FSEP* is the value in the FSEP0 and 1 registers. *TXDATA* is 0 or 1 in transmit mode depending on the data bit to be transmitted. In the receive mode *TXDATA* is always 0. Now to calculate f_{ref} we use the following formula [15]

$$f_{ref} = \frac{f_{xosc}}{REFDIV} \quad (2)$$

f_{xosc} is the crystal oscillator frequency of 14.7456 MHz and *REFDIV* is set to 12. This gives f_{ref} = 1.2288 MHz.

Using all these values in eq. 1, in receive mode $f_{VCO} = 433.152 \times 10^6 Hz$ and in transmit mode $f_{VCO} = 432.96997 \times 10^6 Hz$.

Thus the LO frequency in the receive mode is 433.152 MHz. In the experiments we have used a high side LO injection. So $f_{VCO} = f_{RF} + f_{IF}$ where f_{RF} is the centre frequency and f_{IF} is the Intermediate frequency. For CC1000 f_{IF} is designed to be 150.0375 KHz. So we get f_{RF} = 433.0019625 MHz.

The upper FSK transmit frequency is given by $f_1 = f_0 + f_{sep}$. f_0 is the f_{VCO} frequency calculated above for transmit mode i.e. 432.96997 MHz and f_{sep} is the frequency separation calculated using the formula [15] given below.

$$f_{sep} = f_{ref} \times \frac{FSEP}{16384} \quad (3)$$

Substituting the values $f_{sep} = 63975 Hz$, further using this f_{sep} we get f_1 = 433.03395 MHz. From f_0 and f_1 the centre frequency will be 433.0019625 MHz and is same as in the receive mode.

The transmit power of CC1000 can be varied from -20 dBm to 10 dBm in steps of 1 dB and is controlled by the PA_POW register. We carried out our experiments at four different power level setting as shown in Table 1.

Another parameter that was required for our experiments is the baud rate. This is set using a part of MODEM0 register as shown in Table 2. For our experiments we used 19.2, 38.4 and 76.8 kBaud.

Authorized licensed use limited to: University of Texas at Arlington. Downloaded on December 18, 2009 at 14:48 from IEEE Xplore. Restrictions apply.

Table 1: PA_POW register values and corresponding output power [15]

Output Power (dBm)	PA_POW Register Value (hex)
-20	01
-19	01
-18	02
-17	02
-16	02
-15	03
-14	03
-13	03
-12	04
-11	04

Table 2: MODEM0 register part to set Baud Rate[15]

Register Part Name	Bit & Parameter Value
MODEM0{6:4} BAUDRATE{2:0}	000: 0.6 kBaud 001: 1.2 kBaud 010: 2.4 kBaud 011: 4.8 kBaud 100: 9.6 kBaud 101: 19.2, 38.4 and 76.8 kBaud 110: Not Used 111: Not Used

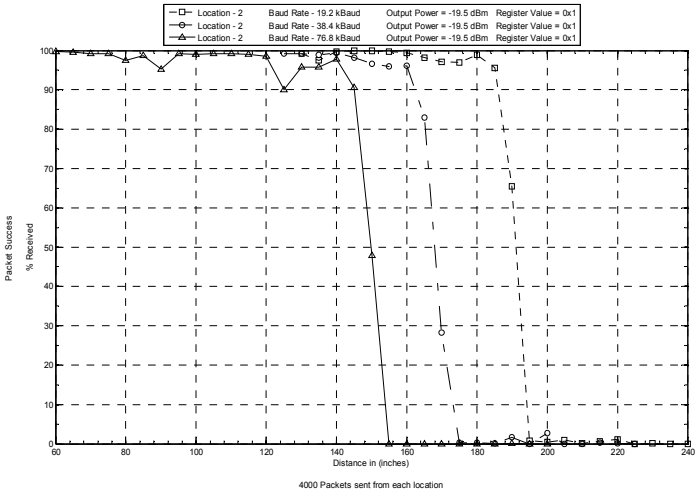
The experiment was carried out in a big warehouse which was used as a lab with minimal office furniture. The Mica2 motes were placed on the ground and were always in line of sight of each other. The following picture was taken during the experiment.



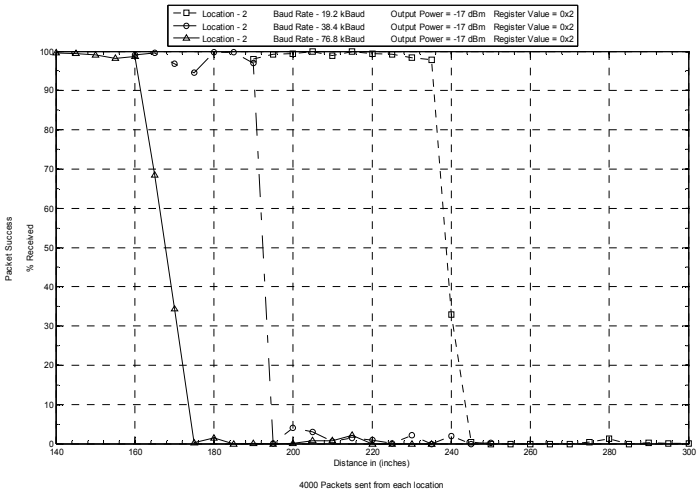
(a) (b)

Figure 1: Experimental Site (a) Front view (b) Top view of motes

For the transmitter mote a certain power level and baud rate is set from the possible options available. Since the wireless channel varies a lot randomly with respect to time there will be some packet loss even when the receiver mote is within the transmission distance. Hence the transmitter mote sends a total of 4000 packets, so as to follow Monte Carlo method, each with a sequence number. The receiver mote keeps a record of the number of packets received and missed and finally transmits a summary packet to the computer attached to it. A resolution of 5 inches was used for the distance between the transmitter and receiver. Once it is found that the receiver is not receiving any packets at all we know that the receiver is out of the transmission range. When it is absolutely sure the receiver is out of range the transmit power or baud rate on the transmitter mote are changed to a different value and the above experiment carried again. The plots in Figure 2 were generated using the data gathered from the experiment.

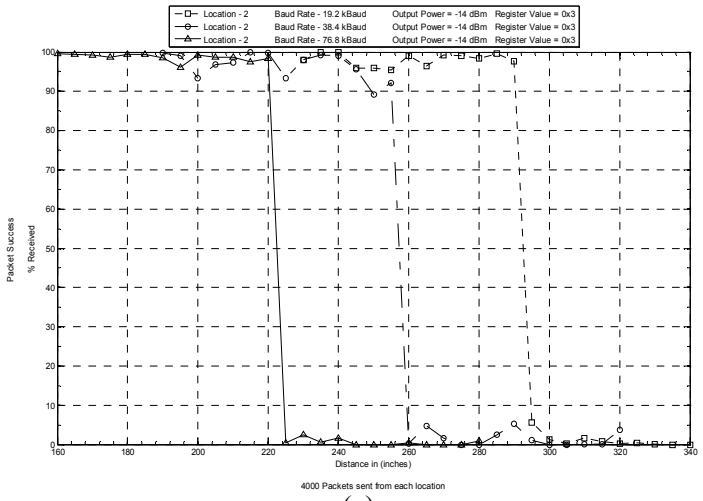


(a)

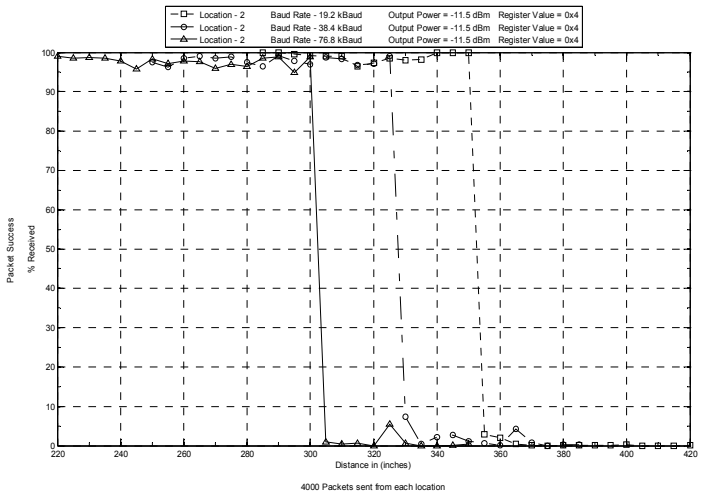


(b)

Authorized licensed use limited to: University of Texas at Arlington. Downloaded on December 18, 2009 at 14:48 from IEEE Xplore. Restrictions apply.



(c)



(d)

Figure 2: Packet success in percentage as a function of transmission distance for power levels of (a) -19.5 dBm, (b) -17 dBm, (c) -14 dBm, (d) -11.5 dBm and for 19.2 kBaud, 38.4 kBaud and 76.8 kBaud

Each curve from the plots in Figure 2 is initially in the region of 90 – 100 % this is because the transmitter and receiver motes are within the transmission range. A few packets are dropped but this could be because of variations in the channel that occur for a very small amount of time and is normal for any wireless channel. As the distance between the transmitter and receiver is increased, after a certain distance the curve drops drastically and the packets received are in the range of 0 – 5 %. This implies the transmitter is out of range of the receiver mote.

IV. DATA FITTING

The empirical data is thought to be derivable from some underlying function. The plots in section III seem to closely follow the Q – function. We used curve fitting using method of least squares to minimize the sum of squared deviations. After fitting Q – function to each curve following plots were generated. All curve fits are not shown in Figure 3 but the data got from all curve fits is shown in Table 3.

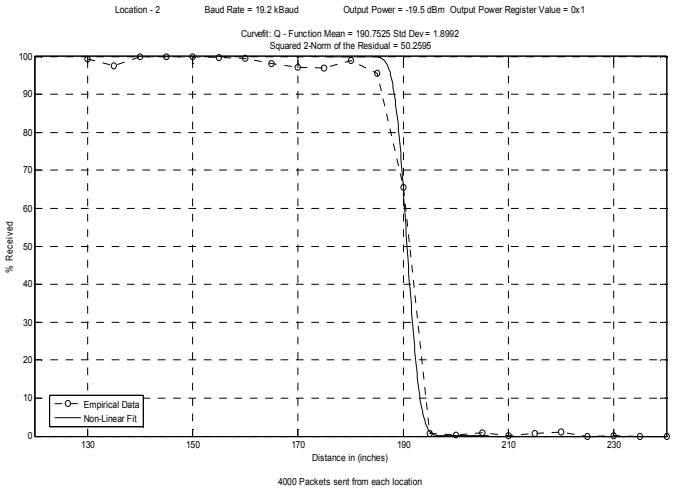


Figure 3: Q–function curve fit at 19.2 kBaud & -19.5 dBm

An initial value of one was used for std. dev. for curve fit and for mean of distance a value where packet success equals 50% was used. The following table shows the parameters got from the curve fit in above plots.

Table 3: Mean, Std. Dev. and Residual Error of curves fit above for different baud rate and transmit power

Baud Rate (kBaud)	Transmit Power (dBm)	Curve Parameters (Inches)		Residual Error
76.8	-19.5	Mean =	149.6819	208.8363
		Std Dev =	3.093	
	-17.0	Mean =	167.642	78.0394
		Std Dev =	4.567	
	- 14.0	Mean =	222.2506	41.3694
		Std Dev =	1.0526	
	- 11.5	Mean =	302.4448	148.6817
		Std Dev =	1.0754	
38.4	-19.5	Mean =	168.0964	57.4137
		Std Dev =	3.2833	
	-17.0	Mean =	191.759	79.4251
		Std Dev =	0.9316	
	- 14.0	Mean =	256.6509	324.2136
		Std Dev =	1.1637	
	- 11.5	Mean =	328.0941	115.0494
		Std Dev =	1.3191	
19.2	-19.5	Mean =	190.7525	50.2595
		Std Dev =	1.8992	
	-17.0	Mean =	239.1081	11.9331
		Std Dev =	2.0253	
	- 14.0	Mean =	292.7798	80.6525
		Std Dev =	1.3931	
	- 11.5	Mean =	353.1259	35.7488
		Std Dev =	0.9846	

Authorized licensed use limited to: University of Texas at Arlington. Downloaded on December 18, 2009 at 14:48 from IEEE Xplore. Restrictions apply.

For all the above std. dev. of distance the average = 1.899 in. The maximum error is 2.668 in. This is the error in the std. dev. of Q – function and not in the transmission distance. In transmission distance the error will be $2.668/2 = 1.334$ in. This is because only the distance between mean and monotonically decreasing part of Q – function is included while measuring transmission distance.

The mean of the distance in Table 3 is related to channel bandwidth and frequency of operation apart from transmit power and baud rate. This is three dimensional and we use surface fit as mentioned below.

A very important result derived by Shannon [16] is

$$C = B_c \times \log_2\left[1 + \frac{P_r}{(N_0 \times B_c)}\right] \quad (4)$$

Here C is the channel capacity in bits per seconds, B_c is the channel bandwidth in Hz, P_r is the received power in watts and N_0 is the single – sided noise power density in watts / Hz. Writing in terms of P_r and converting it to dBm we get

$$P_r(dBm) = 10 \times \log_{10}\left[1000 \times N_0 \times B_c\left(2^{\frac{C}{B_c}} - 1\right)\right] \quad (5)$$

In the wireless channel the received power is calculated using the formula [17] below.

$$P_r(d)[dBm] = P_t[dBm] - PL(d)[dB] \quad (6)$$

Here $P_r(d)$ is the received power in dBm at a distance d from transmitter, P_t is the transmit power in dBm and $PL(d)$ is the path loss in dB at a distance d from transmitter. For finding the path loss $PL(d)$ we use the Log – Distance Path Loss model [17] where

$$PL[dB] = PL(d_0) + \left\{10 \times n \times \log_{10}\left(\frac{d}{d_0}\right)\right\} \quad (7)$$

In this formula $PL[dB]$ is the path loss in dB, $PL(d_0)$ is the path loss at a reference distance d_0, n is the path loss exponent, d is distance in meters at which the path loss is to be calculated and d_0 is the reference distance also in meters.

Substituting eq. (7) in (6) and the result in (5) we get

$$P_t[dBm] - PL(d_0) - \left\{10 \times n \times \log_{10}\left(\frac{d}{d_0}\right)\right\} = 10 \times \log_{10}\left[1000 \times N_0 \times B_c\left(2^{\frac{C}{B_c}} - 1\right)\right]$$

Solving for d we have

$$d = d_0 \times 10^{\frac{P_t - PL(d_0) - 10 \times \log_{10}\left[1000 \times N_0 \times B_c\left(2^{\frac{C}{B_c}} - 1\right)\right]}{10 \times n}} \quad (8)$$

Thus we relate the transmission distance with transmit power, baud rate and channel bandwidth. We use this equation in the surface fit using method of least squares.

In the above equation $PL(d_0)$ is calculated using the Friis free space path loss formula [17] given below.

$$PL(d_0) = -10 \times \log_{10}\left[\frac{\lambda^2}{(4 \times \pi)^2 \times {d_0}^2}\right] \quad (9)$$

Here λ is the wavelength and d_0 is the reference distance. Centre frequency of the motes is 433.002 MHz, as calculated in section III, from which we get λ and the distance d_0 it is said should be in the far – field region of the transmitting antenna. This far – field region or Fraunhofer region of a transmitting antenna is defined as the region beyond the far – field distance d_f which is related to the antenna dimension and wavelength. It is given as follows [17]

$$d_f = \frac{2 \times D^2}{\lambda} \quad (10)$$

Where d_f is the far – field distance, D is the largest physical linear dimension of the antenna and λ is the wavelength.

The Mica2 motes have a monopole whip antenna which is $\lambda/4$ meters high. Using 433.002 MHz frequency we get $\lambda = 0.6928$ m = 27.2767 in and the whip antenna height = 0.1732 m = 6.8 in. So D = 0.1732 m. Putting these values in eq. (10) we get $d_f = 0.086116$ m = 3.3903 in

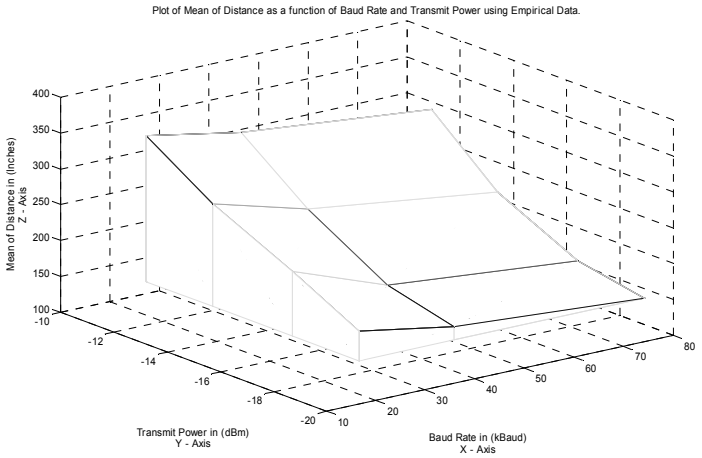
Additional criteria to be in the far – field region are d_f must satisfy

$d_f \rangle\rangle D$ i.e. $d_f \rangle\rangle 6.8$ in and

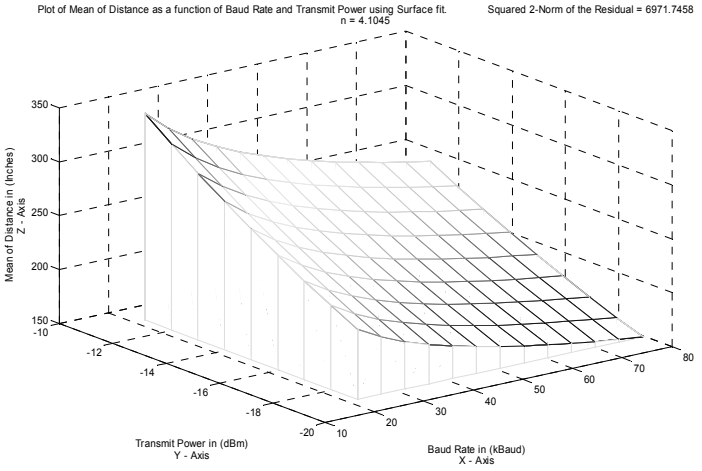
$d_f \rangle\rangle \lambda$ i.e. $d_f \rangle\rangle 27.2767$ in.

So to be in the far – field region we choose our distance d_0 to be 100 in = 2.54 m and from the λ value got above we calculate $PL(d_0)$ and use it in eq. (8). The N_0 in eq. (8) is calculated using $N_0 = k \times T$. k is the Boltzmann constant = $1.3806503 \times 10^{-23}$ m^2 kg s^{-2} K^{-1} and T is the room temperature in degree kelvin = 300^0 k. The channel bandwidth for 433 MHz Mica2 mote, $B_c = 620kHz$ [18]. Using all these values in eq. (8) we try to find the best values for n the path loss exponent such that the error, between the distances calculated using eq. (8) and the values of distance we got from our experimental data, is minimized. To start with, a value of one is assumed for n. After doing the surface fit we get the following graphs.

Authorized licensed use limited to: University of Texas at Arlington. Downloaded on December 18, 2009 at 14:48 from IEEE Xplore. Restrictions apply.



(a)



(b)

Figure 4: Mean of Distance vs Transmit Power and Baud Rate using (a) Empirical Data (b) eq. (8) derived from Shannon theorem and Path Loss Model

The optimized value of path loss exponent n got from surface fit is n = 4.10. The following graph compares distances using both data and also shows the surface.

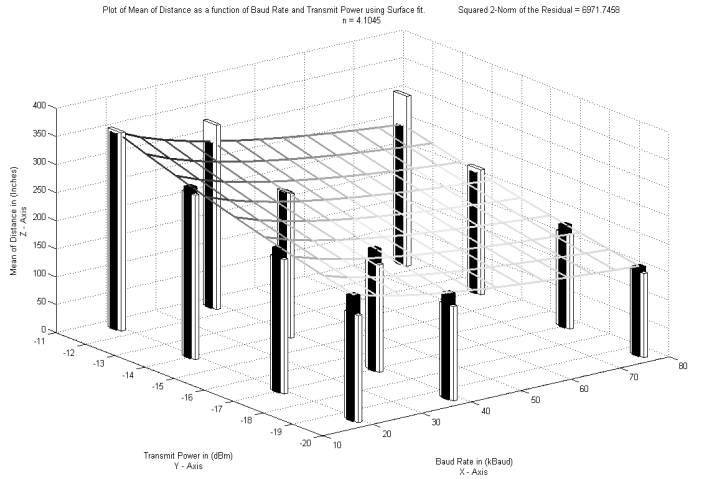


Figure 5: Comparison of Mean of Distance vs. Transmit Power & Baud Rate using Empirical & Surface Fit data

In the plot above the white bars show the distances got using the empirical data at baud rates of 19.2, 38.4 and 76.8 kBaud. The black bars show the distance got using eq. (8). So the difference between the two is the error. For comparison purpose the table below shows the empirical distance, distance obtained using eq. (8), the absolute error between the two and the percentage error.

Table 4: Summary of mean of distance and absolute error

Empirical Data			
Transmit Power	Baud Rate		
	19.2 kBaud	38.4 kBaud	78.6 kBaud
- 19.5 dBm	190.7526	168.0964	149.6819
-17.0 dBm	239.1081	191.7589	167.6420
-14.0 dBm	292.7798	256.6509	222.2506
-11.5 dBm	353.1259	328.0941	302.4448
Shannon Formula Surface Fit - n = 4.10			
Transmit Power	Baud Rate		
	19.2 kBaud	38.4 kBaud	78.6 kBaud
- 19.5 dBm	223.0249	187.8755	157.8458
-17.0 dBm	256.6032	216.1618	181.6109
-14.0 dBm	303.6356	255.7817	214.8980
-11.5 dBm	349.3505	294.2918	247.2528
Absolute Error			
Transmit Power	Baud Rate		
	19.2 kBaud	38.4 kBaud	78.6 kBaud
- 19.5 dBm	32.2723	19.7791	8.1639
-17.0 dBm	17.4952	24.4028	13.9689
-14.0 dBm	10.8558	0.8692	7.3526
-11.5 dBm	3.7754	33.8022	55.1921
Max Error - 55.1921		Min Error - 0.8692	
Percentage Error			
Transmit Power	Baud Rate		
	19.2 kBaud	38.4 kBaud	78.6 kBaud
- 19.5 dBm	16.9184	11.7665	5.4542
-17.0 dBm	7.3168	12.7258	8.3326
-14.0 dBm	3.7078	0.3387	3.3083
-11.5 dBm	1.0691	10.3026	18.2486

Note: All distances in Inches.

The error in the above table is very small. A close comparison of empirical data and surface fit data reveals a mix of positive and negative errors in mean of distance which will reflect in the same way in transmission distance. When this equation is used in a networking protocol most of the time the transmit power and baud rate set will maintain a good link to the receiver. The bad link occurring, in spite of setting the transmit power and baud rate as per eq(8), can happen also because of the dramatic change in the environment for short or long period of time. In this case the transmit power could be slightly increased or the baud rate slightly decreased to maintain a good link. Once done these new values can be used throughout the lifetime of the network.

Authorized licensed use limited to: University of Texas at Arlington. Downloaded on December 18, 2009 at 14:48 from IEEE Xplore. Restrictions apply.

Tuning of the transmission power and baud rate will only increase the network setting time a little but afterwards throughout the operation of the network energy will be conserved. The equation in this paper definitely gives a better starting point at fixing the transmit power and baud rate rather than approximately varying them from minimum to maximum and wasting a lot of time for network setup.

V. CONCLUSION

The key challenge in Wireless Sensor Networks being power conservation, the study in this thesis will support multi – hop routing and clustering algorithms in increasing the power saving in each sensor node. Using Shannon theorem and Log – Distance Path Loss Model the transmission distance is shown to be related to transmit power and baud rate. The extensive empirical data obtained confirms to this relation of transmission distance. The optimized value of the path loss exponent obtained as a result of surface fitting is close to that obtained in other wireless environments. Using this relation along with the knowledge of localization and traffic density between the neighboring mote it will be possible to adjust the transmit power and / or the baud rate to maintain the wireless links between the neighboring motes without loosing the connection and without incurring huge energy costs.

Apart from the advantage of power saving, the correct transmit power level will decrease the level of interference in the network since less motes in the surrounding will hear the conversation. There is also an increase in the network capacity as the packet transmissions are confined only to the small local area and other motes out of the area are free to carry out their own transmissions with some other motes within their area.

ACKNOWLEDGMENT

The authors would like to thank Prasanna M. Ballal of ARRI's DIAL Lab for his help with the experimental testbed used in this paper.

This work was supported in part by Office of Naval Research (ONR) under Grant N00014 – 07 – 1 – 0395, N00014 – 07 – 1 – 1024, and National Science Foundation (NSF) under Grant CNS – 0721515.

REFERENCES

[1] A. Woo, T. Tong and D. Culler, "*Taming the Underlining Challenges of Reliable Multihop Routing in Sensor Networks*" Proc. of 1st Intl. conf. on Embedded Networked Sensor Systems SenSys November 2003.

[2] C. Perkins and E. Royer, "*Ad hoc On – Demand Distance – Vector Routing*". Proc. of 2nd IEEE Workshop on Mobile Computing Systems and Applications, 1999.

[3] D. Braginsky, D. Estrin, "*Rumor Routing Algorithm For Sensor Networks*" Proc. of 1st Intl. Workshop on WSN & App., Sept 2002, Pages: 22 – 31.

[4] C. Intanagonwiwat, R Govindan, D Estrin, J Heidemann, F Silva, "*Directed Diffusion for Wireless Sensor Networking*" IEEE/ACM Trans. on Networking, Vol. 11, No. 1, February 2003 Pages: 2 – 16.

[5] J. Kulik, W. Rabiner and H. Balakrishnan, "*Adaptive Protocols for Information Dissemination in Wireless Sensor Networks*" Proc. 5th Annu. ACM/IEEE Int. Conf. Mobile Computing and Networking (MobiCom 1999), Pages: 174 – 185.

[6] W. Heinzelman, A. Chandrakasan and H. Balakrishnan, "*Energy – Efficient Routing Protocols for Wireless Microsensor Networks*" Proc. of 33rd Hawaii Int. Conf. System Sciences (HICSS), Maui, HI, January 2000.

[7] W. Heinzelman, A. Chandrakasan and H. Balakrishnan, "*An Application – Specific Protocol Architecture for Wireless Microsensor Networks*" IEEE Trans. Wireless Comm., Vol. 1, No. 4, October 2002 Pages: 660 – 670.

[8] A. Wang, W. Heinzelman, and A. Chandrakasan, "*Energy – Scalable Protocols for Battery – Operated Microsensor Networks*" Proc. 1999 IEEE Workshop Signal Processing Systems (SiPS 1999), October 1999, Pages: 483–492.

[9] B. Krishnamachari, D. Estrin, S. Wicker, "*The Impact of Data Aggregation in Wireless Sensor Networks*", Proc. of 22nd Intl. Conf. on Distributed Computing Systems, July 2002, Pages: 575 – 578.

[10] J. Polastre, J. Hill and D. Culler, "*Versatile Low Power Media Access for Wireless Sensor Networks*" Proc. of 2nd Intl. Conf. on Embedded Networked Sensor Systems, November 2004, Pages: 95 – 107.

[11] W. Ye, J. Heidemann, D Estrin, "*An Energy Efficient MAC protocol for Wireless Sensor Networks*" Proc. IEEE Infocom 2002, Vol. 3, Pages: 1567 – 1576.

[12] Q. Ren, Q. Liang, "*A Contention Based Energy – Efficient MAC Protocol for Wireless Sensor Networks*", IEEE Wireless Communications and Networking Conf., Vol. 2, April 2006, Pages: 1154 – 1159.

[13] "*Wireless Instrumentation: Factors Affecting Transmission Distance*", Accutech Tech Note # 215, Accutech Instrumentation Solutions, http://www.savewithaccutech.com/tech-center/technical-articles.asp

[14] "*MPR / MIB User's Manual*", Rev. A September 2005, Crossbow Technology, http://www.xbow.com/Support/wUserManuals.aspx.

[15] "CC1000 Single Chip Very Low Power RF Transceiver Datasheet", Chipcon Corporation, http://www.chipcon.com/files/CC1000_Data_Sheet_2_3.pdf

[16] J. Proakis, "*Digital Communication*", Fourth Edition, McGraw – Hill, 2001.

[17] T. Rappaport, "*Wireless Communications: Principles and Practice*", Second Edition, Pearson Education, 2004.

[18] J. Jeong, S. Kim, "*DOT3 Radio Stack*", www.cs.berkeley.edu/~jaein/presentations/JaeinJeong_ChipconRadioStack.ppt

[19] D.O. Popa and F.L. Lewis, "*Algorithms for robotic deployment of WSN in adaptive sampling applications*" in Wireless Sensor Networks and Applications, ed. Y. Li, M. Thai, and W. Wu, Springer-Verlag, Berlin, 2006, to appear.

Authorized licensed use limited to: University of Texas at Arlington. Downloaded on December 18, 2009 at 14:48 from IEEE Xplore. Restrictions apply.

Superimposed Code Based Channel Assignment in Multi-Radio Multi-Channel Wireless Mesh Networks

Kai Xing, Xiuzhen Cheng & Liran Ma
Department of Computer Science
The George Washington University
Washington, DC 20052, USA
{kaix,cheng,lrma}@gwu.edu

Qilian Liang
Department of Electrical Engineering
The University of Texas at Arlington
Arlington, TX 76019, USA
liang@uta.edu

ABSTRACT

Motivated by the observation that channel assignment for multi-radio multi-channel mesh networks should support both unicast and local broadcast[1], should be interference-aware, and should result in low overall switching delay, high throughput, and low overhead, we propose two flexible localized channel assignment algorithms based on s-disjunct superimposed codes. These algorithms support the local broadcast and unicast effectively, and achieve interference-free channel assignment under certain conditions. In addition, under the primary interference constraints[2], the channel assignment algorithm for unicast can achieve 100% throughput with a simple scheduling algorithm such as the maximal weight independent set scheduling, and can completely avoid hidden/exposed terminal problems under certain conditions. Our algorithms make no assumptions on the underlying network and therefore are applicable to a wide range of MR-MC mesh network settings. We conduct extensive theoretical performance analysis to verify our design.

Categories and Subject Descriptors

C.2.1 [**Network Architecture and Design**]: Wireless Communication

General Terms

Algorithms, Design

Keywords

Multi-radio multi-channel wireless mesh networks, interference, channel assignment, superimposed codes

[1]A broadcast to be heard by all immediate neighbors.

[2]Under the primary interference constraints, each radio can talk with at most one single neighbor at any instant of time. Namely the set of active links supported the same channel at any point of time is a matching.

Permission to make digital or hard copies of all or part of this work for personal or classroom use is granted without fee provided that copies are not made or distributed for profit or commercial advantage and that copies bear this notice and the full citation on the first page. To copy otherwise, to republish, to post on servers or to redistribute to lists, requires prior specific permission and/or a fee.
MobiCom'07, September 9–14, 2007, Montréal, Québec, Canada.
Copyright 2007 ACM 978-1-59593-681-3/07/0009 ...$5.00.

1. INTRODUCTION

With recent advances in wireless technology, the utilization of multiple radios as well as non-overlapping channels provides an opportunity to reduce interference and increase network capacity. Equipped with multiple radios, nodes can communicate with multiple neighbors simultaneously over different channels, and thus can significantly improve the network performance by exploring concurrent transmissions [1].

In a multi-radio multi-channel (MR-MC) mesh network, a key challenging problem for capacity optimization is *channel assignment*. Since practically the number of radios at each node is always much smaller compared to that of orthogonal channels due to reasons such as cost and small form factors, it may be prohibitive to assign one fixed channel to each radio. In other words, a radio may need to switch to different channels as time goes for better performance. This radio constraint makes the channel assignment in MR-MC mesh networks much harder. In this paper, we propose two channel assignment algorithms for interference mitigation and throughput maximization. Our research is motivated by the following observations.

- Current channel assignment approaches lack a support to local broadcast in MR-MC mesh networks. As neighboring nodes tend to use different channels for transmissions, the broadcast packet has to be separately transmitted by the sender on multiple channels. Thus, broadcast can be more expensive than that in single-radio single-channel (SR-SC) networks.
- A number of current channel assignment approaches rely heavily on solving complex optimization problems, which might be impractical for many MR-MC mesh network scenarios. In addition, techniques based on default radio/channel degrade network throughput when the number of radios is much smaller than that of channels.
- Channel switching delay is an important parameter that should be counted in channel assignment. Since the number of radios per node is usually much smaller than that of orthogonal channels, allowing a radio switch among the full range of channels results in higher overall delay since the radio may switch back and forth frequently when multiple different flows traverse the same node simultaneously.
- CSMA/CA is believed to be inadequate to meet the high traffic demand in mesh networks [2]. Any channel assignment that requires RTS/CTS for channel reservation is unfavored due to the high overhead. Since co-channel interference is one of the major reasons for capacity degradation in MR-MC mesh networks, interference-aware channel assignment for throughput optimization should be sought.

In this paper, we propose two channel assignment algorithms based on s-disjunct superimposed codes. The basic idea is sketched as follows. For each node, all available orthogonal channels are labelled as either primary or secondary via a binary channel codeword. This labelling is controlled by an s-disjunct superimposed $(s, 1, N)$-code. The codeword of the transmitting node, together with those of the interferers, determine the channel. Note that primary channels are always preferred during channel assignment. Our analysis indicates that by exploring the s-disjunct property of the $(s, 1, N)$-code, it is possible to achieve interference-free channel assignment for both unicast and broadcast. Comparing with the related literature in Section 2, we have identified the following unique contributions of our paper.

- We have designed two localized simple algorithms that can effectively support both local broadcast and unicast. Under certain conditions, interference-free broadcast and unicast can be achieved.
- Since our algorithms assign channels to transmitters for both unicast and broadcast, and because the channels are selected from a small subset of primary channels whenever possible, our algorithms can effectively decrease the overall switching delay caused by the oscillation of switching back and forth due to the large difference between the numbers of radios and channels.
- With a very simple scheduling algorithm, our channel assignment for unicast is proved to be able to achieve 100% throughput under the primary interference constraints. We also identifies the conditions when hidden and exposed terminal problems are completely avoided with our channel assignment.
- We have conducted extensive theoretical performance analysis to verify our algorithm design. In addition, our algorithms are localized, and have low computation and communication overheads.
- Our algorithms support dynamic, static, and adaptive channel assignment without requesting any complex scheduling and/or channel coordination. These algorithms make no assumptions on the underlying network settings such as traffic patterns and MAC/routing protocols. Therefore they are applicable to a wide range of mesh networks.

The rest of the paper is organized as follows: Section 2 discusses the related work in channel assignment for MR-MC mesh networks. In Section 3, we present our network model and assumptions. Section 4 introduces the s-disjunct superimposed code and links it to the problem of channel assignment in MR-MC mesh networks. In Section 5, we present our channel assignment algorithms for both unicast and broadcast, and analyze their performance theoretically. In Section 6, we discuss a number of related issues. Section 7 summarizes the work and concludes the paper.

2. RELATED WORK

In this section, we survey the most related research in channel assignment for MR-MC mesh networks.

The benefits of using multiple radios and channels have been theoretically studied in [1,3–5] by jointly considering routing, scheduling, and channel assignment. Load-aware channel assignment is studied in [6, 7]. Marina and Das jointly consider channel assignment and topology control in [8].

In Kyasanur and Vaidya [9], the multiple radios at each node are divided into two groups, with one assigned fixed channels for packet reception and ensuring connectivity, and the other assigned switchable channels for capacity increase. This multiple channel management actually handles the channel allocation at the receiver side. Each switchable radio switches to the fixed channel of the destination radio when data transmission needs to be launched. For fixed channel assignment, a node selects random channels for its fixed interfaces initially. To balance the utilization of all channels, nodes collect two-hop neighborhood information and change their fixed channels accordingly. Obviously this fixed channel assignment takes time to converge. In addition, the number of switchable channels is relatively large when the number of radios per node is small, which may cause a large overall switching delay when the node has to switch back and forth in order to simultaneously relay multiple flows to different neighbors. Furthermore, the receiver-based channel assignment does not support broadcast efficiently and each broadcast packet has to be transmitted separately on one of the fixed channels for each neighbor. Our work differs in that we consider transmitter channel assignment, which is expected to incur low overall switching delay and can trivially support efficient broadcast.

A common default channel is introduced in [10–14] to handle the network partition caused by dynamic channel assignment, and to facilitate channel negotiation for data communications. To assign channels to the interfaces other than the default radio, [10] presents a localized greedy heuristic based on an interference cost function defined for pairs of channels. Refs. [11, 12] consider the mesh networks with main traffic flowing to and from a gateway, which is also in charge of the channel computation. In their channel assignment to a non-default radio, nodes closer to the gateway and/or bearing higher traffic load get a better quality channel. In DCA [14], the default channel is used as a control channel. For each node, one of the radios stays on the control channel for exchanging control messages, and other radios dynamically switch to the data channels for transmission. In this case, the utilization of the control channel could be small even though the data channels can be fully utilized. A multi-channel MAC is proposed in [13] for single-radio networks. This MAC protocol requires all nodes to meet at the common channel periodically to negotiate the channels for data communication.

The default channel does not have to be the same for all nodes in the network. In [15], each node fixes one radio on some channel but different nodes possibly use different fixed channels. This channel assignment actually fixes the reception channel for each node, and therefore the remaining radios of the node dynamically switch to its neighbors' fixed channels for data transmission. The same idea is adopted in [9]. In SSCH [16], radios switch among channels following some pseudo-random sequences such that neighboring nodes meet periodically at a common channel. This approach is simple but it requires clock synchronization.

Compared to the works mentioned above, our work does not require any special radio. We consider the channel assignment to all radios in a static fashion. In addition, our channel assignment algorithms are localized and are designed for a mesh network with a more general peer-to-peer traffic pattern.

Another important category of related work is code assignment for hidden terminal interference avoidance in CDMA packet radio networks. Bertossi and Bonuccelli [17] presents a centralized greedy algorithm to assign CDMA codes to vertices such that every pair of nodes at two-hop distance is assigned with a couple of different codes and the number of orthogonal codes utilized is minimized. This is a NP-Complete problem, and therefore the proposed

algorithm is an approximate heuristic. The distributed implementation of the algorithm, which results in a high overhead, is also proposed in [17]. The same code assignment problem is considered in [18] too, where a distributed heuristic is proposed. Note that to ensure hidden terminal interference-free communications, different codes should be assigned to every pair of nodes that are two-hop away. Our work differs from [17, 18] in that we intend to assign channels to nodes with an objective of interference-free unicast and broadcast to their immediate neighbors. In addition, the number of available orthogonal channels in our study is much smaller than that of the CDMA codes in a packet radio network. Furthermore, our localized algorithms are much simpler and results in much lower overhead.

Our work focuses on channel assignment for general MR-MC mesh networks. Each node is associated with a binary channel codeword, and computes its channels based on the codewords of the interferers. The algorithms involved are simple, has very low computation and communication overheads, and can support both unicast and local broadcast effectively.

3. NETWORK MODEL

In this section, we introduce the underlying network model, assumptions, and terminologies employed in the paper.

3.1 Basics

We consider a stationary multi-radio multi-channel (MR-MC) wireless mesh network with $|V|$ nodes. There exist N orthogonal (non-overlapping) frequency channels labelled by $k_1, k_2, \cdots, k_N$. Each node is equipped with Q radio interfaces. In our consideration, $Q \ll N$. This is a practical assumption since the number of radios per node is constrained by cost and form factors. For example, in an IEEE $802.11a$ based mesh network, each node may have 2 or 3 radios but the number of orthogonal channels is 12. We assume that the footprint of a radio is a disk resulting from an omni-directional antenna. In addition, we assume that each radio supports the same set of non-overlapping channels. Note that the number of radios equipped on each mesh node could be different.

For each node, the N available orthogonal channels are divided into two categories: *primary channels* and *secondary channels*. A binary column vector $\vec{c_u}$ of length N, called a *channel codeword*, is associated with each node u to label its channels, with a value 1 representing a primary channel and a value 0 secondary. For example, $\vec{c_u} = (1,0,0,1,0,0,0,1,0,1,0,0)'$ means that channels k_1, k_4, k_8, and k_{10} are primary to u, and k_2, k_3, k_5, k_6, k_7, k_9, k_{11} and k_{12} are secondary to u for a network that can support 12 orthogonal channels. Note that partitioning the channels into two sets can facilitate our algorithm design. Intuitively, a node should favor a channel that is secondary to all its interferers. Therefore for each node, the number of primary channels should be smaller than that of the secondary.

We require that for any two channel codewords $\vec{c_u}$ and $\vec{c_v}$, there exist at least two channels k_1 and k_2 such that k_1 is primary to u but secondary to v, and k_2 is secondary to u but primary to v. In other words, we can always find out a channel that is primary to one node and secondary to another node when the two corresponding channel codewords are different. For simplicity, we assume all nodes have the same number of primary channels. Let this number be w. Then the number of channel codewords satisfying the above condition is $\binom{N}{w}$ for N available orthogonal channels, which reaches its maximum when $w = \frac{N}{2}$. For example, when $N = 12$, there are 66, 495, and 924 available channel codewords for $w = 2, 4, 6$ respectively. We assume that the channel codewords assigned to each node is unique. As explained in Section 6, this assumption can be relaxed when the cellular grid architecture is introduced for salability considerations.

In our study, the network is modelled by a directed graph $G(V, E)$, where V is the set of nodes, and E is the set of directed links. A *channel code*, denoted by a $N \times |V|$ binary matrix $\mathcal{C}$, is associated with G. Therefore sometime G is denoted by $G(V, E, \mathcal{C})$. Each column of $\mathcal{C}$ represents a channel codeword pertaining to a node in the network. For example, the uth column is the channel codeword $\vec{c_u}$ for node u. The purpose of this paper is to assign channels to a node u based on $\vec{c_u}$ and the channel codewords of its interferers in order to mitigate co-channel interference for network capacity maximization, an optimization problem requiring the joint consideration of routing, channel assignment, and packet scheduling. Nevertheless, we focus on channel assignment in this paper, and propose to study joint routing and scheduling based on our channel assignment as a future research.

We assume that a DATA packet sending from u to v is acknowledged with an ACK message from v to u. Therefore even though we use a directed graph to model the network, only bidirectional links are considered. A directed link from node u to v is denoted by $(u \rightarrow v)$. In addition, we use $N_1(u)$ and $N_2(u)$ to represent the sets of neighbors of u within one-hop and two-hop away. We have $u \notin N_1(u)$ and $u \notin N_2(u)$.

3.2 Interference Model

For any node $u \in V$, denoted by $\mathcal{N}(u)$ the set of interferers of u. A node $v \in V$ is an *interferer* of u if v's transmission interferes with u's transmission. Therefore when two-way handshake (DATA-ACK) is adopted for successful packet delivery, the interferers for the unicast from u to v include $N_1(u)$ and $N_1(v)$. For a local broadcast by u, the interferers include all nodes in $N_2(u)$.

4. LINKING SUPERIMPOSED CODES WITH MR-MC NETWORKS

In this section, we first give a brief introduction on *superimposed codes*. Then we link the superimposed $(s, 1, N)$-code, also called the *s-disjunct code*, to channel assignment in MR-MC mesh networks.

4.1 Superimposed codes

Superimposed codes were introduced by Kautz and Singleton [19] in 1964. Since then, they have been extensively studied and applied to various fields, such as multi-access communications [20], [21], cryptography [22], pattern matching [23], circuit complexity [24], and many other areas of computer science. For convenience, we first introduce the basic definitions and properties of superimposed codes.

Let N, t, s, and L be integers such that $1 < s < t$, $1 \leq L \leq t - s$, and $N > 1$. Given a $N \times t$ binary matrix $\mathcal{X}$, denote the ith column of $\mathcal{X}$ by $X(i)$, where $X(i) = (x_1(i), x_2(i), \cdots, x_N(i))'$. We call $X(i)$ a codeword i of $\mathcal{X}$ with a length N. In other words, $\mathcal{X}$ is a *binary code* with each column corresponding to a codeword. Let w and λ be defined as:

$$w_i = \sum_{k=1}^{N} x_k(i), \quad (1)$$

$$\lambda_j = \sum_{k=1}^{t} x_j(k). \quad (2)$$

Therefore w and λ are called the *column weight* and *row weight* of $\mathcal{X}$, respectively. We have $w_{min} = \min_{i=1}^{t} w_i$, $w_{max} = \max_{i=1}^{t} w_i$, $\lambda_{min} = \min_{j=1}^{N} \lambda_j$, and $\lambda_{max} = \max_{j=1}^{N} \lambda_j$. Note that w_i and

$$\begin{pmatrix} 1 & 0 & 0 & 0 & 1 & 0 & 0 & 0 & 0 & 0 & 1 & 0 & 1 \\ 1 & 1 & 0 & 0 & 0 & 1 & 0 & 0 & 0 & 0 & 0 & 1 & 0 \\ 0 & 1 & 1 & 0 & 0 & 0 & 1 & 0 & 0 & 0 & 0 & 0 & 1 \\ 1 & 0 & 1 & 1 & 0 & 0 & 0 & 1 & 0 & 0 & 0 & 0 & 0 \\ 0 & 1 & 0 & 1 & 1 & 0 & 0 & 0 & 1 & 0 & 0 & 0 & 0 \\ 0 & 0 & 1 & 0 & 1 & 1 & 0 & 0 & 0 & 1 & 0 & 0 & 0 \\ 0 & 0 & 0 & 1 & 0 & 1 & 1 & 0 & 0 & 0 & 1 & 0 & 0 \\ 0 & 0 & 0 & 0 & 1 & 0 & 1 & 1 & 0 & 0 & 0 & 1 & 0 \\ 0 & 0 & 0 & 0 & 0 & 1 & 0 & 1 & 1 & 0 & 0 & 0 & 1 \\ 1 & 0 & 0 & 0 & 0 & 0 & 1 & 0 & 1 & 1 & 0 & 0 & 0 \\ 0 & 1 & 0 & 0 & 0 & 0 & 0 & 1 & 0 & 1 & 1 & 0 & 0 \\ 0 & 0 & 1 & 0 & 0 & 0 & 0 & 0 & 1 & 0 & 1 & 1 & 0 \\ 0 & 0 & 0 & 1 & 0 & 0 & 0 & 0 & 0 & 1 & 0 & 1 & 1 \end{pmatrix}$$

Figure 1: An example of a superimposed $(3, 1, 13)$-code of size 13

λ_j record the number of 1's in column i and in row j of $\mathcal{X}$, respectively. Hence w_{min} and w_{max} are the minimum and the maximum column weights of $\mathcal{X}$, respectively; and λ_{min} and λ_{max} are the minimum and the maximum row weights of $\mathcal{X}$, respectively.

The Boolean sum

$$Y = \bigvee_{i=1}^{s} X(i) = X(1) \bigvee X(2) \bigvee \cdots \bigvee X(s)$$

of codewords $X(1), X(2), \cdots, X(s)$ is the binary codeword $Y = (y_1, y_2, \cdots, y_N)'$ such that

$$y_j = \begin{cases} 0, & \text{if } x_j(1) = x_j(2) = \cdots = x_j(s) = 0, \\ 1, & \text{otherwise,} \end{cases}$$

for $j = 1, 2, \cdots, N$. We say that *a binary codeword Y covers a binary codeword Z if the Boolean sum $Y \bigvee Z = Y$.*

Superimposed code (SC): A $N \times t$ binary matrix $\mathcal{X}$ is called a superimposed code of length N, size t, strength s, and $listsize \leq L - 1$ if the Boolean sum of any s-subset[3] of the codewords of $\mathcal{X}$ covers no more than $L - 1$ codewords that are not components of the s-subset. This code is also called a (s, L, N)-code of size t. Fig. 1 shows an example of a superimposed $(3, 1, 13)$-code of size 13.

s-disjunct Code: A binary matrix $\mathcal{X}$ is called an s-disjunct code if and only if it has the property that the Boolean sum of any s codewords in $\mathcal{X}$ does not cover any codeword not in that set of s codewords.

Based on the definitions, a superimposed $(s, 1, N)$-code is a s-disjunct code. Taking the $(3, 1, 13)$-code shown in Fig. 1 as an example, the Boolean sum of the first 3 codewords of $\mathcal{X}$ is $X(1) \bigvee X(2) \bigvee X(3) = (1, 1, 1, 1, 1, 1, 0, 0, 0, 1, 1, 1, 0)'$, which doesn't cover any other codeword of $\mathcal{X}$ but themselves.

According to the s-disjunct characteristic of the superimposed $(s, 1, N)$-code, we can derive the following important property:

LEMMA 4.1. *Given an $(s, 1, N)$ superimposed code $\mathcal{X}$, for any s-subset of the codewords of $\mathcal{X}$, there exists at least one row at which all codewords in the s-subset contains the value 0.*

PROOF. For contradiction we assume that there is no row at which all codewords in the s-subset contain a common value 0. Then the Boolean sum of the s codewords equals $(1, 1, \cdots, 1)'$, which can cover all other codewords in $\mathcal{X}$, contradicting to the fact that $\mathcal{X}$ is a superimposed s-disjunct code. □

[3]An s-subset is a subset of s codewords.

4.2 Superimposed $(s, 1, N)$-codes and Channel Assignment in MR-MC Networks

As elaborated in Subsection 3.1, an MR-MC network is modelled by a directed graph $G(V, E, \mathcal{C})$, where $\mathcal{C}$ is the corresponding channel code. For any given node $u \in V$, $\vec{c}_u \in \mathcal{C}$ is a binary vector with each element corresponding to a channel and its $1/0$ value representing this channel being a primary channel or a secondary channel of node u. This observation helps us to build a direct mapping between a superimposed s-disjunct code $\mathcal{X}$ (represented by a $N \times t$ matrix), and the channel code $\mathcal{C}$ of a network G: N represents the number of available orthogonal channels, and each codeword of $\mathcal{X}$ indicates a possible channel codeword to a node in G. Then the column weight w_i of $\mathcal{X}$ represents the number of primary channels a node i has, and the row weight λ_j represents the number of nodes that take channel k_j as a primary channel.

In this paper, we will design algorithms for channel assignment based on superimposed codes. This research is motivated by the following observation: if the channel code $\mathcal{C}$ of a network G is a superimposed s-disjunct code $\mathcal{X}$, the nice s-disjunct property of $\mathcal{X}$ can be applied to derive the conditions for interference-free channel assignment.

Therefore we assume that the channel code $\mathcal{C}$ of network G is an s-disjunct superimposed code. From now on, we will use $\mathcal{X}$ to represent the channel code. We require that each node gets a unique codeword from $\mathcal{X}$ before participating in the network. In our algorithms, codewords from one-hop or two-hop neighbors are required for channel computation. A natural question is: how to obtain the codewords from neighboring nodes before channel assignment is complete? In this study, we assume that each node broadcasts its channel codeword once on each of its primary channels, or on all channels, to inform the neighbors of its codewords.

5. CHANNEL ASSIGNMENT BASED ON SUPERIMPOSED CODES

In this section, we first propose a generic channel assignment algorithm for MR-MC mesh networks. The generic algorithm assigns channels to nodes instead of links. This can facilitate channel selection for broadcast traffic. Then we propose an algorithm for link channel assignment targeting the unicast traffic. We also analyze the performances of both algorithms in detail.

5.1 The Generic Channel Assignment Algorithm

Let G be an MR-MC wireless mesh network with N available orthogonal channels, and $\mathcal{X}$ be the superimposed $(s, 1, N)$-code for its channel assignment. For any node u in G, a unique codeword $X(u) \in \mathcal{X}$ is associated with u indicating u's primary and secondary channel sets. Denote by $\mathcal{N}(u)$ the set of interferers of u. Algorithm 1 is a generic one that computes a set of channels for node u's transmissions.

Intuitively, u should choose only those channels not being used by any of its interferers from its primary channel set. If none of these primary channels is available, u should choose the secondary channels that are not primary to any of the nodes in $\mathcal{N}(u)$, the set of interferers of u. Since all nodes intend to utilize their primary channels whenever possible, choosing a channel that is secondary to all interferers is a reasonable choice. If u can not find out a channel that is secondary to all interferers, it picks up the primary channels that are primary to the least number of nodes in $\mathcal{N}(u)$.

These primary channels have the smallest row weight in $\mathcal{X}(\mathcal{N}(u))$, the set of codewords of $\mathcal{N}(u)$. Let $CH(u)$ be the set of channels assigned to u.

Algorithm 1 Channel Assignment for Node u

Input: Codewords $X(u)$ and $\mathcal{X}(\mathcal{N}(u))$.
Output: $CH(u)$, the set of channels assigned to u.

1: **function** $CH(u)$=**ChannelSelect**($X(u)$, $\mathcal{X}(\mathcal{N}(u))$)
2: $CH_1(u) \leftarrow Channels(BoolSum(\mathcal{X}(\mathcal{N}(u) \cup \{u\})) \oplus BoolSum(\mathcal{X}(\mathcal{N}(u))))$ ▷ Find the set of primary channels that are secondary to all nodes in $\mathcal{N}(u)$.
3: **if** $CH_1(u) \neq \emptyset$ **then**
4: $CH(u) \leftarrow CH_1(u)$
5: **else**
6: $CH_2(u) \leftarrow Channels(\overline{BoolSum(\mathcal{X}(\mathcal{N}(u) \cup \{u\}))})$ ▷ Find the set of secondary channels that are secondary to all nodes in $\mathcal{N}(u)$.
7: **if** $CH_2(u) \neq \emptyset$ **then**
8: $CH(u) \leftarrow CH_2(u)$
9: **else**
10: $CH_3(u) \leftarrow$ Select $Channels(X(u))$ with the smallest row weight in $\mathcal{X}(\mathcal{N}(u))$ ▷ Select the primary channels with the least row weight in $\mathcal{N}(u)$.
11: $CH(u) \leftarrow CH_3(u)$
12: **end if**
13: **end if**
14: **end function**

The basic idea for Algorithm 1 can be sketched below. Given $X(u)$ and $\mathcal{X}(\mathcal{N}(u))$, the Boolean sum of $\mathcal{X}(\mathcal{N}(u))$ and $\mathcal{X}(\mathcal{N}(u) \cup \{X(u)\})$ are first computed. Then the algorithm computes $CH_1(u)$, the set of u's primary channels that are secondary to all nodes in $\mathcal{N}(u)$. If $CH_1(u) \neq \emptyset$, assign $CH_1(u)$ to u; Otherwise, check $CH_2(u)$, the set of channels that are secondary to all nodes in $\mathcal{N}(u) \cup \{u\}$. If $CH_2(u) \neq \emptyset$, assign $CH_2(u)$ to u; otherwise, assign $CH_3(u)$, the set of primary channels whose corresponding row weights in the set $\mathcal{X}(\mathcal{N}(u))$ are minimum, to u.

Note that the set of primary channels of u are those favored by u. Therefore, $CH_1(u)$ contains the channels favored by u only, and $CH_3(u)$ is the set of channels favored by u and the least number of interferers of u. For $CH_2(u)$, since it contains the set of channels nobody likes to utilize in u's interference range, u should take this advantage. These channel assignment criterions reflect our design principle: *a node always selects a channel that causes the least interference to its neighborhood.*

Also note that Algorithm 1 is a localized one with each node u running a copy and making its channel assignment independently. We will prove in Lemma 5.1 that if there is an unused channel in $CH_1(u)$ for a radio r of u, r's transmission is guaranteed to be interference free.

Since each node may be equipped with multiple radios, the channels in $CH_1(u)$ may not be enough. In this case, assign all channels from $CH_1(u)$ first, then use the channels from $CH_2(u)$, and then from $CH_3(u)$.

Remarks: Algorithm 1 is a generic one that takes the codewords of u and its interferers as inputs. Therefore, Algorithm 1 does not rely on any interference model, as long as the set of u's interferers can be defined. Additionally, since Algorithm 1 assigns channels to the node, or the transmitters of the node, Algorithm 1 is a static channel allocation method. If roles of radios (the role of transmission or reception) are fixed, Algorithm 1 can help to decrease the number of channel switchings significantly compared to dynamic channel assignment. However, Algorithm 1 is dynamic when the set of interferers are collected on-line. Therefore, Algorithm 1 is flexible in that it can support both static and dynamic channel assignments.

Note that the channels determined by Algorithm 1 can be used for both unicast and local broadcast simultaneously. Since Algorithm 1 intends to pick up channels that may not be used by the interferers based on the local knowledge, it is superior in supporting local broadcast compared to existing research (Section 2). We plan to conduct extensive simulations to study the performance of Algorithm 1 when utilized to support broadcast in MR-MC mesh networks.

Example: Take the superimposed 3-disjunct code $\mathcal{X}$ in Fig. 1 as an example. Given a node u and $\mathcal{N}(u) = \{v, w, y\}$. Let $X(u) = X(1)$. If $X(v) = X(2)$, $X(w) = X(3)$, and $X(y) = X(4)$, Algorithm 1 yields $CH_1(u) = \{1, 10\}$, which means that channels 1 and 10 can be assigned to u. In this case, u picks up its primary channels. Since both channels are primary to u, based on Lemma 5.1, the transmission from u will not interfere with any other on-going traffic. If $\mathcal{N}(u) = \{v, w, y, z\}$, and $X(v) = X(3)$, $X(w) = X(10)$, $X(y) = X(12)$, and $X(z) = (13)$, no primary channels of u can be assigned to u but u can get channels $\{5, 7\}$ that are secondary to all nodes in $\mathcal{N}(u) \cup \{u\}$. When $\mathcal{N}(u) = \{v, w, y, z\}$, and $X(v) = X(4)$, $X(w) = X(10)$, $X(y) = X(12)$, and $X(z) = X(13)$, no channel that is secondary to all nodes in $\mathcal{N}(u)$ can be assigned to u. Therefore u picks up channels from its primary channel set $\{1, 2, 4, 10\}$ since all of them have the same row weight of 1 in $\mathcal{N}(u)$.

5.1.1 Conditions for Interference-Free Channel Assignment

In this subsection, we study the conditions for interference-free channel assignment based on Algorithm 1. Note that Algorithm 1 does not require a node u to collect the codewords of all interferers. If u knows nothing about its neighborhood, one of its primary channels will be picked for transmission. However, if $\mathcal{N}(u)$ is the complete set of interferers of node u, interference-free channel assignment is possible. In the following, we will first study the two scenarios when the channels assigned to u based on Algorithm 1 do not conflict with those of any other node in $\mathcal{N}(u)$. Then we study the conditions when interference-free communication in the whole network can be achieved. For simplicity, we assume that each node u in the network is equipped with two radios: one for transmission and one for reception. The results can be generalized to the case of more than two radios.

LEMMA 5.1. *If $CH_1(u) \neq \emptyset$, node u does not interfere with any other node in $\mathcal{N}(u)$.*

PROOF. When $CH_1(u) \neq \emptyset$, node u picks up channels from $CH_1(u)$, a subset of u's primary channel set, for transmission. $CH_1(u)$ contains channels that are primary to u but secondary to all nodes in $\mathcal{N}(u)$. For $\forall v \in \mathcal{N}(u)$, v can't use any channel from $CH_1(u)$ based on Algorithm 1 since v is assigned with either its own primary channels (from $CH_1(v)$ or $CH_3(v)$), which can't be in $CH_1(u)$, or channels that are secondary to all interferers in $\mathcal{N}(v)$ ($CH_2(v)$), which are secondary to u too since $u \in \mathcal{N}(v)$. □

Note that based on Lemma 5.1, if $\mathcal{N}(u)$ is the complete set of interferers of node u, u's transmissions on the channels from $CH_1(u)$ do not cause any interference to other on-going traffic.

THEOREM 5.1. *If $CH_1(u) \neq \emptyset$ holds for $\forall u \in V$ and $\mathcal{N}(u)$ is the complete set of interferers of u in the network $G(V, E)$, the channel assignment based on Algorithm 1 guarantees interference free communications in the network.*

PROOF. The theorem holds from Lemma 5.1. □

Theorems 5.1 indicates that if each node can compute a primary channel that is secondary to all its interferers based on Algorithm 1, interference-free communications in the whole network can be achieved. In the following, we identify another scenario to accomplish interference-free transmission.

LEMMA 5.2. *Given a node u with $CH_1(u) = \emptyset$ and $CH_2(u) \neq \emptyset$, if $CH_1(v_i) \neq \emptyset$ holds for all its interferers $v_1, v_2, \cdots, v_{|\mathcal{N}(u)|}$, node u's transmissions do not interfere with any other node in $\mathcal{N}(u)$.*

PROOF. Since $CH_1(u) = \emptyset$ and $CH_2(u) \neq \emptyset$, the set of channels assigned to u contains u's secondary channels that are secondary to all other nodes in $\mathcal{N}(u)$. If $CH_1(v_i) \neq \emptyset$ holds for all its interferers $v_1, v_2, \cdots, v_{|\mathcal{N}(u)|}$ in $\mathcal{N}(u)$, the set of channels assigned to v_i for $i = 1, 2, \cdots, |\mathcal{N}(u)|$ include v_i's primary channels only. Therefore, u's and its interferers' transmission channels do not overlap, and thus u's transmissions do not interfere with its interferers, and are not interfered by its interferers. □

Note that Theorem 5.1 does not place any restrictions on the size of the interferer set for any node. In the following, we prove that when $s \geq |\mathcal{N}(u)|$ holds for $\forall u \in V$ in the network $G(V, E)$, interference-free communication is guaranteed.

THEOREM 5.2. *If $s \geq |\mathcal{N}(u)|$ and $\mathcal{N}(u)$ is the complete set of interferers of u for $\forall u$ in G, the channel assignment based on Algorithm 1 guarantees interference free communications in the network.*

PROOF. Since $\mathcal{X}$ is an s-disjunct code, $BoolSum(\mathcal{X}(\mathcal{N}(u)))$ does not cover $X(u)$, which means that there exists at least one row in $\mathcal{X}$ at which $X(u)$ has the value 1 and all $\mathcal{X}(\mathcal{N}(u))$ have the value 0 (see Lemma 4.1). Therefore condition $CH_1(u) \neq \emptyset$ holds. Based on Theorem 5.1, the claim holds. □

Theorem 5.2 reports another condition for interference-free communications in the whole network based on Algorithm 1. In other words, if s upper-bounds the cardinality of the complete interferer set of each node in the network, interference-free communications can be achieved. This condition sounds very rigorous. However, for a stationary multi-radio multi-channel mesh network where the mesh routers can be carefully placed, the set of interferers could be small to provide sufficient coverage. In this scenario, channel assignment based on Algorithm 1 yields an interference-free network.

5.1.2 Probabilities for interference-Free Channel Assignment

Note that Lemma 5.1 and Lemma 5.2 report two conditions to achieve interference-free communications with no restrictions on the size of $\mathcal{N}(u)$. In this subsection, we conduct further analysis to derive the probabilities for interference-free channel assignment when $|\mathcal{N}(u)| > s$ based on Algorithm 1. In other words, we will study the probability that a node u can find out a channel to achieve interference-free communication in its local neighborhood when $s' > s$, where $s' = |\mathcal{N}(u)|$.

Let P_1 be the probability that Lemma 5.1 holds for some node u, and P_2 be the probability that Lemma 5.2 holds. Let $\mathcal{N}(u)$ be the complete set of interferers of node u. Under the protocol interference model, $\mathcal{N}(u) = N_2(u)$. We have

$$\begin{aligned} P_1 &= p(CH_1(u) \neq \emptyset), \quad (3) \\ P_2 &= p(CH_2(u) \neq \emptyset, CH_1(u) = \emptyset, \\ &\quad CH_1(v_i) \neq \emptyset, \forall v_i \in \mathcal{N}(u)) \\ &= p(CH_2(u) \neq \emptyset, CH_1(u) = \emptyset) \cdot \\ &\quad p(CH_1(v_i) \neq \emptyset, \forall v_i \in \mathcal{N}(u)) \\ &= p(CH_2(u) \neq \emptyset, CH_1(u) = \emptyset) \cdot \\ &\quad \prod_{i=1}^{|\mathcal{N}(u)|} p(CH_1(v_i) \neq \emptyset) \quad (4) \end{aligned}$$

The last two equalities hold because the channel codeword for each node is randomly and independently assigned. Based on Eq. (3) and (4), to compute P_1 and P_2, we need to first compute the probability that $CH_1(u) \neq \emptyset$ for $\forall u \in V$, and the probability that $CH_1(u) = \emptyset$ and $CH_2(u) \neq \emptyset$ hold simultaneously.

Let m be the number of rows in $BoolSum(\mathcal{X}(\mathcal{N}(u)))$ with a value 0. Given the condition $CH_1(u) \neq \emptyset$ or $CH_2(u) \neq \emptyset$, it implies that $m > 0$. Denote these m rows by row_1, row_2, $\cdots$, row_m. Let λ_{max} be the maximum row weight among $row_1, row_2, \cdots, row_m$. We have $t - s' - \lambda_{max} \geq 0$.

Note that the boolean sum $BoolSum(\mathcal{X}(\mathcal{N}(u)))$ can cover a codeword $X(v)$ in the set $\mathcal{X} \setminus \mathcal{X}(\mathcal{N}(u))$ **iff** $X(v)$ has a value 0 at all the m rows $row_1, row_2, \cdots, row_m$. Therefore, the probability that the boolean sum of $\mathcal{X}(\mathcal{N}(u))$ covers an arbitrary codeword $X(v)$ in $X \setminus \mathcal{X}(\mathcal{N}(u))$ is

$$\begin{aligned} p_{cover|m>0} &= \prod_{i=1}^{m} \frac{|\mathcal{X}| - s' - \lambda_{row_i}}{|\mathcal{X}| - s'} \\ &= \prod_{i=1}^{m} (1 - \frac{\lambda_{row_i}}{|\mathcal{X}| - s'}) \quad (5) \end{aligned}$$

Thus the probability that the boolean sum of $\mathcal{X}(\mathcal{N}(u))$ does not cover any arbitrary codeword $X(v)$ in the set $\mathcal{X} \setminus \mathcal{X}(\mathcal{N}(u))$ is

$$\begin{aligned} p_{uncover|m>0} &= 1 - p_{cover|m>0} \\ &= 1 - \prod_{i=1}^{m} (1 - \frac{\lambda_{row_i}}{|\mathcal{X}| - s'}). \quad (6) \end{aligned}$$

Based on the above analysis, we conclude that a good superimposed code for our channel assignment should have a larger s and larger row weights λ since the higher the probability $p_{uncover}$, the less interference our channel assignment causes. Methods of constructing superimposed (s, L, N)-codes have been extensively studied in [21] [23] [25] [26] [27] [28] [29] [30]. Ref. [31] reports some optimal designs to construct an s-disjunct code with different N, s, t.

Let $p(m > 0|\mathcal{N}(u))$ denote the probability that there exists at least one row with a value 0 in $BoolSum(\mathcal{X}(\mathcal{N}(u)))$. Assuming that each codeword in $\mathcal{X}$ is independent, we have

$$\begin{aligned} p(m > 0|\mathcal{N}(u)) &= 1 - p(m = 0|\mathcal{N}(u)) \\ &= 1 - \prod_{i=1}^{N} (1 - \frac{\binom{t-\lambda_i}{s'}}{\binom{t}{s'}}) \quad (7) \end{aligned}$$

Therefore the probability that $CH_1(u) \neq \emptyset$ is

$$p(CH_1(u) \neq \emptyset) = p(m > 0|\mathcal{N}(u)) \cdot p_{uncover|m>0} \quad (8)$$

Now let's compute the probability that both $CH_1(u) = \emptyset$ and $CH_2(u) \neq \emptyset$ hold. Based on the definition of m, $CH_2(u) \neq \emptyset$ and $CH_1(u) = \emptyset$ hold **iff** the Boolean sum $BoolSum(\mathcal{X}(\mathcal{N}(u)))$

covers the codeword $X(u)$ and $m > 0$. According to Eq.(5), the probability that node u can find a secondary channel for communication is

$$p(CH_2(u) \neq \emptyset, CH_1(u) = \emptyset) = p(m > 0|\mathcal{N}(u)) \cdot p_{cover|m>0} \quad (9)$$

For completeness, we provide the probability that a channel from $CH_3(u)$ is picked. Note that both $CH_1(u) = \emptyset$ and $CH_2(u) = \emptyset$ hold **iff** the boolean sum $BoolSum(\mathcal{X}(\mathcal{N}(u)))$ covers the codeword $X(u)$ and $X(u)$ cannot have a value 0 at any row of the m rows, namely $m = 0$. According to Eq.(7), the probability that $CH_1(u) = \emptyset$ and $CH_2(u) = \emptyset$ is

$$p(CH_1(u) = \phi, CH_2(u) = \phi) = p(m = 0|\mathcal{N}(u)) = \prod_{i=1}^{N}(1 - \frac{\binom{t-\lambda_i}{s'}}{\binom{t}{s'}}) \quad (10)$$

The probability that P_2 holds and the probabilities that u picks up a channel from $CH_1(u)$, $CH_2(u)$, and $CH_3(u)$ with respect to s' for the superimposed $(3, 1, 13)$-code of size 13 (Fig. 1) are illustrated in Fig. 2. Notice that when $s' \leq s$, Algorithm 1 guarantees to choose a channel from $CH_1(u)$ is 1.

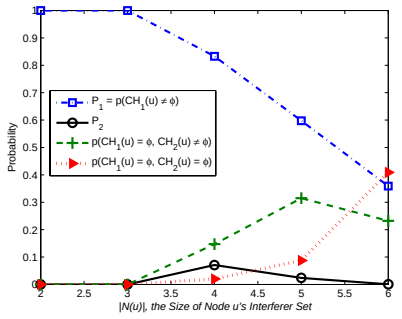


Figure 2: The probabilities that u picks up a channel from $CH_1(u)$, $CH_2(u)$, and $CH_3(u)$, respectively, and the probability that P_2 holds. Here $s = 3$, $t = N = 13$.

5.2 Channel Assignment for Broadcast Traffic

When a channel for broadcast is needed, we can apply Algorithm 1 directly. Let u be any node in a network $G(V, E)$. Let $\mathcal{N}(u)$ be the set of interferers of u. In the topology interference model, $\mathcal{N}(u)$ contains all two-hop neighbors of u, i. e. $\mathcal{N}(u) = N_2(u)$. Let $X(u)$ and $\mathcal{X}(N_2(u))$ be the codewords of u and its interferers. For broadcast channel assignment at node u the inputs to Algorithm 1 are $X(u)$ and $\mathcal{X}(N_2(u))$.

Note that Algorithm 1 does not care whether $\mathcal{N}(u)$ is a complete set of interferers or not. However, if $\mathcal{N}(u)$ is the complete set of interferers of u, and $|\mathcal{N}(u)| \leq s$ holds for $\forall u \in V$, broadcast does not cause any interference (see Theorem 5.2).

In reality, broadcast and unicast coexist. However, broadcast is inferior to unicast, as assumed by IEEE 802.11 standard. Therefore, when applying Algorithm 1 for broadcast channel assignment, u selects an unused channel in $CH_1(u) \neq \emptyset$ first. If fails, u picks up an unused channel in $CH_2(u) \neq \emptyset$. If no channels in $CH_1(u)$ and $CH_2(u)$ is available for u's broadcast, u picks up an unused primary channel from $CH_3(u)$.

5.3 Channel Assignment for Unicast Traffic

In this section, we consider the channel assignment for the unicast traffic from node u to node v, where u and v reside in each other's transmission range. In our consideration, it is u's responsibility to compute the channel for the link $(u \rightarrow v)$. For simplicity, we use $N(u)$ to denote $N_1(u)$, the one-hop immediate neighbor set of u. We have $u \in N(v)$ and $v \in N(u)$.

A simple idea would be to plug-in $X(u)$ and $\mathcal{X}(N(v)) \cup \{X(v)\}$ into Algorithm 1 to compute a channel for $(u \rightarrow v)$. However, since $\mathcal{X}(N(u))$ is available to u too, it is reasonable to use both $\mathcal{X}(N(u))$ and $\mathcal{X}(N(v))$ for $(u \rightarrow v)$ channel assignment. This is our motivation for designing Algorithm 2 for the unicast traffic from u to v. Note that in Algorithm 2 we consider $N(u)$ and $N(v)$ instead of $N_2(u)$ and $N_2(v)$ as the interferers for the unicast traffic from u to v. We will prove that the channel codewords from one-hop neighbors of both the sender and the receiver suffice for Algorithm 2 to achiever 100% throughput with a very simple scheduling algorithm.

Algorithm 2 Channel Assignment for unicast from u to v

Input: Codewords $\mathcal{X}(N(u))$, and $\mathcal{X}(N(v))$
Output: $CH(u \rightarrow v)$, a channel to the link from u to v.

1: **function** $CH(u \rightarrow v)$=**UnicastChannelSelect**($\mathcal{X}(N(u))$, $\mathcal{X}(N(v))$)
2: $CH_1(u) \leftarrow SelectAChannel(BoolSum(\mathcal{X}(N(v) \cup \{v\})) \oplus BoolSum(\mathcal{X}(N(v) \cup \{v\} \setminus \{u\})))$ ▷ Find a primary channel that is secondary to all nodes in $N(v) \cup \{v\} \setminus \{u\}$.
3: **if** $CH_1(u) \neq \emptyset$ **then**
4: $CH(u \rightarrow v) \leftarrow CH_1(u)$
5: **else**
6: $CH_2(u) \leftarrow SelectAChannel(\overline{BoolSum(\mathcal{X}(N(u) \cup \{u\}))} \bigwedge BoolSum(\mathcal{X}(N(v))))$ ▷ Find a secondary channel that is secondary to all nodes in $N(u) \cup \{u\}$ but primary to at least one node in $N(v)$.
7: **if** $CH_2 \neq \emptyset$ **then**
8: $CH(u \rightarrow v) \leftarrow CH_2(u)$
9: **else**
10: $CH_3(u) \leftarrow SelectAChannel(X(u) \bigwedge \overline{X(v)})$ ▷ Select a channel that is primary to u and secondary to v.
11: $CH(u \rightarrow v) \leftarrow CH_3(u)$
12: **end if**
13: **end if**
14: **end function**

The basic idea for Algorithm 2 is sketched below. Node u, the unicast source, first computes a channel that is primary to u but secondary to all nodes in $N(v) \cup \{v\} \setminus \{u\}$. In this case, the channel selected corresponds to a row with a value 1 in $X(u)$ and all 0's in $\mathcal{X}(N(v) \cup \{v\} \setminus \{u\})$. If this primary channel does not exist, u computes a channel that is secondary to all nodes in $N(u) \cup \{u\}$ but primary to at least one node in $N(v)$. If fails again, u picks up a primary channel that is secondary to v. As shown in Theorem 5.6, this channel selection criteria intends to minimize interference and accordingly maximize throughput.

The design motivation for Algorithm 2 is stated as follows. A node should utilize its primary channels if possible; Otherwise, it should choose a secondary channel that is secondary to all nodes in its closed neighborhood, but not secondary to all nodes in the receiver's neighborhood, since otherwise, the receiver may choose the same channel for its own unicast, causing interference.

Note that each node u runs a copy of Algorithm 2 to compute a channel k for the unicast link $(u \rightarrow v)$, where $v \in N(u)$. Therefore Algorithm 2 is a localized transmitter-oriented channel assignment algorithm.

5.3.1 Interference Analysis

An interesting problem is whether Algorithm 2 can compute an interference-free channel for u's transmission to v. Note that there are two different kinds of interferences for the unicast traffic: the direct interference caused by immediate neighbors and the indirect interference caused by the neighbors of the receiver. The first one results in the *exposed terminal problem* while the second one results in the *hidden terminal problem*.

The hidden and exposed terminal problems are well-known phenomenons in wireless networks due to the broadcast nature of the wireless media. For example, in Fig. 3, when node u is transmitting data to node v, the hidden terminal problem occurs when node x, which is unaware of the ongoing transmission, attempts to transmit, thus causing collision at node v. In Fig. 4, when node v is transmitting data to node u, the exposed terminal problem occurs when node x, which is aware of the ongoing transmission, refrains to communicate with y, thus causing degraded network throughput.

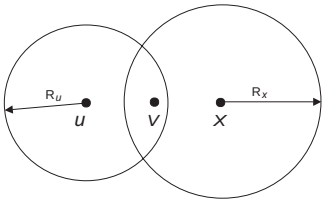


Figure 3: The hidden terminal problem in wireless networks.

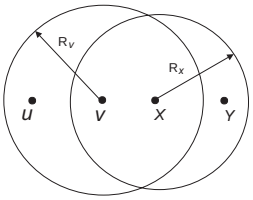


Figure 4: The exposed terminal problem in wireless networks.

In the following we prove that when the number of immediate neighbors of any node in the network is upper-bounded by s, the hidden/exposed problems can be solved and the network communication is free of interference. Note that in the following analysis, we assume that there is no broadcast traffic that can potentially interfere with the unicast traffic.

THEOREM 5.3. *Let u and v be any pair of immediate neighbors in the network $G(V, E)$. If $|N(w)| \leq s$ holds for $\forall w \in V$, Algorithm 2 yields* **hidden** *terminal interference-free channel assignment for the unicast traffic from u to v.*

PROOF. Let x be any hidden terminal, as shown in Fig. 3. We have $x \in N(v)$. Since $|N(v)| \leq s$, $|N(v) \cup \{v\} \setminus \{u\}| \leq s$. Therefore the Boolean sum of all codewords owned by $N(v) \cup \{v\} \setminus \{u\}$ does not cover the codeword of u due to the s-disjunct property of the superimposed code $\mathcal{X}$ used for channel assignment. Thus $CH_1(u) \neq \emptyset$ holds in Algorithm 2 and u can choose one of its primary channels that are secondary to all nodes in $N(v) \cup \{v\} \setminus \{u\}$. Let k be the channel selected by u for the unicast from u to v.

We claim that it is impossible for any node $x \in N(v) \cup \{v\} \setminus \{u\}$ to choose k for unicast based on Algorithm 2. Assume x needs a channel to unicast to y. Since $|N(y)| \leq s$, $CH_1(x) \neq \emptyset$. Therefore x will choose one of its primary channels that are secondary to all nodes in $N(y) \cup \{y\} \setminus \{x\}$ based on Algorithm 2. However, k is secondary to x since $x \in N(v)$. Therefore the unicasts from u to v and from x to y do not interfere since they use different channels.

Note that any node w in $N(u)$ but not in $N(v)$ may choose the same channel as that of u for unicast. But this unicast does not cause interference at v since v is out of w's transmission range. □

THEOREM 5.4. *Let v and u be any pair of immediate neighbors in the network $G(V, E)$. If $|N(w)| \leq s$ holds for $\forall w \in V$, Algorithm 2 yields* **exposed** *terminal interference-free channel assignment for the unicast traffic from v to u.*

PROOF. Let x be any exposed terminal to the unicast from v to u, as shown in Fig. 4. Let y be the destination of the unicast traffic from x. We have $x \in N(v)$, $x \notin N(u)$, and $y \notin N(v) \cup N(u)$. Thus the ACK from y to x does not reach v. For the same reason, the ACK from u to v does not reach x. Therefore, no matter which channels the links $(u \rightarrow v)$ and $(y \rightarrow x)$ receive from Algorithm 2, the two ACKs do not collide at v and x.

Since v and y are hidden with respect to x, based on Theorem 5.3,v and y choose different channels when $|N(w)| \leq s$ holds for $\forall w \in V$ in the network. Therefore, the ACK from y to x and the data from v to u do not collide at x. For the same reason, the ACK from u to v and the data from x to y do not collide at v.

Based on this analysis, Algorithm 2 yields **exposed** terminal-free channel assignment. □

Note that Theorems 5.3 and 5.4 hold when $|N(w)| \leq s$ for $\forall w \in V$ for a network $G(V, E)$. Assuming no interference caused by broadcast traffic (see Subsection 5.2), these two theorems indicate that Algorithm 2 yields interference-free communications in the network G when the maximum node degree (the number of one-hop neighbors) is $\leq s$.

THEOREM 5.5. *If $|N(w)| \leq s$ for $\forall w \in V$ holds for a network $G(V, E)$, Algorithm 2 yields interference-free communications in G.*

PROOF. Proof follows from Theorems 5.3 and 5.4. □

5.3.2 Throughput Analysis

It is interesting to observe that the induced graph of the edges being assigned the same channel via Algorithm 2 is a forest. Recent research [32, 33] indicates that with a simple scheduling algorithm (maximal weight independent set scheduling), a tree graph can achieve 100% throughput under the primary interference constraints. This result can be applied to analyze the achievable throughput via Algorithm 2.

Let's study Algorithm 2 again. It has the following nice feature:

LEMMA 5.3. *Let $(w \rightarrow u)$ and $(u \rightarrow v)$ be two adjacent edges in $G(V, E)$. Assume k_1 is the channel assigned to $(w \rightarrow u)$ and k_2 is the channel to $(u \rightarrow v)$ by Algorithm 2. We have $k_1 \neq k_2$.*

PROOF. Channels k_1 and k_2 are computed by w and u respectively. If $CH_1(w) \neq \emptyset$, $k_1 \in CH_1(w)$. Therefore k_1 is primary to w but secondary to $N(u) \cup \{u\} \setminus \{w\}$. In this case, since k_1 is secondary to u, $k_1 \notin CH_1(u)$ and $k_1 \notin CH_3(u)$. Also because k_1 is primary to w, k_1 can not be in $CH_2(u)$ since $w \in N(u)$ and all channels in $CH_2(u)$ are secondary to $N(u) \cup \{u\}$. Thus channel k_1 can not be selected by u for the edge $(u \rightarrow v)$ if $k_1 \in CH_1(w)$.

If $CH_1(w) = \emptyset$ and $CH_2(w) \neq \emptyset$, k_1 is selected from $CH_2(w)$ by w, which means that k_1 is secondary to all nodes in $N(w) \cup \{w\}$ but primary to at least one node in $N(u)$. Therefore k_1 can not be in $CH_2(u)$ since it contains channels secondary to all nodes in $N(u) \cup \{u\}$. $k_1 \notin CH_1(u)$ and $k_1 \notin CH_3(u)$ hold too since k_1

is secondary to u as $u \in N(w)$. Therefore channel k_1 can not be selected for the edge $(u \to v)$ if $k_1 \in CH_2(w)$.

If k_1 is selected from $CH_3(w)$, k_1 is primary to w and secondary to u, therefore $k_1 \notin CH_1(u)$ and $k_1 \notin CH_3(u)$. We claim that $k_1 \notin CH_2(u)$ too since otherwise k_1 would be secondary to w because $w \in N(u)$ and all channels in $CH_2(u)$ are secondary to the nodes in $N(u) \cup \{u\}$.

Therefor the channel k_1 assigned to the link $(w \to u)$ by Algorithm 2 could not be assigned to the link $(u \to v)$. We have $k_1 \neq k_2$. □

Note that the proof of Lemma 5.3 utilizes the fact that CH_3 is always non-empty. This is guaranteed by the following requirement on the channel codewords: for any two channel codewords $X(u)$ and $X(v)$, there exists two channels k_1 and k_2 such that k_1 is primary to u and secondary to v, and k_2 is primary to v and secondary to u.

COROLLARY 5.1. *Let k_1 and k_2 be the channels assigned to the edges $(u \to v)$ and $(v \to u)$, respectively, by Algorithm 2. Then $k_1 \neq k_2$.*

PROOF. Claim follows from Lemma 5.3. □

Corollary 5.1 indicates that the channels used for DATA and for ACK are always different. Lemma 5.3 indicates that two adjacent links can transmit DATA or ACK concurrently. Therefore, a multihop path can achieve maximum throughput in MR-MC networks since all nodes can transmit simultaneously without causing any collision.

Let $G_k(V, E_k)$ be the induced graph containing all edges receiving channel k based on Algorithm 2. We have

LEMMA 5.4. *For $\forall k \in C$, where C is the set of orthogonal channels, G_k is a forest.*

PROOF. For contradiction we assume that G_k is not a forest. In other words, G_k contains a circle $\mathcal{O}$. Consider any two adjacent edges $(w \to u)$ and $(u \to v)$ in $\mathcal{O}$. Based on Lemma 5.3, the channels assigned to $(w \to u)$ and $(u \to v)$ must be different. Therefore only one of them can appear in G_k. A contradiction to the assumption that $(w \to u)$ and $(u \to v)$ both appear in G_k. Thus no circle $\mathcal{O}$ exists in G_k. □

Lemma 5.3 indicates that each tree in G_k has a star-shaped topology[4], and the number of concurrent transmissions supported equals the total number of stars in all G_k.

COROLLARY 5.2. *Each tree in G_k is a star.*

PROOF. Proof follows from that of Lemma 5.3. □

COROLLARY 5.3. *The number of concurrent transmissions supported by the network equals the total number of stars in all G_k for all $k \in C$.*

PROOF. Since each star topology can support only one unicast at any time, claim follows. □

Brzezinski, Zussman, and Modiano [32] has proved the following lemma:

LEMMA 5.5. *A maximal weight independent set scheduling algorithm achieves 100% throughput for a tree network.*

[4]Since we consider directed links, this topology actually is a star-shaped DAG (Directed Acyclic Graph).

Therefore we have

THEOREM 5.6. *There exists a simple scheduling algorithm such that Algorithm 2 yields 100% throughput.*

PROOF. Proof follows from Lemma 5.4 and Lemma 5.5. □

Brzezinski, Zussman, and Modiano [32] presents multiple algorithms based on matroid intersection to partition the network into subnetworks with large capacity regions to maximize the throughput of each of the subnetwork. Algorithm 2, which is much simpler, maximizes the throughput if each node has a unique channel codewords satisfying the condition elaborated in Section 3.1.

5.3.3 Simulation Study

In this subsection, we conduct simulation to evaluate Algorithm 2 in terms of channel utilization and usage fairness. Our goal is to investigate: 1. the number of concurrent transmissions; 2. the channel usage fairness.

In the simulation we have considered an area of a 100×100 square units with 13 randomly deployed nodes. The simulation settings are listed as follows:

- All simulation results are averaged over 100 different topologies.
- The number of available channels in the network is set to $N = 13$.
- The superimposed $(3, 1, 13)$-code $\mathcal{X}$, as shown in Fig. 1, is applied in the simulation.
- Each node randomly picks a unique codeword from $\mathcal{X}$ as its channel codeword.
- The average node degree is denoted by d, where d varies from 2 to 6.
- The number of radios equipped by each node is denoted by Q, where $Q \in \{2, 4, 6, 8, 10, 12\}$. Q varies under different topologies.

Note that the number of channels utilized by a node can be measured by the number of concurrent transmissions supported by that node. Therefore for an arbitrary node u, we denote its channel utilization by the number of supported concurrent transmissions.

Fig. 5 describes the relationship among the number of concurrent transmissions supported by each node, the average node degree d, and the number of radios Q. For each settings of d and Q, the results are averaged on all the nodes in the network over 100 different topologies. As shown in Fig. 5, when the number of radios is fixed in the network, the smaller the average node degree, the larger the number of concurrent transmissions supported by each node. This is because the smaller the average node degree, the less number of interferers a node may have, namely the more number of channels available for concurrent transmissions.

When the average node degree is fixed, the larger the number of radios, the more the number of concurrent transmissions supported by each node. This result is intuitive since the number of concurrent transmissions is bounded by the number of radios in the network. Comparing the six curves in Fig. 5, we find that the smaller the number of radios, the smaller the number of concurrent transmissions supported by each node. We also find that when $d \leq s$ and Q is fixed, the number of concurrent transmissions supported by each node reaches its maximum, that is Q.

Fairness in channel usage is another important issue in wireless networks. Note that in our simulation study, the channel assignment matrix $\mathcal{X}$ has a constant column weight, which means that

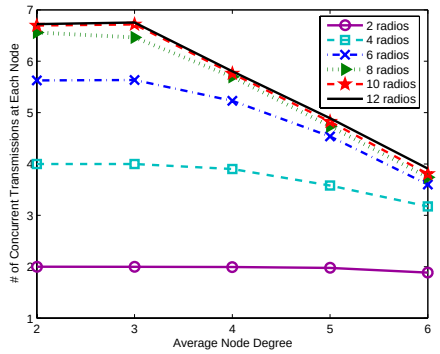


Figure 5: The average number of concurrent transmissions supported by each node.

each node in the network has the same numbers of primary channels and secondary channels. Since the channel codeword is picked randomly and independently for each node, intuitively the channel usage should be fair. This has been validated by our simulation result reported in Fig. 6.

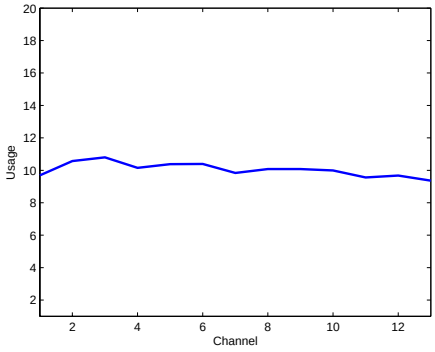


Figure 6: The channel usage of each channel when average node degree is 3.

6. DISCUSSION

6.1 Strength of Algorithms 1 and 2

Note that Algorithms 1 and 2 are both localized. They require the availability of the channel codewords from one or two-hop neighborhood, which results in low communication overhead since the binary codewords are short. In addition, both algorithms have low computation overhead since only simple Boolean algebraic is involved.

Algorithm 1 is generic. It is suitable for both unicast and broadcast traffic. As long as the codewords of the set of interferers are available, an interference-aware channel can be computed. Under certain conditions, this channel causes no interference.

The underlying design principle for unicast channel assignment (Algorithm 2) is the same as that of Algorithm 1: a node always selects a channel that causes the least interference to its neighborhood based on its current knowledge. With a simple scheduling algorithm, Algorithm 2 can achieve 100% throughput.

Neither of the two algorithms relies on the s-disjunct superimposed code, which is introduced to identify the scenarios when interference free communications are possible. However, if the channel codewords form an s-disjunct code, Algorithms 1 and 2 can compute a channel for better interference mitigation. In addition, the larger the s, the better the performance.

Both algorithms can be uploaded to the same node for broadcast and unicast channel computation. However, broadcast may be inferior to unicast, as in IEEE 802.11 standard. In this case, a channel has a higher priority to be assigned for unicast. If the probability of a channel being primary or secondary is the same for all nodes, the channel usage is fair.

Note that even though we assume the frequency channels in our discussion, both algorithms work with any kind of orthogonal channels: time slots, orthogonal codes, etc., as long as the channels can be labelled by a binary string indicating their primary and secondary roles to each node.

6.2 Superimposed Codes

The s-disjunct property elaborated in Lemma 4.1 plays a significant role in interference-free channel assignment. It is clear that the strength s should be strong and the size t should be large for a superimposed code $\mathcal{X}$ of length N to be applicable to a MR-MC network with N available orthogonal channels. Given N, computing a satisfiable superimposed s-disjunct code is non-trivial. As reported by D'yachkov and Rykov in [31], the following relationship of N, t, s, and λ_{max} holds.

LEMMA 6.1. *Let $t > \lambda_{max} > s \geq 1$ and $N > 1$ be integers.*

1. *For any superimposed $(s, 1, N)$-code of length N, size t, and maximum row weight λ_{max}:*

$$N \geq \lceil \frac{(s+1)t}{\lambda_{max}} \rceil \tag{11}$$

2. *If $\lambda_{max} \geq s + 2$, $(s + 1)t = \lambda_{max}N$, and there exists a superimposed $(s, 1, N)$-code $\mathcal{X}$ with size t and maximum row weight λ_{max}, then*

   - *Code $\mathcal{X}$ has a constant column weight $w = s + 1$, and a constant row weight $\lambda = \lambda_{max}$, and the maximal dot product of any two codewords in $\mathcal{X}$ is 1.*
   - *The following inequality holds true:*

$$\lambda^2 - \frac{\lambda(\lambda - 1)}{s + 1} \leq t \tag{12}$$

Note that for a superimposed $(s, 1, N)$-code, the upper bound of s is limited by N. Therefore s cannot be a large number if the number of available channels N in the network is small. However, this should not be a restriction on the application of superimposed codes in IEEE 802.16e based stationary MR-MC wireless mesh networks. The OFDMA technique in IEEE 802.16e [34] [35] allows bandwidth to be divided into many lower-speed sub-channels to increase resistance to multi-path interference. Typically a large number of non-overlapping orthogonal sub-channels are available for simultaneous transmissions. Therefore in this case, s can be large since N is large.

However, the non-overlapping channels in 802.11 standards are limited (3 non-overlapping channels in IEEE 802.11b/g; 12 non-overlapping channels in original IEEE 802.11a). Therefore s in 802.11-based wireless mesh networks is limited to some small number, which may affect the effectiveness of channel assignment.

A good news is that it is very likely that we still have disjunct property with more than s codewords. Let's introduce the definition for α-almost s-disjunct code proposed in [29] [36]: *A binary matrix*

is α-almost s-disjunct if for any randomly selected set of s columns, the probability that they cover no other column is at least α. In [29], authors proposed a study on a 3-disjunct superimposed code of size 30, where the number of codewords is much larger than s. The results indicate that this superimposed code is 0.95-almost 15 disjunct, and 0.6-almost 30 disjunct. This study tells us that a less powerful s-disjunct superimposed code could work well in our channel assignment.

6.3 Scalability Considerations

In superimposed codes, although t increases superlinearly compared to N [31], it is still a bounded number. Therefore, when applying a superimposed code in a MR-MC network, the network size is restricted because a superimposed code can only accommodate at most t nodes. To overcome this problem, we propose the following scalability enhancement.

As shown in Fig. 7, we map the network by cellular grids (regular hexagonal grids). The side length of each grid is R_{max}, where R_{max} is the maximum interference range a node can have in the network. Since the chromatic number of face coloring of such a graph is 3, the cellular grids of the network can be easily classified into 3 categories denoted by A, B, and C.

Given a superimposed $(s, 1, N)$-code $\mathcal{X}$, we evenly divide $\mathcal{X}$ into 3 subsets: t_A, t_B and t_C. Each subset exclusively contains about $1/3$ codewords of $\mathcal{X}$, representing a possible channel assignment for a grid category. For example, nodes belonging to the grids of category A are assigned channels based on t_A; nodes belonging to grids of category B are assigned channels based on t_B; and nodes belonging to grids of category C are assigned channels based on t_C, as shown in Fig. 7.

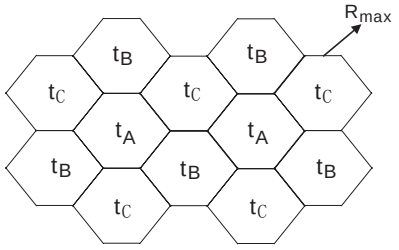


Figure 7: Channel assignment in a scalable network under a cellular grid topology.

Facilitated with a cellular grid topology, the network can scale to infinite size, though the superimposed $(s, 1, N)$-code has a bounded size t.

6.4 Applications to Mobile Mesh Networks

Since both algorithms are localized, and the communication overhead for a node to obtain the channel codewords from its neighborhood is low, channel assignment for mobile MR-MC wireless mesh networks can be easily supported. We will quantitatively study the performance of our algorithms in a mobile mesh network and test their support to popular mobile routing protocols in our future research.

6.5 Future Research

This paper presents our exploratory work toward capacity improvement in MR-MC mesh networks. We will study the performance of our algorithms in an mobile environment and test their capability of simultaneously supporting both unicast and broadcast. Additionally, we will design a MAC protocol based on these two algorithms to efficiently utilize the network resource for throughput maximization. Furthermore, we will explore the impact of channel codeword on the performance of channel assignment based on our algorithms.

7. CONCLUSION

In this paper, we have designed two localized channel assignment algorithms based on s-disjunct superimposed codes for multi-radio multi-channel wireless mesh networks. Our algorithms can effectively support channel allocation for both unicast and local broadcast since channels are pertained to transmitters instead of links even though the interferers at the destination affects channel selection. The selected channels are expected to cause low overall switching delay and low interference to the local neighborhood. In addition, we have identified the conditions when interference-free channel assignment can be achieved and when hidden/exposed terminal problems can be avoided. For unicast, our algorithm results in 100% network throughput with a simple scheduling algorithm. Since we do not make any assumptions on the underlying network settings such as traffic patterns and MAC/routing protocols, our channel assignment algorithms are applicable to a wide range of MR-MC mesh networks.

8. ACKNOWLEDGMENTS

The research of Xing, Cheng, and Ma is supported in part by the NSF CAREER award CNS-0347674. The research of Liang is supported in part by ONR under grant N00014-07-1-0395 and N00014-07-1-1024.

We are grateful to Dr. Lili Qiu, our shepherd, for her help in revising this paper. We are also grateful to the anonymous reviewers for their invaluable and constructive comments and suggestions.

9. REFERENCES

[1] P. Kyasanur and N. H. Vaidya, "Capacity of multi-channel wireless networks: impact of number of channels and interfaces," in *MobiCom '05: Proceedings of the 11th annual international conference on Mobile computing and networking*. ACM Press, 2005, pp. 43–57.

[2] G. Brar, D. M. Blough, and P. Santi, "Computationally efficient scheduling with the physical interference model for throughput improvement in wireless mesh networks," in *MobiCom '06: Proceedings of the 12th annual international conference on Mobile computing and networking*. ACM Press, 2006, pp. 2–13.

[3] M. Alicherry, R. Bhatia, and L. E. Li, "Joint channel assignment and routing for throughput optimization in multi-radio wireless mesh networks," in *MobiCom '05: Proceedings of the 11th annual international conference on Mobile computing and networking*. ACM Press, 2005, pp. 58–72.

[4] M. Kodialam and T. Nandagopal, "Characterizing the capacity region in multi-radio multi-channel wireless mesh networks," in *MobiCom '05: Proceedings of the 11th annual international conference on Mobile computing and networking*. ACM Press, 2005, pp. 73–87.

[5] A. P. Subramanian, R. Krishnan, S. R. Das, and H. Gupta, "Minimum-interference channel assignment in multi-radio wireless mesh networks."

[6] A. Raniwala, K. Gopalan, and T. cker Chiueh, "Centralized channel assignment and routing algorithms for multi-channel wireless mesh networks," *SIGMOBILE Mob. Comput. Commun. Rev.*, vol. 8, no. 2, pp. 50–65, 2004.

[7] A. Raniwala and T. Chiueh, “Architecture and algorithms for an ieee 802.11-based multi-channel wireless mesh network,” in *IEEE Infocom*, 2005.

[8] M. K. Marina and S. R. Das, “A topology control approach for utilizing multiple channels in multi-radio wireless mesh networks,” in *2nd International Conference on Broadband Networks*, 2005, pp. 381– 390.

[9] P. Kyasanur and N. H. Vaidya, “Routing and link-layer protocols for multi-channel multi-interface ad hoc wireless networks,” *SIGMOBILE Mob. Comput. Commun. Rev.*, vol. 10, no. 1, pp. 31–43, 2006.

[10] B.-J. Ko, V. Misra, J. Padhye, and D. Rubenstein, “Distributed channel assignment in multi-radio 802.11 mesh networks,” in *Wireless Communications and Networking Conference (WCNC)*, 2007, pp. 3978–3983.

[11] K. N. Ramachandran, E. M. Belding, K. C. Almeroth, and M. M. Buddhikot, “Interference-aware channel assignment in multi-radio wireless mesh networks,” in *Infocom*, 2006.

[12] H. Skalli, S. K. Das, L. Lenzini, and M. Conti, “Traffic and interference aware channel assignment for multi-radio wireless mesh networks,” in *Technical Report*, 2006.

[13] J. So and N. H. Vaidya, “Multi-channel mac for ad hoc networks: handling multi-channel hidden terminals using a single transceiver,” in *MobiHoc ’04: Proceedings of the 5th ACM international symposium on Mobile ad hoc networking and computing*. ACM Press, 2004, pp. 222–233.

[14] S.-L. Wu, C.-Y. Lin, Y.-C. Tseng, and J.-P. Sheu, “A new multi-channel mac protocol with on-demand channel assignment for multi-hop mobile ad hoc networks,” in *ISPAN ’00: Proceedings of the 2000 International Symposium on Parallel Architectures, Algorithms and Networks (ISPAN ’00)*. IEEE Computer Society, 2000, p. 232.

[15] P.Kyasanur and N.H.Vaidya, “Routing and interface assignment in multi-channel multi-interface wireless networks,” in *Wireless Communications and Networking Conference, 2005 IEEE*, vol. 4, 2005, pp. 2051–2056.

[16] P. Bahl, R. Chandra, and J. Dunagan, “Ssch: slotted seeded channel hopping for capacity improvement in ieee 802.11 ad-hoc wireless networks,” in *MobiCom ’04: Proceedings of the 10th annual international conference on Mobile computing and networking*. ACM Press, 2004, pp. 216–230.

[17] A. A. Bertossi and M. A. Bonuccelli, “Code assignment for hidden terminal interference avoidance in multihop packet radio networks,” *IEEE/ACM Trans. Netw.*, vol. 3, no. 4, pp. 441–449, 1995.

[18] J. Garcia-Luna-Aceves and J. Raju, “Distributed assignment of codes for multihop packet-radio networks,” in *Milcom ’97: Proceedings of the 1997 Military Communications Conference*. IEEE Computer Society, 1997, pp. 450–454.

[19] W. H. Kautz and R. C. Singleton, “Nonrandom binary superimposed codes,” in *IEEE Trans. Inform. Theory*, vol. IT-10, 1964, pp. 363–377.

[20] D. Du and F. Hwang, “Combinatorial group testing and its applications,” *2nd Edition, World Scientific*, 2000.

[21] A. E. F. Clementi, A. Monti, and R. Silvestri, “Selective families, superimposed codes, and broadcasting on unknown radio networks,” in *SODA ’01: Proceedings of the twelfth annual ACM-SIAM symposium on Discrete algorithms*. Society for Industrial and Applied Mathematics, 2001, pp. 709–718.

[22] D. Stinson, T. van Trung, and R. Wei, “Secure frameproof codes, key distribution patterns, group testing algorithms and related structures,” in *Journal of Stat. Planning and Inference*, vol. 86, no. 2, 2000, pp. 595–617.

[23] P. Indyk, “Deterministic superimposed coding with applications to pattern matching,” in *FOCS ’97: Proceedings of the 38th Annual Symposium on Foundations of Computer Science (FOCS ’97)*. IEEE Computer Society, 1997, p. 127.

[24] S. Chaudhuri and J. Radhakrishnan, “Deterministic restrictions in circuit complexity,” in *STOC ’96: Proceedings of the twenty-eighth annual ACM symposium on Theory of computing*. ACM Press, 1996, pp. 30–36.

[25] A. D. Bonis and U. Vaccaro, “Constructions of generalized superimposed codes with applications to group testing and conflict resolution in multiple access channels,” in *Theoretical Computer Science 306*, vol. 1, no. 3, 2003, pp. 223–243.

[26] A. D’yachkov, V. Lebedev, P. Vilenkin, and S. Yekhanin, “Cover-free families and superimposed codes: Constructions, bounds, and applications to cryptography and group testing,” in *IEEE International Symposium on Information Theory*, 2001.

[27] D. Danev, “Some constructions of superimposed codes in euclidean spaces,” *Discrete Appl. Math.*, vol. 128, no. 1, pp. 85–101, 2003.

[28] A. D. yachkov, A. M. Jr, and V.V.Rykov, “New constructions of superimposed codes,” in *Information Theory, IEEE Transactions on*, vol. 46, no. 1, 2000, pp. 284–290.

[29] D. C. Engelhart and A. Sivasubramaniam, “Almost disjunct codes in large scale multihop wireless network media access control,” in *MASCOTS ’05: Proceedings of the 13th IEEE International Symposium on Modeling, Analysis, and Simulation of Computer and Telecommunication Systems*. IEEE Computer Society, 2005, pp. 453–463.

[30] A. J. Macula, “A simple construction of d-disjunct matrices with certain constant weights,” *Discrete Math.*, vol. 162, no. 1-3, pp. 311–312, 1996.

[31] A. G. D’yachkov and V. V. Rykov, “Optimal superimposed codes and designs for renyi’s search model,” *Journal of Statistical Planning and Inference*, vol. 100, no. 2, pp. 281–302, 2002.

[32] A. Brzezinski, G. Zussman, and E. Modiano, “Enabling distributed throughput maximization in wireless mesh networks - a partitioning approach,” in *MobiCom ’06: Proceedings of the 12th annual international conference on Mobile computing and networking*. ACM Press, 2006, pp. 26–37.

[33] A. Dimakis and J. Walrand, “Sufficient conditions for stability of longest queue first scheduling: Second order properties using fluid limits,” *Advances of Applied Probability*, vol. 38, no. 2, pp. 505–521, 2006.

[34] “Wimax/802.16 revealed.” [Online]. Available: http://www.wi-fiplanet.com/tutorials/article.php/3550476

[35] “What is ieee 802.16e.” [Online]. Available: http://www.wimax.com/education/faq/faq45

[36] A. J. Macula, V. V. Rykov, and S. Yekhanin, “Trivial two-stage group testing for complexes using almost disjunct matrices,” *Discrete and Applied Mathematics*, vol. 137, pp. 97–107, 2004.

SVD-QR-T FCM Approach for Virtual MIMO Channel Selection in Wireless Sensor Networks

Jing Liang and Qilian Liang, Senior Member, IEEE
Department of Electrical Engineering
University of Texas at Arlington
Arlington, TX 76019-0016 USA
E-mail: jliang@wcn.uta.edu, liang@uta.edu

Abstract

In this paper, we present Singular-Value Decomposition-QR with Threshold (SVD-QR-T) algorithm to select a subset of channels in virtual MIMO wireless sensor networks (WSN) in order to reduce its complexity and cost. SVD-QR-T selects best subset of transmitters while keeping all receivers active. The threshold is adaptive by means of Fuzzy C-Mean (FCM). Under the constraint of the same total transmission power, this approach is compared against the case without channel selection in terms of capacity, bit error rate (BER) and multiplexing gain in the presence of water-filling as well without. It is shown that in spite of less multiplexing gain, when water-filling is applied, SVD-QR-T FCM provides lower BER at moderate to high SNR; in case of equal transmission power allocation, SVD-QR-T FCM achieves higher capacity at low SNR and lower BER. In general, it provides satisfying performances compared to the case without channel selection but reduced cost and resource.

1 Introduction

1.1 Channel selection in virtual MIMO

Virtual multiple-input-multiple-output (MIMO) has been studied intensively in recent years in order to improve the energy-efficiency in wireless sensor networks (WSN) [1][2][3]. Constrained by its physical size and limited battery, individual sensor is allowed to contain only one antenna. Numerical results show that if these individual sensors jointly form the MIMO system, tremendous energy will be saved while satisfying the required performance. However, a natural drawback of virtual MIMO is the increased complexity and the cost of multiple radio frequency (RF) chains. One technique to reduce the complexity and cost while providing similar capacity and performance is channel selection, or antenna selection.

The knowledge of channels can be obtained by various channel estimation techniques, such as reciprocity principle and feedback channel [4]. When channel side information (CSI) is known to transmitters or receivers, antenna selection can be applied through subset selection algorithms by switchers either at transmitters or receivers, or jointly working at both ends. Therefore the best set of channels are selected to be active while remaining ones are not employed. These switchers typically cost much less than RF chains so that low-cost and low-complexity can be achieved with the benefits of multiple antennas [5] [6]. This system is illustrated in Fig. 1.

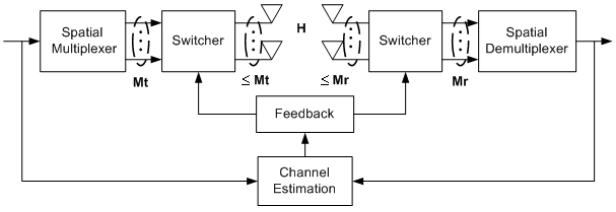


Figure 1. system diagram for virtual MIMO channel selection

Recent years have seen an explosion of interest in MIMO antenna selection and various criteria have been used:

1. Capacity Maximization: In the previous work of [7] [8] [9], channel capacity is used as the optimality criterion, i.e., antennas that achieve the largest capacity are active. [7] demonstrated that in case of no CSI at transmitter (CSIT) but receiver (CSIR), close capacity to that of the MIMO system can be achieved as far as the number of selected receivers is no less than the number of transmitters. [8] and [9] considered CSI

0-7695-2981-X/07 $25.00 © 2007 IEEE
DOI 10.1109/WASA.2007.14

IEEE computer society

Authorized licensed use limited to: University of Texas at Arlington. Downloaded on December 18, 2009 at 14:51 from IEEE Xplore. Restrictions apply.

at transmitter and proposed an exhaustive search algorithm.

2. Minimum Error rate: Apart from maximization of capacity based on Shannon theory, [10] derived another criteria from the respect of minimum error rate when coherent receivers, either maximum likelihood (ML), zero-forcing (ZF) or the minimum mean-square error (MMSE) linear receiver is employed.

3. SNR Maximization: In [11], antenna selection is performed only at the receiver on a basis of largest instantaneous SNR using space-time coding. It is analytically shown that full diversity advantage promised by MIMO can be fully exploited using this criteria as long as the space-time code employed has full spatial diversity.

Although there have been dazzling mathematical studies on antenna selection criteria, practical algorithms of joint transmit and receive antenna selection, i.e., *channel selection* is still open and the problem of corresponding performance analysis require more investigations.

1.2 Contributions and Organization of This Paper

In this paper, under the assumption of quasi-static Rayleigh fading, we propose a practical algorithm to perform channel selection: singular-value decomposition-QR with threshold (SVD-QR-T) employing Fuzzy C-Mean (FCM) to virtually provide adaptive threshold. This algorithm selects rt (see section 3) best subset of transmitters while keeping all receivers active. An example is presented to illustrate each step. Under the constraint of the same total transmission power, this approach is compared against the case without channel selection in terms of capacity, bit error rate (BER) and multiplexing gain. it is shown that in spite of less multiplexing gain, when water-filling is applied, SVD-QR-T FCM provides lower BER at moderate to high SNR; in case of no water-filling and equal transmission power allocation, SVD-QR-T FCM achieves higher capacity at low SNR and lower BER. In general, it provides satisfying performances compared to the case without channel selection but reduced cost and resource.

We organize the remainder of this paper as follows. In Section 2, we introduce our virtual MIMO channel model. Section 3 proposes SVD-QR-T FCM algorithm. Section 4 compares the performances of virtual MIMO after channel selection with those without. Section 5 draws the conclusion and presents future work.

2 Channel Model

Virtual MIMO channel model with M_t transmitters and M_r receivers ($M_t + M_r$ sensors) is illustrated in Fig. 2, where each receiver observes a superposition of the M_t transmitted signals corrupted by Rayleigh flat fading and additive white gaussian noise. Each h_{ji}, $i = 1, 2, \cdots, M_t$ and $j = 1, 2, \cdots, M_r$ represents the channel gain from transmitter i to receiver j [12], which is assumed to be Rayleigh independent and identically distributed (i.i.d.). The additive noise also has i.i.d entries $n_j \sim \mathcal{CN}(0, \sigma^2)$.

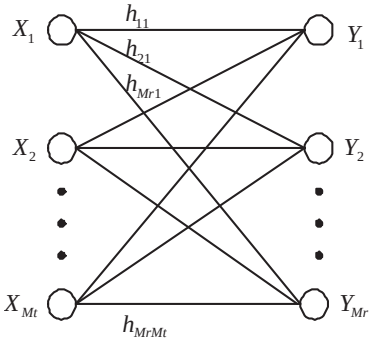


Figure 2. Graphic channel model for virtual MIMO

We may denote this virtual MIMO channel graph with discrete time model:

$$\begin{bmatrix} Y_1 \\ Y_2 \\ \vdots \\ Y_{Mr} \end{bmatrix} = \begin{bmatrix} h_{11} & h_{12} & \cdots & h_{1Mt} \\ h_{21} & h_{22} & \cdots & h_{2Mt} \\ \vdots & \vdots & \vdots & \vdots \\ h_{Mr1} & h_{Mr2} & \cdots & h_{MrMt} \end{bmatrix} \begin{bmatrix} X_1 \\ X_2 \\ \vdots \\ X_{Mt} \end{bmatrix} + \begin{bmatrix} n_1 \\ n_2 \\ \vdots \\ n_{Mr} \end{bmatrix} \quad (1)$$

The above equation can be simplified as $\mathbf{Y} = \mathbf{HX} + \mathbf{n}$, where $\mathbf{H}$ is a $Mr \times Mt$ independent Rayleigh random matrix and $\mathbf{n}$ denotes random noise.

3 SVD-QR-T Virtual MIMO

3.1 SVD-QR-T in virtual MIMO channel selection

SVD has been applied to MIMO channel decomposition in [12], [14], and sensor node selection in [15]. However,

Authorized licensed use limited to: University of Texas at Arlington. Downloaded on December 18, 2009 at 14:51 from IEEE Xplore. Restrictions apply.

these studies are on theoretical analysis only and no algorithm has been proposed on which channels will be physically selected in practice.

We propose SVD-QR-T as follows:

1. Given channel gain matrix $\mathbf{H} \in R^{Mr \times Mt}$ and $r = rank(\mathbf{H}) \leq \min(Mt, Mr)$, determine a numerical estimate rt of the rank r by calculating the singular value decomposition
$$\mathbf{H} = \mathbf{U}\Sigma\mathbf{V}^T, \tag{2}$$
where $\mathbf{U}$ is an $Mr \times Mr$ matrix of orthonormalized eigenvectors of $\mathbf{H}\mathbf{H}^T$, $\mathbf{V}$ is an $Mt \times Mt$ matrix of orthonormalized eigenvectors of $\mathbf{H}^T\mathbf{H}$, and Σ is the diagonal matrix $\Sigma = diag(\sigma_1, \sigma_2, \ldots, \sigma_i, \sigma_r)$, where $\sigma_i = \sqrt{\lambda_i}$ and λ_i is the ith eigenvalue of $\mathbf{H}\mathbf{H}^T$ and $\sigma_1 \geq \sigma_2 \geq \cdots \geq \sigma_r > 0$. σ_i is the singular value of $\mathbf{H}$. In many practical cases, σ_1, σ_1, $\cdots$, σ_{rt} are much larger than $\sigma_{rt+1}, \cdots, \sigma_r$; thus we may set threshold to pick up valuable $\sigma_i, i = 1, 2, \cdots, \sigma_{rt}$ and discard those trivial singular values in order to save resource but maintain satisfying performance. Sometimes rt can be chosen much smaller than the rank r, even 1. In this paper, we propose to use fuzzy c-means (FCM) to determine rt. Details will be discussed in section 3.2.

2. Partition
$$\mathbf{V} = \begin{bmatrix} \mathbf{V}_{11} & \mathbf{V}_{12} \\ \mathbf{V}_{21} & \mathbf{V}_{22} \end{bmatrix} \tag{3}$$
where $\mathbf{V}_{11} \in R^{rt \times rt}$, $\mathbf{V}_{12} \in R^{rt \times (Mt-rt)}$, $\mathbf{V}_{21} \in R^{(Mt-rt) \times rt}$, and $\mathbf{V}_{22} \in R^{(Mt-rt) \times (Mt-rt)}$.

3. Using QR decomposition with column pivoting, determine $\mathbf{E}$ such that
$$[\mathbf{V}_{11}^T, \mathbf{V}_{21}^T]\mathbf{E} = \mathbf{QR}, \tag{4}$$
where $\mathbf{Q}$ is a unitary matrix, and $\mathbf{R} \in R^{rt \times Mt}$ forms an upper triangular matrix with decreasing diagonal elements; and $\mathbf{E}$ is the permutation matrix. The positions of 1 in the first rt columns of $\mathbf{E}$ correspond to the rt ordered *most-significant* transmitters.

3.2 Fuzzy C-Means – Unsupervised Clustering for Adaptive Threshold

In order to keep the balance between performances and cost, we propose FCM clustering approach to divide singular value $(\sigma_1, \sigma_2, \ldots, \sigma_r)$ into two clusters, and thus provides virtual adaptive threshold, so the cluster with higher center would remain for active channels.

FCM clustering is a data clustering technique where each data point belongs to a cluster to a degree specified by a membership grade. This technique was originally introduced by Bezdek [16] as an improvement on earlier clustering methods. Here we briefly summarize it.

Definition 1 (Fuzzy c-Partition) *Let $\mathbf{X} = x_1, x_2, \cdots, x_n$ be any finite set, $\mathbf{V}_{cn}$ be the set of real $c \times n$ matrices, and c be an integer, where $2 \leq c < n$. The* Fuzzy c-partition space *for $\mathbf{X}$ is the set*
$$M_{fc} = U \in V_{cn} | u_{ik} \in [0, 1] \ \forall i, k; \tag{5}$$
where $\sum_{i=1}^{c} u_{ik} = 1 \ \forall k$ and $0 < \sum_{k=1}^{n} u_{ik} < n \ \forall i$. The row i of matrix $U \in M_{fc}$ contains values of the ith membership function, u_i, in the fuzzy c-partition U of $\mathbf{X}$.

The row i of matrix $U \in M_{fc}$ contains values of the ith membership function, u_i, in the fuzzy c-partition U of $\mathbf{X}$.

Definition 2 (Fuzzy c-Means Functionals) *[16] Let $J_m : M_{fc} \times \mathcal{R}^{cp} \rightarrow \mathcal{R}^+$ be*
$$J_m(\mathbf{U}, \mathbf{v}) = \sum_{k=1}^{n} \sum_{i=1}^{c} (u_{ik})^m (d_{ik})^2 \tag{6}$$
where $\mathbf{U} \in M_{fc}$ is a fuzzy c-partition of X; $\mathbf{v} = (\mathbf{v}_1, \mathbf{v}_2, \cdots, \mathbf{v}_c) \in \mathcal{R}^{cp}$, where $\mathbf{v}_i \in \mathcal{R}^p$, is the cluster center of prototype u_i, $1 \leq i \leq c$;
$$(d_{ik})^2 = ||\mathbf{x}_k - \mathbf{v}_i||^2 \tag{7}$$
where $|| \cdot ||$ is any inner product induced norm on $\mathcal{R}^p$; weighting exponential $m \in [1, \infty)$; and, u_{ik} is the membership of $\mathbf{x}_k$ in fuzzy cluster u_i. $J_m(\mathbf{U}, \mathbf{v})$ represents the distance from any given data point to a cluster weighted by that point's membership grade.

The solutions of
$$\min_{\mathbf{U} \in M_{fc}, \mathbf{v} \in \mathcal{R}^{cp}} J_m(\mathbf{U}, \mathbf{v}) \tag{8}$$
are least-squared error stationary points of J_m. An infinite family of fuzzy clustering algorithms — one for each $m \in (1, \infty)$ — is obtained using the necessary conditions for solutions of (8), as summarized in the following:

Theorem 1 *[16] Assume $|| \cdot ||$ to be an inner product induced norm: fix $m \in (1, \infty)$, let $\mathbf{X}$ have at least $c < n$ distinct points, and define the sets ($\forall k$)*
$$I_k = \{i | 1 \leq i \leq c; d_{ik} = ||\mathbf{x}_k - \mathbf{v}_i|| = 0\} \tag{9}$$
$$\tilde{I}_k = \{1, 2, \cdots, c\} - I_k \tag{10}$$
Then $(\mathbf{U}, \mathbf{v}) \in M_{fc} \times \mathcal{R}^{cp}$ is globally minimal for J_m only if (ϕ denotes an empty set)
$$I_k = \phi \Rightarrow u_{ik} = 1 \Big/ [\sum_{j=1}^{c} (\frac{d_{ik}}{d_{jk}})^{2/(m-1)}] \tag{11}$$

Authorized licensed use limited to: University of Texas at Arlington. Downloaded on December 18, 2009 at 14:51 from IEEE Xplore. Restrictions apply.

or

$$I_k \neq \phi \Rightarrow u_{ik} = 0 \ \forall i \in \tilde{I}_k \ and \ \sum_{i \in I_k} u_{ik} = 1, \qquad (12)$$

and

$$\mathbf{v}_i = \sum_{k=1}^{n} (u_{ik})^m \mathbf{x}_k \Big/ \sum_{k=1}^{n} (u_{ik})^m \ \forall i \qquad (13)$$

Bezdek proposed the following iterative method [16] to minimize $J_m(\mathbf{U}, \mathbf{v})$:

1. Fix c, $2 \leq c < n$; choose any inner product norm metric for $\mathcal{R}^p$; and fix m, $1 \leq m < \infty$. Initialize $\mathbf{U}^{(0)} \in M_{fc}$ (e.g., choose its elements randomly from the values between 0 and 1). Then at step l $(l = 1, 2, \cdots)$:
2. Calculate the c fuzzy cluster centers $\mathbf{v}_i^{(l)}$ using (13) and $\mathbf{U}^{(l)}$.
3. Update $\mathbf{U}^{(l)}$ using (11) or (12).
4. Compare $\mathbf{U}^{(l)}$ to $\mathbf{U}^{(l-1)}$ using a convenient matrix norm, i.e., if $||\mathbf{U}^{(l)} - \mathbf{U}^{(l-1)}|| \leq \varepsilon_L$ stop; otherwise, return to step 2.

3.3 Example of SVD-QR-T with FCM in virtual MIMO channel selection

We use the following example to illustrate the SVD-QR-T with FCM application in MIMO-WSN channel selection.

1. *Step 1*. Assume the estimated channel gain is

$$\mathbf{H} = \begin{bmatrix} 0.6211 & 0.7536 & 0.6595 \\ 0.5602 & 0.6596 & 0.1834 \\ 0.2440 & 0.2141 & 0.6365 \\ 0.8220 & 0.6021 & 0.1703 \\ 0.2632 & 0.6049 & 0.5396 \end{bmatrix}$$

By matrix computation, we get:

$$\mathbf{V} = \begin{bmatrix} -0.5856 & -0.5075 & -0.6321 \\ -0.6574 & -0.1589 & 0.7366 \\ -0.4743 & 0.8469 & -0.2406 \end{bmatrix}$$

$diag(\Sigma) = (2.0017, 0.6347, 0.2572)$. Use FCM to divide $diag(\Sigma)$ into 2 clusters, we get

$$\mathbf{v} = \begin{bmatrix} 2.0010 \\ 0.4445 \end{bmatrix}$$

$$\mathbf{U} = \begin{bmatrix} 1.0000 & 0.0190 & 0.0114 \\ 0.0000 & 0.9810 & 0.9886 \end{bmatrix}$$

where entry 1.0000 at $\mathbf{U}$ is the membership that 2.0017 belongs to the cluster with center 2.0010. Therefore, the cluster with higher center is composed of only 2.0017, then 2.0017 is chosen and $rt = 1$.

2. *Step 2*. Obtain $\mathbf{V}_{11}$ and $\mathbf{V}_{21}$ from $\mathbf{V}$:

$$\mathbf{V}_{11} = -0.5856$$

$$\mathbf{V}_{21} = \begin{bmatrix} -0.6574 \\ -0.4743 \end{bmatrix}$$

Based on $[\mathbf{V}_{11}^T \mathbf{V}_{21}^T]$ get $\mathbf{E}$ by QR:

$$\mathbf{E} = \begin{bmatrix} 0 & 1 & 0 \\ 1 & 0 & 0 \\ 0 & 0 & 1 \end{bmatrix}$$

As $rt = 1$, choose the first column of $\mathbf{E}$

$$\mathbf{E}(:, rt) = \begin{bmatrix} 0 \\ 1 \\ 0 \end{bmatrix}$$

3. *Step 3*. Analyze $\mathbf{E}(:, rt)$, 1 appears on the $2nd$ row, and thus the $2nd$ column of $\mathbf{H}$ is selected to construct $\mathbf{H}_s$, which is:

$$\mathbf{H}_s = \begin{bmatrix} 0 & 0.7536 & 0 \\ 0 & 0.6596 & 0 \\ 0 & 0.2141 & 0 \\ 0 & 0.6021 & 0 \\ 0 & 0.6049 & 0 \end{bmatrix}$$

This implies that the channel to be selected are those that connect $2nd$ transmitter and all receivers, i.e., transmitter 2 and all the receivers are selected to be active while other transmitters are not employed to save their battery.

As we may see, the row index in which 1 appears in $\mathbf{E}(:, rt)$ particularly decide which transmitters to be selected, so with regard to SVD-QR-T, $rt \times M_r$ channels are selected to be active.

4 Performance Analysis

Due to the randomness of channel gain matrix, we employ Monte Carlo simulations to analyze the performances

Authorized licensed use limited to: University of Texas at Arlington. Downloaded on December 18, 2009 at 14:51 from IEEE Xplore. Restrictions apply.

on our algorithms in terms of capacity, multiplexing gain and bit error rate (BER). Following steps are applied:

1. Use Jake's Model [19] to randomly generate independent $M_t \times M_r$ Rayleigh channels, take their channel gains at a particular the same time as entries for matrix $\mathbf{H}$.
2. Follow the SVD-QR-T FCM and channel selection algorithm respectively to select channels.
3. Obtain eigenvalue λ_{is} and its rank r_s for $\mathbf{H}_s$. Note that λ_{is} is totally different with λ_i of $\mathbf{H}$.
4. Here we assume $B = 1Hz$. Through 10,000 times Monte Carlo simulations to obtain capacity, BER for QPSK modulation and multiplexing gain with and without water-filling.

4.1 Channel Known At the Transmitter: Water-Filling

When both of CSIT and CSIR are known, water-filling technique can be utilized to optimally allocate power P_i at independent parallel channel i. The sum of capacities on each of these independent parallel channels is the maximal capacity of virtual MIMO [12]. This capacity can be expressed as

$$C = \max_{\sum P_i \le P} \sum_{i=1}^{r} B \log_2(1 + \frac{P_i}{\sigma^2}\lambda_i) \qquad (14)$$

where P is total power constraint for transmitters, r is the rank of $\mathbf{H}$ and λ_i is the eigenvalue of $\mathbf{H}\mathbf{H}^T$. Since the SNR at the ith channel at full power is $SNR_i = \lambda_i P/\sigma^2$, the capacity (14) can also be given in terms of the power allocation P_i as

$$C = \max_{\sum P_i \le P} \sum_{i=1}^{r} B \log_2(1 + \frac{P_i}{P} SNR_i) \qquad (15)$$

where

$$\frac{P_i}{P} = \begin{cases} 1/SNR_0 - 1/SNR_i & SNR_i \ge SNR_0 \\ 0 & SNR_i < SNR_0 \end{cases} \qquad (16)$$

for some cutoff value SNR_0. The final capacity is given as

$$C = \sum_{SNR_i \ge SNR_0} B \log_2(\frac{SNR_i}{SNR_0}) \qquad (17)$$

The value of SNR_0 must be found numerically, owning to no existence of closed-form solution for continues distributions of SNR [21]. This results in Monte Carlo simulations to analyze the capacity performances on SVD-QR-T FCM, which is illustrated in Fig. 3. It is shown that the capacity of 4x4 virtual MIMO is 4 bps/Hz while it becomes 3.4 bps/Hz if SVD-QR-T FCM channel selection is applied. This difference grows up to around 2.2 bps/Hz when SNR reaches 20dB.

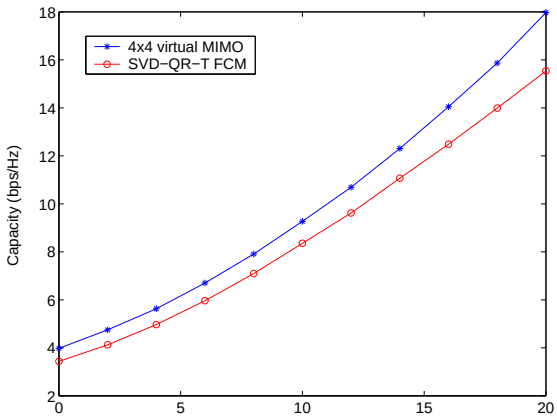


Figure 3. Capacity of SVD-QR-T FCM vs. virtual MIMO with water-filling

Although SVD-QR-T FCM does not seem to provide any advantage in the above figure, it offers lower BER than virtual MIMO without channel selection when SNR is higher than 7dB, which is shown in Fig. 4. This is because SVD-QR-T FCM chooses the best subset of equivalent parallel channels so that SNR allocated at each parallel is larger than that of virtual MIMO as P/σ^2 grows larger. Here we employ QPSK modulation with multiplexing but no space-time coding (STC). Since no diversity gain is obtained, maximal multiplexing does exist.

Maximal multiplexing gain is the number of equivalent multiple parallel spatial channels [22], and also it is referred to as degrees of freedom to communicate [23], which is related with the row and column number of $\mathbf{H}$ and $\mathbf{H}_s$. It has been derived in [23] that the maximal multiplexing gain provided by $M_r \times M_t$ MIMO is $\min(M_t, M_r)$. However, the accurate multiplexing gain is $r = rank(\mathbf{H})$ since it is possible that $\mathbf{H}$ is not full rank. As SVD-QR-T FCM select rt transmitters and all receivers, the maximal multiplexing gain offered by SVD-QR-T FCM is $\min(rt, M_r)$. Note that $rt \le r \le M_r$, therefore the accurate multiplexing gain for SVD-QR-T FCM is rt. However, this values are applicable only for no water-filling. If water-filling are applied, less multiplexing gain will be offered as some singular values with SNR lower than SNR_0 will be cut off.

Under the premise that $\mathbf{H}$ is full rank, we obtain the multiplexing gain on SVD-QR-T FCM and virtual MIMO in Fig. 5.

Authorized licensed use limited to: University of Texas at Arlington. Downloaded on December 18, 2009 at 14:51 from IEEE Xplore. Restrictions apply.

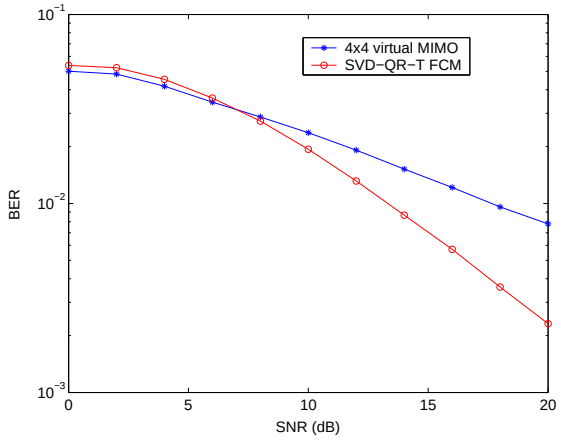


Figure 4. BER of SVD-QR-T vs. 4×4 virtual MIMO with water-filling

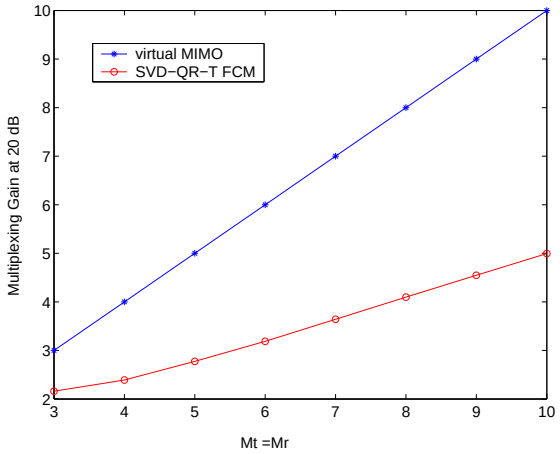


Figure 5. Multiplexing gain of SVD-QR-T FCM vs. virtual MIMO with water-filling at SNR=20dB

4.2 Channel Unknown At Transmitter: Uniform Power Allocation

it is not always the case that both CSIT and CSIR are known. In case of only CSIR, water-filling power optimization can not be applied and people simply allocate equal power to each transmitters, therefore its capacity becomes

$$C = \sum_{i=1}^{r} B \log_2(1 + \frac{SNR_i}{M_t}) \qquad (18)$$

Here we also apply 10,000 time Monte Carlo simulations to obtain the expectation of capacity for SVD-QR-T FCM and 4×4 virtual MIMO at different SNR in Fig. 6. It is shown that SVD-QR-T FCM provides higher capacity than that of virtual MIMO without channel selection if SNR is less than 10dB.

The BER performance is illustrated in Fig. 7. We can see that as SNR increase, BER after SVD-QR-T FCM channel selection become much lower than that of virtual MIMO.

In the mean time, Fig. 8 illustrates that virtual MIMO can achieve larger multiplexing gain than that of SVD-QR-T FCM but that implies more transmitters and RF chains consumption, which is the same situation as in case of water-filling. As no-water-filling is used, here multiplexing gain is not associate with SNR.

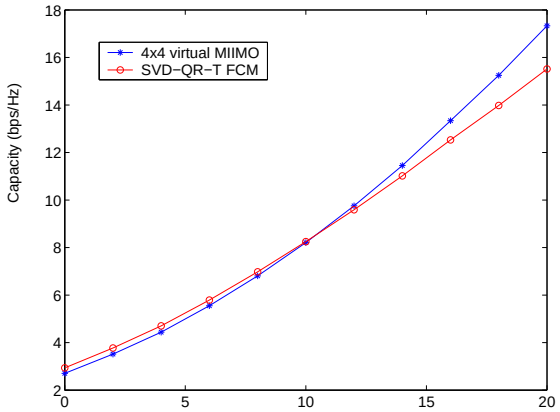


Figure 6. Capacity of SVD-QR-T FCM vs. virtual MIMO without water-filling

5 Conclusions

This paper is a preliminary work on virtual MIMO channel selection problem in practice. SVD-QR-T FCM approach with concrete example is proposed. We not only present the channel selection algorithms, but also provide the detailed approach on performance analysis with Monte Carlo simulations. We demonstrate that with the same total transmission power constraint, SVD-QR-T FCM can offer higher capacity at low SNR without waterfilling and much lower BER at high SNR no matter water-filling is applied or not. Future research tracks might concern the extension of the proposed algorithm to integrate with space time coding (STC) so as to further optimize the system performances.

Authorized licensed use limited to: University of Texas at Arlington. Downloaded on December 18, 2009 at 14:51 from IEEE Xplore. Restrictions apply.

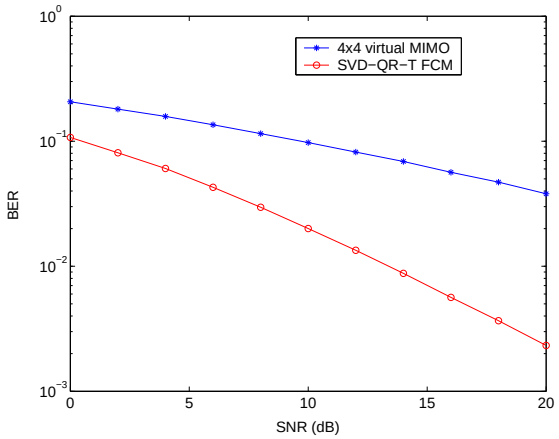


Figure 7. BER of SVD-QR-T vs. 4×4 virtual MIMO without water-filling

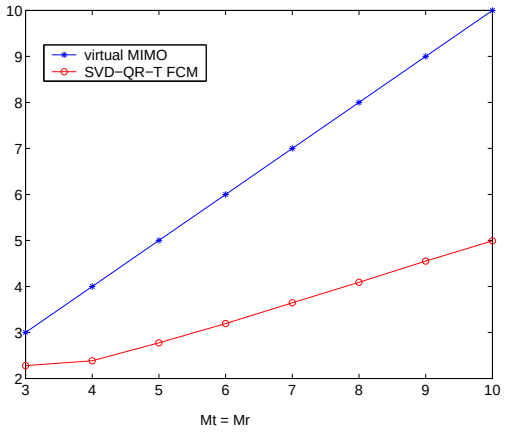


Figure 8. Multiplexing gain of SVD-QR-T FCM vs. virtual MIMO without water-filling

Acknowledgement

This work was supported by the Office of Naval Research (ONR) Young Investigator Award under Grant N00014-03-1-0466, and ONR Award under Grant N00014-07-1-0395.

References

[1] S. Cui and A. Goldsmith "Energy-efficiency of MIMO and Cooperative MIMO Techniques in Sensor Networks" , *IEEE Journal on selected areas in communications*, vol. 22, Aug 2004, pp. 1089-1098

[2] S. K. Jayaweera "Virtual MIMO-based cooperative communication for energy-constrained wireless sensor networks" , *IEEE Transactions on Wireless Communications*, vol. 5, May 2006, pp. 984 - 989

[3] Y. Yuan; Z. He and M. Chen "Virtual MIMO-based cross-layer design forwireless sensor networks" , *IEEE Transactions on Vehicular Technology*, vol. 55, May 2006, pp. 856 - 864

[4] M. Bengtsson and B. Ottersten, "Optimal and suboptimal transmit beamforming", *Handbook of Antennas in Wireless Communications*, L. C. Godara, Ed. Boca Raton, Fl, CRC, 2001

[5] D. A. Gore and A. J. Paulraj, "MIMO antenna subset selection with space-time coding", *IEEE Transactions on Signal Processing*, vol. 50, Oct. 2002

[6] A. Gorokhov, D. A. Gore and A. J. Paulraj, "Receive antenna selection for MIMO flat-fading channels: theory and algorithms", *IEEE Transactions on Information Theory*, vol. 49, Oct. 2003

[7] A. F. Molisch, M. Z. Win and J. H. Winters, "Capacity of MIMO systems with antenna selection", in *Proc. Int. Conf. Communications*, 2001, pp. 570-574

[8] D. A. Gore, R. U. Nabar and A. Paulraj, "Selecting an optimal set of transmit antennas for a low rank matrix channel", in *Proc. Int. Conf. Acoustics, Speech, and Signal Processing*, 2000, pp. 2785-2788

[9] S. Sandhu, R. U. Nabar, D. A. Gore and A. Paulraj, "Near optimal antenna selection of transmit antennas for a MIMO channel based on Shannon capacity", in Proc. 34th Asilomar Conf., Nov. 1999, pp. 567-571

[10] R. W. Heath Jr. and A. Paulraj, "Antenna Selection for spatial multiplexing systems based on minimum error rate", in *Proc. IEEE Int. Control Conf.*, 2001, pp. 2276-2280

Authorized licensed use limited to: University of Texas at Arlington. Downloaded on December 18, 2009 at 14:51 from IEEE Xplore. Restrictions apply.

[11] I. Bahceci, T. M. Duman and Y. Altunbasak "Antenna Selection for Multiple-Antenna Transmission Systems: Performance Analysis and Code Construction *IEEE Transctions on Information Theory*, vol. 49, oct. 2003

[12] A. Goldsmith, *Wireless Communications*, Cambridge University Press, NJ 2001.

[13] D. B. West, *Introduction to Graph Theory (2 Ed.)*, Prentice-Hall of India, NY 2005.

[14] Chen, S., S. A. Billings and W. Luo, "Orthogonal Least Squares Methods and their Application to Non-linear System Identification," *Int. J. Control*, vol. 50, 1989, pp. 1873-1896.

[15] Q. Liang and L. Wang, "Redundancy Reduction in Wireless Sensor Networks Using Singular-Value-QR Decomposition" , *IEEE Military Communication Conference*, Oct. 2005, Atlantic City, NJ.

[16] J. C. Bezdek, *Pattern Recognition with Fuzzy Objective Function Algorithms*, Plenum Press, New York, 1981.

[17] "Xiuzhen Cheng, et al, Strong Minimum Energy Topology: NP-Completeness and Heuristics , IEEE Transaction on Mobile Computing", Vol. 2, No. 3, pp. 248-256, July-September 2003.

[18] Xiuzhen Cheng, et al, "Polynomial-Time Approximation Scheme for Minimum Connected Dominating Set in Ad Hoc Wireless Networks", Networks, Vol. 42, No. 4, pp. 202-208, 2003.

[19] G. Stüber, *Mobile Communications*, 2nd ed., Kluwer Academic Publishers, 2001

[20] M. K. Simon and M. S. Alouini, *Digital Communication over fading channels*, 2nd ed., John Wiley & Sons, 2005

[21] M.-S. Alouini and A. J. Goldsmith, " Capacity of Rayleigh fading channels under different adaptive transmission and diversity combining techniques", *IEEE Trans. Veh. Tech*, pp. 1165-1181, July. 1999

[22] Jr. R. Heath and A. Paulraj, "Switching between multiplexing and diversity based on constellation distance", in *Proc. Allerton Conf. Communication, Contril and Computing*, Oct 2000

[23] L. Zheng, D. N. C. Tse, "Diversity and multiplexing: a fundamental tradeoff in multiple-antenna channels", *IEEE Trans. on Information Theory*, vol. 49, pp. 1073-1096, May 2003

Authorized licensed use limited to: University of Texas at Arlington. Downloaded on December 18, 2009 at 14:51 from IEEE Xplore. Restrictions apply.

Performance Analysis of Energy Detection for Cognitive Radio Wireless Networks

Qingchun Ren and Qilian Liang
Department of Electrical Engineering
University of Texas at Arlington
E-mail: ren@wcn.uta.edu, liang@uta.edu

Abstract

In this paper, considering hidden terminal and exposed node problems, we make a theoretical analysis on the performance of commonly used energy detection methods, such as ideal method, transmitter-independent method and transmitter/receiver-cooperated method, in terms of detection probability. Corresponding analytical models are provided. Performance theoretical curves are acquired to compare the characteristics for individual energy detection methods under various scenarios. Moreover the upper bound for detection probability is achieved and is compared under various system traffic intensity and sensing capability.

1. Introduction

Today's wireless networks are regulated by a fixed spectrum assignment policy. In addition, according to Federal Communications Commission (FCC)[3], temporal and geographical variations in the utilization of the assigned spectrum range from 15% to 85%. There is a dramatic increase in the access to the limited spectrum for mobile services in the recent years. By adapting radios' operating characteristics to the real-time conditions of the environment, cognitive radio (CR) enable flexible, efficient and reliable spectrum use.

In order to ensure cognitive radio network (CRN), which is consisting of CRs, working smoothly, one of important requirements is to sense the spectrum holes successfully. The most efficient detection method is to detect the primary users that are receiving data within the communication range of an secondary user. One common method for detection of unknown signals is energy detection, which measures the energy in the received waveform over an observation time window[4][14]. In [11], energy detection of unknown deterministic signals are studied. Detection performance in terms of detection probability and false alarm probability is formulated. In [1] and [13], multiband/wavelet approach and blind adaptive minimum output energy detection were proposed for capturing the AM-FM components of modulated signals immersed in noise and for DS/CDMA[8] over multipath fading channel separately. Performance of energy detection under channel randomness has been considered in [2] and [5]. In order to improve spectrum sensing, several authors have recently proposed collaboration among secondary users[6][12]. A group of unlicensed deices were exploited for spectrum sensing, which leads to more efficient spectrum utilization from a system-level point of view while decreasing computational complexity of detection algorithms at individual nodes.

However energy detection has been extensively studied in the past, hidden terminal and exposed node problems are ignored through assuming that the environment is same for transmitters and receivers. While this assumption does not always held, especially in high node-density scenarios. In this paper, considering hidden terminal and exposed node problems, we make a theoretical analysis on the performance of energy detection in terms of detection probability. An analytical model is provided for ideal energy detection, transmitter-independent energy detection for CSMA[10]/ALOHA[9]/Schedule-based systems and transmitter/receiver-cooperated energy detection. Theoretical curves are acquired to compare the characteristics for individual energy detection methods under various situations. Moreover the upper bound for detection probability is achieved and compared under various system traffic and sensing error. The theoretical results we acquired can supply a reference on the method selection.

The remainder of this paper is organized as follows. We summary all definitions used through this paper in Section 2. Section 3 and Section 4 describe our theoretical analysis on different energy detection methods. Simulation results are given in Section 5. Section 6 concludes this paper.

0-7695-2981-X/07 $25.00 © 2007 IEEE
DOI 10.1109/WASA.2007.17

IEEE computer society

2 Main Definitions

We classify the frequency band/channel state into three categories:

- *Idle:* When both secondary transmitter and receiver do not sense any signal, we claim the channel is idle. In this case, secondary communication pair can utilize the channel for communications.
- *Busy:* Once a secondary transmitter senses the beacon from a primary receiver and/or a secondary receiver senses the beacon from a primary transmitter, we claim a channel is busy. In this case, secondary communication pair should not utilize the busy channel for communications, since their communication might destroy primary users' or be destroyed by primary users'.
- *Fake Busy:* Just a secondary transmitter senses the beacon from a primary transmitter and/or a secondary receiver senses the beacon from a primary receiver, we claim the channel is fake busy. In this case, secondary communication pair still can utilize the channel for communication, since there is no any unacceptable interference among them.

Generally, network topology, traffic type and communication capability of primary user system determine channel state. In this paper, we exploit p_{id}, p_{bs} and p_{fd} to express the chance of channel state might be at certain point of time. They are always satisfy $p_{id} + p_{bs} + p_{fd} = 1$. The definitions are: p_{id} is the probability of a channel being *Idle*; p_{bs} is the probability of a channel being *Busy*; and p_{fd} is the probability of a channel being *Fake Busy*.

During energy detection, the sensed signal can come from primary transmitters and, for some cases, primary receivers, which is not determined. We use p_{tx} and p_{rx} to stand the probability that the sensed signal coming from primary transmitters and from primary receivers.

The sensing probabilities are defined as:

$$P\{no\ signal\ sensed \mid no\ signal\ exsiting\} = P_{00};$$
$$P\{signal\ sensed \mid signal\ exsiting\} = P_{11};$$
$$P\{no\ signal\ sensed \mid signal\ exsiting\} = P_{10}; and$$
$$P\{signal\ sensed \mid no\ signal\ exsiting\} = P_{01}.$$

The probability of correct decision (P_{cd}) is the probability that a SU makes a correct decision on utilizing or not utilizing a particular frequency band when sensing a particular frequency band is *Idle*/*Fake Busy* or *Busy*, defined as:

$$\begin{aligned} P_{cd} &= P\{transmission\ blocked|channel\ \textit{Busy}\}P\{channel\ \textit{Busy}\} \\ &+ P\{transmission\ processed|channel\ \textit{Idle}/\textit{Fake Busy}\} \\ &\quad P\{channel\ \textit{Idle}/\textit{Fake Busy}\} \end{aligned} \quad (1)$$

3 Generic Environment for Secondary Transmitter and Receiver

While energy detection has been extensively studied in the past, hidden terminal and exposed node problems are ignored through assuming that the environment is often same for transmitters and receivers. However, this assumption can not always hold in the real world. In this section, we use the generic model, in which the signal sensed by secondary transmitters (STs) might not be identical for secondary receivers (SRs). Moreover, in real world, there is always error for signal sensing, i.e., $0 < P_{00}$, P_{11}, P_{01}, $P_{10} < 1$. In this case, for real system design, we evaluate the performance in terms of detection probability for ideal energy detection method, transmitter-independent energy detection method and transmitter/receiver-cooperated energy detection method.

3.1 Ideal Energy Detection

In this case, the primary transmitter (PT) and primary receiver (PR) have the capability to send out special messages such as beacons to indicate they are doing communications. Moreover, for energy detection, not only ST but also SR participate sensing task. Based on the detection results both from STs and SRs, the secondary communication pairs decide their working frequency bands.

We define a 2×2 matrix ($S = \begin{pmatrix} s_{r1} & s_{r2} \\ s_{t1} & s_{t2} \end{pmatrix}$) to express the detection results for secondary communication pairs. s_{r1} and s_{r2} are the detection results referring to PR and PT individually at the SR side. Similarly, s_{t1} and s_{t2} are the detection results referring to PT and PR individually at the ST side. The value for s_{r1}, s_{r2}, s_{t1} and s_{t2} can be 1 or 0 based on signals detected or not. There are totally 16 statuses for S (See Table 1). Note that the signal strength s_{t1} and the signal strength s_{r2} reflect the hidden problem degree and exposed problem degree individually. Therefore, combining the detection at STs and SRs, the detection errors caused by hidden problem and exposed problem can be solved successfully at the same time.

Based on the definition on detection probability (P_{cd}), we derive (2) as following:

$$\begin{aligned} P_{cd} &= (p_{id} + p_{fbs})p_{00}(\gamma_{r2})p_{00}(\gamma_{t1}) + \frac{1}{9}p_{bs}[p_{01}(\gamma_{t1}) \\ &+ p_{01}(\gamma_{r2}) + p_{10}(\gamma_{r2})p_{11}(\gamma_{t1}) + p_{11}(\gamma_{r2})p_{10}(\gamma_{t1}) \\ &+ 3p_{11}(\gamma_{r2})p_{00}(\gamma_{t1}) + 3p_{11}(\gamma_{r2})p_{11}(\gamma_{t1}) \\ &+ 3p_{11}(\gamma_{r2})p_{11}(\gamma_{t1})] \end{aligned} \quad (2)$$

Note that:

- Even though PT, PR, ST and SR participate spectrum sensing, incorrect decision is still possible that for sensing errors of STs and SRs.

Table 1. Channel state classification according to S for ideal energy detection

Channel State	S
Idle	$\begin{pmatrix} 0 & 0 \\ 0 & 0 \end{pmatrix}$
Fake Busy	$\begin{pmatrix} 0 & 0 \\ 0 & 1 \end{pmatrix}, \begin{pmatrix} 1 & 0 \\ 0 & 0 \end{pmatrix}, \begin{pmatrix} 1 & 0 \\ 0 & 1 \end{pmatrix}.$
Busy	$\begin{pmatrix} 0 & 0 \\ 1 & 0 \end{pmatrix}, \begin{pmatrix} 0 & 0 \\ 1 & 1 \end{pmatrix}, \begin{pmatrix} 0 & 1 \\ 0 & 0 \end{pmatrix}, \begin{pmatrix} 0 & 1 \\ 0 & 1 \end{pmatrix}, \begin{pmatrix} 0 & 1 \\ 1 & 0 \end{pmatrix}, \begin{pmatrix} 0 & 1 \\ 1 & 1 \end{pmatrix}, \begin{pmatrix} 1 & 0 \\ 1 & 0 \end{pmatrix}, \begin{pmatrix} 1 & 0 \\ 1 & 1 \end{pmatrix}, \begin{pmatrix} 1 & 1 \\ 0 & 0 \end{pmatrix}, \begin{pmatrix} 1 & 1 \\ 0 & 1 \end{pmatrix}, \begin{pmatrix} 1 & 1 \\ 1 & 0 \end{pmatrix}, \begin{pmatrix} 1 & 1 \\ 1 & 1 \end{pmatrix}.$

- Although both ST and SR implement energy detection according to messages exchanged between PTs and PRs, detection performance in terms of detection probability P_{cd} has nothing with $p(\gamma_{r1})$ and $p(\gamma_{t2})$. That is, only the detection capability referring to PRs of STs, and detection capability referring to PTs of SRs together determines the performance of this ideal energy detection method. This implies that, during detection, to ensure the detection performance the STs only need to monitor the signal from PRs, and the STs need to monitor the signal from PTs. Consequently, the overhead brought by energy detection for STs and STs in CRNs can be safely reduced through making STs/SRs ignore the signal from PTs/PRs.

- Moreover, assuming CRs can correctly detect whether there is transmission processing around them on a particular frequency band, i.e., $p_{00} = 1$, $p_{11} = 1$, $p_{01} = 0$ and $p_{10} = 0$. In this case according to (2), we have $P_{cd} = 1$, which are consisting with our above analysis. For this reason, this ideal energy detection method is an optimal detection way for CRNs.

However, it is too good to be true in real world since overhead caused by transmitting beacons both form primary transmitters and receivers is too heavy to be acceptable or feasible for some systems that utilize certain MAC methods, in which there is no confirmation/response from receivers during data transmission process.

3.2 Transmitter-Independent Energy Detection

In transmitter-independent energy detection method, only STs processes spectrum sensing task. Therefore, the matrix S is reduced into a scalar whose value can be 0 or 1. When a ST senses there is no primary communication pairs doing communication, i.e., $S = 0$, it will decide to use this channel for its communication, otherwise it will not. Generally, there are two categories of primary system based on whether there is confirmation/response from primary receivers. In CSMA/CA primary systems, since besides RTS control packets and data packets transmitted by PTs, another control packets - CTS and ACK are transmitted by PRs[7]. The decision can be done according to the detection with PTs or PRs, in this case, P_{cd} is modified as follows.

$$\begin{aligned} P_{cd} &= p_{tx}\{p_{id}p_{00}(\gamma_{t2}) + \frac{1}{3}p_{fbs}[p_{00}(\gamma_{t2}) + 2p_{10}(\gamma_{t2})] \\ &+ \frac{1}{2}p_{bs}p_{11}(\gamma_{t2})\} + p_{rx}\{(p_{id} + p_{fbs})p_{00}(\gamma_{t1}) \\ &+ \frac{2}{3}p_{bs}p_{11}(\gamma_{t1})\} \end{aligned} \quad (3)$$

Compared with ideal energy detection methods, follows are observed:

- P_{cd} is not only the functions of $p_{\gamma_{t1}}$, but also the functions of $p_{\gamma_{t2}}$ when the detected signal coming from PTs.

- Assuming CRs can correctly detect whether there is transmission processing around them on a particular frequency band, i.e., $p_{00} = 1$, $p_{11} = 1$, $p_{01} = 0$ and $p_{10} = 0$. In this specific case, $P_{cd} = p_{tx}(p_{id} + \frac{1}{3}p_{fbs} + \frac{1}{2}p_{bs}) + p_{rx}(p_{id} + p_{fbs} + \frac{2}{3}p_{bs})$. Since it always has $p_{tx} + p_{rx} = 1$ hold, the upper bound of P_{cd} is $P_{cd,max} = p_{id} + p_{fbs} + \frac{2}{3}p_{bs}$, which is achieved when the detected signals all come from PRs, i.e., $p_{tx} = 0$ and $p_{rx} = 1$.

- Even though only STs are exploited for energy detection in CSMA/CA-based primary system, it can be an optimal energy detection method when channel status only be *Idle* or *Fake Busy*. That is, when $p_{bs} = 0$, $P_{cd,max} = 1$. Otherwise, the performance of transmitter-independent energy detection methods is always $\frac{1}{3}p_{bs}$ worse than the ideal energy detection methods.

- For other primary systems, such as TDMA systems, CSMA systems and ALOHA systems, in which there is no response/confirmation from receivers during data transmission processes, i.e., $p_{tx} = 1$ and $p_{rx} = 0$. In this case, there is $P_{cd,max} = p_{id} + \frac{1}{3}p_{fbs} + \frac{1}{2}p_{bs}$.

3.3 Transmitter/Receiver-Cooperated Energy Detection

Considering the spectrum environment sensed by receiver and transmitter due to different location of them, receiver aiding spectrum sensing method is one of feasible mechanisms to improve the detection performance. Consequently, the detection matrix S is changed into $\begin{pmatrix} 0 \\ 0 \end{pmatrix}$, $\begin{pmatrix} 0 \\ 1 \end{pmatrix}$, $\begin{pmatrix} 1 \\ 0 \end{pmatrix}$ and $\begin{pmatrix} 1 \\ 1 \end{pmatrix}$. Only ST doing frequency sensing, it is impossible to identify the channel is *Busy* or *Fake Busy* when $S = \begin{pmatrix} 0 \\ 1 \end{pmatrix} / \begin{pmatrix} 1 \\ 0 \end{pmatrix}$. Hence, there are two alternative ways to infer the channel state. One is claiming the channel is *Idle* when $S = \begin{pmatrix} 0 \\ 0 \end{pmatrix}$, claiming the channel is *Fake Busy* when $S = \begin{pmatrix} 0 \\ 1 \end{pmatrix}, \begin{pmatrix} 1 \\ 0 \end{pmatrix} and \begin{pmatrix} 1 \\ 1 \end{pmatrix}$ (See Table 2). Then, the P_{cd} is calculated through

Table 2. Channel state classification according to S for transmitter/receiver-cooperated method

Channel State	S
Idle	$\begin{pmatrix} 0 \\ 0 \end{pmatrix}$
Busy	$\begin{pmatrix} 0 \\ 1 \end{pmatrix}, \begin{pmatrix} 1 \\ 0 \end{pmatrix}, \begin{pmatrix} 1 \\ 1 \end{pmatrix}$

$$\begin{aligned} P_{cd} &= p_{tx}\{p_{id}p_{00}(\gamma_{r2})p_{00}(\gamma_{t2}) + \frac{1}{3}p_{fbs}[p_{00}(\gamma_{r2})p_{00}(\gamma_{t2}) \\ &+ 2p_{00}(\gamma_{r2})p_{10}(\gamma_{t2})] + \frac{1}{6}p_{bs}[p_{11}(\gamma_{t2}) + 4p_{11}(\gamma_{r2}) \\ &+ 2p_{10}(\gamma_{r2})p_{01}(\gamma_{t2}) + 2p_{10}(\gamma_{r2})p_{11}(\gamma_{t2}) + p_{01}(\gamma_{r2}) \\ &+ p_{00}(\gamma_{r2})p_{01}(\gamma_{t2})]\} + p_{rx}\{p_{id}p_{00}(\gamma_{r1})p_{00}(\gamma_{t1}) \\ &+ \frac{1}{3}p_{fbs}[p_{00}(\gamma_{r1})p_{00}(\gamma_{t1}) + 2p_{10}(\gamma_{r1})p_{00}(\gamma_{t1})] \\ &+ \frac{1}{6}p_{bs}[4p_{11}(\gamma_{t1}) + p_{11}(\gamma_{r1}) + 2p_{01}(\gamma_{r1})p_{10}(\gamma_{t1}) \\ &+ 2p_{11}(\gamma_{r1})p_{10}(\gamma_{t1}) + p_{10}(\gamma_{r1})p_{01}(\gamma_{t1})]\} \end{aligned} \quad (4)$$

The other is One is claiming the channel is *Idle* when $S = \begin{pmatrix} 0 \\ 0 \end{pmatrix}$, claiming the channel is *Fake Busy* when $S = \begin{pmatrix} 0 \\ 1 \end{pmatrix} / \begin{pmatrix} 1 \\ 0 \end{pmatrix}$, and claiming the channel is Busy when $S = \begin{pmatrix} 1 \\ 0 \end{pmatrix} / \begin{pmatrix} 0 \\ 1 \end{pmatrix} and \begin{pmatrix} 1 \\ 1 \end{pmatrix}$ (See Table 3).

Table 3. channel state classification according to S for transmitter/receiver-cooperated method

Channel State	S
Idle	$\begin{pmatrix} 0 \\ 0 \end{pmatrix}$
Fake Busy	$\begin{pmatrix} 0 \\ 1 \end{pmatrix} / \begin{pmatrix} 1 \\ 0 \end{pmatrix}$
Busy	$\begin{pmatrix} 1 \\ 0 \end{pmatrix} / \begin{pmatrix} 0 \\ 1 \end{pmatrix}, \begin{pmatrix} 1 \\ 1 \end{pmatrix}$

In this case, the P_{cd} is calculated through

$$\begin{aligned} P_{cd} &= p_{tx}\{p_{id}[p_{00}(\gamma_{r2})p_{00}(\gamma_{t2}) + p_{00}(\gamma_{r2})p_{01}(\gamma_{t2})] \\ &+ \frac{1}{3}p_{fbs}[p_{00}(\gamma_{r2})p_{00}(\gamma_{t2}) + 2p_{00}(\gamma_{r2})] + \frac{1}{3}p_{bs}[2p_{11}(\gamma_{r2}) \\ &+ p_{01}(\gamma_{r2})]\} + p_{rx}\{p_{id}[p_{00}(\gamma_{r1})p_{00}(\gamma_{t1}) + p_{01}(\gamma_{r1})p_{00}(\gamma_{t1})] \\ &+ \frac{1}{3}p_{fbs}[p_{00}(\gamma_{r1})p_{00}(\gamma_{t1}) + 2p_{00}(\gamma_{t1}) + \frac{1}{3}p_{bs}[2p_{11}(\gamma_{t1}) \\ &+ p_{01}(\gamma_{t1})]\} \end{aligned} \quad (5)$$

Follows are discussed based above formulas:

- Compared with transmitter-independent energy detection methods, since both STs and SRs participate the detection process, the detection performance is same whatever the detection is based on the signal from PTs or PRs. It is a good news for CRNs that are coexisting with primary systems, in which no response/confirmation from PRs during data transmission processes.
- Assuming CRs can correctly detect whether there is transmission processing around them on a particular frequency band, i.e., $p_{00} = 1$, $p_{11} = 1$, $p_{01} = 0$ and $p_{10} = 0$. In this specific case, the upper bound for detection probability are: $P_{cd,max} = p_{id} + \frac{1}{3}p_{fbs} + \frac{5}{6}p_{bs}$ and $P_{cd,max} = p_{id} + p_{fbs} + \frac{2}{3}p_{bs}$. Note that when $p_{bs} < 4p_{fbs}$, the performance of treating $\begin{pmatrix} 0 \\ 1 \end{pmatrix}$ as *Fake Busy* is worse than treating $\begin{pmatrix} 0 \\ 1 \end{pmatrix}$ as *Busy*.
- Using transmitter/receiver-cooperated energy detection methods, it can acquire better performance for TDMA primary systems, ALOHA systems and CSMA systems. However, for CSMA/CA systems, the transmitter/receiver-cooperated energy detection method treating $\begin{pmatrix} 0 \\ 1 \end{pmatrix}$ as *Busy* achieves better per-

formance when $p_{tx} \geq \frac{4p_{fbs}-p_{bs}}{4p_{fbs}p_{bs}}$, and treating $\begin{pmatrix} 0 \\ 1 \end{pmatrix}$ as *Fake Busy* can always achieve better performance.

- Even though only PTs and PRs are exploited for energy detection, it can be an optimal energy detection method when channel status only be *Idle* or *Fake Busy*. That is, when $p_{bs} = 0$, $P_{cd,max} = 1$. Otherwise, the performance is always $\frac{1}{3}p_{bs}$ worse than the one of ideal energy detection method.

4 Identical Environment for Secondary Transmitter and Receiver Scenario

When the environment for secondary transmitters and receivers are same. In this case, all possible values for S are shown in Table 4. We will obtain P_{cd} for various energy detection methods separately.

Table 4. channel state classification according to S for ideal method

Channel State	S
Idle	$\begin{pmatrix} 0 & 0 \\ 0 & 0 \end{pmatrix}$
Busy	$\begin{pmatrix} 0 & 1 \\ 0 & 1 \end{pmatrix}, \begin{pmatrix} 1 & 0 \\ 1 & 0 \end{pmatrix}, \begin{pmatrix} 1 & 1 \\ 1 & 1 \end{pmatrix}.$

4.1 Ideal Energy Detection

Since the situation for STs and SRs is same, it is validate to make correct decision only according to the detection by STs or SRs. Moreover, for ideal energy detection, PTs and PRs have the capability to send message out, which can be detected by secondary users. In this case, the detection probability P_{cd} is as follows.

$$\begin{aligned} P_{cd} &= p_{id}p_{00}(\gamma_1)p_{00}(\gamma_2) + \frac{1}{3}p_{bs}[p_{01}(\gamma_1) + p_{11}(\gamma_1) + p_{01}(\gamma_2) \\ &+ p_{00}(\gamma_1)p_{11}(\gamma_2) + p_{10}(\gamma_1)p_{11}(\gamma_2) + p_{11}(\gamma_1)p_{00}(\gamma_2)] \end{aligned} \quad (6)$$

p_{γ_1} is the detect probability according to the signal from PRs, and p_{γ_2} is the detect probability according to the signal from PTs. Compared with ideal energy detection performance in generic environment, i.e., the situation for SRs might not be identical with the one for STs, they are same when there are only *Busy* or *Ideal* status existed for channel (i.e., $p_{fbs} = 0$) and the detection results at SRs are same as the one at STs (i.e., $p(\gamma_{r2}) = p(\gamma_2)$ and $p(\gamma_{t1}) = p(\gamma_1)$).

4.2 Transmitter-Independent Energy Detection

When the environment is same for STs and SRs, using the transmitter-independent detection method the detection performance is as following:

$$\begin{aligned} P_{cd} &= p_{tx}\{p_{id}p_{00}(\gamma_2) + \frac{1}{3}p_{bs}[2p_{11}(\gamma_2) + p_{01}(\gamma_2)]\} \\ &+ p_{rx}\{p_{id}p_{00}(\gamma_1) + \frac{1}{3}p_{bs}[2p_{11}(\gamma_1) + p_{01}(\gamma_1)]\} \end{aligned} \quad (7)$$

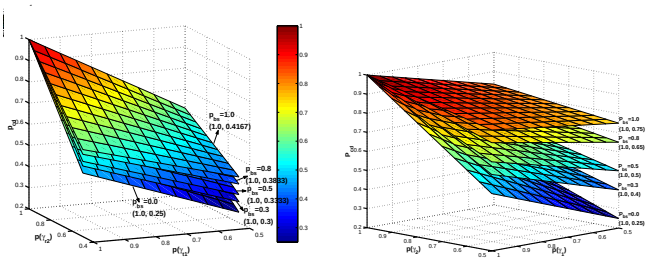
Following characteristics are observed:

- When the situations for STs and SRs are identical, the upper bound of detection performance is same. It is $P_{cd,max} = p_{id} + \frac{2}{3}p_{bs}$.
- Since the situations at STs and SRs are same, it is unnecessary to exploit both secondary transmitter and receiver for better detection performance for CRNs. Therefore, for the special case that there is identical environment for STs and SRs, traditional energy detection method - transmitter-independent energy detection - is an optimal choice.
- Since the situations at STs and SRs are same, obviously, detection probability can be enhanced. However, compared with the performance in generic environment, the upper bound is same as the ones when only monitoring PRs' signals for energy detection, but always better than the ones when only monitoring PTs' signals. It inspired us that some wrong detections are generated for the difference between STs and SRs. That is, in that case, traditional transmitter-independent energy detection is not the best choice. If more signal from PRs can be detected by STs, even for different situation for STs and SRs, better detection performance can be achieved.

5 Simulation and Performance Analysis

5.1 Surface of detection probability P_{cd} for ideal energy detection

Assuming STs and SRs own same sensing capability, that is, $p_{00}(\gamma_{r2}) = p_{11}(\gamma_{r2})$ and $p_{00}(\gamma_{t1}) = p_{11}(\gamma_{t1})$. Moreover, $p_{10}(\gamma_{r2}) = p_{01}(\gamma_{r2}) = 1 - p_{00}(\gamma_{r2})$ and $p_{10}(\gamma_{t1}) = p_{01}(\gamma_{t1}) = 1 - p_{00}(\gamma_{t1})$. Based on (2) and (6), Fig.1 shows the surfaces for P_{cd} under various combinations of traffic load intensity p_{bs}, sensing capability of STs/SRs $p(\gamma_{r2})$/$p(\gamma_{t1})$. Here, the range for $p(\gamma_{r2})$ and $p(\gamma_{t1})$ is [0.5 0.6 0.7 0.8 0.9 1.0], as well as the candidates for p_{bs} are [0.0 0.3 0.5 0.8 1.0]. In those two figures, with p_{bs} the maximum value and minimal value of P_{cd} are shown for each surface. Note that:



(a) (b)

Figure 1. Detection probability P_{cd} for ideal energy detection method for (a) generic environment for secondary transmitters/receivers scenario and (b) identical environment for secondary transmitters/receivers scenario.

- Fixing the traffic intensity of primary systems (i.e., fixing p_{bs}), with the increase of signal detection capability for STs/SRs (i.e., increasing $p(\gamma_{r2})/p(\gamma_{t1})$) there is higher chance to make correct decision for secondary users. It inspire us that enhance the detection capability for secondary users can reduce the interference to primary systems and increase the frequency utilization.

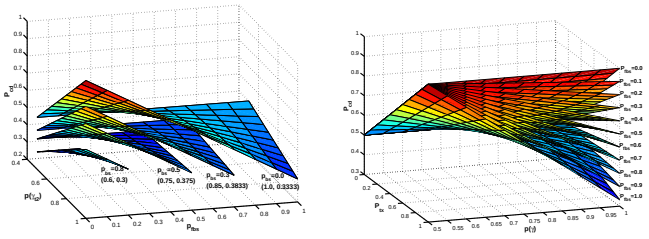
- Fixing the signal detection capability of STs/SRs (i.e., fixing the value for $p(\gamma_{r2})/p(\gamma_{t1})$), when primary system is more often being truly busy (i.e., with higher value for p_{bs}) there is higher chance to make correct decision for secondary users. That is, it is more easy for secondary users to successfully monitor the primary system, which is busy exchanging information. Otherwise, more error will be made for detection.

- Identical environment for STs and SRs can improve the detection performance for CRNs even under same situation, such as same p_{bs}, $p(\gamma_{r2})$ and $p(\gamma_{t1})$, since there is no chance for channel being *Fake Busy*. Therefore, the improvement due to identical environment is reduced when the detection error caused by exposed node problem is less (i.e., less chance for channel being *Fake Busy*). For example, when $p_{bs} = 0.0$, the minimal successful detection probability is same as 0.25 for generic scenario and identical scenario, while when $p_{bs} = 1.0$, the minimal successful detection probability for identical environment is 44.44% ($\frac{0.75-0.4167}{0.75} = 44.44\%$) higher than the one for generic environment.

5.2 Surface of detection probability P_{cd} for transmitter-independent energy detection method

Assuming there is same sensing probability for STs, that is, $p_{00}(\gamma_{t1}) = p_{11}(\gamma_{t1})$ and $p_{10}(\gamma_{t1}) = p_{01}(\gamma_{t1}) = 1 - p_{00}(\gamma_{t1})$. When sensed signal comes from primary transmitters and receivers both, we assume the sensing probability at STs is same. Here, the range for $p(\gamma_{t1})$ is [0.5 0.6 0.7 0.8 0.9 1.0], as well as the candidates for p_{bs} are [0.0 0.3 0.5 0.8].

According to (3), Fig.2 shows the surfaces for P_{cd} under various combinations of traffic load intensity p_{bs}, p_{fbs} and sensing capability of secondary transmitter $p(\gamma_{t1})$ when sensed signal come from PTs or PRs. In above two figures,



(a) (b)

Figure 2. Detection Probability of P_{cd} for Transmitter Independent Energy Detection when Sensed Signal from (a) Primary Transmitter only and (b) Primary Transmitter or Receiver

with p_{bs}, the maximum value and minimal value for P_{cd} are shown for each surface. Note that

- From Fig. 2(a), compared with ideal energy detection method, the more the chance for channel being truly occupied by primary users is, the more the detection error becomes both for generic and identical scenarios. It inspires us that the behavior of primary systems, in which the channel is less often occupied, can be more easy to be monitored by secondary systems only through STs.

- Also from Fig. 2(a), since the channel status can not be accurately monitored only by STs, the chance for channel being *Fake Busy* directly impacts on the detection performance. Fixing the chance for channel being truly busy, the chance for STs to successfully detect the channel status is decreased with the detection error introduced by exposed node problem becoming bigger (i.e., higher value for P_{fbs}). While, in this case, the detection performance can be improved through enhance

the sensing capability for STs (i.e., higher value for $p(\gamma_{t2})$).

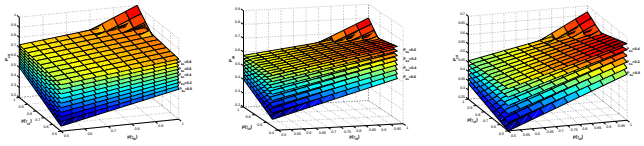
- When sensed signal comes from PTs or PRs (See Fig. 2(b)), it is a negative influence of sensing capability for STs on the detection performance.

- From Fig. 2(b), if more sensed signal comes from PRs, the performance for transmitter-independent detection method can be improved when fixing channel status. Moreover the influence degree of P_{tx} on P_{cd} is changed with the chance for channel being *Fake Busy*. That is, the more the chance for channel being *Fake Busy*, the less the improvement on detection performance caused by more sensed signal coming from PRs. Even more, this positive impact becomes a negative impact when p_γ and P_{fbs} locate in a certain range. The turning points are: $p(\gamma) \geq 0.9$ when $P_{fbs} = 1.0$, $p(\gamma) \geq 0.95$ when $P_{fbs} = 0.9$ and $p(\gamma) = 1.0$ when $P_{fbs} = 0.8$.

5.3 Surface of detection probability P_{cd} for transmitter/receiver-cooperated energy detection

Assuming there is same sensing probability for secondary transmitters and receivers, that is, $p_{00}(\gamma_{t2}) = p_{11}(\gamma_{t2})$ and $p_{00}(\gamma_{r2}) = p_{11}(\gamma_{r2})$. Moreover, $p_{10}(\gamma_{t2}) = p_{01}(\gamma_{t2}) = 1 - p_{00}(\gamma_{t2})$ and $p_{10}(\gamma_{r2}) = p_{01}(\gamma_{r2}) = 1 - p_{00}(\gamma_{r2})$. When sensed signal comes from PRs and PTs both, we assume the sensing probability at STs is same. Here, the range for $p(\gamma_{t1})$ is [0.5 0.6 0.7 0.8 0.9 1.0], as well as the candidates for p_{bs} are [0.0 0.3 0.5 0.8].

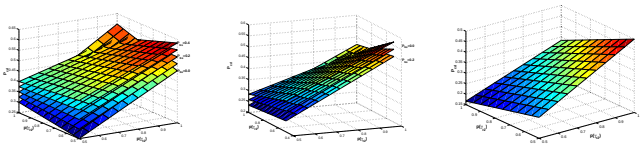
Based on (4), Fig. 3, Fig. 4, Fig. 5 and Fig. 6 show the surfaces for P_{cd} under various combinations of traffic load intensity p_{bs}, p_{fbs} and sensing capability of STs/SRs $p(\gamma_{t2})/p(\gamma_{r2})$ when sensed signal come from PTs/PRs.



(a) (b) (c)

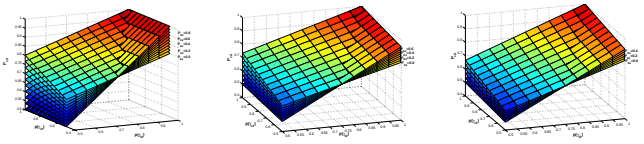
Figure 3. In Generic Scenario, Detection Probability of P_{cd} for Transmitter/Receiver-Cooperated Energy Detection for (a) $P_{fbs} = 0.0$, (b) $P_{fbs} = 0.3$ and (c) $P_{fbs} = 0.5$

Note that



(a) (b) (c)

Figure 4. In Generic Scenario, Detection Probability of P_{cd} for Transmitter/Receiver-Cooperated Energy Detection for (a) $P_{fbs} = 0.6$, (b) $P_{fbs} = 0.8$ and (c) $P_{fbs} = 1.0$

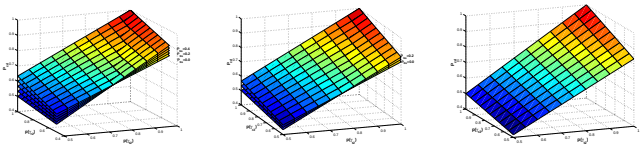


(a) (b) (c)

Figure 5. In Identical Scenario, Detection Probability of P_{cd} for Transmitter/Receiver-Cooperated Energy Detection for (a) $P_{fbs} = 0.0$, (b) $P_{fbs} = 0.3$ and (c) $P_{fbs} = 0.5$

- Similarly with ideal energy detection method, the more the chance for channel being truly occupied by primary users is, the less the detection error becomes both for generic and identical scenarios. It inspires us that the behavior of primary systems, in which the channel is more often occupied, can be more easy to be monitored by secondary systems both through STs and SRs.

- Fixing the chance for channel being *Busy* and *Fake Busy*, the chance for secondary users to successfully detect the channel status is enhanced for utilizing more sensitive STs (i.e., higher value for $p(\gamma_{t2})$).



(a) (b) (c)

Figure 6. In Identical Scenario, Detection Probability of P_{cd} for Transmitter/Receiver-Cooperated Energy Detection for (a) $P_{fbs} = 0.6$, (b) $P_{fbs} = 0.8$ and (c) $P_{fbs} = 1.0$

- There is a watershed for the influence of sensing capacity of SRs on detection performance when the environment for STs and SRs is not identical. When $P_{fbs} \leq 0.5$, the detection performance can be improved through using more sensitive receivers, otherwise when $P_{fbs} \geq 0.5$, less sensitive receivers should be exploited to reduce detection errors. However, this watershed is disappeared when identical environment for STs and SRs.

- Both using STs and SRs for detection, it is still impossible to accurately monitor the operation for primary users for exposed node problem and hidden terminal problem. Identical environment for secondary transmitters and receivers can improve the detection performance

6 Conclusions

While energy detection has been extensively studied in the past, hidden terminal and exposed node problems are ignored through assuming that the environment is same for transmitters and receivers. In this paper, considering hidden terminal and exposed node problems, we make a theoretical analysis on the performance of commonly used energy detection methods, such as ideal method, transmitter-independent method and transmitter/receiver-cooperated method, in terms of detection probability. Corresponding analytical models are provided. Performance theoretical curves are acquired to compare the characteristics for individual energy detection methods under various scenarios. Moreover the upper bound for detection probability is achieved and is compared under various system traffic intensity and sensing capability. From the theoretical results, we found that it is easy to correctly detection the channel status when primary systems are heavily occupied for ideal energy detection method and tansmitter/receiver-cooperated energy detection method. Otherwise, transmitter-independent method is a better scheme to monitor the primary systems. Commonly, increasing the sensitivity of secondary users can upgrade the detection performance. However, in our analysis, it is not true for transmitter-independent method and transmitter/receiriver-cooperated method under certain situations. We have concluded those special cases in this paper. Therefore, the theoretical results can supply a reference on the choosing of energy detection method according to system scenario, such as traffic load, sensing capability, etc..

Acknowledgement

This work was supported by the U.S. Office of Naval Research (ONR) Young Investigator Program Award under Grant N00014-03-1-0466, and ONR Award under Grant N00014-07-1-0395.

References

[1] A. C. Bovik, P. Maragos, and T. F. Quatieri. Am-fm energy detection and separation in noise using multiband energy operators. *IEEE Trans. Signal Processing*, 41(12):3245–3265, 1993.

[2] F. F. Digham, M. Alouini, and M. K. Simon. On the energy detection of unknown signals over fading channels. In *Proc. IEEE International Conference on Communications 2003 (ICC'03)*, pages 3575 – 3579, May 2003.

[3] FCC. Spectrum policy task force report. In *ET Docket No. 02-155*, Nov. 2002.

[4] G. Ganesan and Y. Li. Cooperative spectrum sensing in cognitive radio networks. In *Proc. First IEEE International Symposium on New Frontiers in Dynamic Spectrum Access Networks 2005 (DySPAN2005)*, pages 137–143, Nov. 2005.

[5] A. Ghasemi and E. S. Sousa. Collaborative spectrum sensing for opportunistic access in fading environments. In *Proc. First IEEE International Symposium on New Frontiers in Dynamic Spectrum Access Networks 2005 (DySPAN 2005)*, pages 131–136, Nov. 2005.

[6] T. Kamakaris, M. M. Buddhikot, and R. Iyer. A case for coordinated dynamic spectrum access in celluar networks. In *Proc. First IEEE International Symposium on New Frontiers in Dynamic Spectrum Access Networks 2005 (DySPAN2005)*, pages 289–298, Nov. 2005.

[7] P802.11. Ieee standard for wireless lan medium access control (mac) and physical layer (phy) specifications. Nov. 1997.

[8] M. Schwartz. *Mobile Wireless Communications*. Cambridge University Press, NY, 2005.

[9] B. Sklar. *Digital Communications*. Prentice-Hall, NJ, 2001.

[10] A. S. Tanenbaun. *Comupter Networks*. Prentice-Hall, NJ, 1996.

[11] H. Urkowitz. Energy detection of unknown deterministic signals. *Proceedings of the IEEE*, 55(4):523–531, 1967.

[12] E. Visotsky, S. Kuffner, and R. Peterson. On collaborative detection of tv transmissions in support of dynamic spectrum sharing. In *Proc. First IEEE International Symposium on New Frontiers in Dynamic Spectrum Access Networks 2005 (DySPAN2005)*, pages 338–345, Nov. 2005.

[13] J. F. Weng and T. Le-Ngoc. Rake receiver using blind adaptive minimum output energy detection for ds/cdma over multipath fading channels. *Proceedings of the IEE*, 148(6):385–392, 2001.

[14] M. P. Wylie-Green. Dynamic spectrum sensing by multiband ofdm radio for interference mitigation. In *Proc. First IEEE International Symposium on New Frontiers in Dynamic Spectrum Access Networks 2005 (DySPAN2005)*, pages 619–625, Nov. 2005.

Time Synchronization in Network-Centric Sensor Networks

Sejal Raje and Qilian Liang
Department of Electrical Engineering,
University of Texas at Arlington, 416 Yates Street, Nedderman Hall, Rm 518, Arlington, TX 76019
Email: sejalraje@yahoo.com, liang@uta.edu

***Abstract*— Time Synchronization is a crucial component of infrastructure for wireless sensor networks (WSN). The design of new synchronization methods for WSNs needs to satisfy the unique requirements and constraints in terms of precision, lifetime, energy, and scope of the synchronization. In this paper we have designed and compared three techniques for achieving synchronization in network centric sensor networks, using Sequential least squares, Kalman filter and Fuzzy logic systems. These techniques achieve a highly accurate, long-term and adaptive synchronization by forming a time conversion scale between clocks of two nodes in the network. A synchronization protocol based on any of these techniques will be very energy-efficient, lightweight, multimodal, tunable, and even scalable.**

I. Introduction

A. Overview

In Wireless Sensor Networks (WSN), time synchronization is needed by many applications, for e.g., data fusion, temporal delivery of events, duplicate detection, target detection and tracking etc. Although many solutions have been designed and implemented for problem of time synchronization in traditional networks, many factors in sensor networks, such as *energy constraint*, *dynamic topology*, *variety of applications* and *cost and form factor*, make traditional methods unsuitable for WSNs. After these observations, some design requirements have been formulated to address the challenging task of WSN time-synchronization [1], wherein it is better for any scheme suggested to be energy efficient, adaptive to application's needs, robust and scalable, and provide only the necessary and sufficient synchronization.

The many factors causing errors in clocks of sensor nodes or in synchronization algorithm can be divided into two categories: ***1. Oscillator Characteristics :*** Since sensor nodes' clocks run on very cheap oscillators, the two characteristics of clock oscillators that are the main sources of error are *accuracy* (or resolution), which is a measure of difference between oscillator's expected (ideal) frequency and actual frequency, and *stability*, which is oscillator's tendency to stay at the same frequency over time. ***2. System and Network issues :*** These sources of non-determinism in the message delivery latency have been categorized in four type of delays [4]: '*Send Time*', '*Access Time*', '*Propagation Time*' and '*Receive Time*'. All the above factors finally result in time or phase offset, frequency bias (skew) and frequency drift between the clocks of two nodes. In this paper, we mainly consider the resulting factors due to oscillator problems.

B. Outline of A Synchronization Protocol

Our interests in synchronization arise from a recently suggested approach of synchronizing sensor nodes by forming a time conversion scale between them [2] [3] [4]. As found in many applications, consider a sensor network consisting of many small clusters of nodes; each of them consisting of a clusterhead and many nodes that are within the broadcast range (*single hop* distance) from it. The goals here is to get all the nodes in a cluster to synchronize with the clusterhead. In this scenario, the clusterhead, also referred to as the *sender* (S) node, will broadcast timestamps - containing time in it's own clock - at regular intervals to all other nodes in its cluster, which are the *receivers* (R). Then, using these timestamps and one of the methods suitable for existing conditions, each receiver forms a time-conversion-scale between itself and sender node according to its own clock, and thus predicts the time in the senders clock at any point of time. By having such a reference scale, a node is synchronized with sender, because it can convert the time in it's own clock into other node's time.

Even though similar approaches have been tried before for WSN, the problem with these techniques is that they do not take into account the frequency drift of clocks or environmental effects, which can affect the accuracy of synchronization, especially over a longer period of time. We have tried designing methods that can address these issues while fulfilling the other requirements of WSN time-synch problem.

In the rest of the paper, section II, III, and IV respectively present the designs of Sequential least squares, Kalman filter and Fuzzy logic approaches. Simulations and observations shown in section V and section VI concludes the paper.

II. Sequential Least Squares Approach

Assume that the clocks of S and R are of the same type, so under ideal conditions, they should run at the same frequency, without any initial phase error. But in reality, each clock will drift from its ideal conditions. From [7], [5], an approximation characterizing a clock oscillator, and the resulting eq for drift of a single clock from ideal conditions, are given as:

$$f = f_{nom} + \Delta f_0 + f_d.(t - t_0) + \Delta f_n(t) + \Delta f_e(t) \quad (1)$$

$$\Delta\Phi(t) = \Delta\Phi(t_0) + \Delta f_0.(t - t_0) + \frac{f_d}{2}.(t - t_0)^2 + \Delta f_n(t) + \int_{t_0}^{t} \Delta f_e(\tau) \quad (2)$$

1-4244-0445-2/07/$20.00 ©2007 IEEE

Authorized licensed use limited to: University of Texas at Arlington. Downloaded on January 6, 2010 at 16:11 from IEEE Xplore. Restrictions apply.

where t_0 = starting time ; f_d = frequency drift or aging rate;
f_{nom} = ideal frequency; Δf_0 = initial frequency error;
Δf_n = short-term frequency instability (noise) term;
Δf_e = environmental term.

From the above equations, we can derive the relative clock drift (or time offset) between clocks of two nodes as referred to an ideal clock ($\Delta t_{12}(t)$). Using that expression the offset between the receiver's clock and the sender's clock (Δt_{SR}), at time t_R in the receiver's clock is given as,

$$\Delta t_{SR}(t_R) = (t_{0S} - t_{0R}) + \frac{\Delta f_{0SR}}{f_{nom}}(t_R - t_{0R}) + \Psi_n(t_R) + \frac{f_{d_{SR}}}{2f_{nom}}(t_R - t_{0R})^2 + \Delta t_{eSR}(t_R) \quad (3)$$

and t_{R0} can be assumed to be 0. Thus, the phase or time offset between two clocks at any given time results from a combination of initial phase offset, frequency bias, frequency drift, noise due to the environmental terms, and the random clock jitter. The clock jitter does not lead to accumulated time errors. But as more time passes from the synchronization point, the drift and environmental terms become more significant.

Here, the SLS estimates the clock parameters between a sender and a receiver node, and using those predicts the time-offset between them at the next time step. So node R seeks to predict Δt_k^{SR}, given past m observations of time-offset, $\Delta t_{k-1}^{SR}, ..., \Delta t_{k-m}^{SR}$ from consecutive timestamps received from sender node. In this design, effect of clock drift is considered, but not the environmental terms. Refereing to equation 3, our model for this sequential least squares approach is of the form,

$$\tilde{y_k} = H_k x + v_k \quad (4)$$

where, $\tilde{y}_k = \Delta t_k^{SR}$ denotes the k^{th} measurement,
$H_k = [1 \quad t_k \quad t_k^2]$ is the basis function matrix,
and $x = [x_1 \quad x_2 \quad x_3] = [(t_{0S} - t_{0R}) \quad \frac{\Delta f_{SR}}{f_o} \quad \frac{f_{dSR}}{2f_o}]$ is the parameter matrix. Clock parameters in estimation are initial offset, frequency bias, and frequency drift respectively. The clock jitter term, $\Psi_n(t_R)$, is assumed to be zero mean, white gaussian noise and is used as the measurement noise, v, at any instance of time. Hence the measurement error covariance is given as, $R^{-1} = cov\{\Psi_n(t_R)\}$. The basis functions are independent, and weight matrix remains block diagonal, because the samples Δt_k^{SR} at various times t_k are i.i.d. So as a new timestamp is available, we calculate an updated $(k+1)^{th}$ estimate of clock parameters, using the k^{th} estimates of them and the $(k+1)$ measurements and associated side calculations. We use the covariance recursion form of SLS algorithm. Reader can refer to [9] for further details on working of SLS. The sequential process can be started at any step by initial values for clock parameters - taken either from theory or previous experiments or derived from batch estimation of a few initial measurement samples - i.e., an *a priori* estimate x_0, and the *a priori* estimation error covariance matrix $P_0 = Q = cov(\mathbf{w})$, $\mathbf{w}$ being the errors in *a priori* estimates. Since this design is a minimum-variance (MV) estimator, we get an unbiased estimates of the clock parameters.

III. Kalman Filter Algorithm

Viewed as an extension to the SLS algorithm, Kalman filter approach with it's dynamic system parameters, model for system state estimation and it's *predictor-corrector* form, can prove useful to make the synchronization adaptive to the environmental noise and the dynamic clock drift. Our approach is motivated from various attempts in past of using Kalman filter as a tool in the formation of stable timescales like GPS composite clocks [6]; but the time-synch problem worsens in case of WSN due to cheap oscillators of sensor nodes and severe environmental conditions.

The problem formation is same as that of SLS. For simulating a sensor-network scenario, we have assumed that the clock drift changes after every few seconds due the environmental and other noise. The measurement model will be given as,

$$y_k = x_S(t_k) - x_R(t_k) = H.x_k + v_k \quad (5)$$

where y_k is the phase or time offset between S and R, and $x_S(t_k)$ and $x_R(t_k)$ are the phase states of the sender and the receiver respectively, at time t_k. Even though these expressions are in terms of phase offset, they can be easily converted in terms of time offset, by dividing each term by the ideal frequency of nodes' clocks. Doing so will not change the nature of the problem. For the system model, let x_{SR} be the phase-offset state, y_{SR} the frequency bias state and z_{SR} as the relative drift state between the clocks of sender and receiver. Here, $x_{SR}(t)$ is same as x_k in the equation 5, and $y_{SR}(t)$ should not be confused with y_k. Then the evolution of this offset between S & R from time step $(t-\tau)$ to t is given by following equations:

$$x_{SR}(t) = x_{SR}(t-\tau) + \tau.y_{SR}(t-\tau) + \frac{1}{2}\tau^2.z_{SR}(t-\tau) + w_{x_{SR}}(t) \quad (6)$$

$$y_{SR}(t) = y_{SR}(t-\tau) + \tau.z_{SR}(t-\tau) + w_{y_{SR}}(t) \quad (7)$$

$$z_{SR}(t) = z_{SR}(t-\tau) + w_{z_{SR}}(t) \quad (8)$$

where the process noise vector, which specify the level of relative noise components between the two clocks, is given as

$$W_{SR}(t) = [\ w_{x_{SR}}(t) \quad w_{y_{SR}}(t) \quad w_{z_{SR}}(t)\ ]^T \quad (9)$$

This leads us to a basis vector : $H = [\ 1 \quad 0 \quad 0\ ]$

The random clock jitter is used as the measurement noise, v, at any instance of time. Hence the measurement error covariance is given as, $R^{-1} = cov\{\Psi_n(t_R)\}$ which is assumed to be a zero-mean Gaussian random variable. Hence the state vector is: $x_k = [\ x_{SR}(t) \quad y_{SR}(t) \quad z_{SR}(t)\ ]$ which is updated at every re-synchronization instance, using Φ and W. The transition matrix, showing the transition of states from time step t_k to t_{k+1} is,

$$\Phi = \begin{pmatrix} 1 & \tau & \frac{\tau^2}{2} \\ 0 & 1 & \tau \\ 0 & 0 & 1 \end{pmatrix}$$

Thus the next value of the relative drift between two nodes is obtained by adding some noise to it's previous value; which affects the frequency bias between the two clocks,

Authorized licensed use limited to: University of Texas at Arlington. Downloaded on January 6, 2010 at 16:11 from IEEE Xplore. Restrictions apply.

which in turn changes the phase offset between them. Here, a multiplication factor, τ, which reflects the change in drift over a short time, is taken as the time between subsequent synch pulses. The sources of all the noises lie well in the environmental effects, aging of the oscillator, etc. and it also accounts for the errors in system model. The vector W is derived from the Hadamard and Allan variances - the complete description of which are out of the scope of this work. For a detailed working of Kalman filter, readers can refer to [9].

IV. Fuzzy Logic Algorithm

The rule-based Fuzzy logic systems (FLS) are extensively used for forecasting of time-series [8] [10]. For the FLS solution, first the trend is calculated by a sliding window technique and data is detrended, which is then fed as input to the FLS. Given a collection of these N data points, they are first partitioned into a *training* data subset - used for learning period of FLS - with D data points, $x(1), x(2), ..., x(D)$, and a *testing* data subset - for actual prediction - with $(N - D)$ data points, $x(D+1), ..., x(N)$. For both these subsets, we use the previous 4 data samples as antecedents for forecasting the next sample of data (consequent). I.e. $x(k-3), x(k-2), x(k-1), x(k)$ were used to predict $x(k+1)$. Number of training points were about 30 to 50 for a dataset of 100 samples.

We have chosen *singleton fuzzification*, *product implication* and *Height Defuzzifier*. Each antecedent has two membership functions (MFs) - High and Low, chosen to be Gaussian. The number of rules are $2^4 = 16$. Now, if x_1 is an input value from input set X_1, F_p^l is MF of rule l that is of type p, $\star$ and T are the chosen t-norm, and G^l is rule output fuzzy set. Then the rules are designed as:

R^l : IF $x(k-3)$ is F_1^l and $x(k-2)$ is F_2^l and $x(k-1)$ is F_1^l and $x(k)$ is F_2^l, THEN $x(k+1)$ is G^l.

For singleton fuzzification, the firing level of l^{th} rule is,

$$\mu_{F_1^l}(\acute{x}_1) \star \mu_{F_2^l}(\acute{x}_2) ... \star \mu_{F_p^l}(\acute{x}_p) = T_{i=1}^{p} \mu_{F_i^l}(\acute{x}_i) \tag{10}$$

and the output fuzzy set B^l for rule R^l is such that

$$\mu_{B^l}(y) = [T_{i=1}^{p} \mu_{F_i^l}(x_i)] \star \mu_{G^l}(y) \tag{11}$$

The output of the height defuzzifier, which replaces each G^l by a crisp value at the point, $\bar{y}^l$, having maximum membership grade (height) in l^{th} output set, is given as:

$$y_h(\mathbf{x}) = \frac{\sum_{l=1}^{M} \bar{y}^l \mu_{B^l}(\bar{y}^l)}{\sum_{l=1}^{M} \mu_{B^l}(\bar{y}^l)} \tag{12}$$

For the antecedent MFs, initial mean for 'High' MF was $m_t + \sigma_t$ and that for 'Low' MF was $m_t - \sigma_t$, and the std for both MFs was σ_t, where m_t and σ_t are the mean and std of training data set. The initial consequent fuzzy set comprises of random numbers in the given data range. So, we have total 144 parameters. After setting up the initial design, a steepest descent (back-propagation) algorithm was used to train these parameters using the training data. After training, the rules are fixed and then this FL forecaster is used for the testing subset.

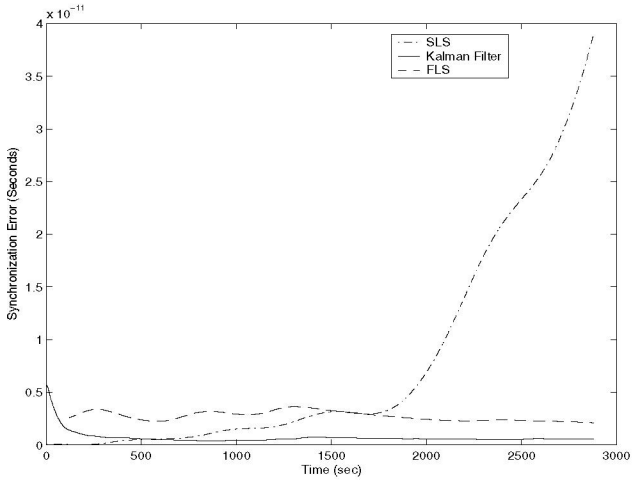


Fig. 1. Mean square synchronization error for dataset 2

The design described above works well with batch mode of prediction; but a better online performance is obtained in this case by a sequential design. For sequential design, after setting the architecture and initial rules, when stored samples are equal to the number of antecedents, it is fed to FLS to predict the next sample. When the next data sample is actually received, the error between predicted and measured value of data is used in the back-propagation algorithm to train the parameters of FLS online, which are then used for prediction at the next time-step.

V. Simulations and Comparisons

We have tested and compared the performances of all the three algorithms, on various datasets, which comprise of the time offset between the sender node and a single receiver node, taken at the sampling rate of 60 to 360 seconds. The first set has constant clock parameters and no environmental noise. In the second dataset, the clock parameters are made dynamic, but environmental noise term is kept low. Both these datasets can be considered to be similar to an indoor-scenario, where the clock parameters and hence the offset between 2 nodes' clock will vary in a non-linear pattern, yet without any drastic random changes. In the third dataset, both variation in the clock parameters and environmental noise are high, which results in highly random changes in clock drift. This dataset is an ideal example of time-offset variation in an outdoor scenario. The mean squared error (mse), i.e. synchronization error, between the predicted value of time-offset and the actual measurement is calculated and plotted for all three approaches. (But due to constraints of space, only few are presented here).

All the methods achieve very good precision on most datasets. The mse is in the range of 10^{-12} or lower, which means that the nodes will be synchronized within an accuracy of less than 10 microseconds. All methods achieved a much higher sampling period (360 seconds) as compared to that obtained from short-term timescale formation of current techniques (10 to 60 seconds). The broadcast nature of the

Authorized licensed use limited to: University of Texas at Arlington. Downloaded on January 6, 2010 at 16:11 from IEEE Xplore. Restrictions apply.

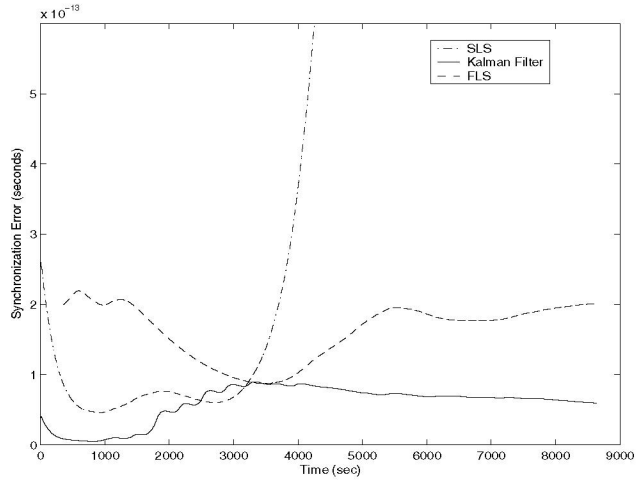


Fig. 2. Mean square synchronization error for dataset 3

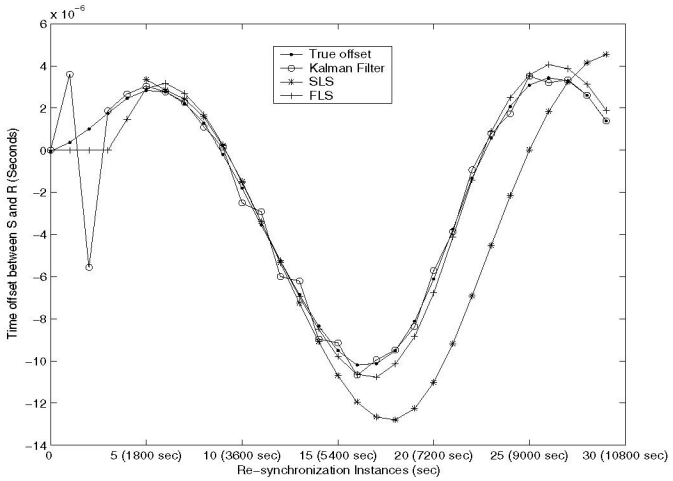


Fig. 3. Measured and estimated values of time offset between Sender and Receiver for Dataset 3

protocol provides a uniform precision over the cluster. All the methods converge very fast, which leaves us room for approximate choice of the initial conditions. FLS and Kalman filter are adaptive to environmental effects on nodes' clocks and hence preserve the accuracy under dynamic conditions. The advantage of FLS over the other two is in its model-free nature, which is very useful when the offset between clocks vary in a highly random fashion. The storage requirement of all techniques is very small, a few samples, though FLS needs more space than other two. SLS and FLS have much less complexity and processing time than Kalman filter approach.

Since the synch pulses are coming after a considerable duration of time, the nodes can sleep in this time and wake-up just to receive the pulses, thus saving a lot of energy. The S-R nature of protocol and a minimum window size keeps the messaging overhead very less. The protocol is flexible and it can adapt easily to provide the 'necessary and sufficient' synchronization for a given application. It is possible to tune it to required accuracy by choosing appropriate values of parameters such as, transition matrix, covariance matrices, mean and std of membership function, window size, and sampling period. The prediction of sender's clock can go on even in the sleep mode, so it will always assure some accuracy in case of both '*Always On*' and '*Post-facto*' synchronization. The performance of these techniques does not depend on the number of nodes in the cluster (density), node failures, or a change of clusterhead. Also, nodes can be synchronized to physical time without much stress on resources, by incorporating only the clusterhead with a GPS receiver.

VI. Conclusion

All the three approaches have been successful in achieving high accuracy of a few microseconds even at a high sampling interval for synchronization beacons, at the same time making the synchronization scheme adaptive to the environmental effects. Owing to it's simpler design, the Sequential Least Squares algorithm can be more useful in an indoor-scenario, whereas because of their recursive and dynamic nature, Kalman Filter and Fuzzy Logic algorithms yield a very good performance for an outdoor-scenario. The nature of the algorithms also provides many other advantages such as: energy-efficiency, multimodal and tunable to the needs of application, scalability, and low overhead. These factors make our schemes applicable in a variety of applications. We suggest some future research to provide in-depth analysis of issues like network-wide synchronization, or adding a correction for network delays, combined with these techniques.

Acknowledgement

This work was supported by the U.S. Office of Naval Research (ONR) Young Investigator Program Award under Grant N00014-03-1-0466.

References

[1] Jeremy Elson, Kay Römer, "Wireless Sensor Networks: A New Regime for Time Synchronization" *ACM SIGCOMM Computer Communication Review*, vol 33, no. 1, January 2003, pp. 149-154

[2] J. Elson, D. Estrin, "Time Synchronization for Wireless Sensor Networks" *Proc. 15th International Parallel and Distributed Processing Symposium*, April 2001, pp. 1965-1970

[3] S. Ganeriwal, D. Ganesan, M. Hansen, M. Srivastava, D. Estrin, "Rate-Adaptive Time Synchronization for Long-lived Sensor Networks" *ACM SIGMETRICS international conference on Measurement and modeling of computer systems*, June 2005, pp. 374-375

[4] Jeremy Elson, Lewis Girod, Deborah Estrin, "Fine-Grained Network Time Synchronization using Reference Broadcasts" *ACM SIGOPS Operating Systems Review: Special issue on Physical Interface*, vol 36, SI Winter 2002, pp. 147-163

[5] An-swol Hu, Sergio D. Servetto, "Asymptotically Optimal Time Synchronization in Dense Sensor Networks" *2nd ACM Int. Conference on Wireless Sensor Networks and Applications* , Sept. 2003, pp. 1-10

[6] Charles A. Greenhall, "Forming stable timescales from the JonesTryon Kalman filter" *IoP Journals: Metrologia: IV International Time-Scale Algorithms Symposium*, vol 40, no. 3, June 2003, pp. 335-341

[7] Douglas Arnold, "Stochastic Model Estimation of Network Time Variance" *Tech. Rep., TRUETIME*,

[8] Qilian Liang, "Ad hoc wireless network traffic-self-similarity and forecasting" *Communications Letters, IEEE*, vol 6, no. 7, July 2002, pp. 297-299

[9] John L. Crassidis, John L. Junkins, "Optimal Estimation of Dynamic Systems" CRC Press, 2004

[10] Jerry M. Mendel, "Uncertain Rule-Based Fuzzy Logic Systems" Prentice Hall PTR, 2000

Authorized licensed use limited to: University of Texas at Arlington. Downloaded on January 6, 2010 at 16:11 from IEEE Xplore. Restrictions apply.

UWB Sensor Networks in Hostile Environment: Interference Analysis and Performance Study

Lingming Wang and Qilian Liang
Department of Electrical Engineering
University of Texas at Arlington
Arlington, TX 76019-0016. USA
E-mail:wang@wcn.uta.edu. liang@uta.edu

***Abstract*— Interferences due to the hostile environment (e.g. jammer) and the Multi-User Access are critical factors affecting performance of the wireless sensor networks. In this paper, we study a hybrid Frequency Hopping/Time Hopping-Pulse Position Modulated (FH/TH-PPM) UWB for wireless sensor networks in hostile environment with partial-band(PB) tone interference. FH and TH are both used to get as much diversity gain as possible. Theoretical analysis is made for the bit error rates performance in the presence of multitone/pulse (tone in frequency domain and pulse in time domain) interference and Multi-User Interference. We also derived theoretical performance formula when the low duty-cycle in UWB system and the large number of sensor nodes in a wireless sensor networks are considered.**

***Index Terms*— Time Hopping, Frequency Hopping, PPM, Wireless sensor networks, UWB, BER**

I. Introduction

Wireless sensor networks are becoming more popular for an ever increasing range of applications with improvements in device size, power control, communications and computing technology. Since 2002 there has been great increasing popularity of commercial applications based on Ultra WideBand. This in turn has ignited interest in the use of this technology for sensor networks. Actually, UWB systems have potentially low complexity and low cost; have a very good time domain resolution, which facilitates location and tracking applications. So, UWB wireless sensor networks are promising.

The rest of this paper is organized as follows. The system models, including the transmission, channel and receiver, will be introduced in Section II. The MUI and hostile interference will be studied in Section III and Section IV respectively, and the SINR and closed-form BER will be derived as well. Numerical results and comparisons will be present in Section V; and conclusions are made in Section VI.

II. System Models

In the proposed system, there are N_F non-overlapping FH bands, each with bandwidth B_h where B_h is the bandwidth required to transmit a TH-PPM signal in the absence of FH. Let $s^k(t)$ denotes the k-th user's signal at time t in this FH/TH-PPM UWB system with totally N_u users, and it takes the form

$$s^k(t) = \sqrt{\frac{E_b}{N_s}} \sum_{j=-\infty}^{+\infty} c_j^{fh}(k) p[t - jT_f - c_j^{th}(k)T_c - d_j(k)\delta]) \tag{1}$$

where $p(t)$is a chip waveform. N_s is the number of pulses used to transmit a single information bit. T_f is the time duration of a frame. E_b is the energy per information bit. $\sqrt{\frac{E_b}{N_s}}$ is the normalized energy in each symbol. $c_j^{th}(k)T_c$ is the time shift introduced by the TH code. T_c is the chip duration. $c_j^{th}(k)$ is the j-th coefficient of the TH sequence used by user k. The $d_j(k)\delta$ term represents the time shift introduced by PPM modulation. $c_j^{fh}(k) = \sqrt{(2)}cos(2\pi f_k j)$ is the k-th user's spreading code during j-th frame.

In WSN, sensor nodes have two states, i.e., active communication status and idle status. In order to save energy, sensor nodes choose to be idle for most of the time. The number of nodes which are actually in the status of active communication is unknown. However, the total number of sensor nodes in the network and the access rate λ, i.e., the rate that a node in the communication status, for each node are assumed to be known. Clearly, the event of status of sensor node is a Bernoulli distribution with mean as λ and variance as $\lambda(1-\lambda)$. Assume there are N_U sensor nodes in a network, each one of them chooses to be idle or active independently. Therefore, the number of sensor nodes which are in active communication status, N_u^T, can be seen as the sum of N_U independent, identically distributed Bernoulli random variable, which is a Binomial distribution. Usually N_U is very large, we can approximate the Binomial distribution to a Gaussian random variable with the mean $N_U\lambda$ and variance $N_U\lambda(1-\lambda)$, as

$$f_{N_u^T}(n_u^t) = \frac{1}{\sqrt{2\pi N_U\lambda(1-\lambda)}} e^{-(n_u^t - N_U\lambda)^2/2N_U\lambda(1-\lambda)} \tag{2}$$

1-4244-0445-2/07/$20.00 ©2007 IEEE

Authorized licensed use limited to: University of Texas at Arlington. Downloaded on December 18, 2009 at 14:54 from IEEE Xplore. Restrictions apply.

For the N_u^T users, they randomly choose one of the sub-bands to transmit the signal according to $c_j^{fh}(k)$ symbol by symbol. It is also a Binomial random variable with the coefficient $1/N_F$. To simplify the problem, we assume that the users are distributed optimally, so the number of users share the same channel, N_u, should be expressed as

$$N_u = N_u^T / N_F. \tag{3}$$

III. Multi-User Interference Analysis

In this section, we will first focus on the analysis of MUI with the absence of hostile jammer interference. We assume there is no inter-channel-interference. Therefore, the received signal of 1-st user's j-th symbol can be expressed as:

$$r_j(t) = r_j^{(1)}(t) + r_{j,mui}(t) + n(t) \tag{4}$$

where $r_{j,mui}(t)$ is the MUI contribution at the receiver input. If the users are many and have comparable powers, we can approximate the MUI as a white Gaussian process by the central limit theorem [5] and, as such, it can be lumped into the additive Gaussian Noise,

$$w_{tot}(t) = r_{j,mui}(t) + n(t) \tag{5}$$

and $w_{tot}(t)$ is still a white Gaussian process. Since the system is asynchronous, we need to consider all cases where a pulse originated by any of the transmitters but TX1, is detected by the receiver. First of all we need to analyze the noise provoked by the presence of one alien pulse at the output of the receiver by using the similar method as in[1],

$$mui^{(k)}(\tau^{(k)}) = \sqrt{E_{RX}^{(k)}} \int_0^{T_c} p(t - \tau^{(k)}) v_t dt \tag{6}$$

where, $E_{RX}^{(k)} = \alpha^{(k)}(E_b/N_s)$, and here we suppose $\alpha^{(k)} = 1\ \forall k$.

Since $\tau^{(k)}$ is uniformly distributed over $[0, T_f)$, and identically distributed for different τ[1], under the hypothesis of perfect power control, e.g., $E_{RX}^{(k)} = E_{RX}\ \forall k$, the total MUI energy is

$$\sigma_{mui}^2 = \frac{E_{RX}}{T_f} \sum_{k=2}^{N_u} \left(\int_0^{T_f} \left(\int_0^{T_c} p(t-\tau) v(t) dt \right)^2 d\tau \right) \tag{7}$$

Define σ_M^2 as

$$\sigma_M^2 = \int_0^{T_f} \left(\int_0^{T_c} p(t-\tau) v(t) dt \right)^2 d\tau \tag{8}$$

we get

$$\sigma_{mui}^2 = \frac{E_{RX}}{T_f} (N_u - 1) \sigma_M^2 \tag{9}$$

Let SNR_{ref} denotes the equivalent signal to noise and MUI ratio over one symbol, it can be written as

$$SNR_{ref} = (SNR_n^{-1} + SIR_{mui}^{-1})^{-1} \tag{10}$$

where SNR_n are the signal to noise ratio over one symbol.

Hence,

$$\begin{aligned} SNR_{ref} &= \left(\left(\frac{E_{RX}}{N_0} \right)^{-1} + \left(\frac{T_f}{(N_u - 1)\sigma_M^2} \right)^{-1} \right)^{-1} \\ &= \frac{T_f}{N_s T_f + (N_u - 1)\sigma_M^2 \left(\frac{E_b}{N_0} \right)} \left(\frac{E_b}{N_0} \right) \end{aligned} \tag{11}$$

where $E_b/N_0$is the system SNR.

IV. Performance Analysis with Multitone/pulse Interference

In this section, the SIR for the hostile interference part is obtained. We make the following assumptions: The multitone/pulse interference has a total power P_J, which is transmitted in a total of q equal power interfering tones spread randomly over the spread spectrum bandwidth. The time duration for the interference pulse is the same as the time duration of the transmitted signal pulse $p(t)$, which is denoted as T_p. To simplify the problem, we suppose $T_c = 2T_p$ and $\delta = T_p$. The hop period of the interference is also T_p, and each hop is independent. The multitone/pulse interference can catch the signal pulse with the perfect timing. We consider the scenario that there is at most one interference per FH sub-band. Hence, in one hop, the probability that a FH band contains an interference tone/pulse is q/N_F. Observe the transmitted signal as in (1), the signal hops both in the frequency domain and in the time domain symbol by symbol. Therefore, our analysis will first focus on one symbol.

We partition the symbol duration as two time slots, hence, for the multitone/pulse interference, there are two hops. In each hop, the interference is independently distributed. There are totally four cases with regard to the jammer interference for each symbol: There is no jammer interference in either of two slots, with the probability as $P\{case1\} = (1 - \frac{q}{N_F}) \cdot (1 - \frac{q}{N_F})$; there is jammer interference in each slot, with the probability as $P\{case2\} = \frac{q}{N_F} \cdot \frac{q}{N_F}$; there is one and only one jammer interference pulse, and it is at the same slot as the signal pulse. The probability of case3 is $P\{case3\} = (1 - \frac{q}{N_F}) \cdot \frac{q}{N_F}$; there is one and only one jammer interference pulse, and it is not at the same slot as the signal pulse. The probability of case4 is $P\{case4\} = (1 - \frac{q}{N_F}) \cdot \frac{q}{N_F}$.

The received signal of the j-th symbol of 1-st user can be expressed as:

$$r_j'(t) = r_j^1(t) + I_{jammer}(t) + w_{tot}(t); \tag{12}$$

Authorized licensed use limited to: University of Texas at Arlington. Downloaded on December 18, 2009 at 14:54 from IEEE Xplore. Restrictions apply.

where $r_j^k(t)$ and $I_{jammer}(t)$ are the jammer interference contributions at the receiver input, and $w_{tot}(t)$ accounts for both the thermal and MUI noise contributions, and is still a white Gaussian process as proved in Section III. Hence, a maximum a posteriori (MAP) approach can be adopted here to get the minimum error probability. For different cases of the jammer interference, the detection boundaries are shown in Fig. 1.

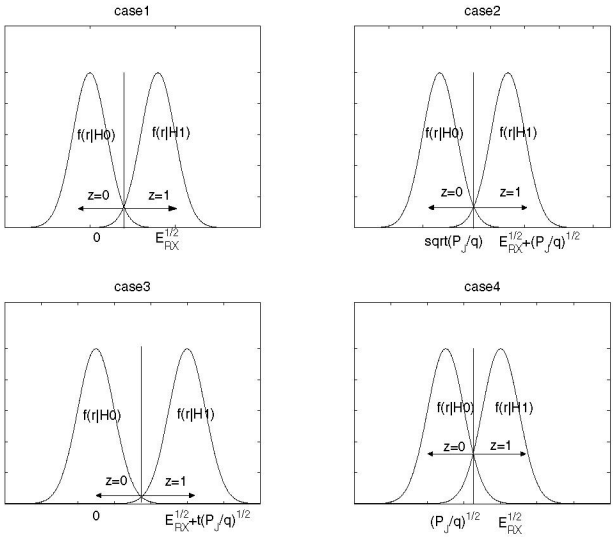


Fig. 1. The MAP detection rule for all the cases.

Hence, we can get the $SINR_{jammer}$ straightforwardly.

$$SINR_{jammer|case1,2} = \frac{E_{RX}}{N_0'}. \tag{13}$$

$$SINR_{jammer|case3} = \frac{(\sqrt{E_{RX}} + \sqrt{\frac{P_J}{q}})^2}{N_0'}. \tag{14}$$

$$SINR_{jammer|case4} = \frac{(\sqrt{E_{RX}} - \sqrt{\frac{P_J}{q}})^2}{N_0'}. \tag{15}$$

Since the error probability of 2-PPM signal is [1], $Pr = Q(\sqrt{SNR_{spec}})$, and after removing the conditioning on cases, we get

$$\begin{aligned} Pr_s' &= \left(\left(\frac{N_F - q}{N_F}\right)^2 + \left(\frac{q}{N_F}\right)^2\right) Q\left(\sqrt{\left(\frac{\frac{E_b}{N_s}}{N_0'}\right)}\right) \\ &+ \left(\frac{N_F - q}{N_F}\right)\left(\frac{q}{N_F}\right)\left(Q\left(\sqrt{\left(\frac{(\sqrt{\frac{E_b}{N_s}} + \sqrt{\frac{P_J}{q}})^2}{N_0'}\right)}\right)\right. \\ &+ \left. Q\left(\sqrt{\left(\frac{(\sqrt{\frac{E_b}{N_s}} - \sqrt{\frac{P_J}{q}})^2}{N_0'}\right)}\right)\right). \end{aligned} \tag{16}$$

Considering only N_u is a random variable, we should take (2) and (3) into (16),

$$Pr_s = \frac{1}{N_F\sqrt{2\pi N_U\lambda(1-\lambda)}} \int_1^{N_U} Pr_s' \, e^{-(n_u - N_U\lambda)^2/2N_U\lambda(1-\lambda)} dn_u \tag{17}$$

After we got the symbol error rate Pr_s, it is easy for us to obtain the bit error rate Pr_b by majority law.

$$Pr_b = \sum_{k=\lceil \frac{N_s}{2} \rceil}^{N_s} C_{Ns}^k Pr_s^k (1 - Pr_s)^{N_s - k} \tag{18}$$

where $\lceil\ \rceil$ is the ceiling operation, and C_{Ns}^k is an N_s-choose-k Binomial coefficient, i.e., $C_{Ns}^k = \frac{k!(N_s-k)!}{N_s!}$.

V. Numerical Results and Comparisons

TABLE I
PARAMETERS OF THE EXAMPLE FH/TH-PPM UWB SYSTEM

Parameter	Notation	2^{nd}-order mono-cycle
shaping factor for the pulse	ϵ	$0.25ns$
time shift introduced by PPM	δ	$0.5ns$
pulse duration	T_p	$0.5ns$
frame duration	T_f	$8ns$
chip duration	T_c	$1ns$
number of hops	N_h	6

The parameters of the example UWB systems are listed in Table I. System performances are evaluated according different values of the pivotal parameters, including N_s, E_B/P_J, q, and λ. The results are shown through Figure. 2 to Figure. 5. We can get following conclusions through the simulations: the more symbols we used to transmit one information bit, and the larger E_b/P_J can both guarantee better performance. However, there are floors in both Figure. 2 and Figure. 3. The curves in Figure. 2 after $15dB$ being flat is caused by jammer interference. The reason for the limited performance gain from $E_b/P_J = 5dB$ to $E_b/P_J = 10dB$ is is when E_b/P_J is higher than some better threshold, the jammer interference is too weak to give any impact to the system. Because large q means not only the probability that a jammer interference bumps the information signal is higher, but also means the energy of the jammer interference for each sub-band is less, the worst and best performances are get at $q = 2$ and $q = 8$ respectively as shown in Figure. 4. Figure. 5 shows though with the same N_U, the difference in λ would yield totally different performance.

VI. Conclusions

In this paper, we make an performance analysis with the presence of the multi-tone/pulse jammer interference

Authorized licensed use limited to: University of Texas at Arlington. Downloaded on December 18, 2009 at 14:54 from IEEE Xplore. Restrictions apply.

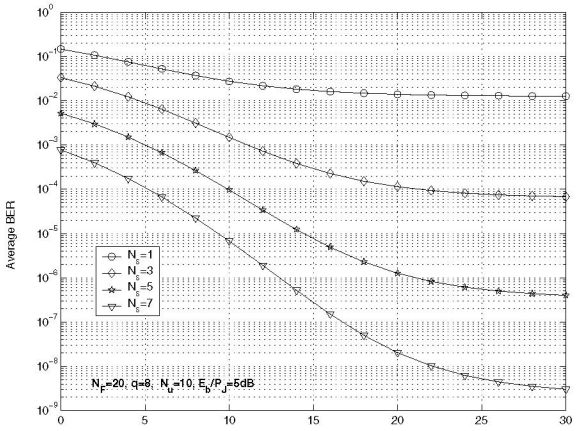


Fig. 2. The average BER for different N_S.

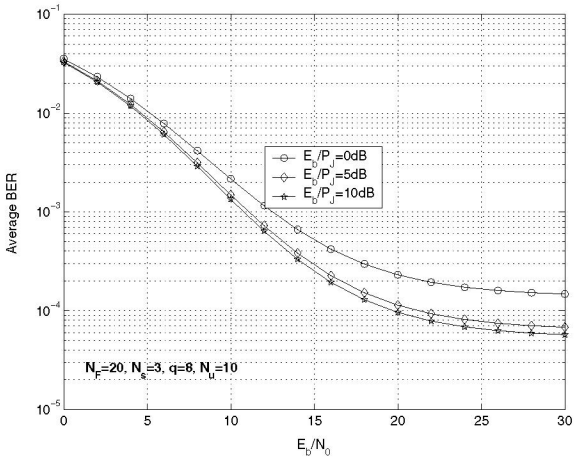


Fig. 3. The average BER for different E_b/P_J.

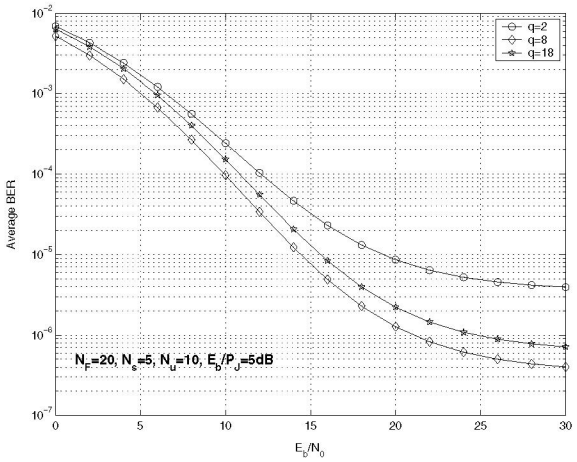


Fig. 4. The average BER for different q.

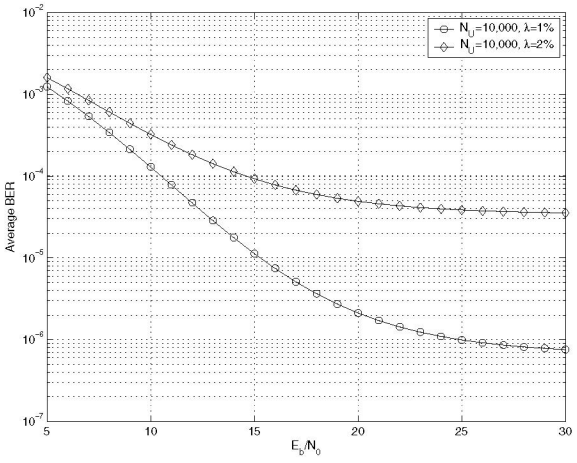


Fig. 5. The average BER for different λ.

and multi-user interference based on the hybrid FH/TH-PPM-UWB system. We get an accurate expressions of SER and BER with the presence of MUI and hostile jammer interference. We evaluate the performances for different number of symbols to carry one information bit N_s; the signal to jammer interference ratio E_b/P_J; the number of tones q of the jammer interference; and the access rate for each sensor nodes λ, in terms of BER so as to show how these parameters affect to the FH/TH-PPM UWB system.

VII. Acknowledgement

This work was supported by the Office of Naval Research (ONR) Young Investigator Award under Grant N00014-03-1-0466.

References

[1] M.D. Benedetto and G. Giancola *Understanding Ultar Wide Band Radio Fundamentals*, Prentice Hall Technical Reference, NJ, USA, 2004

[2] J. Foerster (editor), "Channel Modeling Sub-committee Report Final," IEEE802.15-02/490 (see http://ieee802.org/15/).

[3] V. Lottici, A. D. Andrea and U. Mengali "Channel Estimation for Ultra-Wideband Communications," *IEEE Journal on Selected Areas in Communications*, Vol. 20, No. 9, pp. 1638-1645, Dec 2002.

[4] R. A. Scholtz, "Multiple Access with Time-Hopping Impulse Modulation," *IEEE Militray Communication Conference*, Vol. 2, pp. 447-450, Oct 1993.

[5] M. Z. Win and R. A. Scholtz, "Ultra-wide Bandwidth Time-Hopping Spread-Spectrum Impulse Radio for Wireless Multiple Access Communications," *IEEE Transactions on Communications*, Vol. 48, Issue: 4, pp. 679-691, April 2000.

[6] B. Hu, and N. C. Beaulieu, " Accurate Performance Evaluation of Time-Hopping and Direct-Sequence UWB Systems in Multi-User Interference ," *IEEE Transactions on Communications*, Vol: 53, No. 6, pp. 1053-1062, June. 2005.

[7] L. Yang and G. B. Giannakis "A General Model and SINR Analysis of Low Duty-Cycle UWB Access Through Multipath With Narrowband Interference and Rake Reception," *IEEE Transactions on Communications*, Vol. 4, No. 4, pp. 1818-1833, July 2005.

Authorized licensed use limited to: University of Texas at Arlington. Downloaded on December 18, 2009 at 14:54 from IEEE Xplore. Restrictions apply.

Data Fusion in a Multi-Target Radar Sensor Network

Haining Shu and Qilian Liang
Department of Electrical Engineering
University of Texas at Arlington
Arlington, TX 76019-0016 USA
E-mail: shu@wcn.uta.edu, liang@uta.edu

***Abstract*— In this paper, we consider the decision fusion of Rayleigh fluctuating targets in multi-radar sensor networks. Decision fusion and data fusion in Wireless Sensor Networks (WSNs) has been widely studied in order to save energy. Radar system as a special sensor network, when implemented for battlefield surveillance, faces bandwidth constraint in real-time applications instead of energy restriction. In this work, we study the decision fusion rules of multiple fluctuating targets in multi-radar (MT-MR) sensor networks. The MT-MR decision fusion problem is modeled as a multi-input multi-output (MIMO) system. We assume that each radar makes binary decision for each target from the observation. We derive our *MIMO fusion* rules based on the target fluctuation model and compare against the optimal likelihood ratio method (LR), maximum ratio combiner (MRC) and equal gain combiner (EGC). Simulation results show that the *MIMO fusion* rules approach the optimal-LR and outperforms MRC and EGC at high signal to noise ratio (SNR).**

I. Introduction

Wireless sensor networks (WSN) have attracted growing interest in various applications. Radar as a powerful sensor system, has been employed for the detection and location of reflecting objects such as aircraft, ships, vehicles, people and natural environment. By comparing the received echo signal with the transmitted signal, the location of a target can be determined along with other target related information [1]. Conventional radar system operates as a pure independent entity. While in a resource-constrained WSN, such detached operation may lead to deteriorated performance and waste of limited resources. Collaborative signal and information processing over the network is a very promising area of research and is related to distributed information fusion [2].

A lot of prior research in data fusion are based on the assumption of lossless communication, i.e., the information sent from local sensors is perfectly recovered at the fusion center. For example, in [3] and [4], Vashney *et. al* investigated the optimum fusion rules under the conditional independence assumption. Other papers [5], [6] addressed the problem of distributed detection with constrained system resources, most of which provided the solutions to optimize sensor selection. However, this lossless communication assumption is not practical for many WSNs where the transmitted data suffers from channel fading and multi-user interference. In another hand, decision fusion with non-ideal communication channels are studied at both fusion center level [7], [8] and at the sensor level [9], [10]. Later, Lin *et. al* [11] have extended the channel aware decision fusion rules to more realistic WSN models that involve multi-hop transmissions. The above results, however, are mostly obtained based on one target or one event detection which is not applicable to multi-target situations.

The objective of this work is to derive the decision fusion rules of multiple fluctuating targets in multi-radar (MT-MR) sensor networks. The MT-MR decision fusion is modeled as a multi-input multi-output (MIMO) system. We present the theoretical formulation of the MIMO decision fusion problems. Rayleigh target fluctuation model and Gaussian noise are used in our first stage study.

The remainder of this paper is organized as follows. In the next section, we introduce the concept of target fluctuation model in radar sensor system. In Section III, we briefly overview the previous work on fusion rules. In Section IV, we present our MIMO decision fusion model for multi-target multi-radar sensor networks. Simulation and performance analysis are presented in Section V. Section VI concludes this paper.

II. Target Detection in Radar Sensor System

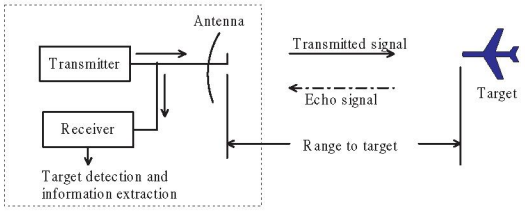


Fig. 1. Basic Principle of Radar System

The basic principle of radar [1] is illustrated in Fig. 1. In active radar sensor networks, the received data usually consists of three parts: white thermal noise, clutter scattered by the land environment, and if a target is present, a reflected or reradiated version of the transmitted signal [12]. That is, we have

$$y^{(t)} = \alpha^{(t)} s^{(t)} + n^{(t)} + \omega^{(t)} \quad (1)$$

in which $s^{(t)}$ and $y^{(t)}$ are the transmitted and received signals, respectively. $\alpha^{(t)}$ is the target cross section or radar

1-4244-0445-2/07/$20.00 ©2007 IEEE

Authorized licensed use limited to: University of Texas at Arlington. Downloaded on January 6, 2010 at 16:13 from IEEE Xplore. Restrictions apply.

cross section (RCS). It is assumed that $n^{(t)}$ is additive noise and $\omega^{(t)}$ is the returned clutter, a distorted version of the transmitted signal $s^{(t)}$.

Classical radar equation takes target cross section or radar cross section (RCS) to determine the power density returned to the radar for a particular power density incident on the target. It has been advantageous to model the target RCSs as a random variable. Some common fluctuation models are now available in the open literature, i.e. Swerling chi , lognormal, Rayleigh, Weibull as a compound Rayleigh distribution, Shadowed Rice target etc. In this work, we treat the target fluctuation as Rayleigh distribution which has the probability density function (pdf) as $f_\nu(\nu) = \frac{\nu}{\sigma_c^2} \exp\left(-\frac{\nu^2}{2\sigma_c^2}\right)$ Where $2\sigma_c^2$ is the mean square value of the envelope ν.

III. Review of Previous Decision Fusion Rules

In a single target, single hop sensor network, the typical parallel fusion structure in a flat fading channel is depicted in Fig. 2. The received signal at the fusion center from kth sensor is $y_k = h_k u_k + n_k$, where h_k is the channel fading envelope and n_k is the zero-mean additive Gaussian noise with variance σ^2. K sensors collect data generated according to either H_0 (there is no target present) or H_1 (there is target present) and transmit these decisions over fading and noisy channels to a fusion center. The fusion center tries to decide which hypothesis is true based on the received data y_k from all k.

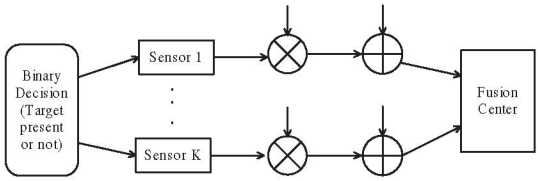


Fig. 2. Single-target, single-hop decision fusion model

Assume that the kth local sensor makes a binary decision $u_k \in \{+1, -1\}$, with false alarm and detection probability P_{fk} and P_{dk} respectively. That is, we have $P_{fk} = P[u_k = 1|H_0]$ and $P_{dk} = P[u_k = 1|H_1]$. Several decision fusion rules have been developed based on the above model in [11]. Throughout this work, we use $\Lambda^{(s)}$ to denote the fusion statistics for the single hop, single target transmission model.

- Optimal LR-based fusion statistic using complete prior knowledge.

$$\Lambda_1^{(s)} = \prod_{k=1}^{K} \frac{P_{dk}\psi_k^{(+)} + (1-P_{dk})\psi_k^{(-)}}{P_{fk}\psi_k^{(+)} + (1-P_{fk})\psi_k^{(-)}} \tag{2}$$

  where $Y = [y_1, ..., y_k]^T$ is a vector containing observations received from all K sensors, $\psi_k^{(+)} = e^{-((y_k-h_k)^2/2\sigma^2)}$ and $\psi_k^{(-)} = e^{-((y_k+h_k)^2/2\sigma^2)}$.
- LR-based fusion rules using only fading statistics for Rayleigh fading channel. Implementing the optimal LR test as in (2) requires that all a priori information, including the instantaneous channel gains.

$$\Lambda_2^{(s)} = \prod_{k=1}^{K} \frac{P_{dk}\Psi_k^{(+)} + (1-P_{dk})\Psi_k^{(-)}}{P_{fk}\Psi_k^{(+)} + (1-P_{fk})\Psi_k^{(-)}} \tag{3}$$

  where $\Psi_k^{(+)} = 1 + \sqrt{2\pi\gamma} y_k e^{(\gamma^2 y_k^2/2)} Q(-y_k\gamma)$, $\Psi_k^{(-)} = 1 - \sqrt{2\pi\gamma} y_k e^{(\gamma^2 y_k^2/2)} Q(y_k\gamma)$ and $\gamma = (\sigma_c/\sigma_n\sqrt{\sigma_c^2+\sigma_n^2})$ with $2\sigma_c^2$ being the mean square value of the fading channel, σ_n^2 is the noise variance.
- A two-stage approximation using the Chair-Varshney fusion rule.

$$\Lambda_3^{(s)} = \sum_{y_k<0} \log\left(\frac{1-P_{dk}}{1-P_{fk}}\right) + \sum_{y_k>0} \log\left(\frac{P_{dk}}{P_{fk}}\right) \tag{4}$$

- Fusion statistics using a maximum ratio combiner (MRC). $\Lambda_4^{(s)} = \frac{1}{K}\sum_{k=1}^{K} h_k y_k$
- Fusion statistics using an equal gain combiner (EGC). $\Lambda_5^{(s)} = \frac{1}{K}\sum_{k=1}^{K} y_k$

IV. Decision Fusion in a Multi-Target Radar Sensor System

In our scenario, we assumed that there are multiple radar sensors and multiple stationary targets in the field. In a multi-hop radar sensor network, the decision data is relayed via several radars to reach the fusion center. When there are multiple radar sensors and multiple targets in the field, the data fusion problem can be roughly modeled as a Multi-Input Multi-Output (MIMO) fusion problem. Fig. 3 illustrates an example of single-hop decision fusion problem.

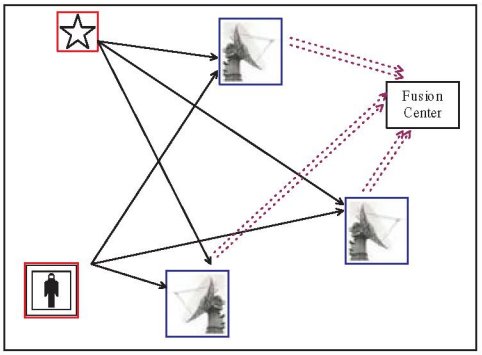


Fig. 3. MIMO fusion model

Let M denote the number of radar sensors and N be the number of targets. The received signal $Y^{(t)}$ at the fusion center at time t is a $N \times M$ matrix. We assume that the radar sensors are geographically dispersed, detection decisions are made at each separate local radar. The element $y_{ij}^{(t)}$ is the decision (target present or absent) of the jth target from the ith radar sensor. $y_{ij}^{(t)}$ can be represented as $y_{ij}^{(t)} = \alpha_{ij}^{(t)} \cdot s_{ij}{}^{(t)} + n_{ij}^{(t)}$.

We next derive the MIMO decision fusion rules for the multi-target radar sensor networks starting from the single-hop radar sensor networks.We use P_f as the fixed false alarm rate and P_{di} to denote the distinct probability of detection at radar sensor i throughout this work.

Authorized licensed use limited to: University of Texas at Arlington. Downloaded on January 6, 2010 at 16:13 from IEEE Xplore. Restrictions apply.

A. Decision fusion rule in multi-target, single-hop radar sensor networks

- Assume we have complete knowledge of the target fluctuation coefficients, the optimal LR-based fusion rule for the jth target was derived as

$$\Lambda_j^{(1)} = \prod_{i=1}^{M} \frac{P_{di}\psi_{ij}^{(+)} + (1-P_{di})\psi_{ij}^{(-)}}{P_f\psi_{ij}^{(+)} + (1-P_f)\psi_{ij}^{(-)}} \quad j = 1, ..., N \tag{5}$$

Complete decision vector for N targets are denoted as $\underline{\Lambda}^{(1)} = [\Lambda_1, \Lambda_1, ..., \Lambda_N]^T$ and

$$\underline{\psi}_i^{(\pm)} = \begin{bmatrix} e^{-(y_{i1} \mp \alpha_{i1})^2/2\sigma^2} \\ . \\ . \\ . \\ e^{-(y_{iN} \mp \alpha_{iN})^2/2\sigma^2} \end{bmatrix} \quad i = 1, ..., M \tag{6}$$

- LR-based fusion rules using only target fluctuation statistics.

$$\Lambda_j^{(2)} = \prod_{i=1}^{M} \frac{P_{di}\Psi_{ij}^{(+)} + (1-P_{di})\Psi_{ij}^{(-)}}{P_f\Psi_{ij}^{(+)} + (1-P_f)\Psi_{ij}^{(-)}} \quad j = 1, ..., N \tag{7}$$

where $\gamma = (\sigma/\sigma_n\sqrt{\sigma^2 + \sigma_n^2})$ with $2\sigma^2$ being the mean square value of the target fluctuation model, σ_n^2 is the noise variance.

$$\underline{\Psi}_i^{(\pm)} = \begin{bmatrix} 1 \pm \sqrt{2\pi\gamma} y_{i1} e^{(\gamma^2 y_{i1}^2/2)} Q(\mp y_{i1}\gamma) \\ . \\ . \\ . \\ 1 \pm \sqrt{2\pi\gamma} y_{iN} e^{(\gamma^2 y_{iN}^2/2)} Q(\mp y_{iN}\gamma) \end{bmatrix} \tag{8}$$

where $i = 1, ..., M$.

- Fusion statistics using a maximum ratio combiner (MRC). $\Lambda_j^{(3)} = \frac{1}{M}\sum_{i=1}^{M} \alpha_{ij} y_{ij} \quad j = 1, ..., N$
- Fusion statistics using an equal gain combiner (EGC). $\Lambda_j^{(4)} = \frac{1}{M}\sum_{i=1}^{M} y_{ij} \quad j = 1, ..., N$

B. Decision fusion for multi-target multi-radar sensor networks

Implementing the decision rules for single target, multi-hop WSNs in [11] to our multi-target, multi-hop radar sensor networks, we get the decision fusion rules as follows.

- Optimal LR-based Fusion Rule
  In multi-hop radar sensor network, we assume only the first hop radar sensors are CFAR with false alarm P_f^0 and probability of detection P_{di}^0. Let P_{di}^c be the probability of detection at the ith radar in the last relay, [11] has proved that for one given target detection, $P_{di}^c \approx P_{di}^0$ and $P_f^c = P_f^0$ at high signal to clutter ratio (SCR). At low SCR, P_{di}^c and P_f^ccan be approximated as

$$P_{di}^c \approx \frac{1}{2} + \frac{2^{M_i}(\prod_{k=0}^{M_{i-1}} \alpha_{ik})}{(\sqrt{2\pi}\sigma)^{M_i}} \left(P_{di}^0 - \frac{1}{2}\right) \tag{9}$$

$$P_f^c \approx \frac{1}{2} + \frac{2^{M_i}(\prod_{k=0}^{M_{i-1}} \alpha_{ik})}{(\sqrt{2\pi}\sigma)^{M_i}} \left(P_f^0 - \frac{1}{2}\right) \tag{10}$$

Assume there are M radar sensors in the last hop, M_i is the number of hops at the ith radar. α_{ik} is RCS value at the kth relay of radar i.
The optimum LR-based fusion rule for multi-target radar sensor networks can be written as

$$\Lambda_j^{(1)} = \prod_{i=1}^{M} \frac{P_{di}^c + (1-P_{di}^c)\cdot\phi_{ij}}{P_f^c + (1-P_f^c)\cdot\phi_{ij}} \quad j = 1, ..., N \tag{11}$$

where

$$\underline{\phi}_i = \begin{bmatrix} e^{-(2y_{i1}\alpha_{i1})^{M_i}/\sigma^2} \\ . \\ . \\ . \\ e^{-(2y_{iN}\alpha_{iN})^{M_i}/\sigma^2} \end{bmatrix} \quad i = 1, ..., M \tag{12}$$

- Denote $\underline{\Lambda}^{(2)}$ as the LR rule that corresponds to the case when only the target RCS statistics are known. $\underline{\Lambda}^{(2)}$ can be derived for the multi-hop MT-MR sensor networks.

$$\Lambda_j^{(2)} = \prod_{i=1}^{M} \frac{1 + [P_{di}^c - Q(\gamma y_{ij})]\sqrt{2\pi}\gamma y_{ij} e^{(\gamma y_{ij})^2/2}}{1 + [P_f^c - Q(\gamma y_{ij})]\sqrt{2\pi}\gamma y_{ij} e^{(\gamma y_{ij})^2/2}} \quad j = 1, ..., N \tag{13}$$

where $\underline{y}_i = [y_{i1}, y_{i2}, ...y_{iN}]$ is a vector containing all N decision data from radar i. P_{di}^c and P_f^c are denoted as in (9) and (10).
- Decision fusion rules of Maximum ratio combiner (MRC) and equal gain combiner (EGC) have the identical format as the single hop case because for both of them, the decision fusion only depends on the last hop.

V. Simulation Results

For multi-target, single-hop radar sensor network and multi-target, multi-hop radar sensor network, we are interested to compare the four decision fusion rules:

- Optimal LR-based rule
- LR-based rule with target RCS statistics only
- MRC rule
- EGC rule

Fig.4 gives the probability of miss detection vs. the SCR for multi-target, single-hop radar sensor network. There are total two stationary targets, three radar sensors in the field. The optimal LR- based fusion rule provides the most powerful detection performance but it requires complete target RCS knowledge. The LR-based rule with target RCS statistics approaches the optimal LR-based rule in low SCR and have about 1dB loss in higher SCR. MRC and EGC have similar

Authorized licensed use limited to: University of Texas at Arlington. Downloaded on January 6, 2010 at 16:13 from IEEE Xplore. Restrictions apply.

performance. Both are little worse than the LR-based rule with target RCS statistics.

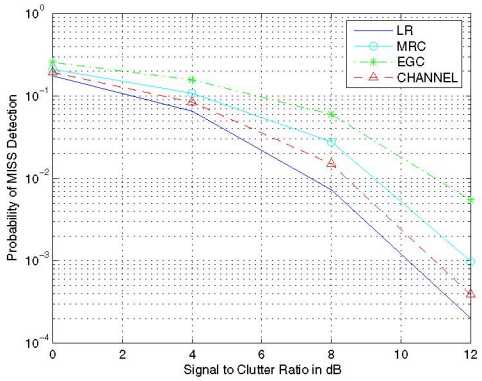


Fig. 4. Single hop

Fig.5 and Fig.6 are the performance for multi-target, multi-hop radar sensor networks. Fig.5 shows the probability of miss detection when each of the three radar sensors reaches the fusion center in two hops. Fig.6 shows the performance when the three radar sensors reach the fusion center in unequal hops. In our simulation, we assume that one radar sensor reaches the fusion center in two hops while the others in single hop. As expected, the probability of detection for the single-hop case outperforms the one for multi-hop.

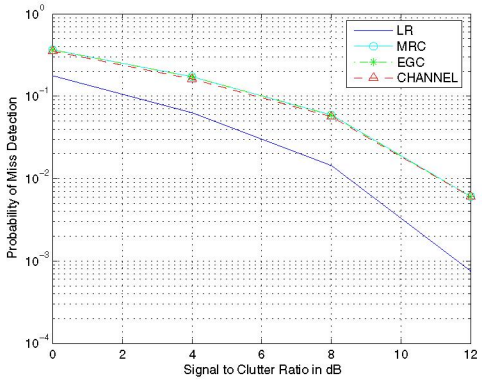


Fig. 5. Multi-hop, equal hops

VI. Conclusions

In this paper, we presented the MIMO decision fusion rules for multi-target, multi-hop radar sensor networks under the assumption that the target RCS is Rayleigh model. We derived the optimum LR-based fusion rule and a sub-optimal LR-based fusion rule with the target RCS statistics only. Simulation results show that the *MIMO fusion* rules approach the optimal-LR and outperforms MRC and EGC at high signal to noise ratio (SNR).

In many cases, two or more local radars may share a common relay node on their way to the fusion center. Under this circumstances, the independent assumption made toward the target RCS may not be held. It is actually a very interesting space correlation issue. As the radar observations always demonstrate time correlation, further research will be focused on this space-time correlation of radar sensor networks.

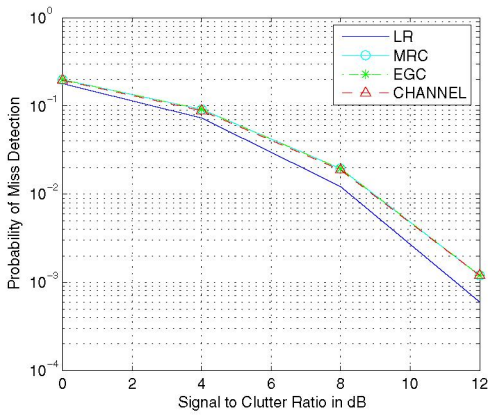


Fig. 6. Multi-hop, unequal hops

Acknowledgment

This work was supported by the Office of Naval Research (ONR) Young Investigator Award under Grant N00014-03-1-0466. The authors would like to thank Dr. Rabinder Madan for helpful discussion and suggestions on radar sensor networks.

References

[1] M. L. Skolnik "Introduction to Radar Systems" *TATA McGRAW HILL*, 10th reprint, 2004

[2] C-Y. Chong and S. P. Kumar "Sensor Networks: Evolution, Opportunities and Challenges" *Proceedings of The IEEE* vol. 91, No. 8, Aug. 2003

[3] Z. Chair and P. K. Varshney "Optimal data fusion in multiple sensor detection systems." *IEEE Transactions on Aerospace and Electronic Systems.*, AES-22, pp. 98-101, Jan. 1986.

[4] P. K. Varshney "Distributed Detection and Data Fusion" *New York: Springer*, 1997

[5] J. Hu and R. Blum "On the optimality of finite-level quantization for distributed signal detection" *IEEE Transactions on Information Theory*, vol. 47, pp. 1665 - 1671, May. 2001.

[6] J. Chamberland and V. V. Veeravalli "Decentralized detection in sensor networks" *IEEE Transactions on Signal Processing*, vol. 51, pp. 407 - 416, Feb. 2003

[7] R. Niu, B. Chen and P. K, Varshney "Decision fusion rules in wireless sensor networks using fading channel statistics" *In Proceedings of CISS 2003*, Baltimore, MD, Mar 2003

[8] S. C. A. Thomopoulos and L. Zhang "Distributed decision fusion with networking delays and channel errors" *Information Science*, vol. 66, pg. 91 - 118, Dec. 1992

[9] B. Chen and P. Willett "Channel optimized binary quantiers for distributed sensor networks" *In Proceedings of IEEE International Conference on Acoustics, Speech, and Signal Processing*, Montreal, Canada, May 2004

[10] B. Liu and B. Chen "Joint Source-Channel coding for distribute sensor networks" *In Proceedings of the 38th Annual Asilomar Conference on Signals, Systemss, and Computers, Pacific Grove*, CA, Nov. 2004

[11] Y. Lin, B. Chen and P. K. Varshney "Decision Fusion Rules in multi-hop wireless sensor networks" *IEEE Transactions on Aerospace and Electronic Systems*, vol.41, no.2,pp 475-488,Apr.2005

[12] Y. Sun, P. Willett and R. Lynch "Waveform Fusion in Sonar Signal Processing" *IEEE Transactions on Aerospace and Electronic Systems*, vol.40, no.2,pp 462-477,Apr.2004

Authorized licensed use limited to: University of Texas at Arlington. Downloaded on January 6, 2010 at 16:13 from IEEE Xplore. Restrictions apply.

RF Emitter Location Using A Network of Small Unmanned Aerial Vehicles (SUAVs)

Jing Liang and Qilian Liang, *Senior Member, IEEE*
Department of Electrical Engineering
University of Texas at Arlington
Arlington, TX 76019-0016 USA
E-mail: jliang@wcn.uta.edu, liang@uta.edu

***Abstract*— In this paper, we design a network of small unmanned aerial vehicles (SUAVs) for passive location of RF emitters. Each small UAV is equipped with multiple electronic surveillance (ES) sensors to provide local mean distance estimation based on received signal strength indicator (RSSI). Fusion center will determine the location of the target through UAV triangulation. Different with previous existing studies, our method is on a basis of an empirical path loss and log-normal shadowing model, from a wireless communication and signal processing vision to offer an effective solution. The performance degradation between UAVs and fusion center is taken into consideration other than assume lossless communication. We analyze the geolocation error and the error probability of distance based on the proposed system. The result shows that this approach provides robust performance for high frequency RF emitters.**

I. Introduction and Motivation

Currently, there is a developing trend to use passive location approach for RF emitters. Unmanned aerial vehicle (UAVs) is of most interest owing to better grazing angles closer to the target than large dedicated manned surveillance platforms [1]. In addition, UAVs are capable of continuous 24-hour surveillance coverage. As a result, they had been developed for battlefield reconnaissance beginning in the 1950s. To this date, UAV is not only limited to an unpiloted aircraft, but unmanned aerial systems (UAS) including ground stations and other elements as well.

Small unmanned aerial systems (SUAS) are rapidly gaining popularity due to the miniaturization of RF components and processors. In particular, given the cutting-edge technology in modern remote sensing (RS), SUAS can be equipped with electronic surveillance (ES) sensors in place of bulky active radars, which result in smaller, lighter and lower-cost counterparts. These types of SUAS are generally classified as having a wing-span of less than 4 meters [2] and a gross vehicle weight less than 15 pounds [3]. A number of UAV manufacturers have developed low-cost TDMA data links that support the cooperative team work of multiple UAVs, which provides higher mobility, survivability and closer proximity to the targeting emitters.

In the present work, [3] and [4] are based on a team of UAVs working cooperatively with on-board camera systems. The location of an object is determined by the fusion of camera images. However, the visual feature can become vulnerable in the following cases: 1)when telemetry and image streams are not synchronized, the target coordinates read by UAV can be particularly misleading; 2)when weather is severe and visibility is low, the image based geolocation may not provide day-or-night, all-weather surveillance; 3)target is well protected and hidden, such as deeply beneath the foliage.

Besides visual feature, the time difference of arrival (TDOA) technique has been adopted in the current work [5]-[9]. In these investigations, a network of at least three UAVs has been employed with on-board ES sensors, a global positioning system (GPS) receiver and a precision clock. When the target is detected by the sensor, the time of arrival would be transmitted to a fusion center, which would finally estimate the emitter location based on their TDOA. Also, Kalman filters is used to track the object. However, TDOA, like other methods including Angle of Arrival (AOA), Frequency of Arrival (FOA), Frequency Difference of Arrival (FDOA) and Phase Difference of Arrival (PDOA) etc., is well known for difficult synchronization issues, such as fine synchronization for location algorithms and coarse synchronization for the coordinating data collected within the area of interest at a common time.

In this paper, we apply netcentric SUAS with on-board multiple ES sensors for RF emitter location. Different from previous work described above, our work describes about a complete system design and analyze the performance in detail. Our method is on a basis of an empirical pass loss and log-normal shadowing model, which has been adopted for reliable high-speed wireless communications for moving users in dynamic environment, but has never been used in the SUAS before, to the best of our knowledge. Also, the performance of multiple ES sensors will be considered for the system as a whole. In addition, we will provide a confidence assessment through error bounding, which has not been seen in the existing approaches.

The rest of paper is organized as follows. Section II presents the system design based on path loss and log-normal shadowing model. Section III analyzes performance of netcentric decision. Section IV presents simulation results and illustrate the characteristics of the approach. Finally, section V draws the conclusion.

II. Path Loss and Log-normal shadowing Approach

In our work, we assume the SUAS is composed of $R(R \geq 3)$ small UAVs. Each UAV is equipped with $N(N \geq 1)$ ES sensors, whose task is to provide received signal strength indicator (RSSI) of RF emitters. A processor is also onboard to compute the current distance from the RF emitter to the sensors based on RSSI. Notice that even though the computation can be achieved in a very fast time on a basis of detected RSSI, estimated distance poses drifts from the real distance due to the relative motion between the UAV and the RF emitter as well as wind gusts during the moment of computation. Thus multiple sensors are employed to provide the receiver diversity. Later we will show that multiple sensors help reduce the distance error and improve the geolocation performance. The processor also applies Equal Gain Combining (EGC) to average out local spatial variations within a UAV. EGC is adopted due to its simplicity and fast computation. Additionally, each UAV works independently and knows its own position either by a GPS receiver or preplanned paths. Also, it is capable of communicating with a fusion center, which makes a final geolocation decision based on the information given by multiple UAVs.

Assume an emitter is sending out RF signal and a UAV d distance away from it detected the signal at this moment. The signal propagating between these two points with no attenuation or reflection follows the free-space propagation law [11]. This commonly adopted path loss model as a function of distance is expressed as

$$\frac{P(d)}{P(d_0)} = \gamma(\frac{d}{d_0})^{-\beta} \tag{1}$$

where d_0 is a close-in distance used as a known received power reference point; β is the path-loss exponent depending on the propagation environment. γ is a unitless constant that depends on the antenna characteristics and the average channel attenuation, which can be defined as

$$\gamma dB = 20\ lg\frac{C}{4\pi f d_0} \qquad (lg = log_{10}) \tag{2}$$

where C is the speed of light and f denotes the frequency. This definition is supported by empirical data for free-space path loss at a transmission distance of 100m [12]. Based on this free-space model, the power in dB form is linearly decreasing with the increase of $log(d)$.

However, in practice, the reflecting surfaces and scattering objects will typically contribute to the random variation of RF signal transmission. The most common model for this additional attenuation is log-normal shadowing, which has been empirically confirmed to model accurately the variation in received power in both outdoor [13] and indoor [14] environments. In this case, the difference between the value predicted by the path loss model and the actual power is a log-normal random variable, i.e., normally distributed in dB, which is denoted by

$$[\frac{P(d)}{P(d_0)}]_{dB} = [\frac{\hat{P}(d)}{P(d_0)}]_{dB} + X \tag{3}$$

where X is a Gaussian random variable, with mean m and variance σ^2.

We will use the combined path loss and log-normal shadowing model to estimate the distance between RF emitter and a UAV through RSSI. This model is illustrated in Fig. **??** with a dotted curve. The power in dB is given by

$$[\frac{P_{ri}}{P(d_0)}]_{dB} = 10lg\gamma - 10\beta lg(\frac{\hat{d}_i}{d_0}) + X \tag{4}$$

where P_{ri} is the RSSI of ES sensor i. Based on (4), when P_{ri} is detected, the processor can easily compute $\hat{d}_i$ in a dB form, which is

$$\hat{d}_{idB} = \frac{1}{\beta}\{\gamma_{dB} + \beta d_{0dB} - [\frac{P_{ri}}{P(d_0)}]_{dB}\} + \frac{X}{\beta} \tag{5}$$

Notice that $d_{idB} = \frac{1}{\beta}\{\gamma_{dB} + \beta d_{0dB} - [\frac{P_{ri}}{P(d_0)}]_{dB}\}$, therefore

$$\hat{d}_{idB} - d_{idB} = \frac{X}{\beta} \tag{6}$$

Then it is obvious that the expectation of distance mean square error based on sensor i is

$$E\{(\hat{d}_{idB} - d_{idB})^2\} = \frac{m^2 + \sigma^2}{\beta^2} \tag{7}$$

N sensors equipped on a UAV are applied to compute the local mean distance that average the local spatial variations. The estimated local mean distance is

$$\hat{D} = \frac{1}{N}\sum_{i=1}^{N}\hat{d}_{idB} \tag{8}$$

This value is obtained based on dB measurement due to the smaller estimation error compared to the linear form [15].

Notice that $D = d_{dB}$. At the detection moment, UAV is d distance away from the RF target, i.e., $d_{idB} = d_{dB}$. Also, each sensor independently obtains the $\hat{d}_{idB}$, i.e., $\hat{d}_{idB} - d_{idB}$ can be considered independent for different i, thus the expectation of *distance mean square error* for each UAV can be expressed as

$$E\{(\hat{D} - D)^2\} = \frac{m^2 + \sigma^2}{N^2\beta^2} \tag{9}$$

This shows that based on path loss and log-normal model, the larger number of sensor N, the smaller distance mean square error will be achieved for each UAV.

As each UAV geolocates RF emitter only based on RSSI and there is no any information about phase, in this situation the current detected area at the moment can be denoted by $a = \pi d^2$. If a is denoted by dB form, then $A = 10lg\pi + 2D$, therefore the expectation of *area mean square error* for each UAV is

$$P_A = E\{(A - \hat{A})^2\} = 4E\{(D - \hat{D})^2\} = \frac{4(m^2 + \sigma^2)}{N^2\beta^2} \tag{10}$$

Finally the upper bound of *geolocation area mean square error* of a UAV network can be denoted by

$$P_e = P(\bigcup_{i=1}^{R} A_i) \leq \sum_{i=1}^{R} P_{Ai} = \frac{4R(m^2+\sigma^2)}{N^2\beta^2} \quad (11)$$

We show this upper bound in Fig. 1, where $R = 3, m = 0, \beta = 2$ are used for illustration.

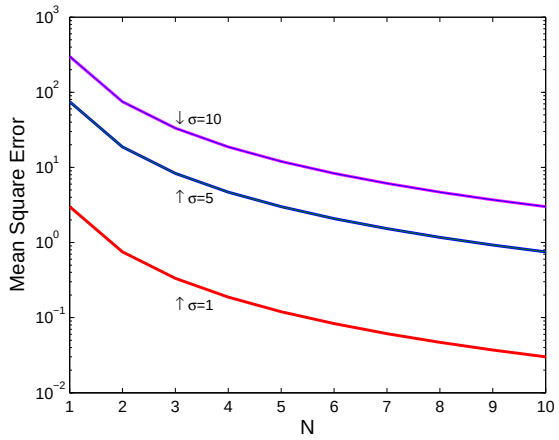


Fig. 1. Upper bound of geolocation area mean square error for a UAV network.

Apart from geolocation performance, we also define *distance range probability* as the probability that the estimated local mean distance $\hat{D}$ falls within $D_1 \leq \hat{D} \leq D_2$, where $D_1 < D_2$ and D_1, D_2 are also in dB form. The corresponding linear form of $\hat{D}, D_1$ and D_2 are $\hat{d}, d_1$ and d_2 respectively.

In order to simplify the expression, we would like to denote

$$S_i = \frac{1}{\sigma}\{\gamma_{dB} + [\frac{P(d_0)}{P_r}]_{dB} - \beta D_i + \beta d_{0dB}\}, \quad i = 1, 2 \quad (12)$$

It's obvious that $S_2 < S_1$. Therefore the distance range probability $P(D_1 \leq \hat{D} \leq D_2)$ (for simplicity, denoted by $P(D_1, D_2)$) turns out to be

$$\begin{cases} Q(S_2) - Q(-S_1) & \text{if (a)} S_1 \leq 0 \text{ or (b)} 0 < S_1 < -S_2 \\ Q(-S_1) - Q(S_2) & \text{if (c)} 0 \leq -S_2 < S_1 \text{ or (d) } S_2 > 0 \end{cases} \quad (13)$$

where the Q-function is defined as the probability that a Gaussian random Z is greater than x:

$$Q(x) = p(Z > x) = \int_x^{\infty} \frac{1}{\sqrt{2\pi}} e^{-\frac{y^2}{2}} dy \quad (14)$$

The (a)-(d) situations are illustrated in the Fig. 2. It's worth mentioning that $P(D_1, D_2) = P(d_1, d_2)$. When D_1 and D_2 are set to be values pretty close to D, (13) turns out to be the probability of correct distance range.

Based on our previous analysis, it's obvious that

$$\hat{D} = D + \frac{X}{N\beta} \quad (15)$$

When the relative motion between UAV and the emitter is very slow, the mean of $\frac{X}{N\beta}$, i.e., $l = \frac{m}{N\beta}$ can be considered zero

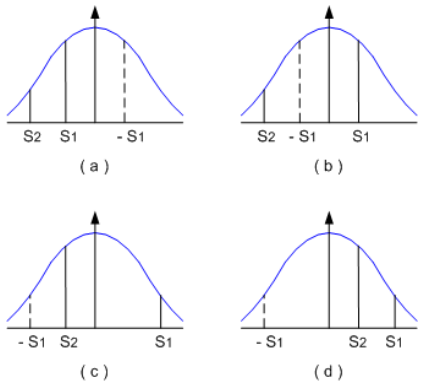


Fig. 2. Distance range probability illustration based on Q function: (a)$S_1 \leq 0$ (b)$0 < S_1 < -S_2$ (c)$0 \leq -S_2 < S_1$ (d) $S_2 > 0$.

because the mean may be considered to describe the average discrepancies in real and estimated distance between the RF emitter and the UAV during the moment of computation. Also, for simplicity and clarity, we use η to denote the variance of $\frac{X}{N\beta}$, which is $\frac{\sigma^2}{N^2\beta^2}$. Therefore, the probability of estimation that RF emitter locate in the range $[D_1, D_2]$ by a single UAV becomes

$$\begin{aligned} & P_{cs}(D_1, D_2) \quad (16) \\ = & \int_{D_1}^{D_2} P(D_1, D_2) f_N(u) du \\ = & \int_{D_1}^{D_2} P(D_1, D_2) \frac{1}{\sqrt{2\pi}\eta} e^{\frac{-(u-D)^2}{2\eta^2}} d\hat{D} \\ = & P(D_1, D_2)[Q(\frac{D_1 - D}{\eta}) - Q(\frac{D_2 - D}{\eta})] \end{aligned}$$

When the relative motion between the UAV and the RF emitter is obvious, due to the random variation, even the mean can be considered as a variable which follows uniform distribution in the range $[L_1, L_2]$(in dB form), where $L_1 < D_1 - D$ and $L_2 > D_2 - D$. In this case, the probability of RF emitter locating in the range $[D_1, D_2]$ by a single UAV becomes

$$\begin{aligned} & P_{cm}(D_1, D_2) \quad (17) \\ = & \int_{D_1}^{D_2} P(D_1, D_2) \int_{L_1}^{L_2} \frac{1}{\sqrt{2\pi}\eta} e^{\frac{-(u-D-v)^2}{2\eta^2}} \cdot \frac{1}{L_2 - L_1} dv du \\ = & \frac{P(D_1, D_2)}{L_2 - L_1} [\int_{L_1}^{L_2} Q(\frac{D_1 - D - v}{\eta}) - \int_{l_1}^{l_2} Q(\frac{D_2 - D - v}{\eta})] dv \end{aligned}$$

III. Netcentric Decision

As soon as each UAV obtains its distance from the RF emitter, this data will immediately be sent to a fusion center through TDMA data links. The fusion center can be a ground station or even mounted on one of the UAVs. Due to the shadowing and multiparth, the signal sent by a UAV will encounter fading before arriving at the fusion center. Assume the instantaneous signal-to-noise ratio (SNR) is y, the statistical averaging probability of error over the fading distribution [16] is

$$P_{e_m_f} = \int_0^{\infty} P_m(y) p_f(y) dy \quad (18)$$

where $P_m(y)$ is the probability of symbol error in AWGN based on a certain modulation scheme and $p_f(y)$ denotes the PDF of the fading amplitude.

Apply the moment generating function (MGF) $M_f(s) = \int_0^\infty p_f(y)e^{sy}dy$ and alternate Q-function $Q(x) = \frac{1}{\pi}\int_0^{\pi/2} e^{\frac{-x^2}{2\sin^2\varphi}}d\varphi$, we derive the probability of symbol error for the UAV network using 4 most common modulation schemes: phase-shift keying (MPSK), pulse amplitude modulation (MPAM), quadrature amplitude modulation (MQAM) and noncoherent frequent-shit keying (MFSK) respectively as follows:

$$P_{e_MPSK_f} = \frac{1}{\pi}\int_0^{\frac{(M-1)\pi}{M}} M_f(-\frac{\sin^2(\pi/M)}{\sin^2\varphi})d\varphi \quad (19)$$

$$P_{e_MPAM_f} = \frac{2(M-1)}{\pi M}\int_0^{\frac{\pi}{2}} M_f(\frac{-3}{\sin^2\varphi(M^2-1)})d\varphi \quad (20)$$

$$\begin{aligned} & P_{e_MQAM_f} \quad (21)\\ = \; & \frac{4}{\pi}(\frac{\sqrt{M}-1}{\sqrt{M}})\int_0^{\frac{\pi}{2}} M_f(-\frac{3}{2(M-1)\sin^2\varphi})d\varphi \\ & -\frac{4}{\pi}(\frac{\sqrt{M}-1}{\sqrt{M}})^2\int_0^{\frac{\pi}{4}} M_f(-\frac{3}{2(M-1)\sin^2\varphi})d\varphi \end{aligned}$$

$$P_{e_MFSK_f} = \sum_{n=1}^{M-1}\binom{M-1}{n}\frac{1}{n+1}M_f(-\frac{n}{n+1}) \quad (22)$$

Assume Rician fading with factor K. Two extreme cases are taken into account. If $K \to 0$, it becomes Rayleigh distribution, therefore (19)-(22) can be denoted using following expressions in this case:

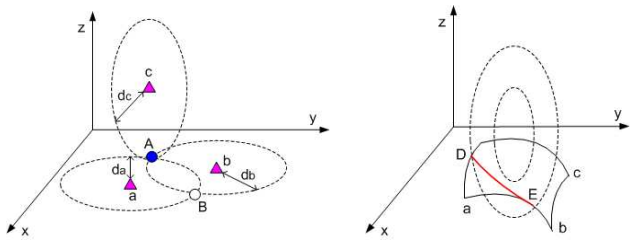
$$P_{e_MPSK_Ray} = 1 - \sqrt{\frac{y\sin^2(\frac{\pi}{M})}{1+y\sin^2(\frac{\pi}{M})}} \quad (23)$$

$$P_{e_MPAM_Ray} = \frac{M-1}{M}\cdot(1-\sqrt{\frac{\frac{3y}{M^2-1}}{1+\frac{3y}{M^2-1}}}) \quad (24)$$

$$\begin{aligned} & P_{e_MQAM_Ray} \quad (25)\\ = \; & \frac{2(\sqrt{M}-1)}{\sqrt{M}}(1-\sqrt{\frac{\frac{3y}{2(M-1)}}{1+\frac{3y}{2(M-1)}}}) - 4(\frac{\sqrt{M}-1}{\sqrt{M}})^2 \\ & \cdot[\frac{1}{4}-\frac{1}{\pi}\sqrt{\frac{\frac{3y}{2(M-1)}}{1+\frac{3y}{2(M-1)}}}arctg\sqrt{\frac{1+\frac{3y}{2(M-1)}}{\frac{3y}{2(M-1)}}}] \end{aligned}$$

$$P_{e_MFSK_Ray} = \sum_{n=1}^{M-1}(-1)^{n+1}\binom{M-1}{n}\frac{1}{n+1}(1+\frac{n}{n+1}y)^{-1} \quad (26)$$

When $K \to \infty$, the Rician fading channel becomes AWGN channel. In this situation, the probability of symbol error based on above modulation schemes have been well studied and the result is provided in [11], Table 6.1.



(a) (b)

Fig. 3. RF emitter Geolocation by SUAS (a) Relative movement between RF emitter and UAVs are slow (b) Relative movement between RF emitter and mini UAVs are obvious.

According to these performance, the best modulation scheme can be chosen to reduce the probability of error. This will be further illustrated in Section IV by simulations.

For simplicity and clarity, we assume the RF emitter is on the ground surface. In the case that the relative motion between the RF emitter and UAVs are quite slow, the UAV a is able to be aware that the RF emitter is somewhere on a circle, of which the center is itself and the radius is d_a, as illustrated in Fig. 3(a). Another UAV b can also identify that there is a RF emitter on a circumference with radius d_b. After combining the information from both a and b, the fusion center will be aware that the target either locates at the position A or B. With the help of a third UAV c, the fusion center will have the knowledge that the RF emitter is at the position A. Therefore with the triangulation, 3 UAVs are able to locate the RF emitter on the ground. In the case that the target is above the ground, 4 UAVs are necessary with one more member providing altitude geolocation information.

When the relative movement between the target and UAVs are obvious, a and b will aware that the RF emitter is moving within a ring area, and the fusion system will understand that the the target is within the intersection of 2 rings. Suppose the intersection area is $\widehat{abc}$ (the intersection can also be 2 independent areas, here we use one case for illustration without loss of generality), shown in Fig. 3(b). When the data from c is obtained, its detected range ring will intersect with $\widehat{abc}$ in a line $\overline{DE}$. Therefore, the trace of the RF emitter DE will be successfully obtained. After a few numbers of measurement, the motion speed, acceleration of the target can be calculated based on range and time difference.

Due to the independence of the distance estimation by each UAV and the transmission of data to the fusion center, the probability that a single UAV accurately provides the location information to the fusion center is $P_{cs}(D_1, D_2)\cdot(1-P_{e_MPSK_f})$ or $P_{cm}(d_1, d_2)\cdot(1-P_{e_MPSK_f})$ for different relative motion situations. Thus the probability of error for the netcentric SUAS made up of R UAVs can be denoted as

$$P_{es_Modulation} \le 1-[P_{cs}(D_1, D_2)\cdot(1-P_{e_Modulation_f})]^R \quad (27)$$

$$P_{em_Modulation} \le 1-[P_{cm}(d_1, d_2)\cdot(1-P_{e_Modulation_f})]^R \quad (28)$$

where $Modulation$ stands for the modulation scheme. The above expressions are error upper bound, this is because the netcentric decision provides much more resilience than a single UAV. For example, in Fig. 3(a) assume UAV a and b accurately geolocate the target while c has a large location error and believes the target is far away from the pint A and B, the whole system may still provide accurate estimation if c determines that the target is closer to A compared with B. Demanding every UAV to provide accurate information to fusion center is a stringent rule, therefore (27) and (28) are upper bounds.

IV. Simulation Results and Performance Analysis

Simulations on a basis of mathematical expressions in Section II and III are presented in this Section for better analysis and illustration about SUAS performance. In the simulation, we assume $d = 100m$, $d_0 = 0.1d$, $\beta = 2$ and $R = 3$.

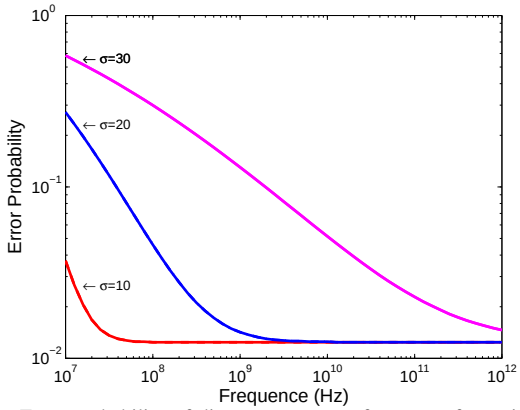


Fig. 4. Error probability of distance range vs. frequency for a single UAV.

Fig. 4 describes about error probability of distance range vs. frequency for a single UAV, where $d_1 = 0.99d$ and $d_2 = 1.01d$ have been used. The curves show that given the same σ (see (3)), the error probability of distance range will be reduced as the frequency increases. However, when the frequency is higher than a certain threshold value, such as 10^8 for $\sigma = 10$, the error probability becomes a constant. This phenomenon is the result of nonlinearity of the Q function. Therefore, this UAV system is more appropriate for geolocate an emitter with higher frequency.

Fig. 5 shows the contribution of another important factor power-rate-to-noise ratio (PRNR) to the correct probability of distance range for a single UAV. We define PRNR as $\frac{P(d_0)}{\sigma P_r}$. It is easy to observe that similar to Fig. 4, there is also a threshold value in correct probability of distance range. The larger the η (see (15)), the smaller the threshold value as well as the probability correctness.

Fig. 6-9 illustrate upper bound error probability for netcentric UAVs based on (27) and (28). Fig. 6 and 7 are in the environment of AWGN while Fig. 8 and 9 are for Rayleigh fading. In the case that relative motion between the RF emitter and UAVs are slow, $d_1 = 0.99d$, $d_2 = 1.01d$ and $\eta = 1$;

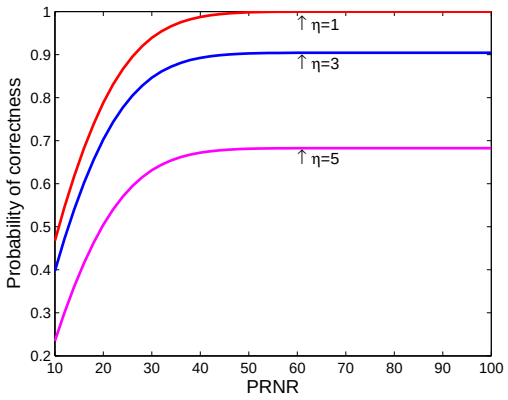


Fig. 5. Correct probability of distance range vs. power-rate-to-noise ratio (PRNR) for a single UAV.

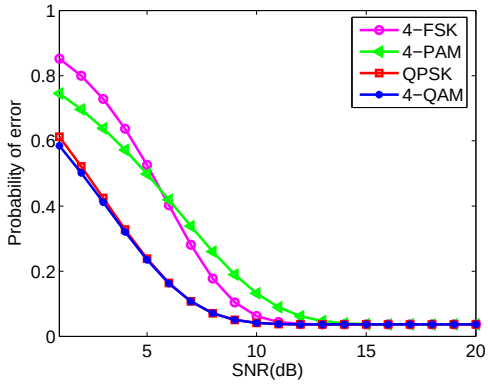


Fig. 6. Upper error bound of the netcentric UAVs in AWGN when relative movement between the RF emitter and UAVs are slow.

when the relative motion is obvious we apply $l_1 = -0.1d$, $l_2 = 0.1d$ and $\eta = 1$, therefore $P_{cs}(D_1, D_2) = 0.9876$ and $P_{cm}(D_1, D_2) = 0.94$. In Figs. 6 and 8, modulation schemes MFSK, MPAM, MPSK and MQAM with $M = 4$ are applied for illustration. This does not mean $M = 2$ can not be used. Actually, the smaller M, the smaller probability of symbol error rate for the same modulation scheme. That partially contributes to the smaller probability of error in Fig. 7. Moreover, the resilience of netcentric design makes the probability of error using BFSK and BPSK much smaller compared to that of 4-FSK and QPSK. This is the same situation while comparing Fig. 9 with 8.

These figures show that no matter the wireless radio channel between UAVS and fusion center is AWGN or Rayleigh, MQAM will provide the smallest probability of error at low SNR while MPSK will provide the smallest probability of error at moderate to high SNR. Therefore MQAM and MPSK can be applied for adaptive modulation for data fusion depending on how large the SNR is at the receiver of fusion center.

V. Conclusions

In this work, we propose a passive geolocation approach to locate RF emitter using a netcentric small UAV systems

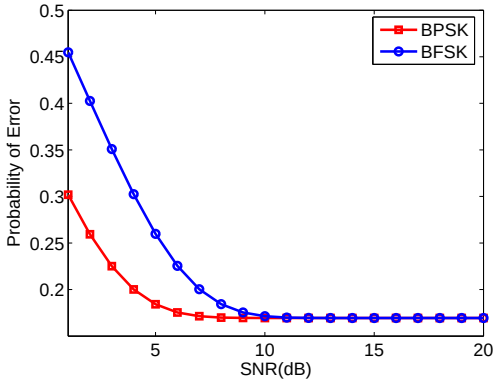


Fig. 7. Upper error bound of the netcentric UAVs in AWGN when relative movement between the RF emitter and UAVs are obvious.

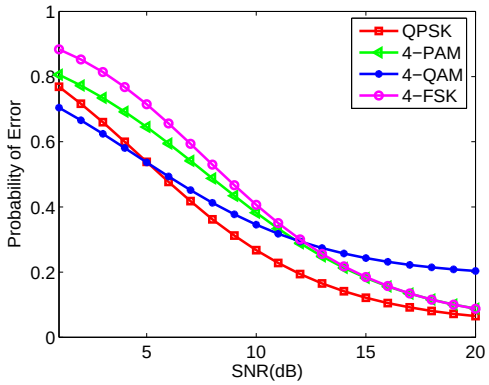


Fig. 8. Upper error bound of the netcentric UAVs in Rayleigh fading when relative movement between the RF emitter and UAVs are slow.

(SUAS) equipped with ES sensors. This approach is based on log-normal shadowing model, which has been empirically confirmed to model accurately the variation in received power in propagation environments. We show that the geolocation error is essentially a log-normal random variable. The larger number of ES sensors, the smaller geolocation area upper bound error. We also analyze the error probability of distance range for the system. We demonstrate that when the emitter frequency is higher than a certain threshold value, the error probability becomes a constant. The situation is similar for power-rate-to-noise ratio (PRNR). Regardless what the wireless radio channel between UAVS and fusion center is, for example AWGN, Rayleigh or Rician, at low SNR MQAM modulation is applied while MPSK will be chosen at moderate to high SNR due to the smallest performance error of the whole system.

ACKNOWLEDGEMENT

This work was supported in part by Office of Naval Research (ONR) under Grant N00014-07-1-0395, N00014-07-1-1024, and National Science Foundation (NSF) under Grant CNS-0721515.

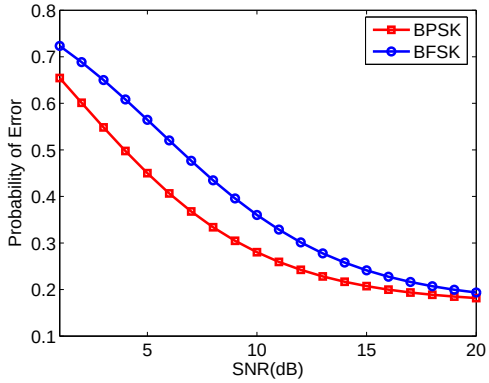


Fig. 9. Upper error bound of the netcentric UAVs in Rayleigh fading when relative movement between the RF emitter and UAVs are obvious.

ACKNOWLEDGEMENT

REFERENCES

[1] K. C. Overman, K. A. Leahy, T. W. Lawrence and R. J. Fritsch, "The future of surface surveillance - revolutionizing the view of the battlefield", *IEEE International Radar Conf.*, pp.1-6, May 2000.

[2] D. Ledger, "Electronic warfare capabilities of mini UAVs", http://aerosonde.com.au/downloads/electronic_warfare_ledger.doc

[3] R. Madison, P. DeBitetto, A. R. Olean and M. Peebles, "Target Geolocation from a Small Unmanned Aircraft System", *2008 IEEE Aerospace Conference*, pp. 1-19, March 2008.

[4] M. Wheeler, B. Schrick, W. Whitacre, M. Campbell, R. Rysdyk and R. Wise, "Cooperative Tracking of Moving Targets by a Team of Autonomous UAVs", *2006 IEEE/AIAA 25th Digital Avionics Systems Conference*, pp. 1-9, Oct. 2006.

[5] N. Okello, "Emitter Geolocation with Multiple UAVs", *2006 9th International Conference on Information Fusion*, pp. 1-8, July, 2006.

[6] N. Okello and D. Musicki, "Measurement Association for emitter geolocation with two UAVs", *2007 10th International Conference on Information Fusion*, pp. 1-8, July 2007.

[7] L. Marsh, D. Gossink, S. P. Drake and G. Calbert, "UAV Team Formation for Emitter Geolocation", *Information, Decision and Control, 2007, IDC'07*, pp. 176-181, Feb. 2007.

[8] A. Mikhalev and R. F. Ormondroyd, "comparison of hough transform and particle filter methods of emitter geolocation using fusion of TDOA Data", *4th Workshop on Positioning, Navigation and Communication 2007, WPNC'07*, pp.121-127.

[9] F. Fletcher, B. Ristic, D. Musicki, "Recursive estimation of emitter location using TDOA measurements from two UAVs", *2007 10th International Conference on Information Fusion*, pp. 1-8, July 2007.

[10] T. S. Rappaport, *Wireless Communications: Principles and Practice*, 2nd ed., Upper Saddle River, NJ: Prentice-Hall, 2002.

[11] A. Goldsmith, *Wireless Communications*, Cambridge University Press, NJ 2001.

[12] V. Erceg, L. J. Greenstein, S. Y. Tjandra, S. R. Parkoff, A. Gupta, B. Kulic, A. A. Julius, and R. Bianchi, "An empirically based path loss model for wireless channels in suburban environments", *IEEE J. Sel. Areas Commun.*, pp. 1205-11, July 1999.

[13] V. Erceg, L. J. Greenstein, S. Y. Tiandra, S. R. Parkoff, A. Gupta, B. Kulic, A. A. Julius, and R. Bianchi, "An empirically based path loss model for wireless channels in suburban environments", *IEEE J. Sel. Aresas Commun.*, pp. 1205-1211, July 1999.

[14] S. S. Ghassemzadeh, L. J. Greenstein, A. Kavcic, T. Sveinsson, and V. Tarokh, "Indoor path loss model for residential and commercial buildings", *Proc. IEEE Veh. Tech, Conf.*, pp. 3115-3119, Oct. 2003.

[15] A. J. Goldsmith, L. J. Greenstein and G. J. Foschini, "Error statistics of real-time power measurements in cellular channels with multipath and shadowing", *IEEE Trans. Veh. Tech.*, pp. 439-446, August, 1994.

[16] M. K. Simon and M.-S. Alouini, *Digital Communication over Fading Channels*, 2nd, Wiley, New Jersy, 2005.

UWB Sensor Networks in Hostile Environment: Interference Analysis and Performance Study

Lingming Wang and Qilian Liang

Department of Electrical Engineering

University of Texas at Arlington

Arlington, TX 76019-0016. USA

E-mail:wang@wcn.uta.edu. liang@uta.edu

Abstract

Interferences due to the hostile environment (e.g. jammer) and the Multi-User Access are critical factors affecting performance of the wireless sensor networks. In this paper, we study a hybrid Frequency Hopping/Time Hopping-Pulse Position Modulated (FH/TH-PPM) UWB for wireless sensor networks in hostile environment with partial-band(PB) tone interference. FH and TH are both used to get as much diversity gain as possible. Theoretical analysis is made for the bit error rates performance in the presence of multitone/pulse (tone in frequency domain and pulse in time domain) interference and Multi-User Interference. We also derived theoretical performance formula when the low duty-cycle in UWB system and the large number of sensor nodes in a wireless sensor networks are considered.

Index Terms : Time Hopping, Frequency Hopping, PPM, Wireless sensor networks, UWB, BER

1 Introduction

Wireless sensor networks are becoming more popular for an ever increasing range of applications with improvements in device size, power control, communications and computing technology. Since 2002 there has been great increasing popularity of commercial applications based on Ultra WideBand. This in turn has ignited interest in the use of this technology for sensor networks. Actually, UWB systems have potentially low complexity and low cost; have a very good time domain resolution, which facilitates location and tracking applications. So, UWB wireless sensor networks are promising.

The rest of this paper is organized as follows. The system models, including the transmission, channel and receiver, will be introduced in Section 2. The MUI and hostile interference will be studied in Section 3 and Section 4 respectively, and the SINR and closed-form BER will be derived as well. Numerical results and comparisons will be present in Section 5; and conclusions are made in Section 6.

2 System Models

In the proposed system, there are N_F non-overlapping FH bands, each with bandwidth B_h where B_h is the bandwidth required to transmit a TH-PPM signal in the absence of FH. Let $s^k(t)$ denotes the k-th user's signal at time t in this FH/TH-PPM UWB system with totally N_u users, and it takes the form

$$s^k(t) = \sqrt{\frac{E_b}{N_s}} \sum_{j=-\infty}^{+\infty} c_j^{fh}(k) p[t - jT_f - c_j^{th}(k)T_c - d_j(k)\delta]) \tag{1}$$

where $p(t)$is a chip waveform, which can take arbitrary time-limited pulse shapes proposed specifically for UWB communication systems, and is normalized to satisfy $\int_{-\infty}^{+\infty} p^2(t)dt = 1$. The notations and parameters are:

- N_s is the number of pulses used to transmit a single information bit. T_f is the time

duration of a frame. In general case, $N_s \geq 1$ pulses carry the information of one bit. The bit duration T_b should satisfy, $T_b \geq T_f N_s$.

- E_b is the energy per information bit. $\sqrt{\frac{E_b}{N_s}}$ is the normalized energy in each symbol.
- $c_j^{th}(k)T_c$ is the time shift introduced by the TH code. T_c is the chip duration. $c_j^{th}(k)$ is the j-th coefficient of the TH sequence used by user k; it is pseudo-random with each element take an integral in the range $[0, N_h - 1]$, where N_h is the number of hops. $T_c \leq T_f/N_h$ should be satisfied.
- The $d_j(k)\delta$ term represents the time shift introduced by PPM modulation. In our system, 2PPM is only considered. Therefore, $d_j(k)$ represents the j-th binary data bit (0 or 1) transmitted by the k-th user; δ is the PPM shift.
- $c_j^{fh}(k) = \sqrt{2}cos(2\pi f_k j)$ is the k-th user's spreading code during j-th frame.

Notice that each symbol chooses one of the N_F sub-bands to transmit the signal, however, in each sub-band, the transmitted signal is TH-2PPM.

In WSN, sensor nodes have two states, i.e., active communication status and idle status. In order to save energy, sensor nodes choose to be idle for most of the time. The number of nodes which are actually in the status of active communication is unknown. However, the total number of sensor nodes in the network and the access rate λ, i.e., the rate that a node in the communication status, for each node are assumed to be known. Clearly, the event of status of sensor node is a Bernoulli distribution with mean as λ and variance as $\lambda(1-\lambda)$. Assume there are N_U sensor nodes in a network, each one of them chooses to be idle or active independently. Therefore, the number of sensor nodes which are in active communication status, N_u^T, can be seen as the sum of N_U independent, identically distributed Bernoulli random variable, which is a Binomial distribution. Usually N_U is very large, we can approximate the Binomial

distribution to a Gaussian random variable with the mean $N_U\lambda$ and variance $N_U\lambda(1-\lambda)$, as

$$f_{N_u^T}(n_u^t) = \frac{1}{\sqrt{2\pi N_U\lambda(1-\lambda)}} e^{-(n_u^t - N_U\lambda)^2/2N_U\lambda(1-\lambda)} \tag{2}$$

For the N_u^T users, they randomly choose one of the sub-bands to transmit the signal according to $c_j^{fh}(k)$ symbol by symbol. It is also a Binomial random variable with the coefficient $1/N_F$. To simplify the problem, we assume that the users are distributed optimally, so the number of users share the same channel, N_u, should be expressed as

$$N_u = N_u^T/N_F. \tag{3}$$

3 Multi-User Interference Analysis

In this section, we will first focus on the analysis of MUI with the absence of hostile jammer interference. We assume there is no inter-channel-interference. Therefore, the received signal of 1-st user's j-th symbol can be expressed as:

$$r_j(t) = r_j^{(1)}(t) + r_{j,mui}(t) + n(t) \tag{4}$$

where $r_{j,mui}(t)$ is the MUI contribution at the receiver input. If the users are many and have comparable powers, we can approximate the MUI as a white Gaussian process by the central limit theorem [5] and, as such, it can be lumped into the additive Gaussian Noise,

$$w_{tot}(t) = r_{j,mui}(t) + n(t) \tag{5}$$

and $w_{tot}(t)$ is still a white Gaussian process. Since the system is asynchronous, we need to consider all cases where a pulse originated by any of the transmitters but TX1, is detected by the receiver. First of all we need to analyze the noise provoked by the presence of one alien pulse at the output of the receiver by using the similar method as in[1],

$$mui^{(k)}(\tau^{(k)}) = \sqrt{E_{RX}^{(k)}} \int_0^{T_c} p(t-\tau^{(k)}) v_t dt \tag{6}$$

where, $E_{RX}^{(k)} = \alpha^{(k)}(E_b/N_s)$, and here we suppose $\alpha^{(k)} = 1\ \forall k$.

Since $\tau^{(k)}$ is uniformly distributed over $[0, T_f)$, and identically distributed for different τ[1], under the hypothesis of perfect power control, e.g., $E_{RX}^{(k)} = E_{RX}\ \forall k$, the total MUI energy is

$$\sigma_{mui}^2 = \frac{E_{RX}}{T_f} \sum_{k=2}^{N_u} \left(\int_0^{T_f} \left(\int_0^{T_c} p(t-\tau)v(t)dt \right)^2 d\tau \right) \tag{7}$$

Define σ_M^2 as

$$\sigma_M^2 = \int_0^{T_f} \left(\int_0^{T_c} p(t-\tau)v(t)dt \right)^2 d\tau \tag{8}$$

we get

$$\sigma_{mui}^2 = \frac{E_{RX}}{T_f}(N_u - 1)\sigma_M^2 \tag{9}$$

Let SNR_{ref} denotes the equivalent signal to noise and MUI ratio over one symbol, it can be written as

$$SNR_{ref} = (SNR_n^{-1} + SIR_{mui}^{-1})^{-1} \tag{10}$$

where SNR_n are the signal to noise ratio over one symbol.

Hence,

$$\begin{aligned} SNR_{ref} &= \left(\left(\frac{E_{RX}}{N_0} \right)^{-1} + \left(\frac{T_f}{(N_u - 1)\sigma_M^2} \right)^{-1} \right)^{-1} \\ &= \frac{T_f}{N_s T_f + (N_u - 1)\sigma_M^2 \left(\frac{E_b}{N_0} \right)} \left(\frac{E_b}{N_0} \right) \end{aligned} \tag{11}$$

where $E_b/N_0$is the system SNR.

4 Performance Analysis with Multitone/pulse Interference

In this section, the SIR for the hostile interference part is obtained. We make the following assumptions: The multitone/pulse interference has a total power P_J, which is transmitted in a total of q equal power interfering tones spread randomly over the spread spectrum bandwidth. The time duration for the interference pulse is the same as the time duration of the transmitted

signal pulse $p(t)$, which is denoted as T_p. To simplify the problem, we suppose $T_c = 2T_p$ and $\delta = T_p$. The hop period of the interference is also T_p, and each hop is independent. The multitone/pulse interference can catch the signal pulse with the perfect timing. We consider the scenario that there is at most one interference per FH sub-band. Hence, in one hop, the probability that a FH band contains an interference tone/pulse is q/N_F. Observe the transmitted signal as in (1), the signal hops both in the frequency domain and in the time domain symbol by symbol. Therefore, our analysis will first focus on one symbol.

We partition the symbol duration as two time slots, hence, for the multitone/pulse interference, there are two hops. In each hop, the interference is independently distributed. There are totally four cases with regard to the jammer interference for each symbol: There is no jammer interference in either of two slots, with the probability as $P\{case1\} = (1 - \frac{q}{N_F}) \cdot (1 - \frac{q}{N_F})$; there is jammer interference in each slot, with the probability as $P\{case2\} = \frac{q}{N_F} \cdot \frac{q}{N_F}$; there is one and only one jammer interference pulse, and it is at the same slot as the signal pulse. The probability of case3 is $P\{case3\} = (1 - \frac{q}{N_F}) \cdot \frac{q}{N_F}$; there is one and only one jammer interference pulse, and it is not at the same slot as the signal pulse. The probability of case4 is $P\{case4\} = (1 - \frac{q}{N_F}) \cdot \frac{q}{N_F}$.

The received signal of the j-th symbol of 1-st user can be expressed as:

$$r'_j(t) = r^1_j(t) + I_{jammer}(t) + w_{tot}(t); \tag{12}$$

where $r^k_j(t)$ and $I_{jammer}(t)$ are the jammer interference contributions at the receiver input, and $w_{tot}(t)$ accounts for both the thermal and MUI noise contributions, and is still a white Gaussian process as proved in Section 3. Hence, a maximum a posteriori (MAP) approach can be adopted here to get the minimum error probability. For different cases of the jammer interference, the detection boundaries are shown in Fig. 2.

Hence, we can get the $SINR_{jammer}$ straightforwardly.

$$SINR_{jammer|case1,2} = \frac{E_{RX}}{N'_0}. \tag{13}$$

$$SINR_{jammer|case3} = \frac{(\sqrt{E_{RX}} + \sqrt{\frac{P_J}{q}})^2}{N_0'}. \tag{14}$$

$$SINR_{jammer|case4} = \frac{(\sqrt{E_{RX}} - \sqrt{\frac{P_J}{q}})^2}{N_0'}. \tag{15}$$

Since the error probability of 2-PPM signal is [1], $Pr = Q(\sqrt{SNR_{spec}})$, and after removing the conditioning on cases, we get

$$\begin{aligned} Pr_s' &= \left(\left(\frac{N_F - q}{N_F}\right)^2 + \left(\frac{q}{N_F}\right)^2\right) Q(\sqrt{\left(\frac{\frac{E_b}{N_s}}{N_0'}\right)}) \\ &+ \left(\frac{N_F - q}{N_F}\right)\left(\frac{q}{N_F}\right)(Q(\sqrt{\left(\frac{(\sqrt{\frac{E_b}{N_s}} + \sqrt{\frac{P_J}{q}})^2}{N_0'}\right)}) \\ &+ Q(\sqrt{\left(\frac{(\sqrt{\frac{E_b}{N_s}} - \sqrt{\frac{P_J}{q}})^2}{N_0'}\right)})). \end{aligned} \tag{16}$$

Considering only N_u is a random variable, we should take (2) and (3) into (16),

$$Pr_s = \frac{1}{N_F\sqrt{2\pi N_U\lambda(1-\lambda)}} \int_1^{N_U} Pr_s' e^{-(n_u - N_U\lambda)^2/2N_U\lambda(1-\lambda)} dn_u \tag{17}$$

After we got the symbol error rate Pr_s, it is easy for us to obtain the bit error rate Pr_b by majority law.

$$Pr_b = \sum_{k=\lceil \frac{N_s}{2} \rceil}^{N_s} C_{Ns}^k Pr_s^k (1 - Pr_s)^{N_s - k} \tag{18}$$

where $\lceil\ \rceil$ is the ceiling operation, and C_{Ns}^k is an N_s-choose-k Binomial coefficient, i.e., $C_{Ns}^k = \frac{k!(N_s-k)!}{N_s!}$.

5 Numerical Results and Comparisons

- The discussion on N_s;

  We fix $N_F = 20$, $q = 8$, $N_u = 10$ and the energy of the signal and jammer interference ratio $E_b/P_J = 5dB$, and compare the Symbol Error Rate (SER) and Bit Error Rate

Table 1: Parameters of the example FH/TH-PPM UWB system

Parameter	Notation	2^{nd}-order mono-cycle
shaping factor for the pulse	ϵ	$0.25ns$
time shift introduced by PPM	δ	$0.5ns$
pulse duration	T_p	$0.5ns$
frame duration	T_f	$8ns$
chip duration	T_c	$1ns$
number of hops	N_h	6

(BER) among $N_s = 1, 3, 5, 7$. The results are shown in Figure. 3 and Figure. 4 respectively. For SER, because, the more symbols used to transmit one bit, the energy for each symbol is less, SER is increasing when the N_s increases. However, BER is more meaningful here, and obviously, the more symbols we used to transmit one information bit, the better performance we can achieve. The curves drop quickly from $SNR = 0dB$ to $15dB$, however, after $15dB$, become flat, which caused by the jammer interference.

- The discussion on E_b/P_J;

  We set $N_F = 20$, $N_s = 3$, $q = 8$, and $N_u = 10$, and compare the SER and BER among $E_b/P_J = 0, 5, 10dB$. Figure. 5 and Figure 6 show the results. For both SER and BER, larger E_b/P_J can guarantee better performance. From $E_b/P_J = 5dB$ to $E_b/P_J = 10dB$, the performance gain is very limited, the reason of which is when E_b/P_J is higher than some better threshold, the jammer interference is too weak to give any impact to the system.

- The discussion on q;

  N_F, N_s, N_u and E_b/P_J are fixed at 20, 5, 10 and $5dB$ respectively.We try to evaluate

the performance for $q = 2, 8, 18$. At the first glance, larger q may be thought to yield worse performance, because large q means the probability that a jammer interference bumps the information signal is higher. However, we need to notice, high q also means the energy of the jammer interference for each sub-band is less, because the total jammer interference power is fixed. We can get the same conclusion in the Figure. 7 and Figure. 8. The worst and best performances are get at $q = 2$ and $q = 8$ respectively.

- The discussion on N_F;

  We evaluate the performance for $N_F = 1, 5, 10, 20$ when $N_s = 1$, and the number of users who are at communication status is 100. We need to evaluate how partitioning N_F can decrease the MUI, therefore, we set it as a jammer interference free channel. Obviously, Figure. 9 shows that we can get better performance when N_F is larger. Considering, more sub-bands partitioned means more cost, the N_F should be set at an appropriate value as long as the Quality of Service (QoS) is satisfying.

- The discussion on N_u;

  We set $N_F = 20$, $q = 8$, $N_s = 5$ and $E_b/P_J = 5dB$. N_u is equal to $5, 10, 15, 20$ respectively to get different performance, which are shown in Figure. 10 and Figure. 11. At high SNR, the performance is degraded quickly when N_u becomes larger. That is because the MUI is related with E_b under the assumption that each user has comparable power.

- The discussion on λ;

  We proved in Section 2 that the N_u is approximately a Gaussian RV.With known N_U, the number of sensor nodes in the WSN, but unknown N_u, the number of users that would share the same sub-band, we need to calculate the SER as in (17). We set $N_U = 10,000$, N_F is set as 20 and we assume the users are optimally distributed. For different access rate, $\lambda = 0.01$ and $\lambda = 0.02$, the performances are shown in Figure 12 and Figure. 13, we can see though the N_U are the same, the difference in λ would yield totally different

performance.

6 Conclusions

In this paper, we make an performance analysis with the presence of the multi-tone/pulse jammer interference and multi-user interference based on the hybrid FH/TH-PPM-UWB system. We get an accurate expressions of SER and BER with the presence of MUI and hostile jammer interference. We evaluate the performances for different number of symbols to carry one information bit N_s; the signal to jammer interference ratio E_b/P_J; the number of tones q of the jammer interference; and the access rate for each sensor nodes λ, in terms of BER so as to show how these parameters affect to the FH/TH-PPM UWB system.

7 Acknowledgement

This work was supported by the Office of Naval Research (ONR) Young Investigator Award under Grant N00014-03-1-0466.

References

[1] M.D. Benedetto and G. Giancola *Understanding Ultar Wide Band Radio Fundamentals*, Prentice Hall Technical Reference, NJ, USA, 2004

[2] J. Foerster (editor), "Channel Modeling Sub-committee Report Final," IEEE802.15-02/490 (see http://ieee802.org/15/).

[3] V. Lottici, A. D. Andrea and U. Mengali "Channel Estimation for Ultra-Wideband Communications," *IEEE Journal on Selected Areas in Communications*, Vol. 20, No. 9, pp. 1638-1645, Dec 2002.

[4] R. A. Scholtz, "Multiple Access with Time-Hopping Impulse Modulation," *IEEE Militray Communication Conference*, Vol. 2, pp. 447-450, Oct 1993.

[5] M. Z. Win and R. A. Scholtz, "Ultra-wide Bandwidth Time-Hopping Spread-Spectrum Impulse Radio for Wireless Multiple Access Communications," *IEEE Transactions on Communications*, Vol. 48, Issue: 4, pp. 679-691, April 2000.

[6] B. Hu, and N. C. Beaulieu, " Accurate Performance Evaluation of Time-Hopping and Direct-Sequence UWB Systems in Multi-User Interference ," *IEEE Transactions on Communications*, Vol: 53, No. 6, pp. 1053-1062, June. 2005.

[7] L. Yang and G. B. Giannakis "A General Model and SINR Analysis of Low Duty-Cycle UWB Access Through Multipath With Narrowband Interference and Rake Reception," *IEEE Transactions on Communications*, Vol. 4, No. 4, pp. 1818-1833, July 2005.

List of Figures

1 An example of the waveform of a 2-PPM signal. 0

2 The MAP detection rule for all the cases. 1

3 The average SER for different N_s. 1

4 The average BER for different N_S. 2

5 The average SER for different E_b/P_J. 2

6 The average BER for different E_b/P_J. 3

7 The average SER for different q. 3

8 The average BER for different q. 4

9 The average BER for different N_F. 4

10 The average SER for different N_u. 5

11 The average BER for different N_u. 5

12 The average SER for different N_U. 6

13 The average BER for different N_U. 6

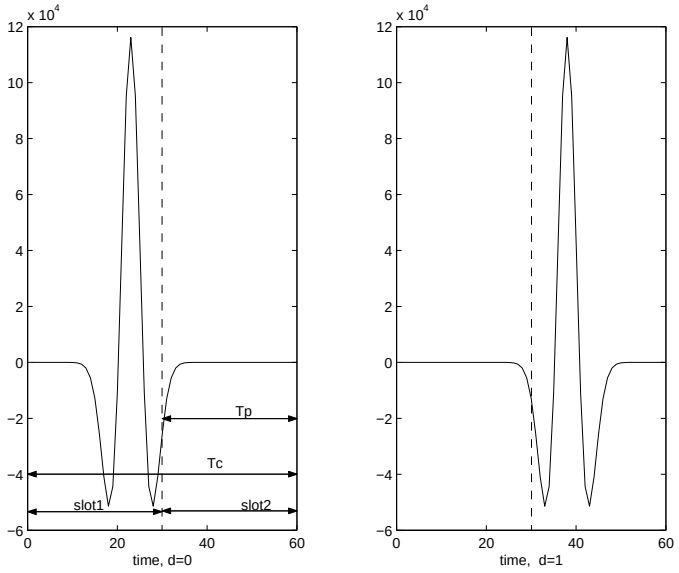


Figure 1: An example of the waveform of a 2-PPM signal.

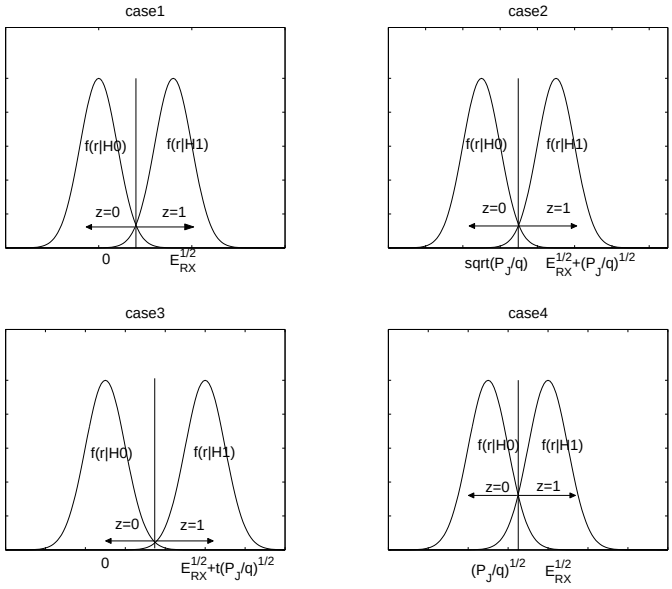


Figure 2: The MAP detection rule for all the cases.

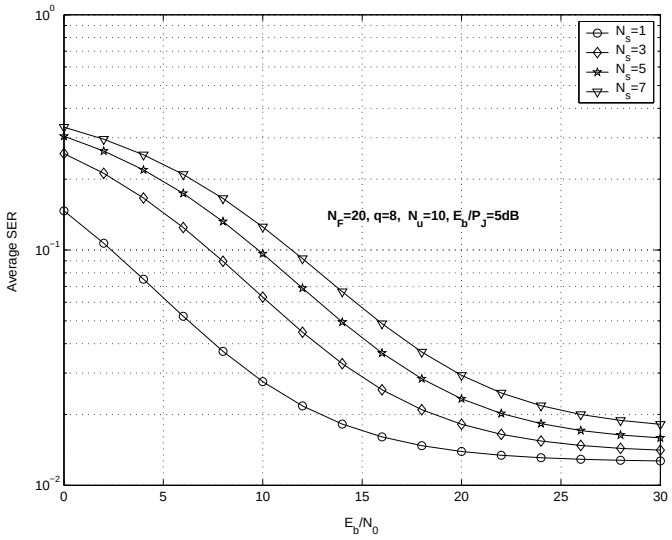


Figure 3: The average SER for different N_s.

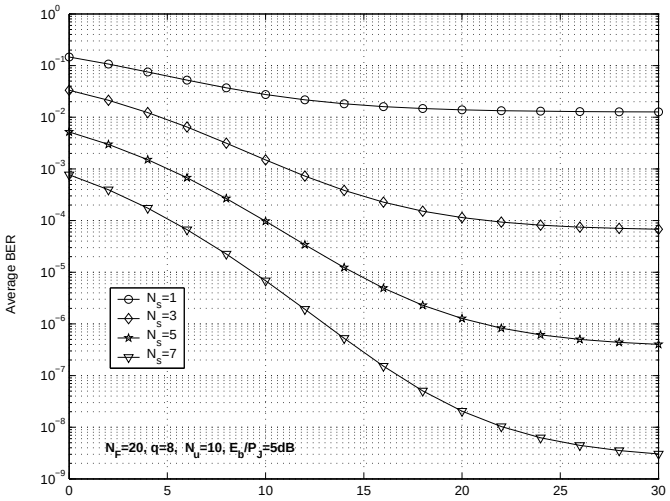


Figure 4: The average BER for different N_S.

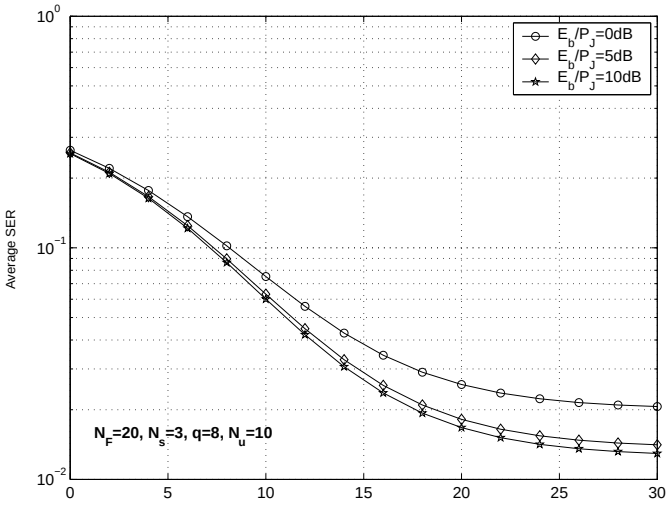


Figure 5: The average SER for different E_b/P_J.

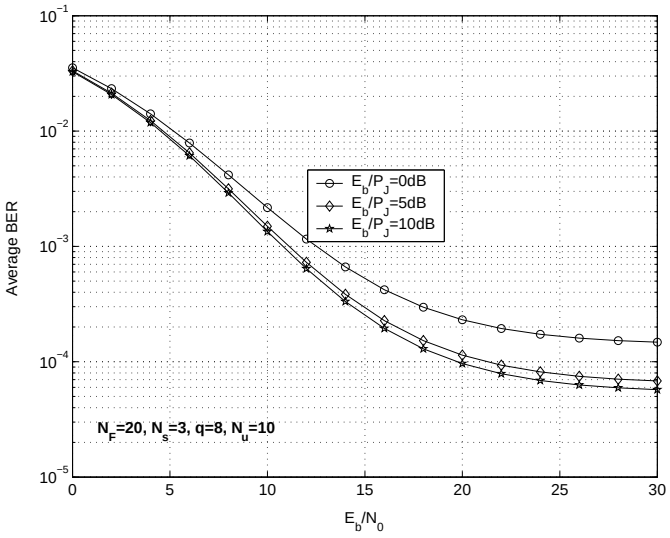


Figure 6: The average BER for different E_b/P_J.

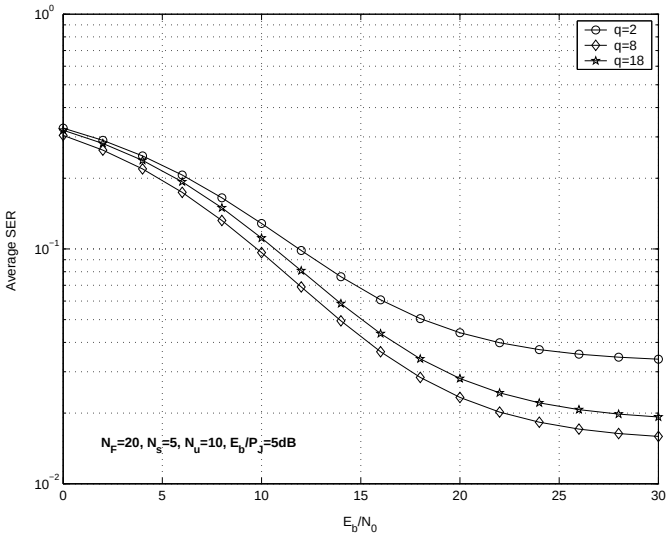


Figure 7: The average SER for different q.

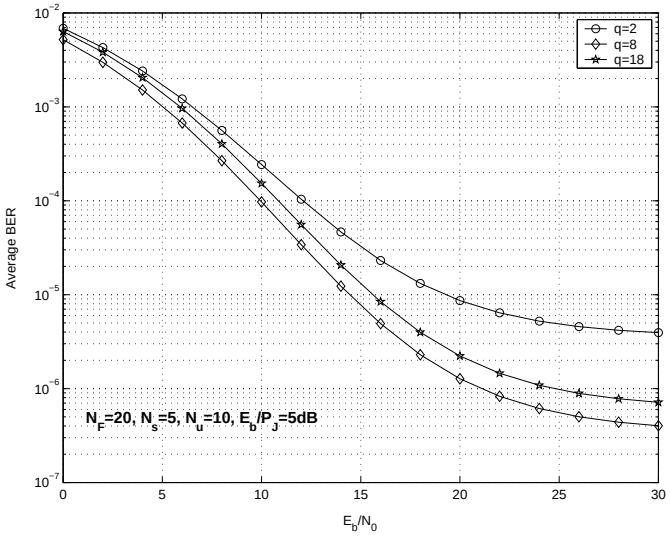


Figure 8: The average BER for different q.

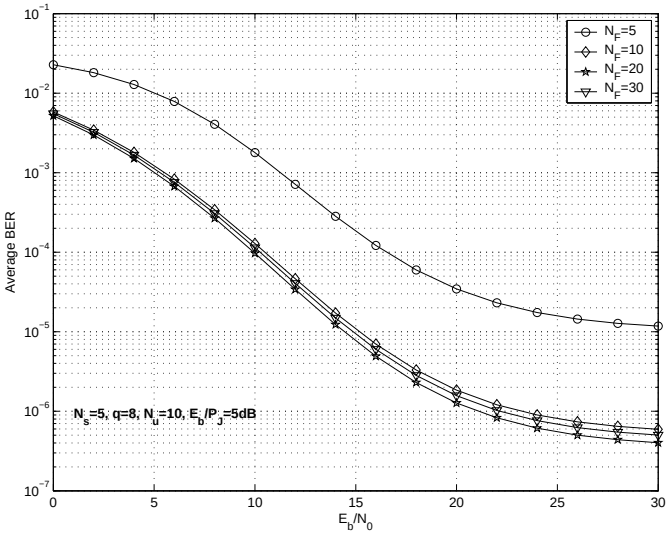


Figure 9: The average BER for different N_F.

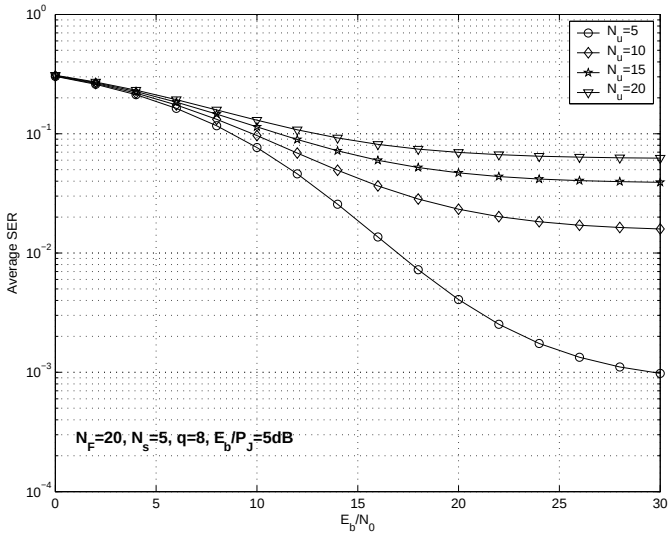


Figure 10: The average SER for different N_u.

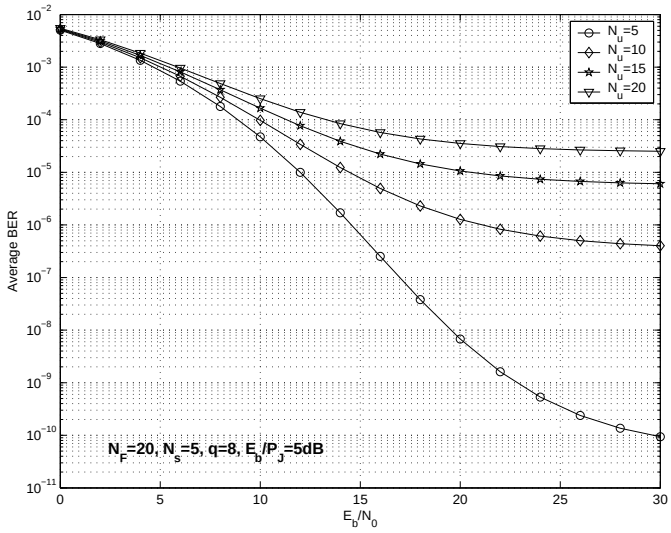


Figure 11: The average BER for different N_u.

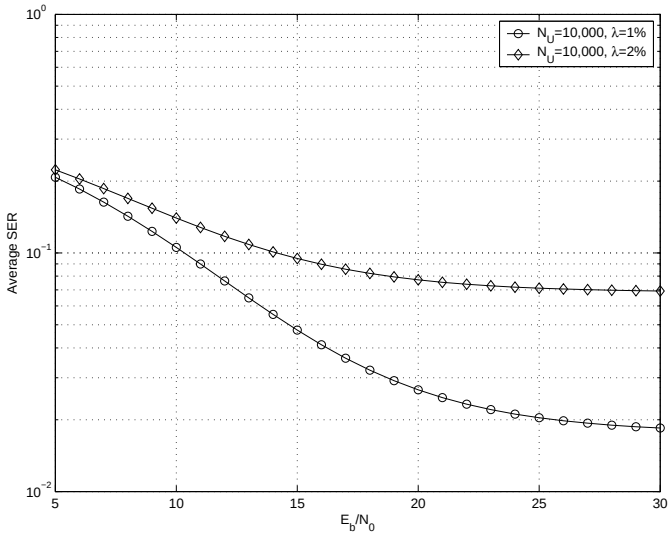


Figure 12: The average SER for different N_U.

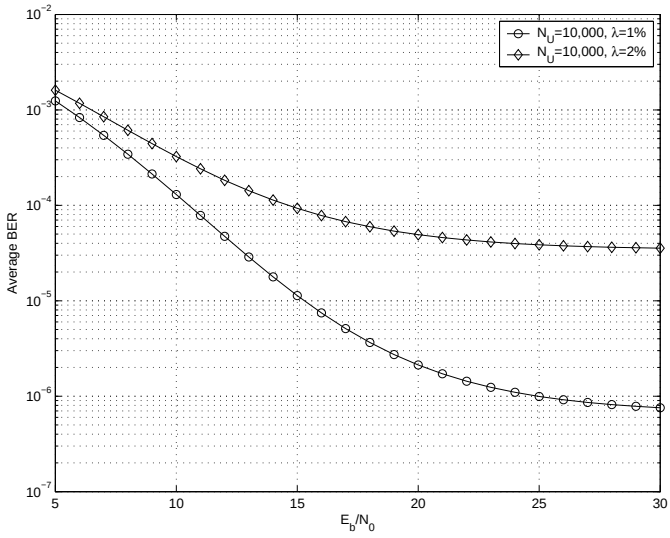


Figure 13: The average BER for different N_U.

Compressive Sensing in Radar Sensor Networks

Qilian Liang
Department of Electrical Engineering
University of Texas at Arlington
Arlington, TX 76019-0016, USA
E-mail: liang@uta.edu

***Abstract*— Motivated by recent advances on Compressive Sensing (CS) and high data redundancy among radars in radar sensor networks, we study CS for radar sensor networks. We demonstrate that the sense-through-foliage UWB radar signals are very sparse, which means CS could be applied to radar sensor networks to tremendously reduce the sampling rate. We propose to apply SVD-QR and maximum likelihood algorithms to CS for radar sensor networks. SVD-QR could vastly reduce the number of radar sensors, and CS is applied to the selected radar sensors for data compression. Simulations are performed and our compression ratio could be 192:1 overall.**

Index Terms : Compressive sensing, radar sensor networks, sense-through-foliage, UWB, sparsity.

I. Introduction

Compressive sensing (CS) is a new method to capture and represent compressible signals at a rate **significantly below the Nyquist rate**. It employs nonadaptive linear projections that preserve the structure of the signal; the signal is then reconstructed from these projections using an optimization process. This leads immediately to new signal reconstruction methods that are successful with surprisingly few measurements, which in turn leads to signal acquisition methods that effect compression as part of the measurement process (hence "compressive sensing"). These recent realizations (though built upon prior work exploiting signal sparsity) have spawned an explosion of research yielding exciting results in a wide range of topics, encompassing algorithms, theory, and applications.

So far, no work has been reported on CS for radar sensor networks. In CS for radar signals, very few works have been reported. In [1], it shows that matched filter could be eliminated if CS is used for radar. In [2], SAR radar image was processed using wavelets basis. In [13], a stylized compressed sensing radar is proposed in which the time-frequency plane is discretized into an N×N grid. In [15], a joint basis selection and sparse parameter estimation (called fast Bayesian mathcing pursuit) algorithm was proposed. In [17], a heuristic, graph-structured, sparse signal representation algorithm for overcomplete dictionaries that can be decomposed into subdictionaries was proposed and applied to SAR imaging. In [3][4], passive radar using OFDM was applied to target signature detection.

The rest of this paper is organized as follows. In Section II, we give an overview of compressive sensing. In Section III, we study the sparsity of narrowband and UWB radar signals. In Section V, we present our results on compressive sensing for UWB radar signals. Section VI concludes this paper.

II. Compressive Sensing: an Overview

CS provides a framework for integrated sensing and compression of discrete-time signals that are sparse or compressible in a known basis or frame. Let z denote a signal of interest, and Ψ denote a sparsifying basis (or called transform domain), such that $z = \Psi\theta$, with $\theta \in \mathbb{R}^N$ being a K-sparse vector, i.e. $\|\theta\|_0 = K$. Traditional transform coding compression techniques acquire first z in its entirety, and then calculate its sparse representation θ in order to encode its nonzero values and their locations, but CS aims to preclude the full signal acquisition by measuring a set y of linear projections of z into vectors ϕ_i, $1 \leq i \leq M$. By stacking these vectors as rows of a matrix Φ (measurement matrix), we can represent the measurements as $y = \Phi z = \Phi\Psi\theta$. The main result in CS states that when the matrix $\Phi\Psi$ holds the restricted isometry property (RIP) [7][10], then the original sparse representation θ is the unique solution to the linear program

$$\hat{\theta} = \arg\min_{\theta\in\mathbb{R}^N} \|\theta\|_{\ell_1} \quad (1)$$

$$s.t.\ y = \Phi\Psi\theta, \quad (2)$$

known as Basis Pursuit, where ℓ_1–norm is defined as ($\|\theta\|_{\ell_1} \equiv \sum_i |\theta_i|$). Thus, the original signal z can be recovered from the measurement vector y in polynomial time. Furthermore, choosing Φ to be a matrix with independent gaussian-distribtued entries satisfies the RIP for $\Phi\Psi$ when Ψ is a basis or tight frame and $M = O(K\log(N/K))$.

III. Sparsity of Narrowband and UWB Radar Signals

Recently, we studied UWB radar sensor signals in a foliage environment and observed that it is very sparse, which satisfies the requirement for compressive sensing. Our work is based on the data collected by AFRL in radar-based sense-through-foliage experiment in late summer and fall. Late summer foliage, because of the limited rainfall, involved foliage with decreased water content. Late fall and winter measurements involved largely defoliated but dense forest, providing a rich scattering environment. Because of wind or different temperatures in dense forest,

it's also a time-varying environment. The sense-through-foliage experiment was constructed on a seven-ton man lift (as shown in Fig. 1a), which had a total lifting capacity of 450 kg. The limit of the lifting capacity was reached during the experiment as essentially the entire measuring apparatus was placed on the lift. The principle pieces of equipment secured on the lift are: Barth pulser, Tektronix model 7704 B oscilloscope, dual antenna mounting stand, two antennas, rack system, IBM laptop, HP signal Generator, Custom RF switch and power supply and Weather shield (small hut). The target is a trihedral reflector (as shown in Fig. 1b). Throughout this work, a Barth pulse source (Barth Electronics, Inc. model 732 GL) was used. The pulse generator uses a coaxial reed switch to discharge a charge line for a very fast rise time pulse outputs. The model 732 pulse generator provides pulses of less than 50 picoseconds (ps) rise time, with amplitude from 150 V to greater than 2 KV into any load impedance through a 50 ohm coaxial line. The generator is capable of producing pulses with a minimum width of 750 ps and a maximum of 1 microsecond. This output pulse width is determined by charge line length for rectangular pulses, or by capacitors for 1/e decay pulses. For the data we used, each sample is spaced at 50 picosecond interval, and 16,000 samples were collected for each collection for a total time duration of 0.8 microseconds at a rate of approximately 20 Hz. The Barth pulse source was operated at low amplitude and 35 pulses reflected signal were averaged for each collection.

We applied the CLEAN algorithm to obtain the channel model based on the transmitted pulses and received echos. The CLEAN algorithm was first introduced in [14] and has been applied to UWB measurements [8][16] and it assumes that the channel is a series of impulses which is consistent with the tapped-delay line channel model. This algorithm searches the received echos iteratively with the transmit pulse to find the maximum correlation [6]. Based on the CLEAN method, we successfully obtained the channel impulse responses based on transmit pulses and receive echoes. For illustration purposes, in Fig. 2, we plot the channel impulse responses for UWB channels using CLEAN method based on one experiment.

Observe Fig. 2c, the channel impulse response $\theta = [\theta_1, \theta_2, \cdots, \theta_n]$ has very few nonzero taps out of 32,000 sample index). Let $\psi(i)$ denote the transmit pulse, The received echo could be represented as (if no noise)

$$z(i) = \theta * \psi(i) = \sum_{j=1}^{n} \theta_j \psi(i-j) = \Psi\theta \qquad (3)$$

where $*$ stands for convolution, and $\Psi = [\psi_1, \psi_2, \cdots, \psi_n]$ are transform domain functions (different time-shifts of transmit pulse). Since most θ_j's are zeroes under the transform basis Ψ, so the UWB radar signals $z(i)$ are very sparse, which validates that CS could be used to reduce the number of samples to collect.



(a)



(b)

Fig. 1. (a) The lift in the experiment. The antennas are at the far end of the lift from the viewer under the roof that was built to shield the equipment from the elements. (b) The target (a trihedral reflector) is shown on the stand at 300 feet from the lift.

IV. Compressive Sensing for Radar Sensor Networks Using SVD-QR Algorithm

We propose to use SVD-QR algorithm [11] [12] to compressive sensing for radar sensor networks. SVD-QR selects a set of independent data sets that minimize the residual error in a least-squares sense:

- Given $P \in R^{N\times M}$ (assuming $N > M$), and $rank(P) = r \leq M$. Determine a numerical estimate $r^{'}$ of the rank of the data sets matrix P by calculating the singular value decomposition

$$P = U \begin{bmatrix} \Sigma & 0 \\ 0 & 0 \end{bmatrix} V^T, \qquad (4)$$

  where, U is an $N \times N$ matrix of orthonormalized eigenvectors of PP^T, V is an $M \times M$ matrix of orthonormalized eigenvectors of P^TP , and Σ is the diagonal matrix $\Sigma = diag(\sigma_1, \sigma_2, \ldots, \sigma_r)$, where σ_i denotes the i^{th} singular value of P, and $\sigma_1 \geq \sigma_2 \geq \cdots \geq \sigma_r > 0$. Select $\hat{r} \leq r^{'}$.
- Calculate a permutation matrix Π such that the columns of the matrix $\Gamma_1 \in R^{N\times\hat{r}}$ in

$$P\Pi = [\Gamma_1, \Gamma_2] \qquad (5)$$

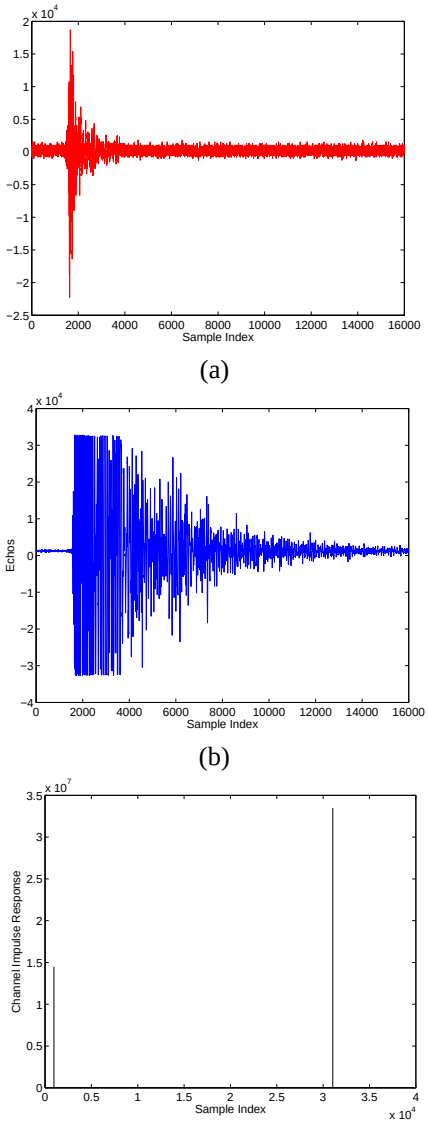


Fig. 2. UWB radar transmitted pulse, received echo, and channel impulse response in one experiment. (a) Transmitted pulse. (b) Received echo. (c) UWB channel impulse responses using CLEAN method.

are independent. The permutation matrix Π is obtained from the QR decomposition of the submatrix comprised of the right singular vectors, which correspond to the $\hat{r}$ ordered *most-significant* singular values.

Our procedures of CS for RSN are as follows:

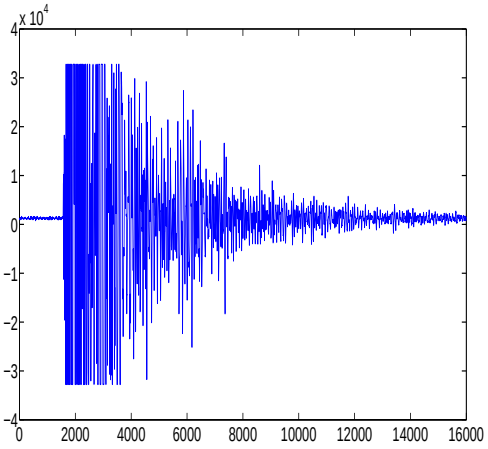
1) Construct matrix $P \in R^{N\times M}$ (assuming $N > M$) where N is the number of time samples and M is the number of radars.
2) Take SVD-QR to matrix P, and determine the principal radar sensors to be used for CS based on the following steps:
   - Decomposes P, from the SVD of P, save V.
   - Observe Σ. Select an appropriate $\hat{r}$.
   - Partition
   $$V = \begin{bmatrix} V_{11} & V_{12} \\ V_{21} & V_{22} \end{bmatrix} \quad (6)$$
   where $V_{11} \in R^{\hat{r}\times\hat{r}}$, $V_{12} \in R^{\hat{r}\times(M-\hat{r})}$, $V_{21} \in R^{(M-\hat{r})\times\hat{r}}$, and $V_{22} \in R^{(M-\hat{r})\times(M-\hat{r})}$. In many practical cases, σ_1 is much larger than $\sigma_{r'}$; thus $\hat{r}$ can be chosen much smaller than the estimate r' of rank(P), even 1.
   - Using QR decomposition with column pivoting, determine Π such that
   $$Q^T[V_{11}^T, V_{21}^T]\Pi = [R_{11}, R_{12}], \quad (7)$$
   where Q is a unitary matrix, and R_{11} and R_{12} form an upper triangular matrix; and Π is the permutation matrix, the column permutation Π is chosen so that $abs(diag(R))$ is decreasing. In short, Π corresponds to the $\hat{r}$ ordered *most-significant* sets, i.e., a sub-set of $\hat{r}$ most important radar sensors are chosen.
3) Perform CS to the $\hat{r}$ most important radar sensors jointly. Explore the redundancy among different sensors in radar sensor network would tremendously reduce the sample sizes. Equation (2) could be extended into matrix format,
   $$\hat{\Theta} = \arg\min_{\theta\in\mathbb{R}^N} \|\Theta\|_F \quad s.t. \ \mathbf{y} = \Phi\Psi\Theta, \quad (8)$$
   where Θ and $\mathbf{y}$ are matrix, and each column is correpsonding to each sensor; $\|\Theta\|_F$ is Frobenius norm for matrix, which is defined as
   $$\|\Theta\|_F = \sqrt{tr(\Theta^H \cdot \Theta)} = \sqrt{tr(\Theta \cdot \Theta^T)} \quad (9)$$
   If AWGN is added, the constraint can be written as
   $$\mathbf{y} = \Phi\Psi\Theta + \mathbf{N} \quad (10)$$
   Since $\mathbf{y}$, $\Phi\Psi$ are known, and $\mathbf{N}$ is AWGN matrix, we use maximal likelihood method to determine Θ.

V. Simulations and Performance Analysis

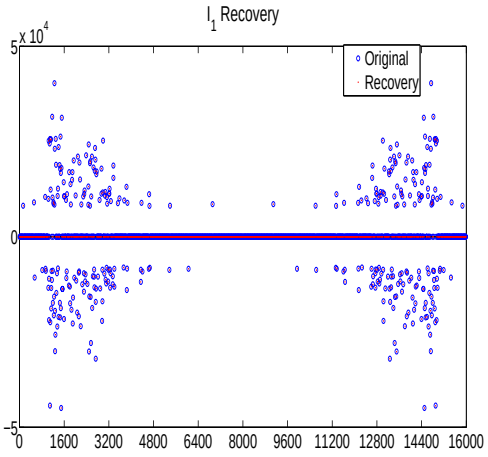
We chose an iid Gaussian random matrix as sensing matrix Φ. $\Phi\Psi$ is also iid Gaussian for various orthonormal bases Ψ such as spikes, sinusoids, wavelets, Gabor functions, curvelets, and so on [10], so we chose $\psi_j(i) = n^{-1/2}\cos(2\pi ji/n), i = 0, 1, \cdots, n-1$. $\Phi\Psi$ is shown to have satisfied RIP with high probability, if $M \geq cK\log(N/K)$, where c is a small constant and hence stable reconstruction is possible with high probability [10]. Note that it is not known in advance which coefficients of Θ are zeroes, or which samples of z are not needed.

We ran simulations based on the above algorithm for a radar sensor networks with 30 radar sensors. Based on the radar sensor network data for 100 collections, we applied SVD-QR to select $\hat{r}$ most important radar sensors, and observed that $\hat{r}$ has mean value 5.23, and std 2.11. For each subset of selected sensors, we performed joint CS, and

it turned that we could used only 500 samples to recover the original 16,000 samples, so the compression ratio is 32:1. Combining the spatial reduction (from 30 sensors to around 5 sensors), we could achieved compression ratio about 192:1 overall. For illustration purpose, in Fig. 3(a), we plot 16,000 samples sense-through-foliage signals in one collection of sense-through-foliage UWB radar sensors. In Fig. 3(b), we plot one column of sparse signals Θ (received echo z projected to cosine basis functions $\psi_j(i)$) and the recovered sparse signals (obtained via (2)). Observe that the original signals could be perfectly recovered.



(a)



(b)

Fig. 3. (a) Original sense-through-foliage received echos (16,000 samples), and (b) ℓ_1-norm recovered sparse signals and the original sparse signals (origianl 16,000 samples projected to the cosine basis functions).

VI. Conclusions

Motivated by recent advances on Compressive Sensing (CS) and high data redundancy among radars in radar sensor networks, we studied CS for radar sensor networks. We demonstrated that the sense-through-foliage UWB radar signals are very sparse, which means CS could be applied to radar sensor networks to tremendously reduce the sampling rate. We proposed to apply SVD-QR and maximum likelihood algorithms to CS for radar sensor networks. SVD-QR could vastly reduce the number of radar sensors, and CS was applied to the selected radar sensors for data compression. Simulations are performed and our compression ratio could be 192:1 overall.

Acknowledgement

The authors would like to thank Dr. Sherwood Samn in AFRL/RHX for providing the radar data.

References

[1] R. Baraniuk and P. Steeghs, "Compressive radar imaging," *IEEE Radar Conference*, Waltham, Massachusetts, April 2007.

[2] S. Bhattacharya, T. Blumensath, B. Mulgrew, and M. Davies, "Fast encoding of synthetic aperture radar raw data using compressed sensing," *IEEE Workshop on Statistical Signal Processing*, Madison, Wisconsin, August 2007)

[3] C. R. Berger, S. Zhou, P. Willett, "Signal Extraction Using Compressed Sensing for Passive Radar with OFDM Signals," *Proc. of the 11th Int. Conf. on Information Fusion*, Cologne, Germany, July 2008.

[4] C. R. Berger, S. Zhou, P. Willett, B. Demissie, J. Heckenbach, "Compressed Sensing for OFDM/MIMO Radar," *Proc. of the 42nd Annual Asilomar Conference on Signals, Systems and Computers*, Pacific Grove, CA, Oct. 2008.

[5] D. Bertsimas, J. N.Tsitsiklis " Introduction to Linear Optimization ," *Athena Scientific* , February, 1997.

[6] R. M. Buehrer, et al, "Characterization of the UWB channel," *IEEE Conf on Ultra Wideband Systems and Technologies*, pp. 26-31, Reston, VA, Nov 2003.

[7] E. Candés, "Compressive sampling," *Int. Congress of Mathematics*, vol. 3, pp. 1433-1452, Madrid, Spain, 2006.

[8] R. J.-M. Cramer, *An Evaluation of Ultrawideband Propagation Channels*, Ph.D Dissertation, USC, 2000.

[9] R. J.-M Cramer, R. A. Scholtz, and M. Z. Win, "Evaluation of an ultra-wide-band propagation channel," *IEEE Transactions on Antennas and Propagation*, vol 50, no. 5, May 2002, pp. 561 - 570.

[10] D. Donoho " Compressed Sensing ," *IEEE Trans. on Information Theory*, Vol.52, No.4, pp.1289-1306, April 2006.

[11] Golub, G. H., and C. F. Van Loan, *Matrix Computations*, Johns Hopkins Univ. Press, MD 1983.

[12] Golub, G.H., "Numerical Methods for Solving Least Squares Problems," *Numer. Math*, no. 7, pp. 206-216, 1965.

[13] M. Herman and T. Strohmer, "High-resolution radar via compressed sensing," to appear in *IEEE Trans. on Signal Processing*

[14] J. A. Hogbom, "Aperture synthesis with a non-regular distribution of interferometer baseline," *Atronomy and Astrophysics Supplement Ser.*, vol. 15, 1974.

[15] L. Potter, P. Schniter, and J. Ziniel, "Sparse reconstruction for RADAR," *SPIE Alg. for Syn. Aperture Radar Imagery XV*, 2008.

[16] R. A. Scholtz, M. Z. Win, and J. M. Cramer, "Evaluation of the Characteristics of the ultra-wideband propagation channel," *Proc of Antenna and Propagation Symposium*, vol. 2, no. 626-630, 1998.

[17] K. R. Varshney, M. etin, J. W. Fisher, and A. S. Willsky, "Sparse representation in structured dictionaries with application to synthetic aperture radar," *IEEE Transactions on Signal Processing*, 56(8), pp. 3548 - 3561, August 2008.

COMPRESSIVE SAMPLING OF SENSE-THROUGH-WALL UWB NOISE RADAR SIGNALS

Ji Wu, Qilian Liang

Department of Electrical Engineering
University of Texas at Arlington
Arlington, TX 76019-0016, USA

Sherwood W. Samn

Air Force Research Laboratory/RHX
Brooks City Base
San Antonio, TX 78235, USA

ABSTRACT

UWB noise radar is one of the novel techniques which are widely used in various sensing-through-wall applications such as emergency rescues and military operations. One of the most challenging problems in UWB noise radar is data storage. In this paper, we apply compressive sampling to UWB noise radar to represent the original signal with far fewer samples. Choosing an iid Gaussian random matrix as measurement matrix is sufficient to capture the information in the UWB noise radar signal, no knowledge of UWB signal is known in advance. Simulation results indicate only 1/5 of original samples are need to perfectly recover the UWB noise radar signal.

Index Terms— compressive sampling, UWB noise radar, Gaussian random matrix

1. INTRODUCTION

Sensing-through-wall techniques have attracted so many interests due to a broad range of military and civilian applications. It will be useful in locating weapons caches during military operations, searching and rescuing people from natural disaster such as earthquakes and providing sustainability assessment of bridges and buildings. Current sense-through-wall systems are mainly based on short-pulse waveforms, which require special antennas to avoid unwanted signal coupling. In addition, periodically transmitted pulses will be easily intercepted by others.

In recent years, UWB waveforms are frequently employed for indoor wireless propagation systems due to its exceptional range resolution and strong penetrating capability. Since UWB radars used for sense-through-wall applications are usually in UHF range (500-1000MHz) for good penetration through walls and building materials. The 500MHz bandwidth will yield a 30cm range resolution. Systems building on existing technology for through-wall sensing are typically heavy and inconvenient to deploy. The major challenge is to develop a simplified architecture which will reduce cost without sacrificing performance. Chip-based arbitrary signal generators can be used as noise sources and field programmable gate array (FPGA) technology can be used for time delay and cross-correlation in UWB noise radar implementation.

Major advantages of UWB noise radar are [1] [2]:

- Immunity from jamming and interference: Unwanted signals caused by jammers or other interfering transmitters will not correlated with the time-delayed transmit replica and hence yield zero at the correlated output.
- Immunity from detection: Since the waveform is not repeatable and spread over a wide band, it cannot be recognized as the intentional signal on other's receiver.
- Frequency diversity: Since the instantaneous noise waveform is spread over a wide frequency range, it achieves the necessary diversity to reduce the clutter and multipath effects.
- Spectral efficiency: Many noise radars can occupy the same spectral band, with negligible cross-interference as the signals will not be correlated with each other.
- Cost-effectiveness: Since thermal noise is easy to generate, expensive modulators and antennas are not needed.
- Thumbtack range-Doppler ambiguity function: Noise radars can achieve high resolution in both range and Doppler and these can be independently controlled by varying the bandwidth and integration time, respectively. It is a unique feature that is present only in noise radars.

Since the UWB signal is usually in UHF range (500-1000MHz), sampling rate should be more than 1GHz/s (Nyquist rate) for alias-free signal sampling which requires plenty of space to store received signal. In this paper, we apply compressive sampling to UWB noise radar signal, which asserts that one can recover it from far fewer samples than traditional Nyquist rate. It also enhances the operational feasibility of UWB noise radar.

The remainder of this paper is organized as follows. In Section 2, we summarize characteristics of UWB noise radar signal and its time-frequency representation. In Section 3, we introduce principles of compressive sampling and its application in data compression. We propose an alternative algorithm to solve the linear program efficiently in (9) in Section 4. We

show final simulation results in Section 5. Conclusions are given in Section 6.

2. UWB NOISE RADAR SIGNAL FUNDAMENTALS

Since UWB noise radar signal is stochastic, it can only be described by its statistics. The UWB noise radar signal $x(t)$ can be described by its following properties:

- Auto-correlation $R_{xx}(\tau)$: impulse or impulse–like at $\tau = 0$.
- Probability density function (PDF) $p_x(X)$: can be characterized as Gaussian distribution.
- Power spectral density (PSD) $S_{xx}(f)$: assumed uniform and bandlimited.

From the above-statistics we can propose the time-frequency model for the UWB noise radar signal as below:

$$x(t) = a(t)\cos\{[\omega_0 + \delta\omega(t)]t\}, \tag{1}$$

where $a(t)$ is the Rayleigh distributed amplitude which describes amplitude fluctuations and $\delta\omega(t)$ is the uniformly distributed frequency fluctuations over the $\pm\Delta\omega$ range, i.e., $[-\Delta\omega \leq \delta\omega \leq +\Delta\omega]$ [3]. Assuming that the random variables $a(t)$ and $\delta\omega(t)$ are uncorrelated, we can show that the average power of the signal x is $\left\langle a^2(t)\right\rangle / 2R_0$, where $\langle\cdot\rangle$ denotes time average and R_0 is the system impedance. The center frequency f_0 and the bandwidth B can be derived as $\omega_0/2\pi$ and $\Delta\omega/\pi$, respectively.

An alternative time–frequency representation of UWB noise radar signal is given by:

$$s(t) = s_I(t)\cos(\omega_0 t) - s_Q(t)\sin(\omega_0 t), \tag{2}$$

where $s_I(t)$ and $s_Q(t)$ are zero-mean Gaussian processes and $f_0 = \omega_0/2\pi$ is the center frequency. This can also be written as:

$$s(t) = a(t)\cos[\omega_0 t + \phi(t)], \tag{3}$$

where $a(t) = \sqrt{s_I^2(t) + s_Q^2(t)}$ is the Rayleigh distributed amplitude and $\phi(t) = \tan^{-1}(s_Q(t)/s_I(t))$ is the uniformly distributed phase.

3. COMPRESSIVE SAMPLING BACKGROUND

Compressive sampling (CS) provides a framework for integrated sensing and compression of discrete-time signals that are sparse or compressible in a known basis or frame. Many natural signals have concise representations when expressed in the proper basis [4]. Mathematically speaking, consider a discrete signal $f \in \mathbb{R}^N$ which can be expanded in an orthonormal basis $\Psi = [\psi_1\psi_2\ \cdots\psi_n]$ as follows:

$$f(t) = \sum_{i=1}^{N} x_i\psi_i(t), \tag{4}$$

where x is the coefficient sequence of f that can be computed from signal f:

$$x_i = \langle f, \psi_i\rangle, i = 1, 2, \cdots, N. \tag{5}$$

It will be convenient to express f as Ψx (where Ψ is the $n \times n$ matrix with $\psi_1\psi_2\ \cdots\psi_n$ as columns). We can say the discrete signal f is K-sparse in the domain Ψ, $K << N$, if only K out of N coefficients in the sequence x are nonzero. Sparsity of signal is a fundamental principle used in the compressive sampling as well as in most modern lossy coders such as JPEG-2000 and many others, since a simple way for image compression would be to compute x from f and then only encode the values and locations of the largest K coefficients. Examples in [5] show that perceptual loss is hardly noticeable from a megapixel image to its approximation obtained by throwing away 97.5% of the coefficients. Unfortunately, this compression process requires computing all N coefficients of signal f and the locations of the significant coefficients, which may not be known in advance.

Compressive sampling suggests this relevant information in the signal f can be captured using a small number of non-adaptive (even random) measurements of the signal. Note that there are only K coefficients are nonzero, so we can remove this "sampling redundancy" by acquiring only M samples of signal f, where $K < M << N$. The new M-length observation vector y can be represented as equation below:

$$y = \Phi f, \tag{6}$$

where Φ is an $M \times N$ measurement matrix. The above equation can be written as

$$y = \Phi\Psi x = \Theta x, \tag{7}$$

where Θ is given by:

$$\Theta = \Phi\Psi, \tag{8}$$

The signal f can be perfectly recovered from M equals to or a little bit more than measurements K, if Θ satisfies the so-called restricted isometry property (RIP)[6]. It suggests that Θ is sufficiently incoherent and Φ cannot sparsely represented basic vectors of matrix Ψ and vice versa.

It has been shown in [4] that choosing an iid Gaussian random matrix as sensing matrix Φ, Θ is also iid Gaussian for various orthonormal bases Ψ such as spikes, sinusoids, wavelets, Gabor functions, curvelets, and so on. Θ is shown to have satisfied RIP with high probability, if $M \geq cK\log(N/K)$, where c is a small constant and hence stable reconstruction is possible with high probability[7]. Note that it is not known in advance which coefficients of f are zeroes, or which samples are not needed.

With the new observation vector y, we decide to recover the signal f by ℓ_1–norm minimization; the proposed reconstruction f^* is given by $f^* = \Psi x^*$, where x^* is the solution to the convex optimization program($\|x\|_{\ell_1} \equiv \sum_i |x|$)

$$\min_{\tilde{x}\in\mathbb{R}^N} \|\tilde{x}\|_{\ell_1} \quad \text{subject to} \quad y = \Phi\Psi\tilde{x}, \tag{9}$$

That is, among all the objects $\tilde{f} = \Psi\tilde{x}$ consistent with the data, we choose the one whose coefficient sequence has minimal ℓ_1–norm. As is well known, minimizing ℓ_1 subject to linear equality constraints can easily be reformulated as a linear program of $O(N^3)$ complexity. However, ℓ_1–minimization is not the only way to recover sparse solutions; other methods, such as greedy algorithm [8], has also been proposed.

4. COMPRESSIVE SAMPLING ALGORITHM IN UWB NOISE RADAR SIGNAL

In this section, we propose an alternative method for dealing with absolute values in linear program problem in (9), which introduces new variables x^+, x^-, constrained to be nonnegative, and let $x_i = x_i^+ - x_i^-$ [9].(Our intention is to have $x_i = x_i^+$ or $x_i = -x_i^-$, depending on whether x_i is positive or negative.) We then replace the occurrence of $|x|$ with $x_i^+ + x_i^-$ and obtain the alternative formulation

$$\min \sum_{i=1}^{N}(x_i^+ + x_i^-) \tag{10}$$

$$\text{subject to} \quad \Phi\Psi x_i^+ - \Phi\Psi x_i^- = y \tag{11}$$

$$x^+, x^- \geq 0, \tag{12}$$

where $x^+ = (x_1^+, x_2^+, \cdots, x_n^+)$, $x^- = (x_1^-, x_2^-, \cdots, x_n^-)$.

The relations $x_i = x_i^+ - x_i^-$, $x^+ \geq 0$, $x^- \geq 0$, are not enough to guarantee that $|x| = x_i^+ + x_i^-$, and the validity of this reformulation may not be entirely obvious. At an optimal solution to the reformulated problem, and for each i, we must have either $x_i^+ = 0$ or $x_i^- = 0$, because otherwise we could reduce both x_i^+ and x_i^- by the same amount and preserve feasibility, while reducing the cost, in contradiction of optimality. Having guaranteed that either $x_i^+ = 0$ or $x_i^- = 0$, the desired relation $|x| = x_i^+ + x_i^-$ now follows.

Let A be the m by $2n$ matrix $[\Phi\Psi \ -\Phi\Psi]$. (11) can be written as:

$$Az = y, \ \ z \geq 0. \tag{13}$$

It has a solution z^*, says, a vector in $\mathbb{R}^{2n}$ which can be partitioned as $z^* = [u^* \, v^*]$, u^* and v^* are solution to x_i^+ and x_i^- respectively; then $x^* = u^* - v^*$ solves (9). The reconstruction signal $f^* = \Psi x^*$. This linear program is typically considered computationally tractable [6].

Intuitively, we can represent UWB noise radar signal in cosine basis based on its representation in (1). The algorithm we used is as follows:

1. Expand the signal in cosine basis Ψ $\psi_j(t) = n^{-1/2}\cos(2\pi jt/n)$, $t = 0, 1, \cdots, n-1$ and obtain coefficient vector x.

2. Choose the parameter M to obtain a new observation vector y by correlating the signal with iid Gaussian matrix with dimension $M \times N$.

3. Create a new sensing matrix A and solve the linear program described in equation (13).

4. Get the estimated coefficient vector x^* and the recovered signal f^*.

5. Compare f^* with f to check whether the reconstruction is exact.

6. If not, go back to step 2 and increase the number of M.

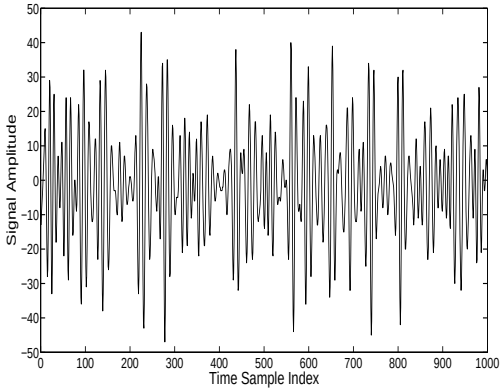


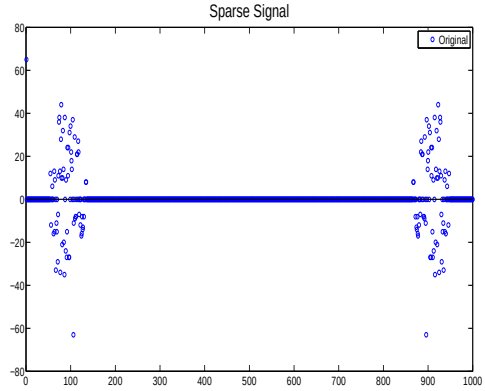
Fig. 1. UWB noise waveforms of received signal

5. SIMULATION RESULTS

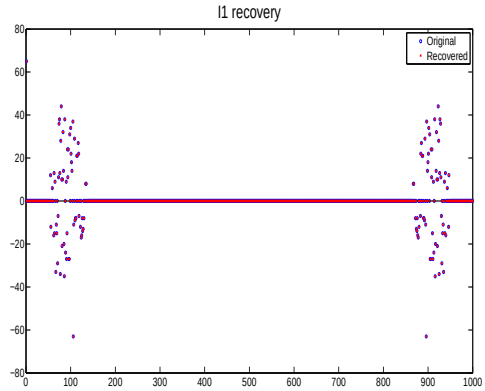
The frequency of the received signal is 400-700 MHz and the sampling rate is 1.5GHz/s. The property and waveform of UWB noise radar signal are illustrated in Fig.1. Our goal is to use M random measurements to exactly recover the original signal.

Fig.2 (a) illustrates the sparse form of UWB noise radar signal in cosine basis. We can see that only a small amount of coefficients are nonzero. In other words, we can say the UWB signal is sparse when expressed in cosine basis ($K << N$). Hence, we can apply the algorithm we proposed in Section 4 to UWB noise radar signal. Fig.2 (b) shows its exactly reconstruction from a new observation vector y with length of 200 samples. It suggests that we can use only 1/5 samples of the original data to represent the UWB noise radar signal without any loss.

In the second experiment, we study the dependence of probability of recovery (Pr) on the number of random measurements M. For each number of M, we performed a Monte Carlo simulation involving 500 realizations of a uniformly random measurements. The role played by probability in compressive sampling is demonstrated in Fig.3. When the random measurements M is less than 177, no algorithm whatsoever would of course be able to reconstruct the signal. The



(a)



(b)

Fig. 2. (a) Sparse UWB noise radar signal in cosine basis (b) its reconstruction by ℓ_1 minimization. The reconstruction is exact.

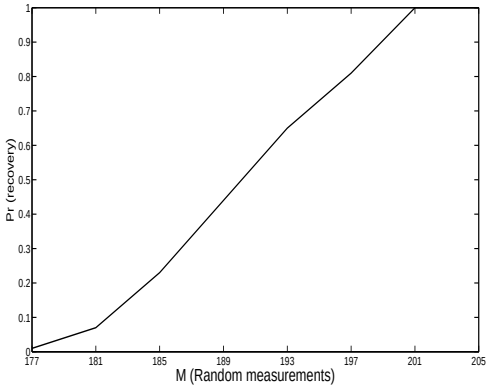


Fig. 3. UWB noise radar signal recovery from M random measurements. The probability of successful recovery depends on the measurements M.

probability of exact reconstruction increases while the number of M increases. The probability of exact recovery does not occur is truly negligible when $M \geq 200$.

6. CONCLUSION

We have applied the novel concept of compressive sampling on a practical problem of sampling UWB noise radar signal. From our investigation, we could draw the following conclusion: 1) The UWB noise radar signal is sparse when expressed in cosine basis Ψ. 2) Gaussian random matrices are largely incoherent with any fixed basis, which can efficiently acquiring the information in the original signal. 3) With 200 random measurements we can reconstruct the signal with negligible probability to fail.

7. REFERENCES

[1] R. M. Narayanan, "Through-wall radar imaging using uwb noise waveforms," Journal of the Franklin Institute, vol. 345(6), pp. 659–678, 2008.

[2] M. G. Di Benedetto and G. Giancola, "*understanding ultra wideband radio fundamentals*," Prentice Hall, *2004.*

[3] P. D. Hoffmeyer J. O. Curtis R. M. Narayanan, Y. Xu, ," in Design,performance, and applications of a coherent ultra wideband random noise radar. Opt.Eng, 1998, vol. 37(6), pp. 1855–1869.

[4] E. Candés and J. Romberg, ," in *Sparse and incoherence in compressive sampling. Inverse problem, 2007, vol. 23(3), pp. 969–985.*

[5] E. Candés and M. Wakin, ," in An introduction to compressive sampling. IEEE Signal Processing Magazine, 2008, pp. 21–30.

[6] D. Donoho, "Compressed sensing," IEEE Trans. on Information Theory, vol. 52, pp. 1289–1306, 2006.

[7] R. Devore R. Baranuik, M. Davenport and M. Wakin, "A simple proof of the restricted isometry property for random matrices," Constructive Approximation, vol. 3, pp. 253–263, December 2008.

[8] J. Tropp and A. C. Gilbert, "Signal recovery from partial information via orthogonal matching pursuit," IEEE Trans. on Information Theory, vol. 53, pp. 4655–4666, 2007.

[9] John N. Tsitsiklis D. Bertsimas, "Introduction to linear optimization," Athena Scientific, February, 1997.

An Amplitude Based Approach for Adaptive Compressive Sampling of UWB Noise Radar Signal

Ji Wu
Department of Electrical Engineering
University of Texas at Arlington
Arlington, TX 76019-0016, USA
Email: wu@wcn.uta.edu

Qilian Liang
Department of Electrical Engineering
University of Texas at Arlington
Arlington, TX 76019-0016, USA
Email: liang@uta.edu

***Abstract*—Compressive sampling(CS) is an emerging filed based on the revelation that a small collection of linear projections of a sparse signal contains enough information for stable, sub-Nyquist signal acquisition. UWB noise radar is one of the novel techniques which are widely used in various applications such as emergence rescues and military operations.Compressive sampling could be applied to UWB noise radar signal due to its sparsity in cosine waveform domain. In this paper, we apply amplitude based approach to compress data without any knowledge in advance. Simulation results indicate that fewer measurements are needed to fully recover original data compared with conventional compressive sampling.**

I. INTRODUCTION

Compressive sensing (CS) is a new method to capture and represent compressible signals at a rate significantly below the Nyquist rate. It employs nonadaptive linear projections that preserve the structure of the signal; the signal is then reconstructed from these projections using an optimization process. This leads immediately to new signal reconstruction methods that are successful with surprisingly few measurements, which in turn leads to signal acquisition methods that effect compression as part of the measurement process (hence "compressive sensing"). These recent realizations (though built upon prior work exploiting signal sparsity)have spawned an explosion of research yielding exciting results in a wide range of topics, encompassing algorithms,theory, and applications.

Since the UWB signal is usually in UHF range (500-1000MHz), sampling rate should be more than 1GHz/s (Nyquist rate) for alias-free signal sampling which requires plenty of space to store received signal. In this paper, we apply amplitude based compressive sampling in UWB noise radar signal, which asserts that one can recover it from far fewer samples than traditional Nyquist rate. It also enhances the operational feasibility of UWB noise radar.

II. OVERVIEW OF COMPRESSIVE SAMPLING

A. Sparsity and undersampled signal recovery

Many natural signals have concise representations when expressed in the proper basis [12]. Mathematically speaking, consider a discrete signal $f \in \mathbb{R}^N$ which can be expanded in an orthonormal basis $\Psi = [\psi_1 \psi_2 \ \cdots \psi_n]$ as follows:

$$f(t) = \sum_{i=1}^{N} x_i \psi_i(t), \tag{1}$$

where x is the coefficient sequence of f that can be computed from the signal f:

$$x_i = \langle f, \psi_i \rangle, i = 1, 2, \cdots, N. \tag{2}$$

It will be convenient to express f as Ψx (where Ψ is the $n \times n$ matrix with $\psi_1 \psi_2 \ \cdots \psi_n$ as columns). We can say the discrete signal f is K-sparse in the domain Ψ, $K << N$, if only K out of N coefficients in the sequence x are nonzero. Sparsity of signal is a fundamental principle used in the compressive sampling as well as in most modern lossy coders such as JPEG-2000 and many others, since a simple way for image compression would be to compute x from f and then only encode the values and locations of the largest K coefficients.Examples in [10] show that perceptual loss is hardly noticeable from a megapixel image to its approximation obtained by throwing away 97.5% of the coefficients.

Unfortunately, this compression process requires computing all N coefficients of signal f and the locations of the significant coefficients, which may not be known in advance. Compressive Sampling suggests this relevant information in the signal f can be captured using a small number of nonadaptive (even random) measurements of the signal. It provides us a potential way to acquire the sparse data efficiently, or equivalently, highly accurate recovery of sparse data from undersampled measurements.

Note that there are only K coefficients are nonzero, so we can remove this "sampling redundancy" by acquiring only M samples of the signal f, where $K < M << N$. The new M-length observation vector y can be represented as equation below:

$$y = \Phi f, \tag{3}$$

where Φ is an $M \times N$ measurement matrix. The above equation can be written as

$$y = \Phi \Psi x = \Theta x, \tag{4}$$

where Θ is given by:

$$\Theta = \Phi\Psi, \tag{5}$$

The signal f can be perfectly recovered from M equals to or a little bit more than measurements K, if Θ satisfies the so-called restricted isometry property (RIP)[8]that we will further investigate. It suggests that Θ is sufficiently incoherent and Φ cannot sparsely represented basic vectors of matrix Ψ and vice versa.

It has been shown [12] that choosing an iid Gaussian random matrix as sensing matrix Φ, Θ is also iid Gaussian for various orthonormal bases Ψ such as spikes, sinusoids, wavelets, Gabor functions, curvelets, and so on. Note that it is not known in advance which coefficients of f are zeroes, or which samples are not needed.

With the new observation matrix y, we decide to recover the signal f by ℓ_1–norm minimization; the proposed reconstruction f^* is given by $f^* = \Psi x^*$, where x^* is the solution to the convex optimization program($\|x\|_{\ell_1} \equiv \sum_i |x|$)

$$\min_{\tilde{x}\in\mathbb{R}^N} \|\tilde{x}\|_{\ell_1} \quad \text{subject to} \quad y = \Phi\Psi\tilde{x}, \tag{6}$$

That is, among all the objects $\tilde{f} = \Psi\tilde{x}$ consistent with the data, we choose the one whose coefficient sequence has minimal ℓ_1–norm. As is well known, minimizing ℓ_1 subject to linear equality constraints can easily be reformulated as a linear program of $O(N^3)$ complexity. However, ℓ_1–minimization is not the only way to recover sparse solutions; other methods, such as greedy algorithm [7], has also been proposed.

B. Partial measurement of compressive sampling

We already know how to recover signal from far fewer samples. The remaining question is that how many measurements we need to have to get original signal fully recovered. It is critical since we need to guarantee the recovery is perfect otherwise the algorithm is meanless, meanwhile; we also want to minimize the number of measurements in order to achieve higher compression ratio to make this algorithm more efficient.

[12] shows that for a fixed signal support T of size $|T| = S$, the program

$$\min_{x\in\mathbb{R}^N} \|x\|_{\ell_1} \quad \text{subject to} \quad y = \Theta_\Omega x, \tag{7}$$

recovers the overwhelming majority of x supported on T and observation subsets Ω of size

$$\|\Omega\| \geq C \cdot \mu^2(\Theta) \cdot S \cdot \log n, \tag{8}$$

where $\mu(\Theta)$ is simply the largest magnitude among the entries in Θ:

$$\mu(\Theta) = \max_{k,j} \|\Theta_{k,j}\|. \tag{9}$$

It is important to understand the relevance of the parameter $\mu(\Theta)$ in (8). $\mu(\Theta)$can interpreted as a rough measure of how concentrated the rows of Θ are. Since each row (or column) of Θ necessarily has an ℓ_2–norm equal to$\sqrt{n}$, μ will take a value between 1 and $\sqrt{n}$. When the rows of Θ are perfectly flat: $\|\Theta_{k,j}\| = 1$ for each k, j , as in the case when Θ is the discrete Fourier transform, we will have $\mu(\Theta) = 1$, and (8) is essentially as good as follows.

$$\|\Omega\| \geq C \cdot S \cdot \log n, \tag{10}$$

If a row of Θ is maximally concentrated– all the row entries but one vanish– then $\mu^2(\Theta) = n$, and (8) offers us no guarantees for recovery from a limited number of samples. This result is very intuitive. Suppose indeed that $\Theta_{k_0,j_0} = \sqrt{n}$ and x is 1-sparse with a nonzero entry in the j_0th location. To reconstruct x, we need to observe the k_0th entry of Θx as otherwise, the data vector y will vanish. In other words, to reconstruct x with probability greater than $1 - 1/n$, we will need to see all the components of Θx, which is just about the content of (8).This shows informally that (8) is fairly tight on both ends of the range of the parameter μ.

In our signal processing application, Θ can be decomposed as a product of a sparsity basis Ψ, and an orthogonal measurement system Φ.Where

$$\Theta = \Phi\Psi, \tag{11}$$

$$\Psi^*\Psi = I, \tag{12}$$

$$\Phi^*\Phi = nI. \tag{13}$$

Result in (8) then tells us how the relationship between the sensingmodality (Φ) and signal model (Ψ) affects the number of measurements required to reconstruct a sparse signal. The parameter μ can be rewritten as

$$\mu(\Phi\,\Psi) = \max_{k,j} |\langle\phi_k, \psi_j\rangle|, \tag{14}$$

and serves as a rough characterization of the degree of similarity between the sparsity and measurement systems. For μ to be close to its minimum value of 1, each of the measuremen vectors (rows of Φ)must be 'spread out'in the Ψ domain. To emphasize this relationship $\mu(\Theta)$ is often referred to as the mutual coherence [15]. The bound (8) tells us that a S-sparse signal can be reconstructed from $\sim S \log n$ samples in any domain in which the test vectors are 'flat', i.e. the coherence parameter is *O*(1).

III. Linear programming in compressive sampling

An alternative method for dealing with absolute values in linear program problem in (6) is to introduce new variables x^+, x^-, constrained to be nonnegative, and let $x_i = x_i^+ + x_i^-$ [14].(Our intention is to have $x_i = x_i^+$ or $x_i = -x_i^-$, depending on whether x_i is positive or negative.) We then replace the occurrence of $|x|$ with $x_i^+ + x_i^-$ and obtain the alternative formulation

$$\min \sum_{i=1}^{N} (x_i^+ + x_i^-) \tag{15}$$

$$\text{subject to} \quad \Phi\Psi x_i^+ - \Phi\Psi x_i^- = y \tag{16}$$

$$x^+, x^- \geq 0, \tag{17}$$

where $x^+ = (x_1^+, x_2^+, \cdots, x_n^+)$ and $x^- = (x_1^-, x_2^-, \cdots, x_n^-)$.

The relations $x_i = x_i^+ + x_i^-$, $x^+ \geq 0$, $x^- \geq 0$, are not enough to guarantee that $|x| = x_i^+ + x_i^-$, and the validity of this reformulation may not be entirely obvious. At an optimal solution to the reformulated problem, and for each i, we must have either $x_i^+ = 0$ or $x_i^- = 0$, because otherwise we could reduce both x_i^+ and x_i^- by the same amount and preserve feasibility, while reducing the cost, in contradiction of optimality. Having guaranteed that either $x_i^+ = 0$ or $x_i^- = 0$, the desired relation $|x| = x_i^+ + x_i^-$ now follows.

Let A be the m by $2n$ matrix $[\Theta \ -\Theta]$. (8) can be written as:

$$Az = y, \ \ z \geq 0. \tag{18}$$

It has a solution z^*, says, a vector in R^{2n} which can be partitioned as $z^* = [u^* \, v^*]$; then $x^* = u^* - v^*$ solves (6). The reconstruction $f^* = \Psi x^*$. This linear program is typically considered computationally tractable [8].

IV. Adaptive compressive sampling algorithm

According to UWB indoor multi-path channel model (IEEE 802.15.SG3a,2003), the average power delay profile(PDP) is characterized by an exponential decay of the amplitude of the clusters [11]. Therefore, we may roughly consider the amplitude of received UWB signal as

$$\hat{y} = \begin{cases} Ae^{-Bx}, & \text{if } y > 0 \\ -Ae^{-Bx}, & \text{if } y < 0 \end{cases}$$

where $\hat{y}$ is the amplitude of estimated received echo, x is sample index and y is the amplitude of original measured data. A and B are constants. These two parameters should be carefully chosen so that $\hat{y}$ is as close as y as possible. In our simulation, we use $A = 35000$ and $B = 0.00025$.

From our investigation, we find that the sparsity of received signal(nonzero coefficients) has a linear relationship with the sample index. If we compress data with every 2000 samples. Then, this relationship can be roughly described as

$$U = 410 - K \cdot I \tag{19}$$

where U is the sparsity of UWB radar signal, I is the first sample index of every 2000 samples. K is a constant,here we use $K = 30/2000$.

From the above relationships, we can apply adaptive compressive sampling algorithm to process the UWB radar data based on the amplitude and the signal and its sparsity. When receiving the signal, we pass it through an envelop detector and an amplifier which coefficient is $K = 1/A = 1/35000$. Hence we get the new signal

$$\tilde{y} = e^{-Bx} \tag{20}$$

where $B = 0.00025$.

we sum up 2000 samples of $\tilde{y}$

$$S_n = \int_n^{n+2000} \tilde{y} dy = \int_n^{n+2000} e^{-Bx} dx \tag{21}$$

$$= e^{-Bn} - e^{-B(n+2000)} \tag{22}$$

where n is index of the first samples of every 2000 samples. Its value can be 0,2000,4000, ...,12000. Where $S_0 = 1 - e^{-2000B} and B = 0.00025$, so we can get all the value of $S_n, n = 0, 1, \ldots, 6$. When we compress the data, we only need to sum up 2000 samples to get(S_{rec})value and compare it with S_n,find n to minimize $|S_{rec} - S_n|$. Then we can plug n in (19) to get the sparsity of the signal. Based on (10), we can adaptively choose the number of measurement in order to achieve higher compression ratio. Note that we can initiate receiving signal at any sample index, what we need to do is to obtain successive16000 successive samples and sum every 2000 samples, hence we can get all the values of S_n and then we could do the compression with the algorithm we mentioned above. The first 16000 can be treated as a kind of taring sequence.

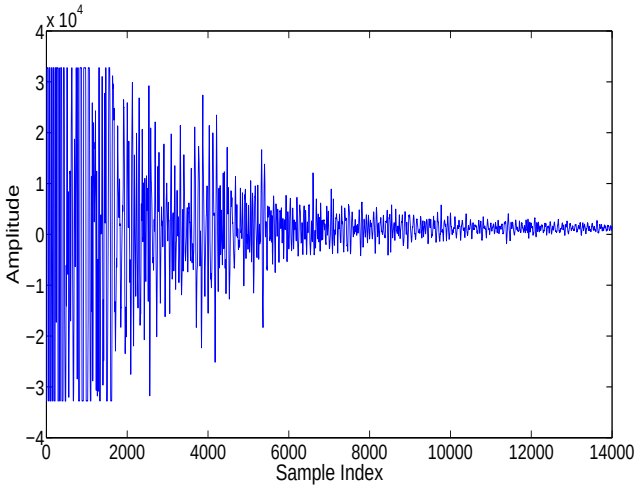
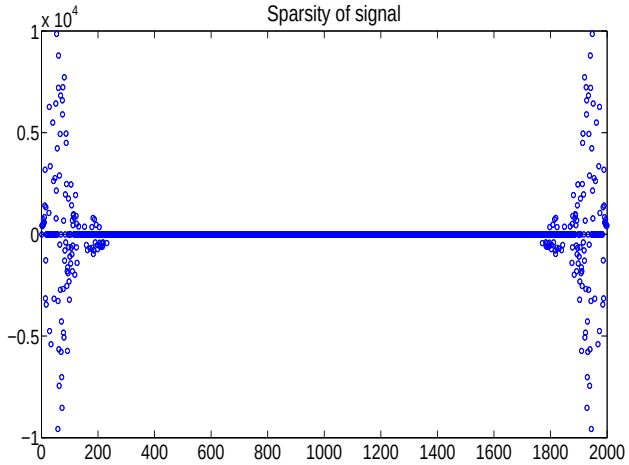


Fig. 1. UWB noise waveforms of transmitted signal

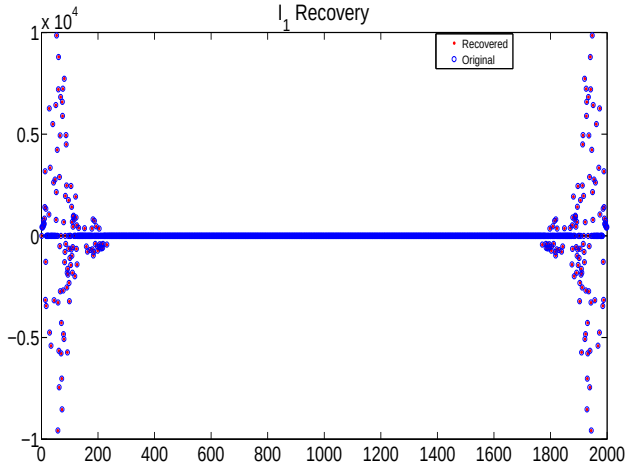
V. Simulation results

Fig.2 (a) illustrates the sparse form of UWB noise radar signal in cosine basis. We can see that only a small amount of coefficients are nonzero. In other words, we can say the UWB signal is sparse when expressed in cosine basis ($K << N$). Hence, we can apply the compressive sampling in UWB noise radar signal. Fig. 2 (b) shows its exactly reconstruction using adaptive compressive sampling from a new observation vector y.

The role played by probability in compressive sampling is demonstrated in Fig.3. When the random measurements M is less than 2000, no algorithm whatsoever would of course be able to reconstruct the signal. The probability of exact reconstruction increases while the number of M increases. From



(a)



(b)

Fig. 2. (a) Sparse UWB noise radar signal in cosine basis (b) its reconstruction by ℓ_1 minimization. The reconstruction is exact.

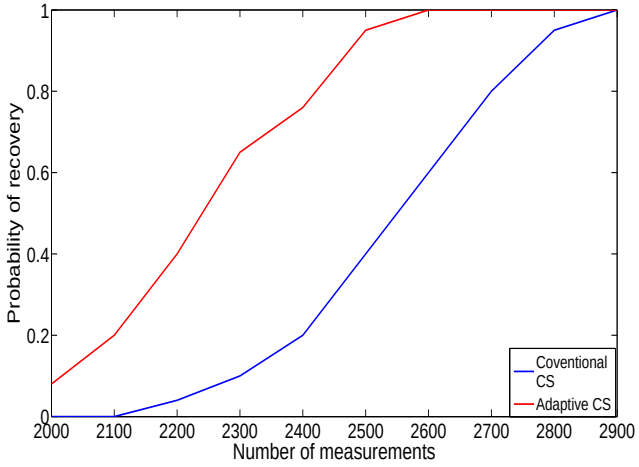


Fig. 3. UWB noise radar signal recovery from M random measurements. The probability of successful recovery depends on the measurements M.

this fig, we can conclude that using our new algorithm, 2600 samples are sufficient to recover the signal with probability almost equal to 1, while using the conventional CS we need around 3000 samples. The probability of exact recovery does not occur is truly negligible when $M \geq 2600$. Thus, we only have to tolerate a probability of failure that is extremely small.

VI. CONCLUSION

We have applied the novel concept of compressive sampling on a practical problem of sampling UWB noise radar signal. From our investigation, we could draw the following conclusion: 1) The UWB noise radar signal is sparse signal when expressed in convenient basis Ψ. 2) Random Gaussian matrices are largely incoherent with any fixed basis, which can efficiently acquiring the information from the original signal. 3) Our proposed algorithm could achieve better compression ratio than conventional CS algorithm; with same number of measurements, we could get higher probability to get original signal fully recovered.

REFERENCES

[1] Devore, *Probability and Statistics for Engineering and the Sciences*, 2nd, London: Artech house, 2005.

[2] M. Barkat, *Signal detection and estimation*, Monterey, CA: BrooksiCole, 1982.

[3] M. G. Di Benedetto and G. Giancola, *Understanding ultra wideband Radio Fundamentals*, Prentice Hall, 2004.

[4] J. H. Reed, *An introduction to Ultra Wideband Communication Systems*, Prentice Hall, 2005.

[5] R. M. Narayanan, " Through-wall radar imaging using UWB noise waveforms ," *Journal of the Franklin Institute*, 345(6), pp. 659-678, Sep 2008.

[6] E. Candés, J.Romberg, and T.Tao, " Robust uncertainty principles: Exact signal reconstruction from highly incomplete frequency information ," *IEEE Trans. on Information Theory*, Vol.52, No.2, pp.485-509, February 2006.

[7] J. Tropp and A.C.Gilbert " Signal recovery from partial information via orthogonal matching pursuit ," *IEEE Trans. on Information Theory*, Vol.53, No.12, pp.4655-4666,2007.

[8] D.Donoho " Compressed Sensing ," *IEEE Trans. on Information Theory*, Vol.52, No.4, pp.1289-1306, April 2006.

[9] R.Baranuik " Compressive Sensing ," *IEEE Signal Processing Magazine*, Vol.24, No.4, pp.118-121, July 2007.

[10] E. Candés and M. Wakin " An introduction to compressive sampling ," *IEEE Signal Processing Magazine*, pp.21-30, March 2008.

[11] R.Baranuik, M. Davenport, R. Devore, and M. Wakin " A simple proof of the restricted isometry property for random matrices ," *Constructive Approximation* , Vol.28, No.3, pp.253-263, December 2008.

[12] E. Candés and J.Romberg " Sparse and incoherence in compressive sampling ," *Inverse problem* , 23(3), 969-985(2007).

[13] R.M. Narayanan, Y.Xu, P.D. Hoffmeyer, J.O. Curtis " Design,performance, and applications of a coherent ultra wideband random noise radar ," *Opt.Eng* , 37(6),(1998) 1855-1869.

[14] Dimitris Bertsimas, John N. Tsitsiklis " Introduction to Linear Optimization ," *Athena Scientific* , February, 1997.

[15] Donoho D L and Huo X " Uncertainty principles and ideal atomic decomposition," *IEEE Trans.Inf.Theory* , 47 2845-62.

WAVEFORM DESIGN AND OPTIMIZATION FOR RADAR SENSOR NETWORK

Lei Xu and Qilian Liang

Department of Electrical Engineering
University of Texas at Arlington
Arlington, TX 76010

ABSTRACT

We investigate the use of information theory to design waveforms for the measurement of extended radar targets in radar sensor networks (RSN). The different channel gains for transmitting signals from different radar sensors are introduced to model the radar system channel. We optimized the estimation waveforms that maximize the mutual information between a target ensemble and the received signal in additive Gaussian noise given the transmitting signals so that characteristics of the target could be well recgonized. We also study the maximum mutual information with the constraints on the number of radar sensors, waveform energy and duration, which could be taken into consideration when waveforms are designed for RSN.

Index Terms— Waveform design, Mutual information, RSN

1. INTRODUCTION

Information theory has been applied to investigating radar system by Woodwar and Davies[1]-[2]. For these works, the information theory is particulary used in the area of radar detection. Considering the application of information theory in radar detection problem, it is summarized to gain information from a mixture of signal and unwanted noise by obtaining as large a signal-to-noise ratio as possible on the grounds in[3].

Meanwhile, much time and efforts has been put into waveform design problem radar system. Wilcox[4] studied the problem of designing waveforms from the radar ambiguity function for narrowband signals. Naparst[5] considered the problem of wideband waveform design and processing to resolve targets in dense target environments. It is not until 1993 when Bell[6] first used mutual information in the design of single radar waveforms and processing to conclude that distributing energy is a good choice to better detect targets..

Radar sensor network (RSN) is a newly studied topic that multiple radar sensors can be combined to form a multiradar system to overcome performance degradation of single radar along with waveform optimization. In [7], Liang studied constant frequency (CF) pulse waveform design and proposed maximum-likelihood (ML) automatic target recognition (ATR) approach for both nonfluctuating and fluctuating targets in a network of multiple radar sensors. In [8], RSN design based on linear frequency modulation (LFM) waveform was studied and LFM waveform design was applied to RSN with application to ATR with delay-Doppler uncertainty by Liang as well. Nevertheless, none of the works have considered the use of information theory in radar waveform design for RSN.

In this paper, we studied the problems of designing a set of radar waveforms for optimal target information extraction in RSN. Here, the radar targets are modeled as extended radar targets of significant physical extent but not the simple point targets for the purpose of extracting information about a target. The problem is modeled to design of radar waveforms which maximize the mutual information between the extended target and the receiver output. Close formula has been derived for the waveform and an example has been illustrated to further study it.

The rest of the paper is organized as follows. In Section 2, we analyze and formulate the problem of waveform design for target estimation in RSN. We further study the estimation waveform problem for target recognition in RSN and derive a close formula for the maximum mutual information between the extended target and the receiver output in Section 3. Section 4, we present an example of performance of waveforms for optimal target estimation problem in RSN. In Section 5, conclusions are drawn on waveform design in application of information theory in RSN .

2. PROBLEM ANALYSIS

In a radar system, we make measurements of a target in order to determine unknown characteristics of it. In other words, we make measurements of a target in order to decrease the *a priori* uncertainty about the target. From the view of information theory, it makes sense that if greater accuracy is required in the measurements, more information must be provided about the object being measured. Thus, it is easy to understand that the greater the mutual information between the target and the received radar signal when the transmitting signal is given, the greater the quantity of information describing the object and the greater the reduction in the *a priori* uncertainty about the target. The waveforms solved for maximizing such mutual information is called information extraction waveforms or estimation waveform which is studied in this paper.

The radar sensor network channel model is shown in Fig. 1. Here, $x_1(t), ..., x_N(t)$ are a set of N finite-energy deterministic waveforms with the total energy E_x transmitted by the transmitter in order to make a measurement of the radar target. Each waveform is assumed to be of the same duration T and confined to the symmetric time interval $[-T/2, T/2]$.

$$E_x = \sum_{i=1}^{N} \int_{-T/2}^{T/2} |x_i(t)|^2 dt \tag{1}$$

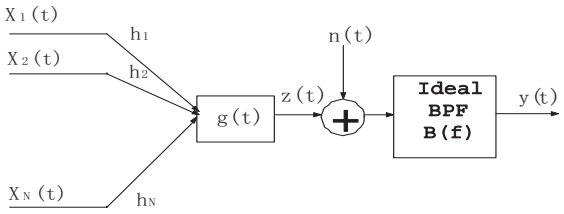


Fig. 1. Radar sensor network channel model

The average power P_x, which satisfies the relation $E_x = NP_xT$, is introduced, since most real radar systems have the energy constraint on the average power of the waveform instead of the total energy. We also assume that each waveform is confined to a frequency interval $w = [f_0, f_0 + W]$ so that only negligible energy resides outside the frequency interval w.

The target has a scattering characteristic modeled by the random impulse response $g(t)$. The resulting scattered

$$z(t) = \sum_{i=1}^{N} \int_{-T/2}^{T/2} g(\tau) x_i(t-\tau) dt \tag{2}$$

The noise process at the receiver is the zero-mean additive Gaussian noise process $n(t)$ which is assumed to be stationary and ergodic, and to have one-sided power spectral density $P_{nn}(f) = 2S_{nn}(f)$ for $f > 0$. $n(t)$ is also statistically independent of both the transmitted waveforms and the target impulse response. he ideal linear time-invariant bandpass filter $B(f)$ is included so that the transmitted signal has no significant energy outside the frequency interval w, neither does $z(t)$ which is the summation of responses of a linear time-invariant system to the transmitted signal. According to the Fig. 1, the problem of Radar Sensor Network can be stated as following. Given a Gaussian target ensemble with random impulse response $g(t)$ having spectral variance $\sigma_G^2(f)$, find the set of waveforms $x_1(t), ..., x_N(t)$ each confined to the symmetric time interval $[-T/2, T/2]$ and having all but a negligible fraction of their energy confined in (one-sided) frequency to $w = [f_0, f_0 + W]$ that maximize the mutual information $I(y(t); g(t)|x_1(t), ..., x_N(t))$ in additive Gaussian noise with one-sided power spectral density $P_{nn}(f)$.

3. WAVEFORMS FOR ESTIMATION IN RADAR SENSOR NETWORK

We are interested in finding the set of waveforms $x_1(t), ..., x_N(t)$ that maximize the mutual information $I(y(t); g(t)|x_1(t), ..., x_N(t))$ between the random target impulse response and the received radar waveform under constraints on their energy and bandwidth. Since it could be shown that $I(y(t); g(t)|x_1(t), ..., x_N(t))$ could be maximized when $I(z(t); g(t)|x_1(t), ..., x_N(t))$ is maximized, we will find the functions $x_1(t), ..., x_N(t)$ that maximize $I(z(t); g(t)|x_1(t), ..., x_N(t))$. We could easily obtain that for the class of functions $x_i(t)$ $x_1(t), ..., x_N(t)$ that maximize $I(y(t); z(t)|x_1(t), ..., x_N(t))$, $I(y(t); g(t)|x_1(t), ...,$
$x_N(t)) = I(y(t); z(t)|x_1(t), ..., x_N(t))$. We do not provide the proof here because of the space limit, but [6] could be referred to for the proving method.

According to the chain rule for mutual information in information theory,

$$\begin{aligned} & I(z(t); g(t)|x_1(t), x_2(t), ..., x_N(t)) \\ \overset{chain\ rule}{=} & \sum_{i=1}^{N} I(z(t); g(t)|x_i(t)) \end{aligned} \tag{3}$$

Then, we consider the small frequency interval $F_k = [f_k, f_k + \Delta f]$ of bandwidth Δf small enough such that for all $f \in F_k, X(f) \approx X(f_k), Z(f) \approx Z(f_k)$, and $Y(f) \approx Y(f_k)$. If $\hat{z_k}(t)$ correspond to the component of $z(t)$ with frequency components in F_k, and $\hat{y_k}(t)$ correspond to the component of $y(t)$ with frequency components in F_k, the mutual information between $\hat{z_k}(t)$ and $\hat{y_k}(t)$, given that $x_i(t)$ is transmitted, could be expressed as [6]

$$\begin{aligned} & I(\hat{y_k}(t); \hat{z_k}(t)|x_i(t)) \\ = & \tilde{T}\Delta f \ln[1 + \frac{2|h_i X_i(f_k)|^2 \sigma_G^2(f_k)}{P_{nn}(f_k)\tilde{T}}] \end{aligned} \tag{4}$$

Here, the observing time interval is $T = [t_0, t_0 + \tilde{T}]$.

We partition the frequency bandwidth into M disjoint frequency intervals F_k, with $\hat{y_k}(t), \hat{z_k}(t)$ and $\hat{n_k}(t)$ in the component in F_k. According to [9], when it is made up of Gaussian random processes with disjoint power spectral densities, such processes corresponding to each F_k are known to be statistically independent. Therefore, the mutual information given that $x(t)$ is transmitted is equal to the sum of each mutual information between $\hat{y_k}(t)$ and $\hat{z_k}(t)$ given that $x(t)$ is transmitted:

$$I(y(t); z(t)|x_i(t)) = \sum_{k=1}^{M} I(\hat{y_k}(t); \hat{z_k}(t)|x_i(t)) \tag{5}$$

If we enlarge the number M of disjoint intervals of bandwidth Δf in the frequency bandwidth $w = [f_0, f_0 + W]$, then $\Delta f \to 0$. In the limit, we achieve an integral for the mutual information $I(y(t); z(t)|x_i(t))$:

$$\begin{aligned} & I(y(t); z(t)|x_i(t)) \\ = & \tilde{T} \int_w \ln[1 + \frac{2|h_i X_i(f)|^2 \sigma_G^2(f)}{P_{nn}(f)\tilde{T}}] df \end{aligned} \tag{6}$$

Take equations (3) and (6) into consideration, we could easily get:

$$\begin{aligned} & I(y(t); z(t)|x_1(t), x_2(t), ..., x_N(t)) \\ = & \sum_{i=1}^{N} \tilde{T} \int_w \ln[1 + \frac{2|h_i X_i(f)|^2 \sigma_G^2(f)}{P_{nn}(f)\tilde{T}}] df \end{aligned} \tag{7}$$

We assume that

$$E_x = \sum_{i=1}^{N} \int_w |X_i(f)|^2 df, \tag{8}$$

and the resulting maximum value of $I(y(t); z(t)|x_1(t), ..., x_N(t))$ is

$$N\tilde{T} \int_w max[0, \ln(\frac{2\sigma_G^2(f)}{NP_{nn}(f)\lambda} \sum_{i=1}^{N} |h_i|^2)] df \tag{9}$$

Proof: According to Jenson's Inequality[10]

$$I(y(t);z(t)|x_1(t),x_2(t),...,x_N(t)) \quad (10)$$
$$\geq (\sum_{i=1}^{N}\tilde{T})[\int_w \ln(1+\frac{2\sigma_G^2(f)\sum_{i=1}^{N}|h_iX_i(f)|^2}{\sum_{i=1}^{N}P_{nn}(f)\tilde{T}})df]$$

Based (8) and (8), we use the Lagrange multiplier technique [11] to form a function

$$\Phi(|X_i(f)|^2) = \sum_{i=1}^{N}\tilde{T}\int_w \ln[1+\frac{2|h_iX_i(f)|^2\sigma_G^2(f)}{P_{nn}(f)\tilde{T}}]df$$
$$-\lambda(\sum_{i=1}^{N}\int_w |X_i(f)|^2df - E_X) \quad (11)$$

The equation (11) is equivalent to maximizing $\varphi(|X_i(f)|^2)$ with respect to $|X_i(f)|^2$, where

$$\varphi(|X_i(f)|^2) = \sum_{i=1}^{N}\tilde{T}\ln[1+\frac{2|h_iX_i(f)|^2\sigma_G^2(f)}{P_{nn}(f)\tilde{T}}]$$
$$-\lambda\sum_{i=1}^{N}|X_i(f)|^2 \quad (12)$$

Here, λ is the Lagrange multiplier which could be determined by the constraint of (8). Thus, maximizing $\Phi(|X_i(f)|^2)$, the $|X_i(f)|^2$ that maximizes $\varphi(|X_i(f)|^2)$ is

$$|X_i(f)|^2 = \tilde{T}/\lambda - \frac{P_{nn}(f)\tilde{T}}{2\sigma_G^2(f)|h_i|^2} \quad (13)$$

Since the magnitude-square spectrum should be no less than zero, we could further rewrite the equation (13) as

$$|X_i(f)|^2 = max[0,\tilde{T}/\lambda - \frac{P_{nn}(f)\tilde{T}}{2\sigma_G^2(f)|h_i|^2}]. \quad (14)$$

We take (14) into (11), and the result could be easily proved.

In addition, substituting the (13) into the constraint of (8), we obtain

$$\sum_{i=1}^{N}\int_w |X_i(f)|^2df = \sum_{i=1}^{N}\int_w(\tilde{T}/\lambda - \frac{P_{nn}(f)\tilde{T}}{2\sigma_G^2(f)|h_i|^2})df$$
$$= E_x \quad (15)$$

Solving it, we have

$$\lambda = \frac{\tilde{T}Nw}{E_x + \sum_{i=1}^{N}\int_w \frac{P_{nn}(f)\tilde{T}}{2\sigma_G^2(f)|h_i|^2}df} \quad (16)$$

As a result, $I(y(t);z(t)|x_1(t),...,x_N(t))$ could be maximized by the $|X_i(f)|^2$ that

$$|X_i(f)|^2 = \frac{E_x + \sum_{i=1}^{N}\int_w \frac{P_{nn}(f)\tilde{T}}{2\sigma_G^2(f)|h_i|^2}df}{Nw} - \frac{P_{nn}(f)\tilde{T}}{2\sigma_G^2(f)|h_i|^2} \quad (17)$$

Observing the equation (14), we see that $|X_i(f)|^2$ is a function of several factors such as $\tilde{T},\lambda,P_{nn}(f)$ and $|h_i|$. $|X_i(f)|^2$ gets larger as $P_{nn}(f)$ gets smaller if all the other factors are held constant for $f \in w$. Oppositely, $|X_i(f)|^2$ gets larger as the variance of $G(f)$ $\sigma_G^2(f)$ or the pulse duration $\tilde{T}$ get larger if all the other factors are held constant. Since we have different channels for different transmitting sensor in a RSN, the effect of different channel gain h_i for each transmitter should be of importance here. If all the other factors are held constant for $f \in w$, we show an interesting interpretation of the relationship between $|X_i(f)|^2$ and $|h_i|$ in Fig. 1.

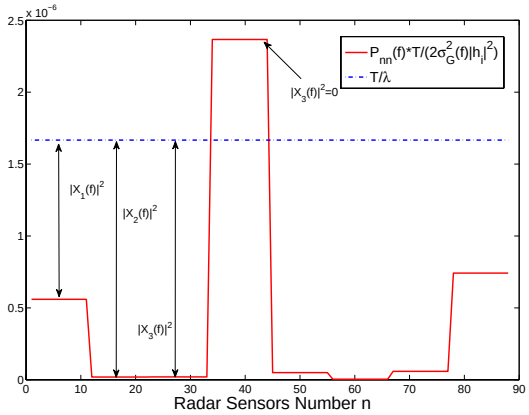


Fig. 2. Waterfilling interpretation of magnitude-squared spectrum $|X_i(f)|^2$

The Fig. 2 is a "waterfilling " strategy which is widely used in problems dealing with power or energy allocation in information theory [12]. As a result, Fig. 2 gives a pictorial view of optimal power allocation strategy for RNS if each channel gain could be properly estimated. The transmitter allocates more power to the stronger channel, taking advantage of the better channel conditions and less or even no power to the weaker ones.

4. RESULTS AND COMPARISON

We will illustrate an example to examine the optimal transmitted signals' spectrum characteristics and the amount of information obtained. From (9), the maximum mutual information is given

$$I_{max}(y(t);z(t)|x_1(t),...,x_N(t))$$
$$= N\tilde{T}\int_w max[0,\ln(\frac{2\sigma_G^2(f)}{NP_{nn}(f)\lambda}\sum_{i=1}^{N}|h_i|^2)]df \quad (18)$$

The Fig. 3 will display the results of numerical solutions of (16) and (18) for the mutual information $I_{max}(y(t);z(t)|x_1(t),...,x_N(t))$ as a function of both the pulse duration T (here, since we assume $T >> 1/w$, then $T = \tilde{T}$) and average power P_x. The value of T equals to $10\mu s, 100\mu s, 1ms 10ms$ and $100ms$, while average power P_x varies over the range from $1W$ to $1000W$ for each T value. And the number of radar sensors in the RSN is 8. Fig. 3 shows that the mutual information $I_{max}(y(t);z(t)|x_1(t),...,x_N(t))$ is proportional to transmitted pulse duration T. In the practical RSN, the duration of the transmitted signal T is often referred to as the "time-on-target" in radar target-recognition problems. It makes sense that if all other factors are equal, the longer the "time-on-target", the better the target could be recognized. This point also well matches

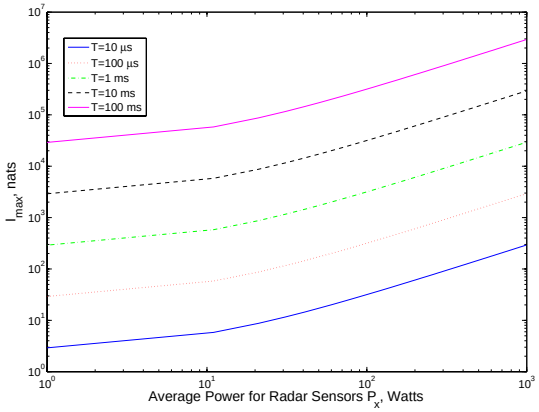
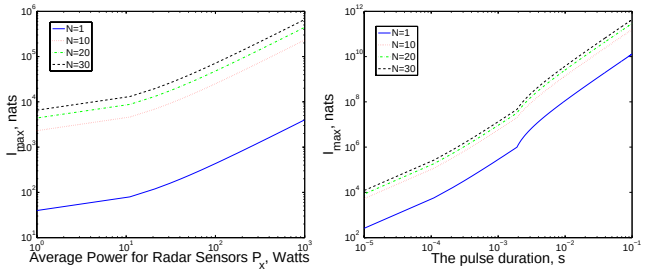


Fig. 3. Maximum mutual information as a function of T and P_x



(a) A function of N and P_x (b) A function of N and T

Fig. 4. Maximum mutual information

up to the expression in (18). In addition, it is easy to see and understand that the more average power allocated on transmitting signals the more mutual information we get at the receiver, as well as the better performance of the target recognition system.

Since RSN is constructed by a number of radar sensors, it is necessary to study the maximum mutual information as a function of the number of radars in RSN N and average power P_x and a function of N and T. The resulting maximum values of $I(y(t); z(t)|x_1(t), ..., x_N(t))$ is plotted in Fig. 4(a). The solution is carried out for values of N equals to $1, 10, 20$ and 30, P_x varies from $1W$ to $1000W$ and T varies over the range from $10\mu s$ to $100ms$. Though the number of radar senors are changing here, we assume the total power allocated on the transmitting sensors are equal in order to compare the target recognition performance. Observing Fig. fig:subfig:a1, the maximum mutual information is proportional to the number of radars in RSN N. Large number of radar sensor such as $N \geq 10$ the increase of the maximum mutual information is not as distinct as when N increase form 1 to 10. The same story happens to the the maximum mutual information as a function of N and T. In a word, the more radar sensors, the better the target could be recognized. However, all three factors N, T and P_x should be carefully decided between the balance of optimizing recognizing performance and the industry implementation cost.

5. CONCLUSION

In this paper, we studied the waveforms design for the measurement of extended radar targets in radar sensor networks (RSN) in the view of information theory. Considering the effect of different channel gains, we investigated the estimation waveforms that maximize the mutual information between a target ensemble and the received signal in additive Gaussian noise given the transmitting signals so that characteristics of the target could be well recgonized. From the study of the maximum mutual information with the constraints on the number of radar sensors, waveform energy and duration, which could be taken into consideration when waveforms are designed for RSN, some useful conclusions for waveforms design in RSN could be drawn. If the channel could be well estimated, the transmitter could allocate more power to the stronger channel to gain better performance. Considering the factors such as the number of radars in RSN N, the signal duration T, and average power P_x, and their relations the corresponding maximum mutual information as a function of them could be used.

6. REFERENCES

[1] P. Woodward and I. Davis, "A theory of radar information," *Phil. Mag.*, vol. 41, pp. 1101–1117, October 1951.

[2] I. Davis, in *On determining the presence of signals in noise*, vol. 99. Proc. IEE, 1952, pp. 45–51.

[3] P. Woodward, *Probability and Information Theory with Applications to Radars*. London: England: Pergamon, 1953.

[4] R. Blahut, W. Miller, and C. Wilcox, *Radar and Sonar*. New York: Springer-Verlag, 1991.

[5] H. Naparst, "Dense target signal processing," *IEEE Trans. Inform, Theory*, vol. IT-37, pp. 317–327, March 1991.

[6] M. Bell, "Information theory and radar: Mutual information and the design and analysis of radar waveforms and systems," *Ph.D. Dissertation, California Inst. Technol.*, 1988.

[7] Q. Liang, in *Waveform Design and Diversity in Radar Sensor Networks: Theoretical Analysis and Application to Automatic Target Recognition*, vol. 2. Sensor and Ad Hoc Communications and Networks, 2006. SECON'06, 2006, pp. 684–689.

[8] ——, in *Radar Sensor Networks for Automatic Target Recognition with Delay-Doppler Uncertainty*, vol. 23-25. Military Communications Conference, 2006. MILCOM 2006, 2006, pp. 1–7.

[9] A. Papoulis, *Probability, Random Variables, and Stochastic Processes*. New York: McGraw-Hill, 1965.

[10] T. Cover and J. Thomas, *Elements of Information Theory*. 2nd ed. John Wiley & Sons, Inc, 2006.

[11] F. Hildebrand, *Advanced Calculus for Applications*. NJ: Prentice-Hall: 2nd ed. Englewood Cliffs, 1976.

[12] R. Gallager, *Information Theory and Reliable Communication*. New York: Wiley, 1968.

Outdoor Propagation Channel Modeling in Foliage Environment

Jing Liang and Qilian Liang
Department of Electrical Engineering
University of Texas at Arlington
E-mail: jliang@wcn.uta.edu, liang@uta.edu

***Abstract*— In this paper, we study the statistical modeling for outdoor non line-of-sight (NLOS) channels in rich scattering and time-varying foliage environment based on extensive data collected by both narrowband and ultra-wideband (UWB) radar sensors. The multipath contributions arrive at the receiver are grouped into clusters. The time of arrival of clusters can be modeled as a Poisson arrival process, while within each cluster, subsequent multipath contributions or rays also arrive according to a Poisson process. However, the parameters are quite different along with the frequency. We also observe that the amplitude of channel coefficient at each path can be more accurately characterized as log-logistic distribution (LLD) other than log-normal, Weibull or Rayleigh due to the best goodness-of-fit and smallest root-mean-square error (RMSE).**

I. Introduction

Forest has been an asymmetric threat environment due to a limited sensing capability of a warfighter. Understanding the signal propagation channels in foliage will assist a range of applications such as target detection, situation monitoring and wireless communications.

There have been many efforts into investigating outdoor propagation channels. In narrowband mobile radio channels, Rayleigh, Rician and Nakagami distributions have been commonly used for the flat fading modeling. For wideband channels, the Ultra-Wideband (UWB) signal is of most interest due to the exceptional range resolution coupled with penetrating capability and low power. [1] has applied UWB radar-like test apparatus to obtain propagation delays, which serves as a preliminary investigation into UWB channel for rural terrain, but more extensive measurements and further analysis are absent for statistical characterization; [2] has characterized UWB channels for outdoor office environment by S-V model with modifications on the ray arrival times and amplitude statistics to fit the empirical data. However, these parameters may not fit foliage environment as trees and branches provide different scattering compared to indoor situation. Some experimental outdoor studies other than UWB are presented in [3][4]. [3] proposes that instead of Rayleigh, Weibull provides better fit to spatially and temporally extended spiking data; [4] shows that the foliage is impulsively corrupted with multipath fading, which leads to inaccuracy of the K-distribution model.

Like indoor environment, the foliage contains a wealth of multiple scattering other than LOS free space. In addition, the movement of leaves, branches and even the tree trunks contribute to the time-variance fading phenomenon. Since the foliage medium can be completely described by its time and space varying feature, one can investigate the channel model based on characterization of the channel impulse response (CIR).

In our investigation, we will apply both narrowband and ultra-wide band (UWB) radar sensors to model the propagation channels, as we believe that foliage is composed of intervening materials that are electromagnetically dispersive, which contributes to the strong frequency dependence of foliage, and thus a narrowband-wideband study would assist with the better understanding of statistic property of the channel. Narrowband signals have been tried at 200, 400 and 600 megahertz respectively, while UWB pulse generator is capable of producing pulses with width 750ps. Each frequency component in a radar signal will sense the foliage in a slightly different manner, therefore provides differences in multipath.

One can easily identify that this work is different from [6]. [6] solely described amplitude of back scattered clutter signals using UWB radars, while the current work analyze temporal property as well as amplitude characterization for both narrowband and UWB CIR.

The rest of this paper is organized as follows. In Section II, we apply CLEAN algorithm to extract CIR for 200MHz, 400MHZ, 600MHz and UWB signals. Section III presents the channel model in view of temporal characterization as well as statistic model comparison. We conclude our work in Section IV.

II. Channel Impulse Response Based on the Measured Data and CLEAN Algorithm

For detailed measurement setup, readers please refer to [6]. The average transmitted and received pulses at position 4 for different frequencies have been illustrated from Figs. 1 - 4. The purpose of average is to remove white Gaussian noise. Note that at a different position the result will be slightly different. However, illustration at one position is sufficient enough to describe the characterization.

The complicated multipath and time-varying CIR can be modeled as follows [7]

$$r(t) \approx \sum_n a_n p_n(t - \tau_n) \tag{1}$$

where a_n and τ_n is referred to as the amplitude and delay of the n^{th} propagation path. In order to extract the CIR from our measurement, the CLEAN algorithm has been used. It was initially introduced in [8] to enhance radio astronomical maps

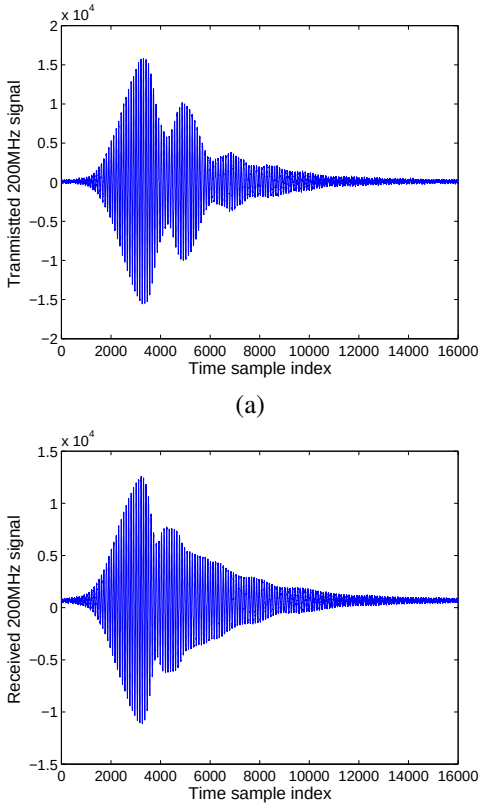


Fig. 1. Measurement of 200MHz and 35 pulses average : (a) transmitted pulse (b) received echoes

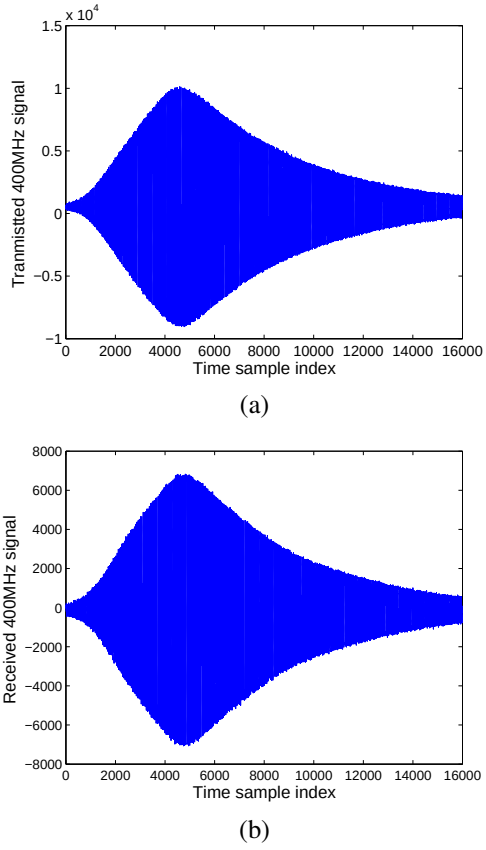


Fig. 2. Measurement of 400MHz and 35 pulses average: (a) transmitted pulse (b) received echoes

of the sky, and has also been employed in narrowband channel modeling [9][10]and UWB channel characterization problems [7][11].

Our steps involved [11] are:

1) Calculate the autocorrelation of the transmitted signal $R_{ss}(t)$ and the cross-correlation of the transmitted with the received waveform $R_{sy}(t)$.
2) Find the largest correlation peak in $R_{sy}(t)$, record the normalized amplitudes α_k and the relative time delay τ_k of the correlation peak.
3) Subtract $R_{ss}(t)$ scaled by α_k from $R_{sy}(t)$ at the time delay τ_k.
4) If a stopping criterion (a minimum threshold) on the peak correlation is not met, go step 2. otherwise stop.

Given the transmission, reception and the CLEAN processing described above, the obtained CIR are illustrated from Fig. 5 to Fig. 8. Note that we plot the absolute value of the UWB channel for the comparison between the outdoor UWB channel with the indoor S-V model [12] (see Fig. 9). It is shown that

1) Both narrowband and UWB channels are made up of multipath components. The time-varying path magnitude implies that fading generally exists, therefore the received pulses are fairly random from one time to another.
2) The UWB channel we obtained looks similar as the CIR in S-V model shown in Fig. 9. However, they are different in the arrival of cluster, subsequent rays and envelope decay.
3) In outdoor environment, the largest scattering, i.e., the highest magnitude does not always appear at the first path. This phenomenon is clearly illustrated in Fig. 5 and 8.
4) Channels are frequency dependent. It has been observed that the intervening materials, such as foliage and soil, have dielectric properties that are strongly frequency dependent. This in part explains the difference among those channels. We will further analyze the detail in the following section.

III. Outdoor Channel Modeling

A. Temporal Characterization

In the S-V model, the arrival of clusters is modelled as a Poisson arrival process with a rate Λ, while within each cluster, subsequent multipath contributions or rays also arrive according to a Poisson process with a rate λ (see Fig. 10). Observe Fig. 5∼8, like in S-V model, multipath contributions arrive at the receiver grouped into clusters and therefore similar methodology used in S-V model studies may be also applied to 200MHz, 400MHz, 600MHz and UWB CIR.

We define:

- T_l = the arrival time of the first path of the l-th cluster;

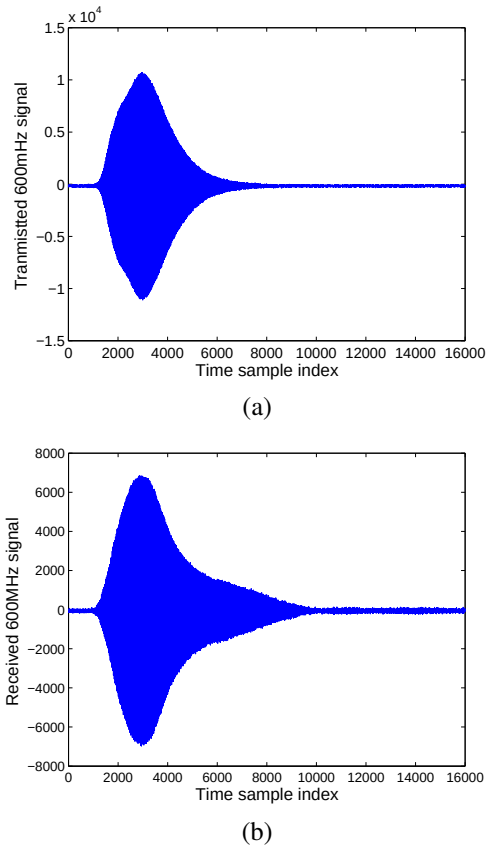


Fig. 3. Measurement of 600MHz and 35 pulses average: (a) transmitted pulse (b) received echoes

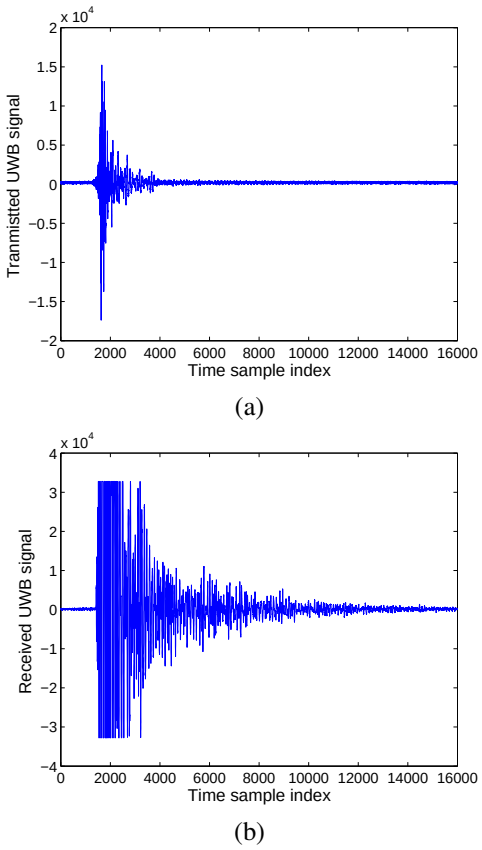


Fig. 4. Measurement of UWB and 35 pulses average: (a)transmitted pulse (b) received echoes

- $\tau_{k,l}$ = the delay of the k-th path within the l-th cluster relative to the first path arrival time T_l;
- Λ = the cluster arrival rate;
- λ = the ray arrival rate, i.e., the arrival rate of the paths within each cluster.

By definition, we have $\tau_{0l} = T_l$. The distributions of the cluster arrival time and the ray arrival time are given by

$$p(T_l|T_{l-1}) = \Lambda \exp\left(-\Lambda(T_l - T_{l-1}), l > 0\right)$$
$$p(\tau_{k,l}|\tau_{(k-1),l}) = \lambda \exp\left(-\lambda(\tau_{k,l} - \tau_{(k-1),l})\right), k > 0 \qquad (2)$$

Specifically, we also observed that the Λ and λ are quite different for 200MHz, 400MHz, 600MHz and UWB CIR. We listed observed parameters in Table I. As for indoor UWB data, we refer [14]. The higher Λ and λ of UWB implies its exceptional range resolution. Lower Λ and λ of outdoor UWB than those of indoor means outdoor environment typically more sparse multiple scattering than that of indoor.

B. Statistical Distribution of Channel Amplitude

In the S-V model, the average Power Decay Profile (PDP) is characterized by an exponential decay of the clusters and a different exponential decay for the pulses within each cluster. In other words, the amplitude follows rayleigh distribution. In the IEEE UWB indoor channel model [13], the clutter approach was adopted (same as S-V model), but a log-normal distribution was suggested for characterizing the multipath gain amplitude, and an additional log-normal variable was introduced for representing the fluctuations of the total multipath gain. In this Section we propose that log-logistic model may better characterize amplitude of the multipath for both outdoor NLOS narrowband and UWB signals in foliage.

TABLE I

TEMPORAL PARAMETERS FOR CHANNEL MODELS

Scenario	$\Lambda(1/ns)$	$\lambda(1/ns)$
200MHz	0.012	0.4
400MHz	0.004	0.128
600MHz	0.002	0.06
Outdoor UWB	0.04	0.8
Indoor UWB Extreme NLOS	0.0667	2.1

1) Statistic Models: In spite of intensive application in precipitation and stream-flow data, so far Log-logistic distribution (LLD) [15] statistical model has never been applied to foliage channel model to the best our knowledge. This model is intended to be employed on a basis of higher kurtosis and longer tails, as well as its shape similarity to log-normal and Weibull distributions.

The PDF for this distribution is given by

$$f(x) = \frac{e^{\frac{lnx-\mu}{\sigma}}}{\sigma x(1+e^{\frac{lnx-\mu}{\sigma}})^2}, \quad x > 0, \ \sigma > 0 \qquad (3)$$

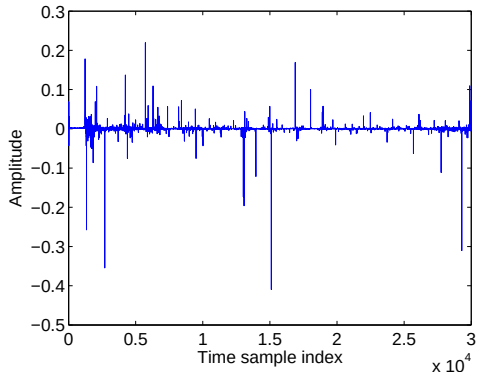


Fig. 5. 200MHz Channel

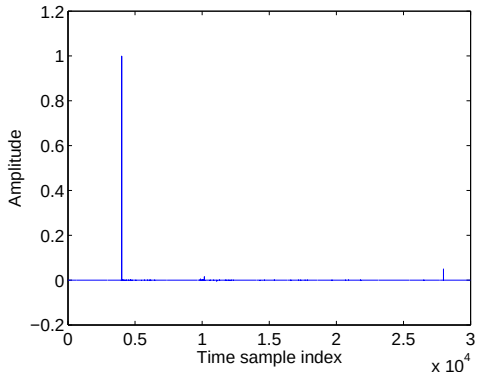


Fig. 7. 600MHz Channel

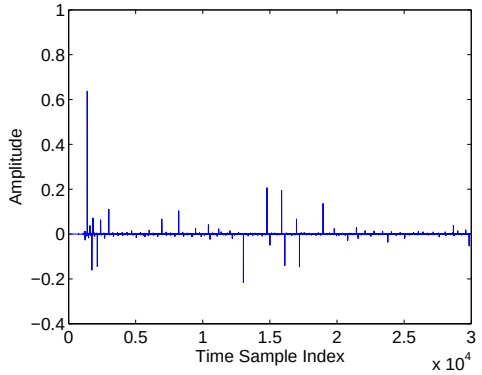


Fig. 6. 400MHz Channel

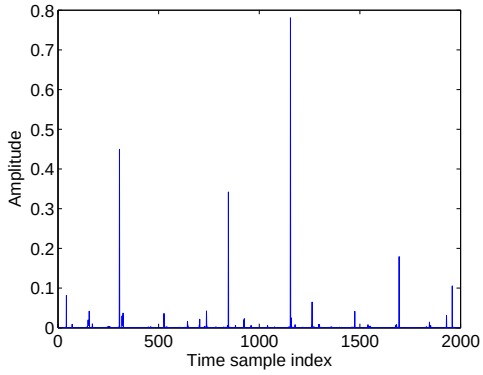


Fig. 8. UWB Channel

where μ is scale parameter and σ is shape parameter. The mean of the the LLD is

$$E\{x\} = e^{\mu}\Gamma(1+\sigma)\Gamma(1-\sigma) \tag{4}$$

where $\Gamma(\cdot)$ is Gamma function. The variance is given by

$$Var\{x\} = e^{2\mu}\{\Gamma(1+2\sigma)\Gamma(1-2\sigma) - [\Gamma(1+\sigma)\Gamma(1-\sigma)]^2\} \tag{5}$$

while the moment of order k is

$$E\{x^k\} = \sigma e^{\mu} B(k\sigma, 1-k\sigma),\ k < \frac{1}{\sigma} \tag{6}$$

where

$$B(m,n) = \int_0^1 x^{m-1}(1-x)^{n-1}dx \tag{7}$$

Similarly, the log-normal distribution [16] is a two-parameter distribution with parameters μ and σ. The PDF for this distribution is given by

$$f(x) = \frac{1}{x\sigma\sqrt{2\pi}} e^{-\frac{(\ln x-\mu)^2}{2\sigma^2}},\quad x>0, \sigma>0 \tag{8}$$

where μ is the scale parameter and σ is the shape parameter.

The Weibull distribution can be made to fit measurements that lie between the Rayleigh and log-normal distribution [17].

The Weibull distribution is also a two-parameter distribution with parameters a and b. The PDF for this distribution is given by

$$f(x) = ba^{-b}x^{b-1}e^{-(x/a)^b},\quad x>0, a>0,\ b>0 \tag{9}$$

where b is the shape parameter and a is the scale parameter.

The Rayleigh distribution, whose real and imaginary components are Gaussian, has the PDF as follows:

$$f(x) = \frac{x}{b^2} e^{-\frac{x^2}{2b^2}},\quad b>0 \tag{10}$$

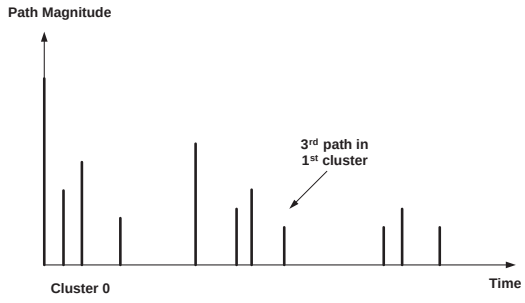


Fig. 9. An illustration of the channel impulse in S-V model.

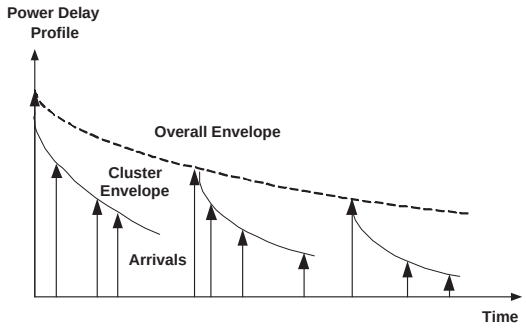


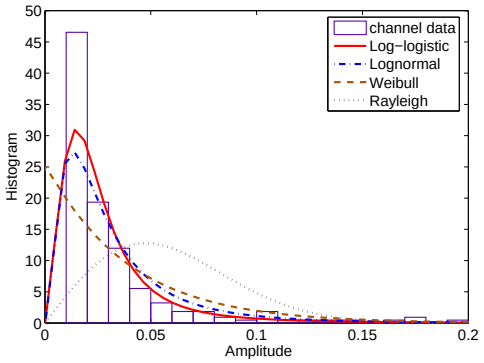
Fig. 10. An illustration of the double exponential decay of the mean cluster power and the ray power within clusters in S-V model.

2) Goodness-of-fit in curve and RMSE: On a basis of CIR cluster amplitude from 12 different positions, we apply Maximum Likelihood Estimation (MLE) approach to estimate the parameters. We obtain $\hat{\mu}$ and $\hat{\sigma}$ for log-logistic, $\hat{\mu}$ and $\hat{\sigma}$ for log-normal, $\hat{a}$ and $\hat{b}$ for weibull and $\hat{b}$ for Rayleigh respectively, which are shown in table II. Note that due to the very small amount of channel sample of 600MHz, its analysis have to be ignored. We also explore the standard deviation (STD) error of each parameter. These descriptions are also shown in table II in the form of ε_x, where x denotes different parameter for each model. It is obvious that log-logistic model provides smaller STD errors than those of log-normal.

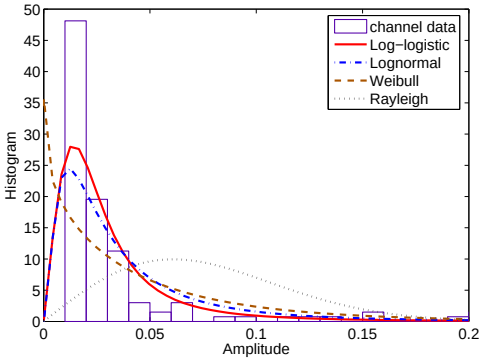
TABLE II
ESTIMATED PARAMETERS FOR STATISTIC MODEL

PDF	Log-Logistic	Log-normal
200MHz	$\hat{\mu}=-3.79907$ $\hat{\sigma}=0.43948$ $\varepsilon_\mu=0.0517626$ $\varepsilon_\sigma=0.0250518$	$\hat{\mu}=-3.69473$ $\hat{\sigma}=0.811659$ $\varepsilon_\mu=0.0550099$ $\varepsilon_\sigma=0.0390963$
400MHz	$\hat{\mu}=-3.75666$ $\hat{\sigma}=0.482505$ $\varepsilon_\mu=0.071783$ $\varepsilon_\sigma=0.035901$	$\hat{\mu}=-3.61265$ $\hat{\sigma}=0.917049$ $\varepsilon_\mu=0.0795182$ $\varepsilon_\sigma=0.0565477$
Outdoor UWB	$\hat{\mu}=-3.30616$ $\hat{\sigma}=0.590192$ $\varepsilon_\mu=0.202988$ $\varepsilon_\sigma=0.101636$	$\hat{\mu}=-3.13344$ $\hat{\sigma}=1.12623$ $\varepsilon_\mu=0.225245$ $\varepsilon_\sigma=0.164277$
PDF	Weibull	Rayleigh
200MHz	$\hat{a}=0.0388139$ $\hat{b}=1.00543$ $\varepsilon_a=0.0027934$ $\varepsilon_b=0.00456447$	$\hat{b}$=0.0474046
400MHz	$\hat{a}=0.0447926$ $\hat{b}=0.903163$ $\varepsilon_a=0.00458706$ $\varepsilon_b=0.0536079$	$\hat{b}$=0.0609159
Outdoor UWB	$\hat{a}=0.080002$ $\hat{b}=0.765597$ $\varepsilon_a=0.0222858$ $\varepsilon_b=0.106023$	$\hat{b}$=0.141188

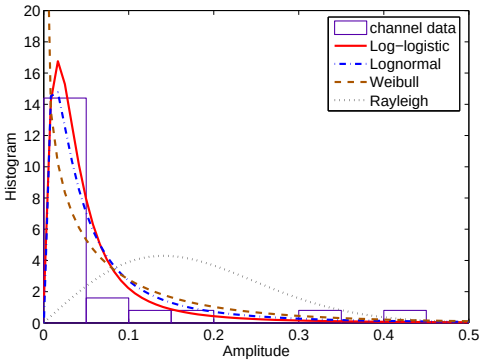
We may also observe that to what extend does the PDF curve of the statistic model match that of CIR cluster amplitude by root mean square error (RMSE). Let i (i=1, 2, $\cdots$, n) be the sample index of CIR amplitude, c_i is the corresponding



(a)



(b)



(c)

Fig. 11. Goodness-of-fit (a)200MHz (b)400MHz (c)UWB

PDF value whereas $\hat{c}_i$ is the PDF value of the statistical model with estimated parameters by means of MSE. RMSE is obtained through

$$\mathrm{RMSE}=\sqrt{\frac{1}{n}\sum_{i=1}^{n}(c_i-\hat{c}_i)^2} \tag{11}$$

where n is the amount of sample index. The RMSE for 200MHz, 400Hz and UWB have been listed in Table III. It demonstrates that LLD turns out to be the model that fits the channel data best.

One may also draw the above conclusion from the Fig. 11,

TABLE III

ROOT MEAN SQUARE ERROR (RMSE) COMPARISON BETWEEN STATISTIC MODELS

PDF	Log-Logistic	Log-normal	Weibull	Rayleigh
200MHz	5.7016	6.2850	8.8810	9.7562
400MHz	5.9023	6.5635	9.7056	10.3359
UWB	2.1867	2.4756	3.0136	4.8975

which describes the the goodness-of-fit in curve. The absolute amplitude of clusters have been plotted in terms of histogram. It can be easily seen that Rayleigh model provides the worst goodness-of-fit compared to LLD, log-normal and Weibull, so that exponential PDP of the clusters adopted in S-V model can not be applied in outdoor NLOS environment. Also, Weibull is not a good choice due to the inaccurate kurtosis and high tails. Compare LLD with log-normal, it is obvious that LLD is able to provide shaper kurtosis, shaper slope, and lower tail. In other word, LLD provides better goodness-of-fit than that of log-normal.

Since the above investigations have shown that LLD can better characterize the multipath gain amplitude for outdoor NLOS narrowband and UWB channels in foliage other than log-normal, we may suggest an additional LLD variable to represent the fluctuations of the total multipath gain. Moreover, similar to the IEEE UWB model, the phase of each path in outdoor NLOS environment may assumed to be either 0 or π with equal probability.

IV. CONCLUSION

In our investigation, we accomplished following conclusions: 1) Outdoor NLOS channels are frequency dependent as intervening materials have dielectric properties that are strongly frequency dependent. 2) Both narrowband and UWB channels are made up of multipath and time-varying components. 3) In outdoor NLOS environment, the largest scattering, i.e., the highest magnitude does not always appear at the first path. 4) The outdoor UWB channels we obtained are similar in their basic features as indoor models. However, they are different in the arrival of cluster and subsequent rays as well as envelope decay. 5) The amplitude of channel coefficient at each path can be more accurately characterized as log-logistic distribution (LLD) other than log-normal, Weibull or Rayleigh due to the best goodness-of-fit and smallest root-mean-square-error (RMSE).

ACKNOWLEDGEMENT

This work was supported in part by Office of Naval Research (ONR) under Grant N00014-07-1-0395 and N00014-07-1-1024, and National Science Foundation (NSF) under Grant CNS-0721515 and CNS-0831902.

REFERENCES

[1] M. Z. Win, F. Ramírez-Mireles, R. A. Scholtz and M. A. Barnes, "Ultra-Wide Bandwidth (UWB) signal propagation for outdoor wireless communications", *Proc. of VTC 1997*, vol. 1, pp. 251-255, May 1997.

[2] C. W. Kim, X. Sun, L. C. Chiam, B. Kannan, F. P. S. Chin and H. K. Garg, "Characterization of ultra-wideband channels for outdoor office environment", *IEEE Wireless Communications and Networking Conference*, vol. 2, pp. 950-955, Mar. 2005.

[3] F. L. Posner , "Spiky sea clutter at high range resolutions and very low grazing angles", *IEEE Transactions on Aerospace and Electronic Systems*, vol. 38, pp. 58-73, Jan. 2002.

[4] Watts, S., "Radar detection prediction in K-distribution sea clutter and thermal noise", *IEEE Transactions on Aerospace and Electronic Systems*, AES-23, pp. 40-45, Jan 1987.

[5] M. Rice, A. Davis and C. Bettweiser, "Wideband Channel Model for Aeronautical Telemetry", *IEEE Transactions on Aerospace and Electronic Systems*, vol. 40, pp. 57-69, Jan. 2004.

[6] J. Liang, Q. Liang and S. W. Samn, "Foliage Clutter Modeling Using the UWB Radar", *IEEE International Conference on Communications, ICC '08*, pp: 1937 - 1941, 19-23 May 2008.

[7] R. J. -M. Cramer, R. A. Scholtz and M. Z. Win, "Evaluation of an ultra-wide-band propagation channel", *IEEE Transactions on Antennas and Propagation*, vol. 50, pp. 561 - 570, May 2002.

[8] J. A. Högbom, "Aperture Synthesis with a non-regular distribution of interferometer baselines", *Astronomy and Astrophysics Supplement Ser.*, vol. 15, pp. 417-426, 1974.

[9] Q. Spencer, M. Rice, B. Jeffs and M. Jensen, "A Statistical Model for the Angle-of-Arrival in Indoor Multipath Propagation", *IEEE Vehicular Technology Conference*, IEEE 1997, pp. 1415-1419.

[10] G. L. Turin, "Introduction to Spread Spectrum Antimultipath Techniques and their Application to Urban Digital Radio", Proc. IEEE, vol. 68, March 1980, pp. 328-354.

[11] J. H. Reed, *An introduction to Ultra Wideband Communication Systems*, Prentice Hall, 2005.

[12] A. A. Saleh and R. A. Valenzuela, "A statistical model for indoor multipath propagation", *IEEE J. on Selected Areas in Communications*, vol. 5, no.2, pp. 128-137, Feb 1987.

[13] IEEE 802. 15. SG3a, "Channel modeling sub-committee report final," *IEEE P802.15-02/490r1-SG3a*, Feb 2003.

[14] M. -G. Di Benedetto and G. Giancola, *Understanding ultra wideband Radio Fundamentals*, Prentice Hall, 2004.

[15] R. C. Gupta, O. Akman and S. Lvin, "A Study of Log-Logistic Model in Survival Analysis", *Biometrical Journal*, 41, pp. 431-443, 1999

[16] E. Limpert, W. Stahel and M. Abbt, "Log-normal Distributions across the Sciences: Keys and Clues", *BioScience*, 51 (5), pp. 341C352, 2001.

[17] W. Weibull, "A statistical distribution function of wide applicability", J. Appl. Mech.-Trans. ASME 18(3), 293-297, 1951.

[18] Devore, *Probability and Statistics for Engineering and the Sciences*, Monterey, CA: BrooksiCole, 1982.

[19] M. Barkat, *Signal deteciton and estimation*, 2nd, London: Artech house, 2005.

TDoA Algorithm for Passive Geolocation Based on Channel Estimation

Qilian Liang
Department of Electrical Engineering
University of Texas at Arlington
Arlington, TX 76019-0016, USA
E-mail: liang@uta.edu

***Abstract*— In this paper, we propose a Time Difference of Arrival (TDoA) algorithm for passive geolocation based on delay estimation of two correlated wireless channels. It's assumed that the passive receiver is carried by a small flying UAV in the sky, and the transmitter is located on the ground (static or mobile), so Rician flat fading model should be used. To estimate the delay of two correlated channels, Block Phase Estimation (BPE) is used for each wireless channel estimation, and then the two estimated channels are compared to get the best time delay. We also compare it against a cross-correlation-based TDoA algorithm. Simulation results show that our TDoA algorithm performs much better than the cross-correlation-based TDoA algorithm with a lower level of magnitude in terms of average TDoA error and Root-Mean-Square-Error (RMSE). Four different Rician fading channel groups are evaluated, and conclusions are drawn for our TDoA algorithm and the cross-correlation-based TDoA algorithm.**

Index Terms : Passive geolocation, Time Difference of Arrival (TDoA), block phase estimation, Rician fading.

I. Introduction

Determining the location of an emitting target is one of the fundamental functions of communication *Electronic Warfare* (EW) systems [8]. The U.S. military has a urgent need to pinpoint an enemy based purely on the reception of radio signals, without the need for using radar. In contrast, locating an enemy actively with radar is to be avoided, since it draws unwanted attention to the platform operating the radar. The measurement of an emitter's position using electronic support (ES) sensors is termed **passive geolocation**, and plays an important part both in electronic support and electronic attack. Existing systems and technology for the precision geolocation of non-cooperative RF emitters are costly and time consuming to develop and deploy, and lack the flexibility to make cost-effective enhancements once deployed. Additionally, existing systems also rely on Global Positioning System (GPS), which is susceptible to jamming. Several techniques of passive geolocation were presented in [8], which includes triangulation, Time of Arrival (ToA), Time Difference of Arrival (TDoA), Angle of Arrival (AoA), etc. In this paper, we are interested in studying passive geolocation from wireless communication point of view and propose a TDoA algorithm for passive geolocation based on wireless channels delay estimation. Some related works in this direction have already been reported. In [6], a TDoA location scheme for the orthogonal frequency division multiplexing (OFDM) based wireless metropolitan area networks (WMANs) was presented. The TDoA algorithm enhances the location performance by utilizing the information in the time and frequency domains obtained from the received location OFDM signals. In [1], a TDoA estimation is carried out for narrowband multipath system using a correlation technique and a super-resolution method - root multiple signal classification (MUSIC). In [2], ultra-wideband (UWB) radio for positioning techniques were overviewed, which include the angle of arrival (AOA), the signal strength (SS), or time delay information, etc. In order to achieve timing error reduction in TDoA, a high-resolution first arriving path detector from propagation channel estimates is derived based on the minimum variance (MV) estimates and normalized minimum variance (NMV) of the power delay profile in [11]. In [7], a received signal phase-based TDoA approach was proposed in [7]. The least squares range difference location problem has been investigated by Schmidt [10] and others. Schmidt showed that the TDoA averaging process produced the geolocation that was the closest feasible one in a lest squared sense based on the measured ranging differences.

In this paper, we propose a TDoA algorithm via wireless channel estimation. The rest of this paper is organized as follows. In Section II, we propose a blind channel phase estimation approach named Block Phase Estimation (BPE) without knowing the unique words. In Section III, we propose our TDoA algorithm based on the estimated phase differences of the two wireless channels. In Section IV, we present our simulation results on our TDoA algorithm and compare it against an existing TDoA approach. Section V concludes this paper.

II. Block Phase Estimation for Wireless Channel

In passive geolocation applications, the passive receiver is carried by a small flying UAV in the sky, and the transmitter is located on the ground (static or mobile). Two parallel antennas with distance d are equipped under the UAV. When $d < 0.38\lambda$ [3], where λ is the wavelength of the RF signal, the two wireless channels are correlated, and one is the delayed version of the other. There exists a Line of Sight (LoS) between transmitter and receiver, and Rician flat fading model should be used.

The general structure of the phase estimator is illustrated in Fig. 1. We are supposed to estimate the phase at the midpoint of the estimation period which is denoted as T_E, it encompass N_E m-ary symbols, and we let $N_E = 2N+1$, where N is the number of samples before and after the sample whose phase is to be estimated. In this context and in the presence of additive white Gaussian noise(AWGN) and zero frequency uncertainty, Fig. 1 with the dotted box eliminated (so that $x_n^{'} = x_n$, $y_n^{'} = y_n$)represents the optimal (maximum likelihood) estimator for $m = 1$, $\Delta f = 0$ which corresponds to an unmodulated carrier. For m-PSK modulated waveform, the phase of each successive symbol should take a different value. Obviously, the above estimator is useless. To solve it, a two-dimentional (complex) nonlinear function is inserted in the dotted box

$$x_n' + iy_n' = F(\rho_n)e^{im\phi_n} \tag{1}$$

where $\rho_n = \sqrt{x_n^2 + y_n^2}$ and $\phi_n = tan^{-1}(y_n/x_n)$. This is a rectangular-to-polar transformation. Multiply phase ϕ_n by m and perform an arbitrary nonlinear transformation on ρ_n; and finally perform a polar-to-rectangular transformation on the result. Obviously by using the preceding and succeeding N symbols to estimate each symbol phase, all but the first and last N symbol estimates can be made unbiased by overlapping estimation periods. For $F(\rho) = \rho^k$, k even,

$$\begin{aligned} E(\frac{\rho^{2k}}{\sigma^{2k}}cos2\epsilon') &= \gamma^k \sum_{n=0}^{m+k} n!\binom{m+k}{n}\binom{m-k+n+1}{n}(\frac{-2}{\gamma})^n \\ &+(-1)^{m+k+1}2^k e^{-\gamma/2}(\frac{2}{\gamma})^{k+1} \\ &\cdot \sum_{n=0}^{m-k-1} \binom{m+k+n}{n}\frac{(m+k)!}{(m-k-n-1)!}(\frac{2}{\gamma})^n, \\ &k \le m-2, \end{aligned} \tag{2}$$

$$E\left(\frac{\rho^{2k}}{\sigma^{2k}}\right) = \sum_{n=0}^{k}\binom{k}{n}^2 \gamma^{k-n}2^n n!, \;\; k = m, \tag{3}$$

where σ^2 is the variance of the real and the imaginary part of each sample. From the above equation, it is shown in [12], for QPSK ($m = 4$), by choosing $F(\rho) = 0, \rho^2$, and ρ^4, the estimator can performs nearly as well as the linear estimator for unmudulated carries with moderate degradation.

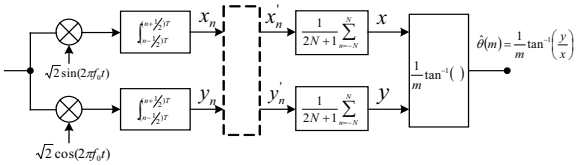


Fig. 1. Block phase estimator for m-PSK carriers

To implement the nonlinear transformation, we need to first multiply the phase by m, along with the final operation of dividing the tan^{-1} function by m, thus gives rise to an m-fold ambiguity in the phase estimate. Liang and Wang applied Unique Words (UW) to remove the ambiguity in wireless channel estimation [5], however the receive antennas don't know any UW in the passive geolocation application. Fortunately, we only need the phase differences of the two correlated wireless channels, so ambiguity is not a problem in our applicaation, and it's automatically canceled by each other of the two wireless channels. After the nonlinear transformation, for each block, we got

$$\hat{\theta}(m) = \frac{1}{m}tan^{-1}(\frac{y}{x}), \tag{4}$$

without considering the phase ambiguity, where $x = \frac{1}{2N+1}\sum_{n=-N}^{N} x_n^{'}$ and $y = \frac{1}{2N+1}\sum_{n=-N}^{N} y_n^{'}$. Using the preceding and succeeding N symbols to estimate each symbol phase individually, so that make the estimation unbiased. That is, approximately $(2N+1)$ as many operations as performing a single estimate are required for all the $(2N+1)$ symbols in the interval [12]. In our scheme, we set up a parameter s denoted as step. For each s symbols, we only do the estimation once, and get the phase of the other $s-1$ symbols by interpolation. Thus, we only need $(2N+1)/s$ operations. It is shown in the simulation result that there is hardly any degradation in terms of the BER.

III. TDoA Finding Algorithm and Comparison with Existing Approach

Based on the BPE algorithm in Section II, we could be able to obtain two channels $g_1(t)$ and $g_2(t)$. Since the two channels are highly correlated, and ideally one is the delay of the other. We construct a cost function,

$$J(\zeta) = \frac{1}{T}\int_0^T [g_1(t-\zeta) - g_2(t)]^2 dt \tag{5}$$

where T is the burst length, and the ζ value that can minimize the cost function is the TDoA value, i.e.,

$$\hat{\zeta} = \inf_{\zeta\in[0,T]} J(\zeta) \tag{6}$$

$$= \arg\inf_{\zeta\in[0,T]} \frac{1}{T}\int_0^T [g_1(t-\zeta) - g_2(t)]^2 dt \tag{7}$$

For discrete case, our TDoA finding algorithm can be represented as

$$\hat{\zeta} = \arg \min_{\zeta \in \{1,2,\cdots,L\}} \frac{1}{L} \sum_{n=0}^{L} [g_1(n-\zeta) - g_2(n)]^2 \quad (8)$$

where L is the total number of symbols of a burst.

Our approach is a channel estimation-based TDoA approach based on the received signals. In the existing approach, a cross-correlation of the received signals based TDoA approach was proposed in [8]. We summarize this approach and will compare with our TDoA algorithm. The received signals from two parallell antennas j and k are

$$r_j(t) = s(t) + n_j(t) \quad (9)$$
$$r_k(t) = As(t-\tau_{jk}) + n_k(t) \quad (10)$$

where A is an attentuation factor and τ_{jk} is the relative time delay between the antennas. The cross correlation of these two received signals is given by

$$C_{jk}(\tau) = \mathcal{E}\{r_j(k) r_k(t-\tau)\} \quad (11)$$
$$= A\mathcal{E}[s(t)s(t-\tau-\tau_{jk})] \quad (12)$$
$$= AC_{ss}(\tau-\tau_{jk}) \quad (13)$$

where $C_{ss}(\tau)$ is the autocorrelation function of $s(t)$. $|C_{jk}(\tau)| \leq 1$ and its maximum value is 1 when $tau = \tau_{jk}$, so the delay τ_{jk} could be estimated based on the cross-correlation of the received signals.

IV. Simulations

We evaluated our TDoA algorithm for different time delays betwen the two wireless channels, and compared it against the cross-correlation-based approach. The burst length is 936 symbols and transmitting 1 burst needs 10ms, so the symbol rate is 93,600 symbols/s. We totally ran two sets of simulations with 100 symbols delay (i.e., $1.07ms$) for the two algorithms. We studied four groups of Rician fading channels and each group has two channels (one is the delayed version of the other): the first group with Rician factor $K = 12dB$, doppler shift $f_d = 200Hz$; the second group of channels $K = 12dB$, $d_d = 500Hz$; the third group of channels $K = 9dB$, $f_d = 200Hz$; and the fourth group of channels $K = 9dB$, $f_d = 500Hz$.

For channel simulation, we chose $N = 60$ (number of scatters), and ran our simulations for different SNR values. At each SNR values, we ran the Monte-Carlo simulations for $MC = 50,000$ bursts, and obtained the average TDoA estimation errors for the two TDoA algorithms which are plotted in Fig. 2(a)(b) for the 100-symbol delay. Observe these figures, the average TDoA errors are not zero, which means both TDoA algorithms are not unbiased, so Cramer-Rao bound can't be used for the TDoA error variance analysis.

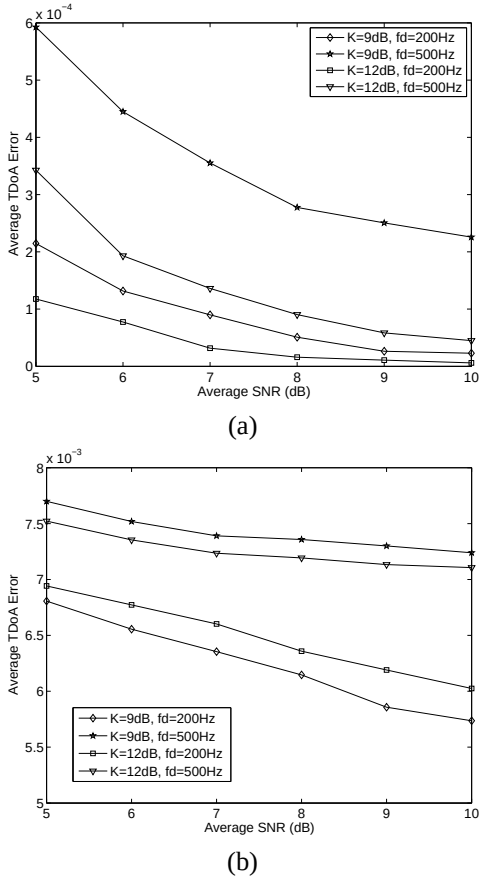


Fig. 2. The average TDoA error versus SNR for four different Rician fading channels with $1.07ms$ (100-symbol) time delay. (a) Our TDoA Algorithm, (b) Cross-correlation-based TDoA algorithm [8].

We evaluated the estimation variance via the Monte-Carlo simulations based on $MC = 50,000$ bursts. We used the root-mean-square-error (RMSE) of the TDoA estimation, which is defined as

$$RMSE = \sqrt{\frac{1}{MC} \sum_{i=1}^{MC} (\hat{\zeta}_i - \zeta_i)^2} \quad (14)$$

where i is the index of bursts in Monte-Carlo simulations. The RMSE for the two TDoA algorithms were plotted in Fig. 3(a)(b) for the 100-symbol delay.

Observe these figures for average TDoA error and RMSE (Figs. 2 and 3),

1) Our TDoA algorithm performs much better than the cross-correlation-based TDoA algorithm with different magnitude level. In terms of average TDoA error as well as RMSE, our TDoA algorithm performs more than 10 times lower than the cross-correlation-based TDoA algorithm. Why the cross-correlation-based TDoA algorithm couldn't perform well? It's because it ignores the channel fading phase dis-

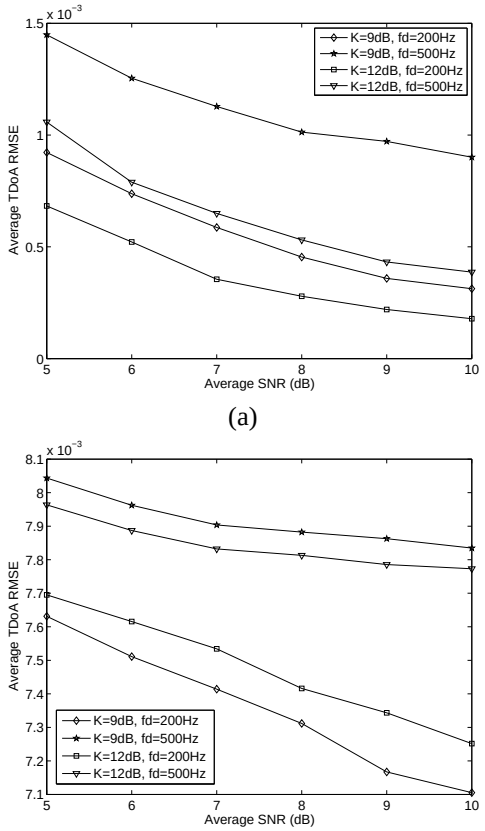


Fig. 3. The TDoA RMSE versus SNR for four different Rician fading channels with $1.07ms$ (100-symbol) time delay. (a) Our TDoA Algorithm, (b) Cross-correlation-based TDoA algorithm [8].

tortion, but channel fading happens in all mobile communications.

2) Our TDoA algorithm performs very well with very low average TDoA error, for example, the average TDoA error is 0.57 symbol time, and RMSE is 16.7 symbol time for channel $K = 12dB$, $f_d = 200Hz$, at $SNR = 10dB$ when the delay is 100-symbol time.
3) The TDoA algorithm performance is related to channel fading condition. According to our simulations, our TDoA algorithm performs in the following order (from the best to the worst):
   - $K = 12dB$, $f_d = 200Hz$;
   - $K = 9dB$, $f_d = 200Hz$;
   - $K = 12dB$, $d_d = 500Hz$;
   - $K = 9dB$, $f_d = 500Hz$.

   It's very clear that larger Doppler shift f_d and lower fading factor K cause TDoA performance degradation. But surprisingly, the cross-correlation-based TDoA algorithm doesn't perform in a consistent order for the four channels because channel fading was not considered in this algorithm.
4) The TDoA performance is sensitive to the time delay. The performance is better for larger time delay case than for smaller time delay. It's because for larger time delay, the time delay finding algorithm will easily locate the delay with less error.

V. Conclusions

We have proposed a Time Difference of Arrival (TDoA) algorithm for passive geolocation based on delay estimation of two correlated wireless channels. It's assumed that the passive receiver is carried by a small flying UAV in the sky, and the transmitter is located on the ground (static or mobile), so Rician flat fading model should be used. To estimate the delay of two correlated channels, Block Phase Estimation (BPE) was used for each wireless channel estimation, and then the two estimated channels are compared to get the best time delay. We also compared our TDoA algorithm against a cross-correlation-based TDoA algorithm. Simulation results showed that our TDoA algorithm performs much better than the cross-correlation-based TDoA algorithm with a lower level of maganitude in terms of average TDoA error and Root-Mean-Square-Error (RMSE).

References

[1] C. R. Comsa, J. Luo; A. Haimovich, S. Schwartz, "Wireless Localization using Time Difference of Arrival in Narrow-Band Multipath Systems," *International Symposium on Signals, Circuits and Systems*, vol. 2, July 2007, pp. 1-4.
[2] S. Gezici, Z. Tian, G. B. Giannakis, H. Kobayashi, A. F. Molisch, H. V. Poor, Z. Sahinoglu, "Localization via ultra-wideband radios: a look at positioning aspects for future sensor networks," *IEEE Signal Processing Magazine*, vol. 22, no. 4, July 2005, pp. 70 - 84.
[3] A. Goldsmith, *Wireless Communications*, Cambridge University Press, New York, NY, 2005.
[4] W. C. Jakes, *Microwave Mobile Communication*, New York, NY: IEEE Press, 1993.
[5] Q. Liang and L. Wang, "Block Phase Estimation with Decision Feedback Demodulator for Satellite-Based Wireless ATM Networks," *62nd IEEE Vehicular Technology Conference*, Dallas, TX, Sept 2005.
[6] H. Ni, G. Ren; Y. Chang; "A TDOA location scheme in OFDM based WMANs," *IEEE Trans on Consumer Electronics*, vol. 54, no. 3, August 2008, pp. 1017 - 1021.
[7] A. G. Piersol, "Time delay estimation using phase data," *IEEE Trans on Acoustic, Speech, and Signal Processing*, vol 29, no. 3, June 1981, pp. 471-477.
[8] R. Poisel, *Electronic Warfare Target Location Method*, Artech House, Boston, 2005.
[9] J. Scheuing and B. Yang, "Disambiguation of TDOA Estimation for Multiple Sources in Reverberant Environments," *IEEE Trans on Audio, Speech, and Language Processing*, vol. 16, no. 8, Nov. 2008, pp. 1479 - 1489.
[10] R. O. Schmidt, "Least squares range difference location," *IEEE Trans on Aerospace and Electronic Systems*, vol. 32, no. 1, Jan 1996, pp. 234-242.
[11] J. Vidal, M. Najar, R. Jativa, "High resolution time-of-arrival detection for wireless positioning systems," *IEEE Vehicular Technology Conference*, 2002, vol. 4, Sept. 2002, pp. 2283 - 2287.
[12] A. J. Viterbi, and A. M. Viterbi, "Nonlinear estimation of PSK modulated carrier phase with application to burst digital transmission," *IEEE Trans. Information Theory*, vol. 32, pp. 432-451, July 1983.

Sparsity and Compressive Sensing of Sense-through-Foliage Radar Signals

Qilian Liang and Ji Wu
Department of Electrical Engineering
University of Texas at Arlington
Arlington, TX 76019-0016, USA
E-mail: liang@uta.edu

***Abstract*— Motivated by recent advances on Compressive Sensing (CS), we study the sparsity of sense-through-foliage radar signals. Based on CLEAN method, we obtain the impulse response for sense-through-foliage communication channels for three different radars, 200MHz, 400MHz, and UWB radars. Channel impulse responses for the above three different kinds of channels demonstrate that the sense-through-foliage signals are very sparse, which means CS is possible to be applied to sense-through-foliage radar signals to tremendously reduce the sampling rate. We apply CS and linear programming to sparse signal compression and recovery, and it turns out that we could achieve compression ratio of 32:1 with perfect recovery for the UWB radar signals.**

Index Terms : Compressive sensing, radars, sense-through-foliage, UWB, sparsity.

I. Introduction

Compressive sensing (CS) is a new method to capture and represent compressible signals at a rate **significantly below the Nyquist rate**. It employs nonadaptive linear projections that preserve the structure of the signal; the signal is then reconstructed from these projections using an optimization process. This leads immediately to new signal reconstruction methods that are successful with surprisingly few measurements, which in turn leads to signal acquisition methods that effect compression as part of the measurement process (hence "compressive sensing"). These recent realizations (though built upon prior work exploiting signal sparsity) have spawned an explosion of research yielding exciting results in a wide range of topics, encompassing algorithms, theory, and applications.

In CS for radar signals, very few works have been reported. In [1], it shows that matched filter could be eliminated if CS is used for radar. In [2], SAR radar image was processed using wavelets basis. In [11], a stylized compressed sensing radar is proposed in which the time-frequency plane is discretized into an N×N grid. In [13], a joint basis selection and sparse parameter estimation (called fast Bayesian mathcing pursuit) algorithm was proposed. In [15], a heuristic, graph-structured, sparse signal representation algorithm for overcomplete dictionaries that can be decomposed into subdictionaries was proposed and applied to SAR imaging. In [3][4], passive radar using OFDM was applied to target signature detection.

The rest of this paper is organized as follows. In Section II, we give an overview of compressive sensing. In Section III, we study the sparsity of narrowband and UWB radar signals. In Section IV, we present our results on compressive sensing for UWB radar signals. Section V concludes this paper.

II. Compressive Sensing: an Overview

CS provides a framework for integrated sensing and compression of discrete-time signals that are sparse or compressible in a known basis or frame. Let z denote a signal of interest, and Ψ denote a sparsifying basis (or called transform domain), such that $z = \Psi\theta$, with $\theta \in \mathbb{R}^N$ being a K-sparse vector, i.e. $\|\theta\|_0 = K$. Traditional transform coding compression techniques acquire first z in its entirety, and then calculate its sparse representation θ in order to encode its nonzero values and their locations, but CS aims to preclude the full signal acquisition by measuring a set y of linear projections of z into vectors ϕ_i, $1 \le i \le M$. By stacking these vectors as rows of a matrix Φ (measurement matrix), we can represent the measurements as $y = \Phi z = \Phi\Psi\theta$. The main result in CS states that when the matrix $\Phi\Psi$ holds the restricted isometry property (RIP) [7][10], then the original sparse representation θ is the unique solution to the linear program

$$\hat{\theta} = \arg\min_{\theta\in\mathbb{R}^N} \|\theta\|_{\ell_1} \quad (1)$$

$$s.t.\ y = \Phi\Psi\theta, \quad (2)$$

known as Basis Pursuit, where ℓ_1–norm is defined as ($\|\theta\|_{\ell_1} \equiv \sum_i |\theta_i|$). Thus, the original signal z can be recovered from the measurement vector y in polynomial time. Furthermore, choosing Φ to be a matrix with independent gaussian-distribtued entries satisfies the RIP for $\Phi\Psi$ when Ψ is a basis or tight frame and $M = O(K\log(N/K))$.

III. Sparsity of Narrowband and UWB Radar Signals

Recently, we studied different radar sensor signals (with narrowband 200MHz, 400MHz, and UWB) in a foliage environment and observed that it is very sparse, which satisfies the requirement for compressive sensing. Our work is based

on the data collected by AFRL in radar-based sense-through-foliage experiment in late summer and fall. Late summer foliage, because of the limited rainfall, involved foliage with decreased water content. Late fall and winter measurements involved largely defoliated but dense forest, providing a rich scattering environment. Because of wind or different temperatures in dense forest, it's also a time-varying environment. The sense-through-foliage experiment was constructed on a seven-ton man lift (as shown in Fig. 1a), which had a total lifting capacity of 450 kg. The limit of the lifting capacity was reached during the experiment as essentially the entire measuring apparatus was placed on the lift. The principle pieces of equipment secured on the lift are: Barth pulser, Tektronix model 7704 B oscilloscope, dual antenna mounting stand, two antennas, rack system, IBM laptop, HP signal Generator, Custom RF switch and power supply and Weather shield (small hut). The target is a trihedral reflector (as shown in Fig. 1b). Throughout this work, a Barth pulse source (Barth Electronics, Inc. model 732 GL) was used. The pulse generator uses a coaxial reed switch to discharge a charge line for a very fast rise time pulse outputs. The model 732 pulse generator provides pulses of less than 50 picoseconds (ps) rise time, with amplitude from 150 V to greater than 2 KV into any load impedance through a 50 ohm coaxial line. The generator is capable of producing pulses with a minimum width of 750 ps and a maximum of 1 microsecond. This output pulse width is determined by charge line length for rectangular pulses, or by capacitors for 1/e decay pulses. For the data we used, each sample is spaced at 50 picosecond interval, and 16,000 samples were collected for each collection for a total time duration of 0.8 microseconds at a rate of approximately 20 Hz. The Barth pulse source was operated at low amplitude and 35 pulses reflected signal were averaged for each collection.

We applied the CLEAN algorithm to obtain the channel model based on the transmitted pulses and received echos. The CLEAN algorithm was first introduced in [12] and has been applied to UWB measurements [8][14] and it assumes that the channel is a series of impulses which is consistent with the tapped-delay line channel model. This algorithm searches the received echos iteratively with the transmit pulse to find the maximum correlation [6]. Based on the CLEAN method, we successfully obtained the channel impulse responses based on transmit pulses and receive echoes. For illustration purposes, in Figs. 2, 3, and 4, we plot the channel impulse responses for 200MHz, 400MHz, and UWB channels using CLEAN method based on one experiment for each case.

Observe Figs. 2c, 3c, and 4c, the channel impulse response $\theta = [\theta_1, \theta_2, \cdots, \theta_n]$ has very few nonzero taps out of 32,000 sample index). Let $\psi(i)$ denote the transmit pulse, The received echo could be represented as (if no noise)

$$z(i) = \theta * \psi(i) = \sum_{j=1}^{n} \theta_j \psi(i-j) = \Psi\theta \qquad (3)$$



(a)



(b)

Fig. 1. (a) The lift in the experiment. The antennas are at the far end of the lift from the viewer under the roof that was built to shield the equipment from the elements. (b) The target (a trihedral reflector) is shown on the stand at 300 feet from the lift.

where $*$ stands for convolution, and $\Psi = [\psi_1, \psi_2, \cdots, \psi_n]$ are transform domain functions (different time-shifts of transmit pulse). Since most θ_j's are zeroes under the transform basis Ψ, so the narrowband and UWB radar signals $z(i)$ are very sparse, which validates that CS could be used to reduce the number of samples to collect. We have some preliminary results on CS for UWB radar signals.

IV. Compressive Sensing and Recovery

We chose an iid Gaussian random matrix as sensing matrix Φ. $\Phi\Psi$ is also iid Gaussian for various orthonormal bases Ψ such as spikes, sinusoids, wavelets, Gabor functions, curvelets, and so on [10], so we chose $\psi_j(i) = n^{-1/2}\cos(2\pi ji/n), i = 0, 1, \cdots, n-1$. $\Phi\Psi$ is shown to have satisfied RIP with high probability, if $M \geq cK\log(N/K)$, where c is a small constant and hence stable reconstruction is possible with high probability [10]. Note that it is not known in advance which coefficients of θ are zeroes, or which samples of z are not needed.

We apply a linear programming algorithm [5] to (2). We introduce new variables θ^+, θ^-, constrained to be nonnegative, and let $\theta_i = \theta_i^+ + \theta_i^-$ [5].(Our intention is to have $\theta_i = \theta_i^+$ or $\theta_i = -\theta_i^-$, depending on whether θ_i is positive or negative.) We then replace the occurrence of $|\theta_i|$

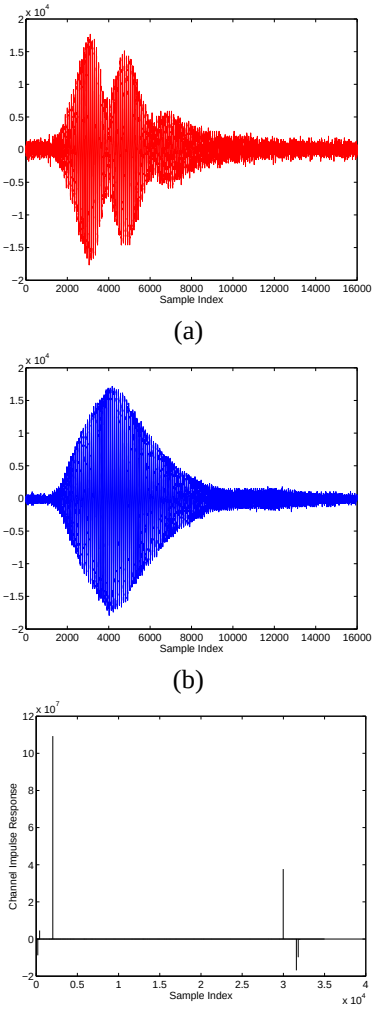


Fig. 2. Narrowband radar (200MHz) transmitted pulse, received echo, and channel impulse response in one experiment. (a) Transmitted pulse. (b) Received echo. (c) Channel impulse responses using CLEAN method.

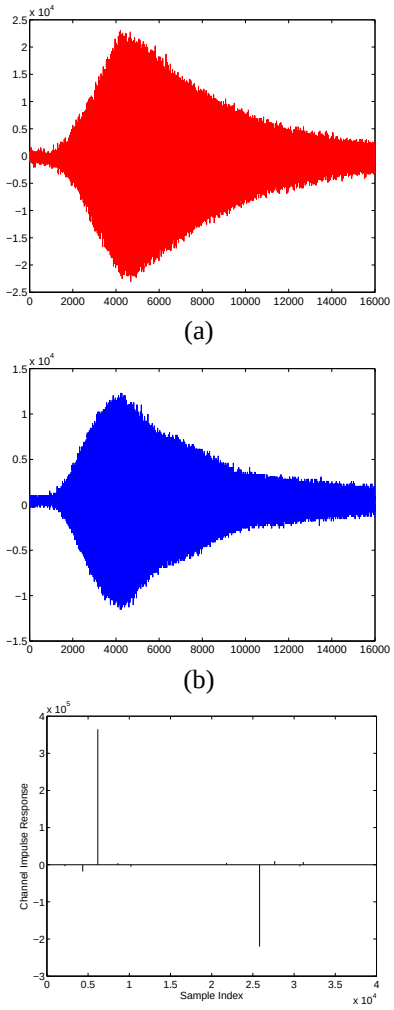


Fig. 3. Narrowband radar (400MHz) transmitted pulse, received echo, and channel impulse response in one experiment.(a) Transmitted pulse. (b) Received echo. (c) Channel impulse responses using CLEAN method.

with $\theta_i^+ + \theta_i^-$ and obtain the alternative formulation

$$\min \sum_{i=1}^{N} (\theta_i^+ + \theta_i^-) \tag{4}$$

$$\text{subject to} \quad \Phi\Psi\theta_i^+ - \Phi\Psi\theta_i^- = y \tag{5}$$

$$\theta^+, \theta^- \geq 0, \tag{6}$$

where $\theta^+ = (\theta_1^+, \theta_2^+, \cdots, \theta_n^+)$ and $\theta^- = (\theta_1^-, \theta_2^-, \cdots, \theta_n^-)$.

The relations $\theta_i = \theta_i^+ + \theta_i^-$, $\theta^+ \geq 0$, $\theta^- \geq 0$, are not enough to guarantee that $|\theta_i| = \theta_i^+ + \theta_i^-$, and the validity of this reformulation may not be entirely obvious. At an optimal solution to the reformulated problem, and for each i, we must have either $\theta_i^+ = 0$ or $\theta_i^- = 0$, because otherwise we could reduce both θ_i^+ and θ_i^- by the same amount and preserve feasibility, while reducing the cost, in contradiction of optimality. Having guaranteed that either $\theta_i^+ = 0$ or $\theta_i^- = 0$, the desired relation $|\theta_i| = \theta_i^+ + \theta_i^-$ now follows.

Let A be the m by $2n$ matrix $[\Phi\Psi, -\Phi\Psi]$. (5) can be written as:

$$Ax = y, \;\; z \geq 0. \tag{7}$$

where $x \triangleq [\theta_i^+, \theta_i^-]^T$ It has a solution x^*, says, a vector in R^{2n} which can be partitioned as $x^* = [u^* v^*]$; then $\theta^* = u^* - v^*$ solves (2). The reconstruction is very straightforward, i.e., $z^* = \Psi\theta^*$

We ran simulations based on the above algorithm and it turned out we could use only 500 samples to recover the original 16,000 samples, so the compression ratio is 32:1. For illustration purpose, in Fig. 5(a), we plot 16,000 samples sense-through-foliage signals in one collection of sense-through-foliage UWB radar sensors. In Fig. 5(b), we plot the original sparse signals θ (received echo z projected to cosine basis functions $\psi_j(i)$) of the and recovered sparse signals (obtained via (2)). Observe that the original signals could be perfectly recovered.

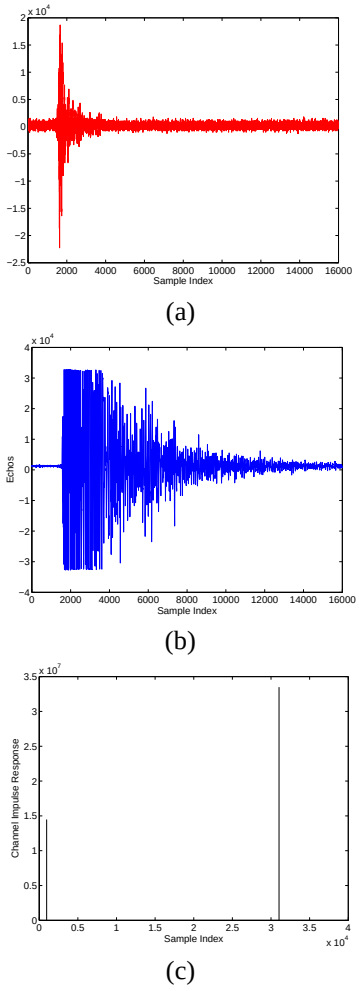


Fig. 4. UWB radar transmitted pulse, received echo, and channel impulse response in one experiment. (a) Transmitted pulse. (b) Received echo. (c) UWB channel impulse responses using CLEAN method.

V. Conclusions

Motivated by recent advances on Compressive Sensing (CS), we studied the sparsity of sense-through-foliage radar sensors. Based on CLEAN method, we obtained the impuse response for sense-through-foliage communication channels for three different radars, 200MHz, 400MHz, and UWB radars. Channel impulse responses for the above three different kinds of channels demonstrated that the sense-through-foliage signals are very sparse, which means CS is possible to be applied to sense-through-foliage radar signals to tremendously reduce the sampling rate. We applied linear programming to sparse signal recovery, and it turned out that we could achieve compression ratio of 32:1 with perfect recovery for the UWB radar signals.

References

[1] R. Baraniuk and P. Steeghs, "Compressive radar imaging," *IEEE Radar Conference*, Waltham, Massachusetts, April 2007.

[2] S. Bhattacharya, T. Blumensath, B. Mulgrew, and M. Davies, "Fast encoding of synthetic aperture radar raw data using compressed sensing," *IEEE Workshop on Statistical Signal Processing*, Madison, Wisconsin, August 2007)

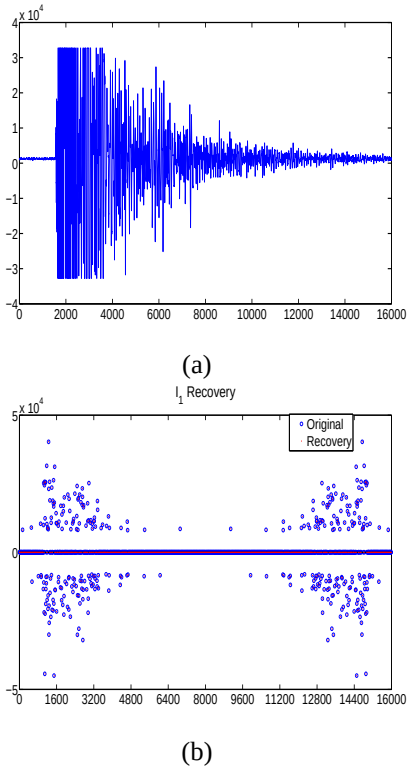


Fig. 5. (a) Original sense-through-foliage received echos (16,000 samples), and (b) ℓ_1-norm recovered sparse signals and the original sparse signals (origianl 16,000 samples projected to the cosine basis functions).

[3] C. R. Berger, S. Zhou, P. Willett, "Signal Extraction Using Compressed Sensing for Passive Radar with OFDM Signals," *Proc. of the 11th Int. Conf. on Information Fusion*, Cologne, Germany, July 2008.

[4] C. R. Berger, S. Zhou, P. Willett, B. Demissie, J. Heckenbach, "Compressed Sensing for OFDM/MIMO Radar," *Proc. of the 42nd Annual Asilomar Conference on Signals, Systems and Computers*, Pacific Grove, CA, Oct. 2008.

[5] D. Bertsimas, J. N.Tsitsiklis " Introduction to Linear Optimization ," *Athena Scientific* , February, 1997.

[6] R. M. Buehrer, et al, "Characterization of the UWB channel," *IEEE Conf on Ultra Wideband Systems and Technologies*, pp. 26-31, Reston, VA, Nov 2003.

[7] E. Candés, "Compressive sampling," *Int. Congress of Mathematics*, vol. 3, pp. 1433-1452, Madrid, Spain, 2006.

[8] R. J.-M. Cramer, *An Evaluation of Ultrawideband Propagation Channels*, Ph.D Dissertation, USC, 2000.

[9] R. J.-M Cramer, R. A. Scholtz, and M. Z. Win, "Evaluation of an ultra-wide-band propagation channel," *IEEE Transactions on Antennas and Propagation*, vol 50, no. 5, May 2002, pp. 561 - 570.

[10] D. Donoho " Compressed Sensing ," *IEEE Trans. on Information Theory*, Vol.52, No.4, pp.1289-1306, April 2006.

[11] M. Herman and T. Strohmer, "High-resolution radar via compressed sensing," to appear in *IEEE Trans. on Signal Processing*

[12] J. A. Hogbom, "Aperture synthesis with a non-regular distribution of interferometer baseline," *Atronomy and Astrophysics Supplement Ser.*, vol. 15, 1974.

[13] L. Potter, P. Schniter, and J. Ziniel, "Sparse reconstruction for RADAR," *SPIE Alg. for Syn. Aperture Radar Imagery XV*, 2008.

[14] R. A. Scholtz, M. Z. Win, and J. M. Cramer, "Evaluation of the Characteristics of the ultra-wideband propagation channel," *Proc of Antenna and Propagation Symposium*, vol. 2, no. 626-630, 1998.

[15] K. R. Varshney, M. etin, J. W. Fisher, and A. S. Willsky, "Sparse representation in structured dictionaries with application to synthetic aperture radar," *IEEE Transactions on Signal Processing*, 56(8), pp. 3548 - 3561, August 2008.

Orthogonal Pulse Compression Codes for MIMO Radar System

Lei Xu
Department of Electrical Engineering
University of Texas at Arlington
Arlington, TX 76010-0016 USA
Email: xu@wcn.uta.edu

Qilian Liang
Department of Electrical Engineering
University of Texas at Arlington
Arlington, TX 76010-0016 USA
Email: liang@uta.edu

***Abstract*— Inspired by recent advances in MIMO radar, we introduce orthogonal pulse compression codes to MIMO radar system in order to gain better target direction finding performance. We propose the concept and the design methodology for the optimized ternary pulse compression codes called the optimized punctured Zero Correlation Zone sequence-Pair Set (ZCZPS). According to codes property analysis, our proposed codes are able to provide the optimized autocorrelation and cross correlation properties during ZCZ. We also present a generalized MIMO radar system model using our proposed codes as pulse compression codes and simulate the target direction finding performance of the fluctuating and nonfluctuating system. The simulation results show that the more antennas used, the better target direction finding performance could be provided.**

I. Introduction

There has been considerable interest in MIMO radars which employ multiple antennas both at the transmitter and at the receiver. The present important research of MIMO radar includes all kinds of techniques. Direction finding [1] is such a technology that a well known waveform is transmitted by an omnidirectional antenna, and a target reflects some of the transmitted energy toward an array of sensors that is used to estimate some unknown parameters, e.g. bearing, range, or speed. Also, beamforming [2] is another important process generally used in direction finding process that an array of receivers can steer a beam toward any direction in space. The advantages of using an array of closely spaced sensors at the receiver are the lack of any mechanical elements in the system, the ability to use advanced signal processing techniques for improving performance, and the ability to steer multiple beams at once.

However, MIMO radars, unlike phased array radars, could transmit different waveforms on the different antennas of the transmitter, which makes it necessary to do the waveform design for the system. In this paper, we design a set of orthogonal ternary codes which are used as pulse compression codes for the MIMO radar system. To the best of our knowledge, it is the first time to introduce pulse compression codes to MIMO radar system. Pulse compression, known as a technique to raise the signal to maximum sidelobe (signal-to-sidelobe) ratio to improve the target detection and range resolution abilities of the radar system, allows a radar to simultaneously achieve the energy of a long pulse and the resolution of a short pulse without the high peak power [3]. Hence, a generalized MIMO radar signal model using our orthogonal ternary codes as pulse compression codes could achieve the high resolution and orthogonality of MIMO radar system simutaneously. In this paper, we focuses on the direction finding performance of the system regarding the orthogonality of the codes and we will consider the resolution performance in the later work. The simulation results show that better direction findsing performance could be obtained by combining MIMO radar and pulse compression codes together.

The rest of the paper is organized as follows. Section 2 introduces the definition and properties of optimized punctured ZCZPS. A method using optimized punctured sequence-pair and Hadamard matrix to construct ZCZPS is also given. Section 3 presents and analyzes a generalized MIMO radar system for our proposed codes. In section 4, some simulation results are provided by using specific examples with different number of uniform linear antennas at the transmitter and receiver of MIMO radar system. In Section 5, conclusions are drawn on our newly provided orthogonal pulse compression codes and MIMO radar system.

II. Orthogonal Pulse Compression Codes

A set of orthogonal pulse compression codes could be used in the MIMO radar system to gain the diversity and improve the direction finding performance. In this section, we will propose and analyze the concept and design methodology for a new ternary codes which could be applied to MIMO radar system.

A. Definition and Design for Optimized Punctured ZCZ Sequence-Pair Set

Matsufuji and Torii have provided some methods of constructing ZCZ sequences in [4] [5]. In this section, a set of novel ternary codes, namely the optimized punctured ZCZ sequence-pair set, is constructed through applying the optimized punctured sequence-pair [6] to the zero correlation zone. In other words, optimized punctured ZCZPS is a specific kind of ZCZPS.

Definition 2-1 [6] Sequence $\mathbf{u} = (u_0, u_1, ..., u_{N-1})$ is the punctured sequence for $\mathbf{v} = (v_0, v_1, ..., v_{N-1})$,

$$u_j = \begin{cases} 0, & \text{if } u_j \text{ is punctured} \\ v_j, & \text{if } u_j \text{ is Non-punctured} \end{cases} \quad (1)$$

Where P is the number of punctured bits in sequence $\mathbf{v}$, suppose $v_j \in (-1, 1)$, $u_j \in (-1, 0, 1)$, $\mathbf{u}$ is P-punctured binary sequence, $(\mathbf{u}, \mathbf{v})$ is called a punctured binary sequence-pair.

Definition 2-2 [6] The autocorrelation of punctured sequence-pair $(\mathbf{u}, \mathbf{v})$ is defined

$$R_{\mathbf{uv}}(\tau) = \sum_{i=0}^{N-1} u_i v_{(i+\tau) mod N}, 0 \le \tau \le N-1 \quad (2)$$

If the punctured sequence-pair has the following autocorrelation property:

$$R_{\mathbf{uv}}(\tau) = \begin{cases} E, & \text{if } \tau \equiv 0 \text{mod} N \\ 0, & \text{otherwise} \end{cases} \quad (3)$$

the punctured sequence-pair is called optimized punctured sequence-pair [6]. Where, $E = \sum_{i=0}^{N-1} u_i v_{(i+\tau) mod N} = N - P$, is the energy of punctured sequence-pair.

Definition 2-3 Assume $(\mathbf{X}, \mathbf{Y})$ to be sequence-pair set of length N and the number of sequence-pairs K, where $i = 1, 2, 3, ..., N-1, p = 0, 1, 2, ..., K-1$, if all the sequences in the set satisfy the following equation:

$$R_{\mathbf{x}^{(p)}\mathbf{y}^{(q)}}(\tau) = \sum_{i=0}^{N-1} x_i^{(p)} y_{(i+\tau)mod(N)}^{(q)*} = \sum_{i=0}^{N-1} y_i^{(p)} x_{(i+\tau)mod(N)}^{(q)*}$$

$$= \begin{cases} \lambda N, & \text{for } \tau = 0, p = q \\ 0, & \text{for } \tau = 0, p \neq q \\ 0, & \text{for } 0 < |\tau| \leq Z_0 \end{cases} \quad (4)$$

where $0 < \lambda \leq 1$, then $(\mathbf{x}^{(p)}, \mathbf{y}^{(p)})$ is called a ZCZ sequence-Pair, $ZCZP(N, K, Z_0)$ is an abbreviation. $(\mathbf{X}, \mathbf{Y})$ is called a ZCZ sequence-Pair Set, and $ZCZPS(N, K, Z_0)$ is an abbreviation.

Definition 2-4 If $(\mathbf{X}, \mathbf{Y})$ in **Definition 2-3** is constructed by optimized punctured sequence-pair and a certain matrix, such as Hadamard matrix or an orthogonal matrix, here

$$x_i^{(p)} \in (-1, 1), \quad i = 0, 1, 2, ..., N-1$$
$$y_i^{(q)} \in (-1, 0, 1), \quad i = 0, 1, 2, ..., N-1.$$

Then $(\mathbf{X}, \mathbf{Y})$ can be called optimized punctured ZCZ sequence-pair set.

Based on odd length optimized punctured binary sequence pairs and a Hadamard matrix, an optimized punctured ZCZPS can be constructed on following steps:

Step 1: Considering an optimized punctured binary sequence-pair $(\mathbf{u}, \mathbf{v})$ of odd length N_1.

Step 2: A Hadamard matrix B (consisting of several Walsh sequences) of order N_2 is considered. The length of the sequence of the matrix is also N_2.

Step 3: Processing bit-multiplication on the optimized punctured binary sequence-pair and each row of Hadamard matrix B, then sequence-pair set (X, Y) is obtained.

Because of space limit, the steps would be described in detail in the later version, as well as the proof.

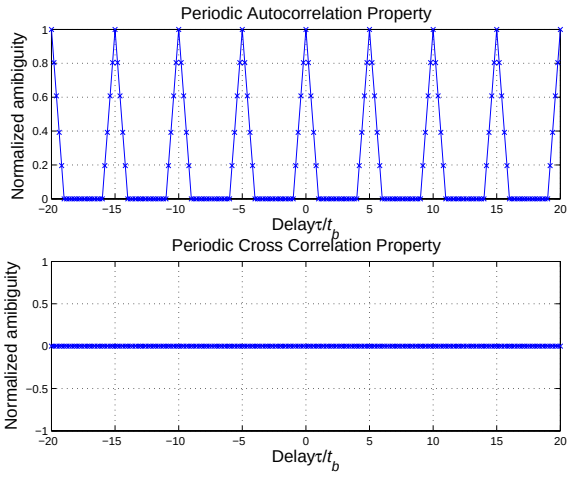
Since the optimized punctured binary sequence-pairs here are of odd lengths and the lengths of Walsh sequence are $2^n, n = 1, 2, ...$, common divisor of N_1 and N_2 is 1, $GCD(N_1, N_2) = 1$. The sequence-pair set $(\mathbf{X}, \mathbf{Y})$ is optimized punctured ZCZPS and $N_1 - 1$ is the zero correlation zone Z_0. The length of each sequence in optimized punctured ZCZPS is $N = N_1 * N_2$. The number of sequence-pairs in optimized punctured ZCZPS rests on the order of the Hadamard matrix. The sequence $\mathbf{x}^{(p)}$ in sequence set $\mathbf{X}$ and the corresponding sequence $\mathbf{y}^{(p)}$ in sequence set $\mathbf{Y}$ construct a sequence-pair $(\mathbf{x}^{(p)}, \mathbf{y}^{(p)})$ that can be used as a pulse compression code.

B. Properties of Optimized Punctured ZCZ Sequence-pair Set

In this section, the optimized punctured ZCZPS $(\mathbf{X}, \mathbf{Y})$ is constructed by 5-bit length optimized punctured binary sequence-pair $(\mathbf{u}, \mathbf{v}), \mathbf{u} = [+ + - + -], \mathbf{v} = [+ + 000]$ (using $'+'$ and $'-'$ symbols for $'1'$ and $'-1'$) and Hadamard matrix H of order 4. We follow the three steps presented in the previous part to construct an optimized punctured ZCZPS. The number of sequence-pairs here is 4, and the length of each sequence is $5 * 4 = 20$. Each row of each matrix $\mathbf{X} = [\mathbf{x}^{(1)}; \mathbf{x}^{(2)}; \mathbf{x}^{(3)}; \mathbf{x}^{(4)}]$ and $\mathbf{Y} = [\mathbf{y}^{(1)}; \mathbf{y}^{(2)}; \mathbf{y}^{(3)}; \mathbf{y}^{(4)}]$ constitute a certain optimized punctured ZCZP $(\mathbf{x}^{(p)}, \mathbf{y}^{(p)})$. The autocorrelation property and cross correlation property of 20-bit length optimized punctured ZCZ sequence pair set $(\mathbf{X}, \mathbf{Y})$ are shown in Fig. 1.

From the Fig. 1, the sidelobe of autocorrelation of the codes can be as low as 0 when the time delay is kept within $Z_0 = N_1 = 5$ (zero correlation zone) and the cross correlation value is kept as low as 0 during the whole time domain.

Fig. 1. Correlation property of optimized punctured ZCZPS



It is known that a suitable criterion for evaluating pulse compression code of length N is the ratio of the peak signal divided by the peak signal sidelobe (PSR). The sidelobe of the new code shown in Fig. 1 can be as low as 0, so the PSR can be as high as infinite which could effectively avoid masking mainlobes of the other targets. In addition, the zero cross correlation properties make those codes well cooperate in the MIMO radar system without introducing the interference. Hence, our proposed codes could be used as a set of orthogonal pulse compression codes in the MIMO radar system.

III. Signal Model Of MIMO Radar

In this section, we describe a signal model for the MIMO radar system using orthogonal pulse compression codes. Assume a radar system that utilizes an array with M antennas at the transmitter, and N antennas at the receiver. For simplicity, we assume that the arrays at the transmitter and receiver are parallel. A transmitting linear array made up of M elements equally spaced a distance d apart. The elements are assumed to be isotropic radiators in that they have uniform response for signals from all directions. The first antenna will be taken as the reference with zero phase. The signal radiated by the transmit antenna impinges at angle θ which is the angle of arrival (AOA) relative to the transmitting array normal. From simple geometry, the difference in path length between adjacent elements for signals transmitting at an angle θ with respect to the normal to the antenna, is $dsin\theta$. This gives a phase difference between adjacent elements of $\phi = 2\pi(d/\lambda)sin\theta$, where λ is wavelength of the received signal. And the phase difference for m-th transmit antenna is $\phi_m = 2\pi((m-1)d/\lambda)sin\theta$ [3]. For convenience, we take the amplitude of the received signal at each element to be unity. A pulse compression code $C^{(m)} = \sum_{p=0}^{N-1} C_p^{(m)}(t - p\tau_c)$ is applied to m-th transmit antenna, and the signal vector induced by the m-th transmit antenna is given by

$$g^{(m)} = e^{-j\phi_m}[C_0^{(m)}, C_1^{(m)}, C_2^{(m)}, ..., C_{P-1}^{(m)}]^T, 1 \leq m \leq M \quad (5)$$

The signal vectors are organized in the $M \times P$ transmit matrix $\mathbf{G} = [g^{(1)}, g^{(2)}, ..., g^{(M)}]^T$. The transmitted waveforms are listed along the diagonal of the matrix $\mathbf{S} = diag(s_1, ..., s_M)$. The transmitted waveforms could be normalized such that $|s_i|^2 = 1/M$. The normalizing method ensures that transmitted power is not dependent of the

number of transmitting antennas. Suppose, all antennas transmit the same waveform, $\mathbf{S} = s\mathbf{I}_M$, where the subscript M denotes the order of the unity matrix.

Similar to the transmitter, the model for the array at the receiver could be developed, resulting in an $N \times P$ channel matrix K. Similarly, the first antenna on the receiving part will be taken as the reference with zero phase. The signal radiated by the receive antenna impinges at angle θ_0 which is the angle of arrival (AOA) relative to the receiving array normal. The phase difference for n-th transmit antenna is $\varphi_n = 2\pi((n-1)d_r/\lambda)sin\theta_0$. For phase-modulated pulse compression waveforms, the corresponding pulse compression codes $C^{'(n)} = \sum_{p=0}^{P-1} C_p^{'(n)}(t - p\tau_c)$ have to be applied to each receive antenna to implement the matched filter. The signal vector arrived at the n-th receive antenna could be given by

$$k^{(n)} = e^{-j\varphi_n}[C_0^{'(n)}, C_1^{'(n)}, C_2^{'(n)}, ..., C_{P-1}^{'(n)}]^T, 1 \le n \le N;$$
$$\mathbf{K} = [k^{(1)}, k^{(2)}, ..., k^{(N)}]^T \quad (6)$$

Since we study the pulse compression technique in the MIMO radar system, the number of matched filters on the receiving side should be the same as the number of transmitting signals. For the further research in this paper, we assume the number of transmitting antennas and that of receiving antennas are the equivalent. Here, $N = M$.

Assume there is a far field complex (multiple scatters) target and it is known that small changes in the aspect angle of complex targets can cause major changes in the radar cross section (RCS). Here, RCS for each receiver antenna is assumed to have isotropic reflectivity modeled by zero-mean, unit-variance per dimension, independent and identically distributed (i.i.d.) Gaussian complex random variables λ_i. The target is then modeled by the diagonal matrix

$$\Sigma = \frac{1}{\sqrt{2M}} \begin{bmatrix} \lambda_0 & 0 & \cdots & 0 \\ 0 & \lambda_1 & \ddots & \vdots \\ \vdots & \ddots & \ddots & 0 \\ 0 & ... & 0 & \lambda_{M-1} \end{bmatrix} \quad (7)$$

where the normalization factor makes the target average RCS$=\frac{\sum_{i=0}^{M-1}|\lambda_i|^2}{2M}$ independent of the number of receiving antennas in the model. The nonfluctuating target modeled using non-zero constants for λ_i is identified as "$Swerling0$" or "$Swerling5$" model. For the fluctuating target, if the target RCS is drawn from the Rayleigh pdf and vary independently from pulse to pulse, the target model represents a classical "$Swerling2$" model.

Processing the transmit matrix, the target matrix and the receive matrix together, the MIMO radar channel model is given by $M \times M$ matrix shown in (8).

According to the (8), it is easy to notice that $\sum_{p=0}^{P-1} C_p^{(m)} C_p^{'(n)}$ specified by the pulse compression codes exists at each position of the matrix. If we select orthogonal pulse compression codes for transmit and receive antennas, it is satisfied that

$$\sum_{p=0}^{P-1} C_p^{(m)} C_p^{'(n)} = \begin{cases} E_s & m = n \\ 0 & m \ne n \end{cases} \quad (9)$$

The **H** matrix turns to be shown as (10).

As a result, the signal vector received by the MIMO radar is given by

$$r = \mathbf{HS} + n \quad (11)$$

Where the additive white Gaussian noise vector n consists of i.i.d, zero-mean complex normal distributed random variables. In this case we assume that all antennas transmit the same waveform, $\mathbf{S} = \mathbf{s}I_M$.

If receiver antenna uses a beamformer to steer towards direction $\theta_0^{'}$, $\varphi_n^{'} = 2\pi((n-1)d_r/\lambda)sin\theta_0^{'}$. The beamformer is modeled by a diagonal matrix

$$\beta(\theta_0') = \begin{bmatrix} e^{j\varphi_1^{'}} & 0 & \cdots & 0 \\ 0 & e^{j\varphi_2^{'}} & \cdots & 0 \\ \vdots & \vdots & \ddots & \vdots \\ 0 & ... & 0 & e^{j\varphi_M^{'}} \end{bmatrix} \quad (12)$$

The output of the beamformer is shown in (13).

Processing the output of **y**, we obtain the diagonal of the output matrix **y** and change it into a $M \times 1$ vector $\mathbf{y}'$. The output of the beamformer at the receiver antenna is

$$y' = [\lambda_0 e^{j(\phi_1 + \varphi_1^{'} - \varphi_1)} E_s s, \lambda_1 e^{j(\phi_2 + \varphi_2^{'} - \varphi_2)} E_s s, \cdots, \lambda_{M-1} e^{j(\phi_N + \varphi_N^{'} - \varphi_N)} E_s s]^T + n^{'} \quad (14)$$

where $E_s >> \sigma^2(n')$.

In MIMO radar for direction finding (DF) purpose, the transmit antennas are sufficiently separated, so the phase shifts at the transmitter are set to zero. It is easy to see that when $\theta = 0$, $\phi_m = 2\pi(d/\lambda)sin\theta = 0$ and $g^{(m)} = [C_m^{(0)}, C_m^{(1)}, C_m^{(2)}, ..., C_m^{(N-1)}]^T$. If the beamformer can well estimate the direction θ_0 at the receiver antenna, stating differently, $\theta_0^{'} \cong \theta_0$ and $\varphi_n = \varphi_n'$. The result at the MIMO receiver antennas is

$$y'' = [\lambda_0 E_s s, \lambda_1 E_s s, \ldots, \lambda_{M-1} E_s s]^T + n^{'} \quad (15)$$

Here, we apply MSE (mean square error) to the output y' of receiver antennas to estimate direction finding error. Similar to RAKE receiver, we can choose the path which could provide the minimum phase difference in $y^{'}$ to find the direction of the target, which could be called Selective Combining. Considering target detection or recognition, we could also sum up all the paths in order to achieve the diversity gain, however, we only focus on the research of direction finding in this paper.

IV. Simulations and Analysis

In this section, we are running MATLAB simulations of the MIMO radar system using different number of antennas to see the direction finding performance. The numbers of transmitting and receiving antennas are both M, the transmit antennas are spaced sufficiently and the antenna array is used in the receiving part. The target fluctuating model in which the channel fluctuated according to a Rayleigh distribution is considered besides the nonfluctuating model. Estimation MSE is used as the common figure of merit for comparing the performance.

We choose the path which provides the best performance before estimate MSE called Selective Combining method. Using nonfluctuating and fluctuating target model, the MIMO radar systems of different antennas are illustrated in Fig. 2.

From the Fig. 2, it is easy to see that under the situation of both nonfluctuating and fluctuating modelss the system with more antennas could always achieve less MSE than the system with less antennas especially when the SNR value is not large. However, considering the nonfluctuating model, when the SNR increases the advantage becomes less distinct. Comparing the Fig.2(a) and 2(b), the performance of our system for fluctuating modeal is degraded because of the Rayleigh fading. According to the results, a general conclusion

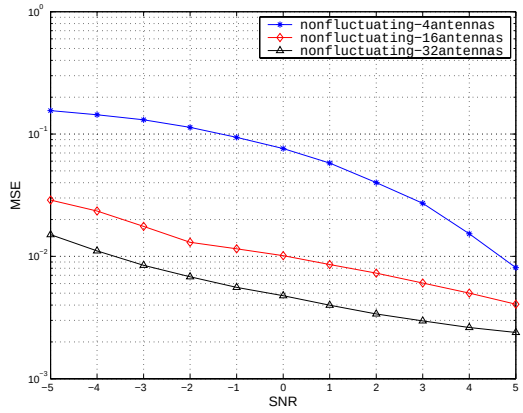
$$\mathbf{H} = \mathbf{K}[\mathbf{G}^{\mathbf{H}}\Sigma] = \begin{bmatrix} k_1 \\ k_2 \\ \vdots \\ k_M \end{bmatrix} [g_1^* g_2^* \dots g_M^*] \begin{bmatrix} \lambda_0 & 0 & \cdots & 0 \\ 0 & \lambda_1 & \ddots & \vdots \\ \vdots & \ddots & \ddots & 0 \\ 0 & \dots & 0 & \lambda_{M-1} \end{bmatrix} \tag{8}$$

$$= \begin{bmatrix} \lambda_0 e^{j(\phi_1-\varphi_1)} \sum_{p=0}^{P-1} C_1^{(p)} C_1^{'(p)} & \lambda_1 e^{j(\phi_2-\varphi_1)} \sum_{p=0}^{P-1} C_2^{(p)} C_1^{'(p)} & \dots & \lambda_{M-1} e^{j(\phi_M-\varphi_1)} \sum_{p=0}^{P-1} C_M^{(p)} C_1^{'(p)} \\ \lambda_0 e^{j(\phi_1-\varphi_2)} \sum_{p=0}^{P-1} C_1^{(p)} C_2^{'(p)} & \lambda_1 e^{j(\phi_2-\varphi_2)} \sum_{p=0}^{P-1} C_2^{(p)} C_2^{'(p)} & \dots & \lambda_{M-1} e^{j(\phi_M-\varphi_2)} \sum_{p=0}^{P-1} C_M^{(p)} C_2^{'(p)} \\ \vdots & \vdots & \ddots & \vdots \\ \lambda_0 e^{j(\phi_1-\varphi_M)} \sum_{p=0}^{P-1} C_1^{(p)} C_M^{'(p)} & \lambda_1 e^{j(\phi_2-\varphi_M)} \sum_{p=0}^{P-1} C_2^{(p)} C_M^{'(p)} & \dots & \lambda_{M-1} e^{j(\phi_M-\varphi_M)} \sum_{p=0}^{P-1} C_M^{(p)} C_M^{'(p)} \end{bmatrix}.$$

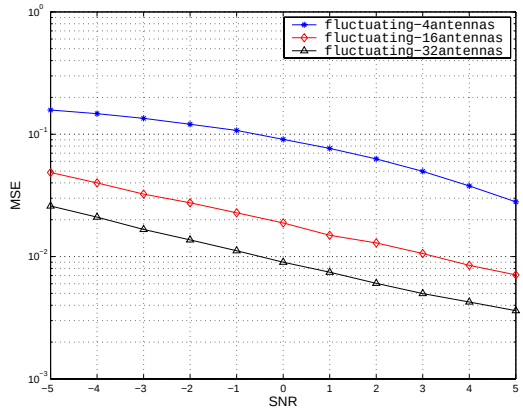
$$\mathbf{H} = \begin{bmatrix} \lambda_0 e 0^{j(\phi_1-\varphi_1)} E_s & 0 & \cdots & 0 \\ 0 & \lambda_1 e^{j(\phi_2-\varphi_2)} E_s & \cdots & 0 \\ \vdots & \vdots & \ddots & \vdots \\ 0 & \dots & 0 & \lambda_{M-1} e^{j(\phi_M-\varphi_M)} E_s \end{bmatrix} \tag{10}$$

$$\mathbf{y} = r\beta(\theta_0^{'}) = \mathbf{HS}\beta(\theta_0^{'}) + n^{'} = \begin{bmatrix} \lambda_0 e^{j(\phi_1-\varphi_1+\varphi_1^{'})} E_s s & 0 & \dots & 0 \\ 0 & \lambda_1 e^{j(\phi_2-\varphi_2+\varphi_2^{'})} E_s s & \dots & 0 \\ \vdots & \vdots & \ddots & \vdots \\ 0 & 0 & \dots & \lambda_{M-1} e^{j(\phi_M-\varphi_M+\varphi_M^{'})} E_s s \end{bmatrix} + n^{'} \tag{13}$$

Fig. 2. MSE of beamforming at the receiver



(a) nonfluctuating model



(b) fluctuating model

could be drawn that the more antennas MIMO radar system utilized the better direction finding performance could achieved in the both models.

V. Conclusions

In this paper, we introduced the orthogonal pulse compression codes to the MIMO radar system which has the same number of transmit and receive antennas to improve the radar direction finding performance. We provided a set of new optimized triphase pulse compression codes, gave a specific example and analyzed the codes' properties. We presented and analyzed a generalized MIMO radar system model for our provided framework. Simulation results showed that significant SNR gain could be obtained in MIMO radar system using orthogonal pulse compression codes. The MIMO radar system using more antennas outperformes the one having less antennas.

References

[1] S. Pasupathy and A. N. Venetsanopoulos, "Optimum active array processing structure and space-time factorability," *IEEE Trans. Aerosp. Electron. syst.*, vol.10, pp. 770-778, 1974.

[2] S. Haykin, J. Litva and T. J. Shepherd, *Radar Array Processing*, Springer-Verlag, New York, 1st edition, 1993.

[3] S. Ariyavisitakul, N. Sollenberger, and L. Greenstein, *Introduction to Radar System*, Tata McGraw-Hill, 2001.

[4] S. Matsufuji, N Suehiro , N Kuroyanagi and P Z Fan, "Two types of polyphase sequence set for approximately synchronized CDMA systems," *IEICE Trans. Fundamentals*, E862A(1): pp. 229-234, Jan. 2003.

[5] H. Torii, M. Nakamura and N. Suehiro, "A new class of zero correlation zone sequences," *IEEE Tran. Inform.Theory*, Vol.50: pp. 559-565, Mar. 2004.

[6] T. Jiang, *Research on Quasi-Optimized Binary Signal Pair and Perfect Punctured Binary Signal Pair Theory*, Ph.D Dissertation: Yanshan University, 2003.